

Fan Li  
Sajid Bashir  
Jingbo Louise Liu *Editors*

# Nanostructured Materials for Next-Generation Energy Storage and Conversion

Fuel Cells

[MATERIALS.SPRINGER.COM](https://www.materials.springer.com)

 Springer

---

# Nanostructured Materials for Next-Generation Energy Storage and Conversion

---

Fan Li • Sajid Bashir • Jingbo Louise Liu  
Editors

# Nanostructured Materials for Next-Generation Energy Storage and Conversion

Fuel Cells

With 255 Figures and 41 Tables

 Springer

*Editors*

Fan Li  
Beijing Key Laboratory for Catalysis and  
Separation, Department of Chemistry  
and Chemical Engineering  
College of Environmental and Energy  
Engineering  
Beijing University of Technology  
Beijing, China

Sajid Bashir  
Department of Chemistry  
Texas A&M University-Kingsville  
Kingsville, TX, USA

Jingbo Louise Liu  
Department of Chemistry  
Texas A&M University-Kingsville  
Kingsville, TX, USA

ISBN 978-3-662-56363-2      ISBN 978-3-662-56364-9 (eBook)  
<https://doi.org/10.1007/978-3-662-56364-9>

Library of Congress Control Number: 2018930880

© Springer-Verlag GmbH Germany, part of Springer Nature 2018, corrected publication 2018

This work is subject to copyright. All rights are reserved by the Publisher, whether the whole or part of the material is concerned, specifically the rights of translation, reprinting, reuse of illustrations, recitation, broadcasting, reproduction on microfilms or in any other physical way, and transmission or information storage and retrieval, electronic adaptation, computer software, or by similar or dissimilar methodology now known or hereafter developed.

The use of general descriptive names, registered names, trademarks, service marks, etc. in this publication does not imply, even in the absence of a specific statement, that such names are exempt from the relevant protective laws and regulations and therefore free for general use.

The publisher, the authors and the editors are safe to assume that the advice and information in this book are believed to be true and accurate at the date of publication. Neither the publisher nor the authors or the editors give a warranty, express or implied, with respect to the material contained herein or for any errors or omissions that may have been made. The publisher remains neutral with regard to jurisdictional claims in published maps and institutional affiliations.

Printed on acid-free paper

This Springer imprint is published by the registered company Springer-Verlag GmbH, DE part of Springer Nature.

The registered company address is: Heidelberger Platz 3, 14197 Berlin, Germany



---

## Preface

The increase in the human population has jumped from 2.8 billion in 1955 (US President Eisenhower) to 7.5 billion in 2017 (US President Trump). This significant increase has meant that more CO<sub>2</sub> is generated through combustion of carbon-based fuels, which currently are the dominant fuel-mix used in transportation, heating and cooling, and electric power generation. One consequence of the continued rise of CO<sub>2</sub> emission is the ability of CO<sub>2</sub> to trap sunlight as a greenhouse gas (GHG) with subsequent worldwide redistribution of trapped heat, contributing to changes in global weather patterns. One possible approach is reducing GHG emissions and managing global warming by displacement of fossil fuels by fuel cells (FC) and FC based vehicles (FCVs), which do not generate CO<sub>2</sub> as a by-product but water via a redox reaction  $[2\text{H}_2(\text{g}) + \text{O}_2(\text{g}) \rightarrow 2\text{H}_2\text{O}(\text{l})]$ . In addition, hydrogen when used as a fuel feedstock is a near-zero CO<sub>2</sub> emission source at point of use, and is available in the oxidized form in water (H<sub>2</sub>O) or as the hydride of carbon in natural gas (methane, CH<sub>4</sub>) that can be generated by electrolysis of water or reformation of natural gas.

The total number of electric vehicles including FCVs reached an excess of 1.25 million in 2015, of which 550,000 were new registrations. It is anticipated that by 2025, there will be 5 million FCVs with a projected FC system cost of \$30–\$40/kW. The gradual tightening of fuel economy and emission standards is also likely to stimulate FC development, deployment, and wide societal acceptance if the total cost of ownership can be reduced to the cost of conventional technologies.

This book focuses on the design, characteristics, and development potential of FC technologies in light of changing energy requirement and related challenges. The technological factors that influence the dynamics, flexibility, and operating costs of FC operation are highlighted. Moreover, the potential for using FC technologies in the mobility sector, stationary industrial sector, and the heat thermodynamics is discussed, as these factors determine the extent to which the future ‘value’ of stationary and portable FC technology applies to other industries. This ‘valuation’ for FC development will guide the development and direction of newer, less developed technologies, such as cost of development, ease of integration into the infrastructure, power density output, operational lifetime, and cost of operation relative to current ICEs.

The advantages of FC technologies coupled with renewable hydrogen are synergistic and offer considerable advantages over the internal combustion engine–gasoline combination. The proton exchange membrane fuel cell efficiency can be estimated as  $\eta = 1 - T\Delta S/\Delta H$  and using the Gibbs free energy ( $\Delta G = -237.13$  kJ/mol) and heating value of hydrogen ( $\Delta H = 285.85$  kJ/mol) is around 83% efficient. The introduction of FCVs will deliver immediate benefits in air quality in large urban centers, as the usage and importance of FCs for both portable and stationary applications is expected to increase at the expense of fossil fuels.

The editors are fortunate to have renowned experts in the field contribute to this book. As a result, this book not only serves as an introduction to individuals who are new to the field, but also to individuals who are seasoned experts. All the chapters give a solid overview of the subject under discussion followed by an extension into the area of expertise of the specific author. Due to the self-contained nature of each chapter, the reader does not need to reference several chapters to get the concept, which is an advantage. The reader may see a trend in which each author presents introductory themes with their point of view.

The book is composed of three themes. The first theme is related to energy policy and electric power. In ► [Chap. 1](#), the energy policy as initially proposed and actually executed is discussed between two presidencies spanning 40 years in terms of federal support in various areas deemed critical to this nation's energy security. In the second chapter, "Electric Power and Hydrogen Redox" (HREG, ► [Chap. 2](#)), a hydrogen redox electric power and hydrogen generation systems (HREG) are discussed, which enable electrostatic-to-chemical energy conversion in the water electrolysis for both stationary and portable applications. The third chapter (► [Chap. 3](#)) deals with evaluation of cell performance and durability for cathode catalysts during simulated fuel cell vehicle (FCV) operation. Specifically, cell performance and durability testing for cathode catalysts on two types of supports, carbon black and conducting ceramic nanoparticles, were discussed, including startup/shutdown cycles and load cycles.

This leads to the second theme in the book relating to optimization of FCs through design and synthesis of novel catalysts. This section begins with the design and application of metal carbonyl cluster as electrocatalyst (► [Chap. 4](#)) based on thermolysis or pyrolysis of osmium, ruthenium, iridium, and rhodium *n*-decacarbonyl derivatives. These materials are discussed with respect to benchmarking the oxygen reduction reaction (ORR) and hydrogen oxidation reaction (HOR) electrocatalyst reactions. The theme is continued in ► [Chap. 5](#), where the use of noncarbon supports in low-temperature FCs is discussed in terms of performance. ► [Chapter 6](#) focuses on the design, synthesis, and evaluation of noble metal electrocatalysts applied in polymer electrolyte fuel cells. This type of development is critical because there is insufficient worldwide Pt to meet the anticipated demand for the next 25 years in FCVs. The strategies to reduce electrocatalyst costs are a fabrication of either nonplatinum electrocatalysts with similar performance to Pt or alloying to reduce Pt loading. The electrocatalyst activity is usually increased through nanostructuring of the catalyst support that is the focus of the next chapter. In ► [Chap. 7](#), low power

density and fuel utilization of catalysts in PEMFCs and/or DMFCs are discussed and expanded upon. These shortcomings are related respectively to poor reaction kinetics and methanol crossover and are overcome through the use of graphene or carbon nanotubes as newer support surfaces. The theme is concluded with a discussion of nanostructured catalysts for solid oxide fuel cells (SOFC, ► Chap. 8). The factors related to design and application of new nano-sized electrode catalyst to decrease the activation polarization resistance and to improve the SOFC performance are discussed.

The third and final theme of the book is related to optimization of fuel cells through modeling and simulation. The section starts with a modeling analysis of water management in a PEMFC (► Chap. 9). The effect of relative humidity and stoichiometry of reactants on the water saturation, back-diffusion of water from the cathode to the anode, is considered and strategies to reduce possible flooding and increase FC performance and operational reliability are discussed. The chapter is followed by development of a computational thermodynamic model to better understand the cathode electrolyte in SOFCs (► Chap. 10). The development of density functional theory (DFT) of varying sophistications to model and evaluate with experimental data to the activity and stability of the ORR of the PEMFC electrocatalysts (► Chap. 11). The modeling is expanded to an entire FCV in ► Chap. 12. Here, the optimization strategies of hydrogen FCs as range extenders in electric vehicles are discussed. In the following chapter (► 13), a comprehensive treatment of a totalized hydrogen energy utilization system (THEUS) for stationary applications is introduced. The parameters for THEUS related to load leveling and cogeneration in commercial buildings from renewable energy sources such as solar photovoltaics (PVs) and wind power are explored. These two chapters tie-in a critical and often overlooked feature of the environment in which the FC operate, which is outside the finely controlled environment of the research laboratory. The influence of impurities in the air on nanostructured electrocatalysts in a PEMFC is comprehensively explored (► Chap. 14), and the physical or chemical hybrid materials used for hydrogen storage are discussed. In ► Chap. 15, hydrogen storage based on manganese oxide anchored to a polymeric matrix, as examples of solid state materials for hydrogen storage, is compared and contrasted with conventional approaches.

These types of strategies are critical to the widespread application and usage of FCVs, where the hydrogen fuel is supplied to the FCs that supply electrical energy via a power inverter to the electric motor as described in the previous chapters. The FCV could also be configured where the FC stack is channeled to the DC/DC converter and the inverter and electric motor, with an onboard auxiliary power unit. In ► Chap. 14, pollutants in their air and their effect on the cathode catalyst were investigated. In the following chapter (► 16), the effects of fabrication design on the bipolar plate and membrane electrode assembly are discussed in terms of how stresses can lead to component failure in real world settings. In many laboratory-based bench test experiments, the “purity” of the oxidant (air) and effect of actual stress and strain on the catalyst layer, or membrane electrode assembly, are often neglected. The authors of these two chapters (► 14 and ► 16) give practical

hands-on perspective coupled with research data to orientate the postdoctoral researcher or graduate student who may fabricate such components to include best practices in their FC designed tests. The design, fabrication, modeling, and evaluation of a new tubular electrode for SOFC are discussed next (► Chap. 17). The section concludes with a discussion of the safety aspects related to use and disposal of these electrocatalysts (► Chap. 18), which is not usually discussed in monographs on FC designs, development, and applications, but is an area that will gain prominence as FCs become more available and are disposed after usage. Today, we are aware of the toxicological and safety “costs” related to the disposal of aluminum or lead components and the realization of potential toxicity with aluminum or lead ion migration in soil or water after disposal. The chapter (► 18) outlines that nanometals, unlike their bulk counterparts, are not inert but reactive with a variety of cells.

These chapters (► 1 – ► 18) will offer the catalyst development, fuel cell design, and operation to research students, postgraduate researchers, young investigators, experienced principal investigators, and industrialists. The treatise aims to provide the current state-of-the-art information from theoretical framing of the problem to actual hands-on activities that authors have gained through their decades of experience. The expertise and knowledge are passed down to current practitioners in the field to make an informative monograph, which can serve both a reference source book and a how-to-guide.

The general aim has been to learn how to assess the technical impact of new electrocatalysts and how to improve fuel cell technology in terms of operational reliability, cost, ease of use, and safety. Lastly, the stellar contribution of the authors, their research group, and institutions are duly acknowledged. We also would like to extend our deep appreciation to our institution, colleagues, and students as well as the editorial staff at Springer publishing who has strived to deliver the best possible scholarly product. As always, errors and omission are the responsibility of the editors, for which we as preface authors ask forgiveness.

August 04, 2017

Sajid Bashir  
Nancy KingSanders  
Jingbo Louise Liu

---

# Contents

<b>1 Fuel Cell Technology: Policy, Features, and Applications – A Mini-review</b> .....	1
Sajid Bashir, Nancy KingSanders, and Jingbo Louise Liu	
<b>2 Concept of Hydrogen Redox Electric Power and Hydrogen Energy Generators</b> .....	27
Katsutoshi Ono	
<b>3 Evaluation of Cell Performance and Durability for Cathode Catalysts (Platinum Supported on Carbon Blacks or Conducting Ceramic Nanoparticles) During Simulated Fuel Cell Vehicle Operation: Start-Up/Shutdown Cycles and Load Cycles</b> .....	53
Makoto Uchida, Katsuyoshi Kakinuma, and Akihiro Iiyama	
<b>4 Metal Carbonyl Cluster Complexes as Electrocatalysts for PEM Fuel Cells</b> .....	115
Jorge Uribe-Godínez	
<b>5 Non-carbon Support Materials Used in Low-Temperature Fuel Cells</b> .....	145
Xuecheng Cao, Fan Li, and Ruizhi Yang	
<b>6 Noble Metal Electrocatalysts for Anode and Cathode in Polymer Electrolyte Fuel Cells</b> .....	171
Surbhi Sharma and Carolina Musse Branco	
<b>7 Nanomaterials in Proton Exchange Membrane Fuel Cells</b> .....	199
Yufeng Zhang, Rui Xue, Weijian Yuan, and Xiaowei Liu	
<b>8 Nanostructured Electrodes for High-Performing Solid Oxide Fuel Cells</b> .....	227
Hanping Ding	
<b>9 Modeling Analysis for Species, Pressure, and Temperature Regulation in Proton Exchange Membrane Fuel Cells</b> .....	249
Zhaohui Wang	

<b>10</b>	<b>The Application of Computational Thermodynamics to the Cathode-Electrolyte in Solid Oxide Fuel Cells</b> .....	281
	Shadi Darvish, Mohammad Asadikiya, Mei Yang, and Yu Zhong	
<b>11</b>	<b>Application of DFT Methods to Investigate Activity and Stability of Oxygen Reduction Reaction Electrocatalysts</b> .....	337
	Xin Chen, Qingan Qiao, and Fan Li	
<b>12</b>	<b>Hydrogen Fuel Cell as Range Extender in Electric Vehicle Powertrains: Fuel Optimization Strategies</b> .....	359
	Roberto Álvarez and Sergio Corbera	
<b>13</b>	<b>Totalized Hydrogen Energy Utilization System</b> .....	385
	Hiroshi Ito and Akihiro Nakano	
<b>14</b>	<b>Influence of Air Impurities on the Performance of Nanostructured PEMFC Catalysts</b> .....	407
	Olga A. Baturina, Boris Dyatkin, and Tatyana V. Reshetenko	
<b>15</b>	<b>Solid-State Materials for Hydrogen Storage</b> .....	443
	Rolando Pedicini, Irene Gatto, and Enza Passalacqua	
<b>16</b>	<b>Stress Distribution in PEM Fuel Cells: Traditional Materials and New Trends</b> .....	469
	Javier de la Cruz, Tatiana Romero, and Ulises Cano	
<b>17</b>	<b>Recent Progress on the Utilization of Nanomaterials in Microtubular Solid Oxide Fuel Cell</b> .....	497
	Mohd Hilmi Mohamed, Siti Munira Jamil, Mohd Hafiz Dzarfan Othman, Mukhlis A Rahman, Juhana Jaafar, and Ahmad Fauzi Ismail	
<b>18</b>	<b>Nanostructured Materials for Advanced Energy Conversion and Storage Devices: Safety Implications at End-of-Life Disposal</b> .....	517
	Sajid Bashir, Pranitha Hanumandla, Hsuan-Yi Huang, and Jingbo Louise Liu	
	<b>Correction to: Evaluation of Cell Performance and Durability for Cathode Catalysts (Platinum Supported on Carbon Blacks or Conducting Ceramic Nanoparticles) During Simulated Fuel Cell Vehicle Operation: Start-Up/Shutdown Cycles and Load Cycles</b> .....	E1
	<b>Index</b> .....	543

---

## Abbreviations

A/E	Anode/Electrolyte layer interface
AA	Acetylacetone
AC	Alternating current or Activated carbon
AE	Alkaline earth
AEC	Atomic Energy Commission
AES	Auger electron spectroscopy
AFC	Alkaline fuel cell
AFCMS	Adaptive fuel consumption minimization strategy
Ag	Argentum (silver)
ALD	Atomic layer deposition
APS	Ammonium persulfate
ARSM	Atmospheric resistive switching mechanism
AS	Air start
ATO	Antimony-doped tin oxide
Au	Auric (gold)
B	Boron
BAAEDI	Bisacetylacetoneethylenedi imine
BAWE	Bipolar alkaline water electrolyzer
BDC	Benzene-dicarboxylate
BEV	Battery electric vehicles
BN	Boron nitride
BOPs	Balance of plants
BSAEDI	Bissalicylaldehyde-ethylenediimine
BSCF	Barium strontium cobalt ferrite
BW	Bounded Warburg element
C	Carbon
C/A	Cubic/Amorphous
Ca	Calcium
CALPHAD	CALculation of PHase Diagram
CB	Carbon black
CCM(s)	Catalyst coated membrane(s)
Cd	Cadmium

---

Ce	Cerium
CE	Counter electrode
CEM	Compound energy model
CFE	Carbon fiber electrode
CHP	Cogeneration of heat and power
Cl( $\bar{\text{r}}$ )	Chlorine(/chloride)
CL(s)	Catalyst layer(s)
Cm	Curium
CNLS	Complex nonlinear least squares
CNT(s)	Carbon nanotube(s)
CO	Carbon monoxide
Co	Cobalt
CO <sub>2</sub>	Carbon dioxide
COR(s)	Carbon oxidation reaction(s)
CP	Carbon paper or Coordination polymers
CPE	Constant phase element
CPO	Coordination polymer of Oslo
Cr	Chromium
Cs	Cesium
CTE	Coefficient of thermal expansion
Cu	Cuprum (Copper)
CV	Cyclic voltammetry
CVD	Chemical vapor deposition
DARPA	Defense Advanced Research Projects Agency
DC	Direct current
DEFC	Direct ethanol fuel cell
DFAFC	Direct formic acid fuel cell
DFT	Discrete Fourier transform or Density functional theory
DHE	Dynamic hydrogen electrode
DHW	Domestic hot water
DMFC	Direct methanol fuel cell
DOE	Department of Energy
DTU	Technical University of Denmark
EC(s)	Electrochemical cell(s)
ECA	Electrochemical area
ECSA	Electrochemical surface area
EDL	Electrical double layer
EDS	Energy dispersive spectroscopy
Ee	Total cell voltage
EELS	Electron energy loss spectroscopy
EG	Ethylene glycol
EIS	Electrochemical impedance spectroscopy
EL	Water electrolyzer
EMF	Electromotive force



---

EQCM	Electrochemical quartz crystal microbalance
EREV	Extended range electric vehicle
ESA	Electrochemical surface area
ESI-PSE	Electrostatic-induction potential-superposed electrolysis
EUDC	European Union Driving Cycle
EXAFS	Extended X-ray absorption fine structure
FC(s)	Fuel cell(s)
FCC	Face centered cubic
FCCJ	Fuel Cell Commercialization Conference of Japan
FCHJU	Fuel Cells and Hydrogen Joint Undertaking
FCV(s)	Fuel cell powered vehicle(s)
FCX	Fuel cell experimental (vehicle)
Fe	Ferrum (Iron or Ferrous or Ferric)
FFT	Fast Fourier transform
FIB	Focus(ed) ion beam
FRA	Frequency response analyzer
FSZ	Fully stabilized zirconia
FT	Fourier transform
FUN(s)	Functional unit(s)
FWHM	Full-width-at-half-maximum
GA(s)	Graphene aerogel or Genetic algorithm(s)
GCB	Graphitized carbon black
Gd	Gadolinium
GDC	Gadolinium doped ceria
GDE(s)	Gas diffusion electrode(s)
GDL(s)	Gas diffusion layer(s)
GDQ	Generalized differential quadrature
GGA	Generalized gradient approximation
GHG(s)	Greenhouse gas(es)
GIXD	Glancing incidence X-ray diffraction
GNT(s)	Graphene nanotube(s)
GO	Graphene oxide
GOA	Graphene oxide aerogel
H <sub>2</sub>	Hydrogen
HA	<i>Hygrophila auriculata</i> plant extract
HAADF	High-angle angular dark-field
HAXPES	Hard X-ray photoelectron spectroscopy
HCP	Hexagonal close pack
HF	High frequency
HFAA	Hexafluoro acetylacetone
HFR	High-frequency resistance
Hg	Hydrargyrum (Mercury)
HKUST	Hong Kong University of Science and Technology
HLG	HOMO-LUMO gap

---

HOMO	Highest occupied molecular orbital
HOR(s)	Hydrogen oxidation reaction(s)
HREG(s)	Hydrogen generation system(s)
HRTEM	High resolution transmission electron microscope
HT	Heat treated/treatment
IAE	Ionized air reference electrode
ICE(s)	Internal combustion engine(s)
I-E(s)	Current-potential curve(s)
IFP(s)	Imidazolate framework(s) Potsdam
In	Indium
INT(s)	Interface(s)
IR	Internal reforming or Infrared spectroscopy
IRMOF(s)	Isorecticular metal organic framework(s)
ITO(s)	Indium oxide(s)
JUC	Jilin University China
K	Kalium (Potassium)
KCL	Kirchhoff's current law
K-K	Kramers-Kronig
KMC(s)	Kinetic Monte Carlo simulation(s)
KVL	Kirchhoff's voltage law
La	Lanthanum
LANL	Los Alamos National Laboratory
LCA	Life cycle assessment
LDA	Local density approximation
Li	Lithium
LSC	Lanthanum strontium cobaltite
LSCF	Lanthanum strontium cobalt ferrite
LSCM	Lanthanum strontium chromium manganite
LSGM	Lanthanum strontium gallium magnesium oxide
LSM	Lanthanum strontium manganite
LST	Lanthanum strontium gallium or Linear systems theory
LUMO	Lowest unoccupied molecular orbital
LZO	Lanthanum zirconium oxide
M/T	Monoclinic/Tetragonal
MCFC(s)	Molten carbonate fuel cell(s)
MEA	Membrane electrode assembly
MEMS	Micro electro mechanical system
MFC	Mass flow controller
MFFCS	Multifunctional fuel cell system
MFU	Metal-Organic Framework Ulm University
Mg	Magnesium
MHT	Metal hydride tank
MIEC	Mixed ionic and electronic conductor
MIL	Materials of Institut Lavoisier

---

Mn	Manganese
MNP(s)	Magnetic nanoparticle(s)
Mo	Molybdenum
MO(s)	Metal oxide(s)
MOF(s)	Metal-organic framework(s)
MOR(s)	Methanol oxidation reaction(s)
Mpc(s)	Metallic phthalocyanine(s)
MPGe	Miles per gallon equivalent
MWNT(s)	Multi-walled carbon nanotube(s)
N <sub>2</sub>	Nitrogen
NASA	National Aeronautics and Space Administration
Nb	Niobium
NCL	Nitrogen-doped carbon layer
NCP(s)	Nanoscale coordination polymer(s)
NEDC	New European Driving Cycle
NHE	Normal hydrogen electrode
NI	Necking index
Ni	Nickel
NL(s)	Normal liter(s)
NLLS	Nonlinear least squares
NM(s)	Nanomaterial(s)
NO	Nitric oxide
NOTT	University of Nottingham
NP(s)	Nanoparticle(s)
NSF	National Science Foundation
NU	Northwestern University
O	Atomic oxygen
O <sub>2</sub>	Molecular oxygen
OCV	Open circuit voltage
ODA	Oxygen depleted air
OER(s)	Oxygen evolution reaction(s)
OP	Optimization problem
ORR(s)	Oxygen reduction reaction(s)
Os	Osmium
Ox	Oxidant
P	Phosphorus
PAFC(s)	Phosphoric acid fuel cell(s)
PAH(s)	Polycyclic aromatic hydrocarbon(s)
PANI	Polyaniline
PBCO	Praseodymium barium cobaltite oxide
PBFM	Praseodymium barium ferrite magnesium oxide
PBFM(s)	Praseodymium barium ferrite magnesium oxide(s)
PBI	Polybenzimidazole
PBMO(s)	Praseodymium barium magnesium oxide(s)

---

PC(s)	Phthalocyanine(s)
PCI	Pressure-concentration isotherm
PCN(s)	Porous coordination network(s)
Pd	Palladium
PD	Polydopamine
PDFV	Polyvinylidene fluoride
PDU	Power distributor unit
PEC	Predictive environmental concentration
PEEK	Poly-ether-ether-ketone
PEFC(s)	Polymer electrolyte fuel cell(s)
PEM	Proton exchange membrane
PEMFC(s)	Polymer electrolyte membrane fuel cell(s)
PEO	Polyethylene oxide
PFSA	Perfluorosulfonic acid
PGM(s)	Platinum group metal(s)
PHEV(s)	Plug-in hybrid electric vehicle(s)
PIM	Intrinsic microporosity
PLD	Pulsed laser deposition
POP(s)	Porous organic polymer(s)
PPy	Polypyrrole
PPY-PSS	Polypyrrole polystyrene sulfonate
PSCFN(s)	Praseodymium strontium cobalt iron niobium oxide(s)
PSZ	Partially stabilized zirconia
Pt	Platinum
PTFE	Polytetrafluoroethylene
PV(s)	Photovoltaic(s)
PVDF	Polyvinylidene fluoride
Q-HQ	Quinone-hydroquinone
RA(s)	Risk assessment(s)
RC	Resistor-capacitor
RCL	Resistor-capacitor-inductor
Rd	Reductant
RDE(s)	Rotating disk electrode(s)
RDS	Rate-determining step
RE	Reference electrode
RES	Renewable energy sources
RF	Radio frequency
rGO(s)	Reduced graphene oxide(s)
Rh	Rhodium
RH(/s)	Relative humidity (/humidities)
RHE	Reversible hydrogen electrode
RL	Resistor-inductor
ROS	Reactive oxygen species
RPE	Retinal pigment epithelium
RPM(s)	Robust porphyrinic material(s)

---

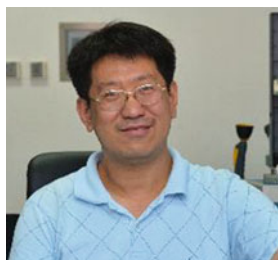
RRDE	Rotating ring-disk electrode
RS	Red seed extract of <i>Hydrophilia auriculata</i>
RT	Room temperature
Ru	Ruthenium
S	Sulfur
SBA	Santa Barbara amorphous type mesoporous silica
SBU(s)	Second building unit(s)
Sc	Scandium
SCE	Saturated calomel electrode
SEM	Scanning electron microscope
SFM	Strontium ferrite molybdate
SGTE	Scientific Group Thermodata Europe
SHE	Standard hydrogen reference electrode
Si	Silicon
Sm	Samarium
SMMO(s)	Strontium magnesium molybdenum oxide(s)
SMSI	Strong metal-support interaction
Sn	Tin
SNU	Seoul National University
SoC	State of charge
SOFC(s)	Solid oxide fuel cell(s)
Sr	Strontium
SSC	Samaria strontium cobaltite
SSE	Single voltage source electrolysis
SSFF	Stainless steel fiber felt
STEM	Scanning transmission electron microscopy
SU/SD	Start-up/Shutdown
SWCNT(s)	Single-walled carbon nanotube(s)
SZO	Strontium zirconate
T/C	Tetragonal/Cubic
Ta	Tantalum
TAA	Dibenzotetraaza anulenes
TaC	Tantalum carbide
TDS	Thermal desorption spectroscopy
TEM	Transmission electron microscope
TGA	Thermogravimetric analysis
THEUS	Totalized hydrogen energy utilization system
Ti	Titanium
TiB	Titanium boride(s)
TiC(s)	Titanium carbide(s)
TiN(s)	Titanium nitride(s)
TiO	Titanium oxide or Titania
TMC(s)	Transition metal carbide(s)
TMPP(s)	Tetrametoxiphenyl porphyrin(s)
TOE(s)	Tonne of oil equivalent(s)

---

TPB	Triple phase boundary
TPP	Tetraphenyl porphine
TPR	Temperature-programmed reduction
TXRF	Total reflection X-ray fluorescence
UiO	University of Oslo
UMCM	University of Michigan Crystalline Material
URFC(s)	Unitized reversible fuel cell(s)
USP	Ultrasonic spray pyrolysis
UTSA	University of Texas at San Antonio
UV	Ultraviolet
V	Vanadium
W	Tungsten
WC(s)	Tungsten carbide(s)
WE	Working electrode
WGSR(s)	Water gas shift reaction(s)
WWII	Second World War
XAS	X-ray absorption spectroscopy
XPS	X-ray photoelectron spectroscopy
XRD	X-ray diffraction
Y	Yttrium
YST	Yttrium-stabilized titania
YSZ	Yttria-stabilized zirconia
ZIF(s)	Zeolite imidazolate framework(s)
Zn	Zinc
Zr	Zirconium
ZTC	Zeolite template carbon

---

## About the Authors



**Fan Li** received his Ph.D. in Materials Science and Engineering from Royal Institute of Technology (KTH), Sweden, 2007, and Physical Chemistry in Metallurgy from the University of Science and Technology Beijing in 2008. He is an Associate Professor at Beijing University of Technology. He has directed and participated in (>10) projects supported by National Natural Science Foundation of China (NSFC), Beijing Natural Science Foundation, Ministry of Education, and Ministry of Science and Technology of P.R. China. Dr. Li is focused on electrochemical properties of the transition metal oxides with mixed valence states and applied them in polymer electrolyte membrane fuel cell. The preparation and characterization of nano-structured electro-catalyst with low content noble metals is his main study field. Dr. Li has authored and coauthored textbook, book, and book chapters and peer-reviewed journal articles (>50). During the past 9 years, he taught over 500 students and trained more than 100 undergraduate and postgraduate students.



**Sajid Bashir** received his Ph.D. in Analytical Chemistry from the University of Warwick, England, 2001. He was a Postgraduate Research Associate at Cornell University to conduct research in field of plant genetics. He is a Full Professor at Texas A&M University-Kingsville (TAMUK) and a Faculty Fellow at the US Air Force. He has directed and participated in (>20) projects supported by the Welch Foundation, TAMUK, Texas Workforce Commission, and US National Institute of Health. He has coauthored more than 80 book chapters and peer-reviewed journal articles. He is a Fellow and Chartered Chemist of the Royal Society of Chemistry, and a

Chartered Scientist. During his service in TAMUK, he trained more than 3,000 students on both undergraduate and graduate levels. He created online courses and established safety training protocols in conjunction with the risk management. Currently, he collaborated with the local law enforcement as a consultant.



**Jingbo Louise Liu** received her Ph.D. in Materials Science and Engineering from the University of Science and Technology Beijing in 2001. She is a Full Professor at Texas A&M University – Kingsville (TAMUK) and focused on materials preparation, characterization, and applications. She is the DEBI Faculty Fellow at the US Air Force Research Laboratory. She has authored and coauthored, books, book chapters, and peer-reviewed journal articles (>90). During her 11-year services in TAMUK, she taught >7,000 students and trained to conduct leading edge research. She directed and/or participated in the projects (>40) supported by the NSF (USA and China), NSERC (Canada), ACS Petroleum Research Funds, and Department of Education as PI, Co-PI, and senior personnel.



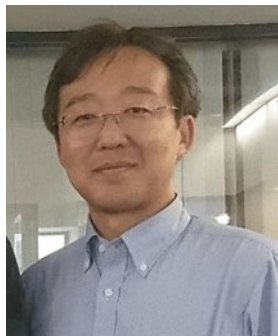
**Katsutoshi Ono** received B. Eng. Degree from Kyoto University, Japan, in 1961 and degree of Dr. Sci. from Faculté des sciences, Université de Paris in 1967. He was researcher at Ecole des Mines de Paris, 1965–1967, Professor of Materials Science, Kyoto University, 1982–1997, Energy Science and Technology, 1997–2001. He is currently a Professor Emeritus. He taught Chemical Thermodynamic Thermodynamics for under graduate course, and Thermal Chemistry and Chemistry and Statistical Mechanics for graduate course. As the laboratory experiments, he conducted the measurements of free energy and the equilibrium phase diagrams of the binary and ternary metal-oxide systems at high temperatures, 1983–1990. He focused his works on the industrial field of metallurgy, 1990–2001: Application of vacuum metallurgy to the steelmaking and the electron-



beam melting of high-melting-point metals and alloys. From 2001 to 2010, he was engaged in the development of a new process for titanium production (OS process). He published “Design, Test and Theoretical Assessments for Reduction of Titanium Oxide to Produce Titanium in Molten Salt” in 2016. He is now working on the hydrogen energy. It is basically a study of how to achieve self-sustainable electrical power generation. Recently, he proposed the theoretical concept of hydrogen redox electric power and hydrogen energy generators.



**Makoto Uchida** received his Ph.D. in Engineering Science from the University of Yamanashi (UoY) in 1999. He was attached in Panasonic Corporation from 1987 to 2008. He established a basic design of the fuel cell stack and membrane electrode assembly (MEA) for Panasonic Fuel Cell co-generation system (ENE-FARM), and promoted the product planning and the business project. He was related to the decision of the Japan Industrial Standard of the polymer electrolyte fuel cell (PEFC) power system as the chief member of The Japan Electrical Manufacturers' Association. In 2008, he moved from Panasonic to UoY and was inducted to a Professor and a manager of Metals Research Division, Fuel Cell Nanomaterials Center, which was established at that time, and promoted the “Research on Nanotechnology for High Performance Fuel Cells (HiPer-FC)” project which was founded from the New Energy and Industrial Technology Development Organization (NEDO) of Japan. Currently, he is also promoting the next “Superlative, Stable, and Scalable Performance Fuel Cell” (S-Per-FC) project founded by NEDO from 2015 and other collaboration researches with many companies. He is establishing MEA to advance performance and durability of PEFCs and directs researches of new fabrication methods for MEAs. He has authored and coauthored textbook, book, and book chapters and peer reviewed journal articles (>70). During his 9-year services in UoY, he trained >100 graduate students to conduct leading edge research. He received the Technical Development Award of the Electrochemical Society of Japan in 2006.



**Katsuyoshi Kakinuma** received his Ph.D. in Engineering Science from the Tokyo University of Science in 1998. He joined Kanagawa University as a Research Associate and invented the new oxide-ion conductor for solid oxide fuel cells (SOFC). In 2008, he moved from Kanagawa University to University of Yamanashi as an Associate Professor at Fuel cell nanomaterials center and was then promoted as a Professor of the center in 2011. He also promoted “HiPer-FC” from 2008 to 2014 and “S-Per-FC” project from 2015 founded from NEDO. He is establishing invention of high durable and high active catalysts supported on conducting ceramics nanoparticles for PEFC. He has authored and coauthored textbook, book, book chapters, and peer-reviewed journal articles (>90). He was in charge of the editorial board of *Electrochemistry* (The Electrochemical Society of Japan, 2010–2012). His awards include the Young Researcher Award of the Electrochemical Society of Japan (Sano Award) in 2005.



**Akihiro Iiyama** received his Ph.D in Mechanical Engineering from the University of Tokyo (UoT) in 1991. He joined Nissan Motor Co., Ltd. in 1982 and worked for the R&D of the diesel engines and gasoline engines. In April 2008, he was appointed the General Manager, Fuel Cell Laboratory, Nissan Research Center, Nissan Motor Co., LTD.; in April 2010, he was appointed the General Manager, EV System Laboratory, Nissan Research Center, Nissan Motor Co., LTD.; and in April 2011: Expert Leader, EV System Laboratory, Nissan Research Center, Nissan Motor Co., LTD. During these periods, he led the R&D activity on the MEA degradation mechanism analysis, their mitigation technology, fuel stack and its system development, and prototype FCV development in Nissan Motor Co., LTD. In February 2015, he moved to the University of Yamanashi as a Project Professor and became the Director of Fuel Cell Nanomaterials Center, University of Yamanashi in April 2015, to manage the “SPer-FC” project funded by the NEDO, Japan, a position he still occupies. He has authored and coauthored textbook, book, and book chapters and peer-reviewed journal

articles (>30). He received the 2013 FY Thermal Engineering Award, Distinguished Engineers, from the Japan Society of Mechanical Engineers.



**Jorge Uribe Godínez** received his Ph.D. in Materials Science from the Research and Advanced Studies Center of the National Polytechnique Institute (CINVESTAV, Campus Queretaro), Mexico, 2011. He was also a postdoctoral research fellow at Institute of Chemistry of the National Autonomous University of Mexico (UNAM) to conduct research in the field of electrocatalysis and PEM fuel cells (2014). Currently, he works at National Center of Metrology of Mexico (CENAM) as researcher. He is directing the re-establishment of the Primary National System for Measurement of Electrolytic Conductivity in Mexico. In addition, he keeps collaboration with colleagues from UNAM and CINVESTAV, to develop new electrocatalysts and to evaluate them in hydrogen PEM fuel cells. Dr. Uribe has authored some journal articles, and he is co-inventor of a patent about mono- and poly-metallic electrocatalysts and its application in hydrogen fuel cells. He also peer reviewed some journal articles and presented more than 40 research works at different scientific congress. Since 2012, he has trained seven undergraduate students and six graduate students and he has participated as Professor of courses to both undergraduate and graduate levels. Dr. Uribe has received more than ten awards for his research work.



**Xuecheng Cao** received his B.E. degree in New Energy Materials and Devices at Soochow University in 2014. He is currently a Ph.D. student in Prof. Ruizhi Yang's research group. His research interests focus on the design and understanding of nanostructured carbon-free cathode materials for lithium-oxygen batteries (LOBs), transition metal oxide based electrocatalysts for oxygen reduction reaction (ORR) and oxygen evolution reaction (OER). He aims to develop materials with tunable structure and improve the energy conversion efficiency of LOBs.



**Ruizhi Yang** received her Ph.D. in Condensed Matter Physics from the Institute of Physics, Chinese Academy of Sciences in 2005. She was a Postdoctoral Fellow at Dalhousie University (2005–2008) and Research Associate at Stanford University (2008–2011). She is a Professor at Soochow University. Her research interests mainly focus on the development of advanced electrode materials for fuel cells, lithium-air batteries, and other metal-air batteries at an atomic scale; the fundamental understanding of electrocatalysis in fuel cells and metal-air batteries; and also understanding of the structural dynamics of nanoparticles, thin films, and single crystals in electrocatalytic processes. Prof. Yang has directed and participated in more than 10 projects supported by National Natural Science Foundation of China (NSFC), the National Key Research and Development Program of China, Natural Science Foundation of Jiangsu Province, etc. She has authored and coauthored book chapters and peer-reviewed journal articles (>60) and held patents (>20). She received the Electrochemistry Award for Young Talent, China, in 2013. During her service in Soochow University, she taught over 300 students and trained more than 50 graduate students to conduct leading edge research.



**Dr. Surbhi Sharma** completed her B.Sc. (Hons) in Physics, University of Delhi, followed by MSc. in Nanoscience from Amity University, India. She received her Ph.D. degree from Ulster University, UK, 2011, where her work was conferred with the Best Thesis Award. She joined the University of Birmingham as a Teaching Fellow in fuel cells in 2011. She taught and trained students at the undergraduate and postgraduate level for carrying out systematic and innovative research and also attained professional teaching qualifications and is a Fellow of Higher Education Academy since 2013. She has also co-supervised doctoral students' studies to completion. As the Work Package Leader for the multi-partner project STAMPPEM (2012–2015), funded by the European Union's Fuel Cells and Hydrogen Joint Undertaking (FCH-JU), 7th Framework Program, she delivered hybrid polymer-metal NP conductive, corrosion protection coatings for stainless

steel. She has research interests in the field of energy materials and novel energy applications with a focus on exploring graphene oxide and its oxygen functional group interactions with metal nanoparticles and reduced graphene based materials along with metal nanoparticles for CO-tolerant electrocatalyst-support systems, composite and multilayer proton conducting membranes, electrochemical sensors/biosensors, and corrosion protection coatings. She has reviewed research articles and book proposals and is on the editorial board for a number of journals. She has authored and published 29 peer-reviewed articles and book chapters along with a patent on nitrogenated graphene. She has been awarded research funds from Defence Science and Technology Laboratories (DSTL), Royal Academy of Engineering (RAE), and Materials Research Society (MRS).



**Carolina Musse Branco** graduated in Material Engineering at Universidade Federal do Rio Grande do Sul (Brazil) in 2011. There she continued her masters on electrolyte polymer/cellulose membranes for PEMFC with hydrogen at the Laboratory of Polymeric Materials. In 2013, she joined the Centre for Hydrogen and Fuel Cell Research at the University of Birmingham, UK, as a Ph.D. student, which was finalized in July of 2017. During the Ph.D., she investigated multilayer membranes for intermediate temperature PEFC.



**Yufeng Zhang** received his Ph.D. in Microelectronics and Solid State Electronics from Harbin Institute of Technology China, 2004. He was also a postgraduate research associate at Harbin Institute of Technology to conduct research in the field of power MEMS. As a Professor at Harbin Institute of Technology, he has directed and participated in (>10) projects supported by the Chinese National Natural Science Foundation, 863 Program, 973 Program, Doctoral Fund in Universities, etc. He has coauthored book chapters and peer-reviewed journal articles and delivered more than a dozen presentations at various scientific conferences.

Currently, Dr. Zhang is an IEEE Fellow and member of Editorial Board of *Scientific World Journal and Advances in Materials Science and Engineering*, being as reviewer of many international journals as well. During his service in Harbin Institute of Technology, he taught more than 500 undergraduate students and trained more than 100 graduate students to conduct leading edge research. The team he leads is the best in micro power field.



**Hanping Ding** received his Ph.D. in Mechanical Engineering from the University of South Carolina in 2014. He has over 11 years' experience in developing solid-state electrochemical devices for energy conversion and storage. His specific research interests are focused on advanced functional materials and microstructures for intermediate-temperature solid oxide fuel cells, direct hydrocarbon fuel cells, proton ceramics, and fuel cell stack system. Currently, Dr. Ding is the Postdoctoral Fellow at the Colorado Fuel Cell Center in Colorado School of Mines. Dr. Ding has authored and coauthored two book chapters and over 40 peer-reviewed journal articles. He served as reviewer for dozens of energy-related international journals. He received several awards by the University of Science and Technology of China and CoorsTek Company (USA).

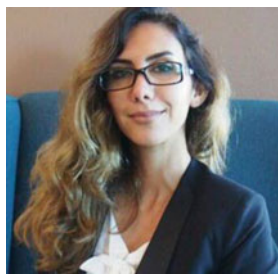


**Zhaohui Wang** received his Ph.D. in Electrical and Computer Engineering from the University of Arizona in 2011. He also received Master of Science in Bioengineering from the University of Toledo in 2005 and Master of Science in Mechanical Engineering from the University of Arizona in 2008. From 2011, he continued postdoctoral training in the University of Pittsburgh Medical Center. In 2014, he was promoted to visiting Assistant Professor of Electrical Engineering and Computer Science at Texas A&M University-Kingsville. During the 3-year service in TAMUK, he taught 1930 graduate students and trained five master's students to conduct leading edge research. He reviewed more than 40 journal articles and served as NDSEG panelist. He is researching into micro/nano-electronic devices and bio-medical imaging. By now, Dr. Wang authored 29 peer-reviewed journal articles and proceeding papers, and contributed to three patents on innovative medical devices.





**Dr. Yu Zhong** is currently an Associate Professor in Worcester Polytechnic Institute (WPI). He received his Ph.D. from Penn State (2005). After a short-term working as Research Associate, he joined Saint-Gobain High Performance Research Center in Northborough, MA. He had spent his 8-year career there working as internal technical consultant focusing on the application of thermodynamics and kinetics to various materials R&D projects. In 2013, he moved to Florida International University (FIU) as Assistant Professor. He received the TMS FMD Young Leaders Professional Development Award in 2016 and ONR summer faculty fellowship in 2015, 2016, and 2017. Dr. Zhong has more than 33 peer-reviewed journal papers published/accepted, two book chapters, and two patents. His research is currently supported by Department of Energy (DOE) and American Chemical Society (ACS).



**Shadi Darvish** is a final year Ph.D. candidate in Materials Science and Engineering and will be graduating in December 2017 from Florida International University. She has started her Ph.D. in Integrated Materials and Processes Design (IMPD) group on spring 2014. During her Ph.D., she has carried out research on several topics, including thermodynamic investigation of defect chemistry inside the perovskites, thermodynamic predictions of electronic and thermomechanical properties of perovskites, and the impact of atmosphere impurities on solid oxide fuel cells' (SOFC) cathode. She is also collaborated in several industrial projects while she worked as an intern at QuesTek Innovation LLC. Her efforts during her Ph.D. study resulted in publishing several articles for ceramic-based membranes and SOFCs.



**Mohammad Asadikiya** is a Ph.D. candidate in the Department of Mechanical and Materials Engineering of Florida International University (FIU). He received his M. Sc. from Sharif University of Technology (2009) in corrosion and protection of materials. He spent several years in various industrial sections, mainly to control corrosion and protect different types of materials. He was the manager of R&D section of Maham imensaz Co. until 2013, working to develop new corrosion inhibitors and scale removers.

Mr. Asadikiya has published several peer-reviewed journal and conference papers and presented in various scientific conferences. He has also published one book chapter and holds one patent. He is currently working on the reassessment of thermodynamic database of yttria-stabilized zirconia as the electrolyte in solid oxide fuel cells (SOFCs). He is also investigating the sintering behavior of boron carbide by applying the CALPHAD approach.



**Dr. Mei Yang** is currently working in Worcester Polytechnic Institute (WPI) as Assistant Research Professor and Associate Technical Director of Center for Heat Treating Excellence (CHTE) following her position as a Senior R&D Engineer in H.C. Starck, where she was in charge of the alloy development for various niobium, tantalum, and molybdenum alloys. Her expertise is integrated materials and processes development for both metals and ceramics by combining modeling and experimental investigation. Her current research is focused on advanced heat treatment techniques.



**Xin Chen** received his Ph.D. in Environmental Science from the Beijing University of Technology, China, 2014. Then he worked in the College of Chemistry and Chemical Engineering of Southwest Petroleum University and is currently an Associate Professor. From 2014–2016 he did his postdoctoral research at Peking University with Professor Dingguo Xia. His current research interests include the structure and properties for energy conversion and storage materials, ammonia decomposition catalyst, electrochemical reactions, and the applications of computational chemistry.





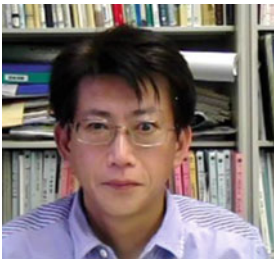
**Qing-An Qiao** received her Ph.D. in Physical Chemistry from Shandong University, China, 2004. She is an Associate Professor and works in School of Chemistry and Materials Science, Ludong University. Her current research interests include the properties and mechanisms for biological systems, the molecular modeling for function materials, and other fields for computational chemistry application.



**Roberto Álvarez** is an Electrical Engineer with a Ph.D. in Manufacturing Process Engineering. He currently heads the Mechanical Engineering Department at Nebrija University (Madrid, Spain). He has over 14 years of experience as a Lecturer in electric machines, manufacturing processes, environmental science, and electric vehicles and serves as a consultant on these topics for various companies in Spain. He is the author of numerous articles and delivered more than 20 contributions to scientific conferences related to energy and greenhouse gas emissions. High-profile journal contributions include *Energy Policy*, *Energy*, *Land Use Policy*, *Journal of Automobile Engineering*, and *Journal of Cleaner Production*. He has also reviewed articles for journals. He has coauthored books: *Carbon Footprint and Urban Planning* (Springer), *Carbon Footprint and the Industrial Life Cycle* (Springer) and textbooks: *Mathematics for Engineers* (Ed. Paraninfo). He has acted as a supervisor of Ph.D. thesis, and currently he is supervising two Ph.D. students. He has directed and participated in (>10) research projects.



**Sergio Corbera** received B.Tech. degree in Mechanical Engineering from the Technical University of Madrid, Spain, 2012, and M.S. degree in Advanced Machines and Transports from the Carlos III University, Madrid, 2013. He worked for 4 years (2012 to 2014) as nonlinear structural engineer in the aerospace industry. Since 2015, he is writing his Ph.D. thesis on methodologies for intelligent design at Nebrija University (Madrid, Spain). His research activities are focused on algorithms and methodologies for intelligent product development, with special application to the field of automobiles and motorcycles. In addition, his research interests include vehicle dynamics, fuel consumption, chassis design, and structural optimization. He has been author and coauthor of different research papers in specialized journals as *ISA Transactions* and *Structural and Multidisciplinary Optimization*.



**Hiroshi Ito** is a Senior Researcher of Thermofluid System Group in Research Institute for Energy Conservation, National Institute of Advanced Industrial Science and Technology (AIST). He received a MEng in Nuclear Engineering from the Tokyo Institute of Technology (1993) and a Ph.D. in Fundamental Energy Science from the Kyoto University (2004). Dr. Ito joined the AIST in 1993 and was a guest researcher in the Institute of Energy Technology (IFE) in Norway from 2007 to 2008. He has also participated in activities of Hydrogen Technology Collaboration Programme (HTCP) of International Energy Agency (IEA) since 2004 and served as Operating Agent of Task 29 (Distributed Community Hydrogen – DISCO-H<sub>2</sub>) from 2013 to 2016. His areas of interest include polymer based electrochemical energy conversion device and system analysis of hydrogen based energy system.



**Akihiro Nakano** received his Ph.D. in Engineering from the University of Tsukuba, Japan, in 1993. He was a Postdoctoral Fellow in JSPS from 1993 to 1996, and he was also a visiting researcher in the low temperature physics group at NASA Jet Propulsion Laboratory (JPL) from 1994 to 1996. Dr. Nakano is a Leader of Thermofluid System Group in Research Institute for Energy Conservation, Department of Energy and Environment at the National Institute of Advanced Industrial Science and Technology (AIST). Thermal

engineering, fluid mechanics, cryogenics, and hydrogen energy are his fields, and he has engaged in research and development of hydrogen systems and their elemental technologies from 2009. Dr. Nakano was a visiting researcher at Savannah River National Laboratory (SRNL) and a Visiting Professor at the University of South Carolina in 2011 for the research of the totalized hydrogen energy utilization system (THEUS) under the joint research program of METI in Japan and DOE in USA. He has coauthored the book chapter of THEUS.



**Boris Dyatkin** received his Ph.D. in Materials Science and Engineering from Drexel University (USA) in 2015. He completed his graduate studies in the Nanomaterials Research Group of Professor Yury Gogotsi. His Ph.D. research focused on carbon nanomaterials for energy storage. He completed visiting research fellowships at the US Army Research Laboratory (2014), Dalian University of Technology (2014), and Oak Ridge National Laboratory (2015). He is the recipient of the Department of Energy's SCGSR Fellowship (2014) and Drexel University's Outstanding Promise Award (2016). He is a fellow of the Clean Energy Leadership Institute. He has published over 20 peer-reviewed publications and delivered over 25 presentations at conferences in the USA and around the world. Currently, he is a National Research Council (NRC) postdoctoral researcher at the US Naval Research Laboratory (NRL) in Washington, DC. His present research focuses on refractory ceramics and high-performance composites.



**Olga A. Baturina** received her Ph.D. in Electrochemistry from Moscow State University (Russia) in 1986. From 1986 until 2001, she worked as Research Scientist at Moscow State University and the Russian Academy of Sciences. Her research addressed structure of the electrical double layer at the electrode/solution interface and development of more efficient primary lithium/SOCl<sub>2</sub> batteries. Since 2001, her research area shifted into proton exchange membrane fuel cells (PEMFCs). In particular, she worked on the development of

nanostructured oxide-supported Pt catalysts for the oxygen reduction reaction and researched the effect of impurities on the performance of the PEMFC cathode catalysts. Currently, she holds the position of a Research Scientist at the US Naval Research Laboratory in Washington, DC. She has published over 80 scientific publications in peer-reviewed journals and coauthored three book chapters.



**Tatyana V. Reshetenko** received her Ph.D. in Catalysis from Novosibirsk State University and Boreskov Institute of Catalysis (Russia) in 2003. Her Ph.D. thesis was devoted to investigation of iron-based catalysts for the methane decomposition for production of multiwall carbon nanotubes and pure hydrogen. Subsequently, Dr. Reshetenko worked at Samsung SDI (South Korea) on optimizing the structure and composition of membrane electrode assembly (MEA) for direct methanol fuel cells for portable applications. She has been with Hawaii Natural Energy Institute since December 2007 and currently, she holds the position of Assistant Researcher. Her research interests involve studies of spatial proton exchange membrane fuel cells (PEMFCs) performance under different operating conditions, local variations of MEA materials properties, and fuel/air contaminants exposure in a segmented cell system. She has authored over 50 peer-reviewed publications and delivered over 30 presentations at conferences. Dr. Reshetenko leads as PI in a project supported by US Army Research Office devoted to fundamental understanding of mass transport phenomena at PEMFCs.



**Rolando Pedicini** is a researcher with permanent position at CNR – Institute for Advanced Energy and Technologies “Nicola Giordano” of Messina, Italy. He obtained a Master Degree in Chemistry, on March 2000, at the University of Messina (Italy). Its scientific activity includes: nonperfluorosulfonic polymers functionalization like PEEK, PSF, etc.; development of different kinds of polymeric membranes; chemical-physical characterization; and materials development for solid state H<sub>2</sub> storage applications (metallic oxides anchored to a polymeric

matrix; coverage of metallic alanate; and study and characterization of natural material for H<sub>2</sub>). Actually, Dr. Pedicini is the person in charge of the research unit “Hydrogen storage: materials and applications” pertaining to the “Fuel Cells for Polymer Electrolyte (PEFC) and Hydrogen Storage.” Since 2011, he is a member of the “COST ACTION MP1103 – WG1 Session.” From 2013 until now he is a member of the Editorial Board of the following scientific journals: *The Scientific World Journal: Energy*, *Energy Research Journal*, *MAYFEB Journal of Energy*, *SCIREA Journal of Energy*. Since 2015, he is a member of “New European Research Grouping on Fuel Cells and Hydrogen” (N-ERGHY). Since 2015, he is Technical Coordinator of two MoU with the Instituto Tecnológico de Chetumal (Mexico) and Universidad de Quintana Roo (Mexico). Currently, Dr. Pedicini is involved in several research projects (14) on national and European funds serving as a part of the ITAE research. In 2014, he worked as an evaluator for national projects banned from the Ministry of Education, University and Research. Dr. Pedicini performs regularly as a “Reviewer” for different scientific international journals. He is author/coauthor of 26 papers on international scientific journals, 62 congress communications, and 29 scientific reports for EU and national projects and for industrial contractors.



**Dr. Irene Gatto** is a permanent researcher at CNR – Institute for Advanced Energy Technologies “Nicola Giordano” of Messina, Italy. She obtained a B.Sc. degree in Chemistry (1998) from University of Messina (Italy) and a Ph.D. in Engineering and Materials Chemistry (2005) from University of Messina. From 2013 she is the Head of the “Polymer Electrolyte Fuel Cells (PEFC) and Hydrogen storage” group at the CNR – ITAE institute. Her current research is focused on polymer electrolyte fuel cells and hydrogen storage. The activity concerns development and characterization of components for fuel cells polymer electrolyte; electrochemical characterization measurements in test stations with different size from 5 to 200 cm<sup>2</sup> both as a single cell and stack; design and realization of demonstration systems and test stations for the characterization of single cells and stacks with a power ranging from 10 W to 5 kW; and design and realization of demonstration systems for

hydrogen storage. She is involved in various research programs related to the previously mentioned topics. She was the scientist responsible of CNR-ITAE unit in the 7th Framework Programme Collaborative Project No. 303452, “Improved Lifetime of Automotive Application Fuel Cells with Ultra-Low Pt-Loading (IMPACT).” She published about 148 articles (more than 783 citations and H-index: 15 from SCOPUS Database) – 47 in international journals, one book chapter (Springer), and she had about 101 contributions in national and international conferences. She is a reviewer for several international scientific journals. She was member of the scientific committee of conferences.



**Dr. Enza Passalacqua** is graduated in Industrial Chemistry and specialized in Chemistry and Catalysis Technology at University of Messina. She is a researcher at Institute for advanced energy technologies “Nicola Giordano” (ITAE) of CNR since 1988 and a Research Manager since 2010. From 1993 to 2012 she has coordinated the research activity “Polymer electrolyte fuel cells (PEFC) and hydrogen storage” at CNR-ITAE, and currently is research manager and collaborates with the same research group. She has been technical leader of several national and European projects addressed to the development and characterization of components (gas diffusion electrodes, membranes, membrane/electrodes assembly) and to the realization of small size PEFC stack and systems. She is author of 97 papers for international journals and more than 200 for international congresses. In 2008, she was teacher in the II level Master in “Systems for Production and Transport of Hydrogen and Fuel Cell” of the University of Messina-Department of Industrial Chemistry and Materials Engineering. From 2009–2011 she was a component of the Female Researchers in Europe Window (FRIEND) of CNR to help and push female researchers to participate in the project. From 2011–2013 she has carried out technical and scientific activity in the Joint Programme of European Energy Research Alliance (EERA) as expert for CNR. From 2016 she is in the Panel Transport as CNR expert to evaluate MiSE Projects.





**Javier de la Cruz** received his Ph.D. in Electrical Engineering from the CINVESTAV, Mexico, 2014. He has been a Lecturer since 2010 in three Mexican universities, including UNAM. He is a CONACYT Researcher at the INEEL since 2014. He has participated in more than five projects supported by CONACYT. Now he is leading a national project on small wind turbine technology with international collaborations. He has published journal conference and journal papers in fuel cell technology.



**Dr. T. Romero** received her Ph.D. in Transport Phenomena in Proton Exchange Membrane Fuel Cells from the University of British Columbia in 2008. She has expertise in electrocatalysts, membranes and membrane electrode assembly fabrication, and integration of nanomaterials for improving fuel cells performance. At the Institute for Fuel Cell Innovations (IFCI), Dr. Romero worked developing new methodologies and designing novel testing apparatus for fuel cell transport phenomena studies. From 2000 onwards, she has worked at the Instituto Nacional de Electricidad y Energías Limpias (INEEL) where she works on fuel cell systems development, coordinating multidisciplinary national and international teams. Dr. Romero graduated *summa cum laude* with a MASc. in Electrocatalysts for Fuel Cells from the Universidad Nacional Autónoma de México (UNAM). In 2001, she took an appointment in the National Research Energy Laboratory (NREL), in Colorado, where she developed a MEA fabrication methodology. Dr. Romero has authored more than 20 peer-reviewed papers and has two patents granted.



**Dr. U. Cano-Castillo** carried out his D.Phil. in Materials Science at the University of Oxford working on environmentally assisted corrosion cracking of composite materials. Since then, he has been working on electrochemistry applied to energy systems including membrane fuel cells, automotive batteries, and electrolysis. He is founder of the Hydrogen and Fuel Cells group at the Electricity Research Institute in Mexico where he has led several applied projects, including fuel cell systems for transportation applications. He has several patents granted on that technology. Dr. Cano-Castillo is

Mexico's representative to the Technology Collaboration Programme on Advanced Fuel Cells of the International Energy Agency. His interests range from innovative materials for electrochemical applications, electrochemical energy storage to practical energy systems.



**Hilmi Mohamed** is currently enrolled as a Ph.D. student in Gas Engineering in Universiti Teknologi Malaysia since 2014. His major research area is triple layer hollow fiber applied for the solid oxide fuel cells (SOFCs). His research goals are to develop fibers with unique structure to enhance the stability and mechanics of the SOFCs. He has authored and coauthored peer-reviewed journal papers with high impact factors. He had also presented his research discoveries in national and international conferences.



**Dr. Siti Munira Jamil** received her Ph.D. in Gas Engineering from Universiti Teknologi Malaysia, Malaysia, 2017. She was promoted to a Postdoctoral Researcher at Universiti Teknologi Malaysia due to her outstanding achievement in her Ph.D. study. She has authored and coauthored peer-reviewed journal articles and book chapters and delivered a few presentations at various international and national conferences. Currently, she is an active researcher in bringing the new technology of microtubular solid oxide fuel cell (MT-SOFC) in Malaysia.



**Siti Halimah Ahmad** received her Master in Gas Engineering from Universiti Teknologi Malaysia in 2016. Her research interests emphasize the nanoparticles for solid oxide fuel cells (SOFCs). Her future research will focus on the development series of nanoparticles with different tunable structures and advancement of the robustness of the SOFCs. She has authored and coauthored peer-reviewed journal publications with high impact factors.





**Dr. Mohd Hafiz Dzarfan Othman** is an Associate Professor in Department of Energy Engineering, Faculty of Chemical and Energy Engineering, Deputy Director of Advanced Membrane Technology Research Centre (AMTEC), and also Head of Renewable Energy Research Group. He received his Bachelor's and Master's degrees from Universiti Teknologi Malaysia, Malaysia, and Ph.D. from Imperial College London, United Kingdom. Up to May 2017, he has supervised 23 Ph.D. students and 18 master's students, with research interests in ceramic/polymeric membranes for energy generation, gas separation, and water reclamation. He has published more than 80 articles in Scopus-indexed journals with h-index of 13. He has led 18 research/consultancy projects, including recently received international grants *Kurita Water and Environment Foundation* and *Nippon Sheet Glass Foundation for Materials Science and Engineering*, besides co-researcher of another 50 projects, which in total worth RM16 million (about USD 4 million). Through these projects, his research team has successfully developed sustainable membranes for the treatment of various pollutants in water as well as an economical fuel cell for efficient electricity generation and has been granted two patents (four more are currently being examined). Some of the research products have also been recognized in the national and international level by winning several awards, for instance Asian Invention Excellence Award in *28th International Invention, Innovation and Technology Exhibition (ITEX'17)*, Best Invention Award in *18th Industrial Art and Technology Exhibition (INATEX2016)*, Jury Award in *17th Industrial Art and Technology Exhibition (INATEX2015)*, Most Distinguished Award in *Persidangan Dan Eskpo Ciptaan Institusi Pengajian Tinggi Antarabangsa (PECIPTA) 2013*, Double Gold Medal in *British Invention Show (BIS) 2008*, and Best of the Best Award in *Malaysia Technology Expo (MTE) 2008*.



**Dr. Mukhlis A. Rahman** graduated with B. Eng. (Chemical Engineering) in 2003. He was involved in research activities since 2004 when he became a master's student at Universiti Teknologi Malaysia. He worked on the preparation of polymer precursor for the development of carbon fiber locally, in collaboration with SIRIM and other public universities. He published two ISI research articles and one patent has been granted. Dr. Mukhlis A. Rahman later received his M. Eng. (Gas Engineering) in 2006. He started his academic career when he was appointed as a Lecturer in 2007 in the Department of Gas Engineering, Faculty of Chemical and Energy Engineering. Shortly after that, he was granted with a scholarship from Ministry of Higher Education to further his Ph.D. study in Chemical Engineering at Imperial College London, focusing his scope on ceramic membrane for microreactor incorporated with palladium membrane for hydrogen separation. Through his works, seven ISI research articles were published in the area. He was able to complete his Ph.D. study in 3 years and 8 months before coming back to UTM on August 2011 to continue his academic career. Due to excellent achievement during his Ph.D. study, he was awarded an Excellent Service Award 2011 from UTM. Dr. Mukhlis A. Rahman has great passion in "research and innovation" fields. He and his research group have developed ceramic and glass membranes locally to be used for water purification. Until now, he has supervised four Ph.D. students and six master's students, with research interests in ceramic membranes incorporated with porous materials for water reclamation. He has published more than 40 articles in Scopus-indexed journals with h-index of 13. He has led 10 research projects, besides coresearcher of more than 50 projects, which in total worth more than RM10 million.



**Dr. Juhana Jaafar** graduated with a B.Eng. (Chemical Engineering) from Universiti Teknologi Malaysia in 2004. She was then granted with National Science Fellowship under Ministry of Higher Education (MOHE) to pursue her M.Sc. in Gas Engineering from Universiti Teknologi Malaysia. In 2011, she graduated with a Ph.D. in Gas Engineering from the same university specializing in advanced membrane manufacturing for energy application. She has started her academic career

at UTM in 2007. Currently, she is the Lecturer of Gas Engineering Department, Faculty of Chemical and Energy Engineering. Her outstanding outputs in research were evident from her receiving distinguished awards at national and international levels including Asian Invention Excellent Award, 28th International Invention, Innovation and Technology Exhibition (ITEX 2017), Gold Medal, International Invention, Innovation and Design Johor 2017 (IIDJ 2017), Most Distinguished Award – Higher Education International Conference, Innovation Expo of Institute of Higher Education (PECIPTA 2013), Best of the Best awards at the Malaysian Technology Expo (MTE 2008), and Double Gold Medal in British Invention Show (BIS 2008). Her outstanding achievement has been publicized in mass media such as *Berita Harian*, *Harian Metro*, and *Malaysia Hari Ini*.



**Ahmad Fauzi Ismail** is Professor at Faculty of Chemical and Energy Engineering, UTM. His research interests are in the development of polymeric, inorganic, and novel mixed matrix membranes for water desalination, waste water treatment, gas separation processes; membrane for palm oil refining; photocatalytic membrane for removal of emerging contaminants; and development of hemodialysis membrane and polymer electrolyte membrane for fuel cell applications. He obtained his Ph.D. in Chemical and Process Engineering in 1997 from University of Strathclyde and M.Sc. and B.Sc. from Universiti Teknologi Malaysia in 1992 and 1989, respectively. He is the author and coauthor of over 500 refereed journals. He has authored 6 books, 45 book chapters, and 4 edited books, 4 Patents granted, and 16 Patents pending. His h-index is 50 with cumulative citation of over 10112. He has won more than 120 awards nationally and internationally. He is a Fellow of The Academy of Sciences Malaysia, Chartered Engineer in the UK, and a Fellow of the Institution of Chemical Engineers. Ahmad Fauzi also served as the Editorial Board Member of *Journal of Membrane Water Treatment*, *Jurnal Teknologi*, *Journal of Membrane Science and Research*, and *Journal of Membrane and Separation Technology* and the Advisory Editorial Board Member of *Journal of Chemical Technology and*

*Biotechnology.* He involved extensively in R&D&C for national and multinational companies related to membrane-based processes for industrial application. He is the founder of Advanced Membrane Technology Research Center, which is now known as Higher Education Center of Excellence. Currently, Ahmad Fauzi is the Deputy Vice Chancellor of Research and Innovation, UTM.



**Dr. Nancy KingSanders'** background in higher education spans more than 27 years to include a current appointment as Associate Vice-President for Student Success at Texas A&M University-Kingsville, a position she has held since 2011. Prior appointments include Associate Dean for Graduate Studies, Administrative Intern for Academic Affairs, Graduate Music Education Coordinator, as well as attaining tenure and the rank of Full Professor in the Music Department at Texas A&M University-Kingsville. Under her administrative leadership at TAMUK, she established the Center for Student Success to include AVID (Advancement Via Individual Determination) for Higher Education, the First-Year Experience, a two-semester First-Year Seminar Course, Centralized Academic Advising, the Graduation Pathway Success Mentoring Center, the Pathway Academic Assistance Tutoring Center, Freshman Interest Groups, Academic Career Literacy, Mapping First-Year Seminar Curriculum to General Education Component Area Options, and Javelina Common Read Program, resulting in a 15.9% increase in First-Time in College retention at Texas A&M University-Kingsville. She was also selected as a National First-Year Student Advocate by Cengage and the National Resource Center for the First-Year Experience and Students in Transition. Dr. KingSanders' other responsibilities include all academic support for undergraduate students and Co-Principal Investigator for a Title V Individual \$2.625 Million Hispanic Serving Institution Grant to embed research into undergraduate courses.

---

## Contributors

**Roberto Álvarez** Department of Engineering, Universidad Nebrija, Madrid, Spain

**Mohammad Asadikiya** Department of Mechanical and Materials Engineering, Florida International University, Miami, FL, USA

Center for the Study of Matter at Extreme Conditions (CeSMEC), Florida International University, Miami, FL, USA

**Sajid Bashir** Department of Chemistry, Texas A&M University-Kingsville, Kingsville, TX, USA

**Olga A. Baturina** Naval Research Laboratory, Washington, DC, USA

**Carolina Musse Branco** School of Chemical Engineering, University of Birmingham, Birmingham, UK

**Ulises Cano** INEEL, Cuernavaca, Mexico

**Xuecheng Cao** Soochow Institute for Energy and Materials InnovationS, College of Physics, Optoelectronics and Energy & Collaborative Innovation Center of Suzhou Nanoscience and Technology, Soochow University, Suzhou, Jiangsu, China

**Xin Chen** The Center of New Energy Materials and Technology, College of Chemistry and Chemical Engineering, Southwest Petroleum University, Chengdu, China

**Sergio Corbera** Department of Engineering, Universidad Nebrija, Madrid, Spain

**Javier de la Cruz** CONACYT-INEEL, Cuernavaca, Mexico

**Shadi Darvish** Department of Mechanical and Materials Engineering, Florida International University, Miami, FL, USA

Center for the Study of Matter at Extreme Conditions (CeSMEC), Florida International University, Miami, FL, USA

**Hanping Ding** Department of Mechanical Engineering, Colorado Fuel Cell Center, Colorado School of Mines, Golden, CO, USA

Energy & Environmental Science and Technology, Idaho National Laboratory, Idaho Falls, USA

**Boris Dyatkin** Naval Research Laboratory, Washington, DC, USA

**Irene Gatto** Institute for Advanced Energy Technologies, Messina, Italy

**Pranitha Hanumandla** The Department of Chemistry, Texas A&M University-Kingsville, Kingsville, TX, USA

**Hsuan-Yi Huang** The Department of Chemistry, Texas A&M University-Kingsville, Kingsville, TX, USA

**Akihiro Iiyama** Fuel Cell Nanomaterials Center, University of Yamanashi, Kofu, Yamanashi, Japan

**Ahmad Fauzi Ismail** Advanced Membrane Technology Research Centre, Universiti Teknologi Malaysia, Johor, Malaysia

Renewable Energy Research Group, Department of Energy Engineering, Faculty of Chemical and Energy Engineering, Universiti Teknologi Malaysia, Johor, Malaysia

**Hiroshi Ito** Research Institute for Energy Conservation, National Institute of Advanced Industrial Science and Technology (AIST), Tsukuba, Japan

**Juhana Jaafar** Advanced Membrane Technology Research Centre, Universiti Teknologi Malaysia, Johor, Malaysia

Renewable Energy Research Group, Department of Energy Engineering, Faculty of Chemical and Energy Engineering, Universiti Teknologi Malaysia, Johor, Malaysia

**Siti Munira Jamil** Advanced Membrane Technology Research Centre, Universiti Teknologi Malaysia, Johor, Malaysia

Renewable Energy Research Group, Department of Energy Engineering, Faculty of Chemical and Energy Engineering, Universiti Teknologi Malaysia, Johor, Malaysia

**Katsuyoshi Kakinuma** Fuel Cell Nanomaterials Center, University of Yamanashi, Kofu, Yamanashi, Japan

**Nancy KingSanders** Texas A&M University-Kingsville, Kingsville, TX, USA

**Fan Li** Beijing Key Laboratory for Catalysis and Separation, Department of Chemistry and Chemical Engineering, College of Environmental and Energy Engineering, Beijing University of Technology, Beijing, China

**Jingbo Louise Liu** Department of Chemistry, Texas A&M University-Kingsville, Kingsville, TX, USA

**Xiaowei Liu** MEMS Center, Harbin Institute of Technology, Harbin, China

**Mohd Hilmi Mohamed** Advanced Membrane Technology Research Centre, Universiti Teknologi Malaysia, Johor, Malaysia

Renewable Energy Research Group, Department of Energy Engineering, Faculty of Chemical and Energy Engineering, Universiti Teknologi Malaysia, Johor, Malaysia

**Akihiro Nakano** Research Institute for Energy Conservation, National Institute of Advanced Industrial Science and Technology (AIST), Tsukuba, Japan

**Katsutoshi Ono** Department of Energy Science and Technology, Kyoto University, Kyoto, Japan

**Mohd Hafiz Dzarfan Othman** Advanced Membrane Technology Research Centre, Universiti Teknologi Malaysia, Johor, Malaysia

Renewable Energy Research Group, Department of Energy Engineering, Faculty of Chemical and Energy Engineering, Universiti Teknologi Malaysia, Johor, Malaysia

**Enza Passalacqua** Institute for Advanced Energy Technologies, Messina, Italy

**Rolando Pedicini** Institute for Advanced Energy Technologies, Messina, Italy  
Dipartimento di Fisica, Università della Calabria, Arcavacata di Rende, CS, Italy

**Qingan Qiao** School of Chemistry and Materials Science, Ludong University, Yantai, China

**Mukhlis A. Rahman** Advanced Membrane Technology Research Centre, Universiti Teknologi Malaysia, Johor, Malaysia

Renewable Energy Research Group, Department of Energy Engineering, Faculty of Chemical and Energy Engineering, Universiti Teknologi Malaysia, Johor, Malaysia

**Tatyana V. Reshетенko** Hawaii Natural Energy Institute, University of Hawaii, Honolulu, HI, USA

**Tatiana Romero** INEEL, Cuernavaca, Mexico

**Surbhi Sharma** School of Chemical Engineering, University of Birmingham, Birmingham, UK

**Makoto Uchida** Fuel Cell Nanomaterials Center, University of Yamanashi, Kofu, Yamanashi, Japan

**Jorge Uribe-Godínez** Centro Nacional de Metrología, El Marqués, Querétaro, Mexico

**Zhaohui Wang** Department of Electrical Engineering and Computer Science, Texas A&M University-Kingsville, Kingsville, TX, USA

**Rui Xue** MEMS Center, Harbin Institute of Technology, Harbin, China

**Ruizhi Yang** Soochow Institute for Energy and Materials InnovationS, College of Physics, Optoelectronics and Energy & Collaborative Innovation Center of Suzhou Nanoscience and Technology, Soochow University, Suzhou, Jiangsu, China

**Mei Yang** H.C. Starck Inc., Newton, MA, USA

**Weijian Yuan** MEMS Center, Harbin Institute of Technology, Harbin, China

**Yufeng Zhang** MEMS Center, Harbin Institute of Technology, Harbin, China

**Yu Zhong** Department of Mechanical and Materials Engineering, Florida International University, Miami, FL, USA

Center for the Study of Matter at Extreme Conditions (CeSMEC), Florida International University, Miami, FL, USA

Mechanical Engineering Department, Worcester Polytechnic Institute, Worcester, MA, USA





# Fuel Cell Technology: Policy, Features, and Applications – A Mini-review

# 1

Sajid Bashir, Nancy KingSanders, and Jingbo Louise Liu

*Dedicated to Peter J. Derrick and Rakesh Prajapat*

## Contents

1.1	Introduction .....	2
1.1.1	President Eisenhower and Energy Policy .....	3
1.1.2	From Analytics to Policy: Department of Energy: History, Challenges, and Possible Future .....	6
1.1.3	Current Challenges: Fossil Fuel Technology Improvement Program .....	8
1.1.4	Department of Energy (DOE) Policies in Prior Administrations .....	9
1.1.5	Transition to a Non-carbon Economy: The Issues .....	12
1.1.6	The Potential Pitfalls and Hazards Toward Becoming a Non-carbon Economy .....	13
1.1.7	Economic Impacts .....	14
1.1.8	Carbon Dioxide (CO <sub>2</sub> ) Emission Reduction .....	15
1.1.9	Fuel Cell Technology: Policy, Features, and Applications .....	15
1.2	Conclusion .....	20
	References .....	21

## Author Contribution

The first draft of this chapter was written by SB. The data in the figures and charts were by SB and modified by JL. The first draft was reviewed and edited by NKS. All three authors collectively conceived and discussed the concept of this chapter.

S. Bashir · J. L. Liu (✉)

Department of Chemistry, Texas A&M University-Kingsville, Kingsville, TX, USA

e-mail: [Br9@tamuk.edu](mailto:Br9@tamuk.edu); [kfjll00@tamuk.edu](mailto:kfjll00@tamuk.edu)

N. KingSanders

Texas A&M University-Kingsville, Kingsville, TX, USA

e-mail: [Nancy.kingsanders@tamuk.edu](mailto:Nancy.kingsanders@tamuk.edu)

---

**Abstract**

When Dwight D. Eisenhower became the 34th president of the United States, he was the first incumbent of the office that did not hold any political office within state government or within the US Congress, excluding military service, since Ulysses Grant. No president prior to or since has crafted and influenced energy policy to the degree of President Eisenhower. As the first officeholder without a past “congressional” career, he was viewed as pro-business and pro-military, and the expectations of his government were that nuclear energy would provide cheaper electricity. The challenges during his administration enabled him to adopt a more orthodox policy stance, and the nuclear energy policies did not proceed as anticipated or planned. The 45th President of the United States, Donald Trump, is the only individual since Eisenhower without a prior congressional-type political career. Since he has a foundation in real estate business, like Eisenhower, he is perceived as “pro-business,” and it is pertinent to compare similar energy policies under the current administration. Although the current administration is only 100 days old, statements during the primaries, general election, and first 100 days in office and first proposed federal budget suggest that tax credits for electric vehicles and other tax assistance credits will be discontinued and that certain brackets of taxes will be eliminated or greatly reduced. And many federal policies enacted under the Obama administration related to environment and energy will be rolled back, favoring coal, drilling, and Keystone XL and the Dakota Access Pipelines. Whether these policies will promote domestic energy production, reduce the import-to-export gap, or lower the “energy deficiency” is too early to gauge. The introduction of potential import fees or border taxes may promote coal extraction at the expense of natural gas exploration. This may also impact gasoline prices at the pump since crude oil imported from other countries would have taxes or fees levied on it. Coupled with limiting environmental regulations and capping liabilities, lower corporate tax rates for oil exploration companies may promote domestic energy production, because of lower operating costs and liabilities, and may increase corporate profits, although these trends may not be observable within the lifetime of the first term of President Trump. In addition, the projected 3% growth in employment over the current 1.7% is again too early to discern, although most economist’s opinions are that these targets will not be met since these currently are proposals and not implemented policy.

---

**1.1 Introduction**

The International Energy Outlook survey in 2009 projected that the total world energy demands would increase from an estimated 308 Quad Btu’s in 1985 to 678 Btu’s by 2030 [1] up from 95 Quad Btu’s in 1950 when Dwight Eisenhower was the President of the United States [2]. One certainty is that the demand for energy both domestically and internationally is likely to increase as projected by the

IEA [3]. Within the United States, the energy demand was around 37 Quad Btu's [4] to approximately 100 Quad Btu's when President Trump was inaugurated [5]. One major difference between the two administrations is the perception of using renewable energy resources that were not significant in the 1950s. The role of carbon dioxide (CO<sub>2</sub>) as a potential greenhouse gas and its link with global warming was also not a policy consideration; however, there are policy considerations that have remained constant since World War II, namely, energy security and the main drivers behind policy related to energy and consumption of energy.

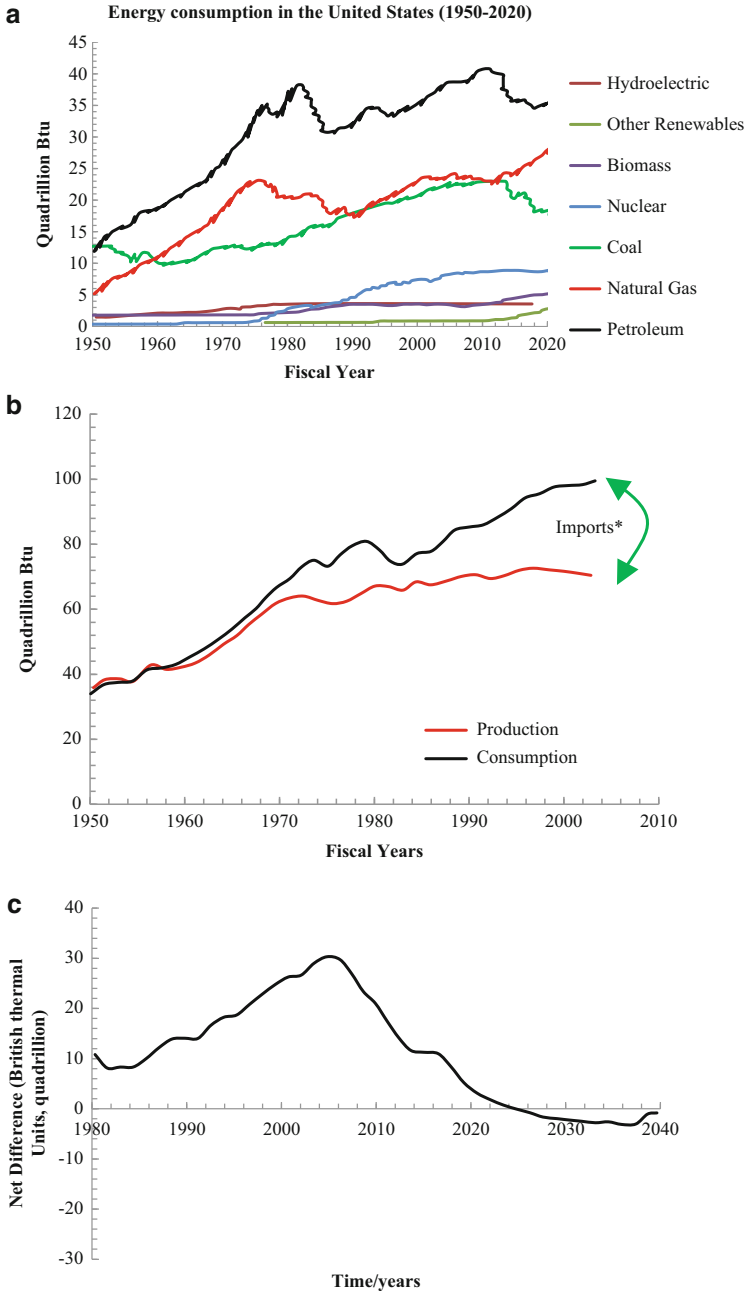
President Dwight Eisenhower, elected to the highest office, was one of the few political leaders that were not a career politician, in the sense of serving in local, state, or federal government legislative bodies or as a governor. President Trump likewise does not have a political background [6]. It is instructive to examine US energy policy over these decades and view how the current policies were derived. One important note is the demand for energy as indexed against nonrenewable fossil fuels, shown in Fig. 1.1 [7]. Since Eisenhower's energy declaration of the United States, the usage of coal has increased during the presidency of every president [8]. They left office with the country consuming more coal than when they entered [9]. In the 1950s, this metric shifted to petroleum, and from Eisenhower to George W. Bush, coal consumption was higher at the end of their term than when entering the office. Only under President Obama's second term did petroleum importation decrease with the expectation to become surplus around 2040 (Fig. 1.1a–c) [7].

The forecast indicates a decrease in terms of net oil usage, because of two factors [10]. More electricity is generated from natural gas rather than coal, lowering carbon dioxide emissions. Also, general residential usage is less, with renewable or more efficient devices being used. The net result is that around 2025 the United States will become a net exporter of energy and most likely oil [11]. Whether or not this is a result of the executive action and market action is difficult to quantify, although outcomes are influenced by energy policy.

### 1.1.1 President Eisenhower and Energy Policy

President Eisenhower launched the age of commercial nuclear energy with his December 8, 1953, "Atoms for Peace" speech to the United Nations General Assembly [12]. Today nuclear fission accounts for about 12% of America's total energy [13]. Despite the urban myth that nuclear engineers promised that electricity generated from uranium would be "too cheap to meter," records show that those sober engineers knew that nuclear energy was more expensive than conventional power but offered many compelling strategic and environmental benefits [14].

In the pantheon of historical pivots in the energy arena, there is irony in Eisenhower's iconic signing of the 1956 National Interstate Highway Act as an implicit, if unintentional, energy policy [15]. The Interstate system spurred not just a great economic expansion but facilitated the rise of the age of oil consumption; highways are where over 20% of American energy is consumed, creating a large demand for energy production and usage. To stimulate domestic production, the



**Fig. 1.1** (a) Domestic energy production from 1950 for sustainable and fossil fuel sources [7]. (b) Domestic oil production and usage from 1950 to 2020\* and resulting net export status for the United States (\*predicted, Ref. [7]). (c) US Net Energy Balance [7]

Eisenhower administration introduced import quotas and price controls (on natural gas) [16]. The net result was to stimulate domestic production and consumption, enabling wealth to be redistributed within the oil sections from production entities to refineries, creating a supply shortage that is met by the use of substitute oils and increases in price for the consumer (because of import quotas). The intent of these policies is to promote domestic production and usage but to keep prices low, particularly for citizens who are on the lower-income scale, and to minimize large profits for oil companies and owners. Research tends to indicate that price controls as a form of “fairness” to the “poor” are an inefficient method since the poor often use the resources to a lesser degree than the average-income family. Furthermore, tax credits and incentives would target lower-income citizens directly and be more useful than price controls, which are contrary to a free-market economy [17]. The larger profit concern is addressed through the realization that many of the larger oil fields either offshore or inland are on state or federal lands. The result of these policies has been an oil shortage, an inefficient use of capital investment, and a heavy reliance on oil “tax or sales receipts” by some states [18]. There are a number of generalizations that can be stated here before detailing specifics.

The three big government policies which impact practically every citizen are (1) access to and the cost of healthcare, (2) energy (electricity, diesel, or gasoline), and (3) taxation. Therefore, energy policy is significant and over the last two decades has incorporated environmental factors in addition to engineering or business technical issues [19].

Since the Civil War, the cost of energy has risen slightly in terms of cost-to-earnings ratio, which was documented during the end of the World War II and the Korean War, intersecting with governance by President Eisenhower. The number of natural oil (one million barrels) or gas (6 billion cubic feet) declined from approximately 3% in the 1940s to 1.5% in the 1950s with an increase in the cost of 30% (adjusted for inflation). These increases could not be offset by production gains introduced by newer technology [20]. The availability of cheap and abundant oil made use of other sources unnecessary, and environmental concerns were deemed less important than staving off two possible economic recessions during his tenure. The carbon versus non-carbon debate had not happened yet, but the president recognized that the use of uranium and plutonium for peaceful purposes had environmental and cost benefits, particularly in providing electricity. The cost of electricity was low, but historic demand approximately doubled every decade. The regulatory framework set ensured the federal government had control and regulation of nuclear fuels, but the policy makers had underestimated the technical challenges and the cost of business, as well as disposal of the used fuel. In addition, federal research and development in non-defense energy have remained relatively low (Fig. 1.2a).

Using the Atomic Energy Commission/Department of Energy (AEC/DOE) as a yardstick to gauge government policy with regard to coal-, natural gas-, and petroleum-based research, it can be seen that federal research has fluctuated, based on external events. The peak in funding was a result of external pressures related to oil prices and a policy to enable the United States to become less dependent on

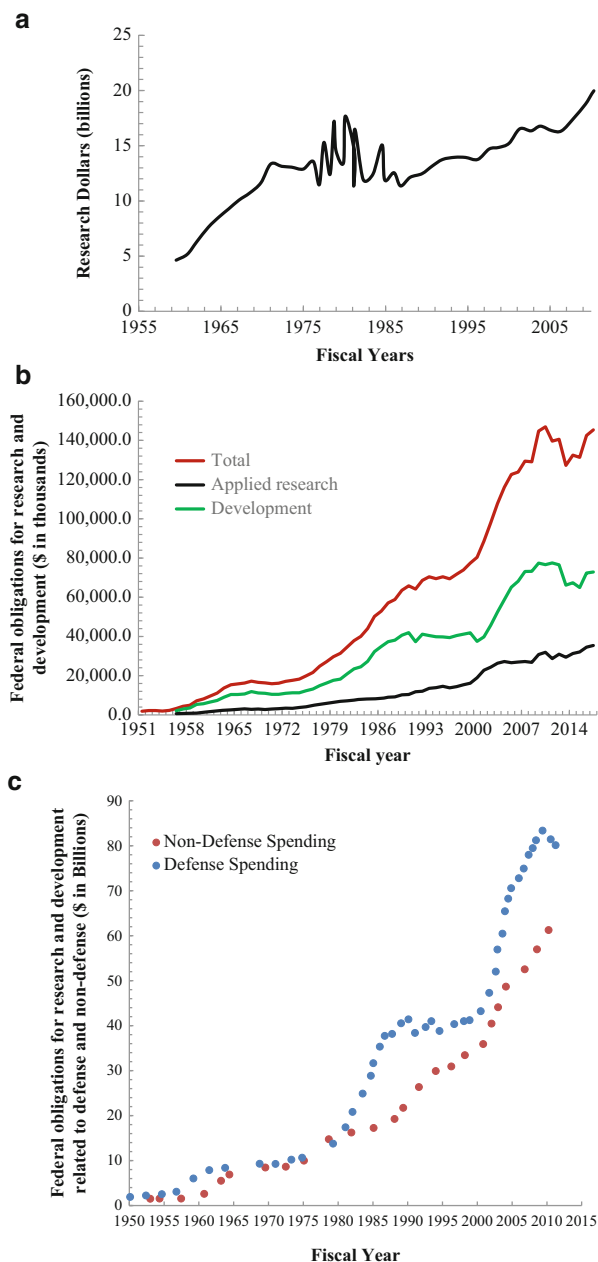
foreign oil. Toward this end, successive administrations have introduced either price caps, import quotas, the use of strategic reserves, or creation of oversight or regulatory agencies including the continuation of research policy undertaken during the Roosevelt administration of creation of a brain trust. The idea of federal funds and universities to solve technical challenges is one foundation of federal research; however, the level of support to the overall desire of lessening the reliance on foreign energy has not been consistent with the stated aims. We see a federal fund surge during the late 1970s and late 2010s, but general energy funding has always remained lower than defense or healthcare funding. Federal funding for energy has steadily increased over the years to an approximate track of \$80 billion that has fluctuated between decades and been approximately set to around 2.5% of gross domestic product (GDP), although actual percentage was as low as 1.5% in the early phase of the Eisenhower administration but rose steadily to above 2.5% during the mid-1960s (Fig. 1.2b) [21].

The historic spending on the Department of Energy has fluctuated from a low of 0.9% of GDP to a high of 12.6% depending on the specific administration and political challenges faced. The higher spending during 1979 was a direct response to the second oil crisis and “stimulus money” in energy (excluding atomic energy). The values are difficult to compare since certain programs were reclassified as general science rather than energy, diminishing the percent spent listed [20]. One constant theme from World War II (WWII) onward is that federal spending on defense (51.08%) and health and human services (26.68%) accounts for the bulk of federal research and development (R&D) funds. All other agencies are allocated a total of 3.25% between them, except the DOE (7.42%), National Science Foundation (NSF) (4.57%), National Aeronautics and Space Administration (NASA) (4.45%), United States Department of Agriculture (USDA) (1.70%), and Department of Commerce (0.86%). The overall split between basic research and applied research and development is highly dependent on the specific agency and its mission (Fig. 1.2c). With the Department of Energy, the split is even between basic and applied, noting that much of the research is undertaken by federally funded research and development centers, such as Sandia, Oak Ridge, or Los Alamos National Laboratories, although they received approximately 7.5% of federal R&D dollars (2009) and universities [22].

### **1.1.2 From Analytics to Policy: Department of Energy: History, Challenges, and Possible Future**

The federal government particularly from WWII onward has invested in research and has co-opted private industry to contribute, chiefly through tax credits. While much of the funds are geared toward basic research, select agencies have been funded for applied research. Post-World War II policy has followed suggestions by Vannevar Bush that the federal government undertakes basic research and in inference leaves more mature and profitable technologies to private enterprise [23]. The federal government has on the whole adopted this vision across successive

**Fig. 1.2** (a) Federal research invested in non-defense energy-related research (1953–2010) from the non-defense component of the Atomic Energy Commission to the Department of Energy which took over the responsibility for non-defense energy-related research. (b) Federal research invested in applied and development areas (1953–2014). (c) Federal research invested in defense and non-defense areas (1953–2010)



administrations, except within a few federal agencies whose mission is more applied, such as the NASA, Defense Advanced Research Projects Agency (DARPA), and Office of Homeland Security [24]. While a medium value relative to GDP can be loosely ascertained, there are no spending guidelines that set a floor or ceiling on

research dollars that are influenced by external events, such as the oil embargo in the late 1970s. The Departments of Energy, Defense and Agriculture are the major agencies responsible for biofuels. The research dollars from a high in 1978 to a 20-year time point suggest a significant reduction (\$6–\$0.5 billion adjusted for inflation). A direct comparison is difficult since the portfolio of energies and relative emphasis has changed. In the 1950s–1960s, the emphasis was on nuclear power; the current 2000–2020 emphases are on renewable and fossil and nuclear energy through the Office of Science. This funding mechanism has supported research in materials science impacting solar energy, biomass-derived fuels, and hydrogen fuel initiative in addition to funding for fossil and nuclear energy programs [20].

In the last two administrations, the potential markers for the Trump administration are policies and initiatives in biomass-derived fuels, hydrogen-powered fuel cells, and the wind and solar technologies for electricity generation. The end goal is displacement of oil in the transportation sector by ethanol and hydrogen. The end goal for wind and solar is displacement of coal as a fuel used in the generation of electricity [25].

The use of ethanol is problematic in that the production and infrastructure are greater than with gasoline, because of the reliance on corn as a primary source for the generation of ethanol and its corrosive properties in the distribution network. The use of fast-growing grasses, such as agricultural waste by-products, could alleviate some of these feedstock issues, although the cost of production is relatively high. In terms of promoting the hydrogen economy, considerable federal and private funds have been invested and may continue under the Trump administration, although at a much reduced fund level. This is because the proposed DOE goals have not been met, chiefly a fuel-cell-powered vehicle with a refueling cycle of 300 miles, a life-span of 150,000 miles, and costs comparable to gasoline [26]. The DOE has invested in upgrading wind infrastructure, to increase land-based wind turbines, distributed energy systems, and storage devices as a means of supplying electricity to remote residential units or agricultural machinery (as a means of generating electricity). Lastly, solar technologies face similar challenges of being competitive with conventional technologies with less expensive semiconductor materials rather than crystal-line silicon [27].

### **1.1.3 Current Challenges: Fossil Fuel Technology Improvement Program**

The DOE research is increasingly focused on domestic fossil fuel production through improvements in exploration technologies and techniques. The focus is on enhanced oil recovery, protection, and accessibility to areas that are currently difficult such as deep-sea oil deposits. A similar focus is found on natural gas technologies, such as developing deep-sea drilling technologies to tap into deep gas reservoirs including methane hydrates in permafrost and ocean floor [28]. Above-ground, the DOE is focused on cleaner coal technologies and techniques including implementation of integrated gasification combined cycle technologies. The clean



coal power initiative includes carbon capture, carbon sequestration, and near-zero CO<sub>2</sub> emissions by use of low-CO<sub>2</sub> technologies for a certain energy generation [29]. It is clear that the current Trump administration will scale back some of these policies. However, it is not clear whether lessening enforcement of environmental policies will spur development on increased demand for coal-based energy [30].

Other challenges include fostering electrical generation using generation III nuclear power reactors and advanced fuel cycle initiatives with a sodium-cooled fast reactor that can use a variety of nuclear fuels [31]. It seems likely the Trump administration will continue to promote these initiatives but scale back on regulations which they deem are negative on the business model type of growth [32].

### 1.1.4 Department of Energy (DOE) Policies in Prior Administrations

The DOE is the central intellectual warehouse for ideas, funding, and innovation within the United States. Although historic funding levels are lower than under Eisenhower and the late 1970s, the DOE has budget authority in a wide variety of energy markets, such as renewable, fossil, and nuclear. A central mandate of the oil embargo that all US administrations have followed is the independence of foreign oil imports, and although considerable research funds have been expended, this is not the current reality. The nation is reliant predominately on fossil fuels, although, with increased demand for renewable, natural gas, it appears that the United States will meet its primary target of self-sustainability within the next decade. The secondary target of less reliance on fossil fuels is more of a technical challenge since the bulk of electrical and transport energies are still fossil fuel based. President Eisenhower's government-promoted nuclear energy program, however, compared with the previous administration's Manhattan Project or the incoming administration's Apollo program, has lower funding which has consistently remained low over the last 30 years. As with the Manhattan and Apollo projects, federal funding was used for a specifically applied goal, and toward this goal, other tangibles were generated, enabling early-stage technologies to be adopted by private enterprise, in addition to the generation of new innovative products, intellectual products, and strategies that revolutionized contemporary markets. Federal government policy directed toward investment is an essential component in reducing barriers to commercialization and update of newer technologies, also creating a culture to bring in the next generation of scientists and business entrepreneurs [33]. The historic funding levels between FY1950-FY1955 and FY2005-FY2014 for various energies are summarized in Table 1.1.

Energy-related research has been a cornerstone of the federal government, beginning with coal-based synthetic petroleum and nuclear research prior to and during the Eisenhower administration, although there has been a shift in emphasis from fossil fuels (25–24%) and nuclear (49–28%) to renewable (12–19%) between 1948 and 2014. Although the Trump administration has been in office for 100 days (at the time of writing this chapter), it is premature to speculate on energy policy. The indications are that fossil fuel policies will be promoted at the expense of

**Table 1.1** AEC/DOE energy average yearly funding total (USD billions)

Energy resource	FY1950-FY1955 <sup>a</sup>	FY2005-FY2015 <sup>b</sup>
Fossil energy	3.68	10.00
Nuclear energy	7.27	11.66
Renewable energy	1.71	7.87

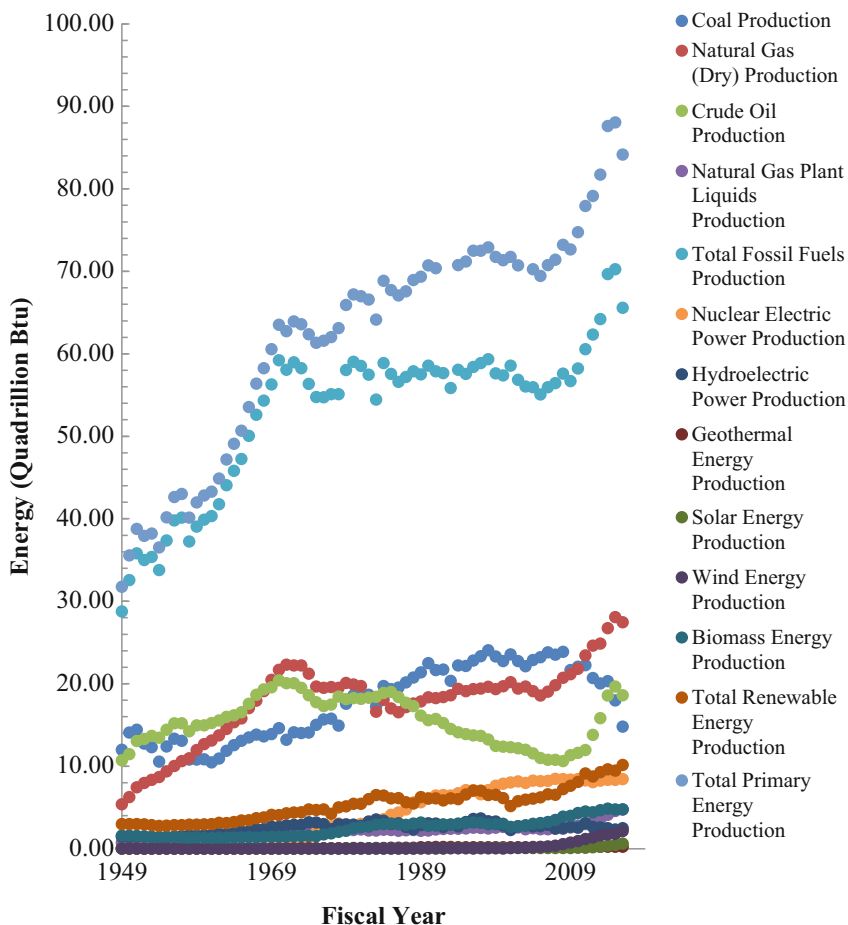
Gross Domestic Product and Deflators Used in the Historical Tables 1940–2019.

<sup>a</sup>Values averaged from 1949 to 1954 and

<sup>b</sup>2005 to 2014. The average assumed constant funding over those cumulative years. US dollar calculated based on 2013 value [34].

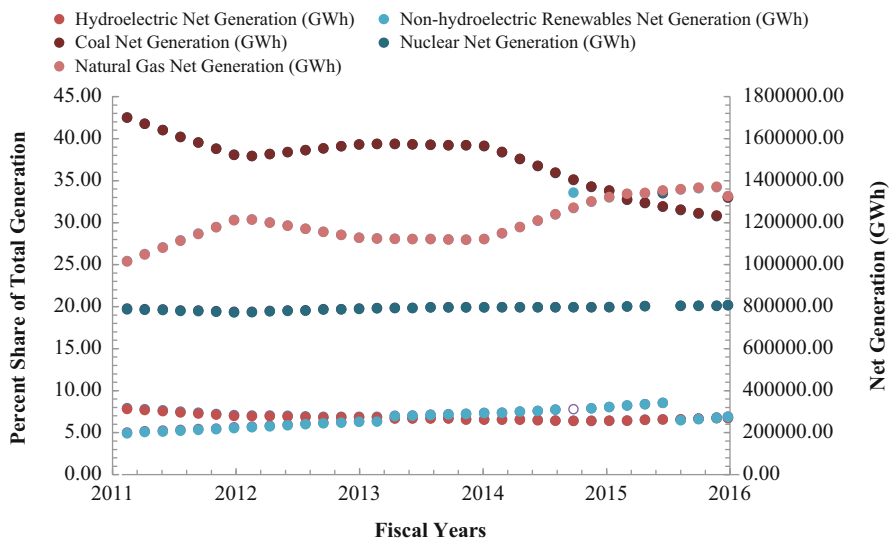
environmental regulations that are deemed “uncompetitive to businesses.” This does not preclude supportive action on renewable energy sources, specifically fuel cell-based technologies since these are considered business opportunities, which can create American jobs. Before an assessment of what the impact of fuel cells in transport will be, the historic mix of fuels is summarized below (Fig. 1.3).

Two general trends are seen: first, the amount of total energy the country consumed around 1955 was 40 quadrillion British thermal units (Btu’s), of which over three-quarters was fossil fuel based [36]. In 2015 the demand had risen to over 98 quadrillion Btu’s, of which over 80% was fossil fuel based. Thus, electrical demand is likely to increase for the next 20 years, although the rate of increase may slow. The second was that President Eisenhower’s expectation for nuclear energy to become the dominant supplier of domestic energy was not realized. This second trend of a dominant energy resource, like coal and nuclear, is unlikely to happen [37]. The three major fossil fuels, coal, natural gas, and petroleum, have dominated the domestic energy market during this time period, with nuclear being a distinct second, but it is unlikely coal will dominate to the extent it has dominated in the past [38]. Coal, the primary fuel other than wood in the previous century, peaked in 2008 and has steadily declined. The decline is because of lesser demand from electricity generators that have been transitioned to natural gas [39]. This is reflected in higher natural gas production than the prior years. Greater efficiency and cost-saving technologies have contributed to increased production of natural gas from shale formations [40]. In addition, production of natural gas plant liquids extracted from natural gas has increased as consumer demand has increased. Lastly, crude oil production has been on a steady decline beginning from the 1970s until 2008 [41]. Cost-saving technologies again assisted increased production particularly in Texas and North Dakota [42]. Sustainable energy has increased steadily because of increased output from the wind and solar energies. In 2015, the total primary energy consumption sectors were electric power (39%), transportation (28%), industrial usage (22%), residential usage (7%), and commercial (4%). This demand was met from the production of natural gas (32%), crude oil and natural gas plant liquid-based petroleum (28%), coal (21%), renewable energies (11%), and nuclear electric power generation (9%) [43]. A major driving force for the switch between coal and natural gas usage has been the demand for generation of electricity that has used natural gas and less coal. The trends are summarized in Fig. 1.4 [45].



**Fig. 1.3** Primary energy production by source and year [35] (<https://www.eia.gov/totalenergy/data/annual/showtext.php?t=ptb0102>)

The electricity generated from natural gas is the largest slice of total US generation (33.8%), followed by coal (30.4%). This decline for coal and increase for natural gas are a result of the retirement of older coal-fired generators and increased infrastructure investment in natural gas renewable as favorable investment opportunities relative to coal. The decline in coal was also because of increased use of renewables (the wind, biomass, solar, geothermal, and hydro) to 8.4%. This is in response to energy policies such as the federal production tax credit, the investment tax credit, and state-level renewable portfolio standards. It appears that the Trump administration will scale back some of these credits including clean power implementation. These rollbacks are unlikely to impact capital costs for development of the wind and solar technologies that are on a downward trajectory compared with other technologies in the energy sector [46]. These savings have often been passed to



**Fig. 1.4** Primary energy production by source and year [44] (<https://www.eia.gov/electricity/monthly/update/archive/april2017/>)

the end user. The tax credits have also spurred growth in electric utilities using the wind with capacity steadily increasing until 2022 when tax credits are expected to lapse. It appears that 90% or more of the capacity building will occur before or by 2022. A slower growth was also observed for the use of solar energy, but with the tax credits expiring or declining beginning in 2018, it is expected to reach parity with wind energy generation by 2040 [47].

### 1.1.5 Transition to a Non-carbon Economy: The Issues

Two considerations regarding the movement from fossil fuels to sustainable energy are as follows: (1) with the current rate of usage, fossil fuels will not last more than 300 years [9], and (2) greenhouse gas is attributed to increases in global temperature and factors affecting health. Historically, research in California linked volatile organic compounds to ozone production and human disease. This led to Phase II Reformulated Gasoline which contained 10% methyl tertiary [48, 49]. Human health issues can further be subdivided into occupational, environmental, ecological, regional, and global exposure with increasing distance from the source [50]. Occupational is direct exposure to diesel particulate matter, volatile organics, carbon monoxide, or other residues. Environmental exposure would be exposed to air pollutants, such as particulate matter, ozone, sulfur oxides ( $SO_x$ ), nitrogen oxides ( $NO_x$ ), carbon monoxide, and dioxide [51]. Heavy metal and organometallics, such as arsenic, nickel, vanadium, benzene, naphthalene, and 1,3-butadiene, are examples of the type of pollutants that are found in common fuels [52]. The ecological impact is related to storage,

transportation, and spillage of potential fuels, including combustion by-products such as fly ash, heavy metals, persistent organic pollutants, eutrophication assisting inorganic nutrients, or phytotoxic elicitors including acidic species that promote acid deposition. Common examples include polycyclic aromatic hydrocarbons, ozone, and  $\text{SO}_x$ , which are also toxic to plants [53]. Nitrite deposits can promote acid deposition and eutrophication, in addition to  $\text{SO}_x$  and organic acids [54].

Regional impact is well documented from the 1952 Great Smog of London that caused 4,000 deaths resulting in the introduction of the 1956 Clean Air Act from particulate matter, dust, sulfate, and nitrate aerosols, including combustion by-products from fuels. Volatile organic species react with particulate matter and create a smog or haze affecting visibility and health [55]. These species also affect weather patterns through depletion of ozone in the stratosphere as a result of interactions with ultraviolet (UV) radiation. Species that can potentially degrade ozone are  $\text{NO}_x$  and chlorofluorocarbons [56]. The reactive species from nitrogen via combustion can accelerate ozone depletion and is another concern other than the known catalyst effects of chlorine. These species can be generated or released by spillage or leakage, such as leakage of methane from the storage and distribution network [57]. These emissions emanate from a pressure differential between the storage tank and the atmosphere, which may be remedied by lowering the vapor pressure of gasoline when a gasoline blend with alcohol is generated, including emission of methane and coal dust [58]. In transport, combustion can lead to the emission of gasses that are higher under cold start than stable higher operating temperatures, or where the engines are improperly tuned, allowing higher than expected emissions [59].

### 1.1.6 The Potential Pitfalls and Hazards Toward Becoming a Non-carbon Economy

Particulate matter from 2.5  $\mu\text{m}$  to 10  $\mu\text{m}$  can be generated and is short-lived, but can travel hundreds of meters and is the result of direct emission from combustion or oxidation of gas-phase emissions which form particulate matters during atmospheric aging. The most common are in the range of 10  $\mu\text{m}$  as a result of mechanical wear and tear of the engine or synthetic oil [60].

The role of greenhouse gasses and carbon dioxide ( $\text{CO}_2$ ) has not been explored and is an important consideration in moving away from carbon-based fuels. Carbon dioxide is a by-product of respiration or combustion and in 2010 contributed to almost 82% of emissions [61] and is unlikely to decrease in the short term to midterm (<10 years, [62]). The movement toward economically feasible non-carbon alternatives would be a prudent first step and potentially a new business opportunity to create jobs and grow the utility market. Taking 2011 as a baseline year, the total primary energy consumption was 12.27 Mtonne of oil equivalent (toe) which topped 13.00 Mtoe by 2015. Basically, world consumption is increasing approximately 2,000 Mtoe/decade related to electricity generation and use in transportation, residential, and business sectors of the economy. In 2011, for the first time, China become the world dominant power in domestic electricity consumption

(4,052 TWh) with the United States being second (3,883 TWh). In 2013, China topped 5,000 TWh consumption for the first time (5,447 TWh) which has slowed down, mainly to the slowdown in China [63]. These factors of the slowdown in China for 2015/2016 and previous record highs have driven some countries to seek energy generation from renewable energy sources, known in policy circles as energy security. The Middle East conflict and oil embargo in 1973 controlled petroleum prices in the United States, making policy makers aware of the importance of energy independence as a form of security. This area was not a concern during the pre-industrial era since energy was decentralized, local, and related to the wind, water (hydro), the sun, wood, and peat (biomass). During the industrial revolution, coal became the engine that drove the economy [64]. A study by Delucchi and Murphy [65] concluded the cost of Persian Gulf oil upon the US military is as high as \$37 billion per year or \$0.15 per gallon. If this oil was replaced by domestic sources such as renewables, shale gas, or a reconfiguration (fewer gasoline automobiles and a mixture of electric, methanol, natural gas, or fuel cell), the security savings could be substantial. This area was not a concern during the pre-industrial era since energy was decentralized, local and related to the wind, water (hydro), the sun, wood, and peat (biomass). During the industrial revolution, coal became the engine that drove the economy [64]. A study by Delucchi and Murphy [65] concluded the cost of Persian Gulf oil upon the US military is as high as \$37 billion per year or \$0.15 per gallon. If this oil was replaced by domestic sources such as renewables, shale gas or a reconfiguration (fewer gasoline automobiles and a mixture of electric, methanol, natural gas, or fuel cell), the security savings could be substantial.

### 1.1.7 Economic Impacts

The current Trump administration is known for its business approach to federal problems [66]. The emphasis on job creation, industrial innovation, and fairness in trade treaties (balance of payment) is a central legislative platform [67]. The push for renewables has two business-centric advantages. In the first case, there will be lesser reliance on fossil fuels, even if this is restricted to the generation of electricity. This will improve the balance of payments or at least redistribute payments more domestically. The second includes energy-saving technologies and policies that can be sold to other countries, much like the sale of cars, airplanes, or banking services [68], and indirectly will create jobs, through export of technology. This approach could serve as a business model for countries that do not have an abundance of fossil resources. The International Energy Agency modeled a scenario where the 2005 carbon dioxide emissions were lowered by 50% (2DS model) and found that over \$100 trillion would be saved over 40 years (2010–2050) by implementing the 2DS model resulting in reduced fossil fuel importation and/or usage by approximately 210 Gtoe, which in turn would lead to lower fuel prices (\$150 trillion over the same period, Ref. [69]).

The model also estimates that five million new jobs could be created. The Global Status Report estimated 1.5 million jobs in the biofuel sector, over 800,000 in solar

photovoltaics, and over 650,000 in wind power [70] with renewable energy accounting for almost 15% of the energy-generating sector in Germany, with a European Union target of 20% by 2020. The study also concluded that no major job losses would occur in the fossil fuel sector if the transition was managed with tax credits, training credits with programs to migrant workers from one sector to the other, a net growth could occur. The biggest trend would be a reduction in CO<sub>2</sub> emissions.

### 1.1.8 Carbon Dioxide (CO<sub>2</sub>) Emission Reduction

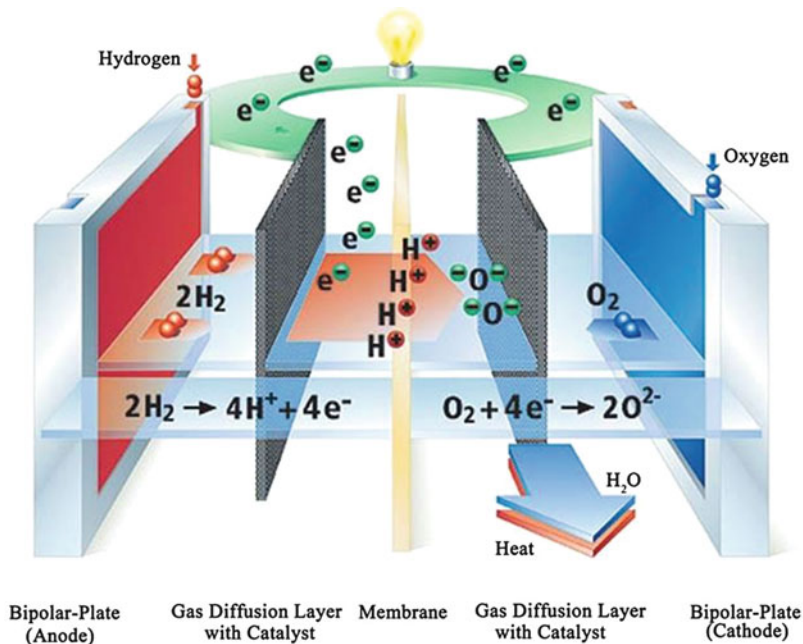
While CO<sub>2</sub> is not harmful to plants that require it in photosynthesis, higher levels are toxic for animals that undergo aerobic respiration and generate CO<sub>2</sub>. A comparative study showed that renewable energy technologies reduce carbon dioxide emissions by a greater degree than nonrenewable technologies, to the level of 1.7 Gt CO<sub>2</sub> emissions in 2008 [71]. The International Energy Agency and World Economic Outlook estimated that over 5 Gt of CO<sub>2</sub> emissions could be saved if Brazil, Russia, India, China, and South Africa switched to renewable sources for power generation by 2030 lowering CO<sub>2</sub> to less than 450 parts-per-million (ppm) [72]. If China were able to reduce CO<sub>2</sub> emissions to the 450 ppm target by 2030, this would represent a reduction of approximately 2.2 Gt relative to no reduction or set target [73]. This could be managed by a straight fuel replacement (fossil by renewables) or a hybrid approach using carbon dioxide capture and storage technologies, artificial leaf for enhanced photosynthesis, and long-term storage in caves, salt mines, and undersea stores [74].

### 1.1.9 Fuel Cell Technology: Policy, Features, and Applications

A number of initiatives have related to fuel cell development, from research during World War II on fuel cells [75] to NASA's development on Gemini [76] and revisited during the oil crisis of the 1970s [77] particularly as an alternative to gasoline in automobiles [78]. The program supporting the National Energy Technology Laboratory was a key policy program to support aggressive fuel cell development particularly of solid oxide fuel cells (SOFCs) [79] FutureGen program [80] in addition to a FreedomCAR tailored toward automobiles [81]. The latter program focus is the incorporation of proton-exchange membrane fuel cells (PEMFCs). The intent with the hydrogen fuel initiative is to design, develop, and proof technologies for essentially a fuel stack to replace the internal combustion engine powered by gasoline. This would result in significant reduction in the combustion of gasoline and emission of greenhouse emissions [82]. For any "fuel cell" initiatives to be viable and successful, four key challenges need to be met and overcome:

1. The incorporation of non-precious metal or substitution of platinum by cheaper catalysts, if mass production is to be an economically profitable venture [83].





**Fig. 1.5** Schematic of single PEMFC (From Garrain et al. [87], with permission)

2. If the fuel is hydrogen from electrolysis using sunlight, then durable photocatalysts are required [84].
3. Hydrogen storage materials operating at low pressure and high volumetric density [85].
4. A low-cost pipeline, distribution network similar to the one used for natural gas is required [86].

The PEMFCs generate electrical energy when hydrogen is combined with oxygen (from air) to generate water and consist of an electrolytic polymer membrane and platinum electrocatalyst in the form of a stack constructed of a membrane electrode assembly (MEA) which is between the ion-exchange membrane and electrodes as shown in Fig. 1.5 [87]. The electrodes are in turn between a gas diffusion layer and flow path. The stack is thus built of layers of these individual cells. Each cell operates between 0.7 V and 1 V depending on electrical current. The output drives the electric motor which requires between 250 V and 300 V. The early-generation cars had a 288 V, requiring approximately  $(288/0.7)$  410 cells [88].

Unlike an internal combustion engine where the energy goes into heat, an electrical engine can achieve over 50% or greater efficiency to a theoretical limit of 83% [89]. The PEMFC would require fuel, and this can either be onboard stored hydrogen gas or where some precursor is converted to hydrogen using a reformer.



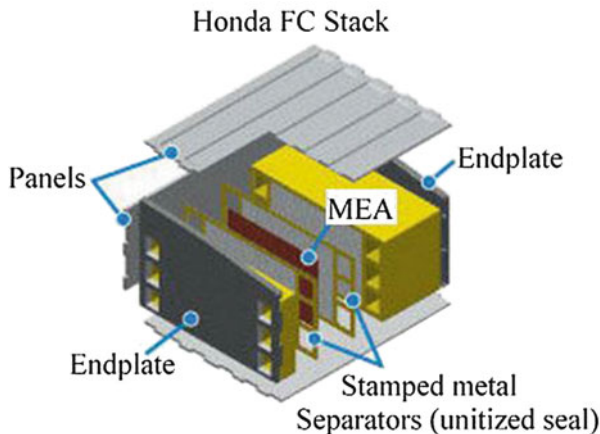
The approach used by Honda, for example, was to use pure hydrogen gas to eliminate the potential of CO<sub>2</sub> production since the only by-product was water [90].

The fuel stack is thus packaged in the form of a membrane electrode assembly (MEA) with three types of components [91]: the membrane component, the catalyst layer, and the gas diffusion layer (GDL). The stack would then be configured with end plates, flow-field plate, seal, and MEA, with the plates also serving to cool or move heat flow. Most research has focused on the membrane and electrocatalyst design. The most common type of membrane is a perfluorosulfonic acid with a polytetrafluoroethylene-based backbone with  $-O-(CF_2)_n-O$  ether-type side chain and a sulfonic acid anchor [92]. Hydrogen ion mobility occurs upon membrane hydration and movement from sulfonic acid sites. The backbone is also resistant to chemical oxidation or reduction [89] with high ion conductivity (at least 0.2 S/cm or  $0.05 \Omega \text{ cm}^2/100 \mu$ ) [93]. The manufacturing costs of perfluorosulfonic acid (PFSA)-type materials are relatively high, and they are prone to generate toxic aerosols above 150 °C [94]. Since these membranes have to be hydrated to retain high proton conductivity, this feature raises unit costs. Other alternates to fully fluorinated membranes are partially fluorinated or non-fluorinated, or some composites, such as trifluoro styrene, sulfonated polybenzimidazoles, sulfonated polyether ketones, and polytetrafluoroethylene or poly(vinylidene fluoride) cross-linked with divinylbenzene-linked polymers, are examples of promising alternatives [95]. Other alternatives include MEA, where the catalyst is applied to the GDL or the catalyst is applied to the membrane and followed by GDL addition [96].

Proton-exchange membrane fuel cells also offer the advantage of a different fuel intake such as methanol. The problem of methanol reformate is the addition of carbon dioxide and carbon monoxide; the latter can irreversibly bind and deactivate the catalyst. Onboard fuel reforming can include selective oxidation for CO removal to <10 ppm within the tolerance limit of most PEMFCs (~100 ppm) [97]. Alternatively, the reformed methanol may be passed over a platinum catalyst or hydrogen peroxide bleeding, because of oxygen bleed from the decomposition of the peroxide in the anode humidifier. This problem is avoided if pure hydrogen gas is used instead [98]. Catalyst alloying is another method to counter potential CO poisoning by the formulation of two- or three-metal anode catalysts. The most common are Pt or carbon (Pt/C), Pt-ruthenium (Ru)/C, Pt-molybdenum (Mo)/C, Pt-Ru-Mo/C, Pt-tungsten (W)/C, Pt-Ru-W/C, Pt-Re-magnesium hydride (Pt-Re-(MgH<sub>2</sub>)), and Pt-Ru-aluminum (Al<sub>4</sub>) [99]. The Pt catalyst at the cathode is expensive, and much research has been targeted to lower the amount of Pt at the cathode [100].

The gas diffusion layer needs thickness to be stable but thin enough to allow gas diffusion to occur. Typical thickness ranges from 100  $\mu\text{m}$  to 300  $\mu\text{m}$  enabling the gas to reach the catalyst on the membrane electrode assembly. The gas diffusion layer (GDL) also assists with water channeling, since water vapor is required to reach the membrane to enable it to be moist. The GDL needs to channel water produced at the cathode to migrate, to avoid flooding the electrode by having the membrane coated with polytetrafluoroethylene [101]. For efficient packaging of PEMFC, six areas need to be addressed: membrane materials that are durable, safe to use, and temperature resistant, catalyst materials that are affordable and rely on non-precious

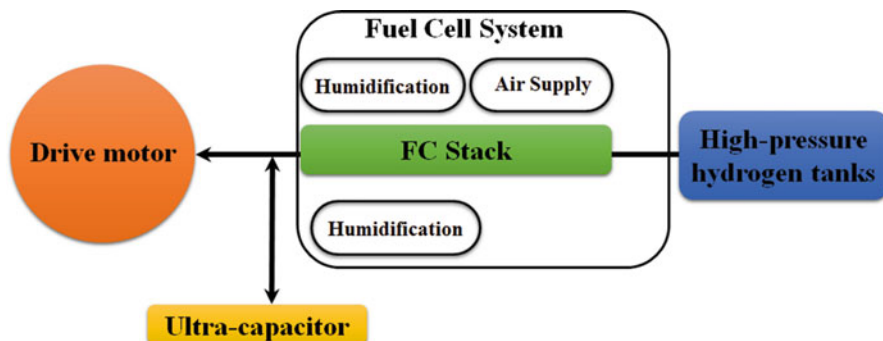
**Fig. 1.6** 3D schematic of Honda FC stack with stamped metal separator (With permission, <http://world.honda.com/FuelCell/FCX/fcstack/>). The Honda FCX utilizes two fuel cell (FC) stacks with a humidifier module that can produce 130 kW output [103]



metals, GDL materials that promote gas diffusion and electrical conductivity, cathode catalyst limiting Pt  $< 0.1 \text{ mg/cm}^2$  (as demonstrated by Ref. [100]), bipolar plate material, and design. The bulk of the design issue is dominated by material selection, such as whether the membrane polymer should be fluorinated, sulfonated, or impregnated with Lewis acids or basic groups. Likewise, the catalyst needs alloys that are resistant to CO poisoning, using non-Pt-based alloys. In the area of MEA manufacturing, catalyst preparation and design dominate research, exemplified by a catalyst layer with a thickness of  $5 \text{ }\mu\text{m}$  with bipolar plate design also being a critical area. The approach taken by Honda was to use compressed hydrogen gas as a fuel source. They used an aromatic polymer structured around sulfonic ester of 2,5-dichlorobenzophenone [102]. The membrane and a stamped metal separator yield high electrical and thermal conductivity, within  $-20 \text{ }^\circ\text{C}$  to  $+90 \text{ }^\circ\text{C}$  (shown in Fig. 1.6).

The third generation design four new design features: (a) a smaller form factor for the fuel cell that is more tolerant to shocks; (b) electric turbo air compressor; (c) fuel cell voltage control unit and a (d) downsize drive unit. The initial drive motor. The drive motor 80 kW permanent magnetic alternating current synchronous motor with high heat-resistant magnets to suppress eddy currents and heat. A supplemental power source in the form of an ultra-capacitor is included. The two-layered condenser uses activated carbon electrodes to improve onboard electrical storage capacity greater than nickel-hydride batteries. The capacitor achieves an energy density of 9.2 F and an output of 3.1 kW/L and can be configured in three models (Fig. 1.7) [103].

The previously configured system may be operated in capacitor mode with the ultra-capacitor feeding the motor and the fuel cell stack providing power as necessary or in a battery-assisted mode with the battery via high-voltage controller providing power with the fuel-cell stack in reserve or fuel-cell mode, where the fuel cell directly powers the motor. The configuration where a capacitor provides power

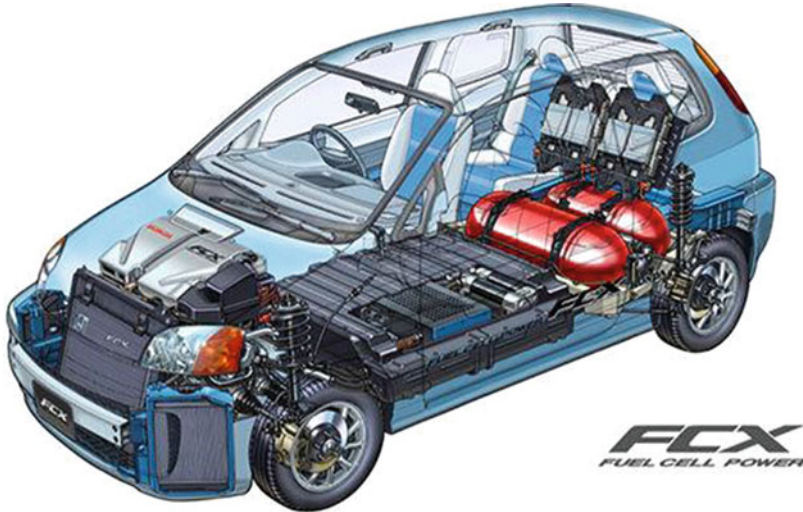


**Fig. 1.7** Schematic of the type of configuration in FCX vehicle (With permission, <http://world.honda.com/FuelCell/FCX/powertrain/>). In the current design, the ultra-capacitor is not included. In the newer designs, the fuel cell voltage control unit was adopted to provide voltage to the traction motor in order to reduce the number of stacks in a fuel cell. High-frequency switching at 30 kHz enabled the capacitor and inductor to be downsized. The redesign enables the current FCV to be approximately 40% in volume. This reduction in size enables the power control unit to be installed under the front hood and integrated with the traction motor [103]

to assist the fuel cell stack during transitional response will improve fuel efficiency. The capacitor follows the voltage characteristics of the fuel cell stack and does not require a high-voltage controller. The transitions such as start-up, acceleration, and immediate power are provided by the capacitor in the previous design configuration until the fuel cell kicks in. Under idle or city traffic, the fuel cell output may be sufficient. During braking, the drive motor's counter-electromotive force can recover the braking energy and send it to the capacitor. The distance traveled on 1 kilogram of hydrogen gas is a measure to compare with miles per gallon, since 1 kilogram of hydrogen has similar energy to 1 gallon of gasoline and can be equivalent to 50 miles per gallon equivalent (MPGe), similar to hybrid cars but greater than gasoline-powered compact cars (summarized in Fig. 1.7).

The last one is the fuel storage system. The Honda FCX series of automobiles have an onboard hydrogen storage system in the form of liquid hydrogen, hydrogen gas under pressure, or hydrogen-absorbing metal alloy or resin. Honda utilizes compressed gas storage in an aluminum-lined carbon/glass fiber [104]. The three layers provide strength, and corrosion resistance at 70 MPa to store up to almost 157 L of hydrogen capacity twin-tank. The automobile can drive up to 265 MPGe on a full tank of 11 kg of hydrogen [105] or an approximate distance of 800 km per tank with a refuel time of 3 minutes [103].

The Honda fuel cell vehicle (shown in Fig. 1.8) is powered by an electric motor powered by an 86 kW fuel stack using compressed hydrogen optimized fuel cell voltage control unit. Considering factors such as energy efficiency during power generation and driving, overall system weight, and packaging efficiency, Honda equipped the FCX with a system that combines a fuel cell stack and fuel cell voltage control unit with onboard high-pressure hydrogen tanks of powertrain dimensions similar to a typical V6 engine [103].



**Fig. 1.8** 3D schematic of Honda's FCX (with permission <http://world.honda.com/FuelCell/FCX/overview/>). [In the current design, a smaller hydrogen tank is under the rear seat, with the battery being under the front seat and larger hydrogen tank under the rear axle. The installation of the tank below the rear seat lowered the center of gravity and improved vehicle statistic stability factor by 5%] [103]

Although electric vehicles total approximately 1% of sales, their percent growth from 2016 has more than doubled and is estimated to top 5 million unit sales by 2025 [106]. The manufacturing costs of batteries will drop the number of unit sales, particularly with China and India becoming significant players, which will increase the global market share during the Trump administration. Within the United States, it is likely that tax credit will continue in the short term and these would add a further economic boost [107], although indications are that they will be phased out [108].

---

## 1.2 Conclusion

The outcome of energy policy is historically nonlinear from what we knew for President Eisenhower to what we anticipate for President Trump. President Eisenhower was perceived as “pro-business,” favoring low taxation, and having no political experience, although he had directed the military operations during World War II. His vision of nuclear energy as a dominant energy mix for electricity was not realized due to economic and technical challenges and the public fear of all things “nuclear.” President Trump, the second individual after President Eisenhower, who held no political office prior to the office of the presidency and although it is too early, appears that he favors coal as a dominant energy mix. This is reflected in withdrawal, cancellation or renegotiation from multination treaties (NAFTA,

Paris, TPI) that are deemed uncompetitive to American economic interests. It is too early whether coal will become the dominant energy source for generation of electricity. The trend over the last 5 years suggests that global demand for electricity will increase at a slower rate and taper out. The demand will be met from natural gas and sustainable resources to a greater degree than ever before. This will also promote the hydrogen economy via challenging the pole position of petroleum/diesel as fuels for automobiles for hydrogen or electricity, particularly from international combustion engineer to proton-exchange membrane fuel cell stacks [109]. Although the cost analyses of gasoline, electric, and hydrogen fuel cell cars have been completed, the environmental and toxicological assessment of fuel cells remains to be determined. (see ► Chap. 9, “Modeling Analysis for Species, Pressure, and Temperature Regulation in Proton Exchange Membrane Fuel Cells”) will discuss the cytotoxicity of electrocatalysts used in the fuel cells.

**Acknowledgments** The College of Arts and Sciences (CoA&S, Dr. Bashir, 160336-00002), American Chemical Society, Petroleum Research Funds (Dr. Liu, 53827-UR10), Summer Faculty Fellowship Program (Dr. Bashir), Welch Departmental Grant (AC-0006), and Department of Education (Dr. KingSanders, P031S150096 – I-CARE) at Texas A&M University-Kingsville (TAMUK) were duly acknowledged for their funding and student support. The Microscopy and Imaging Center (MIC) at TAMU and the Department of Chemistry at TAMUK were also duly acknowledged for their technical support and nanostructure characterization.

**Dedication** This chapter is dedicated to Professor Peter J. Derrick who passed away on February 6, 2017, during the preparation of this manuscript. Dr. Derrick was a Ph.D. advisor of SB at the University of Warwick. Dr. Derrick was someone who expected not only high academic rigor but also high ethical and professional standards. We deeply mourn the loss of this chemistry hero. We also celebrate his life and profession through the publication of peer-reviewed research.

SB also mourns the loss of his best friend Rakesh Prajapat with whom they shared their childhood until both were admitted by the universities. It seems incredible someone so young who is no longer present. SB deeply misses his loving company and excellent counsel, forever. SB would be delighted to pass his deepest condolences to Miss Sophie Prajapat, who will carry out her father’s legacy of being the utmost professional, a best friend, a reliable neighbor, and a decent person. SB is proud and privileged to call Mr. Rakesh Prajapat a “friend” in deed.

---

## References

1. IEO, US Department of Energy and International Energy Outlook 2009 and technical report DOE/EIA-0484 (2009), <http://large.stanford.edu/courses/2013/ph241/roberts2/docs/WEO2009.pdf>
2. M. Roser, Energy production & changing energy sources. I: empirical view (2010), <https://ourworldindata.org/energy-production-and-changing-energy-sources/>
3. IEA, (2017), <http://energyatlas.iea.org/#!/tellmap/-1002896040/0>
4. EIA, (2016), [http://www.eia.doe.gov/ieo/pdf/0484\(2009\).pdf](http://www.eia.doe.gov/ieo/pdf/0484(2009).pdf)
5. EIA, (2016), [https://www.eia.gov/outlooks/aeo/pdf/0383\(2017\).pdf](https://www.eia.gov/outlooks/aeo/pdf/0383(2017).pdf)
6. J.P. Tomain, The dominant model of United States energy policy. U. Colo. L. Rev. **61**, 355–358 (1990)
7. AEO, (2017), <https://www.eia.gov/outlooks/aeo/>
8. J.A. Hausman, Project independence report: an appraisal of US energy needs up to 1985. Bell J. Econ. **6**, 517–551 (1975)

9. S. Shafiee, E. Topal, When will fossil fuel reserves be diminished? *Energ. Policy* **37**(1), 181–189 (2009)
10. EY, (2017), [http://www.ey.com/Publication/vwLUAssets/EY-us-energy-policy-in-the-trump-administration/\\$File/EY-us-energy-policy-in-the-trump-administration.pdf](http://www.ey.com/Publication/vwLUAssets/EY-us-energy-policy-in-the-trump-administration/$File/EY-us-energy-policy-in-the-trump-administration.pdf)
11. EIA, (2017), <https://www.eia.gov/petroleum/supply/weekly/>
12. D.D. Eisenhower, Atoms for peace. *IAEA Bull.* **45**(2), 62–67 (2003)
13. J. Chow, R.J. Kopp, P.R. Portney, Energy resources and global development. *Science* **302** (5650), 1528–1531 (2003)
14. R.G. Hewlett, J.M. Holl, *Atoms for Peace and War, 1953–1961: Eisenhower and the Atomic Energy Commission*, vol. 3 (University of California Press, Berkeley, 1989), <http://blog.nuclearsecrecy.com/misc/1989-Hewlett-Holl-AtomsforPeaceandWar.pdf>
15. A. Chandra, E. Thompson, Does public infrastructure affect economic activity?: evidence from the rural interstate highway system. *Reg. Sci. Urban Econ.* **30**(4), 457–490 (2000)
16. C.E. Phelps, R.T. Smith, *Petroleum Regulation: The False Dilemma of Decontrol* (vol. 1951, No. RC) (Rand Corp, Santa Monica, 1977), <https://www.rand.org/content/dam/rand/pubs/reports/2006/R1951.pdf>
17. R.S. Pindyck, The optimal exploration and production of nonrenewable resources. *J. Polit. Econ.* **86**(5), 841–861 (1978)
18. W.J. Mead, The performance of government in energy regulations. *Am. Econ. Rev.* **69**(2), 352–356 (1979)
19. B. Hannon, R.A. Herendeen, P. Penner, *Energy Conservation Tax: Impacts and Policy Implications* (No. NP-2900771; ERG-267). (Illinois University Office of Vice Chancellor for Research, Urbana, 1979), <https://www.osti.gov/scitech/biblio/6075619>
20. NSF, (2017), <https://www.nsf.gov/statistics/srvyfedfunds/#tabs-2>
21. A.M. Weinberg, Nuclear energy: salvaging the atomic age. *Wilson Q.* **3**(3), 88–112 (1979)
22. J.V. Kennedy, The sources and uses of US science funding. *New Atlantis* **36**, 3–22 (2012)
23. V. Bush, As we may think. *Atlantic Month.* **176**(1), 101–108 (1945)
24. G.T. Shen, Resource 2. Federal R&D funding: quick agency profiles (2017), <http://www.proposalxponent.com/federalprofiles.html>
25. G.F. Nemet, D.M. Kammen, US energy research and development: declining investment, increasing need, and the feasibility of expansion. *Energ. Policy* **35**(1), 746–755 (2007)
26. A. Simons, C. Bauer, A life-cycle perspective on automotive fuel cells. *Appl. Energy* **157**, 884–896 (2015)
27. N.S. Lewis, Research opportunities to advance solar energy utilization. *Science* **351**(6271), AAD1920-4 (2016), <http://science.sciencemag.org/content/351/6271/aad1920>
28. R. Boswell, Is gas hydrate energy within reach? *Science* **325**(5943), 957–958 (2009), <http://science.sciencemag.org/content/325/5943/957>
29. J.D. Figueroa, T. Fout, S. Plasynski, H. McIlvried, R.D. Srivastava, Advances in CO<sub>2</sub> capture technology – the US Department of Energy’s Carbon Sequestration Program. *Int. J. Greenhouse Gas Control* **2**(1), 9–20 (2008)
30. H. Tabuchi, What’s at stake in Trump’s proposed E.P.A. cuts (2017), [https://www.nytimes.com/2017/04/10/climate/trump-epa-budget-cuts.html?\\_r=0](https://www.nytimes.com/2017/04/10/climate/trump-epa-budget-cuts.html?_r=0)
31. D.C. Crawford, D.L. Porter, S.L. Hayes, Fuels for sodium-cooled fast reactors: US perspective. *J. Nucl. Mater.* **371**(1), 202–231 (2007)
32. J. Worland, President Trump’s energy policy remains a work in progress (2017), <http://time.com/4662244/donald-trump-energy-policy-unclear/>
33. J.H. Gibbons, Report to the president on federal energy research and development for the challenges of the twenty-first century. President’s Committee of Advisors on Science and Technology, Executive Office of the President of the United States of America (1997), [https://science.energy.gov/~media/bes/pdf/accomplishments/files/pcast\\_energy\\_r\\_d\\_nov1997.pdf](https://science.energy.gov/~media/bes/pdf/accomplishments/files/pcast_energy_r_d_nov1997.pdf)
34. F.J. Sissine, Renewable energy R&D funding history: a comparison with funding for nuclear energy, fossil energy, and energy efficiency R&D. Congressional Research Service, Library of



- Congress (2008), <http://www.nationalaglawcenter.org/wp-content/uploads/assets/crs/RS22858.pdf>
35. EIA, (2016), <https://www.eia.gov/totalenergy/data/browser/?tbl=T01.01#/?f=A>
  36. S.H. Schurr, B.C. Netschert, Energy in the American economy, 1850–1975. *Challenge* **10**(9), 41–44 (1960), [http://www.jstor.org/stable/pdf/40718553.pdf?seq=1#page\\_scan\\_tab\\_contents](http://www.jstor.org/stable/pdf/40718553.pdf?seq=1#page_scan_tab_contents)
  37. O. Hohmeyer, The social costs of electricity-renewables versus fossil and nuclear energy. *Int. J. Sol. Energy* **11**(3–4), 231–250 (1992)
  38. D. Kearney, Energy information administration. Department of Energy, **92010**(9), 1–15 (2010), [https://www.stb.gov/STB/docs/RETAC/2010/March/EIA\\_AEO\\_2010.pdf](https://www.stb.gov/STB/docs/RETAC/2010/March/EIA_AEO_2010.pdf)
  39. P. Jaramillo, W.M. Griffin, H.S. Matthews, Comparative life-cycle air emissions of coal, domestic natural gas, LNG, and SNG for electricity generation. *Environ. Sci. Technol.* **41** (17), 6290–6296 (2007)
  40. R.S. Pindyck, The long-run evolution of energy prices. *Energy J.* **20**(2), 1–27 (1999)
  41. S.P. Brown, M.K. Yücel, What drives natural gas prices? *Energy J.* **29**(2), 45–60 (2008)
  42. E. Worrell, C. Galitsky, Energy efficiency improvement and cost saving opportunities for petroleum refineries, Lawrence Berkeley National Laboratory (2005), <http://escholarship.org/uc/item/96m8d8gm>
  43. G.L. Kyriakopoulos, G. Arabatzis, Electrical energy storage systems in electricity generation: energy policies, innovative technologies, and regulatory regimes. *Renew. Sust. Energ. Rev.* **56**, 1044–1067 (2016)
  44. EIA, (2016), <https://www.eia.gov/outlooks/aeo/data/browser/#/?id=2-AEO2017&cases=ref2017&sourcekey=0>
  45. M. Kovacevic, M. Lambic, L. Radovanovic, I. Kucora, M. Ristic, Measures for increasing consumption of natural gas. *Energ. Source. B. Econ. Plann. Policy* **12**(5), 443–451 (2017)
  46. M.Z. Jacobson, M.A. Delucchi, G. Bazouin, Z.A. Bauer, C.C. Heavey, E. Fisher, T.W. Yeskoo, 100% Clean and renewable wind, water, and sunlight (WWS) all-sector energy roadmaps for the 50 United States. *Energ. Environ. Sci.* **8**(7), 2093–2117 (2015)
  47. V. Devabhaktuni, M. Alam, S.S.S.R. Depuru, R.C. Green, D. Nims, C. Near, Solar energy: trends and enabling technologies. *Renew. Sust. Energ. Rev.* **19**, 555–564 (2013)
  48. S.C. Mayotte, V. Rao, C.E. Lindhjem, M.S. Sklar, Reformulated gasoline effects on exhaust emissions: phase II: continued investigation of the effects of fuel oxygenate content, oxygenate type, volatility, sulfur, olefins and distillation parameters (no. 941974). SAE technical paper (1994), <http://papers.sae.org/941974/>
  49. A.A. Keller, L.F. Fernandez, S. Hitz, H. Kun, A. Peterson, B. Smith, M. Yoshioka, An integral cost-benefit analysis of gasoline formulations meeting California phase II reformulated gasoline requirements. UC TSR&TP Report to the Governor of California (1998), <http://citeseerx.ist.psu.edu/viewdoc/download?doi=10.1.1.15.9224&rep=rep1&type=pdf>
  50. F.E. Ahmed, Toxicology and human health effects following exposure to oxygenated or reformulated gasoline. *Toxicol. Lett.* **123**(2), 89–113 (2001)
  51. R.E. Morris, Y. Jia, The impact of biodiesel fuels on air quality and human health: task 4 report (2003), [http://biodiesel.org/reports/20030501\\_gen-365.pdf](http://biodiesel.org/reports/20030501_gen-365.pdf)
  52. M. Strum, R. Scheffe, A national review of ambient air toxics observations. *J. Air Waste Manage. Assoc.* **66**(2), 120–133 (2016)
  53. W.R. Hartley, A.J. Englande, D.J. Harrington, Health risk assessment of groundwater contaminated with methyl tertiary butyl ether (MTBE). *Water Sci. Technol.* **39**(10–11), 305–310 (1999)
  54. A.A. Meharg, in *Ecological Impact of Major Industrial Chemical Accidents*, ed. by G.W. Ware. Reviews of Environmental Contamination and Toxicology (Springer, New York, 1994), pp. 21–48
  55. P. Brimblecombe, The clean air act after 50 years. *Weather* **61**(11), 311–314 (2006)
  56. T.R. Fanshawe, P.J. Diggle, S. Rushton, R. Sanderson, P.W.W. Lurz, S.V. Glinianaia, T. Pless-Mulloli, Modeling spatiotemporal variation in exposure to particulate matter: a two-stage approach. *Environmetrics* **19**(6), 549–566 (2008)

57. S.M. Bernard, J.M. Samet, A. Grambsch, K.L. Ebi, I. Romieu, The potential impacts of climate variability and change on air pollution-related health effects in the United States. *Environ. Health Perspect.* **109**(Suppl 2), 199–205 (2001)
58. K. Ito, G.D. Thurston, C. Hayes, M. Lippmann, Associations of London, England, daily mortality with particulate matter, sulfur dioxide, and acidic aerosol pollution. *Arch. Environ. Health* **48**(4), 213–220 (1993)
59. C. Ji, S. Wang, Combustion and emissions performance of a hybrid hydrogen–gasoline engine at idle and lean conditions. *Int. J. Hydrog. Energy* **35**(1), 346–355 (2010)
60. T. Johnson, Diesel engine emissions and their control. *Platin. Met. Rev.* **52**(1), 23–37 (2008)
61. IEA, *CO<sub>2</sub> Emissions from Fuel Combustion 2012* (OECD Publishing, Paris, 2012), <http://www.pbl.nl/en/publications/2012/co2-emissions-from-fuel-combustion-2012-edition>
62. J. Conti, P. Holtberg, International energy outlook 2011. US energy information administration, (EIA) (2011), [https://www.iea.org/publications/freepublications/publication/WEO2011\\_WEB.pdf](https://www.iea.org/publications/freepublications/publication/WEO2011_WEB.pdf)
63. Global Energy Statistical Yearbook, (2016), <https://yearbook.enerdata.net/energy-consumption-data.html>
64. M. Asif, T. Muneer, Energy supply, its demand and security issues for developed and emerging economies. *Renew. Sust. Energ. Rev.* **11**(7), 1388–1413 (2007)
65. M.A. Delucchi, J.J. Murphy, US military expenditures to protect the use of Persian Gulf oil for motor vehicles. *Energ. Policy* **36**(6), 2253–2264 (2008)
66. The Economist, The Trump administration's trade strategy is dangerously outdated (2017), <http://www.economist.com/news/finance-and-economics/21717998-it-will-be-hard-deal-china-today-if-it-were-japan-1980s-trump>
67. D.J. Hirschfeld, Trump sends NAFTA renegotiation notice to congress (2017), [https://www.nytimes.com/2017/05/18/us/politics/nafta-renegotiation-trump.html?\\_r=0](https://www.nytimes.com/2017/05/18/us/politics/nafta-renegotiation-trump.html?_r=0)
68. A. Heshmati, Demand, customer baseline and demand response in the electricity market: a survey. *J. Econ. Surv.* **28**(5), 862–888 (2014)
69. IEA, *Energy Technology Perspectives 2012* (OECD Publishing, Paris, 2012) [https://www.iea.org/publications/freepublications/publication/ETP2012\\_free.pdf](https://www.iea.org/publications/freepublications/publication/ETP2012_free.pdf)
70. E. Martinot, J. Sawin, Renewables global status report. Renewables 2012 Global Status Report, REN21 (2012), [http://www.martinot.info/REN21\\_GSR2012.pdf](http://www.martinot.info/REN21_GSR2012.pdf)
71. S. Ölz, Renewable energy policy considerations for deploying renewables (2011), [http://environmentportal.in/files/file/Renew\\_Policies.pdf](http://environmentportal.in/files/file/Renew_Policies.pdf)
72. L. Wu, S. Liu, D. Liu, Z. Fang, H. Xu, Modeling and forecasting CO<sub>2</sub> emissions in the BRICS (Brazil, Russia, India, China, and South Africa) countries using a novel multi-variable gray model. *Energy* **79**, 489–495 (2015)
73. V. Bosetti, J. Frankel, Politically feasible emissions targets to attain 460 ppm CO<sub>2</sub> concentrations. *Rev. Environ. Econ. Policy* **6**(1), 86–109 (2012)
74. K.S. Lackner, A guide to CO<sub>2</sub> sequestration. *Science* **300**(5626), 1677–1678 (2003), <http://science.sciencemag.org/content/300/5626/1677>
75. F.T. Bacon, T.M. Fry, Review lecture: the development and practical application of fuel cells. *Proc. R. Soc. Lond. A. Math. Phys. Eng. Sci.* **334**(1599), 427–452 (1973)
76. M. Warshay, P.R. Prokopius, The fuel cell in space: yesterday, today and tomorrow. *J. Power Sources* **29**(1–2), 193–200 (1990)
77. K.V. Kordesch, 25 Years of fuel cell development/1951–1976. *J. Electrochem. Soc.* **125**, 77 (1978)
78. K.C. Tangri, U.S. Patent No. 4,085,709, U.S. Patent and Trademark Office, Washington, DC (1978), <https://www.google.com/patents/US4085709>
79. W. Surdoval, US DOE fossil energy fuel cell program. *ECS Trans.* **7**(1), 11–15 (2007)
80. M.C. Williams, J.P. Strakey, W.A. Surdoval, The US Department of Energy, the office of fossil energy stationary fuel cell program. *J. Power Sources* **143**(1), 191–196 (2005)
81. S. Gottesfeld, T.A. Zawodzinski, Polymer electrolyte fuel cells. *Adv. Electrochem. Sci. Eng.* **5**, 195–302 (1997)



82. D.E. Curtin, R.D. Lousenberg, T.J. Henry, P.C. Tangeman, M.E. Tisack, Advanced materials for improved PEMFC performance and life. *J. Power Sources* **131**(1), 41–48 (2004)
83. S. Gronich, 2010–2025 Scenario analysis (2010), [https://energy.gov/sites/prod/files/2014/03/fl0/gronich\\_scenario\\_analysis.pdf](https://energy.gov/sites/prod/files/2014/03/fl0/gronich_scenario_analysis.pdf)
84. J. Rodriguez, P.X. Thivel, E. Puzenat, Photocatalytic hydrogen production for PEMFC supply: a new issue. *Int. J. Hydrog. Energy* **38**(15), 6344–6348 (2013)
85. S. Satyapal, J. Petrovic, C. Read, G. Thomas, G. Ordaz, The US Department of Energy's National Hydrogen Storage Project: progress towards meeting hydrogen-powered vehicle requirements. *Catal. Today* **120**(3), 246–256 (2007)
86. J.J. Winebrake, B.P. Creswick, The future of hydrogen fueling systems for transportation: an application of perspective-based scenario analysis using the analytic hierarchy process. *Technol. Forecast. Soc. Chang.* **70**(4), 359–384 (2003)
87. D. Garraín, Y. Lechón, C. de la Rúa, Polymer electrolyte membrane fuel cells (PEMFC) in automotive applications: environmental relevance of the manufacturing stage. *Smart Grid Renew. Energy* **2**(2), 68–72 (2011)
88. B. Ibeh, C. Gardner, M. Ternan, Separation of hydrogen from a hydrogen/methane mixture using a PEM fuel cell. *Int. J. Hydrog. Energy* **32**(7), 908–914 (2007)
89. A. Emadi, K. Rajashekara, S.S. Williamson, S.M. Lukic, Topological overview of hybrid electric and fuel cell vehicular power system architectures and configurations. *IEEE Trans. Veh. Technol.* **54**(3), 763–770 (2005)
90. S. Kawasaki, M. Ogura, T. Ono, Y. Kami, Development of the HONDA FCX fuel cell vehicle. *Honda R&D Tech. Rev.* **15**(1), 1–6 (2003)
91. B.C. Steele, A. Heinzl, Materials for fuel-cell technologies. *Nature* **414**(6861), 345–352 (2001), <https://www.nature.com/nature/journal/v414/n6861/full/414345a0.html>
92. D. Chu, R. Jiang, Performance of polymer electrolyte membrane fuel cell (PEMFC) stacks: part I. Evaluation and simulation of an air-breathing PEMFC stack. *J. Power Sources* **83**(1), 128–133 (1999)
93. L. Nguyen, F. Mighri, Y. Deyrail, S. Elkoun, Conductive materials for proton exchange membrane fuel cell bipolar plates made from PVDF, PET and co-continuous PVDF/PET filled with carbon additives. *Fuel Cells* **10**(6), 938–948 (2010)
94. V. Mehta, J.S. Cooper, Review and analysis of PEM fuel cell design and manufacturing. *J. Power Sources* **114**(1), 32–53 (2003)
95. H. Zhang, P.K. Shen, The recent development of polymer electrolyte membranes for fuel cells. *Chem. Rev.* **112**(5), 2780–2832 (2012)
96. S. Zhang, X. Yuan, H. Wang, W. Mérida, H. Zhu, J. Shen, J. Zhang, A review of accelerated stress tests of MEA durability in PEM fuel cells. *Int. J. Hydrog. Energy* **34**(1), 388–404 (2009)
97. J.P. Breen, J.R. Ross, Methanol reforming for fuel cell applications: development of zirconia-containing Cu–Zn–Al catalysts. *Catal. Today* **51**(3), 521–533 (1999)
98. S. Velu, K. Suzuki, M. Okazaki, M.P. Kapoor, T. Osaki, F. Ohashi, Oxidative steam reforming of methanol over CuZnAl (Zr)-oxide catalysts for the selective production of hydrogen for fuel cells: catalyst characterization and performance evaluation. *J. Catal.* **194**(2), 373–384 (2000)
99. S. Zhang, Y. Shao, G. Yin, Y. Lin, Recent progress in nanostructured electrocatalysts for PEM fuel cells. *J. Mater. Chem. A* **1**(15), 4631–4641 (2013)
100. Y. Yuan, J.A. Smith, G. Goenaga, D.J. Liu, Z. Luo, J. Liu, Platinum-decorated aligned carbon nanotubes: electrocatalyst for improved performance of proton exchange membrane fuel cells. *J. Power Sources* **196**(15), 6160–6167 (2011)
101. S. Shimpalee, U. Beuscher, J.W. Van Zee, Analysis of GDL flooding effects on PEMFC performance. *Electrochim. Acta* **52**(24), 6748–6754 (2007)
102. K. Goto, I. Rozhanskii, Y. Yamakawa, T. Otsuki, Y. Naito, Development of aromatic polymer electrolyte membrane with high conductivity and durability for the fuel cell. *Polym. J.* **41**(2), 95–102 (2009)
103. Honda R&D Technical Review provided by Honda Patents & Technologies North America, LLC, 3, 1–10 (2009)

104. M. Matsunaga, T. Fukushima, K. Ojima, Powertrain system of Honda FCX Clarity fuel cell vehicle. *World Electr. Veh. J.* **3**, 1–10 (2009)
105. B.D. James, A.B. Spisak, Mass production cost estimation of direct H<sub>2</sub> PEM fuel cell systems for transportation applications: 2012 update. Report by Strategic Analysis, Inc., under award number DEEE0005236 for the US Department of Energy, vol. 18 (2012), pp. 1–186, [https://energy.gov/sites/prod/files/2014/11/f19/fcto\\_sa\\_2013\\_pemfc\\_transportation\\_cost\\_analysis.pdf](https://energy.gov/sites/prod/files/2014/11/f19/fcto_sa_2013_pemfc_transportation_cost_analysis.pdf)
106. Y. Orbach, G.E. Fruchter, Forecasting sales and product evolution: the case of the hybrid/electric car. *Technol. Forecast. Soc. Chang.* **78**(7), 1210–1226 (2011)
107. B. Nykvist, M. Nilsson, Rapidly falling costs of battery packs for electric vehicles. *Nat. Clim. Chang.* **5**(4), 329–332 (2015)
108. J.B. Stronberg, Renewable Energy Tax Credits in the Age of Trump (Civil Notion, 2017). <https://civilnotionblog.weebly.com/home/renewable-energy-tax-credits-in-the-age-of-trump>
109. A. Walker, M. Galea, C. Gerada, A. Mebarki, D. Gerada. A topology selection consideration of electrical machines for traction applications: towards the FreedomCar 2020 targets. In *Ecological Vehicles and Renewable Energies (EVER)*, 2015 Tenth International Conference on IEEE (2015), pp. 1–10, <http://ieeexplore.ieee.org/document/7112923/>



# Concept of Hydrogen Redox Electric Power and Hydrogen Energy Generators

# 2

Katsutoshi Ono

## Contents

2.1	Introduction .....	28
2.2	Theoretical Backgrounds .....	29
2.2.1	“Zero Power Input” Electrostatic Field .....	29
2.2.2	Theoretical Power Requirement of Water Electrolysis .....	33
2.2.3	Direct Electrostatic-to-Chemical Energy Conversion in Water Electrolysis .....	33
2.3	Electrostatic-Induction Potential-Superposed Water Electrolysis .....	36
2.3.1	Principle .....	36
2.4	Hydrogen Redox Electric Power and Hydrogen Energy Generators .....	40
2.4.1	Suggested Generators .....	40
2.4.2	Hydrogen Redox Electric Power Generator (HREG) .....	40
2.4.3	Hydrogen Redox Hydrogen Energy Generator .....	44
2.5	Theories of the Onboard HREG System for Fuel Cell Vehicles with Infinite Cruising Range .....	44
2.5.1	Outline of the Onboard HREG System .....	44
2.5.2	Basic Equations for Infinite Cruising Range .....	46
2.5.3	Weight Evaluation of the Onboard HREG System .....	49
2.6	Conclusion .....	50
	References .....	50

## Abstract

The purpose of this paper is to review the hydrogen redox electric power and hydrogen generation systems (HREG). It offers considerable conceptual advantage such that it functions with zero energy input, zero matter input, and zero emission

## Author Contribution

KO conceived and wrote the entire manuscript, as well as edits and revisions.

K. Ono (✉)

Department of Energy Science and Technology, Kyoto University, Kyoto, Japan

e-mail: [ono6725@tg8.so-net.ne.jp](mailto:ono6725@tg8.so-net.ne.jp)

without violating the laws of thermodynamics. Its application ranges from the large-scale central station power generation down to the small-scale onboard power generation system for electric vehicles with infinite cruising range. The hydrogen redox hydrogen generator also works with zero power input. To attain a highly positive energy balance, the advantage was taken of the electrostatic energy that appears in the water electrolysis when a constant static voltage is applied across parallel electrodes. A feature and an essential part of these generators are then the electrostatic-to-chemical energy conversion in the water electrolysis. The method proposed here for supplying energy to the electrolytic cell, which has been termed electrostatic-induction potential-superposed electrolysis (ESI-PSE), theoretically reduces the power requirement for water electrolysis down to 17% of the total energy required. If the ESI-PSE electrolyzer, which delivers pure stoichiometric  $\text{H}_2\text{-O}_2$  fuel for a fuel cell, is combined with a fuel cell to form an energy cycle, then this may lead to the concepts of hydrogen redox electric power and hydrogen energy generators. According to the calculations using the data of operational conditions for the commercial electrolyzers and fuel cells, more than 70% of the power delivered from the fuel cell can be extracted outside the cycle as net power output. Because of the simplicity, effectiveness, cleanliness, and self-exciting, these novel generators may offer a potential route for its practical application to the electricity and hydrogen production systems of the future. In addition, attempts were made to examine the possibilities of the onboard HREG system for an infinite cruising range of regular passenger cars.

---

## 2.1 Introduction

This energy cycle can be viewed as a two-stage generator that consists of two different energy conversion devices. The hydrogen generation device is an electrostatic-induction potential-superposed electrolytic cell that enables the  $\text{H}_2\text{O} \rightarrow \text{H}_2 + \frac{1}{2}\text{O}_2$  reduction reaction, based on electrical-to-chemical energy conversion. The power-producing device is a fuel cell in which the reverse reaction occurs, i.e., the  $\text{H}_2 + \frac{1}{2}\text{O}_2 \rightarrow \text{H}_2\text{O}$  oxidation reaction, based on chemical-to-electrical energy conversion. Part of the power generated by the fuel cell is returned to the ESI-PSE water electrolytic cell, and the remainder represents the net power output. In addition to cycling the generated power,  $\text{H}_2\text{O}$ , which contains heat from the exothermic reaction in the fuel cell, is transferred to the electrolytic cell to be utilized for the endothermic reaction. The problem is how to achieve a highly positive power balance for this cycle, such that more than 70% of the power delivered from the fuel cell can be extracted outside the cycle as net power output. If a process is thermodynamically reversible, then the amount of electrical energy delivered by the fuel cell must equal the amount of electrical energy required by the electrolytic cell for a given  $\text{H}_2$  circulation rate. However, the electrical energy delivered by the fuel presents self-sustaining electric power generation cycle to be successful. This electrical power generation system is based on a thermodynamic cycle where the electrical energy

delivered by the fuel cell is the total power, whereas the electrical energy required by the ESI-PSE electrolyzer specifically for electrolytic decomposition of a chemically stable compound such as  $\text{H}_2\text{O}$  is mainly electrostatic energy free of power: theoretically, 82% of the total energy, i.e., the standard enthalpy change required for the reduction of  $\text{H}_2\text{O}$ , is the electrostatic energy for which the outside voltage source is not required to provide power, only a static voltage. To carry out the direct electrostatic-to-chemical energy conversion free of power in water electrolysis, and thus achieve a highly positive power balance of the energy cycle, attempts have been made to connect an external energy supply circuit based on the ESI-PSE mode to the electrodes of water electrolytic cells [1–3]. The experimental verification of the ESI-PSE has been performed and reported previously [3]. In this paper, we intend to address:

1. The theoretical foundation for the alternative energy supply system to be connected to the electrodes of typical water electrolytic cells and the performance of the system in the cell undergoing electrolysis. Most of the interest has centered on the field of electrostatic-to-chemical energy conversion. This field largely depends on the fundamental theories proposed by Guggenheim [4–6] and later Christopher and Shipman [7].
2. Principle and performance of the electrostatic-induction potential-superposed water electrolysis.
3. The system design concept of the combined energy cycle consisting of an existing bipolar water electrolyzer and fuel cell.
4. Simulation of the hydrogen redox electric power generator using the operational condition data for commercially available electrolyzers and fuel cells.
5. The onboard hydrogen redox electric power propulsion system for regular passenger cars to achieve infinite driving range.

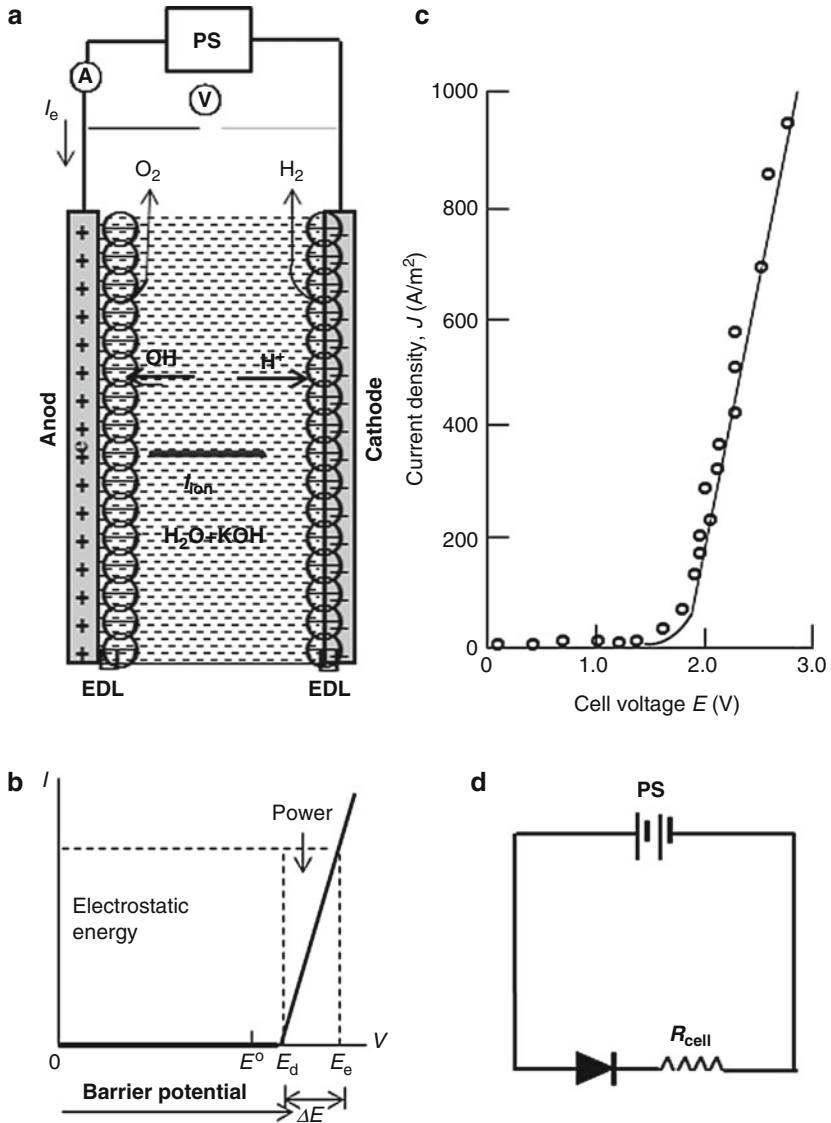
---

## 2.2 Theoretical Backgrounds

### 2.2.1 “Zero Power Input” Electrostatic Field

The nature and mechanism of the electrolysis are absolute and, thus, unchangeable, but the electrical energy supply mode can be changed. To find a solution for ultimate reduction in the power requirement of the water electrolysis, it is essential to have a clear understanding of the theories forming the basic aspects of the standard water electrolytic processes.

Figure 2.1a shows how the alkaline water electrolytic cell works. The nonlinear  $V$ - $I$  characteristic curve for a practical water electrolytic cell typically shows the amount of current measured at the point between the cell and the power supply as a function of cell voltage (voltage between the electrodes), as seen in the schematic  $V$ - $I$  curve (Fig. 2.1b). In the voltage range over the practical decomposition voltage  $E_d$ , the external current flows due to the electrode reactions between electrons and ions in the cell are the total power, whereas the electrical energy specifically required by the electrolytic cell for electrolytic decomposition of a chemically stable compound



**Fig. 2.1** Standard water electrolysis in operation. **(a)** Structure of standard alkaline water electrolysis. Electrical double layer (EDL);  $I_e$ , electrolytic current (A);  $I_{ion}$ , current in electrolyte due to the migration of ions (A); **(b)** generalized voltage-current characteristic curve.  $E^0$  (V), theoretical decomposition voltage;  $\Delta E$ , extra applied voltage over  $E_d$  (V); **(c)** measured  $V$ - $I$  curve; and **(d)** ideal model of the electrolytic cell as a forward biased diode

such as  $\text{H}_2\text{O}$  is essentially electrostatic energy. The process occurring in the voltage range less than  $E_d$  is called *nonfaradaic process* exerted by the electrostatic energy: the behavior of the electrode-electrolyte interface is analogous to that of a capacitor [8]. Therefore, the amount of energy stored is given by Eq. 2.1:

$$W = (1/2)CE^2 \quad (2.1)$$

where  $C$  is the capacitance and  $E$  is the inter-electrode voltage. In the case of the water electrolysis, the capacitive energy is stored specifically in the electrical double layers. In the consecutive region where practical electrolysis occurs, the current increases in an almost linear relationship with the applied voltage, as evidenced experimentally (Fig. 2.1c). The experimental method is outlined as follows. The electrolytic cell, which was made of acrylic resin, contained four  $62 \times 40$  mm electrodes, 0.5 mm thick, made of rectangular stainless steel sheets. These were set in parallel and fixed to the side wall and the bottom of the tank. The electrodes formed two walls of a square channel, with insulators forming the other two walls. The distance between the cell electrodes was 20 mm. No diaphragm to prevent a back reaction of hydrogen with oxygen was used because the present study was not concerned with current efficiency. The maximum voltage was applied to the field generator electrodes so that if there were any opening in the inner cell electrode plates, an unexpected leakage of current would occur. An  $\text{H}_2\text{O}$ -10 % NaOH at 300 K was selected as the electrolyte common to all tests.

An electrolytic cell is essentially an electrical device used as an electrical circuit element; it consists of two metallic electrode plates separated by an electrolyte solution. This is the model for standard single-voltage source electrolysis (SSE). Water electrolysis to produce  $\text{H}_2$  and  $\text{O}_2$  normally uses an aqueous solution containing the conducting ionic species  $\text{H}^+$  and  $\text{OH}^-$ . Its electronic behavior as a circuit element can be represented by a nonlinear  $V$ - $I$  characteristic curve, shown in Fig. 2.1b, in its generalized form, neglecting the residual background current and assuming a linear line in the voltage range greater than  $E_d$ . The null-current voltage in the range from 0 to  $E_d$  contributes to a major portion of the total applied voltage,  $E_c$ . Once the voltage reaches  $E_d$ , the current begins to increase drastically.  $E_d$  is then the upper limit of the voltage where no current flows in the external circuit.

The  $V$ - $I$  curve implies that the total cell voltage  $E_c$  is the superposition of two separate voltages: (1) the practical decomposition voltage,  $E_d$ , and (2) the additional applied voltage  $\Delta E$ , which, when superposed on  $E_d$ , yields the electrolytic current;  $\Delta E$  is then identified with the electromotive force (*emf*) for the current,  $I_c$ , to flow in the external circuit. The relationship between the amount of current and the amount of  $\text{H}_2$  and  $\text{O}_2$  produced is given by the Faraday law, that is, the passage of  $2F$  coulombs produces 1 mole of  $\text{H}_2$  at the negative electrode (cathode) and one-half mole of  $\text{O}_2$  at the positive electrode (anode), where  $F$  is the Faraday constant ( $\text{C}\cdot\text{mol}^{-1}$ ). Because the decomposition voltage  $E_d$  is an upper limit to the null-current static condition, it may be identified with the barrier potential [9–12]. The  $V$ - $I$  behavior of the electrolytic cell may be approximated by that of a forward biased diode, as shown in Fig. 2.1d.

When the forward voltage reaches the barrier potential,  $E_d$ , the current begins to increase.

During electrolysis, the voltage source external to the electrolytic cell must supply a voltage  $E_e$  given by Eq. 2.2:

$$E_e = E_d + \Delta E \quad (2.2)$$

When  $I_e$  flows, owing to a total applied voltage of  $E_e$ , the product ( $I_e E_e$ ) represents the total power that the voltage source is required to provide (W). The value of this power depends on the value of  $E_d$ , as expressed by Eq. 2.3:

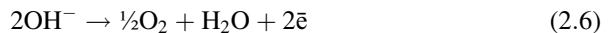
$$P_{el} = I_e(E_d + \Delta E) \quad (2.3)$$

The first term  $I_e E_d$  represents the energy provided by the source to the current to overcome the barrier potential. The current  $I_e$  flows because of the *emf*  $\Delta E$ , not  $E_d + \Delta E$ , so that the second term  $I_e \Delta E$  is the electrical power consumed in the cell. Thus, the electrical energy required by the SSE is the total power. The process occurring at the voltage corresponding to the barrier potential is related to the internal energy creation and storage under a constant electrostatic field established between the electrodes impressed at  $E_d$ ; the internal energy becomes maximum so that  $H_2O$  is placed in the decomposition state: the energy created and stored becomes maximum. The water enters the decomposition state represented by the reaction



where  $H^+$  and  $OH^-$  represent the ions in the fully charged double layer at the negative and positive electrode, respectively. Because the cell carries out the internal energy creation without delivering current to the external circuit, the voltage source does not need to provide power, the just voltage to place the water in the decomposition state.

During electrolysis, the entire process is governed by the mass-transfer mechanism. When an extra voltage  $\Delta E$  additional to  $E_d$  is applied to the cell, it produces an external current,  $I_e$ , according to the charge-transfer reactions between the ions in the decomposition state and electrons on the electrodes:



If a half-cell is considered, as  $H_2$  leaves from the electrode/solution interface because of  $\Delta E$ , a flux of  $H^+$  ions always occurs from the bulk solution to fully charge the EDL by migration resulting from the Coulomb force exerted by the electrostatic field established between the electrodes at the potential of  $E_d$ . Thus, at any time during electrolysis, internal energy is continuously created. Because, in this potential condition, the ion migration contributes to the current only within the solution phase, and electrons cannot cross the interface, this process does not generate any current in the external circuit, and thus no power is needed. Therefore, this kinetic process may



be defined as continuous energy creation. The entire electrolytic process is then characterized by the superposition of two elementary processes: continuous energy creation in the solution and charge-transfer reactions at the electrode-electrolyte interfaces.

### 2.2.2 Theoretical Power Requirement of Water Electrolysis

According to the thermodynamic data at 300 K,  $\Delta G^\circ = 237 \text{ kJ/mol}\cdot\text{H}_2$  [13], and the total energy change (enthalpy change) is  $\Delta H^\circ = 286 \text{ kJ/mol}\cdot\text{H}_2$ . Hence, theoretically, 83 % of the total energy required for the electrolytic reduction of  $\text{H}_2\text{O}$  is the electrostatic energy for which the outside voltage source is not required to provide power, only voltage. The reason that the highly efficient HREG may be feasible is that the real power requirement of water electrolysis is only 17% of total energy requirement if the reversible process is assumed. Because the ion-conducting process in the electrolyte occurs in the absence of power, the power supply external to the cell only provides the energy for the electronic conduction external to the cell. The cell voltage  $E_c$  is the superposition of  $\Delta E$  on  $E_d$ , and the entire corresponding electrolytic process is the superposition of the charge-transfer process where  $\Delta E$  is applied (i.e., where power is used) on the electrostatic process where  $E_d$  is applied (i.e., where power is not used). If the current  $2F$  flows to produce 1 mole of  $\text{H}_2$  and one-half mole of  $\text{O}_2$ , and because the current efficiency is known from experimental evidence to be near unity, the net power requirement reduces to the generalized form for any given cell, regardless of the decomposition voltage  $E_d$ , temperature, pressure, composition of solution, and cell dimension:

$$P_{\text{el}}^* = 2F\Delta E \quad (2.7)$$

where  $F$  is the Faraday constant ( $\text{C}\cdot\text{mol}^{-1}$ ). It is expected, therefore, that the barrier potential effect can be avoided by means of an alternative power supply mode.

### 2.2.3 Direct Electrostatic-to-Chemical Energy Conversion in Water Electrolysis

The essential part of the HREG system is the electrostatic-to-chemical energy conversion in the water electrolysis. Because this power-free electrostatic energy is the original source of the net power output from the HREG system, it is indispensable, therefore, to prove theoretically that this electrostatic process does not use power but only the static voltage between the electrodes. For this purpose, it must be shown that the free energy change of the  $\text{H}_2\text{O}$  decomposition reaction is related to the power-free electrostatic field strength  $E$ . During electrolysis, the power supply does not need to provide power, but merely voltage to the electrodes for the ionic current to flow in the electrolyte solution between the electrodes. It is essential to clarify theoretically the presence of the power-free electrostatic

energy when undergoing electrolysis. The null-current voltage range from 0 to  $E_d$  contributes to a major portion of the total applied voltage,  $E_e$ . If alkaline water electrolysis is assumed, then at  $V = E_d$  the reversible cell enters the decomposition state represented by the half reactions that occur at the negative and positive electrodes, which correspond to Eqs. 2.5 and 2.6, respectively. If this process proceeds reversibly without the production of current in the circuit external to the cell, then the net gain in energy of  $H_2O$  from the constant electrostatic field is given by the Gibbs free energy change of the reaction,  $H_2O = H_2 + \frac{1}{2}O_2$ , and related to  $E_d$  as  $\Delta G = 2FE_d$ .

The electrostatic energy is directly converted to the chemical energy of the electrolyte solution, and water is placed in the decomposition state. The direct electrostatic-to-chemical energy conversion may then be proved as follows. The Gibbs free energy  $G$  represents the chemical energy stored because  $G$  is a thermodynamic quantity that is responsible for the mutual energy conversion with electrical energy (J).  $G$  is typically a function of independent parameters, the temperature (K), the pressure (Pa), and the mole number of ions ( $NJ$ ), present in the electrolyte solution [14]. If an electrostatic field is present (V/m), then the charge on the electrode  $Q$  ( $C$ ) must be added as one of the independent parameters [6]:

$$G = G(T, P, n_j, Q) \quad (2.8)$$

The differential of  $G$  takes the form;

$$dG = (\partial G/\partial T)dT + (\partial G/\partial P)dP + (\partial G/\partial n_j)dn_j + (\partial G/\partial Q)dQ \quad (2.9)$$

Since  $dT = dP = dn_j = 0$  and  $(\partial G/\partial Q) = V$  ( $V$ , potential difference between the electrodes), Eq. 2.9 reduces to

$$dG = VdQ \quad (2.10)$$

If we let  $L$  be the inter-electrode distance,  $A$  the electrode surface area, and  $v$  the volume of the field (i.e., the volume of the electrolyte solution), then  $LA = v$ . By definition,  $V = LE$ ,  $Q = AD$ , and  $D = \epsilon E$  where  $E$  is the electric field strength,  $D$  is the electric displacement, and  $\epsilon$  is the permittivity. Using these relations, Eq. 2.10 is reformed to

$$dG = v\epsilon EdE \quad (2.11)$$

Integration of Eq. 2.11 with respect to  $E$  from 0 where the field is not present (i.e.,  $E = 0$  and  $G = 0$ ) to  $E$  where the field is present gives the equation for quasi-static energy conversion:

$$\Delta G = (1/2)v\epsilon ED = (1/2)v\epsilon E^2. \quad (2.12)$$

$\Delta G$  becomes a function of  $E$  alone; fixing  $E$  within the stability range of the electrolyte solution fixes its equilibrium state. Equation 2.12 suggests that in the

presence of a time-invariant electrostatic field, the spontaneous increase in the chemical energy of species present in an electrolyte solution is thermodynamically favorable.

The electrostatic field,  $E$ , is defined in one-dimensional form as

$$E = -(\partial\varphi/\partial x), \quad (2.13)$$

where  $\varphi$  is the electrical potential. Coulomb's law describes the interaction force between two statically charged particles,  $Q_1$  and  $Q_2$ . In its scalar form, the law is

$$F = Q_1Q_2/4\pi\epsilon r^2, \quad (2.14)$$

where  $r$  is the distance between the charges and  $\epsilon$  is the permittivity of the medium considered. If  $Q_1$  is the static charge on an electrode and  $Q_2$  is an ion in an electrolyte solution, then the ion experiences a force at a distance and migrates through the electrolyte under the influence of an electrostatic field. Here we show the definitive evidence indicating the existence of the power-free electrostatic energy. When undergoing electrolysis, the free electrons flow exclusively through the power supply, and the conducting lead wires and electrodes, inducing the electronic current  $I_e$ . No electronic conduction is allowed in the electrolyte solution where the ionic current,  $I_{\text{ion}}$ , is induced by the migration of ions. The  $I_{\text{ion}}$  in the electrolyte flows as a result of the constant electric field generated by the time-invariable potential difference between the electrodes. The power-free electrostatic energy created in the electrolyte across the electrodes is also observed when a fuel cell operates. When  $H_2$  and  $O_2$  are applied to the anode and cathode, respectively, a voltage is invested between the electrodes as a result of chemical-to-electrical energy conversion reaction. It is important to note that a fuel cell provides the electric power originated from the chemical energy of fuel exclusively to the load: it does not provide power for the ion transfer process that occurs in the electrolyte but provides electrostatic energy. Thus, it can be seen that the electrostatic field established by the static charges on the electrodes is an internally self-sustaining energy source. In other words, because the free energy change of the hydrogen burning reaction is totally converted into the electrical power produced in the load outside the cell, the power is not used for the ion transfer process in the cell. In addition, the ionic current flowing in the electrostatic field induced by a constant potential difference between electrodes is typically formulated as a function of the electrostatic field [8, 15–17]:

$$I_{\text{ion}} = Az^2F^2nv(-\partial\varphi/\partial x), \quad (2.15)$$

where  $A$  is the electrode surface area ( $\text{cm}^2$ ),  $z$  is the number of charges,  $F$  is the Faraday constant ( $\text{C}\cdot\text{mol}^{-1}$ ),  $n$  is the number of moles of ions per unit volume, and  $v$  is the ion migration velocity ( $\text{C}\cdot\text{s}^{-1}$ ). This also implies that the ionic current flows under the influence of the electrostatic field in the absence of power.

## 2.3 Electrostatic-Induction Potential-Superposed Water Electrolysis

### 2.3.1 Principle

The method termed ESI-PSE supplies potentials to the electrodes in a dual mode as shown in Fig. 2.2a, i.e., the superposition of two voltages on the electrodes with two independent voltage sources; one is a bias voltage source (PS1), which induces  $E_d$  at the cell electrodes, and the other is a power supply (PS2), which provides power to the cell. Figure 2.2b shows how the system works, and Fig. 2.2c is an equivalent closed circuit with two voltage sources connected in opposing directions. These sources can act in parallel independently, and supply the cell electrodes with individual potentials, which yields a superposition such that the resulting voltage between the cell electrodes equals the magnitude of the algebraic sum of the individual potential, i.e.,  $E_d + \Delta E$ . The performance of the cell can be explained by a series of steps. Firstly, when the PS2 output voltage  $V_{PS2} = E_d$ ,  $I = 0$  (null point) because of the usual condition of uniformity of the electrochemical potential throughout the electrolyte solution [7]. Secondly, if  $V_{PS2}$  is increased from the null point, then an electrolytic current  $I = I_c$  flows due to the total source voltage (*emf*) of  $\Delta E = V_{PS2} - E_d$ . Hence, the two sources can be replaced by a single source that delivers  $\Delta E$ , according to the superposition theorem of dc circuit [9, 18]. The bias voltage source does not need to produce electrical current, but only a static voltage because of the null-current condition at  $E_d$ . The total power requirement is then given by Eq. 2.7.

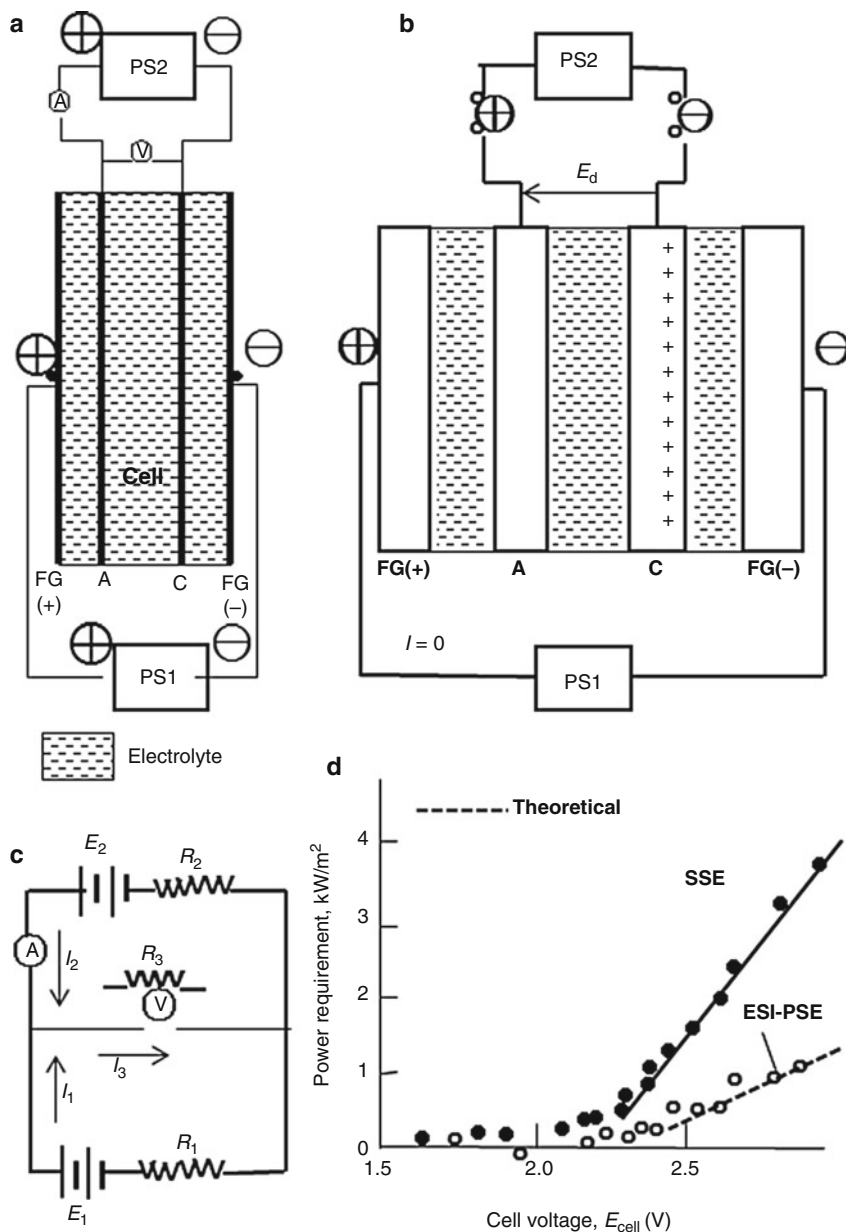
Equation 2.7 can also be obtained by numerical analysis using the superposition theorem of dc circuit. Equivalent network when the cell is undergoing electrolysis with current flowing is represented in Fig. 2.2c in the generalized form. To evaluate the currents and voltages, we impose the notations,  $E_1$ ,  $E_2$ ,  $R_1$ , and  $R_2$  for the field-induced decomposition voltage, the output voltage of PS2, the cell resistance, and the internal resistance of the voltmeter, respectively, as depicted in Fig. 2.2c. The branch currents are given by the following equations [18]:

$$I_1 = \frac{(R_3 + R_2)E_1 - R_3E_2}{R_1R_3 + R_3R_2 + R_2R_1} \quad (2.16)$$

$$I_2 = \frac{(R_1 + R_3)E_2 - R_3E_1}{R_1R_3 + R_3R_2 + R_2R_1} \quad (2.17)$$

$$I_3 = \frac{R_1 + R_3 + R_3E_1}{R_1R_3 + R_3R_2 + R_2R_1} \quad (2.18)$$

- (1) If  $R_3 \gg R_1$  and  $R_3 \gg R_2$ ,



**Fig. 2.2** Electrostatic-induction potential-superposed electrolysis. **(a)** Cell structure of ESI-PSE: FG, field generator; A, anode; C, cathode. **(b)** Principle of ESI-PSE. PS, power supply; **(c)** equivalent linear network involving two independent voltage sources.  $E_1$ , induced decomposition voltage;  $E_2$ , output voltage of PS2;  $R_1$ , cell resistance;  $R_2$ , internal resistance of the voltmeter;  $R_3$ , internal resistance of PS2; and **(d)**, power requirements as a function of the cell voltage for both SSE and ESI-PSE

$$I_1 = \frac{E_1 - E_2}{R_1 + R_2}, I_3 = 0 \text{ and } I_2 = \frac{E_2 - E_1}{R_1 + R_2}$$

Then  $I_1 = -I_3$ .

(2) If  $R_3 \gg R_1, R_3 \gg R_2$ , and  $E_1 = E_2$ ,

then  $I_1 = I_2 = I_3 = 0$

This situation corresponds to the null point where the electrolytic reaction begins to occur.

(3) If  $R_3 \gg R_1, R_3 \gg R_2$ , and  $E_1 > E_2$ ,

putting  $(E_2 - E_1) = \Delta E$ , we obtain  $I_2(R_1 + R_2) = \Delta E$ . This means that the electrolytic current is driven exclusively by the *emf*,  $\Delta E$ , provided by PS2. The voltage source PS1 does not need to deliver an electrical current, but merely a static voltage because of the null-current condition. Therefore, the electric power required to conduct this electrolysis may be given by Eq. 2.7.

The experimental verification of the ESI-PSE was made by direct power measurements on the power supply circuit external to the cell: the experimental apparatus and procedures are introduced elsewhere [2]. Fig. 2.2d shows the power requirements as a function of cell voltage for both the SSE and ESI-PSE electrolyzers which were measured using the same cell. From Eqs. 2.3 and 2.7, the power requirement relationship between SSE and ESI-PSE is given by

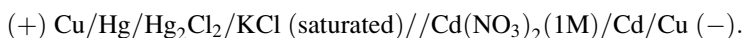
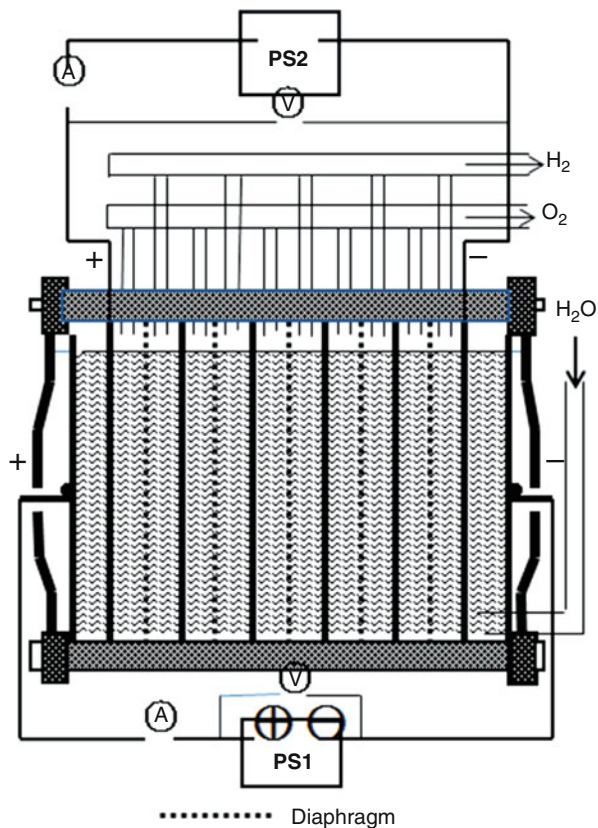
$$P_{\text{el}}^* = [\Delta E / (E_d + \Delta E)] P_{\text{el}}. \quad (2.19)$$

The power requirements for ESI-PSE calculated using Eq. 2.19 are in good agreement with the experimental values.

A single ESI-PSE cell generates a limited amount of  $\text{H}_2$  and  $\text{O}_2$ . In practice, many cells are assembled into a stack, with the principles being the same. For example, the bipolar electrolyzer [19] currently in use in the industry offers considerable advantages, in that it may be used directly with the present cell structure as shown in Fig. 2.3. This is a type of electrostatic-induction electrolyzer, but it remains a barrier potential type electrolyzer. The electrolyzer is typically operated with a single power supply PS1, which is responsible for the total power, i.e., the number of cells times the power per cell,  $I(E_d + \Delta E)$ . To change the power supply mode into the ESI-PSE scheme, it is sufficient to introduce minor modifications as follows. (1) The outermost pair of electrodes is used as a field generator and should be connected to the power supply PS1. (2) The power supply responsible for providing power should be connected to the electrodes next to the field generator electrodes with the opposing polarity depicted there. There is no need for lead wires to take current from each of the inner cells.

The potential-superposed electrolysis may be considered as indicative of the electronic performance of a schematic cell system proposed by Bard and Faulkner [8]:

**Fig. 2.3** Longitudinal cross section through series-connected ESI-PSE cells



The open-circuit potential is 0.64 V. When the power supply is connected to this cell with opposing polarity and when the voltage,  $V_{PS}$ , applied by the external power supply is equal and opposite to the cell voltage (i.e.,  $I = 0$ ) because the circuit electromotive force (*emf*) is zero. At this stage, the dissolved Cd ( $\text{NO}_3)_2$  spontaneously reaches the decomposition equilibrium (i.e.,  $\text{Cd}^{2+} + 2\bar{e} = \text{Cd}$ ). The null-current electrostatic field established by the static electrons on the electrodes imposed at 0.64V spontaneously creates and stores the internal energy within the fully charged electrical double layer. Because of the null-current condition, the power source does not need to provide power but merely a voltage. Therefore, a net energy increase is observed as  $\text{Cd(NO}_3)_2$  changes from the dissolved state to a decomposition state. When  $V_{PS}$  is increased (i.e.,  $\Delta E = V_{PS} - 0.64$ ), the cell behaves as an electrolytic cell in which Cd deposition ( $\text{Cd}^{2+} + 2\bar{e} \rightarrow \text{Cd}$ ) occurs. The system can now be replaced with an equivalent circuit comprising two voltage sources that are in series and exert their voltages in opposing directions. As a result, electrolytic current flow (i.e.,  $I = 2F$ ) owing to an *emf* of magnitude  $\Delta E$  superimposed on a

voltage of 0.64 V. The total power requirement then becomes the same form as Eq. 2.7,  $P = 2F\Delta E$ , independent of 0.64V. Furthermore, Bard and Faulkner showed that because the electrolytic current begins to flow only after the applied voltage exceeds the decomposition voltage  $E_d$ ,  $\Delta E$  is the *emf* (total source voltage) that the external power supply provides to the cell for the Cd deposition reaction to occur at the electrode/solution interface. The induced energy is then recovered in the form of the energy state of pure Cd.

---

## 2.4 Hydrogen Redox Electric Power and Hydrogen Energy Generators

### 2.4.1 Suggested Generators

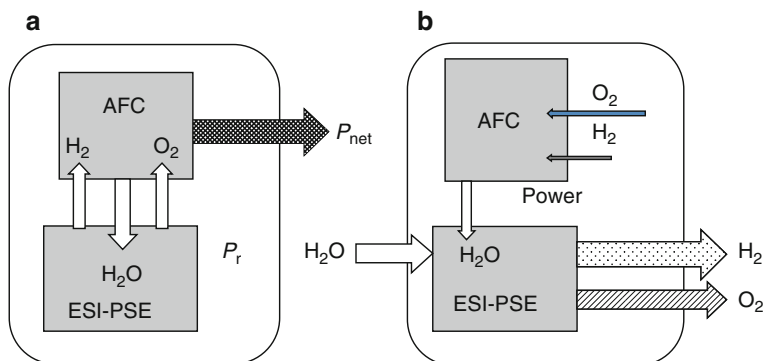
Figure 2.4a and b shows the system designs for hydrogen redox electric power and hydrogen redox hydrogen energy generators, respectively. A commercially available electrolyzer and fuel cell are assumed to employ for the application of ESI-PSE mode. The low-temperature bipolar alkaline water electrolyzer (BAWE) and the low-temperature alkaline fuel cell (AFC) with the same electrolyte ( $\text{H}_2\text{O}$ -30% KOH) as that for the electrolyzer were selected for both generators to assess the energy efficiencies for the reason that they are suited to large-scale power station applications.

Among all types of fuel cells, low-temperature (ca. 25–70 °C) AFCs operate well at room temperature, yielding the highest voltages at comparable current densities. An AFC can be built from carbon materials and plastics that are anti-corrosive and low-cost. Therefore, this type of fuel cells is able to achieve a long operating life, approximately 2 years. The AFC is installed in a closed system; therefore, contamination of the alkaline electrolyte ( $\text{H}_2\text{O}$ -KOH) by  $\text{CO}_2$  can be avoided. On the other hand, the BAWE also has the same advantages with respect to lifetime, construction materials, and stability of the electrolyte. The same alkaline electrolyte is used for both devices so that mutual contamination can be avoided. The preliminary system design is based on consideration of the mutual consistency for a stable operation of the total system. To maintain the mass balance in the system, the electrolyzer current must be controlled such that the rate of hydrogen consumption in the fuel cell equals the rate of hydrogen emission from the electrolyzer if the current efficiency of the electrolyzer is unity. This system does not require the compressed hydrogen gas tank which is an explosion hazard.

### 2.4.2 Hydrogen Redox Electric Power Generator (HREG)

This generation system functions with zero energy input, zero matter input, and zero emission, without any violation of the laws of thermodynamics. To predict the energy efficiency of the total energy cycle, the energy efficiencies of the individual electrolyzer and fuel cell in the system were first examined. The energy efficiency of





**Fig. 2.4** Schematic diagrams of (a) hydrogen redox electric power and (b) hydrogen energy generators

**Table 2.1** Nominal parameters and related values of alkaline water electrolytic cells operated in industries

Electrolytic temperature (K)	Current density (A/m <sup>2</sup> )	Theoretical voltage (V)	Decomposition electrolytic voltage (V)
353	1750	1.18	1.75
393	1000	1.15	1.80

a commercially available BAWE with ESI-PSE electrodes may be estimated as follows. The operating conditions of the standard low-temperature alkaline water electrolysis are temperature, 60–80 °C; pressure, 1 atm; current density, 1000–3000 A/m<sup>2</sup>; cell voltage,  $E_c$ , 1.9–2.2 V; and electrolyte, H<sub>2</sub>O-30% KOH.

If the  $\text{H}_2\text{O} = \text{H}_2 + \frac{1}{2}\text{O}_2$  reduction reaction is performed using the cell voltage,  $E_c = E_d + \Delta E = 1.8 + 0.25 = 2.05$  V, then the total energy provided for a cell is  $2FE_d + 2F\Delta E = 395.6$  kJ where  $F$  is the Faraday constant, the term  $2FE_d$  is the electrostatic energy created in situ, and  $2F\Delta E$  is the electrical power provided for the electrode reactions to occur. The standard enthalpy change of the reduction reaction is  $\Delta H^\circ = 285$  kJ/mol H<sub>2</sub>O at 333 K (60 °C), which gives the energy efficiency,  $(\Delta H^\circ/395.6) \times 100 = 72\%$ . Nominal parameters and related values of alkaline water electrolyzers operated in industries are tabulated in Table 2.1.

The electrolyzer is assumed to be a low-temperature bipolar alkaline water electrolyzer (BAWE), and the fuel cell is a low-temperature alkaline fuel cell (AFC) with the same electrolyte (H<sub>2</sub>O-30% KOH) as that for the electrolyzer. The factors that mainly affect the energy efficiency of the AFC are the utilization efficiency of fuels at the electrode reactions, the  $\Delta G/\Delta H$  ratio of the  $\text{H}_2 + \frac{1}{2}\text{O}_2 = \text{H}_2\text{O}$  oxidation reaction, and the voltage degradation factor, i.e., the voltage efficiency  $\theta = E_f/E_f^\circ$  [20, 21] for the operating AFC, where  $E_f$  is the actual voltage of a cell undergoing oxidation and  $E_f^\circ$  is the theoretical open-circuit voltage. The overall energy efficiency of a commercially available low-temperature AFC is in the order

of 60%. If the AFC is combined with the BAWE to form a closed single energy cycle, the energy efficiency of the developed energy cycle equals the energy efficiency of the AFC in the system for the reasons described below. The energy sources for the BAWE with ESI-PSE electrodes are the internally provided electrostatic energy plus the power returned from the AFC. The energy efficiency of a fuel cell is usually designated by the relation,

$$\lambda = \beta(\Delta G^\circ / \Delta H^\circ)\theta, \quad (2.20)$$

$\beta$  = fuel utilization efficiency

$\Delta G^\circ$  = standard free energy change of the reaction,  $\text{H}_2 + \frac{1}{2}\text{O}_2 = \text{H}_2\text{O}$

$\Delta H^\circ$  = standard enthalpy change (heat) for the exothermic reaction

$\theta = E_f/E_f^\circ$  = degradation of cell voltage (voltage efficiency), where  $E_f^\circ$  is the theoretical open-circuit voltage of the fuel cell (1.23 V at 300 K)

The pure stoichiometric  $\text{H}_2\text{-O}_2$  fuel completes the reaction,  $\text{H}_2 + \frac{1}{2}\text{O}_2 = \text{H}_2\text{O}$ ; therefore, the utilization efficiency of the fuel may be deleted from the factors that affect the energy efficiency of the AFC. The oxidation by-product,  $\text{H}_2\text{O}$ , which contains the heat liberated by the exothermic reaction, is transferred to the BAWE and used for the endothermic reduction reaction. The thermodynamic factor,  $\Delta G^\circ/\Delta H^\circ$ , is thus also deleted, which leaves the voltage efficiency as the only factor,  $\theta = E_f/E_f^\circ$ .

In this combined energy cycle, the main device is the fuel cell to produce electricity. The electrolyzer in this system is a backup reactor to synthesize fuel for the fuel cell. Part of the power generated by the fuel cell is returned to the electrolyzer, and the remainder represents the net power output. To represent the productive capacity, the cycle power efficiency is introduced as the figure of merit and defined as the ratio  $\xi_p$  of the net power extracted from the cycle,  $P_{\text{net}}$ , to the power produced by the pure stoichiometric  $\text{H}_2\text{-O}_2$  fuel,  $P_f$ :

$$\xi_p = P_{\text{net}}/P_f. \quad (2.21)$$

If the voltage efficiency is taken into account, then for 1 mole of  $\text{H}_2$ ,

$$P_f = 2F\theta E_f^\circ. \quad (2.22)$$

Mass balance in the cycle requires equality of the electrolytic and galvanic currents. If the current efficiency is assumed to be unity, then Eq. 2.7 is subtracted from Eq. 2.22 to yield the theoretical net power output of the cycle,  $P_{\text{net}}$ . Hence, the cycle power efficiency is rearranged in the form

$$\xi_p = P_{\text{net}}/P_f = 1 - \Delta E/\theta E_f^\circ. \quad (2.23)$$

Assessments have been made on the achievable cycle power efficiencies for the hydrogen redox power generation system when a commercially available AFC is combined with an existing BAWE that is connected to the ESI-PSE mode. Because  $\Delta E = E_c - E_d$ , Eq. 2.23 is revised to

**Table 2.2** Operational conditions of BAWE and AFC for high cycle power efficiencies

BAWE		AFC	
Single cell voltage	Current density	Voltage efficiency	Cycle power efficiency of hydrogen redox power generator
$V_{cell}$ (V)	$J$ (A/m <sup>2</sup> )	$\theta$	$\xi_p$ (%)
2.2	3000	0.8	60
2.1	2200	0.8	70
2.0	1400	0.8	80

$$E_e = \theta E_t^\circ (1 - \xi_p) + E_d. \quad (2.24)$$

An evaluation of the energy efficiencies for the total generation system require the  $V$ - $I$  characteristics for the BAWE and the voltage efficiency of the AFC. The  $V$ - $I$  characteristics were determined using data for the operating conditions of typical electrolyzers, with  $j = 1000, 3000,$  and  $4500$  A/m<sup>2</sup> at  $E_c = 1.9, 2.2,$  and  $2.4$  V, respectively, and also with reference to the literature [22, 23]. Commercially available AFCs operate with a voltage efficiency of  $\theta = 0.8$  on average [24]. Table 2.2 summarizes the result of calculations using the commercial data for the operational conditions, which showed that highly positive power balance ranging from 60 to 80% may be achievable for the hydrogen redox power generator using commercially available devices.

The energy efficiency for this energy cycle where the energy is created within the system is defined as follows. The purely stoichiometric H<sub>2</sub>-O<sub>2</sub> fuel produced by the electrolyzer is the source of energy to convert into electricity so that the H<sub>2</sub> + ½O<sub>2</sub> = H<sub>2</sub>O oxidation reaction is performed in the fuel cell. The heat released is recycled for use in the endothermic reduction reaction at the electrolyzer; therefore, the standard free energy change for the oxidation reaction,  $|\Delta G^\circ|$ , is responsible for the electric power generation. On the other hand, the electrical energy delivered by the fuel cell is  $2F\eta E_d^\circ$ . The energy efficiency is then given by the ratio of  $2F\eta E_d^\circ$  to  $|\Delta G^\circ|$ :

$$\xi_E = 2F\theta E_d^\circ / |\Delta G^\circ| = \theta. \quad (2.25)$$

The power output outside the generator is dependent on the rate of H<sub>2</sub>O circulation inside the system. If the circulation rate is 1 mole of H<sub>2</sub>O per second, then the power output is given by

$$P = |\Delta G^\circ| \xi_E \text{ (kW)} \quad (2.26)$$

$|\Delta G^\circ| = 232$  kJ/mole H<sub>2</sub>O at 330 K and  $\theta = 0.8$ ; therefore, if H<sub>2</sub>O circulates at a rate of 1 kg/s, then the real power supplied to the load outside the system would be  $1.03 \times 10^4$  kW.

### 2.4.3 Hydrogen Redox Hydrogen Energy Generator

Figure 2.4b outlines the combined cycle of AWE electrolyzer with ESI-PSE and AFC to produce hydrogen. This system is of mutual consistency with the HREG system shown in Fig. 2.1a and is able to generate the stoichiometric H<sub>2</sub>-O<sub>2</sub> fuel without receiving electric power from outside of the cycle. Part of the fuel generated by the ESI-PSE electrolyzer is returned to the fuel cell, and the remainder represents the net hydrogen output. In addition to cycling the generated fuel, H<sub>2</sub>O, which contains heat from the exothermic reaction in the fuel cell, is transferred to the electrolyzer for the use to its endothermic reaction.

The hydrogen cycle efficiency,  $\xi_H$ , is defined as the ratio of the hydrogen output rate from the generator to the total hydrogen generation rate from the ESI-PSE electrolyzer, which can be calculated from the hydrogen balance relationships, and  $\xi_H$  is expressed in the same form as Eq. 2.26:

$$\xi_H = 1 - \Delta E / \theta E_f^0. \quad (2.27)$$

This system may achieve a highly positive hydrogen balance such that the net hydrogen output of this cycle exceeds, for example, 70% of the hydrogen delivered by the ESI-PSE electrolyzer.

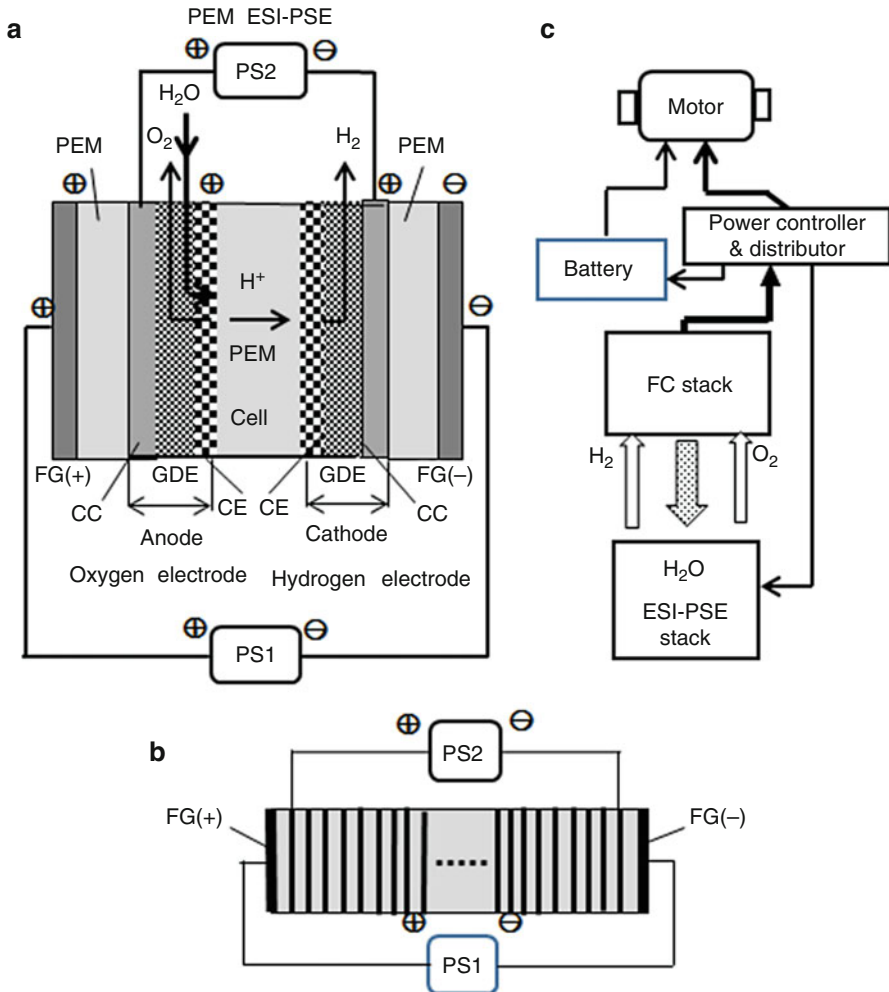
---

## 2.5 Theories of the Onboard HREG System for Fuel Cell Vehicles with Infinite Cruising Range

### 2.5.1 Outline of the Onboard HREG System

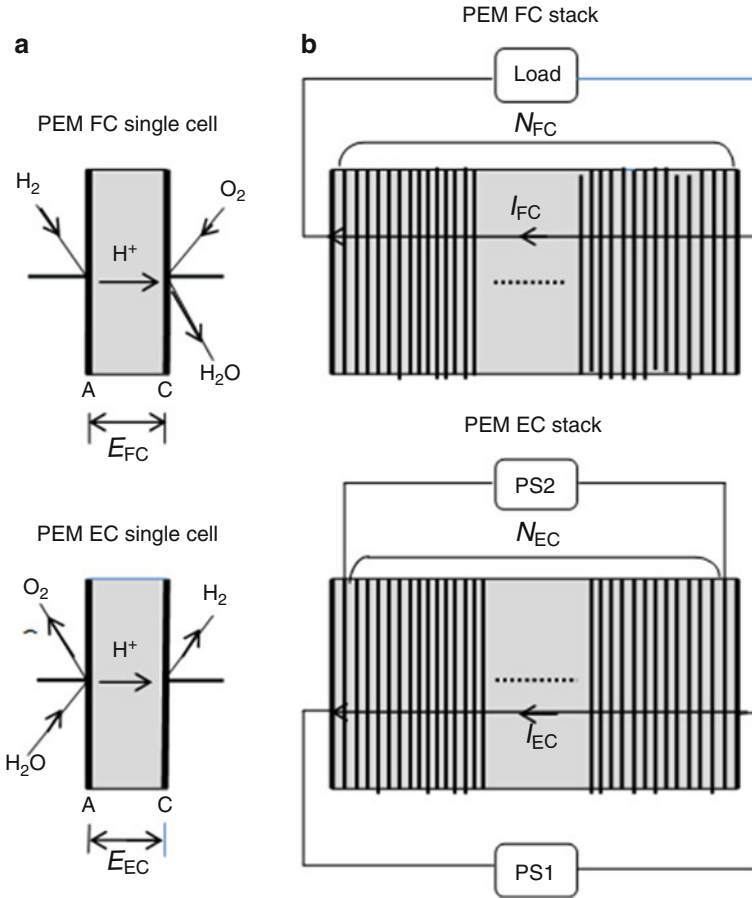
The use of hydrogen-burning fuel cell stack has received wide publicity in the last several years. To achieve an unlimited driving range in the transportation applications, a fuel cell stack is combined with an ESI-PSE stack to form an onboard HREG propulsion system, so that the pure stoichiometric H<sub>2</sub>-O<sub>2</sub> fuel for the fuel cell can be generated by the traveling EV cars. The solid polymer membrane electrolyte (PEM) is used for both fuel cell (FC) and ESI-PSE water electrolytic cell (EC), due to its solid structure and ability to operate at high current densities [25]. Figure 2.5a illustrates a multilayer structure of the PEM ESI-PSE cell sandwiched between two field generators. The cell electrodes normally consist of a current collector, gas diffusion electrode, and catalyzed electrode [26]. Because these components are electrically conductive, the field generators can induce potentials on the inner electrodes. The EC cells are assumed to use in the bipolar configuration shown in Fig. 2.5b. Figure 2.5c illustrates a simplified conceptual block diagram of the onboard HREG propulsion system.

The approach toward optimizing the onboard HREG system and designing the system to be compact is of preferential importance. The PEM HREG system is essentially an energy cycle with the close conjunction of two electrochemical devices. It is important to note that with respect to the structure, the PEM EC cell



**Fig. 2.5** The onboard hydrogen redox electric power generation system. (a) Schematic structure of the ESI-PSE water electrolysis using solid polymer electrolyte; (b) longitudinal cross section through series-connected ESI-PSE cells; and (c) configuration of the components for an onboard hydrogen redox electric power generator. FG, field generator; PEM, polymer electrolyte membrane; CC, a current collector; GDE, gas diffusion electrode; CE, catalyzer electrode

must be identical with the typical PEM FC cell which has established feasibility so far. Both the FC and EC stacks must be constructed in the same form of a bipolar series connection. Only the number of cells connected in series may be different from each other. Figure 2.6a shows the performances of a single PEM FC and PEM EC. The cell stacks with bipolar configuration are shown schematically in Fig. 2.6b.



**Fig. 2.6** Schematic diagrams of the onboard HREG system for electric vehicles. (a) Performance of the PEM FC and PEM EC cells. A, anode; C, cathode. (b) Longitudinal cross section of the PEM FC and PEM EC stacks. PS, power supply

## 2.5.2 Basic Equations for Infinite Cruising Range

The assessment of the HREG system has been made by making the following assumptions and conditions:

1. The dimensions, structure, and materials of the PEM fuel cell (PEM FC) and the PEM EC cells must be exactly the same. All the individual cells in both FC and EC stacks have then the same weight and the same electrode area.
2. Equality of the H<sub>2</sub>-O<sub>2</sub> consumption rate in the PEM FC stack and the H<sub>2</sub>-O<sub>2</sub> generation rate in the PEM EC stack is required.
3. The estimation is given in terms of the weight ratio of the ESI-PSE EC stack responsible for supplying the FC stack with the H<sub>2</sub>-O<sub>2</sub> fuel to that of the typical

onboard FC stack. The typical FC stack is the FC stack currently used for the FC vehicles.

4. The gas pressure level selected for the PEM EC is ordinarily about 5 atm. High pressure applied to the PEM FC contributes to the increase in its open-circuit voltage. If higher pressure is required to the PEM FC cells, then a compressor may be used.

The concerned parameters are given below:

$E_{FC}$	Fuel cell voltage.
$E_{EC}$	Electrolytic cell voltage.
$\theta$	Voltage efficiency of a PEM FC cell due to voltage degradation resulting from polarization. $\theta$ is equal to the energy efficiency of a PEM FC.
$\Xi$	Cycle power efficiency of the HREG system, defined as Eq. 2.23 where $\theta E_T^o = E_{FC}$ .
$P_T^o$	Maximum power output from an existing FC stack.
$P_T$	Maximum power output from an FC stack in the HREG system.
$P_r$	Power returned from the FC stack to the EC stack.
$M_{FC}^o$	Weight of an existing FC stack.
$M_{EC}$	Weight of a single EC stack in the HREG system.
$M_{FC}^{(r)}$	Weight of a set of the FC cells responsible for producing the power returned.
$M_T$	Gross weight of the HREG system.
$N_{FC}$	Number of the FC cells connected in series in the FC stack.
$N_{FC}^o$	Number of the FC cells connected in series in the existing FC stack.
$N_{EC}$	Number of the EC cells connected in series in the EC stack.
$N_{FC}^{(r)}$	Number of the FC cells generating the power returned from the FC stack to the EC stack.
$I_{FC}$	Current flowing through the FC stack.
$I_{EC}$	Current flowing through the EC stack.
$J_{FC}$	Current density of the FC cell.
$J_{EC}$	Current density of the EC cell.

Part of the power  $P_r$  delivered by the PEM FC stack is returned to the PEM ESI-PSE EC stack; the remaining represents the real power to drive the motor. The cycle power efficiency of the HREG system is defined as

$$\xi = (P_{net}/P_T) = (P_T - P_r)/P_T \quad (2.28)$$

The maximum power output,  $P_T$ , of the HREG system must be the sum of the maximum power output from the existing FC stack,  $P_T^o$ , plus the power returned from the FC stack to the EC stack:

$$P_T = P_T^o + P_r, \quad (2.29)$$

where  $P_T^o$  is the nominal maximum power of the FC stack on the typical regular passenger car.

From Eqs. 2.28 and 2.29, we have

$$P_T = (1/\xi)P_T^0 \quad (2.30)$$

The power output of the FC stack is proportional to the number of cells connected in series. By the condition that the FC stack consists of identical cells, the stack current,  $I_{FC}$ , does not depend on the number of cells,  $N_{FC}$ : the increase in  $N_{FC}$  does not change  $I_{FC}$ . The FC stack current produces the same magnitude of power in every cell in the stack. According to the Faraday law, the number of moles of  $H_2$  consumed in each cell in a unit of time is proportional to  $I_{FC}$ , assuming the current efficiencies to be unity. The number of  $H_2$  moles consumed in the entire sack must be proportional to the product,  $N_{FC} I_{FC}$ . This amount of  $H_2$  is to be provided by the PEM EC stack, in which the rate of  $H_2$  emission may be written in the form of  $N_{EC} I_{EC}$ . Therefore, from Eq. 2.30 we obtain the relation

$$N_{EC}I_{EC} = (1/\xi)N_{FC}^0I_{FC} \quad (2.31)$$

The currents  $I_{EC}$  are related to the current densities,  $J_{EC}$  and  $J_{FC}$  as  $I_{EC} = A J_{EC}$  and  $I_{FC} = A J_{FC}$ , respectively, where  $A$  is the electrode area. Because the electrode surface area for all cells in the HREG system is the same, Eq. 2.31 can be written in the form

$$N_{EC}/N_{FC}^0 = (1/\xi)(J_{FC}/J_{EC}) \quad (2.32)$$

The selected design parameters of the FC stack, EC stack, and HREG system were determined as follows:

- (1) The cycle power efficiency of 70% ( $\xi = 0.7$ ) was used.
- (2) The FC cell voltage  $E_{FC}$  of the existing regular passenger FCV is lowered down to the level of  $E_{FC} = 0.7$  V from the theoretical value of 1.23 V when the car is driven at the maximum power. It is the consequence of the appreciable polarization effect involved inevitably in the FC cell.
- (3) If  $\xi = 0.7$  and  $E_{FC} = 0.7$  V, the extra applied voltage  $\Delta E$  in Eq. 2.23 was calculated to be  $\Delta E = 0.21$  V. Then,  $E_{EC} = 1.23 + 0.21 = 1.44$  V.
- (4) The polarization study indicates that the  $J_{FC}$  value corresponding to  $E_{FC} = 0.7$  V is  $J_{FC} = 0.50$  A/cm<sup>2</sup> [27].
- (5) The current density of the EC stack,  $J_{EC}$ , was determined by using the  $V$ - $I$  relation as [28]

$$J_{EC} = 2.0 E_{EC} - 2.4 (J_{EC} \text{ in A/cm}^2 \text{ and } E_{EC} \text{ in volt}).$$

Putting  $E_{EC} = 1.44$  V,  $J_{EC} = 0.48$  A/cm<sup>2</sup> from the above equation. If we operate the HREG system with  $\xi = 0.7$ ,  $J_{FC} = 0.50$  A/cm<sup>2</sup>, and  $J_{EC} = 0.48$  A/cm<sup>2</sup>, then the  $N_{EC}/N_{FC}^0$  ratio becomes 1.49 from Eq. 2.32. This result of calculation indicates that the number of cells required for the ESI-PSE EC stack must be 1.5 times as much as that of the existing FC stack for the HREG system to be self-consistent.



### 2.5.3 Weight Evaluation of the Onboard HREG System

The first requirement in a theoretical investigation of the onboard HREG system is its applicability to the FC vehicles. One item of considerable interest to predict the possibility for transportation application has been the question related to the gross weight of the onboard HREG system to replace the typical FC power generation system. The weight ratio of the EC stack to the existing FC stack is then given by

$$M_{EC}/M_{FC}^{\circ} = N_{EC}/N_{FC}^{\circ} = I_{FC}/I_{EC}. \quad (2.33)$$

Thus,

$$M_{EC} = (J_{FC}/J_{EC})M_{FC}^{\circ}. \quad (2.34)$$

To evaluate the total weight,  $M_T$ , of the HHREG system,  $M_T$  must be related to  $M_{FC}^{\circ}$  through a nondimensional factor,  $\alpha$ , as

$$M_T = \alpha M_{FC}^{\circ}. \quad (2.35)$$

Using Eqs. 2.29 and 2.30, we obtain

$$P_T = [(1 - \xi)/\xi]P_T^{\circ}. \quad (2.36)$$

It follows that

$$N_{FC}^{(r)} = [(1 - \xi)/\xi]N_{FC}^{\circ}. \quad (2.37)$$

If the number of cells is proportional to the weight, then Eq. 2.37 may be replaced by

$$M_{FC}^{(r)} = [(1 - \xi)/\xi]M_{FC}^{\circ} \quad (2.38)$$

Therefore, the total weight of the HREG system can be obtained using Eqs. 2.34 and 2.38 as

$$M_T = M_{FC}^{\circ} + M_{FC}^{(r)} + M_{EC} = \alpha M_{FC}^{\circ}, \quad (2.39)$$

where  $\alpha$  is a nondimensional factor given by

$$\alpha = 1 + (1 - \xi)/\xi + (J_{FC}/J_{EC}) \quad (2.40)$$

For numerical evaluation of the total weight of the onboard HREG system and predicting its acceptability to the regular passenger cars,  $\alpha$ -value may be an index with respect to weight and volume. Finally, the resulting  $\alpha$ -value for  $\xi = 0.7$ ,  $J_{EC} = 0.48$  A/cm<sup>2</sup>, and  $J_{FC} = 0.50$  A/cm<sup>2</sup> is  $\alpha = 2.47$ . A typical weight of an existing onboard FC stack is on the order of 60 kg. Then, the HREG system weighs  $2.47 \times 60 = 148$  kg. The weight of the HREG system does not exceed that of the existing FC

system consisting of the FC stack of 60 kg plus the high-pressure hydrogen tank of 100 kg [29], i.e., 160 kg. Although the present evaluation is preliminary in nature, the results obtained imply that the new power system HREG may be applicable to the regular passenger vehicles.

---

## 2.6 Conclusion

The principle and performance of the electrostatic induction potential-superposed water electrolysis for the synthesis of a fully sustainable stoichiometric  $H_2-O_2$  fuel for a fuel cell. This system works on the mechanism of continuous creation of internal energy and extraction of the created energy from the system in the form of the energy state of stoichiometric  $H_2-O_2$  fuel. The basic concept of an electrolyzer-fuel cell combined cycle satisfying both the full sustainability of the fuel and the highest possible energy efficiency of the fuel cell was introduced. This power generation concept assumes to use a low-temperature AFC and a low-temperature BAW, both of which are commercially available. This system works on the mechanism of continuous creation and storage of internal energy and extraction of the created energy from the system in the form of the energy state of stoichiometric  $H_2-O_2$  fuel. We have confirmed the phenomenon of the internal energy creation and measured the quantity of energy thus created. The result of calculations using the commercial data for the operational conditions showed that more than 70% of the power delivered from the fuel cell can be extracted outside the cycle as net power output. This energy cycle is also applied to produce pure hydrogen without using electricity. This system may achieve the hydrogen output of more than 70% of the hydrogen delivered by the ESI-PSE water electrolyzer.

In addition, this approach demonstrated the transportation applications of the hydrogen redox electric power generator. To bring the ESI-PSE electrolytic stack onboard, it is required not to be heavy. Its weight was presumed theoretically to be the same order as the weight of the existing onboard fuel cell stack. A union between the transportation and the hydrogen redox electric power generator is a natural one with prospects for profitable commercial application in near future.

**Acknowledgments** The technological outline of the fuel cell electric vehicle and the structure of the fuel cell stack is available on the internet official sites (2017) by Toyota Motor Co. and Sumitomo Riko, Inc. The data values for this study are deeply appreciated. The author thanks the editors in allowing me to extend my previously published works [K. Ono, The Institute of Electrical Engineers of Japan, 2013; International Journal of Hydrogen Energy, 2016.].

---

## References

1. K. Ono, Fundamental theories on a combined energy cycle of electrostatic induction hydrogen electrolytic cell and a fuel cell to produce sustainable hydrogen energy. IEEJ Trans. Fundam. Mater. **133**, 615 (2013)

2. K. Ono, Energetically self-sustaining electric power generation system based on the combined cycle of electrostatic induction hydrogen electrolyzer and fuel cell. *IEEJ Trans. Fundam. Mater.* **135**, 22 (2013)
3. K. Ono, Hydrogen redox electric power and hydrogen energy generators. *Int. J. Hydrogen Energy* **41**, 10284–10291 (2016)
4. E.A. Guggenheim, *Thermodynamics*, 2nd edn. (North-Holland Publishing, Amsterdam, 1950)
5. E.A. Guggenheim, *Thermodynamics*, 3rd edn. (North-Holland Publishing, Amsterdam, 1957)
6. E.A. Guggenheim, *Thermodynamics*, 5th edn. (North-Holland Publishing, Amsterdam, 1967), pp. 333–337
7. H.A. Christopher, C.W. Shipman, Poisson's equation as a condition of equilibrium in electrochemical systems. *J. Electrochem. Soc.* **115**, 501–506 (1968)
8. A.J. Bard, L.R. Faulkner, *Electrochemical Methods Fundamentals and Applications* (Wiley, Hoboken, 2001)
9. T.L. Floyd, *Electronics Fundamentals* (Pearson Education, Upper Saddle River, New Jersey, 2004)
10. W.J. Weir, *Electronic Circuit Fundamentals* (Prentice-Hall, Englewood Cliffs, 1987)
11. R.A. Smith, *Semiconductors* (McGraw-Hill Kogakusha, Tokyo, 1971)
12. S.M. Sze, *Physics of Semiconductor Devices* (Wiley International Edition, New York, 1969)
13. I. Barin, O. Knacke, *Thermochemical Properties of Inorganic Substances* (Springer-Verlag, Berlin, 1973)
14. I. Prigogine, R. Defay, *Thermodynamic Chimique* (Edition Desoer, Liège, 1944)
15. R. Tamamushi, *Electrochemistry* (Tokyo Kagaku Dounn, Sengoku, Bunkyo-Ku, Japan, 1967)
16. J. Newman, K.E. Thomas-Alyea, *Electrochemical Systems*, 3rd edn. (Wiley-Interscience, New York, 2004)
17. J. Goodisman, *Electrochemistry: Theoretical Foundations* (Wiley, New York, 1987)
18. T. Satoh, T. Sasaki, *Electromagnetics and Electrical Circuit* (Nikkan Kogyo Shinbun-sha, Nihombashi Koami-cho, Chuo-ku, Tokyo, Japan 2001)
19. S. Nagai, Electrochemical Association of Japan, *Handbook of Electrochemistry* (Maruzen Shuppan Co. Ltd, Kanda Jimbo-cho Bldg. 6F, Kanda Jimbo-cho 2-17, Chiyoda-ku, Tokyo, Japan, 1942), p. 81
20. K. Ota, Principle of fuel cells for application, GS Yuasa Technical Report, vol. 2, No. 1 (2005)
21. R.P. O'Hayre, S.W. Cha, W. Colella, F.B. Prinz, *Fuel Cell Fundamentals* (Wiley, Hoboken, 2006)
22. R.L. LeRoy, M.B. Janjua, R. Renaud, U. Leuenberger, Analysis of time-variation effects in water electrolysis. *J. Electrochem. Soc.* **126**, 1674 (1979)
23. I. Abe, Hydrogen Production by Water Electrolysis Hydrogen Energy System, 33.19 (2008)
24. A.J. Applby, F.R. Foulkes, *Fuel Cell Handbook* (Van Nostrand Reinhold, New York, 1989)
25. R.O. Hayre, C. Suk-Won, W. Colella, F.B. Prinz, *Fuel Cells* (Wiley, Hoboken, 2006)
26. T. Yoshida, *Innovative Batteries Enhanced Power Supply for the Next Stage* (N.T.S, Tokyo, 2006)
27. F. Barbir, *PEM Fuel Cells, Theory and Practice* (Elsevier, Amsterdam, 2013)
28. Annual Reports, Natural Resources, and Energies, 1999/2000, The Agency for Resources and Energies, Japan
29. Y. Kojima, The existing state and the future of hydrogen storage technologies for fuel cell vehicles. *Hydrogen Energy Syst.* **33**, 49–58 (2008)



# Evaluation of Cell Performance and Durability for Cathode Catalysts (Platinum Supported on Carbon Blacks or Conducting Ceramic Nanoparticles) During Simulated Fuel Cell Vehicle Operation: Start-Up/Shutdown Cycles and Load Cycles

Makoto Uchida, Katsuyoshi Kakinuma, and Akihiro Iiyama

## Contents

3.1	Introduction .....	54
3.2	Evaluation of Cell Performance and Durability for Pt/CBs Under the Simulated Operation of both SU/SD Cycles and Load Cycles .....	58
3.2.1	Electrochemical and Raman Spectroscopic Evaluation of Pt/GCB Catalyst Durability for SU/SD Operation .....	59
3.2.2	Investigation of the Corrosion of Carbon Supports in Polymer Electrolyte Fuel Cells Using Simulated SU/SD Cycling .....	63
3.2.3	Deleterious Effects of Interim CV on Pt/CB Degradation During SU/SD Cycling .....	66
3.2.4	Durability of Pt/GCB During Gas-Exchange SU Operation .....	69
3.2.5	Degradation Mechanisms of CBs Under Hydrogen Passivation SU/SD Process .....	75
3.2.6	Load Cycle Durability of a Pt/GCB .....	79
3.3	Synthesis and Evaluation of Cell Performance and Durability for Pt Supported on Conducting Ceramic Nanoparticles During Simulated SU/SD Cycles .....	86
3.3.1	Degradation of Carbon Support and Alternative Support Materials .....	86

The original version of this chapter was revised: The correction to this chapter is available online at [https://doi.org/10.1007/978-3-662-56364-9\\_19](https://doi.org/10.1007/978-3-662-56364-9_19)

## Author Contributions

This work was coordinated by Makoto Uchida and Akihiro Iiyama. Katsuyoshi Kakinuma carried out the preparation and characterization of catalysts and performed the electrochemical measurements. Makoto Uchida contributed to the catalyst preparations, the electrochemical measurements, the durability evaluations, and all of the characterization. All the authors contributed equally to the data interpretation, discussion, and preparation of the manuscript, and Makoto Uchida revised the final version of the paper. The authors further acknowledge that there is no financial relationship with the editors or publisher and have contributed original work in this chapter, other than what is acknowledged or appropriately cited with copyright permission.

M. Uchida (✉) · K. Kakinuma · A. Iiyama

Fuel Cell Nanomaterials Center, University of Yamanashi, Kofu, Yamanashi, Japan

e-mail: [uchidam@yamanashi.ac.jp](mailto:uchidam@yamanashi.ac.jp); [kkakinuma@yamanashi.ac.jp](mailto:kkakinuma@yamanashi.ac.jp); [aaiyama@yamanashi.ac.jp](mailto:aaiyama@yamanashi.ac.jp)

3.3.2 Pt Supported on Titanium Nitride (Pt/TiN) and Carbide (Pt/TiC) .....	88
3.3.3 Pt Supported on SnO <sub>2</sub> Catalysts .....	90
3.3.4 “ARSM” Effect of Pt Supported on Ta-TiO <sub>2</sub> Catalysts .....	101
3.4 Conclusions .....	105
References .....	106

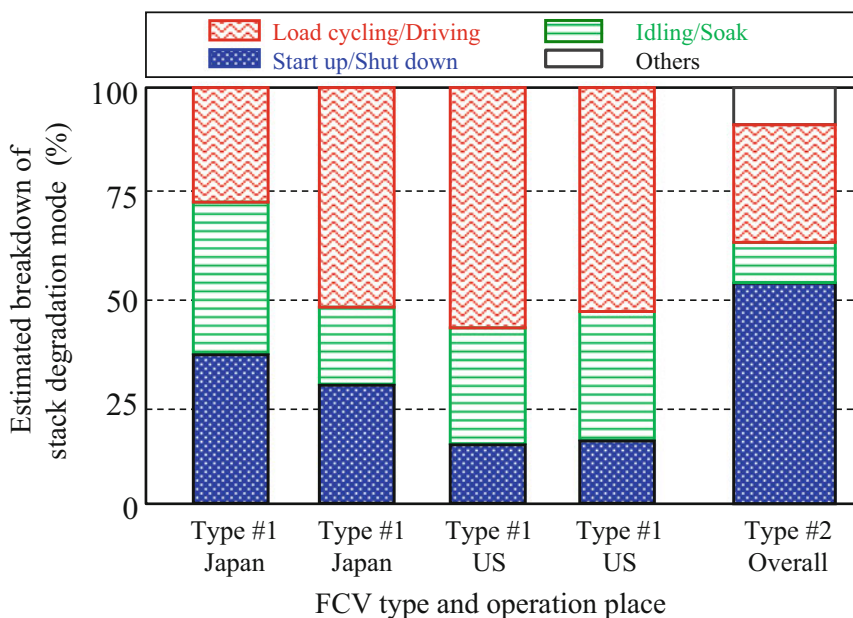
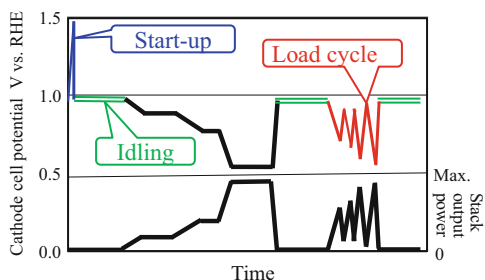
## Abstract

We summarized investigations on the evaluation of cell performance and durability for cathode catalysts on two types of supports, carbon blacks (CBs) and conducting ceramic nanoparticles, during simulated fuel cell vehicle (FCV) operation, including start-up/shutdown (SU/SD) cycles and load cycles. In cathode catalyst layers (CLs) using Pt supported on CBs (Pt/CBs), the effects of graphitized CB (GCB) and Pt nanoparticle size, as well as its dispersion state on the GCB, were investigated on both the performance and durability. The negative effects of the interim cyclic voltammetric measurements on the Pt/CB catalyst degradation during SU/SD cycling evaluation, which led to an overestimation of the degradation process, were also suggested. We found that catalyst degradation occurred not only in the outlet region but also in the inlet region during the gas-exchange SU. Degradation of CBs during a hydrogen passivation SU/SD process was found to decrease but still to occur, due to local cells arising from nonuniform distributions of ionomer and Pt particles. The effects of load cycle conditions, which involved open circuit and load holding times, and variations of current density, and humidity, on the durability of the cathode were also investigated. The buildup of Pt oxides at higher potentials during open circuit and re-reduction at lower potentials during high current density operation led to accelerated degradation; these conditions have relevance to ordinary operation with drastic load changes. For the intrinsic improvement of SU/SD durability, we synthesized conducting ceramic nanoparticles. The durability of the cathode CLs, using Pt supported on conducting ceramic nanoparticles with a fused-aggregate network structure, was superior to that of Pt/GCB. We also proposed that the cathode CL degradation can be mitigated by the use of ceramic nanoparticles in the anode because of the significant reduction of the reverse current due to the high resistivity in the air, termed the “atmospheric resistive switching mechanism” (ARSM).

## 3.1 Introduction

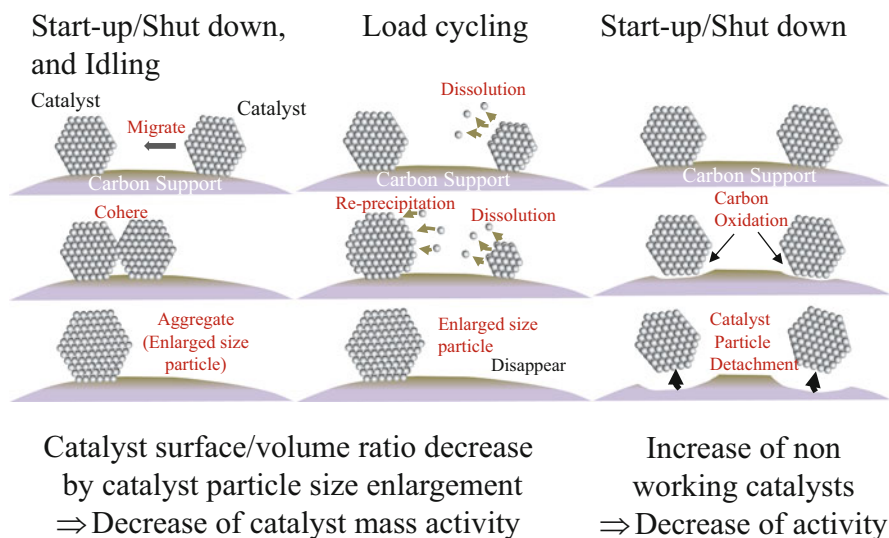
During actual fuel cell vehicle (FCV) operation, cells in the FCV stack will be exposed to various potential patterns, as shown in Fig. 3.1. For example, during the startup (SU) process, hydrogen will be introduced to the anode channel, replacing air, and the cathode cell potential can reach 1.5 V. After SU, the FCV will be at idle condition, during which the cathode cell potential will be near the open circuit voltage (OCV) potential for some time. During driving, the FCV will accelerate and decelerate, and the cathode cell potential will cycle between low and high potentials, respectively. Due to the exposure to cell potential variations, the FCV stack performance will degrade.

**Fig. 3.1** Typical FCV operation mode and cell potential



**Fig. 3.2** Estimated breakdown of stack performance degradation mode during FCV operation for FCV type #1 [1], FCV type #2 [2]

There are several reports on such actual FCV performance degradation and breakdown during normal public road operation. Figure 3.2 summarizes the FCV stack performance degradation reported by Nissan [1] and Honda [2]. Nissan reported that the FCV performance degradation can be fully explained by the degradation occurring during the three main vehicle operation modes, i.e., during the startup (SU) and shutdown (SD) processes, during load cycling, and during idling, based on their FCV durability test data obtained on typical public roads, both in the United States and Japan. The performance degradation was estimated by use of the stack voltage time record of each FCV during vehicle operation, compared with the FCV stack performance degradation measured by the chassis dynamo after the driving test. Both the estimated degradation and measured degradation matched



**Fig. 3.3** Degradation mechanism during FCV operation mode

well [1]. FCVs in Japan tend to be operated for shorter mileage in daily use, and in each trip, the main degradation occurs during SU/SD and idling. FCVs in the USA tend to be operated for longer mileage, and the main degradation occurs during load cycling.

Honda has also reported their FCV performance degradation results. The detailed actual testing conditions were not disclosed, but they concluded that the catalyst degradation during SU/SD was the main cause of FCV degradation. The difference between the Honda and the Nissan results might be attributed to differences in the FCV stack material and the system and control configuration, which would affect the actual cell degradation degree and potential time history during each FCV operation, even if conditions were similar.

Many papers have reported the degradation mechanism during each FCV operation mode. Figure 3.3 illustrates three phenomena from the viewpoints of the Pt nanoparticles and carbon support particles during the degradation process. The cause of the degradation during SU is considered to be the carbon support oxidation near the outlet of the cathode of the high cathode potential caused by the hydrogen front [3]. The Pt catalyst particles will detach from the oxidized carbon support and will no longer be active because they lose electronic contact with the carbon support.

During load cycling, the cathode catalyst will be exposed to the potential cycles, and catalyst oxidation and reduction will proceed cyclically. Smaller catalyst particles will dissolve faster due to their higher chemical potential, and dissolved Pt ions will redeposit on the larger Pt particles (Ostwald ripening). The larger size particles become larger, the surface and mass ratios decrease, and the mass activities decrease [4]. During idling, catalyst particles are exposed to high potentials, near the OCV. During such high potential holding, the catalyst particles migrate and aggregate to

form larger size particles, and thus the performance degrades. At high potentials during SU/SD and potential cycling, such catalyst particle migration and aggregation also occurs.

The degradation mechanism mentioned above can be explained in terms of the three phenomena shown in Fig. 3.3. In order to suppress the FCV stack performance degradation, it is necessary to suppress these phenomena. Both material improvement and system operation control modification would be necessary to mitigate the degradation. From the viewpoint of system operation control, cell potential control will be effective, i.e., to suppress the cathode potential increase during the SU process by means of electrical circuit modification.

Material characteristics improvement is also important. For the Pt catalyst particles, uniform size distribution would be effective in suppressing the Pt dissolution from smaller size particles and redeposition on larger size particles. For the carbon support, the usage of a more graphitized carbon can be effective in suppressing the carbon oxidation during the SU process. The usage of ceramic materials for the catalyst support is expected to be one of the ultimate mitigation technologies. Uniform catalyst particle dispersion on the support will be effective to suppress the particle aggregation.

The Japanese industrial consortium, the Fuel Cell Commercialization Conference of Japan (FCCJ), which was organized to promote a hydrogen energy economy and fuel cell commercialization, has proposed test protocols to evaluate materials durability for the SU/SD and load cycling in order to promote materials research and development [5]. For SU/SD, they have proposed to apply a triangular potential cycle (1.0–1.5 V) to the cathode catalyst to evaluate the support oxidation characteristics. For load cycling, they have proposed to apply a rectangular potential cycle (0.6–1.0 V) to evaluate the catalyst dissolution and redeposition characteristics. This protocol is widely utilized by the New Energy and Industrial Technology Development Organization (NEDO) of Japan in their funded projects to establish a common basis for a materials evaluation data set.

The following sections in this chapter will describe the research carried out at the University of Yamanashi on the cathode catalyst-support performance and degradation by utilizing the FCCJ protocols as well as further improved protocols that have been developed through collaborative research with the automotive industry. The membrane-electrode assembly (MEA) has been targeted for research on the degradation mechanism in preference to the half-cell due to the MEA's close relationship to actual FCV phenomena. As a result, it has been clearly revealed that in the actual MEA catalyst layer during realistic operation, the three material degradation phenomena described above occur simultaneously and three dimensionally in a closely related manner. Based on the MEA analysis, the most promising directions for technical development can be clearly pointed out.

In Sect. 3.2, the catalyst degradation which is supported on the carbon will be introduced. In Sect. 3.3, the ceramics support, which would be the ultimate solution for the high potential degradation mitigation, will be introduced. In Sect. 3.2, the SU/SD degradation research utilizing the MEA will be introduced first (Potential cycle 2.1–2.3, Gas replacement 2.4, Hydrogen-enriched SU 2.5). Then, actual load

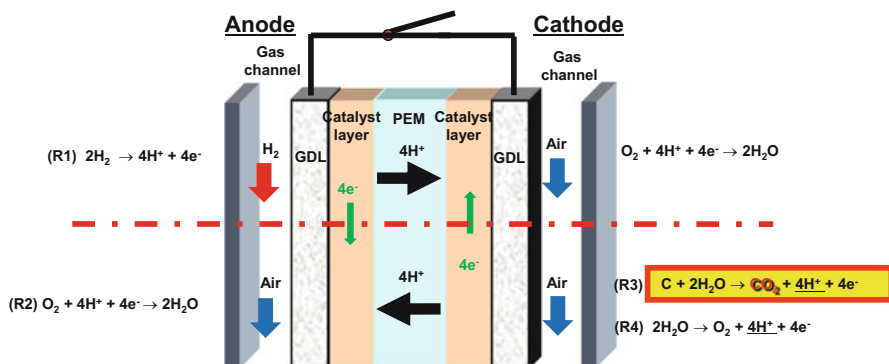


cycle degradation with applied electric load for degradation mechanism confirmation will be introduced, comparing the potential cycle-only case and showing the technical direction for improvement (2.6). From this performance degradation research, it is demonstrated that the combination of the SU/SD and the load cycling enhances the degradation (2.2, 2.3, 2.4, and 2.5). In Sect. 3.3, new ceramic supports will be introduced, which have been prepared through unique synthesis methods and show equivalent cell performance and superior SU/SD degradation characteristics, which have been confirmed by MEA testing. It is also confirmed that the ceramic supports can suppress SU/SD degradation when used at the anode catalyst layer, by suppressing the cathode catalyst high potential by changing its own electric conductivity at the anode.

---

## 3.2 Evaluation of Cell Performance and Durability for Pt/CBs Under the Simulated Operation of both SU/SD Cycles and Load Cycles

It is usual that the anode compartment of a fuel cell is purged with air during the SD process, which eventually results in an equilibrium condition, with a zero potential difference between anode and cathode [6]. However, before equilibrium is reached, hydrogen and air can coexist at the anode, as shown in Fig. 3.4. The same situation also occurs during SU, when hydrogen is reintroduced into the anode compartment. During both SU and SD the potential and the nature of the reaction can thus vary significantly within each electrode due to the inhomogeneity of the gaseous environment [3]. The anode can be considered to be divided into two distinct regions, with the one region supporting mainly the hydrogen oxidation reaction (HOR, R1) and the second region supporting mainly the oxygen reduction reaction (ORR, R2). Even though the actual potential across the electrode does not vary greatly, the differing gaseous environments control the reactions at the anode surface [7]. During SU and SD, there is no current flow, so there is an OCV ( $E_{\text{cell,OC}}$ ) condition, and in the hydrogen-rich region, this would be a typical value for a hydrogen/air cell, i.e., ca. 1.0 V. In contrast, in the air-rich region at the anode, the low potential that generally exists due to the presence of hydrogen in the hydrogen-rich region necessarily leads to  $\text{O}_2$  being reduced; i.e., the ORR occurs. This process requires protons, and thus, to supply those, water is oxidized, i.e., the oxygen evolution reaction (OER, R4) at the cathode in the region just opposite, which necessitates an anodic current and therefore a high potential (ca. 1.5 V). The latter also leads to an oxidation of the carbon black (CB) support, i.e., the carbon oxidation reaction (COR) (R3) and thus degradation in the cathode catalyst layer (CL). Of course, it is conceivable that the protons for the ORR (R2) occurring in the air-rich region could also be supplied by the HOR (R1) occurring in the hydrogen-rich region, as are the electrons. However, this scenario is unlikely due to the long distances involved, on the order of centimeters, through the very thin membrane and/or

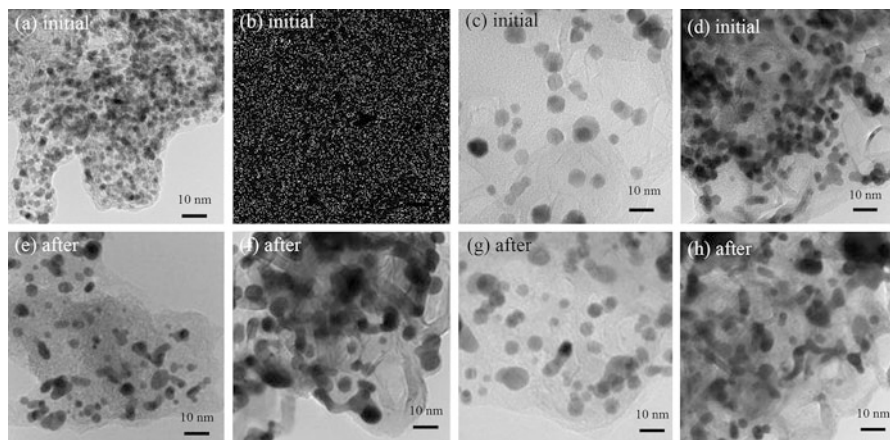


**Fig. 3.4** Carbon corrosion mechanism during the SU processes

anode CL. Thus, there is effectively a large ohmic resistance for this pathway. Thus, due to the much lower resistance, the required protons are supplied directly, over a short distance (tens of  $\mu\text{m}$ ) through the membrane by either the COR (R3) or the OER (R4) in the cathode CL, then combining with oxygen (ORR) at the anode [3, 7, 8]. This process has been termed the “reverse current mechanism” [3]. Thus, the SD and SU give rise to processes, most importantly carbon oxidation or corrosion, that lead to severe degradation of the Pt/CB cathode catalyst. As a result of the carbon corrosion, the Pt catalyst particles can easily detach from the carbon support surface, leading to a decrease of catalytic performance [8–11]. Furthermore, the dimensions and hydrophobicity of the pores in the CL are adversely affected [12], which leads to poorer gas mass transport. A summary of the previous research on load-cycle durability is described in the beginning of Sect. 3.2.6.

### 3.2.1 Electrochemical and Raman Spectroscopic Evaluation of Pt/GCB Catalyst Durability for SU/SD Operation

As outlined above, SU/SD cycles can induce excursions of the cathode potential to values greater than 1.2 V due to the reverse current mechanism [3, 13], at which the COR proceeds at significant rates [14]. In order to impede this reaction, highly graphitized CBs (GCBs) have been found to be useful [14–16]. As a further strategy to enhance catalytic performance and durability, we have developed a method to prepare Pt/GCB catalysts, termed the nanocapsule method [14, 17, 18]. With this method, it is possible to obtain high dispersions of Pt nanoparticles on the GCB supports, which have yielded improved ORR activity and durability, both in electrolyte solution (half-cell testing) and MEAs [14, 18]. These studies have demonstrated the importance of the support carbon and the state of dispersion of the Pt nanoparticles for the achievement of high durability and performance. Therefore, in order to monitor the degradation of the catalyst, an effective approach would be to



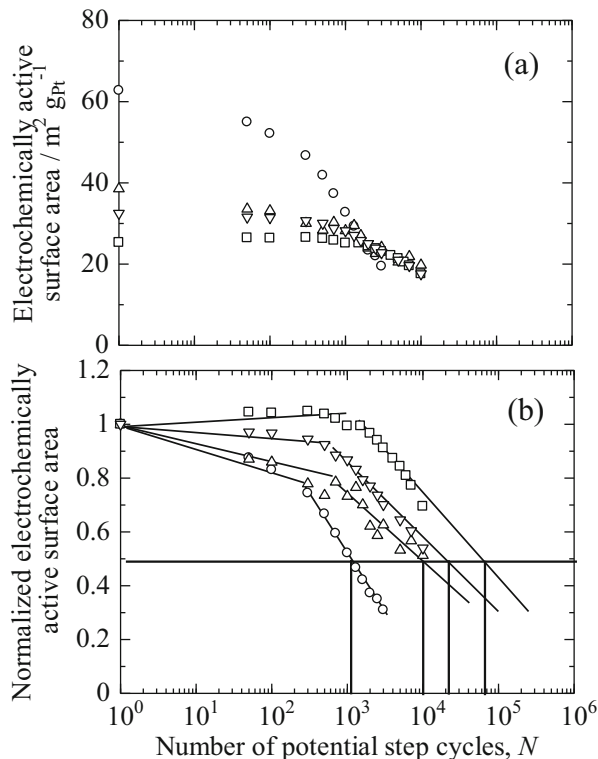
**Fig. 3.5** TEM images of uncycled catalysts (a) c-Pt/CB, (b) c-Pt/GCB, (c) Pt/GCB-HT and (d) n-Pt/GCB, and of durability-test cycled catalysts: (e) c-Pt/CB, (f) c-Pt/GCB, (g) Pt/GCB-HT, and (h) n-Pt/GCB

sensitively examine the state of the carbon support, which would help to elucidate the relationships between the various electrocatalyst characteristics, including the nature of the support and the dispersion method, and the durability.

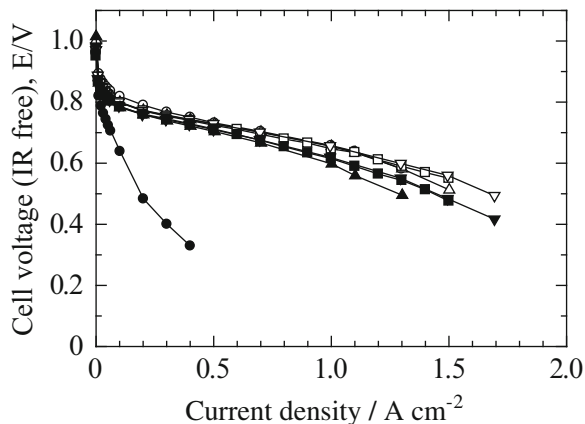
The durability of Pt nanoparticle catalysts was examined for two types of carbon supports, CB and GCB, for 50 wt % Pt-loaded catalysts (commercial Pt/CB: TEC10E50E, Pt/GCB: TEC10EA50E and heat-treated (HT) Pt/GCB, Tanaka Kikinzoku Kogyo K.K., and an in-house-prepared nanocapsule Pt/GCB). The catalysts were characterized by the use of electrochemical and Raman spectroscopic methods. The catalysts were tested by use of a standard potential step protocol (0.9 V  $\leftrightarrow$  1.3 V vs. RHE, holding 30 s at each potential and taking 1 min for one cycle, 3000 potential cycles for commercial Pt/CB and 10,000 cycles for commercial Pt/GCB, Pt/GCB-HT, and nanocapsule Pt/GCB) in MEAs at 65 °C with 100% RH H<sub>2</sub> (anode) and N<sub>2</sub> (cathode) (Figs. 3.5, 3.6, and 3.7). Higher corrosion resistance of the GCB was evidenced by the slower degradation of the electrochemically active surface area (ECA) and smaller mass activity losses before versus after durability testing (Table 3.1).

In order to maintain the cell performance during voltage cycling, the essential factors were found to include a support material with high corrosion resistance, a uniform dispersion of the Pt nanoparticles, and a slightly increased Pt particle size. For a Pt/GCB catalyst, changes in the Raman spectra were clearly detected before and after durability testing, while surprisingly, for a commercial Pt/CB, only slight differences of spectra were found. The degree of degradation of the GCB support was determined from changes in the band area of the D1 band (ca. 1325 cm<sup>-1</sup>), which is associated with a loss of symmetry at the graphene layer edge, normalized to the G band (ca. 1575 cm<sup>-1</sup>) area, as estimated by spectral curve fitting [19–21] (Fig. 3.8).

**Fig. 3.6** Plot of the progress of (a) electrochemically active surface area (ECA) degradation and (b) normalized ECA (normalized to the initial ECA values) for c-Pt/CB ( $\circ$ ), c-Pt/GCB ( $\Delta$ ), Pt/GCB-HT ( $\square$ ), and n-Pt/GCB ( $\nabla$ ) catalysts as a function of the logarithm of the cycle number



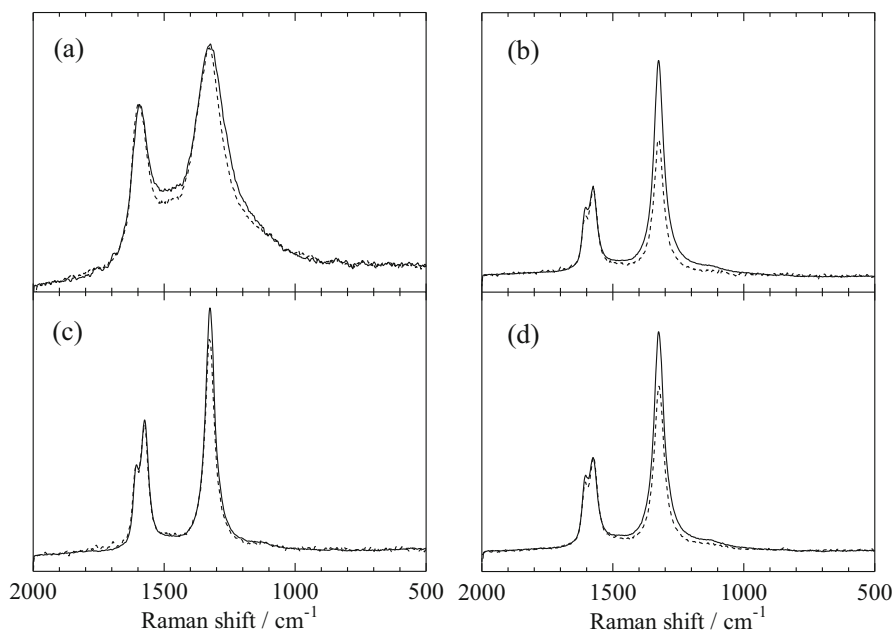
**Fig. 3.7** Cell performance  $I$ - $E$  curves for initial (open symbols) and after (filled symbols) durability testing for c-Pt/CB ( $\circ$ ), c-Pt/GCB ( $\Delta$ ), Pt/GCB-HT ( $\square$ ), and n-Pt/GCB ( $\nabla$ ) catalysts at  $65^\circ\text{C}$ , 100% RH with  $\text{H}_2$  and air (0.1 MPa). MEA: Pt loading (cathode/anode)  $0.5 \text{ mg-Pt cm}^{-2}$ , Nafion (NRE212), active electrode-area  $29.2 \text{ cm}^2$ , Japan Automotive Research Institute (JARI) standard cell [13]



It was found that the degradation of the GCB support was suppressed by a combination of heat treatment of the catalyst and uniform dispersion of the Pt nanoparticles, based on the examination of the  $A_{\text{D1-band}}/A_{\text{G-band}}$  values. Both the Raman spectra and the results obtained for the ECA and  $I$ - $E$  measurements produced

**Table 3.1** Typical properties of the c-Pt/CB, c-Pt/GCB, Pt/GCB-HT, and n-Pt/GCB cathode catalysts before and after the application of potential cycling ( $N = 10,000$ , except  $N = 3000$  for c-Pt/CB) for their durability tests

sample	Pt loading (wt%)	cycle number, N	ECA ( $\text{cm}^2 \text{g}^{-1}$ )		Half-life period (cycles)	$d_{\text{TEM}}$ (nm)	
			initial	after		initial	after
c-Pt/CB	46.1	3000	62.8	19.5	1000	$2.5 \pm 0.6$	$4.4 \pm 1.6$
c-Pt/GCB	46.7	10,000	38.6	19.8	9000	$3.4 \pm 0.7$	$4.8 \pm 1.0$
Pt/GCB-HT	50.1	10,000	25.3	17.6	60,000	$7.0 \pm 2.0$	$6.5 \pm 2.0$
n-Pt/GCB	46.1	10,000	32.5	17.6	20,000	$3.0 \pm 0.4$	$4.5 \pm 1.2$



**Fig. 3.8** Raman spectra for (a) c-Pt/CB, (b) c-Pt/GCB, (c) Pt/GCB-HT, and (d) n-Pt/GCB catalysts before (dotted line) and after (solid line) start-stop potential cycle testing [13]

consistent estimates of the degradation rates for the GCB-supported catalysts (Table 3.2).

The D3 band (ca.  $1495 \text{ cm}^{-1}$ ) area, originating from the amorphous carbon component, normalized to the G band area ( $A_{\text{D3-band}}/A_{\text{G-band}}$ ), also increased after the durability test. The after/before ratios of the  $A_{\text{D3-band}}/A_{\text{G-band}}$  ratios decreased in the order, c-Pt/CB > c-Pt/GCB > n-Pt/GCB > Pt/GCB-HT, which was the same order as that for the degradation rates of the ECA values. This band corresponds only to the amorphous carbon component, not a defective graphite layer caused by carbon corrosion (Fig. 3.8 and Table 3.2). We suggest that the D3 band can be used as an

**Table 3.2** Relative band area ratios of the D1 and D3 bands to the G band,  $A_{Dx\text{-band}}/A_{G\text{-band}}$  ( $x = 1, 3$ ), calculated from the Raman spectra for the c-Pt/CB, c-Pt/GCB, Pt/GCB-HT, and n-Pt/GCB catalysts obtained before and after the durability testing ( $N = 10,000$ , except  $N = 3000$  for c-Pt/CB)

	Pt/CB	c-Pt/GCB	Pt/GCB-HT	n-Pt/GCB
$A_{D1\text{-band}}/A_{G\text{-band}}$				
before	4.170	2.143	2.328	2.274
after	4.112	3.916	2.526	3.264
ratio change	0.986	1.827	1.085	1.435
$A_{D3\text{-band}}/A_{G\text{-band}}$				
before	0.314	0.145	0.214	0.136
after	1.256	0.290	0.202	0.164
ratio change	3.997	2.006	0.942	1.209

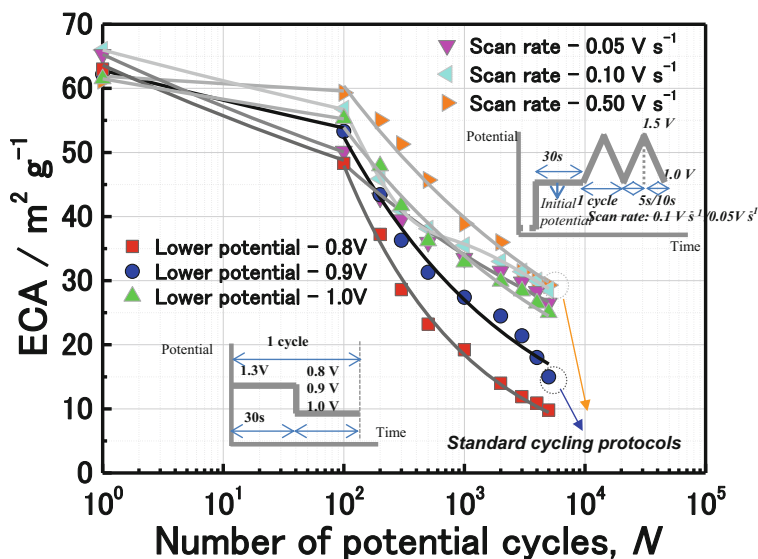
Ratio change = after / before

indicator of CB corrosion and thus the use of the  $A_{D3\text{-band}}/A_{G\text{-band}}$  ratio as a means to evaluate the degradation of c-Pt/CB as well as Pt/GCB catalysts.

In general, we found that the type of support material, Pt nanoparticle size, and the degree of Pt dispersion on the support all affected the degradation characteristics of the catalysts. In particular, the Raman spectroscopic measurements were found to be useful in the evaluation of the state of degradation of GCB-supported Pt catalysts.

### 3.2.2 Investigation of the Corrosion of Carbon Supports in Polymer Electrolyte Fuel Cells Using Simulated SU/SD Cycling

The effects of SU/SD in terms of the corrosion of CB support materials in PEFCs have been studied by several groups using potentiostatic tests (from 1.0 V to 1.4 V vs. the reversible hydrogen electrode, RHE) [22–28] and potential cycling tests (various potential ranges within 0.02–1.4 V vs. RHE) [27–34]. Based on these studies, reasonable results have been presented concerning the corrosion of the carbon support and the resulting Pt area loss. Nevertheless, most of these studies were performed under conditions relevant to the carbon corrosion itself and not under conditions simulating the actual SU/SD processes of PEFCs, and thus there has still been a need for a systematic, realistic approach to the evaluation of the SU/SD processes. We found in our previous study [35] that corrosion of the CB support in the cathode is accelerated mainly by raising the potential above 0.90 V versus RHE during daily SU/SD operation of residential PEFCs. For FCV SU/SD cycles, the potential of the cathode reached ca. 1.5 V versus RHE at low flow rates due to the reverse current mechanism, and the cathode potential exhibited a triangular sweep behavior [5]. Therefore, there appear to be two different types of relevant cathode potential cycling protocols to simulate the SU/SD processes, either a potential step cycle or a single triangular potential cycle above 0.9 V. Indeed, both of these two types of protocols have been recommended by the FCCJ for durability testing. The major automakers in Japan and the FCCJ have recently proposed the



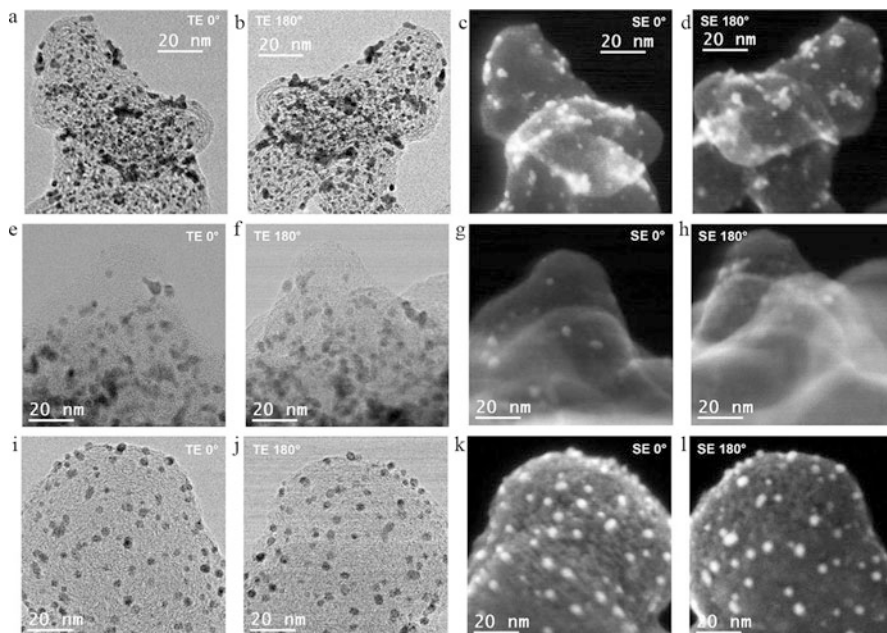
**Fig. 3.9** Effect of scan rate ( $0.50 \text{ V s}^{-1}$ ,  $0.10 \text{ V s}^{-1}$ , and  $0.05 \text{ V s}^{-1}$ ) for the triangular wave cycling and lower potential limit (0.8 V, 0.9 V, and 1.0 V) for the square wave cycling at  $80^\circ\text{C}$ , 100% RH with  $\text{H}_2$  and  $\text{N}_2$  (0.1 MPa). MEA: Pt loading (cathode/anode)  $0.5 \text{ mg-Pt cm}^{-2}$ , Nafion (NRE212), active electrode-area  $29.2 \text{ cm}^2$ , JARI standard cell [22]

triangular wave cycling protocol, based on the actual triangular sweep behavior caused by the gas exchange process in the operating fuel cell. Thus, this protocol correctly simulates the actual SU/SD behavior. Moreover, it uses a much shorter cycle time (2 s vs. 30 s for the step protocol), resulting in acceleration of the testing. Interestingly, the sweep mode is intrinsically more destructive for the same time period [36, 37].

We have compared the two protocols in investigating the corrosion of the CB support material and the degradation of the Pt/CB cathode catalyst by applying either a square wave cycling (2007 FCCJ protocol, potential  $E = 0.9\text{--}1.3 \text{ V}$  vs. RHE, holding 30 s at each  $E$  value, 1 min for one cycle) [18, 35] or a triangular wave cycling (2011 FCCJ protocol,  $E = 1.0\text{--}1.5 \text{ V}$  vs. RHE, at a scan rate of  $0.5 \text{ V s}^{-1}$ , 2 s for one cycle) [5]. During the SU/SD cycling, we examined the changes in ECA by use of cyclic voltammetry (CV) and the performance degradation of the MEAs with current-potential ( $I\text{-}E$ ) curves. The CB support corrosion was analyzed by use of scanning electron microscopy (SEM), transmission electron microscopy (TEM), and scanning transmission electron microscopy (STEM), providing detailed information on the corrosion process and catalyst degradation.

The standard cycling protocols are shown in Fig. 3.9, together with the cycle number  $N$  dependence of the ECA. The latter, as well as the mass activity, Tafel slope, and ohmic resistance showed that the square wave cycling caused more significant degradation of the catalyst than the triangular wave cycling, in terms of the number of cycles. However, as discussed later, the triangular cycling was





**Fig. 3.10** STEM images of the Pt/CB cathode catalyst before and after the durability test: (a) initial TEM image at 0°, (b) initial TEM image at 180°, (c) initial SEM image at 0°, (d) initial SEM image at 180°, (e) TEM image at 0° after 500 square wave cycles, (f) TEM image at 180° after 500 square wave cycles, (g) SEM image at 0° after 500 square wave cycles, (h) SEM image at 180° after 500 square wave cycles, (i) TEM image at 0° after 5000 triangular wave cycles, (j) TEM image at 180° after 5000 triangular wave cycles, (k) SEM image at 0° after 5000 triangular wave cycles, and (l) SEM image at 180° after 5,000 triangular wave cycles

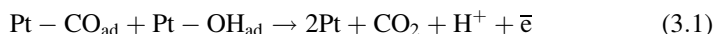
actually more destructive in terms of time. For the square wave cycling, the cycle half-life  $N_{1/2}$ , i.e., the  $N$  value at which ECA decreased to half its initial value, was 10 times shorter than that for the triangular wave cycling. The difference in durability for the two cycling modes was ascribed to the degree of carbon corrosion in the Pt/CB cathode catalyst. As a result of the square wave cycling, nearly all of the Pt particles were detached from the CB support, and the CL exhibited a significant decrease in thickness, ca. 86%, due to the severe carbon support corrosion and amorphization. During the square wave cycling, the corrosion of the CB support also occurred significantly in the interior of the CB particles in addition to the surface (Fig. 3.10e–h). During the triangular wave cycling, the CB support corrosion was less extensive and was observed more locally at unstable CB surface defects (Fig. 3.10i–l). However, the degradation caused by the triangular wave cycling mode was actually greater than expected on the basis of time spent at high potentials (>1.0 V, effect of scan rate in Fig. 3.9), because, during the fast cycling, the time that the Pt spends in a passivated state is minimized, increasing its activity in catalyzing the carbon corrosion. Further supporting this idea, it was found that a decreased value of lower potential used in the square wave cycling (from 0.9 V to 0.8 V) led to



very severe carbon corrosion, due to more complete Pt depassivation. Thus, it can clearly be seen that carbon corrosion has a strong effect on the durability of the Pt cathode catalyst during the SU/SD cycling of PEFCs.

### 3.2.3 Deleterious Effects of Interim CV on Pt/CB Degradation During SU/SD Cycling

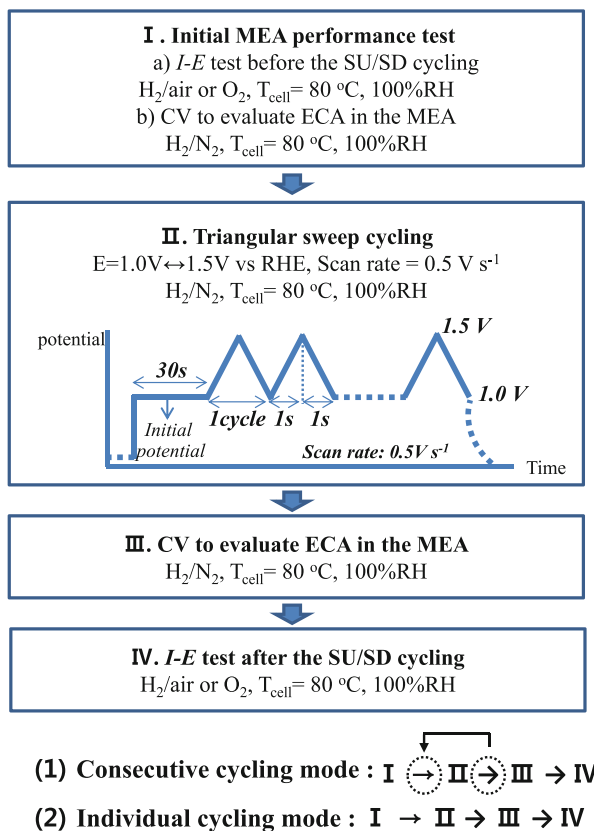
The rate of carbon corrosion is greatly increased at elevated potentials at the cathode during SU/SD [38]. Specifically, we found that CB corrosion in residential PEFCs is accelerated at operating potentials above 0.9 V versus RHE during daily SU/SD operation [35]. During FCV SU/SD, the cathode potential can reach ca. 1.5 V versus RHE at low flow rates due to the reverse current mechanism [5], leading to severe carbon corrosion. In addition, the presence of Pt nanoparticles can strongly accelerate the carbon corrosion due to a catalytic effect. The mechanisms remain to be understood in detail at present. Based on the work of Lebedeva et al., one possible mechanism involves the Pt-catalyzed oxidation of CO to CO<sub>2</sub> (Eq. 3.1) at higher potentials [39]:



In this way, platinum would accelerate the adjustment of the thermodynamic equilibrium. A similar effect was suggested by Maass et al. to be involved in MEA support degradation [31]. Wickman et al. [40] and Gubler et al. [6] have also reported the catalytic effect of platinum on carbon corrosion. Wickman et al. used the electrochemical quartz crystal microbalance (EQCM), in which a Pt particle layer on a carbon electrode exhibited a much larger mass loss compared with either a Pt-only or a carbon-only sample. Gubler et al. pointed out that the catalytic activity of platinum is limited by the formation of a passivating oxide layer on the platinum, based on the fact that the rate of platinum-catalyzed carbon corrosion is strongly dependent on the upper and lower potential limits. Sugawara et al. have also pointed out this type of phenomenon, focusing on the corrosion of the platinum in a carbon-supported catalyst [36]; Gallagher et al. focused on the corrosion of CB with no platinum present [37]. These studies have concluded that the formation and reduction of Pt oxides can accelerate the corrosion of both the carbon support and the Pt nanoparticles. Therefore, it is important to control the cathode potential behavior for the SU/SD process; for example, when the potential exhibits a triangular sweep between 1.0 V and 1.5 V during a short cycle time, a passive layer can form on Pt, thus limiting its catalytic effect, providing protection against PEFC performance degradation.

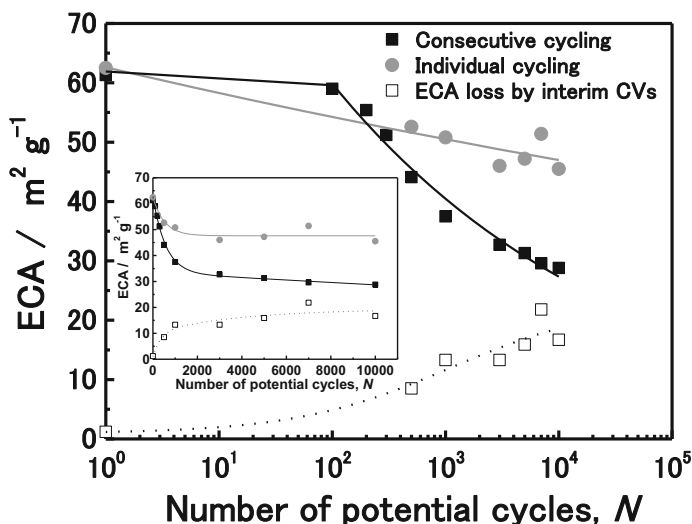
In this research, the adverse effects of interim CV measurements on Pt/CB catalyst durability, including Pt-catalyzed carbon corrosion, were examined during SU/SD cycling by use of two different experimental approaches (Fig. 3.11). In the industrial fuel cell community, researchers typically carry out interim CV measurements to monitor the Pt ECA, which usually decreases, during durability testing; see,

**Fig. 3.11** Experimental procedures for investigating the effects of interim CV measurements on Pt/CB catalyst degradation during SU/SD cycling evaluation: the first (1) is the consecutive cycling mode, and the second (2) is the individual cycling mode [38]



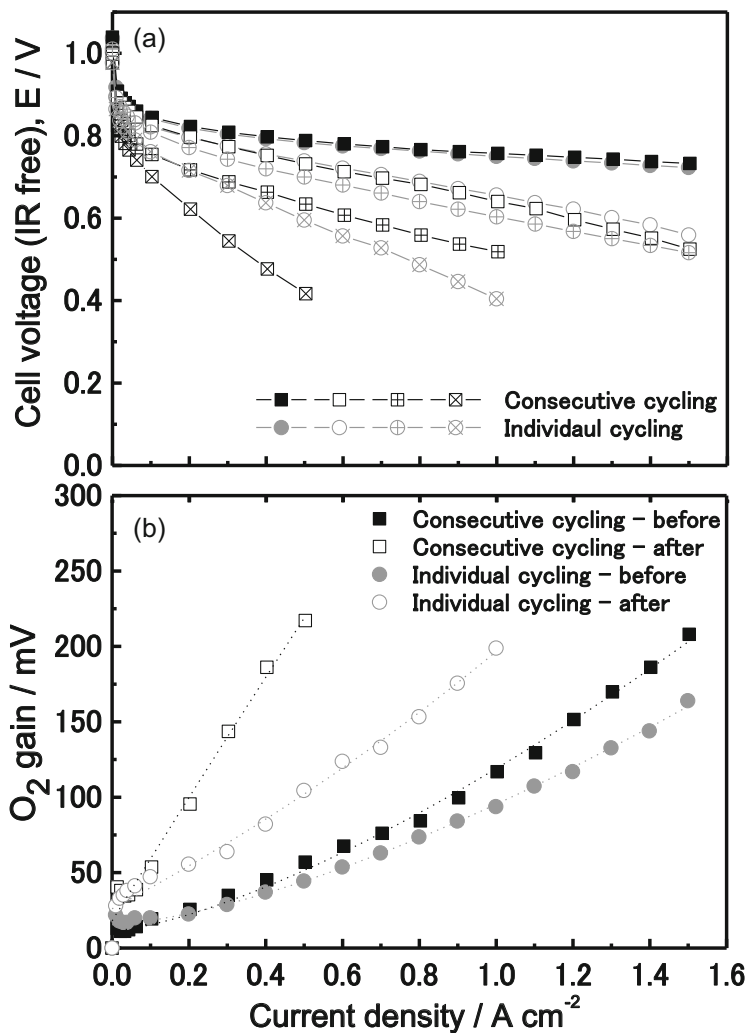
for example, the US DRIVE Partnership Fuel Cell Technical Team protocol, as reported by the US Department of Energy [41], and the FCCJ protocol [35]. The DOE protocol specifies interim CVs to be measured every 24 h, for a total of 17 times, during a cycling test of 400 h [41]. Indeed, researchers in the fuel cell/automotive industry generally have recognized that frequent interruptions of a durability test, e.g., to measure CV, can adversely impact the durability; however, such effects have not been examined and documented systematically. Recent results from our laboratory have clearly demonstrated for the first time, as far as we are aware, the adverse effects of interim CV measurements on Pt/CB catalyst durability during SU/SD cycling, providing important new information in terms of both durability testing and practical PEFC operation.

In our examination of the effects of interim CV measurements on Pt/CB catalyst degradation and Pt-catalyzed carbon corrosion during SU/SD cycling, the results for ECA losses and cycle half-life  $N_{1/2}$  proved that, with the conventional protocol, termed “consecutive cycling,” which included interim CV measurements, there was more advanced Pt/CB catalyst degradation in comparison with a protocol that involved CV measurements only at the beginning and end, termed “individual



**Fig. 3.12** Changes of ECA values of Pt/CB catalyst resulting from the consecutive cycling and individual cycling. MEA: Pt loading (cathode/anode) 0.5 mg-Pt cm<sup>-2</sup>, Nafion (NRE212), active electrode-area 29.2 cm<sup>2</sup>, JARI standard cell [38]

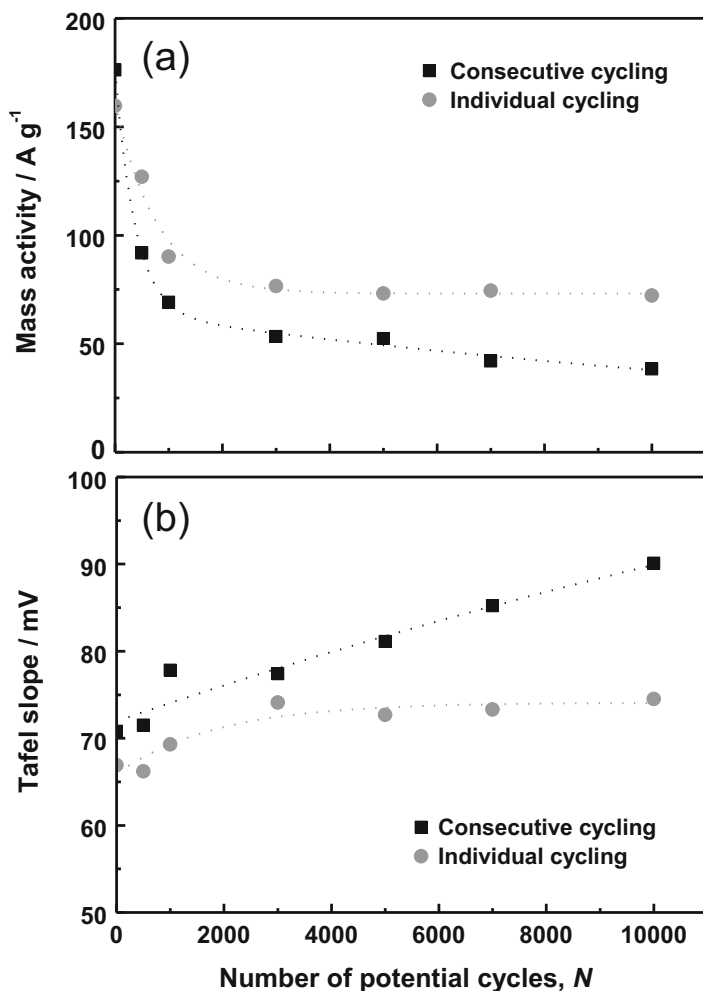
cycling” (Fig. 3.12). As a result of consecutive cycling, ECA losses were a factor of two greater after 10,000 cycles. Additional results, including *IR*-free *I-E* curves (Fig. 3.13a), oxygen gains (Fig. 3.13b), mass activity (Fig. 3.14a), and Tafel slope (Fig. 3.14b) showed that the deterioration of the Pt/CB CL structure, particularly the CB support corrosion, and the decrease of Pt utilization, due to Pt nanoparticle degradation, led to severe performance degradation and ECA loss due to the consecutive cycling. The consecutive cycling mode also led to the observation of larger current for the quinone-hydroquinone (Q-HQ) redox couple, evidence for severe carbon oxidation, which was ascribed to Pt catalysis, which had become depassivated at low potentials during the interim CV measurements. After the cycling tests, the SEM and TEM examinations showed that severe degradation of the Pt/CB catalyst resulted from platinum dissolution and CB support corrosion due to the interim CV measurements. Based on these results, we concluded that the negative effects of the interim CV measurements have an adverse effect on Pt/CB catalyst durability during SU/SD cycling evaluation, which can lead to overestimation of the effect of SU/SD on the degradation process. It has come to our attention that researchers in the auto industry are also at work to modify the SU/SD procedures and test protocols in order to minimize the cathode degradation. As an additional note, the phenomena described above, including Pt oxidation at high potential and oxide re-reduction at a low potential, are also important for ordinary operation, during which there can be significant load changes, and thus accelerated degradation can also result. Therefore, mitigation strategies are needed.



**Fig. 3.13** (a) IR-free polarization curves and (b) oxygen gains; comparisons before and after the SU/SD cycling (10,000 cycles). MEA: Pt loading (cathode/anode) 0.5 mg-Pt cm<sup>-2</sup>, Nafion (NRE212), active electrode-area 29.2 cm<sup>2</sup>, JARI standard cell [38]

### 3.2.4 Durability of Pt/GCB During Gas-Exchange SU Operation

In order to improve the performance and durability of our cathode catalysts, several years ago, we developed a GCB-supported Pt catalyst in which the Pt deposition was carried out by use of a type of reverse micelle technique that was termed the “nanocapsule method” (n-Pt/GCB) [12, 13, 42]. This method affords a high dispersion of the Pt nanoparticle particles on the GCB support, compared with

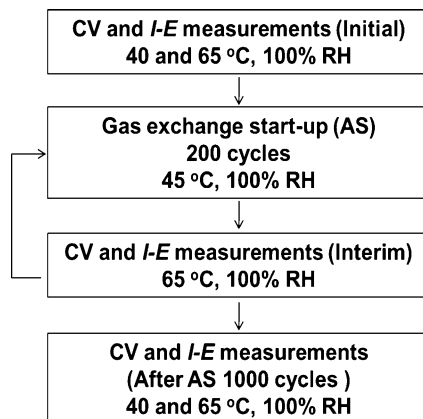


**Fig. 3.14** Changes of (a) mass activity and (b) Tafel slope; measured during the SU/SD cycling: anode gas, H<sub>2</sub> (70% utilization); cathode gas, O<sub>2</sub> (40% utilization); operating temperature, 80 °C; relative humidity (RH), 100% [38]

conventional techniques, leading to enhanced ORR activity. It was expected that the GCB itself would provide enhanced durability, but it was also found that the high dispersion of Pt further enhanced the n-Pt/GCB durability during potential cycling that simulated the PEFC SU/SD processes. Thus, it was demonstrated that the support carbon and the state of dispersion of the Pt particles play important roles in providing high performance and durability for PEFC electrocatalysts.

Several groups have worked to elucidate the performance degradation mechanisms under actual PEFC SU/SD conditions. Kreitmeier et al. examined carbon corrosion via the measurement of CO<sub>2</sub> production by use of online mass spectrometry [43].

**Fig. 3.15** Experimental procedures for the AS durability evaluation [42]



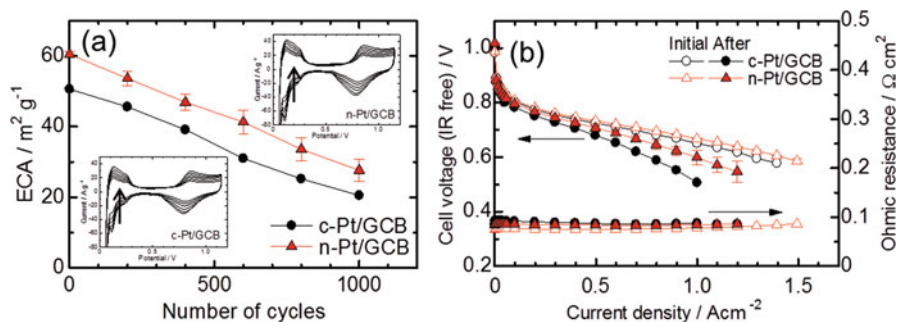
**Table 3.3** Conditions of anode and cathode gas for AS cycle [42]

	Anode gas, mL/min	Cathode gas, mL/min	Time, s
Step 1	Air: 360 Dry	Air: 360 Wet	90
Step 2	H <sub>2</sub> : 38 Wet	Air: 360 Wet	90
Step 3	N <sub>2</sub> : 180 Dry	N <sub>2</sub> : 180 Dry	60

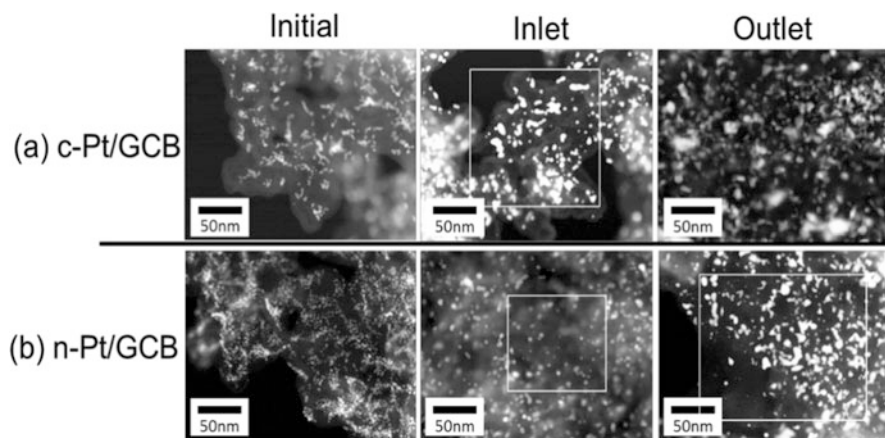
Lamibrac et al. made use of a segmented cell to measure internal currents within the cathode during PEFC SU/SD [44]. Durst et al. also made use of a segmented cell and were able to find correlations between the local CL performance loss and its degradation [45]. These measurements have been instructive, but have not distinguished between the effects of the SU and the SD on the cell performance and degradation, and thus the individual effects are remaining for in-depth investigation.

Three unique points of this research can be summarized as follows. First, in our previous research, we found that the well-dispersed Pt catalyst, n-Pt/GCB, exhibited higher durability than commercial Pt/GCB during a potential cycling protocol that simulates SU/SD. In more recent research, we have demonstrated the durability during a gas exchange protocol simulating air-start (AS), which is similar to actual FCV SU conditions (Fig. 3.15 and Table 3.3). The cycle number dependence of the ECA (Fig. 3.16a), cell performance (Fig. 3.16b), and particle size distribution of Pt and the degradation of the carbon were studied by TEM, STEM (Fig. 3.17 and Table 3.4), and micro-Raman spectroscopy.

Second, we also made use of glancing incidence X-ray diffraction (GIXD [46], Figs. 3.18 and 3.19) to analyze the Pt degradation in the CL and membrane. As far as we are aware, this is the first application of GIXD in the PEFC field. GIXD is a simple, nondestructive analytical technique to analyze Pt degradation quickly. Third, as already mentioned, even though it has been well accepted that the cathode CL degrades severely under SU conditions, caused by the reverse current mechanism



**Fig. 3.16** (a) ECA changes of c-Pt/GCB and n-Pt/GCB at 65 °C with 100% RH  $\text{N}_2$  in the cathode and 100% RH  $\text{H}_2$  in the anode measured during the AS cycling and (b) *I-E* curves of c-Pt/GCB and n-Pt/GCB at 65 °C with 100% RH  $\text{H}_2$  in the anode and air in the cathode before and after the entire AS-SU durability evaluation. MEA: Pt loading (cathode/anode)  $0.5 \text{ mg-Pt cm}^{-2}$ , Nafion (NRE212), active electrode-area  $29.2 \text{ cm}^2$ , JARI standard cell [42]



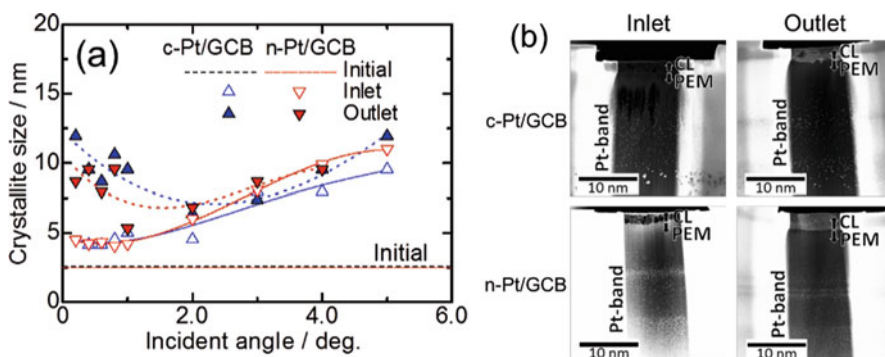
**Fig. 3.17** Dark-field STEM images of (a) c-Pt/GCB and (b) n-Pt/GCB of the initial state and both the inlet and outlet regions after the AS cycling. Mean sizes of Pt particles were calculated from the Pt particles that were not directly on the top surfaces of each of the FIB slices of the CLs within the white frames shown in the images of the inlet region for c-Pt/GCB and both inlet and outlet regions for n-Pt/GCB [42]

[3], particularly in the gas outlet region, we found that catalyst degradation also occurs in the inlet region during AS. With the use of a single cell with two RHEs, the degradation in the inlet region was found to be associated with ORR-induced potential excursions during the AS [42].

One of the main points of our recent research is that the well dispersed, nanocapsule-based n-Pt/GCB catalyst exhibited higher durability than that for a similar commercial sample (c-Pt/GCB) under AS conditions (Fig. 3.16). The ECA

**Table 3.4** Pt particle diameters (nm) of c-Pt/GCB and n-Pt/GCB in the initial state and both inlet and outlet regions at several depth positions after the AS durability evaluation obtained by STEM images (Fig. 3.17). Values in parentheses show distances from the interface between the membrane and the CL ( $\mu\text{m}$ ). [42] \*These values could not be measured due to severe catalyst degradation.

	Initial nm	After AS durability evaluation					
		Inlet nm ( $\mu\text{m}$ )			Outlet nm ( $\mu\text{m}$ )		
		membrane side	center	GDL side	membrane side	center	GDL side
c-Pt/GCB	3.3	5.0 (0)	6.3 (10)	6.4 (20)	NA*		
n-Pt/GCB	2.4	4.8 (0)	6.2 (16)	5.9 (32)	6.7 (0)	6.3 (3)	5.3 (5)



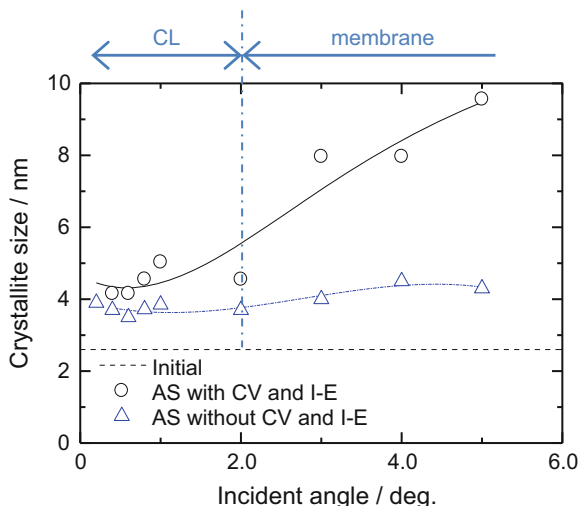
**Fig. 3.18** (a) Relationship between the incident X-ray angle and the crystallite size of c-Pt/GCB and n-Pt/GCB before and after the AS durability evaluation in the inlet and outlet regions and (b) dark-field STEM images of MEA cross-sections of c-Pt/GCB and n-Pt/GCB after the AS durability evaluation in the inlet and outlet region. The CL thicknesses for c-Pt/GCB and n-Pt/GCB became small due to the ion beam used to prepare the ultrathin slices of the membranes [42]

values and the  $I$ - $E$  performance of the n-Pt/GCB cathode were maintained at higher levels than that for the c-Pt/GCB cathode after 1000 durability cycles.

As a second main point, the spatial distribution of the carbon-supported Pt degradation was examined in order to evaluate in more detail the fuel cell durability under AS conditions, in which the anode was successively fed with air, hydrogen, and nitrogen. (Figs. 3.17, 3.18 and Table 3.4). As indicated by STEM and GIXD measurements, the n-Pt/GCB catalyst's highly uniform Pt particle distribution largely impeded their aggregation, particularly in the outlet region, compared with the less uniformly distributed c-Pt/GCB. Raman spectral measurements [13] also indicated that carbon corrosion was suppressed by n-Pt/GCB's uniform Pt distribution [42]. It was also shown by STEM and GIXD measurements that the Pt catalyst degradation occurred in the inlet region as well as the outlet region. With GIXD, the sizes of the Pt particles were examined as a function of incident angle  $\theta$  (Fig. 3.18a). Increasing  $\theta$  corresponds to increasing distance from the gas-side of the cathode



**Fig. 3.19** The relationship between the incident X-ray angle and the crystallite sizes of c-Pt/GCB before and after the durability evaluation of AS with and without interim measurements (CV and *I-E*) [42]



CL. For both catalysts, there was a trend of increasing Pt crystallite size with increasing  $\theta$ . This result applies to Pt particles both in the CL and also within the membrane because the XRD also detects particles in deeper positions in the interior of the membrane (Fig. 3.18a). For  $2.0^\circ < \theta < 5.0^\circ$ , which corresponds to the membrane region, it is concluded that Pt in ionic form had diffused and deposited as the metal via reduction by hydrogen that had permeated from the anode; the Pt crystallite size was then dependent on the hydrogen concentration, which would have been higher near the anode (Fig. 3.18b).

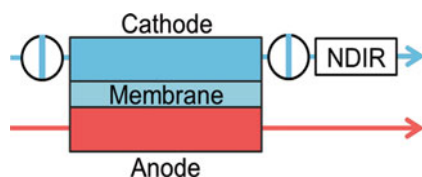
As a final point, the Pt particle degradation in the inlet region was ascribed to a combination of the interim CV measurements [38], which were carried out every 200 cycles, and the ORR-induced potential excursions in the inlet region resulting from the AS evaluation. As shown in Fig. 3.19, even after the AS without interim measurements, the Pt crystallites also increased slightly in size. Within the membrane, the increase of the size of the Pt crystallites after the AS evaluation without interim CV was much smaller than that for the AS with interim CV. Based on these results, it can be concluded that the AS accelerated Pt dissolution in the inlet region and the interim measurements caused the severe growth of the Pt crystallites. Thus, the degradation of the Pt particles in the inlet region was ascribed to the ORR-induced potential cycling in the inlet region during the AS durability evaluation. Additionally, the severe Pt catalyst degradation resulting from the interim CV was concluded to occur in the inlet region as well as in the outlet region. Notably, this condition was seen to be similar to load cycling in actual FCV operation.

In summary, we conclude that the cathode catalyst is degraded under SU conditions in both the gas inlet and outlet regions, even though previous work has focused more on the outlet region degradation [7, 47]. The result suggests that the degradation of the Pt catalyst and carbon support under the combined conditions of SU/SD cycling and the load cycling can be severe.

### 3.2.5 Degradation Mechanisms of CBs Under Hydrogen Passivation SU/SD Process

It has been proposed that, in order to improve the durability during SU/SD cycling of FCV PEFCs, a so-called hydrogen passivation process ( $H_2$ -SU/SD) can be implemented [48, 49]. In this process, during SD, the cathode gas valves are closed at both the inlet and outlet (Fig. 3.20, step 2 of the air-air cycle in Table 3.5), so that the  $O_2$  in the cathode is consumed by  $H_2$  permeating from the anode, and then the  $H_2$  supply is also stopped. During SU, both sets of valves are again opened, supplying air to the cathode and  $H_2$  to the anode (step 3 in Table 3.5). This  $H_2$ -SU/SD process is designed to prevent the construction of local cells, which are the basis of the reverse current mechanism [3], and it is also designed to suppress the COR and Pt aggregation that are usually observed during air-SU/SD (Table 3.6) [7, 42, 47].

We studied the COR during this  $H_2$ -SU/SD process, as outlined above (Fig. 3.20, step 2 of air-air cycle in Table 3.5) and found that the amount of oxidized CB decreased to approximately one-eighth compared with that for air-SU/SD (Table 3.6), mainly because the reverse current mechanism was suppressed (Fig. 3.21). Nevertheless, even this much-decreased amount of COR should not be ignored for long-term FCV operation, because the extent of oxidative degradation (55 ppm after 100 cycles) during  $H_2$ -SU/SD would lead to a 5.5% loss of carbon



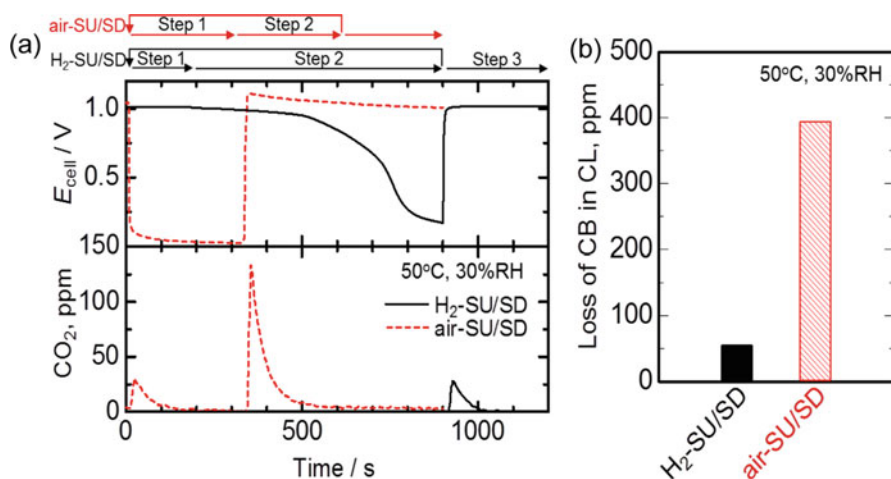
**Fig. 3.20** Schematic of the cell with gas lines equipped with two solenoid valves and a non-dispersive infrared (NDIR) detector. CCMs were constructed from CB both with and without Pt catalysts (CB (Ketjenblack EC), Pt/CB (TEC10E50E)) on each side of the membrane (Nafion NRE 211). The Pt loading:  $0.50 \text{ mg-Pt cm}^{-2}$ , active electrode-area  $29.2 \text{ cm}^2$ , JARI standard cell [48]

**Table 3.5** Conditions of anode and cathode gas for both the air-air cycle ( $H_2$ -SU/SD process) and the  $N_2$ -air cycle at  $50^\circ\text{C}$  and 30% RH under ambient pressure [48]

	Anode gas (ml / min)	Cathode gas (ml / min)		Time (s)
		air-air	$N_2$ -air	
Step 1		$N_2$ : 80	$N_2$ : 100	180
		$O_2$ : 20		
Step 2	$H_2$ : 100	$N_2$ : 0	$N_2$ : 0	720
Step 3		$N_2$ : 80	$N_2$ : 80	
		$O_2$ : 20	$O_2$ : 20	

**Table 3.6** Conditions of anode and cathode gas for the air-SU/SD cycle at 50 °C and 30% RH under ambient pressure [42, 48]

	Anode gas (mL/min)	Cathode gas (mL/min)	Time (s)
Step 1	Air: 360 Dry	N <sub>2</sub> : 80 O <sub>2</sub> : 20 Wet	300
Step 2	H <sub>2</sub> : 38 Wet	N <sub>2</sub> : 80 O <sub>2</sub> : 20 Wet	300

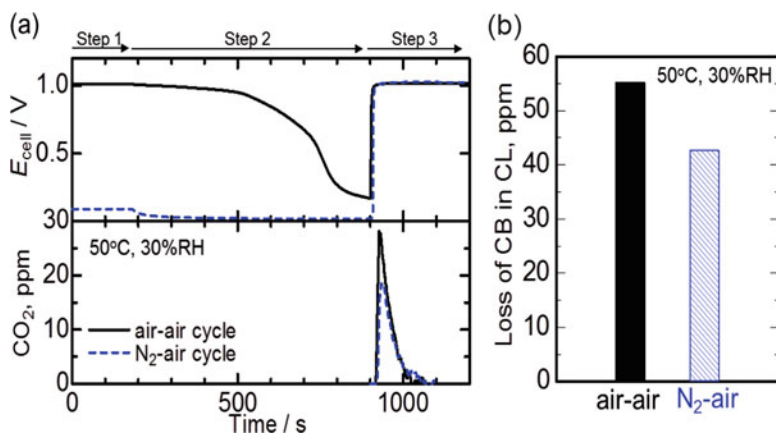
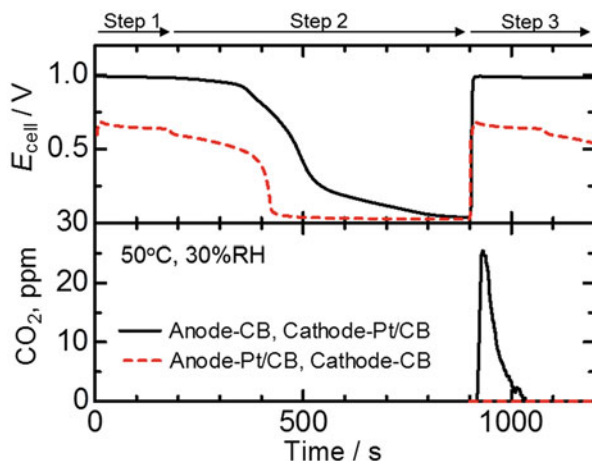
**Fig. 3.21** (a) Changes of the  $E_{\text{cell}}$  and  $\text{CO}_2$  concentration and (b) ratio of the oxidized CB to the total CB in the CL during both the air-SU/SD and  $\text{H}_2$ -SU/SD processes [48]

after 1000 cycles; moreover, the ECA and MA losses, even at 100 cycles, were ca. 13% and 26%, respectively [48].

We attempted to clarify the mechanisms for the COR occurring during  $\text{H}_2$ -SU/SD by examining (1) the effect of the presence of Pt by comparing CLs consisting of CB either with or without Pt on either side of the membrane (Fig. 3.22), (2) the time dependence of the COR during  $\text{H}_2$ -SU/SD by comparing the amounts of CB being oxidized for  $\text{N}_2$  versus air supply to the cathode in the first step (Table 3.5, Fig. 3.23), and (3) the correlation between the COR and the state of Pt oxidation by comparing the amounts of CB being oxidized during  $\text{H}_2$ -SU/SD with versus without a cathode potential hold (Fig. 3.24).

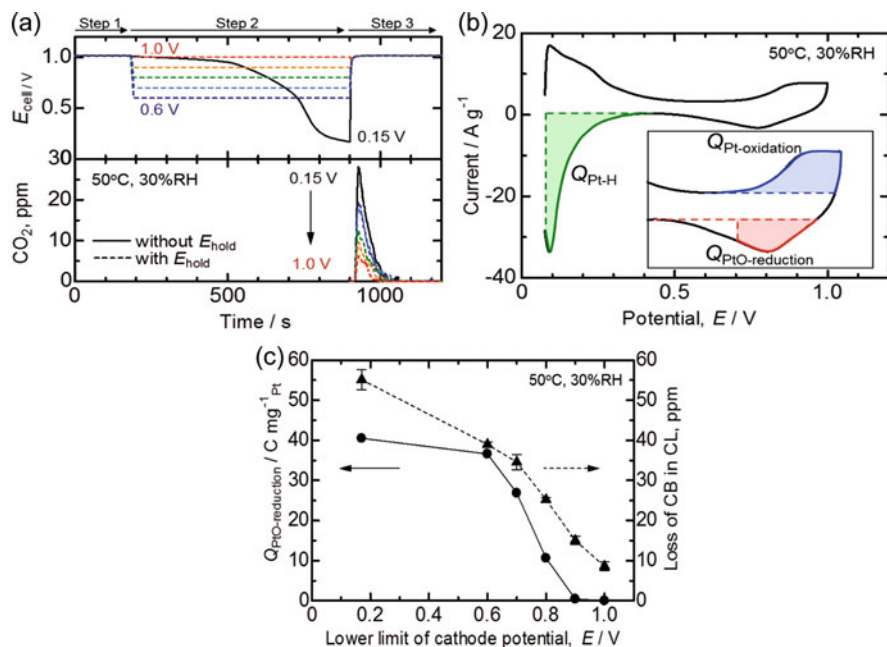
Based on these results (Fig. 3.22), it can be seen that the COR occurred only to a negligible extent in the absence of Pt in the cathode but was greatly accelerated in the presence of Pt. Comparing the air-air and  $\text{N}_2$ -air cycles, the difference in the amounts of CB being oxidized corresponds to the amount of CB oxidized in step 2 of the  $\text{H}_2$ -SU/SD process (Fig. 3.23, Table 3.5). These results indicate that the percentages of COR occurring during  $\text{H}_2$  permeation were 23% and during air re-introduction were 77%.

**Fig. 3.22** Changes of the  $E_{cell}$  and  $CO_2$  concentration with CB and Pt/CB both in the anode and cathode during the  $H_2$ -SU/SD process (air-air cycle in Table 3.1) [48]



**Fig. 3.23** (a) Changes of the  $E_{cell}$  and  $CO_2$  concentration and (b) ratio of the oxidized CB to the total CB in the CL during both air-air cycles and  $N_2$ -air cycles in Table 3.5 [48]

The changes both of  $E_{cell}$  and the  $CO_2$  concentration during the air-air cycle with and without the  $E_{hold}$  in step 2 can be seen in Fig. 3.24a. The  $CO_2$  concentration was found to decrease with increasing holding potential. The electric charges for both Pt oxidation ( $Q_{Pt-oxidation}$ ) and Pt oxide reduction ( $Q_{PtO-reduction}$ ) occurring at the various holding potentials were obtained from the CVs in order to relate the amount of CB being oxidized to the Pt oxidation state.  $Q_{PtO-reduction}$  values with various lower potential limits and  $Q_{Pt-H}$  values were determined from the areas under the CVs, as shown in Fig. 3.24b. The relationships between the holding potential and both (right axis, Fig. 3.24c) the amount of oxidized CB and (left axis)  $Q_{PtO-reduction}$  obtained during the air-air cycles, with and without the  $E_{hold}$  in step 2 of  $H_2$ -SU/SD, are shown. Both the amounts of oxidized CB and  $Q_{PtO-reduction}$  decreased with increasing

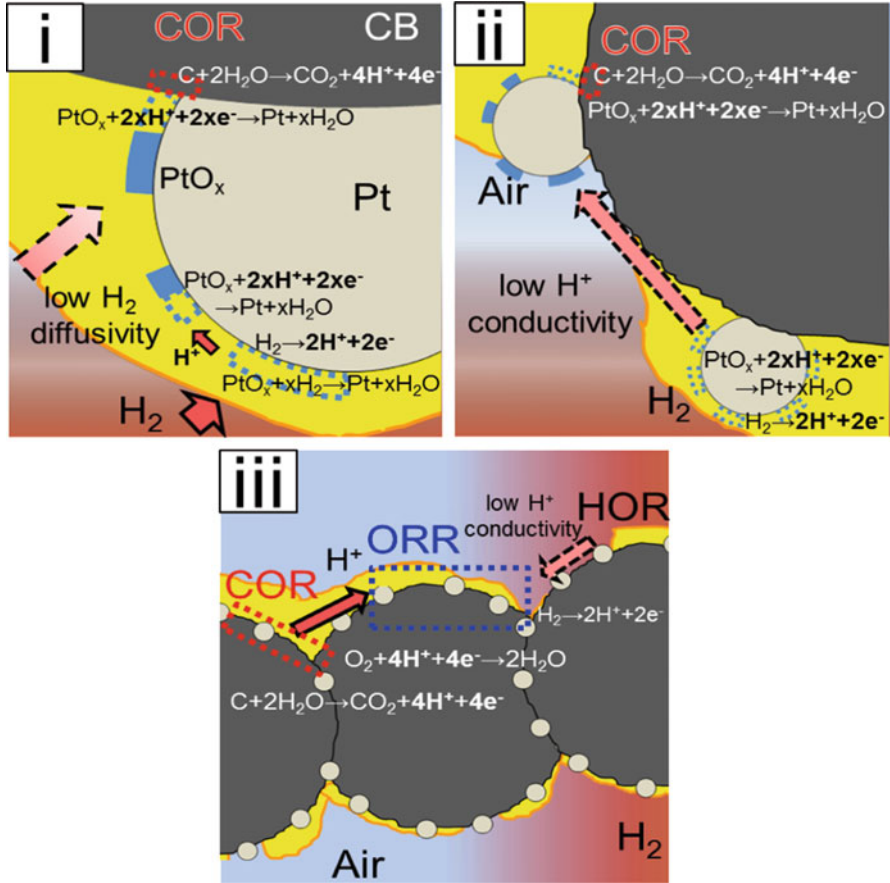


**Fig. 3.24** (a) Changes of the  $E_{\text{cell}}$  and  $\text{CO}_2$  concentration during air-air cycles with and without the  $E_{\text{hold}}$ , (b) CVs at 50 °C with 30% RH  $\text{N}_2$  in the cathode and 30% RH  $\text{H}_2$  in the anode, and (c) relationships both of the oxidized CB ratio to the total CB in the CL during the  $\text{H}_2$ -SU/SD process and  $Q_{\text{PtO-reduction}}$  with the lower limit of the cathode potential [48]

holding potential. This result clearly indicates that the extent of COR was correlated with the amount of Pt oxide reduction. On the other hand, as reported by Linse et al., a higher cathode potential served to decrease the extent of COR; the degree of Pt oxidation increased in the potential range from 0.4 V to 1.0 V [6]. Thus, we can propose a practical strategy that could be implemented in FCV systems would be to hold the cathode potential at relatively high values during  $\text{H}_2$ -SU/SD to suppress the COR.

Based on the above results, we propose three different types of mechanisms for the COR in both steps 2 and 3 of  $\text{H}_2$ -SU/SD due to the nonuniform distributions of both ionomer and Pt particles (Fig. 3.25). The COR was caused by local cells that arose due to (i) a limited access of  $\text{H}_2$  or limited access of protons associated with (ii) the reduction of the Pt oxide during the  $\text{H}_2$  permeation from the anode to cathode and (iii) the ORR at metallic Pt sites during the air re-introduction.

In order to improve the durability of PEFCs in FCVs, the use of higher stability support materials, such as GCB [13, 42] or metal oxides [50–58], is an effective approach to inhibit the COR during the  $\text{H}_2$ -SU/SD process. Based on the COR mechanisms (i), (ii), and (iii), the uniform distribution of the ionomer in the cathode CL can prevent both the inhibition of the  $\text{H}_2$  supply and the shortage of  $\text{H}^+$ , which lead to the COR associated with the reduction of the Pt oxide and the ORR. The



**Fig. 3.25** Oxidation mechanisms of the carbon support due to local cells during step 2 ( $H_2$  permeating to the cathode from the anode) both with (i) a single Pt particle and (ii) two or more Pt particles, and (iii) during the step 3 (artificial air resupplied) during the  $H_2$ -SU/SD process [48]

increase of the exchange speed of air in the cathode also mitigates the COR caused by a mechanism (iii). The effects of these approaches on the durability during the SU/SD process can be further enhanced by the preservation of a more highly oxidized state of the Pt.

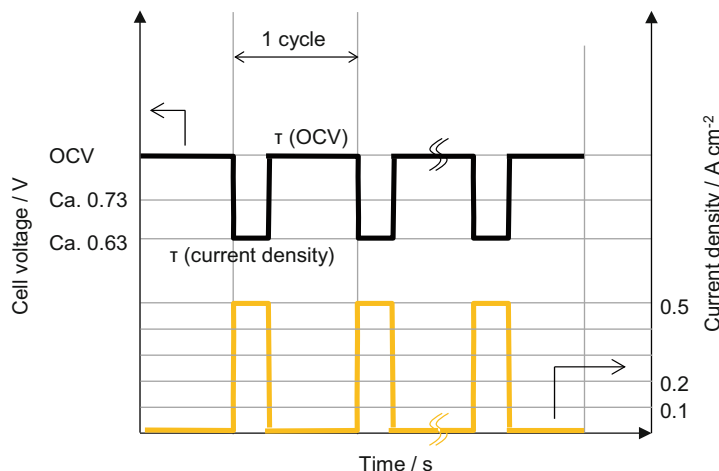
### 3.2.6 Load Cycle Durability of a Pt/GCB

This research focused on load cycling, which can accelerate the degradation of the Pt nanoparticles (NPs), due to dissolution [59–62] and particle growth [63, 64]. Many researchers have attempted to address this issue. It is well known that the degradation of Pt NPs is evaluated by potential cycling, which simulates load cycling, using a

potentiostat. The degradation of Pt has been intensively investigated under various potential cycling conditions by Mitsushima et al. [65–68]. According to these papers, the degradation of Pt under potential cycling is accelerated by a high positive-going sweep rate and a low negative-going sweep rate [66], increasing temperature, and decreasing pH [67]. Moreover, other researchers have also reported the degradation of Pt under various potential cycling regimes [69–71]. Uchimura et al. have reported that the degradation of Pt was accelerated to a greater extent during potential cycling involving asymmetric triangular profiles with lower negative-going sweep rates compared with those with low positive-going sweep rates [69]. Yasuda et al. found that Pt deposition in the membrane was accelerated by the presence of hydrogen transported through the membrane from the anode. This deposition was also affected by the presence of oxygen in the cathode [71]. Kongkanand et al. also concluded that the electrooxidation of Pt is accelerated more by the presence of oxygen than the presence of nitrogen at lower potentials [72]. The degradation of Pt NPs during potential cycling is primarily caused by Ostwald ripening and place exchange. As already mentioned, Ostwald ripening leads to increased Pt particle size, because the smaller particles have a higher surface energy and thus are less stable than the larger particles [68, 71, 73, 74]. Oxygen atoms adsorbed on the Pt surface can enter the Pt lattice by place exchange at potentials greater than 1.1 V [75–78]. These studies have revealed that the degradation of Pt during potential cycling is correlated strongly with the oxidation of Pt NPs. However, it has been suspected that the actual degradation of Pt is different from that observed with potential cycling with H<sub>2</sub>/N<sub>2</sub> because the FCV operating condition includes load cycling with H<sub>2</sub>/air.

In this research (Fig. 3.26 and Table 3.7), we investigated the degradation of the electrocatalyst in terms of Pt dissolution, Pt deposition, and Pt particle growth in both the CL and membrane under various conditions, as follows: load cycling involving OCV and load holding times at a high current density (sample names A1, A2, and A3); at a lower current density (A5); and at OCV (A4) under 100% RH and a lower RH (A6). The electrochemical evaluation was carried out with CV and *I-E* curve measurements (Figs. 3.27 and 3.28). The electrodes were analyzed by TEM (Fig. 3.29), scanning ion microscopy (SIM, Fig. 3.30), and STEM energy-dispersive X-ray spectroscopy (EDX) before and after the load cycling evaluations (Fig. 3.31). These results provide information on the degradation of Pt under realistic FCV operating conditions.

The Pt degradation on the GCB support was examined during load cycling as a function of the holding times of OCV/load at 80 °C and 100% RH, and it was found that the interim load cycles between the OCV holding periods clearly affected the degradation of the cathode electrocatalyst (Figs. 3.27 and 3.28d, A3 > A1 > A2, and A3 > A4). This phenomenon corresponds to the previous results of our group, as described above, which reported the deleterious effects of interim CV and *I-E* on Pt/CB catalyst degradation during SU/SD cycling evaluation [38, 42]. In addition, the Pt dissolved from the cathode CL was significantly deposited in the membrane during load cycles with longer OCV holding times (Fig. 3.29c). The results of Figs. 3.30 and 3.31 indicate the effect of both the RH (A6) and the current density



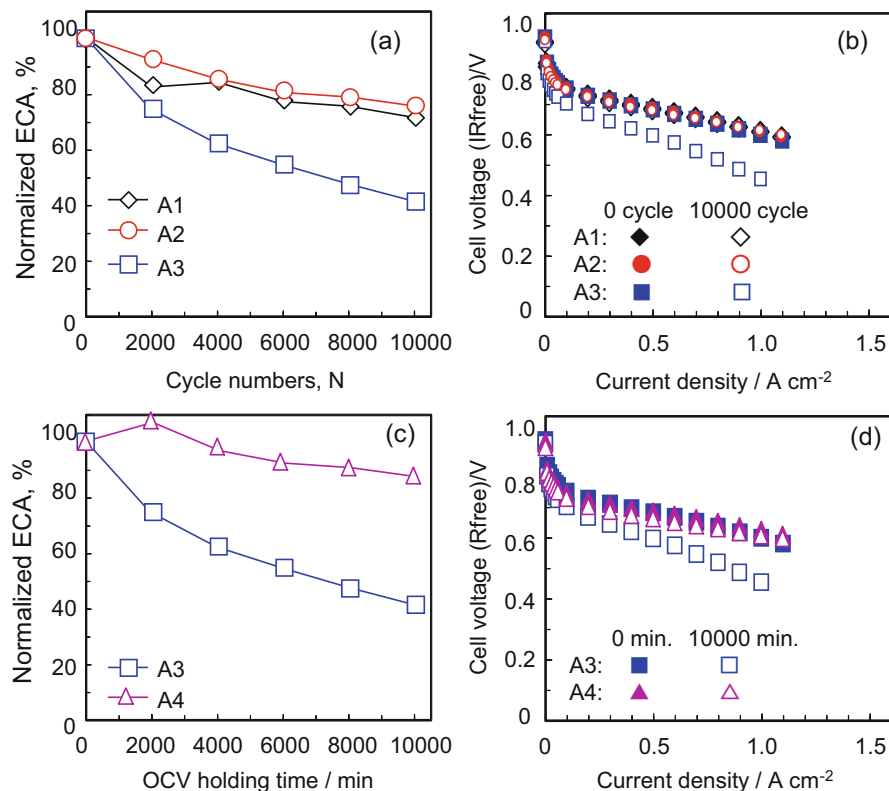
**Fig. 3.26** Protocol for the simulation of fuel cell load cycles with OCV and various current loads (0, 0.1, 0.2, 0.5  $\text{A cm}^{-2}$ ) with supply of  $\text{H}_2$ /air at either 50 or 100% RH; holding time at OCV,  $\tau(\text{OCV}) = 3, 60$  and  $600,000$  s, and holding time under current load,  $\tau(\text{CL}) = 0, 3$  and  $60$  s [59]

**Table 3.7** Load cycle conditions [59]

Sample name	Nominal cell potential range, (V)	OCV holding time, (s)	Load current density, ( $\text{A cm}^{-2}$ )	Load holding time, (s)	Cycle number	Total OCV holding time, (s (min))	Relative Humidity, % RH
A1	Ca. 0.63 ↔ OCV	3	0.5	3	10,000	30,000 (500)	100
A2	Ca. 0.63 ↔ OCV	3	0.5	60	10,000	30,000 (500)	100
A3	Ca. 0.63 ↔ OCV	60	0.5	3	10,000	600,000 (10000)	100
A4	OCV	600,000	0	0	–	600,000 (10000)	100
A5	Ca. 0.73 ↔ OCV	60	0.1	3	10,000	600,000 (10000)	100
A6	Ca. 0.63 ↔ OCV	60	0.2	3	10,000	600,000 (10000)	50

on the Pt degradation during load cycles with longer OCV holding times; specifically, it was found that the load cycle with lower current density (A5), i.e., higher operating potential, accelerated the Pt particle growth but suppressed the Pt dissolution. It was also revealed that both the dissolution and the redeposition of Pt were effectively suppressed during load cycles at lower RH due to the decrease of the water content in both ionomer and membrane, which contributed to the poor transport of Pt ions and the suppression of Pt oxidation. The degradation of the

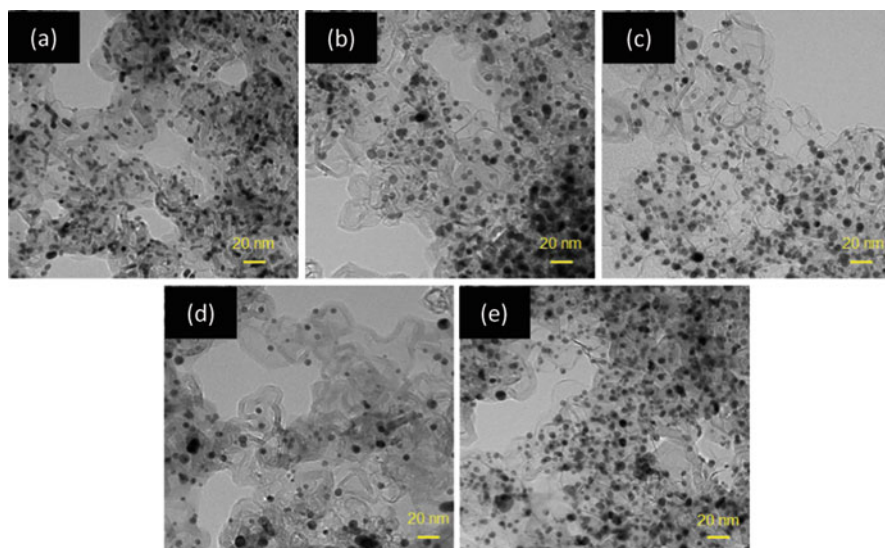




**Fig. 3.27** (a) Normalized ECA changes during the durability evaluations of load cycles with holding times of OCV/load ( $0.5 \text{ A cm}^{-2}$ ) between ca.  $0.63 \text{ V}$  and OCV at  $80^\circ \text{C}$  and  $100\% \text{ RH}$ ,  $\diamond$ :  $3 \text{ s}/3 \text{ s}$  (A1),  $\circ$ :  $3 \text{ s}/60 \text{ s}$  (A2),  $\square$ :  $60 \text{ s}/3 \text{ s}$  (A3), (b) IR-free  $I$ - $E$  curves before and after the durability evaluations at  $80^\circ \text{C}$  and  $100\% \text{ RH}$  under  $\text{H}_2/\text{air}$ , (c) Normalized ECA changes during the load cycles and the OCV holding at  $80^\circ \text{C}$  and  $100\% \text{ RH}$ ,  $\square$ : OCV/load holding time of  $60 \text{ s}/3 \text{ s}$  (A3),  $\triangle$ : OCV holding time of  $10,000 \text{ min}$  (A4), (d) IR-free  $I$ - $E$  curves before and after the load cycles and OCV holding at  $80^\circ \text{C}$  and  $100\% \text{ RH}$  under  $\text{H}_2/\text{air}$  ( $0.1 \text{ MPa}$ ), Pt loading (cathode/anode)  $0.1/0.5 \text{ mg-Pt cm}^{-2}$ , Nafion (NRE211), active electrode-area  $29.2 \text{ cm}^2$ , JARI standard cell [59]

electrocatalyst in the case of the high current density range (A3, ca.  $0.63 \text{ V}$ - OCV, Fig. 3.31a), in the presence of large amounts of crossover  $\text{H}_2$  and back-diffusing water, was preferentially caused by the Pt dissolution near the membrane boundary. That in the case of low current density (A5, ca.  $0.73 \text{ V}$ - OCV, Fig. 3.31b), in the presence of small amounts of crossover  $\text{H}_2$  and back-diffusing water, was preferentially caused by Pt particle growth. On the other hand, in the durability evaluation at low RH (A6, Fig. 3.31c), in the presence of small amounts of water, both the Pt dissolution and Pt particle growth were effectively suppressed.

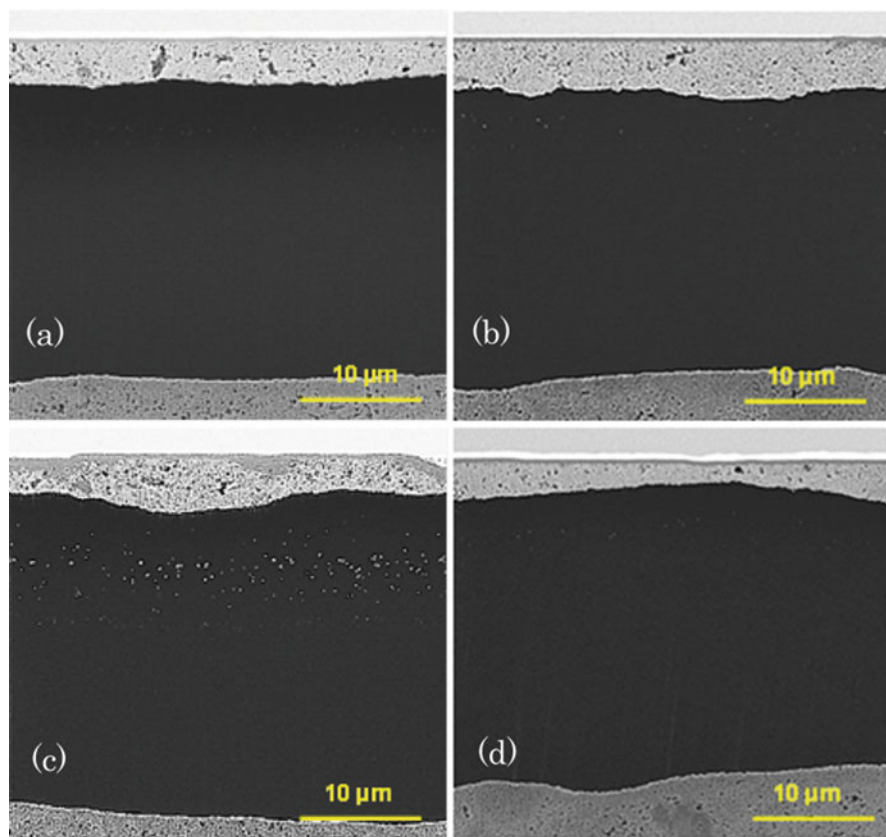
We illustrate the models of both the Pt degradation and the suppression in Fig. 3.32. The Pt oxidation dependence on the holding potential might also depend on the holding time at a high cell voltage such as the OCV. Uchimura et al. reported



**Fig. 3.28** TEM images of Pt/GCB cathode catalyst before and after the durability evaluations: (a) initial Pt/GCB cathode electrocatalyst after conditioning, (b) after the durability evaluation with holding times of OCV 3 s/load 3 s (A1), (c) OCV 3 s/load 60 s (A2), (d) OCV 60 s/load 3 s (A3), (e) OCV holding time of 10,000 min without load cycle (A4) [59]

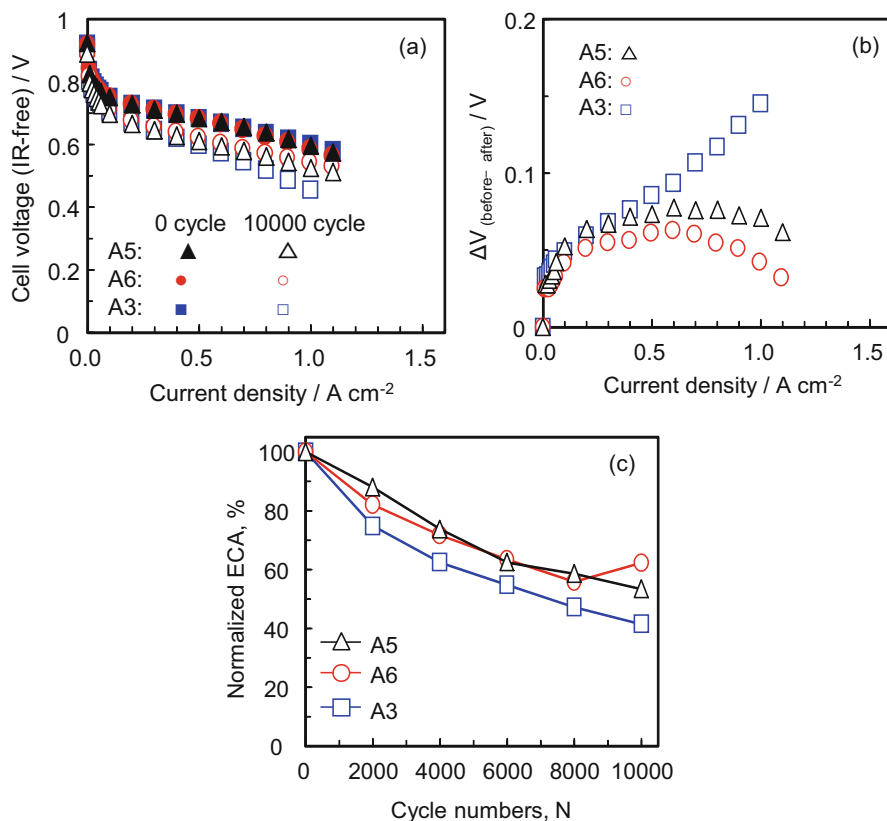
that the Pt surface is covered with oxide species during the potential cycling in the potential range from 0.80 V to 0.95 V [70]. Kongkanand and Alsabet have also reported that Pt is more oxidized at higher potentials and longer holding times [72, 79]. The Pt dissolution is accelerated when the upper potential limit is greater than 0.8 V [36]. In addition, the presence of  $O_2$  can induce place-exchange [72]. Therefore, similar to results presented in the previous Section, these results suggest that the degradation from Pt dissolution is accelerated by both deep oxidation and reduction of PtO, which are caused by both the longer OCV holding and the lower potential limit, respectively (A3). The reduction of PtO is well known to produce  $Pt^{2+}$  [36]. The Pt dissolution during the load cycles occurs particularly in the cathode CL near the membrane side, as shown in Fig. 3.31a. The dissolved  $Pt^{2+}$  ions diffuse into the membrane and are deposited therein by crossover  $H_2$  from the anode, as shown in Fig. 3.29c. These Pt degradation modes in the CL are illustrated in Fig. 3.31a. The cell performance in the high current density region decreases remarkably because the proton paths are extended by the Pt dissolution in the cathode CL near the membrane side (A3 in Figs. 3.27b, d, 3.30b, c, and 3.31a).

In the load cycles of condition A5 (low current density, ca. 0.73 V, and OCV), the deterioration of the cell performance was suppressed to a greater extent than that in the A3 condition (high current density, ca. 0.63 V, and OCV). The comparison of the Pt distribution after the load cycles between conditions A3 and A5 (Fig. 3.31) indicates that the disappearance of Pt in the CL near the membrane side was suppressed by the low current load of the A5 condition. However, the Pt particle



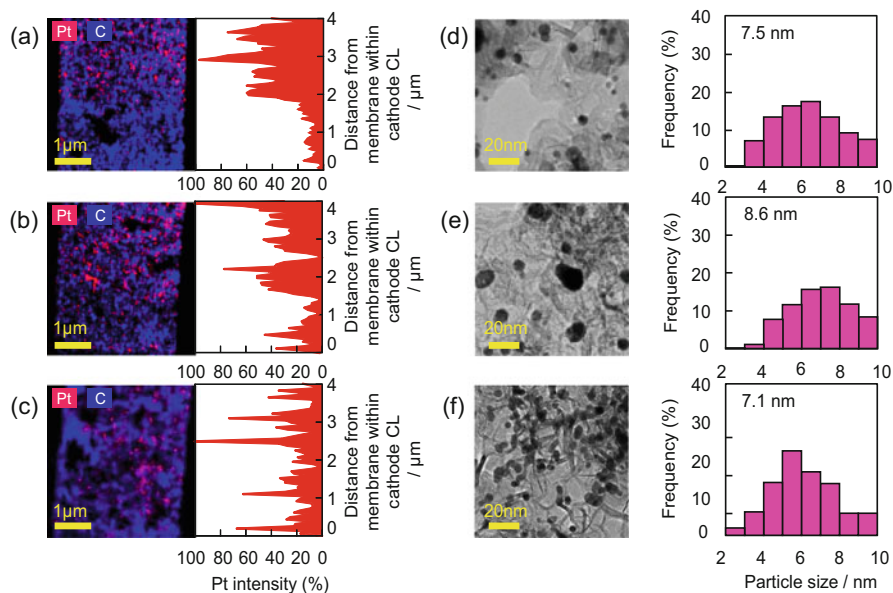
**Fig. 3.29** SIM images of the cross-sections of MEAs after the durability evaluations: (a) with OCV/load holding times of 3 s/3 s (A1), (b) 3 s/60 s (A2), (c) 60 s/3 s (A3), (d) OCV holding time of 10,000 min (A4) [59]

growth was enhanced by the A5 condition, which seems to have been caused by electrochemical Ostwald ripening. With the lower potential of ca. 0.63 V, more PtO is reduced, producing  $\text{Pt}^{2+}$ , which can then diffuse into the membrane, whereas at ca. 0.73 V, less PtO is reduced, and the  $\text{Pt}^{2+}$  tends to be deposited within the CL. In addition, the increase of water back-diffusion is suppressed at the lower current density of  $0.1 \text{ A cm}^{-1}$ , compared with the higher current density of  $0.5 \text{ A cm}^{-1}$ , which would otherwise help to carry the  $\text{Pt}^{2+}$  ions into the membrane. Crossover  $\text{H}_2$  may also be suppressed, which otherwise would have caused Pt to be deposited in the membrane at the lower current density. The operating condition with current load affects the amount of water associated with transporting protons [80]; increased humidity has been shown to enhance the  $\text{H}_2$  permeability [81], so we hypothesize that increased load leads to increased  $\text{H}_2$  crossover. These Pt degradation modes are consistent with Fig. 3.31b and are illustrated in Fig. 3.32b.



**Fig. 3.30** (a) IR-free I-E curves before and after the durability evaluations, (b) difference of cell voltages before and after the durability evaluations using A3, A5, A6 conditions, (c) Normalized ECA changes of the cathode during the durability evaluations using A3, A5, A6 conditions,  $\square$ : load cycle with OCV/load holding times of 60 s/3 s (A3),  $\triangle$ : load cycle with low current density (A5),  $\circ$ : load cycle at low RH (A6), [59]

In the case of the low RH condition of A6, the deterioration of the cell performance and the  $Q_{PtO}$  were smaller than those of the other conditions (Fig. 3.30). The thicknesses of both the ionomer and the membrane would decrease with decreasing RH, and the water contents would also decrease. The Pt ion transport in the ionomer and membrane would decrease with the shrinking of the water (and ionic) channel networks due to the decrease of the water content [33]. In addition, the oxidation of Pt was suppressed during the load cycles under low RH conditions [59]. Uchimura et al. have also reported that Pt dissolution is suppressed at low RH (ca. 30% RH) [67]. Therefore, the Pt dissolution and particle growth during the load cycling under lower RH conditions was suppressed (Fig. 3.31c, f), because the Pt ion transport was low, the oxidation of Pt was limited, and the redeposition of Pt was inhibited, as illustrated in Fig. 3.32c. Consequently, we found that low RH operation during load



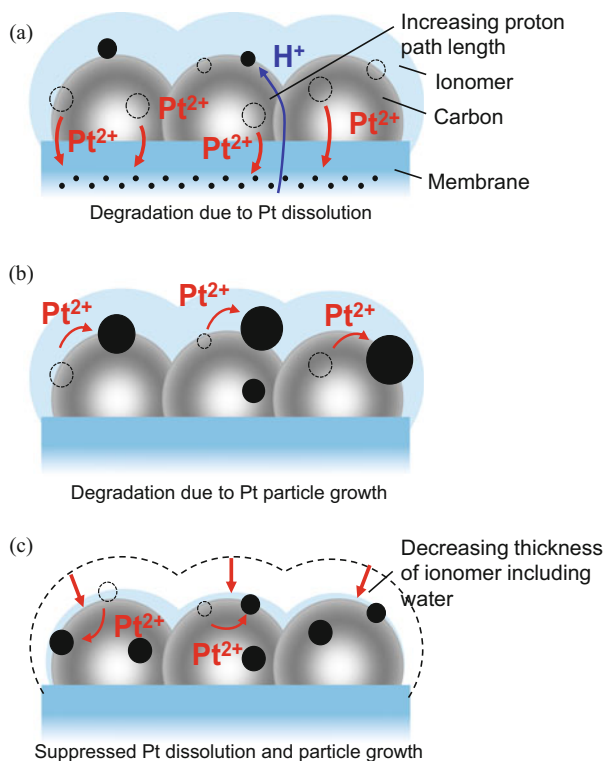
**Fig. 3.31** Pt distribution by EDX element mapping (left) and Pt line scan (right) in the cathode CL near side of the membrane after the durability evaluations using (a) load cycle with long OCV holding time (A3), (b) with low current density (A5), and (c) at low RH (A6). The vertical axis shows the CL distance from the membrane. TEM images of Pt particles on GCB support (left) and particle size distribution of Pt (right) after the durability evaluations; (d) load cycles with long OCV holding time (A3), (e) with low current density (A5), and (f) at low RH (A6) [56]

cycling is important in suppressing the Pt degradation from Pt dissolution and Pt particle growth in the cathode CL. Thus, we conclude that the Pt degradation during load cycling can be suppressed by operation with a suitably low RH, even for longer OCV holding times, such as during idling and immediately after fuel cell SU.

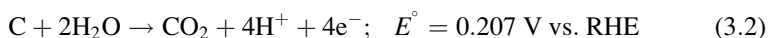
### 3.3 Synthesis and Evaluation of Cell Performance and Durability for Pt Supported on Conducting Ceramic Nanoparticles During Simulated SU/SD Cycles

#### 3.3.1 Degradation of Carbon Support and Alternative Support Materials

In the previous Section, we focused on the problem of the degradation of the carbon support, which should be solved in order for the fuel cell to find widespread application in vehicles and residential power units. The carbon support has an intrinsic thermodynamic instability as a result of its oxidative corrosion to carbon dioxide (Eq. 3.2) under the typical PEFC operating condition of low pH and high humidity [34, 82].



**Fig. 3.32** Schematic of Pt (black) degradation on the GCB (gray) support in the cathode for (a) load cycles with a longer OCV holding time (A3, ca. 0.63 V – OCV, 100% RH), (b) that with a low current density range (A5, ca. 0.73 V – OCV, 100% RH), (c) that at low RH (A6, ca. 0.63 V – OCV, 50% RH) [59]



Operation in the higher potential range ( $>0.9$  V), particularly under automotive SU/SD conditions, accelerates the degradation of the cathode catalyst and leads to the deterioration of the PEFC performance, as we have described in detail in the previous Sections.

The development of alternative supports to carbon with high electrical conductivity and stability in the high potential range is thus an extremely important issue to address in order to ensure the success of fuel cell commercialization. A number of candidates have been reported, such as  $TiO_2$ ,  $SnO_2$ , TiB, TiN,  $WO_3$ , TiC, WC,  $In_2O_3$ ,  $IrO_2$ ,  $In_2O_3-SnO_2$ ,  $Ti_4O_7$ , and  $TiO_x$  [50, 83–93]. Moreover, alternative non-carbon supports also require the high surface area to maintain a high dispersion of the Pt nanoparticles. Mesoporous particles [94, 95], nanoparticles [96, 97], nanotubes [98], and nanowires [99] have been reported as preferred microstructures to construct high surface area supports. In addition, the electrocatalyst of the PEFC is

necessarily in the form of a gas diffusion electrode, which requires not only a high surface area but also electrically conductive pathways and gas diffusion pathways.

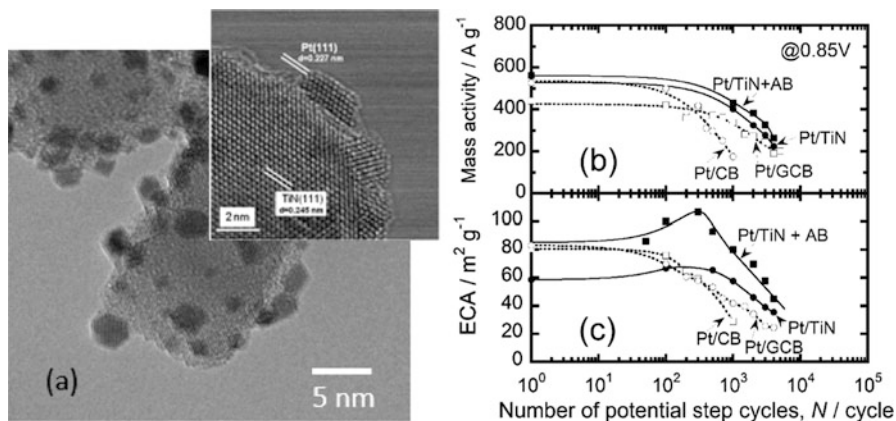
To meet these requirements, we proposed nanoparticle nitride/carbide supports, specifically, TiN and TiC [100–103], and the nanoparticle oxide supports SnO<sub>2</sub> and TiO<sub>2</sub> with fused-aggregate network structures to be applied to PEFC cathodes [56, 104–110]. In particular, the fused-aggregate network structure, involving fusion of nearest-neighbor particles to form a random branching structure, is similar to that of CB and GCB. We have examined the performance and durability of these catalysts by rotating disk electrode (RDE) and single cell measurements.

### 3.3.2 Pt Supported on Titanium Nitride (Pt/TiN) and Carbide (Pt/TiC)

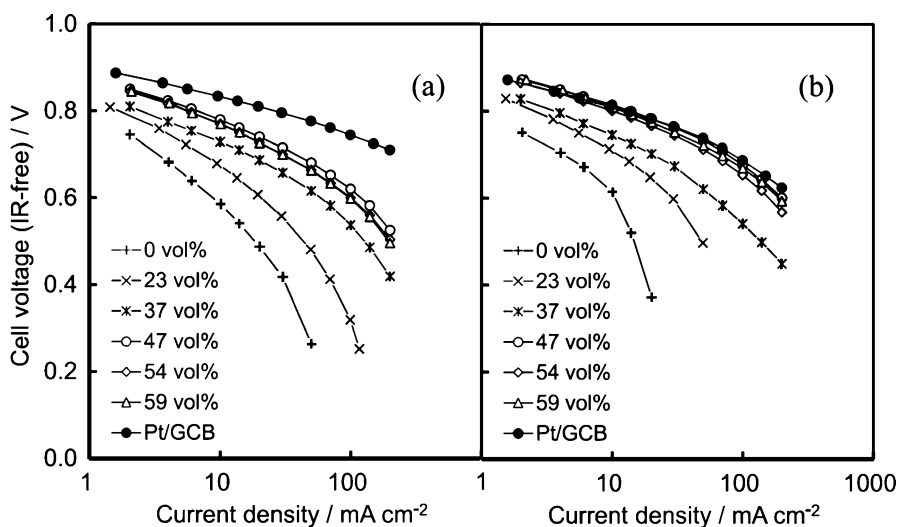
Titanium nitride (TiN) is known to be exceptionally stable under acidic conditions, and therefore, it has been used as a corrosion-resistant coating on stainless steel [100–103]. TiN also has more than a factor of ten greater electrical conductivity compared to those of typical oxides or carbons. TiN nanoparticles with high surface area were obtained in a tailor-made fashion by use of a radio frequency (RF) plasma method (Nisshin Engineering Co.). The surface area of the TiN support was measured to be 40 m<sup>2</sup> g<sup>-1</sup> by the BET adsorption method (BELSORP-max, MicrotracBEL, Inc.). We synthesized Pt catalysts supported on titanium nitride nanoparticles (Pt/TiN, Pt loading, 8.9 wt %) by a colloidal method. The Pt nanoparticles were found to exhibit a characteristic hexahedral shape, with clear faceting and a lattice structure that was highly oriented to that of the TiN support, indicating a strong interaction between the Pt nanoparticles and the TiN support. We evaluated the electrochemical activity of the Pt/TiN both without and with mixing with electrically conducting acetylene black (AB), the latter denoted as Pt/TiN + AB. The ECA of Pt in Pt/TiN + AB was noticeably larger than that of Pt/TiN, reaching 108 m<sup>2</sup>g<sub>Pt</sub><sup>-1</sup> as a maximum, which was close to the geometrically estimated Pt surface area (127 m<sup>2</sup>g<sub>Pt</sub><sup>-1</sup>), based on TEM. By means of a potential step cycling test (0.9~1.3 V vs. RHE, 30 s) simulating SU/SD cycles in PEFCs, it was found that both of the TiN-based catalysts exhibited superior durability compared to commercial Pt catalysts supported on Pt/CB or Pt/GCB, based on the ECA values in Fig. 3.33c. The mass activities at 0.85 V of both of the TiN-based catalysts for the ORR were also higher than those for commercial Pt/CB or Pt/GCB during the potential step cycling test shown in Fig. 3.33b. Similar results were also obtained for Pt catalysts supported on titanium nitride nanoparticles (Pt/TiC).

We also successfully fabricated practical-size MEAs with well-dispersed Pt/TiN + AB cathode CLs. The electrical resistance and the ECA can be controlled by the amount of AB additive, as predicted by percolation theory. For AB contents greater than 37 vol.%, the AB networks were nearly as effective as that for Pt/GCB. The Pt utilization ( $U_{\text{Pt}}$ ) value was close to 100% in a practical-sized MEA using a Pt/TiN + 47 vol.% AB cathode. According to the Tafel slope analysis, it was also found that the percolated AB network supplied effective gas transport pathways that were not flooded by generated water, thus enhancing the oxygen mass transport. The





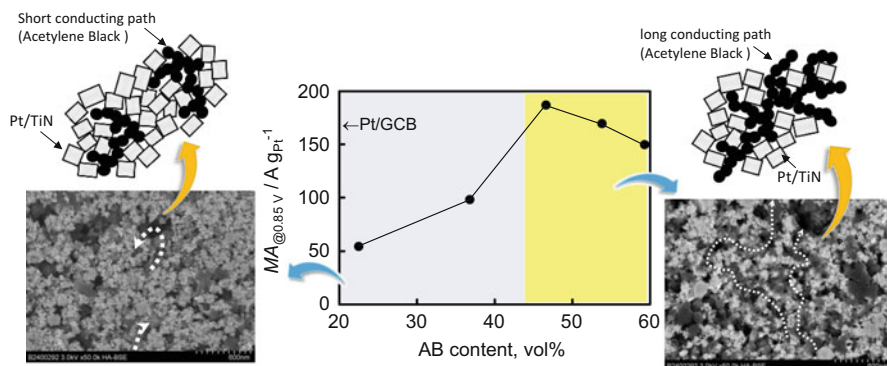
**Fig. 3.33** TEM image of Pt/TiN (a). The change of mass activity (@0.85 V) (b) and ECA of Pt/TiN during the accelerated durability test (0.9–1.3 V, 30 sec.) (c) [101]



**Fig. 3.34** *I-E* curves of the single cell using Pt/TiN and Pt/TiN + x vol.% GCB cathode catalyst ((a): 80 °C, 80%RH, (b): 80 °C, 100% RH) [101]

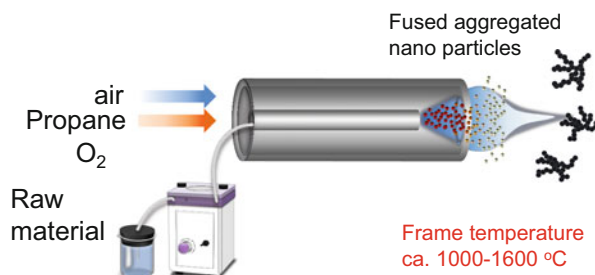
practical-sized MEA using Pt/TiN + 47 vol.% AB showed 1.5 times greater mass activity compared with an MEA using a commercial Pt/GCB catalyst (Fig. 3.34). We have recognized that these alternative supports require the capability of constructing both electrically conductive pathways and gas diffusion pathways (Fig. 3.35).





**Fig. 3.35** Mass activity at 0.85 V in 80 °C, 80% RH. High mass activity was obtained above the GCB additive of 45 vol.%, which would rely on the percolation law [101]

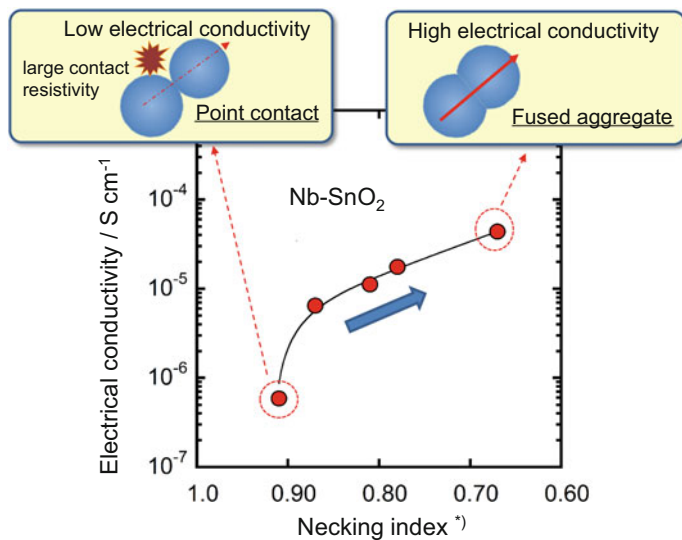
**Fig. 3.36** Schematic image of flame oxide-synthesis method



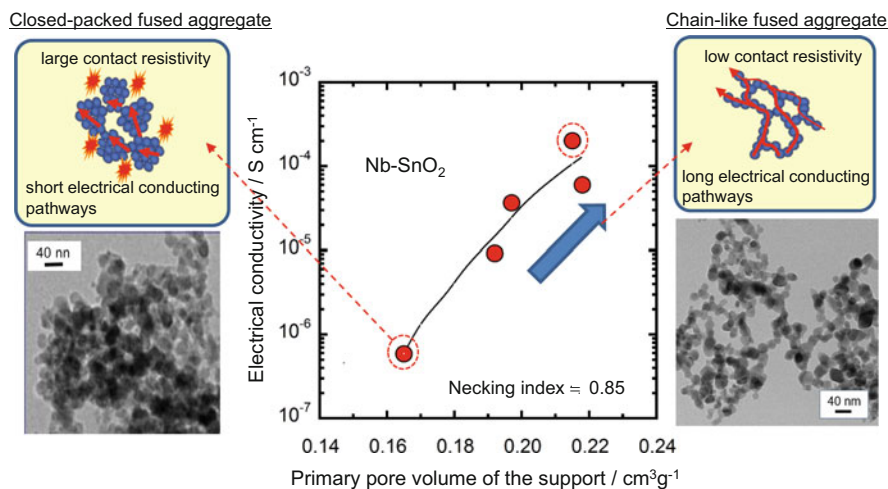
### 3.3.3 Pt Supported on SnO<sub>2</sub> Catalysts

#### 3.3.3.1 Synthesis of Pt/SnO<sub>2</sub> Catalyst

In the previous Section, it was pointed out that high performance for new support materials requires the construction of both electrically conductive pathways and gas diffusion pathways, in addition to the high surface area [56, 104–110]. The flame oxide-synthesis method is one of the well-known bottom-up techniques for nanoparticle synthesis by use of a flame spray (Fig. 3.36), and it has been found to produce particles with carbon-like microstructure. The nanoparticles are characterized by a highly crystallized single phase and relatively high surface area (20–100 m<sup>2</sup> g<sup>-1</sup>). The particles can be produced with partial necking to nearest neighbor particles, as evaluated by a “necking index” or NI: (NI = BET surface area/estimated geometrical surface area from the crystallite size defined by XRD). We have investigated the relationship between NI and electrical conductivity. The electrical conductivity of Nb-SnO<sub>2</sub> nanoparticles was found to increase with increasing NI (Fig. 3.37). The electrical conductivity of the support was also enhanced by changing the microstructure from a close-packed fused-aggregate type to a chain-

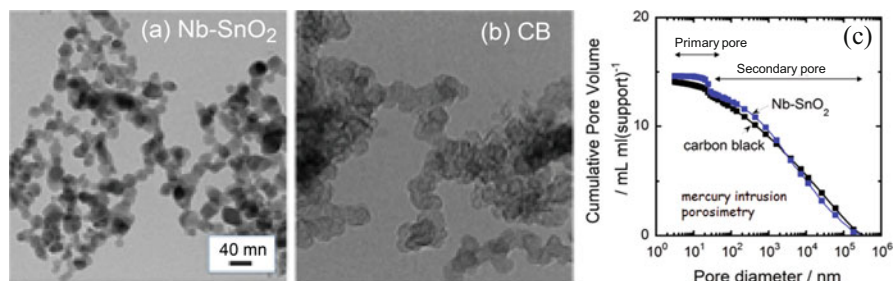


**Fig. 3.37** The electrical conductivity behavior of Nb-SnO<sub>2</sub> as a function of necking index [106]

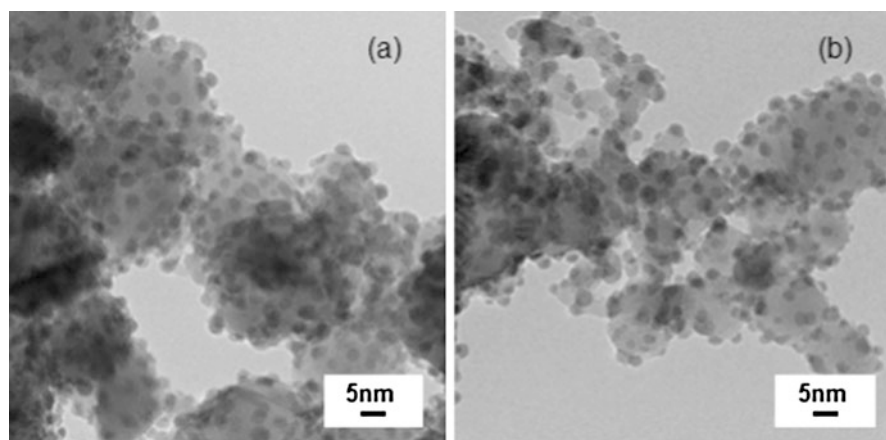


**Fig. 3.38** The electrical conductivity of Nb-SnO<sub>2</sub> with fused-aggregated network structure as a function of primary pore volume [106]

like type (Fig. 3.38). The Nb-SnO<sub>2</sub> obtained was found to exhibit the same microstructure of that of CB, based on the comparison of TEM images. In particular, the pore volume of the Nb-SnO<sub>2</sub> with chain-like fused-aggregate structure was also comparable to that of CB (Fig. 3.39).



**Fig. 3.39** (a) TEM images of Nb-SnO<sub>2</sub> with a chain-like fused-aggregated network structure, (b) CB, and (c) cumulative pore volume of the Nb-SnO<sub>2</sub> and CB [106]

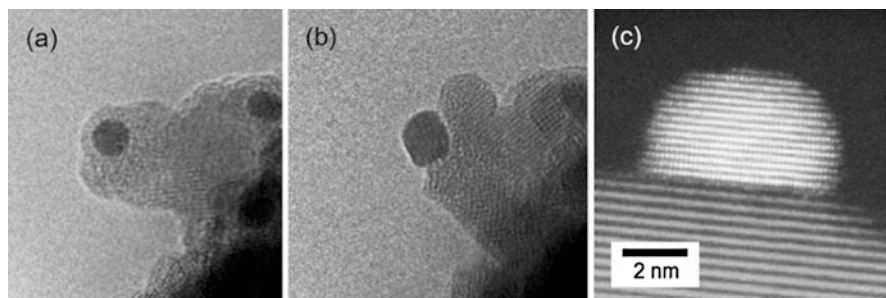


**Fig. 3.40** (a) TEM images of typical Pt catalysts supported on SnO<sub>2</sub> Pt-Ta-SnO<sub>2</sub> and (b) Pt/Nb-SnO<sub>2</sub> [106, 107]

### 3.3.3.2 Evaluation of Pt/SnO<sub>2</sub> Catalyst by RDE

Pt catalysts supported on Sb-SnO<sub>2</sub>, Nb-SnO<sub>2</sub>, and Ta-SnO<sub>2</sub> nanoparticles (Pt/Sb-SnO<sub>2</sub>, Pt/Nb-SnO<sub>2</sub>, Pt-Ta-SnO<sub>2</sub>) were synthesized by a colloidal method (Fig. 3.40). The Pt nanoparticles had a characteristic hexahedral shape with clear faceting and a lattice structure that indicated high orientation to that of the Nb-SnO<sub>2</sub> support. The mean Pt particle sizes were also from 2.6 nm to 3.1 nm with a well-controlled narrow dispersion. The Pt loadings amount for each catalyst were from 15.0 wt % to 20.0 wt %.

The Fig. 3.41 shows a successive series of environmental TEM images of a Pt/Sb-SnO<sub>2</sub>. The Pt/Sb-SnO<sub>2</sub> catalyst was kept at 300 °C in 1 Pa of nitrogen atmosphere for 4 h. We observed that the encapsulated phase with an amorphous thin layer of several nm in thickness was on the Pt surface (Fig. 3.41a). The amorphous thin layer was characterized by a high-resolution, atomic-scale transmission electron microscope equipped with EDX, and Sn, Sb, and O peaks were



**Fig. 3.41** (a) In situ TEM images of Pt/Sb-SnO<sub>2</sub>, 300 °C in N<sub>2</sub> 1 Pa, (b) change to 300 °C in 1% hydrogen (N<sub>2</sub> balance), (c) high-resolution TEM images of Pt/Nb-SnO<sub>2</sub> (c) [56, 104]

detected. We concluded that the encapsulated thin layer on Pt surface was the amorphous Sb-SnO<sub>2</sub> phase. Such encapsulation of Pt nanoparticles by SnO<sub>2</sub> was also reported by Kamiuchi et al. [109, 110]. We also found that the most of the amorphous layer on the Pt nanoparticle surfaces decreased in size or disappeared after changing the atmosphere to 1.0 Pa 1%-H<sub>2</sub> (balance N<sub>2</sub>), as shown in Fig. 3.41b. We considered that the encapsulated amorphous layer on the surface of Pt nanoparticles would degrade the catalytic activity, and thus we sought to produce a clean Pt surface via a heat treatment procedure.

Moreover, the loaded Pt particles were found to be hemispheric in shape and oriented to the SnO<sub>2</sub> support after the sintering procedure. This result relies on a strong interaction between the Pt and highly crystallized Nb-SnO<sub>2</sub> support (Fig. 3.41c). We expected that such interaction between the Pt catalysts and the Nb-SnO<sub>2</sub> support could also have prevented the Pt nanoparticle migration and that the durability of the catalysts under operating conditions would be improved.

The apparent electrical conductivities of the Pt/Nb-SnO<sub>2</sub> under air condition as a function of the Pt loading amount was shown in Fig. 3.42. We found that the apparent electrical conductivities of the Pt/Nb-SnO<sub>2</sub> were enhanced greatly with increasing Pt loading amount, by more than two orders of magnitude, compared to that of the support alone. Generally, the electrical conductivity of nanometer-sized metal oxide particles is influenced on the adsorbed molecules. Chemisorbed, charged oxygen species (O<sub>2</sub><sup>-</sup>, O<sup>-</sup>, O<sup>2-</sup>) can be generated on the oxide surface by the reduction of oxygen molecules by electrons supplied from the oxide [111–113].

We measured in more detail the behavior of the electrical conductivity of the Pt/Nb-SnO<sub>2</sub> and Nb-SnO<sub>2</sub> under various gas atmospheres. The rectangular shape of pressed sample was set in the electrical conducting measurement system and pre-treated at 150 °C under argon for 1.5 h to desorb the adsorbed molecules on the surface, following a reported procedure [112], and then cooled in an argon atmosphere without exposure to ambient atmosphere. The atmosphere in the system was replaced with pure oxygen for 3 h and then replaced by argon again. The sequence of temperature and atmosphere treatments was shown in Fig. 3.43. During this sequence, the electrical conductivities at 25 °C were monitored and were shown in

**Fig. 3.42** Apparent electrical conductivities of Pt/Nb-SnO<sub>2</sub> particles in air atmosphere plotted versus the Pt loading [106]

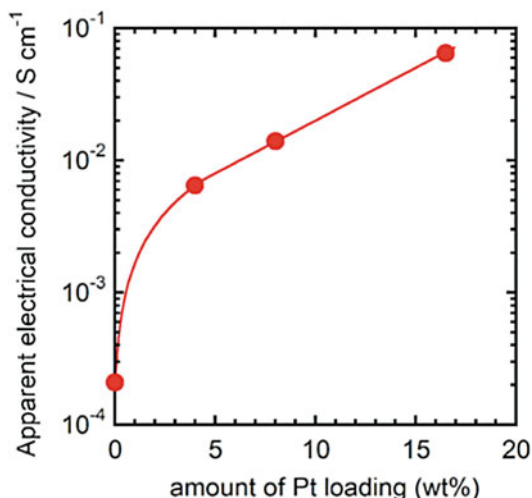
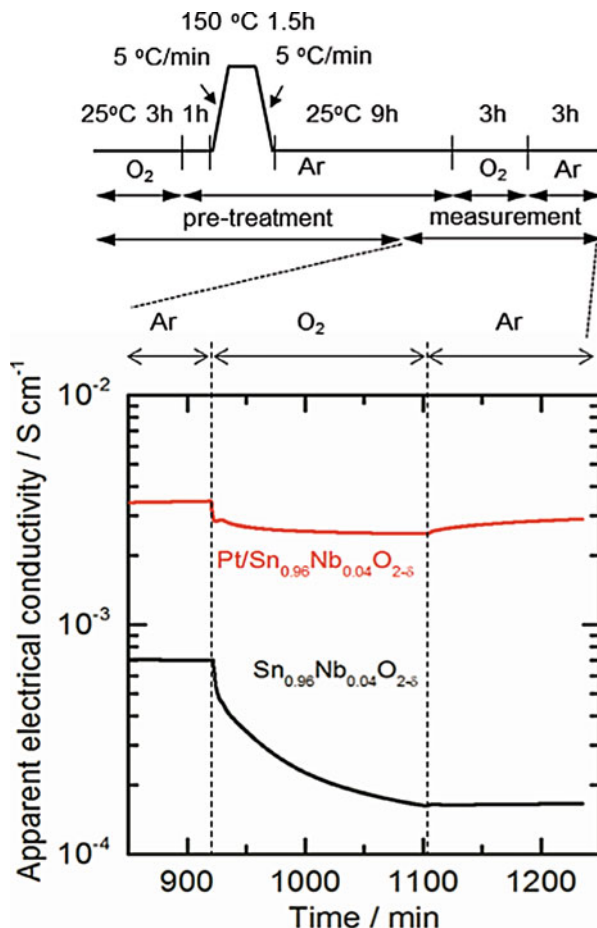


Fig. 3.43. We found an electrical conductivity at Pt/Nb-SnO<sub>2</sub> decreased abruptly but slightly as the atmosphere was changed to oxygen, but the conductivity recovered slowly after changing back to an argon atmosphere. However, the conductivity of the Nb-SnO<sub>2</sub>, which was heat-treated in the same procedure, decreased markedly in an oxygen atmosphere, and the conductivity did not recover after changing from oxygen back to the argon atmosphere.

We consider that the Pt nanoparticles might diminish the influence of adsorbed oxygen species on the charge carriers on the tin oxide nanoparticle surface. On the nanosized tin oxide, the charged oxygen species ( $O_2^-$ ,  $O^-$ ,  $O^{2-}$ ) are thought to introduce a depletion layer, with band bending, on the surface of the oxide [111], as shown in Fig. 3.44a, b. This band bending in the depletion layer increases the grain boundary resistance and interparticle resistance of the nanoparticles, thus interrupting the electron conduction in the oxide [112, 113]. The development of necking decreased the grain boundary and interparticle resistances (Fig. 3.44c–e). Moreover, our results indicated that Pt nanoparticles mitigated the influence of adsorbed oxygen species on the Nb-SnO<sub>2</sub> nanoparticle surface, by analogy with similar phenomena for titanium dioxide [111]. The result would shrink the depletion layer with the relief of band bending and would suppress the grain boundary and interparticle resistances (Fig. 3.44c–e).

The RDE measurements were conducted in 0.1 M HClO<sub>4</sub> solution saturated with N<sub>2</sub> at 25 °C. The CVs for Pt/Sb-SnO<sub>2</sub>, Pt/Nb-SnO<sub>2</sub>, and Pt/Ta-SnO<sub>2</sub> showed the hydrogen adsorption/desorption peaks clearly. Anodic current due to oxide formation on the platinum surface also arose above 0.7 V versus RHE. These peak positions and behavior were matched well with those for the commercial Pt/CB or Pt/GCB for the similar potential sweep range (0.05 V to 1.0 V vs. RHE), as reported in previous work [18, 104, 105]. The kinetically controlled current density and mass activity at 0.85 V of Pt/Sb-SnO<sub>2</sub>, Pt/Nb-SnO<sub>2</sub>, Pt/Ta-SnO<sub>2</sub>, commercial Pt/CB, and

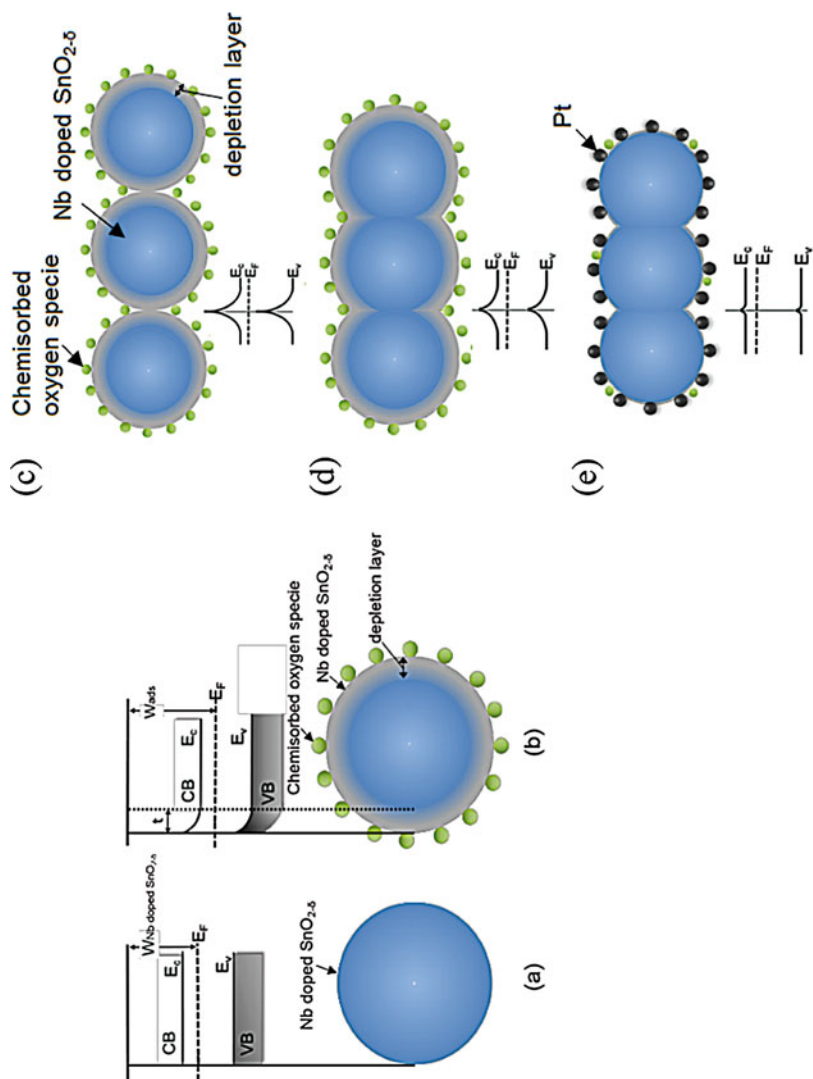
**Fig. 3.43** The apparent electrical conductivity of Nb-SnO<sub>2</sub> and Pt/Nb-SnO<sub>2</sub> monitored under Ar and O<sub>2</sub> atmospheres. The sequence shows the temperature and atmosphere during the heat treatment and conductivity measurements, a variation of the apparent electrical conductivity of Nb-SnO<sub>2</sub> and Pt/Nb-SnO<sub>2</sub> by changing atmospheric conditions. Each sample was pretreated at 150 °C in argon and cooled to room temperature under the same atmosphere, without exposure to the ambient atmosphere [106]



commercial Pt/GCB were summarized in Fig. 3.45. Thus, superior ORR activities of Pt/Sb-SnO<sub>2</sub>, Pt/Nb-SnO<sub>2</sub>, and Pt/Ta-SnO<sub>2</sub>, of which the supports were synthesized by flame oxide-synthesis method, were apparent in the other commercial Pt catalyst supported on carbon. We concluded that the SnO<sub>2</sub> materials with fused-aggregate network structure were promising candidates for catalyst supports for PEFC cathodes.

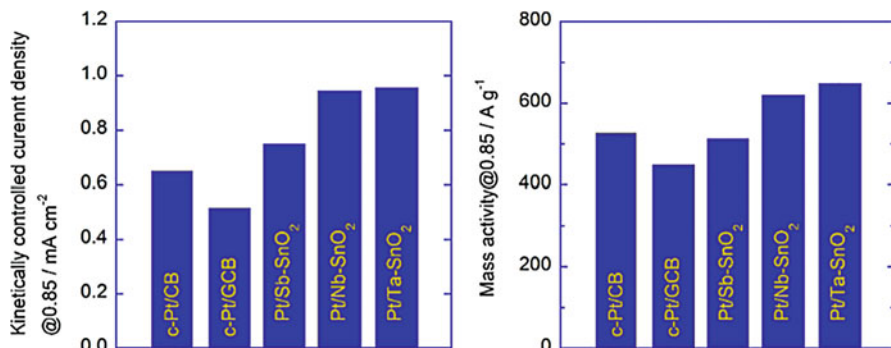
### 3.3.3.3 Evaluation of Pt/SnO<sub>2</sub> CL by MEA

We also evaluated the single cell performances of PEFCs using Pt/Nb-SnO<sub>2</sub> with/without GCB. The single cell using Pt/GCB was also evaluated as a reference. The cross-sections of the Pt/Nb-SnO<sub>2</sub> cathode layer with/without GCB (13 vol.%) are investigated by SEM and TEM as shown in Fig. 3.46a–d, respectively. The CL of Pt/Nb-SnO<sub>2</sub> with fused-aggregate network structure constructed a porous structure, and the CL of Pt/Nb-SnO<sub>2</sub> with GCB also formed a porous structure (Fig. 3.46a–c).



**Fig. 3.44** Schematic image of the electrical structure of Nb-SnO<sub>2</sub> nanoparticles in vacuum condition (a), oxygen condition (b), electronic structure of Nb-SnO<sub>2</sub> without fused-aggregated network structure (c), with fused-aggregated network structure (d) and Pt/Nb-SnO<sub>2</sub> with fused-aggregated network structure (e) [106]





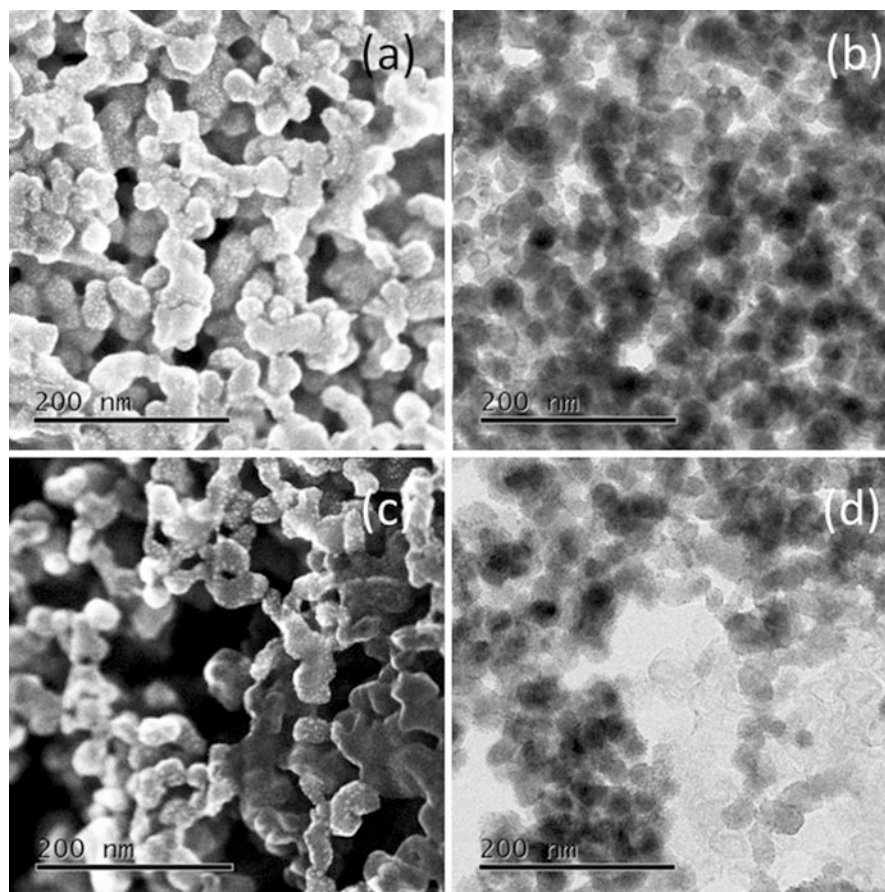
**Fig. 3.45** Kinetically current density and mass activity @0.85 V in each catalyst

The added GCB (lighter gray particles) was well-mixed with the metal oxide (dark gray) as shown in Fig. 3.46d. These observations for the mixed CL of Pt/Nb-SnO<sub>2</sub> + GCB was constructed by the CL consisted of segregated agglomerates with a similar size (sub- $\mu\text{m}$ ) of highly hydrophilic and hydrophobic phases.

Figure 3.47 demonstrated the *IR*-free *I-E* curves and ohmic resistances of the cells using Pt/Nb-SnO<sub>2</sub> and Pt/GCB as cathodes (Pt loading, 0.05 mg·cm<sup>-2</sup>) at 80 °C under various operating conditions, as indicated in the figure caption. The ohmic resistances of the two cells, or the Pt/Nb-SnO<sub>2</sub> and Pt/GCB cathodes, were similar to each other in the whole current density regions as well as all humidity conditions measured. These resistances largely rely on those of the electrolyte membranes, not of the CLs from the results of impedance measurement of the frequency of around 10 kHz. The performance of the cell with Pt/Nb-SnO<sub>2</sub> measured under air was lower than that of the Pt/GCB cathode at 100% RH, but equal at 80% RH. The superior performance of the cell using Pt/Nb-SnO<sub>2</sub> to those for Pt/GCB appeared in the low humidity region, from 30% to 53% RH. Though the resistances of the cell were similar to each other, the *IR*-free performances of the cells and cathode polarizations exhibited significant differences. This dependence of the cathode performances on the humidity should rely on the different performances of each cathode CLs. We should consider the controlling factors, such as the electrical conductivity of the catalyst supports, protonic conductivity of the Nafion binder, or diffusivity of reactant air or product H<sub>2</sub>O. In our previous research [106, 107], the fused-aggregate network structure of the Nb-SnO<sub>2</sub> was constructed and supplied the electrically conductive networks, which affect the decrease of the cell resistances up to that using Pt/CB. Therefore, the electrical conductivity was not a possible reason for the significant dependence of the performance on humidity.

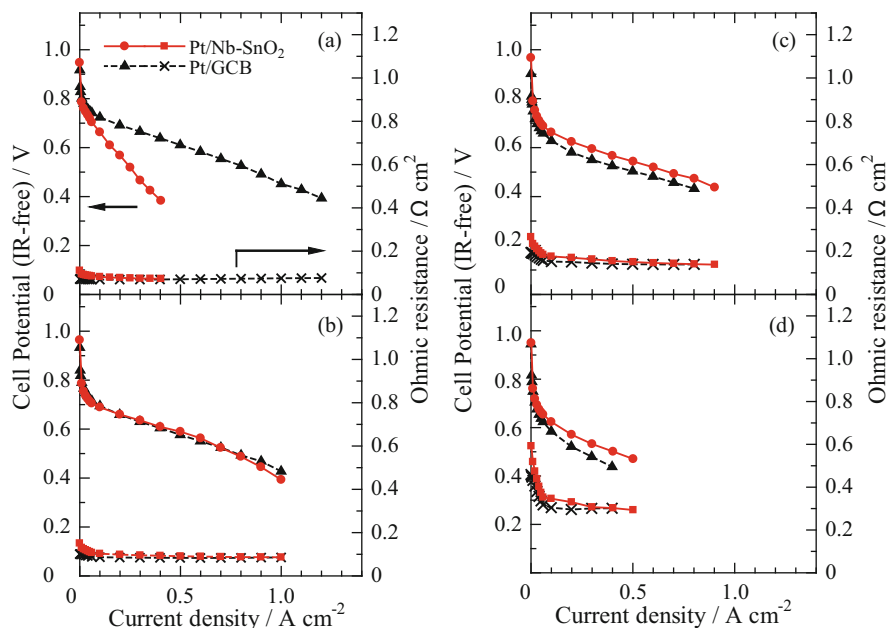
The Pt/Nb-SnO<sub>2</sub> surface is a hydrophilic character and may play a significant advantageous role in improving the protonic conductivity of the binder in the low humidity condition, compared with GCB surface. But the surface property may play a disadvantageous role under excess humidification conditions, e.g., at 100% RH. In general, the cell performance in the high current density region is also obeyed with an increase of the diffusivity of reactants and/or products in the CLs. In our previous





**Fig. 3.46** SEM images and TEM images of cathode catalyst layers, (a) SEM and (b) TEM images of Pt/Nb-SnO<sub>2</sub>, (c) SEM and (d) TEM images of Pt/Nb-SnO<sub>2</sub> with 13 vol.% of GCB [56]

research, it was reported that the adding AB in the Pt/TiN cathode can provide electrically conductive pathways in the CL, and mitigated the ohmic resistance of the cell, with the behavior consistent with percolation theory [102]. However, significant improvement of the cell resistance did not appear by the addition of GCB. It is certain that the Nb-SnO<sub>2</sub> with fused-aggregate network structure supplies excellent electrically conductive pathways, even compared with the GCB support. Therefore, the electrical conductivity in CL of Pt/Nb-SnO<sub>2</sub> would not be the main reason for the improvement of the cell performance. The Pt-mass powers at 0.5 V of each cell are shown in Fig. 3.48. The mass power of the Pt/Nb-SnO<sub>2</sub> cathode without GCB between 30% and 80% RH was higher than that of the Pt/GCB cathode. However, the mass power decreased to half that for Pt/GCB at 100% RH due to the flooding of the CL. But, the Pt-mass powers of Pt/Nb-SnO<sub>2</sub> + AB are clearly able to be improved



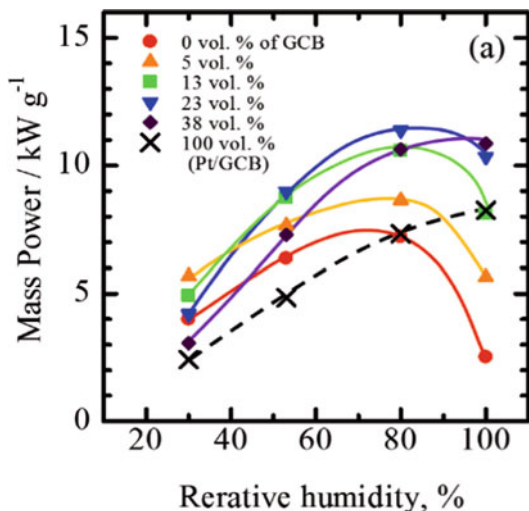
**Fig. 3.47** IR-free  $I$ - $E$  curve and ohmic resistances of versus current density in the cells using Pt/Nb-SnO<sub>2</sub> and Pt/GCB as cathode catalysts at 80 °C, supplied air/H<sub>2</sub>, humidifying at (a) 100% RH, (b) 80% RH, (c) 53% RH, (d) 30% RH, under ambient pressure. Pt loadings 0.05 mg<sub>Pt</sub> cm<sup>-2</sup> [56]

over the whole humidity range, as shown in Fig. 3.48, even though the 100% RH, and reached high values greater than 10 kW g<sup>-1</sup> over 23 vol.% of GCB.

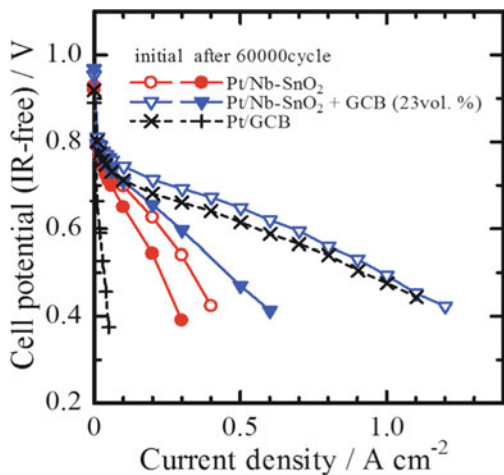
Figure 3.49 shows the IR-free  $I$ - $E$  curves of the cells at initial and 60,000 potential cycles at 80 °C and 100% RH. The initial performance of the Pt/Nb-SnO<sub>2</sub> cathode with GCB was superior to that without GCB and still higher than that of Pt/GCB. After 60,000 potential cycles, the cell performance of the Pt/Nb-SnO<sub>2</sub> cathode without GCB was highest in the other CLs.

The performance of Pt/Nb-SnO<sub>2</sub> without GCB, which had the highest ECA after the durability evaluation, was not exceeded to that with GCB. These results demonstrate that the degradation tendency of the actual cell performance did not correspond to the ECA change. The changes of ECA are shown as a function of the number of potential sweep cycles in Fig. 3.50. The initial ECA of Pt/Nb-SnO<sub>2</sub> with/without GCB (23 vol.%) were 45 m<sup>2</sup> g<sub>Pt</sub><sup>-1</sup> and 46 m<sup>2</sup> g<sup>-1</sup>, respectively, and were well retained, decreasing only to 70% after 60,000 potential cycles. The initial ECA of Pt/GCB (38 m<sup>2</sup> g<sub>Pt</sub><sup>-1</sup>) was lower than that of Pt/Nb-SnO<sub>2</sub> with/without GCB, and decreased to about 35% of the initial value after 60,000 cycles. The severe ECA losses for Pt/GCB were due to severe carbon corrosion accompanied with both aggregation and isolation of Pt particles [13]. We concluded that the Pt/Nb-SnO<sub>2</sub>

**Fig. 3.48** Pt-mass power at 0.5 V (IR-free) on Pt/Nb-SnO<sub>2</sub> cathodes with/without GCB and on Pt/GCB cathode as a function of RH [56]



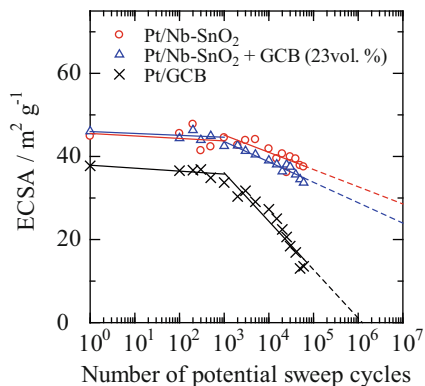
**Fig. 3.49** IR-free *I-E* curves of the cells using Pt/Nb-SnO<sub>2</sub> cathode with added GCB in comparison with that of a commercial Pt/GCB cathode at 80 °C, 100% RH, air/H<sub>2</sub> before/after 60,000 cycles of potential sweep cycle evaluation [56]



cathode with/without GCB (23 vol.%) exhibits excellent durability for high cathode potentials, based on these results for ECA and IV performance evaluation.

TEM images of the Pt/Nb-SnO<sub>2</sub> CL and Pt/GCB CL both before and after durability evaluation are shown in Fig. 3.51. The Pt nanoparticle size on the Pt/Nb-SnO<sub>2</sub> surface changed from  $3.0 \pm 0.6$  nm (initial state) to  $4.9 \pm 0.8$  nm (after 60,000 cycles) in diameter during durability evaluation. The Pt particle shape changed from hemisphere to spherical, which caused the decrease of ECA for Pt/Nb-SnO<sub>2</sub> (Fig. 3.51a, b). This phenomenon can be explained by a growth mechanism of the Pt nanoparticles via dissolution and redeposition originated from the Ostwald ripening [14, 62, 112]. In contrast, the Pt particles on GCB

**Fig. 3.50** Plot of the progress of ECA degradation for Pt/Nb-SnO<sub>2</sub>, Pt/Nb-SnO<sub>2</sub>

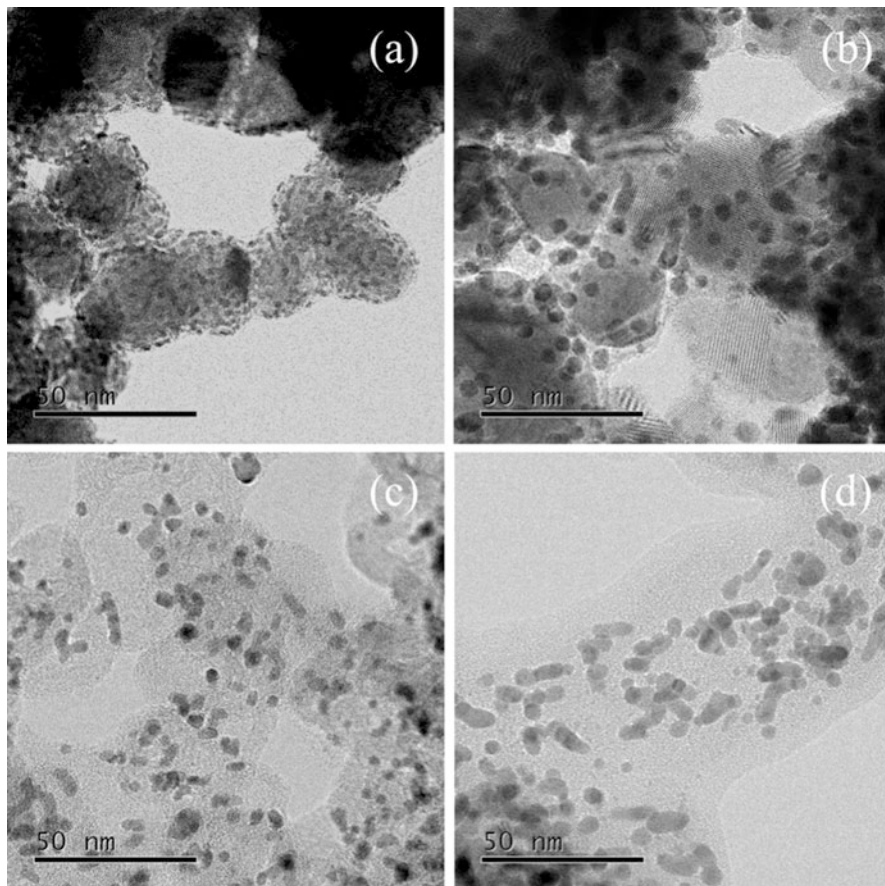


aggregated each other and formed elongated clusters, after 60,000 cycles as shown in Fig. 3.51d. Raman analysis of the GCB support in the Pt/GCB cathode indicated the severe corrosion, which promoted Pt particle coalescence via migration of Pt nanoparticles on the support [14]. The high stability of the Nb-SnO<sub>2</sub> support was able to mitigate the migration of Pt nanoparticles. Moreover, we confirmed that the Pt (111) lattice planes were parallel to those of SnO<sub>2</sub> (110), indicating that the Pt nanoparticles were well oriented on the Nb-SnO<sub>2</sub> surface at the initial state, as shown in Fig. 3.41c. We consider that such interaction between the Pt nanoparticles and the Nb-SnO<sub>2</sub> support could also have prevented the migration of the Pt nanoparticles during the durability evaluation, as discussed in earlier research [104, 105]. We conclude that the Pt/Nb-SnO<sub>2</sub> with/without GCB cathode exhibited outstanding durability during the SU/SD potential sweep evaluation in PEFCs.

The addition of GCB to the Pt/Nb-SnO<sub>2</sub> cathode was able to construct gas diffusion pathways in the CL. Over 23 vol.% of GCB adding the mass power from 80% to 100% RH reached more than 10 A g<sub>Pt</sub><sup>-1</sup> for the Pt/Nb-SnO<sub>2</sub> cathode, which was superior to that of the Pt/GCB cathode. The durability of the Pt/Nb-SnO<sub>2</sub> cathode with/without GCB during the SU/SD potential sweep operation exceeded to that of Pt/GCB cathode. We confirmed that the degree of degradation of GCB in the Pt/Nb-SnO<sub>2</sub> cathode was lower than that in the Pt/GCB cathode from the results of the Raman spectra in Fig. 3.52. These results indicated that the added GCB can provide gas diffusion pathways, which improve the performance of the cell even after extensive cycling because of the absence of Pt catalyst particles on the GCB. We conclude that the Pt/Nb-SnO<sub>2</sub> catalyst and Pt/Nb-SnO<sub>2</sub>-based cathodes with GCB are expecting alternatives for the cathodes of PEFCs.

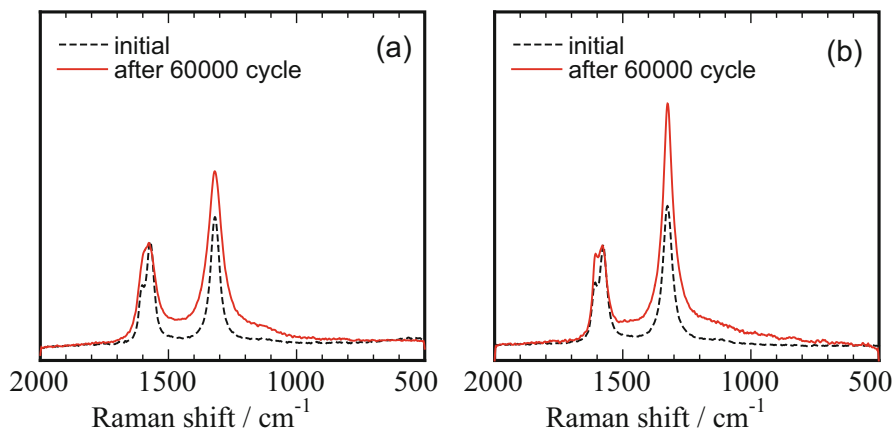
### 3.3.4 “ARSM” Effect of Pt Supported on Ta-TiO<sub>2</sub> Catalysts

We also synthesized a Ta-doped TiO<sub>2</sub> support with a fused-aggregate network structure and prepared an MEA from a Pt catalyst supported on it (Pt/Ta-TiO<sub>2</sub>) as the anode catalyst [114]. The resistance of the Pt/Ta-TiO<sub>2</sub> anode cell was similar to



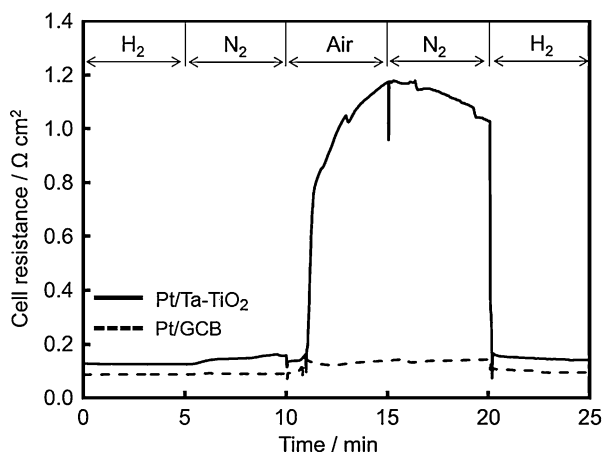
**Fig. 3.51** TEM images of Pt/Nb-SnO<sub>2</sub> with GCB CL before (a) and after (b) 60,000 cycles of durability evaluation, and Pt/GCB CL before (c) and after (d) 60,000 cycles of durability evaluation [56]

that of the Pt/GCB anode cell in the H<sub>2</sub> atmosphere, i.e., ca. 0.13 and 0.10 Ω cm<sup>2</sup>, respectively, but drastically increased after changing to an air atmosphere. The resistivity of the Pt/GCB anode cell increased negligibly after changing the atmosphere to air. The resistance of the Pt-Ta-TiO<sub>2</sub> anode cell in air atmosphere reached a level up to 9.3 higher than that in the H<sub>2</sub> atmosphere (Fig. 3.53). Various resistivity phenomena involving oxide supports, including increases in oxidizing atmospheres, were discussed in Sect. 3.3.3.2. As already mentioned, chemisorbed molecules, such as charged oxygen species (O<sub>2</sub><sup>-</sup>, O<sup>-</sup>, O<sup>2-</sup>), are generated by the reduction of oxygen molecules to cause a depletion layer with band bending on the surface. This band bending in the depletion layer impedes electron transport across grain boundaries and particles, thus increasing the resistance of the oxide semiconductors. An increase



**Fig. 3.52** Raman spectra for (a) Pt/Nb-SnO<sub>2</sub> cathode with 23 vol.% of GCB and (b) Pt/GCB cathode, initial (dotted line) and after 60,000 cycles of durability test cycling (solid line) [56]

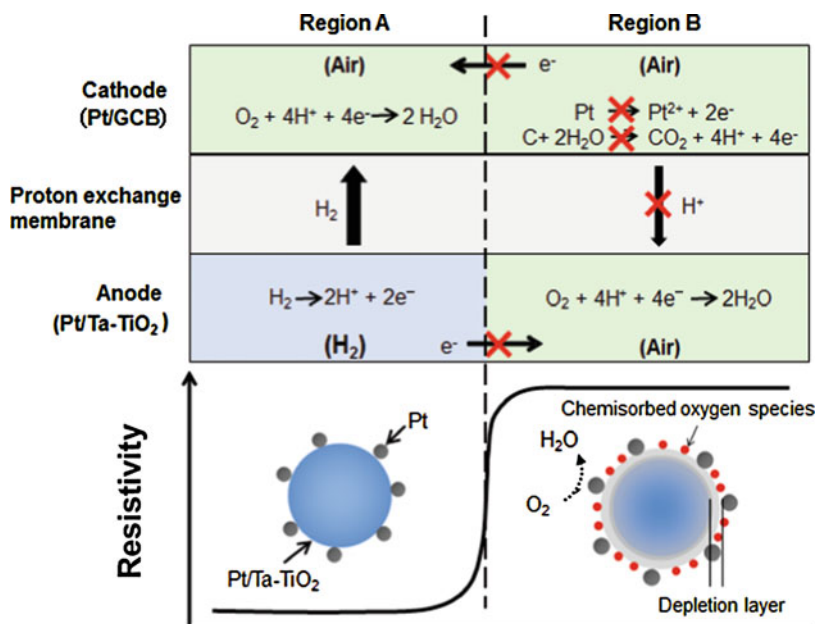
**Fig. 3.53** Cell resistances of Pt/Ta-TiO<sub>2</sub> anode cell (solid line) and Pt/GCB anode cell (dashed line) measured at 65 °C in over-humidified (75 °C dew point) H<sub>2</sub>, N<sub>2</sub>, and air atmospheres [114]



of the resistance for the Pt/Ta-TiO<sub>2</sub> anode cell in air atmosphere must bring about a lowering of the catalytic activity of the supported Pt catalyst.

We applied this phenomenon to the air/air SU of the fuel cell, with the expectation of the following type of behavior. During the stoppage of cell operation, the activity of Pt/Ta-TiO<sub>2</sub> anode would be diminished over the whole gas-flow field due to the presence of air, either from leakage or due to intentional purging. By supplying the H<sub>2</sub> into the flow field, the boundary line of activated Pt catalyst, indicated by the dotted line in Fig. 3.54, shifts to the right, in the down-flow direction. During this condition, the Pt catalyst of the cathode and anode in Region B can be maintained in a passivated state, and the carbon corrosion at the cathode should be suppressed. In the case of the Pt/GCB anode, the Pt catalyst is in an activated condition in Region B,





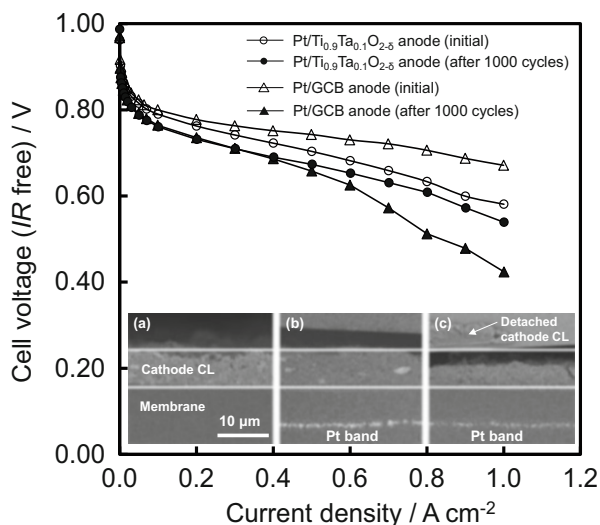
**Fig. 3.54** Schematic image of “ARSM” mechanism [114]

even immediately after the introduction of  $\text{H}_2$  into the flow field, resulting in carbon corrosion in the cathode catalyst for longer times and wider areas compared to that for the Pt/Ta- $\text{TiO}_2$  anode. From these results, we proposed a new strategy for alleviating the reverse current phenomenon using a unique “atmospheric resistive switching mechanism” (ARSM) of a metal oxide semiconductor support, such that the electrical resistivity changes depending on the gas atmosphere. These results demonstrate the mitigating cathode catalyst degradation during air/air SU cycling by the effectiveness of the ARSM.

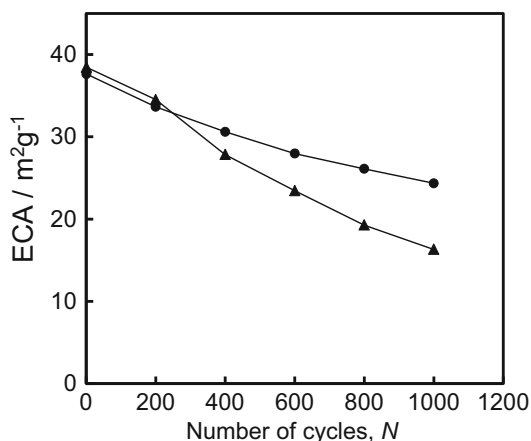
During the simulation of air/air SU cycling by gas switching from air to  $\text{H}_2$ , the losses of ECA and ORR activity of the cathode catalyst was reduced by the use of the Pt/Ta- $\text{TiO}_2$  anode (Fig. 3.55), and thus the corrosion of the cathode carbon was dramatically decreased. The MEA with the Pt/Ta- $\text{TiO}_2$  anode showed higher performance than the MEA with the Pt/GCB anode after air/air SU cycling. The variation of the cathode ECA during the simulated air/air SU cycling is shown in Fig. 3.56. The initial cathode ECA values of the Pt/Ta- $\text{TiO}_2$  anode cell and Pt/GCB anode cell were similar to each other. The retention of the ECA at 1000 cycles was 64.7% for the Pt/Ta- $\text{TiO}_2$  anode cell and 42.4% for the Pt/GCB anode cell. It was found that the use of the Pt/Ta- $\text{TiO}_2$  catalyst for the anode alleviated the loss of ECA in the Pt/GCB cathode during air/air SU cycling.

Therefore, the superior performances of the Pt/Ta- $\text{TiO}_2$  anode cell to those of the Pt/GCB anode cell at high current density were attributed to the difference of cathode carbon corrosion during the air/air SU cycling. We conclude that the reverse

**Fig. 3.55** IR-free  $I$ - $E$  curves of Pt/Ta-TiO<sub>2</sub> anode cell (circles) and Pt/GCB anode cell (triangles) in H<sub>2</sub>/air at 65 °C and 100% RH, initially (open symbols) and after the air/air SU cycling (solid symbols); H<sub>2</sub> utilization 70%, oxygen utilization 40%, ambient pressure. The insert shows the cross-sectional SEM images of Pt/GCB cathode regions; for (a) the pristine MEA with Pt/GCB anode and the SU-tested MEAs with (b) Pt/Ta-TiO<sub>2</sub> anode and (c) Pt/GCB anode [114]



**Fig. 3.56** Plots of the cathode ECA of Pt/Ta-TiO<sub>2</sub> anode cell (circles) and Pt/GCB anode cell (triangles) as a function of the number of air/air SU cycles measured at 45 °C in H<sub>2</sub> (anode) and N<sub>2</sub> (cathode) with 100% RH [114]



current was significantly diminished by the use of the Pt/Ta-TiO<sub>2</sub> anode due to the ARSM effect originating from its high resistivity in an air atmosphere, which impeded the cathode catalyst degradation during air/air SU cycling.

### 3.4 Conclusions

We investigated the cell performance and durability for the cathode CL using two types of supports, i.e., CBs and conducting ceramic nanoparticles, under the simulated operation of both SU/SD cycles and load cycles for FCVs.



We found that the type of CB, Pt nanoparticle size, as well as its dispersion state on the CB affected the degradation properties of the catalysts. We also found that Raman spectroscopic measurements were useful for the evaluation of the degradation of the CBs and clarified also that the reduction from the passivated state of Pt acts effectively to catalyze the carbon corrosion. The interim performance measurements during SU/SD cycling evaluation were found to enhance the Pt/CB degradation, leading to overestimation of the degradation process. The catalyst degradation occurred not only in the outlet region but also in the inlet region during the gas-exchange SU due to the local ORR in the inlet region. We proposed three different types of mechanisms for the COR in the cathode CL in the hydrogen passivation SU/SD process due to the nonuniform distributions of both ionomer and Pt particles. The COR was caused by local cells that arose due to (i) a limited access of H<sub>2</sub> or limited access of protons associated with (ii) the reduction of the Pt oxide during the H<sub>2</sub> permeation from the anode to cathode and (iii) the ORR at metallic Pt sites during the air re-introduction. The load cycle conditions, which involved OCV and load holding times, current densities, and gas humidities, on the durability of the cathode were also investigated. We conclude that the Pt degradation during load cycling is able to be suppressed by operation with a suitable low RH, even for longer OCV holding times, such as during idling and immediately after fuel cell SU. These results indicated that the combinations of both the SU/SD cycles and the load cycles which arise during the interim evaluation and local cell in the cathode enhanced the degradation of the cathode catalyst in the inlet region. The buildup of Pt oxides at higher potentials and re-reduction at lower potentials also have relevance to ordinary operation with drastic load changes, which also can lead to accelerated degradation.

We also proposed the use of conducting ceramic nanoparticles as candidate supports in order to make intrinsic improvements in the SU/SD durability. Pt/TiN, Pt/TiC, and Pt/SnO<sub>2</sub> [115, 116] catalysts showed higher ORR activity and SU/SD durability than those of commercial Pt/CB and Pt/GCB. In particular, the morphology of the fused-aggregate network structure of conducting ceramic nanoparticles is a key concept in order to fabricate highly active, durable cathodes for PEFCs. We also proposed a novel strategy to alleviate the carbon corrosion by use of ARSM in the conducting ceramic support. The degradation of the cathode carbon support was effectively mitigated by applying the ARSM technique to Pt/TiO<sub>2</sub> at the anode side of the MEA.

**Acknowledgments** This work was supported by funds for the “Research on Nanotechnology for High Performance Fuel Cells (HiPer-FC) and Superlative, Stable, and Scalable Performance Fuel Cell (SPer-FC) project” from the NEDO of Japan and the JSPS KAKENHI Grant Number B24350093. We are also grateful to Honda R&D Co., Ltd. and Mitsubishi Motors Corporation for discussion concern with evaluation methods for more practical operation.

---

## References

1. R. Shimoi, T. Aoyama, A. Iiyama, Development of fuel cell stack durability based on actual vehicle test data: current status and future work. *SAE Int. J. Engines* **2**, 960–970 (2009). <https://doi.org/10.4271/2009-01-1014>

2. M. Yamamoto, H. Matsumori, Empirical model for polymer electrolyte fuel cell electro catalyst degradation using platinum stress. *Honda Techn. Rev.* **28**(1), 37–44 (2016). <https://www.hondarandd.jp/summary.php?sid=49&lang=en>. Accessed 23 Feb 2017
3. C.A. Reiser, L. Bregoli, T.W. Patterson, J.S. Yi, J. Deliang, M.L. Perry, T.D. Jarvi, A reverse-current decay mechanism for fuel cells. *Electrochem. Solid-State Lett.* **8**, A273–A276 (2005). <https://doi.org/10.1149/1.1896466>
4. P.J. Ferreira, G.J. la O', Y. Shao-Horn, D. Morgan, R. Makharia, S. Kocha, H.A. Gasteiger, Instability of Pt/C electrocatalysts in proton exchange membrane fuel cells. A mechanistic investigation. *J. Electrochem. Soc.* **152**, A2256–A2271 (2005). <https://doi.org/10.1149/1.2050347>
5. A. Ohma, K. Shinohara, A. Iiyama, T. Yoshida, A. Daimaru, Membrane and catalyst performance targets for automotive fuel cells by FCCJ membrane, catalyst, MEA WG. *ECS Trans.* **41**, 775–784 (2011). <https://doi.org/10.1149/1.3635611>
6. N. Linse, L. Gubler, G.G. Scherer, A. Wokaun, The effect of platinum on carbon corrosion behavior in polymer electrolyte fuel cells. *Electrochim. Acta* **56**, 7541–7549 (2011). <https://doi.org/10.1016/j.electacta.2011.06.093>
7. Y. Ishigami, K. Takada, H. Yano, J. Inukai, M. Uchida, Y. Nagumo, T. Hyakutake, H. Nishide, M. Watanabe, Corrosion of carbon supports at cathode during hydrogen/air replacement at anode studied by visualization of oxygen partial pressures in a PEFC-start-up/shut-down simulation. *J. Power Sources* **196**, 3003–3008 (2011). <https://doi.org/10.1016/j.jpowsour.2010.11.092>
8. R. Darling, J. Meyers, Kinetic model of platinum dissolution in PEMFCs. *J. Electrochem. Soc.* **150**, A1523–A1527 (2003). <https://doi.org/10.1149/1.1613669>
9. J. Xie, D.L. Wood, D.M. Wayne, T.A. Zawodinski, P. Atanassov, R.L. Borup, Durability of PEFCs at high humidity conditions. *J. Electrochem. Soc.* **152**, A104–A113 (2005). <https://doi.org/10.1149/1.1830355>
10. J. Xie, D.L. Wood, K.L. More, P. Atanassov, R.L. Borup, Microstructural changes of membrane electrode assemblies during PEFC durability testing at high humidity conditions. *J. Electrochem. Soc.* **152**, A1011–A1020 (2005). <https://doi.org/10.1149/1.1873492>
11. T.W. Patterson, R.M. Darling, Damage to the cathode catalyst of a PEM fuel cell caused by localized fuel starvation. *Electrochem. Solid-State Lett.* **9**, A183–A185 (2006). <https://doi.org/10.1149/1.2167930>
12. Z.Y. Liu, B.K. Brady, R.N. Carter, B. Litteer, M. Budinski, J.K. Hyun, D.A. Muller, Characterization of carbon corrosion-induced structural damage of PEM fuel cell cathode electrodes caused by local fuel starvation. *J. Electrochem. Soc.* **155**, B979–B984 (2008). <https://doi.org/10.1149/1.2956198>
13. M. Hara, M. Lee, C.-H. Liu, B.-H. Chen, Y. Yamashita, M. Uchida, H. Uchida, M. Watanabe, Electrochemical and Raman spectroscopic evaluation of Pt/graphitized carbon black catalyst durability for the start/stop operating condition of polymer electrolyte fuel cells. *Electrochim. Acta* **70**, 171–181 (2012). <https://doi.org/10.1016/j.electacta.2012.03.043>
14. M. Lee, M. Uchida, K. Okaya, H. Uchida, M. Watanabe, Durability of Pt/graphitized carbon catalyst prepared by the nanocapsule method for the start/stop operating condition of polymer electrolyte fuel cells. *Electrochemistry* **79**, 381–387 (2011). <https://doi.org/10.5796/electrochemistry.79.381>
15. P.V. Shanahan, L. Xu, C. Liang, M. Waje, S. Dai, Y.S. Yan, Graphitic mesoporous carbon as a durable fuel cell catalyst support. *J. Power Sources* **185**, 423–427 (2008). <https://doi.org/10.1016/j.jpowsour.2008.06.041>
16. C. Wang, M. Waje, X. Wang, J.M. Tang, R.C. Haddon, Y.S. Yan, Graphitic mesoporous carbon as a durable fuel cell catalyst support. *Nano Lett.* **4**, 345–348 (2004). <https://doi.org/10.1021/nl034952p>
17. H. Yano, M. Kataoka, H. Yamashita, H. Uchida, M. Watanabe, Oxygen reduction activity of carbon-supported Pt–M (M = V, Ni, Cr, Co, and Fe) alloys prepared by nanocapsule method. *Langmuir* **23**, 6438–6445 (2007). <https://doi.org/10.1021/la070078u>

18. H. Yano, T. Akiyama, P. Bele, H. Uchida, M. Watanabe, Durability of Pt/graphitized carbon catalysts for the oxygen reduction reaction prepared by the nanocapsule method. *Phys. Chem. Chem. Phys.* **12**, 3806–3814 (2010). <https://doi.org/10.1039/b923460h>
19. Y. Wang, D.C. Alsmeyer, R.L. McCreery, Raman spectroscopy of carbon materials: structural basis of observed spectra. *Chem. Mater.* **2**, 557–563 (1990). <https://doi.org/10.1021/cm00011a018>
20. A. Sadezky, H. Muckenhuber, H. Grothe, R. Niessner, U. Poschl, Raman microspectroscopy of soot and related carbonaceous materials: spectral analysis and structural information. *Carbon* **43**, 1731–1742 (2005). <https://doi.org/10.1016/j.carbon.2005.02.018>
21. M. Marcinek, L.J. Hardwick, G.Z. Zukowska, R. Kostecki, Microwave plasma chemical vapor deposition of graphitic carbon thin films. *Carbon* **48**, 1552–1557 (2010). <https://doi.org/10.1016/j.carbon.2009.12.052>
22. Y.-C. Park, K. Kakinuma, M. Uchida, D.A. Tryk, T. Kamino, H. Uchida, M. Watanabe, Investigation of the corrosion of carbon supports in polymer electrolyte fuel cells using simulated start-up/shutdown cycling. *Electrochim. Acta* **91**, 195–207 (2013). <https://doi.org/10.1016/j.electacta.2012.12.082>
23. P.L. Antonucci, F. Romeo, M. Minutoli, E. Alderucci, N. Giordano, Electrochemical corrosion behavior of carbon black in phosphoric acid. *Carbon* **26**, 197–203 (1988). [https://doi.org/10.1016/0008-6223\(88\)90037-1](https://doi.org/10.1016/0008-6223(88)90037-1)
24. M.F. Mathais, R. Makharia, H.A. Gasteiger, J.J. Conley, T.J. Fuller, C.J. Gittleman, S.S. Kocha, D.P. Miller, C.K. Mittelsteadt, T. Xie, S.G. Yan, P.T. Yu, Two fuel cell cars in every garage? *Electrochem. Soc. Interface* **14**, 24–35 (2005). [https://www.electrochem.org/dl/interface/fal/fal05/IF8-05\\_Pg24-35.pdf](https://www.electrochem.org/dl/interface/fal/fal05/IF8-05_Pg24-35.pdf). Accessed 23 Feb 2017
25. C.S. Ball, S.L. Hudson, D. Thompsett, B. Theobald, An investigation into factors affecting the stability of carbons and carbon supported platinum and platinum/cobalt alloy catalysts during 1.2 V potentiostatic hold regimes at a range of temperatures. *J. Power Sources* **171**, 18–25 (2007). <https://doi.org/10.1016/j.jpowsour.2006.11.004>
26. K.H. Lim, O. HS, S.E. Jang, Y.J. Ko, H.J. Kim, H. Kim, Effect of operating conditions on carbon corrosion in polymer electrolyte membrane fuel cells. *J. Power Sources* **193**, 575–579 (2009). <https://doi.org/10.1016/j.jpowsour.2009.04.006>
27. M. Cai, M.S. Ruthkosky, B. Merzougui, S. Swathirajan, M.P. Balogh, O. SH, Investigation of thermal and electrochemical degradation of fuel cell catalysts. *J. Power Sources* **160**, 977–986 (2006). <https://doi.org/10.1016/j.jpowsour.2006.03.033>
28. K.J.J. Mayrhofer, J.C. Meier, S.J. Ashton, G.K.H. Wiberg, F. Kraus, M. Hanzlik, M. Arenz, Fuel cell catalyst degradation on the nanoscale. *Electrochem. Commun.* **10**, 1144–1147 (2008). <https://doi.org/10.1016/j.elecom.2008.05.032>
29. J. Wang, G. Yin, Y. Shao, Z. Wang, Y. Gao, Electrochemical durability investigation of single-walled and multi-walled carbon nanotubes under potentiostatic conditions. *J. Power Sources* **176**, 128–131 (2008). <https://doi.org/10.1016/j.jpowsour.2007.10.057>
30. L. Li, Y. Xing, Electrochemical durability of carbon nanotubes in noncatalyzed and catalyzed oxidations. *J. Electrochem. Soc.* **153**, A1823–A1828 (2006). <https://doi.org/10.1149/1.2234659>
31. S. Maass, F. Finsterwalder, G. Frank, R. Hartmann, C. Merten, Carbon support oxidation in PEM fuel cell cathodes. *J. Power Sources* **176**, 444–451 (2008). <https://doi.org/10.1016/j.jpowsour.2007.08.053>
32. W. Li, A.M. Lane, Investigation of Pt catalytic effects on carbon support corrosion of the cathode catalyst in PEM fuel cells using DEMS spectra. *Electrochem. Commun.* **11**, 1187–1190 (2009). <https://doi.org/10.1016/j.elecom.2009.04.001>
33. W. Bi, Q. Sun, Y. Deng, T.F. Fuller, The effect of humidity and oxygen partial pressure on degradation of Pt/C catalyst in PEM fuel cell. *Electrochim. Acta* **54**, 1826–1833 (2009). <https://doi.org/10.1016/j.electacta.2008.10.008>
34. F. Ettingshausen, J. Kleemann, A. Marcu, G. Toth, H. Fuess, C. Roth, Dissolution and migration of platinum in PEMFCs investigated for start/stop cycling and high potential degradation. *Fuel Cells* **11**, 238–245 (2011). <https://doi.org/10.1002/fuce.201000051>

35. T. Yoda, H. Uchida, M. Watanabe, Effects of operating potential and temperature on degradation of electrocatalyst layer for PEFCs. *Electrochim. Acta* **52**, 5997–6005 (2007). <https://doi.org/10.1016/j.electacta.2007.03.049>
36. Y. Sugawara, T. Okayasu, A.P. Yadav, A. Nishikata, T. Tsuru, Dissolution mechanism of platinum in sulfuric acid solution. *J. Electrochem. Soc.* **159**, F779–F786 (2012). <https://doi.org/10.1149/2.017212jes>
37. K.G. Gallagher, D.T. Wong, T.F. Fuller, The effect of transient potential exposure on the electrochemical oxidation of carbon black in low-temperature fuel cells. *J. Electrochem. Soc.* **155**, B488–B493 (2008). <https://doi.org/10.1149/1.2891138>
38. Y.-C. Park, K. Kakinuma, M. Uchida, H. Uchida, M. Watanabe, Deleterious effects of interim cyclic voltammetry on Pt/carbon blackcatalyst degradation during start-up/shutdown cycling evaluation. *Electrochim. Acta* **123**, 84–92 (2014). <https://doi.org/10.1016/j.electacta.2013.12.120>
39. N.P. Lebedeva, M.T.M. Koper, J.M. Feliu, R.A. van Santen, Mechanism and kinetics of the electrochemical CO adlayer oxidation on Pt(111). *J. Electroanal. Chem.* **524–525**, 242–251 (2002). [https://doi.org/10.1016/S0022-0728\(02\)00669-1](https://doi.org/10.1016/S0022-0728(02)00669-1)
40. B. Wickman, H. Gronbeck, P. Hanarp, B. Kasemo, Corrosion induced degradation of Pt/C model electrodes measured with electrochemical quartz crystal microbalance. *J. Electrochem. Soc.* **157**, B592–B598 (2010). <https://doi.org/10.1149/1.3309730>
41. U.S. DRIVE Partnership Fuel Cell Technical Team, Cell component accelerated stress test and polarization curve protocols for polymer electrolyte membrane fuel cells (electrocatalysts, supports, membranes, and membrane electrode assemblies), [http://www1.eere.energy.gov/hydrogenandfuelcells/pdfs/component\\_durability\\_may\\_2010.pdf](http://www1.eere.energy.gov/hydrogenandfuelcells/pdfs/component_durability_may_2010.pdf). Accessed 8 Feb 2017
42. Y. Yamashita, S. Itami, J. Takano, M. Kodama, K. Kakinuma, M. Hara, M. Watanabe, M. Uchida, Durability of Pt catalysts supported on graphitized carbon-black during gas-exchange start-up operation similar to that used for fuel cell vehicles. *J. Electrochem. Soc.* **163**, F644–F650 (2016). <https://doi.org/10.1149/2.0771607jes>
43. S. Kreitmeier, A. Wokaun, B. u. FN, Local catalyst support degradation during polymer electrolyte fuel cell start-up and shutdown. *J. Electrochem. Soc.* **159**, F787–F793 (2012). <https://doi.org/10.1149/2.019212jes>
44. A. Lamibrac, G. Maranzana, O. Lottin, J. Dillet, J. Mainka, S. Didierjean, A. Thomas, C. Moyne, Experimental characterization of internal currents during the start-up of a proton exchange membrane fuel cell. *J. Power Sources* **196**, 9451–9458 (2011). <https://doi.org/10.1016/j.jpowsour.2011.07.013>
45. J. Durst, A. Lamibrac, F. Charlot, J. Dillet, L.F. Castanheira, G. Maranzana, L. Dubau, F. Maillard, M. Chatenet, O. Lottin, Degradation heterogeneities induced by repetitive start/stop events in proton exchange membrane fuel cell: inlet vs. outlet and channel vs. land. *Appl. Catal. B-Environ.* **138**, 416–426 (2013). <https://doi.org/10.1016/j.apcatb.2013.03.021>
46. R.D. Tarey, R.S. Rastogi, K.L. Chopra, Characterization of thin films by glancing incidence X-ray diffraction. *Rigaku J.* **4**, 11–15 (1987), <http://rigaku.com/downloads/journal/Vol4.1987/tarey.pdf>. Accessed 23 Feb 2017
47. Y. Ishigami, I. Maeda, K. Takada, T. Hyakutake, T. Suga, J. Inukai, M. Uchida, Y. Nagumo, H. Nishide, M. Watanabe, Real-time visualization of CO<sub>2</sub> generated by corrosion of the carbon support in a PEFC cathode. *Electrochem. Solid-State Lett.* **15**, B51–B53 (2012). <https://doi.org/10.1149/2.018204esl>
48. Y. Yamashita, S. Itami, J. Takano, M. Kodama, K. Kakinuma, H. Uchida, M. Watanabe, A. Iiyama, M. Uchida, Degradation mechanisms of carbon supports under hydrogen passivation startup and shutdown process for PEFCs. *J. Electrochem. Soc.* **164**, F181–F187 (2017). <https://doi.org/10.1149/2.0101704jes>
49. K. Miyata, C. Wake, Japanese patent 5,647,079, 2014
50. T. Ioroi, T. Akita, M. Asahi, S. Yamazaki, Z. Siroma, N. Fujiwara, K. Yasuda, Platinum-titanium alloy catalysts on a Magnéli-phase titanium oxide support for improved durability in polymer electrolyte fuel cells. *J. Power Sources* **223**, 183–189 (2013). <https://doi.org/10.1016/j.jpowsour.2012.09.063>

51. S.-Y. Huang, P. Ganesan, B.N. Popov, Electrocatalytic activity and stability of niobium-doped titanium oxide supported platinum catalyst for polymer electrolyte membrane fuel cells. *Appl. Catal. B Environ.* **96**, 224–231 (2010). <https://doi.org/10.1016/j.apcatb.2010.02.025>
52. T.B. Do, M. Cai, M.S. Ruthkosky, T.E. Moylan, Niobium-doped titanium oxide for fuel cell application. *Electrochim. Acta* **55**, 8013–8017 (2011). <https://doi.org/10.1016/j.electacta.2010.03.027>
53. H. Chhina, S. Campbell, O. Kesler, Ex situ and in situ stability of platinum supported on niobium-doped titania for PEMFCs. *J. Electrochem. Soc.* **156**, B1232–B1237 (2009). <https://doi.org/10.1149/1.3184155>
54. A. Kumar, V. Ramani, Strong metal-support interactions enhance the activity and durability of platinum supported on tantalum-modified titanium dioxide. *Electrocatalysts ACS Catal.* **4**, 1516–1525 (2014). <https://doi.org/10.1021/cs500116h>
55. A. Masao, S. Noda, F. Takasaki, K. Ito, K. Sasaki, Carbon-free Pt electrocatalysts supported on SnO<sub>2</sub> for polymer electrolyte fuel cells. *Electrochem. Solid-State Lett.* **12**, B119–B122 (2009). <https://doi.org/10.1149/1.3152325>
56. Y. Chino, K. Taniguchi, Y. Senoo, K. Kakinuma, M. Hara, M. Watanabe, M. Uchida, Effect of added graphitized CB on both performance and durability of Pt/Nb-SnO<sub>2</sub> cathodes for PEFCs. *J. Electrochem. Soc.* **162**, F736–F743 (2015). <https://doi.org/10.1149/2.0651507jes>
57. E. Fabri, A. Rabis, R. Kotz, T.J. Schmidt, Pt nanoparticles supported on Sb-doped SnO<sub>2</sub> porous structures: developments and issues. *Phys. Chem. Chem. Phys.* **16**, 13672–13681 (2014). <https://doi.org/10.1039/C4CP00238E>
58. Y. Liu, E.W. Mustain, Stability limitations for Pt/Sn-In<sub>2</sub>O<sub>3</sub> and Pt/in-SnO<sub>2</sub> in acidic electrochemical systems. *Electrochim. Acta* **115**, 116–125 (2014). <https://doi.org/10.1016/j.electacta.2013.10.155>
59. C. Takei, K. Kakinuma, K. Kawashima, K. Tashiro, M. Watanabe, M. Uchida, Load cycle durability of a graphitized carbon black-supported platinum catalyst in polymer electrolyte fuel cell cathodes. *J. Power Sources* **324**, 729–737 (2016). <https://doi.org/10.1016/j.jpowsour.2016.05.117>
60. D.C. Johnson, D.T. Napp, S. Bruckenstein, A ring-disk electrode study of the current/potential behaviour of platinum in 1.0 M sulphuric and 0.1 M perchloric acids. *Electrochim. Acta* **15**, 1493–1509 (1970). [https://doi.org/10.1016/0013-4686\(70\)80070-6](https://doi.org/10.1016/0013-4686(70)80070-6)
61. D.A.J. Rand, R. Woods, A study of the dissolution of platinum, palladium, rhodium and gold electrodes in 1 M sulphuric acid by cyclic voltammetry. *J. Electroanal. Chem. Interfacial Electrochem.* **35**, 209–218 (1972). [https://doi.org/10.1016/S0022-0728\(72\)80308-5](https://doi.org/10.1016/S0022-0728(72)80308-5)
62. X. Wang, R. Kumar, D.J. Myers, Effect of voltage on platinum dissolution: relevance to polymer electrolyte fuel cells batteries, fuel cells, and energy conversion. *Electrochem. Solid-State Lett.* **9**, A225–A227 (2006). <https://doi.org/10.1149/1.2180536>
63. J.A. Bett, K. Kinoshita, P. Stonehart, Crystallite growth of platinum dispersed on graphitized carbon black. *J. Catalysis* **35**, 307–316 (1974). [https://doi.org/10.1016/0021-9517\(74\)90209-7](https://doi.org/10.1016/0021-9517(74)90209-7)
64. J.A.S. Bett, K. Kinoshita, P. Stonehart, Crystallite growth of platinum dispersed on graphitized carbon black: II. Effect of liquid environment. *J. Catalysis* **41**, 124–133 (1976). [https://doi.org/10.1016/0021-9517\(76\)90207-4](https://doi.org/10.1016/0021-9517(76)90207-4)
65. S. Kawahara, S. Mitsushima, K. Ota, N. Kamiya, Deterioration of Pt catalyst under potential cycling. *ECS Trans.* **3**, 625–631 (2006). <https://doi.org/10.1149/1.2356183>
66. S. Mitsushima, S. Kawahara, K. Ota, N. Kamiya, Consumption rate of Pt under potential cycling. *J. Electrochem. Soc.* **154**, B153–B158 (2007). <https://doi.org/10.1149/1.2400596>
67. S. Mitsushima, Y. Koizumi, S. Uzuka, K. Ota, Dissolution of platinum in acidic media. *Electrochim. Acta* **54**, 455–460 (2008). <https://doi.org/10.1016/j.electacta.2008.07.052>
68. F. Hiraoka, K. Matsuzawa, S. Mitsushima, Degradation of Pt/C under various potential cycling patterns. *Electrocatalysis* **4**, 10–16 (2013). <https://doi.org/10.1007/s12678-012-0105-2>
69. M. Uchimura, S.S. Kocha, The impact of cycle profile on PEMFC durability. *ECS Trans.* **11**, 1215–1226 (2007). <https://doi.org/10.1149/1.2781035>

70. M. Uchimura, S. Sugawara, Y. Suzuki, J. Zhang, S.S. Kocha, Electrocatalyst durability under simulated automotive drive cycles. *ECS Trans.* **16**, 225–234 (2008). <https://doi.org/10.1149/1.2981858>
71. K. Yasuda, A. Taniguchi, T. Akita, T. Ioroi, Z. Siroma, Platinum dissolution and deposition in the polymer electrolyte membrane of a PEM fuel cell as studied by potential cycling. *Phys. Chem. Chem. Phys.* **8**, 746–752 (2006). <https://doi.org/10.1039/B514342J>
72. A. Kongkanand, J.M. Ziegelbauer, Surface platinum electrooxidation in the presence of oxygen. *J. Phys. Chem. C* **116**, 3684–3693 (2012). <https://doi.org/10.1021/jp211490a>
73. R.L. Borup, J.R. Davey, F.H. Garzon, D.L. Wood, M.A. Inbody, PEM fuel cell electrocatalyst durability measurements. *J. Power Sources* **163**, 76–81 (2006). <https://doi.org/10.1016/j.jpowsour.2006.03.009>
74. S. Chen, H.A. Gasteiger, K. Hayakawa, T. Tada, Y. Shao-Horn, Platinum-alloy cathode catalyst degradation in proton exchange membrane fuel cells: nanometer-scale compositional and morphological changes. *J. Electrochem. Soc.* **157**, A82–A97 (2010). <https://doi.org/10.1149/1.3258275>
75. B.E. Conway, Electrochemical oxide film formation at noble metals as a surface-chemical process. *Prog. Surf. Sci.* **49**, 331–452 (1995). [https://doi.org/10.1016/0079-6816\(95\)00040-6](https://doi.org/10.1016/0079-6816(95)00040-6)
76. H. Imai, K. Izumi, M. Matsumoto, Y. Kubo, K. Kato, Y. Imai, In situ and real-time monitoring of oxide growth in a few monolayers at surfaces of platinum nanoparticles in aqueous media. *J. Am. Chem. Soc.* **131**, 6293–6300 (2009). <https://doi.org/10.1021/ja810036h>
77. G. Jerkiewicz, G. Vatanhah, J. Lessard, M.P. Soriaga, Y.-S. Park, Surface-oxide growth at platinum electrodes in aqueous H<sub>2</sub>SO<sub>4</sub> reexamination of its mechanism through combined cyclic-voltammetry, electrochemical quartz-crystal nanobalance, and auger electron spectroscopy measurements. *Electrochim. Acta* **49**, 1451–1459 (2003). <https://doi.org/10.1016/j.electacta.2003.11.008>
78. M. Wakisaka, S. Asizawa, H. Uchida, M. Watanabe, In situ STM observation of morphological changes of the Pt (111) electrode surface during potential cycling in 10 mM HF solution. *Phys. Chem. Chem. Phys.* **12**, 4184–4190 (2010). <https://doi.org/10.1039/B923956A>
79. M. Alsabet, M. Grden, G. Jerkiewicz, Comprehensive study of the growth of thin oxide layers on Pt electrodes under well-defined temperature, potential, and time conditions. *J. Electroanal. Chem.* **589**, 120–127 (2006). <https://doi.org/10.1016/j.jelechem.2006.01.022>
80. Q. Yan, H. Toghiani, J. Wu, Investigation of water transport through membrane in a PEM fuel cell by water balance experiments. *J. Power Sources* **158**, 316–325 (2006). <https://doi.org/10.1016/j.jpowsour.2005.09.013>
81. S. Takaichi, H. Uchida, M. Watanabe, Distribution profile of hydrogen and oxygen permeating in polymer electrolyte membrane measured by mixed potential. *Electrochem. Commun.* **9**, 1975–1979 (2007). <https://doi.org/10.1016/j.elecom.2007.05.011>
82. T. Aoki, A. Matsunaga, Y. Ogami, A. Maekawa, S. Mitsushima, K. Ota, H. Nishikawa, The influence of polymer electrolyte fuel cell cathode degradation on the electrode polarization. *J. Power Sources* **195**, 2182–2188 (2010). <https://doi.org/10.1016/j.jpowsour.2009.10.074>
83. D.H. Lim, W.J. Lee, N.L. Macy, W.H. Smyrl, Electrochemical durability investigation of Pt/TiO<sub>2</sub> nanotube catalysts for polymer electrolyte membrane fuel cells. *Electrochem. Solid-State Lett.* **12**, B123–B125 (2009). <https://doi.org/10.1149/1.3152333>
84. S. Yin, S. Mu, M. Pan, Z. Fu, A highly stable TiB<sub>2</sub>-supported Pt catalyst for polymer electrolyte membrane fuel cells. *J. Power Sources* **196**, 7931–7936 (2011). <https://doi.org/10.1016/j.jpowsour.2011.05.033>
85. B. Avasarala, P. Haldar, Electrochemical oxidation behavior of titanium nitride based electrocatalysts under PEM fuel cell conditions. *Electrochim. Acta* **55**, 9024–9034 (2010). <https://doi.org/10.1016/j.electacta.2010.08.035>
86. Y. Liu, W.E. Mustain, High stability, high activity Pt/ITO oxygen reduction electrocatalysts. *J. Am. Chem. Soc.* **135**, 530–533 (2013). <https://doi.org/10.1021/ja307635r>
87. F. Takasaki, S. Matsuie, Y. Takabatake, Z. Noda, A. Hayashi, Y. Shiratori, K. Ito, K. Sasaki, Carbon-free Pt electrocatalysts supported on SnO<sub>2</sub> for polymer electrolyte fuel cells:



- electrocatalytic activity and durability. *J. Electrochem. Soc.* **158**, B1270–B1275 (2011). <https://doi.org/10.1149/1.3625918>
88. S. Keerthi, H. Rob, C. Stephen, Y. Siyu, Z. Jiujun, Electrocatalytic activity and durability of Pt/NbO<sub>2</sub> and Pt/Ti<sub>4</sub>O<sub>7</sub> nanofibers for PEM fuel cell oxygen reduction reaction. *Electrochim. Acta* **59**, 538–547 (2012). <https://doi.org/10.1016/j.electacta.2011.11.005>
89. B. Wickman, M. Wesselmark, C. Lagergren, G. Lindbergh, Tungsten oxide in polymer electrolyte fuel cell electrodes—a thin-film model electrode study. *Electrochim. Acta* **56**, 9496–9503 (2011). <https://doi.org/10.1016/j.electacta.2011.08.046>
90. A. Ignaszak, C. Song, W. Zhu, J. Zhang, A. Bauer, R. Baker, V. Neburchilov, S. Ye, S. Campbell, Titanium carbide and its core-shelled derivative TiC@TiO<sub>2</sub> as catalyst supports for proton exchange membrane fuel cells. *Electrochim. Acta* **69**, 397–405 (2012). <https://doi.org/10.1016/j.electacta.2012.03.039>
91. W. Yao, J. Yang, J. Wang, Y. Nuli, Chemical deposition of platinum nanoparticles on iridium oxide for oxygen electrode of unitized regenerative fuel cell. *Electrochem. Commun.* **9**, 1029–1034 (2007). <https://doi.org/10.1016/j.elecom.2006.12.017>
92. T. Ioroi, H. Senoh, S. Yamazaki, Z. Siroma, N. Fujiwara, K. Yasuda, Stability of corrosion-resistant magnéli-phase Ti<sub>4</sub>O<sub>7</sub>-supported PEMFC catalysts at high potentials. *J. Electrochem. Soc.* **155**, B321–B326 (2008). <https://doi.org/10.1149/1.2833310>
93. T. Ioroi, Z. Siroma, N. Fujiwara, S. Yamazaki, K. Yasuda, Sub-stoichiometric titanium oxide-supported platinum electrocatalyst for polymer electrolyte fuel cells. *Electrochem. Commun.* **7**, 183–188 (2005). <https://doi.org/10.1016/j.elecom.2004.12.007>
94. Y. Wang, S. Song, V. Maragou, P.K. Shen, P. Tsiakaras, High surface area tungsten carbide microspheres as effective Pt catalyst support for oxygen reduction reaction. *Appl Catal B* **89**, 223–228 (2009). <https://doi.org/10.1016/j.apcatb.2008.11.032>
95. S.Y. Huang, P. Ganesan, B.N. Popov, Titania supported platinum catalyst with high electrocatalytic activity and stability for polymer electrolyte membrane fuel cell. *Appl Catal B* **102**, 71–77 (2011). <https://doi.org/10.1016/j.apcatb.2010.11.026>
96. N.R. Elezovic, B.M. Babic, V.R. Radmilovic, L.M. Vracar, N.V. Krstajic, Nb-TiO<sub>2</sub> supported platinum nanocatalyst for oxygen reduction reaction in alkaline solutions. *Electrochim. Acta* **56**, 9020–9026 (2011). <https://doi.org/10.1016/j.electacta.2011.04.075>
97. C.V. Subban, Q. Zhou, A. Hu, T.E. Moylan, F.T. Wagner, F.J. DiSalvo, Sol-gel synthesis, electrochemical characterization and stability testing of Ti<sub>0.7</sub>W<sub>0.3</sub>O<sub>2</sub> nanoparticles for catalyst support applications in proton-exchange membrane fuel cells. *J. Am. Chem. Soc.* **132**, 17531–17536 (2010). <https://doi.org/10.1021/ja1074163>
98. C. Zhang, H. Yu, Y. Li, L. Fu, Y. Gao, W. Song, Z. Shao, B. Yi, Simple synthesis of Pt/TiO<sub>2</sub> nanotube arrays with high activity and stability. *J. Electroanal. Chem.* **701**, 14–19 (2013). <https://doi.org/10.1016/j.jelechem.2013.04.012>
99. M.S. Saha, R. Li, M. Cai, X. Sun, High electrocatalytic activity of platinum nanoparticles on SnO<sub>2</sub> nanowire-based electrodes. *Electrochem. Solid-State Lett.* **10**, B130–B133 (2007). <https://doi.org/10.1149/1.2745632>
100. K. Kakinuma, Y. Wakasugi, M. Uchida, T. Kamino, H. Uchida, M. Watanabe, Synthesis and electrochemical characterization of new Pt catalyst supported on well crystallized titanium nitride nano-meter sized particles for polymer electrolyte fuel cell. *Electrochemistry* **79**, 399–403 (2011). <https://doi.org/10.5796/electrochemistry.79.399>
101. K. Kakinuma, Y. Wakasugi, M. Uchida, T. Kamino, H. Uchida, S. Deki, M. Watanabe, Preparation of titanium nitride-supported platinum catalysts with well controlled morphology and their properties relevant to polymer electrolyte fuel cells. *Electrochim. Acta* **77**, 279–284 (2012). <https://doi.org/10.1016/j.electacta.2012.06.001>
102. H. Shintani, K. Kakinuma, H. Uchida, M. Watanabe, M. Uchida, Performance of practical-sized membrane-electrode assemblies using titanium nitride-supported platinum catalysts mixed with acetylene black as the cathode catalyst layer. *J. Power Sources* **280**, 593–599 (2015). <https://doi.org/10.1016/j.jpowsour.2015.01.132>

103. M. Chiwata, K. Kakinuma, M. Wakisaka, M. Uchida, S. Deki, M. Watanabe, H. Uchida, Oxygen reduction reaction activity and durability of Pt catalysts supported on titanium carbide. *Catalysts* **5**, 966–980 (2015). <https://doi.org/10.3390/catal5020966>
104. K. Kakinuma, M. Uchida, T. Kamino, H. Uchida, M. Watanabe, Synthesis and electrochemical characterization of Pt catalyst supported on  $\text{Sn}_{0.96}\text{Sb}_{0.04}\text{O}_{2-8}$  with a network structure. *Electrochim. Acta* **56**, 2881–2887 (2011). <https://doi.org/10.1016/j.electacta.2010.12.077>
105. K. Kakinuma, Y. Chino, Y. Senoo, M. Uchida, T. Kamino, H. Uchida, M. Watanabe, Characterization of Pt catalysts on Nb-doped and Sb-doped  $\text{SnO}_{2-8}$  support materials with aggregated structure by rotating disk electrode and fuel cell measurement. *Electrochim. Acta* **110**, 316–324 (2013). <https://doi.org/10.1016/j.electacta.2013.06.127>
106. Y. Senoo, K. Kakinuma, M. Uchida, H. Uchida, S. Deki, M. Watanabe, Improvements in electrical and electrochemical properties of Nb-doped  $\text{SnO}_{2-8}$  supports for fuel cell cathodes due to aggregation and Pt loading. *RSC Adv.* **4**, 32180–32188 (2014). <https://doi.org/10.1039/c4ra03988b>
107. Y. Senoo, K. Kakinuma, M. Uchida, H. Uchida, S. Deki, M. Watanabe, Cathodic performance and high potential durability of Ta- $\text{SnO}_{2-8}$ -supported Pt catalysts for PEFC cathodes. *Electrochem. Commun.* **51**, 37–40 (2015). <https://doi.org/10.1016/j.elecom.2014.12.005>
108. K. Kakinuma, I. Kim, Y. Senoo, H. Yano, M. Watanabe, M. Uchida, Electrochemical oxidation of hydrolyzed poly oxymethylene-dimethyl ether by PtRu catalysts on Nb-doped  $\text{SnO}_{2-8}$  supports for direct oxydation fuel cells. *ACS Appl. Mater. Interfaces* **6**, 22138–22145 (2014). <https://doi.org/10.1021/am505553b>
109. N. Kamiuchi, K. Taguchi, T. Matsui, R. Kikuchi, K. Eguchi, Sintering and redispersion of platinum catalysts supported on tin oxide. *Appl. Catal. B Environ.* **89**, 65–72 (2009). <https://doi.org/10.1016/j.apcatb.2008.11.026>
110. N. Kamiuchi, T. Matsui, R. Kikuchi, K. Eguchi, Nanoscopic observation of strong chemical interaction between Pt and Tin oxide. *J. Phys. Chem. C* **111**, 16470–16476 (2007). <https://doi.org/10.1021/jp0745337>
111. J.F. Boyle, K.A. Jones, The effects of CO, water vapor and surface temperature on the conductivity of a  $\text{SnO}_2$  gas sensor. *J. Electron. Mater.* **6**, 717–733 (1977). <https://doi.org/10.1007/BF02660346>
112. N. Barsan, U. Weimar, Conduction model of metal oxide gas sensors. *J. Electroceram.* **7**, 143–167 (2001). <https://doi.org/10.1023/A:1014405811371>
113. A. Fujishima, X. Zhang, A.D. Tryk,  $\text{TiO}_2$  photocatalysis and related surface phenomena. *Surf. Sci. Rep.* **63**, 515–582 (2008). <https://doi.org/10.1016/j.surfrep.2008.10.001>
114. H. Shintani, Y. Kojima, K. Kakinuma, M. Watanabe, M. Uchida, Novel strategy to mitigate cathode catalyst degradation during air/air startup cycling via the atmospheric resistive switching mechanism of a hydrogen anode with a platinum catalyst supported on tantalum-doped titanium dioxide. *J. Power Sources* **294**, 292–298 (2015). <https://doi.org/10.1016/j.jpousour.2015.06.072>
115. Y. Chino, K. Kakinuma, D.A. Tryk, M. Watanabe, M. Uchida, Influence of Pt loading and cell potential on the HF ohmic resistance of an Nb-doped  $\text{SnO}_2$ -supported Pt cathode for PEFCs. *J. Electrochem. Soc.* **163**, F97–F105 (2016). <https://doi.org/10.1149/2.0571602jes>
116. K. Takahashi, R. Koda, K. Kakinuma, M. Uchida, Improvement of cell performance in low-Pt-loading PEFC cathode catalyst layers with Pt/Ta- $\text{SnO}_2$  prepared by the electrosplay method. *J. Electrochem. Soc.* **164**, F235–F242 (2017). <https://doi.org/10.1149/2.0251704jes>





# Metal Carbonyl Cluster Complexes as Electrocatalysts for PEM Fuel Cells

# 4

Jorge Uribe-Godínez

## Contents

4.1	Introduction .....	116
4.1.1	Platinum and Other Catalysts .....	117
4.1.2	Metal Carbonyl Cluster Complexes as Electrocatalysts for PEMFCs .....	119
4.2	Experimental .....	122
4.2.1	Synthesis of the Catalytic Materials .....	122
4.2.2	Electrochemical Characterization .....	122
4.2.3	Structural Characterization .....	123
4.2.4	Electrode Evaluation .....	124
4.3	Results and Discussion .....	124
4.3.1	Synthesis of the Catalytic Materials .....	124
4.3.2	Study and Electrochemical Characterization of the Metal Carbonyl Clusters ...	127
4.3.3	Structural and Morphological Characterization .....	135
4.3.4	PEM Fuel Cell Evaluation .....	136
4.4	Conclusion .....	140
	References .....	141

## Abstract

New mono- and polymetallic electrocatalysts were synthesized from the carbonyl cluster compounds through thermolysis and pyrolysis methods. The precursor compounds used were triosmium dodecacarbonyl  $[\text{Os}_3(\text{CO})_{12}]$ , triruthenium dodecacarbonyl  $[\text{Ru}_3(\text{CO})_{12}]$ , tetrairidium dodecacarbonyl  $[\text{Ir}_4(\text{CO})_{12}]$ , and

## Author Contribution

J. Uribe-Godínez compiled the material presented and selected the figures and tables included, as well as performed the final technical revision.

J. Uribe-Godínez (✉)

Centro Nacional de Metrología, El Marqués, Querétaro, Mexico

e-mail: [juribe@cenam.mx](mailto:juribe@cenam.mx)

hexarhodium hexadecacarbonyl [ $\text{Rh}_6(\text{CO})_{16}$ ]. In the syntheses by thermolysis, the reaction time (between 5 and 20 h) and the temperature were modified as a function of the solvent used (dimethyl sulfoxide, *o*-dichlorobenzene, *n*-nonane, and *o*-xylene). The pyrolysis variables, including the temperature (90–500 °C), atmosphere gases (nitrogen and hydrogen), and reaction time (controlled at 5 h), were optimized. The precursor compounds and final products were structurally and morphologically characterized using spectroscopic and microscopic analyses. It was found that some of the products showed a metallic character and others were more nonmetallic due to the incorporation of carbonyl groups in their structures. The oxygen reduction reaction (ORR) and hydrogen oxidation reaction (HOR) were measured to evaluate the electrochemical performance of these synthesized electrocatalysts, in the absence and presence of methanol and carbon monoxide, respectively (both contaminants in different concentrations). The materials were tested by rotating disk electrode (RDE), cyclic voltammetry (CV), and linear sweep voltammetry (LSV).

The electrochemical analyses indicated that majority of the electrocatalysts exhibit a dual electrocatalytic behavior toward ORR and HOR. These catalysts are also tolerant to methanol and carbon monoxide, respectively. The synthesized catalysts have superior performance relative to commercial platinum catalysts, which are easily poisoned by CO (ppm). Some iridium-based materials were found to be able to oxidize methanol and ethanol, although their catalytic activity remains to be improved. The most kinetically active catalysts were incorporated into a proton exchange membrane fuel cells (PEMFCs), as part of a Research and Advanced Studies Center, Campus Querétaro (CINVESTAV-Querétaro) fuel cell test system. Under different cell operating conditions, electrical power was generated sufficiently to drive appliances even when a fuel mixture of  $\text{H}_2/0.5\%$  CO was introduced. This design opens a new paradigm to apply reforming hydrogen into PEMFCs, with a reduced manufacturing costs and energy balance. The other advantage of this approach is the tolerance of the electrocatalyst to CO, which can poison traditional platinum-based catalysts.

---

## 4.1 Introduction

There is a wide variety of materials with different structures and geometries, which can be used as catalysts for electrochemical reactions, such as the oxygen reduction reaction (ORR) and the hydrogen oxidation reaction (HOR). The kinetics of the ORR is low in acid electrolytes; therefore it is necessary that the catalysts used as electrodes have a large specific surface area in order to reach practical electrochemical velocities in PEMFCs. Generally, these electrodes have a porous morphology that provides an extended interfacial region, where the electrochemical reactions can occur. The main characteristics of an electrocatalyst include rough surface electrodes, acceptable electronic conductivity, good chemical/electrochemical stability in electrolytes, and simple fabrication. Carbon powders with different specific surface areas (ranging from 10 to 100  $\text{m}^2 \text{g}^{-1}$ ) have many desirable characteristics

for the elaboration of PEMFC's electrodes. Unfortunately, these materials are susceptible to gradual electrochemical oxidation and degradation at high anodic potential values.

The typical electrocatalysts used for the ORR and HOR are metallic particles, metal complexes with macrocyclic ligands, and metal oxides; however, when such materials are used, they can be oxidized at high anodic potential values. The metallic particles supported by nanosized carbon play an important role as electrocatalysts of the ORR and HOR. Platinum and some of its alloys are the best examples of supported electrocatalysts to perform the electrochemical reactions mentioned occurring in PEMFCs [1].

### 4.1.1 Platinum and Other Catalysts

Platinum is the best and the most commonly used catalyst to carry out the ORR and HOR in PEMFCs, due to facile adsorption-desorption of  $O_2$  and  $H_2$  gases, at the surface of the electrodes which influence its catalytic reactivity [2]. Platinum is also relatively inert in acid media which results in robustness of the PEMFC. A drawback of using Pt lies in its high cost (30% of fuel stack), its availability [3], and its susceptibility to contaminates. These include methanol and carbon monoxide that reduce catalytic activity, requiring research into the development of alternative catalysts that are low-Pt or non-Pt based and more tolerant to either poison (CO) or contaminates ( $CH_3OH$ ) [4].

A first approximation consisted in the use of a platinum monolayer deposited over some other metal, alloys, or another nanoparticle substrate to create a new and large surface area. The typical platinum load in a PEM fuel cell is a few  $mg\ cm^{-2}$ . In the last few years, platinum deposited over carbon with a high specific surface area (XC-72; Cabot) has become the standard commercial catalyst for fuel cells. Around 1980, the first platinum alloy supported over nanoparticle carbon (Pt/C) was synthesized, which had a better catalytic activity for the ORR than pure platinum. The next few years, many other binary and ternary nano-alloys were synthesized, which presented a higher catalytic activity than platinum; for example,  $Pt_x-Co_y$  and  $Pt_x-Ni_y$ , were evaluated to perform the ORR.

The catalytic activity of these nano-alloys can be attributed to different factors, such as the distribution of platinum active sites could be changed due to the formation of the alloy (joint effect). It could also change the local geometry through chemical bond formation (structural effect) or could modify directly the reactivity of specific surface platinum sites (electronic effect). The latter was an idea to produce catalysts that can be used as cathodes and anodes in PEMFCs [5]. Platinum nano-alloys supported over carbon have been used as anodic catalysts to perform the HOR, especially to evaluate their tolerance to carbon monoxide. In these cases, metals such as ruthenium or molybdenum are co-alloyed with platinum to produce oxygenated species (such as  $Ru_xO$ ) at low overpotential values, in order to oxidize the adsorbed CO over platinum.

Different platinum alloys (binary: Pt-Ru, Pt-Ir, Pt-V, Pt-Rh, Pt-Cr, Pt-Co, Pt-Ni, Pt-Fe, Pt-Mn, Pt-Pd; and ternary: Pt-Ru-W, Pt-Ru-Mo, Pt-Ru-Sn) have been

exhaustively studied in the presence of carbon monoxide in a fuel cell, to determine which of them were the most resistant to the fuel supply contaminant. It was demonstrated that the Pt-Ru alloy was the best one; in fact, this alloy presented the same behavior as pure platinum, using a 0.15 mPa of fuel feed with 100 ppm of CO, at 80 °C. The best ternary alloy in a fuel cell operating at 75 °C and using a fuel feed with 150 ppm of CO was Pt-Ru-W. These results were for current density values smaller than 300 mA·cm<sup>-2</sup>; however, for practical density currents (higher than 25 mA·cm<sup>-2</sup>), all the alloys showed a less effective performance than that with pure hydrogen. Therefore, the use of platinum alloys as anodic catalysts in the presence of CO is not effective enough for practical applications [6]. A major drawback of using these platinum alloys (binary or ternary) is related to their long-term stability, since platinum segregation or the noble metal lixiviation at fuel cell operation conditions can occur, which causes the catalytic activity reduction, polymer membrane conductivity reduction, and catalytic layer resistance increase at electrodes, affecting directly the performance of a fuel cell [2, 7–9].

An attractive solution to the listed problems is the use of non-Pt catalysts, such as Pd and Ru nano-alloys [10–12], or even the use of free non-noble metal catalysts, such as Ni, Fe, Co, Cr, Cu, W, Se, Sn, and Mo, which are more abundant. In this way, several papers report the catalytic activity of chalcogenides, metal oxides, non-noble metal carbides and nitrides, and recently carbon catalysts doped with nitrogen. Although the catalytic activity and the stability of these materials are lower than platinum catalysts, they are promising due to their cost, stability, and improved catalytic performance [4, 7, 13]. For example, metal oxides have been used as electrocatalysts of the ORR and HOR, due to their wide conductivity range (from metallic to nonconducting), which depends on their composition and preparation method. Three of the most common solid oxide structures used as electrocatalysts are spinel, perovskite, and rutile. Metal oxides exhibit a wide number of applications because of several and important characteristics such as their electrochemical stability at anodic potential values and electrocatalytic activity to perform the oxygen evolution reaction [1].

The preparation of metal transition complexes with macrocyclic ligands for electrocatalysis usually involves procedures that are common in organic and inorganic synthesis. The composition and molecular structures of the macrocycles are controlled by the appropriate selection of the precursor compounds and the experimental synthesis conditions. The metallic phthalocyanines (MPc), the cobalt phthalocyanine (CoPc), and iron phthalocyanine (FePc) have received particular attention due to their electrocatalytic activity for the ORR in alkaline and acid media, respectively. The number of metals that can be incorporated into the MPc's structure is limited, since it only includes metals such as Fe, Co, Ni, and noble metals.

The ORR has also been studied on the porphyrin series, called cofacials. Other compounds, such as transition metal tetramethoxyphenyl porphyrins (TMPP) and dibenzotetraazaanulenes (TAA), have played an important role as electrocatalysts based on non-noble metals for the ORR. In particular, the cobalt TAA shows an electrocatalytic activity comparable with platinum in alkaline media [1]. In addition, different heterocyclic polymers, such as a polypyrrole with metallic ions (Co or Fe) in

their structures and polyaniline (PANI), have been used as ORR electrocatalysts. This kind of catalysts is notable because of its good stability when they are used as electrodes in a PEMFC, although their catalytic activity is similar to that of catalysts without Pt, which is lower when they are compared with platinum-based catalysts [3].

### 4.1.2 Metal Carbonyl Cluster Complexes as Electrocatalysts for PEMFCs

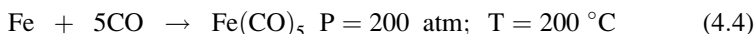
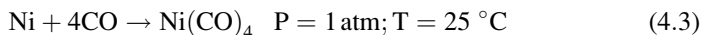
A redox reaction involves a very low electronic transfer, so that it is necessary to apply higher potential values than its standard potential. Such reactions can be accelerated using a catalytic material on the original surface of the working electrode. The catalyst facilitates the electron transfer between the analyte and the electrode [14]. In most cases, the reaction sequence (for a reduction process) is the following:



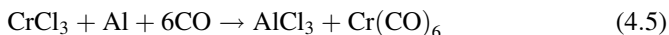
where M represents the catalyst and A the analyte. Therefore, the electronic transfer takes place between the electrode and the catalyst and not directly between the electrode and the analyte. In addition, the active catalyst form is electrochemically regenerated. The result of this electronic exchange is the decrease of the overpotential to the normal potential value of the catalyst, as well as an increase of the current density response. The electrocatalytic process efficiency depends on the distances between the bonding redox sites and the surface since the electronic transfer decreases exponentially when the distance traveled by the electron increases [14]. The use of modified electrodes with catalysts increases the activity and selectivity of the electrochemical process. The search for materials with high catalytic activity is a challenge, since the more frequently used and expensive catalysts for ORR and HOR are nanostructured platinum supported on carbon. In addition to cost, other drawbacks of Pt catalysts are a gradual loss of catalytic activity when the platinum particle surface decreases, due to incrustation processes, dissolution, physical detachment, and/or impurities absorption [15–17]. Only limited Pt-based materials have presented a certain degree of resistance to methanol [16–18].

The research to find new electrocatalysts to perform the ORR and HOR has been focused on transition metal complexes [19, 20] as another alternative area. For example, nitrogenated complexes of Fe and Co have been successfully demonstrated for the ORR in acid media [21–24]. Other approaches include the use of ruthenium impregnated on nanoparticle carbon and modified with phenanthroline iron complexes [25]. Ruthenium-based materials are relatively resistant to the presence of methanol, with incorporation of Se and/or Mo atoms in their structure [26–29]. Osmium-based catalysts were reported for HOR and methanol oxidation reaction (AOR), when combined with platinum [30, 31]. The osmium complexes are relatively tolerant to methanol when they perform the ORR [32].

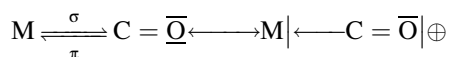
On the other hand, metal carbonyl clusters are composed of a metal core surrounded by ligands and display different geometries and surfaces for chemisorption processes and electrocatalytic reactivity. Most transition metals can form complexes with the carbonyl ligands. These complexes are important because (1) the carbonyl ligand is considered a Lewis base and can form strong coordinative covalent bonds with the metal core in the complexes; (2) the metals always have a low oxidation state, formally at or near zero; and (3) frequently these compounds obey the octodeca rule ( $18 \bar{e}$ ). The family of metal carbonyl complexes has important applications in organic and organometallic synthesis because of their theoretical and structural properties. The great capacity of the CO ligand to accept  $p$  electron retrodonation is responsible for their stability. These complexes can be neutral metal carbonyls (zero oxidation state of the transition metal), anionic metal carbonyls (negative oxidation state), or mixed compounds with CO and other ligands [33]. In general, the molecular structures adopted by simple carbonyl complexes can be predicted using valence shell electron pair repulsion theory. The carbonyl complexes can be synthesized by direct metal (finely divided) interaction with carbon monoxide (Eqs. 4.4 and 4.5).



Most of the carbonyl compounds are obtained by metal reduction in the presence of carbon monoxide (Eqs. 4.5 and 4.6).



In fact, the carbon monoxide in Eq. (4.6) acts as a reducing agent. The  $-\text{C} \equiv \text{O}$  representation indicates that the CO-ligand bonding with a single metal does not experience a large dipole shift compared with the free carbon monoxide. This observation is due to the  $\sigma$  and  $\pi$  bonding between carbon and oxygen atoms. The bond order of C and O is three with a symmetrical and asymmetrical stretching frequencies of 2143 and 2150–1820  $\text{cm}^{-1}$ , respectively [34]. The orbital interaction between a transition metal and the CO group can be explained as follows [33]. The CO  $\sigma$  donation to the metal impoverishes carbon, and the  $\pi$  retrodonation to the antibonding orbitals of carbonyl enriches carbon and oxygen simultaneously. As a result, the CO ligand is polarized and prone to nucleophilic attack over the polarized atom carbon (with a partially positive charge). If the  $\pi$  metal retrodonation is more important, the antibonding  $\pi^*$  orbital of carbonyl is more densely occupied, resulting in weakening the C-O bond and strengthening the M-C bond. It is possible to use two mesomeric forms to describe the M-C-O bond sequence, one neutral and another ionic form.



When the CO ligands form bridges, the bond order equals 2 is similar to the CO in organic compounds (such as acetone). This bond order is reflected in lowering carbon and oxygen stretching frequencies of 1850 and 1700  $\text{cm}^{-1}$  for CO ligands in bridged compounds and 1715  $\text{cm}^{-1}$  for saturated ketones. The bridge formation between carbonyl and metal is accompanied by a metal-metal bond, which produces polarization of M-C-M bonds, including the metal orbital superposition with CO  $\sigma$  and  $\pi$  orbitals [34]. The polynuclear metal transition cluster carbonyls are an important model to obtain nanoparticles with catalytic activity. The total or partial decarbonylation of this type of compounds is the most successful method for the preparation of high-nuclear metallic clusters. Normally, when the metallic complex is used in a thermolysis synthesis method, two types of chemical reactions occur:

1. Decarbonylation, in which there is a loss of carbonyl groups
2. Condensation, in which the decarbonylated metals can form a molecular cluster bigger than the precursor with more metal-metal bonds

The synthesis temperature is an important variable in the compound formation. In general, tri-, tetra-, and pentanuclear compounds are formed when the synthesis temperature is around 125 °C. While for temperatures up to 200 °C, the nuclearity of the compounds is higher and can form hexa- and heptanuclear compounds. The high nuclearity of the metal carbonyls causes a poor solubility in organic solvents; therefore, their purification and structural characterization become difficult [35]. For example, when the triosmium dodecacarbonyl complex  $[\text{Os}_3(\text{CO})_{12}]$  is heated in a sealed tube, the precursor is decarbonylated, and a new material with five or eight osmium atoms is formed. At the same time, these new compounds can be converted in carbonylate ions and carbonyl hydrides [35, 36].

The studies on transition metal carbonyl clusters show that some of these compounds are good candidates for their use as electrocatalysts of the ORR and HOR [37, 38]. The carbonyl groups in these cluster compounds presumably protect the metal centers, thus avoiding their interaction with undesired similar molecules, such as reforming CO. It was also found that the syntheses of some electrocatalysts based on osmium and ruthenium carbonyl compounds  $[\text{Os}_3(\text{CO})_{12}$  and  $\text{Ru}_3(\text{CO})_{12}]$  can be achieved by different reaction routes. These methods include solid-state reactions using oxidative, neutral, or reductive atmospheres, as well as synthesis in solution, using different solvents (coordinating and non-coordinating). The complexes exhibit catalytic activity to perform the ORR and HOR [37, 39–41].

This chapter proposes the use of other metal carbonyl cluster compounds with different nuclearity, such as iridium dodecacarbonyl and hexarhodium hexadecacarbonyl, as precursor compounds in the synthesis of new electrocatalytic materials to perform the ORR and HOR even in the presence of fuel supply contaminants (methanol and carbon monoxide) at different concentrations. This approach can also be tailored to synthesize new catalysts for alcohol oxidation reactions (AOR). The electrochemical analyses of the precursor compounds and the new materials synthesized from them were performed by the rotating disk electrode (RDE) technique, using cyclic voltammetry, linear sweep voltammetry,

and chronoamperometry. The RDE technique allowed evaluation of the electrocatalytic activity of such materials for subsequent later application as anodes and cathodes in hydrogen PEMFCs (described below).

## 4.2 Experimental

### 4.2.1 Synthesis of the Catalytic Materials

The syntheses of the osmium-, ruthenium-, iridium-, and rhodium-based materials were carried out using triosmium dodecacarbonyl  $[\text{Os}_3(\text{CO})_{12}]$ , triruthenium dodecacarbonyl  $[\text{Ru}_3(\text{CO})_{12}]$ , tetrairidium dodecacarbonyl  $[\text{Ir}_4(\text{CO})_{12}]$ , and hexarhodium hexadecacarbonyl  $[\text{Rh}_6(\text{CO})_{16}]$ . All starting materials were received from Sigma-Aldrich Química, S. L. (Toluca, Mexico) and used as precursor compounds.

- (a) Thermolysis: These syntheses were performed with 50 mg of the corresponding carbonyl compound and 50 mL of the selected solvent: dimethyl sulfoxide (DMSO, b. p. = 190 °C), *o*-dichlorobenzene (*o*-DCB, b. p. = 183 °C), *n*-nonane (*n*-Non, b. p. = 150 °C), or *o*-xylene (*o*-Xyl, b. p. = 143 °C). The mixture was placed in a 100 mL round-bottom flask and heated under reflux conditions for 5 or 20 h for DMSO and 20 h for the other solvents. In all cases, the products (blackish powders) were centrifuged, washed with diethyl ether (98%, J. T. Baker, Nuevo León, Mexico) in order to eliminate precursor and solvent residues, and dried at room temperature under normal pressure (air).
- (b) Pyrolysis: The materials were prepared by heating of 50 mg of the metal carbonyl precursor selected at different temperatures (90–500 °C), in a heated porcelain vessel for 5 h, under a continuous gas feed (neutral,  $\text{N}_2$ ; and reductive,  $\text{H}_2$ ), on a Lindberg Blue tube furnace at a 10 °C  $\text{min}^{-1}$  heating rate. The polymetallic materials were prepared by pyrolysis of 50 or 60 mg of the corresponding metal carbonyl mixture (25 mg of each precursor for the bimetallic materials, 20 mg of each one for the tri-metallic materials, and 15 mg for the tetra-metallic catalysts). The products (blackish powders) were recovered and stored under normal atmosphere (air).

### 4.2.2 Electrochemical Characterization

The rotating disk electrode (RDE) studies were performed using a potentiostat/galvanostat (Princeton Applied Research, Model 263A) and a Radiometer Analytical BM-EDI101 glassy carbon rotating disk electrode (with a CTV101 speed control unit), at 25 °C, in a conventional electrochemical cell with three compartments for the work, counter, and reference electrode, respectively. A mercury sulfate electrode ( $\text{Hg}|\text{Hg}_2\text{SO}_4|0.5 \text{ mol}\cdot\text{L}^{-1} \text{ H}_2\text{SO}_4||$ ) was used as a reference; however, the potential values reported are referred to the normal hydrogen electrode (NHE); a carbon cloth was used as counter electrode. The  $0.5 \text{ mol}\cdot\text{L}^{-1} \text{ H}_2\text{SO}_4$  electrolyte was



prepared with 98% sulfuric acid (J. T. Baker) and deionized water ( $18.2 \text{ M}\Omega\cdot\text{cm}^{-1}$ ). The working electrode for the RDE measurements was prepared with 1 mg of the catalyst, 1 mg of carbon powder (Vulcan<sup>®</sup> XC72R; Cabot), and 20  $\mu\text{L}$  of a 5% Nafion<sup>®</sup>/isopropanol solution (Electrochem) mixed in an ultrasonic bath for 5 min; 3  $\mu\text{L}$  of the resulting slurry was deposited on the glassy carbon disk electrode (geometrical area =  $0.07 \text{ cm}^2$ ) and dried in air.

**Cyclic voltammetry.** The CV experiments were done to clean, activate, and characterize the electrode surface to evaluate ORR and HOR activities. The electrolyte was deoxygenated with nitrogen (Infra, UHP) for 30 min before each CV measurement; then it was subjected to 30 potential sweeps between 0.0 and 1.03 V/NHE, at a 20 mV/s scan rate (stabilization was usually reached after 20 potential sweeps). The open-circuit potential (OCP) of the electrode in the  $\text{N}_2$  saturated electrolyte ( $E_{\text{OC}}^{\text{N}_2}$ ) was measured at the end of each experiment. Then, in the case of the ORR, molecular oxygen (Infra, UHP) was bubbled into the electrolyte for 15 min, and the OCP of the electrode in the presence of  $\text{O}_2$  ( $E_{\text{OC}}^{\text{O}_2}$ ) was measured. For the HOR, hydrogen (Infra, UHP) was bubbled into the electrolyte. In the presence of methanol and carbon monoxide, respectively, the same procedure was followed, except that after the CV and linear sweep voltammetry (LSV) measurements with pure  $\text{O}_2$  or  $\text{H}_2$ , the electrolyte was purged with nitrogen for 30 min, and CV measurements were again performed (three potential sweeps between 0.0 and 1.03 V/NHE, at a 20 mV/s rate). Absolute methanol ( $\text{CH}_3\text{OH}$ , J. T. Baker) was then added to the electrolyte to reach a final  $\text{CH}_3\text{OH}$  concentration of 1.0 or 2.0  $\text{mol}\cdot\text{L}^{-1}$ . In the case of the HOR, the  $\text{H}_2/\text{CO}$  mixture ( $[\text{CO}] = 100 \text{ ppm}$  and 0.5%, Infra) was then bubbled to the electrolyte until the OCP value of 0.0 V/NHE was reached. The CV measurements (three potential scans under the above conditions) were subsequently done to detect possible current peaks associated to methanol or carbon monoxide oxidation.

**Linear sweep voltammetry.** The LSV technique was used to study the ORR and HOR activities. The electrolyte was saturated with molecular oxygen in the absence and presence of methanol (1.0 and 2.0  $\text{mol}\cdot\text{L}^{-1}$ ) or with pure  $\text{H}_2$  or  $\text{H}_2/\text{CO}$  mixtures ( $[\text{CO}] = 100 \text{ ppm}$  and 0.5%), respectively. The OCPs ( $E_{\text{OC}}^{\text{O}_2}$  and  $E_{\text{OC}}^{\text{H}_2}$ , respectively) were measured for each process. Current-potential ( $I$ - $V$ ) curves were obtained in the  $E_{\text{OC}}^{\text{O}_2}$  to 0.1 V/NHE and  $E_{\text{OC}}^{\text{H}_2}$  to 0.4 V/NHE ranges, respectively, at a 5 mV/s rate. The rotation rates ranged from 100 to 900 rpm. All measurements were performed at least three times.

**Chronoamperometry.** The methanol oxidation reaction was studied on some iridium-based materials, by chronoamperometry at different concentrations (1.0, 2.0 and 3.0  $\text{mol}\cdot\text{L}^{-1}$ ) in 0.5  $\text{mol}\cdot\text{L}^{-1}$   $\text{H}_2\text{SO}_4$  purged with UHP  $\text{N}_2$  at 25 °C during the potential step from 0.3 to 0.8 V/NHE. The 1:1 Pt-Ru 20%/Vulcan<sup>®</sup> (Electrochem) was also used as catalyst under the same conditions for comparison purposes.

### 4.2.3 Structural Characterization

The structural characterization of the new material was performed by means of diffuse reflectance Fourier transform infrared spectroscopy (FTIR), on a PerkinElmer-GX3

spectrometer, with the samples dissolved in FTIR-grade KBr. Complementary micro-Raman studies were carried out on a Dilor Labram spectrometer, with a He/Ne (632.8 nm) laser and using a 50 $\times$  objective lens. The diffractograms were obtained by X-ray diffraction, on a Rigaku D/max-2100 diffractometer (Cu K $\alpha_1$  radiation, 1.5406 Å). The chemical composition was determined on a field-emission electron probe microanalyzer (JEOL JXA 8530F). A scanning electron microscope (Philips, XL30ESEM) was used for the morphological characterization.

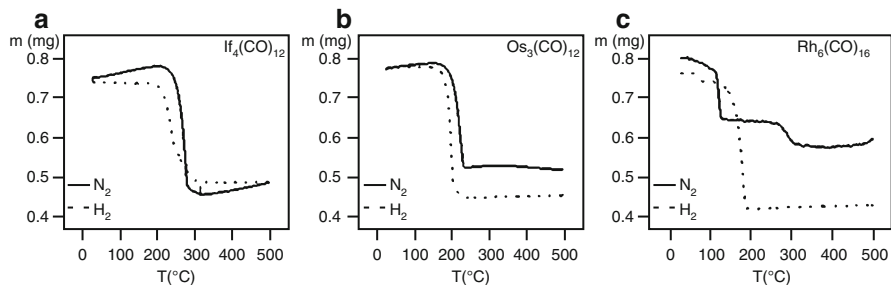
#### 4.2.4 Electrode Evaluation

The study of the catalysts as cathodes and anodes in a single PEMFC, designed and built at CINVESTAV-Queretaro, was performed on a fuel cell test system at room temperature. This fuel cell test system was incorporated with flow and pressure sensors. The flow sensor had a control range of 0–200 cm<sup>2</sup>·min<sup>-1</sup> (mass-flow controller, MKS Type 1497A), while the pressure sensors had a measurement range of 0 to 150 psi (PX4202-150G). The relative humidity was controlled between 5 and 95 RH % and monitored using humidity sensors (Gefran, T1500C1H4). The operating temperature was controlled using a Peltier device (100 W power and an operation range between -90 °C and 90 °C). The total catalyst loading was 1.0 mg·cm<sup>-2</sup> as cathodes (Pt/C anode, 0.5 mg cm<sup>-2</sup>) and 0.5 mg·cm<sup>-2</sup> anodes (Pt/C cathode, 1.0 mg cm<sup>-2</sup>). A Nafion<sup>®</sup>-117 membrane was used as the electrolyte. Aluminum serpentine flow field collector plates were used with an effective area of 17.64 cm<sup>2</sup>. A Pt/Pt membrane-electrode assembly (MEA) was also evaluated for comparison purposes. Pure O<sub>2</sub> was used as the oxidant in all measurements and pure hydrogen or H<sub>2</sub>/CO mixtures as the fuel. The discharge and power density curves were obtained to evaluate fuel cell performance using open-circuit potential ( $E$ ), current ( $I$ ), current density ( $J$ ), power density ( $P$ ), and efficiency ( $\eta$ ) of the fuel cell composed of the synthesized materials as electrodes.

### 4.3 Results and Discussion

#### 4.3.1 Synthesis of the Catalytic Materials

The catalyst synthesis was carried out by two different methods: (a) thermolysis in different solvents and (b) pyrolysis under a neutral (N<sub>2</sub>) and a reductive (H<sub>2</sub>) atmosphere. When the materials were obtained by thermolysis, the solvent plays an important role to direct the reaction, in which solvents with different polarities and hydrophilicities were selected. Three solvents, dimethyl sulfoxide (DMSO), *o*-dichlorobenzene (*o*-DCB), and *o*-xylene (*o*-XYL), with different polarities and functional groups were incorporated into the catalyst's structure. The nonpolar solvent, *n*-nonane (*n*-NON), is relatively inert without possibilities to coordinate into the metallic centers of the precursors. All solvents have different boiling points, allowing for synthesis of products with different structural and electrochemical characteristics.



**Fig. 4.1** Thermograms of the metal carbonyl complexes, in the different atmosphere at a  $10\text{ }^{\circ}\text{C}\cdot\text{min}^{-1}$  rate. The gas feed stream was  $50\text{ mL}\cdot\text{min}^{-1}$

When the catalysts were produced using pyrolysis, the atmosphere plays an important role. Therefore, the neutral ( $\text{N}_2$ ) and reductive ( $\text{H}_2$ ) media were selected as one of the synthesis variables, alongside the temperature. The role of temperature is to guide the decarbonylation rate and other decomposition products. The precursor compounds, which are subjected to a pyrolysis in different atmospheres, were analyzed by a thermogravimetric technique (TGA) to study their behavior (Fig. 4.1).

The TGA data indicated that the decarbonylation of the metal carbonyl used as precursor compounds occurs in a single step, regardless of the atmosphere used. For the iridium carbonyl complex (Fig. 4.1a), the loss of the carbonyl groups took place at a lower temperature range ( $\sim 220\text{--}350\text{ }^{\circ}\text{C}$ ) than that for the osmium precursor derivative (Fig. 4.1b,  $\sim 150\text{--}320\text{ }^{\circ}\text{C}$ ). In both cases, the decarbonylation process was faster under hydrogen than nitrogen medium. In the case of rhodium carbonyl precursor (Fig. 4.1c), the decarbonylation occurred in a single step and was faster under  $\text{H}_2$  atmosphere. In the nitrogen atmosphere, the loss of the carbonyl groups occurred in two steps: one at  $90\text{--}105\text{ }^{\circ}\text{C}$  range and another (of lower intensity) between  $280$  and  $310\text{ }^{\circ}\text{C}$ . These experiments corroborated the atmosphere synthesis effect over the pyrolytic process of the metal carbonyl compounds used as precursors and allowed for obtaining materials with different structural and catalytic properties. The thermolysis syntheses over the reaction time were compared and found to be similar to our previous findings [37, 40, 41]. The actual time has a bearing on the final structure and catalytic properties, with catalysts compared to each other where generated at a thermolysis time of 5 and 20 h. Other time points were not selected, since our previous data indicated that 5 h were enough to modify the precursor compounds to generate the new catalysts [42].

The synthesized materials showed similar physical characteristics as obtained by thermolysis and pyrolysis. The materials obtained by thermolysis were fine blackish powders, while by pyrolysis were fine gray powders, with exception of two iridium-based materials. The material obtained under nitrogen atmosphere at  $190\text{ }^{\circ}\text{C}$  for 5 h was a dark-brown powder, and the one obtained under hydrogen atmosphere at  $90\text{ }^{\circ}\text{C}$  for 5 h was a dark-green powder.

In general, the syntheses in DMSO at 5 h using osmium carbonyl and iridium carbonyl precursors produce two types of products, one soluble and another

insoluble in the reaction media; the reaction performance was  $\sim 15\%$  regardless of precursor compound used; in addition, the materials exhibited no activity toward ORR, HOR, or AOR. When the reaction time was extended to 20 h, the reaction performance of the main product was increased to  $\sim 40\%$ . However, these two products were electrochemically inactive.

The materials based on rhodium carbonyl showed catalytic activity for the ORR and HOR, regardless of synthesis time. The catalysts were synthesized using two variables that were the time and the aromaticity of the solvents (*o*-dichlorobenzene and *o*-xylene and the aliphatic solvent, *n*-nonane). The solvents have different boiling points (183 °C, 143 °C, and 150 °C, respectively), and they can be part of the final product structure. The performance of these prepared products was  $\sim 35\%$ . The best catalytic behavior was for the catalyst obtained in *o*-DCB; therefore, the synthesis was repeated but using the iridium carbonyl precursor. The new iridium-based material showed catalytic activity toward ORR, HOR, and AOR.

Syntheses by pyrolysis method generated products whose reaction performance was  $\sim 45\%$ , except for the osmium carbonyl precursor, whose performance was  $< 5\%$ ; therefore, the use of osmium carbonyl precursor for the generation of catalysts was discontinued, in spite of their ORR and HOR activities.

Rhodium carbonyl-based materials produced by pyrolysis were obtained at 190 °C in  $N_2$  or  $H_2$  atmospheres, generating metallic product particles with activity for the ORR and HOR. The HOR reactivity was greater under the catalyst generated under nitrogen than the one generated under hydrogen. This is due to the presence of hydrogen atoms on the catalyst surface-limiting reactive sites; therefore, future synthesis under hydrogen with rhodium-based carbonyl was discontinued. The research indicates that rhodium precursors under  $N_2$  at low temperature ( $< 190$  °C) may produce active (ORR and HOR) catalysts which have incorporated CO into their structures.

Iridium carbonyl-based materials produced by pyrolysis were obtained at 190 °C for 5 h in  $N_2$  or  $H_2$  atmospheres, generating two types of products with differing activity for the ORR and HOR. One product based on iridium carbonyl exhibited ORR and HOR activity, while the other metallic product, as a result of decarbonylation of the precursor, exhibited similar ORR and HOR in addition to AOR activity. Two types of catalysts can be generated that exhibit ORR and HOR activity. One type of catalyst was fabricated under nitrogen at high temperatures ( $\geq 350$  °C) to facilitate decarbonylation of the precursor. The other was fabricated under hydrogen at low temperature ( $\leq 230$  °C) to facilitate incorporation of CO into the catalyst structure. In this manner, the synthesis of bi-, tri-, and tetra-metallic catalysts was achieved by tuning the gases ( $N_2$  or  $H_2$ ) or temperatures (90–100 °C) via the pyrolysis method at 5 h' reaction time. Under these conditions, fine black powders were obtained that exhibited ORR and HOR reactivity as well as limited AOR reactivity for the iridium-based catalyst. The structural, morphological, and electrochemical characterization of catalytic materials synthesized from transition metal carbonyl cluster complexes allowed for generation of new knowledge to guide further catalyst development.

### 4.3.2 Study and Electrochemical Characterization of the Metal Carbonyl Clusters

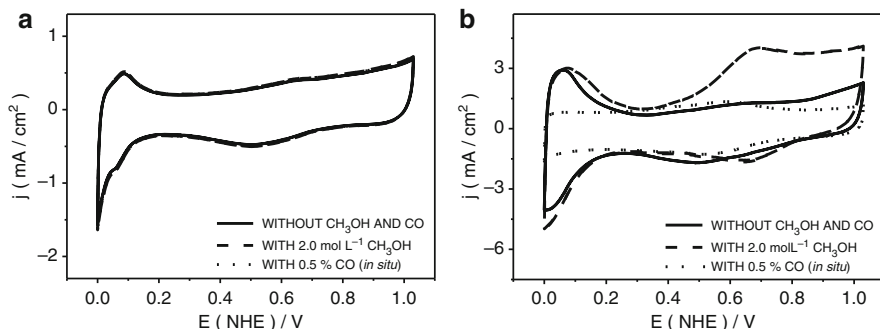
This section shows the results of the electrochemical characterization and analysis of the synthesized materials, from rotating disk electrode (RDE) technique, using cyclic voltammetry (CV), linear sweep voltammetry (LSV), and chronoamperometry (for aliphatic AOR study).

#### 4.3.2.1 Precursor Compounds

The osmium, ruthenium, iridium, and rhodium carbonyl compounds were produced with well-defined geometries and structures. For example, the iridium carbonyl  $[\text{Ir}_4(\text{CO})_{12}]$  adopts a  $T_d$  point group symmetry arrangement with three terminally bonded CO ligands per metal atom. The observed solid-state structure of  $\text{Ir}_4(\text{CO})_{12}$  is the result of inserting the tetrahedral  $\text{Ir}_4$  cluster unit into the energetically “less favorable” cuboctahedral arrangement of CO ligands [43]. The rhodium carbonyl  $[\text{Rh}_6(\text{CO})_{16}]$  adopts a  $\bar{4}3m$  crystal symmetry arrangement ( $T_d$  point group) where 12 of 16 carbonyl ligands are terminal groups, while the remaining four are located on threefold axes above four of the octahedral faces. Each of these latter four carbonyls which are directed toward the vertices of a tetrahedron is bonded to three rhodium atoms forming the corresponding bridge carbonyls [44]. The  $\text{Os}_3(\text{CO})_{12}$  and  $\text{Ru}_3(\text{CO})_{12}$  have a similar geometry and planar structure to  $D_{3h}$  point group structures ( $\bar{6}m2$  crystal group).

These transition metal carbonyl clusters have interesting structural and functional properties; they possess a core with metallic properties, with surrounding carbonyl groups bonded to them [45]. Several preparation methods have been described, most of which require high pressure; however, three methods to synthesize  $\text{Ir}_4(\text{CO})_{12}$  at atmospheric pressure have been reported [46]. For many decades, organometallic compounds have played an important role as precursors for important homogeneous transition metal-catalyzed reactions, such as hydrogenation and hydroformylation, which are both used for the syntheses of fine chemicals and pharmaceuticals [47]; however, their application as catalysts for electrochemical reactions had not been reported until 7 years ago.

The author published the electrocatalytic activity for ORR and HOR of two discrete metal carbonyl clusters with a well-defined molecular and crystal structures,  $\text{Ir}_4(\text{CO})_{12}$  and  $\text{Rh}_6(\text{CO})_{16}$  [38, 48]. These metal carbonyl clusters are capable of performing the ORR and HOR even in the presence of fuel cell contaminants (methanol and carbon monoxide, respectively). The electrocatalytic properties of these complexes most likely arise from their electron-rich iridium and rhodium atom cores, with the carbonyl ligands exerting the observed protective effect against poisoning agents and potential oxidation. The tetra- and hexa-nuclear complexes are capable of performing the two basic reactions in hydrogen fuel cell, while other compounds with similar composition but different nuclearity, e.g.,  $\text{Ru}_3(\text{CO})_{12}$  and  $\text{Os}_3(\text{CO})_{12}$ , are inactive. Hence, this research further investigated the nuclearity and structure of transition metal carbonyl clusters as alternative catalysts to platinum for PEM fuel cells [49–51].



**Fig. 4.2** Representative cyclic voltammograms of (a) Rh-Ir-based material ( $N_2/90\text{ }^\circ\text{C}/5\text{ h}$ ) and (b) Rh-Ir-Os-based catalyst ( $H_2/90\text{ }^\circ\text{C}/5\text{ h}$ ) in the absence and presence of fuel cell contaminants ( $CH_3OH$  and  $CO$ ) at different concentrations. The electrolyte was  $0.5\text{ mol}\cdot\text{L}^{-1}\text{ H}_2\text{SO}_4$  and the sweep rate  $20\text{ mV/s}$

#### 4.3.2.2 New Catalytic Materials Based on Metal Carbonyl Cluster Compounds

The cyclic voltammetry (CV) allows to carry out an electrochemical characterization of the electrode materials to evaluate their electrochemical activities. The homogeneity of the surface can be probed using the sweep potential over a specified time. The analyses of the CV plot can yield the catalytic activity for selected electrochemical reaction, such as carbon monoxide oxidation and aliphatic alcohol oxidation (methanol, ethanol, and isopropanol). The analysis can determine the hydrogen and oxygen evolution reactions using the selected materials. The higher energetic surfaces that are catalytically unfavored may be accessed with the appropriate potential sweep over a certain time period (1 h), enabling these sites to be accessible to substrate and to facilitate catalysis (oxygen, hydrogen, methanol, or ethanol). Figure 4.2a shows representative cyclic voltammograms of a bimetallic catalyst based on  $Ir_4(CO)_{12}/Rh_6(CO)_{16}$  synthesized in a  $N_2$  atmosphere at  $90\text{ }^\circ\text{C}$  for 5 h. The CVs were obtained in  $N_2$  saturated  $0.5\text{ mol}\cdot\text{L}^{-1}\text{ H}_2\text{SO}_4$ , in the absence and presence of methanol ( $2.0\text{ mol}\cdot\text{L}^{-1}$ ). The CV of the compounds in the presence of a hydrogen/carbon monoxide mixture ( $[CO] = 0.5\%$ ) was also examined. The electrochemical behavior of the Rh-Ir-based cluster was similar in the absence or presence of methanol or carbon monoxide. The data suggests that the catalyst is tolerant to such PEM fuel supply contaminants. The CV showed anodic-cathodic peaks in the  $0.5\text{--}0.7\text{ V/NHE}$  region, which are ascribed to the Vulcan<sup>®</sup> support, as well as a hydrogen evolution zone in the  $0.0\text{--}0.2\text{ V/NHE}$  range. The oxidation peaks of either methanol or carbon monoxide are not observed, in contrast with platinum, which easily oxidizes both compounds [52].

Figure 4.2b shows representative CV of Rh-Ir-Os-based catalyst (tri-metallic material synthesized in the  $H_2$  atmosphere using a mixture of  $Rh_6(CO)_{16}/Ir_4(CO)_{12}/Os_3(CO)_{12}$  at  $90\text{ }^\circ\text{C}$  for 5 h). The CVs were obtained under the same conditions as the Rh-Ir-based carbonyl. The voltammograms in the absence of contaminants showed

anodic-cathodic peaks in the 0.4–0.7 V/NHE region, ascribed to the Vulcan<sup>®</sup> support, a hydrogen adsorption/desorption and evolution ( $\sim 0.0$ – $0.15$  V/NHE) region, as well as the first stage of an O<sub>2</sub> evolution process ( $\sim 0.9$ – $1.0$  V/NHE). No electrochemical signs of decomposition processes were observed, indicating catalyst stability as evaluated upon continuous cycling over 1.5 h approximately. Probably, the Ir/Rh couple is overlapping their signals with Rh; at potential range of 0.4–0.7 V/NHE, two peaks are recorded (anodic and cathodic, respectively). These peaks are attributed to the formation of rhodium hydroxyl and rhodium oxidized species on the catalytic surface, which are reduced at cathodic potentials by an irreversible mechanism, since the potential difference ( $\Delta E$ ) is higher than 0.06 V/NHE [14].

The CV of Rh-Ir-Os-based material is not affected in the presence of CO, with no oxidation peaks being observed. In contrast, in the presence of methanol, the voltammogram of this material shows a methanol oxidation peak in the 0.4–0.9 V/NHE range, indicating its sensitivity to this alcohol [11, 49].

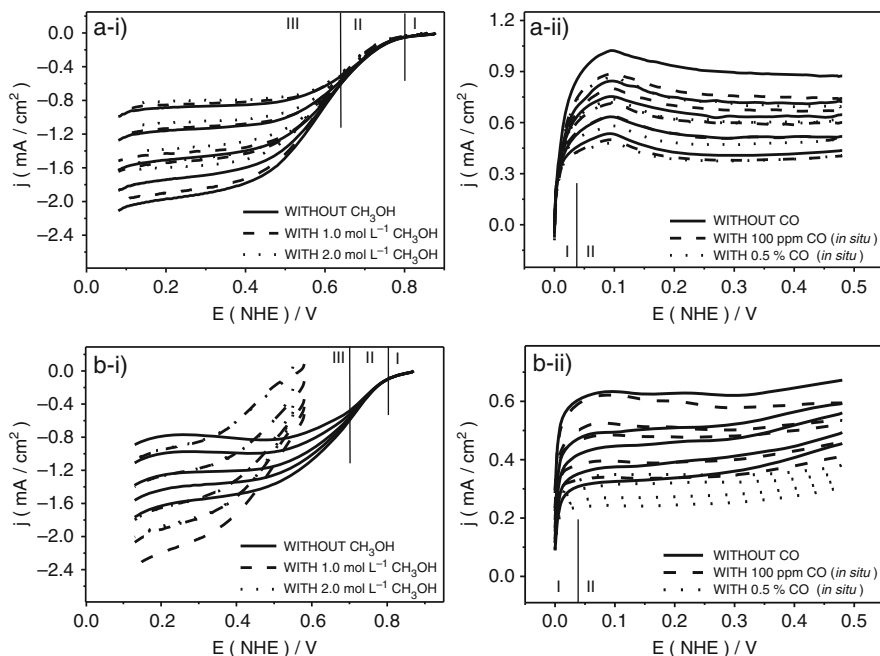
The catalytic activity of some materials to perform the alcohol oxidation reaction is attributed to the presence of metallic iridium particles in the final products obtained or to an iridium-based material partially decarbonylated, independent of the synthesis method; both types of iridium catalysts are capable of performing the oxidation of aliphatic alcohols, such as methanol and ethanol [49]. The synthesis conditions influence the electrochemical, morphological, and structural characteristics of the products, since the reductive atmosphere (H<sub>2</sub>) stimulates metallic particle formation. Under these conditions, the decarbonylation of the precursor compounds occurs quickly with total decarbonylation forming metal particles (probable alloys in these cases) or metal particles and some new metal carbonyl compound mixtures, capable of performing the alcohol oxidation [49]. Synthesis under a N<sub>2</sub> atmosphere generates metal carbonyl compounds without catalytic properties to oxidize the contaminant. Similar results were obtained with the synthesis by thermolysis of an Ir-based material in *o*-DCB at 20 h, since it also presented catalytical activity toward methanol oxidation.

In general, the CV characterization of most new catalytic materials did not show the corresponding peaks to oxidation of fuel contaminants, suggesting that mono- and poly-metallic materials are not active to the methanol and carbon monoxide oxidation in different concentrations, respectively.

#### 4.3.2.3 Study of the Oxygen Reduction, Hydrogen Oxidation, and Methanol Oxidation Reactions

The linear sweep voltammetry (LSV) is another electrochemical method, to study catalyst reactivity toward ORR or HOR by applying a potential sweep, but unlike CV, this sweep can only be applied in one cathodic or anodic direction. By obtaining the polarization curves for each catalytic material at different rotation velocities of work electrode (RDE), the catalytical activity can be evaluated. Most the synthesized materials showed *dual* catalytic activity toward the ORR and HOR, similar to platinum catalysts.

Figure 4.3a-i and a-ii shows representative ORR and HOR polarization curves of the Rh-Ir-based catalyst (synthesized in N<sub>2</sub> at 90 °C). This catalyst demonstrated efficient dual reactivity (ORR and HOR) in the absence of fuel cell contaminants,



**Fig. 4.3** (a-i-ii) Representative ORR and HOR current-potential curves for a bimetallic catalyst. (b-i-ii) Representative ORR and HOR current-potential curves for a tri-metallic material. Both in the absence and presence of 1.0 and 2.0 mol L<sup>-1</sup> methanol solutions for the ORR and 100 ppm and 0.5% CO/H<sub>2</sub> mixtures for the HOR. The sweep rate was 5 mV/s for the ORR and 10 mV/s for the HOR. The rotation rates were 100, 200, 400, 600, and 900 rpm for both cases

since the polarization curves are well defined. The characteristic zones include I-kinetic control zone (between 0.88 and 0.80 V/NHE), II-mixed control zone (0.80–0.65 V/NHE), and III-diffusional control zone (0.65–0.05 V/NHE) for the ORR. For the HOR, two zones I-mixed control zone (0.0–0.04 V/NHE) and II-diffusional control zone between 0.05 and 0.5 V/NHE were observed due to its rapid reactivity compared with the ORR. Therefore, it is impossible to observe the HOR kinetic control zone under these experimental conditions. These zones are almost the same in the presence of fuel cell contaminants, CH<sub>3</sub>OH and CO, respectively. The tri-metallic material obtained in a hydrogen atmosphere at 90 °C, was active to the HOR even in the presence of carbon monoxide with different concentrations. The tri-metallic material found to be active for the ORR in the absence of methanol only (Fig. 4.3b-i, b-ii), since when the Rh-Ir-Os-based catalyst is in direct contact with methanol, its catalytic activity for the ORR is lost. As a result, the corresponding polarization curves do not present the characteristic zones previously mentioned, and the OCP is unfavorable to perform the ORR. This is an indication that its active sites have been blocked by the contaminant species, which hinder the efficient catalytical performance. However, this approach can be utilized to study the methanol oxidation reaction using different catalysts to replace Pt or Pt-Ru [50].



Most the catalysts based on metal carbonyl cluster compounds are capable to perform the ORR and HOR, even in the presence of fuel supply contaminants. The polarization curves presented well-defined characteristic zones, OCP values, and current density data, which are similar to platinum catalysts. The advantage of these metal carbonyl catalysts is that it can maintain their catalytic activity in the presence of the fuel contaminants unlike platinum and its alloys.

It has been established that to obtain the total electrocatalytic activity of a material for the ORR or HOR, the kinetic and diffusion currents must be known. The Koutecky-Levich equation at a given potential is

$$\frac{1}{j} = \frac{1}{j_k} + \frac{1}{j_d} \quad (4.7)$$

where  $j$  is the measured disk current,  $j_k$  the kinetic current, and  $j_d$  the diffusion controlled current. This equation may be used to separate  $j_k$  from  $j_d$  and get the real electrocatalyst activity [53]. For the rotating disk electrode experiment, in the laminar flow regime, the diffusion current is a function of the rotation velocity; hence, Eq. (4.7) may be written as

$$\frac{1}{j} = \frac{1}{j_k} + \frac{B}{\omega^2} \quad (4.8)$$

where  $\omega$  is the electrode rotation velocity in rpm and  $B$  is a constant given by Eq. (4.9) [54]. For the case of ORR

$$B = \frac{1}{200nFA\nu^{\frac{1}{6}}D_{O_2}^{\frac{2}{3}}C_{O_2}} \quad (4.9)$$

where  $n$  is the number of electrons exchanged per mol of  $O_2$ ,  $F$  the Faraday constant (96,485 C·mol<sup>-1</sup>),  $A$  the catalytic effective surface area (cm<sup>2</sup>),  $\nu$  the kinematic viscosity of the electrolyte (cm<sup>2</sup>·s<sup>-1</sup>),  $D$  the oxygen diffusion coefficient (cm<sup>2</sup>·s<sup>-1</sup>), and  $C$  the bulk oxygen concentration in the electrolyte (mol·cm<sup>-3</sup>); the values used in this work were 0.01 cm<sup>2</sup> s<sup>-1</sup> for the kinematic viscosity, 1.4 × 10<sup>-5</sup> cm<sup>2</sup> s<sup>-1</sup> for the oxygen diffusion coefficient, and 1.1 × 10<sup>-6</sup> mol·cm<sup>-3</sup> for the bulk oxygen concentration [54]. These parameters for the HOR are different to the ones described in Eqs. (4.7, 4.8, and 4.9) [55].

According to Eq. (4.8), a plot of  $1/j$  vs.  $1/\omega^{1/2}$  for various potentials should yield straight and parallel lines with intercepts corresponding to the inverse of the real kinetic current,  $j_k$ , and slopes yielding the values of  $B$ . The number of electrons transferred in the ORR can be assessed with the values of  $B$ , according to Eq. (4.9). The value  $B$  was calculated the theoretical (using  $n = 2$  and 4;  $A =$  electrode geometric area, 0.072 cm<sup>2</sup>) and experimental Koutecky-Levich plots at two different methanol concentrations, at a given potential value. Most of the catalysts show plots that resemble curves calculated for an  $n$  value of 4 process, rather than a plot indicating a two-electron process. This suggests that  $O_2$  is most likely reduced to

H<sub>2</sub>O, following a direct, four-electron pathway at the solid electrode/solution interface. Similar results were obtained for the 30% Pt/Vulcan<sup>®</sup> electrodes in the absence of methanol. Results indicate that the fabricated catalysts can perform an ORR at similar velocity to a platinum catalyst, without the hydrogen peroxide formation. That would be detrimental to overall fuel cell efficiency, where the ORR is limiting reaction step. On this basis, the effective catalytic surface area,  $A_{\text{eff}}$ , can be calculated from Eq. (4.10), using the experimental Koutecky-Levich slope,  $B_{\text{exp}}$ , and  $n = 4$ :

$$A_{\text{eff}} = \frac{1}{200nFB_{\text{exp}}v^{\frac{1}{6}}D_{\text{O}_2}^{\frac{2}{3}}C_{\text{O}_2}} \quad (4.10)$$

All currents measured (cyclic voltammograms, polarization curves, and Tafel plots) were normalized to this effective area.

All materials synthesized showed linear  $1/j$  vs.  $1/\omega^{1/2}$  plots, which can be associated with a first-order reaction with respect to the oxygen dissolved in the electrolyte [56, 57]. Moreover, such linearity is not affected by the presence of methanol. However, the reaction order,  $m$ , was calculated from the slope of the  $\log j$  vs.  $\log [1 - (j/j_d)]$  plots (where  $j$  is the total current and  $j_d$  the diffusion current) for several rotation rates at a given potential [58], and it was demonstrated that the reaction order was unity with respect to dissolved O<sub>2</sub> in the 0.5 mol L<sup>-1</sup> H<sub>2</sub>SO<sub>4</sub> electrolyte.

Normally, the kinetic current values obtained from the interception of the Koutecky-Levich plots are used to generate the Tafel curves ( $\log j_k$  vs.  $E$ ); however, very precise results may not be obtained due to inevitable variations in the experimental conditions. For this reason, the current-potential curves were corrected by a previously described procedure [54], in order to get the correct kinetic current:

$$j_k = \frac{j^*j_d}{j_d - j} \quad (4.11)$$

The mass-transport-corrected Tafel plots ( $\log [j \cdot j_d / (j_d - j)]$  vs.  $E$ ) for the ORR can be obtained using Eq. (4.11). The same procedure can be followed to obtain the Tafel plots and the corresponding kinetic parameters for the HOR. In agreement with the previous polarization curves, the form of such Tafel curves is similar, regardless in the presence of methanol. Kinetic parameters (obtained from the Tafel plots) and OCP ( $E_{\text{OC}}^{\text{O}_2}$  and  $E_{\text{OC}}^{\text{H}_2}$ ) of representative electrocatalysts are presented in Table 4.1.

In the case of ORR, the kinetic parameters were calculated from the corresponding mass-transfer-corrected Tafel plots and are listed in Table 4.1, along with the reaction orders ( $m$ ). The Tafel slope,  $b$ , is related with the reaction mechanism; and the charge transfer coefficient,  $\alpha$ , is related with the energy necessary to perform the reaction; the ORR values for the bimetallic material are very close than those reported for platinum nanoparticles ( $b = 118 \text{ mV dec}^{-1}$ ;  $\alpha = 0.5$ ) [37]. These results suggest that the ORR mechanism adopted by the Rh-Ir-based material is similar to that followed by Pt. The corresponding values for the tri-metallic material are smaller and higher, respectively, than those calculated for platinum, indicating

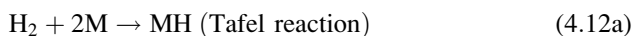
**Table 4.1** ORR and HOR kinetic parameters of representative catalysts based on metal carbonyl clusters. The open-circuit potential values are also shown

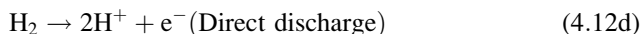
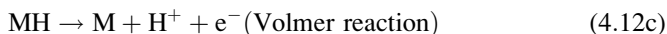
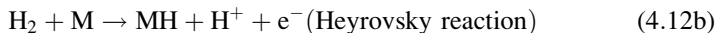
Reaction	Catalyst	$[\text{CH}_3\text{OH}]$ ( $\text{mol L}^{-1}$ )	$E_{OC}^{O_2}$ (V/NHE)	$m$	$b$ ( $\text{mV dec}^{-1}$ )	$\alpha$	$j_0$ ( $\text{mA cm}^{-2}$ )
ORR	Rh-Ir ( $\text{N}_2/90\text{ }^\circ\text{C}/5\text{ h}$ )	0.0	0.880	0.99	111.04	0.54	$1.51 \times 10^{-5}$
		1.0	0.864	0.98	106.87	0.56	$8.46 \times 10^{-6}$
		2.0	0.847	0.96	101.08	0.59	$5.24 \times 10^{-6}$
	Rh-Ir-Os ( $\text{H}_2/90\text{ }^\circ\text{C}/5\text{ h}$ )	0.0	0.875	1.00	94.71	0.63	$2.17 \times 10^{-6}$
		1.0	0.560	–	–	–	–
		2.0	0.535	–	–	–	–
Reaction	Catalyst	$ \text{co} $	$E_{OC}^{H_2}$ (V/NHE)	$m$	$B$ ( $\text{mV dec}^{-1}$ )	$\alpha$	$j_0$ ( $\text{mA cm}^{-2}$ )
HOR	Rh-Ir ( $\text{N}_2/90\text{ }^\circ\text{C}/5\text{ h}$ )	0.0	0.0	–	31.07	0.94	0.34
		100 ppm (in situ)	0.0	–	35.75	0.93	0.28
		0.5% (in situ)	0.0	–	30.95	0.68	0.18
	Rh-Ir-Os ( $\text{H}_2/90\text{ }^\circ\text{C}/5\text{ h}$ )	0.0	0.0	–	65.60	0.98	0.39
		100 ppm (in situ)	0.0	–	60.80	0.97	0.38
		0.5% (in situ)	0.0	–	61.79	0.92	0.29

that the ORR mechanism is possibly different. The exchange current density,  $j_0$ , which is related with the reaction rate constant,  $k$  [54], is considered one of the most important parameters to determine the real catalytic activity of a material; for the bimetallic material, it was found to be one order of magnitude higher in the absence of methanol than that for platinum nanoparticles,  $j_0 = 1.41 \times 10^{-6} \text{ mA/cm}^2$  [37]. The  $j_0$  values of the catalyst do not decrease importantly even in the presence of methanol, which confirms the resistance properties of the rhodium-iridium complex to this contaminant; therefore it can be used as a direct methanol fuel cell (DMFC) cathode.

Although the tri-metallic catalyst does not exhibit catalytic activity for ORR in the presence of methanol, its kinetic parameters in the absence of such contaminant are close to those for the platinum catalyst, which suggests these types of complexes can be utilized as potential *non-platinum alternative catalysts*.

As for the HOR, the kinetic parameters, i.e., the Tafel slope ( $B$ ), exchange current density ( $j_0$ ), and the charge transfer coefficient ( $\alpha$ ), were calculated from the corresponding mass-corrected Tafel plots, and the results are summarized in Table 4.1. The accepted mechanisms of the HOR involve the following reactions, depending on the electrocatalyst (M) and electrolyte used and shown in Eqs. 4.12a, 4.12b, 4.12c, and 4.12d [55]:





A sequence of Tafel/Volmer or Heyrovsky/Volmer steps is considered for most electrode materials, while a concerted mechanism (direct discharge) is suggested when the rates of reactions are similar [55]. In the present case, the average Tafel slopes of  $\sim 32 \text{ mV}\cdot\text{dec}^{-1}$  for the bimetallic material, and of  $\sim 62 \text{ mV}\cdot\text{dec}^{-1}$  for the tri-metallic catalyst, were obtained using pure hydrogen and mixtures ( $\text{H}_2/\text{CO}$ ). These results suggest a reversible direct discharge mechanism and an irreversible direct discharge mechanism, respectively [55].

Although the exchange current density ( $j_0$ ) values of both synthesized materials are lower than those exhibited by platinum ( $0.47 \text{ mA}/\text{cm}^2$  [37]), the significant CO tolerance is shown by both catalysts based on metal carbonyl clusters, which is an advantage over Pt catalysts. The  $j_0$  values of the clusters are similar in the absence or presence of CO, indicating that catalysts can be used in PEMFCs with reforming hydrogen as a fuel supply. Similar tolerance to CO was also observed for the most of the fabricated electrocatalysts. This class of metal carbonyl cluster catalysts exhibits an important advantage over Pt-based materials in their ability to catalyze ORR and HOR with fuel supplies containing  $\text{CH}_3\text{OH}$  or CO. This type of selectivity is not observed with Pt-based catalysts that become deactivated when in contact with contaminant species. Therefore, metal carbonyl cluster catalysts can be evaluated as cathodes and anodes in PEMFCs.

The methanol oxidation reaction was studied using different mono- and poly-metallic carbonyl cluster catalysts containing iridium. The catalysts showed activity independent of the fabrication method. The most facile reactions were observed when the catalyst was fabricated using pyrolysis under  $\text{H}_2$  atmosphere. When using iridium carbonyl cluster as precursor compound under  $\text{N}_2$  environment at  $230^\circ\text{C}$ ,  $350^\circ\text{C}$ , and  $500^\circ\text{C}$ , the materials were also active to methanol oxidation. This activity can be attributed to the presence of metal particles of iridium [49]. The catalyst fabricated by thermolysis with high boiling point solvents at 20 h was also active.

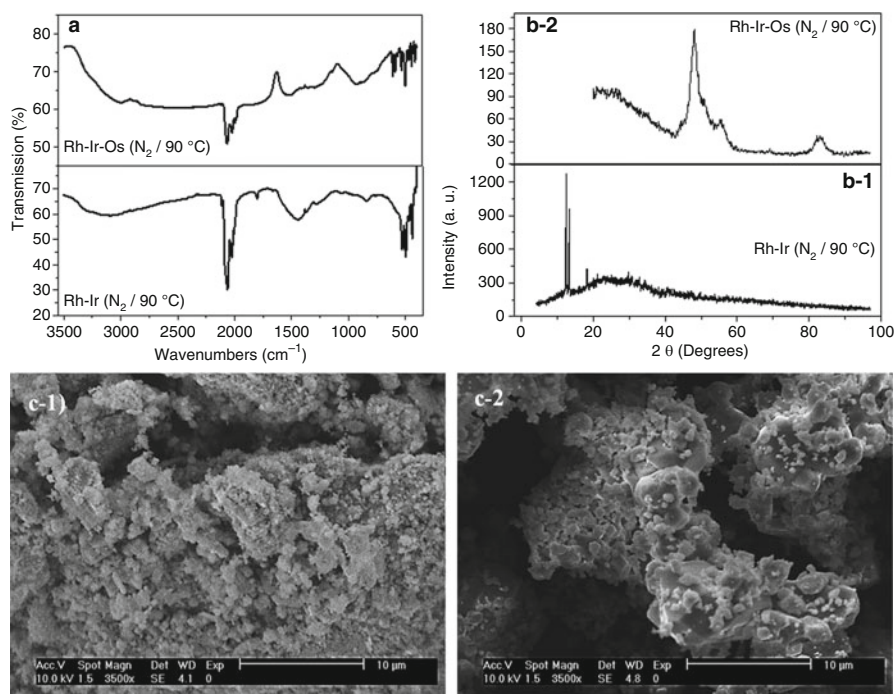
The methanol oxidation reaction was studied using the carbonyl cluster catalysts by CV and chronoamperometry, under different methanol concentrations (1.0, 2.0, and  $3.0 \text{ mol}\cdot\text{L}^{-1}$   $\text{H}_2\text{SO}_4$ ). In general, the potential range (0.35–0.9 V/NHE) in which the AOR occurs was determined from the CV plots. The data from the CV plots was used to optimize measurements by chronoamperograms. The measurement parameters were controlled at a total time of 30 s and a sample time of 15 s at different potential values, for each methanol concentration. From the latter, the stationary  $j/E$  curves for the AOR on the different electrodes could be plotted. Although the current density for the catalysts was found to be proportional to the alcohol concentration, its values are significantly smaller than those of Pt-Ru/Vulcan<sup>®</sup>. However, the anode overpotential of the different materials is similar to that of the commercial catalyst, indicating high catalytic property of the carbonyl cluster [50].

These results show that the new materials are good potential candidates to be evaluated as both cathodes and anodes in a reforming hydrogen PEMFC and as anodes in a direct methanol fuel cell.

### 4.3.3 Structural and Morphological Characterization

The structural and morphological characterization of the different catalysts indicated that the precursor compounds have well-defined structures and geometries [38, 48]. The products exhibited different structural, morphological, and electrochemical properties, depending on the thermic processes of precursor compounds, such as in different solvents and synthesis atmosphere, temperature, time, and reaction media. It was also found that performance of catalysts produced by pyrolysis (free solvent reactions) was higher than fabricated by thermolysis. In short, the structural, morphological, and electrochemical evaluation of the catalysts can guide the optimization of synthesis parameters.

The synthesized materials presented crystallite size  $<60$  nm (even for those which products were a mixture: metal particles and some metal carbonyl cluster), which were calculated by the Scherrer equation [59] using the full width at half maximum (FWHM) of the crystallographic peaks. This property is very important for electrocatalyst since the reactions occur on surface, which are favored when this area is greater. Representative FT-IR, XRD pattern, and SEM images of two catalytic materials synthesized from mixtures of  $\text{Rh}_6(\text{CO})_{16}/\text{Ir}_4(\text{CO})_{12}$  (relation weight 1:1) and of  $\text{Rh}_6(\text{CO})_{16}/\text{Ir}_4(\text{CO})_{12}/\text{Os}_3(\text{CO})_{12}$  (relation weight 1:1:1) are presented in Fig. 4.4. The FTIR (Fig. 4.4a) spectra show carbonyl stretching bands around  $2060\text{ cm}^{-1}$ , as well as a group of bands around  $505\text{ cm}^{-1}$ , associated with the terminal carbonyl group and metal-carbonyl vibrations, respectively [60, 61]. Such bands are an indication of the presence of carbonyl metal complexes; however, their intensity is weaker for the material synthesized in  $\text{H}_2$  (Fig. 4.4a-2) than for the catalyst obtained in  $\text{N}_2$  (Fig. 4.4a-1), which means that the decarbonylation process is favored in a reductive atmosphere. This was confirmed by a chemical composition analysis of the catalysts, using EDS technique, Rh 32.81, Ir 37.40, C 14.36, and O 15.41 wt. % for the material obtained in  $\text{N}_2$  and Rh 23.98, Ir 37.43, Os 28.61, C 7.52, and O 2.45 wt. % for the catalyst synthesized in  $\text{H}_2$ , and by the X-ray diffraction patterns are shown in Fig. 4.4b. The pattern of Fig. 4.4b1 can be assigned to a new Rh-Ir-based carbonyl complex obtained in  $\text{N}_2$ , while the pattern of the material synthesized in  $\text{H}_2$  (Fig. 4.4b2) shows some peaks attributed to metal particles, with a larger contribution from the iridium carbonyl precursor, according to the EDS analysis. Calculations based on the full width at half maximum (FWHM) of the main XRD peaks, using the Scherrer equation [59], suggest that the average particle size is  $\sim 62$  nm for the catalyst obtained in a nitrogen atmosphere and  $\sim 38$  nm for that synthesized in the  $\text{H}_2$  atmosphere. Figure 4.4c1–2 shows SEM images of the bi- and tri-metallic electrocatalysts; both materials exhibit a porous spongelike surface morphology, although the tri-metallic material had higher particle porosity than the

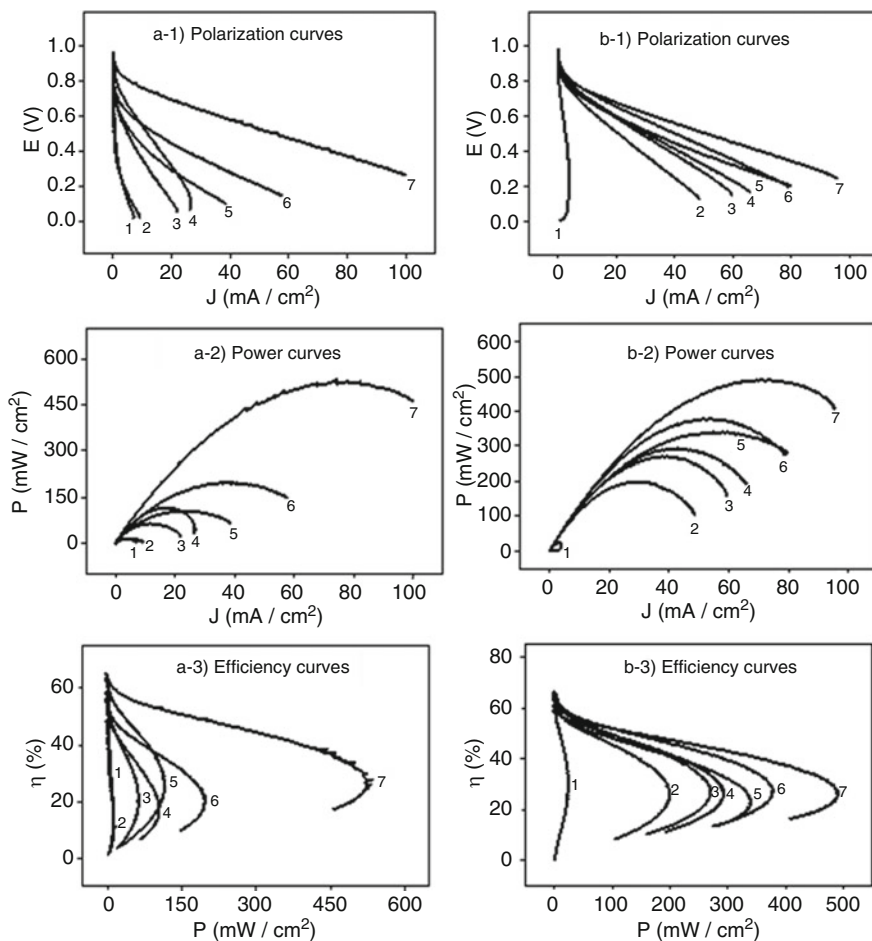


**Fig. 4.4** Structural analyses of the catalyst. (a) The FTIR study to determine the metal-carbonyl vibrations, (b) the XRD data to determine the crystalline structure, and (c) SEM image to evaluate the surface morphology

bimetallic material. The small particle diameter and high porosity can be an advantageous property for their use as catalysts.

#### 4.3.4 PEM Fuel Cell Evaluation

The optimal catalysts as determined by electrochemical and structural characterization were selected in order to be evaluated as cathodes and anodes in a hydrogen PEMFC. To conduct this study, single fuel cells (with different flow channel geometries) and the test system were designed and built. The different variables, such as feed stream, relative humidity, and pressure of reactive gases, and the operation temperature of the cell were accurately controlled. The parameters including open-circuit potential, current density, power density, and the discharge and power curves of each material were measured to evaluate electrocatalyst performance using a membrane-electrode assembly (MEA). The fuel cell test system was more cost-effective to be built than a commercial design. This system was evaluated



**Fig. 4.5** Electrochemical study of the PEMFCs. **(a1–3)** Fuel cell performance of representative catalysts used as *cathodes*: (1)  $\text{Ir}_y(\text{CO})_n\text{-Ir}_y(\text{N}_2/230\text{ }^\circ\text{C})$ , (2)  $\text{Ir}_4(\text{CO})_{12}$ , (3)  $\text{Ir}_y(\text{H}_2/190\text{ }^\circ\text{C})$ , (4)  $\text{Rh}_z(\text{N}_2/190\text{ }^\circ\text{C})$ , (5)  $\text{Rh}_6(\text{CO})_{16}$ , (6)  $\text{Rh}_z(o\text{-DCB})$ , (7)  $\text{Pt/Vulcan}^{\text{®}}$  (30%). For all cases the anode was  $\text{Pt/Vulcan}^{\text{®}}$  (30%). **(b1–3)** Fuel cell performance of representative catalysts used as *anodes*: (1)  $\text{Ir}_4(\text{CO})_{12}$ , (2)  $\text{Rh}_z(o\text{-DCB})$ , (3)  $\text{Ir}_y(\text{CO})_n\text{-Ir}_y(\text{N}_2/230\text{ }^\circ\text{C})$ , (4)  $\text{Rh}_z(\text{N}_2/190\text{ }^\circ\text{C})$ , (5)  $\text{Ir}_y(\text{H}_2/190\text{ }^\circ\text{C})$ , (6)  $\text{Rh}_6(\text{CO})_{16}$ , (7)  $\text{Pt/Vulcan}^{\text{®}}$  (30%). For all cases the cathode was  $\text{Pt/Vulcan}^{\text{®}}$  (30%).

using the platinum ( $\text{Pt/Pt}$ : cathode/anode) as reference and the fabricated metal carbonyl cluster catalysts. The higher current density and power density ( $100.8\text{ mA cm}^{-2}$  and  $527.5\text{ mW cm}^{-2}$ ) were obtained using collector plates with flow channels of serpentine geometry than using parallel or interdigital geometries. This is attributed to the low-pressure drop of the reactive gases in a serpentine



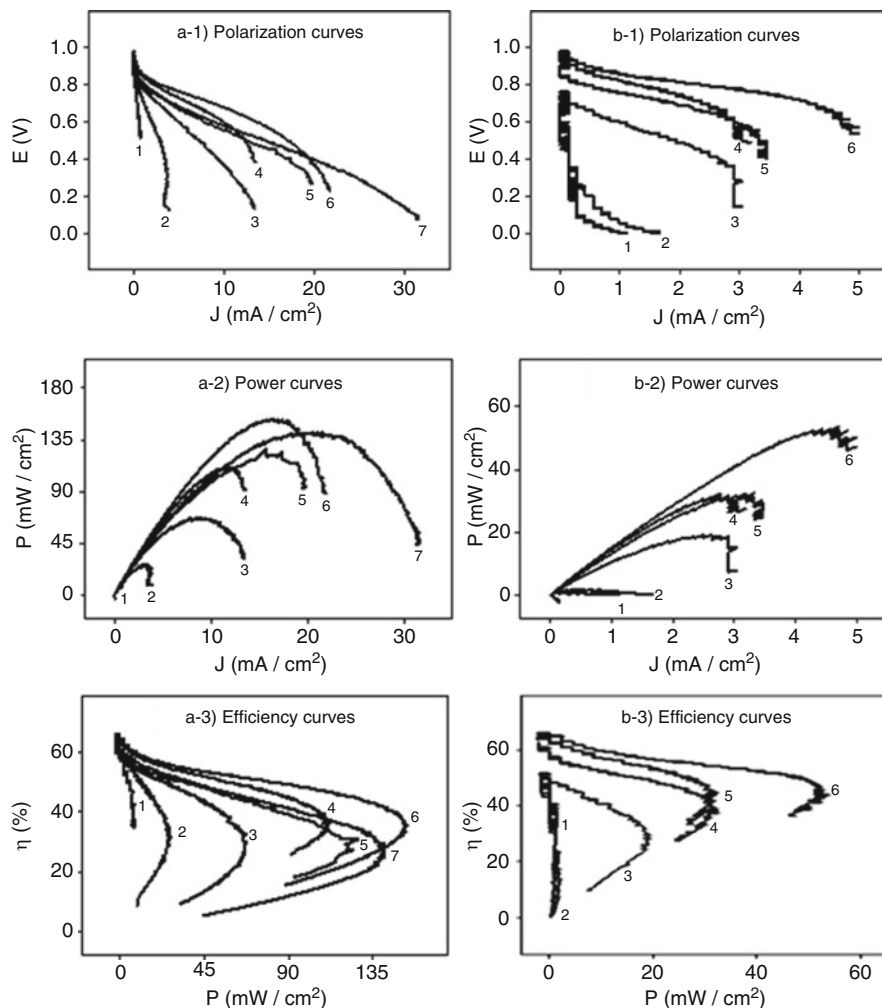
**Table 4.2** Fuel cell performance of representative catalysts based on metal carbonyl clusters as cathodes and its comparison with platinum (The anode was Pt/Vulcan® 30% for all cases). T = 20 °C; R. H. = 60% for O<sub>2</sub> and H<sub>2</sub>

MEA	Fuel cell conditions		Fuel cell parameters				
	Feed stream (sccm)		<i>E</i> (V)	<i>I</i> (mA)	<i>J</i> (mA cm <sup>-2</sup> )	<i>P</i> (mW cm <sup>-2</sup> )	<i>η</i> (%)
	O <sub>2</sub>	H <sub>2</sub>					
Ir <sub>y</sub> (CO) <sub>n</sub> -Ir <sub>y</sub> (N <sub>2</sub> /230 °C)	100	30	0.83	0.12	6.92	13.11	14.24
Ir <sub>4</sub> (CO) <sub>12</sub>	200	200	0.74	0.18	10.51	17.64	10.32
Ir <sub>y</sub> (H <sub>2</sub> /190 °C)	120	20	0.87	0.38	21.86	63.56	20.12
Rh <sub>z</sub> (N <sub>2</sub> /190 °C)	120	30	0.93	0.46	26.15	116.40	25.61
Rh <sub>6</sub> (CO) <sub>16</sub>	100	10	0.83	0.66	37.92	105.17	16.98
Rh <sub>z</sub> ( <i>o</i> -DCB/183 °C)	120	200	0.83	1.01	57.57	198.43	20.12
Pt/Vulcan® (30%)	120	20	0.96	1.77	100.89	527.53	26.79

geometry [6]. Figure 4.5a shows the fuel cell performance using representative catalytic materials as cathodes. Although the performance of the carbonyl catalyst was lower than that exhibited by platinum, it was enough to power some electronic devices, similar to Pt/Pt assembly, which is attributed to similar efficiency values (Fig. 4.5a3). The best catalytic material evaluated as a cathode in a PEMFC was obtained by thermolysis from rhodium carbonyl in *o*-DCB (Table 4.2).

When the novel materials were evaluated as anodes in a single-hydrogen PEMFC at room temperature, the best performance was for the precursor compound Rh<sub>6</sub>(CO)<sub>16</sub> followed very close by an Ir-based catalyst (obtained by pyrolysis in a reductive atmosphere at 190 °C); both showed a similar performance to that of platinum using pure hydrogen. The performance of the material obtained by pyrolysis of the rhodium carbonyls in N<sub>2</sub> at 190 °C (Fig. 4.5b1–3) is also similar to that of Pt. Studies were also performed in the presence of 100 ppm and 0.5% CO in the hydrogen feed stream. In the presence of 100 ppm CO, the Ir<sub>y</sub>(H<sub>2</sub>/190 °C) catalyst exhibited slightly higher cell potential values than Pt and Rh<sub>6</sub>(CO)<sub>16</sub> within a certain current density range (Fig. 4.6a1–3); other catalytic materials based on rhodium and iridium (obtained by thermolysis and pyrolysis, respectively) also have a good stability and performance under this fuel cell operating conditions. In the presence of 0.5% CO, however, the CO-resistant properties of the novel catalysts are more evident (Fig. 4.6b1–3), since the cell potential is virtually maintained for most of them, while it drops dramatically for Pt catalyst. Although the current density decreases considerably for all materials, they were capable to generate electrical power sufficiently to drive two appliances at the same time in contrast with platinum catalyst. These results verified that the new materials present a better performance





**Fig. 4.6** Fuel cell performance of representative catalysts used as *anodes* in the presence of CO in different concentration (in situ). **(a1–3)** 100 ppm CO: (1)  $\text{Ir}_4(\text{CO})_{12}$ , (2)  $\text{Rh}_2(\text{N}_2/190^\circ\text{C})$ , (3)  $\text{Rh}_2(o\text{-DCB})$ , (4)  $\text{Ir}_y(\text{CO})_n\text{-Ir}_y(\text{N}_2/230^\circ\text{C})$ , (5)  $\text{Rh}_6(\text{CO})_{16}$ , (6)  $\text{Ir}_y(\text{H}_2/190^\circ\text{C})$ , (7)  $\text{Pt/Vulcan}^{\text{®}}$  (30%). **(b1–3)** 0.5% CO: (1)  $\text{Rh}_2(\text{N}_2/190^\circ\text{C})$ , (2)  $\text{Pt/Vulcan}^{\text{®}}$  (30%), (3)  $\text{Rh}_6(\text{CO})_{16}$ , (4)  $\text{Rh}_2(o\text{-DCB})$ , (5)  $\text{Ir}_y(\text{CO})_n\text{-Ir}_y(\text{N}_2/230^\circ\text{C})$ , (6)  $\text{Ir}_y(\text{H}_2/190^\circ\text{C})$ . For all cases the cathode was  $\text{Pt/Vulcan}^{\text{®}}$  (30%)

than platinum catalyst when the fuel is a mixture of  $\text{H}_2/\text{CO}$  in different concentrations (Table 4.3). Some bimetallic Ru-Os catalysts obtained by thermolysis method also showed similar performance when they were evaluated as electrodes in a PEMFC [42].

**Table 4.3** Fuel cell performance of representative catalysts based on metal carbonyl clusters as anodes and its comparison with platinum (The cathode was Pt/Vulcan® 30% for all cases). T = 20 °C; R. H. = 60% for O<sub>2</sub> and H<sub>2</sub>

MEA	Fuel cell conditions		Presence of CO  x	Fuel cell parameters				
	Feed stream (sccm)			E (V)	I (mA)	J (mA cm <sup>-2</sup> )	P (mW cm <sup>-2</sup> )	η (%)
Anode	O <sub>2</sub>	H <sub>2</sub>						
Ir <sub>y</sub> (CO) <sub>n</sub> -Ir <sub>y</sub> (N <sub>2</sub> /230 °C)	120	30	0.0	0.95	1.05	59.98	276.50	28.08
			100 ppm	0.94	0.23	13.54	112.92	36.84
			0.5%	0.95	0.05	3.18	32.12	38.81
Ir <sub>4</sub> (CO) <sub>12</sub>	120	80	0.0	0.90	0.07	4.01	30.28	29.16
			100 ppm	0.89	0.007	0.43	8.42	–
			0.5%	–	–	–	–	–
Ir <sub>y</sub> (H <sub>2</sub> /190 °C)	120	30	0.0	0.98	1.38	78.49	385.28	27.25
			100 ppm	0.97	0.38	21.98	155.08	35.43
			0.5%	0.97	0.08	4.99	54.18	44.53
Rh <sub>z</sub> (N <sub>2</sub> /190 °C)	120	30	0.0	0.87	1.16	66.01	299.44	26.48
			100 ppm	0.92	0.007	4.09	28.61	29.43
			0.5%	0.70	0.01	1.12	1.11	28.10
Rh <sub>6</sub> (CO) <sub>16</sub>	120	20	0.0	0.96	1.41	80.10	345.13	23.80
			100 ppm	0.95	0.34	19.70	128.50	28.72
			0.5%	0.95	0.06	3.50	32.81	44.53
Rh <sub>z</sub> ( <i>o</i> -DCB/ 183 °C)	120	30	0.0	0.93	0.85	48.31	204.91	26.85
			100 ppm	0.92	0.23	13.31	68.93	31.21
			0.5%	0.92	0.05	3.06	20.08	9.86
Pt/Vulcan® (30%)	120	20	0.0	0.96	1.69	95.80	497.01	26.85
			100 ppm	0.94	0.55	31.66	143.18	26.26
			0.5%	0.72	0.02	1.68	2.49	12.72

## 4.4 Conclusion

New mono-, bi-, tri-, and tetra-catalytic materials based on osmium, ruthenium, iridium, and rhodium carbonyl clusters were developed, in order to perform the oxygen reduction and hydrogen oxidation reactions. The direct application of these new materials as electrodes in a PEMFC showed their real activity. This is because the experimental conditions in an electrochemical cell and in a fuel cell are different and yield different results. The electrochemical study is a first approximation of the kinetic behavior of the materials in order to perform the ORR and HOR (even in the presence of fuel supply contaminants, such as methanol and carbon monoxide, respectively). However, this behavior can be modified when these materials are evaluated as cathodes or anodes in a PEMFC. This was the case of the materials presented in this chapter, since the electrochemical study and kinetic analysis

indicated that most of the fabricated catalysts were capable of performing the HOR in the absence or presence of carbon monoxide at different concentration without losing their catalytic activity and without major changes in their polarization curves and kinetic parameters. However, when different catalytic materials were evaluated as anodes in a PEMFC using pure hydrogen, 100 ppm, and 0.5% CO in the hydrogen feed stream, the materials have different performance: using pure H<sub>2</sub>, the carbonyl cluster catalysts showed a similar performance to that of platinum; while current density and power density values decreased considerably for all materials with CO in the fuel supply, however, the cell potentials remained virtually unchanged but dropped dramatically for Pt catalyst.

Finally, with the direct application of the new metal carbonyl materials as electrodes in a PEMFC, it was possible to power some electronic devices of different powers, such as little fans, toys, LEDs, and a disk man CD player, even when using a fuel mixture (0.5% CO/H<sub>2</sub>). This opens the possibility to use reforming hydrogen, helping to decrease the high cost of fuel cell technology, as well as the hydrogen production for fuel cells. In addition, for some applications, the platinum catalyst could be successfully substituted by some carbonyl clusters, since they can perform both reactions (ORR and HOR), but with the important advantage of being resistant to fuel cell contaminants (CH<sub>3</sub>OH and CO, respectively), which also helps to decrease the cost of fuel cells.

**Acknowledgments** The author thanks V. García-Montalvo and O. Jiménez-Sandoval for their support in his postgraduate research training at the Institute of Chemistry, National Autonomous University of Mexico (UNAM), and CINVESTAV-Querétaro, respectively. C. I. Zuñiga-Romero, A. Mauricio-Sánchez, J. E. Urbina-Alvárez, M. A. Hernández-Landaverde and F. Rodríguez-Melgarejo are acknowledged for technical support; and E. G. Santillán-Rivero is also duly acknowledged for bibliographical assistance (CINVESTAV-Querétaro). The author is grateful to CONACYT for a graduate scholarship and DGAPA-UNAM for a postgraduate fellowship. Finally, the author would like to thank his parents for their invaluable moral support and Miriam Millán-Rocha, for her valuable patience and for accompanying him in this satisfactory experience.

---

## References

1. K. Kinoshita, *Electrochemical Oxygen Technology* (Wiley, Berkeley, 1992)
2. O.T. Holton, J.W. Stevenson, The role of platinum in proton exchange membrane fuel cells. *Platinum Mater. Rev.* **57**, 259–271 (2013)
3. C. Sealy, The problem with platinum. *Mater. Today* **11**, 65–68 (2008)
4. A. Brouzgou, S. Song, P. Tsiakaras, Low and non-platinum electrocatalysts for PEMFCs: current status, challenges, and prospects. *Appl. Catal. B Environ.* **127**, 371–388 (2012)
5. F. Raimondi, G. Scherer, R. Kotz, A. Wokaun, Nanoparticles in energy technology: Examples from electrochemistry and catalysis. *Angew. Chem. Int. Ed. Engl.* **44**, 2190–2209 (2005)
6. X. Li, *Principles of Fuel Cells* (Taylor and Francis, New York, 2006)
7. J. Zhang, *PEM Fuel Cell Electrocatalyst and Catalyst Layers* (Springer, Vancouver, 2008)
8. A. Rabis, P. Rodriguez, T.J. Schmidt, Electrocatalysis for polymer electrolyte fuel cells: Recent achievements and future challenges. *ACS Catal.* **2**, 864–890 (2012)
9. Y. Shao, G. Yin, Y. Gao, Understanding and approaches for the durability issues of Pt-based catalysts for PEM fuel cell. *J. Power Sources* **171**, 558–566 (2007)

10. R.C. Urian, A. Gullá, S. Mukerjee, Electrocatalysis of reformat tolerance in proton exchange membranes fuel cells: part I. *J. Electroanal. Chem.* **554–555**, 307–324 (2003)
11. J.W. Lee, B.N. Popov, Ruthenium-based electrocatalysts for oxygen reduction reaction-a review. *J. Solid State Electrochem.* **11**, 1355–1364 (2007)
12. S. Maheswari, P. Sridhar, S. Pitchumani, Pd-RuSe/C as ORR specific catalyst in alkaline solution containing methanol. *Fuel Cells* **12**, 963–970 (2012)
13. R. Othman, A.L. Dicks, Z. Zhu, Non-precious metal catalysts for the PEM fuel cell cathode. *Int. J. Hydrog. Energy* **6**, 357–372 (2012)
14. J. Wang, *Analytical Electrochemistry* (Wiley-VCH, New York, 2000)
15. F.C. Anson, C. Shi, B. Steiger, Novel multinuclear catalysts for the Electroreduction of dioxygen directly to water. *Acc. Chem. Res.* **30**, 437–442 (1997)
16. A.K. Shukla, R.K. Raman, Methanol tolerant electrocatalysts for the oxygen reduction reaction. *Annu. Rev. Mater. Res.* **33**, 155–168 (2003)
17. Z. Juogs, R.J. Behm, Simultaneous oxygen reduction and methanol oxidation on a carbon-supported Pt catalyst and mixed potential formation-revisited. *Electrochim. Acta* **49**, 3891–3900 (2004)
18. R.-F. Wang, S.-J. Liao, H.-Y. Liu, H. Heng, Synthesis and characterization of Pt-se/C electrocatalyst for oxygen reduction and its tolerance to methanol. *J. Power Sources* **171**, 471–476 (2007)
19. V. Le Rhun, E. Garnier, S. Pronier, N. Alonso-Vante, Electrocatalysis on nanoscale ruthenium-based material manufactured by carbonyl decomposition. *Electrochem. Commun.* **2**, 475–479 (2000)
20. M. Bron, P. Bogdanoff, S. Fiechter, et al., Carbon supported catalysts for oxygen reduction in acid media prepared by thermolysis of  $\text{Ru}_3(\text{CO})_{12}$ . *J. Electroanal. Chem.* **517**, 85–94 (2001)
21. S. Marcotte, D. Villers, N. Guillet, et al., Electroreduction of oxygen on co-based catalysts: Determination of the parameters affecting the two-electron transfer reaction in an acid medium. *Electrochim. Acta* **50**, 179–188 (2004)
22. G. Faubert, R. Côté, D. Guay, et al., Iron catalysts prepared by high-temperature pyrolysis of tetraphenyl porphyrins adsorbed on carbon black for oxygen reduction in polymer electrolyte fuel cells. *Electrochim. Acta* **43**, 341–353 (1998)
23. M. LeFèvre, J.P. Dodelet, Fe-based catalysts for the reduction of oxygen in polymer electrolyte membrane fuel cell conditions: determination of the amount of peroxide released during electroreduction and its influence on the stability of the catalysts. *Electrochim. Acta* **48**, 2749–2760 (2003)
24. G. Lalonde, R. Côté, D. Guay, Is nitrogen important in the formulation of Fe-based catalysts for oxygen reduction in solid polymer fuel cells? *Electrochim. Acta* **42**, 1379–1388 (1997)
25. M. Bron, P. Bogdanoff, S. Fiechter, et al., Enhancement of oxygen electro-reduction activity via surface modification of carbon-supported ruthenium nanoparticles: a new class of electrocatalysts. *J. Electroanal. Chem.* **578**, 339–344 (2005)
26. H. Tributsch, M. Bron, M. Hilgendorff, et al., Methanol-resistant cathodic oxygen reduction catalysts for methanol fuel cells. *J. Appl. Electrochem.* **31**, 739–748 (2001)
27. A.L. Ocampo, R.H. Castellanos, P.J. Sebastian, Kinetic study of the oxygen reduction reaction on  $\text{Ru}_y(\text{CO})_n$  in acid medium with different concentrations of methanol. *J. New Mater. Electrochem. Syst.* **5**, 163–168 (2002)
28. T.J. Schmidt, U.A. Paulus, H.A. Gasteiger, Oxygen reduction on  $\text{Ru}_{1.92}\text{Mo}_{0.08}\text{SeO}_4$ , Ru/carbon, and Pt/carbon in pure and methanol-containing electrolytes. *J. Electrochem. Soc.* **147**, 2620–2624 (2000)
29. N. Alonso-Vante, P. Bogdanoff, H. Tributsch, On the origin of the selectivity of oxygen reduction of ruthenium-containing electrocatalysts in methanol-containing electrolyte. *J. Catal.* **190**, 240–246 (2000)
30. E.I. Santiago, E.A. Ticianelli, The performance of carbon-supported PtOs electrocatalysts for the hydrogen oxidation in the presence of CO. *Int. J. Hydrog. Energy* **30**, 159–165 (2005)

31. S.M. Bonilla, C.F. Zinola, J. Rodríguez, Catalytic effects of ruthenium and osmium spontaneous deposition on platinum surfaces toward methanol oxidation. *J. Colloid Interface Sci.* **288**, 377–386 (2005)
32. R.H. Castellanos, A.L. Ocampo, J.P. Sebastian,  $\text{Os}_x(\text{CO})_n$  based methanol-tolerant Electrocatalyst for  $\text{O}_2$  Electroreduction in acid electrolyte. *J. New Mater. Electrochem. Syst.* **5**, 83–90 (2002)
33. D. Astruc, *Química Organometálica* (Reverté, Barcelona, 2003)
34. J.E. Huheey, E.A. Keiter, R.L. Keiter, *Química Inorgánica. Principios de Estructura y Reactividad* (Alfa-Omega, México, 2005)
35. F.A. Cotton, G. Wilkinson, *Química Inorgánica Avanzada* (Limusa, México, 1996)
36. R.D. Adams, The synthesis, structures, bonding and unusual reactivity of sulfido osmium carbonyl cluster compounds. *Polyhedron* **4**, 2003–2031 (1985)
37. J. Uribe-Godínez, R.H. Castellanos, E. Borja-Arco, et al., Novel osmium-based electrocatalysts for oxygen reduction and hydrogen oxidation in acid conditions. *J. Power Sources* **177**, 286–295 (2008)
38. J. Uribe-Godínez, R.H. Castellanos, O. Jiménez-Sandoval, Hexadecacarbonylhexarhodium as a novel electrocatalyst for oxygen reduction and hydrogen oxidation in the presence of fuel cell contaminants. *J. Power Sources* **195**, 7243–7245 (2010)
39. R.H. Castellanos, E. Borja-Arco, A. Altamirano-Gutiérrez, Electrocatalytic properties of novel ruthenium-based compounds for the oxygen reduction reaction in 0.5 M  $\text{H}_2\text{SO}_4$ : effects of the synthesis atmosphere and temperature. *J. New Mater. Electrochem. Syst.* **8**, 69–75 (2005)
40. A. Altamirano-Gutiérrez, O. Jiménez-Sandoval, J. Uribe-Godínez, et al., Methanol resistant ruthenium electrocatalysts for oxygen reduction synthesized by pyrolysis of  $\text{Ru}_3(\text{CO})_{12}$  in different atmospheres. *Int. J. Hydrog. Energy* **34**, 7983–7994 (2009)
41. E. Borja-Arco, R.H. Castellanos, J. Uribe-Godínez, et al., Osmium–ruthenium carbonyl clusters as methanol tolerant electrocatalysts for oxygen reduction. *J. Power Sources* **188**, 387–396 (2009)
42. Uribe-Godínez J, Borja-Arco E, Jiménez-Sandoval O (2015) Bimetallic Electrocatalysts resistance to carbon monoxide and methanol for application in a polymer electrolyte fuel cell. Patent. Folio number 40335
43. B.F.G. Johnson, Y.V. Roberts, E. Parisini, Solid state studies into the possible rearrangement mechanisms for the fluxional behavior of the tetranuclear carbonyls  $\text{M}_4(\text{CO})_{12}$  and their derivatives. *J. Organomet. Chem.* **478**, 21–28 (1994)
44. E.R. Corey, L.F. Dahl,  $\text{Rh}_6(\text{CO})_{16}$  and its identity with previously reported  $\text{Rh}_4(\text{CO})_{11}$ . *J. Am. Chem. Soc.* **85**, 1202–1203 (1963)
45. D.M.P. Mingos, D.J. Wales, *Introduction to Cluster Chemistry* (Prentice Hall, Englewood Cliffs, 1990)
46. R. Della Pergola, L. Garlaschelli, S. Martinengo, Chemistry of iridium carbonyl clusters. Preparation of  $\text{Ir}_4(\text{CO})_{12}$ . *J. Organomet. Chem.* **331**, 271–274 (1987)
47. A.D. Allian, Y. Wang, M. Saeys, et al., The combination of deconvolution and density functional theory for the mid-infrared vibrational spectra of stable and unstable rhodium carbonyl clusters. *Vib. Spectrosc.* **41**, 101–111 (2006)
48. J. Uribe-Godínez, O. Jiménez-Sandoval, Study of the electrocatalytic properties of  $\text{Ir}_4(\text{CO})_{12}$  for the oxygen reduction and hydrogen oxidation reactions, in the absence and presence of fuel cell contaminants. *Int. J. Hydrog. Energy* **3**, 9477–9484 (2012)
49. J. Uribe-Godínez, V. García-Montalvo, O. Jiménez-Sandoval, Development of Ir-based and Rh-based catalyst electrodes for PEM fuel cell applications. *Int. J. Hydrog. Energy* **38**, 7680–7683 (2013)
50. J. Uribe-Godínez, V. García-Montalvo, O. Jiménez-Sandoval, A novel Rh-Ir electrocatalyst for the oxygen reduction reaction and the hydrogen and methanol oxidation reactions. *Int. J. Hydrog. Energy* **39**, 9121–9127 (2014)

51. J. Uribe-Godínez, V. García-Montalvo, O. Jiménez-Sandoval, Study of the oxygen reduction and hydrogen oxidation reactions on RhIrRu-based catalysts. *Int. J. Hydrog. Energy* **41**, 22520–22528 (2016)
52. T.R. Ralph, M.P. Hogarth, Catalysis for low-temperature fuel cells. Part III: challenges for the direct methanol fuel cell. *Platin. Met. Rev.* **46**, 146–164 (2002)
53. V.Y. Filinovsky, Y.V. Pleskov, *Rotating Disk, and Ring-Disk Electrodes* (Consultants Bureau, New York, 1976)
54. E. Gileadi, *Electrode kinetics for chemists, chemical engineers and material scientists* (Wiley-VCH, New York, 1993)
55. R. Mello, E.A. Ticianelli, Kinetic study of the hydrogen oxidation reaction on platinum and Nafion<sup>®</sup> covered platinum electrodes. *Electrochim. Acta* **42**, 1031–1039 (1997)
56. N. Alonso-Vante, H. Tributsch, O. Solorza-Feria, Kinetics studies of oxygen reduction in the acid medium on novel semiconducting transition metal chalcogenides. *Electrochim. Acta* **40**, 567–576 (1995)
57. A. Damjanovic, M.A. Genshaw, B.J. O'M, The mechanism of oxygen reduction at platinum in alkaline solutions with special reference to H<sub>2</sub>O<sub>2</sub>. *J. Electrochem. Soc.* **114**, 1107–1112 (1967)
58. T. Jiang, G.M. Brisard, Determination of the kinetic parameters of oxygen reduction on copper using a rotating ring single crystal disk assembly (RRD<sub>Cu(th k l)E</sub>). *Electrochim. Acta* **52**, 4487–4496 (2007)
59. B.D. Cullity, *Elements of X-Ray Diffraction* (Addison-Wesley, Reading, 1978)
60. K. Nakamoto, *Infrared and Raman Spectra of Inorganic and Coordination Compounds, Part B: Applications in Coordination, Organometallic, and Bioinorganic Chemistry*, 6th edn. (Wiley, Hoboken, 2009)
61. D. Lin-Vien, N. Colthup, W.G. Fateley, et al., *The Handbook of Infrared and Raman Characteristic Frequencies of Organic Molecules* (Academic, San Diego, 1991)



# Non-carbon Support Materials Used in Low-Temperature Fuel Cells

# 5

Xuecheng Cao, Fan Li, and Ruizhi Yang

## Contents

5.1 Support Materials in Low-Temperature Fuel Cells .....	146
5.2 Metal Oxide-Based Support Materials .....	148
5.3 Metal-Doped Oxide-Based Support Materials .....	153
5.4 Carbide-Based Support Materials .....	157
5.5 Nitride-Based Support Materials .....	159
5.6 Boride-Based Support Materials .....	160
5.7 Mesoporous Silica-Based Support Materials .....	161
5.8 Metal-Based Support Materials .....	161
5.9 Conducting Polymer-Based Support Materials .....	162
5.10 Conclusion .....	163
References .....	167

## Author Contributions

FL and RY collectively conceived this topic. XC generated the data table and completed the literature survey. FL wrote the sections of metal, metal oxide, and conducting polymer. RY wrote the sections of carbides, nitrides, borides, and mesoporous silica as support materials. All authors reviewed and edited this manuscript.

X. Cao · R. Yang (✉)

Soochow Institute for Energy and Materials InnovationS, College of Physics, Optoelectronics and Energy & Collaborative Innovation Center of Suzhou Nanoscience and Technology, Soochow University, Suzhou, Jiangsu, China  
e-mail: [yangrz@suda.edu.cn](mailto:yangrz@suda.edu.cn)

F. Li

Beijing Key Laboratory for Catalysis and Separation, Department of Chemistry and Chemical Engineering, College of Environmental and Energy Engineering, Beijing University of Technology, Beijing, China  
e-mail: [vanadiumli@bjut.edu.cn](mailto:vanadiumli@bjut.edu.cn)

## Abstract

To improve electrochemical performance of the fuel cell devices, various nano-scaled materials were produced using different methods such as colloidal chemistry, physical deposition, pyrolysis, and solid-state chemistry. Series of materials such as Pt-catalytic support materials are described and include doped metal oxides, carbides, nitrides, borides, mesoporous silica, metal, and conducting polymer-based support materials for Pt class of electrocatalysts. In this chapter, we summarized the recent developments in the advanced synthesis of electrodes for low-temperature fuel cells, cathode, and anode catalyst for proton exchange membrane fuel cells (PEMFCs). The structures of these materials were highly diversified, including core-shell, hybrid catalytic materials, and skinned-shell structures. We also discuss tolerance to acidic media and CO of catalysts supported by metal and mixed metal oxide nanocatalysts with mesoporous, hollow, or multilayered structures. Their representative catalytic applications in the fuel cell devices particularly in oxygen reduction reaction (ORR), hydrogen oxidation reactions (HOR), and methanol oxidation reaction (MOR) are discussed. We highlighted perspectives for their challenges ahead and opportunities for their use in low-temperature fuel cells and PEMFCs. Based on the structural characterization and performance of the devices, we further listed the ideal support material characteristics to enhance the stability and durability of these carbon-based and non-carbon-based support materials for Pt and non-Pt nanocatalysts used in low-temperature fuel cells.

## 5.1 Support Materials in Low-Temperature Fuel Cells

Fuel cells, especially low-temperature fuel cells, are promising to be the future energy device for vehicles and grid energy storage because of their high energy efficiency and low to zero emission [1]. The fuel cells can be classified into several classes by the fuel supplies (such as  $H_2$ ,  $CH_3OH$ ,  $CH_4$ , and  $C_2H_6$ ). Hydrogen has the highest specific energy density in all candidates when used as anode fuel. Proton exchange membrane fuel cells (PEMFCs), sometimes using pure hydrogen as anode fuel and working at a lower temperature than  $100\text{ }^\circ\text{C}$ , is a promising energy conversion device used in electric vehicles and other fields. And this fuel cell technology has also been shown to be competitive with conventional energy conversion devices such as lead-acid battery and Li-ion battery [2]. Although there are many advantages in this energy system, there are still several challenges that hinder the wide commercialization of low-temperature fuel cells, including the high expense of platinum usage in both cathode and anode catalyst and the poor durability.

Platinum (Pt) or Pt-based catalysts are used in both anode and cathode compartments. Different Pt or Pt-based materials are catalyzing the oxidation reaction of the fuels such as hydrogen, alcohol, aldehyde, and carboxylic acid in the anode compartment and catalyzing the oxygen reduction reaction (ORR) in the cathode compartment, respectively. Usually, the catalysts are in nanoscale dimension and need to



be dispersed in the support materials. The support materials can provide the large specific surface area to promote loading and dispersing the nanocatalyst. The supporting materials should also be electron conductors to transport the electron charge for the redox reactions.

Carbon materials, especially commercial Vulcan XC-72 carbon black, are the most commonly used support materials, which can be used to facilitate catalysis in both anode and cathode compartments in low-temperature fuel cell systems. Such materials have several advantages, including high electrical conductivity, high specific surface area, and low mass density. However, the corrosion and decomposition of carbon materials during prolonged operation will cause the catalysts to lose their activity and reduce the durability [3]. Development of novel support materials is essential to solve this problem and to advance commercialization of low-temperature fuel cells. A characteristic of robust fuel cells depends on the quality of support materials, which should also include uniform particle size distribution and excellent electrochemical stability. For example, the most currently used catalysts in the low-temperature fuel cells are platinum (Pt) and Pt alloy-based catalysts supported by the porous and conductive carbon-based materials with a high specific surface area of  $>100 \text{ m}^2 \text{ g}^{-1}$  [4]. The Pt nanoparticles with a uniform particle size were dispersed on the surface of the carbon homogeneously to provide enough three-phase interface to facilitate electrocatalysis. Although this carbon support has excellent electronic conductivity and outstanding specific surface area, the corrosion of carbon support materials caused by the electrochemical oxidation during the operation process (high potential: about 1.4 V vs reversible hydrogen electrode (RHE)) has been identified to be the major drawback of catalysts durability, which limits the large-scale commercialization of fuel cells [5]. In the cathode chamber, the high voltage and presence of oxygen promote the carbon material corrosion, while in the anode chamber with limited fuel supplies, carbon materials replace the fuel, resulting in corrosion.

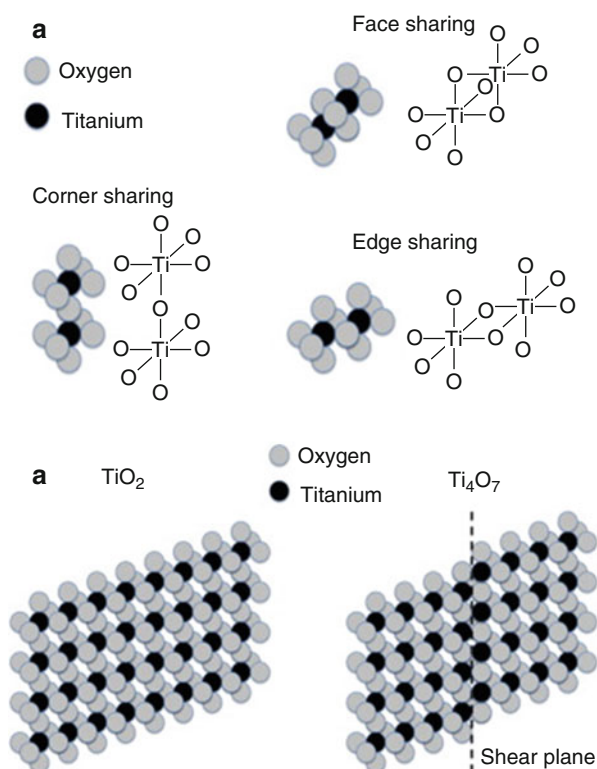
To address the corrosion of catalyst support, researchers have focused on the development of alternative support materials to replace the traditional carbon support materials used in a low-temperature fuel cell. To maintain the high catalytic activity of the noble metal catalyst, the support materials should meet several requirements during the operation of a low-temperature fuel cell. First, when the fuel cell operates at a high potential, support materials must be stable under this rigorous oxidation state to remain the electronic conductivity on its surface. Second, the non-carbon support materials should have a strong interaction at the interface between the catalysts and support to maintain the high dispersity of noble metal catalysts without agglomeration and detachment. And this interaction may change the electron structure at the interface, in which catalytic performance is degraded. With respect to the exploration of non-carbon support materials for noble metal catalysts, considerable work has been done in the past decades. In this chapter, we discuss the non-carbon support materials used in a low-temperature fuel cell. Lots of support materials have been developed including metal, metal oxide, metal carbide, metal nitride, metal boride, and conducting polymer. Firstly, we start with a metal oxide.

## 5.2 Metal Oxide-Based Support Materials

In recent years, oxygen-deficient titania ( $\text{Ti}_n\text{O}_{2n-1}$ , where  $n$  is between 4 and 10) has attracted wide attention as a promising electrode support material to facilitate electrocatalysis [6]. Figure 5.1 shows the different orientations of  $\text{TiO}_2$  octahedra (Fig. 5.1a) and the face-sharing shear plane (Fig. 5.1b) present in  $\text{Ti}_4\text{O}_7$ . This structure, known as Magnéli phase, is characterized by the presence of ordered planes of oxygen vacancies, also known as shear planes, and it has been shown that they can form conducting channels inside TiO-based memristor devices [7]. Among the  $\text{Ti}_n\text{O}_{2n-1}$  family, several oxides ( $\text{Ti}_4\text{O}_7$ ,  $\text{Ti}_5\text{O}_9$ ) exhibit high electronic conductivity at room temperature, which is similar to that of traditional carbon-based materials [8]. These conductive oxides displayed high electrical conductivity, chemical and electrochemical stability, and high tolerance to the corrosive media, such as salt solution, acid solution, and alkaline liquors [9]. The electronic conductivity of  $\text{Ti}_4\text{O}_7$  bulk is about  $2000 \text{ S cm}^{-1}$ , exhibiting the highest electrical conductivity and stability, which has been widely studied in electrocatalysis.

Phase-pure  $\text{Ti}_4\text{O}_7$  can be synthesized by several procedures, including pure  $\text{H}_2$  reduction and carbon thermal reaction. This  $\text{Ti}_4\text{O}_7$  powder was used as catalyst

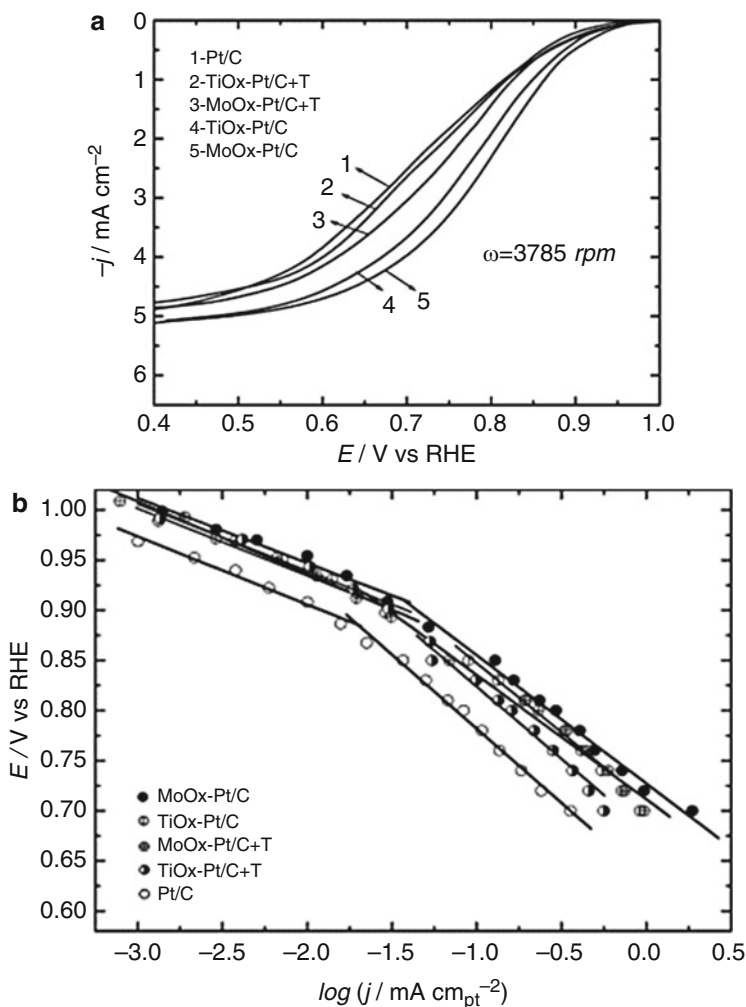
**Fig. 5.1** (a) The different orientations of  $\text{TiO}_2$  octahedra in Magnéli phase materials; edges and face- and corner-sharing of oxygen. (b) Edge-sharing  $\text{TiO}_2$  and  $\text{Ti}_4\text{O}_7$  octahedral sheets showing the face-sharing shear plane which is present in  $\text{Ti}_4\text{O}_7$  (The figure was adapted from [6] with permission of Elsevier)



support for several noble metals such as Pt [10] and iridium (Ir) [11]; and the obtained hybrid catalysts showed high electrocatalytic activity and durability. The  $\text{Ti}_4\text{O}_7$ -supported Pt hybrid nanocatalysts showed comparable specific activities for oxygen reduction reaction (ORR) as compared to a conventional porous carbon-supported Pt catalyst both under the three-electrode testing system and fuel cell operating conditions. Ioroi et al. firstly demonstrated the effect of high-potential conditions of activity and stability of Pt-deposited  $\text{Ti}_4\text{O}_7$  catalyst [12]. For a high-potential holding test, Pt- $\text{Ti}_4\text{O}_7$  catalyst showed greater stability than a conventional Pt/XC72 catalyst. The instability of Pt/XC72 catalyst is due to the corrosion of carbon support materials, while the  $\text{Ti}_4\text{O}_7$  support is more stable in this potential region.

The interaction between the precious metal and support materials can promote the catalytic activity and boost the durability of hybrid catalyst, which is called strong metal-support interaction (SMSI) [13]. Farndon et al. [14] discussed the surface interaction between the Pt particles and the as-supplied Ebonex support in Pt/ $\text{Ti}_4\text{O}_7$  hybrid catalysts. Slavcheva et al. [15] synthesized Pt and Pt-cobalt (Co) nanoparticles supported on Ebonex support by the borohydride reduction method. Because of the metal-support interaction, the Pt-Co-Ebonex catalyst was shown to facilitate the ORR, which started at a lower onset potential. For ORR, the Pt-Co-Ebonex catalyst gave a high reaction rate as compared with those catalyzed by Pt-Ebonex and pure Pt-Co catalysts. This result was suggested that the improved catalytic performance is attributed to the strong interface interaction between Pt nanoparticles and the Ebonex support as well as the d-band coupling mechanism, where the surface activity is given by the energy shift of the surfaced states with respect to the Fermi level. The stability of Pt-Ebonex was performed in different kinds of the electrolyte. Chen et al. investigated that the Pt-Ebonex catalyst has a stable performance in a basic electrolyte (1 M NaOH), while the electrochemical durability of Pt-Ebonex in acidic solution (0.5 M  $\text{H}_2\text{SO}_4$ ) under the conditions of oxygen is limited [16]. Yao et al. prepared fiber-like nanostructured  $\text{Ti}_4\text{O}_7$ , into which the Pt nanoparticles were deposited with a modified ethylene glycol reduction method. The prepared Pt/nanostructured (NS)- $\text{Ti}_4\text{O}_7$  catalysts exhibited superior durability as well as activity, in comparison to the commercial Pt/C catalyst in acidic solution (0.5 M  $\text{H}_2\text{SO}_4$ ). The XPS results indicated the strong metal-support interaction between Pt and NS- $\text{Ti}_4\text{O}_7$ , which is propitious to the improvement of the catalyst durability [17].

Besides  $\text{Ti}_4\text{O}_7$ , other Magnéli phase titanium oxides have been synthesized by other methods and used for electrochemical catalysis. Shen et al. synthesized Magnéli phase  $\text{Ti}_8\text{O}_{15}$  nanowires via a one-step evaporation-deposition synthesis method in a hydrogen atmosphere [18]. The electrical conductivity of a single as-fabricated  $\text{Ti}_8\text{O}_{15}$  nanowire is  $2060 \text{ S m}^{-1}$  at 300 K, which is much higher than carbon black ( $\sim 100 \text{ S m}^{-1}$ ) and graphite ( $\sim 1000 \text{ S m}^{-1}$ ) and similar to graphene ( $\sim 2000 \text{ S m}^{-1}$ ). Palladium (Pd) nanoparticles deposited on  $\text{Ti}_8\text{O}_{15}$  nanowires are synthesized through a pulsed electrodeposition method. The Pd/ $\text{Ti}_8\text{O}_{15}$  hybrid catalysts show a significantly enhanced activity for ethanol oxidation reaction (EOR) and excellent durability compared to the commercial Pt/C catalyst.

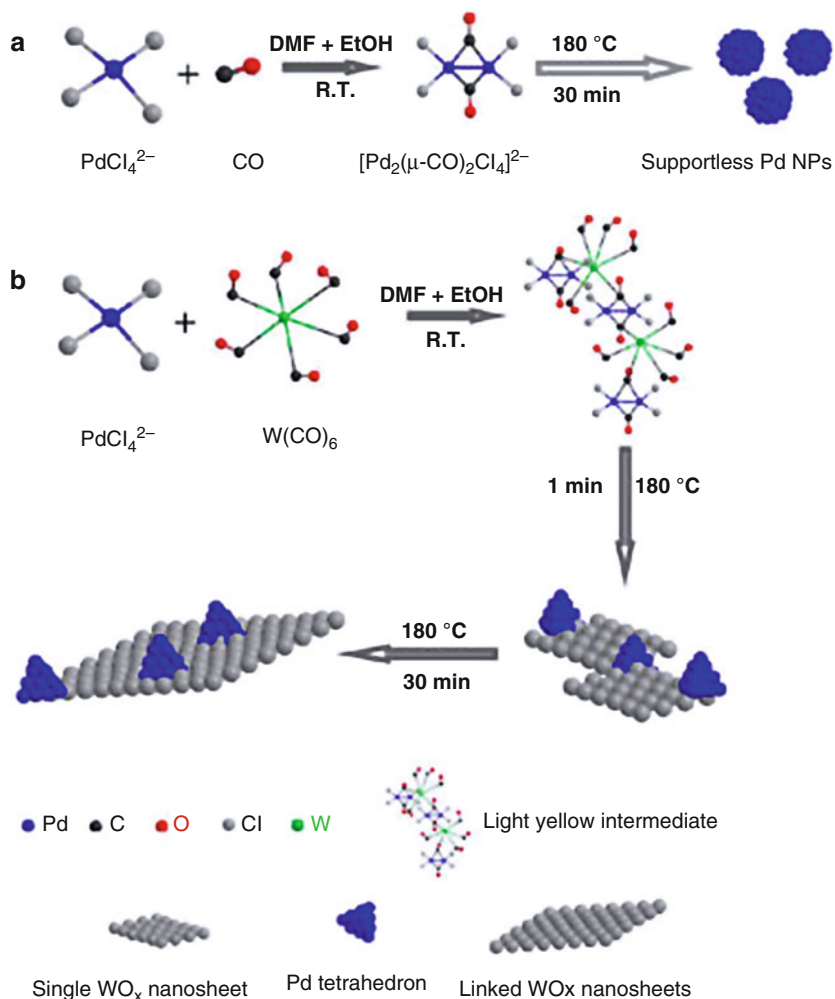


**Fig. 5.2** (a) Polarization curves obtained with rotating disk electrode for an O<sub>2</sub> reduction in a 0.5 mol dm<sup>-3</sup> HClO<sub>4</sub> electrolyte at Pt/C, TiO<sub>x</sub>-Pt/C, and MoO<sub>x</sub>-Pt/C electrodes, at 3785 rpm. (b) Tafel plots normalized to the electrochemically active surface area for an O<sub>2</sub> reduction in a 0.5 mol dm<sup>-3</sup> HClO<sub>4</sub> electrolyte at Pt/C, TiO<sub>x</sub>-Pt/C, and MoO<sub>x</sub>-Pt/C electrodes (The figure was adapted from [20] with permission of Elsevier)

Molybdenum (Mo) oxides, especially Magnéli phase molybdenum oxides, have attracted many researchers' interest for the applications in low-temperature fuel cells. There are four Magnéli phase molybdenum oxides, Mo<sub>4</sub>O<sub>11</sub>, Mo<sub>5</sub>O<sub>14</sub>, Mo<sub>8</sub>O<sub>23</sub>, and Mo<sub>9</sub>O<sub>26</sub>, between the composition of MoO<sub>2</sub> and MoO<sub>3</sub>. These oxides can coexist or form glass-like structures marked as MoO<sub>x</sub>. The formation of hydrogen molybdenum bronze on the surface of molybdenum oxides can form a strong metal-support interaction, which will enhance the ORR activity of noble metal

support on the supporting oxides. Chen et al. investigated the hydrogen molybdenum bronze formation and revealed hydrogen spillover on  $\text{MoO}_3$  with the presence of Pt [19]. Elezovic et al. synthesized  $\text{MoO}_x$ -Pt/C catalyst by the polyol method combined with  $\text{MoO}_x$  post-deposition for ORR and MOR [20]. Figure 5.2a, b depicted the ORR polarization curves at 3785 rpm and Tafel slopes of different samples, respectively. The ORR activity of  $\text{MoO}_x$ -Pt/C catalyst is much higher than that of commercial Pt/C, which was explained by the synergetic effects due to the formation of the interface between oxide supports and Pt nanoparticles. And the Tafel slope of  $\text{MoO}_x$ -Pt/C is similar to the value of Pt/C, which demonstrates its high catalytic activity. Mixed valence state of molybdenum oxide was investigated by Wang et al. [21]. They prepared Pt/ $\text{MoO}_x$  catalysts by electrodeposition method and proposed promotion mechanism of  $\text{MoO}_x$  for MOR, causing the removal of the adsorbed CO poisons at lower potentials. Ioroi et al. [22] prepared carbon-supported Pt/Mo oxide catalysts and the reformate tolerances of Pt/ $\text{MoO}_x$ /C, and conventional Pt-ruthenium (Ru)/carbon (C) anodes were examined to clarify the feature and differences between these catalysts. The Pt/ $\text{MoO}_x$  showed better CO tolerance than PtRu in the presence of CO (80 ppm)/ $\text{H}_2$  mixture, especially at higher fuel utilization conditions, which is mainly due to the higher catalytic activity of Pt/ $\text{MoO}_x$  catalyst for the water-gas shift reaction and electrooxidation of carbon monoxide (CO). In contrast, the carbon dioxide ( $\text{CO}_2$ ) tolerance of Pt/ $\text{MoO}_x$ /C was much worse than that of PtRu/C. Some researchers found that crystallized  $\text{Mo}_4\text{O}_{11}$  have two phases ( $\gamma$ - $\text{Mo}_4\text{O}_{11}$  and  $\eta$ - $\text{Mo}_4\text{O}_{11}$ ), with good electrical conductivity, which have been proved theoretically and experimentally [23–25]. Yang et al. [26] reported  $\text{Mo}_4\text{O}_{11}$  with a trace amount of  $\text{MoO}_2$  mixed with Pt black. This composited catalyst plays the anti-poisoning role of the intermediate product  $-\text{CH}_x\text{O}$ , but the durability remains to be improved.

Tungsten-based materials can also be used as support materials in a low-temperature fuel cell. The defected tungsten oxide ( $\text{WO}_x$ ) is an n-type semiconductor with a bandgap between 2.6 and 2.8 eV which could be applied in a low-temperature fuel cell. Xu et al. investigated the improvement of sulfur tolerance of noble metal catalyst by tungsten oxide-induced effects [27].  $\text{WO}_x$  is adopted for the first time to modify such noble metal catalysts to acquire an excellent sulfur tolerance, due to its unique nature with hydrophilicity, redox couple in lower valence, as well as proton spillover effect. The Pt/ $\text{WO}_x$ -C catalysts with different  $\text{WO}_x$  contents were synthesized and tested by cycling voltammetry (CV) and rotating ring-disk electrode (RRDE) methods. The higher catalytic activity of Pt/ $\text{WO}_x$ -C hybrid catalyst toward ORR is studied in comparison with commercial Pt/C after both were poisoned by  $\text{SO}_x$  where the electron transfer number of the Pt/ $\text{WO}_x$ -C is near four, whereas the Pt/C is not equal to four. The electronic interaction between Pt and  $\text{WO}_x$  is evidently confirmed by X-ray photoelectron spectroscopy (XPS) analysis, and the results strongly indicated that complete electron transfer is the crucial factor for the ORR improvement. Li et al. studied Magnéli phase tungsten oxide  $\text{W}_{18}\text{O}_{49}$  as a support for Pt catalyst [28]. The XPS results showed a strong metal-support interaction between Pt and  $\text{W}_{18}\text{O}_{49}$ , in which the valence state of W in  $\text{W}_{18}\text{O}_{49}$  was found to be +5 and +6, respectively. This mixed valence state may promote the hydrogen spillover and oxygen buffering effects. When tested in a



**Fig. 5.3** The synthesis mechanism of Pd/ $\text{W}_{18}\text{O}_{49}$  hybrid nanomaterials by  $\text{W}(\text{CO})_6$  precursor (The figure was adapted from [29] with permission of the American Chemical Society)

half-cell system, the Pt/ $\text{W}_{18}\text{O}_{49}$  catalyst exhibited the greater MOR activity and higher stability than commercial Pt/C and Pt black.

Lu et al. also developed a robust method for the synthesis of strongly coupled Pd/ $\text{W}_{18}\text{O}_{49}$  catalyst and demonstrated its high activity for ORR and excellent stability [29]. Tetrahedron-like Pd nanocrystal supported on  $\text{W}_{18}\text{O}_{49}$  nanosheets were fabricated using a unique  $[\text{Pd}_2(\mu\text{-CO})_2\text{Cl}_4]^{2-}$ - $\text{W}(\text{CO})_6$  structure. Figure 5.3 showed the synthesis mechanism of Pd/ $\text{W}_{18}\text{O}_{49}$  hybrid nanomaterials (Fig. 5.3a). Although the non-supported Pd nanoparticles or pristine  $\text{W}_{18}\text{O}_{49}$  has low ORR activity, the hybrid displayed a superior activity to commercial Pt/C. The stability

of this hybrid catalyst is greater than that of the commercial Pd/C and Pt/C catalysts, which is attributed to the synergistic interaction between Pd nanocrystal and  $W_{18}O_{49}$  nanosheets (Fig. 5.3b).

Ruthenium oxide ( $RuO_2$ ) has also been explored as a catalyst support [30]. The Pt/ $RuO_2$  catalyst shows the bifunctional mechanism in MOR, in which the presence of Ru-OH bonds on the  $RuO_2$  surface plays a beneficial role in catalytic activity enhancement for this MOR. It is known that Ru-OH<sub>ad</sub> can facilitate Pt-CO<sub>ad</sub> oxidation at a lower potential by providing adsorbed OH<sub>ad</sub> groups adjacent to active Pt atoms. To further exploit the beneficial property of the Pt/ $RuO_2$  catalyst, Chen et al. [31] synthesized Pt/ $RuO_2$ -H<sub>2</sub>O catalyst by a solution-based method to achieve the superior performance. This catalyst showed higher catalytic activity toward MOR than that of Pt-Ru black catalyst. Conducting metal oxides are considered to be good candidates for catalyst support. However, the chemical stability and electronic conductivity of the nonstoichiometric oxides should be increased for a long-term operation. Doping of heteroatoms into the matrix of metal oxide may provide an efficient way to increase both electrocatalytic performance and stability.

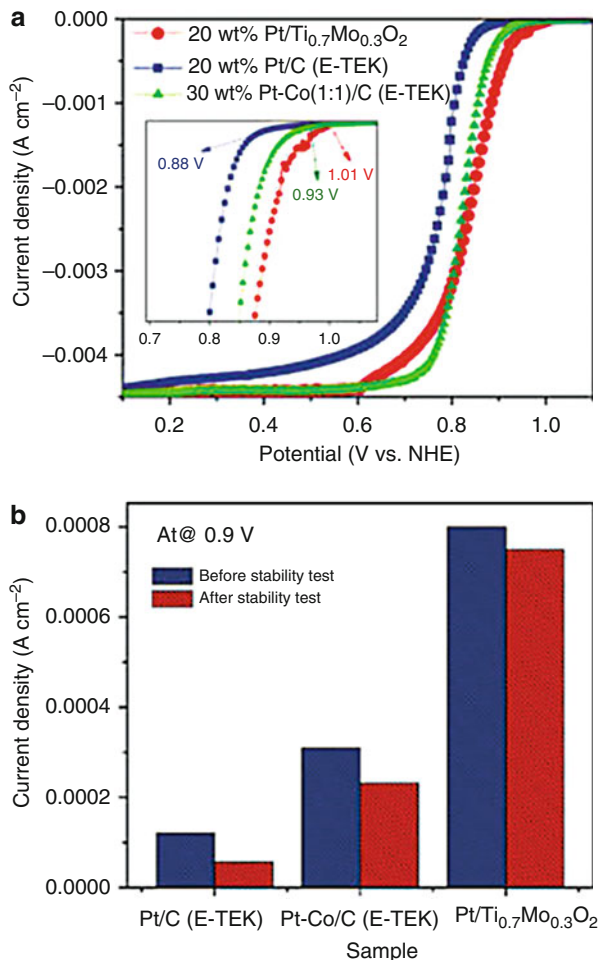
### 5.3 Metal-Doped Oxide-Based Support Materials

The use of metal oxide as support materials in a fuel cell is a promising approach due to their stability. However, the electrical conductivity of most of these materials remains to be further developed. Doping is one of the efficient methods to increase the electrical conductivity of metal oxide, and numerous elements were selected for doping. Park and Seol prepared niobium (Nb)-doped  $TiO_2$  material using hydrothermal synthesis and produced Pt-based catalyst using this support material for the ORR [32]. The as-synthesized Nb-doped titania ( $TiO_2$ ) support has an average particle size of 10 nm, and the size of Pt particle supported on the surface of Nb-doped  $TiO_2$  was 3 nm. The Pt/Nb- $TiO_2$  catalyst showed an outstanding ORR performance and stability because of the strong metal-support interactions (SMSI) between Pt and Nb-doped  $TiO_2$  support materials. Hass et al. [33] fabricated Ru-doped  $TiO_2$  support materials by using a sol-gel routine. They found that the conductivity of the support could be increased with the increasing of ruthenium mole fraction. The Ru-doped  $TiO_2$  support has an average particle size of 200 nm, and the Pt particles were deposited on this support using a chemical deposition process. The Pt/Ru- $TiO_2$  hybrid catalyst has a comparative ORR activity to commercial Pt/C in 0.5 M phosphoric acid electrolyte. Wang et al. [34] successfully synthesized  $Ru_{0.1}Ti_{0.9}O_2$  nanopowder by using TiN nanoparticles and  $RuCl_3$  as precursors by the impregnation-thermal decomposition method, and then the Pt nanoparticles were deposited on the surface of this support material to form Pt/ $Ru_{0.1}Ti_{0.9}O_2$  hybrid catalysts. Fuel cell tests using this material in the cathode catalyst layer showed fairly high catalyst performance and stability.

Hwang et al. presented a new approach by exploring  $Ti_{0.7}Mo_{0.3}O_2$  used as functionalized catalytic support for Pt nanoparticles [35]. The  $Ti_{0.7}Mo_{0.3}O_2$  support was synthesized by a single-step hydrothermal method without any surfactant or



**Fig. 5.4** (a) Polarization curves showing the ORR current of Pt/Ti<sub>0.7</sub>Mo<sub>0.3</sub>O<sub>2</sub> catalyst and two kinds of commercial Pt/C (E-TEK) and Pt-Co/C (E-TEK) catalysts. (b) Stability characterization of Pt/Ti<sub>0.7</sub>Mo<sub>0.3</sub>O<sub>2</sub> and commercial Pt/C (E-TEK) and Pt-Co/C (E-TEK) catalysts at 0.9 V before and after stability by 5000 potential cycles (The figure was taken from [35]; reproduced with permission of the American Chemical Society)



stabilizer. Figure 5.4a, b showed polarization curves and stability of Pt/Ti<sub>0.7</sub>Mo<sub>0.3</sub>O<sub>2</sub> and commercial Pt/C (E-TEK) and Pt-Co/C (E-TEK) catalysts, respectively. They found the ORR current density generated using catalytic Pt/Ti<sub>0.7</sub>Mo<sub>0.3</sub>O<sub>2</sub> is ~7 mA cm<sup>-2</sup> and about 2.6-fold higher than those of commercial Pt/C and Pt-Co/C catalysts [36] when calculated with the same Pt loading (Fig. 5.4a). The high catalytic performance is based on the novel nanostructure Ti<sub>0.7</sub>Mo<sub>0.3</sub>O<sub>2</sub> support with “electronic transfer mechanism” from Ti<sub>0.7</sub>Mo<sub>0.3</sub>O<sub>2</sub> support to Pt that can modify the surface electronic structure of surface Pt, attributing to a shift in the d-band center of the surface Pt atoms. Because of the strong metal-support interaction, the stability of Pt/Ti<sub>0.7</sub>Mo<sub>0.3</sub>O<sub>2</sub> is higher than those of Pt/C and Pt-Co/C catalysts in both acidic and oxidation environments. These results showed that Ti<sub>0.7</sub>Mo<sub>0.3</sub>O<sub>2</sub> is a promising candidate as non-carbon catalyst support material for a low-temperature fuel cell with outstanding performance and excellent stability (Fig. 5.4b). Kim et al. [37] also

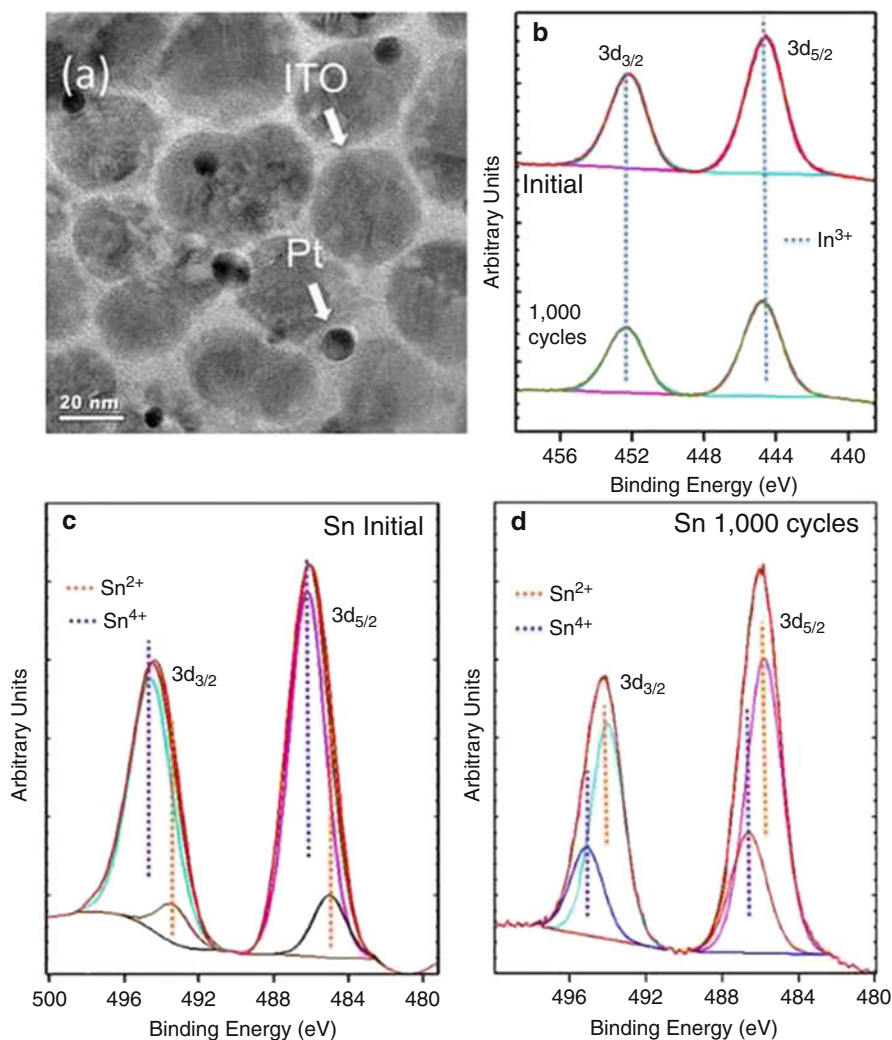


studied different doping elements into  $\text{TiO}_2$  and their ORR performances. Transition metals such as V, Cr, and Nb as a different dopant are introduced into  $\text{TiO}_2$  matrix, and they found that the vanadium-doped  $\text{TiO}_2$  has a comparable strain at the Pt surface by extended X-ray absorption fine structure (EXAFS) analysis. It was confirmed that the shorter Pt interatomic bond length is correlated with the better ORR specific activity. In addition, Pt/V- $\text{TiO}_2$  gave the best durability due to the anchoring effect of Pt nanoparticles which is derived from the strong metal-support interaction.

Besides  $\text{TiO}_2$ , tin oxide ( $\text{SnO}_2$ ) has also been explored as a support for electrocatalysts. Although  $\text{SnO}_2$  itself is a poor electrical conductor, doping  $\text{SnO}_2$  using some metal such as Sb and Ru can significantly increase the electronic conductivity, making it possible to use as a catalyst support. The conductivity of Ru-doped  $\text{SnO}_2$  support material has a conductivity of around  $2.5 \times 10^{-3} \text{ S cm}^{-1}$  [38]. Besides the large surface area of such a supported catalyst, the doping metals such as Sb also have beneficial effects such as adsorption of OH species and electronic effects for improving the electrooxidation of small alcohols. These all facilitate the electrocatalytic performance of the doped  $\text{SnO}_2$ .

Santos et al. [39] found that the Sb-doped  $\text{SnO}_2$  (ATO) films were effective for the dispersion of Pt nanoparticles. Lee et al. also deposited colloidal Pt particles on ATO particles with various Pt loadings [40]. The powdered X-ray diffraction patterns for these Pt/ATO catalysts showed typical polycrystalline patterns, indicating that the Sb ions partially replaced Sn ions in the cassiterite  $\text{SnO}_2$  polycrystal structure without the formation of any other phases of Sb compounds. These catalysts were tested for both methanol and ethanol electrooxidation, and the results showed that their catalytic activities were enhanced when compared to the value of a commercial Pt/C catalyst. In addition, the electrochemical stability of Pt/ATO is higher than the commercial Pt/C, which is tested under the fuel cell condition. Besides Sb elements, Ru was also used as a doping metal for  $\text{SnO}_2$  to form support materials. Pang et al. prepared some Ru-doped  $\text{SnO}_2$  support materials by chemical precipitation and followed by calcination at 823 K [41]. The Ru-doped  $\text{SnO}_2$  nanoparticles were found to have high stability in an acidic electrolyte. The Pt/Ru- $\text{SnO}_2$  catalysts showed higher electrochemical activity and stability than Pt/ $\text{SnO}_2$  catalysts.

Sn-doped indium oxide (ITO) nanoparticles were conceived as a high stability non-carbon support for Pt nanoparticles by Liu et al., and the activity and stability of Pt/ITO catalyst for the ORR were investigated and shown in Fig. 5.5 [42]. The TEM image exhibited Pt nanoparticles supported on the surface of ITO particles (Fig. 5.5a). Sn was employed as the dopant in the  $\text{In}_2\text{O}_3$  oxide to exploit the strong interaction between Sn and Pt that was previously used to enhance the activity of Pt on Pt/ITO. The mass activity of Pt was extremely high on the Pt/ITO hybrid, and the enhanced ORR performance of Pt/ITO was attributed to the strong metal-support interaction between Pt and ITO supports, which can be confirmed by XPS results (Fig. 5.5b). The ITO support materials provide enough electronic conductivity which ensures the electron transfer during the reaction and also changes the surface electron structure of Pt (Fig. 5.5c). The stability of the hybrid catalyst after 1000 cycles is



**Fig. 5.5** (a) TEM image of Pt/ITO electrocatalyst after 1000 cycles. XPS spectra of (b) In 3d and Sn 3d of Pt/ITO (c) before and (d) after 1000 cycles (The figure was taken from [42]; reproduced with permission of the American Chemical Society)

much higher than the commercial Pt/C catalyst, while the minor degradation is assumed to be the surface dissolution of Sn pieces (Fig. 5.5d).

Sulfated zirconium oxides (S-ZrO<sub>2</sub>) have also been explored as catalyst supports for many chemical reactions. The ZrO<sub>2</sub> itself with low electronic conductivity cannot be used as support materials in fuel cell directly. However, after modification by sulfonation, S-ZrO<sub>2</sub> was formed which has a high electrical conductivity used in many reactions. Hara and Miyayama employed different synthesis methods for

S-ZrO<sub>2</sub> samples [43]. They found that the surface of a S-ZrO<sub>2</sub> with heat treatment showed the strong bonding between SO<sub>x</sub> species and Zr atoms. When used in the fuel cells, Pt supported on S-ZrO<sub>2</sub> catalyst displayed a high electrocatalytic performance. Suzuki et al. synthesized sulfated zirconia-supported Pt (Pt/S-ZrO<sub>2</sub>) using ultrasonic spray pyrolysis (USP) [44]. They found that the Pt was evenly dispersed on the surface of S-ZrO<sub>2</sub> supports as nanoparticles with a diameter of about 8 nm. The performance of fuel cell using S-ZrO<sub>2</sub> as support materials is higher than using commercial Pt/C if both of the catalyst layers were not impregnated with Nafion ionomer. This indicated that the Pt/S-ZrO<sub>2</sub> could reduce the usage of Nafion ionomer in the catalyst layer. The USP is one of the one-step synthesis methods to directly prepare materials like metal oxide-supported metal electrocatalyst with high surface area support. Recently, USP has been also demonstrated as a facile method to prepare meso- and macroporous support materials. The summary of doped metal oxides is listed in Table 5.1.

Besides metal oxide, other metal compounds such as metal carbide, metal nitride, and metal boride can also be used as catalyst supporting materials in fuel cell and show excellent performance.

---

## 5.4 Carbide-Based Support Materials

Carbides are compounds composed of carbon and a less electronegative element. According to the chemical bonding types, all carbides exhibit some level of covalent character. Four types of carbides were classified as (1) saltlike, (2) covalent compounds, (3) interstitial compounds, and (4) intermediate transition metal carbides. Commonly intermediate transition metal carbides have the highest stability in both acidic and basic electrolyte with a good electrical conductivity, which makes them promising candidate as support materials for noble metal catalysts.

Titanium carbide (TiC) was investigated as a useful support material in electrochemical catalysis and fuel cell applications. TiC has an excellent stability toward electrochemical oxidation, although TiC as support materials is still limited. Jalan et al. [45] showed that TiC with a relatively large surface area of 25–125 m<sup>2</sup> g<sup>-1</sup> could be synthesized by placing titanium tetrachloride (TiCl<sub>4</sub>) in a gas flow stream containing unsaturated hydrocarbon and hydrogen in the temperature range of 500–1250 °C. In this synthesizing process, TiC was formed with a desirable chain-like morphology, which has an open porous structure. This open porous structure cannot only maintain high electrical conductivity but also provide diffusion paths for oxygen and electrolyte during the catalytic reaction.

Besides TiC, tungsten carbide (WC) was suggested to be an ideal support material due to its unique chemical and physical properties. Weigert et al. studied electrochemical behaviors of WC and Pt-modified WC as electrochemical catalysts in a direct methanol fuel cell (DMFC) [46]. Evidence of improved anode kinetics was observed by increasing the fuel concentration and operating temperature. It was evident that the most limiting factor of this catalyst used in DMFC is the low surface area of the anode catalyst. Wang et al. [47] prepared tungsten carbide microsphere

**Table 5.1** Comparison of differently doped metal oxides as support

Samples	Matrix	Doping formula	Catalysis reaction	Performance	Proposed mechanism	Ref.
1	TiO <sub>2</sub>	Nb-TiO <sub>2</sub>	ORR	Excellent activity and durability	The interaction between oxide support and a metal catalyst	[32]
2	TiO <sub>2</sub>	Ru <sub>0.1</sub> Ti <sub>0.9</sub> O <sub>2</sub>	ORR	The catalysts had an active platinum surface area comparable to commercial catalysts on a carbon support	Ruthenium mole fraction increased the electronic conductivity and improve performances	[33, 34]
3	TiO <sub>2</sub>	Ti <sub>0.7</sub> Mo <sub>0.3</sub> O <sub>2</sub>	ORR	ORR current density is ~7 and 2.6-fold higher than Pt/C and Pt-Co/C with same Pt loading	SMSI between Pt particles and Ti <sub>0.7</sub> Mo <sub>0.3</sub> O <sub>2</sub> support	[35]
4	TiO <sub>2</sub>	V(Cr/Nb)-TiO <sub>2</sub>	ORR	Pt/V-TiO <sub>2</sub> exhibits excellent durability	More compressive strain in Pt/M-TiO <sub>2</sub> than Pt/TiO <sub>2</sub> and Pt/C and the shorter Pt interatomic bond	[37]
5	SnO <sub>2</sub>	Sb-SnO <sub>2</sub>	MOR EOR	Larger intrinsic electrocatalytic activity	Higher roughness factors than platinumized Pt electrodes	[39, 40]
6	In <sub>2</sub> O <sub>3</sub>	Sn-In <sub>2</sub> O <sub>3</sub>	ORR	The mass activity of Pt was high as 621 ± 31 mA/mg <sub>Pt</sub> and the stability of Pt/ITO was also very impressive	The strong interaction between Pt and ITO limits the surface Sn dissolution to those parts of ITO without Pt support	[42]
7	ZrO <sub>2</sub>	S-ZrO <sub>2</sub>	ORR	No large IR loss in single cell performance up to 2.5 Acm <sup>-2</sup>	S-ZrO <sub>2</sub> support act as a proton conductor in the catalyst layer	[43, 44]

with high surface area ( $256 \text{ m}^2 \text{ g}^{-1}$ ) by hydrothermal synthesis. They found that the ORR performance including onset potential and mass activity of Pt-WC microsphere is higher than that of Pt supported on the carbon microsphere. This catalytic improvement was attributed to the higher electrochemical surface area (ESA), as well as to the synergistic strong metal-support interaction between the Pt and WC support materials. Hara et al. fabricated WC-based support by carburizing of tungsten nitrides ( $\text{W}_2\text{N}$ ) and tungsten sulfides ( $\text{WS}_2$ ) as precursors from different starting materials [48]. The results indicated that WC, which was obtained from  $\text{W}(\text{CO})_6/\text{S}$  and  $(\text{NH}_4)_2\text{WS}_4$ , gives a much higher specific surface area than others. And the mass activity of Pt/WC was superior to the commercial Pt/C catalyst. Electrochemical testing was performed by applying oxidation cycles between +0.6 V and +1.8 V to the support catalyst material combinations and monitoring the activity of the supported catalyst over 100 oxidation cycles. The electrocatalytic activity of Pt/C decreased quickly, while the Pt/WC catalyst maintains its catalytic activity after 100 accelerated oxidation cycles.

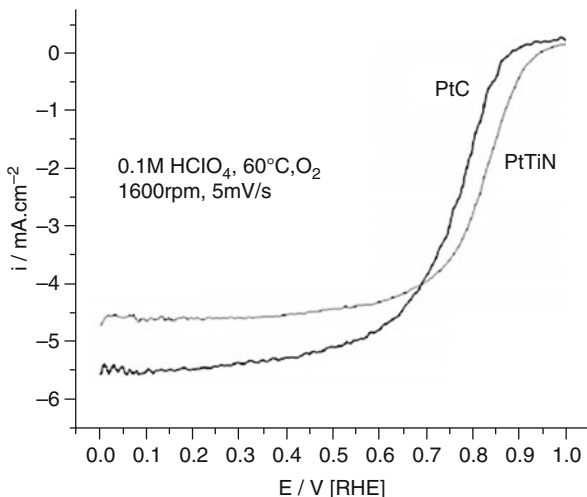
Silica carbide is also used as a conductive support for ORR in PEMFC and exhibits good catalytic performance. Lobato et al. deposited nanoscale Pt on the SiC supports [49]. For the first time, the SiC-based supports were applied for about 100 h at  $160^\circ\text{C}$  and compared with commercial Pt/C. Their results showed the SiC(TiC)-Pt hybrid catalysts exhibited a high catalytic durability in half-cell experiments and a low degradation rate of the electrochemical surface area. Dhiman et al. had synthesized SiC particles with two different sizes (50–150 nm and 25–35 nm) supported Pt nanoparticles [50]. The SiC supports are subjected to an acid treatment to introduce surface groups, which help to anchor the Pt nanoparticles. The SiC-based catalysts have been found to have a higher electrochemical activity than commercially available Vulcan-based catalysts. These promising results signal a new era of SiC-based catalyst supports for future fuel cell applications.

---

## 5.5 Nitride-Based Support Materials

Titanium nitride (TiN) was reported as catalyst support in terms of fuel cell applications because of its high electrical conductivity and outstanding oxidation and corrosion resistances. Avasarala et al. synthesized a Pt/TiN hybrid electrocatalyst with Pt nanoparticles supported on commercial TiN nanoparticles with an average particle size of 20 nm and a specific surface area of  $40\text{--}55 \text{ m}^2 \text{ g}^{-1}$  and performed electrochemical tests to evaluate its electrochemical surface area and mass and specific activities under the PEM fuel cell testing conditions [51]. Figure 5.6 showed ORR polarization curves of Pt/TiN and Pt/C. The ORR activity of Pt/TiN was higher than commercial Pt/C in 0.1 M  $\text{HClO}_4$  electrolyte because of the more positive half-wave potential of Pt/TiN. The improved activity and ECSA of Pt/TiN in the electrochemical half-cell may be attributed to the superior dispersion of Pt nanoparticles on the TiN nanoparticle supports. The XPS analysis revealed the presence

**Fig. 5.6** Oxygen reduction current densities on 20 wt% Pt/TiN and BASF 20 wt% Pt/C with a Pt loading of  $20 \mu\text{g}_{\text{Pt}}\cdot\text{cm}^{-2}$  on a glassy carbon electrode at 1600 rpm (The figure was taken from [51]; reproduced with permission of the Royal Society of Chemistry)



of an oxygen-rich layer on the surface of non-platinized and platinized TiN particles. The high surface oxygen content is due to a thin oxide/oxy-nitride layer on the TiN surface because of its oxidation from exposure to oxygen or moisture. This oxide layer has a positive effect to protect the deeper TiN supports away from the oxidation and did not indicate a poor conductivity due to the ultra-thin layer (a few nanometer) of this oxide (of a few nanometer thickness).

Besides TiN, boron nitride (BN) is another potential candidate as support material for catalysts. The lattice structure of BN is similar to the graphite with a hexagonal structure. And the stability, chemical inertness, and conductivity with respect to less dissolution and chemical reactivity are promising for applications under harsh conditions. Perdigon-Melon et al. [52] prepared porous BN samples using sol-gel deposition method to increase the specific surface area of BN powder. The porous structure of the obtained BN supported highly dispersed Pt nanoparticles on its surface for providing enough three-phase interface. Although current results are limited, preliminary data suggests that the BN particles have potential as support materials to enhance the performance of electrocatalysis.

## 5.6 Boride-Based Support Materials

Titanium diboride ( $\text{TiB}_2$ ) is an electrically conducting ceramic with good electrical conductivity, excellent thermal stability, and corrosion resistance in acid medium, which makes it a promising support material in a low-temperature fuel cell. Yin et al. [53] demonstrated that  $\text{TiB}_2$  is a novel catalyst support material with excellent electrical conductivity and electrochemical stability. The as-synthesized  $\text{Pt/TiB}_2$  was obtained by a colloidal route, and highly dispersed Pt nanoparticles on the

surface of  $\text{TiB}_2$  support materials were generated. The electrochemical performances of  $\text{Pt/TiB}_2$  were investigated by the rotating disk electrode (RDE) technique in a 0.5 M  $\text{H}_2\text{SO}_4$  electrolyte. It was found that the  $\text{Pt/TiB}_2$  catalyst has similar ORR catalytic activity to the commercial  $\text{Pt/C}$ . The stability of  $\text{Pt/TiB}_2$  is approximately four times higher than that of the  $\text{Pt/C}$ , endowing this catalyst with an excellent stability resulting from the  $\text{TiB}_2$  supports and also possibly from polymer stabilization effects. The use of  $\text{TiB}_2$  powders with large particle size as support materials will reduce the utilization efficiency of Pt catalyst. The results showed that greater improvements in the use of  $\text{Pt/TiB}_2$  hybrid catalysts can be achieved.

---

## 5.7 Mesoporous Silica-Based Support Materials

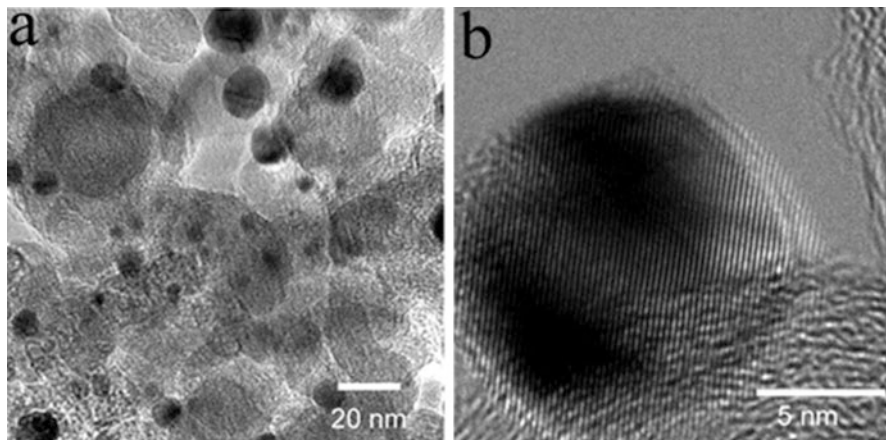
Mesoporous silica with a high surface area and uniform pore structure has attracted attention as a fuel cell support material. Although the conductivity of pristine support materials is low, the noble metal catalysts supported on the surface of this mesoporous silica will improve its electronic conductivity. Dalai et al. synthesized mesoporous Santa Barbara Amorphous-15 (SBA-15) and deposited Pd-Zn alloy on its surface [54]. The Pd-Zn alloy formation was favored when the catalyst was reduced above 400 °C, but yielded a lower chemisorption capacity; hence the total metallic Pd surface area was reduced.

---

## 5.8 Metal-Based Support Materials

Metals can also be used as support materials in a low-temperature fuel cell. In some synthesis processes, the attachment of metal supports and catalysts may produce some degree of alloying, which generates a positive effect for catalysis. Sasaki et al. [55] prepared an Au-supported Pt electrocatalyst, in which a Pt submonolayer was deposited on Au nanoparticles with the exposition of special Au (111) crystal face. Zhang et al. also synthesized some similar catalysts, in which Pt submonolayer was deposited on Pd (111) face [56]. Figure 5.7a, b showed the Pt submonolayer was deposited on the Pd (111) lattice planes. The results also showed a significant improvement of ORR catalytic performance of this Pt-Pd (111) catalysts over commercial  $\text{Pt/C}$ . Stamenkovic et al. [57] thought that the ORR performance was dependent on the arrangement of Pt on the surface of support materials. And a Pt-skin surface may strongly enhance the catalytic activity. Another Pt surface, called Pt-skeleton surface, can be formed by Pt-transition metal (TM) alloy in an acidic environment, in which TM atoms on the surface could be dissolved and remain a Pt-containing outermost layer [58]. Due to the metal elements usually existing as the alloy components in the catalyst, and core-shell structure design of the catalyst is the common synthesis approach. It was hypothesized that these metal-support catalysts should belong to the bimetal or tri-metal core-shell catalyst





**Fig. 5.7** (a) Low magnification and high magnification overview of Pd supported on the carbon surface. The one-dimensional lattice fringes correspond to (111) lattice planes in Pd (The figure was taken from [56]; reproduced with permission of the American Chemical Society)

family. Therefore, a very brief introduction of the delegations of these metal supports is provided.

## 5.9 Conducting Polymer-Based Support Materials

The electronic conducting polymer is a family of polymer which has high electronic conductivity and chemical stability. The electronic conducting polymer with their unique electrochemical and mechanical properties is a promising support material in a low-temperature fuel cell. Some polymer such as polyaniline (PANI) and polypyrrole (PPy) have been used as conducting support materials for catalysts in a low-temperature fuel cell. The conductivity levels of PANI can be as high as  $100 \text{ S}\cdot\text{cm}^{-1}$ , and the chemical stability of PANI in aqueous solution is also very high. Laborde et al. [59] prepared Pt-modified polyaniline electrode. They found the electrocatalytic activity of MOR of Pt-PANI hybrid catalyst is higher than the bulk platinum electrode. Nanostructured Pt/PANI catalyst was also obtained by Rajesh et al. [60]. They found that nanotube-like PANI as support materials increase the catalytic activity and stability of Pt. Polypyrrole is a mechanically and chemically stable conducting polymer and is easy to be prepared. The electronic conductivity of PPy is about  $500 \text{ S cm}^{-1}$  which is enough for electron transfer to occur during electrocatalysis. Zhao et al. [61] prepared a PPy-XC72 composite support by in situ chemical polymerization of pyrrole on XC-72, followed by the chemical deposition of Pt particles on its surface. The obtained catalyst revealed a higher MOR catalytic performance and better CO tolerance than commercial Pt/C catalyst. Some PPy-containing bimetallic catalysts, such as Pt-Ru/PPy-C, [62] Pt-Fe/PPy-C [63], and Pt-Co/PPy-C [64], have also been investigated to exhibit high electrocatalytic



performance. To enhance the conductivity of the support materials, sometimes the carbon nanotubes were applied simultaneously with the conductive polymer. But the electronic conducting polymer provides a possibility to produce the soft electrode, which is the key technique to produce a collapsible and wearable PEMFC, as a portable electrical source for devices.

---

## 5.10 Conclusion

In summary, carbon-based supporting materials for Pt-based catalysts have many problems such as carbon oxidation or corrosion during the process of fuel cell operation. To address these issues of carbon oxidation, the non-carbon supporting materials are a promising candidate for low-temperature fuel cell catalysts. These non-carbon supporting materials include Magnéli phase oxide, metal ion-doped oxide, metal carbides, metal nitrides, and metal borides. In comparison with carbon-based supporting materials, some significant drawbacks still exist for non-carbon supporting materials.

First, the specific surface area and pore volume are much smaller than porous carbon materials. Second, the electronic conductivity of non-carbon supporting materials is still lower than carbon support. Last, some oxide supporting materials have higher solubility in electrolyte than carbon-based support materials, which will lead to a failure in fuel cell operation. Therefore, to produce an ideal non-carbon supporting material, the following requirements should be met:

- (a) Stability. The stability of supporting materials including low solubility in the electrolyte and high resistance to oxidation.
- (b) Electronic conductivity. The high electronic conductivity is a basic requirement for a supporting material.
- (c) Surface area. For better-supporting catalysts, non-carbon supporting materials should have a high specific surface area to achieve more active sites.
- (d) The strong interaction between catalysts and supporting materials. The interaction between supporting materials and catalysts makes the catalysts stable on the surface of the supporting materials.
- (e) Low price and ease of the fabrication. The synthesis process of ideal non-carbon supporting materials should be feasible. The large application of the non-carbon supporting materials requires low cost, which needs a low-cost source to synthesize support materials.

Although much of progress has been made to improve the activity and durability of the low-temperature fuel cell, it is clear that more research and attentions should be put on the development of non-carbon support materials. The conclusion of all the support materials mentioned above is shown in Table 5.2.

**Table 5.2** The sum of varied support materials and their application in fuel cells

Samples	Formula	Classification	Reaction of catalysis	Performance	Combined with (without) carbon	Reference
1	Ti <sub>4</sub> O <sub>7</sub>	Defected oxide	ORR	Better catalytic performance and excellent durability	Single support	[10–12]
2	MoO <sub>x</sub>	Defected oxide	MOR	ORR mechanism on MoO <sub>x</sub> -Pt/C was direct four-electron process	Combined with carbon	[20, 22]
3	W <sub>18</sub> O <sub>49</sub>	Defected oxide	ORR	Pd/W <sub>18</sub> O <sub>49</sub> hybrid exhibited not only surprisingly high ORR activity but also excellent stability	Combined with carbon/single support	[27–29]
4	RuO <sub>2</sub>	Oxide	MOR	High reactivity and durability	Single support	[30, 31]
5	Nb-TiO <sub>2</sub>	Doped oxide	ORR	Excellent activity and durability	Single support	[32]
6	Ru <sub>0.1</sub> Ti <sub>0.9</sub> O <sub>2</sub>	Doped oxide	ORR	The catalysts had an active platinum surface area comparable to commercial catalysts on a carbon support	Single support	[33, 34]
7	Ti <sub>0.7</sub> Mo <sub>0.3</sub> O <sub>2</sub>	Doped oxide	ORR	ORR current density is ~7 mA cm <sup>-2</sup> and 2.6-fold higher than Pt/C and Pt-Co/C with same Pt loading	Single support	[35]
8	V-TiO <sub>2</sub>	Doped oxide	ORR	Pt/V-TiO <sub>2</sub> exhibits excellent durability	Single support	[37]
9	Sb-SnO <sub>2</sub>	Doped oxide	MOR EOR	Larger intrinsic electrocatalytic activity	Single support	[39, 40]
10	Sn-In <sub>2</sub> O <sub>3</sub>	Doped oxide	ORR	The mass activity of Pt was high as 621 ± 31 mA/mg <sub>Pt</sub> and the stability of Pt/ITO was also very impressive	Single support	[42]

(continued)

**Table 5.2** (continued)

Samples	Formula	Classification	Reaction of catalysis	Performance	Combined with (without) carbon	Reference
11	S-ZrO <sub>2</sub>	Doped oxide	ORR	No large IR loss in single cell performance up to 2.5 Acm <sup>-2</sup>	Single support	[43, 44]
12	TiC	Carbide	–	–	Single support	[45]
13	WC	Carbide	MOR ORR	Pt/WC catalyst enhanced the ORR activity by more than 200%	Single support	[46–48]
14	SiC	Carbide	ORR	The SiC-based catalysts have been found to have a higher electrochemical activity than commercially available Vulcan-based catalysts	Single support	[49, 50]
15	TiN	Nitride	ORR	Pt/TiN shows a higher reduction current in comparison with carbon support catalyst	Single support	[51]
16	BN	Nitride	–	Potential application	–	[52]
17	TiB <sub>2</sub>	Boride	ORR	The electrochemical stability of TiB <sub>2</sub> was investigated and showed almost no changes in redox region after oxidation during 48 h at 1.20 V	Single support	[53]
18	Pt-Au(111)	Noble metal	ORR	The Pt <sub>0.75</sub> Pd <sub>0.25</sub> monolayer on Au/C equals the activity of a Pt/C catalyst with 2.5 times larger Pt loading	Single support	[55]

(continued)

**Table 5.2** (continued)

Samples	Formula	Classification	Reaction of catalysis	Performance	Combined with (without) carbon	Reference
19	Pt-Pd(111)	Noble metal	ORR	The mass activity of Pt-Pd(111) electrode is five to eight times higher than that of Pt/C electrocatalyst	Single support	[56]
20	Pt-Ni and Pt-Co	Noble metal	ORR	The reaction mechanism on Pt-Ni and Pt-Co surfaces is the same as the one on pure Pt with lower mass loading	Single support	[57, 58]
21	PANI	Conductive polymer	MOR	The Pt incorporated polyaniline nanotube electrode exhibited excellent catalytic activity and stability	Single support	[59, 60]
22	PPy-XC72	Conductive polymer	MOR	The Pt nanoparticles deposited on polypyrrole-carbon exhibit better catalytic activity than those on plain carbon	Combined with carbon	[61]
23	PPy-C	Conductive polymer	ORR and MOR	Pt and Pt-Ru particles deposited on PPy-CNT composite polymer films exhibit excellent catalytic activity and stability	Combined with carbon	[62–64]

**Acknowledgment** The authors would express thanks to Dr. Gong Hongyu and Ms. Zheng Xiangjun for their kindly help and to the National Nature Science Foundation of China (51572181, 51472009, 51172007) and Natural Science Foundation of Jiangsu Province, China (BK20151226), for their financial support.

## References

1. A.S. Arico, P. Bruce, B. Scrosati, J.M. Tarascon, W. Van Schalkwijk, Nanostructured materials for advanced energy conversion and storage devices. *Nat. Mater.* **4**(5), 366–377 (2005)
2. B.C.H. Steele, A. Heinzel, Materials for fuel cell technologies. *Nature* **414**, 345–352 (2001)
3. L.M. Roen, C.H. Paik, T.D. Jarvi, Electrocatalytic corrosion of carbon support in PEMFC cathodes. *Electrochim. Solid-State Lett.* **7**(1), A19–A22 (2004)
4. P. Serp, M. Corrias, P. Kalck, Carbon nanotubes and nanofibers in catalysis. *Appl. Catal. A* **253**(2), 337–358 (2003)
5. S.D. Knights, K.M. Colbow, J. St-Pierre, D.P. Wilkinson, Aging mechanisms and a lifetime of PEFC and DMFC. *J. Power Sources* **127**(1–2), 127–134 (2004)
6. F.C. Walsh, R.G.A. Wills, The continuing development of Magnéli phase titanium sub-oxide and Ebonex<sup>®</sup> electrodes. *Electrochim. Acta* **55**, 6342–6351 (2010)
7. S. Andersson, B. Collen, U. Kuylenstierna, A. Magnéli, Phase analysis studies on the titanium-oxygen system. *Acta Chem. Scand.* **11**, 1641–1652 (1957)
8. M. Marezio, D.B. McWhan, P.D. Demier, J.P. Remeika, Structural aspects of the metal-insulator transitions in Ti<sub>4</sub>O<sub>7</sub>. *J. Solid State Chem.* **6**(2), 213–221 (1973)
9. J.E. Graves, D. Pletcher, R.L. Clarke, F.C. Walsh, The electrochemistry of Magnéli phase titanium oxide ceramic electrodes Part I. The deposition and properties of the metal coating. *J. Appl. Electrochem.* **21**(10), 848–857 (1991)
10. L.M. Vracar, N.V. Krstajic, V.R. Radmilovic, M.M. Jaksic, Electrocatalysis by nanoparticles-oxygen reduction on Ebonex/Pt electrode. *J. Electroanal. Chem.* **587**(1), 99–107 (2005)
11. L. Wang, P. Lettenmeier, U. Golla-Schindler, P. Gazdzicki, N.A. Canas, T. Morawietz, R. Hiesgen, S.S. Hosseiny, A.S. Gago, K.A. Friedrich, Nanostructured Ir-supported on Ti<sub>4</sub>O<sub>7</sub> as a cost effective anode for proton exchange membrane (PEM) electrolyzers. *Phys. Chem. Chem. Phys.* **18**(6), 4487–4495 (2016)
12. T. Ioroi, H. Senoh, S. Yamazaki, Z. Siroma, N. Fujiwara, K. Yasuda, Stability of corrosion-resistant Magnéli-phase Ti<sub>4</sub>O<sub>7</sub>-supported PEMFC catalysts at high potentials. *J. Electrochem. Soc.* **155**(4), B321–B326 (2008)
13. S.J. Tauster, S.C. Fung, R.T.K. Baker, J.A. Horsley, Strong interactions in support-metal catalysts. *Science* **211**(4487), 1121–1125 (1981)
14. E.E. Farndon, D. Pletcher, A. Saraby-Reintjes, The electrodeposition of platinum onto a conducting ceramic Ebonex. *Electrochim. Acta* **42**(8), 1269–1279 (1997)
15. E. Slavcheva, V. Nikolova, T. Petkova, E. Lefterova, I. Dragieva, T. Vitanov, E. Budevski, Electrocatalytic activity of Pt and Pt-Co deposited on Ebonex by BH reduction. *Electrochim. Acta* **50**(27), 5444–5448 (2005)
16. G.Y. Chen, S.R. Bare, T.E. Mallouk, Development of supported bifunctional electrocatalysts for unitized regenerative fuel cells. *J. Electrochem. Soc.* **149**(8), A1092–A1099 (2002)
17. C.H. Yao, F. Li, X. Li, D.G. Xia, Fiber-like nanostructured Ti<sub>4</sub>O<sub>7</sub> used as durable fuel cell catalyst support in oxygen reduction catalysis. *J. Mater. Chem.* **22**(32), 16560–16565 (2012)
18. P.K. Shen, C.Y. He, S.Y. Chang, X.D. Huang, Z.Q. Tian, Magnéli phase Ti<sub>8</sub>O<sub>15</sub> nanowires as conductive carbon-free energy materials to enhance the electrochemical activity of palladium nanoparticles for direct ethanol oxidation. *J. Mater. Chem. A* **3**, 14416–14423 (2015)
19. L. Chen, A.C. Cooper, G.P. Pez, H.S. Cheng, On the mechanisms of hydrogen spillover in MoO<sub>3</sub>. *J. Phys. Chem. C* **112**(6), 1755–1758 (2008)

20. N.R. Elezovic, B.M. Babic, V.R. Radmilovic, L.M. Vracar, N.V. Krstajic, Synthesis and characterization of  $\text{MoO}_x\text{-Pt/C}$  and  $\text{TiO}_x\text{-Pt/C}$  nano-catalysts for oxygen reduction. *Electrochim. Acta* **54**(9), 2404–2409 (2009)
21. Y. Wang, E.R. Fachini, G. Cruz, Y.M. Zhu, Y. Ishikawa, J.A. Colucci, C.R. Cabrera, Effect of surface composition of electrochemically deposited platinum/molybdenum oxide on methanol oxidation. *J. Electrochem. Soc.* **148**(3), C222–C226 (2001)
22. T. Ioroi, T. Akita, S. Yamazaki, Z. Siroma, N. Fujiwara, K. Yasuda, Comparative study of carbon-supported Pt/Mo-oxide and PtRu for use as Co-tolerant anode catalysts. *Electrochim. Acta* **52**(2), 491–498 (2006)
23. M. Koyano, A. Miyata, H. Hara, Anisotropic behavior of electrical conductivity and collective motion of charge density wave in quasi-two-dimensional conductor  $\text{g-Mo}_4\text{O}_{11}$ . *Phys. B Condens. Matter* **284-285**, 1663–1664 (2000)
24. T. Sato, T. Dobashi, H. Komatsu, T. Takahashi, M. Koyano, Electronic structure of  $\eta\text{-Mo}_4\text{O}_{11}$  studied by high-resolution angle-resolved photoemission spectroscopy. *J. Electron Spectrosc. Relat. Phenom.* **144-147**, 549–552 (2005)
25. M.S. da Luz, A. de Campos, B.D. White, J.J. Neumeier, Electrical resistivity, high-resolution thermal expansion, and heat capacity measurements of the charge-density-wave compound  $\gamma\text{-Mo}_4\text{O}_{11}$ . *Phys. Rev. B* **79**, 233106-1–233106-4 (2009)
26. F. Yang, F. Li, Y. Wang, X. Chen, D.G. Xia, J.B. Liu, Enhanced electrocatalytic performance for methanol oxidation with a Magnéli phase molybdenum oxide/Pt-black composite. *J. Mol. Catal. A Chem.* **400**, 7–13 (2015)
27. R. Xu, F. Xu, M. Pan, M. SC, Improving sulfur tolerance of noble metal catalysts by tungsten oxide-induced effects. *RSC Adv.* **3**, 764–773 (2013)
28. F. Li, H.Y. Gong, Y. Wang, H. Zhang, Y.Z. Wang, S.N. Liu, S. Wang, C.W. Sun, Enhanced activity, durability and anti-poisoning property of  $\text{Pt/W}_{18}\text{O}_{49}$  for methanol oxidation with a substoichiometric tungsten oxide  $\text{W}_{18}\text{O}_{49}$  support. *J. Mater. Chem. A* **2**, 20154–20163 (2014)
29. L. YZ, Y.Y. Jiang, X.H. Gao, X.D. Wang, W. Chen, Strongly coupled Pd nano tetrahedron/tungsten oxide nanosheet hybrids with enhanced catalytic activity and stability as oxygen reduction electrocatalysts. *J. Am. Chem. Soc.* **136**(33), 11687–11697 (2014)
30. X.B. Zhu, H.M. Zhang, Y.M. Liang, Y. Zhang, B.L. Yi, A novel PTFE-reinforced multilayer self-humidifying composite membrane for PEM fuel cell. *Electrochem. Solid-State Lett.* **9**(2), A49–A52 (2006)
31. Z.G. Chen, X.P. Qiu, B. Lu, S.C. Zhang, W.T. Zhu, L.Q. Chen, Synthesis of hydrous ruthenium oxide-supported platinum catalysts for direct methanol fuel cells. *Electrochem. Commun.* **7**(6), 593–596 (2005)
32. K. Park, K. Seol, Nb-TiO<sub>2</sub> supported Pt cathode catalyst for polymer electrolyte membrane fuel cells. *Electrochem. Commun.* **9**(9), 2256–2260 (2007)
33. O.E. Hass, S.T. Briskeby, O.E. Kongstein, M. Tsytkin, R. Tunold, B.T. Boerresen, Synthesis and characterization of  $\text{Ru}_x\text{Ti}_{1-x}\text{O}_2$  as a catalyst support for the polymer electrolyte fuel cell. *J. New Mater. Electrochem. Syst.* **11**(1), 9–14 (2008)
34. A.P. Wang, X. HB, L. YH, H. JZ, X.F. Kong, B.L. Tian, H. Dong, Synthesis and characterization of ruthenium-titanium composite oxide and a platinum catalyst supported on it. *Chin. J. Catal.* **30**(3), 179–181 (2009)
35. V. Ho, C.J. Pan, J. Rick, S. WN, B.J. Hwang, Nanostructured  $\text{Ti}_{0.7}\text{Mo}_{0.3}\text{O}_2$  supported enhances electron transfer to Pt: high-performance catalysts for oxygen reduction reaction. *J. Am. Chem. Soc.* **133**(30), 11716–11724 (2011)
36. P. Yu, M. Pemberton, P. Plasse, Pt-Co/C cathode catalyst for improved durability in PEMFCs. *J. Power Source* **144**(1), 11–20 (2005)
37. J.H. Kim, G. Kwon, H. Lim, C. Zhu, H. You, Y.T. Kim, Effects of transition metal doping in Pt/M-TiO<sub>2</sub> (M=V, Cr, Nb) on oxygen reduction reaction activity. *J. Power Sources* **320**, 188–195 (2016)
38. T. Saraidarov, R. Reisfeld, E. Zigansky, A. Sashchiuk, E. Lifshitz, Electrical conductivity of doped porous glasses as possible sensors for oxygen. *Opt. Appl.* **38**(1), 109–117 (2008)

39. A.L. Santos, D. Profeti, P. Olivi, Electrooxidation of methanol on Pt microparticles dispersed on SnO<sub>2</sub> thin films. *Electrochim. Acta* **50**(13), 2615–2621 (2005)
40. K.S. Lee, I.S. Park, Y.H. Cho, D.S. Jung, N. Jung, H.Y. Park, Y.E. Sung, Electrocatalytic activity and stability of Pt supported on Sb-doped SnO<sub>2</sub> nanoparticles for direct alcohol fuel cells. *J. Catal.* **258**(1), 143–152 (2008)
41. H.L. Pang, X.H. Zhang, X.X. Zhong, B. Liu, X.G. Wei, Y.F. Kuang, J.H. Chen, Preparation of Ru-doped SnO<sub>2</sub>-supported Pt catalysts and their electrocatalytic properties for methanol oxidation. *J. Colloid Interface Sci.* **319**(1), 193–198 (2008)
42. Y. Liu, W.E. Mustain, High stability, high activity Pt/ITO oxygen reduction electrocatalysts. *J. Am. Chem. Soc.* **135**(2), 530–533 (2013)
43. S. Hara, M. Miyayama, Proton conductivity of super acidic sulfated zirconia. *Solid State Ionics* **168**(1–2), 111–116 (2004)
44. Y.C. Suzuki, A. Ishihara, S. Mitsushima, N. Kamiya, K. Ota, Sulfated-zirconia as a support of Pt catalyst for polymer electrolyte fuel cells. *Electrochem. Solid-State Lett.* **10**(7), B105–B107 (2007)
45. V. Jalan, D.G. Frost, U.S. Patent 4,795,684 1989
46. E.C. Weigert, S. Arisetty, S.G. Advani, A.K. Prasad, J.G. Chen, Electrochemical evaluation of tungsten monocarbide (WC) and platinum-modified WC as alternative DMFC electrocatalysts. *J. New Mater. Electrochem. Syst.* **11**, 243–251 (2008)
47. Y. Wang, S.Q. Song, V. Maragou, P.K. Shen, P. Tsiakaras, High surface area tungsten carbide microsphere as effective Pt catalyst support for oxygen reduction reaction. *Appl Catal B* **89** (1–2), 223–228 (2009)
48. Y. Hara, N. Minami, H. Matsumoto, H. Itagaki, New synthesis of tungsten carbide particles and synergistic effect with Pt metal as a hydrogen oxidation catalyst for fuel cell applications. *Appl. Catal. A* **332**(2), 289–296 (2007)
49. J. Lobato, H. Zamora, J. Plaza, P. Canizares, M.A. Rodrigo, Enhancement of high-temperature PEMFC stability using catalysts based on Pt supported on SiC-based materials. *Appl. Catal. B Environ.* **198**, 516–524 (2016)
50. R. Dhiman, E. Johnson, E.M. Skou, P. Morgen, S.M. Andersen, SiC nanocrystals as Pt catalyst supports for fuel cell applications. *J. Mater. Chem. A* **1**, 6030–6036 (2013)
51. B. Avasara, T. Murray, W.Z. Li, P. Haldar, Titanium nitride nanoparticles based electrocatalysts for proton exchange membrane fuel cells. *J. Mater. Chem.* **19**, 1803–1805 (2009)
52. J.A. Perdigon-Melon, A. Auroux, C. Guimon, B. Bonnetot, Micrometric BN powders used as catalyst support: influence of the precursor on the properties of BN ceramic. *J. Solid State Chem.* **177**(2), 609–615 (2004)
53. S.B. Yin, S.C. Mu, H.F. Lv, N.C. Cheng, M. Pan, Z.Y. Fu, A highly stable catalyst for PEM fuel cell based on durable titanium diboride support and polymer stabilization. *Appl Catal B* **93** (3–4), 233–240 (2010)
54. I. Eswaramoorthi, A.K. Dalai, A comparative study on the performance of mesoporous SBA-15 supported Pd-Zn catalysts in partial oxidation and steam reforming of methanol for hydrogen production. *Int. J. Hydrog. Energy* **34**(6), 2580–2590 (2009)
55. K. Sasaki, Y. Mo, J.X. Wang, M. Balasubramanian, F. Uribe, J. Mcbreen, R.R. Adzic, Pt submonolayers on metal nanoparticles-novel Electrocatalysts for H<sub>2</sub> oxidation and O<sub>2</sub> reduction. *Electrochim. Acta* **48**(25–26), 3841–3849 (2003)
56. J. Zhang, Y. Mo, M.B. Vukmirovic, R. Klie, K. Sasaki, R.R. Adzic, Platinum monolayer electrocatalysts for O<sub>2</sub> reduction: Pt monolayer on Pd (111) and on carbon-supported Pd nanoparticles. *J. Phys. Chem. B* **108**(30), 10955–10964 (2004)
57. V. Stamenkovic, T.J. Schmidt, P.N. Ross, N.M. Markovic, Surface composition effects in electrocatalysis: kinetics of oxygen reduction on well-defined Pt<sub>3</sub>Ni and Pt<sub>3</sub>Co alloy surfaces. *J. Phys. Chem. B* **106**(46), 11970–11979 (2002)
58. V.R. Stamenkovic, B.S. Mun, K.J.J. Mayrhofer, P.N. Ross, N.M. Markovic, Effect of surface composition on electronic structure, stability, and electrocatalytic properties of Pt-transition

- metal alloys: Pt-skin versus Pt-skeleton surfaces. *J. Am. Chem. Soc.* **128**(27), 8813–8819 (2006)
59. H. Laborde, J.M. Leger, C. Lamy, Electrocatalytic oxidation of methanol and C1 molecules on highly dispersed electrodes Part1: platinum in polyaniline. *J. Appl. Electrochem.* **24**(3), 219–226 (1994)
  60. B. Rajesh, K.R. Thampi, J.M. Bonard, H.J. Mathieu, N. Xanthopoulos, B. Viswanathan, Nanostructured conducting polyaniline tubules as catalyst support for Pt particles for possible fuel cell applications. *Electrochem. Solid-State Lett.* **7**(11), A404–A407 (2004)
  61. H.B. Zhao, L. Li, J. Yang, Y.M. Zhang, Nanostructured polypyrrole/carbon composite as Pt catalyst support for fuel cell applications. *J. Power Sources* **184**(2), 375–380 (2008)
  62. V. Selvaraj, M. Alagar, Pt and Pt-Ru nanoparticles decorated polypyrrole/multiwalled carbon nanotubes and their catalytic activity towards methanol oxidation. *Electrochem. Commun.* **9**(5), 1145–1153 (2007)
  63. H.B. Zhao, L. Li, J. Yang, Y.M. Zhang, H. Li, Synthesis and characterization of bimetallic Pt-Fe/polypyrrole-carbon catalyst as DMFC anode catalyst. *Electrochem. Commun.* **10**(6), 876–879 (2008)
  64. H.B. Zhao, J. Yang, L. Li, H. Li, J.L. Wang, Y.M. Zhang, Effect of over-oxidation treatment of Pt-Co/polypyrrole-carbon nanotube catalysts on methanol oxidation. *Int. J. Hydrog. Energy* **34**(9), 3908–3914 (2009)





# Noble Metal Electrocatalysts for Anode and Cathode in Polymer Electrolyte Fuel Cells

Surbhi Sharma and Carolina Musse Branco

## Contents

6.1	Introduction .....	172
6.2	Current State of the Art for Noble Metal Electrocatalysts .....	173
6.3	Hydrogen Oxidation (Anode) Electrocatalysts .....	175
6.3.1	Hydrogen Oxidation (Anode) Electrocatalysts in Alcohol Systems .....	175
6.4	Oxygen Reduction (Cathode) Electrocatalysts .....	176
6.5	Factors Affecting Electrocatalyst Performance .....	178
6.5.1	Role of Nanocatalyst Size and Morphology .....	179
6.5.2	Role of Alloying .....	186
6.5.3	Separation Between Electrocatalyst Nanoparticles .....	189
6.5.4	Electrocatalyst Dispersion and Loading on Support .....	190
6.6	Recycling Precious Metal Electrocatalysts .....	191
6.7	Future Prospects and Outlook .....	192
	References .....	193

## Abstract

The chapter begins with a brief introduction of the importance and role of electrocatalysts in fuel cells. The following sections discuss the current state-of-the-art for noble metal electrocatalysts in polymer electrolyte fuel cells (PEFCs) along with an examination of recent developments in various noble metal (Pt, Pd, Au, Ag, Ir, Ru) electrocatalysts used in anode and cathode of a PEFC. Various 0D, 1D, 2D, and 3D nanostructured morphologies of electrocatalysts are

## Author Contributions

Sections 5.5.1.1–5.5.1.4 were contributed by Dr Carolina Musse Branco. Sections 5.1–5.5, 5.5.2–5.5.4 and 5.6 were contributed by Dr Surbhi Sharma, and Sect. 5.5.1 was jointly completed by Dr Surbhi Sharma and Dr Carolina Musse Branco.

S. Sharma (✉) · C. M. Branco

School of Chemical Engineering, University of Birmingham, Birmingham, UK

e-mail: [S.Sharma.1@bham.ac.uk](mailto:S.Sharma.1@bham.ac.uk); [carol\\_mbranco@hotmail.com](mailto:carol_mbranco@hotmail.com)

scrutinized. Different factors responsible for influencing and manipulating the electrocatalytic response and the stability of electrocatalysts are also discussed. The need and scope for recycling of precious metal electrocatalysts are examined and finally expected future trends are deliberated.

---

## 6.1 Introduction

Polymer electrolyte fuel cells (PEFCs) are regarded as the most promising alternatives to the existing internal combustion engine (ICE) based transportation system, which is currently 95% dependent upon fossil fuels. With the reality of climate change daunting on the world along with the dwindling crude oil reserves, the hydrogen-based PEFCs have the potential to dramatically improve our urban air quality, offer better energy security, and reduce the carbon footprint as they are suitable not just for application in transportation but also for portable electronics and combined heat and power systems. Besides being the greener energy solution with zero or near zero greenhouse gas emissions, the PEFC systems also offer significantly higher energy efficiencies (PEFC have 50–60% efficiency) as opposed to the existing ICE systems, which have a maximum efficiency of just 20% [1–6]. Among the various types of fuel cells, the low temperature (operating at 80–120 °C) acid-based hydrogen fuel cells are the best choice for transportation applications, offering quick start-up along with good efficiency. Fuel cells, in general, have an added benefit over other electrochemical systems such as batteries, as they do not need charging and continue to supply power as long as the fuel (hydrogen in case of PEMFCs) and oxidant (oxygen/air) are in continuous supply. They also have the advantages of being lightweight, quick hydrogen refill time, and being more economical over battery-operated alternatives.

Fuel cell powered vehicles (FCVs) are a reality. Toyota Mirai was the first mass-produced FCV, which has been commercially sold since 2014 in Japan and since 2015 in North America [7]. While all major automotive companies have by now launched their concept fuel cell vehicles such as Toyota FCV-R, Mercedes-Benz F-cell, Honda FCX-clarity, and Chevrolet Equinox Fuel Cell, the high cost of these vehicles and fuel supply availability limit their large-scale commercial viability against the existing ICE systems [8–13]. The major component costs of this system are contributed by the platinum (Pt) based electrocatalysts, which are responsible for catalyzing reactions at the anode and cathode of the fuel cell. The breakdown of hydrogen at the anode and the reduction of oxygen to combine with protons and electrons to form water at the cathode cannot take place in the absence of a catalyst at such low temperatures. Anode reaction is quick and simple, requiring relatively low amounts of Pt catalyst. However, the cathode reactions are extremely sluggish requiring very high Pt loadings to carry out the reactions efficiently.

The fundamental characteristics required for an effective electrocatalyst (for anode or cathode) in a PEFC system are (a) activity – to enable adsorption of reactants and facilitate reaction, (b) selectivity – to produce the desired product and minimize undesirable intermediate and byproducts, (c) stability – toward the harsh PEFC environment (high temperature, presence of radicals, and strong oxidants), and (d) resistance – toward poisoning from impurities (CO<sub>2</sub>, sulfur-based gases in feed gas) [14]. Tremendous efforts have been made using a variety of approaches to reduce the amount of electrocatalysts costs over the past two to three decades. These approaches to reduce costs owing to electrocatalysts have mainly focused on reducing the Pt loading and increasing the efficiency of the electrocatalyst, and can be categorized as follows: (1) replacing bulk Pt with nanostructured catalysts; (2) alloying with other noble metals; (3) alloying with non-noble, transition/d-block metals; (4) Pt and noble metal-free catalysts; and (5) enhancing supports for electrocatalysts to improve electrocatalytic efficiency.

This chapter focuses on the noble metal-based electrocatalysts systems (excluding noble-transition metal alloys) for anode and cathode applications in PEMFCs, explaining the current state of the art, the role, and functions of anode and cathode electrocatalysts as well as factors affecting the electrocatalytic performance such as morphology, alloying, loading, and distribution. It will further discuss parameters for enhancing efficiency and minimizing Pt and other noble metal loading along with exploring current noble metal recycling options.

---

## 6.2 Current State of the Art for Noble Metal Electrocatalysts

Before going into the discussion about the state of the art, it is important to recall what is a noble metal and which metals are included in the list of noble metals. Noble metals are defined as those elements in the periodic table, which are least reactive or extremely resistant to oxidation/corrosion even under conditions of high temperature. Based on this, gold (Au), silver, (Ag), mercury (Hg), platinum (Pt), and Pt group metals, i.e., metals belonging to the groups VIIB, VIIIB, and IB of the second and third transition series of the periodic table are considered as noble metals. Specifically, Pt group metals include palladium (Pd), rhodium (Rd), rhenium (Rh), ruthenium (Ru), and osmium (Os) as noble metals.

The Pt nanoparticles supported on carbon black or Pt/C is the accepted industry standard catalyst for PEFCs. There is a wide variety of carbon black but the most commonly used carbon black is Vulcan carbon (manufactured by E-TEK) or Ketjen black (manufactured by TKK). The standard Pt loading for the anode (0.05 mg/cm<sup>2</sup>) and cathode (~0.4 mg/cm<sup>2</sup>) are significantly different due to the quick and efficient hydrogen oxidation as compared to sluggish oxygen reduction reaction at the cathode. According to the 2016 United States Department of Energy (DOE) reports, the 2015 status of Pt group metal (PGM) total loading (both anode and cathode) was 0.13 mg<sub>PGM</sub>/cm<sup>2</sup>. The target for 2020 is a loading of 0.125 mg<sub>PGM</sub>/cm<sup>2</sup>.

Further estimates based on the data available in 2015 suggest that the cost of an 80-kW<sub>net</sub> automotive PEFC system operating on direct hydrogen to be \$53/kW when manufactured at a volume of 500,000 units/year. With the 2015 status of total catalyst content of 0.16 g<sub>PGM</sub>/kW, the electrocatalyst still accounts for more than 30% of the total cost of a PEFC system [15].

As mentioned earlier, myriad approaches have been extensively explored to look for reducing these costs. The use of transition or d-block metals with Pt as well as other noble metals to make binary, tertiary, and ternary alloys is one of the most widely explored options for reducing electrocatalyst costs in PEFCs. Many of the reported studies suggest promising future potential for binary and higher combinations as electrocatalysts [16–18]. However, problems such as catalyst-support degradation and loss of electrocatalyst often lead to leaching of these metals into the PEFC system, thereby entering other components. Several studies on single cell PEFC systems have identified that the ions of various d-block elements, such as iron (Fe), copper (Cu), cobalt (Co), and nickel (Ni), which are also popular choices for most Pt-alloy electrocatalysts, enter into polymer membrane and actively react with hydrogen peroxide (another byproduct) resulting in membrane degradation [19]. Moreover, estimates and calculations reported in recent reviews of the available literature have revealed that the current state of non-noble electrocatalyst systems is not ready for transportation applications due to their durability and performance limitations. These systems, in their current state, are better suited for low-power portable PEFC applications only. Comparisons with Pt/C electrodes tested in real FC systems reveal that even for portable FC systems, these suffer from poor durability, with just around 16% power (in comparison to Pt/C) being delivered after 700 h of operation. These figures are drastically below the 2015 targets of DOE where durability is defined as a maximum of 20% power loss (i.e., 80% power remaining as compared to initial power) after 5000 h of FC operation [7]. For automotive applications the DOE targets are even stricter, requiring 5000 h of durability with less than 10% loss of performance [15]. Thus, the need for continuously improving the efficiency and durability of the noble metal systems in order to minimize their usage and the net PEFC costs till the noble metal free systems can achieve the required targets of peak power and durability for commercialization.

Thorough studies have been systematically carried out in developing the noble metal electrocatalysts and in exploring the novel methods to minimize the loading without compromising on the performance and efficiency. These include approaches such as 0-, 1-, 2-, and 3-dimensional nanostructures (including core-shell structures) and chalcogenides, all consisting of pure as well as alloyed noble metal systems. However, before investigating the numerous varieties of electrocatalyst morphologies, it is essential to understand the anode and cathode operations in a PEFC. Therefore, the next two sections will explain the role of anode and cathode electrocatalysts, respectively. Following this, Sect. 6.5 will delve into the discussion about the various types of electrocatalysts and how their various attributes play a role in their electrocatalytic performances.

### 6.3 Hydrogen Oxidation (Anode) Electrocatalysts

Hydrogen oxidation reaction or HOR is a simple, single-step reaction. As the hydrogen gas flows into the anode of the PEFC, the hydrogen molecule ( $H_2$ ) reaches the electrocatalyst surface and is adsorbed on the electrocatalytically active reaction site. Here the H-H bond undergoes hemolytic cleavage to generate two adsorbed hydrogen atoms. Subsequently, the H atoms are each oxidized to produce a proton ( $H^+$ ) and an electron ( $e^-$ ), respectively. The proton leaves the catalyst surface to diffuse through the proton exchange membrane to reach the cathode, while the electron flows from anode to the cathode to complete the external circuit, producing current, respectively [14]. The kinetics of HOR is relatively fast and leads to minimal potential loss (less than 5 mV). As such, very low Pt loadings ( $0.05 \text{ mg/cm}^2$ ) are sufficient to carry out the reaction effectively and efficiently. Consequently, more emphasis has been given to improve the efficiency of the cathode electrocatalyst, where very high loading of electrocatalysts are required to reduce voltage losses and improve the sluggish reaction kinetics.

#### 6.3.1 Hydrogen Oxidation (Anode) Electrocatalysts in Alcohol Systems

Alcohol-based fuel cells, especially direct methanol fuel cells (DMFC), are often considered a subcategory of PEFC. Since methanol is utilized as the source of hydrogen in this system, the anode reactions are slightly different in this system. It is actually quite a challenging situation unlike the anode setup of a conventional hydrogen-based PEFC. The breakdown of methanol involves several proposed pathways with quite a few reaction intermediaries, including HCOO, carbon monoxide (CO), and other residual carbon species as products like  $CO_2$ , formaldehyde, and formic acid [20]. These reaction intermediaries interfere with the normal catalyst functioning at the anode. This is particularly true for CO molecules, which bond strongly to the electroactive sites of the electrocatalyst, inhibiting the other reactants from coming together at the reaction sites for further methanol oxidation reactions (MORs). This phenomenon is referred to as electrocatalyst poisoning. The overall MOR at the anode is more complicated in the DMFC system (than a  $H_2/O_2$  PEFC), and the commercially accepted anode catalyst here is PtRu alloy. Oxyphilic metals like Ru prevent the blocking of the reaction sites on the Pt surface by lowering the oxidation potential of the adsorbed CO thus enabling faster conversion and release of  $CO_2$  [20, 21].

Consequently, extensive work has been carried out on DMFC anode electrocatalysts in order to make them more tolerant to poisoning and for improving their efficiency and durability. Noble metals are known to be particularly suitable in such systems due to their resistance to oxidation and stability in acidic environments. This will be further discussed in Sect. 6.5, which elaborates on the factors influencing electrocatalytic performance.

## 6.4 Oxygen Reduction (Cathode) Electrocatalysts

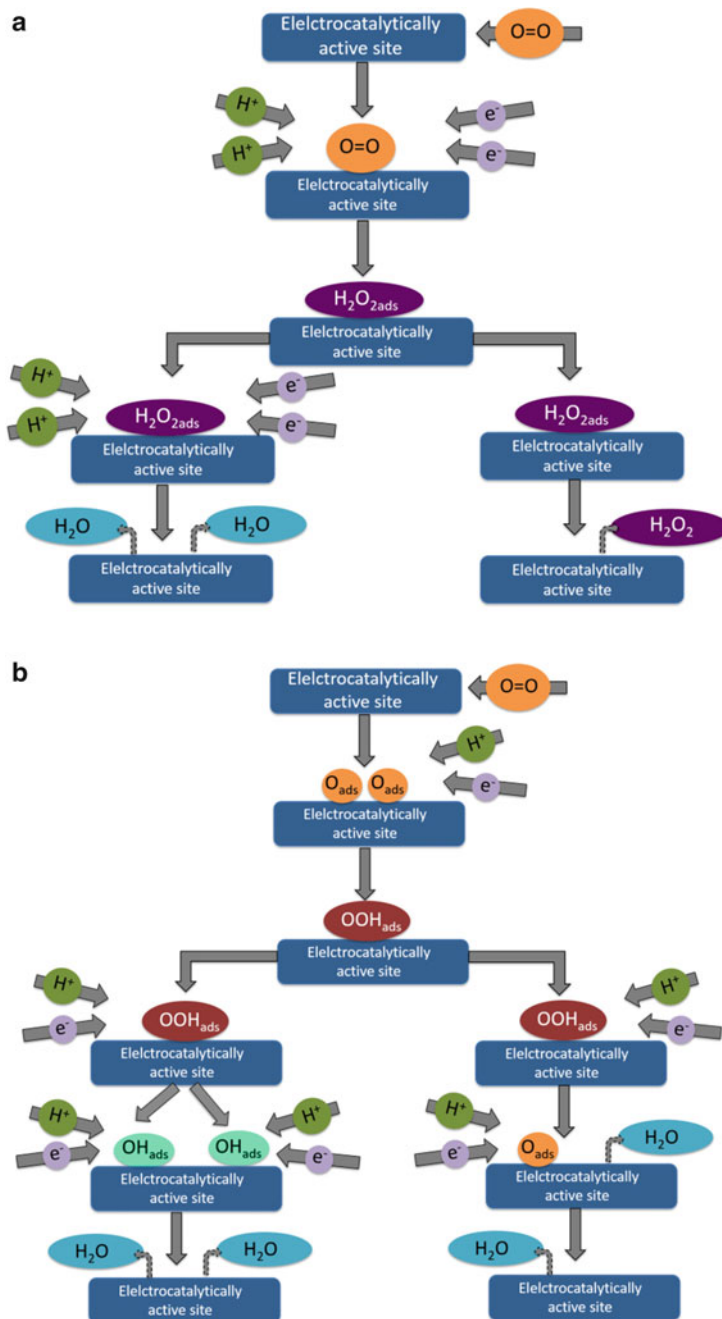
The oxygen reduction reaction (ORR), which takes place at the cathode, is a multistep reaction making it sluggish. The ORR can take place via two different pathways, namely:

1. Partial reduction, involving a two electron process
2. Full reduction, involving a four electron process

In the case of partial reduction, an oxygen molecule is adsorbed at the electrocatalyst reaction sites followed by two hydrogen ions ( $H^+$ ) and incoming electrons ( $\bar{e}$ ) resulting in the formation of adsorbed hydrogen peroxide ( $H_2O_{2ads}$ ) molecule. This is referred to as an associative process as the adsorption of the oxygen molecule does not result in the  $O=O$  bond breaking. The  $H_2O_{2ads}$  either undergoes a further reduction to generate two water molecules or simply dissociates from the reaction sites, giving rise to a free  $H_2O_2$  molecule. Which one of the two paths the  $H_2O_{2ads}$  takes may depend on factors such as availability of more hydrogen in the cathode compartment. However, the complete details are unknown. Nevertheless, the production and presence of free  $H_2O_2$  in the fuel cell system is highly undesirable. This is due to its ability to promote radical oxidative degeneration and chain scission reactions in the polymer membrane. The schematic in Fig. 6.1a shows the partial reduction process.

The full reduction is a dissociative process where an oxygen molecule is first adsorbed on the electrocatalytically active site, which is followed by the  $O=O$  bond breaking, resulting in two adsorbed oxygen atoms ( $2O^*_{ads}$ ). The incoming hydrogen ions (or protons) and  $\bar{e}$  then result in protonation and reduction of the adsorbed  $O^*$  atoms leading to the formation of adsorbed  $OOH_{ads}$  groups. From here the reaction can proceed in two different ways depending on where the addition of second  $H^+$  takes place. If the second  $H^+$  addition is at the  $O_{ads}$  to the electrocatalyst, it results in the formation of two  $OH_{ads}$  groups. Subsequent protonation and electron reductions at each  $OH_{ads}$  result in formation and release of two water ( $H_2O$ ) molecules. On the other hand, if the  $H^+$  addition occurs at the oxygen bound to the first hydrogen ( $O-H$ ), it leads to a water molecule formation, which desorbs from the surface. Another two  $\bar{e}$  and  $H^+$  reacting with the  $O_{ads}$  then result in the second water molecule release. The former reaction (resulting in the simultaneous production of two water molecules) has been found to be the thermodynamically favored pathway according to density functional theory simulation studies. Thus, the full reduction is the more efficient, preferred reaction pathway resulting in the formation of stable water molecules; as opposed to radical  $H_2O_2$  in the half reduction [2, 14, 22–25]. Figure 6.1b shows a schematic with flow charts describing the reaction pathways for ORR.

The complexity of the ORR process demanded awareness and knowledge of the factors that can play a crucial role in improving catalytical performance. It further necessitated an extensive understanding of how each factor can drive the various reaction steps of the ORR process. This has led to several studies on (a) morphology



**Fig. 6.1** Schematic showing (a) partial reduction process and, (b) full reduction process, for the ORR at PEFC cathode

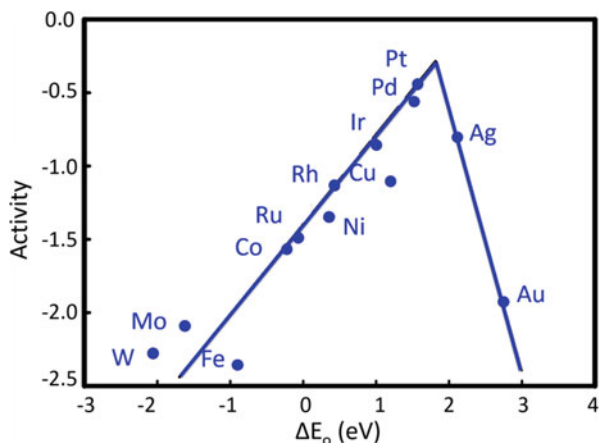
(shape, size, roughness); (b) combination of alloying materials; and (c) loading and distribution of electrocatalyst [2, 7, 26, 27]. The next section will focus on the factors influencing electrocatalytic performance.

## 6.5 Factors Affecting Electrocatalyst Performance

In order to efficiently complete the sluggish and complex ORR process, several factors need to be ascertained when choosing an electrocatalyst. Catalytic performance of any PEFC electrocatalyst depends on several influential aspects. Not just the type of metal but aspects such as nanoparticle size, shape, crystal facets/index plane (especially in single crystal Pt), the amount of electrocatalyst loading and its distribution on the carbon/noncarbon support, the interaction of the catalyst with the support also influence the catalyst performance and the dynamics of ORR. For example, a reactant must bind to the electrocatalyst in such a way that the bond is strong enough for the reaction to occur but also weak enough to enable a quick dissociation or release of the product from the reaction site. This is known as the Sabatier principle. If the bond is too strong electrocatalyst poisoning occurs (either due to the reactants or the reaction intermediaries) as the reaction site is no longer available for participating in the electrocatalytic reactions. On the other hand, if the bond between the oxygen molecule and the electrocatalytic site is too weak, the O=O bond cleavage and electron transfer process will become difficult. Thus, the metal-oxygen interactions alone can significantly impact the speed and potential loss in the overall ORR process [28–31].

Volcano plots (oxygen binding energy versus oxygen reduction activity) are a useful tool, which is used to compare the oxygen binding energy ( $\Delta E^\circ$ ) of different metals and identify the electrocatalysts for ORR. As can be seen in Fig. 6.2, Pt (followed by Pd) assumes a prime position (if not ideal) for ORR electrocatalysts.

**Fig. 6.2** Volcano plot showing the variation in activity for oxygen reduction reaction with respect to change in oxygen binding energy calculated using Sabatier Analysis (Modified from Ref. [36] with permission from the American Chemical Society © 2004)





Since the peak of the volcano plot is not occupied by any element one can assume there is scope for improvisation [2].

Alloying of Pt with other metals, to make bi-, tri-, and quaternary alloy systems, is one of the oldest approaches to fine tune the electronic properties of metals. The shift in the d-band center due to alloying also correlates to the oxygen adsorption energies. In the case of alloy electrocatalysts, consideration also needs to be given to the choice of metals as well as the ratio of alloying along with the chosen morphology. Tweaking the lattice planes and crystal facets on the surface of the electrocatalyst is another creative approach. Different crystal planes of each metal possess different surface energies resulting in diverse metal-oxygen interactions. This further leads to the morphology of the nanostructured electrocatalysts since, morphology is shaped by the dominant crystal facet of the metal or alloy under the specific temperature, pressure and other growth constraints. The presence of edge sites is found to enhance electrocatalytic activity. These, of course, tend to vary depending on the shape as well as the size of the electrocatalyst structures [32–35].

### 6.5.1 Role of Nanocatalyst Size and Morphology

Size and morphology are two primary factors, which have been studied extensively to optimize electrocatalyst behavior. Several studies have projected complex and contradictory results about how particles sizes (<5, 1–5, and 3–7 nm) affect the specific activity. Centi et al. defended the idea that the diameter size is fundamental [37]. Chen et al. affirmed that the catalyst activity increases three times as the particle size is reduced [38]. The Pt nanoparticles with 3–4 nm (diameter) and 3–10 nm are most commonly used for ORR and MOR, respectively [39–42]. Besides the activity, the size of the particles also affects the stabilization of defects. This stabilization is proportional to the decrease in the particle size. Defects compromise the mechanical structure, stability and also affect the electronic conductivity of the electrocatalyst. Therefore, reducing the diameter of the particles to extremely low values can have a trick effect in increasing the defects. Thus, a balance between conductivity, defects, and catalyst activity is essential when the particles size is defined.

Nevertheless, all these size-related effects on electrocatalytic activity are often attributed to the electronic state, electronic properties, and geometry arising due to the size limitations [43–45]. In order to understand the size behavior in nanostructures, one must appreciate the role of Miller indices and lattice planes in metal electrocatalyst nanostructures. For example, the oxygen molecule adsorbs too strongly to the Pt{111} facet limiting the overall ORR kinetics due to the slow removal of the adsorbed oxygen containing species [7]. Being the most widely investigated metal, low index surfaces of Pt, i.e., {111}, {110} and {100}, facets have been the focus of several detailed ex situ (or half-cell ORR) studies over the last two decades [46]. The ex situ studies are generally performed using electrolytes such as sulfuric acid (H<sub>2</sub>SO<sub>4</sub>) and perchloric acid (HClO<sub>4</sub>). The key conclusions of these comprehensive studies include:

- (a) ORR activity for Pt increases in the order  $\{100\} < \{111\} < \{110\}$ . However, it must be mentioned here that this trend is only true in the case of weakly adsorbed electrolytes, such as  $\text{HClO}_4$ . The trend changes to  $\{111\} < \{100\} < \{110\}$  in the case of  $\text{H}_2\text{SO}_4$ , which is an adsorbing electrolyte where the bisulfate anions upon adsorption inhibit the activity of  $\{111\}$  facets.
- (b) In the case of high index Pt surfaces, the ORR activity has been found to be highly dependent on the orientation of the steps and terraces on the surfaces. Their activity seems to increase with an increase in terrace density except for  $n$   $\{110\}$ – $\{111\}$  surfaces [7, 47–51].

Efforts have, therefore, been made to maximize the ORR activity using the high activity planes,  $\{111\}$  and  $\{100\}$ , of Pt by synthesizing nanostructures with controlled shapes. Nanoparticles with high index planes with at least one Miller index larger than unity, such as tetrahedron  $\{hk0\}$ , trisoctahedron  $\{hkk\}$ , and trapezohedron  $\{hkk\}$ , have demonstrated higher activity than  $\{111\}$ . These surfaces need to be especially designed and are not very stable when subjected to potential cycling as they have a tendency to evolve into a more thermodynamically equilibrated shape. Moreover, the mechanism behind the higher ORR activity of the high index planes is not very clear yet [52–54].

Contrary to the idea defended by some other studies, it has been suggested that in case of 5–1 nm Pt nanoparticles, the distribution of terrace sites, i.e.,  $\{111\}$  and  $\{100\}$ , decreases and the low coordination number edges, which have stronger interaction with oxygen, dominate; leading to drastically reduced ORR activity as size decreases below 3 nm. Studies using X-ray photoemission spectroscopy (XPS) and in situ X-ray absorption spectroscopy (XAS) data have also identified that binding energy of  $\text{Pt}4f_{3/2}$  and  $4f_{5/2}$  states for Pt nanoparticles becomes higher with decreasing particle size. These have been further corroborated by density functional theory (DFT) calculations [55–57].

Effect of particle size on MOR has also been reported in several studies and are largely akin to ORR results suggesting that for particle size  $< 5$  nm activity decreases as the particle size decreases. This too is ascribed to the increased interaction between oxygenated species (such as CO), present during MOR, with the low index edge sites of Pt nanoparticles limiting the adsorption of methanol. The FT-IR studies combined with voltammetry by Park et al. have proposed the Pt site “ensemble effect.” According to this, the breakdown of methanol to form reaction intermediaries (including CO) is impeded by the limited availability of the adjacent Pt terrace sites in particles  $< 4$  nm [58, 59]. Some contradictory studies have also been reported which observed a reverse effect of decreasing particle size. More importantly, studies by Yoo et al. and earlier by McNicol have found that Pt and PtRu particle size-MOR activity relationship goes through a maximum at 2.3 and 2.6 nm, respectively [60, 61].

Similar studies on the effect of particle size and crystal indices, although limited, have also been performed for other noble metals. The Pd is one such metal, which demonstrates ORR activity five times lower than Pt and has an electronic structure very similar to that of Pt. The Pd is also an important choice as it is significantly

cheaper ( $\frac{1}{4}$ – $\frac{1}{5}$  the cost of Pt). In the case of Pd, {110} facet is far more active than its other facets (14 times more active than Pd{111}). It also shows twice the activity of Pt{111} in acidic media [62, 63]. Although Pd binds more strongly with oxygen than Pt (and hence the lower ORR activity), DFT studies show that Pd{100} binds slightly less strongly than {111}, which partially explains the significantly higher activity of Pd{100} [64].

Apart from the size, the shape or morphology also plays a critical role in defining the properties of the electrocatalysts. Together, the size and shape can result in the unique surface to volume ratios, which is essential in reducing the amount of metal used as electrocatalyst and maximizing its effectiveness. The next section explores the wide range of morphologies that have been studied for application in PEFCs.

### 6.5.1.1 Zero-Dimensional (0-D) Structures

To control the shape, various parameters are to be considered (such as precursor, solvent, capping and reducing agents) depending on the synthesis or deposition process used [65]. Morphology and choice of metal together can play a defining role in achieving excellent ORR or MOR activity. Both are interdependent since different index planes show distinctive electrocatalytic activity in different metals as discussed above for Pt and Pd.

A variety of shapes has been synthesized for monometallic Au, Pt, and Pd along with other noble metals owing to their face-centered cubic lattice structures. However, cubic and octahedral nanostructures are more common as these are relatively easy to prepare due to their low surface energies. The Pd nanocubes have shown better activity than octahedral and conventional Pd/C [7, 63]. The nanocages, which are hollow structures, have recently attracted attention. Zhang et al. reported Pt cubic and octahedral nanocages enclosed by {100} and {111} facets [66]. Other studies have also reported work on Pt nanocages demonstrating higher ORR activity than Pt/C [67].

With the aim to minimize Pt usage in PEMFCs, the trend over the past few years has been toward exploring alloyed 0-D structures and moving away from pure Pt (or other noble metals) based nanostructures. Moreover, the higher dimensional structures are also gaining interest due to their intrinsic advantages. These have been discussed in the following sections.

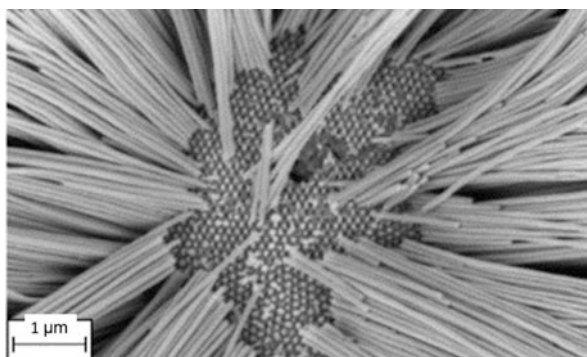
### 6.5.1.2 One-Dimensional (1-D) Structures

The 1-D nanocatalysts can be synthesized in the form of tubes, wires, and rods. More complex 1-D morphologies include nanochain, dendritic nanotubes, and nano lances [68]. In these structures, not all size parameters are necessarily nanosized. This characteristic makes the wires and tubes easier to handle, improving the general distribution and reducing agglomeration of the electrocatalyst. These 1-D electrocatalysts can be further organized into 2-D and 3-D aligned structures using techniques, such as chemical vapor deposition, stamping, and printing [69]. In comparison to 0-D electrocatalysts, 1-D systems demonstrate increased mass transport and present higher electrocatalytic activity. Many of these advantages come

from the anisotropy and surface properties of the structure. Above all, the enhanced durability and stability of 1-D Pt structures (compared with 0-D) is the most significant benefit. The higher stability in 1-D nanostructures is due to the smaller number of defect sites on the surface of single crystalline 1-D nanostructures than those on 0-D structures. Defects reduce the electrocatalytic activity of the material as the defective crystallographic plane gives rise to local variations in the surface energy and coordination numbers. The defect sites also reduce stability and contribute to the decomposition and irreversible oxidation of the catalyst [70–72]. This is certainly not desirable in the PEFC operation. The 1-D nanostructures are predisposed to anisotropic growth as they tend to minimize the surface energy. They also have larger surfaces and longer crystalline planes. Consequently, their lattice planes have fewer lattice boundaries than 0-D. These lattice boundaries are prejudicial for electroactivity. The anisotropic growth works efficiently for Pt 1-D electrocatalysts as it results in the preferential exposure of low index planes, which are the most active for ORR, i.e., {100} and {111}, in the case of Pt [70]. These nanowires and tube structures can be synthesized horizontally or vertically with length and diameter being the two size parameters. Ultrathin Pt nanowires (diameter 1.5–3 nm) with high surface to volume ratio have been found to not only demonstrate good electrochemical surface area (ECSA), but also do not seem to undergo physical ripening, aggregation, and mass transport limitation in practical application. It has also been evidenced that proper cleaning of these ultrathin wires to wash off amorphous Pt deposits can significantly enhance their performance by ensuring exposure of electroactive sites [68, 73].

Similar to 0-D nanocatalysts, the distribution and density are important factors that affect the electrocatalysts final properties. Apart from this, the growing arrangement is another fundamental factor. The wires and tubes can be grown randomly, oriented or part oriented. The substrate or matrix on which the nanowires will grow or be deposited also influences the nanowire morphology. Napolskii et al. grew nanowires by electrochemical deposition onto a porous alumina matrix, as seen in Fig. 6.3. After the elimination of the matrix, the resultant nanowires presented diameter similar to the pores of the matrix [74]. Similar to nanoparticles, the diameter of nanowires plays a crucial role in their electrochemical properties

**Fig. 6.3** Pt nanowire grown on porous alumina matrix using electrochemical deposition process (Modified with permission from Ref. [74], Elsevier ©2007)



(as seen in the case of ultrathin Pt nanowires) and it is one of the parameters, which must be controlled. The common method to define the diameter of nanowires is with the help of tunnel and channels on the substrate. However, it is very difficult to synthesize single crystalline nanowires without the use of a surfactant, which can later interfere with the electrocatalyst performance if not cleaned properly [75]. One of the most popular supports to grow 1-D electrocatalysts are the carbon nanotubes (CNTs), as they offer good electrical conductivity and high chemical stability. The support, when used to grow the electrocatalyst on it, can significantly affect the dispersion, uniformity, and morphology of the electrocatalyst. Besides CNTs, a broad range of carbon and noncarbon nanostructures are also used as support.

To grow these electrocatalysts, the most common method is chemical and physical vapor deposition by the vapor-liquid-solid method, especially to obtain aligned and oriented 1-D catalysts. The vapors of catalyst initiators and precursor are introduced into a confined space onto a sample substrate inside the chamber. The vapors transform to liquid phase as catalyst particles on the substrate surface and these particles grow to 1D catalyst in solid state [69]. Besides these vacuum deposition methods, electrodeposition and wet chemical solution based methods are also widely used, where the growth of nanostructures can be controlled and manipulated by innumerable variables, such as the current, potential, reaction time, precursor concentration, inclusion of surface, etc.

Besides Pt, 1-D electrocatalysts using other noble metals have also been explored. The Pd is the next widely explored noble element in electrocatalysts. The Pd nanorods were reported to show ten times higher activity than Pd nanoparticles [76, 77]. Alloyed 1-D structures have also been explored, which include core-shell type structures (the intricacies and properties of core-shell structures have been discussed in detail in the Sect. 5.6.2). The Pt-Pd, Pt-Au, and Pt-Ag porous nanorods have been shown to be resistant to dissolution, aggregation, and Ostwald ripening, besides showing enhanced ORR activity due to weaker Pt-O binding energy [78–81]. The core-shell nanowires are particularly highlighted for Pd-Pt combination. One method to prepare Pt-Pd alloy in nanowire formats is to use a sacrificial metal such as Cu, which is then replaced by Pd core, followed by Pt outer shell. This technique results in a polycrystalline structure with higher activity than Pt nanotubes. This improvement in the activity is mainly due to two effects: (1) ligand effect and (2) the Pd in the Pt surface. The Pt-Pd lattice shrinks slightly in comparison to Pt lattice. This leads to a reduced affinity toward oxygen improving the ORR [70].

The Pt-Ru alloy nanowires, core-shell nanowires, and hybrid combinations such as Ru nanowires decorated with Pt have been explored as the Pt-Ru duo is widely popular as anode electrocatalysts in DMFC due to the high tolerance toward CO poisoning offered by them [82–84]. While the Pt-Rh and Pt-Ru nanowires present higher stability than the equivalent nanoparticles, the Pt-free, Pd alloy-based 1-D structures such as Pd-Au and Pd-Ag are also showing promising performance in alcohol-based fuel cells. Bimetallic Au-Pd nanorods have also attracted attention for alkaline fuel cells [39].

Unlike nanoparticles, 1-D electrocatalysts can also be synthesized without support or on gas diffusion layers as hybrid electrocatalyst-GDL systems or gas diffusion

electrodes (GDE). Initial reports on the *in situ* single cell studies of these GDEs show promising potential for future [85, 86].

### 6.5.1.3 Two-Dimensional (2-D) Structures

The 2-D and 3-D electrocatalysts are complex networks comprising 0-D and 1-D nanostructures. The 1-D nanowires can grow vertically on the substrate forming 2-D nanowalls [87]. This highly oriented array, with a high surface to volume ratio, is a desired characteristic for the electrocatalysts. The porous nanoparticles forming 0-D catalysts can also be arranged into 2-D structures. Moreover, the hollow 2-D structures can increase the electrocatalytic activity without increasing the net amount of Pt. However, unlike 1-D, 2-D structures are less stable and are more likely to be decomposed. This is due to the presence of edges and borders, which aggravate their decomposition in aggressive environments. Among the multiplicity of Pt 2-D structures are nanowalls, nanosheets, nano prisms, nanodisks, and nanoplates. These structures consist of compacted Pt atoms linked through metallic bonds [88]. However, most of these structures are synthesized with the help of surfactants, which make the growth process very slow and inefficient for mass production.

Just like nanowires to nanowalls, nanoparticles can also be used to form 2-D nanoplate structures. Core-shell nanoplates have generated a lot of interest for use in PEFCs with the spotlight again being on the Pd@Pt combination [40, 89]. This structure enhances the electrocatalytic activity by reducing the adsorption of oxygen species, especially in ORR. Just like in the 0-D core-shell, in the 2D structure the core metal is first synthesized in the nanoplate form. Following this, Pt epitaxially grows over the core metal, resulting in the nanoplate core-shell. The surface of the nanoplates can be extremely smooth and the facets with the highest electrocatalytic activity can be chosen for exposure during the growth, increasing the overall performance. The Pt nanosheets is another structure that can be made from different types of crystals and internal structures, such as spheres and wires. For example, Song et al. prepared flat nanosheet with platinum dendrites. The authors reported that this structure was more resistant to ripening when exposed to FC environment than 0-D spheres or even 3-D structures prepared from 0-D [90].

Another interesting 2-D structure is nano wheel. The nanowheels consist of flat nanodisc with Pt forming disc-like micelles (called bicelles) synthesized using biceller surfactant templates. This unique and complex structure is gaining popularity but its use in fuel cells so far is elusive, which may be due to the intricate surfactant based preparation method [91].

Apart from Pt-Pd systems, 2-D and 3-D arrays of Pt-Au dendrites also seem to offer some advantages. The Au is chemically more stable and durable than Pd [92]. The Au 2-D electrocatalyst can form unique square sheets. Here Au crystallizes in the hexagonal close pack (hcp) structure instead of the traditional fcc structure as seen in spheres and particles. These differences change the properties of the nanostructure considerably as the exposed facets are no longer the same. Here, Au tends to stabilize Pt in the structure, especially during potential cycling, when Pt may suffer from dissolution, making Au-Pt an attractive alloy system, especially in complex 2-D formats [88].



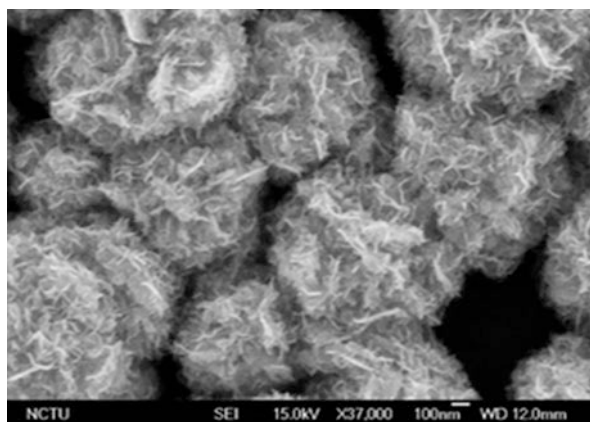
### 6.5.1.4 Three Dimensional (3-D) Structures

The Pt 3-D structures have higher catalytic activity than 0-D, 1-D, and 2-D structures. However, these structures are difficult to synthesize and it is not easy to control their homogeneity. In order to achieve 3-D morphology, Pt can be synthesized on the surface of a support [93]. The substrates used for growing 3-D nanostructures can vary from a large range of materials and shapes, such as carbon black spheres, graphene oxide sheets, a metallic substrate, and others. As mentioned earlier, the substrates influence the final properties of the electrocatalyst and must be carefully chosen. The 3-D structures can consist of electrocatalysts with 1-D structure, such as nanowires organized into a 3-D network. Besides increasing the activity, the formation of 3-D structures increases the stability of the electrocatalyst. While 2-D nanostructures present harsh edges, 3-D nanostructures do not necessarily possess these. The elimination of the edges increases their durability.

One popular form of 3-D electrocatalysts is ordered arrays which are especially good for liquid fuel-based FCs [39]. The array arrangement increases the distribution and, consequently, the utilization of the liquid fuel. Nano dendrite is another common form of 3-D catalyst. Similar to other structures, it can be made of Pt and/or Pt alloys. The nanocubes shaped from nanowires are common displays of the 3-D structure. These nanocubes are highly ordered, which can enhance electrocatalytic properties due to the exposure of the highly active facets.

Besides Pt nanotubes and nanowires arranged in different arrays, another common 3-D structure is a nanoflower. Tiwari et al. reported a new technique using potential pulse plating to manufacture Pt nanoflowers (Fig. 6.4). These nanoflowers demonstrated higher electrocatalytic activity than Pt thin-film towards MOR and also showed better tolerance toward CO [94]. In a step further, Sun et al. developed a method to produce Pt nanoflower catalyst from the arrangement of nanowires for large-scale manufacturing. This method requires only 16 h to grow nanoparticles to nanowires and finally into nanoflowers [95]. The production of Pt high activity electrocatalyst with any structure is still very costly and one of the main challenges in a PEFC. The fact that the nanoflowers could be mass-produced generates potential

**Fig. 6.4** Pt Nanoflowers with preferential {100} and {110} facets synthesized on Si substrate using potential pulse plating (Printed with permission from Ref. [94] Royal Society of Chemistry ©2009)



for turning this high activity electrocatalyst into a good alternative for future commercialization.

Similar to 2-D nanostructures, the porous nanoparticles can grow and generate complex 3-D arrangements. The nanoflower morphology can also be prepared with the porous particles, further reducing the amount of Pt utilized [96]. However, agglomeration and nonuniform distribution is more common in porous structures and requires a much more controlled manufacturing method.

The hollow 3-D structure is another interesting approach for Pt catalyst. This approach maximizes the surface to volume ratio and has the potential to reduce the loading of Pt to lower values (compared to pure Pt catalysts). Hollow cubes can be made from hollow nanospheres or hollow nanowires. However, these structures are even more complex than the ones discussed above, resulting in difficult synthesis and homogeneity control. One example of this structure is the 3-D dendritic Pt nanostructure prepared by Wang et al. [97].

The technology of Pt nanowires is far more developed than the technology of the other noble metals. Thus, many of the 3-D arrangements with other precious metals are still being developed with support materials, such as carbon nanostructures, polymers, and metal oxides.

The Pd nanowire arrays and Pd-Ru have been used as electrocatalyst [39] and demonstrate higher electrocatalytic activity than particles and 2-D Pd structures. The Pt-Pd and Pt-Ru 3-D arrays with nanowires have shown higher electrocatalytic activity than the Pt-based electrocatalysts due to the ligand effect [70]. Compared with 1-D electrocatalysts, these alloyed 3-D structures have the same advantages as Pt 3-D structures but also face the same challenges. However, as reported in the 2-D section, Au presents superior chemical stability. For this reason, Fang et al. prepared Au 3-D dendrite arrangements as an electrocatalyst, obtaining complex structures [98]. Interestingly, the 3-D arrangement of Pt-Ru in the ratio 1:1 presents enormous holes and spaces, but the ORR activity is not compromised when compared with 0-D Pt-Ru nanoparticles [99]. Unfortunately, despite all efforts from the scientific community to investigate 3-D catalyst structures for fuel cells, very few mass production techniques have been found. Therefore, these 3-D electrocatalysts are still far from commercial application.

### 6.5.2 Role of Alloying

Alloys of two or more metals have been studied exhaustively over the past few decades to explore better electrocatalytic activity. The Pt, although the best-known electrocatalyst material, suffers from stability issues due to Ostwald ripening in the acidic PEMFC environment. Alloying with other noble metals is, therefore, useful in not only reducing the Pt-related costs but also improving durability and electrocatalytic activity. The specific advantage of alloys is the opportunity to modify electronic properties leading to shifting in the d-band center in order to achieve enhanced interaction and optimum bonding with oxygen species to improve ORR and MOR efficiencies. There is also the economic advantage when alloying Pt with



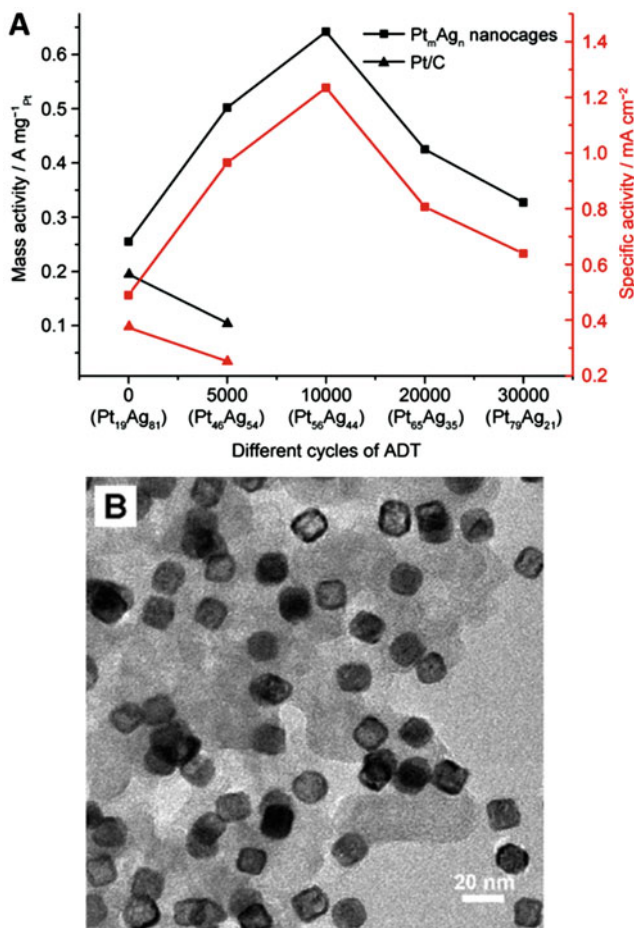
other less expensive noble metals to improve the overall reaction efficiency of ORR. The key parameters to alloying are the choice of metals and ratio of alloying. The optimized alloying ratio will, in turn, depend on factors like synthesis method used, annealing temperatures, and other synthesis conditions.

The most commonly used noble metal for alloying with Pt is Ru, which has been extensively studied for DMFC anode applications. The noble metals, Au, Ag, and Pd have also been very popular [100]. Coreduction using strong reducing agents is one of the most widely used methods to prepare alloys with predetermined compositions. Selection of metal precursor, reaction time duration, and temperature are also essential for driving the reaction kinetics to tune the nanostructures of the Pt-alloy [101, 103]. As previously mentioned, Pd nanocubes are capable of very efficient ORR. However, these suffer from low stability. Yan et al. alloyed Pd with Rh using highly controlled reaction kinetics to form cubic as well as octahedral Pd-Rh alloys for ORR application. The alloys demonstrated excellent stability with less than 25% loss in mass activity as compared to more than 56% for commercial Pt/C in ex situ ORR studies [104]. More recently, ordered alloys with defined and innovative structures using Pt-Pd, Pt-Ag have gathered significant interest [105]. Yang et al. synthesized Pt-Ag hollow nanocages of different compositions using a galvanic replacement method. These 18 nm nanocages with 3 nm wall thickness demonstrated ORR activity 3.3 times higher than that of commercial Pt/C in ex situ rotating disc electrode tests and significantly higher durability, which can be seen in Fig. 6.5 [106]. Kodama et al. reported a unique modified stepped Pt single crystal structure with Au atoms selectively deposited on {100} step sites, as PEFC cathode catalysts. The modified structures were reported to show 70% increase in ORR [107]. In some studies, core-shell structures are also considered as alloys. Indeed these are alloys with a defined structure. Thus, in this chapter, we have discussed core-shells within the alloys as structured alloys.

### 6.5.2.1 Structured Alloys: Core-Shell Structures

A core-shell structure consists of a non-Pt core covered by a Pt shell. These can be prepared using various methods (Cu-mediated deposition, atomic layer deposition, electrochemical deposition, etc.) and a variety of studies exploring effects of core composition, shell thickness, size as well as different architectures (icosahedra, tetrahedron, octahedron, and nanowires) have been carried out [108]. Such a structure offers three main benefits over conventional 0-, 1-, and 2-D morphologies.

- (a) Improvement of the utilization of Pt atoms. In conventional nano electrocatalysts, only the surface atoms are exposed for participation in the electrochemical reactions leaving about 60–70% of the atoms inside the particles as unused.
- (b) Cost reduction. By replacing the core with less expensive metals (Pd, Ru, Re), the cost of the catalyst can be significantly reduced.
- (c) Strain and ligand effect. The Pt atom monolayer shell on the core experiences tensile and compressive strain when deposited on a non-Pt core due to the lattice constant mismatch. This strain can be utilized to shift the d-band center of Pt in



**Fig. 6.5** (a) Graph showing mass activity and specific activity of Pt-Ag nanocages of different compositions in comparison with Pt/C; (b) TEM image of Pt-Ag nanocages supported on carbon black (Modified with permission from Ref. [106] American Chemical Society © 2016)

order to modulate the binding energies of the reaction species (adsorbates). The DFT studies have also confirmed the presence of the electronic (ligand) effect arising due to coupling between the core and Pt shell [7, 109, 110].

Zang et al. thoroughly explored the correlations between d-band activities and the choice of noble metal forming the core (Ir, Ru, Rh, Pd, Ag, and Au) [111]. Various other studies have also investigated the tuning of ORR activity via core-shell method. The Pd{111} core shows a significant lowering of Pt d-band center. Alloys of Pd with other noble metals (Ir, Au) have also been studied as core shells. The Au {111} has a significantly larger lattice constant than Pt, and a tensile stress occurs when Pt monolayer is supported on this core. However, Au@Pt (using Au{111})

were found to be two times more active than bulk Pt{111}. It has also been reported that the compressive strain on Au nanoparticles (3 nm) results in higher activity than the same sized Pd nanoparticles [112, 113]. Use of another interlayer, between the core and shell, (or multilayered core-shell) has also been studied with promising results. The Pd@Pt ORR activity shows three times enhancement with the introduction of a Pd@Au interlayer. Structures other than spherical, such as cubes and octahedrons, for the core have also shown promising performance. A number of studies have reported excellent performance by Ir@Pt and Au@Pt nano dendritic structures. Apart from the interaction between the core and the Pt shell, the improved activity was attributed to a higher number of corner and edge sites present in such structures. Different ratios of Ir/Re in the core with Pt and Pt/Pd shell reportedly resulted in different OH binding energies, hence modifying ORR activity [113–116].

Core-shells, however, suffer from degradation occurring due to many reasons including, core depletion, particle growth, and coalescence due to Pt dissolution resulting in thicker Pt shell and complete loss of core-shell morphology due to evolution of nanoporosity (formation of hollow particles) [108]. Scaling up of the production of such structures is also a concern if these need to be explored for real PEFC systems. Initial in situ tests, however, have been quite encouraging where Pd@Pt system showed only a 37% loss (after 100,000 potential cycles) in mass activity as opposed to 70% loss (in 60,000 cycles) in the case of commercial Pt/C [117].

### 6.5.3 Separation Between Electrocatalyst Nanoparticles

The separation between particles is defined as the interparticle distance, which is the center-to-center distance between two adjacent particles. A few studies have looked into this aspect and found that when particles are close to each other within a certain critical distance there is some kind of mutual influence and interaction. There are, however, conflicting reports over whether this has a positive or negative influence on the PEFC performance. One theory suggests the occurrence of a shielding or diffusion effect where nanoparticles, within a critical distance (suggested to be  $\leq 18$  for oxygen and  $\leq 20$  nm for air by Watanabe et al.), modify the spherical diffusion of isolated Pt nanoparticle to a planar diffusion similar to that in Pt films reducing the ORR activity [118–120]. Some other studies have also argued this to be the effect of the ratio of interparticle distance and particle size. There is another theory, which supports a more positive influence of interparticle distance or the ratio of interparticle distance and particle size. This one advocates that when adjacent particles are close enough such that their interparticle distance is equal to the sum of their radii then these form an extended layer increasing catalytic activity due to the potential drop in the electrochemical double layer. This has been correlated with experimental studies showing a shift of the Pt oxide reduction peak toward higher potentials, confirming weaker adsorption of oxygen species and the consequently increased ORR activity [119, 121, 122]. There is also a lack of consensus among researchers over whether the mass activity is dependent on particle size or interparticle distance. Nevertheless, results from various systematic studies over

the years surely confirm that the activity of electrocatalysts is not dependent on just one parameter. Interparticle distance, particle size as well as ratio of the two along with the metal loading and dispersion on the support, all play their distinctive roles in shaping the overall electrocatalytic behavior [7, 123, 124].

#### 6.5.4 Electrocatalyst Dispersion and Loading on Support

To achieve a homogeneous and good dispersion of the electrocatalyst on the support, it is important to control the homogeneity in the size and shape of Pt nanoparticles. Four major parameters must be considered for this. During the nucleation process, for the clusters of Pt atoms to form nuclei and then grow into nanoparticles, they must overcome the barrier known as critical free energy. The clusters, which do not overcome this value, disintegrate easily. The second important parameter is the critical radius, which is the minimum radius that the cluster must achieve in order to avoid disintegration. The third parameter is the number of clusters in function of the radius. The fourth major parameter is the nucleation rate, i.e., the rate at which the nanoparticle clusters grow [65]. Uniformity in the size of these clusters is also important to the electrochemical properties of the catalyst, which further depends on the growth process as well as the support or the substrate on which the electrocatalyst is grown or deposited. A huge variety of carbon and noncarbon nanostructured supports have been studied. These supports are not only important for dispersion and distribution of electrocatalysts but with their conductivity properties and other synergistic interactions with an electrocatalyst, nanostructured supports are also known to have the potential to enhance their catalytic activity and improve tolerance towards poisoning. Several reviews have extensively reported on the vast selection of catalyst supports studied over the decades [125–128].

The electrocatalyst loading is defined as the amount (usually in weight%) of nanostructured electrocatalyst deposited on the support. Together the catalyst-support it forms the catalyst layer (CL), which is supported on a gas diffusion layer inside the fuel cell system. For achieving a desired net amount of electrocatalyst (at anode or cathode), the choice of a high or low Pt loading catalyst-support system also entails a significant change in the amount of carbon support and Nafion (binder) added to the CL. The changes in the Pt:C ratio and the carbon:Nafion ratio and the resultant CL composition and thickness can thus significantly influence the overall PEFC performance. This is because the diffusivity of reactant gases is dependent on the thickness and porosity of the CL. Low Pt:C ratios give rise to increased mass transport resistance toward the diffusion of gases due to the more complex and longer reactant pathway, negatively influencing the PEFC performance. On the other hand, a high Pt:C ratio results in very little Nafion which decreases the protonic conductivity. Several studies have been performed to optimize the CL and Pt loading. It is for this reason that a 20 wt.% loading is used in commercial Pt/C for PEFC applications. Moreover, the diffusivity of an oxygen molecule is slower as compared to hydrogen.

Thus a longer path due to higher CL can further slowdown the ORR process [26, 129–131]. Studies on similar lines have also been performed on DMFC anode. A study by Lee et al. revealed that 80 wt.% PtRu/C with thinnest CL showed superior performance in the DMFC single cell test as compared to 40 and 60 wt.% catalysts [129]. One can expect these ratios to vary when studies using the variety of 1-, 2-, and 3-D structures are performed and optimized in real FC systems.

It is important to appreciate that the within a working fuel cell, many more parameters come into play (apart from those related to catalysts alone as discussed here), a flavor of which can be gained from the complexity of CL and its interaction with diffusion gases.

---

## 6.6 Recycling Precious Metal Electrocatalysts

The global production of Pt in 2016 was just over 170 metric tons [132]. Based on the estimated production of 100 million cars each with a 50 kW unit with the targeted 2020 Pt usage of 0.125 g/W, an annual production of nearly 689 tons of Pt is required [15]. The total Pt reserves in the world are estimated to be 40,000 tons (assuming mining down to the depth of 2 km) [133]. Based on the above estimates, it is evident that recycling of Pt, as well as other noble metals (which also have limited availability on earth), must be investigated and undertaken on a large scale in order to make large-scale fuel cell production and usage sustainable.

It is essential to remind oneself that catalysts are not consumed in any chemical or electrochemical reaction (the role of a catalyst is to facilitate a reaction and not participate in it). Hence, the recycling of metals is a practical and feasible solution. Recycling of precious as well as other metals extends beyond their use in just fuel cells (precious metals such as Au, Pd are used in electronic applications like computer motherboards, catalytic converters, other metals used in photovoltaics, rechargeable batteries). Even in the case of applications/reactions, where metals are converted to oxides or other forms, pure metal can always be reclaimed.

Recycling is not just important from economic perspectives but it also has very positive environmental implications. A state-of-the-art recycling facility is capable of achieving up to 95% recovery of platinum group metals. The traditional recycling facilities consist of integrated smelter-refinery set ups that depend on the recycling chain (collection of old products, sorting/dismantling, preprocessing, etc.) for a regular supply of materials for recycling [134].

More recently, other biological methods have been explored for reclaiming precious metals from waste leachates, mixed metal liquid wastes, and spent automotive catalysts. The traditional smelter refineries face limitations concerning economic viability when it comes to recycling small amounts of metals. For example, the ultrathin coated computer hard disc does not normally have a positive net value due to the processing costs involved. Similar implications could be faced in the case of small FC stacks (using low quantities of electrocatalyst). The use of easy to grow bacterial cultures can maximize the recycling of precious metals by utilizing untapped sources, which are otherwise considered negative net value in the

traditional recycling industry. The use of a variety of bacteria such as *D. desulfurizing*, *Escherichia*, *Shewanella*, *Ralstonia*, and *Cupriavidus* have been studied which are highly capable of selectively absorbing precious metal salts to reduce them to pure metals in the form of nanoparticles. These bacteria have special enzymes and hydrogenases to allow the identification, uptake, and internalization of metal salts into the bacterial cells where these are reduced to metal nanoparticles [134–137]. Many of the bacteria are commonly used in the biotechnology industry and can be sourced as waste cultures, thereby further reducing the costs of this bioreclamation process. These precious metal nanoparticles supported on the carbon-based bacterial scaffold have also demonstrated potential as electrocatalyst support systems with minimum further treatment and show promising potential for future use in PEFCs [138–140].

---

## 6.7 Future Prospects and Outlook

An enormous body of research has been put into the search for the most durable, efficient (electrocatalytically active), and economic electrocatalysts for anode and cathode application in PEFCs. Promising results on novel alloys and nanostructured morphologies combining a variety of metals have been extensively explored. While anode loading of Pt has been minimized to achieve the 2020 DOE targets, the cathode loading still needs to be reduced further to improve the commercial viability of FCs. Despite tremendous efforts made to study and improve the efficiency of non-precious metals toward ORR, even the best of these systems are either not durable enough or not efficient enough to be comparable with the Pt and other noble metal-based electrocatalyst systems. Their current state does not make them suitable for commercial applications as that would only lead to higher overall costs. Nonetheless, it must be appreciated that some of these non-precious metal systems certainly hold prospects for improvement and investigations on these must continue.

The Pt continues to be the most effective electrocatalyst, especially in the absence of sufficient long-term, in situ, single cell PEFC studies of the freshly identified electrocatalysts, which seem to offer tremendous potential. Alloys of Pt with other precious metals along with the use of innovative morphological structures such as core-shells, nanocages, nanowires, and dendritic, hollow 3-D structures have shown immense potential as ORR electrocatalysts. The Pd and Au seem to be the more promising among other precious metals, although these are also the most widely investigated noble metals (following Pt). In fact, Pd@Pt structures have shown the potential to decrease Pt loading to as low as 0.025 mg/cm<sup>2</sup> but the stability of these remains a concern [141]. Single cell studies including long-term accelerated stress tests and durability studies need to be performed on the selectively optimized and identified noble metal electrocatalyst systems to understand their performance and challenges in real PEFC systems. Other, less studied noble metals like Rh and Ir have shown good potential in combination with Pd, Pt, and Au but more studies will be needed to better understand and help improve the durability of these alloy systems. It is imperative that all potential electrocatalysts be thoroughly investigated with a

variety of material characterization techniques (such as transmission electron microscopy, X-ray diffraction, XPS, and high-angle annular dark-field imaging) along with relevant *ex-situ* electrochemical characterizations in order to have a good overall understanding of their behavior and potential before being tested in real PEFC systems. Development of noble metal electrocatalysts will continue to be of extreme importance in the foreseeable future in order to realize the dream of large-scale commercialization of PEFC-based transport and other portable applications with suitable economic viability. Hence, research and development must continue to minimize costs and maximize the efficiency of noble metal electrocatalysts until other cheaper alternatives (such as noble metal-free electrocatalysts or even metal-free electrocatalysts) can reach the desirable performances.

---

## References

1. J.-J. Hwang, *Renew. Sust. Energ. Rev.* **19**, 220–229 (2013)
2. J. Stacy, Y.N. Regmi, B. Leonard, M. Fan, *Renew. Sust. Energ. Rev.* **69**, 401–414 (2017)
3. G.A. Florida's, P. Christodoulides, *Environ. Int.* **35**(2), 390–401 (2009)
4. M. Irani, M. Fan, H. Ismail, A. Tewari, B. Dutcher, A.G. Russell, *Nano Energy* **11**, 235–246 (2015)
5. Y. Kong, G. Jiang, M. Fan, X. Shen, S. Cui, A.G. Russell, *Chem. Commun.* **50**(81), 12158–12161 (2014)
6. S. Cui, W. Cheng, X. Shen, M. Fan, A. Russell, Z. Wu, X. Yi, *Energy Environ. Sci.* **4**(6), 2070–2074 (2011)
7. M. Shao, Q. Chang, J.-P. Dodelet, R. Chenitz, *Chem. Rev.* **116**, 3594–3657 (2016)
8. M. Matsunaga, T. Fukushima, K. Ojima, *World Electric Vehicle Journal* **3**, 2032–6653 (2009)
9. S. Aso, M. Kizaki, Y. Nonobe, Development of fuel cell hybrid vehicles in Toyota, in *Proceedings of the Power Conversion Conference*, Nagoya, Apr 2007. <https://doi.org/10.1109/PCCON.2007.37317>
10. D. Wenger, W. Polifke, E. Schmidt-Ihn, T. Abdel-Baset, S. Maus, *Int. J. Hydrog. Energy* **34**, 6265–6270 (2009)
11. Mercedes-Benz F-cell world drive in Europe: legs 1–5. <http://www.emercedesbenz.com/autos/mercedes-benz/concept-vehicles/mercedes-benz-f-cell-world-drive-in-europe-legs-1-5/>. Accessed 03 Mar 2017
12. V.P. McConnell, *Fuel Cells Bull.* **1**, 12–15 (2007)
13. J.R. Healey, Fuel cell cars, in *Earth 3.0*, *Scientific American* (Sept 2008)
14. O.T. Holton, J.W. Stevenson, *Platin. Met. Rev.* **57**(4), 259–271 (2013)
15. Fuel cell technologies office multi-year research, development, and demonstration plan. [https://energy.gov/sites/prod/files/2014/12/f19/fcto\\_myrd\\_d\\_fuel\\_cells.pdf](https://energy.gov/sites/prod/files/2014/12/f19/fcto_myrd_d_fuel_cells.pdf)
16. M. Chokai, T. Daidou, Y. Nabae, *ECS Trans.* **64**(3), 261–270 (2014)
17. G. Wu, K.L. More, C.M. Johnston, P. Zelenay, *Science* **332**(6028), 443–447 (2011)
18. C.H. Choi, H.-K. Lim, M.W. Chung, J.C. Park, H. Shin, H. Kim, S.I. Woo, *J. Am. Chem. Soc.* **136**(25), 9070–9077 (2014)
19. M.P. Rodgers, L.J. Bonville, H.R. Kunz, D.K. Slattery, J.M. Fenton, *Chem. Rev.* **112**(11), 6075–6103 (2012)
20. D. Cao, G.Q. Lu, A. Wieckowski, S.A. Wasileski, M. Neurock, *J. Phys. Chem. B* **109**(23), 11622–11633 (2005)
21. S. Sriramulu, T.D. Jarvi, E.M. Stuve, *J. Electroanal. Chem.* **467**, 132–142 (1999)
22. C. Song, J. Zhang, Electrocatalytic oxygen reduction reaction, in *PEM Fuel Cell Electrocatalysts and Catalyst Layers*, (Springer, London, 2008), pp. 89–134



23. R.F. Morais, A.A. Franco, P. Sautet, D. Loffred, *Phys. Chem. Chem. Phys.* **17**, 11392–11400 (2015)
24. L. Zhang, Z. Xia, *J. Phys. Chem.* **C115**(22), 11170–11176 (2011)
25. D.-H. Lim, J. Wilcox, *J. Phys. Chem. C* **116**(5), 3653–3660 (2012)
26. E. Antolini, *Appl. Catal. B Environ.* **181**, 298–313 (2016)
27. J. Zhang, Q. Kuang, Y. Jiang, Z. Xie, *Nano Today* **11**, 661–667 (2016)
28. O. Deutschmann, H. Knözinger, K. Kochloeff, T. Turek, Heterogeneous catalysis and solid catalysts, in *Ullmann's Encyclopedia of Industrial Chemistry* (2009). [https://doi.org/10.1002/14356007.a05\\_313.pub2](https://doi.org/10.1002/14356007.a05_313.pub2)
29. J. Cheng, P. Hu, *J. Am. Chem. Soc.* **130**(33), 10868–10869 (2008)
30. T. Bligaard, J.K. Nørskov, S. Dahl, J. Matthiesen, C.H. Christensen, J. Sehested, *J. Catal.* **224**, 206–217 (2004)
31. P. Sabatier, Hydrogénations et deshydrogénations par catalyze. *Ber. der Dtsch. Chem. Ges.* **44** (3), 1984–2001 (1911)
32. A.R. Morris, M.D. Skoglund, J.H. Holles, *Appl. Catal. A Gen.* **489**, 98–110 (2015)
33. K.A. Kuttiyiel, K. Sasaki, Y.M. Choi, D. Su, P. Liu, R.R. Adzic, *Energy Environ. Sci.* **5**(1), 5297–5304 (2012)
34. K. Zhou, Y. Li, *Angew. Chem. Int. Ed.* **51**(3), 602–613 (2012)
35. J.X. Wang, H. Inada, L. Wu, Y. Zhu, Y. Choi, P. Liu, W.P. Zhou, R.R. Adzic, *J. Am. Chem. Soc.* **131**(47), 17298–17302 (2009)
36. J.K. Nørskov, J. Rossmeisl, A. Logadottir, L. Lindqvist, *The. J. Phys. Chem. B* **108**(46), 17886–17892 (2004)
37. G. Centi, S. Perathoner, *Eur. J. Inorg. Chem.* **2009**, 3851–3878 (2009)
38. A. Chen, P.F. Holt-Hindle, *Chem. Rev.* **110**, 3767–3804 (2010)
39. Y. Qiao, C.M. Li, *J. Mater. Chem.* **21**, 4027–4036 (2011)
40. L. Bu, N. Zhang, S. Guo, X. Zhang, J. Li, J. Yao, T. Wu, G. Lu, J.-Y. Ma, D. Su, X. Huang, *Science* **354**, 1410–1414 (2016)
41. C.W.B. Bezerra, L. Zhang, H. Liu, K. Lee, A.L.B. Marques, E.P. Marques, H. Wang, J. Zhang, *J. Power Sources* **173**, 891–908 (2007)
42. S. Garbarino, A. Pereira, C. Hamel, E. Irissou, M. Chaker, D. Guay, *J. Phys. Chem. C* **114**, 2980–2988 (2010)
43. Y. Liu, L. Zhang, B.G. Willis, W.E. Mustain, *ACS Catal.* **5**(3), 1560–1567 (2015)
44. L.R. Merte, F. Behafarid, D.J. Miller, D. Friebel, S. Cho, F. Mbuga, D. Sokaras, R. Alonso-Mori, D. Weng T-C Nordlund, A. Nilsson, B.R. Cuenya, *ACS Catal.* **2**(11), 2371–2376 (2012)
45. K. Yamamoto, T. Imaoka, W.-J. Chun, O. Enoki, H. Katoh, M. Takenaga, A. Sono, *Nat. Chem.* **1**(5), 397–402 (2009)
46. N.M. Marković, T.J. Schmidt, V. Stamenković, P.N. Ross, *Fuel Cells* **1**(2), 105–116 (2001)
47. M.D. Maciá, J.M. Campiña, E. Herrero, J.M. Feliu, *J. Electroanal. Chem.* **564**(0), 141–150 (2004)
48. A. Kuzume, E. Herrero, J.M. Feliu, *J. Electroanal. Chem.* **599**(2), 333–343 (2007)
49. A.M. Gómez-Marín, R. Rizo, J.M. Feliu, *Beilstein J. Nanotechnol.* **4**, 956–967 (2013)
50. A.M. Gómez-Marín, J.M. Feliu, *Catal. Today* **244**(0), 172–176 (2015)
51. N. Hoshi, M. Nakamura, A. Hitotsuyanagi, *Electrochim. Acta* **112**, 899–904 (2013)
52. B. Wu, N. Zheng, *Nano Today* **8**(2), 168–197 (2013)
53. B.Y. Xia, H.B. Wu, X. Wang, X.W. Lou, *Angew. Chem.* **125**(47), 12563–12566 (2013)
54. D. Li, C. Wang, D.S. Strmcnik, D.V. Tripkovic, X. Sun, Y. Kang, M. Chi, J.D. Snyder, D. Van der Vliet, Y. Tsai, V.R. Stamenkovic, S. Sun, N.M. Markovic, *Energy Environ. Sci.* **7**(12), 4061–4069 (2014)
55. M. Shao, A. Peles, K. Shoemaker, *Nano Lett.* **11**, 3714–3719 (2011)
56. S. Mukerjee, J. McBreen, *J. Electroanal. Chem.* **448**, 163–171 (1998)
57. Y. Takasu, Y.N. Ohashi, X.G. Zhang, Y. Murakami, H. Minagawa, S. Sato, K. Yahikozawa, *Electrochim. Acta* **41**, 2595–2600 (1996)
58. S. Park, Y. Xie, M.J. Weaver, *Langmuir* **18**, 5792–5798 (2002)



59. K. Bergamaski, A.L.N. Pinheiro, E. Teixeira-Neto, F.C. Nart, *J. Phys. Chem. B* **110**(39), 19271–19279 (2006)
60. B.D. McNicol, P. Attwood, R.T. Short, *J. Chem. Soc. Faraday Trans.* **77**, 2017–2028 (1981)
61. S.J. Yoo, Y.T. Jeon, Y.H. Cho, K.S. Lee, Y.E. Sung, *Electrochim. Acta* **55**, 7939–7944 (2010)
62. M. Shao, *J. Power Sources* **196**(5), 2433–2444 (2011)
63. M. Shao, T. Yu, J.H. Odell, M. Jin, Y. Xia, *Chem. Commun.* **47**(23), 6566–6568 (2011)
64. L. Ou, S. Chen, *J. Phys. Chem. C* **117**(3), 1342–1349 (2013)
65. Z. Peng, H. Yang, *Nano Today* **4**, 143–164 (2009)
66. L. Zhang, L.T. Roling, X. Wang, M. Vara, M. Chi, J. Liu, S. Choi, J. Park, J.A. Herron, Z. Xie, M. Mavrikakis, Y. Xia, *Science* **349**(6246), 412–416 (2015)
67. X. Wang, L. Figueroa-Cosme, X. Yang, M. Luo, J. Liu, Z. Xie, Y. Xia, *Nano Lett.* **16**(2), 1467–1471 (2016)
68. Y. Lu, S. Du, R. Steinberger-Wilkens, *Appl. Catal. B Environ.* **199**, 292–314 (2016)
69. R.K. Joshi, J.J. Schneider, *Chem. Soc. Rev.* **41**, 5285–5312 (2012)
70. C. Koenigsmann, S.S. Wong, *Energy Environ. Sci.* **4**, 1161–1176 (2011)
71. Y. Shao, G. Yin, Y. Gao, *J. Power Sources* **171**, 558–566 (2007)
72. K. MTM (ed.), *Fuel Cell Catalysts* (Wiley-Interscience, Hoboken, 2009)
73. C. Koenigsmann, W.P. Zhou, R.R. Adzic, E. Sutter, S.S. Wong, *Nano Lett.* **10**, 2806–2811 (2010)
74. K.S. Napolskii, P.J. Barczuk, S.Y. Vassiliev, A.G. Veresov, G.A. Tsirlina, P.J. Kulesza, *Electrochim. Acta* **52**, 7910–7979 (2007)
75. S. Sun, F. Jaouen, J.-P. Dodelet, *Adv. Mater.* **20**, 3900–3904 (2008)
76. L. Xiao, L. Zhuang, Y. Liu, J. Lu, H.D. Abruña, *J. Am. Chem. Soc.* **131**(2), 602–608 (2009)
77. S. Choi, H. Jeong, K.-H. Choi, J.Y. Song, J. Kim, *ACS Appl. Mater. Interfaces* **6**(4), 3002–3007 (2014)
78. T.H. Yeh, C.W. Liu, H.S. Chen, K.W. Wang, *Electrochem. Commun.* **31**, 125–128 (2013)
79. Y.C. Tseng, H.S. Chen, C.W. Liu, T.H. Yeh, K.W. Wang, *J. Mater. Chem. A* **2**, 4270–4275 (2014)
80. Y.T. Liang, S.P. Lin, C.W. Liu, S.R. Chung, T.Y. Chen, J.H. Wang, K.W. Wang, *Chem. Commun.* **51**, 6605–6608 (2015)
81. Y.T. Liang, C.W. Liu, H.S. Chen, T.J. Lin, C.Y. Yang, T.L. Chen, C.H. Lin, M.C. Tu, K.W. Wang, *RSC Adv.* **5**, 39205–39208 (2015)
82. G.-Y. Zhao, C.-L. Xu, D.-J. Guo, H. Li, H.-L. Li, *J. Power Sources* **162**(1), 492–496 (2006)
83. C. Koenigsmann, D.B. Semple, E. Sutter, S.E. Tobierre, S.S. Wong, *ACS Appl. Mater. Interfaces* **5**(12), 5518–5530 (2013)
84. L. Yang, M.B. Vukmirovic, D. Su, K. Sasaki, J.A. Herron, M. Mavrikakis, S. Liao, R.R. Adzic, *J. Phys. Chem. C* **117**(4), 1748–1753 (2013)
85. W.C. Choi, S.I. Woo, *J. Power Sources* **124**, 420–425 (2003)
86. K. Lin, Y. Lu, S. Du, X. Li, H. Dong, *Int. J. Hydrog. Energy* **41**(18), 7622–7630 (2016)
87. H.T. Ng, J. Li, M.K. Smith, P. Nguyen, A. Cassell, J. Han, M. Meyyappan, *Science* **300**, 1249–1249 (2003)
88. Z. Fan, X. Huang, C. Tan, H. Zhang, *Chem. Sci.* **6**, 95–111 (2015)
89. W. Wang, Y. Zhao, Y. Ding, *Nanoscale* **7**, 11934–11939 (2015)
90. Y. Song, M.A. Hickner, S.R. Challa, R.M. Dorin, R.M. Garcia, H. Wang, Y.-B. Jiang, P. Li, Y. Qiu, F. van Swol, C.J. Medforth, J.E. Miller, T. Nwoga, K. Kawahara, W. Li, J.A. Shelnett, *Nano Lett.* **9**, 1534–1539 (2009)
91. Y. Song, R.M. Dorin, R.M. Garcia, Y.-B. Jiang, H. Wang, P. Li, Y. Qiu, F. van Swol, J.E. Miller, J.A. Shelnett, *JACS* **130**, 12602–12603 (2008)
92. S. Guo, E. Wang, *Nano Today* **6**, 240–264 (2011)
93. A.A. Ensafi, M. Jafari-Asl, B. Rezaei, *Electrochim. Acta* **130**, 397–405 (2014)
94. J.N. Tiwari, F.-M. Pan, K.-L. Lin, *New J. Chem.* **33**, 1482–1485 (2009)
95. S.H. Sun, D.Q. Yang, D. Villers, G.X. Zhang, E. Sacher, J.P. Dodelet, *Adv. Mater.* **20**, 571–574 (2008)

96. X. Teng, X. Liang, S. Maksimuk, H. Yang, *Small* **2**, 249–253 (2006)
97. L. Wang, Y. Yamauchi, *Chem. Mater.* **21**, 3562–3569 (2009)
98. J. Fang, X. Ma, H. Cai, X. Song, B. Ding, *Nanotechnology* **17**, 5841–5845 (2006)
99. A. Morozan, B. Jousselme, S. Palacin, *Energy Environ. Sci.* **4**, 1238–1254 (2011)
100. G. Fu, K. Wu, J. Lin, Y. Tang, Y. Chen, Y. Zhou, T. Lu, *J. Phys. Chem. C* **117**(19), 9826–9834 (2013)
101. M.-S. Hyun, S.-K. Kim, B. Lee, D. Peck, Y. Shul, D. Jung, *Catal. Today* **132**(1–4), 138–145 (2008)
102. Y.H. Lee, G. Lee, J.H. Shim, S. Hwang, J. Kwak, K. Lee, H. Song, J.T. Park, *Chem. Mater.* **18** (18), 4209–4211 (2006)
103. Y.-J. Wang, N. Zhao, B. Fang, H. Li, X.T. Bi, H. Wang, *Chem. Rev.* **115**, 3433–3467 (2015)
104. Y. Yan, F. Zhan, J. Du, Y. Jiang, C. Jin, M. Fu, H. Zhang, D. Yang, *Nanoscale* **7**, 301–307 (2015)
105. J.W. Hong, S.K. Kang, B.-S. Choi, D. Kim, S.B. Lee, S.W. Han, *ACS Nano* **6**(3), 2410–2419 (2012)
106. X. Yang, L.T. Rolling, M. Vara, A.O. Elnabawy, M. Zhao, Z.D. Hood, S. Bao, M. Mavrikakis, Y. Xia, *Nano Lett.* **16**, 6644–6649 (2016)
107. K. Kodama, R. Jinnouchi, N. Takahashi, H. Murata, Y. Morimoto, *J. Am. Chem. Soc.* **138**(12), 4194–4200 (2016)
108. M. Oezaslan, F. Hasché, P. Strasser, *The. J. Phys. Chem. Lett.* **4**(19), 3273–3291 (2013)
109. B. Hammer, J.K. Nørskov, *Adv. Catal.* **45**, 71–129 (2000)
110. F. Calle-Vallejo, M.T.M. Koper, A.S. Bandarenka, *Chem. Soc. Rev.* **42**(12), 5210–5230 (2013)
111. J.L. Zhang, M.B. Vukmirovic, Y. Xu, M. Mavrikakis, R.R. Adzic, *Angew. Chem. Int. Ed.* **44** (14), 2132–2135 (2005)
112. Y. Iijima, T. Kondo, Y. Takahashi, Y. Bando, N. Todoroki, T. Wadayama, *J. Electrochem. Soc.* **160**(8), F898–F904 (2013)
113. M. Shao, A. Peles, K. Shoemaker, M. Gummalla, P.N. Njoki, J. Luo, C.-J. Zhong, *J. Phys. Chem. Lett.* **2**, 67–72 (2011)
114. B. Lim, X. Lu, M. Jiang, P.H.C. Camargo, E.C. Cho, E.P. Lee, Y. Xia, *Nano Lett.* **8**(11), 4043–4047 (2008)
115. G. Zhang, Z.-G. Shao, W. Lu, G. Li, F. Liu, B. Yi, *Electrochem. Commun.* **22**, 145–148 (2012)
116. H.I. Karan, K. Sasaki, K. Kuttiyiel, C.A. Farberow, M. Mavrikakis, R.R. Adzic, *ACS Catal.* **2** (5), 817–824 (2012)
117. K. Sasaki, H. Naohara, Y. Cai, Y.M. Choi, P. Liu, M.B. Vukmirovic, J.X. Wang, R.R. Adzic, *Angew. Chem. Int. Ed.* **49**(46), 8602–8607 (2010)
118. M. Watanabe, H. Sei, P. Stonehart, *J. Electroanal. Chem.* **261**, 375–387 (1989)
119. H. Yang, S. Kumar, S. Zou, *J. Electroanal. Chem.* **688**, 180–188 (2013)
120. R.W. Lindstrom, Y.E. Seidel, Z. Jusys, M. Gustavsson, B. Wickman, B. Kasemo, R.J. Behm, *J. Electroanal. Chem.* **644**, 90–192 (2010)
121. K. Tammeveski, M. Arulepp, T. Tenno, C. Ferrater, J. Claret, *Electrochem. Acta* **42**, 2961–2967 (1997)
122. J. Speder, L. Altmann, M. Baumer, J.J.K. Kirkensgaard, K. Mortensen, M. Arenz, *RSC Adv.* **4**, 14971–14978 (2014)
123. M. Nesselberger, S. Ashton, J.C. Meier, I. Katsounaros, K.J.J. Mayrhofer, M. Arenz, *J. Am. Chem. Soc.* **133**(43), 17428–17433 (2011)
124. M. Nesselberger, M. Roefzaad, R.F. Hamou, P.U. Biedermann, F.F. Schweinberger, S. Kunz, K. Schloegl, G.K.H. Wiberg, S. Ashton, U. Heiz, K.J.J. Mayrhofer, M. Arenz, *Nat. Mater.* **12** (10), 919–924 (2013)
125. S. Sharma, B.G. Pollet, *J. Power Sources* **208**, 96–119 (2012)
126. N.S. Veizaga, V.I. Rodriguez, S.R. de Migue, *J. Electrochem. Soc.* **164**(2), F22–F31 (2017)
127. S. Sharma, M.N. Groves, J. Fennell, N. Soin, S.L. Horsewel, C. Malardier-Jugroot, *Chem. Mater.* **26**(21), 6142–6151 (2014)
128. Q. Xue, Z.Y. Yang, *Int. J. Hydrog. Energy* **41**(15), 6310–6315 (2016)
129. J.S. Lee, K.I. Han, S.O. Park, H.N. Kim, H. Kim, *Electrochim. Acta* **50**, 807–810 (2004)
130. A.L. Dicks, *J. Power Sources* **156**, 128–141 (2006)

131. E.A. Ticianelli, C.R. Derouin, S. Srinivasan, *J. Electroanal. Chem.* **251**, 275–295 (1998)
132. <https://www.statista.com/statistics/273645/global-mine-production-of-platinum>. Accessed 22 Mar 2017
133. R.G. Cawthorn, *S. Afr. J. Sci.* **95**, 481–489 (1999)
134. C. Hagelüken, *Platin. Met. Rev.* **56**(1), 29–35 (2012)
135. P. Yong, N.A. Rowson, J.P.G. Farr, I.R. Harris, L.E. Macaskie, *Environ. Technol.* **24**, 289–297 (2003)
136. A.N. Mabbett, D. Sanyahumbi, P. Yong, L.E. Macaskie, *Environ. Sci. Technol.* **40**, 1015–1021 (2006)
137. P. Yong, I.P. Mikheenko, K. Deplanche, M.D. Redwood, L.E. Macaskie, *Biotechnol. Lett.* **32**, 1821–1828 (2010)
138. S. Dimitriadis, N. Nomikou, A.P. McHale, *Biotechnol. Lett.* **29**, 545–551 (2007)
139. P. Yong, M. Paterson-Beedle, I.P. Mikheenko, L.E. Macaskie, *Biotechnol. Lett.* **29**, 539–544 (2007)
140. R.E. Priestley, A. Mansfield, J. Bye, K. Deplanche, A.B. Jorge, D. Brett, L.E. Macaskie, S. Sharma, *RSC Adv.* **5**(102), 84093–84103 (2015)
141. A. Kongkanand, N.P. Subramanian, Y. Yu, Z. Liu, H. Igarashi, D.A. Muller, *ACS Catal.* **6**, 1578–1583 (2016)



# Nanomaterials in Proton Exchange Membrane Fuel Cells

# 7

Yufeng Zhang, Rui Xue, Weijian Yuan, and Xiaowei Liu

## Contents

7.1	Introduction .....	200
7.2	Carbon Nanotubes (CNT) Used in Direct Methanol Fuel Cells (DMFCs) .....	202
7.3	Graphene Applied in Direct Methanol Fuel Cells (DMFCs) .....	207
7.3.1	Graphene Used as Barrier Layer .....	207
7.3.2	Graphene Used in Catalyst .....	209
7.4	Other Nanomaterials Applied in PEMFC .....	218
7.4.1	Zero-Dimensional Nanomaterials .....	218
7.4.2	One-Dimensional Nanomaterials .....	219
7.4.3	Two-Dimensional Nanomaterials .....	219
7.4.4	Three-Dimensional Nanomaterials .....	220
7.5	Conclusion .....	221
	References .....	221

## Abstract

With the rapid development of modern science and technology in the current society, environmental conservation and taking advantage of new energy sources have become the core strategies of sustainable development for society. Micro-energy technology has boasted a huge potential in market demand and attracted a great deal of interest in research and development since it is safe, efficient, and

## Author Contributions

Weijian Yuan is responsible for the part of “Graphene Used in Catalyst” and “Other Nanomaterials Applied in PEMFC.” Rui Xue is responsible for the part of “CNT Used in Catalyst” and “Graphene Used as Barrier Layer.” Yufeng Zhang and Xiaowei Liu are in charge of the design, modification, and validation of the whole manuscript.

Y. Zhang (✉) · R. Xue · W. Yuan · X. Liu  
MEMS Center, Harbin Institute of Technology, Harbin, China  
e-mail: [yufeng\\_zhang@hit.edu.cn](mailto:yufeng_zhang@hit.edu.cn)

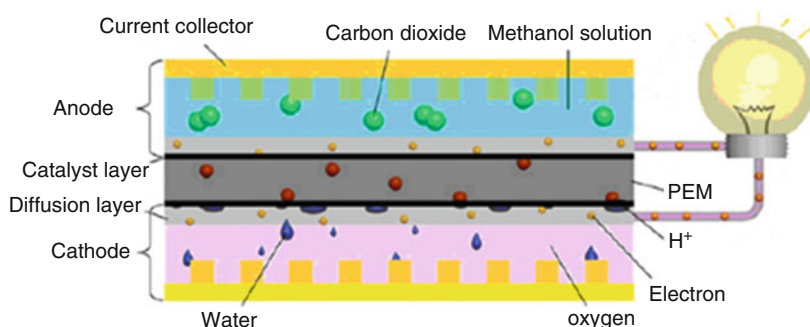
environmentally friendly and meets the goals for portable devices on the exterior, weight, and endurance. Although significant advancements have been achieved for proton exchange membrane fuel cells (PEMFCs) in recent years, PEMFCs still suffer from the key problems of low power density and fuel utilization, which are related, respectively, to poor reaction kinetics and methanol permeation through the membrane (*viz.*, methanol crossover). Nanomaterials recently have attracted lots of attention owing to their distinguishing physical and chemical characteristics. Among them, carbon-based nanostructured materials such as graphene (G) and carbon nanotube (CNTs) have been successfully applied in fuel cells. PEMFC combined with nanostructured materials has remarkable improvements compared with the traditional fuel cells.

---

## 7.1 Introduction

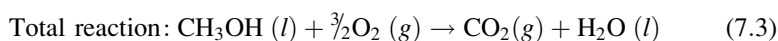
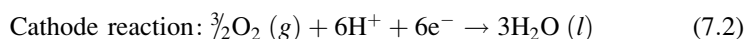
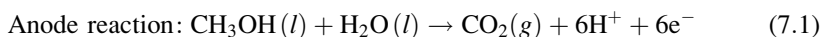
The increase in population and migration of individuals forming large metropolitan population centers requires a vast infrastructure to accommodate, transport, and feed. This necessitates the use of energy in the form of fossil fuels from the industrial revolution that caused an increase in carbon dioxide emission and potential global warming. The current approach is to lessen energy production from fossil fuels using alternative energy resources such as fuel cells, which convert chemical energy to electrical energy with zero or near-zero emission of harmful gases. With the rapid development and increasing market demand for micro-power sources, direct methanol fuel cell (DMFC) based on microelectromechanical system (MEMS) technology is currently becoming the research hotspot due to its great application prospect in the future. The DMFC has drawn significant attention due to its advantages such as eco-friendly, efficiency, high energy density, abundant reserves, and convenient for storage and transport [1–5].

The basic structure of DMFC is shown in Fig. 7.1 (from Yuan et al., with permission License 4153521292378 [6]), mainly composed of the anode plate, the membrane electrode assembly (MEA), and cathode plates. The MEA is made up of the diffusion layer (DL), catalyst, and proton exchange membrane (PEM). The anode plate of the flow field structure is mainly used to support the DL, distribute reactants, and collect current. The diffusion layers serve three purposes, as a gas, liquid, and electron channels, which are mainly used as a support for the catalytic layer, a collection of electrons, and the conduction of reactants and products. The catalytic layer provides a place for electrochemical reaction. The PEM as a key component in MEA serves as a proton conduction and separates the fuel and oxidant at the same time. In the anode reaction of DMFC, methanol solution flow field reaches the catalytic layer through the anode diffusion layer by convection and diffusion. Under the effect of catalyst particles, an oxidation reaction occurs, generating carbon dioxide ( $\text{CO}_2$ ) gas and releasing hydrogen protons ( $\text{H}^+$ ) and electron ( $\bar{e}$ ) simultaneously. The  $\text{CO}_2$  gas returns to the anode flow channel through the diffusion layer and ultimately discharges with the methanol solution flow. Meanwhile, the



**Fig. 7.1** Schematic of the basic structure of a DMFC [6]

electrons transfer from the anode compartment through the external circuit to the cathode compartment, generating direct electricity. The protons ( $H^+$ ) directly diffuse to the surface of the cathode catalyst layer through the PEM. These protons will react with oxygen, which transports through the diffusion layer to the surface of the cathode catalyst layer. The electrochemical reaction will result in  $H_2O$  production. Detailed chemical reaction Eqs. (7.1), (7.2), and (7.3) are shown as follows:



However, the key challenges for the intensive research on DMFC lie in the enhancement of DMFC performance. Current FC performance is suboptimal even with laboratory-based stacks, whose performance rapidly deteriorates in real FC industrial applications. There are a number of reasons for this suboptimal performance. One of the disadvantages is cathode flooding related to water management. After the water molecules on the surface of the cathode catalyst layer are generated, the molecule migrates through the diffusion layer into the cathode flow channel; however, if the gas flow rate is too low, some quantity of water molecules cannot be efficiently discharged into the air, causing flooding. The cathode water-flooding phenomenon will block both porosities of the porous diffusion layer and cathode flow channel. This blocking will cause a serious impediment to oxygen transport, and as a result, a shortage of the cathode gas supply will occur that, in turn, will lead to an increase in polarization, lowering FC performance. Therefore, the water generated in the cathode compartment should be discharged as quickly as possible. But at the same time, the PEM should contain water content, in order to mitigate mass transfer resistance. The DMFC cathode water management is a complex process, which is one of the key factors in limiting FC performance. One method to decrease cathode flooding is an introduction of high-speed airflow, which allows

water to flow at increased velocities. This area of research can be tailored toward design and construction of air-breathing DMFCs. To solve the key components of the material and structure design, researchers must focus on the development of nanostructured materials [7–14].

Methanol crossover is a second key problem hindering the development of DMFC. In the internal DMFC, part of methanol molecules which was not involved in the electrochemical reaction transmit through the PEM from the anode directly to the cathode. This phenomenon is called the methanol crossover. (1) Methanol crossover can cause degradation of DMFC performance, which mainly results from oxidizing reaction of methanol molecules penetrating to the cathode that will produce a mixed over potential, reducing the working voltage of DMFC; and (2) methanol crossover is a waste of fuel, and produces excess heat, which also degrades FC performance [15–19].

Low catalyst activity is the third technical DMFC obstacle especially under the condition of low temperature. Herein, anodic oxidation catalyst activity needs to be improved for optimal FC performance. If the anode catalyst activity increases, the methanol consumption will also be increased; on the other hand, osmotic quantity will be decreased. This process will also reduce the negative effect of methanol crossover, improving FC performance.

With the increased development of nanometer-sized materials in recent years, miniature DMFCs based on nanomaterials have received great attention. The nanostructured materials used in DMFC include carbon nanotube paper (i.e., Bucky paper), carbon nanotube (CNT) film, graphene (G) aerogels and hydrogel, etc.. Considering the nanostructure material, graphene which has an excellent physical and chemical performance and stability is a suitable material for DMFC-based catalyst.

---

## 7.2 Carbon Nanotubes (CNT) Used in Direct Methanol Fuel Cells (DMFCs)

In an MEA, the gas diffusion layer has two major functions. First, the microporous structure allows the reactants in the diffusion layer to spread into the catalyst layer. Here, the reactants can also uniformly disperse on the catalytic layer, which provides the effective area of the electrochemical reaction, and the layer arrangement gives the highest surface area. The second function is to export the electrons from the anode electrochemical reaction generated by the external circuit and import electrons from open circuit potential (OCP) into the catalyst layer. Therefore, the selection of gas diffusion layer material must be able to provide a conduction and is an important consideration.

A novel MEA structure of DMFC controls water management and decreases methanol crossover. The CNT paper replacing carbon paper (CP) as a gas diffusion layer (GDL) enhances water back diffusion which passively prevents flooding in the cathode and promotes low methanol crossover [20]. Generally, porous materials such as CP or carbon cloth are chosen as components of the GDL. The FC produces

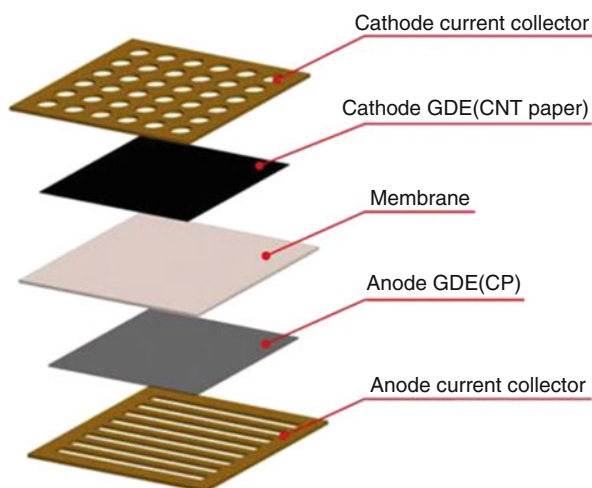
water during operation, as working FC temperatures are below the boiling point of water, so water always exists in liquid form in the compartment. When large amounts of water are stored around the electrodes, the water-flooding phenomenon causes increased oxygen mass transfer resistance and serious cathode polarization, leading to a rapid decrease in FC performance. So as the GDL, CP or carbon cloth must be of a certain hydrophobicity, and the general processing is to add polytetrafluoroethylene (PTFE) in carbon paper to improve the GDL paper hydrophobicity [21].

In this work, the water transmittal layer is CNT paper made from an aggregate of CNTs. The CNTs are allotropes of carbon with a cylindrical nanostructure which is supplied by Suzhou Creative-Carbon Nanotechnology Co. Ltd., China. For purification and chemical modification, the multi-walled carbon nanotubes (MWNTs) are dispersed into concentrated sulfuric acid (98%) and concentrated nitric acid (70%) mixture solution of 3:1 v/v by ultrasonication for 8 h. The mixture solution is diluted by large quantities of water to remove acid and filtered by polyvinylidene fluoride (PVDF) membrane. After chemical modification, the MWNTs have oxygenated functional groups which make MWNTs hydrophilic, and the wetting angle is 73.5°. The mixture of 100 mg of purified MWNT and 1 g Triton X-100 (a surfactant) was dispersed into 100 mL of deionized water by ultrasonication for 2.5 h [22]. The as-prepared MWNT suspension was filtered through the wetted PVDF membrane by a positive nitrogen gas pressure of 500 kPa to produce a well-known Bucky paper. Due to the van der Waals forces, the interaction of CNT surface and surfactant can be strong and stable. Subsequently, the produced Bucky paper is flushed in an effective solvent (2:1 v/v, water to methanol) to remove residual Triton X-100 surfactant after being rinsed by deionized water. Afterward, the produced Bucky paper is dried in a vacuum oven for 5 h and then peeled off from the PVDF membrane. The thickness of the CNT papers is controlled by the concentration of the MWNT suspension. Finally, the CNT paper is cut into 10 × 10 mm as a water transmittal layer. A piece of five-layered MEA with an active area of 10 × 10 mm is fabricated in a self-breathing DMFC by the catalyst-coated membrane (CCM) and hot press method. The hydrophilic catalyst layer is prepared to utilize the decal transfer method to form the CCM, with an anode catalyst layer of platinum-ruthenium (Pt-Ru) black (4.0 mg·cm<sup>2</sup>) and a cathode catalyst layer of Pt black (2.0 mg·cm<sup>2</sup>) and a Nafion 117 membrane between them. Then, for forming the GDL, CP (TGPH-090, Toray Inc.) is prepared by the hydrophobic (10 wt. % PTFE for the anode and 30 wt. % PTFE for the cathode, respectively) and pore-formed (ammonium hydrogen carbonate, NH<sub>4</sub>HCO<sub>3</sub>) pretreatment. Finally, the CCM is sandwiched between two GDLs and hot-pressed under the condition of 130 °C and 4 MPa for 120 s. The CNT is embedded between the five-layered MEA and cathode current collector which serves as a collector and distributor layer of water and electron as shown in Fig. 7.2. Figure 7.2 is from Deng et al., with permission License 4153540257896 [20].

Stainless steel plates with a thickness of 300 μm are chosen to fabricate the anode and cathode current collectors, and the structure of anode and cathode is fabricated by MEMS technology. A 500 nm layer of gold (Au) is deposited on the current collectors by the magnetron sputtering ion plating (MSIP) to reduce contact



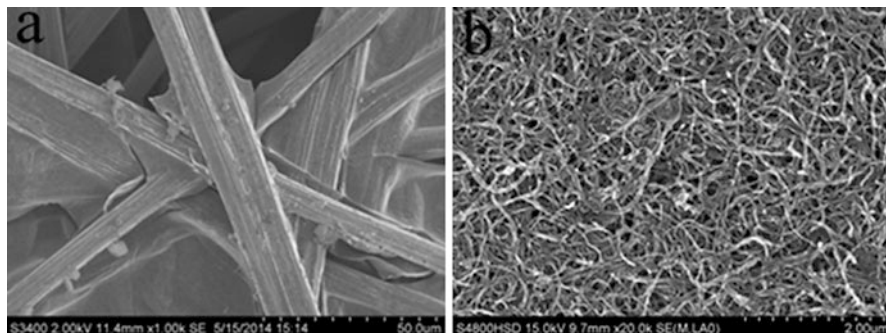
**Fig. 7.2** The CNT embedded between the five-layered MEA and cathode current collector [21]



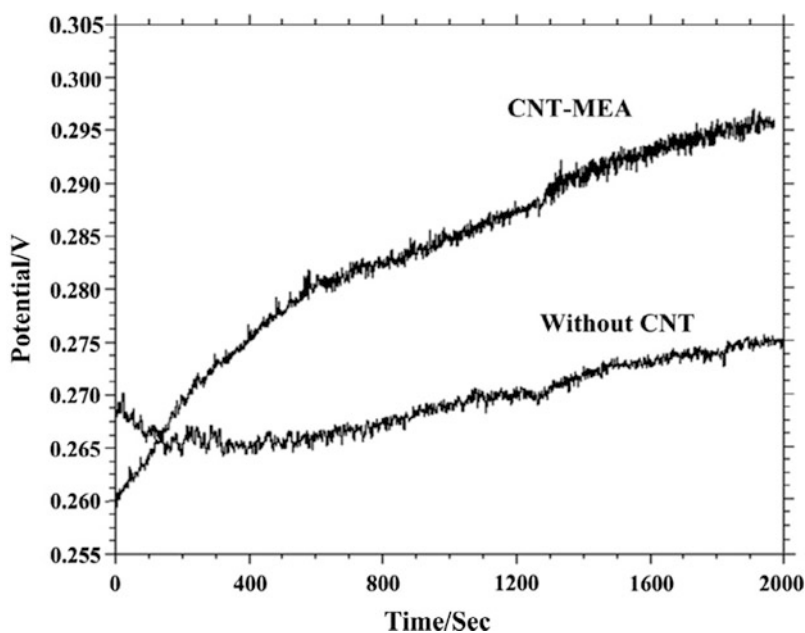
resistance and avoid chemical corrosion. A CNT paper with a thickness of 150  $\mu\text{m}$  is utilized to absorb water from the cathode which keeps MEA in a proper hydration and prevent cathode flooding. From the SEM image of CNT paper shown in Fig. 7.3 (from Deng et al., with permission License 4153540257896) [20], we can see that the CNT paper contains a high porous ratio structure which causes it to have a capillary phenomenon, and the high porous ratio structure also makes the oxygen diffuse through CNT expediently. The CNT paper is hot-pressed on the cathode side of MEA at 130  $^{\circ}\text{C}$  and 4 MPa for 120 s to form the CNT-MEA compound structure.

As the radius of self-breathing openings on the cathode current collector is very small, long-term operation of the self-breathing DMFC will cause cathode flooding easier than conventional designs. In order to determine the flooding behavior of DMFC with and without CNT-MEA which uses the CNT paper as water transmittal layer, a short-term voltage assessment with 3 M methanol solution and flow rates of 1 mL/min was conducted at ambient conditions. A measurement comparison of cell potential as a function of time between the DMFC without and with CNT as the water transmittal layer is summarized in Fig. 7.4 (from Deng et al., with permission License 4153540906158) [21].

The output voltage versus time measurements is recorded for 2000 s at a current of 120 mA. It can be seen that the voltage of the DMFC composed of CP-MEA is higher than that of DMFC composed of CNT-MEA during the first 150 s. After this time point, the voltage of DMFC composed of CNT-MEA constantly increases and exceeds that of DMFC composed of CP-MEA. It was also found the voltage of DMFC composed of CP-MEA decreases at 430 s of operation and then improves. The performance of DMFC composed of CNT-MEA is inferior to that of the DMFC composed of CP-MEA at the beginning of operation because oxygen needs time to diffuse through the CNT layer which leads to an oxygen starvation for a short time period. At the same time, the DMFC composed of CP-MEA is flooded, leading to voltage declination and then voltage inclination after 430 s due to DMFC which

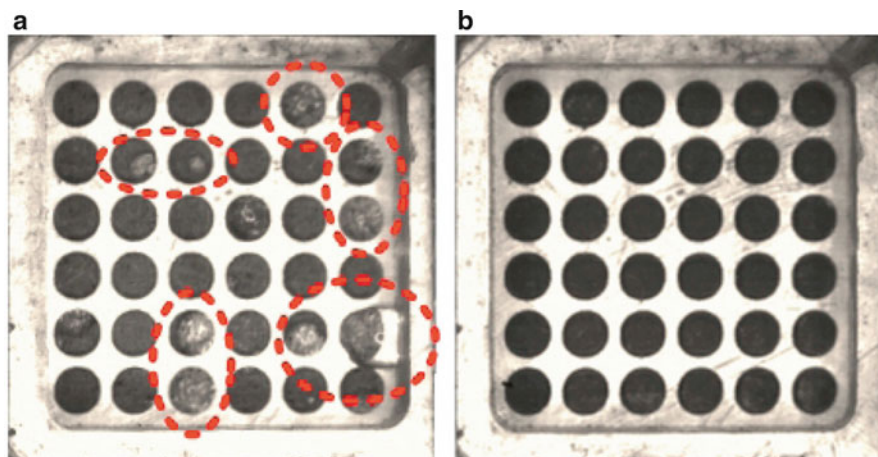


**Fig. 7.3** Morphological analyses. (a) Carbon paper and (b) carbon nanotube paper [21]



**Fig. 7.4** Output potential of traditional and  $\mu$ -DMFC based on CNT [20]

produces heat that aids the activity of catalyst and the water evaporation rate. The voltage of the DMFC composed of CNT-MEA is more stable within about 400 min than the DMFC composed of CP-MEA. This stability is in part due to CNT layer transport of water from GDL to the outside, which avoids flooding in GDL. The lower likelihood of flooding ensures the cathode reaction areas to remain active for longer periods. The DMFC composed of CNT-MEA produces more heat, which improves the mass transport velocity of oxygen. In spite of CNT-MEA gas blockage and limited gas penetration into GDL, the performance of the DMFC composed of CNT-MEA is superior to that of the cell composed of CP-MEA. The above gas



**Fig. 7.5** Cathode surface of traditional and DMFC based on CNT after the long-term operation. (a) Traditional DMFC and (b) CNT-based DMFC [20]

blockage was found to dissipate in a short time. A large quantity of water is generated on the surface of GDL by chemical reaction and then condensed on the surface of the GDL in a liquid phase, during the long-term operation of the air-breathing DMFC. When the rate of water generation is higher than that of water evaporation, water will be condensed as droplets on the GDL surface which can be seen through the openings on the cathode. Flooding in the cathode prevents oxygen from entering into the GDL and decreases reaction area which leads to low efficiency and inhomogeneous distribution of oxygen mass transport in GDL, hindering performance advancement of air-breathing DMFC.

Figure 7.5 (from Deng et al., with permission License 4153540906158) shows the visual degradation of the surface phenomenon of cathode based on the voltage profile shown in Fig. 7.4. The DMFC was operated for 15 min and examined for degradation. Figure 7.5 (a) presents the cathode surface phenomenon of DMFC composed of CNT-MEA, which uses the CNT paper as water transmittal layer. Figure 7.5 (b) presents the cathode surface phenomenon of the DMFC composed of CP-MEA. We can see that the cathode surface of DMFC composed of CP-MEA has a degree of hydration (seen as droplets of water); but the DMFC composed of CNT-MEA water transmittal layer appears anhydrous at the cathode surface, which proves that using the CNT-MEA structure can prevent cathode flooding. Moreover, the unique structure of CNT paper can also enhance the efficiency of oxygen mass transport and catalyst utilization. The DMFC composed of CNT-MEA exhibits significantly higher performance than DMFC composed of CP-MEA and can operate in high methanol concentration, showing a peak power density of  $23.2 \text{ mW cm}^{-2}$ . The energy efficiency and fuel utilization efficiency are obviously improved from 11.54% to 22.7% and 36.61% to 49.34%, between MEAs composed of CP and CNTs, respectively. The water transport coefficient is 0.47 (dimensionless) from CNT-MEA, which is lower than previously reported DMFC composed of CP-MEA.

## 7.3 Graphene Applied in Direct Methanol Fuel Cells (DMFCs)

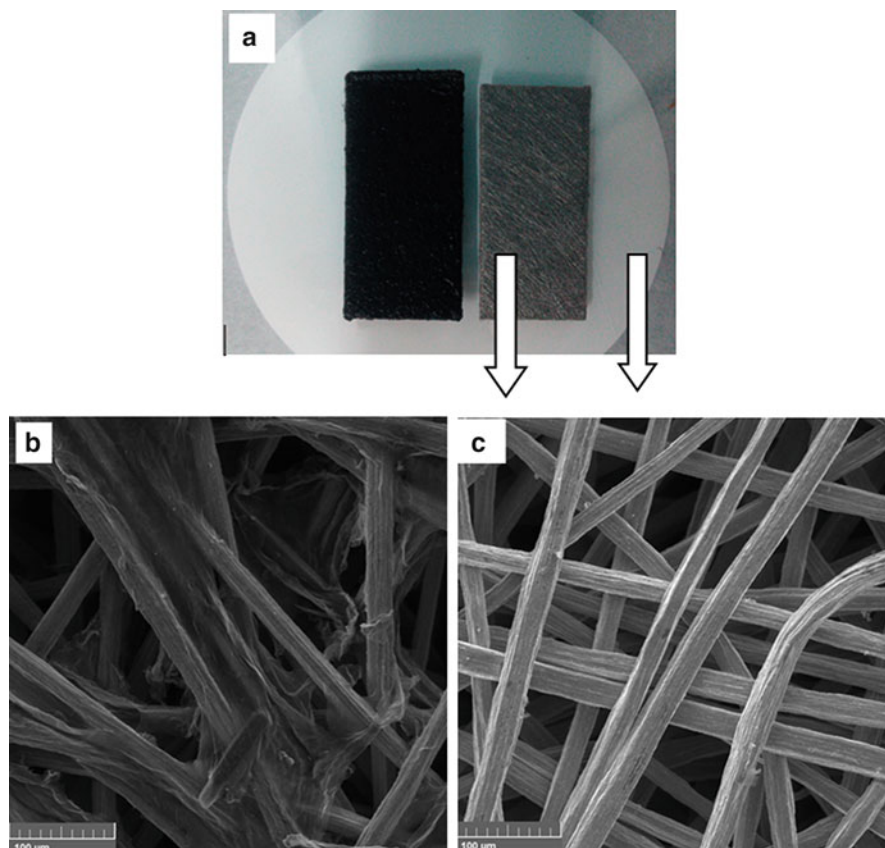
### 7.3.1 Graphene Used as Barrier Layer

In this section, the authors discuss the development of a novel anode mass transfer barrier layer for a DMFC to mitigate methanol crossover. The novel barrier layer was a composite material of stainless steel fiber felt (SSFF) and reduced graphene oxide (rGO), which was prepared by dipping a piece of SSFF plate into the graphene oxide solution and subsequently experiencing a reduction process. Using this composite material as dual-use anode barrier layer and current collector, respectively, a passive DMFC was fabricated and tested. The results showed that the novel barrier layer effectively increased the methanol mass transport resistance, lowering methanol crossover, and thus allowed the cell to operate at a higher methanol concentration. In addition, the cell fabricated with the novel barrier layer showed higher discharging stability and lower inner resistance at the same time when compared with a traditional cell.

In previous work, sintered stainless steel fiber felt (SSFF) was studied in a new anode structure, in which the anode diffusion layer also played an important role as a current collector [23]. To improve current collector efficiency, reduced graphene oxide (rGO) is proposed due to graphene hydrogels' excellent electrical properties, and porosity was constructed composed of rGO and SSFF composite structure to reduce the porosity and increase current, as a novel barrier layer for DMFC. A procedure previously described in the fabrication of graphene and foam-nickel composite was adopted [24]. Briefly, GO was scattered in deionized water, using ultrasound, in order to expel any residual air out of the SSFF, and a wafer of SSFF (0.62 mm thick) was also ultrasonically vibrated. Then GO was deposited into SSFF by leaching, with  $5 \text{ mol}\cdot\text{mL}^{-1}$  GO solution. The resulting SSFF-G hydrogel composite film was then immersed in vitamin C (VC) solution ( $10.0 \text{ mg}\cdot\text{mL}^{-1}$ ) overnight and subsequently heated at  $60^\circ\text{C}$  for 2 h. During this process, GO sheets were reduced to generate rGO. Then the composite sheets were placed into a freeze dryer at  $-20^\circ\text{C}$  for 48 h after a rapid freezing by immersion in liquid nitrogen.

After the rGO-SSFF composite was generated, it was evaluated as an anode gas diffusion backing and current collector by fabricating an MEA for a DMFC. The MEA with an active area of  $1 \times 1 \text{ cm}$  was fabricated by traditional procedures. Both the anode and cathode GDEs are purchased from Johnson Matthey, Inc. Nafion 117 membrane utilized had a width of  $170 \mu\text{m}$ , which was sandwiched between the anode GDE and cathode GDE by 18 MP hot-pressing for 5 minutes. The methanol capacity of both the new cell (SSFF-rGO) and the conventional cell was 2 mL whose performance was compared and contrasted to each other [25]. After testing the FC performance, the internal morphology of the obtained SSFF-rGO was evaluated using scanning electron microscope (SEM) and structural modifications compared with a piece of unprocessed SSFF. The SSFF-rGO performance under different methanol concentrations was also evaluated.

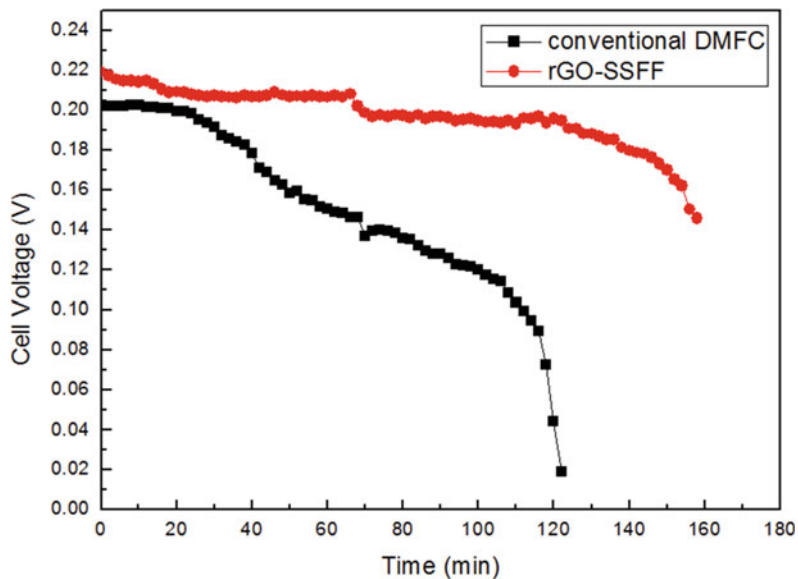
The physical picture of SSFF-rGO produced using the above procedure is shown in Fig. 7.6a (from Zhang et al., with permission License 4153541289218 [25]). The



**Fig. 7.6** Photograph of the (a) SSFF-rGO and SSFF, SEM of the (b) SSFF-rGO and (c) SSFF [25]

micrograph indicates that the graphene hydrogels successfully covered the surface of SSFF. The scanning electron micrographs of the SSFF-rGO composite are shown in Fig. 7.6b, c. The SEM image of SSFF-rGO (Fig. 7.6b) shows that graphene has been successfully deposited in the micropores of the whole SSFF (Fig. 7.6c). As shown in Fig. 7.6b, the SSFF-rGO with the graphene hydrogels is distributed evenly in holes of SSFF, which can potentially hinder methanol transport. The SEM images confirm that the composite possesses uniform porous inner configuration, which makes the SSFF-rGO a suitable substitute for the mass transfer barrier layer for DMFC at high methanol concentration and also guarantees high mechanical strength and superb ductility [25].

To evaluate the stability of the two materials, the fabricated cell was discharged under a constant current density of  $80 \text{ mA} \cdot \text{cm}^{-2}$  at room temperature, with the novel cell at 7 M and traditional cell at 3 M shown in Fig. 7.7 (from Zhang et al., with permission License 4153541289218) [25]. It can be seen that besides a long discharging time, the novel cell has a higher and more stable cell voltage profile



**Fig. 7.7** Transient discharging curves of the  $\mu$ -DMFCs under a constant current density of  $80 \text{ mA cm}^{-2}$  at  $298 \text{ K}$  [25]

compared with conventional DMFC. The differences between discharging results demonstrate and confirm the ability of the rGO-SSFF material in reducing methanol crossover under high concentration condition by taking advantages of its internal porous structure.

### 7.3.2 Graphene Used in Catalyst

As MEA is the core of PEMFC, the catalyst layer is the core of MEA, which makes it a significant parameter in evaluating the output performance of PEMFC. The current low efficiency, poor stability, and high cost of the catalyst remain as the biggest hurdles for the commercialization of PEMFC. In order to maintain high catalytic activity and good stability, metal particles are usually dispersed onto a support material. The catalyst support material not only determines the dispersion of metal nanoparticles but also interacts with metal particles, which in turn affects the activity and stability of the catalyst [26]. Catalyst support used in PEMFC should have the following characteristics:

1. High specific surface area, which would enhance the dispersion of metal nanoparticles and improve the catalyst surface utilization
2. Excellent conductivity that can quickly transfer the electrons of electrode reaction
3. Reasonable pore structure, which makes rapid transfer and diffusion of reactants and products



4. Strong corrosion resistance, to prevent catalyst performance in the electrolyte from rapid degradation

In summary, the most suitable material for PEMFC catalyst support currently is carbon. Graphene, an intriguing member of the carbon material family, was discovered in 2004 [27] and is a possible replacement for carbon as a structural support material. With its unique two-dimensional, single-atom layer thickness structure, graphene exhibits a large theoretical specific surface area (up to  $2600 \text{ m}^2 \text{ g}^{-1}$ ), high electrical conductivity, high thermal conductivity, and excellent mechanical properties. In addition, chemically transformed graphene has an interlayer structure containing lattice defects (vacancies, holes) and surface functional groups (carboxyl, epoxy, and hydroxyl) that can anchor metal particles on their surface. This strong interaction between the metal and the substrate can improve the stability of the nanocatalyst [28, 29]. Fampiou et al. [28] used density functional theory (DFT) and bond-order potential calculations to prove that the defects of the surface of graphene can be a strong confinement trap of Pt nanoclusters, making Pt-graphene hybrid show excellent long-term stability. Besides, the charge transfer between the catalyst and the graphene substrate increases, and the catalytic activity of the catalyst is enhanced. Therefore, much work has been done to investigate the issue, and experiment results show graphene-based catalysts have better catalytic activity and stability than their traditional counterparts.

### 7.3.2.1 Graphene-Supported Catalyst for Methanol Oxidation Reaction (MOR)

Direct methanol fuel cell plays a dominant role in all kinds of P. Its fuel, methanol, has a low molecular weight, high energy density, and simple structure, which makes it one of the most suitable fuels of all kinds.

#### Platinum/Graphene Catalyst

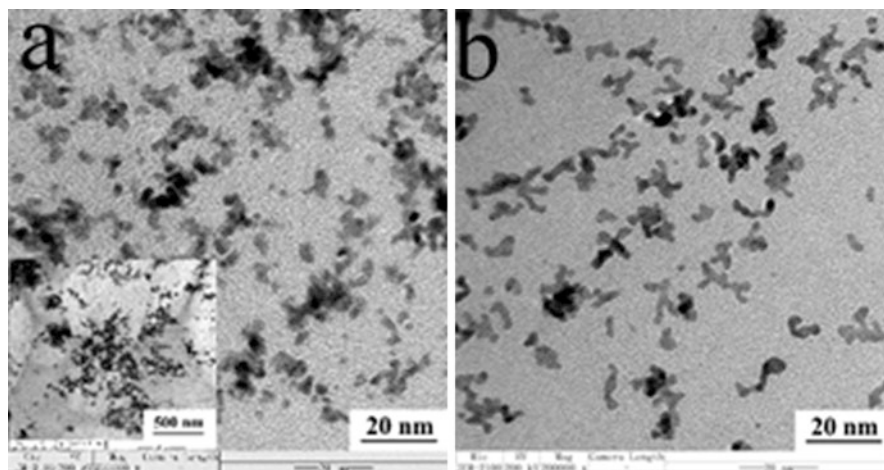
Although other metal-based and nonmetal catalysts have been discovered and studied, platinum (Pt)-based catalyst still remains one of the most widely used species due to their high Pt activity toward methanol. There are three general methods to prepare Pt-based graphene hybrid. One is a chemical reduction [30–32]. Herein, Pt or other metal precursors, such as hexachloroplatinic acid ( $\text{H}_2\text{PtCl}_6$ ), ruthenium (III), and chloride ( $\text{RuCl}_3$ ), are mixed with graphene or GO. Then reductants, such as hydrazine hydrate ( $\text{N}_2\text{H}_4$ ), sodium borohydride ( $\text{NaBH}_4$ ), or hydroiodic acid (HI), are carefully added to the mixture. The reduction reaction will take place either at room temperature or at higher temperatures, depending on the chemical reductant utilized. The reduced sample is then filtered, washed, and dried under vacuum, yielding the catalyst sample which is applied on DMFC. The second method is electrodeposition [33, 34]. By applying cyclic voltammetry (CV), square wave scanning, chronoamperometry, and other electrochemical methods to electrolyte solution of precursors, the corresponding catalyst can be obtained. Potential, current density, and deposition time are parameters to control the synthesis procedure. However, the particles prepared by

electrodeposition are large, and using this method, it is difficult to fabricate materials on a large scale. The third method is microwave-assisted synthesis [35–37]. Here, the new catalyst preparation method has the advantages of simplicity, short preparation period, simple reaction control, and uniformity of the produced particles. Microwave irradiation can generate homogeneous and rapid heating of the reaction mixture that can take from seconds to one minute of reaction time. In addition, the microwave heating technique can also promote the formation of a large number of initial nuclei in the reaction, generating synthesized nanoparticles that exhibit uniform and small diameters.

Among the three synthesis methods, microwave-assisted heating with ethylene glycol (EG) method is the widely used technique [37]. Herein, a certain amount of GO is dispersed uniformly into the mixture of ethylene glycol ( $C_2H_6O_2$ ) and isopropyl alcohol ( $C_3H_8O$ ) with the ratio of 4:1 v/v using ultrasound dispersion. The chloroplatinic acid-ethylene glycol ( $H_2PtCl_6$ -EG “ink”) solution is added and stirred for 3 h. The pH value of the ink is adjusted by sodium hydroxide (NaOH) generating an alkaline NaOH-EG solution through drop-by-drop addition until pH of the ink is  $>7$ . Using 1 M NaOH, this corresponds approximately to the addition of 12 drops of the base. To the ink argon (Ar), gas is fed to expel ( $O_2$ ) oxygen. The oxygen-depleted ink is microwave heated between 1 and 3 minutes. After cooling down to room temperature, dilute nitric acid ( $HNO_3$ ) solution was added to the mixture to adjust pH value to 4. The mixture was continually stirred for 12 h, and then the product was washed repeatedly with ultrapure water until no chloride anion ( $Cl^-$ ) was detected. A solid catalyst was generated after the drying process.

During the preparation of the catalyst, aggregation between GO sheets by van der Waals forces can decrease the high intrinsic specific area of graphene and thus limit the enhancement of catalytic activity. To reduce the degree of aggregation, polymers, such as poly(diallyl dimethyl ammonium) chloride (PDDA) [38, 39], chitosan [40], and N-acetylcholine (N-ACh) [41], have been used to modify graphene nano-sheets. Experimental results show that the functionalized graphene sheets have excellent efficiency and increased dispersion of noble metal nanoparticles. In our previous work, aniline ( $C_6H_5NH_2$ ) was utilized to form nitrogen-doped carbon layer (NCL) to prevent the aggregation among graphene nano-sheets [42]. Typically, aniline monomers in 0.5 M  $H_2SO_4$  were added to the GO solution and stirred for 3 h. The GO was subsequently reduced by sodium borohydride (rGO). The above solution was further mixed with ammonium persulfate (APS,  $(NH_4)_2S_2O_8$ ), and polymerization was then carried out for 20 h at room temperature. Afterward, the sample was filtered and dried, and the resulting product was heat treated under 500 °C with argon gas flow for 3 h. The Pt nanoparticles were dispersed onto the composite obtained above via chemical reduction by sodium borohydride. The catalyst prepared was denoted as Pt/NCL-rGO. Figure 7.8 (from Zhang et al., with permission License 4153550310970) [42] shows transmission electron microscope (TEM) images of the synthesized Pt/NCL-rGO and Pt/rGO composite catalysts. The distribution of Pt nanoparticles on the NCL-rGO was more uniform than that on rGO. The electrochemical surface area (ECSA) of the Pt/NCL-rGO estimated by the cyclic voltammetry (CV) curves obtained in 0.5 M sulfuric acid ( $H_2SO_4$ ) was  $58.72 \text{ m}^2 \text{ g}^{-1}$ , which was larger than



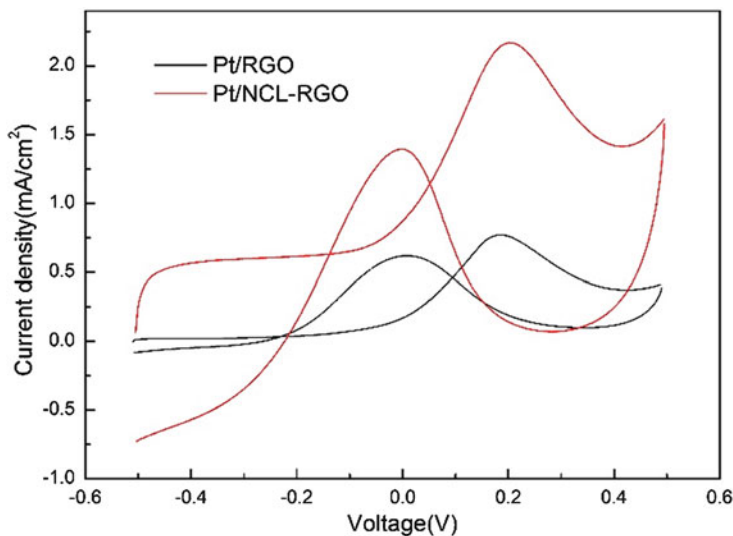


**Fig. 7.8** TEM images of (a) Pt/NCL-rGO and (b) Pt/rGO [42]

the ECSA for Pt/rGO. These results were further confirmed by generating corresponding CV curves for methanol oxidation (MOR) and are shown in Fig. 7.9 (from Zhang et al., with permission License 4153550310970) [42]. Both curves have two oxidation peaks. The one located at 0.2 volts (V) in the positive scanning direction is for MOR, and the other located at 0 V in the negative direction is for the oxidation of intermediate product(s). It can be seen that the peak current density of Pt/NCL-rGO is almost twice that of Pt/rGOs. The greater ECSA of the Pt/NCL-rGO catalyst indicates better dispersal of Pt nanoparticles into the NCL-rGO layer exhibiting higher electrocatalytic activity than in the Pt/rGO catalyst layer.

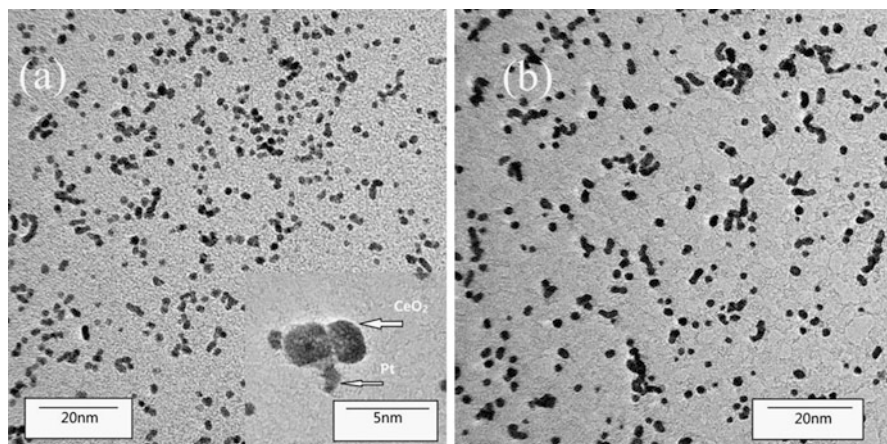
### Binary Pt-Based/Graphene Catalyst

The MOR process involves the adsorption of methanol and subsequent dissociation into adsorbed intermediates such as adsorbed carbon monoxide ( $\text{CO}_{\text{ads}}$ ), carboxylate ( $\text{COOH}_{\text{ads}}$ ), and aldehyde ( $\text{CHO}_{\text{ads}}$ ) intermediary products [43]. These products will poison the Pt particles and lead to a sharp decrease of DMFC performance. To overcome this poisoning hurdle, a bifunctional mechanism has been proposed in which other metals or metal oxides are added to form the binary catalyst, which may be more tolerant to potential poisoning. So far, various binary Pt-based/graphene catalysts have been reported, and they exhibit excellent electrocatalytic activity for MOR, such as Pt-ruthenium (Ru)/graphene [44, 45], Pt-palladium (Pd)/graphene [46, 47], Pt-nickel (Ni)/graphene [48, 49], Pt-iron (Fe)/graphene [50], and Pt-tin (Sn)/graphene [51]. Ruthenium is the most widely used co-metal in commercial catalysts. Dong et al. [44] used EG reduction method and dispersed Pt particles and Ru particles onto graphene sheets. Their as-obtained catalyst showed better efficiency and activity than the commercial Pt-Ru/Vulcan XC-72R, the catalyst used in DMFC.

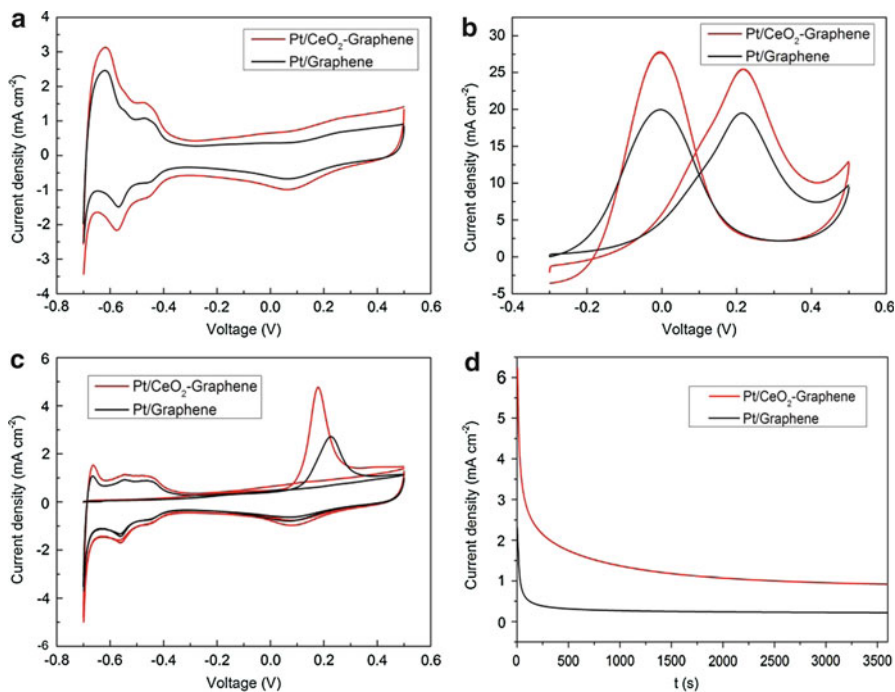


**Fig. 7.9** CV curves of Pt/NCL-rGO and Pt/rGO in 0.5 M H<sub>2</sub>SO<sub>4</sub> and 0.5 M methanol [42]

Among those widely used metal oxides, the rare earth cerium oxide (Ce<sub>x</sub>O<sub>y</sub>) attracted considerable interest because of its fluorite structure whose action (where  $x = 2$  and  $y = 3$  corresponding to +3 and  $x = 1$  and  $y = 2$  corresponding to +4 oxidation states for Ce, respectively) added advantage of Ce acting as an oxygen buffer [52]. We prepared Pt nanoparticles on the cerium (IV) oxide (CeO<sub>2</sub>)-graphene composites by a fast and efficient one-step microwave-assisted EG method [37]. In the method, EG is regarded as a reducing agent for the metal salt compounds and a protecting agent for the metal nanoparticles. Pt/graphene was also prepared for comparison. Figure 7.10 (from Zhang et al., with permission License 4153550689598) shows the TEM images of Pt/graphene and Pt/CeO<sub>2</sub>-graphene. Compared with Fig. 7.10b, the sizes of platinum particles, shown in Fig. 7.10a, become smaller and are better dispersed on graphene support owing to ceria incorporation. High-resolution (HR) TEM analyses suggest that the reduced Pt particles have successfully adhered to the ceria particles deposited onto the graphene sheets. Figure 7.11 (from Zhang et al., with permission License 4153550689598) [37] images demonstrate electrochemical evaluation of the Pt/CeO<sub>2</sub>-graphene and Pt/graphene catalysts. The CV curves reveal that the former has a larger ECSA and better activity toward methanol electrooxidation than the latter catalyst. This improved catalysis is due to facile desorption of the CO<sub>ads</sub> electro-oxides from the catalyst surface due to the effect of CeO<sub>2</sub> as a co-catalyst and oxygen storage material. The adsorbed hydroxyl (OH<sub>ads</sub>) species on CeO<sub>2</sub> can transform (fully oxidize) CO-like poisoning species to CO<sub>2</sub>, releasing the bound active sites on Pt surface for further MOR catalysis. Figure 7.11c shows CO adsorption-oxidation curves. Compared to the Pt/graphene catalyst, the onset and the peak potentials for adsorbed carbon monoxide (CO<sub>ads</sub>) oxidation on Pt/CeO<sub>2</sub>-graphene catalyst were



**Fig. 7.10** TEM images of Pt/CeO<sub>2</sub>-graphene (a) and Pt/graphene (b) [37]



**Fig. 7.11** Electrochemical properties tests. (a) CVs in 0.5 M H<sub>2</sub>SO<sub>4</sub>. (b) CVs in 1 M CH<sub>3</sub>OH + 0.5 M H<sub>2</sub>SO<sub>4</sub>. (c) CO<sub>ads</sub> stripping voltammograms. (d) Chronoamperometric curve [37]

shifted to a more negative potential, indicating that the addition of CeO<sub>2</sub> contributed to weakening the CO adsorptive bond on the Pt active sites. The ECSA from CO stripping voltammetry can directly reflect the CO-oxidizing ability of the catalysts,

assuming the formation of a monolayer of linearly adsorbed CO and the Columbia charge required for oxidation of  $\text{CO}_{\text{ads}}$  to be  $484 \mu\text{C cm}^{-2}$ . The calculated ECSA for the two catalysts were  $16.3 \text{ m}^2 \text{ g}^{-1}$  and  $11.4 \text{ m}^2 \text{ g}^{-1}$ , respectively, by using the  $\text{CO}_{\text{ads}}$  oxidation charge after subtracting the background current, which implies that  $\text{CeO}_2$ -metal oxide can improve catalytic activity for  $\text{CO}_{\text{ads}}$  electrooxidation. Figure 7.11d shows typical current density-time responses for MOR measured at a fixed potential of 1.02 V. The Pt/ $\text{CeO}_2$ -graphene catalyst shows better stability than its non-metal oxide counterpart.

### Non-Pt-Based/Graphene Catalyst

As one of the most expensive noble metals, the high cost and short storage of Pt impede the full commercialization of DMFC. To solve this problem, researchers used other metal particles as substitutes for Pt, among which Pd, which is either replaced or alloyed with other noble metals such as gold (Au) and silver (Ag) and the composite catalyst used for MOR process. Palladium (Pd) is one of the most promising alternatives to Pt, due to its similar physical and electrical properties but with the added advantage of lower procurement cost. The Pd-based catalyst in the anode of DMFC reveals stronger resistance to CO poisoning. The preparation of Pd-based/graphene is similar to Pt/graphene. The modification of graphene and bifunctional mechanism also helps to boost the activity and stability of Pd-based/graphene catalyst. The electrochemical test results suggest that Pd-based/graphene catalyst possesses better catalytic performance and durability than traditional carbon materials supported Pd nanoparticles [53, 54].

In recent years, Au- and Ag-based/graphene catalysts also have attracted increasing attention [55–58] due to lower cost of usage, but with similar physical and electrical properties. The most common preparation process is a chemical reduction of metal precursors in the presence of graphene or GO. Goncalves et al. [58] used a simple chemical method in an aqueous medium and successfully prepared Au/graphene. It should be noted that no Au particles can be formed on totally reduced graphene nano-sheets since the oxygen functionalities at the graphene sheets provide reactive sites for the nucleation and growth of Au nanoparticles.

#### 7.3.2.2 Graphene-Supported Catalyst for Hydrogen Oxidation Reaction (HOR)

Proton exchange membrane fuel cells with hydrogen as a fuel have the advantages of high energy density and zero emission and generation of water as a by-product. The FCs are widely applied in large devices such as cars; however, the widespread usage is hampered by availability, access, and storage of hydrogen, as well as the size (dimensions and mass) of the onboard PEMFC system.

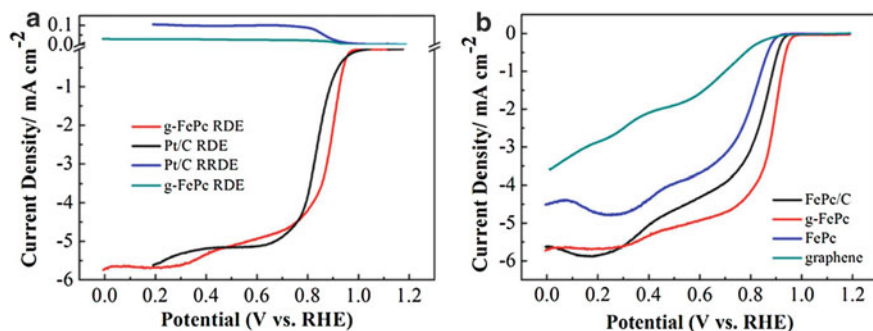
Platinum-based catalysts have the highest performance for HOR with low mass fuels, due to the lower redox potential. Since the kinetics of hydrogen oxidation is more facile than the corresponding ORR, the kinetics of the HOR are usually faster at lower potentials than for the ORR, reflecting the lower Pt load (mass % of the catalyst) at the anode in PEMFC. Different types of carbon materials have been studied as the support materials for the HOR to further lower Pt load on the anode

catalyst [59]. In a pure hydrogen atmosphere, Pt/carbon black shows similar electrocatalytic activities for HOR to either Pt-Ru/carbon black or Pt/graphene in spite of the addition of Ru and the difference of supporting materials. However, at the PEMFC front-end hydrogen fuel supply is obtained through hydrogen generators, such as methanol reformer, which also produce carbon monoxide at low parts-per-million concentrations. Therefore, catalyst tolerance to CO is an essential factor in evaluating catalyst performance for the HOR. Incorporation of the sub-nano-dimension of Pt clusters supported on graphene reported by Yoo et al. exhibited better CO tolerance than the catalyst supported on carbon black [60]. The activity of the former catalyst for HOR was determined to be 52% in the presence of H<sub>2</sub> and 11% with H<sub>2</sub> containing 500 ppm of CO.

### 7.3.2.3 Graphene-Supported Catalyst for Oxygen Reduction Reaction (ORR)

The ORR, which takes place at the cathode of PEMFC, has a slow electrochemical kinetics compared to HOR, due to the higher potential load requirement, necessitating higher Pt catalyst loading. Therefore, fabrication of a high-efficiency catalyst for the ORR at lower Pt loading is essential for wide-scale commercialization of an FC, providing similar FC performance can be obtained to FCs using current Pt loading of 0.4 mg·Pt. The ORR is different from the MOR and HOR, in that the mechanism of catalysis can proceed by two reaction pathways depending on the reaction conditions. One is the four-electron reduction of O<sub>2</sub> to water as the end product ( $O_2 + 4H^+ + 4e^- \rightarrow 2H_2O$ ) and the other is a two-step, two-electron reduction procedure, involving the formation of H<sub>2</sub>O<sub>2</sub> as an intermediate ( $O_2 + 4H^+ + 2e^- \rightarrow H_2O_2 + 2H^+ + 2e^- \rightarrow 2H_2O$ ) [61]. The former reaction pathway is more efficient than the latter one.

Like all the other reactions in PEMFC and DMFC, Pt-based catalysis requires the highest Pt load for viable activity for the ORR, and current investigators are focused on reducing the Pt loading without reducing catalytic efficiency, through either use of new forms of structural support materials or lower Pt as composite materials (coating with metals oxides, forming composite alloys, hollow shells using sacrificial Si, or as two- or three-dimensional structures are examples of how the Pt loading could be reduced without reducing the Pt catalytic efficiency for the ORR). Kou et al. [62] found that Pt nanoparticles supported on the functionalized graphene sheets exhibit larger ECSA, higher ORR activity, and enhanced stability in acid solution compared to the commercial Pt/C catalyst. Their research gave additional evidence that graphene sheets could enhance the performance of Pt catalyst at lower Pt loading than in a conventional Pt/C FC. The Pt/graphene support for ORR faces technical challenge of high cost and low durability due to the methanol crossover. The Pt alloys/graphene and other metal-based catalysts such as Pd/graphene have been fabricated as catalysts for ORR [63–66]. Yue et al. [64] found that Pt-cobalt (Co)/graphene exhibited higher ORR catalytic activity than pure Pt in alkaline solutions. Zhang et al. [65] dispersed the acid-treated Pt-Ni alloy on graphene and found that Pt-Ni/graphene had higher ORR activity than that of pure Pt catalysts in both acidic



**Fig. 7.12** (a) RDE and RRDE measurements of ORR at FePc/G and Pt/C catalyst in  $O_2$ -saturated 0.1 M KOH. The ring electrode is polarized at 0.5 V (vs Ag/AgCl) with a rotation rate of 1600 rpm and a potential scan rate of 10 mV/s. (b) Comparison of the RDE polarization curves of FePc, graphene, FePc/G, and FePc supported on carbon (FePc/C) in  $O_2$ -saturated 0.1 M KOH at 1600 rpm [72]

and alkaline solutions. Liu et al. [66] synthesized Pd-Ag nano-rings supported on graphene nano-sheets (Pd-Ag/GNs) and studied their ORR performance under alkaline circumstances. The Pd-Ag/GNs not only showed higher ORR catalytic performance but also revealed higher methanol tolerance when compared to Pd/C and Pt/C catalysts, respectively. Unlike the MOR or HOR, non-noble metal-based catalysts for use in ORR are a second major area of focus by investigators [67–70]. Among them, iron (Fe) or cobalt (Co) metal (M) incorporated onto nitrogen-doped (N) carbon (C) [M-N-C] catalysts is one promising class of cathode-supported catalyst [71]. Byon et al. [69] prepared Fe-based catalyst on rGO (Fe-N-rGO), in which the dopant nitrogen was derived from pyridine ( $C_5H_5N$ ). The Fe-N-rGO exhibited higher ORR mass activity and improved stability than the Fe-N-C catalysts prepared from carbon black (CB) or oxidized CB in acid solution. Jiang et al. [72] modified graphene with iron phthalocyanine ( $C_{32}H_{16}FeN_8$ , FePc/G) through  $\pi$ - $\pi$  interaction. The as-obtained FePc/G was studied as a catalyst for ORR in alkaline solution. Figure 7.12 demonstrates rotating disk electrode (RDE) and rotating ring-disk electrode (RRDE) measurements of ORR at FePc/G and Pt/C catalyst in  $O_2$ -saturated 0.1 M KOH. The electrochemical results indicate that the graphene support can significantly improve the ORR performance of the FePc catalyst, and the FePc has a better ORR activity than the carbon-supported FePc catalyst (FePc/C).

Recently, researchers found out that N-doped graphene itself can serve as ORR catalyst without any metal particles involved [73–75]. Geng et al. [76] prepared N-doped graphene with different content of three types of nitrogen at different temperatures. It was found that the optimum temperature was 900 °C. The resulting catalyst had a very high ORR activity through a four-electron transfer process in  $O_2$ -saturated 0.1 M KOH.



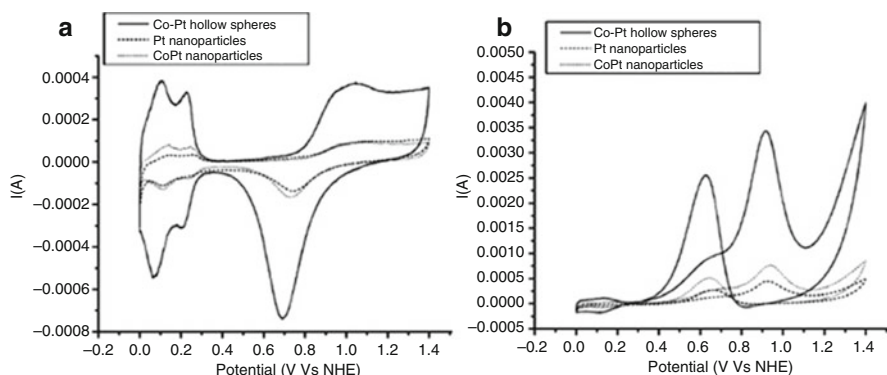
## 7.4 Other Nanomaterials Applied in PEMFC

Apart from carbon nanotubes (CNT) and graphene, there are other nanomaterials applied in DMFC and PEMFC. The research mainly focused on the metal catalyst supported on CNTs or graphene structured as dimensional surfaces summarized in the next sections.

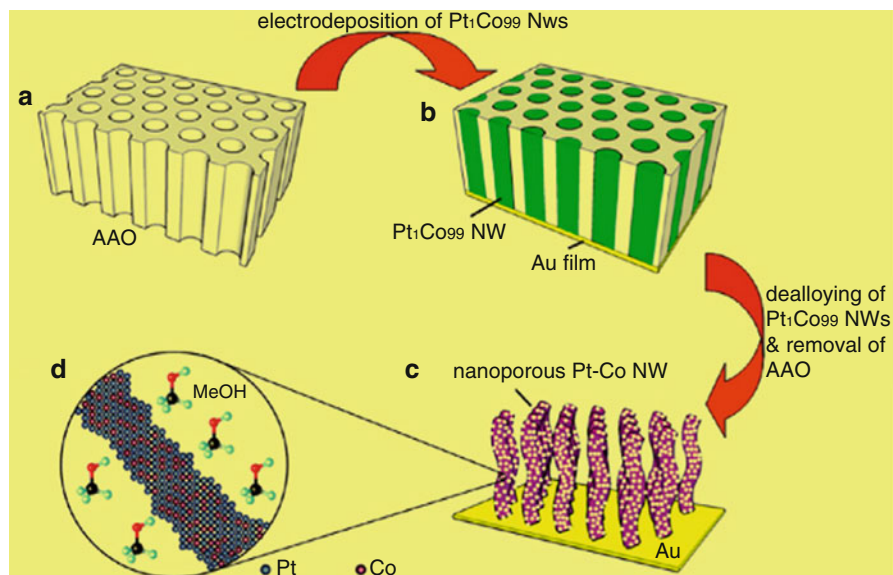
### 7.4.1 Zero-Dimensional Nanomaterials

In the past few years, stabilizing Pt nanoparticle clusters through forming zero-dimension structures had attracted researcher as potential low-loading Pt catalyst for PEMFC applications. The clusters stabilizing Pt nanoparticles are formed in order to maximize the active number of surface versus the inactive number of Pt atoms. Bimetallic clusters have also been investigated, not only to enhance CO tolerance of catalyst but also to decrease the Pt loading. By optimizing the synthetic conditions, a very thin surface layer of Pt can be generated [77]. Chen et al. [78] reported the synthesis of a Co-Pt catalyst with a hollow sphere structure via a simple thermolytic procedure (Fig. 7.13). The as-fabricated catalyst performance was compared with Pt nanoparticle and Co-Pt nanoparticles, respectively. The Co-Pt catalyst was generated in the form of hollow spheres which exhibited a superior electrocatalytic activity toward the MOR at the same Pt loading as the Pt catalyst.

Graphene quantum dot (GQD) has been used as a new zero-dimensional (0-D) nanomaterial and has become a promising nanomaterial for fuel cell applications, due to its excellent characteristics, such as high electrical conductivity, high surface area, tunable photoluminescence, and excellent dispersion in various solvents [79–82]. Recently, Hasanzadeh et al. reported a novel nano-catalyst based on graphene quantum dot functionalized by chitosan (GQD-CS) and  $\beta$ -cyclodextrin (GQD- $\beta$ -CD) toward MOR in alkaline solution.



**Fig. 7.13** (a) CVs of Co-Pt hollow spheres, Co-Pt nanoparticles, and Pt nanoparticles in a 0.5 M  $H_2SO_4$  solution; (b) CVs of Co-Pt hollow spheres, Co-Pt nanoparticles, and Pt nanoparticles in a 0.5 M  $H_2SO_4$  solution + 1 M methanol solution [78]



**Fig. 7.14** (a–c) The schematic diagram explains the nano-porous Pt-Co nanowire fabrication process; (d) enlarged view of the ligaments [85]

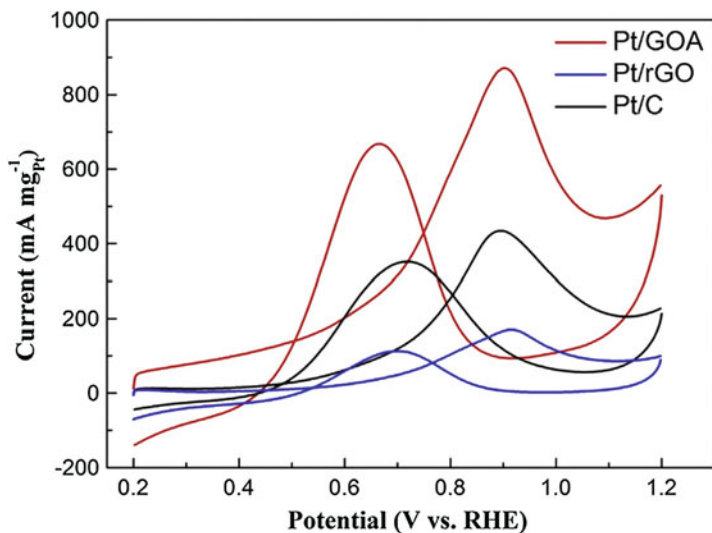
## 7.4.2 One-Dimensional Nanomaterials

One-dimensional (1-D) nanomaterials which form the basis of higher-dimensional materials have been extensively studied. Apart from CNT, researchers have also applied nanowires, nanorods, and nano-belts in the 1-D catalyst for PEMFC, [83, 84]. Ksar et al. [83] synthesized Pd nanowires in a hexagonal mesosphere via electron beam irradiation, which showed superior electrocatalytic activity and stability for ethanol oxidation. Liu et al. [84] fabricated the nano-porous Pt-Co alloy nanowires by de-alloying electrodeposited Pt<sub>1</sub>Co<sub>99</sub> nanowires in the presence of porous aluminum oxide (AO) membrane in a mild acidic medium, and electrochemical tests were conducted. Fig. 7.14 (from Liu et al., with permission License 501290469) [84] illustrates the preparation process. However, the specific surface area of the 1-D nanomaterials was smaller than that of the two-dimensional material, which limits their further improvement of catalytic performance.

## 7.4.3 Two-Dimensional Nanomaterials

Two-dimensional (2-D) nanomaterials represented by graphene have shown great advantages in energy conversion and storage applications during the past few years. For example, nanostructured transition metal sulfides have been explored as the catalyst for HOR [85, 86]. Recently, there are several literature reports involving new classes of 2-D materials being applied in PEMFC and DMFC, such as transition





**Fig. 7.15** Cyclic voltammetric curves of Pt/GOA, Pt/rGO, and commercial Pt/C in  $N_2$ -saturated  $0.5\text{ M CH}_3\text{OH} + 0.5\text{ M H}_2\text{SO}_4$  solution with a scan rate of  $50\text{ mV s}^{-1}$

metal compound arrays [87–89]. Due to the similarity of the electronic states to Pt at the Fermi level, group VI transition metal carbides (TMCs) exhibit catalytic properties analogous to Pt [90]. He et al. report a successful synthesis of Pt nanoparticles loaded onto the 2-D support of tantalum carbide (TaC)-nano-sheet and graphene hybrid impregnated with Pt (Pt/TaC/G) as an efficient and durable electrocatalyst for MOR. The catalyst was analyzed by X-ray photoelectron spectroscopy (XPS) and X-ray absorption spectroscopy (XAS) which indicated synergetic chemical coupling effects between the Pt and TaC/G that led to increased improvement in ORR catalytic activity and catalyst durability.

#### 7.4.4 Three-Dimensional Nanomaterials

Two-dimensional nanomaterials have a tendency to stack during the utilization process, due to layer-to-layer interactions. To minimize stacking higher-order three-dimensional (3-D) materials have been proposed and fabricated by researchers. These nanomaterials hold unique morphologies that provide a larger surface area which enhance the transfer of reactants and products. Graphene oxide aerogel (GOA) and graphene aerogel (GA), as the 3-D constructs of graphene, have attracted significant attention [91–93]. Graphene oxide aerogel can be obtained by supercritical  $\text{CO}_2$  drying or freeze-drying of GOA prepared by cross-linking graphene nano-sheets with multivalent metal ions or amino groups. Moreover, GA can also be prepared by supercritical  $\text{CO}_2$  drying or freeze-drying of graphene hydrogel that is prepared by hydrothermal treatment of GO. The as-prepared GOA or GA not only

maintain the intrinsic properties of 2-D graphene sheets but also exhibit other excellent functions of GO with improved catalytic performance. Our group successfully dispersed Pt nanoparticles on GOA via chemical reduction and examined its performance as a catalyst for DMFC [94]. The prepared Pt/GOA showed a low degree of graphitization as ascertained by an analysis of XRD spectrum, indicating that the graphene sheets did not stack. The SEM images also indicated that Pt/GOA maintained excellent 3-D porous structure, which not only facilitated reaction mass transfer but also avoided the detrimental influence of reduced active surface area of Pt particles due to the stacking of the graphene sheets.

The CV results also revealed that the ECSA of Pt/GOA reached  $95.5 \text{ m}^2 \cdot \text{g}^{-1}$ , which was twice that of commercial Pt/C. Fig. 7.15 (from Duan et al., with permission License 501290464) [94] demonstrated the CV curves of Pt/GOA, Pt/rGO, and commercial Pt/C in  $\text{N}_2$ -saturated  $0.5 \text{ M CH}_3\text{OH} + 0.5 \text{ M H}_2\text{SO}_4$  solution. The peak current density of Pt/GOA was  $876 \text{ mA} \cdot \text{mg}^{-1}_{\text{Pt}}$ , which was much higher than the other two samples. The CV data demonstrate that the Pt/GOA catalyst exhibited greater electrochemical activity (ESA) than either the Pt/rGO or the Pt/C catalyst, which resulted in the higher ECSA of Pt nanoparticles on Pt/GOA due to lower layer stacking and higher area. In addition, chronoamperometric measurements indicated that the catalytic stability toward MOR was also strongly enhanced.

---

## 7.5 Conclusion

A diverse type and structuring of nanomaterials have played a significant role enabling improved performance of PEMFCs and DMFCs by researchers during the past decade. The wide application of 0-, 1-, 2-, and 3-D nanomaterials contributed to the decrease in FC cost due to lower Pt loading and increased improvement of FC performance. Yet the performance of PEMFCs and DMFCs cannot meet the expected demand through increased commercialization, due to Pt loading being the limiting factor in FC design. With the emergence and development of new nanomaterials that greatly diminish Pt loading without loss of performance, FCs with more innovative structure and lesser Pt loading are expected to lead to improved FC performance, which in turn will lower FC cost and increase availability for a variety of applications. The greater usage of PEMFCs and DMFCs will lead to reduced use of fossil fuels mitigating the negative effects of global warming and increased access to portable power to rural areas that are not electrified, benefiting rural societies.

**Acknowledgment** This research is financially supported by the National Natural Science Funds of China (Agreement Codes 61404037 and 61376113).

---

## References

1. T.J. Yen, N. Fang, X. Zhang, G.Q. Lu, C.Y. Wang, A micro methanol fuel cell operating at near room temperature. *Appl. Phys. Lett.* **83**, 4056–4058 (2003)

2. C. Xu, T.S. Zhao, A new flow field design for polymer electrolyte-based fuel cells. *Electrochem. Commun.* **9**, 497–503 (2007)
3. H. Dai, H.M. Zhang, Q.T. Luo, Y. Zhang, C. Bi, Properties and fuel cell performance of proton exchange membranes prepared from disulfonated poly (sulfide sulfone). *J. Power Sources* **185**, 19–25 (2008)
4. Y.F. Zhang, P. Zhang, B. Zhang, J.M. Li, H.C. Deng, X.W. Liu, Development of an air-breathing direct methanol fuel cell with the cathode shutter current collectors. *Int. J. Hydrog. Energy* **35**, 5638–5646 (2010)
5. B. Zhang, Y.F. Zhang, H. He, J.M. Li, Z.Y. Yuan, C.R. Na, X.W. Liu, Development and performance analysis of a metallic micro-direct methanol fuel cell for high-performance applications. *J. Power Sources* **195**, 7338–7348 (2010)
6. Z. Yuan, Y. Zhang, J. Leng, Y. Gao, X. Liu, Development of a 4-cell air-breathing micro direct methanol fuel cell stack. *J. Power Sources* **202**, 134–142 (2012)
7. T.S. Zhao, C. Xu, R. Chen, W.W. Yang, Small direct methanol fuel cells with passive supply of reactants. *J. Power Sources* **191**, 185–202 (2009)
8. F. Achmad, S.K. Kamarudin, W.R.W. Daud, E.H. Majlan, Passive direct methanol fuel cells for portable electronic devices. *Appl. Energy* **88**, 1681–1689 (2011)
9. T.S. Zhao, C. Xu, R. Chen, W.W. Yang, Mass transport phenomena in direct methanol fuel cells. *Prog. Energy Combust. Sci.* **35**, 275–292 (2009)
10. R. Chen, T.S. Zhao, Porous current collectors for passive direct methanol fuel cells. *Electrochim. Acta* **52**, 4317–4324 (2007)
11. Y. Li, X.L. Zhang, L. Nie, Y.F. Zhang, X.W. Liu, Stainless steel fiber felt as cathode diffusion backing and current collector for a micro direct methanol fuel cell with low methanol crossover. *J. Power Sources* **245**, 520–528 (2014)
12. S.C. Yao, X.D. Tang, C.C. Hsieh, Y. Alyousef, M. Vladime, G.K. Fedder, C.H. Amon, Micro-electro-mechanical systems (MEMS)-based micro-scale direct methanol fuel cell development. *Energy* **31**, 636–649 (2006)
13. H. Peng, P. Chen, H. Chen, C. Chieng, T. Yeh, C. Pan, F. Tseng, Passive cathodic water/air management device for micro-direct methanol fuel cells. *J. Power Sources* **195**, 7349–7358 (2010)
14. Y.A. Zhou, X.H. Wang, X. Guo, X.P. Qiu, L.T. Liu, A water collecting and recycling structure for silicon-based micro direct methanol fuel cells. *Int. J. Hydrog. Energy* **37**, 967–976 (2012)
15. M.M.H.-S. rabadi, E. Dashtimoghadam, F.S. Majedi, S.H. Emami, H. Moaddel, A high-performance chitosan-based double layer proton exchange membrane with reduced methanol crossover. *Int. J. Hydrog. Energy* **36**, 6105–6111 (2011)
16. J. Kim, J.-D. Jeon, S.-Y. Kwak, Delamination of microporous layered silicate by acid-hydrothermal treatment and its use for reduction of methanol crossover in DMFC. *Microporous Mesoporous Mater.* **168**, 148–154 (2013)
17. H. Deligöz, S. Yilmaztürk, T. Gümüşoğlu, Improved direct methanol fuel cell performance of layer-by-layer assembled composite and catalyst containing membranes. *Electrochim. Acta* **111**, 791–796 (2013)
18. Y. Xue, S. Chan, Layer-by-layer self-assembly of CHI/PVS-Nafion composite membrane for reduced methanol crossover and enhanced DMFC performance. *Int. J. Hydrog. Energy* **40**, 1877–1885 (2015)
19. Y.-C. Park, D.-H. Kim, S. Lim, S.-K.Y. Kim, D.-H. Peck, D.-H. Jung, Design of a MEA with multi-layer electrodes for high concentration methanol DMFCs. *Int. J. Hydrog. Energy* **37**, 4717–4727 (2012)
20. H. Deng, Y. Zhang, Z. Xue, L. Yang, X. Zhang, X. Liu, A CNT (carbon nanotube) paper as cathode gas diffusion electrode for water management of passive  $\mu$ -DMFC (micro-direct methanol fuel cell) with highly concentrated methanol. *Energy* **82**, 236–241 (2015)
21. H. Deng, Y. Zhang, Y. Li, X. Zhang, X. Liu, A CNT-MEA compound structure of micro-direct methanol fuel cell for water management. *Microelectron. Eng.* **110**, 288–291 (2013)
22. S.H. Ng, J. Wang, Z.P. Guo, J. Chenb, et al., *J. Electrochim. Acta* **51**, 23 (2005)

23. R. Xue, S. Sang, H. Jin, Q. Shen, Y. Zhang, X. Liu, X. Zhang, Stainless steel fiber felt as the anode diffusion backing and current collector for  $\mu$ -DMFC. *Microelectron. Eng.* **119**, 159–163 (2014)
24. S. Ye, F. Jiachun, W. Peiyi, Deposition of three-dimensional graphene aerogel on nickel foam as a binder-free supercapacitor electrode. *ACS Appl. Mater. Interfaces* **5**, 7122–7129 (2013)
25. Y. Zhang, R. Xue, X. Zhang, J. Song, X. Liu, rGO deposited in stainless steel fiber felt as mass transfer barrier layer for  $\mu$ -DMFC. *Energy* **91**, 1081–1086 (2015)
26. J. Rajeswari, B. Viswanathan, Tungsten trioxide nanorods as supports for platinum in methanol oxidation. *Mater. Chem. Phys.* **106**(2–3), 168–174 (2007)
27. K.S. Novoselov, A.K. Geim, S.V. Morozov, D. Jiang, Y. Zhang, S.V. Dubonos, A.A. Firsov, Materials and methods: Electric field effect in atomically thin carbon films. *Science* **306**(5696), 666–669 (2004)
28. I. Fampiou, A. Ramasubramaniam, Binding of Pt nanoclusters to point defects in graphene: Adsorption, morphology, and electronic structure. *J. Phys. Chem. C* **116**(11), 6543–6555 (2012)
29. R. Kou, Y. Shao, D. Mei, Z. Nie, D. Wang, C. Wang, et al., Stabilization of electrocatalytic metal nanoparticles at metal-metal oxide-graphene triple junction points. *J. Am. Chem. Soc.* **133**(8), 2541–2547 (2011)
30. C. Huang, C. Li, G. Shi, Graphene based catalysts. *Energy Environ. Sci.* **5**(10), 8848–8868 (2012)
31. B. Seger, P.V. Kamat, Electrocatalytically active graphene-platinum nanocomposites. Role of 2-d carbon support in PEM fuel cells. *J. Phys. Chem. C* **113**(19), 7990–7995 (2009)
32. R.I. Jafri, T. Arockiadoss, N. Rajalakshmi, S. Ramaprabhu, Nanostructured Pt dispersed on graphene-multiwalled carbon nanotube hybrid nanomaterials as electrocatalyst for PEMFC. *J. Electrochem. Soc.* **157**(6), B874 (2010)
33. H. Meng, C. Wang, P.K. Shen, G. Wu, Palladium thorn clusters as catalysts for electrooxidation of formic acid. *Energy Environ. Sci.* **4**(4), 1522–1526 (2011)
34. Y.G. Zhou, J.J. Chen, F.B. Wang, Z.H. Sheng, X.H. Xia, A facile approach to the synthesis of highly electroactive Pt nanoparticles on graphene as an anode catalyst for direct methanol fuel cells. *Chem. Commun.* **46**(32), 5951–5953 (2010)
35. S. Sharma, A. Ganguly, P. Papakonstantinou, X. Miao, M. Li, J.L. Hutchison, et al., Rapid microwave synthesis of CO tolerant reduced graphene oxide-supported platinum electrocatalysts for oxidation of methanol. *J. Phys. Chem. C* **114**(45), 19459–19466 (2010)
36. P. Kundu, C. Nethravathi, P.A. Deshpande, M. Rajamathi, G. Madras, N. Ravishankar, Ultrafast microwave-assisted route to surfactant-free ultrafine Pt nanoparticles on graphene: Synergistic co-reduction mechanism and high catalytic activity. *Chem. Mater.* **23**(11), 2772 (2011)
37. H. Chen, J. Duan, X. Zhang, Y. Zhang, C. Guo, L. Nie, et al., One step synthesis of Pt/CeO<sub>2</sub>-graphene catalyst by microwave-assisted ethylene glycol process for direct methanol fuel cell. *Mater. Lett.* **126**, 9–12 (2014)
38. Z. Wang, J. Xia, X. Guo, Y. Xia, S. Yao, F. Zhang, et al., Platinum/graphene functionalized by PDDA as a novel enzyme carrier for hydrogen peroxide biosensor. *Anal. Methods* **5**(2), 483–488 (2012)
39. J.D. Qiu, G.C. Wang, R.P. Liang, X.H. Xia, H.W. Yu, Controllable deposition of platinum nanoparticles on graphene as an electrocatalyst for direct methanol fuel cells. *J. Phys. Chem. C* **115**(31), 15639–15645 (2011)
40. Z. Cui, C.M. Li, S.P. Jiang, PtRu catalysts supported on heteropolyacid and chitosan functionalized carbon nanotubes for methanol oxidation reaction of fuel cells. *Phys. Chem. Chem. Phys.* **13**(36), 16349 (2011)
41. J. Duan, X. Liu, H. Chen, Y. Zhang, J. Du, X. Zhang, Poly(n-acetylaniline) functionalized graphene nanosheets supported Pt electrocatalysts for methanol oxidation. *Microelectron. Eng.* **121**(4), 100–103 (2014)
42. X. Zhang, W. Yuan, J. Duan, Y. Zhang, X. Liu, Graphene nanosheets modified by nitrogen-doped carbon layer to support Pt nanoparticles for direct methanol fuel cell. *Microelectron. Eng.* **141**, 234–237 (2015)

43. J.M. Léger, Mechanism aspects of methanol oxidation on platinum-based electrocatalysts. *J. Appl. Electrochem.* **31**, 767–771 (2001)
44. L. Dong, R.R.S. Gari, Z. Li, M.M. Craig, S. Hou, Graphene-supported platinum and platinum–ruthenium nanoparticles with high electrocatalytic activity for methanol and ethanol oxidation. *Carbon* **48**(3), 781–787 (2010)
45. H. Li, X. Zhang, H. Pang, C. Huang, J. Chen, PMo12-functionalized graphene nanosheet-supported PtRu nanocatalysts for methanol electro-oxidation. *J. Solid State Electrochem.* **14** (12), 2267–2274 (2010)
46. H. Ji, M. Li, Y. Wang, F. Gao, Electrodeposition of graphene-supported PdPt nanoparticles with enhanced electrocatalytic activity. *Electrochem. Commun.* **24**(1), 17–20 (2012)
47. Y. Lu, Y. Jiang, H. Wu, W. Chen, Nano-PtPd cubes on graphene exhibit enhanced activity and durability in methanol electrooxidation after CO stripping–cleaning. *J. Phys. Chem. C* **117**(6), 2926–2938 (2013)
48. Y. Hu, P. Wu, Y. Yin, H. Zhang, C. Cai, Effects of structure, composition, and carbon support properties on the electrocatalytic activity of Pt-Ni-graphene nanocatalysts for the methanol oxidation. *Appl. Catal. B Environ.* **111**(6), 208–217 (2011)
49. Y. Hu, P. Wu, H. Zhang, C. Cai, Synthesis of graphene-supported hollow Pt-Ni nanocatalysts for highly active electrocatalysis toward the methanol oxidation reaction. *Electrochim. Acta* **85** (4), 314–321 (2012)
50. Z.Y. Ji, G.X. Zhu, X.P. Shen, H. Zhou, C.M. Wu, M. Wang, Reduced graphene oxide supported FePt alloy nanoparticles with high electrocatalytic performance for methanol oxidation. *New J. Chem.* **36**(9), 1774–1780 (2012)
51. F. Han, X. Wang, J. Lian, Y. Wang, The effect of Sn content on the electrocatalytic properties of Pt-Sn nanoparticles dispersed on graphene nanosheets for the methanol oxidation reaction. *Carbon* **50**(15), 5498–5504 (2012)
52. C.L. Perkins, M.A. Henderson, C.H.F. Peden, G.S. Herman, Self-diffusion in ceria. *J. Vacuum Sci. Tech. Vacuum Surfaces Films* **19**(4 PT 2), 217–218 (2001)
53. R. Awasthi, R.N. Singh, Graphene-supported Pd-Ru nanoparticles with superior methanol electrooxidation activity. *Carbon* **51**(1), 282–289 (2013)
54. P. Xi, F. Chen, G. Xie, C. Ma, H. Liu, C. Shao, et al., Surfactant free rGO/Pd nanocomposites as highly active heterogeneous catalysts for the hydrolytic dehydrogenation of ammonia borane for chemical hydrogen storage. *Nanoscale* **4**(18), 5597 (2012)
55. E.J. Lim, S.M. Choi, H.S. Min, Y. Kim, S. Lee, W.B. Kim, Highly dispersed ag nanoparticles on nanosheets of reduced graphene oxide for oxygen reduction reaction in alkaline media. *Electrochem. Commun.* **28**(1), 100–103 (2013)
56. X. Liu, X. Wang, P. He, L. Yi, Z. Liu, X. Yi, Influence of borohydride concentration on the synthesized au/graphene nanocomposites for direct borohydride fuel cell. *J. Solid State Electrochem.* **16**(12), 3929–3937 (2012)
57. S.J. Cho, A. Suri, X. Mei, J. Ouyang, In situ deposition of gold nanostructures with well-defined shapes on unfunctionalized reduced graphene oxide through chemical reduction of a dry gold precursor with ethylene glycol vapor. *RSC Adv.* **3**(3), 1201–1209 (2012)
58. G. Goncalves, P.A.A.P. Marques, C.M. Granadeiro, H.I.S. Nogueira, M.K. Singh, J. Grácio, Surface modification of graphene nanosheets with gold nanoparticles: The role of oxygen moieties at graphene surface on gold nucleation and growth. *Chem. Mater.* **21**, 4796–4802 (2009)
59. M. Carmo, V.A. Paganin, J.M. Rosolen, E.R. Gonzalez, Alternative supports for the preparation of catalysts for low-temperature fuel cells: The use of carbon nanotubes. *J. Power Sources* **142** (1), 169–176 (2005)
60. E.J. Yoo, T. Okada, T. Akita, M. Kohyama, I. Honma, J. Nakamura, Sub-nano-Pt cluster supported on graphene nanosheets for CO tolerant catalysts in polymer electrolyte fuel cells. *J. Power Sources* **196**(1), 110–115 (2011)
61. E. Yeager, Electrocatalysts for molecular oxygen reduction. *Electrochim. Acta* **29**, 1527–1537 (1984)

62. R. Kou, Y. Shao, D. Wang, M.H. Engelhard, J.H. Kwak, J. Wang, et al., Enhanced activity and stability of Pt catalysts on functionalized graphene sheets for electrocatalytic oxygen reduction. *Electrochem. Commun.* **11**(5), 954–957 (2009)
63. H.J. Kim, S.M. Choi, H.S. Min, S. Green, G.W. Huber, W.B. Kim, Efficient electrooxidation of biomass-derived glycerol over a graphene-supported PtRu electrocatalyst. *Electrochem. Commun.* **13**(8), 890–893 (2011)
64. Q. Yue, K. Zhang, X. Chen, L. Wang, J. Zhao, J. Liu, J. Jia, Generation of OH radicals in oxygen reduction reaction at Pt–Co nanoparticles supported on graphene in alkaline solutions. *Chem. Commun.* **46**(19), 3369–3371 (2010)
65. K. Zhang, Q. Yue, G. Chen, Y. Zhai, L. Wang, H. Wang, H. Li, Effects of acid treatment of Pt–Ni alloy nanoparticles@ graphene on the kinetics of the oxygen reduction reaction in acidic and alkaline solutions. *J. Phys. Chem. C* **115**(2), 379–389 (2010)
66. M. Liu, Y. Lu, W. Chen, Electrocatalysts: PdAg nanorings supported on graphene nanosheets: Highly methanol-tolerant cathode electrocatalyst for alkaline fuel cells (adv. Funct. Mater. 10/2013). *Adv. Funct. Mater.* **23**(23), 1348–1348 (2013)
67. Z.S. Wu, S. Yang, S. Yi, K. Parvez, X. Feng, K. Müllen, 3D nitrogen-doped graphene aerogel-supported Fe<sub>3</sub>O<sub>4</sub> nanoparticles as efficient electrocatalysts for the oxygen reduction reaction. *J. Am. Chem. Soc.* **134**(22), 9082 (2012)
68. C. Zhang, R. Hao, H. Yin, F. Liu, Y. Hou, Iron phthalocyanine and nitrogen-doped graphene composite as a novel non-precious catalyst for the oxygen reduction reaction. *Nanoscale* **4**(23), 7326–7329 (2012)
69. H.R. Byon, S. Jin, S.H. Yang, Graphene-based non-noble-metal catalysts for oxygen reduction reaction in acid. *Chem. Mater.* **23**(23), 3421–3428 (2011)
70. R.J. Toh, H.L. Poh, Z. Sofer, M. Pumera, Transition metal (Mn, Fe, Co, Ni)-doped graphene hybrids for electrocatalysis. *Chem. Asian J.* **8**(6), 1295–1300 (2013)
71. M. Lefèvre, E. Proietti, F. Jaouen, Dodelet, Supporting material for: Iron-based catalysts with improved oxygen reduction activity in polymer electrolyte fuel cells. *Science* **324**(5923), 71–74 (2009)
72. Y. Jiang, Y. Lu, X. Lv, D. Han, Q. Zhang, L. Niu, et al., Enhanced catalytic performance of Pt-free iron phthalocyanine by graphene support for efficient oxygen reduction reaction. *ACS Catal.* **3**(6), 1263–1271 (2013)
73. Z. Yang, H. Nie, X. Chen, X. Chen, S. Huang, Recent progress in doped carbon nanomaterials as effective cathode catalysts for fuel cell oxygen reduction reaction. *J. Power Sources* **236**(16), 238–249 (2013)
74. C. Zhang, R. Hao, H. Liao, Y. Hou, Synthesis of amino-functionalized graphene as metal-free catalyst and exploration of the roles of various nitrogen states in oxygen reduction reaction. *Nano Energy* **2**(1), 88–97 (2013)
75. C. He, Z. Li, M. Cai, M. Cai, J.Q. Wang, Z. Tian, et al., A strategy for mass production of self-assembled nitrogen-doped graphene as catalytic materials. *J. Mater. Chem. A* **1**(4), 1401–1406 (2012)
76. D. Geng, Y. Chen, Y. Chen, Y. Li, R. Li, X. Sun, et al., High oxygen-reduction activity and durability of nitrogen-doped graphene. *Energy Environ. Sci.* **4**(3), 760–764 (2011)
77. J.B. Raoof, R. Ojani, S. Rashid-Nadimi, Electrochemical synthesis of bimetallic Au@Pt nanoparticles supported on gold film electrode by means of self-assembled monolayer. *J. Electroanal. Chem.* **641**(1–2), 71–77 (2010)
78. G. Chen, D. Xia, Z. Nie, Z. Wang, L. Wang, J. Zhang, et al., Facile synthesis of co-Pt hollow sphere electrocatalyst. *Chem. Mater.* **19**(7), 1840–1844 (2007)
79. C.S. Lim, K. Hola, A. Ambrosi, R. Zboril, M. Pumera, Graphene and carbon quantum dots electrochemistry. *Electrochem. Commun.* **52**, 75–79 (2015)
80. M. Bacon, S.J. Bradley, T. Nann, Graphene quantum dots. *Part. Part. Syst. Charact.* **31**(4), 415–428 (2014)

81. Q. Li, B.W. Noffke, Y. Liu, L.S. Li, Understanding fundamental processes in carbon materials with well-defined colloidal graphene quantum dots. *Curr. Opin. Colloid Interface Sci.* **20**(5-6), 346–353 (2015)
82. L. Lin, M. Rong, F. Luo, D. Chen, Y. Wang, X. Chen, Luminescent graphene quantum dots as new fluorescent materials for environmental and biological applications. *TrAC Trends Anal. Chem.* **54**, 83–102 (2013)
83. F. Ksar, L. Ramos, B. Keita, L. Nadjo, P. Beaunier, H. Remita, Bimetallic palladium– gold nanostructures: Application in ethanol oxidation. *Chem. Mater.* **21**(15), 3677–3683 (2009)
84. L. Liu, E. Pippel, R. Scholz, U. Gösele, Nanoporous Pt-Co alloy nanowires: Fabrication, characterization, and electrocatalytic properties. *Nano Lett.* **9**(12), 4352–4358 (2009)
85. P. Du, Y. Zhu, J. Zhang, D. Xu, W. Peng, G. Zhang, et al., Metallic 1t phase MoS<sub>2</sub> nanosheets as a highly efficient co-catalyst for the photocatalytic hydrogen evolution of CdS nanorods. *RSC Adv.* **6**(78), 74394–74399 (2016)
86. L.F. Zhang, G. Ou, L. Gu, Z.J. Peng, L.N. Wang, H. Wu, A highly active molybdenum multisulfide electrocatalyst for the hydrogen evolution reaction. *RSC Adv.* **6**(109), 107158–107162 (2016)
87. S. Mu, X. Chen, R. Sun, X. Liu, H. Wu, D. He, et al., Nano-size boron carbide intercalated graphene as high performance catalyst supports and electrodes for PEM fuel cells. *Carbon* **103**, 449–456 (2016)
88. P. Wu, H. Lv, T. Peng, D. He, S. Mu, Nano conductive ceramic wedged graphene composites as highly efficient metal supports for oxygen reduction. *Sci. Rep.* **4**(2), 3968 (2014)
89. X. Chen, D. He, H. Wu, X. Zhao, J. Zhang, K. Cheng, et al., Platinized graphene/ceramics nano-sandwiched architectures and electrodes with outstanding performance for PEM fuel cells. *Sci. Rep.* **5**, 16246 (2015)
90. C. He, J. Tao, Y. Ke, Y. Qiu, Graphene-supported small tungsten carbide nanocrystals promoting a Pd catalyst towards formic acid oxidation. *RSC Adv.* **5**(82), 66695–66703 (2015)
91. M. Nawaz, W. Miran, J. Jang, D.S. Lee, One-step hydrothermal synthesis of porous 3d reduced graphene oxide/TiO<sub>2</sub> aerogel for carbamazepine photodegradation in aqueous solution. *Appl. Catal. B Environ.* **203**, 85–95 (2017)
92. X. Jia, J. Wang, X. Zhu, T. Wang, F. Yang, W. Dong, et al., Synthesis of lightweight and flexible composite aerogel of mesoporous iron oxide threaded by carbon nanotubes for microwave absorption. *J. Alloys Compd.* **697**, 138–146 (2016)
93. X. Xu, Y. Sun, W. Qiao, X. Zhang, X. Chen, X. Song, et al., 3D MoS<sub>2</sub>-graphene hybrid aerogels as catalyst for enhanced efficient hydrogen evolution. *Appl. Surf. Sci.* **396**(8), 1520–1527 (2017)
94. J. Duan, X. Zhang, W. Yuan, H. Chen, S. Jiang, X. Liu, et al., Graphene oxide aerogel-supported Pt electrocatalysts for methanol oxidation. *J. Power Sources* **285**, 76–79 (2015)



# Nanostructured Electrodes for High-Performing Solid Oxide Fuel Cells

# 8

Hanping Ding

## Contents

8.1	Introduction .....	228
8.2	Nanostructured Cathode for High-Performing Solid Oxide Fuel Cell (SOFC) .....	231
8.2.1	Embedding of Catalyst Nano-network into Cathode by Infiltration Method ....	231
8.2.2	Performance Improvements by Infiltrated Cathode .....	232
8.3	Nanostructured Anode for Solid Oxide Fuel Cell (SOFC) .....	235
8.3.1	Nanostructured Nickel-Based Anode .....	236
8.3.2	Nanostructured Cu-Based Anode .....	237
8.3.3	Nanostructured Ceramic Oxide Anode .....	238
8.4	Conclusion .....	243
	References .....	243

## Abstract

Solid oxide fuel cell (SOFC) is an all-solid-state ceramic electrochemical device for converting chemical energy (fuels) to electricity with high energy efficiency and ultralow harmful emissions. These classes of FCs have received significant attention by researchers as a potential replacement for petroleum-based energy devices. In order to broaden the material selection and increase material system durability, the development of intermediate- or low-temperature SOFC is critical to making their commercialization viable. Therefore, the SOFC performance at lowered operating

## Author Contributions

Dr. Ding would like to thank Prof. Neal P. Sullivan, the Director Colorado Fuel Cell Center, for providing numerous supports during author's academic stay in Colorado School of Mines.

H. Ding (✉)

Department of Mechanical Engineering, Colorado Fuel Cell Center, Colorado School of Mines, Golden, CO, USA

Energy & Environmental Science and Technology, Idaho National Laboratory, Idaho Falls, USA

e-mail: [hanpingding@gmail.com](mailto:hanpingding@gmail.com); [Hanping.ding@inl.gov](mailto:Hanping.ding@inl.gov)



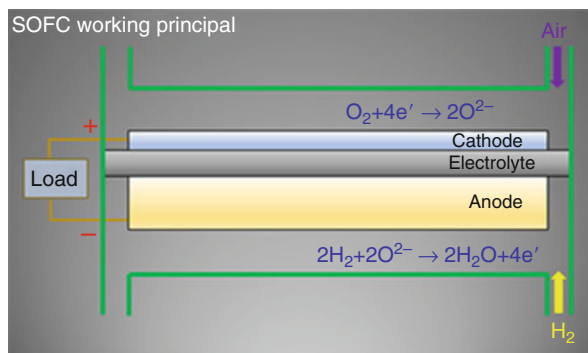
temperatures must be improved by the innovation of materials and microstructures. The nanostructure engineering of electrodes has demonstrated their improved catalytic performance due to minimization of the electrode polarization resistances for oxygen reduction reaction and fuel oxidation reaction at the nanoscale compared to the traditional electrode design. The synthesis technique strategy was based on wet chemistry catalyst infiltration into electrode structure and has been demonstrated improvements in power density and electrode stability. In this chapter, the technical process of ion infiltration method is discussed; and the different routes in fabricating nanostructured electrodes to achieve high-performing SOFC in hydrogen and hydrocarbon fuels are reviewed. The electrode parameters that lead to improvement of SOFC performance are also summarized. By fabricating electrodes at the nanoscale, a significant increase in specific area was obtained that can provide greater active catalysis sites for electrode reactions, as well as a decrease in the activation polarization resistance which collectively led to improved SOFC performance.

---

## 8.1 Introduction

The solid oxide fuel cell (SOFC) is an attractive technology for chemical-to-electrical energy conversion due to its advantages such as high efficiency, low operation cost, and fuel flexibility [1–4]. As a ceramic device, the FC operates at a high temperature which facilitates its high efficiency when combined with a gas turbine. The absence of expensive catalyst material and resistance against fuels containing carbon monoxide contributes to its lower manufacturing cost [5–7]. Investigators have aimed to increase SOFC power efficiencies from a variety of fuel feedstocks through research and development of functional materials used in SOFCs. Researchers have focused on new cell design; fabrication of composite electrode or new electrode structures, mathematical analysis of gas flow patterns, and thermodynamic modeling of catalysis at the electrode surface are examples of areas of research which will lead to improvements in FC electrochemical performance. The higher operating temperature also requires the FC design to incorporate materials that result in increased physical and chemical compatibility with other cell components, the capability of system incorporation into the stack, which in turn enables the FC to be operated at a lower temperature increasing long-term FC stability [8–10]. The commercialization trend of an SOFC system for distributed power sources has become more widespread, due to improvements in optimized operating conditions, resulting in better longevity and lower manufacturing costs. At present, while this technology exhibits great promise to be applied in society, there remain three major engineering and scientific hurdles. Firstly, the relative high operating temperature requires the SOFC materials and other key components in the stacks such as sealing and interconnecting materials to be compatible resulting in increased reliability of the stack system [11, 12]; secondly, the use of petroleum-based fuels faces technical problems such as coking and sulfur poisoning when nickel-based anode catalysts are used, although researchers have proposed some strategies to avoid the degradation of FCs when using fuels containing carbon and sulfur [13–15]; thirdly, the higher operating temperature leads to a

**Fig. 8.1** The working principle of a solid oxide fuel cell (SOFC)



degradation in performance over time affecting their longevity, and contributing to increased manufacturing and maintenance costs, and ultimately FC efficiency [16, 17]. Therefore, researchers have focused efforts on developing materials and structures and operating conditions that have been made to optimize the performance of single-cell level and stack compatibility [18, 19]. Since the high operating temperature restricts potential SOFC material selection and reliability, various technical routes have been explored to increase FC robustness and performance. The introduction of more active catalysts, or catalyst with an increased specific surface, and more conductive materials is shown to contribute to improved FC electrochemical performance at lower temperatures.

A typical oxide-ion conducting-based SOFC is composed of two electrodes and one electrolyte (Fig. 8.1). The oxygen ions are formed by oxygen molecules associating with two electrons at the cathode compartment that is transported through the dense electrolyte to reach the anode compartment. The oxygen ions can react with hydrogen fuel to form the water. During this process, the electrons released from hydrogen pass through the external circuit to form the electricity. The SOFC performance is directly determined by the internal resistance which is related with the overpotential polarization of each component contributed by imperfections in materials, microstructure, and design of the fuel cell [20]. There are three main polarization resistances contributed by different physical or electrochemical phenomenon: ohmic resistance, concentration polarization, and activation polarization.

Firstly, the ohmic resistance is determined by the conductivities of these three components. The resistance is mainly determined by the electrolyte material since the electronic conductivities of the cathode (usually conductive oxide) and anode (nickel metal in cermet composite) are several magnitudes higher than that of electrolyte which is ionic and conductive in nature.

Therefore, the ohmic resistance of electrolyte dominates the total resistance; consequently, the conductivity and thickness of the electrolyte become two important parameters to control the resistance. The electrolyte resistance can be minimized through the incorporation of high conductive electrolyte materials and techniques for fabricating thin membranes. Secondly, the concentration polarization resistance results from limitations on the mass transport within the electrode structure [21, 22].

The reactants may be consumed by the electrochemical reaction faster than they can diffuse into the reaction boundaries, which causes the reactant concentration to be lower than required for optimal performance. The concentration polarization occurs in both the anode and cathode compartments. This polarization is in part due to electrode design that is very thin and highly porous. The reaction products of steam can dilute the fuel stream which must transport through the whole anode substrate to the three-phase boundary. The relevant optimization strategies of anode microstructure such as increasing porosity and grade electrode can decrease this polarization resistance significantly with the compromise of other properties. Lastly, the activation polarization is the result of catalytic activity toward oxygen reduction reaction (ORR) and fuel oxidation reaction, which is closely related to the catalytic activity of the employed materials and microstructure [23].

In a typical anode-supported SOFC with electrolyte thin membrane operated in hydrogen, the cell performance is affected by the ohmic resistance of electrolyte film and activation resistance from cathode material. The electrolyte resistance can be significantly reduced by using very thin film, and concentration polarization can be decreased by optimizing the microstructure for improved gas diffusion; the cathode activation polarization is the dominant factor in the total cell resistance. Therefore, the development of highly active materials and optimal electrode morphology is critical to improving the FC performance. Therefore the relationship of good material candidates to improved electrochemical catalysis requires improvements in oxygen diffusion efficiency and increased surface exchange kinetics, which are empirically or experimentally associated with mixed electrical conductivity. Researchers have significant efforts in developing newer cathode materials with high catalytic activity for oxygen reduction reaction (ORR) [24–26]. Many types of materials such as perovskite, spinel, and layered perovskite have been demonstrated as promising cathodes for high-performing SOFC [27–30]. In direct hydrocarbon-fueled SOFC with ceramic oxide anode, performance is constrained by the degree of electrode polarization resistance arising from both the cathode in the oxidizing condition and anode in the reducing atmosphere. Therefore, the propensity of ceramic oxide anode as a catalyst under complex gaseous conditions requires a greater understanding of catalyst kinetics, materials engineering, and electrode design for enhanced catalysis. There are several material candidates that are being developed for stable operation SOFC in hydrogen, methane, and other hydrocarbon fuels in the form of nanostructured catalysts [31–33].

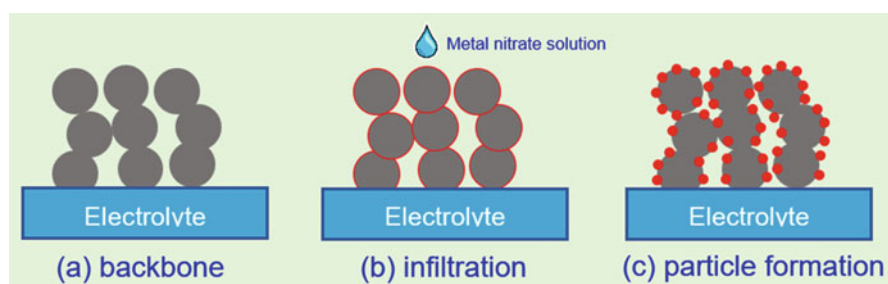
Nano-engineering of the cathode electrode to form nano-network has been shown to significantly increase the ORR through the availability of more active sites at the electrode surface that in turn lead to increased SOFC performance. The conventional cathode layer is prepared by sintering the ceramic particles to form a porous electrode microstructure for gaseous diffusion and reaction. The length of three-phase boundaries for ORR reaction is closely related to electrochemical performance. To maximize the three-phase boundaries (TPBs) for high-performing SOFC, a new cathode structure with the higher specific surface area can be achieved by various technique routes, which enable nanostructured catalyst to be fabricated. The introduction of the nano-sized catalyst into the cathode backbone has been regarded as an effective way

to increase the surface area and ultimately FC performance [34–37]. There are many methods to embed the catalyst metal into the nano-network for increased SOFC performance [38–40]. The ion filtration or impregnation method via metal salt solution implanting into electrode structure attracts increasing attention and becomes the most effective way to develop a catalytic nano-network for extremely extended reaction sites. The ion filtration method can not only increase the specific surface area but also effectively avoid thermal or chemical compatibility problems between cathode and electrolyte. The technique of ion infiltration and development status, as well as perspective, is introduced and reviewed [41–44]. The significant increase of active sites for ORR or fuel oxidation in SOFC nanostructured electrodes can enhance catalytic activity with decreased electrode polarization resistance. The development status of nanostructured electrodes for high-performing SOFC operated in various fuels is discussed in this chapter.

## 8.2 Nanostructured Cathode for High-Performing Solid Oxide Fuel Cell (SOFC)

### 8.2.1 Embedding of Catalyst Nano-network into Cathode by Infiltration Method

Conventional cathode sintering requires high temperature to facilitate good mechanical bonding and necking between cathode and electrolyte, which cause rough microstructure with large particle size. The basic process of ion infiltration method is to deposit two-dimensional or three-dimensional catalysts into cathode layer by firing aqueous metal ion solution with fast ramping rate to control nuclei rate. The nano-network is vulnerable to the high temperature; therefore, it demands a new route to obtaining nano-sized catalyst in the cathode: (a) the conducting electrolyte or electrode backbone/framework is sintered onto electrolyte at normal sintering temperature; and (b) nano-sized catalysts are impregnated into the rigid electrode structure at low temperatures afterward. The nanostructured cathode is formed after this two-step preparation (Fig. 8.2). For yttria-stabilized zirconia (YSZ)-based cell,



**Fig. 8.2** The typical process of infiltration method: (a) YSZ backbone; (b) dropping solution onto particle surface; (c) formation of catalyst particles

for example, (a) the pure and porous YSZ structure with thickness about 10–30  $\mu\text{m}$  was firstly deposited onto YSZ electrolyte after sintering at 1100–1200  $^{\circ}\text{C}$ ; (b) the prepared solution with stoichiometric amount of metal salts for a specific chemical composition (e.g., lanthanum strontium manganite, LSM) is dipped into the YSZ backbone and then fired at relatively low temperature of 700  $^{\circ}\text{C}$  to form the LSM nanoparticles; and (c) the loading of LSM cathode particles is controlled by the infiltration cycling times.

There are several technical advantages for this infiltration method: (a) the generated nano-network can be well maintained at the relatively low formation temperature, while good mechanical strength between electrode and electrolyte is reached by the backbone layer; (b) the form of nano-network can be differentiated by various preparation conditions, such as heating/cooling rate and concentration of the metal nitrate solution, and (c) diverse materials with compositional complexity can be in situ synthesis and sintered in the electrode. For the different conducting interface required for ORR, two kinds of electrode structures are fabricated. If the cathode is composed of a pure electronic conductive material, a porous electrolyte scaffold/skeleton is fabricated on the dense electrolyte first to form oxide-ion conducting path, and then the cathode catalyst of nano-sized particles or wires is deposited onto the surface to extend the reaction TPB to the whole surface of electrolyte/electrode interface.

If the cathode is a mixed ionic-electronic conductor, there are two possible ways to fabricate the cathode. First, the scaffold can be the electrolyte for conducting only oxygen ions or mixed ionic-electronic conductors (MIEC) cathode for conducting both ions and electrons. The second step is to infiltrate the cathode catalyst onto the scaffold so that both backbone and surface catalyst can conduct electrons and ions simultaneously while ORR takes place on the nanoparticles.

## 8.2.2 Performance Improvements by Infiltrated Cathode

Many catalytically active oxides have been developed as the cathode materials for SOFC, in which perovskite structure is commonly used due to the capability of accepting oxygen vacancies readily and electronic conductivity by multivalent transition metals. Examples of perovskite-based cathode materials include lanthanum strontium manganite (LSM,  $\text{La}_{0.8}\text{Sr}_{0.2}\text{MnO}_3$ ) [45], lanthanum strontium cobaltite (LSC,  $\text{La}_{0.6}\text{Sr}_{0.4}\text{CoO}_3$ ) [46], samaria strontium cobaltite (SSC,  $\text{Sm}_{0.5}\text{Sr}_{0.5}\text{CoO}_3$ ) [47], and barium strontium cobalt ferrite (BSCF,  $\text{Ba}_{0.5}\text{Sr}_{0.5}\text{Co}_{0.8}\text{Fe}_{0.2}\text{O}_3$ ) [48]. The electrode backbone can be electrolyte material with ionic conduction or mixed ionic and electronic conductor.

In the conventional LSM-based cathode, the fluorite-structured yttrium-stabilized zirconia YSZ is introduced to the LSM nanoparticles by impregnation. The fabrication of such composite cathode can not only increase the reaction sites for oxygen reduction, but the materials also enhance the mechanical adhesion between electrode and electrolyte since the YSZ backbone is sintered at high temperature to easily form the good ceramic necking. Furthermore, the low-phase formation temperature can

also avoid the potential chemical reaction of LSM and YSZ in the case of direct sintering of composite electrode. He and Gorte et al. prepared LSM with perovskite phase by infiltrating mixed nitrate solution into a porous YSZ matrix, followed by a sintering process at various temperatures [49]. With uniform fine LSM particles, the electrical conductivity at 700 °C in the air with a porosity of 28% reached 3.16 S/cm. The cathode polarization resistance can be decreased to 0.5  $\Omega\cdot\text{cm}^2$  [50]. The anode-supported single cell with such fabricated cathode exhibited about 360  $\text{mW}\cdot\text{cm}^{-2}$  at 700 °C in humidified  $\text{H}_2$ . Armstrong and Virkar et al. also prepared infiltrated LSM electrode using nitrate-salt solution and achieved power density as high as 1.2  $\text{W}\cdot\text{cm}^{-2}$  for a cell operating in hydrogen at 800 °C [51]. Jiang et al. found that a proper chelating agent should be added to the nitrate solution to avoid segregation of individual metal ions during firing process to form pure LSM phase structure [52]. Because the infiltration process is an in situ wet chemistry method, the mobility of different metal ions can be reduced by encircling stable metal-chelate complexes steadily into the backbone by growing polymer network. For example, by using Triton X-100 as a chelating agent and one-step infiltration process, the LSM particles with a size of 30–100 nm were deposited on the outer wall of the pre-sintered porous YSZ, which provided a high density of active sites for oxygen reduction reaction [53]. A power density of 0.3  $\text{W}\cdot\text{cm}^{-2}$  at a low temperature of 650 °C was obtained. Furthermore, the infiltrated LSM nanoparticles were demonstrated to be electrochemically stable for 500 h at 650 °C when the cell was discharged at 150  $\text{mA}\cdot\text{cm}^{-2}$  [54].

As a mixed ionic and electronic conductor (MIEC), lanthanum strontium cobaltite (LSC) is a highly conductive perovskite material that has been used as a cathode material. To increase catalysis, the specific area of the catalyst area was increased by the design of a tubular structure. The LSC cathode was synthesized by using a pore-wetting technique [55]. The LSC nanotube yielded low electrode polarization resistance of 0.21  $\Omega\cdot\text{cm}^2$  at 700 °C measured from the prepared symmetric cell. However, the LSC cathode was not very stable under cathodic conditions. Huang et al. proved that the high ORR activity could be retained by coating the surface with a conformal layer of nanoscale zirconia ( $\text{ZrO}_2$ ) film by atomic layer deposition (ALD) method [56]. The nanostructured LSC cathode showed the low resistance of 0.04  $\Omega\cdot\text{cm}^2$  at 700 °C in the air for 4000 h. However, the LSC perovskite-based cathode material cannot be widely used because it reacts rapidly with YSZ at 1000 °C, the required minimum sintering temperature to get ceramic bonding, to form insulating phases of lanthanum zirconia ( $\text{La}_2\text{Zr}_2\text{O}_7$ ) and strontium zirconia ( $\text{SrZrO}_3$ ) that in turn lower catalysis efficiency [57]. Therefore, infiltrating the LSC electrode can avoid this problem by decreasing the temperature of forming perovskite phase. The cell with a cathode composed of 30 vol. % LSC in a YSZ scaffold exhibited a peak power density of 2.1  $\text{W}\cdot\text{cm}^{-2}$  at 800 °C in hydrogen ( $\text{H}_2$ ) [58].

Another promising material for high-performing cathode is rare earth element-based oxides such as barium strontium cobalt ferrite (BSCF) developed by Shao and Haile et al. Incorporated into a thin-film doped ceria single fuel cell, the electrode exhibited high power densities in the FC of 1010  $\text{mW}\cdot\text{cm}^{-2}$  at 600 °C and 402  $\text{mW}\cdot\text{cm}^{-2}$  at 500 °C when operated in humidified hydrogen and air [48]. The

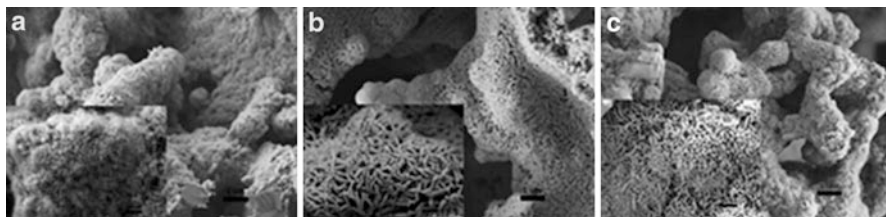
area-specific resistance (ASR) was determined from the symmetric cell as remarkably as low between 0.055 and 0.071  $\Omega\cdot\text{cm}^2$  at 600 °C and between 0.51 and 0.6  $\Omega\cdot\text{cm}^2$  at 500 °C. The mechanism responsible for the increased performance was hypothesized from the oxygen permeation measurement. The high oxygen diffusivity through BSCF bulk yields its high rate of oxygen electrooxidation, while oxygen surface exchange process is the rate limiting step at low operating temperatures. Therefore, the superior high-performing SOFC at low temperatures can be possible after implementing the nanostructured BSCF cathode. There are two general strategies to achieve the nanostructured BSCF electrodes based upon pulse laser deposition (PLD) and wet chemistry ion infiltration method. Because of the low electrical conductivity of BSCF limiting the cathode catalysis activity, the thin catalyst layer is believed to enhance the ORR. Liu and Cheng et al. fabricated 800-nm-thick BSCF layer consisted of small nanoparticles with average particle size of about 40 nm onto YSZ/nickel oxide (NiO)-YSZ composite substrate with increased FC performance [59].

The nanoparticles grow to a dense layer on the YSZ electrolyte with agglomerated grains with characteristic diffraction peaks representing the {110}, {211}, {220}, and {310} crystal planes. The maximum power density with PLD-prepared BSCF cathode was 1.12  $\text{W}\cdot\text{cm}^{-2}$  in  $\text{H}_2$  at 800 °C, compared with 0.45  $\text{W}\cdot\text{cm}^{-2}$  for conventional screen-printing BSCF cathode. With the infiltration of the stoichiometric metal salt solution, ~20 wt % BSCF nanoparticles with size about ~30 nm were formed on the surface of scaffold particles [60]. For the infiltrated composite cathode, the ORR occurred not only at the TPB but also at the prolonged cathode surface. It is found that electrode polarization resistance ( $R_p$ ) reached the minimum value when the backbone is infiltrated with 16.2 wt % BSCF, e.g., 0.043  $\Omega\cdot\text{cm}^2$  at 700 °C.

The nanostructured BSCF electrode was also achieved by depositing other kinds of nanoparticles such as LSM or Ag onto the BSCF backbone [61, 62]. For example, the  $R_p$  of 1.8  $\text{mg}\cdot\text{cm}^{-2}$  BSCF-impregnated LSM cathode was 0.18  $\Omega\cdot\text{cm}^2$  at 800 °C, which its resistance was about 12 times lower than that of pure LSM, leading to increased FC performance. The YSZ electrolyte-based single cell with the nanostructured BSCF/LSM cathode exhibited maximum power densities of 1.21 and 0.32  $\text{W}\cdot\text{cm}^{-2}$  at 800 and 650 °C, respectively.

Strontium-doped samarium cobaltite (SSC) as a compositional cathode material has been extensively investigated by researchers for SOFC with different electrolytes [63–65]. Xia et al. found that the composite cathode of SSC and samarium-doped ceria (SDC, 10 wt %) significantly reduced the interfacial resistance from 2.0  $\Omega\cdot\text{cm}^2$  for pure SSC to less than 0.18  $\Omega\cdot\text{cm}^2$  at 600 °C under open circuit potential (OCP) condition. With combustion chemical vapor deposition (CVD) method, the composite cathode particles (70 wt % SSC and 30 wt % SDC) were about 50 nm in diameter. The electrode/electrolyte interfacial resistance is about 0.17  $\Omega\cdot\text{cm}^2$  at 600 °C. The maximum power densities were 60, 108, 159, 202, and 243  $\text{mW}\cdot\text{cm}^{-2}$  at 500, 550, 600, 650, and 700 °C, respectively [66]. Xia et al. also fabricated a nano-network of SSC by infiltration method for low-temperature SOFC. The nano-network consisted of well-connected SSC nanowires serving as conducting path for oxygen ion and





**Fig. 8.3** Morphology of cathodes with impregnated SSC nanoparticles fired at different heating rates: (a)  $5\text{ }^{\circ}\text{C min}^{-1}$ ; (b)  $10\text{ }^{\circ}\text{C min}^{-1}$ ; (c)  $30\text{ }^{\circ}\text{C min}^{-1}$  [67]

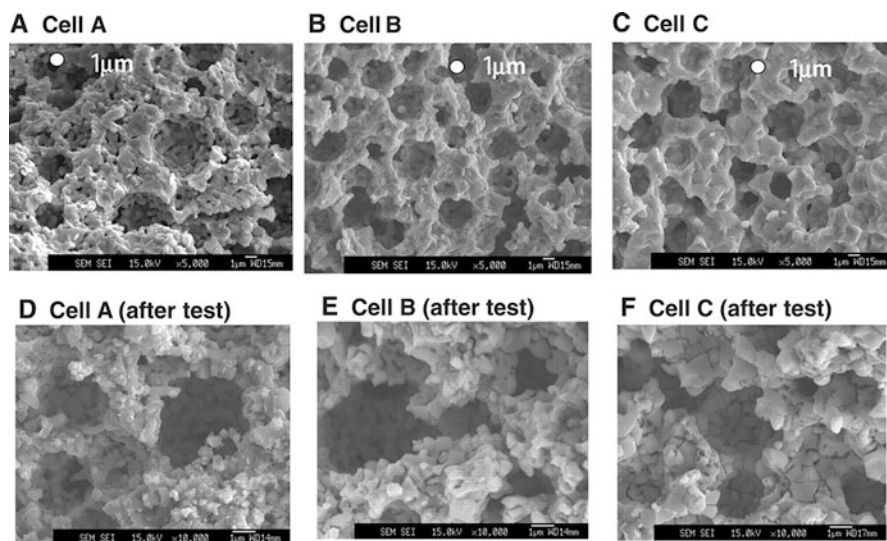
electron conduction and catalysis sites, respectively [67]. The morphology was found to closely relate to a process of nucleation and growth affected by the heating rate (Fig. 8.3).

At a low heating rate, more time for solid nucleation and growth resulted in the formation of particles of large diameter that were distributed randomly on the outer surface of the SDC backbone frame, whereas with the higher heating rate, smaller diameter particles were generated due to the faster nucleation reaction, increased nucleation, and smaller nuclei nanoparticle clustering. The SSC nanoparticle formed a network as a cathode; the single cell with a nickel (Ni)-SDC anode and a  $10\text{-}\mu\text{m}$ -thick SDC electrolyte showed peak power density of  $0.44\text{ W}\cdot\text{cm}^{-2}$  at  $500\text{ }^{\circ}\text{C}$  and  $0.81\text{ W}\cdot\text{cm}^{-2}$  at  $600\text{ }^{\circ}\text{C}$ .

### 8.3 Nanostructured Anode for Solid Oxide Fuel Cell (SOFC)

The SOFC anode is where the fuel ( $\text{H}_2$ ,  $\text{C}_x\text{H}_y\text{O}_z$ , or  $\text{NH}_3$ ) is oxidized by oxygen ions after electrons are released to pass the external circuit to form the electricity. In terms of fuel flexibility of SOFC, it is critical to developing a well-defined anode structure for high-performing SOFC. For over four decades, nickel-zirconia dual-phase cermet has been regarded as the dominant anode material. Nickel is an excellent metal catalyst for fuel oxidation, and Ni possesses a high degree of electronic conductance as an anode material. The reduction of NiO to Ni also produces a considerable amount of porosity for fuel gas diffusion. The use of zirconia is to provide ion conduction for extending sites of HOR and also to mechanically support the whole fuel cell. The importance of anode functioning as fuel oxidation chamber is mainly summarized in two aspects. Firstly, the anode performance using hydrogen fuel can be effectively improved by minimizing the polarization resistance when the microstructure of the anode is optimized because concentration polarization basically dominates the anode polarization. Meanwhile, as a place where the internal reforming takes place when the anode is fed with hydrocarbon fuels, the choice of anode material and decoration of microstructure with metals are critical to developing stable and high-performing anode in such fuels. Secondly, nickel-free ceramic oxides have also been studied as alternative anode materials. Due to low electrical conductivity and sluggish catalytic activity,





**Fig. 8.4** Scanning electron microscopy images of Ni-YSZ anode microstructure before and after test [68]

the optimization of anode property and morphology is necessary to improve the anode performance. Therefore, the nanostructured anode for SOFC is discussed for nickel-based and nickel-free-based anode, respectively.

### 8.3.1 Nanostructured Nickel-Based Anode

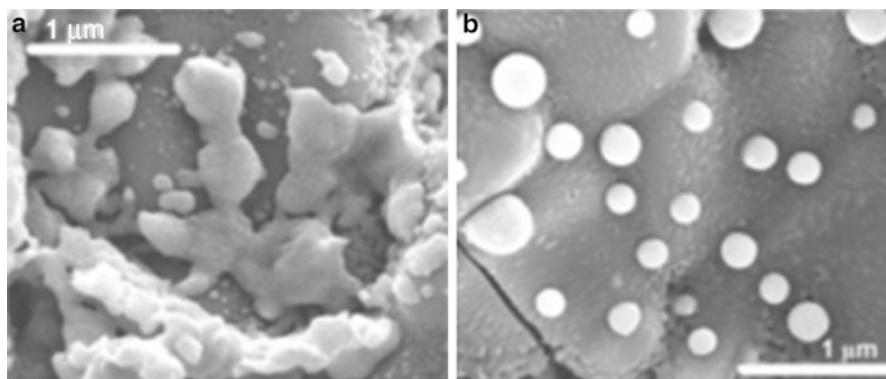
Since nickel is the sole catalyst for fuel oxidation while the ceramic phase provides only mechanical support for the fuel cell, decreasing the anode particle size can significantly improve the electrochemical performance due to increased availability of reaction active sites. The effect of anode microstructure on SOFC performance has been studied by many researchers. Suzuki et al. correlated the microstructure of anode with electrochemical performance on a tubular SOFC design. With a conventional preparation method, the NiO-YSZ anode tube was prepared with high-porosity and nano-sized NiO particles (Fig. 8.4) [68]. Meanwhile, the YSZ electrolyte membrane was sintered on with a thickness only about 3 μm to minimize the ohmic resistance of the whole cell. The SOFC had a peak power density of more than 1 W·cm<sup>-2</sup> at 600 °C.

The investigation of the hydrogen fuel flow rate affecting performance was performed to better understand the relationship between structure and SOFC power output. Zhan and Barnett et al. fabricated a thin LSGM electrolyte-based SOFC with nanostructured nickel oxide using a three-step procedure which employed (1) ion impregnation method to generate nano-catalyst [69], (2) depositing of a 30 μm LSGM layer onto LSGM dense pellet to form bilayer electrolyte/support

structure and sintering cathode and current collector layers, and (3) impregnation of the nickel nitrate solution into the porous LSGM structure and calcination at 700 °C in the air to generate a thin layer of NiO nanoparticles on the LSGM structure surface. The Ni loading was controlled by varying the impregnation cycles and solution concentration. The nanostructured SOFC showed high power densities of 1.20 W·cm<sup>-2</sup> at 650 °C and 0.39 W·cm<sup>-2</sup> at 550 °C when operated using humidified hydrogen as a fuel and air as an oxidant. The average diameters of synthesized Ni particles varied from ~30 nm when Ni volume loading is about 0.84% to ~90 nm at 2.51 vol. %. The increase in particle size was caused by repeated calcination cycles; therefore, it was a compromise between Ni loading and thermal cycle to yield the optimal performance. Some more dedicated studies further clarified the role of the nanostructured anode in the high-performance fuel cell by comparing the effect of anode functional layer located at TPB active area on decreasing cell polarization resistance. Park and Son et al. investigated the impact of a nanostructured Ni-YSZ anode on low-temperature SOFC performance by modifying the processing (ALD) technique to fabricate an anode-supported cells based on thin-film (~1 μm) electrolyte with and without the nanostructured Ni-YSZ anode. The Ni-YSZ anode functional layer with grain size about ~100 nm was fabricated [70]. It was determined that the anode with functional nano-sized particles increased FC significantly performance, particularly at a low temperature of 500 °C. The electrochemical analysis also revealed that the TPB density was increased near the electrolyte/anode interface because of increased number of active sites for charge transfer and fuel oxidation reaction. Their work also demonstrated that while cathode resistance was considered as the main factor in determining whole cell resistance, the anode structure could also affect the low-temperature performance. Yamaguchi and Barnett et al. also studied the nanostructured anode functional layer thickness playing a role in gaining better contact resistance [71]. With a thicker functional layer, the power density was gradually improved; and it was expected that the porosity of the catalytic layer started to be a negative effect on FC performance when the layer thickness was further increased to some threshold value, which has not been optimized.

### 8.3.2 Nanostructured Cu-Based Anode

As conventional nickel anode are vulnerable to hydrocarbon fuels when fuels are not reformed either internally or externally, alternative anode materials are proposed to replace potential problems such as coking and/or sulfur poisoning. One method proved to be an effective anode was anode containing copper due to the metals high electronic conductivity for fuel oxidation reaction and is inertness to coking. Therefore, a Cu anode can effectively inhibit carbon deposition and minimize degradation in catalysis. However, Cu anode is not active toward fuel catalysis; therefore, other forms of catalyst should be implemented into anode structure. Gorte et al. proposed a Cu-based anode with ceria nanoparticles for a direct-methane SOFC [72]. Because the melting temperature of CuO is as low as 1235 °C, the anode cermet co-sintering method cannot be used to prepare CuO-ceria composite anode at high sintering



**Fig. 8.5** SEM images of a Cu-CeO<sub>2</sub>-YSZ composite (18 vol% Cu, 9 vol% ceria) reduced in H<sub>2</sub> at (a) 700 °C and (b) 900 °C [73]

temperature for densifying the electrolyte membrane [73,74]. Therefore, the YSZ anode backbone was prepared by tape casting to form the porous structure after pre-sintering, and then Cu was added by aqueous impregnation with a concentrated solution of Cu(NO<sub>3</sub>)<sub>2</sub>, followed by firing in the air to form the nanoparticles (Fig. 8.5).

With a 60- $\mu\text{m}$ -thick YSZ electrolyte and Cu-ceria anode, the cell was demonstrated to show direct oxidation of various hydrocarbons (methane, ethane, 1-butene, n-butane, and toluene) with products of carbon dioxide (CO<sub>2</sub>) and water. The maximum power densities were 0.34 W·cm<sup>-2</sup> for H<sub>2</sub> and 0.18 W·cm<sup>-2</sup> for n-butane at 800 °C. Because Cu was used primarily as the current collector and ceria (CeO<sub>2</sub>) for catalytic activity for fuel oxidation reaction, the infiltration of ceria was necessary to construct a catalytically active nanostructured Cu-ceria anode [75]. Some other metal-phase catalysts were also added into Cu-ceria anode by infiltration method to show more promise when the anode was operated using methane as a fuel feedstock [76].

### 8.3.3 Nanostructured Ceramic Oxide Anode

Several ceramic oxides with a perovskite structure have been extensively studied for alternative anode materials, which are mixed ionic-electronic conductors in the anodic conditions and catalytically even more active than ceria for oxidation of various fuels. Perovskites could readily accept oxygen vacancies and contain transition-metal cations in the octahedral sites due to their high tolerance against crystal distortion. Based on these several oxide-based perovskites, such as lanthanum strontium chromium manganite type (LSCM, La<sub>0.75</sub>Sr<sub>0.25</sub>Cr<sub>0.5</sub>Mn<sub>0.5</sub>O<sub>3</sub>) [77] with other metals such as lanthanum strontium titanium oxide type (LSTO, La<sub>0.33</sub>Sr<sub>0.67</sub>Ti<sub>1-x</sub>M<sub>x</sub>O<sub>3</sub>, where *M* was either titanium (Ti), iron (Fe<sup>n+</sup>), manganese (Mn<sup>n+</sup>), or scandium (Sc)) [78], nonstoichiometric ordered perovskite strontium

molybdate-type transition metal oxides  $\text{Sr}_2M\text{MoO}_6$  (SMMO, where  $M$  is either magnesium (Mg), iron (Fe), or cobalt (Co)) [33, 79, 80] and praseodymium strontium niobium-type oxides (PSNO) with cobalt or iron ( $\text{Pr}_{0.8}\text{Sr}_{1.2}(\text{Co}, \text{Fe})_{0.8}\text{Nb}_{0.2}\text{O}_4$ ) [81] have been investigated as the potential anode materials. These conductive anode materials have high resistance against both coking and sulfur poisoning and limited stability under reducing condition. However, these anodes also showed other limitations, such as insufficient electrical conductivity and low catalytic activity when compared to those of the conventional Ni-YSZ anode. For instance, pure perovskite lanthanum strontium titanium-type oxide (LSTO) or lanthanum and strontium chromium-type manganite (LSCM) anode without a palladium (Pd) or nickel (Ni) catalyst provided lower catalytic performance using  $\text{H}_2$  as a fuel source below  $900^\circ\text{C}$ , and the anode catalytic activity toward  $\text{CH}_4$  oxidation was also lower than with the anodes with the Ni catalyst [82,83]. It was further observed that the catalytic pathways for reforming methane during the cell operation could be blocked by the residual strontium carbonate ( $\text{SrCO}_3$ ) and strontium molybdate ( $\text{SrMoO}_4$ ) on the surface of the SMMO anode [84]. To enhance the performance of the FC using hydrogen and other fuels, it was hypothesized that nanostructuring of the ceramic oxide anode was able to significantly increase the number of active sites on functional nanoparticles catalyst that lead to increased performance.

### 8.3.3.1 Precious Metal

The impregnation of highly catalytic precious metals can enhance the performance of ceramic oxide anodes. The commonly used catalysts are a ruthenium (Ru), Pt, and Pd. The impregnated anodes demonstrate enhanced catalytic activity to fuel oxidation reaction. S. P. Jiang et al. [85] and Y. Ye et al. [86] both fabricated anodes with Pd nanoparticles by ion infiltration method, followed by determination of the electrocatalytic activity of composite LSCM/YSZ anode for the methane and ethanol oxidation reaction, which was significantly improved. At  $800^\circ\text{C}$ , the electrode polarization resistance for methane oxidation was reduced by a factor of 3 with  $0.1\text{--}0.66\text{ mg}\cdot\text{cm}^{-2}$  loading of Pd. Kinetic analyses indicated that the oxygen transfer and methane decomposition processes were also promoted. It was determined that impregnation of Pd had a negligible effect on hydrogen oxidation using wet  $\text{H}_2$ . The study reported by R. J. Gorte et al. also investigated the improvement of catalysis by LSCM/YSZ anode by infiltrating different catalysts of Pt, Ni, Pd, and ceria [82]. For comparison, the electrode impedance (e.g.,  $1.5\ \Omega\cdot\text{cm}^2$ ) was measured for a variety of anode materials without and with a metal catalyst. The resistance decreased to  $0.36\ \Omega\cdot\text{cm}^2$  with the addition of 5 wt % ceria and to  $0.08\ \Omega\cdot\text{cm}^2$  with 0.5 wt % Pd and 5 wt % ceria. It is hypothesized that the metals Pd or Pt primarily enhance the diffusion and dissociation related with electrode processes at low frequencies in impedance spectra, which facilitates the mass transfer of reaction species. The combination of ceria and Pd or Pt nanoparticles can further enhance the performance of the anode. For example, Ru- $\text{CeO}_2$  (50%) and YST ( $\text{Sr}_{0.88}\text{Y}_{0.08}\text{TiO}_3$ ) (50%) anode YSZ ( $\text{Y}_{0.08}\text{Zr}_{0.92}\text{O}_2$ ) electrolyte exhibited peak power densities of  $510\text{ mW}\cdot\text{cm}^{-2}$  in  $\text{H}_2$  and  $470\text{ mW}\cdot\text{cm}^{-2}$  in  $\text{H}_2$  with 10 ppm  $\text{H}_2\text{S}$  at  $800^\circ\text{C}$  [87].

### 8.3.3.2 Non-precious Metal

One major drawback of fuel cell-related manufacturing costs is related to the cost of utilization of precious metal catalysts. The cost could be lowered by substitution of the precious metals by catalytically active non-precious metal in the electrode as demonstrated by Liu [88]. Uchida et al. [89] introduced a small amount of Ni catalyst (6–8 vol. %) into the ceramic frame for increasing the active area for reaction significantly. Fu and Irvine found that yttrium-substituted SrTiO<sub>3</sub> (YST) was a very good electronic conductor with conductivity about 20–100 S·cm<sup>-2</sup> at 800 °C but showed limited catalytic activity [90]. By implementing the required ionic conductivity and catalytic activity, YSZ was combined with YST to supply the ionic conduction path, and the composite material was fabricated as the ceramic frame. A small amount of Ni catalyst was incorporated into the two-phase ceramic network to enhance the reaction activity. The R<sub>p</sub> with 0%, 5%, and 10% Ni loaded into YST/YSZ anodes in wet 5% hydrogen (H<sub>2</sub>)/balanced by argon (Ar) at 850 °C was determined, and the anode showed a decreasing trend in ohmic resistance from 0.49 to 0.17 and then 0.13 Ω·cm<sup>2</sup>, respectively [90]. The Ni nanoparticles with a size of 50–100 nm were fabricated to potentially offer a large number of active sites for the HOR, and it was determined that the nanoparticles were effectively separated by strontium yttria titania (SYT)/yttria-stabilized zirconia (YSZ) particles with a minor degree of grain coarsening. The Ni nanoparticles were also employed into different ceramic anodes. Boulfrad and Irvine et al. coated 5 wt % nickel onto lanthanum strontium chromium manganese oxide-type (LSCM, La<sub>0.75</sub>Sr<sub>0.25</sub>Cr<sub>0.5</sub>Mn<sub>0.5</sub>O<sub>3-δ</sub>) perovskite particles to form the nanostructured ceramic oxide particles which are then mixed with different amounts of gadolinium-doped ceria (CGO, Ce<sub>0.9</sub>Gd<sub>0.1</sub>O<sub>1.95-δ</sub>) material as the anode [91]. Under examinations of scanning transmission electron microscopy (STEM) and X-ray energy dispersive spectroscopy (EDS), nickel was observed to be precipitated in the form of nanoparticles under reducing condition. The Ni nanoparticles led to a decrease in anodic activation energy by half, and the electrode polarization resistance also dropped by 60% at 800 °C. Yoo et al. reported a maximum power density of ~0.63 W·cm<sup>-2</sup> in H<sub>2</sub> at 800 °C for a lanthanum strontium gallium magnesium oxide (LSGM)-type (~250 μm) electrolyte-supported SOFC with Ni-impregnated lanthanum gallate, strontium, and titanium cobaltite-gadolinium-doped ceria-type ((La<sub>0.2</sub>Sr<sub>0.8</sub>Ti<sub>0.98</sub>Co<sub>0.02</sub>O<sub>3</sub>)-Ni-GDC) composite anode [92].

Xiao and Chen et al. used temperature-programmed reduction (TPR) technique to study the promotion effect of Ni (~2 wt %) on hydrogen oxidation when it is infiltrated onto a double perovskite strontium ferrite molybdate (SFM, Sr<sub>2</sub>Fe<sub>1.5</sub>Mo<sub>0.5</sub>O<sub>6</sub>) ceramic anode [93]. With the Ni-modified SFM anode, the metal reduction signal starts to shift toward lower temperature, indicating the interaction between Ni hydrogen increased. The scanning electron microscopy (SEM) analyses during the reduction process indicated that the oxidation of hydrogen was more facile. A cell with nickel-strontium ferrite molybdate (Ni-SFM) as the anode, lanthanum strontium gallium magnesium oxide type (LSGM, La<sub>0.8</sub>Sr<sub>0.2</sub>Ga<sub>0.83</sub>Mg<sub>0.17</sub>O<sub>3</sub>) as the electrolyte, and lanthanum strontium

cobalt ferrite type (LSCF,  $\text{La}_{0.6}\text{Sr}_{0.4}\text{Co}_{0.2}\text{Fe}_{0.8}\text{O}_3$ ) as the cathode showed a high peak power density of  $1166 \text{ mW}\cdot\text{cm}^{-2}$  at  $800^\circ\text{C}$  using  $\text{H}_2$  as the fuel and ambient air as the oxidant. The cell polarization resistance is only about  $0.145 \Omega\cdot\text{cm}^2$  at  $800^\circ\text{C}$  which was much lower than that of the cell with pure SFM anode ( $0.243 \Omega\cdot\text{cm}^2$ ) under the same testing conditions. However, it was also found that SFM anode with dispersive Ni on the surface could be poisoned by trace levels of hydrogen sulfide ( $\text{H}_2\text{S}$ ) in the fuel. The current density of the cell operated at a constant voltage of  $0.7 \text{ V}$  at  $800^\circ\text{C}$  in  $\text{H}_2$  with 100 parts-per-million (ppm)  $\text{H}_2\text{S}$  dropped from  $1.34$  to  $1.1 \text{ A}\cdot\text{cm}^{-2}$  after 20 h continuous operation. Such a fast degradation rate was much higher than that observed in SFM without Ni coating. Therefore, the modified Ni-modified SFM anode demonstrated limitations on the Ni before the  $\text{H}_2\text{S}$ -poisoning problem was solved.

Some other transition metals such as Co, Fe, or Co-Fe were also reported to be used in enhancing the SOFC anode performance by infiltration and in situ precipitation from the surface. For example, Yang and Chen et al. reported a composite anode consisting of potassium tetrafluoride nickelate (II) ( $\text{K}_2\text{NiF}_4$ )-type-structured praseodymium strontium cobalt iron-doped niobium oxide-type (K-PSCFN,  $\text{Pr}_{0.8}\text{Sr}_{1.2}(\text{Co}, \text{Fe})_{0.8}\text{Nb}_{0.2}\text{O}_{4+\delta}$ ) matrix with homogeneously dispersed nano-sized Co-Fe alloy by annealing the perovskite praseodymium strontium cobalt iron-doped niobium oxide-type (P-PSCFN,  $\text{Pr}_{0.4}\text{Sr}_{0.6}\text{Co}_{0.2}\text{Fe}_{0.7}\text{Nb}_{0.1}\text{O}_{3-\delta}$ ) using  $\text{H}_2$  at  $900^\circ\text{C}$  [81]. The fabricated Co-Fe nanostructured ceramic anode was demonstrated to yield comparable performance to the Ni-based cermet anode with enhanced sulfur tolerance and coking resistance. In pure  $\text{H}_2$ , the electrolyte-supported cell with a structure of K-PSCFN-cobalt iron alloy (CFA)|LSGM|P-PSCFN electrolyte showed a maximum power density of  $0.96 \text{ W}\cdot\text{cm}^{-2}$  at  $850^\circ\text{C}$ , compared with  $0.21 \text{ W}\cdot\text{cm}^{-2}$  without the Co-Fe catalyst. The cell also exhibited high power density using  $\text{H}_2$  fuel containing  $\text{H}_2\text{S}$  of  $0.92 \text{ W}\cdot\text{cm}^{-2}$  at 50 ppm  $\text{H}_2\text{S}$  and of  $0.89 \text{ W}\cdot\text{cm}^{-2}$  at 100 ppm  $\text{H}_2\text{S}$  operated at  $850^\circ\text{C}$ . The results demonstrate the impact of Co-Fe alloying on the catalytic activity of ceramic anode. The Co-Fe nanostructured anode also showed long-term stability in  $\text{H}_2\text{S}$ -containing fuel and hydrocarbon fuels ( $\text{CH}_4$  and  $\text{C}_3\text{H}_8$ ) when the cell was discharged at different constant voltages. The redox cyclic stability of the anode was examined by switching the gas at anode side from  $\text{H}_2$  to air repeatedly to show the reversibility of the Co-Fe alloy. A study by G. Kim et al. recently developed a double perovskite material containing praseodymium barium magnesium oxide type (PBMO,  $\text{PrBaMn}_2\text{O}_{5+\delta}$ ) as a ceramic anode for high-performing direct hydrocarbon SOFC [94]. The PBMO anode was prepared by in situ annealing PBMO perovskite under reducing condition. With a 15 wt % Co-Fe catalyst under humidified  $\text{H}_2$ ,  $\text{C}_3\text{H}_8$ , and  $\text{CH}_4$  fuels (3%  $\text{H}_2\text{O}$ ), the single cell exhibited peak power densities of 1.77, 1.32, and  $0.57 \text{ W}\cdot\text{cm}^{-2}$  at  $850^\circ\text{C}$  using humidified hydrogen and propane fuels, respectively.

### 8.3.3.3 Ceramic Oxides

The incorporation of ceramic anode nanoparticles into the anode is complicated due to the difficulty of infiltrating multiple metal ions into the ceramic structure and



forming the correct phase structure after treatment. The fabricated nanostructured ceramic anodes exhibit a longer TPB length by extending the oxide catalyst throughout the electrode. Lee and Gorte et al. infiltrated 45 wt % lanthanum strontium gallium titanium oxide type (LST,  $\text{La}_{0.3}\text{Sr}_{0.7}\text{TiO}_3$ ) into 65% porous YSZ electrode scaffold to form the composite anode. The microstructure of infiltrated anode was greatly affected by the calcination temperature [95]. With conductivity of 0.4 S/cm at 900 °C in  $\text{H}_2$  comparable to traditional anodes, however, the cell (LST-YSZ anode | YSZ electrolyte  $\sim 60\ \mu\text{m}$  | LSF-YSZ cathode) operated in humidified  $\text{H}_2$  at 800 °C showed only a peak power density of  $20\ \text{mW}\cdot\text{cm}^{-2}$ . With the addition of 5% ceria and 0.5 wt % Pd, the power density was dramatically increased to  $780\ \text{mW}\cdot\text{cm}^{-2}$ , indicating the low electrochemical activity for hydrogen oxidation by LST itself. Lack of catalytic activity after infiltrating the ceramic catalyst nanoparticles also occurred on the LSCM anode, owing to its low electrical conductivity [96–99]. By infiltrating 45 wt % LSCM into a porous YSZ layer, the power density of the SOFC with 60- $\mu\text{m}$ -thick YSZ electrolyte reached  $500\ \text{mW}\cdot\text{cm}^{-2}$  in  $\text{H}_2$  at 700 °C with the addition of 0.5–1% Pd, rhodium (Rh), or Ni metals as catalysts. Therefore, the catalytic activity of the ceramic oxide itself was critical in obtaining comparable performance with Ni-based cermet anode. Recently, Ding and Zhang et al. reported a highly redox-stable ceramic oxide with an *A*-site-deficient layered perovskite structure, praseodymium barium ferrite magnesium oxide type ( $\text{PrBa}_{0.95}\text{Fe}_{0.9}\text{Mo}_{0.1}\text{O}_{5+\delta}$ ) (PBFM), as the anode material in a direct methane-fueled SOFC [100]. Firstly, the selection of this material was based on four general considerations. (1) Perovskites with high tolerance against crystal structure distortion could fine-tune the material's chemical stability and also the electrical/catalytic/mechanical properties through doping strategy; (2) iron-rich perovskite containing mixed-valence  $\text{Fe}^{2+}/\text{Fe}^{3+}$  redox couple could provide high electronic conductivity even though these redox ions only partially occupy the sub-lattice; (3) layered perovskite structure could be fabricated to yield high electrical conductivity and the ordered *A*-cations localizing oxygen vacancies within the rare earth layers, which could make a contribution to fast oxygen surface exchange/bulk diffusion and catalytic activity toward both hydrogen and hydrocarbon oxidation processes; and (4) our experiments lead us to hypothesize that the PBFM perovskites are stable upon partial removal of lattice oxygen and that the use of sixfold-coordinated Mo(VI)/Mo(V) couple at the *B* site could stabilize the material with stronger chemical bond under crude anodic conditions. The single cell of a lanthanum strontium gallium magnesium oxide-type (LSGM,  $\text{La}_{0.8}\text{Sr}_{0.2}\text{Ga}_{0.8}\text{Mg}_{0.2}\text{O}_{2.8}$ ) electrolyte-supported SOFC with the configuration of praseodymium barium ferrite magnesium oxide type (PBFM), LSGM, and praseodymium barium cobaltite type (PBCO,  $\text{PrBaCo}_2\text{O}_{5+\delta}$ ) [PBFM|LSGM|PBCO] showed maximum power densities of 1.72, 1.05, and  $0.56\ \text{W}\cdot\text{cm}^{-2}$  at 800, 700, and 600 °C, respectively. The PBFM anode was nanostructured by infiltrating the nitrates solution with the same stoichiometry as the prime backbone material. The as-prepared cell showed an enhanced performance, for example, the power densities of 2.3, 1.5, and  $0.8\ \text{W}\cdot\text{cm}^{-2}$  at 800, 700, and 600 °C in  $\text{H}_2$  were achieved, respectively.

## 8.4 Conclusion

Nano-engineering electrodes for SOFC operating in various fuels at intermediate temperatures through ion impregnation method to increase the catalysis active sites for ORR or fuel oxidation reaction have become a crucial strategy in enhancing FC performance. The optimization of the electrode microstructure can effectively minimize the activation polarization resistance when the nano-sized particles were incorporated into the electrode scaffold. There have been extensive studies focusing on the addition of different types of functional catalyst into electrodes. The research findings indicate that the nano-engineering electrode was a very promising route to facilitate the intermediate temperature operation of SOFC, while new material development was also under way.

---

## References

1. N.Q. Minh, Ceramic fuel cells. *J. Am. Ceram. Soc.* **76**, 563–588 (1993)
2. A.J. Jacobson, Materials for solid oxide fuel cells. *Chem. Mater.* **22**, 660–674 (2010)
3. D.J.L. Brett, A. Atkinson, N.P. Brandon, S.J. Skinner, Intermediate temperature solid oxide fuel cells. *Chem. Soc. Rev.* **37**, 1568–1578 (2008)
4. R.M. Ormerod, Solid oxide fuel cells. *Chem. Soc. Rev.* **32**, 17–28 (2003)
5. Y. Yi, A.D. Rao, J. Brouwer, G.S. Samuelsen, *J. Power Sources* **144**, 67–76 (2005)
6. S.C. Singhal, Solid oxide fuel cells for stationary, mobile, and military applications. *Solid State Ionics* **152–153**, 405–410 (2002)
7. W.G. Coors, Protonic ceramic fuel cells for high-efficiency operation with methane. *J. Power Sources* **118**, 150–156 (2003)
8. L. Yang, C.D. Zuo, S.Z. Wang, Z. Cheng, M. Liu, A novel composite cathode for low-temperature SOFCs based on oxide proton conductors. *Adv. Mater.* **20**, 3280–3283 (2008)
9. N.M. Sammes, Y. Du, R. Bove, Design and fabrication of a 100 W anode-supported tubular SOFC stack. *J. Power Sources* **145**, 428–434 (2005)
10. T. Fukui, S. Ohara, K. Mukai, Long-term stability of Ni-YSZ anode with a new microstructure prepared from composite powder. *Electrochem. Solid-State Lett.* **29**(1), 120–122 (1998)
11. A. Atkinson, S. Barnett, R.J. Gorte, J.T.S. Irvine, A.J. McEvoy, M. Mogensen, S.C. Singhal, J. Vohs, Advanced anodes for high-temperature fuel cells. *Nat. Mater.* **3**, 17–27 (2004)
12. T. Zhang, W.G. Fahrenholtz, S.T. Reis, R.K. Brow, Borate volatility from SOFC sealing glasses. *J. Am. Ceram. Soc.* **91**, 2564–2569 (2008)
13. E.P. Murray, T. Tsai, S.A. Barnett, A direct-methane fuel cell with a ceria-based anode. *Nature* **400**, 649–651 (1999)
14. S. McIntosh, R.J. Gorte, Direct hydrocarbon solid oxide fuel cells. *Chem. Rev.* **104**, 4845–4865 (2004)
15. Y.H. Huang, R.I. Dass, Z.L. Xing, J.B. Goodenough, Double perovskites as anode materials for solid oxide fuel cells. *Science* **312**, 254–257 (2006)
16. R. Steinberger-Wilckens, F. Tietz, M.J. Smith, J. Mougins, B. Rietveld, O. Bucheli, J.V. Herle, R. Rosenberg, M. Zahid, P. Holtappels, Real-SOFC—a joint European effort in understanding SOFC degradation. *ECS Trans.* **7**, 67–76 (2007)
17. A. Hagen, R. Barfod, P.V. Hendriksen, Y.-L. Liu, S. Ramousse, Degradation of anode-supported SOFCs as a function of temperature and current load. *J. Electrochem. Soc.* **153**, A1165–A1171 (2006)



18. M.L. Liu, M.E. Lynch, K. Blinn, F.M. Alamgir, Y.M. Choi, Rational SOFC material design: new advances and tools. *Mater. Today* **14**, 534–546 (2011)
19. J.-H. Lee, J.-W. Heo, D.-S. Lee, J. Kim, G.-H. Kim, H.-W. Lee, H.S. Song, J.-H. Moon, The impact of anode microstructure on the power generating characteristics of SOFC. *Solid State Ionics* **158**, 225–232 (2003)
20. K.J. Yoon, P. Zink, S. Gopalan, U.B. Pal, Polarization measurements on single-step co-fired solid oxide fuel cells (SOFCs). *J. Power Sources* **172**, 39–49 (2007)
21. A.V. Virkar, J. Chen, C.W. Tanner, J.-W. Kim, The role of electrode microstructure on activation and concentration polarizations in solid oxide fuel cells. *Solid State Ionics* **131**, 189–198 (2000)
22. S.H. Chan, K.A. Khor, Z.T. Xia, A complete polarization model of a solid oxide fuel cell and its sensitivity to the change of cell component thickness. *J. Power Sources* **93**, 130–140 (2001)
23. D.A. Noren, M.A. Hoffman, Clarifying the Butler-Volmer equation and related approximations for calculating activation losses in solid oxide fuel cell models. *J. Power Sources* **152**, 175–181 (2005)
24. Z.P. Shao, S.M. Haile, A high-performance cathode for the next generation of solid-oxide fuel cells. *Nature* **431**, 170–173 (2004)
25. S.B. Adler, Factors governing oxygen reduction in solid oxide fuel cell cathodes. *Chem. Rev.* **104**, 4791–4843 (2004)
26. C.W. Sun, R. Hui, J. Roller, Cathode materials for solid oxide fuel cells: a review. *J. Solid State Electrochem.* **14**, 1125–1144 (2010)
27. S.J. Skinner, Recent advances in perovskite-type materials for solid oxide fuel cell cathodes. *Int. J. Inorg. Mater.* **3**, 113–121 (2001)
28. A. Tarancón, S.J. Skinner, R.J. Chater, F. Hernández-Ramírez, J.A. Kilner, Layered perovskites as promising cathodes for intermediate temperature solid oxide fuel cells. *J. Mater. Chem.* **17**, 3175–3181 (2007)
29. L. Shao, Q. Wang, L. Fan, P. Wang, N. Zhang, K. Sun, Copper-cobalt spinel as a high-performance cathode for intermediate temperature solid oxide fuel cells. *Chem. Commun.* **52**, 8615–8618 (2016)
30. Q. Fu, F. Tietz, D. Sebold, S. Tao, J.T.S. Irvine, An efficient ceramic-based anode for solid oxide fuel cells. *J. Power Sources* **171**, 663–669 (2007)
31. G. Xiao, F. Chen, Redox stable anodes for solid oxide fuel cells. *Front. Energy Res.* **2**, 1–13 (2014)
32. K. Huang, J. Wan, J.B. Goodenough, Oxide-ion conducting ceramics for solid oxide fuel. *Cell* **36**, 1093–1098 (2001)
33. J.B. Goodenough, Y.-H. Huang, Alternative anode materials for solid oxide fuel cells. *J. Power Sources* **173**, 1–10 (2007)
34. P.G. Bruce, B. Scrosati, J.-M. Tarascon, Nanomaterials for rechargeable lithium batteries. *Angew. Chem.* **47**, 2930–2946 (2008)
35. L. Zhang, T.J. Webster, Nanotechnology and nanomaterials: promises for improved tissue regeneration. *Nano Today* **4**, 66–80 (2009)
36. Q. Peng, Y.-C. Tseng, S.B. Darling, J.W. Elam, A route to nanoscopic materials via sequential infiltration synthesis on block copolymer templates. *ACS Nano* **5**, 4600–4606 (2011)
37. J. Martin, C. Mijangos, Tailored polymer-based nanofibers and nanotubes by means of different infiltration methods into alumina nanopores. *Langmuir* **25**, 1181–1187 (2009)
38. T.Z. Sholkapper, H. Kurokawa, C.P. Jacobson, S.J. Visco, L.C. De Jonghe, Nanostructured solid oxide fuel cell electrodes. *Nano Lett.* **7**, 2136–2141 (2007)
39. C.C. Chao, C.M. Hsu, Y. Cui, F.B. Prinz, Improved solid oxide fuel cell performance with nanostructured electrolytes. *ACS Nano* **5**, 5692–5696 (2011)
40. L. Baque, A. Caneiro, M.S. Moreno, A. Serquis, High-performance nanostructured IT-SOFC cathodes prepared by the novel chemical method. *Electrochem. Commun.* **10**, 1905–1908 (2008)

41. D. Ding, X. Li, S.Y. Lai, K. Gerdes, M. Liu, Enhancing SOFC cathode performance by surface modification through infiltration. *Energy Environ. Sci.* **7**, 552–575 (2014)
42. J.M. Vohs, R.J. Gorte, High-performance SOFC cathodes prepared by infiltration. *Adv. Mater.* **21**, 943–956 (2009)
43. S.P. Jiang, A review of wet impregnation – an alternative method for the fabrication of high performance and nanostructured electrodes of solid oxide fuel cells. *Mater. Sci. Eng.* **418**, 199–210 (2006)
44. S.P. Jiang, Nanoscale and nanostructured electrodes of solid oxide fuel cells by infiltration: advances and challenges. *Int. J. Hydro. Energy* **37**, 449–470 (2012)
45. M.J. Jorgensen, M. Mogensen, Impedance of solid oxide fuel cell LSM/YSZ composite cathodes. *J. Electrochem. Soc.* **148**, A433–A442 (2001)
46. M. Shiono, K. Kobayashi, T.L. Nguyen, K. Hosoda, T. Kato, K. Ota, M. Dokiya, Effect of the CeO<sub>2</sub> interlayer on ZrO<sub>2</sub> electrolyte/la(Sr)CoO<sub>3</sub> cathode for low-temperature SOFCs. *Solid State Ionics* **170**, 1–7 (2004)
47. L. Yang, C.D. Zuo, S.Z. Wang, Z. Cheng, M.L. Liu, A novel composite cathode for low-temperature SOFCs based on oxide proton conductors. *Adv. Mater.* **20**, 3280–3283 (2008)
48. Z.P. Shao, S.M. Haile, A high-performance cathode for the next generation of solid-oxide fuel cells. *Nature* **431**, 170–173 (2004)
49. H. He, Y. Huang, J. Regal, M. Boaro, J.M. Vohs, R.J. Gorte, Low-temperature fabrication of oxide composites for solid-oxides fuel cells. *J. Am. Ceram. Soc.* **87**, 331–336 (2004)
50. Y. Huang, J.M. Vohs, R.J. Gorte, Characterization of LSM-YSZ composites prepared by impregnation methods. *J. Electrochem. Soc.* **152**, A1347–A1353 (2005)
51. T.J. Armstrong, A.V. Virkar, *204th Meeting of the Electrochemical Society* (Electrochemical Society, Pennington, 2003). Abstract 1113
52. Z. Jiang, Z. Lei, B. Ding, C. Xia, F. Zhao, F. Chen, Electrochemical characteristics of solid oxide fuel cell cathodes prepared by infiltrating (La,Sr)MnO<sub>3</sub> nanoparticles into yttria-stabilized bismuth oxide backbones. *Int. J. Hydrog. Energy* **35**, 8322–8330 (2010)
53. T.Z. Sholklipper, C. Lu, C.P. Jacobson, S.J. Visco, L.C. De Jonghe, LSM-infiltrated solid oxide fuel cell cathodes. *Electrochem. Solid-State Lett.* **9**, A376–A378 (2006)
54. T.Z. Sholklipper, V. Radmilovic, C.P. Jacobson, S.J. Visco, L.C.D. Jonghe, *Electrochem. Solid-State Lett.* **10**, B74–B76 (2007)
55. M.G. Bellino, J.G. Scannell, D.G. Lamas, A.G. Leyva, N.E. Walsøe de Reca, High-performance solid-oxide fuel cell cathodes based on cobaltite nanotubes. *J. Am. Chem. Soc.* **129**, 3066–3067 (2007)
56. Y. Gong, D. Palacio, X. Song, R.L. Patel, X. Liang, X. Zhao, J.B. Goodenough, K. Huang, Stabilizing nanostructured solid oxide fuel cell cathode with atomic layer deposition. *Nano Lett.* **13**, 4340–4345 (2013)
57. Y.L. Liu, A. Hagen, R. Barfod, M. Chen, H.J. Wang, F.W. Poulsen, P.V. Hendriksen, Microstructural studies on the degradation of the interface between LM-YSZ cathode and YSZ electrolyte in SOFCs. *Solid State Ionics* **180**, 1298–1304 (2009)
58. T.J. Armstrong, J.G. Rich, Anode-supported solid oxide fuel cells with La<sub>0.6</sub>Sr<sub>0.4</sub>CoO<sub>3-δ</sub>-Zr<sub>0.84</sub>Y<sub>0.16</sub>O<sub>2-δ</sub> composite cathodes fabricated by an infiltration method. *J. Electrochem. Soc.* **153**, A515–A520 (2006)
59. B. Liu, X. Chen, Y. Dong, S.S. Mao, M. Cheng, A high-performance, a nanostructured Ba<sub>0.5</sub>Sr<sub>0.5</sub>Co<sub>0.8</sub>Fe<sub>0.2</sub>O<sub>3-δ</sub> cathode for solid oxide fuel cells. *Adv. Energy Mater.* **1**, 343–346 (2011)
60. D. Han, X. Liu, F. Zeng, J. Qian, T. Wu, Z. Zhan, A micro-nano porous oxide hybrid for efficient oxygen reduction in reduced-temperature solid oxide fuel cells. *Sci. Rep.* **2**, 462 (2012)
61. N. Ai, S.P. Jiang, Z. Lü, K. Chen, W. Su, Nanostructured (Ba,Sr)(Co,Fe) O<sub>3-δ</sub> impregnated (La,Sr) MnO<sub>3</sub> cathode for intermediate-temperature solid oxide fuel cells. *J. Electrochem. Soc.* **157**, B1033–B1039 (2010)

62. R. Su, Z. Lü, S.P. Jiang, Y.B. Shen, W.H. Su, K.F. Chen, Ag decorated (Ba,Sr)(Co,Fe)O<sub>3</sub> cathodes for solid oxide fuel cells prepared by electroless silver deposition. *Int. J. Hydrog. Energy* **38**, 2413–2420 (2013)
63. C. Xia, M. Liu, A simple and cost-effective approach to fabrication of dense ceramic membranes on porous substrates. *J. Am. Ceram. Soc.* **84**, 1903–1905 (2001)
64. C. Xia, F. Chen, M. Liu, Reduced-temperature solid oxide fuel cells fabricated by screen printing. *Electrochem. Solid-State Lett.* **4**, A52–A54 (2001)
65. H.Y. Tu, Y. Takeda, N. Imanishi, O. Yamamoto, Ln<sub>1-x</sub>Sr<sub>x</sub>CoO<sub>3</sub> (Ln=Sm, Dy) for the electrode of solid oxide fuel cells. *Solid State Ionics* **100**, 283–288 (1997)
66. Y. Liu, S. Zha, M. Liu, Novel nanostructured electrodes for solid oxide fuel cells fabricated by combustion chemical vapor deposition (CVD). *Adv. Mater.* **16**, 256–260 (2004)
67. F. Zhao, Z. Wang, M. Liu, L. Zhang, C. Xia, F. Chen, Novel nano-network cathodes for solid oxide fuel cells. *J. Power Sources* **185**, 13–18 (2008)
68. T. Suzuki, Z. Hasan, Y. Funahashi, T. Yamaguchi, Y. Fujishiro, M. Awano, Impact of anode microstructure on solid oxide fuel cells. *Science* **325**, 852–855 (2009)
69. Z. Zhan, S.A. Barnett, A reduced temperature solid oxide fuel cell with nanostructured anodes. *Energy Environ. Sic.* **4**, 3951–3954 (2011)
70. J.H. Park, S.M. Han, K.J. Yoon, H. Kim, J. Hong, B.-K. Kim, J.-H. Lee, J.-W. Son, Impact of nanostructured anode on low-temperature performance of thin-film-based anode-supported solid oxide fuel cells. *J. Power Sources* **315**, 324–330 (2016)
71. T. Yamaguchi, H. Sumi, K. Hamamoto, T. Suzuki, Y. Fujishiro, J.D. Carter, S.A. Barnett, Effect of nanostructured anode functional layer thickness on the solid-oxide fuel cell performance in the intermediate temperature. *Int. J. Hydrog. Energy* **39**, 19731–19736 (2014)
72. S. Park, J.M. Vohs, R.J. Gorte, Direct oxidation of hydrocarbons in a solid-oxide fuel cell. *Nature* **404**, 265–267 (2000)
73. R.J. Gorte, S. Park, J.M. Vohs, C. Wang, Anodes for direct oxidation of dry hydrocarbons in a solid-oxide fuel cell. *Adv. Mater.* **12**, 1465–1469 (2000)
74. M.D. Gross, J.M. Vohs, R.J. Gorte, Recent progress in SOFC anodes for direct utilization of hydrocarbons. *J. Mater. Chem.* **17**, 3071–3077 (2007)
75. X.-F. Ye, B. Huang, S.R. Wang, Z.R. Wang, L. Xiong, T.L. Wen, Preparation and performance of a Cu–CeO<sub>2</sub>–ScSZ composite anode for SOFCs running on ethanol fuel. *J. Power Sources* **164**, 203–209 (2007)
76. R.J. Gorte, J.M. Vohs, Nanostructured anodes for solid oxide fuel cells. *Curr. Opin. Colloid Interface Sci.* **14**, 236–244 (2009)
77. S.W. Tao, J.T.S. Irvine, A redox-stable efficient anode for solid oxide fuel cells. *Nat. Mater.* **2**, 320–323 (2003)
78. X.W. Zhou, N. Yan, K.T. Chuang, J.L. Luo, Progress in La-doped SrTiO<sub>3</sub> (LST)-based anode materials for solid oxide fuel cells. *RSC Adv.* **4**, 118–131 (2014)
79. Y.H. Huang, R.I. Dass, Z.L. Xing, J. Goodenough, Double perovskites as anode materials for solid oxide fuel cells. *Science* **312**, 254–257 (2006)
80. Q. Liu, X.H. Dong, G.L. Xiao, F. Zhao, F.L. Chen, A novel electrode material for symmetric SOFCs. *Adv. Mater.* **22**, 5478–5482 (2010)
81. C.H. Yang, Sulfur-tolerant redox-reversible anode material for direct hydrocarbon solid oxide fuel cells. *Adv. Mater.* **24**, 1439–1443 (2012)
82. J.S. Kim, V.V. Nair, J.M. Vohs, R.J. Gorte, A study of the methane tolerance of LSCM-YSZ composite anodes with Pt, Ni, Pd and ceria catalysts. *Scr. Mater.* **65**, 90–95 (2011)
83. K.B. Yoo, G.M. Choi, LST-GDC composite anode on LaGaO<sub>3</sub>-based solid oxide fuel cell. *Solid State Ionics* **192**, 515–518 (2011)
84. Y.H. Huang, Double-perovskite anode materials Sr<sub>2</sub>MMoO<sub>6</sub> (M = Co, Ni) for solid oxide fuel cells. *Chem. Mater.* **21**, 2319–2326 (2009)
85. S.P. Jiang, Y. Ye, T. He, S.B. Ho, Nanostructured palladium–La<sub>0.75</sub>Sr<sub>0.25</sub>Cr<sub>0.5</sub>Mn<sub>0.5</sub>O<sub>3</sub>/Y<sub>2</sub>O<sub>3</sub>–ZrO<sub>2</sub> composite anodes for direct methane and ethanol solid oxide fuel cells. *J. Power Sources* **185**, 179–182 (2008)

86. Y. Ye, T. He, Y. Li, E.H. Tang, T.L. Reitz, S.P. Jiang, Pd-promoted  $\text{La}_{0.75}\text{Sr}_{0.25}\text{Cr}_{0.5}\text{Mn}_{0.5}\text{O}_3/\text{YSZ}$  composite anodes for direct utilization of methane in SOFCs. *J. Electrochem. Soc.* **155**, B811–B818 (2008)
87. H. Kurokawa, J. Yang, C. Jacobson, L. DE Jongle, S. Visco, Y-doped  $\text{SrTiO}_3$  based sulfur tolerant anode for solid oxide fuel cells. *J. Power Sources* **164**, 510–518 (2007)
88. S. Primdahl, Y.L. Liu, Ni catalyst for hydrogen conversion in Gadolinia-doped ceria anodes for solid oxide fuel cells. *J. Electrochem. Soc.* **149**, A1466–A1472 (2002)
89. H. Uchida, S. Suzuki, M. Watanabe, High performance electrode for medium-temperature solid oxide fuel cells. *Electrochem. Solid-State Lett.* **6**, A174–A177 (2003)
90. Q. Fu, F. Tietz, D. Sebold, S. Tao, J. Irvine, An efficient ceramic-based anode for solid oxide fuel cells. *J. Power Sources* **171**, 663–669 (2007)
91. S. Boulfrad, M. Cassidy, E. Traversa, J.T.S. Irvine, Improving the performance of SOFC anodes by decorating perovskite with Ni nanoparticles. *ECS Trans.* **57**, 1211–1216 (2013)
92. K.B. Yoo, B.H. Park, G.M. Choi, Stability and performance of SOFC with  $\text{SrTiO}_3$ -based anode in  $\text{CH}_4$  fuel. *Solid State Ionics* **225**, 104–107 (2012)
93. G. Xiao, C. Jin, Q. Liu, A. Heyden, F. Chen, Ni modified ceramic anodes for solid oxide fuel cells. *J. Power Sources* **201**, 43–48 (2012)
94. S. Sengodan, S. Choi, A. Jun, T.H. Shin, Y.-W. Ju, H.Y. Jeong, J. Shin, J.T.S. Irvine, G. Kim, Layered oxygen-deficient double perovskite as an efficient and stable anode for direct hydrocarbon solid oxide fuel cells. *Nat. Mater.* **14**, 205–209 (2015)
95. S. Lee, G. Kim, J.M. Vohs, R.J. Gorte, SOFC anodes based on infiltration of  $\text{La}_{0.3}\text{Sr}_{0.7}\text{TiO}_3$ . *J. Electrochem. Soc.* **155**, B1179–B1183 (2008)
96. G. Kim, S. Lee, J.Y. Shin, G. Corre, J.T.S. Irvine, J.M. Vohs, R.J. Gorte, Investigation of the structural and catalytic requirements for high-performance SOFC anodes formed by infiltration of LSCM. *Electrochem. Solid-State Lett.* **12**, B48–B52 (2009)
97. G. Corre, G. Kim, M. Cassidy, J.M. Vohs, R.J. Gorte, J.T.S. Irvine, Activation and ripening of impregnated manganese containing perovskite SOFC electrodes under redox cycling. *Chem. Mater.* **21**, 1077–1084 (2009)
98. G. Kim, G. Corre, J.T.S. Irvine, J.M. Vohs, R.J. Gorte, Engineering composite oxide SOFC anodes for efficient oxidation of methane. *Electrochem. Solid-State Lett.* **11**, B16–B19 (2008)
99. J.-S. Kim, N.L. Wieder, A.J. Abraham, M. Cargnello, P. Fornasiero, R.J. Gorte, J.M. Vohs, Highly active and thermally stable core-shell catalysts for solid oxide fuel cells. *J. Electrochem. Soc.* **158**, B596–B600 (2011)
100. H. Ding, Z. Tao, S. Liu, J. Zhang, A high-performing sulfur-tolerant and redox-stable layered perovskite anode for direct hydrocarbon solid oxide fuel cells. *Sci. Rep.* **5**, 18129 (2015)



# Modeling Analysis for Species, Pressure, and Temperature Regulation in Proton Exchange Membrane Fuel Cells

9

Zhaohui Wang

## Contents

9.1	Introduction of PEM Modeling .....	250
9.2	Static Modeling of PEM Fuel Cell .....	252
9.2.1	Modeling Assumptions .....	254
9.2.2	Ionic and Electronic Currents at Electrodes .....	254
9.2.3	Gas Species in Flow Channels .....	257
9.2.4	Fluid Flow in Porous Media .....	259
9.2.5	Conservation of Liquid Water .....	260
9.2.6	Heat Transport .....	261
9.2.7	Boundary Conditions .....	262
9.3	Humidity and Pressure Regulation .....	264
9.3.1	State Feedback Controller .....	266
9.3.2	Static Output Feedback Controller .....	268
9.4	Gas Flow Rate Regulation .....	268
9.4.1	Controller Design Under Gas Flow Rate Constraints .....	268
9.4.2	Predictive Control of Cathode Exhaust Gas Mass Flow .....	270
9.5	Temperature Regulation .....	270
9.5.1	Predictive Thermal Model .....	270
9.5.2	Lumped Thermal Model .....	271
9.5.3	Energy Balanced Thermal Model .....	272
9.5.4	Active Disturbance Rejection Temperature Control System .....	273
9.6	Discussion .....	275
9.6.1	Cathode Relative Humidity .....	275
9.6.2	Anode Relative Humidity .....	275
9.6.3	Stoichiometry .....	276

## Author Contributions

Zhaohui Wang is solely responsible for this review on the modeling analysis of the PEM fuel cell.

Z. Wang (✉)

Department of Electrical Engineering and Computer Science, Texas A&M University-Kingsville, Kingsville, TX, USA

e-mail: [Zhouhui.wang@tamuk.edu](mailto:Zhouhui.wang@tamuk.edu)

9.6.4	Operation Temperature .....	276
9.6.5	Flow Distribution .....	277
9.6.6	Pressure Drop .....	277
9.6.7	Compression Pressure .....	278
9.7	Summary .....	279
	References .....	279

## Abstract

The performance degradation of proton exchange membrane or polymer electrolyte membrane fuel cell (PEMFC) stems from air starvation and water flooding. In the mathematical modeling, the conservation equations were applied for momentum, mass, species, charge, and energy, to investigate the heat transfer and temperature distribution in the cathode along with the multiphase and multi-species transport under the steady-state condition. This model shows the effect of stoichiometry of reactants and relative humidity on the water saturation. The back-diffusion of water from the cathode to the anode is considered to reduce possible flooding. The feedback controls are used to address the transient water, pressure, and temperature management problems of a PEMFC system. An anode recirculation system measures the feedback signals to regulate the anode and cathode humidities and the pressure difference between the anode and cathode compartments. It was found that the robust nonlinear controller is insensitive to parametric uncertainty, maintaining performance around any equilibrium point.

## 9.1 Introduction of PEM Modeling

The proton exchange membrane (PEM) or polymer electrolyte membrane fuel cell (PEMFC) has been the subject of numerous researches, promising to deliver a cleaner, more efficient, and more durable power stack. The PEMFC contains advantages over other types of fuel cells such as solid oxide fuel cells (SOFCs) of operating at a lower temperature, being lighter in weight, and more compact, which makes them ideal for applications such as cars. PEMFC-based power-train systems have been in a relatively more developed stage for ground vehicle systems because PEMFC has a lower operating temperature ( $\sim 80^\circ\text{C}$ ), a rapid start-up time from freezing conditions, a lighter weight, and a more compact size. For the low-temperature PEMFCs, the  $\sim 80^\circ\text{C}$  operating temperature is too low for cogeneration like in SOFCs, and the electrolyte must be water saturated. The fuel cell that operates without humidifier relies on rapid water generation and high-rate back-diffusion through thin membranes to maintain the hydration of the membrane as well as the ionomer in the catalyst layers. The high-temperature PEMFCs, operating between  $100^\circ\text{C}$  and  $200^\circ\text{C}$ , potentially offer benefits to electrode kinetics, heat management, and better tolerance to fuel impurities, particularly CO in reformate. These improvements potentially could lead to higher overall system efficiencies. However, the gold standard perfluorinated sulfonic acid (PFSA) membranes lose

function rapidly at 100 °C and above if hydration drops below ~100% and begin to creep in this temperature range, resulting in localized thinning and overall lower system lifetimes.

The static modeling of PEMFC applies the conservation equations for momentum, mass, species, charge, and energy and shows the multiphase and multi-species transport under the steady-state condition along with the heat transfer and temperature distribution in the cathode. The fuel, hydrogen, is injected into the anode, while the oxygen, usually in the form of air, is supplied to the cathode. At the anode, the hydrogen molecule is split into hydrogen ions (or protons,  $H^+$ ), called charge carrier, and electrons ( $e^-$ ). The electrons flow through an external circuit and produce electric power. The hydrogen ions permeate across the electrolyte to the cathode, where the oxygen combines with the electrons and the hydrogen ions to produce water. The catalyst layers are made from a mixture of graphite powder, PEM powder, and a catalyst, usually, platinum, bonded to the gas diffuser. The semipermeable polymer electrolyte membrane is made from ionomers and designed to conduct protons while acting as an electronic insulator and reactant barrier, e.g., to oxygen and hydrogen gas. The transparent PEM film with a thickness less than a millimeter is composed of macromolecules, enabling protons from the sulfonate site to detach and hop from site to site throughout the film. This film can be incorporated into a membrane electrode assembly (MEA) to separate the reactants and transport protons while blocking a direct electronic pathway through the membrane. The fluoropolymer (PFSA, perfluorosulfonic acid) Nafion<sup>®</sup> is one of the most common and commercially available PEM materials because Nafion is an ionomer with a perfluorinated backbone like Teflon<sup>®</sup>. Other structural motifs, polyaromatic polymers or partially fluorinated polymers, can be made ionomers for proton exchange membranes. The fuel cell performance degradation stems from water flooding and air starvation. Several control schemes are applied for regulating humidity, pressure, and temperature.

Fuel cell starvation is where a shortage of oxygen or hydrogen occurs. For tank inerting on aircraft, the multifunctional fuel cell system (MFFCS) can provide oxygen depleted air (ODA)-gas with an oxygen content of 10–11% to prevent ignition of fuel vapors and a low humidity to prevent icing and contamination inside the tanks [1]. Not all system states can be measured and some states measured exhibit a significant time delay. A nonlinear state estimation strategy builds the entire system state and compensates for the delay. An observer-based feedback and feedforward controller manage the trade-off between reduction of parasitic losses and fast fuel cell net power response during rapid current demands [2].

Optimal fuel cell performance is dependent upon water management. The stability of the membrane is determined by its water content, and proper hydration of the membrane is crucial for maintaining mechanical stability and membrane conductivity. Appropriate flow stoichiometry can increase liquid water removal. The lack of sensors for measuring the amount of liquid water in a compartment makes water management an interesting control problem. The feedback control used to address the transient water management problem of a PEMFC system is an area of current development by researchers [3]. The required cathode inlet humidity is maintained by flowing the air through a humidifier, while the anode water removal is controlled

by the unconsumed fuel (hydrogen) leaving the anode. The performance objectives were satisfied using a gain-scheduled static output feedback scheme which adjusts the controller gains when the cathode vapor pressure arrives at the saturation pressure of water vapor.

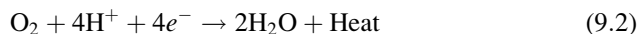
## 9.2 Static Modeling of PEM Fuel Cell

The anode of PEM fuel cell is fed with the humidified hydrogen of mass fractions for  $H_2/H_2O$ . The cathode is supplied with the humidified oxygen and water fractions for  $O_2/H_2O/N_2$ , where  $N_2$  is considered to be an inert gas and serves as a diluent. Two electrochemical reactions exist concurrently on the membrane of a PEM fuel cell. One is hydrogen oxidation reaction (HOR) in the anodic catalyst layer, where humidified hydrogen is injected into the inlet channels of the anode. The other one is oxygen reduction reaction (ORR) in the cathodic catalyst layer, where the air is supplied to the inlet channels of the cathode (Fig. 9.1).

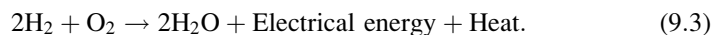
The hydrogen from the anode gas channel is consumed in the anodic catalyst layer, where the created protons carry the ionic current to the cathode (Eq. 9.1):



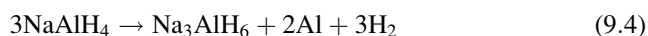
In the cathodic catalyst layer, oxygen reacts with protons coming from the anode through the PEM and with the electrons coming from the anode through an external circuit (Eq. 9.2):



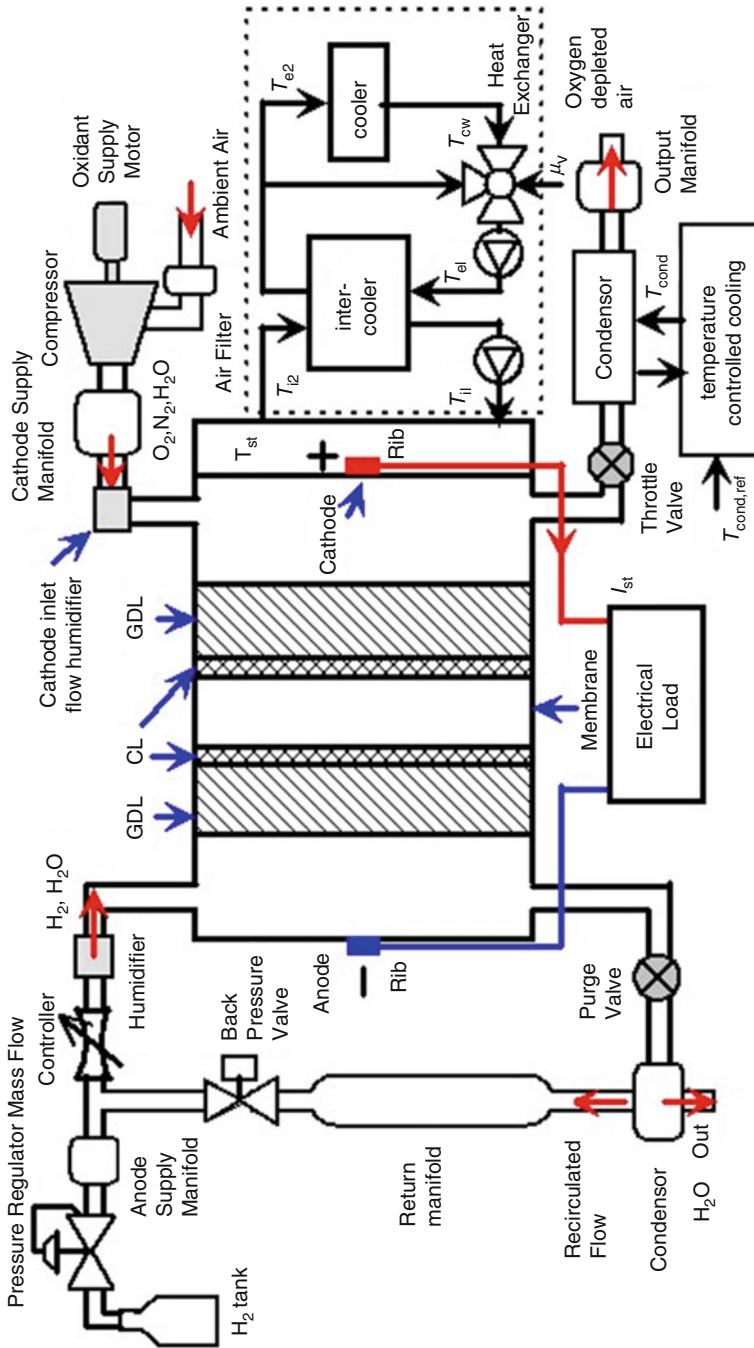
Considered all together, the chemical reaction inside the fuel cell is [4] described in Eq. (9.3):



The hydrogen storage material for the PEM fuel cell can be the complex sodium aluminum hydride that decomposes in two steps with a theoretical reversible hydrogen content of 5.5 wt. % [5]: (1) 3.7 wt. %  $H_2$  is released in the 1st step at approximately 100 °C and (2) 1.8 wt. %  $H_2$  in the 2nd step at approximately 150 °C. The kinetics of the decomposition and rehydrogenation of the complex hydride can be improved by doping with 4 mol. %  $TiCl_3$  which are summarized in Eqs. (9.4) and (9.5):







**Fig. 9.1** Schematic of a PEM fuel cell and its control system

### 9.2.1 Modeling Assumptions

In the mathematical model, the following assumptions are used [6, 7]:

1. The fuel cell is operating at steady and isothermic state (temperature remains constant,  $\Delta T$ ).
2. The flow is incompressible and laminar everywhere due to small gas pressure gradient and low Reynolds number (Re).
3. The gas diffusion layer and catalyst layer are isotropic porous media and hydrophobic with contact angle larger than  $90^\circ$ .
4. The PEM is impermeable to reactant gases that behave as the ideal gas mixture.
5. The production of water in the catalyst layer is in vapor state for high-temperature PEMFC or fluid state for low-temperature PEMFC.
6. The protons can only transport through the electrolyte and electrons through the external electric load.
7. Three species including oxygen, water, and nitrogen are considered on the cathode side, while hydrogen and water are considered on the anode side.
8. In a high-temperature PEMFC ( $T > T_{\text{H}_2\text{O},v}$ , where  $T_{\text{H}_2\text{O},v}$  is the evaporation temperature of water with default value of  $100^\circ\text{C}$ ), the production of water in the catalyst layer (CL) is in vapor form, while in a low-temperature PEMFC ( $T < T_{\text{H}_2\text{O},v}$ ), the production of water in the CL is in fluid phase.

### 9.2.2 Ionic and Electronic Currents at Electrodes

In a PEMFC, the current continuity equation is applied to the electrical current in conducting materials that include porous electrodes and membrane, so the current is split into two parts: (1) ionic current  $i_s$  that is formed by protons traveling through the ionic conductor (membrane) and (2) electronic current  $i_m$  where the electrons transfer through the solid matrix of electrodes (Eq. 9.6):

$$\nabla \cdot i = \nabla \cdot i_s + \nabla \cdot i_m = 0 \quad (9.6)$$

The conservation of charge to the electron transport, which describes the solid potential  $\phi_s$  in the bipolar plate, a gas diffusion layer (GDL), and catalyst layer, and the conservation of charge to the proton transport, which describes the electrolyte potential  $\phi_m$  in the membrane [6], are summarized in Eqs. (9.7) and (9.8):

$$\nabla \cdot i_s = \nabla \cdot (-\sigma_s^{\text{eff}} \nabla \phi_s) = -S_s \quad (9.7)$$

$$\nabla \cdot i_m = \nabla \cdot (-\sigma_m^{\text{eff}} \nabla \phi_m) = S_e \quad (9.8)$$

At anode catalyst layer (CL), the source terms are summarized in Eq. (9.9):

$$S_e = j_a, \quad S_s = -j_a \quad (9.9)$$

Similarly, at cathode CL the source terms are summarized in Eq. (9.10):

$$S_e = j_c, \quad S_s = -j_c \quad (9.10)$$

where  $j_a$  and  $j_c$  are the transfer current density corresponding to the electrochemical reaction at the anode and cathode catalyst layers, which can be formulated by two methods: (1) the agglomerate model and (2) Butler-Volmer equation. In the catalyst layers, the agglomerate is formed by the dispersed catalyst, and this zone is filled with electrolyte [7]. The oxygen is dissolved into the electrolyte and reaches the catalyst site. The agglomerate model describes the transfer current density (Eqs. 9.11, 9.12, 9.13, and 9.14) as the following [8, 9]:

$$j_a = -\frac{6(1-\varepsilon)FD_H^{\text{agg}}}{(R^{\text{agg}})^2} \left( c_H^{\text{agg}} - c_H^{\text{ref}} \exp\left(-\frac{\alpha_a F}{RT} \eta\right) \right) (1 - K_a \coth(K_a)) \quad (9.11)$$

$$j_c = \frac{12(1-\varepsilon)FD_O^{\text{agg}}}{(R^{\text{agg}})^2} c_O^{\text{agg}} (1 - K_c \coth(K_c)) \quad (9.12)$$

where

$$K_a = \sqrt{\frac{\alpha_a j_{0,a} s}{2F c_H^{\text{ref}} D_H^{\text{agg}}}} R^{\text{agg}} \quad (9.13)$$

$$K_c = \sqrt{\frac{\alpha_c j_{0,c} s}{4F c_O^{\text{ref}} D_O^{\text{agg}}}} \exp\left(-\frac{\alpha_c F}{RT} \eta\right) R^{\text{agg}} \quad (9.14)$$

where  $c^{\text{agg}}$  (mol/m<sup>3</sup>) is the gas concentration at the surface of the agglomerates,  $c^{\text{ref}}$  (mol/m<sup>3</sup>) is the dissolved gas concentration at a reference state,  $F$  (coulomb/mol) is the Faraday constant,  $D^{\text{agg}}$  (m<sup>2</sup>/s) the diffusion coefficient of the dissolved gas inside the agglomerate,  $R^{\text{agg}}$  (m) the agglomerate radius,  $j_0$  (Am<sup>-2</sup>) is the exchange current density,  $s$  (m<sup>2</sup>/m<sup>3</sup>) is the specific surface area, and  $\eta$  (V) is the electrochemical overpotential, which is expressed by the potential difference between solid matrix and electrolyte and is defined by Eq. (9.15) as

$$\eta = \begin{cases} \phi_s - \phi_m & \text{at anode} \\ \phi_s - \phi_m - U_{\text{oc}} & \text{at cathode} \end{cases} \quad (9.15)$$

where the open-circuit potential  $U_{\text{oc}}$  is defined by Eq. (9.16) as

$$U_{\text{oc}} = 0.23 - 0.9 \times 10^{-3} (T - 298) \quad (9.16)$$

The transfer coefficients  $\alpha_a$  and  $\alpha_c$  depend on many parameters, including temperature. At the anode side, a well-recognized value of 0.5 (dimensionless unit) was assumed. At the cathode side, the reported values vary within a certain range: 0.73

for the behavior of the base system [10], 0.67 at 150 °C for O<sub>2</sub> reduction on Pt in 85% H<sub>3</sub>PO<sub>4</sub> [11], 0.777 [12], and 0.89 [9].

The Butler-Volmer equation can derive the anodic and cathodic volumetric current densities,  $j_a$  and  $j_c$ , for the electrochemical reaction at the catalyst layers as Eqs. (9.17–9.18) [6, 35]:

$$j_a = (1 - S)A_a i_0^{\text{ref}} \left\{ \left( \frac{c_{H_2}}{c_{H_2}^{\text{ref}}} \right)^2 \exp \left[ \frac{4\alpha_a F}{RT} (\phi_s - \phi_m) \right] \right\} \quad (9.17)$$

$$j_c = (1 - S)A_c i_0^{\text{ref}} \left\{ \left( \frac{c_{O_2}}{c_{O_2}^{\text{ref}}} \right) \exp \left[ \frac{4\alpha_c n F}{RT} (\phi_m - \phi_s) \right] - \left( \frac{c_{H_2O}}{c_{H_2O}^{\text{ref}}} \right)^2 \exp \left[ -\frac{4(1 - \alpha_c) F}{RT} (\phi_m - \phi_s) \right] \right\} \quad (9.18)$$

where  $A_a$  and  $A_c$  (default value used was 100 cm<sup>2</sup>) are the anodic and cathodic effective specific catalyst area,  $c_{H_2}^{\text{ref}}$ ,  $c_{O_2}^{\text{ref}}$  (default value used was 3.38 mol m<sup>-3</sup>), and  $c_{H_2O}^{\text{ref}}$  are the reference concentration of hydrogen, oxygen, and water, respectively,  $\alpha_a$  (default value used was 1 dimensionless unit) and  $\alpha_c$  (default value used was 0.5 dimensionless unit) are the symmetric factors. The reference exchange current density,  $i_0^{\text{ref}}$ , in A cm<sup>-3</sup> can be calculated as follows [13], defined in Eq. (9.19):

$$i_0^{\text{ref}} = 10^{3.507 - 4001/T} \quad (9.19)$$

The effective saturation  $S$  is defined by Eq. (9.19) as

$$S = \frac{s - S_{\text{res}}}{S_{\text{max}} - S_{\text{res}}} \quad (9.20)$$

where  $S_{\text{res}}$  (default value used was 0.102 dimensionless unit) and  $S_{\text{max}}$  (default value used was 0.924 dimensionless unit) are the residual and maximum saturation, respectively, of the wetting fluid.

The effective electrical conductivity  $\sigma_s^{\text{eff}}$  and the effective electrolyte conductivity  $\sigma_m^{\text{eff}}$  are given by Eqs. (9.21) and (9.22):

$$\sigma_s^{\text{eff}} = \begin{cases} \sigma_s (1 - \xi_{\text{GDL}})^{1.5} & \text{in GDL} \\ \sigma_s (\varepsilon_s)^{1.5} & \text{in CL} \end{cases} \quad (9.21)$$

$$\sigma_m^{\text{eff}} = \sigma_m (\xi_{\text{CL}} \varepsilon_m)^{1.5} \quad (9.22)$$

where  $\xi_{\text{GDL}}$  is the GDL porosity (default value used was 0.5 dimensionless unit),  $\xi_{\text{CL}}$  is the CL porosity or void region in the catalyst layer,  $\varepsilon_s$  is the solid fraction in CL

(default value used was 0.3 dimensionless unit),  $\varepsilon_m$  is the electrolyte fraction in CL (default value used was 0.15 dimensionless unit), and  $\sigma_s$  is the electric conductivity (default value used was 300 S m<sup>-1</sup>). The electrolyte conductivity  $\sigma_m$  can be described by Eq. (9.23) as [36]

$$\sigma_m = -100 \exp \left[ 1268 \left( \frac{1}{303} - \frac{1}{T} \right) \right] \times [0.00326 - 0.005139\lambda] \quad (9.23)$$

where  $T$  is the operating temperature (default value used was 80 °C for low-temperature PEMFC). The hydration of the membrane or water content  $\lambda$  is defined by Eq. (9.24) as follows:

$$\lambda = 0.3 + 6a[1 - \tanh(a - 0.5)] + 3.9\sqrt{a} \left[ 1 + \tanh \left( \frac{a - 0.89}{0.23} \right) \right] \quad (9.24)$$

The activity of water  $a$  is defined by Eq. (9.25) as

$$a = \frac{x_{\text{H}_2\text{O}} p_g}{p_{\text{sat}}} \quad (9.25)$$

where  $x_{\text{H}_2\text{O}}$  is the mole fraction of water and  $p_g$  is the gas pressure. Saturation pressure in atmosphere  $P_{\text{sat}}$  is estimated using Eq. (9.26) as

$$p_{\text{sat}} = 10^{-2.1794 + 0.02953(T-273) - 9.1837 \times 10^{-5}(T-273)^2 + 1.4454 \times 10^{-7}(T-273)^3} \quad (9.26)$$

### 9.2.3 Gas Species in Flow Channels

The multicomponent diffusion and convection for the species transport in flow channels are described by the Stefan-Maxwell equation [6], which solves for the fluxes in terms of mass fractions defined in Eq. (9.27):

$$\rho u \cdot \nabla \omega_i - \nabla \cdot \left\{ \rho \omega_i \sum_{j=1}^N (1-S)^{1.5} D_{ij}^{\text{eff}} \left[ \frac{M}{M_j} \left( \nabla \omega_j + \omega_j \frac{\nabla M}{M} \right) + (x_j - \omega_j) \frac{\nabla p}{p} \right] \right\} = S_i \quad (9.27)$$

where the subscript  $i$  (or  $j$ ) represents each species of H<sub>2</sub> and H<sub>2</sub>O on the anode side ( $N = 1$ ) and O<sub>2</sub>, H<sub>2</sub>O, and N<sub>2</sub> on the cathode side ( $N = 2$ ),  $u$  is velocity vector (m/s),  $\omega_i$  is the mass fraction of species  $i$ ,  $x$  is the mole fraction,  $p$  is the pressure (Pa),  $M$  is the molecular mass (kg/mol), and  $S_i$  is the source term of species  $i$ .  $D_{ij}^{\text{eff}}$ , the effective diffusion coefficient of species  $i$  in the GDL and CL, is obtained from the Bruggemann's correction, defined in Eqs. (9.28) and (9.29):

$$D_{ij}^{\text{eff}} = \varepsilon_{\text{GDL}}^{1.5} D_{ij} \quad (9.28)$$

$$D_{ij}^{\text{eff}} = \varepsilon_{\text{CL}}^{1.5} D_{ij} \quad (9.29)$$

where  $D_{ij}$  is the binary diffusion coefficient that can be calculated from the empirical correlation given Eq. (9.30) by [14, 15]:

$$D_{ij} = D_{ij}^0(T_0, P_0) \frac{P}{P_0} \left( \frac{T}{T_0} \right)^{1.5} \quad (9.30)$$

According to the  $D_{ij}^0$  [14],  $D_{\text{O}_2, \text{N}_2} = 0.22 \times 10^{-4} \times (T/293.2)^{1.5} \text{m}^2/\text{s}$ ,  $D_{\text{O}_2, \text{H}_2\text{O}} = 0.282 \times 10^{-4} \times (T/308.1)^{1.5} \text{m}^2/\text{s}$ ,  $D_{\text{H}_2\text{O}, \text{N}_2} = 0.293 \times 10^{-4} \times (T/298.2)^{1.5} \text{m}^2/\text{s}$ , and  $D_{\text{H}_2, \text{H}_2\text{O}} = 0.915 \times 10^{-4} \times (T/307.1)^{1.5} \text{m}^2/\text{s}$ . The effective diffusivity of oxygen for the flooded electrode and CL model can be derived from the effective oxygen diffusivity in water vapor and liquid water [16].

The density of mixture gas  $\rho$  is a function of mixture components which is given by Eq. (9.31):

$$\rho = \left( \sum_i x_i M_i \right) \frac{p}{RT} \quad (9.31)$$

where  $x_i$  is the mole fraction of species  $i$ ,  $R$  is the universal gas constant ( $8.314 \text{ J}\cdot\text{mol}^{-1} \text{ K}^{-1}$ ), and  $T$  is the cell temperature (K). The subscript  $i$  represents each species of hydrogen and water on the anode side and oxygen, water, and nitrogen on the cathode side.

On the cathode side, the third species can be derived from the other two solved species, summarized in Eq. (9.32):

$$\omega_{\text{N}_2} = 1 - \omega_{\text{O}_2} - \omega_{\text{H}_2\text{O}} \quad (9.32)$$

While on the anode side, the mass fraction of water can be expressed by that of hydrogen and also summarized in Eq. (9.33):

$$\omega_{\text{H}_2\text{O}} = 1 - \omega_{\text{H}_2} \quad (9.33)$$

The source term  $S_i$  comes from the electrochemical kinetics, where consumption of the reactants of species  $i$  on the anode or cathode side produces a current as given by Eqs. (9.34), (9.35), and (9.36):

$$S_{\text{H}_2} = R_{\text{H}_2} \quad (9.34)$$

$$S_{\text{O}_2} = R_{\text{O}_2} \quad (9.35)$$

$$S_{\text{H}_2\text{O}} = \begin{cases} R_{\text{H}_2\text{O}} + R_{v \leftrightarrow 1} & T > T_{\text{H}_2\text{O},v} \\ R_{\text{H}_2\text{O}} & T < T_{\text{H}_2\text{O},v} \end{cases} \quad (9.36)$$

where  $T_{\text{H}_2\text{O},v}$  is the evaporation temperature of water, the reaction rate of species  $i$   $R_i$ , [7, 17, 18] is given by Eqs. (9.37), (9.38), and (9.39),  $R_{v \leftrightarrow 1}$  representing the condensation and evaporation of the water is given by Eq. (9.40):

$$R_{\text{H}_2} = -\frac{j_a}{2F} M_{\text{H}_2} \quad (9.37)$$

$$R_{\text{O}_2} = \frac{j_c}{4F} M_{\text{O}_2} \quad (9.38)$$

$$R_{\text{H}_2\text{O}} = -\frac{j_c}{2F} M_{\text{H}_2\text{O}} \quad (9.39)$$

$$R_{v \leftrightarrow 1} = \chi \varepsilon \frac{M_{\text{H}_2\text{O}}}{RT} (x_{\text{H}_2\text{O}} p_g - p_{\text{sat}}) (1 - S) q \\ + E \varepsilon \frac{M_{\text{H}_2\text{O}}}{RT} S (x_{\text{H}_2\text{O}} p_g - p_{\text{sat}}) (1 - q) \quad (9.40)$$

where  $\chi$  is the condensation constant with default value of  $100 \text{ s}^{-1}$ ,  $E$  is the evaporation constant with default value of  $100 \text{ s}^{-1}$ , and  $q$  is the switch function (Eq. 9.40), which is related to the relative humidity (RH) inside the GDL and CL:

$$q = \begin{cases} 0 & \text{if } a \leq 1 \\ 1 & \text{if } a > 1 \end{cases} \quad (9.41)$$

## 9.2.4 Fluid Flow in Porous Media

Since gas diffusion layers (GDL) and catalyst layers are porous media, the fluid flow  $u$  in the porous media is described by the Darcy equation and the mass conservation in Eqs. (9.42) and (9.43):

$$u = -\frac{\kappa}{\eta} \nabla p \quad (9.42)$$

$$\nabla \cdot (\rho u) = S_m \quad (9.43)$$

where  $\kappa$  represents the permeability,  $\rho$  is the density,  $\eta$  is the dynamic viscosity, and  $p$  is the pressure. The source term  $S_m$  ( $\text{kg m}^{-3} \text{ s}^{-1}$ ) accounts for the consumption of hydrogen at the anode CL and the consumption of oxygen, and the net production of water due to the electrochemical reactions at cathode CL is given in Eq. (9.44):

$$S_m = \begin{cases} -R_{H_2} & \text{at anode CL} \\ -R_{O_2} + R_{H_2O} & \text{at cathode CL} \end{cases} \quad (9.44)$$

$S_m$  represents (Eq. 9.45) an extra drag force inversely proportional to the permeability of a porous medium but proportional to fluid viscosity and velocity:

$$S_m = -(\eta/\kappa)u_g \quad (9.45)$$

where  $\kappa$  is the permeability (default value used was  $5.5 \times 10^{-11} \text{ m}^2$ ) and  $\eta$  is the fluid viscosity (default value used was  $2.1 \times 10^{-5} \text{ Pa s}$ ).

## 9.2.5 Conservation of Liquid Water

The saturation of liquid water  $S$  can be solved by the conservation of mass as defined by Eq. (9.46) [19]:

$$\nabla \cdot \left( \rho_l \left[ -D_c \nabla S + \frac{\mu_g \kappa_l}{\mu_l \kappa_g} u_g \right] \right) = S_l \quad (9.46)$$

where  $S_l$  (Eq. 9.47) is the source term for liquid water and is defined according to the operating temperature  $T$  as follows:

$$S_l = \begin{cases} R_{v \leftrightarrow 1} & T > T_{H_2O, v} \\ R_{v \leftrightarrow 1} + R_{H_2O} & T < T_{H_2O, v} \end{cases} \quad (9.47)$$

where  $T_{H_2O, v}$  is the evaporation temperature of water, the source term  $R_{v \leftrightarrow 1}$  describes the evaporation or condensation of liquid water due to phase change from liquid to vapor or vice versa in the gas diffusion and catalyst layers, and the source term  $R_{H_2O}$  describes the addition of liquid water created from the electrochemical reaction and it is only evaluated in the CL and equal to zero in the GDL since no reaction takes place there.

The capillary diffusion coefficient,  $D_c$ , is defined by Eqs. (9.48), (9.49), (9.50), and (9.51) as

$$D_c = -\frac{\kappa_l}{\mu_l} \frac{dp_c}{dS} \quad (9.48)$$

$$\kappa_l = \kappa \kappa_{rl}, \quad \kappa_g = \kappa \kappa_{rg}, \quad \kappa_{rl} = S^3, \quad \kappa_{rg} = (1 - S)^3 \quad (9.49)$$

$$p_c = \sigma \cos \theta_c \left( \frac{\varepsilon}{\kappa} \right)^{0.5} g(S) \quad (9.50)$$



$$g(S) = \begin{cases} 1.417(1-S) - 2.12(1-S)^2 + 1.263(1-S)^3 & \text{if } 0 \leq \theta_c < \pi/2 \\ 1.417S - 2.12S^2 + 1.263S^3 & \text{if } \pi/2 \leq \theta_c < \pi \end{cases} \quad (9.51)$$

where the Leverett function expression of capillary pressure  $p_c$  is dependent on the contact angle  $\theta_c$ ,  $\varepsilon$  is the porosity (0–1) and the porosity of CL  $\varepsilon_{CL}$  has a default value used of 0.4 dimensionless unit,  $\sigma$  is the surface tension (default value used was 0.062 N/m), and  $\kappa$  is the permeability (default value used was  $5.5 \times 10^{-11} \text{ m}^2$ ).

Electroosmotic drag and back-diffusion characterize the water vapor flux between GDL and CL as defined by Eq. (9.52):

$$N_w = -D_\lambda \nabla \cdot \lambda + \frac{n_d J}{F} \quad (9.52)$$

where  $n_d$  is defined by Eq. (9.53) and  $D_\lambda$  is defined by Eq. (9.54):

$$n_d = \frac{2.5\lambda}{22} \quad (9.53)$$

$$D_\lambda = \exp \left[ 2416 \left( \frac{1}{303} - \frac{1}{T} \right) \right] \times \begin{cases} 10^{-6} & \lambda < 2 \\ 10^{-6} [1 + 2(\lambda - 2)] & 2 \leq \lambda < 3 \\ 10^{-6} [3 - 1.67(\lambda - 3)] & 3 \leq \lambda < 4.5 \\ 1.25 \times 10^{-6} & 4.5 \leq \lambda \end{cases} \quad (9.54)$$

## 9.2.6 Heat Transport

Heat is generated due to the electrochemical reaction and resistance to the transport of protons, electrons, and species. The energy equation governing the transport of heat can be expressed in Eq. (9.55) as follows:

$$(\rho c_p)^{\text{eff}} \mathbf{u}_{\text{mix}} \cdot \nabla \cdot T = \nabla \cdot (k^{\text{eff}} \nabla T) + \dot{Q} \quad (9.55)$$

where the effective heat capacity of each layer  $(\rho c_p)^{\text{eff}}$  exists in three domains: bipolar plate, backing layer, and catalyst layer, and is weighted by the volume fraction of each phase in the layer defined by Eq. (9.56):

$$(\rho c_p)^{\text{eff}} = \varepsilon_g (\rho c_p)_g + \varepsilon_s (\rho c_p)_s + \varepsilon_l (\rho c_p)_l + \varepsilon_m (\rho c_p)_m \quad (9.56)$$

The effective thermal conductivity,  $k^{\text{eff}}$ , is evaluated for each layer as defined by Eq. (9.57):

$$k^{\text{eff}} = \varepsilon_g k_g + \varepsilon_s k_s + \varepsilon_l k_l + \varepsilon_m k_m \quad (9.57)$$

where  $\varepsilon_l$ ,  $\varepsilon_m$ ,  $\varepsilon_s$ , and  $\varepsilon_g$  represent the volume fraction of liquid water, a membrane electrolyte, solid matrix, and gas pore, respectively. Hence, the summation of the  $\varepsilon$  terms equals unity (dimensionless unit).

The mixture velocity  $\mathbf{u}_{\text{mix}}$  can be found using Eq. (9.58) for the mixture properties as

$$\mathbf{u}_{\text{mix}} = \frac{\rho_l \mathbf{u}_l + \rho_g \mathbf{u}_g}{\rho_l S + \rho_g (1 - S)} \quad (9.58)$$

where  $\mathbf{u}_l$  and  $\mathbf{u}_g$  are the velocity of phase liquid and gas.

The total heat generation is composed of reversible and irreversible heat releases. The irreversible heat release can be further divided into activation and Ohmic heating since in the present formulation the activation polarization actually includes the overpotential due to the mass transfer as well as defined in Eq. (9.59):

$$\begin{aligned} \dot{Q} &= \dot{Q}_{\text{rev}} + \dot{Q}_{\text{act}} + \dot{Q}_{\text{ohm}} + \dot{Q}_{\text{phase}} \\ &= \underbrace{\left| \frac{J}{nF} \right| (T\Delta S)}_{\text{rev}} + \underbrace{|nJ|}_{\text{act}} + \underbrace{\left( \frac{J_s^2}{\sigma_s^{\text{eff}}} + \frac{J_m^2}{\sigma_m^{\text{eff}}} \right)}_{\text{ohm}} + \underbrace{h_{fg} R_{v \leftrightarrow l}}_{\text{phase}} \end{aligned} \quad (9.59)$$

where  $\Delta S$  represents the entropy change of the overall reaction;  $\eta$  is the activation overpotential;  $J$  is the reaction rate;  $\sigma_s$  (default value used was  $115 \text{ S m}^{-1}$ ) and  $\sigma_m$  are the electronic and protonic conductivities, respectively;  $J_s$  and  $J_m$  are the electronic and protonic current densities, respectively; and  $h_{fg}$  is the enthalpy of vaporization of water.

### 9.2.7 Boundary Conditions

The flow inlet is the interface between the inlet channel and GDL. The boundary conditions of mass fraction  $m_i$  are defined by Eqs. (9.60) and (9.61):

$$\omega_{\text{O}_2} = \omega_{\text{O}_2, \text{in}}, \quad \omega_{\text{H}_2\text{O}} = \omega_{\text{H}_2\text{O}, \text{in}}, \quad \omega_{\text{H}_2} = \omega_{\text{H}_2, \text{in}} \quad \text{on the flow inlet} \quad (9.60)$$

$$\mathbf{n} \cdot (\nabla \omega) = 0 \quad \text{for other boundaries} \quad (9.61)$$

The boundary conditions of  $p$  are defined by Eqs. (9.62–9.64):

$$p = p_{\text{in}} = p_{\text{in}, 0} \quad \text{on the flow inlet between GDL and inlet channel} \quad (9.62)$$

$$p = p_{\text{ref}} \quad \text{on the flow outlet between GDL and outlet channel} \quad (9.63)$$

$$\mathbf{n} \cdot (\nabla p) = 0 \quad \text{for other boundaries} \quad (9.64)$$

where  $p_{i,0}$  represents the initial inlet pressure that is dependent on the stoichiometric value, the gas pressure  $p$  is specified as equal to the inlet pressure,  $p_{\text{ref}}$  is the back pressure set to the atmospheric pressure

The boundary conditions of  $S$  are defined by Eqs. (9.65) and (9.68):

$$S = 0 \quad \text{between GDL and channel} \quad (9.65)$$

$$\mathbf{n} \cdot (D_c \nabla S) = \frac{n_d i M_{\text{H}_2\text{O}}}{F \rho_l S \varepsilon_{\text{CL}}} \quad \text{between CL and membrane} \quad (9.66)$$

$$\mathbf{n} \cdot (\nabla S) = 0 \quad \text{for other boundaries} \quad (9.67)$$

$$i = (1 - S) i_0^{\text{ref}} \left( \frac{c_{\text{O}_2}}{c_{\text{O}_2, \text{ref}}} \right)^{\gamma_{\text{O}_2}} \left\{ \exp \left[ \frac{\alpha F}{RT} (\phi_m - \phi_s) \right] - \exp \left[ -\frac{\alpha F}{RT} (\phi_m - \phi_s) \right] \right\} \quad (9.68)$$

where  $\alpha$  is the symmetric factor (default value used was 0.5 dimensionless unit),  $\gamma_{\text{O}_2}$  is the order of reaction (default value used was 1.0 dimensionless unit). The electroosmotic drag coefficient ( $\text{H}_2\text{O}/\text{H}^+$ ),  $n_d$ , of water molecules through the electrolyte membrane is dependent on the water activity  $a$ , defined by Eq. (9.69).

$$n_d = \begin{cases} 1.0 & \text{if } \lambda < 9 \\ 0.117\lambda - 0.053 & \text{if } \lambda \geq 9 \end{cases} \quad (9.69)$$

The boundary conditions of  $\phi_m$  are defined by Eqs. (9.70) and (9.71):

$$\phi_m = 0 \quad \text{between CL and membrane} \quad (9.70)$$

$$\mathbf{n} \cdot (\nabla \phi_m) = 0 \quad \text{for other boundaries} \quad (9.71)$$

The boundary conditions of  $\phi_s$  determine the electrode potential distribution between channel and GDL using Eqs. (9.72) and (9.73):

$$\phi_s = \begin{cases} V_{\text{cell}} & \text{at cathode} \\ 0 & \text{at anode} \end{cases} \quad (9.72)$$

$$\mathbf{n} \cdot (\nabla \phi_s) = 0 \quad \text{for other boundaries} \quad (9.73)$$

The boundary conditions of  $T$  are defined by Eqs. (9.74), (9.75), and (9.76):

$$T = T_{\text{st}} \quad \text{at cathode} \quad (9.74)$$

$$\mathbf{n} \cdot (k^{\text{eff}} \nabla T) \Big|_{\text{solid\_side}} = h_T (T_{\text{st}} \Big|_{\text{channel\_side}} - T \Big|_{\text{solid\_side}}) \quad \text{around the channels} \quad (9.75)$$

$$\mathbf{n} \cdot (\nabla T) = 0 \quad \text{for other boundaries} \quad (9.76)$$

where  $T_{st}$  is the cathode temperature maintained by the cooling system and  $h_T$  is the convective heat transfer coefficient which can be derived from the Nusselt number correlation [20]:  $Nu = h_T d_h / k_i = 3.61$  (dimensionless unit).

### 9.3 Humidity and Pressure Regulation

The lumped-parameter control-oriented model of a PEMFC system involves ten states [3] defined by Eq. (9.77):

$$x = [m_{H_2,a}, m_{H_2O,a}, m_{H_2,r}, m_{H_2O,r}, m_{H_2,sm,a}, m_{O_2,ca}, m_{H_2O,ca}, m_{N_2,ca}, m_{sm,ca}, m_{om,ca}]^T \quad (9.77)$$

where  $m_{i,j}$  denotes the mass of species “ $i$ ” in manifold “ $j$ .” The subscripts “a,” “sm, a,” “ca,” “om,ca,” “sm, ca,” and “r” represent the anode, anode supply manifold, cathode, cathode outlet manifold, cathode supply manifold, and return manifold, respectively. The system dynamics of the fuel cell system, maintained at a constant temperature, are modeled by utilizing mass conservation to each species in a given manifold as defined by Eq. (9.78):

$$\frac{dm_{i,j}}{dt} = W_{i,j}^{in} - W_{i,j}^{out} \quad (9.78)$$

where  $W_{i,j}^{in}$  and  $W_{i,j}^{out}$ , defined by Eqs. (9.79) and (9.80), represent the mass flow rates of species “ $i$ ” entering (or generated) and leaving (or consumed) manifold “ $j$ ,” respectively:

$$\frac{dm_{H_2O,ca}}{dt} = W_{H_2O,gen} - W_{H_2O,in,ca} - W_{H_2O,out,ca} + W_{memb} \quad (9.79)$$

$$\frac{dm_{H_2O,a}}{dt} = W_{H_2O,in,a} - W_{H_2O,out,a} + W_{memb} \quad (9.80)$$

where  $W_{memb}$ , the water transport through the membrane from the anode to the cathode, is defined by Eqs. (9.81), (9.82), and (9.83):

$$W_{memb} = M_{H_2O} A_{fc} n_{cells} (N_{drag} - N_{diff}) \quad (9.81)$$

$$N_{drag} = \frac{I_{st}}{A_{fc} F} n_d \quad (9.82)$$

$$N_{diff} = \bar{D}_w (\lambda_c - \lambda_a) \quad (9.83)$$

where  $A_{fc}$  denotes the active fuel cell area,  $n_d$  is the drag coefficient,  $n_{cells}$  is the number of cells in the stack,  $\bar{D}_w$  is the diffusion coefficient,  $F$  is the Faraday's constant, and  $\lambda_a$  and  $\lambda_c$  are the anode and cathode water contents, respectively.

Water activity,  $a_{w,j}$ , in an electrode compartment is the ratio of the mass of water in the compartment to its saturation value, defined in Eq. (9.84):

$$a_{w,j} = \frac{m_{H_2O,v,j}}{m_{H_2O,v,j}^{sat}} \quad (9.84)$$

where “j” is replaced by “ca” for the cathode and “a” for the anode.  $m_{H_2O,v,j}^{sat}$  denotes the maximum mass of water vapor in an electrode compartment “j,” defined in Eq. (9.85):

$$m_{H_2O,v,j}^{sat} = \frac{p_{sat}(T_j)V_j}{R_{H_2O}T_j} \quad (9.85)$$

where  $V_j$  denotes the lumped volume of the compartment “j,”  $p_{sat}(T_j)$  represents the saturation pressure at temperature  $T_j$ , and  $R_{H_2O}$  is the gas constant of water vapor.

The relative humidity of manifold “j” is defined in Eq. (9.86) as

$$\varphi_j = \min \left\{ \frac{m_{H_2O,j}}{m_{H_2O,v,j}^{sat}}, 1 \right\} \quad (9.86)$$

Note that, for subsaturating cases,  $a_{w,j} = \varphi_j$ . The total pressure in the manifold,  $p_j$ , and the partial pressure of species “i” in manifold “j,”  $p_{i,j}$ , are given by Eqs. (9.87) and (9.88):

$$p_{i,j} = \begin{cases} m_{i,j} \frac{R_i T_j}{V_j} & \text{for } i \neq H_2O \\ \min \{ m_{i,j}, m_{H_2O,v,j}^{sat} \} & \text{for } i = H_2O \end{cases} \quad (9.87)$$

$$p_j = \sum_i p_{i,j} \quad (9.88)$$

where  $R_i$  is the gas constant for species “i.” Therefore, the states defined by Eq. (9.89) can be used to describe the system dynamics:

$$x = [p_a, a_{w,a}, p_r, \varphi_r, p_{sm,a}, p_{ca}, a_{w,ca}, p_{O_2,ca}, p_{sm,ca}, p_{om,ca}]^T \quad (9.89)$$

The control inputs are defined by Eq. (9.90), where feedback controllers are built for the actuators on the anode side of fuel cell stack.

$$u = [W_{sup}, u_{bpv}]^T \quad (9.90)$$

where the flow rate of dry hydrogen,  $W_{\text{sup}}$ , is supplied from the hydrogen fuel source and  $u_{\text{bpv}}$  denotes the normalized back pressure valve opening. The exogenous input  $w$  is defined by Eq. (9.91) as

$$w = [I_{\text{st}}, \varphi_{\text{in, ca}}, W_{\text{comp}}]^T \quad (9.91)$$

where  $I_{\text{st}}$  is the load,  $W_{\text{comp}}$  is the air flow through the compressor, and  $\varphi_{\text{in, c}}$  represents the cathode inlet humidity.

The performance variables are defined by Eq. 9.92) as

$$z = [a_{\text{w, a}} - a_{\text{w, a}}^*, a_{\text{w, ca}} - a_{\text{w, ca}}^*, p_{\text{a}} - p_{\text{a}}^*]^T \quad (9.92)$$

where  $p_{\text{a}}$ ,  $a_{\text{w, ca}}$ , and  $a_{\text{w, a}}$  are the anode pressure, the cathode water activity, and the anode water activity, respectively. The quantities  $a_{\text{w, a}}^*$  and  $a_{\text{w, ca}}^*$  represent the desired water activities for the anode and cathode, respectively, ensuring the two compartments of the fuel cell stack maintain high humidity conditions (barely below saturation) and yet subsaturation at equilibrium. The anode pressure  $p_{\text{a}}$  is regulated to follow the pressure on the cathode side to maintain an acceptable pressure difference across the membrane throughout the operating range. The desired anode pressure  $p_{\text{a}}^*$  is obtained from the cathode supply manifold pressure  $p_{\text{sm, ca}}$  by Eq. (9.93) as

$$p_{\text{a}}^* = 0.923p_{\text{sm, ca}} + 4850 \quad (9.93)$$

where both  $p_{\text{a}}^*$  and  $p_{\text{sm, ca}}$  are in Pa.

These performance variables deviate from  $z = 0$  with a load change that (1) shifts their desired steady-state values and (2) changes the water activities and pressures inside the electrodes. A proper actuation of  $u$  from the control system can minimize the deviations in  $z$  during the load transients and restore  $z$  to the desired equilibrium ( $z = 0$ ).

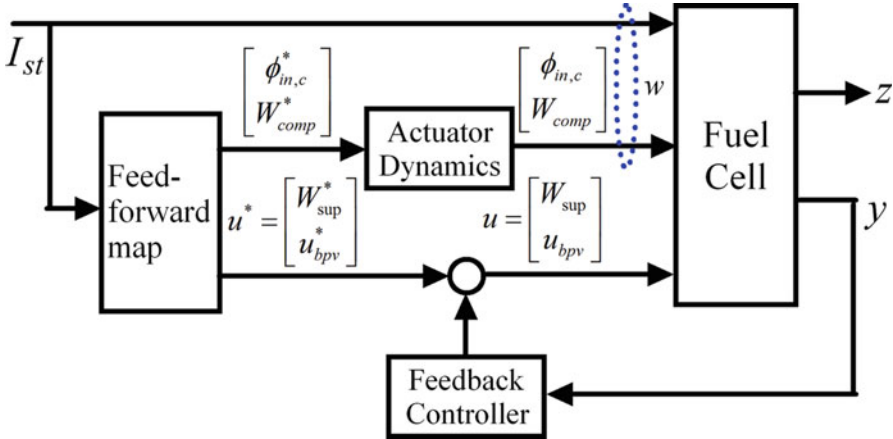
In the modularity of control design for the anode recirculation system, the measured variables for the feedback contain only anode side humidity and pressure measurements, as defined in Eq. (9.94):

$$y = [p_{\text{a}}, p_{\text{r}}, p_{\text{sm, a}}, \varphi_{\text{a}}] \quad (9.94)$$

where  $p_{\text{sm, a}}$  and  $p_{\text{r}}$  are the pressures in the anode supply manifold and the anode return manifold. For a full-state feedback controller,  $y = x$ .

### 9.3.1 State Feedback Controller

The feedforward map  $u^* = [W_{\text{sup}}^*, u_{\text{bpv}}^*]$  contributes to the state feedback controller  $u$  as illustrated in Fig. 9.2 and defined by Eq. (9.95):



**Fig. 9.2** The controller for the fuel cell uses the feedforward and feedback control signals.  $w$ ,  $y$ ,  $u$ , and  $z$  are exogenous inputs, measured variables, control inputs, and performance variables. The type of controller determines the choice of  $y$  (Modified figure from [3])

$$u = u^* + K_{sf}(x - x^*) \tag{9.95}$$

where  $x^*$  is the desired steady-state operating condition and  $K_{sf}$  is the state feedback gain. A linear quadratic regulator approach is used to realize an optimal full-state feedback controller that meets the desired transient criteria. The performance cost function  $J$  is given by Eq. (9.96):

$$J = \int_0^\infty (z^T Q z + (u - u^*)^T R (u - u^*)) dt \tag{9.96}$$

where  $K_{sf}$  is obtained by tuning  $R$ , a  $2 \times 2$  diagonal matrix, and  $Q$ , a  $3 \times 3$  diagonal matrix, with trial and a marginal change to reduce error in the closed-loop performance [3]. The cost function  $J$  is minimized by the optimal state feedback controller gains  $K_{sf}$  given by Eq. (9.97):

$$K_{sf} = -R^{-1} B_u^T \bar{P} \tag{9.97}$$

where  $\bar{P}$  is a solution to the algebraic Riccati Eq. (9.98):

$$AP + \bar{P}A + C_z^T Q C_z - \bar{P} B_u R^{-1} B_u^T \bar{P} = 0 \tag{9.98}$$

where the matrices  $A$ ,  $B_u$ ,  $B_w$ , and  $C_z$  are obtained through symbolic linearization using MATLAB for the dynamic system that is represented by an equilibrium condition, defined in Eqs. (9.99) and (9.100):

$$\delta \dot{x} = A \delta x + B_u \delta u + B_w \delta w \tag{9.99}$$

$$\delta z = C_z \delta x \tag{9.100}$$

where  $\delta(\cdot)$  represents the deviation of the variable from the equilibrium condition and  $\delta x = x - x^*$ .

### 9.3.2 Static Output Feedback Controller

The control action of the combined static output feedback and feedforward controller is given by Eq. (9.101):

$$u = u^* + K_y(y - y^*) \quad (9.101)$$

Let the linear representation of the measured variables be given by Eq. (9.102):

$$\delta y = C_y \delta x \quad (9.102)$$

where  $\delta y$  is the deviation of  $y$  from its equilibrium condition,  $y^*$ . The optimal feedback gain  $K_y$  minimizes the cost function  $J$  and is then given by Eq. (9.103):

$$K_y = -R^{-1} B_u^T S L C_y^T (C_y L C_y^T)^{-1} \quad (9.103)$$

where the matrices  $S$  and  $L$  are obtained by solving the coupled Riccati Eqs. (9.104), (9.105), and (9.106) as

$$A_{cl}^T S + S A_{cl} + C_z^T Q C_z + C_y^T K_y^T R K_y C_y = 0 \quad (9.104)$$

$$A_{cl} L + L A_{cl}^T + I = 0 \quad (9.105)$$

$$A_{cl} = A + B_u K_y C_y = 0 \quad (9.106)$$

## 9.4 Gas Flow Rate Regulation

### 9.4.1 Controller Design Under Gas Flow Rate Constraints

By denoting the state variables including the activation overvoltage, the hydrogen partial pressure, and the oxygen partial pressure,  $x^T = [V_{act}, p_{H_2}, p_{O_2}]^T$ ; the control inputs including the hydrogen and oxygen input flow rate,  $u^T = [\dot{m}_{H_2, in}, \dot{m}_{O_2, in}]^T$ ; and the varying system parameters including the current and temperature,  $\theta^T = [I, T]^T$ , the system nonlinear dynamics [21, 22] can be expressed by Eq. (9.107) as

$$\dot{x} = f(x, u, \theta) \quad (9.107)$$

When the air is supplied instead of the pure oxygen, the control input of oxygen input flow rate can be alternatively replaced by the air flow rate or the fan voltage. The activation overvoltage can be described by Eqs. (9.108), (9.109), (9.110), and (9.111):



$$\frac{dV_{\text{act}}}{dt} = \frac{V_{\text{act}}I}{\eta_{\text{act}}C_{dl}} + \frac{I}{C_{dl}} \quad (9.108)$$

$$\eta_{\text{act}} = -0.984 + (0.00286 + 0.0002\ln(A_{\text{cell}}) + 4.3 \cdot 10^{-5}\ln(C_{\text{H}_2}))T + 7.6 \cdot 10^{-5}T\ln(C_{\text{O}_2}) - 1.93 \cdot 10^{-4}T\ln I \quad (9.109)$$

$$C_{\text{H}_2} = 9.174 \cdot 10^{-7} p_{\text{H}_2} \exp\left(\frac{-77}{T}\right) \quad (9.110)$$

$$C_{\text{O}_2} = 1.97 \cdot 10^{-7} p_{\text{O}_2} \exp\left(\frac{498}{T}\right) \quad (9.111)$$

where  $A_{\text{cell}}$  is the cell active area. The hydrogen partial pressure can be described by Eqs. (9.112), (9.113), and (9.114):

$$\frac{V_{\text{an}}}{RT} \frac{dp_{\text{H}_2}}{dt} = \dot{m}_{\text{H}_2, \text{in}} - k_{\text{an}}(p_{\text{H}_2} - p_{\text{H}_2, \text{tank}}) - \frac{NI}{2F} \quad (9.112)$$

$$\dot{m}_{\text{H}_2, \text{out}} = k_{\text{an}}(p_{\text{H}_2} - p_{\text{H}_2, \text{tank}}) \quad (9.113)$$

$$\dot{m}_{\text{H}_2, \text{used}} = \frac{NI}{2F} \quad (9.114)$$

where  $p_{\text{H}_2, \text{tank}}$  is the hydrogen tank pressure. The oxygen partial pressure can be described by Eqs. (9.115), (9.116), and (9.117):

$$\frac{V_{\text{ca}}}{RT} \frac{dp_{\text{O}_2}}{dt} = \dot{m}_{\text{O}_2, \text{in}} - \dot{m}_{\text{O}_2, \text{out}} - \dot{m}_{\text{O}_2, \text{used}} \quad (9.115)$$

$$\dot{m}_{\text{O}_2, \text{out}} = k_{\text{ca}}(p_{\text{O}_2} - p_{\text{O}_2, \text{BP}}) \quad (9.116)$$

$$\dot{m}_{\text{O}_2, \text{used}} = \frac{NI}{4F} \quad (9.117)$$

where  $P_{\text{O}_2, \text{BP}}$  is oxygen back pressure. The equilibrium operating conditions of the nonlinear dynamics of the PEM fuel cell can be derived from  $\dot{x} = 0$ . Then we have the equilibrium values of the state variables  $x^*, \text{T} = [V_{\text{act}}^*, p_{\text{H}_2}^*, p_{\text{O}_2}^*]^{\text{T}}$ , defined in Eqs. (9.118), (9.119), and (9.120):

$$V_{\text{act}}^* = -\eta_{\text{act}}(p_{\text{H}_2}^*, p_{\text{O}_2}^*, I, T) \quad (9.118)$$

$$p_{\text{H}_2}^* = \frac{1}{k_{\text{an}}} \left( \dot{m}_{\text{H}_2, \text{in}}^* - \frac{NI}{2F} \right) + p_{\text{H}_2, \text{in}} \quad (9.119)$$

$$p_{\text{O}_2}^* = \frac{1}{k_{\text{ca}}} \left( \dot{m}_{\text{O}_2, \text{in}}^* - \frac{NI}{4F} \right) + p_{\text{O}_2, \text{out}} \quad (9.120)$$

## 9.4.2 Predictive Control of Cathode Exhaust Gas Mass Flow

The predictive cathode exhaust gas mass flow control model can describe the behavior of oxygen depleted air, called ODA-gas, mass flow, and its oxygen content, defined by Eq. (9.121) as

$$\dot{x}_g = f_g(x_g, u_g). \quad (9.121)$$

In this model, the vector of inputs is  $u_g = [I_{st}, \zeta_{O_2}]^T$ , the state vector is  $x_g = [W_{mfc}, W_{oda}, c_{O_2}, z]^T$ , and the output vector is  $y_g = [W_{oda}, c_{O_2}]^T$ , where  $I_{st}$  is stacked current,  $\zeta_{O_2}$  is stoichiometry,  $W_{mfc}$  is the feed air mass flow provided by a controlled valve (mass flow controller) with a time constant  $\tau_{mfc}$ ,  $W_{oda}$  is the ODA-gas mass flow through the downstream pipes with a time constant  $\tau_{fc}$ , and  $z$  is the disturbance mass flow. This model is defined by Eqs. (9.122), (9.123), (9.124), and (9.125) [1]:

$$\tau_{mfc} \dot{W}_{mfc} = W_{mfc, ref} - W_{mfc} \quad (9.122)$$

$$\tau_{fc} \dot{W}_{oda} = W_{mfc} + z - I_{st} \frac{n_{cells}}{4F} M_{O_2} - W_{oda} \quad (9.123)$$

$$\tau_{O_2} \dot{c}_{O_2} = c_{O_2, ca} - c_{O_2} \quad (9.124)$$

$$\dot{z} = 0 \quad (9.125)$$

where  $F$  is the Faraday constant and  $n_{cells}$  is the number of cells in the fuel cell stack. The solutions are provided in Eqs. (9.126), (9.127), (9.128), and (9.129):

$$W_{mfc, ref} = I_{st} \zeta_{O_2} \frac{n_{cells}}{4F} \left( M_{O_2} + \frac{0.79}{0.21} M_{N_2} \right) \quad (9.126)$$

$$c_{O_2, ca} = N_{O_2, ca} / (N_{O_2, ca} + N_{N_2, ca}) \quad (9.127)$$

$$N_{O_2, ca} = (\chi_{O_2} / M_{O_2}) / (W_{mfc} + z) - \frac{n_{cells}}{4F} I_{st} \quad (9.128)$$

$$N_{N_2, ca} = (\chi_{N_2} / M_{N_2}) / (W_{mfc} + z). \quad (9.129)$$

## 9.5 Temperature Regulation

### 9.5.1 Predictive Thermal Model

In the predictive thermal dynamics model Fig 9.1, while the output vector is  $y_{th} = [T_{st}, T_{i1}, T_{e1}, T_{cw}, T_{cond}, X_{oda}]^T$ , the state vector  $x_{th} = [T_{st}, T_{i1}, T_{i2}, T_{e1}, T_{e2}, T_{cw}, T_{cond}]^T$  includes stack temperature  $T_{st}$ , stack cooling system temperatures  $T_{i1}$ ,  $T_{i2}$ ,  $T_{e1}$ ,  $T_{e2}$ , and  $T_{cw}$ , and condenser cooling temperature  $T_{cond}$ , summarized in Eq. (9.130).

$$\dot{x}_{th} = f_{th}(x_g, x_{th}, u_g, u_{th}). \quad (9.130)$$

where the input vector  $u_{th} = [T_{cond, ref}, u_v]^T$  comprises the condenser cooling system reference temperature  $T_{cond, ref}$  and the stack cooling system cooling valve position  $u_v$ . ODA-gas water loading  $X_{oda}$  is determined by the mean pressure of a fully saturated flow in the condenser, outlined by Eq. (9.131):

$$X_{oda} = \frac{p_V^{sat}(T_{cond})}{0.5(p_3 + p_4) - p_V^{sat}(T_{cond})} \frac{R_{oda}}{R_V} \quad (9.131)$$

where water loading  $X$  of a humid gas is defined by Eq. (9.132) as

$$X = \frac{m_v}{m_g} = \frac{\text{mass of vapor}}{\text{mass of dry gas}} \quad (9.132)$$

The stack and condenser cooling system temperatures are described by a predictive thermal model described in Eqs. (9.133), (9.134), (9.135), (9.136), (9.138), and (9.139) as follows [1]:

$$C_{st}\dot{T}_{st} = \dot{Q}_{st} - W_i c_i (T_{st} - T_{i1}). \quad (9.133)$$

$$m_{i1}\dot{T}_{i1} = W_i \left( \left( T_{i2} - \frac{\dot{Q}_{ic}}{C_i} \right) - T_{i1} \right) \quad (9.134)$$

$$m_{i2}\dot{T}_{i2} = W_i (T_{s2} - T_{i2}) \quad (9.135)$$

$$m_{e1}\dot{T}_{e1} = W_e (u_v T_{cw} + (1 - u_v) T_{e2} - T_{e1}) \quad (9.136)$$

$$m_{e2}\dot{T}_{e2} = W_e \left( 0.94 \left( T_{e1} + \frac{\dot{Q}_{ic}}{C_e} \right) u_v T_{cw} + 0.06 T_{e1} - T_{e2} \right) \quad (9.137)$$

$$m_{cw}\dot{T}_{cw} = u_v W_e (T_{e2} - T_{cw}) - \frac{UA_{cw}}{c_e} (T_{e2} - T_{cw}) \quad (9.138)$$

$$\tau_c \dot{T}_{cond} = T_{cond, ref} - T_{cond} \quad (9.139)$$

## 9.5.2 Lumped Thermal Model

The temperature model can be described by a lumped thermal model [23] summarized in Eq. (9.140):

$$\frac{dT_{st}}{dt} = \frac{\dot{Q}_{sou} - W_c C_{pc} (T_{st} - T_{c,in})}{m_{st} C_{pst}} \quad (9.140)$$

where  $m_{st}$  is the heat mass of the stack,  $C_{pst}$  and  $C_{pc}$  are the specific heat,  $W_c$  is the coolant flow rate considered as a control variable,  $T_{c,in}$  is the coolant temperature at the stack inlet, and  $v_{act}$  is the activation loss at catalyst layer.  $\dot{Q}_{sou}$  is the internal energy source that is calculated as a function of the stack current  $I_{st}$ , temperature  $T$ , electrical resistance of stack layers  $R_{ohm}$ , Faraday's number  $F$ , and the entropy change  $\Delta s$ , as described by Eq. (9.141):

$$\dot{Q}_{sou} = I_{st} \left( -\frac{T\Delta s}{4F} + v_{act} + I_{st} R_{ohm} \right) \quad (9.141)$$

For the observer design of this completely nonlinear model, the state vector is  $x = [P_{O_2}, P_{H_2}, P_{N_2}, p_{sm}, m_{sm}, p_{v,an}, p_{v,ca}, p_{rm}, T_{st}]^T$ , where  $P_{H_2}$  is the hydrogen pressure in the anode,  $m_{sm}$  is the mass of air in supply manifold,  $p_{v,a}$  is the vapor partial pressure in the anode,  $p_{v,ca}$  is the vapor partial pressure in the cathode,  $p_{rm}$  is the pressure of return manifold, and  $T_{st}$  is the stack temperature.

### 9.5.3 Energy Balanced Thermal Model

The thermal model can be obtained from an energy balance, taking into account the energy produced in the chemical reaction of water formation (which is supposed to be formed as water steam)  $\dot{H}_{reac}$ , the energy supplied in the form of electricity  $P_{elect}$  and the amount of heat evacuated by radiation  $\dot{Q}_{rad,B2amb}$ , and both natural and forced convection  $\dot{Q}_{conv,B2amb}$ . Heat removal is completed through forced convection by a small fan. In bigger fuel cell stack systems, where the amount of heat is considerably larger, water cooling is necessary. The energy balance is summarized in Eq. (9.142) [24]:

$$m_{st} C_{st} \frac{dT_{st}}{dt} = \dot{H}_{reac} - P_{elect} - \dot{Q}_{rad,B2amb} \quad (9.142)$$

where  $m_{st}$  is the mass of fuel cell (default value used was 5 kg) and  $C_{st}$  is heat capacity of the fuel cell (default value used was  $1100 \text{ JK}^{-1} \text{ kg}^{-1}$ ). The enthalpy flow rate described in Eqs. (9.143), (9.144), (9.145), and (9.146) will be

$$\dot{H}_{reac} = \dot{m}_{H_2, reac} \Delta h_{H_2} + \dot{m}_{O_2, reac} \Delta h_{O_2} - W_{H_2O, gen(g)} \left( h_{f, H_2O(g)}^0 \Delta h_{H_2O(g)} \right) \quad (9.143)$$

$$\Delta h_{H_2} = c_{p, H_2} (T_{anch, in} - T^0) \quad (9.144)$$

$$\Delta h_{\text{O}_2} = c_{p, \text{O}_2} (T_{\text{cach, in}} - T^0) \quad (9.145)$$

$$\Delta h_{\text{H}_2\text{O}} = c_{p, \text{H}_2\text{O}(g)} (T_{\text{st}} - T^0) \quad (9.146)$$

where  $h_{\text{f}, \text{H}_2\text{O}(g)}^0$  is the mass-specific enthalpy of formation of water steam;  $c_{p, \text{H}_2}$ ,  $c_{p, \text{O}_2}$ , and  $c_{p, \text{H}_2\text{O}(g)}$  are the specific heats of hydrogen, oxygen, and water steam respectively; and  $T^0$  is the reference temperature for the enthalpy. Energy yielded in the form of electricity is calculated using Eq. (9.147):

$$P_{\text{elect}} = V_{\text{st}} I_{\text{st}} \quad (9.147)$$

Heat exchanged as radiation is modeled by Eq. (9.148) as

$$\dot{Q}_{\text{rad, B2amb}} = \varepsilon \sigma A_{\text{B2amb, rad}} (T_{\text{st}}^4 - T_{\text{amb}}^4) \quad (9.148)$$

where  $\varepsilon$  is the emissivity (default value used was 0.9 dimensionless unit),  $\sigma$  is the Stefan-Boltzmann constant (default value used was  $5.678 \times 10^{-8} \text{ W m}^{-2} \text{ K}^{-4}$ ), and  $A_{\text{B2amb, rad}}$  is the radiation exchange area (default value used was  $0.141 \text{ m}^2$ ). The convective term is composed by the natural convection  $\dot{Q}_{\text{conv, B2amb, nat}}$  and the forced convection  $\dot{Q}_{\text{conv, B2amb, forc}}$  as defined in Eqs. (9.149–9.151):

$$\dot{Q}_{\text{conv, B2amb}} = \dot{Q}_{\text{conv, B2amb, nat}} + \dot{Q}_{\text{conv, B2amb, forc}} \quad (9.149)$$

$$\dot{Q}_{\text{conv, B2amb, nat}} = h_{\text{B2amb, nat}} A_{\text{B2amb, conv}} (T_{\text{st}} - T_{\text{amb}}) \quad (9.150)$$

$$\dot{Q}_{\text{conv, B2amb, forc}} = h_{\text{B2amb, forc}} A_{\text{B2cool, conv}} (T_{\text{st}} - T_{\text{cool}}) \quad (9.151)$$

where  $h_{\text{B2amb, nat}}$  (default value used was  $14 \text{ W kg}^{-1}$ ) and  $h_{\text{B2amb, forc}}$  are the convective heat transfer coefficients and they are different, just as the exchange areas ( $A_{\text{B2amb, conv}}$  and  $A_{\text{B2cool, conv}}$ ) are, because natural convection takes place in the fuel cell lateral walls, and forced convection occurs across the internal walls of the cells, which are constructed as a radiator in Eq. (9.152):

$$h_{\text{B2amb, forc}} = K_{h1} (W_{\text{cool}})^{K_{h2}} \quad (9.152)$$

where  $K_{h1}$  has default value used was 0.0156 dimensionless unit and  $K_{h2}$  has a default value of unity (also dimensionless unit).

#### 9.5.4 Active Disturbance Rejection Temperature Control System

In the active disturbance rejection temperature control system, the PEMFC temperature system is described in Eq. (9.153) as [25]

$$\frac{dT_{st}}{dt} = f_{\text{total}} + bW_{cl} \quad (9.153)$$

where  $W_{cl}$  is the coolant water flow as a control variable to control the stack temperature,  $f_{\text{total}}$  is defined in Eq. (9.154) and  $b$  is the gain of the control variable as defined in Eq. (9.155):

$$f_{\text{total}} = (Q_{\text{in}} - Q_{\text{out}} + Q_{\text{rea}} - Q_{\text{amb}} - P)/(m_s c_{p,s}) \quad (9.154)$$

$$b = -c_{p,\text{H}_2\text{O}}(T_{st} - T_{\text{wc}}^{\text{in}})/(m_s c_{p,s}) \quad (9.155)$$

where  $c_{p,s}$  is the specific heat of the PEMFC (default value used was  $4000 \text{ JK}^{-1} \text{ kg}^{-1}$ ),  $c_{p,\text{H}_2\text{O}}$  is the specific heat of water (default value used was  $75.37 \text{ J mol}^{-1} \text{ kg}^{-1}$ ), and  $T_{\text{wc}}^{\text{in}}$  is the inlet chilling water temperature (default value used was  $333 \text{ K}$ ). In the temperature control system, the state variables are  $x = [x_1, x_2]$ , where  $x_1 = T_{st}$  and  $x_2 = f_{\text{total}}$ ; output is  $y = x_1 = T_s$ ; control variable is  $u = W_{cl}$ ; the observed value of states is  $z = [z_1, z_2]$ , where  $z_1 = \hat{y} \approx x_1 = T_{st} = y$ ,  $z_1 = \hat{f}_{\text{total}} \approx x_2 = f_{\text{total}}$ , and  $\hat{f}_{\text{total}}$  is the estimate of  $f_{\text{total}}$ . This control system is described in Eq. (9.156) as follows [25]:

$$\begin{cases} e(k) = z_1(k) - x_1(k) \\ z_1(k+1) = z_1(k) + h(z_2(k) - \beta_{01}g_1(e(k)) + bW_{cl}(k)) \\ z_2(k+1) = z_2(k) - h\beta_{02}g_2(e(k)) \end{cases} \quad (9.156)$$

where  $\beta_{01}$  (default value used was 28 dimensionless unit) and  $\beta_{02}$  (default value used was unity, a dimensionless unit) are adjustable parameters. The objective is to keep  $e_0 = (v_{\text{set}} - z_1) = (v_{\text{set}} - \hat{y})$  around zero (also a dimensionless unit). The  $g$  term is defined by Eqs. (9.157), (9.158), and (9.159):

$$g_1(e) = \text{fal}(e, 0.5, \delta) \quad (9.157)$$

$$g_2(e) = \text{fal}(e, 0.25, \delta) \quad (9.158)$$

$$\text{fal}(e, \alpha, \delta) = \begin{cases} e/\delta^{\alpha-1} & |e| \leq \delta \\ |e|^\alpha \text{sign}(e) & |e| > \delta \end{cases} \quad (9.159)$$

The final control law  $u$  can be obtained using Eq. (9.160):

$$u(k) = W_{cl}(k) = u_0(k) - \frac{1}{b} \hat{f}_{\text{total}}(k) \quad (9.160)$$

where  $u_0$  and its  $s$  terms are defined in Eqs. (9.161) and (9.162):

$$u_0(k) = u_{\text{con}} \left( \frac{s(k)}{|s(k)| + \sigma} \right) + \zeta \quad (9.161)$$

$$s(k) = \alpha(v_{\text{set}} - z_1(k)) = \alpha(v_{\text{set}} - \hat{T}_{\text{st}}(k)) \quad (9.162)$$

where  $u_{\text{con}}$  is a constant (default value used was 25 dimensionless unit),  $\sigma > 0$  is rejection chattering factor, and  $\zeta > 0$  provides that  $s(k)\dot{s}(k) < 0$  satisfies the Lyapunov stability principle.

## 9.6 Discussion

### 9.6.1 Cathode Relative Humidity

More liquid water is created in the cathode GDL while the cathodic relative humidity (RH<sub>c</sub>) increases. When the anodic RH is at 100%, a lower RH<sub>c</sub> improves cathodic local current densities and lowers liquid water buildup, thus decreasing possible water flooding and enhancing cell performance. The mass transport limitation caused by cathodic flooding is the major factor that determines cell performance at higher operating currents, as liquid water saturations at the lower operating voltage are far higher than those at the higher operating voltage. Though the RH<sub>a</sub> is 100%, the mass flow rate of water from the cathode to the anode by back-diffusion decreases at a higher operating voltage due to lower cathodic water saturation. Therefore, membrane hydration gradually turns into the key factor that affects cell performance.

The higher water saturation improves the back-diffusion of water and effectively ensures membrane hydration, thus improving PEMFC performance. The minimum current density occurs at the outlet channel, while the maximum current density exists near the inlet channel. More liquid water is produced with increasing RH<sub>c</sub>, while the local current density decreases. The increase of instantaneous resistance at the GDL-CL interface leads to the decrease of local current density. However, the increase in local current may build up more water created by more active electrochemical reactions. Excessively produced liquid water clogs the gas pores in the CL and GDL, potentially leading to cathodic flooding.

### 9.6.2 Anode Relative Humidity

When RH<sub>c</sub> = 100%, a lower RH<sub>a</sub> supplies more hydrogen into the CL to join the electrochemical reaction and enlarges the difference between the water concentrations at the cathode and anode. The enhanced back-diffusion of water from the cathode to the anode reduces possible cathodic flooding. Therefore, a lower RH<sub>a</sub> provides better performance than a higher RH<sub>a</sub>. An increase of the RH<sub>a</sub> increases the water fraction as well, leading to a decrease in the hydrogen molar fraction.

The operating currents do not have significant effects on the distributions of the molar fraction, that is, the molar ratio between anodic water and hydrogen. The decrease of RH<sub>a</sub> significantly results into the increase of hydrogen mass flow rates, so that more hydrogen can be transported into the CL to join the electrochemical

reactions, improving fuel cell performance. Membrane resistance along with Ohmic voltage losses in the membrane is usually increased by lower anodic relative humidities, where cathodic relative humidities were kept at values far less than 100%.

When  $RH_c$  is maintained at 100%, high cathodic RH provides sufficient water to maintain membrane hydration by water back-diffusion. It is also found that a lower  $RH_a$  reduces the local resistance of the cathodic GDL-CL interface, leading to better fuel cell performance.

### 9.6.3 Stoichiometry

Under the assumption of equal cathodic and anodic stoichiometries, the critical condition of the stoichiometries  $\zeta$  ensures that the amount of water delivered out in the vapor phase is greater than the rate of water generation in the cell. If flow rates are faster than this stoichiometry, the accumulated liquid water evaporates. If flow rates are slower than this stoichiometry, the liquid water generated in the cell will accumulate and lead to flooding defined in Eq. (9.163) [26] as

$$\zeta = 0.29 \left( \frac{P}{p_{\text{sat}}(T)} - 1 \right) + 0.44 \quad (9.163)$$

When  $RH_a = 100\%$  and  $RH_c = 100\%$ , liquid water delivered from the cathode to the anode GDL by back-diffusion can be consumed by higher anode stoichiometries. As excess anodic stoichiometry decreases anode water concentration, more water is produced from the cathode to anode, leading to less liquid water accumulated at the cathodic GDL-CL interface. The local current density variation due to anodic stoichiometry variations is different from that of cathodic stoichiometry variations. Higher anodic stoichiometries can transfer more current densities to the cathodic GDL-CL interface, showing better PEM fuel cell performance.

### 9.6.4 Operation Temperature

The PEM fuel cell has several critical issues in the performance and longevity, such as relatively low operation temperature, flexible size, quick start-up, system robustness, and pollution-free operation. Its operating temperature is typically less than 100 °C, and the product water usually remains in liquid form in the cell. Water transport inside the fuel cell determines the temperature distribution that will further affect the water and oxygen diffusivity and reaction kinetics [27]. Inadequate thermal and water management may cause the creation of local hotspots in the cell, degrading the cell components and shorting the lifetime of the cell [28].

The highest temperature change occurs in the GDL, both in the in-plane and across-the-plane directions, while the highest temperature is reached in the CL



[13]. The high thermal conductivity of the plate leads to a relatively uniform distribution of temperature in the bipolar plate. The absorption of heat during the evaporation of liquid water in the GDL and CL decreases the maximum temperature, causing a decrease in the inlet relative humidity of the air stream. The increase in permeability of the cathode shows a nonuniformity of the temperature distribution, especially in the CL. The decrease of the channel shoulder to channel width ratio causes a nonuniform distribution of temperature, especially in the channel areas.

### 9.6.5 Flow Distribution

The objective of water management is to reach a delicate balance between achieving membrane hydration and avoiding electrode flooding. Proper water management is determined by the two-phase flow of water and reactant gases in the gas distribution channels of PEM fuel cells. Externally humidified air and hydrogen gas streams can control sufficient water within the fuel cell to maintain the proton conductivity of the polymer electrolyte membrane, removing excess water from the cell to avoid flooding. The condensed liquid water may flood inside a fuel cell and block gas transport pathways in the catalyst layers, gas diffusion layers (GDLs), and the gas channels, inducing large mass-transport losses.

The hydration of the membrane is crucial to minimize Ohmic losses and resistivity in the fuel cell. Because insufficient reacting water can't achieve full hydration of the membrane, especially in the cathode inlet regions, external humidification is often used but leads to excess water buildup further into the cell. The flooding in the catalyst layer leads to a reduction of the active reaction area, along with a drop in cell performance. The water accumulated in gas channels eventually results in an increase of parasitic pumping power and even channel clogging [6].

### 9.6.6 Pressure Drop

The pressure difference inside the PEMFC arises due to load variations, causing the pressure difference between anode and cathode. This problem can be resolved by equalizing anode and cathode pressures, to protect the fuel cell from permanent damage.

Low superficial air velocities (air stoichiometry below 5) make the two-phase flow dominated by slugs or semi-slugs and cause severe flow maldistribution and large fluctuations in the pressure drop. Higher air velocities form a water film on the channel walls that are hydrophilic [29].

The smaller but frequent fluctuations in the pressure drop for the film flow come from the water buildup at the channel-exit manifold interface. The water film formation along the channel is dictated by the Concus-Finn condition [30], defined in Eq. (9.164):

$$\theta_c + \alpha < \frac{\pi}{2} \quad (9.164)$$

where  $\theta_c$  is the contact angle of water on the channel wall and  $\alpha$  is the half interior angle formed by the channel corner. The two-phase friction multiplier, defined as the ratio of the two-phase pressure drop to the single gas phase pressure drop, can describe the water buildup in the gas channels at the two-phase flow [31], defined in Eq. (9.165):

$$\phi_g^2 = \frac{\Delta P_{TP}}{\Delta P_g} \quad (9.165)$$

where  $\Delta P_{TP}$  and  $\Delta P_g$  are the pressure drop in two-phase flow and with only single-phase gas flow in the channel, respectively. The two-phase friction multiplier increases with the increasing water flow rate.

## 9.6.7 Compression Pressure

A certain compression pressure must be exerted on the assembled fuel cell to achieve adequate contact between the components and to ensure proper gas sealing, while excessive compression decreases GDL porosity and impedes reactant transport and may also destroy typical paper-type GDLs and other components [32]. Usually, increasing compression enhances the electric conductivity of GDL, reduces the contact resistance at the interfaces, and further forms the preferential pathway for liquid water transport in the compressed part of the GDL. One pressure-sensitive film was inserted between two membranes and used to measure the internal pressure after all parts are assembled together [33]. This film was removed during the operation.

The effect of compression pressure on the mechanical and thermal properties of gas diffusion layers (GDL) was investigated by Nitta et al. [34]. The stress-strain curve of the GDL shows one nonlinear and two piecewise linear regions within the compression pressure range of 0–5.5 MPa [34]. In an actual fuel cell assembly, the rib/channel structure of the neighboring bipolar plate leads to inhomogeneous compression pressure over the GDL. The compression force is exerted practically only on the GDL under the rib of the bipolar plate but not under the channel. Therefore, the GDL under the rib is deformed and becomes thinner, while the GDL under the channel partially intrudes into the channel.

The thermal conductivity of the compressed gas diffusion layers (GDL) is approximated to be  $1.18 \pm 0.11 \text{ Wm}^{-1} \text{ K}^{-1}$  at room temperature and is independent of the compression pressure. The computer modeling shows that the thermal contact resistance between the GDL and graphite is comparable to the thermal bulk resistance of the GDL and decreased nonlinearly with increasing compression pressure. A temperature drop of 1.7–4.4 °C was also predicted across the GDL and catalyst layer depending on compression pressures.

## 9.7 Summary

Mathematical modeling used conservation equations for momentum, mass, species, charge, and energy, to investigate the heat transfer and temperature distribution in the cathode along with the multiphase and multi-species transport under the steady-state condition. This model shows that (1) the water saturation is under the influence of stoichiometry of reactants and relative humidity and (2) the possible flooding can be reduced by the back-diffusion of water from the cathode to the anode. Multiple feedback control schemes are used to address the transient water, pressure, and temperature management problem of a PEMFC system. The pressure regulation requirement stems from membrane safety consideration. The resultant nonlinear controller is robust and is proved to be insensitive to parametric uncertainty, maintaining performance around any equilibrium point.

**Acknowledgment** The author thanks Dr. Jingbo Liu and Dr. Bashir for their support and encouragement to finish this review chapter.

## References

1. M. Schultze, J. Horn, Modeling, state estimation and nonlinear model predictive control of cathode exhaust gas mass flow for PEM fuel cells. *Control. Eng. Pract.* **49**, 76–86 (2016)
2. R.T. Meyer, B. Yao, Modeling and simulation of a modern PEM fuel cell system, in *ASME 2006 4th International Conference on Fuel Cell Science, Engineering and Technology* (American Society of Mechanical Engineers, 2006), pp. 133–150
3. A.Y. Karnik, J. Sun, A.G. Stefanopoulou, J.H. Buckland, Humidity and pressure regulation in a PEM fuel cell using a gain-scheduled static feedback controller. *IEEE Trans. Control Syst Technol* **17**(2), 283–297 (2009)
4. Peraza, C., Diaz, J. G., Arteaga-Bravo, F. J., Villanueva, C., Francisco Gonzalez-Longatt, F., Modeling and simulation of PEM fuel cell with bond graph and 20sim, in *American Control Conference* (2008), pp. 5104–5108
5. R. Urbanczyk, S. Peil, D. Bathen, C. Heßke, J. Burfeind, K. Hauschild, M. Felderhoff, F. Schüth, HT-PEM fuel cell system with integrated complex metal hydride storage tank. *Fuel Cells* **11**(6), 911–920 (2011)
6. Y.B. Kim, Study on the effect of humidity and stoichiometry on the water saturation of PEM fuel cells. *Int. J. Energy Res.* **36**, 509–522 (2012)
7. Z. Shi, X. Wang (2008). Two-dimensional PEM fuel cells modeling using COMSOL Multiphysics, in *Modelling and Simulation*, ed. by G. Petrone, G. Cammarata, pp. 677–688. Retrieved from: [http://www.intechopen.com/books/modelling\\_and\\_simulation/twodimensional\\_pem\\_fuel\\_cells\\_modeling\\_using\\_comsol\\_multiphysics](http://www.intechopen.com/books/modelling_and_simulation/twodimensional_pem_fuel_cells_modeling_using_comsol_multiphysics)
8. E. Robalinho, Z. Ahmed, E. Cekinski, M. Linardi, Advances in PEM fuel cells with CFD techniques, in *Proceedings of the 5th International Workshop on Hydrogen and Fuel Cells* (2010)
9. C. Siegel, G. Bandlamudi, A. Heinzl, Systematic characterization of a PBI/H 3 PO 4 sol-gel membrane-modeling and simulation. *J. Power Sources* **196**(5), 2735–2749 (2011)
10. T. Sousa, M. Mamlouk, K. Scott, An isothermal model of a laboratory intermediate temperature fuel cell using PBI doped phosphoric acid membranes. *Chem. Eng. Sci.* **65**(8), 2513–2530 (2010)
11. K. Klinedinst, J.A.S. Bett, J. Macdonald, P. Stonehart, Oxygen solubility and diffusivity in hot concentrated H<sub>3</sub>PO<sub>4</sub>. *J. Electroanal. Chem. Interfacial Electrochem.* **57**(3), 281–289 (1974)

12. A.A. Kulikovskiy, H.F. Oetjen, C. Wannek, A simple and accurate method for high-temperature PEM fuel cell characterization. *Fuel Cells* **10**(3), 363–368 (2010)
13. N. Zamel, X. Li, Non-isothermal multi-phase modeling of PEM fuel cell cathode. *Int. J. Energy Res.* **34**, 568–584 (2010)
14. E.L. Cussler, *Diffusion-Mass Transfer in Fluid Systems* (Cambridge University Press, London, 1969)
15. T. Henriques, B. César, P.C. Branco, Increasing the efficiency of a portable PEM fuel cell by altering the cathode channel geometry: a numerical and experimental study. *Appl. Energy* **87**(4), 1400–1409 (2010)
16. H. Wu, X. Li, P. Berg, Numerical analysis of dynamic processes in fully humidified PEM fuel cells. *Int. J. Hydrog. Energy* **32**(12), 2022–2031 (2007)
17. I. Matraji, S. Laghrouche, M. Wack, Pressure control in a PEM fuel cell via second order sliding mode. *Int. J. Hydrog. Energy* **37**(21), 16104–16116 (2012)
18. Z. Shi, X. Wang, Comparison of Darcy’s law, the Brinkman equation, the modified NS equation and the pure diffusion equation in PEM fuel cell modeling, in *COMSOL Conference*, (2007)
19. N. Zamel, X. Li, A parametric study of multi-phase and multi-species transport in the cathode of PEM fuel cells. *Int. J. Energy Res.* **32**, 698–721 (2008)
20. R.K. Shah, A.L. London, *Laminar Flow Forced Convection in Ducts* (Academic, New York, 1978)
21. P.C. Chen, The dynamics analysis and controller design for the PEM fuel cell under gas flow rate constraints. *Int. J. Hydrog. Energy* **36**, 3110–3122 (2011)
22. P.C. Chen, Output-feedback voltage tracking control for input-constrained PEM fuel cell systems. *Int. J. Hydrog. Energy* **36**(22), 14608–14621 (2011)
23. J. Liu, W. Lin, F. Alsaadi, T. Hayat, Nonlinear observer design for PEM fuel cell power systems via second order sliding mode technique. *Neurocomputing* **168**, 145–151 (2015)
24. A.J. Real, A. Arce, C. Bordons, Development and experimental validation of a PEM fuel cell dynamic model. *J. Power Sources* **173**, 310–324 (2007)
25. D. Li, C. Li, Z. Gao, Q. Jin, On active disturbance rejection in temperature regulation of the proton exchange membrane fuel cells. *J. Power Sources* **283**, 452–463 (2015)
26. I.S. Hussaini, C.Y. Wang, Dynamic water management of polymer electrolyte membrane fuel cells using intermittent RH control. *J. Power Sources* **195**(12), 3822–3829 (2010)
27. M. Coppo, N.P. Siegel, M.R. Spakovskiy, On the influence of temperature on PEM fuel cell operation. *J. Power Sources* **159**(1), 560–569 (2006)
28. M. Cai, M.S. Ruthkosky, B. Merzougui, S. Swathirajan, M.P. Balogh, S.H. Oh, Investigation of thermal and electrochemical degradation of fuel cell catalysts. *J. Power Sources* **160**(2), 977–986 (2006)
29. Z. Lua, S.G. Kandlikara, C. Ratha, M. Grimmer, W. Domigana, A.D. Whitea, M. Hardbargera, J.P. Owejanb, T.A. Traboldb, Water management studies in PEM fuel cells, part II: Ex situ investigation of flow maldistribution, pressure drop and two-phase flow pattern in gas channels. *Int. J. Hydrog. Energy* **34**, 3445–3456 (2009)
30. P. Concus, R. Finn, On the behavior of a capillary surface in a wedge. *Appl. Math. Sci.* **63**, 292–299 (1969)
31. R.W. Lockhart, R.C. Martinelli, Proposed correlation of data for isothermal two-phase, two-component flow in pipes. *Chem. Eng. Prog.* **45**, 39–48 (1949)
32. C. Lee, W. Mérida, Gas diffusion layer durability under steady-state and freezing conditions. *J. Power Sources* **164**, 141–153 (2007)
33. W.K. Lee, C.H. Ho, J.W.V. Zee, M. Murthy, The effects of compression and gas diffusion layers on the performance of a PEM fuel cell. *J. Power Sources* **84**, 45–51 (1999)
34. I. Nitta, O. Himanen, M. Mikkola, Thermal conductivity and contact resistance of compressed gas diffusion layer of PEM fuel cell. *Fuel Cells* **8**(2), 111–119 (2008)
35. F. Barbir, *PEM Fuel Cells Theory and Practice* (Academic Press, 2012)
36. V. Gurau, H. Liu, S. Kakac, A two-dimensional model for proton exchange membrane fuel cells. *AIChE J.* **44**(11), 2410–2422 (1998)



# The Application of Computational Thermodynamics to the Cathode-Electrolyte in Solid Oxide Fuel Cells

# 10

Shadi Darvish, Mohammad Asadikiya, Mei Yang, and Yu Zhong

## Contents

10.1	Introduction .....	283
10.1.1	Solid Oxide Fuel Cell .....	283
10.1.2	Cathode .....	284
10.1.3	Electrolyte .....	284
10.1.4	Anode .....	285
10.1.5	Current Status of SOFC Development .....	285

## Author Contribution

Author YZ is in charge of the cathode-electrolyte inter-reaction and the overall SOFC thermodynamic investigations. Author MY was in charge of the  $\text{LaCoO}_3$  perovskite thermodynamic database development. Author SD was in charge of the  $\text{CO}_2$ 's effect to the cathode (LSM and LSCF), the electronic conductivity prediction for LSM, and the thermomechanical property prediction for LSM. Author MA was in charge of the ionic conductivity prediction for YSZ and the phase diagram development for the nano  $n$ -YSZ particles. The authors further acknowledge that there is no financial relationship with the editors or publisher and have contributed original work in this chapter, other than what acknowledged or appropriately cited with copyright permission. The authors compiled this chapter based on their previous publications, " $\text{La}_{0.6}\text{Sr}_{0.4}\text{Co}_{0.2}\text{Fe}_{0.8}\text{O}_{3 \pm \delta}$ - $\text{CO}_2$ - $\text{O}_2$  system for application in solid oxide fuel cells," *Journal of Power Sources*; "Phase diagram for a nano-yttria-stabilized zirconia system," *RSC Advances*; "Weight loss mechanism of  $(\text{La}_{0.8}\text{Sr}_{0.2})_{0.98}\text{MnO}_{3 \pm \delta}$  during thermal cycles," *Ceramic Engineering*; and "Quantitative defect chemistry analysis and electronic conductivity prediction of  $\text{La}_{0.8}\text{Sr}_{0.2}\text{MnO}_{3 \pm \delta}$  perovskite," *Journal of the Electrochemical Society*. Information was also adapted from "Defect analysis and thermodynamic modeling of  $\text{LaCoO}_{3 - \delta}$ ," *Solid State Ionics*.

S. Darvish · M. Asadikiya

Department of Mechanical and Materials Engineering, Florida International University, Miami, FL, USA

Center for the Study of Matter at Extreme Conditions (CeSMEC), Florida International University, Miami, FL, USA

10.2	Previous Efforts on Improvement of Cathode-Electrolyte Properties .....	286
10.2.1	Electrical Conductivity of LSM .....	286
10.2.2	Gas Species Impact on Cathode .....	289
10.2.3	Phase Stability at Cathode-Electrolyte Interface .....	290
10.2.4	Thermomechanical Properties of Perovskites .....	291
10.2.5	The YSZ Electrolyte .....	292
10.3	Background of Computational Thermodynamics and Modeling .....	293
10.3.1	The CALPHAD Approach .....	293
10.3.2	Gibbs Energy Description for Individual Phases .....	293
10.3.3	Thermodynamic Database Development for Perovskites .....	295
10.3.4	Thermodynamic Database for Bulk YSZ .....	302
10.3.5	Phase Diagram for YSZ Nanoparticles .....	304
10.3.6	Database Development for Perovskite-Fluorite Reactions .....	306
10.4	Recent SOFC-Related Results from the CALPHAD Approach .....	306
10.4.1	Defect Chemistry and Quantitative Brouwer Diagram .....	306
10.4.2	Electrical Conductivities .....	306
10.4.3	Cathode-Electrolyte Triple Phase Boundary Stabilities .....	312
10.4.4	Thermomechanical Properties of Perovskites .....	314
10.4.5	Stability of the Perovskite in Atmosphere Containing CO <sub>2</sub> .....	317
10.4.6	Phase Diagrams for Nanoparticles .....	325
10.5	Summary .....	329
	References .....	330

## Abstract

The fundamentals of solid oxide fuel cell (SOFC) and computational thermodynamics, using the CALPHAD (CALculation of PHase Diagrams) approach, are reviewed in this chapter. The thermodynamic database development for perovskites and fluorites is especially discussed. In addition, the application of computational thermodynamics to the cathode and electrolyte of SOFC is also discussed in detail including the defect chemistry and quantitative Brouwer diagrams, electronic and ionic conductivity, cathode-electrolyte triple phase boundary (TPB) stability, thermomechanical properties of perovskite cathode, the effect of gas impurities like CO<sub>2</sub> to the phase stability of cathode, and phase diagram development for nano (*n*-)yttria-stabilized zirconia (YSZ) particles.

---

M. Yang  
H.C. Starck Inc., Newton, MA, USA

Y. Zhong (✉)  
Department of Mechanical and Materials Engineering, Florida International University, Miami, FL, USA

Center for the Study of Matter at Extreme Conditions (CeSMEC), Florida International University, Miami, FL, USA

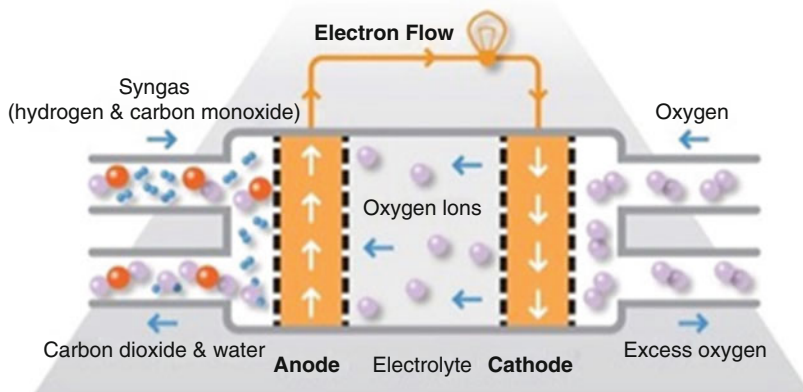
Mechanical Engineering Department, Worcester Polytechnic Institute, Worcester, MA, USA  
e-mail: [yzhong@wpi.edu](mailto:yzhong@wpi.edu)

## 10.1 Introduction

### 10.1.1 Solid Oxide Fuel Cell

A state-of-the-art fuel cell is considered an electrochemical conversion device, which is able to produce electricity directly from oxidizing a fuel. Fuel cells are mainly classified by their electrolyte material. Solid oxide fuel cells (SOFCs) have a solid oxide or ceramic electrolyte to conduct oxygen ions from the cathode side to the anode side. High efficiency, long-term stability, fuel flexibility, low emission, and relatively low cost are all included as advantages of this class of fuel cells. However, besides all these advantages, high operating temperature (500–1000 °C), which results in longer start-up times and mechanical and chemical compatibility issues, is the most significant disadvantage of this device. Figure 10.1 shows a scheme of a SOFC and its parts. A SOFC is mainly made up of three layers of cathode, electrolyte, and anode. There is also a layer of interconnections between them.

A single SOFC, consisting of these three layers stacked together, has dimensions of a few millimeters in thickness and connects hundreds of these cells in a series forming an SOFC stack. The electrical and ionic activation of cell parts occurs when high temperature is reached, and as a consequence, the stacks have to run at temperatures ranging from 500 °C to 1000 °C. The oxygen reduction reaction (ORR) in order to form oxygen ions occurs at the cathode compartment as illustrated in Eq. 10.1. These ions diffuse through the electrolyte to the anode, where they electrochemically oxidize the fuel. In the anode reaction, a water by-product is given off as well as two electrons as shown in Eq. 10.2. These electrons then flow through an external circuit, where they can do useful work. The cycle then repeats as those electrons enter the cathode material again. The SOFCs have a wide variety of applications, such as its use as auxiliary power units in hybrid or electronic vehicles or stationary power generation with outputs from 100 W to 2 MW. The higher operating temperatures make SOFCs suitable candidates for application with heat



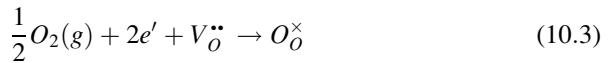
**Fig. 10.1** Solid oxide fuel cell parts and reaction scheme [1]

engine energy recovery devices or combined heat and power, which further increase overall fuel efficiency [2] and Eqs. 10.1 and 10.2:



### 10.1.2 Cathode

The cathode is a thin porous ceramic layer on the electrolyte where oxygen reduction reaction (ORR) takes place. The overall ORR is written in Kroger-Vink notation (Eq. 10.3):



where  $e'$  represents an electron,  $V_O^{\bullet\bullet}$  vacancy of oxygen site with double positive charge, and  $O_O^{\times}$  an oxygen ion sitting on an oxygen lattice site with neutral charge.

Cathode ceramic must be electronically conductive. Currently, lanthanum strontium manganite (LSM) is the choice of cathode material especially for commercial use due to their compatibility with doped zirconia electrolytes. Thermomechanically, LSM has a similar coefficient of thermal expansion (CTE) to yttria-doped zirconia (YSZ) and thus limits stress buildup due to mismatch in the CTE. Additionally, the LSM has low level of chemical reactivity with YSZ electrolyte, which avoids degradation of the cathode and electrolyte materials and extends their lifetime. On the other hand, LSM is considered a poor ionic conductor, and this property results in an electrochemically active reaction which is limited only to the triple phase boundaries (TPBs), where the electrolyte, *air*, and electrode interact. The LSM works well as a cathode at high temperatures (800–1200 °C). However, its performance quickly drops as the operating temperature is lowered below 800 °C. A potential cathode material must be able to conduct both electrons and oxygen ions in order to increase the reaction zone beyond the TPBs. To address these issues, composite cathode composed of LSM-YSZ has been used to increase the reaction length. Mixed ionic and electronic conducting (MIEC) ceramics, such as perovskite lanthanum strontium cobalt ferrite (LSCF), are also being researched for use in intermediate temperature SOFCs as they are more active and can make up for the increase in activation energy of the reaction [3].

### 10.1.3 Electrolyte

Electrolyte in SOFCs is a dense ceramic, which can conduct oxygen anions. The electronic conductivity of electrolyte has to be as low as possible to



prevent energy losses. The high operating temperatures of SOFCs allow the kinetics of oxygen ion transport to ensure good performance. However, as the operating temperature approaches the lower limit for SOFCs, the electrolyte begins to have large ionic transport resistances and affect performance. Popular electrolyte materials are YSZ (often 8 mol% yttria-8YSZ), scandia-stabilized zirconia (ScSZ) (usually 9 mol%  $\text{Sc}_2\text{O}_3$ -9ScSZ), and gadolinium-doped ceria (GDC) [4]. The electrolyte material has a critical influence on the cell performance [5]. Therefore, it is important to select a material for the electrolyte, which does not chemically interact with cathode or anode materials. The current target in the related research areas is to reduce the SOFCs' functional temperature without reducing the ionic conductivity. This can broaden material choices for SOFC, and many existing problems such as degradation of the cell at high temperature can be potentially solved.

### 10.1.4 Anode

The ceramic anode layer must be very porous to allow the fuel to flow toward the electrolyte. Similar to the cathode, the anode must conduct electrons, with ionic conductivity, which is considered a positive attribute. The most common anode material used and commercially utilized is a cermet made up of nickel mixed with the ceramic material that is used for the electrolyte in that particular cell, typically YSZ nanomaterial-based catalysts. The anode is commonly the thickest and strongest layer in each individual cell and is often the layer that provides the mechanical support. One of the functions of the anode allows for the oxygen ions to diffuse through the electrolyte to oxidize the hydrogen fuel. The redox reaction between the oxygen ions and the hydrogen produces heat as well as water and electricity as shown in Eq. 10.2 [3].

### 10.1.5 Current Status of SOFC Development

All the research efforts are going now in the direction of lower-temperature SOFCs (600 °C). Low-temperature systems can reduce the overall costs by reducing insulation, material design, start-up time, and degradation-related costs. Higher operating temperatures result in temperature gradient increase and the severity of thermal stresses [2]. Another possibility for intermediate temperature (650–800 °C) systems is the use of cheaper metallic materials with better mechanical properties and thermal conductivity.

There are a lot of fundamental works, which have been undertaken on the cathode improvement in order to accelerate the ORR and increase the total efficiency of the cell. This extensive research on defect chemistries of the cathode, electrolyte, and anode has been carried out for almost a century as it is closely linked with the thermodynamic equilibria, thermomechanical properties, electrical conductivity, electromechanical properties, superconductivity, catalytic activity, and

thermoelectric properties in metal oxides [6]. Even though those efforts were proven successful for certain binary and ternary compounds [7], there is still lack of approach to effectively understand the accurate defect chemistry, especially for multicomponent metal oxides [8, 9].

The other issue on the cathode side, which is widely being studied, is formation of new secondary phases on the surface (solid-gas interface) and at the TPBs due to the chemical reactivity of the cathode constituents with the gas species in the *air*, such as CO<sub>2</sub>. The CO<sub>2</sub> is considered the main gas-phase impurity on the cathodic side in SOFCs. Any leakage of exhaust gas from the anode side as a result of anode reaction, which may contain up to 30 vol.% CO<sub>2</sub>, can lead to exposing the cell components, especially the cathode, to high concentrations of CO<sub>2</sub> [10, 11]. The cathode degradation, due to the formation of unwanted secondary phases as a result of reactions among cathode, electrolyte, and certain gas-phase species, would impact the long-term stability of the device and lower its efficiency. Studies have shown that the formation of Sr-containing phases, especially below the operating temperatures, is the main reason for lowering the electronic conductivity and blocking oxygen-transferring path for ORR [12–14].

Most commonly, solid electrolyte materials which are used in SOFCs are YSZ, doped ceria (e.g., gadolinium-doped, GDC, and samaria-doped ceria, SDC), stabilized Bi<sub>2</sub>O<sub>3</sub>, and strontium/magnesium-doped lanthanum gallate (SMLG). A typical SOFC has an electrolyte with YSZ; since YSZ-based SOFCs are required to operate at high temperature of 800–1000 °C, researches are underway to replace YSZ with another material, which can operate at lower temperatures, with at least the same efficiency as YSZ [15]. In the following section, the most prominent experimental and simulation efforts to address the SOFCs' current issues have been summarized.

---

## 10.2 Previous Efforts on Improvement of Cathode-Electrolyte Properties

As it was discussed previously, the electrical conductivity, thermomechanical properties, and phase stability of cathode-electrolyte are considered the main issues of current SOFCs that need to be solved for their efficiency enhancement. In this regard, outcomes from the different research groups have been reviewed, and limitations of these works have been discussed.

### 10.2.1 Electrical Conductivity of LSM

The dominant conduction mechanism, which is widely used for perovskite, is shown in Eq. 10.4:

$$\sigma_{tot} = \sigma_{ion} + \sigma_e + \sigma_h \quad (10.4)$$

where  $\sigma_{tot}$ ,  $\sigma_{ion}$ ,  $\sigma_e$ , and  $\sigma_h$  illustrate the total electrical conductivity, ionic conductivity, and the electronic conductivities due to electrons and electron-holes, respectively. In LSM,  $\sigma_{ion}$  is extremely low, and the dominant electronic conductivity is determined by the electron-hole mechanism, i.e.,  $\sigma_e$  can be neglected [16–18].

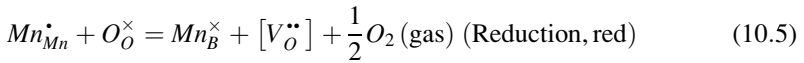
Several different conduction mechanisms have been proposed for LSM from various groups [16–20]. They all agreed that conductivity is closely related to the defect chemistry inside LSM. The  $\sigma_{ion}$  is proportional to the  $[V_O^{\bullet\bullet}]$ , while  $\sigma_e$  and  $\sigma_h$  are proportional to  $[Mn'_{Mn}]$  ( $'$ , single negative charge) and  $[Mn^{\bullet}_{Mn}]$  ( $\bullet$ , single positive charge) due to the electron jump between  $Mn^{2+}$  and  $Mn^{3+}$  states as well as  $Mn^{4+}$  and  $Mn^{3+}$  states, respectively. It was also reached an agreement that the concentration of  $Mn^{2+}$  should be much less than that of  $Mn^{4+}$  [16–18]. However, the quantitative concentration of critical species, such as  $Mn^{2+}$ ,  $Mn^{3+}$ , and  $Mn^{4+}$ , is still not clear.

The Brouwer diagram developed in 1954 [21] is still considered as the most classical method for quickly capturing the involved defect chemistries. In previous approaches, the defect equilibria in the Brouwer diagrams were divided into several regimes; in each regime, only the dominant equilibria are considered, which show the trends of point-defect concentrations, but the quantitative relationships between species concentrations with various parameters are not typically available. In order to address this issue, some critical assumptions were considered to calculate the species concentrations quantitatively [16–18]. There were mainly two different models, which are summarized as the random-defect model and the cluster-defect model. Both of these models assume various species inside, contributing to the defects. In the cluster-defect model, it was assumed that certain clusters may form due to the strong local species interactions. In the cluster-defect model proposed by Van Roosmalen and Cordfunke [22], charge disproportionation was also considered. However, it was assumed that the neutral defect cluster is  $\langle Mn'_{Mn} - [V_O^{\bullet\bullet}] - Mn^{\bullet}_{Mn} \rangle$  based on the consideration of the  $MnO_6$  octahedron local structure. In the random-defect model,  $Sr'_{La}$ ,  $Mn^{\bullet}_{Mn}$ , and  $V_O^{\bullet\bullet}$  were initially considered as the main defects [23] based on the previous effort in the modeling of  $LaCrO_3$  [24–26]. It was assumed that the addition of Sr introduced charge imbalance into the system, which was balanced electronically by the formation of  $Mn^{4+}$  from oxidation of  $Mn^{3+}$  ions and ionically forming oxygen vacancies. This model was later improved by considering the critical charge disproportionation reaction, i.e., a pair of  $Mn^{3+}$  ions decomposed into a pair of  $Mn^{2+}$  and  $Mn^{4+}$  ions, proposed by Kuo et al. [27] to interpret the defect chemistry reactions for oxygen nonstoichiometry ( $\delta$ ) modeling, as well as electrical conductivity calculation of  $(La,Sr)MnO_3$ , which was similar to the one proposed for  $La_{1-x}Sr_xFeO_{3-\delta}$  [28].

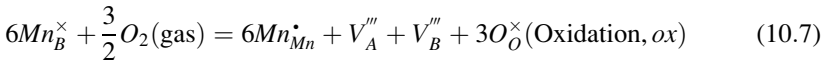
Based on the comparison and also the study of defects of mole fraction for the two models by Yasuda and Hishinuma [23], the cluster-defect model was chosen, as it was assumed that electrons would be trapped in the cluster and not contribute to the electronic conductivity. The only contribution would come from the electron-hole mechanism, which was associated with the free  $Mn^{4+}$  ions. The main argument was the model had better agreement with the thermogravimetric experimental data in comparison with that from the random-defect model. However, the later

comparisons of these two models were carried out in other studies, which proved the random-defect model was able to better reproduce the thermogravimetric data [28]. All of the following researchers preferred the random-defect model to predict defect sides. For example, Nowotny and Rekas [18] assumed the dominant conduction mechanism was from the  $Mn^{4+}$  ions and carefully compared the random-defect model and the cluster-defect model for  $(La,Sr)MnO_{3\pm\delta}$  with experimental data from Kuo et al. [29]. It was concluded that the random-defect model matched better with experimental data [18]. Willy Poulsen [16] and Zhou and Anderson [17] also investigated the defect chemistry to calculate the electrical conductivity of perovskites. Their model is essentially close to Nowotny and Rekas' [18] proposed model, with the assumption  $Mn'_{Mn}$  can be neglected. As a result,  $Mn^{\bullet}_{Mn}$  can be considered as the only charge carrier.

One recent defect chemistry analysis was carried out by Lee and Morgan [30]. The relationships of defect formation enthalpies with defect concentration were obtained from the calculated ab initio defect energies and oxygen non-stoichiometry of  $LaMnO_3$ , which also adopted the random-defect model. It is in general agreed that the dominant defect reactions for LSM based on the random-defect model [16–18, 30] are listed in Eqs. 10.5, 10.6, 10.7, 10.8, 10.9, and 10.10:



$$K_{red} = \frac{[Mn^{\times}_B][V^{\bullet\bullet}_O][P_{O_2}]^{\frac{1}{2}}}{[Mn^{\bullet}_{Mn}][O^{\times}_O]} \quad (10.6)$$



$$K_{ox} = \frac{[Mn^{\bullet}_{Mn}]^6 [V'''_A][V'''_B][O^{\times}_O]^3}{[Mn^{\times}_B]^6 [P_{O_2}]^{\frac{3}{2}}} \quad (''' , \text{triple negative charge}) \quad (10.8)$$



$$K_{ch.disp} = \frac{[Mn'_{Mn}][Mn^{\bullet}_{Mn}]}{[Mn^{\times}_B]^2} \quad (10.10)$$

which is the same as the dominant defect reactions in  $LaMnO_3$ ; the addition of Sr will only change the reaction constants.

However, the above defect chemistry analyses and the proposed conduction models on LSM share the following common problems:

1. They were all developed based on certain assumptions on the concentration relationship of different elements or ions, which might be valid only in certain composition ranges.

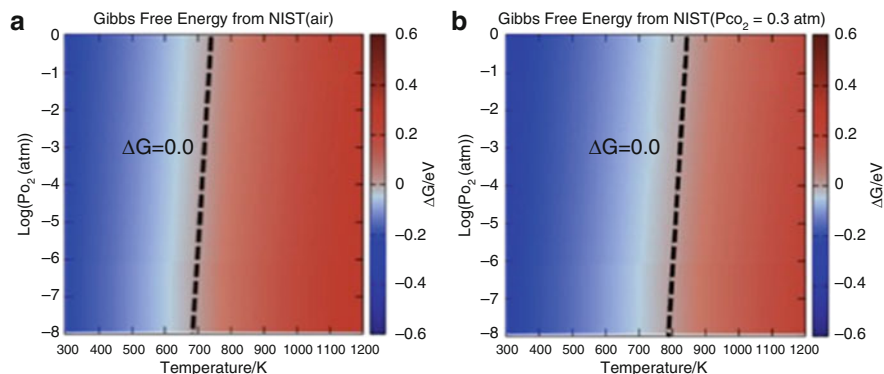
2. Their models did not consider phases other than the LSM perovskite inside the La-Sr-Mn-O system.
3. The Gibbs free energy of LSM perovskite was not considered in their model. Thus, the quantitative concentration of species could be significantly different from the real concentrations.
4. None of the nonstoichiometric compositions, i.e., the composition ratio in *A* site and *B* site away from 1:1, was not considered.

## 10.2.2 Gas Species Impact on Cathode

Despite the potential of the LSM and LSCF as a cathode, chemical instability on the surface (solid-gas interface) and at the triple phase boundaries (TPBs) was reported as a result of impurities, such as CO<sub>2</sub>, in the atmosphere. The formation of SrCO<sub>3</sub> on the surface of LSM has been reported experimentally by Hu et al. [31, 32] as a result of the introduction of CO<sub>2</sub> to the system. In their work, it was claimed that the segregated particles might be SrCO<sub>3</sub> due to the high atomic percentage of Sr, C, and O on the surface according to Auger electron spectroscopy (AES) data. Similar researches have been carried out for La<sub>0.6</sub>Sr<sub>0.4</sub>Co<sub>0.2</sub>Fe<sub>0.8</sub>O<sub>3±δ</sub> (LSCF-6428) by Oh et al. [33], Zhao et al. [34], Yu et al. [10], and Simmer et al. [35]. In Oh et al.'s work [33], it was observed that submicron particles are formed on the surface after heat treatment in the *air*; and a higher area density of secondary phases was formed with increasing temperature. Some unidentified Sr-O compounds were reported with the observed increase of Sr peak intensity and the decrease of La, Co, and Fe peak intensities. However, the exact phase and composition of these particles were not clearly reported. In addition, it was observed that no secondary phases were formed on the surface of the samples, which were heat treated in an N<sub>2</sub> atmosphere containing 0.1 vol.% O<sub>2</sub>, even at higher temperatures.

In another study by Zhao et al., pressed LSCF-6428 powders were sintered at 1350 °C for 5 h in the *air* [34]. These samples were heat treated at 800 °C in the *air* for 96 h. The formation of micron-sized particles on the grain boundaries and submicron particles on the grain surface of heat-treated samples was observed. The EDS mapping revealed that submicron particles are Co-rich (corresponded with Co<sub>3</sub>O<sub>4</sub>), while the fine particles are Sr-rich. Due to the majority of segregated particles on the grain boundaries (Co-rich), it was suggested that migration and segregation of Co species are more favorable as compared to Sr-rich segregated particles. Such observation was also mentioned in several other works [36, 37].

In Yu et al.'s work [10], LSCF-6428 thin films deposited by pulsed laser deposition (PLD) were exposed to two different atmospheres containing 30% CO<sub>2</sub>-21% O<sub>2</sub>-49% N<sub>2</sub> (referred to as high CO<sub>2</sub> atmosphere) and 21% O<sub>2</sub>-79% N<sub>2</sub> (referred to as CO<sub>2</sub>-free atmosphere). It is worth noting that ~400 ppm CO<sub>2</sub> existed in their "CO<sub>2</sub>-free atmosphere." Real-time total reflection X-ray fluorescence (TXRF) spectroscopy results showed Sr segregation on the surface of LSCF during annealing in both high CO<sub>2</sub> and CO<sub>2</sub>-free atmospheres. The results obtained from ex situ hard X-ray photoelectron



**Fig. 10.2** Calculated phase diagram plotted as  $\log(P_{O_2})$  versus temperature, where  $\delta = 0$  and (a)  $P_{CO_2} = 360$  ppm, (b)  $P_{CO_2} = 0.3$  atm [10]

spectroscopy (HAXPES) were fitted, and the formation of the surface oxide and carbonate was reported, which corresponded with SrO and SrCO<sub>3</sub>. Additionally, it was reported that the precipitates formed in the high CO<sub>2</sub> atmosphere are significantly larger than those in the CO<sub>2</sub>-free atmosphere. Two different mechanisms were proposed: (1) two-step mechanism, i.e., Sr reacts with O to form SrO, and then SrCO<sub>3</sub> forms as a result of the reaction between SrO and CO<sub>2</sub>, and (2) one-step mechanism, i.e., LSCF reacts with CO<sub>2</sub>, directly, to form SrCO<sub>3</sub>. These mechanisms were analyzed using density functional theory (DFT) to calculate the Gibbs free energy changes as a function of  $P_{CO_2}$  and temperature for La<sub>0.75</sub>Sr<sub>0.25</sub>Co<sub>0.25</sub>Fe<sub>0.75</sub>O<sub>3</sub> at fixed oxygen vacancy concentrations to obtain stability diagrams. These stability diagrams provided SrCO<sub>3</sub> stability thresholds that can be discerned from the computed  $\Delta G$  values as shown in Fig. 10.2. Increasing  $P_{CO_2}$  and decreasing temperature result in the formation of more SrCO<sub>3</sub>. Overall, it was predicted that the secondary phase formed on the surface of heat-treated sample in 30 vol.% CO<sub>2</sub>, which was claimed as SrCO<sub>3</sub>, acted as a diffusion barrier and enhanced the segregation kinetics. Similar phenomenon was claimed in the follow-up article [38].

In Simmer's work [35], the LSCF-6428 cathode was screen printed on an anode-supported YSZ electrolyte and sintered at 1050 °C for 2 h. The atmosphere containing 48.5% H<sub>2</sub>-48.5% N<sub>2</sub>-3% H<sub>2</sub>O was flowed to the anode and *air* to the cathode. Electrochemical impedance spectroscopy (EIS) revealed a decline in the cell performance, while X-ray photoelectron spectroscopy (XPS) data revealed Sr segregation from the cathode. Field-assisted kinetic demixing was suggested as a possible mechanism for the Sr segregation, which led to cell degradation.

### 10.2.3 Phase Stability at Cathode-Electrolyte Interface

It has been reported that two zirconated phases, i.e., La<sub>2</sub>Zr<sub>2</sub>O<sub>7</sub> (LZO) and SrZrO<sub>3</sub> (SZO), would be formed at the TPB under different conditions, and their formation is influenced by different factors like the stoichiometry of LSM and YSZ, the

LSM/YSZ ratio, the microstructure of the interface, and the temperature [39–44]. The electrical conductivity of these two zirconated phases is of several magnitudes lower than those of LSM and YSZ [45–47], both zirconate phases formed at the interface lead to an increase in both the resistance and the overpotential of the LSM cathode. Even inclusion of very low amounts of zirconate will greatly damage the performance of the whole cell. Understanding the factors influencing the zirconate formation is obviously advantageous not only to improve the initial performance of SOFCs but also to reduce the long-term degradation of SOFCs operated at intermediate temperatures (800–900 °C).

### 10.2.4 Thermomechanical Properties of Perovskites

Thermomechanical property of alkaline earth (AE) metal-doped lanthanum manganite  $\text{La}_{1-x}\text{AE}_x\text{MnO}_{3+\delta}$  (LMO) is one of the most important reasons to be considered as the promising materials to be used as a cathode in solid oxide fuel cell (SOFC) [48]. However, it has been shown that the interface stability may become a problem in the long-term application, and the thermomechanical property may be one of the most important failure mechanisms [49].

It is well known that the thermomechanical property and weight loss mechanism of perovskites are linked with each other. A study by Mori [50] showed that sintered  $\text{La}_{1-x}\text{Sr}_x\text{MnO}_{3+\delta}$  perovskites with Sr content of  $x \sim 0\text{--}0.4$  shrink during thermal cycling between 600 and 1100 °C under an oxidizing atmosphere, which generates stress in the SOFC stack. This volume change is attributed to the change in the oxygen vacancy by absorbing and releasing oxygen in high temperatures [51]. In addition to the generated stress in cathode under current load, cation vacancies in LSM could also cause the diffusion of cations from the interface to an outside environment. Due to an increase in the number of TPBs, this phenomenon might look helpful at first, but its continuation increases the interface resistance and deteriorates adhesion at the interface. Mori et al. [50] have also reported a permanent change in sample dimensions with thermal cycle experiments. The *A* site metal in lanthanum manganite and oxygen create a cubic close packed structure, in which oxygen content is 3 and excessive oxygen is attributed to cation vacancies rather than interstitial oxygen atoms. Mori [52, 53] hypothesized that the release of oxygen at high temperature and formation of vacancies are due to charge compensation. Since ionic radius of  $\text{Mn}^{3+}$  (978.5 pm) and  $\text{Mn}^{2+}$  (81 pm) is larger than  $\text{Mn}^{4+}$  (67 pm), by reducing the  $\text{Mn}^{4+}$  to  $\text{Mn}^{3+}$ , the crystal lattice expands with charge compensation. However, in the case of alkaline earth (AE) metal-doped LMO compound, the structure is more complex at high temperatures. Under oxidizing atmosphere at high temperatures, various perovskite compounds are present in the structure that complicates the behavior of the material in that condition.

Despite the various investigations that show the thermomechanical behavior of LSM at high temperatures, the exact mechanism of this phenomenon has not established yet, and most of the research is focused on suppressing the effect by changing the composition of the compound [54, 55]. It has been shown [56] that



replacing Mn in LSM structure by Mg, Cr, Co, Al, and especially Ni could prevent the thermal cycling shrinkage. Changing the concentration of lanthanum and partially replacing it by another lanthanide could also enhance the volume stability in high-temperature cycles.

## 10.2.5 The YSZ Electrolyte

The yttria-stabilized zirconia (YSZ) is of particular importance due to its critical application. Tetragonal polymorph is applied as an advanced structural ceramic-like tooth crowns and jet engines due to its high toughness [57–59]. Cubic polymorph is capable of conducting oxygen ions due to the high oxygen vacancy concentration, which increases with temperature increase [58]. This special characteristic has made cubic polymorph as a perfect choice for oxygen sensors and electrolyte in SOFCs [60–62].

Pure zirconia ( $\text{ZrO}_2$ ) undergoes a phase transformation from monoclinic, which is stable at room temperature, to tetragonal at about 1000 °C and then to cubic phases at about 2370 °C, with  $\text{ZrO}_2$  melting at about 2690 °C [58, 63]. Obtaining stable sintered zirconia ceramic product is difficult because of the large volume change in the transformation between tetragonal and monoclinic [64]. On the other hand, cubic phase needs to be stable in the wider range of temperature to be applicable in desired applications.

Ruff and Ebert [65] found that stabilizing tetragonal (*t*-) or cubic (*c*-) phases can be achieved by doping, and one of the appropriate dopants for zirconia is yttria ( $\text{Y}_2\text{O}_3$ ). By adjusting the molar percentage of yttria, tetragonal or cubic phases can be stabilized. Therefore, the problem of large volume change in tetragonal to monoclinic transition will be removed since there is no tetragonal to monoclinic transformation anymore. Also, the cubic phase will be stable at lower temperatures and can be applied in various applications. When the tetragonal phase is stable, it is called partially stabilized zirconia (PSZ), and when the cubic phase is stable, it is called fully stabilized zirconia (FSZ). The  $\text{Y}_2\text{O}_3$  makes cubic or tetragonal phases stable by the substitution of some of the  $\text{Zr}^{+4}$  ions (with small ionic radii) with  $\text{Y}^{+3}$  ions (which are larger ionic radii) [66]. This produces oxygen vacancies, as three  $\text{O}^{-2}$  ions replace four  $\text{O}^{-2}$  ions.

Several research groups have tried to evaluate the changes in the transformation temperatures as a function of grain size for the (nano) *n*-YSZ system [57, 58, 67, 68]. The total surface energy is consisting of specific surface energy and surface area. Thus, to define Gibbs energy of the *n*-YSZ system, the specific surface energy has to be measured. According to the capability of microcalorimetry method to measure the specific surface energy of nanoparticles, Drazin and Castro applied water adsorption microcalorimetry theory to measure multiple specific surface energies in the *n*-YSZ system for yttria mole fraction of 0–0.2 (dimensionless unit) at room temperature [69, 70]. The experiments were done for *m*- $\text{ZrO}_2$ , *t*- $\text{ZrO}_2$ , *c*- $\text{ZrO}_2$ , and amorphous phases with the particle size of 32.4–39.8 nm, 14.2–17.7 nm, 4–6.3 nm, and 1–1.1 nm, respectively. The stability range of each crystal structure is determined by the particle size, temperature, and composition [71]. The electrical conductivity of *n*-YSZ can be significantly different in different crystal structures, temperatures, and compositions.



## 10.3 Background of Computational Thermodynamics and Modeling

The CALPHAD (*calculation of phase diagram*) approach models complex phase equilibria in multicomponent systems through computer coupling of phase diagrams and thermochemistry [72, 73]. Its theoretical basis is the thermodynamic description of individual phases. The model used here is with respect to the compound energy formalism [74] based on the CALPHAD approach proposed by Grundy [28]. The compound energy formalism is determined to model the thermodynamic features of phases with more than one sublattice.

### 10.3.1 The CALPHAD Approach

The thermodynamic description of perovskites and fluorites has been developed with the CALPHAD approach through computer coupling of phase diagrams and thermochemistry [72, 73]. Its theoretical basis is thermodynamic modeling of individual phases. This approach was initially introduced by Kaufman [72] to model the complex phase equilibria in multicomponent alloys.

### 10.3.2 Gibbs Energy Description for Individual Phases

#### 10.3.2.1 Pure Elements and Stoichiometric Compounds

For pure elements, the most commonly used model is suggested by the Scientific Group Thermodata Europe (SGTE) [75] and has the following form (Eq. 10.11):

$$G_m - H_m^{SER} = a + bT + cT \ln T + dT^2 + \dots \quad (10.11)$$

The left-hand side of Eq. 10.11 is defined as the Gibbs energy relative to a standard element reference state (SER), where  $H_m^{SER}$  is the enthalpy of the element in its stable state at 298.15 K. Coefficients a, b, c, and d are the model parameters. This model is also preferable for stoichiometric compounds when heat capacity information is available. For those stoichiometric compounds that heat capacity information is not available, Neumann-Kopp's rule is assumed, which is  $\Delta C_p = 0$ . The Gibbs energy of the binary stoichiometric compound  $A_{1-x}B_x$  can be expressed in Eq. 10.12:

$${}^\circ G_m^{A_{1-x}B_x} = (1-x) {}^\circ G_A^\Phi + x {}^\circ G_B^\Phi + a + bT \quad (10.12)$$

where  ${}^\circ G_i^\Phi$  is the molar Gibbs energy of the pure element i with the structure  $\Phi$  from Dinsdale [76].

#### 10.3.2.2 Multicomponent Solution Phases

For multicomponent solution phases, the Gibbs energy is expressed by the following general formula in Eq. 10.13:

$$G_m = {}^\circ G_m + \Delta^{\text{ideal}} G_m + \Delta^{\text{xs}} G_m \quad (10.13)$$

where  ${}^\circ G_m$  is the Gibbs energy of a mechanical mixture of pure components,  $\Delta^{\text{ideal}} G_m$  denotes the contribution from the configurational entropy of mixing, and  $\Delta^{\text{xs}} G_m$  is the excess Gibbs energy due to interactions between the components. Sublattice models have been used to describe solution phases [77, 78]. For example, intermetallic phases in an A-B-binary system can be described by a two-sublattice model, written as (A, B)<sub>an</sub>(A, B)<sub>b</sub>, where subscripts a and b denote the number of sites of each sublattice, respectively. The three terms are expressed in Eqs. 10.14, 10.15, and 10.16:

$${}^\circ G_m = y_A^I y_A^{II} {}^\circ G_{A:A}^\Phi + y_A^I y_B^{II} {}^\circ G_{A:B}^\Phi + y_B^I y_A^{II} {}^\circ G_{B:A}^\Phi + y_B^I y_B^{II} {}^\circ G_{B:B}^\Phi \quad (10.14)$$

$$\Delta^{\text{ideal}} G_m = aRT (y_A^I \ln y_A^I + y_B^I \ln y_B^I) + bRT (y_A^{II} \ln y_A^{II} + y_B^{II} \ln y_B^{II}) \quad (10.15)$$

$$\begin{aligned} \Delta^{\text{xs}} G_m^\Phi = & y_A^I y_B^{II} \left( y_A^{II} \sum_{k=0}^k L_{A,B:A}^\Phi (y_A^I - y_B^I)^k + y_B^{II} \sum_{k=0}^k L_{A,B:B}^\Phi (y_A^I - y_B^I)^k \right) \\ & + y_A^{II} y_B^I \left( y_A^I \sum_{k=0}^k L_{A:A,B}^\Phi (y_A^I - y_B^I)^k + y_B^I \sum_{k=0}^k L_{B:A,B}^\Phi (y_A^I - y_B^I)^k \right) \end{aligned} \quad (10.16)$$

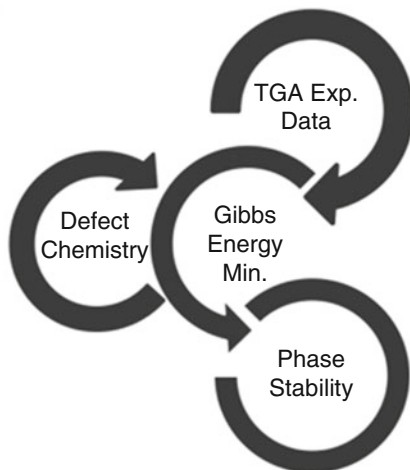
where  $y^I$  and  $y^{II}$  are the site fractions of A and B in the first and second sublattices, respectively. The  ${}^\circ G_{IJ}^\Phi$  is the Gibbs energy of the end-member of  $I_a J_b$ ;  ${}^k L_{A,B}^\Phi$  ( ${}^k L_{*:A,B}^\Phi$ ) are the interaction parameters between component A and B in the first (second) sublattice. In this notation, a colon (:) separates components occupying different sublattices, and a comma (,) separates interacting components in the same sublattice. These equations can be generalized for phases with multicomponents and multisublattices [78], and they reduce to a random substitutional model when there is only one sublattice.

### 10.3.2.3 Ionic Solid Solution Phases

Different from the typical description of solution phases as mentioned above, the ionic solid solutions are described in this work for perovskites and fluorites by the compound energy model (CEM) [78], in which ionic species are assumed to mix independently on a series of separate sublattices.

The description of a solution phase in terms of sublattices defines a volume in composition space in which the phase is contained. The CEM is based on the Gibbs energy of the corner points of this volume, which are regarded as “compounds.” For ionic solutions, some corner points may correspond to charged compounds which are then used purely in a formal way. Only neutral compounds can have a physical meaning. Furthermore, the neutral corner points may represent stable and metastable compounds as well as unstable hypothetical ones. For example, in the ionic solid phase  $(A^{x+}, B^{y+})_a (C^{z-}, Va)_b$ , the four end-members are  $(A^{x+})_a (C^{z-})_b$ ,  $(A^{x+})_a (Va)_b$ ,  $(B^{y+})_a (C^{z-})_b$ , and  $(B^{y+})_a (Va)_b$ , and its Gibbs energy is described in Eq. 10.17:

**Fig. 10.3** Inputs for thermodynamic database development in the CALPHAD approach



$$\begin{aligned}
 G_m^{(A^{x+}, B^{y+})_a(C^{z-}, Va)_b} = & y_{A^{x+}} y_{C^{z-}} {}^0G_{A^{x+};C^{z-}} + y_{A^{x+}} y_{Va} {}^0G_{A^{x+};Va} \\
 & + y_{B^{y+}} y_{C^{z-}} {}^0G_{B^{y+};C^{z-}} + y_{B^{y+}} y_{Va} {}^0G_{B^{y+};Va} \\
 & + RT[a(y_{A^{x+}} \ln y_{A^{x+}} + y_{B^{y+}} \ln y_{B^{y+}}) + b(y_{C^{z-}} \ln y_{C^{z-}} + y_{Va} \ln y_{Va})] \\
 & + {}^{xs}G_m^{(A^{x+}, B^{y+})_a(C^{z-}, Va)_b}
 \end{aligned}
 \tag{10.17}$$

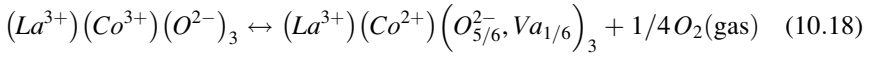
### 10.3.3 Thermodynamic Database Development for Perovskites

The most significant advantage of the CALPHAD approach is that all the possible defect reactions have been already considered by the modeling choice, which was initiated by Grundy for  $\text{LaMnO}_3$  perovskite [79], which is different from alloys. The successful thermodynamic database development for perovskites relies on three important inputs as shown in Fig. 10.3: first, the experimental data on phase equilibria; second, the experimental data with the TGA test; and third, analysis of the dominant defect reactions. With the Gibbs energy description of the perovskites by using the ionic model, it was proven that only the thermodynamic model, which correctly captured the defect chemistry involved in perovskites, was able to fit the experimental data, as shown in similar works such as those described for La-Co-O [80], La-Ca-Fe-O [81], La-Sr-Co-O [82–84], and La-Sr-Cr-Mn-O [85] systems. In the following subsections, the details of how the thermodynamic database was constructed will be elaborated by using the example of  $\text{LaCoO}_{3-\delta}$ .

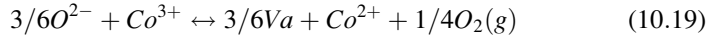
#### 10.3.3.1 Defect Analysis

Defect analysis was carried out to study appropriate thermodynamic models for  $\text{LaCoO}_{3-\delta}$ . Conventionally,  $\text{Co}^{2+}$  and  $\text{Co}^{3+}$  were assumed in  $\text{LaCoO}_{3-\delta}$ , to take into account the oxygen deficiency, and a simple three sublattice model,  $(\text{La}^{3+})_1(\text{Co}^{2+}$ ,

$(\text{Co}^{3+})_1(\text{O}^{2-}, \text{Va})_3$ , was initially used to describe  $\text{LaCoO}_{3-\delta}$  with Va representing vacancies. The reaction of charge transfer is described in Eq. 10.18:



Casting the Kroger-Vink notation [86] to the current sublattice model, the defect reaction can be written as described in Eq. 10.19:



The equilibrium constant of this reaction in terms of compositions is described in Eq. 10.20:

$$K_2 = \frac{[\text{Va}]^{1/2} [\text{Co}^{2+}] P_{\text{O}_2}^{1/4}}{[\text{O}^{2-}]^{1/2} [\text{Co}^{3+}]} \quad (10.20)$$

where  $P_{\text{O}_2}^{1/4}$  is the oxygen partial pressure. For small defect concentrations,  $[\text{O}^{2-}]^{1/2} [\text{Co}^{3+}]$  is approximately equal to 1.  $[\text{Co}^{2+}] = 1/2[\text{Va}]$  can be obtained from Eq. 10.18 for electroneutrality. Therefore, the relationship can be expressed as that described in Eq. 10.21:

$$P_{\text{O}_2}^{-1/4} \propto [\text{Va}]^{3/2} \quad \text{i.e.} \quad \log[\text{Va}] \propto -\frac{1}{6} \log P_{\text{O}_2} \quad (10.21)$$

That means when  $\log[\text{Va}]$  is plotted as a function of  $\log P_{\text{O}_2}$ , the slope would be about  $-1/6$ . However, the slopes from experimental data are close to  $-1/2$  as shown in Fig. 10.4. Therefore,  $(\text{La}^{3+})_1(\text{Co}^{2+}, \text{Co}^{3+})_1(\text{O}^{2-}, \text{Va})_3$  is not a proper model to describe the oxygen defects of  $\text{LaCoO}_{3-\delta}$ .

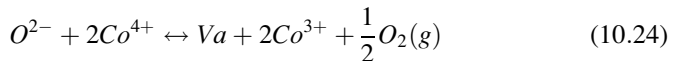
The charge disproportionation defect reaction can be expressed as the following Eq. 10.22:



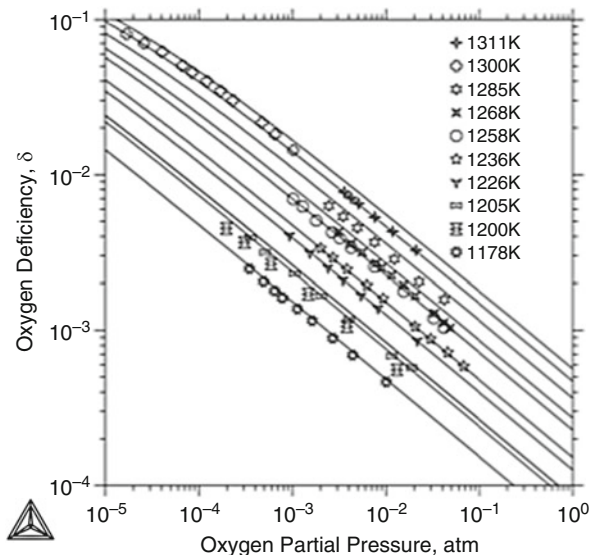
The equilibrium constant of this reaction is described in Eq. 10.23:

$$K_5 = \frac{[\text{Co}^{2+}][\text{Co}^{4+}]}{[\text{Co}^{3+}]^2} \quad (10.23)$$

The oxygen deficiency can be generated when  $\text{Co}^{4+}$  transfers into  $\text{Co}^{3+}$  or  $\text{Co}^{3+}$  transfers into  $\text{Co}^{2+}$ , which would give similar results. The former can be expressed as described in Eq. 10.24:



**Fig. 10.4** The oxygen deficiency of  $\text{LaCoO}_{3-\delta}$  as a function of oxygen partial pressure compared with the experimental data by Seppanen et al. [87] at different temperatures. The deviation of calculated  $\log(\text{PO}_2)$  relative to experimental data is 4.0% [80]



Its equilibrium constant is described in Eq. 10.25:

$$K_7 = \frac{[\text{Co}^{3+}]^2 [\text{Va}] P_{\text{O}_2}^{1/2}}{[\text{Co}^{4+}]^2 [\text{O}^{2-}]} \quad (10.25)$$

At low oxygen deficiencies, the charge disproportionation reaction is dominant, and  $[\text{Co}^{2+}] = [\text{Co}^{4+}]$  can be assumed from Eq. 10.22, and then Eq. 10.26 is derived:

$$K_5 \cdot K_7 = [\text{Va}] P_{\text{O}_2}^{1/2} \quad (10.26)$$

which gives Eq. 10.27:

$$\log[\text{Va}] \propto -1/2 \log P_{\text{O}_2} \quad (10.27)$$

This slope is in agreement with the experimental data in the literature shown in Fig. 10.4 as mentioned above.

### 10.3.3.2 Perovskite Gibbs Energy Construction

Based on the above discussions,  $\text{LaCoO}_{3-\delta}$  was modeled using the compound-energy model [88] to describe the mixing of ions and vacancies on the three sublattices,  $(\text{La}^{3+}, \text{Va})_1(\text{Co}^{2+}, \text{Co}^{3+}, \text{Co}^{4+}, \text{Va})_1(\text{O}^{2-}, \text{Va})_3$ , where Va stands for the vacancy.

The Gibbs energy of this phase is represented by the weighted sum of 16 end-members plus the entropy of mixing in each sublattice and the excess Gibbs energy as shown in Eq. 10.28:

$$\begin{aligned}
 G_m^{LaCoO_{3-\delta}} = & y_{La^{3+}}y_{Co^{2+}}y_{O^{2-}} \circ G_{La^{3+}:Co^{2+}:O^{2-}} \\
 & + y_{La^{3+}}y_{Co^{3+}}y_{O^{2-}} \circ G_{La^{3+}:Co^{3+}:O^{2-}} + y_{La^{3+}}y_{Co^{4+}}y_{O^{2-}} \circ G_{La^{3+}:Co^{4+}:O^{2-}} \\
 & + y_{La^{3+}}y_{Co^{2+}}y_{Va}^{III} \circ G_{La^{3+}:Co^{2+}:Va} + y_{La^{3+}}y_{Co^{3+}}y_{Va}^{III} \circ G_{La^{3+}:Co^{3+}:Va} \\
 & + y_{La^{3+}}y_{Co^{4+}}y_{Va}^{III} \circ G_{La^{3+}:Co^{4+}:Va} + y_{La^{3+}}y_{Va}^{II} \circ G_{La^{3+}:Va:O^{2-}} \\
 & + y_{La^{3+}}y_{Va}^{III} \circ G_{La^{3+}:Va:Va} + y_{Va}^I y_{Co^{2+}}y_{O^{2-}} \circ G_{Va:Co^{2+}:O^{2-}} \\
 & + y_{Va}^I y_{Co^{3+}}y_{O^{2-}} \circ G_{Va:Co^{3+}:O^{2-}} + y_{Va}^I y_{Co^{4+}}y_{O^{2-}} \circ G_{Va:Co^{4+}:O^{2-}} \\
 & + y_{Va}^I y_{Co^{2+}}y_{Va}^{III} \circ G_{Va:Co^{2+}:Va} + y_{Va}^I y_{Co^{3+}}y_{Va}^{III} \circ G_{Va:Co^{3+}:Va} \\
 & + y_{Va}^I y_{Co^{4+}}y_{Va}^{III} \circ G_{Va:Co^{4+}:Va} + y_{Va}^I y_{Va}^{II} \circ G_{Va:Va:O^{2-}} \\
 & + y_{Va}^I y_{Va}^{III} \circ G_{Va:Va:Va} + RT [(y_{La^{3+}} \ln y_{La^{3+}} + y_{Va}^I \ln y_{Va}^I) \\
 & + (y_{Co^{2+}} \ln y_{Co^{2+}} + y_{Co^{3+}} \ln y_{Co^{3+}} + y_{Co^{4+}} \ln y_{Co^{4+}} + y_{Va}^{II} \ln y_{Va}^{II}) \\
 & + 3(y_{O^{2-}} \ln y_{O^{2-}} + y_{Va}^{III} \ln y_{Va}^{III})] + {}^{xs}G_m
 \end{aligned} \tag{10.28}$$

where  $y_i^j$  is the site fraction of  $i$  in the sublattice  $j$ ,  $\circ G_{i;j:k}$  the Gibbs energy of the end-member  $i(j)(k)_3$  with the superscript  $LaCoO_{3-\delta}$  omitted, and  ${}^{xs}G_m$  the excess Gibbs energy due to non-ideal mixing.

Since most end-members are not electroneutral, there are no experimental data available to evaluate their Gibbs energy functions. On the other hand, there are five independent neutral compounds in the system with the first and second sublattices containing only one cation and vacancy, respectively, i.e.,  $(La^{3+})(Co^{3+})(O^{2-})_3$ ,  $(La^{3+})(Co^{2+})(O_{5/6}^{2-}, Va_{1/6})_3$ ,  $(La^{3+})(Co_{3/4}^{4+}, Va_{1/4})(O^{2-})_3$ ,  $(La_{2/3}^{3+}, Va_{1/3})(Co^{4+})(O^{2-})_3$ , and  $(Va)(Va)(Va)_3$ . Their Gibbs energies can be represented in terms of formation energy from La, Co, and  $O_2$  as shown in Eqs. 10.29, 10.30, 10.31, 10.32, and 10.33:

$$\begin{aligned}
 G(La^{3+})(Co^{3+})(O^{2-})_3 = & GL3O = \circ G_{La} + \circ G_{Co} + \frac{3}{2} \circ G_{O_2} \\
 & + \Delta G(La^{3+})(Co^{3+})(O^{2-})_3
 \end{aligned} \tag{10.29}$$

$$\begin{aligned}
 G(La^{3+})(Co^{3+})(O_{5/6}^{2-}, Va_{1/6})_3 = & GL2OV = \circ G_{La} + \circ G_{Co} + \frac{5}{4} \circ G_{O_2} \\
 & + \Delta G(La^{3+})(Co^{3+})(O_{5/6}^{2-}, Va_{1/6})_3
 \end{aligned} \tag{10.30}$$

$$G^{(La^{3+})}(Co_{3/4}^{4+}, Va_{1/4})(O^{2-})_3 = GL4O = {}^\circ G_{La} + \frac{3}{4} {}^\circ G_{Co} + \frac{3}{4} {}^\circ G_{O_2} + \Delta G^{(La^{3+})}(Co_{3/4}^{4+}, Va_{1/4})(O^{2-})_3 \quad (10.31)$$

$$G^{(La_{2/3}^{3+}, Va_{1/3})}(Co^{4+})(O^{2-})_3 = GV4O = \frac{2}{3} {}^\circ G_{La} + {}^\circ G_{Co} + \frac{3}{2} {}^\circ G_{O_2} + \Delta G^{(La_{2/3}^{3+}, Va_{1/3})}(Co^{4+})(O^{2-})_3 \quad (10.32)$$

$$G^{(Va)(Va)(Va)_3} = GVVV = 3 {}^\circ G_{Va} = 0 \quad (10.33)$$

where  $\Delta G_{La}^0$ ,  $\Delta G_{Co}^0$ , and  $\Delta G_{O_2}^0$  are the Gibbs energies of hexagonally close packet (hcp)-La, hcp-Co, and oxygen gas taken from Dinsdale [89] and  $\Delta G$  is the Gibbs energy of formation represented by using  $\Delta H - T\Delta S$ , with  $\Delta H$  and  $\Delta S$  to be evaluated.

Following the same approach described in Ref. [90] and assuming ideal mixing, the above Gibbs energies can be related to the Gibbs energies of corresponding end-members as described in Eqs. 10.34, 10.35, 10.36, 10.37, and 10.38:

$$GL3O = {}^\circ G_{La^{3+}:Co^{3+}:O^{2-}} \quad (10.34)$$

$$GL2OV = \frac{5}{6} {}^\circ G_{La^{3+}:Co^{2+}:O^{2-}} + \frac{1}{6} {}^\circ G_{La^{3+}:Co^{2+}:Va} + 3RT \left( \frac{5}{6} \ln \frac{5}{6} + \frac{1}{6} \ln \frac{1}{6} \right) \quad (10.35)$$

$$GLV4O = \frac{2}{3} {}^\circ G_{La^{3+}:Co^{4+}:O^{2-}} + \frac{1}{3} {}^\circ G_{Va:Co^{4+}:O^{2-}} + RT \left( \frac{2}{3} \ln \frac{2}{3} + \frac{1}{3} \ln \frac{1}{3} \right) \quad (10.36)$$

$$GL4VO = \frac{3}{4} {}^\circ G_{La^{3+}:Co^{4+}:O^{2-}} + \frac{1}{4} {}^\circ G_{La^{3+}:Va:O^{2-}} + RT \left( \frac{3}{4} \ln \frac{3}{4} + \frac{1}{4} \ln \frac{1}{4} \right) \quad (10.37)$$

$$GVVV = 3 {}^\circ G_{Va} = 0 \quad (10.38)$$

For other end-members, we assume  ${}^\circ G_{Va:Va:O^{2-}} = GVVV + 3/2 {}^\circ G_{O_2}^{Gas}$  plus the following reciprocal relations [90] described in Eqs. 10.39, 10.40, 10.41, 10.42, 10.43, 10.44, 10.45, 10.46, 10.47, and 10.48:

$$\Delta G_{r1} = {}^\circ G_{La^{3+}:Co^{3+}:O^{2-}} + {}^\circ G_{Va:Co^{3+}:Va} - {}^\circ G_{La^{3+}:Co^{3+}:Va} - {}^\circ G_{Va:Co^{3+}:O^{2-}} \quad (10.39)$$

$$\Delta G_{r2} = {}^\circ G_{La^{3+}:Va:O^{2-}} + {}^\circ G_{Va:Va:Va} - {}^\circ G_{La^{3+}:Va:Va} - {}^\circ G_{Va:Va:O^{2-}} \quad (10.40)$$

$$\Delta G_{r3} = {}^\circ G_{La^{3+}:Co^{2+}:O^{2-}} + {}^\circ G_{Va:Co^{3+}:O^{2-}} - {}^\circ G_{La^{3+}:Co^{3+}:O^{2-}} - {}^\circ G_{Va:Co^{2+}:O^{2-}} \quad (10.41)$$

$$\Delta G_{r4} = {}^\circ G_{La^{3+}:Co^{3+}:O^{2-}} + {}^\circ G_{Va:Co^{4+}:O^{2-}} - {}^\circ G_{La^{3+}:Co^{4+}:O^{2-}} - {}^\circ G_{Va:Co^{3+}:O^{2-}} \quad (10.42)$$

$$\Delta G_{r5} = {}^\circ G_{La^{3+}:Co^{4+}:O^{2-}} + {}^\circ G_{Va:Va:O^{2-}} - {}^\circ G_{La^{3+}:Va:O^{2-}} - {}^\circ G_{Va:Co^{4+}:O^{2-}} \quad (10.43)$$

$$\Delta G_{r6} = {}^\circ G_{La^{3+}:Co^{2+}:Va} + {}^\circ G_{Va:Co^{3+}:Va} - {}^\circ G_{La^{3+}:Co^{3+}:Va} - {}^\circ G_{Va:Co^{3+}:Va} \quad (10.44)$$

$$\Delta G_{r7} = {}^\circ G_{La^{3+}:Co^{3+}:Va} + {}^\circ G_{Va:Co^{4+}:Va} - {}^\circ G_{La^{3+}:Co^{4+}:Va} - {}^\circ G_{Va:Co^{3+}:Va} \quad (10.45)$$

$$\Delta G_{r8} = {}^\circ G_{La^{3+}:Co^{2+}:O^{2-}} + {}^\circ G_{La^{3+}:Co^{3+}:Va} - {}^\circ G_{La^{3+}:Co^{2+}:Va} - {}^\circ G_{La^{3+}:Co^{3+}:O^{2-}} \quad (10.46)$$

$$\Delta G_{r9} = {}^\circ G_{La^{3+}:Co^{3+}:O^{2-}} + {}^\circ G_{La^{3+}:Co^{4+}:Va} - {}^\circ G_{La^{3+}:Co^{3+}:Va} - {}^\circ G_{La^{3+}:Co^{4+}:O^{2-}} \quad (10.47)$$

$$\Delta G_{r10} = {}^\circ G_{Va:Co^{3+}:O^{2-}} + {}^\circ G_{Va:Va:Va} - {}^\circ G_{Va:Co^{3+}:Va} - {}^\circ G_{Va:Va:O^{2-}} \quad (10.48)$$

where  $\Delta G_r$  is the change of Gibbs energy for each reaction representing derivations from ideality. With these 16 equations, the Gibbs energies of 16 end-members can be calculated as shown in Ref. [90]. Since the nonstoichiometry is rather small, all 10  $\Delta G_r$  values are set to 0.

The excess Gibbs energy described in Eq. 10.11,  ${}^{xs}G_m$ , is expressed in terms of Redlich-Kister polynomial [91] shown in Eq. 10.49:

$${}^{xs}G_m = \sum_s \sum_{t \neq s} \sum_i \sum_j y_i^s y_j^t \sum_{p \neq t} \sum_m \sum_{n > m} y_m^p y_n^p \sum_{k=0}^k L(y_m^p - y_n^p)^k \quad (10.49)$$

where  ${}^kL$  is the  $k^{th}$  interaction parameter between  $m$  and  $n$  in sublattice and  $p$  with  $i$  and  $j$  in sublattice  $s$  and  $t$ , respectively, and can be temperature dependent. Due to the lack of data, the only interaction parameters considered are an interaction between  $O^{2-}$  and Va in the third sublattice,  ${}^0L(La^{3+})_1(i)_1(O^{2-}, Va)_3$  with  $i$  being the  $Co^{2+}$ ,  $Co^{3+}$ , and  $Co^{4+}$  in the second sublattice, all of which were assumed to be the same.

### 10.3.3.3 Evaluation of Model Parameters and Discussions

The model parameters of  $LaCoO_{3-\delta}$  to be evaluated include enthalpy and entropy of formation of the five chosen neutral endpoints. The GL3O function, the Gibbs energy of  $(La^{3+})(Co^{3+})(O^{2-})_3$ , is modified from the Gibbs energy of  $LaCoO_3$ ,  $G_m^{LaCoO_3}$ , in the Scientific Group Thermodata Europe *substance* (SSUB) database [75] which represents the compound  $(La^{3+})(Co^{2+}, Co^{3+}, Co^{4+})(O^{2-})_3$  with  $Co^{2+}$ ,  $Co^{3+}$ , and  $Co^{4+}$  in the second sublattice defined in Eq. 10.50:

$$G_m^{LaCoO_3} = y_{Co^{2+}} {}^\circ G_{La^{3+}:Co^{2+}:O^{2-}} + y_{Co^{3+}} {}^\circ G_{La^{3+}:Co^{3+}:O^{2-}} + y_{Co^{4+}} {}^\circ G_{La^{3+}:Co^{4+}:O^{2-}} + RT(y_{Co^{2+}} \ln y_{Co^{2+}} + y_{Co^{3+}} \ln y_{Co^{3+}} + y_{Co^{4+}} \ln y_{Co^{4+}}) + {}^{xs}G_m^{LaCoO_3} \quad (10.50)$$



Assuming the ideal reciprocal relation and using  $y_{Co^{2+}} = y_{Co^{4+}}$ , one obtains the expression defined in Eq. 10.51:

$$G_m^{LaCoO_3} = {}^\circ G_{La^{3+};Co^{3+};O^{2-}} + y_{Co^{2+}} \left[ {}^\circ G_{Va;Co^{2+};Va} + {}^\circ G_{Va;Co^{4+};Va} - 2 {}^\circ G_{Va;Co^{3+};Va} \right] + RT \sum y_i \ln y_i + {}^{xs} G_m^{LaCoO_3} \quad (10.51)$$

The second term on the right-hand side represents the Gibbs energy of reaction  $2Co^{3+} = Co^{2+} + Co^{4+}$ , which can be represented by  $\Delta G = \Delta H - T\Delta S$ . The third term represents the ideal mixing of three Co species in the second sublattice. The fourth term is the excess Gibbs energy of  $Co^{2+}$ ,  $Co^{3+}$ , and  $Co^{4+}$ , which can be expressed as  ${}^{ex}G = {}^{ex}H - T{}^{ex}S$ . As the first order of approximation, Eq. 10.51 can thus be written in the form described by Eq. 10.52:

$$G_m^{LaCoO_3} = {}^\circ G_{La^{3+};Co^{3+};O^{2-}} + A + BT \quad (10.52)$$

The GL3O function is thus modeled as described in Eq. 10.53:

$$GL3O = {}^\circ G_{La^{3+};Co^{3+};O^{2-}} = G_m^{LaCoO_3} + A^{GL3O} + B^{GL3O}T \quad (10.53)$$

The enthalpy and entropy of formation for  $(La^{3+})(Co^{2+})(O_{5/6}^{2-}, Va_{1/6})_3$  are evaluated as model parameters. The calculated oxygen deficiency for the compositions of  $(La_{2/3}^{3+}, Va_{1/3})(Co^{4+})(O^{2-})_3$ ,  $(La^{3+})(Co_{3/4}^{4+}, Va_{1/4})(O^{2-})_3$ , and  $(Va)(Va)(Va)_3$  is significantly different from the observed oxygen deficiency, and their Gibbs energies have limited contributions to the stability of  $LaCoO_{3-\delta}$ . Their enthalpy and entropy of formation are thus assumed to be zero. The Gibbs energies of other phases in the La-Co-O system were taken from the SSUB database [75].

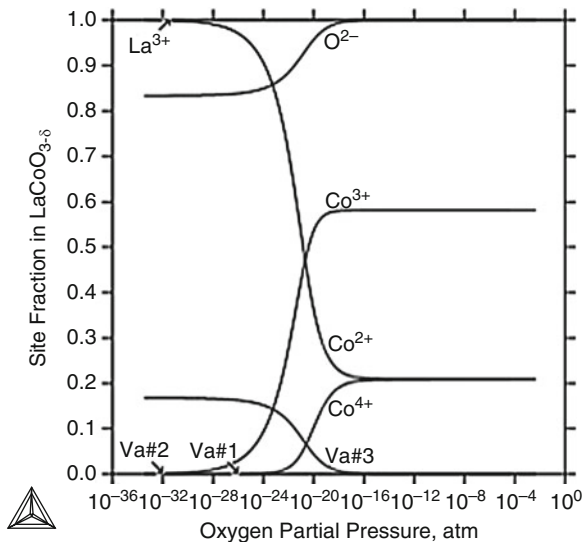
With the Gibbs energy of  $LaCoO_{3-\delta}$ , thus obtained, a wide range of stable and metastable equilibria can be calculated for all ranges of oxygen partial pressures. No cation vacancy can be found in the first and second sublattice under the assumption of ideal mixing. The charge disproportionation,  $2Co^{3+} \leftrightarrow Co^{2+} + Co^{4+}$ , can be seen when  $\log(P_{O_2})$  is high, with  $y_{Ce^{2+}}$  and  $y_{Ce^{4+}}$  around 20%. This charge disproportionation contributes to the good electrical conduction of  $LaCoO_{3-\delta}$ , as  $Co^{4+}$  and  $Co^{2+}$  can be represented by  $Co^{3+} + \bar{e}$  and  $Co^{3+} + h$  with  $\bar{e}$  and  $h$  representing electrons and holes, respectively. With the decrease of the oxygen partial pressure, the contents of  $Co^{4+}$  and  $Co^{3+}$  decrease, and those of  $Co^{2+}$  increase. That means at low oxygen partial pressures, the oxygen vacancy defect reaction  $2O^{2-} + 2Co^{3+} + Co^{4+} \leftrightarrow Va + 3Co^{2+} + 3Co^{2+} + O_2(g)$  becomes dominant.

The site fraction of different species in  $LaCoO_{3-\delta}$  at 1123 K versus oxygen partial pressure is shown in Fig. 10.5.

#### 10.3.3.4 The Merged Perovskite Database

In order to examine the stability of perovskite (LSM and LSCF) in the  $CO_2$ -air atmosphere, the assessed La-Sr-Mn-O and La-Sr-Co-Fe-O databases were merged

**Fig. 10.5** Site fractions calculated for  $\text{LaCoO}_{3-\delta}$  at 1123 K as a function of oxygen partial pressure. The site fractions of  $(\text{Va})_1$  and  $(\text{Va})_2$  are close to 0, and  $\text{La}^{3+}$  is close to 1 in various oxygen partial pressures



separately with the SSUB-5 database [75]. The Gibbs energies of stoichiometric solid phases and the gas phase from SSUB-5 were added to perovskite databases. As a result, the assessed La-Sr-Mn-O-C and La-Sr-Co-Fe-O-C databases are developed with the following major assumptions:

1. Perovskite does not have or only has very limited solubility of C in its lattice.
2. The impact of humidity in the *air* is negligible on the reaction between perovskite and  $\text{CO}_2$ .

It is worth mentioning that the merged databases are able to provide practical predictions under SOFC operating conditions based on the minimization of the Gibbs energy for all the species, phases, and constituents. Therefore, it is able to provide valid guidance on the secondary phase formation in LSM/YSZ/ $\text{CO}_2$  and LSCF/ $\text{CO}_2$  system in different operating conditions.

### 10.3.4 Thermodynamic Database for Bulk YSZ

An assessed thermodynamic database can be applied in various applications [92–96]. The thermodynamic database for the  $\text{ZrO}_2\text{-Y}_2\text{O}_3$  system, developed by Chen et al. [97], was applied to calculate the Gibbs energy of each phase for the bulk YSZ at different temperatures. The Gibbs free energy of bulk materials is defined by Eq. 10.54:

$$\Delta G_{\text{bulk}} = \Delta H + T\Delta S \quad (10.54)$$

in which H is the enthalpy, T is the absolute temperature, and S is the entropy.

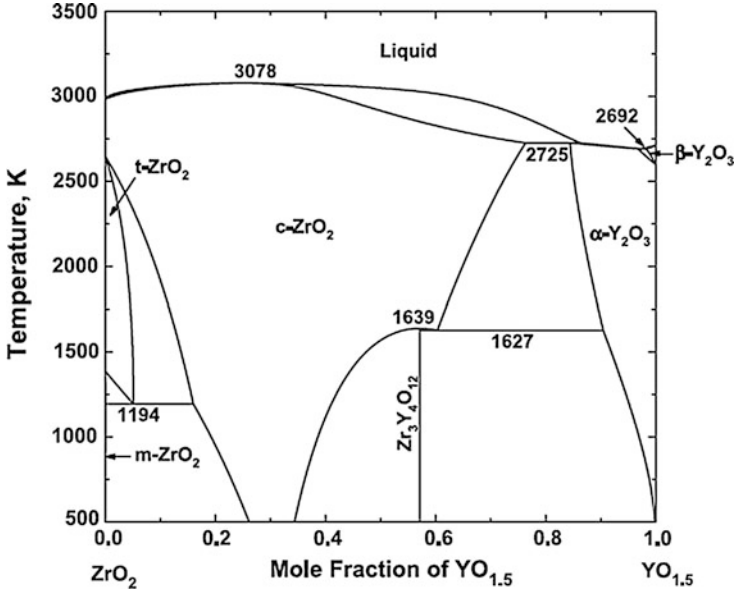


Fig. 10.6 Calculated  $ZrO_2$ - $YO_{1.5}$  phase diagram by Ming Chen et al. (2004) [97]

Figure 10.6 shows the calculated  $ZrO_2$ - $YO_{1.5}$  phase diagram. Each polymorph of YSZ has been clearly labeled in this diagram.

The model to define  $m$ - $ZrO_2$  (monoclinic YSZ phase) and  $t$ - $ZrO_2$  (tetragonal YSZ phase) in the database by Chen et al. is  $(Y^{3+}, Zr^{4+})_1(O^{2-}, Va)_2$  [97]. The first sublattice of this model is occupied by  $Y^{3+}$  and  $Zr^{4+}$  ions, and the second one is occupied by  $O^{2-}$  ion and vacancy. The model used for  $c$ - $ZrO_2$  (cubic YSZ phase) is  $(Y, Y^{3+}, Zr, Zr^{4+})_1(O^{2-}, Va)_2$ . Therefore, the Gibbs energy of the  $m$ - $ZrO_2$  and  $t$ - $ZrO_2$  phases is given by Eq. 10.55:

$$G_m = y_Y^{3+}y_O^{2-}G_{Y^{3+}:O^{2-}} + y_{Zr}^{4+}y_O^{2-}G_{Zr^{4+}:O^{2-}} + y_Y^{3+}y_{Va}G_{Y^{3+}:Va} + y_{Zr}^{4+}y_{Va}G_{Zr^{4+}:Va} + RT[y_Y^{3+}\ln y_Y^{3+} + y_{Zr}^{4+}\ln y_{Zr}^{4+} + 2(y_O^{2-}\ln y_O^{2-} + y_{Va}\ln y_{Va})] + {}^E G_m \quad (10.55)$$

And the Gibbs energy of the  $c$ - $ZrO_2$  phase is given by Eq. 10.56:

$$G'_m = y_Y^{3+}y_O^{2-}G_{Y^{3+}:O^{2-}} + y_{Zr}^{4+}y_O^{2-}G_{Zr^{4+}:O^{2-}} + y_Y^{3+}y_{Va}G_{Y^{3+}:Va} + y_{Zr}^{4+}y_{Va}G_{Zr^{4+}:Va} + y_Y y_O^{2-}G_{Y:O^{2-}} + y_{Zr} y_O^{2-}G_{Zr:O^{2-}} + y_Y y_{Va}G_{Y:Va} + y_{Zr} y_{Va}G_{Zr:Va} + RT[y_Y \ln y_Y + y_Y^{3+} \ln y_Y^{3+} + y_{Zr} \ln y_{Zr} + y_{Zr}^{4+} \ln y_{Zr}^{4+} + 2(y_O^{2-} \ln y_O^{2-} + y_{Va} \ln y_{Va})] + {}^E G'_m \quad (10.56)$$

where  $y_j$  is site fraction of species  $j$  in a particular sublattice. The excess Gibbs energy,  $E_{G_m}$ , is defined by Eq. 10.57:

$$E_{G_m} = y_Y^{3+} y_{Zr}^{4+} y_O^{2-} \sum_{i=0}^n {}^iL_{Y^{3+}, Zr^{4+}:O^{2-}} (y_Y^{3+} - y_{Zr}^{4+})^i + y_Y^{3+} y_{Zr}^{4+} y_{Va} \sum_{i=0}^n {}^iL_{Y^{3+}, Zr^{4+}:Va} (y_Y^{3+} - y_{Zr}^{4+})^i \quad (10.57)$$

And the excess Gibbs energy,  $E_{G'_m}$ , is defined by Eq. 10.58:

$$E_{G'_m} = y_Y^{3+} y_{Zr}^{4+} y_O^{2-} \sum_{i=0}^n {}^iL_{Y^{3+}, Zr^{4+}:O^{2-}} (y_Y^{3+} - y_{Zr}^{4+})^i + y_Y^{3+} y_{Zr}^{4+} y_{Va} \sum_{i=0}^n {}^iL_{Y^{3+}, Zr^{4+}:Va} (y_Y^{3+} - y_{Zr}^{4+})^i + y_{Zr} y_{Zr}^{4+} y_O^{2-} \sum_{i=0}^n {}^iL_{Zr, Zr^{4+}:O^{2-}} (y_{Zr} - y_{Zr}^{4+})^i + y_{Zr} y_{Zr}^{4+} y_{Va} \sum_{i=0}^n {}^iL_{Zr, Zr^{4+}:Va} (y_{Zr} - y_{Zr}^{4+})^i \quad (10.58)$$

where  ${}^iL$  is the interaction parameter with the form of  $A + BT$ . When  $i = 0$ , the solution is regular; if  $i = 1$ , the solution is sub-regular; and when  $i = 2$ , the solution is sub-sub-regular.

The  $m$ -ZrO<sub>2</sub> phase was considered as an ideal solution since yttria concentration in  $m$ -ZrO<sub>2</sub> is extremely low. The  $t$ -ZrO<sub>2</sub> phase was treated as a regular solution, and  $c$ -ZrO<sub>2</sub> was considered as a sub-regular solution in the database by Chen et al. [97].

### 10.3.5 Phase Diagram for YSZ Nanoparticles

In the Gibbs energy of nanoparticles, the surface area plays an effective role. Therefore, the Gibbs energy definition for nanoparticles is as Eq. 10.59:

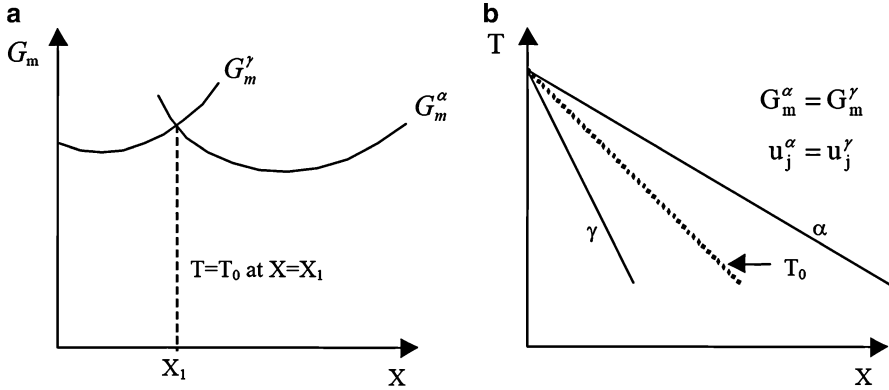
$$\Delta G_{total} = \Delta G_{buk} + \gamma A = \Delta H_{buk} - T \Delta S_{buk} + \gamma A \quad (10.59)$$

in which  $\gamma$  is specific surface energy and  $A$  is surface area of the nanoparticles. The particles were considered spherical to enhance surface area calculations. The specific surface energy of (nano)  $n$ -YSZ polymorphs at room temperature by Drazin and Castro [70] was applied to calculate surface energy.

To determine the phase boundaries of monoclinic, tetragonal, and cubic ZrO<sub>2</sub>, the T-zero temperature method was adopted. In addition, the amorphous phase was modeled by using the ionic liquid description in the  $n$ -YSZ system.

(a) T-zero temperature method to determine phase boundaries:

The  $T_0$  boundary is plotted as a metastable phase boundary, and it is assumed to be a line on which the Gibbs energy of two adjacent phases is equal in a determined composition. The  $T_0$  temperature method is a partial equilibria simulation suggested by Kaufman and Cohen [98], which is applied in the



**Fig. 10.7** T-zero temperature method. (a)  $T_0$  temperature as a point at a defined composition, (b)  $T_0$  temperature as a line when the composition changes [71]

systems like YSZ since the kinetics is very slow in them. In order to capture the  $T_0$  temperature for the monoclinic-tetragonal phase transformation, the starting transition temperature of tetragonal to monoclinic phases during cooling and also the starting transition temperature of monoclinic to tetragonal phases during heating are recorded, and the average of these two temperatures is considered as the  $T_0$  temperature point. The  $T_0$  temperature is located in the two-phase region, and it is a theoretical limit for a diffusionless transformation as illustrated in Fig. 10.7. In this figure,  $u_j$  is defined as the site fraction of element  $j$  with reference to the substitutional sublattices only.

(b) Amorphous phase modeling:

To model an amorphous phase in the CALPHAD approach, one method is to extrapolate the liquid model to lower temperatures as a supercooling liquid. Some minor errors are expected in this simulation since the structure and physical state of a supercooling liquid are different from amorphous phase; however, they are still very similar, and the results are close to reality. In the thermodynamic database by Chen et al., the liquid phase was modeled as  $(Y^{3+}, Zr^{4+})_p(O^{2-})_q$ , in which  $p = 2y_{O^{2-}}$  and  $q = 3y_{Y^{3+}} + 4y_{Zr^{4+}}$  [97]. The Gibbs energy description of liquid is given by Eq. 10.60:

$$G_m^L = y_Y^{3+} y_{O^{2-}} G_{Y^{3+}, O^{2-}}^{L, Y^{3+}} + y_{Zr^{4+}} y_{O^{2-}} G_{Zr^{4+}, O^{2-}}^{L, Zr^{4+}} + pRT [y_Y^{3+} \ln y_Y^{3+} + y_{Zr^{4+}} \ln y_{Zr^{4+}}] + {}^E G_m^L \quad (10.60)$$

The excess Gibbs energy,  ${}^E G_m^L$ , is defined by Eq. 10.61:

$${}^E G_m^L = y_Y^{3+} y_{Zr^{4+}} y_{O^{2-}} \sum_{i=0}^n i L_{Y^{3+}, Zr^{4+}, O^{2-}}^{3+, 4+, 2-} (y_Y^{3+} - y_{Zr^{4+}})^i \quad (10.61)$$

The ionic liquid was considered as sub-sub-regular solution ( $i = 2$ ) in the database by Chen et al. [97].

### 10.3.6 Database Development for Perovskite-Fluorite Reactions

The original La-Mn-O-Y-Zr database was developed by Chen et al. [99] based on the CALPHAD approach. In their work, the thermodynamic descriptions of quaternary sub-systems of  $\text{LaO}_{1.5}\text{-YO}_{1.5}\text{-ZrO}_2$ ,  $\text{LaO}_{1.5}\text{-MnO}_x\text{-YO}_{1.5}$ ,  $\text{LaO}_{1.5}\text{-MnO}_x\text{-ZrO}_2$ , and  $\text{LaO}_{1.5}\text{-MnO}_x\text{-YO}_{1.5}\text{-ZrO}_2$  were obtained by ideal extrapolation of the ternary systems such as La-Y-O or Y-Zr-O due to the limitation of experimental data for the quaternary systems. Subsequently, the description of La-Mn-O-Y-Zr was obtained based on quaternary sub-systems. With the same approach, the La-Mn-O-Y-Zr database was expanded to La-Sr-Mn-O-Y-Zr by Chen [99].

## 10.4 Recent SOFC-Related Results from the CALPHAD Approach

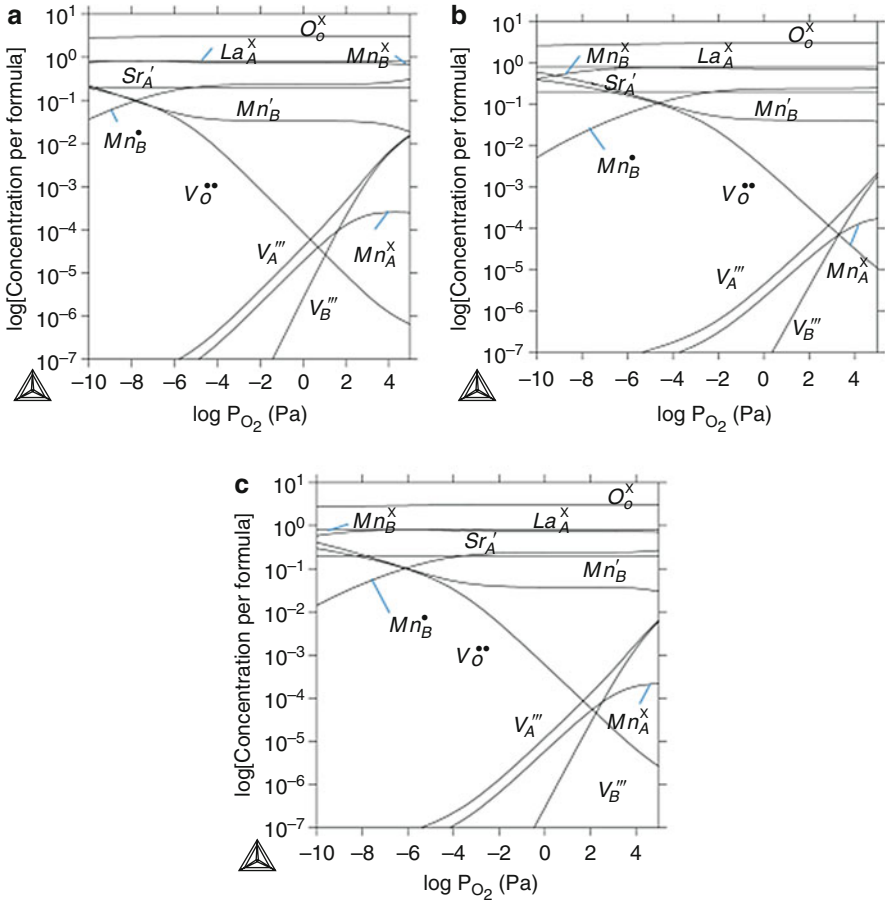
### 10.4.1 Defect Chemistry and Quantitative Brouwer Diagram

With the correct choice of the thermodynamic model and also the Gibbs energy description, the first quantitative Brouwer diagram for LSM perovskite, based on the CALPHAD approach, was developed. This approach maps out the quantitative concentration of all the species at different conditions as shown in Fig. 10.8 for LSM-20 ( $\text{La}_{0.8}\text{Sr}_{0.2}\text{MnO}_{3\pm\delta}$ ). All the defect reactions including the dominant reactions listed in Eqs. 10.5, 10.7, and 10.9 are considered. As a result of quantitative calculation of the concentration of each species, especially the ones considered in dominant reactions, the system behavior such as the electrical conductivity could be predicted and tuned based on the application requirements. Considering the reduction reaction (Eq. 10.5) with the increase of oxygen partial pressure, i.e.,  $\text{O}_2$  (gas) concentration, the reaction is pushed to the reverse direction (reactant), which caused a decrease of  $[V_{\text{O}}^{\bullet\bullet}]$  and  $[Mn_B^{\times}]$ , as well as the increase of  $[Mn_{Mn}^{\bullet}]$  and  $[O_{\text{O}}^{\times}]$ , as shown in Fig. 10.8. It also can be seen that the increase of  $P_{\text{O}_2}$  in Eq. 10.6 will push the reaction to the forward direction (products), which will cause the increase of  $[V_{\text{A}}^{\prime\prime}]$ ,  $[V_{\text{B}}^{\prime\prime}]$ , and  $[Mn_{Mn}^{\bullet}]$  and the decrease of  $[Mn_B^{\times}]$ . Considering all the parameters affect the electrical conductivity, it is noteworthy that  $[V_{\text{O}}^{\bullet\bullet}]$  decreases with the increase of  $P_{\text{O}_2}$ . The concentration is very low, which is  $6.48 \times 10^{-7}$  per formula at  $P_{\text{O}_2} = 10^5$  Pa and  $2.7 \times 10^{-5}$  per formula at  $P_{\text{O}_2} = 1$  Pa. Therefore, its oxygen ionic conductivity is substantially low in typical operation conditions and can be neglected. Thus,  $\text{La}_{0.8}\text{Sr}_{0.2}\text{MnO}_{3\pm\delta}$  is not considered as an oxygen ionic conductor in general.

### 10.4.2 Electrical Conductivities

#### 10.4.2.1 Electronic Conductivities

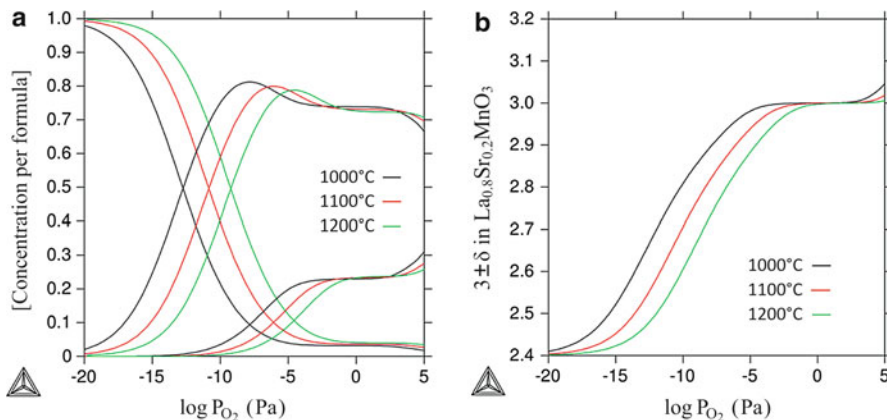
The charge disproportionation among the three states of Mn ions, i.e.,  $\text{Mn}^{2+}$ ,  $\text{Mn}^{3+}$ , and  $\text{Mn}^{4+}$ , in manganite perovskite plays the main role in electronic conduction mechanism. Figure 10.9a illustrates the charge disproportionation (Eq. 10.9) in



**Fig. 10.8** Quantitative Brouwer diagrams of  $\text{La}_{0.8}\text{Sr}_{0.2}\text{MnO}_{3\pm\delta}$  including all the species in LSM-20 at (a) 1000 °C, (b) 1100 °C, and (c) 1200 °C [8]

$\text{La}_{0.8}\text{Sr}_{0.2}\text{MnO}_{3\pm\delta}$  perovskite. It can be seen that, with the increase of temperature, more  $\text{Mn}^{2+}$  ions form in the whole oxygen partial pressure range as a result of  $\text{Mn}^{3+}$  disproportionation. Increasing oxygen partial pressure will cause the decrease of  $Mn'_{Mn}$  and the increase of  $[Mn^{\bullet}_{Mn}]$ . In the random-defect model proposed by Nowotny and Rekas [18],  $\text{Mn}^{4+}$  ions are considered as the only charge carriers in LSM perovskites. However, based on the compound energy formalism model, which is close to the random-defect model [18], both  $\text{Mn}^{2+}$  and  $\text{Mn}^{4+}$  (charge disproportionation effect) should be considered as carriers in the electrical conductivity calculation. However,  $\text{Mn}^{2+}$  is not considered based on the following two reasons:

1. Based on the typical operating condition of LSM-20 ( $P_{\text{O}_2} > 1 \text{ Pa}$ ), the  $\text{Mn}^{4+}$  ions, which have higher concentration than  $\text{Mn}^{2+}$ , are considered as the main carriers in our calculation. In LSM perovskites by substitution of  $\text{Sr}^{2+}$  in the *A* site, the total



**Fig. 10.9** (a) Charge disproportionation diagrams of  $\text{La}_{0.8}\text{Sr}_{0.2}\text{MnO}_{3\pm\delta}$  at 1000, 1100, and 1200 °C and (b) oxygen stoichiometry as a function of oxygen partial pressure of  $\text{La}_{0.8}\text{Sr}_{0.2}\text{MnO}_{3-\delta}$  at 1000, 1100, and 1200 °C [8]

A site valence becomes less than +3; thus, the B site valence increases by the increase of  $\text{Mn}^{4+}$  ion concentrations.

- The Seebeck coefficient of LSM was positive in the whole  $P_{\text{O}_2}$  range, which indicated that LSM was  $p$ -type oxides, i.e., the electronic conductivity was mainly contributed by  $\text{Mn}^{4+}$  ions [29].

Another significant result achieved from Fig. 10.9a is that  $\text{Mn}^{3+}$  never reaches 100%. It suggests that in the considered temperatures and oxygen partial pressure range,  $\text{Mn}^{3+}$  partially disproportionates into  $\text{Mn}^{4+}$  and  $\text{Mn}^{2+}$ , as the same reported for  $\text{LaMnO}_3$  [79].

At a constant oxygen partial pressure, oxygen deficiency ( $\delta$ ) decreases with the increase of temperature as exhibited in Fig. 10.9b. Consequently, the oxygen site valence state and  $Mn'_{Mn}$  will increase. It is shown that in  $P_{\text{O}_2} < 10^{-15}$  Pa, the oxygen stoichiometry ( $3 \pm \delta$ ) in  $\text{La}_{0.8}\text{Sr}_{0.2}\text{MnO}_{3\pm\delta}$ , which is too low, causes high concentration of  $Mn'_{Mn}$  in this range. The most important outcome comparing Fig. 10.9a, b is a plateau starting at  $P_{\text{O}_2} \sim 10^{-5}$  Pa in  $\delta$  versus  $\log P_{\text{O}_2}$ , which explains the plateau for all Mn ion state curves in the same oxygen partial pressure range. Thus, it is worth noting that the charge disproportionation behavior is affected directly by oxygen nonstoichiometry and temperature.

One significant thermodynamic parameter discussed [16–18] for the defect chemistry analysis was the equilibrium constant of the dominant defect reactions. Calculation of this parameter leads to the calculation of further involved thermodynamic parameters as a result of the calculation of the oxygen partial pressure inside the system [27]. Comparison of the calculated equilibrium constant from electrical conductivity with thermogravimetric data was carried out by Kuo et al. [29]. Discrepancies between these two sets of data were mentioned due to the assumption of constant mobility used in conductivity calculation for each oxygen partial pressure,



which was actually due to the assumption of the defect model and the summarized relationship among species. One recent effort to calculate the defect reaction equilibrium constants was carried out by Lee and Morgan for lanthanum manganite (LMO) [30]. Based on their assumption, the independence of equilibrium constant to  $P_{O_2}$  (Pa) in intermediate region ( $10^{-15} \leq P_{O_2} \leq 10^{-10}$ ), which has small amount of oxygen and cation vacancies, results to the consideration of system as an ideal solution. They concluded that with the change of the oxygen nonstoichiometry ( $\delta$ ), the equilibrium constants will change accordingly. Significant error may occur especially in the intermediate region where  $\delta$  is close to zero and hard to measure, which may cause the errors in the further calculations on the defect reaction enthalpies and entropies. In most of the previous works [16–18], the calculation of species concentration was carried out as a function of one or two specific species concentration, which can be determined from thermogravimetric experimental data. To predict the equilibrium constants, not only  $\delta$  and cation vacancy concentrations will affect the equilibrium constant of the dominant reactions; the other species concentration in dominant reactions, e.g.,  $[Mn_{Mn}^{\bullet}]$  and  $[V_O^{\bullet\bullet}]$ , should be calculated accurately as well.

The prediction of conductivity for LSM-20 perovskite is carried out using the quantitative Brower diagrams presented previously based on Eq. 10.4; the oxygen vacancy is the carrier for ionic conductivity, while the  $B$  site defect concentrations are responsible for electronic conductivity as shown in Eq. 10.62:

$$\sigma = e\mu_h[Mn_{Mn}^{\bullet}] + e\mu_e[Mn'_{Mn}] \quad (S.cm^{-1}) \quad (10.62)$$

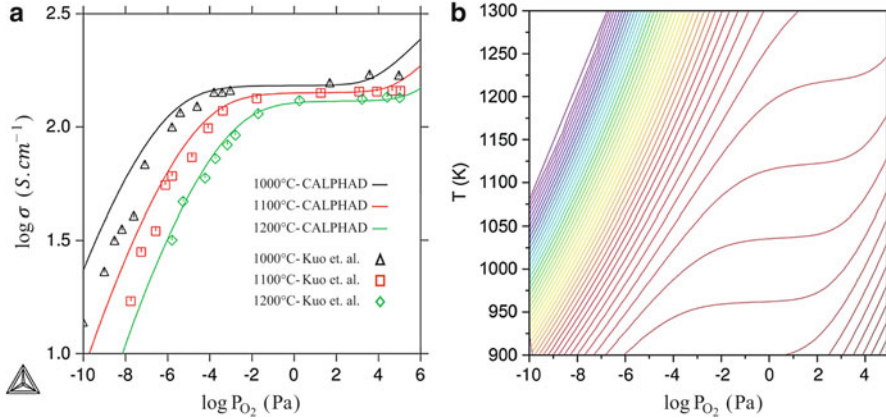
where  $\bar{e}$  is the electron charge,  $[Mn_{Mn}^{\bullet}]$  and  $[Mn'_{Mn}]$  are the carrier concentrations, and  $\mu_h$  and  $\mu_e$  define electron-hole mobility and electron mobility, respectively.

The  $Mn_{Mn}^{\bullet}$  is considered as the dominant carrier for the electronic conductivity, considering the LSM operation conditions. Thus, the electron-hole mechanism {the first part of Eq. 10.62} proposed by Nowotny and Rekas [18] for electronic conductivity prediction is used in this work as well. The electron mobility is not discussed in this work due to the neglecting of  $[Mn'_{Mn}]$  in this  $p$ -type oxide.

The  $\mu_h$  (electron-hole mobility) in Eq. 10.62, which is a measure of electron-hole scattering in a system, is presented in following Eq. 10.63:

$$\mu_h = 2.3\exp\left(\frac{-0.27 \pm 0.04 \text{ eV}}{kT}\right) \quad (cm^2.s^{-1}) \quad (10.63)$$

As illustrated in Eq. 10.63, two constants are considered in the electron-hole mobility calculation from Nowotny and Rekas's work [18]. The energy barrier value from [18] was adopted as the start value and slightly shifted to  $(-0.27 \pm 0.04 \text{ eV})$ . Figure 10.10a demonstrates the electronic conductivity ( $\sigma$ ) as a function of oxygen partial pressure in the temperature range of 1000–1200 °C for  $La_{0.8}Sr_{0.2}MnO_{3 \pm \delta}$ . The model matches the experimental data provided by Kuo et al. [29] very well for this perovskite, especially at  $P_{O_2} \geq 10^{-6}$  Pa. The charge disproportionation reaction



**Fig. 10.10** (a) Electronic conductivity ( $\sigma$ ) experimental and calculated data of  $\text{La}_{0.8}\text{Sr}_{0.2}\text{MnO}_{3\pm\delta}$  at 1000, 1100, and 1200 °C versus  $P_{\text{O}_2}$  (b) 2-D projection of electronic conductivity as a function of oxygen partial pressure and temperature [8]

is considered as the main factor affecting the electronic conductivity. With the increase of  $[Mn_{Mn}^{\bullet}]$ , the increase of the electronic conductivity in LSM is observed. Since the standard ion in the  $B$  site has a valence of +3, if the  $\text{Mn}^{4+}$  ion existed in this site, an electron-hole in the  $B$  site will be created. Thus, the created electron-hole is directly proportional to the  $\text{Mn}^{4+}$  concentration, i.e.,  $[Mn_{Mn}^{\bullet}]$ . There are some differences observed in  $P_{\text{O}_2} < 10^{-6}$  Pa, which might be due to the contribution of  $[Mn_B']$  which is increased in this region as shown in Fig. 10.9a. The 2-D projection of electronic conductivity as a function of temperature and  $P_{\text{O}_2}$  is plotted in Fig. 10.10b.

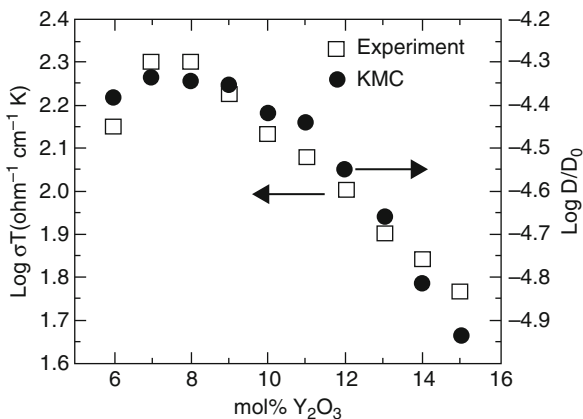
In the case of ionic conductivity, the oxygen vacancies in the third sublattice are determined as the carrier. Since the oxygen vacancy ( $V_O^{\bullet\bullet}$ ) has substantially low concentration, especially in oxygen-deficient region, the ionic conductivity is negligible, and the LSM can be considered as pure electronic conductor. Similar investigation was carried out for  $\text{La}_{1-x}\text{Ca}_x\text{FeO}_{3\pm\delta}$ , and the thermodynamic model using the CALPHAD approach was presented [100].

#### 10.4.2.2 Ionic Conductivity of YSZ

It is known that the conductivity can be determined by Eq. 10.64 [101, 102]:

$$\sigma = zn\mu \quad (10.64)$$

According to Eq. 10.64, the ionic conductivity of YSZ is related to the charge of oxygen ions as carriers ( $z$ ), oxygen vacancy concentration ( $n$ ), and the mobility of oxygen vacancies ( $\mu$ ). The charge of oxygen ions is  $-2$ ; therefore, by knowing the oxygen vacancy concentration and mobility, it is possible to calculate the ionic conductivity. The mobility also can be determined by Eq. 10.65 [61, 103]:



**Fig. 10.11** (Y) Logarithmic plot of conductivity versus mol% Y<sub>2</sub>O<sub>3</sub> in YSZ obtained experimentally from Ref. [105] at 1273 K. (●) Logarithmic plot of D/D<sub>0</sub> (normalized oxygen self-diffusion coefficients) versus Y<sub>2</sub>O<sub>3</sub> doping concentration in YSZ obtained by kinetic Monte Carlo (KMC) simulation of 5X5X5 unit cell with 2,000,000 jumps averaged over 12 initial configurations at 1050 K [104]

$$\mu = A e^{-\frac{E_a}{kT}} \quad (10.65)$$

in which  $E_a$  is the activation energy and  $A$  is a pre-exponential factor.

Quantum simulations complemented with kinetic Monte Carlo (KMC) simulations using density functional theory (DFT)-derived probabilities have been used to predict ionic conductivity in 6–15 mol% YSZ [104]. This approach provides results with qualitative agreement relative to the experimental observations. The quantum simulations suggest that the decrease in conductivity at high doping concentrations mostly arises from the higher migration energy required to traverse across the two adjacent tetrahedra containing the Y-Zr or Y-Y common edge during the diffusion process [104].

The calculated optimum ionic conductivity at 7–8 mol% YSZ agrees well with the experimental observations [104]. The KMC results reveal that the increase in the overall migration energy at higher yttria concentration is due to the higher probability that oxygen vacancies encounter the Zr-Y and Y-Y pairs. The binding energy of  $V_O^{\bullet\bullet}$  Y<sub>Zr}' and Y<sub>Zr}'Y<sub>Zr}' was extracted to the fourth nearest-neighbor interactions. The strongest binding energy was found when  $V_O^{\bullet\bullet}$  was the second nearest neighbor to Y<sub>Zr}' which is in a good agreement with the experimental observations [104].</sub></sub></sub></sub>

It was suggested that this technique can be used to predict ionic conductivity in different types of electrolytes to find optimum dopant concentrations [104]. Furthermore, by considering the effect of all cations in both adjacent tetrahedra, this technique could improve the ability to predict the effect of the dopant concentration on the ionic conductivity [104]. In Fig. 10.11, the compatibility of KMC simulations and experimental results are compared.

### 10.4.3 Cathode-Electrolyte Triple Phase Boundary Stabilities

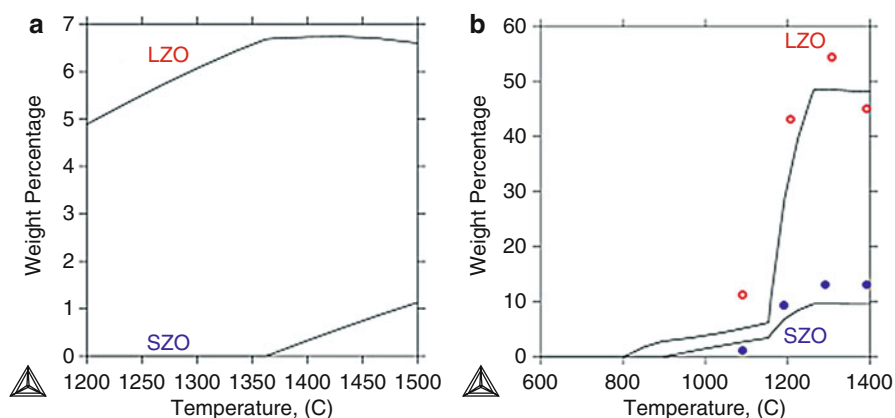
The thermodynamic calculations were done with the La-Sr-Mn-Y-Zr-O thermodynamic database based on Chen's dissertation [15] and reports by Grundy [16]. It is to understand the effects of temperature, *A* site deficiency, Sr content in the *A* site of LSM, and LSM/YSZ ratio to the zirconate phase stabilities at TPB at the sintering and operation conditions. For the calculation results, the weight percentages of LZO and SZO were plotted out, while the other phases, i.e., LSM, YSZ, and MnO, were not plotted.

In the current investigation, to simulate the sintering conditions in the *air*,  $P_{(O_2)} = 0.21$  atm was adopted, while to simulate the operation conditions,  $P_{(O_2)} = 10^{-5}$  atm was used to simulate the low oxygen partial pressure at TPB due to the polarization.

#### 10.4.3.1 Predictions from Computational Thermodynamics

The calculations of the phase stabilities of zirconate at different temperatures were done for the 50 wt.%, 2% *A*-LSM-20, and 50 wt.% 8-YSZ mixture. 2% *A*-LSM-20 was used because it is the most common cathode composition in SOFC, in which, there is a 2% *A* site deficiency. Figure 10.12a shows the calculated results of phase equilibria for the sintering condition. With the sintering temperatures varying from 1200 to 1400 °C, less than 6.73 wt.% LZO may form, while SZO will essentially not form. The lesser LZO phase will form by decreasing the sintering temperature.

However, much more zirconate (about 10 wt.% SZO and 48 wt.% LZO will form at 1400 °C) will form in the operating condition as shown in Fig. 10.12b. There are



**Fig. 10.12** Weight percentages of the two zirconates calculated from the mixture of 2%A-LSM-20 and 8-YSZ (50–50 wt.%) at two different conditions. (a) Sintering in the air at different temperatures. (b) Operation at different temperatures in comparison with experimental data from 1100 °C to 1400 °C (red circles represent LZO and blue dots represent SZO) [107]

three stages for the both zirconates. In stage I, a very large amount of LZO and SZO will be formed at high temperatures, which is around 1300 to 1400 °C; in stage II, a very sharp drop of LZO and SZO happens around 1200 °C; and in stage III, limited LZO and SZO will form, which happens lower than 1200 °C. Overall, fewer zirconates will form with the decrease of temperature. Furthermore, SZO will not form at temperatures lower than 900 °C, and LZO will not form below 800 °C. The common operation temperature, which is around 800 ~ 900 °C, lies in the sensitive region. A small change of powder compositions or operating conditions can greatly affect the stabilities of the two zirconates at TPB. By comparing Fig. 10.12a, b, it shows that the formation of the two zirconates at operation conditions is far more critical than at sintering conditions.

#### 10.4.3.2 Experimental Results

(a) Thermodynamic stabilities of zirconates:

Thermodynamic calculations can only provide a trend of the stabilities of the two zirconate phases at various conditions. Experimental verifications in the *air* and  $N_2$  are needed to show the reliability of the calculation results.

Having a good understanding of the zirconate stabilities at the operating temperatures is very critical to reduce the long-term degradation of the SOFC performance. However, it is difficult to have the direct understanding of the zirconate formation at operation conditions, i.e., 800–900 °C, which lies in the sensitive region, as shown in Fig. 10.12b. Instead, investigations at high temperatures, i.e., 1200–1400 °C, are adopted based on the following two reasons:

1. The formation of zirconates is very limited at the typical operation temperatures, while much more zirconates will be formed at temperatures greater than 1200 °C based on the thermodynamic calculation results, as shown in Fig. 10.12b.
2. It is practically impossible to reach equilibrium at the normal operating temperatures due to the slow reaction rates. It would be desired to get such information in much shorter time. The phase equilibria between 1200 and 1400 °C are much easier to reach as the reaction rate at those temperatures is much higher than the real operation temperatures.

(b) Zirconates stabilities in  $N_2$ :

The mixture of the 50 wt.% LSM-20 and 50 wt.% 8-YSZ heat treated in  $N_2$  at 1200 °C, 1300 °C, and 1400 °C and the weight percentages of both zirconates are summarized in Fig. 10.12b. The formation of both zirconates shows pretty good agreement with the thermodynamic calculation results: A lot of LZO and SZO form at 1300 °C and 1400 °C (stage I); the results from 1200 °C show the drop of the zirconates (stage II) as predicted by the thermodynamic calculation results in Fig. 10.12b. Formation of SZO was reported in the other works as well [106].

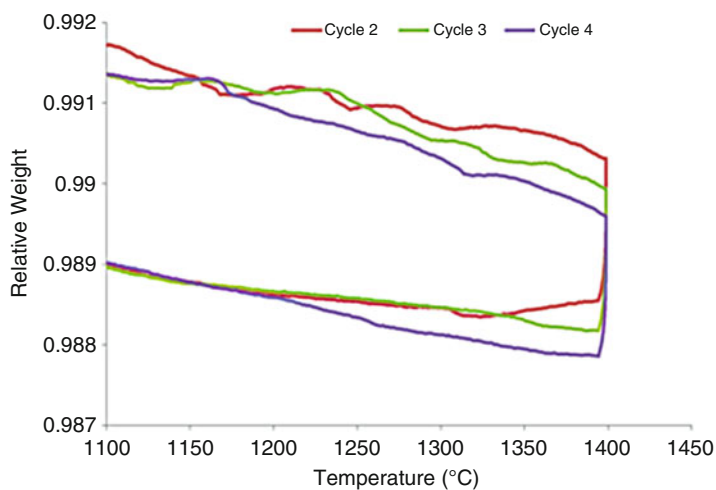
## 10.4.4 Thermomechanical Properties of Perovskites

### 10.4.4.1 Experimental Results

The weight loss behavior along with the thermomechanical properties is pretty complicated as it is a combination of thermodynamics and kinetics. In this section, a preliminary experimental investigation on the weight loss behavior of LSM is presented.

The as received LSM powder was heated up to 1400 °C and was maintained at 1400 °C for 8 h. The heated sample was then quickly cooled to room temperature to keep the oxygen concentration close to the equilibrium condition at 1400 °C. The heat-treated powder was heated to 1400 °C with 10 °C/min ramp. The powder was kept at 1400 °C for 30 min and then cooled down with the same rate, i.e., 10 °C/min. The cycle was repeated for another three times to study the effect of temperature on the performance of the LSM powder. The results are shown in Fig. 10.13. During the first cycle, close constant weight was observed during the heating up process, which is not shown here. The sample was cooled down at a relatively slow rate, i.e., 10 °C/min. Starting from the second run, it shows very clearly that the weight is losing during the heating up process and keep dropping at 1400 °C during the 30-min holding time, and when the sample was cooled down, the weight of the sample starts to increase again. Furthermore, the more the cycle, the more weight loss it shows. The maximum weight loss at the end of holding time at 1400 °C in the fourth cycle is 1.2 wt.%. Only four cycles were chosen because of the limitation of the SDT Q660 instrumentation.

Even though the weight change behavior of LSM-20 powder was mainly due to the thermodynamic equilibrium especially at a slow heating rate, the diffusion



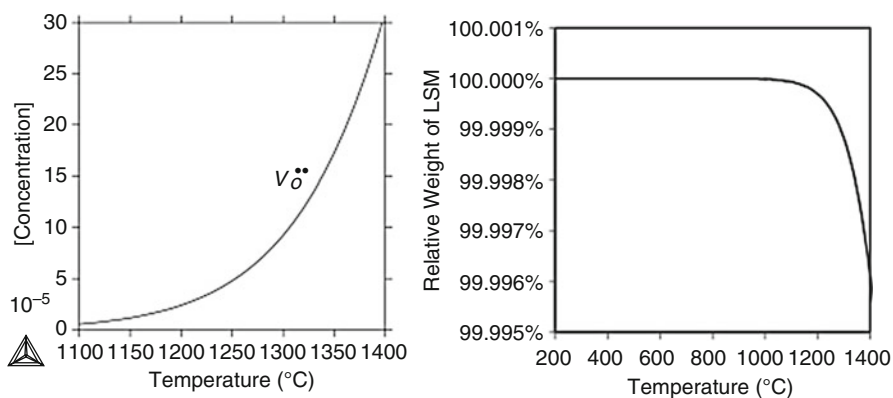
**Fig. 10.13** Weight change behavior of the quenched LSM-20 powder in an air atmosphere in various temperature cycles [108]

process of oxygen into and out of the LSM crystal is a kinetically controlled process, which will also play an important role. As a consequence, the holding time, especially at 1400 °C, could affect the weight loss behavior of the LSM powder. The results clearly show that the sample hasn't reached the final equilibrium within the four cycle's procedure. If low enough holding time could be achieved, much more weight loss was expected.

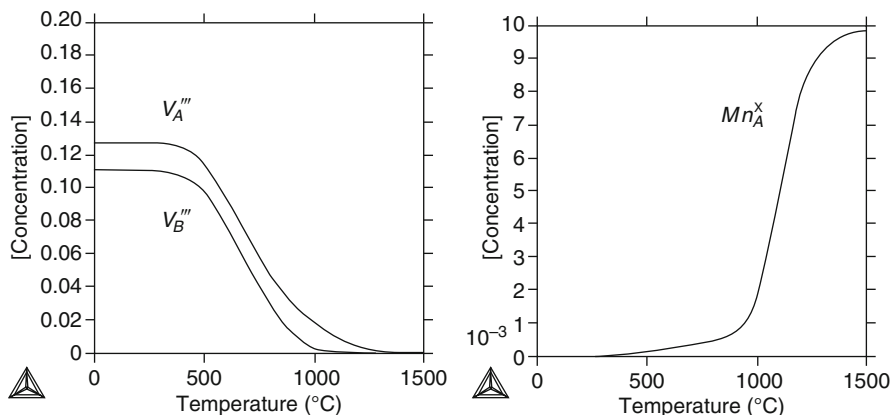
#### 10.4.4.2 Simulation Results

It is well known that the weight change of LSM is due to the absorption and release of the oxygen from the LSM. It was believed that the weight loss is due to the oxygen site vacancy concentration change. However, the accurate defect chemistry indicated a totally different mechanism regarding weight loss. The model used in this work is in accordance with the precepts of the compound energy formalism based on the CALPHAD approach proposed by Grundy [109]. The generated data set was carefully compared with the associate model proposed by Yokokawa et al. [110]. In the latter model, a nonstoichiometric perovskite was considered as a mixture of molecule-like associates. At the end, both models were compared with standard established classical defect chemistry model, and the accuracy of the compound energy formalism was demonstrated to capture the defect chemistry inside  $\text{LaMnO}_3$  more realistically than the classical model.

The breakthrough in thermodynamic modeling is the correct model choice for LSM and the accurate Gibbs energy description; the quantitative Brouwer diagram at various conditions can be plotted out for the first time with the support of the CALPHAD approach with Thermo-Calc [111]. The quantitative Brouwer diagram indicated that the concentration of each species can be quantitatively plotted out. Specifically, the concentration of  $V_{\text{O}}^{\bullet\bullet}$  was plotted in Fig. 10.14. It shows the concentration of  $V_{\text{O}}^{\bullet\bullet}$  sites increases with temperature; however, it is less than



**Fig. 10.14** The quantitative Brouwer diagram on the concentration of  $V_{\text{O}}^{\bullet\bullet}$  at different temperature (left panel); the relative weight loss of LSM calculated based on  $V_{\text{O}}^{\bullet\bullet}$  concentration change (right panel) [108]

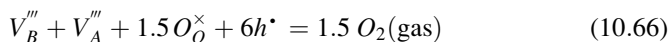


**Fig. 10.15** The quantitative Brouwer diagram of LSM-20 for the concentration of  $V_A'''$  and  $V_B'''$  (left panel) and the antisite  $Mn_A^x$  in the temperature range from room temperature to 1400 °C in the air (right panel) [108]

0.03% at 1400 °C. The weight loss due to  $V_O^{2\bullet}$  also increases and was also plotted in Fig. 10.14, which is 0.004% and lesser than what we observed and is in contradictory with older literature publications. The current observations rule out the possibility that the weight loss is mainly due to  $V_O^{2\bullet}$  sites.

However, at the same time, the thermodynamic calculation on the weight change of the LSM from room temperature to 1400 °C was predicted. It was predicted that the maximum weight change of LSM-20 can be as large as 2.5 wt.%, assuming the thermodynamic equilibrium is reached at each temperature. It is also found out that the molar change of LSM-20 can be as large as 8%. That is, for every 1 mole LSM-20 at 1400 °C, when the sample is cooled down to room temperature, LSM-20 will increase to 1.08 moles.

The detail defect chemistry analysis shows the concentration of cation vacancies, i.e.,  $V_A'''$  and  $V_B'''$  are almost decreasing in pairs with the increase of temperature (Fig. 10.15). It clearly indicated the weight loss and molar change are due to the Schottky defects described in Eq.10.66:



At the same time, it can be observed that there is concentration difference between the two cation vacancies, which is mainly due to the A site deficiency. It shows with the increase of temperature that the difference will drop, which is due to the formation of antisite Mn ions ( $Mn_A^x$ ). Further analysis with the combined approach with quantitative defect chemistry analysis and experimental investigations will yield insight into the problem.



### 10.4.5 Stability of the Perovskite in Atmosphere Containing CO<sub>2</sub>

In the present work, we apply computational thermodynamics and electrochemistry to understand the effect of operating parameters, such as temperature, gas composition, as well as cathode characteristics, like material composition and thickness, on the formation of secondary phases using the CALPHAD approach.

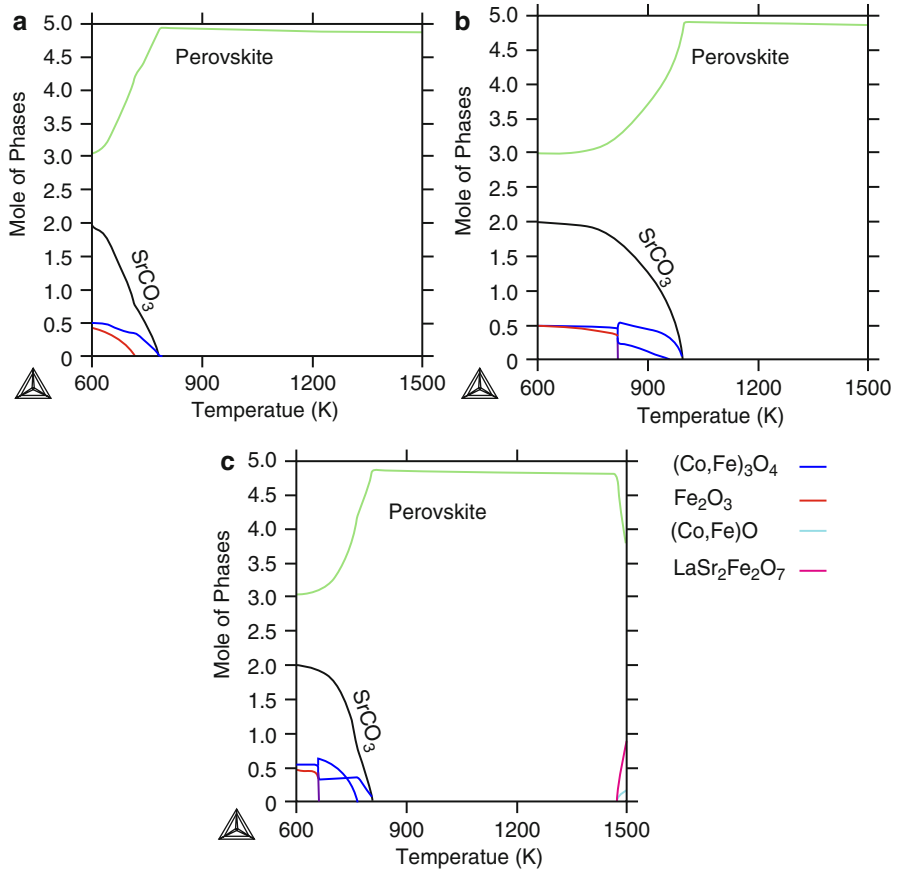
The concentration of CO<sub>2</sub> in the atmosphere is considered as the other significant impact of the atmosphere on the cells. Typical CO<sub>2</sub> concentration in the *air* is assumed to be 360 ppm; however, in order to predict the system behavior in extreme condition, and to compare with existing experimental observations,  $P_{CO_2}$  up to 0.3 atm is considered in this simulation in addition to comparisons with many other experimental conditions. When water vapor pressure is neglected in all the considered atmosphere conditions, *CO<sub>2</sub>-free air* contains 21% O<sub>2</sub>-79% N<sub>2</sub> (C#1); *nitrogen gas* has  $P_{O_2} = 10^{-5}$  atm with no CO<sub>2</sub> (C#2); and *air* is considered with  $P_{CO_2} = 360$  ppm and  $P_{O_2} = 0.21$  atm (C#3). The most extreme case (*30 vol.% CO<sub>2</sub>-air* (C#4)) comprised 30 vol.% CO<sub>2</sub> and 21 vol.% O<sub>2</sub>. The C#5 represents the *reducing atmosphere* ( $P_{O_2} = 10^{-5}$  atm) with the typical CO<sub>2</sub> partial pressure that exists in the air ( $P_{CO_2} = 360$  ppm). In the above conditions, it is worth noting that the *CO<sub>2</sub>-free air* (C#1) in our simulation is totally CO<sub>2</sub>-free, which was different from the experimental CO<sub>2</sub>-free atmosphere in Yu et al.'s work, which contained CO<sub>2</sub> [10]. The experimental CO<sub>2</sub>-free atmosphere in Yu et al.'s work [10] is actually corresponding to the C#3 condition in our simulation. Also the nitrogen gas (C#2) is adopted to simulate the phase stability in reducing condition ( $P_{O_2} = 10^{-5}$  atm) and also the default  $P_{O_2}$  at the TPBs as indicated in Eq. 10.67:

$$p_{O_2}(i) = p - (p - p_{O_2}^0) \exp \left[ \frac{jRTl_c}{4FD_{eff}^{O_2-N_2} p} \right] \quad (10.67)$$

The default oxygen partial pressure drop at the TPBs, due to the cathodic polarization, is assumed as  $P_{O_2} = 10^{-5}$  atm in our thermodynamic simulation. In the following sections, predictions are presented in special atmospheric conditions, which are listed in Table 10.1.

**Table 10.1** Atmospheric assumption representation

Condition #	Experimental condition	Prediction condition
C#1	CO <sub>2</sub> -free <i>air</i>	$P_{O_2} = 0.21$ atm
C#2	Nitrogen	$P_{O_2} = 10^{-5}$ atm
C#3	Air	$P_{CO_2} = 360$ ppm, $P_{O_2} = 0.21$ atm
C#4	30 vol.% CO <sub>2</sub> - <i>air</i>	$P_{CO_2} = 0.3$ atm, $P_{O_2} = 0.21$ atm
C#5	360 ppm CO <sub>2</sub> in <i>reducing atmosphere</i>	$P_{CO_2} = 360$ ppm, $P_{O_2} = 10^{-5}$ atm



**Fig. 10.16** Mole of secondary phases of 1 mol LSCF-6428 within a wide range of temperature in conditions (a) C#3, (b) C#4, (c) C#5 [13]

In the following, thermodynamic predictions are discussed on the formation of secondary phases in a broad range of temperature,  $P_{CO_2}$ ,  $P_{O_2}$ , and material composition for LSCF using the CALPHAD approach.

#### 10.4.5.1 Secondary Phase Stability at Different Temperatures

It has been observed that secondary phases will form on the surface of LSCF. However, various phases were identified ex situ in different works [10, 33–35]. The basis for the current simulation is 1 mole of atoms occupying the *A* site, 1 mole of atoms on the *B* site, and 3 moles of atoms on the oxygen site, for a total of 5 moles of atoms for LSCF-6428. However, the total moles are slightly lower than 5 due to the existence of *A* site, *B* site, and oxygen site deficiencies. Results from calculation at C#1 and C#2 illustrate that no secondary phases form except a very small amount of Sr<sub>6</sub>Co<sub>5</sub>O<sub>15</sub> at very low temperatures, which may not be experimentally observed due to slow kinetics. Changing the atmosphere to N<sub>2</sub>

causes the formation of  $(\text{La, Sr})_3\text{Fe}_2\text{O}_7$  and  $(\text{Co, Fe})\text{O}$  (halite), which was also predicted by Zhang [84], at temperatures higher than  $\sim 1450$  K, which was the typical sintering temperature range for LSCF-6428. It is worth mentioning that in the typical operating temperature range for SOFCs (1023–1223 K), LSCF-6428, the system is stable, and no secondary phase forms at  $P_{\text{O}_2} = 0.21$  atm and  $P_{\text{O}_2} = 10^{-5}$  atm.

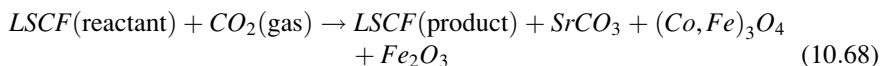
Figure 10.16 shows the thermodynamic equilibria in condition (a) C#3, (b) C#4, and (c) C#5 for 1 mole per formula unit of LSCF-6428 and plots the stability regions under different conditions, i.e., (a) *air* (C#3), (b) *30 vol.% CO<sub>2</sub>-air* (C#4), and (c) *reducing atmosphere* (C#5). It was observed from Fig. 10.16a that at temperatures higher than 780 K, no secondary phase forms and that the LSCF-6428 is stable in condition C#3. At temperatures lower than 780 K, secondary phases including  $\text{SrCO}_3$ ,  $\text{Fe}_2\text{O}_3$  (corundum), and  $(\text{Co, Fe})_3\text{O}_4$  (spinel) become stable. The  $\text{CO}_2$  exposure ( $P_{\text{CO}_2} = 0.3$  atm) results in considerable increase in the concentration of low-temperature secondary phases and also a significant increase in the threshold temperature of the  $\text{SrCO}_3$  precipitation (996 K) as shown in Fig. 10.16b.

Figure 10.16c applies to conditions that can be established in two different ways: (i) holding the LSCF sample in a *reducing atmosphere* and (ii) a reduction in the cathode surface oxygen partial pressure due to the cathode polarization under cell operating conditions. The data showed that the LSCF-6428 was stable in the operating temperature range of SOFCs. In addition, holding the LSCF-6428 sample under reducing conditions at a temperature higher than 1475 K leads to the formation of  $(\text{La, Sr})_3\text{Fe}_2\text{O}_7$  and  $(\text{Co, Fe})\text{O}$ . Furthermore, the *reducing atmosphere* will slightly increase the stability temperature range of  $\text{SrCO}_3$ ,  $\text{Fe}_2\text{O}_3$  (corundum), and  $(\text{Co, Fe})_3\text{O}_4$  (spinel) phases to 800 K. It is worth noting that two  $(\text{Co, Fe})_3\text{O}_4$  spinels were considered in the thermodynamic database as shown in Fig. 10.16b, c. One of them is the Co-rich spinel, which is close to  $\text{Co}_3\text{O}_4$ , and the other one is the Fe-rich spinel, which is close to  $\text{Fe}_3\text{O}_4$ . The Fe-rich spinel is stable at elevated temperature, while Co-rich spinel is the only stable spinel at room temperature. Overall,  $\text{SrCO}_3$  will be the dominant secondary phase at low temperatures. The high  $\text{CO}_2$  partial pressure and low  $\text{O}_2$  partial pressure will increase the stability of  $\text{SrCO}_3$ . However,  $\text{SrCO}_3$  is predicted not to form under typical operating conditions.

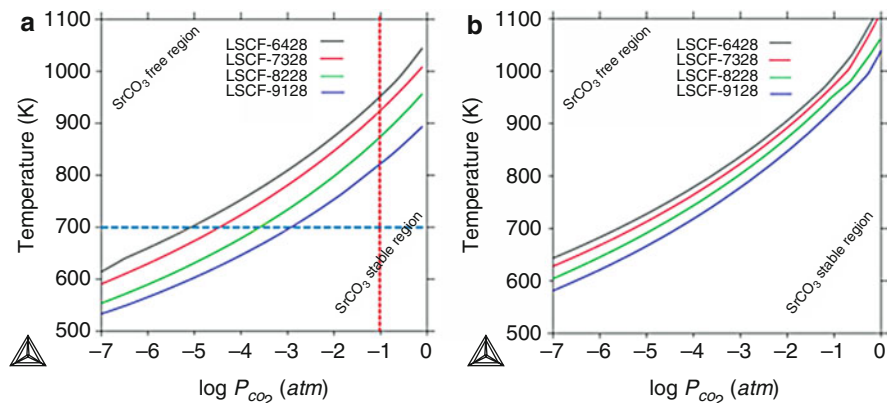
#### 10.4.5.2 $\text{SrCO}_3$ Stability

a)  $\text{SrCO}_3$  threshold diagram:

According to the predictions from Fig. 10.16,  $\text{SrCO}_3$ ,  $(\text{Co, Fe})_3\text{O}_4$ , and  $\text{Fe}_2\text{O}_3$  may precipitate from LSCF with the  $\text{CO}_2$  exposure especially at low temperatures. The products of the reactions can be slightly different at various conditions; however, the dominant reaction under most conditions is summarized in Eq. 10.68:



where LSCF (reactant) is in the LSCF sample before the  $\text{CO}_2$  exposure and LSCF (product) is the sample after the  $\text{CO}_2$  exposure. The resulting material may have a



**Fig. 10.17** SrCO<sub>3</sub> stability threshold diagram for SrCO<sub>3</sub> stability for various LSCF compositions in the (a) air and (b) N<sub>2</sub> ( $P_{O_2} = 10^{-5} \text{ atm}$ ) [13]

different composition than the LSCF (reactant) because of the formation of new phases, such as SrCO<sub>3</sub>. The threshold prediction for the precipitation of SrCO<sub>3</sub> is one critical information that needs to be taken into account for the re-optimization of LSCF cathode compositions and the cathode gas impurity control if CO<sub>2</sub> plays a significant role in the long-term degradation of SOFC.

The threshold diagram for the SrCO<sub>3</sub> stability in the LSCF system is plotted in Fig. 10.17 for the first time proposed in this chapter. The threshold diagram represents a mapping of the Gibbs free energy for the dominant reactions ( $\Delta G_{rxn(2)}$ ) as a function of temperature,  $P_{CO_2}$ , and Sr concentration. In accordance with this diagram, each line is a locus of temperature and  $P_{CO_2}$  where  $\Delta G_{rxn(2)} = 0$  (curves in Fig. 10.17) for SrCO<sub>3</sub> formation. If  $\Delta G_{rxn(2)}$  is negative, at the lower right corner of the diagram, SrCO<sub>3</sub> is stable (SrCO<sub>3</sub> stable region), and if  $\Delta G_{rxn(2)}$  is positive, as defined in upper left quadrant of Fig. 10.17, the system is free of SrCO<sub>3</sub> (SrCO<sub>3</sub> free region). This is a useful aid for complicated multicomponent systems, such as SOFC cathodes, and can be only developed by the CALPHAD approach. During the simulations, the threshold that was defined as SrCO<sub>3</sub> is a stable phase; however, its concentration was zero. The advantage of the CALPHAD approach is that it does not a priori assume specific SrCO<sub>3</sub> formation reactions as a basis for equilibrium simulations. It automatically considers the correct reactions given a set of temperatures and gas-phase and solid-phase compositions. This relieves the material designer from the burden of accounting for correct reaction schemes.

Overall, it is also seen in the threshold diagrams that by decreasing the temperature, as well as by increasing the  $P_{CO_2}$  and Sr concentration, the propensity to form SrCO<sub>3</sub> increases. For example, at a fixed  $P_{CO_2}$  (0.1 atm, the red dash line in Fig. 10.17a), LSCFs with lower Sr concentration have lower SrCO<sub>3</sub> formation temperatures; at fixed temperature (700 K, the blue dash line in Fig. 10.17a), the LSCFs with higher Sr

concentration have lower SrCO<sub>3</sub> formation  $P_{CO_2}$ . Additionally, the impact of  $P_{O_2}$  on the SrCO<sub>3</sub> stability threshold has also been examined by considering two cases: (i)  $P_{O_2} = 0.21$  atm and (ii)  $P_{O_2} = 10^{-5}$  atm as shown in Fig. 10.17a, b.

The threshold trends for both oxygen partial pressures are the same. However, the difference is that in a more reducing atmosphere, i.e., lower  $P_{O_2}$ , SrCO<sub>3</sub> is stable down to lower CO<sub>2</sub> partial pressures at a fixed temperature in comparison with higher  $P_{O_2}$ .

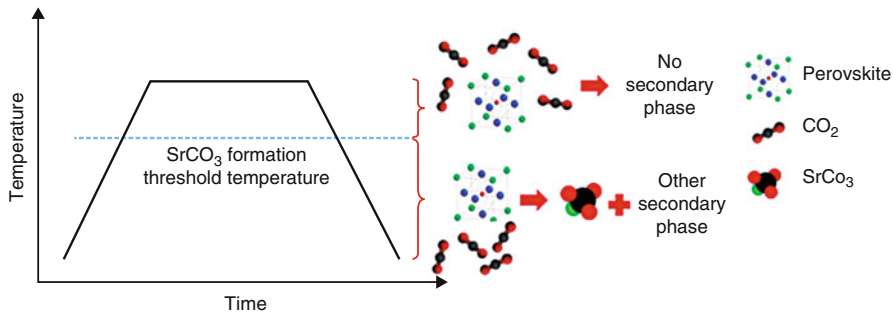
The thermodynamic predictions regarding the phase formation in LSCF-6428 system in a wide range of temperature,  $P_{CO_2}$ ,  $P_{O_2}$ , and LSCF composition have been conducted based on the CALPHAD approach and compared with the previous investigations [13].

It is anticipated that  $P_{O_2}$  at the TPBs will be significantly lower than the  $P_{O_2}$  in the air just outside the cathode surface during operation. The  $P_{O_2}$  at the TPBs is dependent on the temperature, LSCF layer thickness, and the current density. At the same current density, the higher the operating temperature, the higher the  $P_{O_2}$  at TPBs; the thicker the LSCF layer, the lower the  $P_{O_2}$  at the TPBs. In agreement with this model, accordingly the  $P_{O_2}$  at the TPBs will be significantly lower than  $P_{O_2}$  in the air and is in the range of  $10^{-3}$  to  $10^{-5}$  atm.

In the current thermodynamic simulations, the default  $P_{O_2}$  at the TPBs was assumed to be  $10^{-5}$  atm based on the cathode polarization conditions. Overall, the predictions regarding CO<sub>2</sub> exposure to the LSCF system are in agreement with the previous experimental and modeling investigations [10, 33, 34, 36, 37]. The modeling confirms that the Sr-O compounds observed by Oh et al. [33] are most likely SrCO<sub>3</sub>. It also confirms the formation of spinel phases in the air from LSCF [34, 36, 37], and it confirms the conclusion that SrCO<sub>3</sub> will become much more stable in high CO<sub>2</sub> concentration as indicated by Yu et al. [10]. The SrCO<sub>3</sub> threshold diagrams predicted with CALPHAD approach, as demonstrated in Fig. 10.17, also show good agreement with the conclusion from the threshold diagrams predicted by first-principle calculation carried out by Yu et al. [10].

However, some of the current predictions are significantly different from the previous experimental investigations.

1. It was claimed that LSCF-6428 segregation occurs during the heat treatment of the samples in the *air* at operating temperature, i.e., 1023–1223 K. The simulation on LSCF-6428 stability without the CO<sub>2</sub> exposure shows LSCF-6428 is stable in operating condition in the *air* or in *reducing condition* due to the cathode polarization. However, it is found that by the exposure of CO<sub>2</sub> to the system, secondary phases, including SrCO<sub>3</sub> and Co- and/or Fe-rich spinels in the form of (Co, Fe)<sub>3</sub>O<sub>4</sub>, will form at low temperature. It is predicted the experimental-observed LSCF phase separation in the *air* is not due to the solubility limit of LSCF itself. Instead, it may be due to the existence of CO<sub>2</sub> in the *air*.
2. The formation condition of SrCO<sub>3</sub> from the thermodynamic simulation results conflicts with the experimental observations. It was claimed that SrCO<sub>3</sub> will



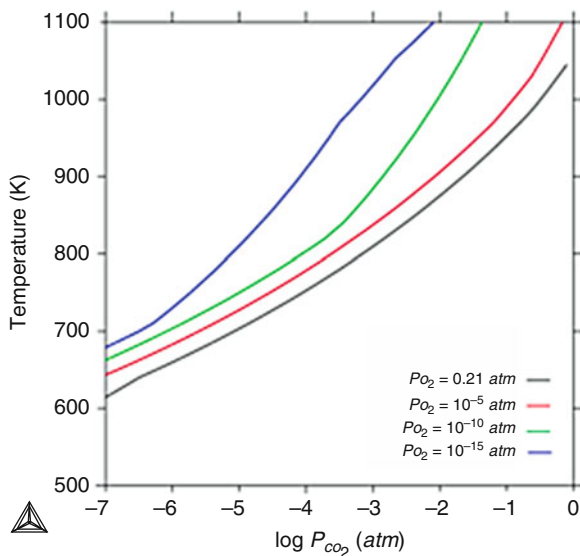
**Fig. 10.18** Schematic demonstration of a thermal-cycle for LSCF-6428 in an atmosphere containing  $\text{CO}_2$  [13]

form at the operating condition [10], while the thermodynamic simulation prediction shows  $\text{SrCO}_3$  only form at low temperature. The predicted  $\text{SrCO}_3$  precipitation temperature for LSCF-6428 is lower than the typical operating temperature (1023–1223 K) in both gas with low  $\text{CO}_2$  concentration (*air* with 360 ppm  $\text{CO}_2$ ) and gas with high  $\text{CO}_2$  concentration (30 vol.%  $\text{CO}_2$ ). Figure 10.18 shows the schematic demonstration of the formation of secondary phases in a typical thermal-cycle based on the prediction from our thermodynamic simulations. It shows secondary phases, including  $\text{SrCO}_3$ , might form during the heating up and cooling down of the system, and, due to the kinetics of reactions, they do not completely dissolve back, and they may remain on the surface or at the TPBs.

The disparities between prior experiments [10] and the current thermodynamic simulations of the  $\text{SrCO}_3$  formation may due to the difference between the real experimental condition and our three simulation conditions:

- (i) The experiments from Yu et al. [10] were performed on thin films deposited on single crystal substrates. Depending on the lattice mismatch, these could result in highly strained layers, which could shift the stability boundaries for  $\text{SrCO}_3$  formation in LSCF. By contrast, the present simulations are applicable to nominally strain-free LSCF, which is a more realistic condition for porous electrodes.
- (ii) The composition of the surface of the LSCF layer is very different from the nominal composition; the real-time TXRF experiments show 8%–32% Sr on the surface of LSCF. However, the nominal Sr composition of LSCF-6428 is 40%. It is reasonable to believe that the concentration of the other elements La, Co, and Fe is also very different from the nominal composition. The composition difference may significantly affect the  $\text{SrCO}_3$  formation, which cannot be used for direct comparison with the thermodynamic prediction of LSCF-6428 from the current work.
- (iii) Because of the local geometry in the cathode layer, it is possible that  $P_{\text{O}_2}$  at certain TPB locations is very different from the value calculated from Eq. 10.67

**Fig. 10.19** SrCO<sub>3</sub> stability threshold diagram for SrCO<sub>3</sub> stability for LSCF-6428 at various  $P_{O_2}$  [13]



and the default value we adopted in our thermodynamic simulations, for example, the thermodynamic simulation from  $P_{O_2} = 10^{-15}$  atm to  $P_{O_2} = 0.21$  atm. Figure 10.19 shows that SrCO<sub>3</sub> formation threshold temperature can be significantly low at low  $P_{CO_2}$  conditions. With  $P_{O_2} < 10^{-15}$  atm, the SrCO<sub>3</sub> may become stable at the typical operating temperature (1073 K). The current densities in Eq. 10.67 are averages normalized to the geometrical projected contact area between the cathode and the electrolyte. The asperities in the cathode combined with local low-porosity regions could significantly increase the local current density and such that very low  $P_{O_2}$  ( $\sim 10^{-15}$  atm) becomes possible within the cathode.

In addition, it compares LSM-20 and LSCF-6428 cathodes from the long-term degradation point of view. It is concluded that a mole of secondary phases, especially SrCO<sub>3</sub> that forms on the LSM-20 surface, were much lower than that on LSCF-6428. It was concluded that CO<sub>2</sub> was not deleterious for LSM-20 under typical operating  $P_{CO_2}$ , but for LSCF-6428, it was a critical parameter to consider for the SOFC long-term degradation.

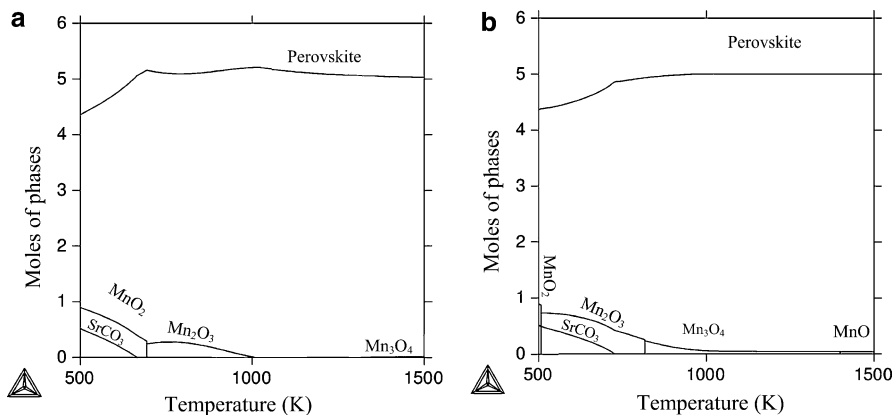
Overall, our predictions show that the propensity to form SrCO<sub>3</sub> is thermodynamically more favorable at higher  $P_{CO_2}$ , lower  $P_{O_2}$ , and lower temperatures. Thus, thermal-cycle is considered as the main reason for SrCO<sub>3</sub> formation, which may block the oxygen reduction reaction (ORR) sites. In SOFC industrial applications, it is suggested to include two considerations: (1) the SrCO<sub>3</sub> stability into the LSCF compositional optimization and (2) avoidance of unnecessary thermal cycles and reducing the holding time in the SrCO<sub>3</sub> stable regions.

The CALPHAD approach has a unique advantage for the prediction of CO<sub>2</sub> effect on the SrCO<sub>3</sub> formation: The composition effect of *A* and *B* sites of LSCF was simulated for the first time in the current chapter. It shows that the stability of SrCO<sub>3</sub> decreases at fixed temperature and  $P_{CO_2}$  by decreasing the Sr concentration in *A* site or Co concentration in *B* site. This provides prudent guidance on how to design the composition of LSCF, as CO<sub>2</sub> is an important factor for long-term degradation, which was not previously considered during the compositional optimization of LSCF. On the other hand, comparing with the first-principle calculations [10], which were limited to the specific LSCF composition (La<sub>0.75</sub>Sr<sub>0.25</sub>Co<sub>0.25</sub>Fe<sub>0.75</sub>O<sub>3</sub>), its prediction accuracy drops significantly with the increase of temperature, not to mention the uncertainties of the potentials used in DFT calculations. The current work provides crucial guidance on the design of the next generation of LSCF and on other possible cathode candidates using the CALPHAD approach. It is planned to apply this approach to obtain stability maps for other material systems to be used in solid-state ionic devices.

#### 10.4.5.3 Effect of CO<sub>2</sub> on LSM and LSCF

The LSM-20 and LSCF-6428 are two leading competitors for the SOFC cathode. The LSCF-6428 is considered as a candidate because of its excellent mixed ionic and electronic conductivity [33], and also its thermal expansion coefficient (TEC) matches with the rare earth (RE)-doped ceria (RE<sub>2</sub>O<sub>3</sub>-CeO<sub>2</sub>, where RE = Gd, Sm, Y etc.) [112]. While its TEC is higher than that of yttria-stabilized zirconia (YSZ), it reacts with YSZ to form insulating phases. The results indicate that LSCF can be employed as the cathode material in combination with YSZ electrolytes through the application of a barrier layer of RE<sub>2</sub>O<sub>3</sub>-CeO<sub>2</sub>. On the other hand, LSM-20 has significantly high electronic conductivity, excellent electrocatalytic activity, and an excellent TEC match with the electrolyte, key parameters for a functional SOFC cathode [31]. Despite these advantages, both systems suffer from long-term stability issues such as surface segregation and secondary phase formation. According to Hu et al. [31], SrCO<sub>3</sub> formation causes initial degradation at the LSM surface. However, it was observed that the effect of CO<sub>2</sub> in the *air* on the electrochemical performance of the cell is negligible. For LSCF-6428, it was reported by Yu et al. [10] that formation of SrCO<sub>3</sub> drives the segregation kinetics of Sr at the surface until a steady state is reached. The steady state occurs due to the blocking of the surface by secondary phases. In the current work, thermodynamic predictions are carried out to compare the stability of both cathodes under the same conditions. The predictions for LSM-20 were comprehensively discussed in our previous report [12]. As illustrated in Fig. 10.20a, b, the mole of phases as a function of temperature was predicted for LSM-20 in the (a) *air* ( $P_{O_2} = 0.21$  atm) containing 30 vol.% CO<sub>2</sub> and (b) *N<sub>2</sub>* ( $P_{O_2} = 10^{-5}$  atm) containing 30 vol.% CO<sub>2</sub>, respectively. It is worth noting that 1 mole per formula of LSM-20, i.e., (La<sub>0.8</sub>Sr<sub>0.2</sub>)<sub>0.98</sub>MnO<sub>3 ± δ</sub>, is adopted in the current simulation. The perovskite phase is slightly different from 5 moles in total due to the *A* site, *B* site, and oxygen site deficiencies as well as secondary phase formation. Surprisingly, the concentration of secondary phases in LSM-20 is much lower than that predicted for LSCF-6428 in Fig. 10.16. At low temperatures (< 1000 K), MnO<sub>2</sub>, Mn<sub>2</sub>O<sub>3</sub>, and SrCO<sub>3</sub> are predicted as secondary phases in the LSM-20





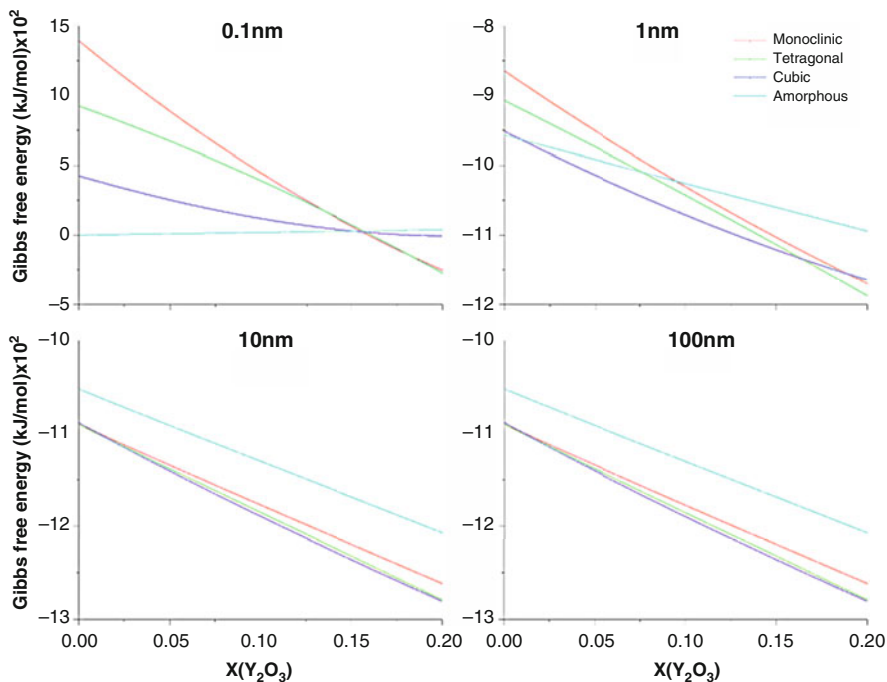
**Fig. 10.20** Moles of secondary phases of 1 mol of LSM-20 within a wide range of temperature in condition (a) air ( $P_{O_2} = 0.21 \text{ atm}$ ) containing 30 vol.%  $\text{CO}_2$  and (b)  $\text{N}_2$  ( $P_{O_2} = 10^{-5} \text{ atm}$ ) containing 30 vol.%  $\text{CO}_2$  [13]

system. For both systems, secondary phases form below 1000 K in 30 vol.%  $\text{CO}_2$ -air, while no secondary phase is stable in the operating temperature range, i.e., 1023–1223 K. The  $\text{Mn}_3\text{O}_4$  is predicted to form on LSM-20 surface at temperatures higher than  $\sim 1273$  K in Fig. 10.20a. However, no secondary phase was predicted to form in LSCF-6428 system at high temperatures. By comparing the amount of secondary phases in both systems shows the significant differences between them. The total amount of segregated phases, especially  $\text{SrCO}_3$ , is much higher in LSCF-6428 than LSM-20 due to the higher reactivity of LSCF-6428 with  $\text{CO}_2$  in the air ( $P_{O_2} = 0.21 \text{ atm}$ ) containing 30 vol.%  $\text{CO}_2$ .

Although no secondary phase is predicted to form in the LSM-20 system within the operating temperature range in the air ( $P_{O_2} = 0.21 \text{ atm}$ ) containing 30 vol.%  $\text{CO}_2$ , conditions in experiments could be different due to the limitation of reaction kinetics. Because of the heating up and cooling down of the cell, secondary phases form on the surface, and at the TPBs, and they may remain or dissolve by changes in the experimental conditions. For instance,  $\text{Mn}_3\text{O}_4$  forms during sintering (1473 K) and may not completely dissolved back into LSM by cooling down the sample, and a tiny amount of this phase might remain on the surface. Thus, the more precipitates form, the more remain on the surface and may cause more and faster degradation of the cathode. In conclusion, LSM-20 is more stable than LSCF-6428 for long-term operation due to the slower rate of degradation at different temperature and atmospheres.

#### 10.4.6 Phase Diagrams for Nanoparticles

In this section, it is shown how to develop the  $n$ -YSZ phase diagram, by applying the CALPHAD approach. Due to important applications of the zirconia-rich YSZ, the calculations are focused on the yttria mole fraction between 0 and 0.2.



**Fig. 10.21** The Gibbs energy versus yttria mole fraction at room temperature for  $n$ -YSZ with different particle sizes [71]

Drazin and Castro derived four equations to explain the specific surface energy of each  $n$ -YSZ polymorph [70] described in Eqs. 10.69, 10.70, 10.71, and 10.72:

$$\gamma_m = (1.9278) - (9.68)x \quad (10.69)$$

$$\gamma_t = (1.565) - (4.61)x \quad (10.70)$$

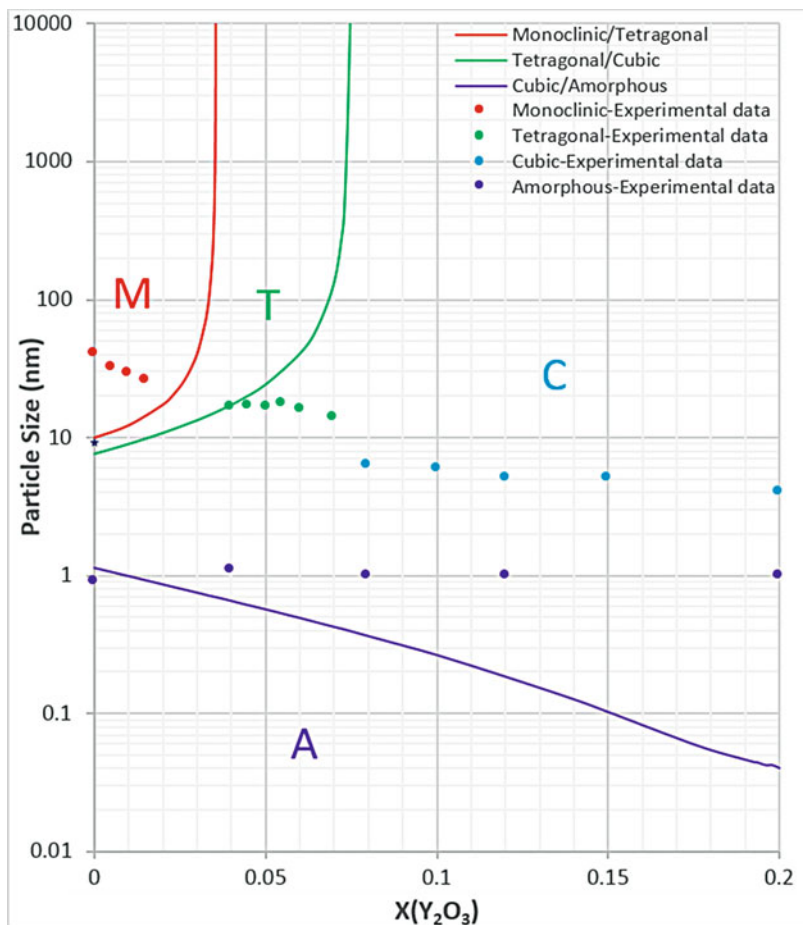
$$\gamma_c = (1.1756) - (3.36)x + (7.77)x^2 \quad (10.71)$$

$$\gamma_a = (0.8174) - (0.11)x \quad (10.72)$$

where  $x$  is the yttria mole fraction and  $\gamma_m$ ,  $\gamma_t$ ,  $\gamma_c$ , and  $\gamma_a$  are specific surface energies of monoclinic, tetragonal, cubic, and amorphous phases, respectively.

Combining the Gibbs energy of bulk YSZ and the surface energy of each polymorph at room temperature, the total Gibbs energy of the  $n$ -YSZ system is predicted as shown in Fig. 10.21.

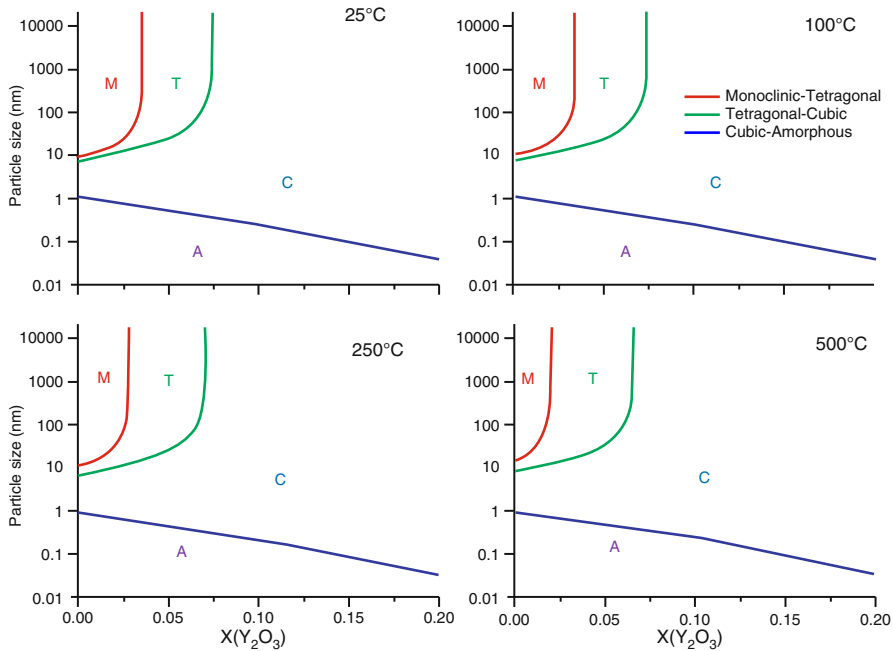
The intersection of different phases of Gibbs energies is changing with particle size as shown in Fig. 10.21. The amorphous phase is not stable when the particle size is 10 or 100 nm, while for the particle size as small as 1 nm, the amorphous phase is stable in low yttria concentrations (Fig. 10.21). The Gibbs energy minimization is a



**Fig. 10.22** The phase diagram for the *n*-YSZ system at room temperature in comparison with the experimental data which represent experimentally measured crystal structure by Drazin and Castro [70]. ★ sign indicates the largest tetragonal pure zirconia particle size experimentally observed [70] (M, monoclinic; T, tetragonal; C, cubic; A, amorphous) [71]

key factor to make a phase stable. By decreasing the particle size, the effect of surface energy increases, which causes the change of all involved phases of Gibbs energies and leads to stability of amorphous phase.

The intersections represent  $T_0$  temperature points at which the Gibbs energies of the two involved phases are equal at a certain composition. By combining the Gibbs energy diagrams and yttria concentration for various particle sizes, the *n*-YSZ phase diagram at room temperature was plotted as shown in Fig. 10.22. In this figure, each curve indicates the boundary between phases, by which the stability range of each polymorph versus particle size and composition (mole fraction of Y<sub>2</sub>O<sub>3</sub>) is determined at room temperature.



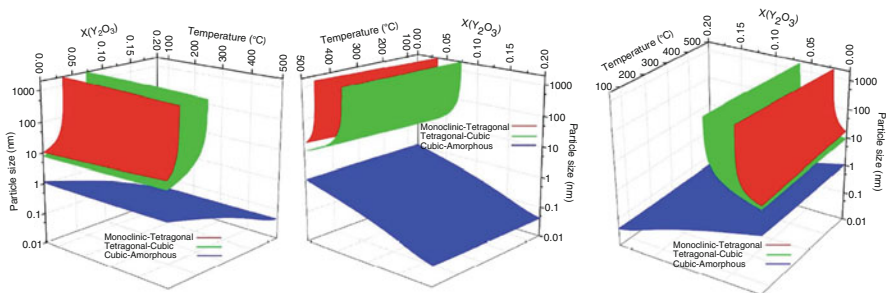
**Fig. 10.23** The phase diagram for an  $n$ -YSZ system at 25 °C, 100 °C, 250 °C, and 500 °C (M, monoclinic; T, tetragonal; C, cubic; A, amorphous) [71]

The errors are expected for the amorphous phase because of the simplifications explained in Sect. 10.3.5; however, the results clearly show the ability of CALPHAD approach to predict the amorphous stability range. According to Fig. 10.22, the tetragonal phase region and the related superimposed experimental data show some discrepancy, which is related to the bulk YSZ thermodynamic database provided by Chen et al. [97]. This shows an improvement is needed in tetragonal + cubic/cubic phase boundary of the database.

The Gibbs energy calculation of bulk YSZ can be extended to higher temperatures since the CALPHAD approach has been applied. Considering the effect of surface energy, the  $n$ -YSZ phase diagram at various temperatures is plotted as shown in Fig. 10.23. The specific surface energy changes by temperature [113]; however, it was assumed to be small and negligible.

According to the diagrams in Fig. 10.23, the  $c$ -ZrO<sub>2</sub> region is enlarged and the stability range of  $m$ -ZrO<sub>2</sub> shrinks with the increase of temperature. In addition, the T/C curve shifts toward the left and also moves up by increasing temperature.

Based on Fig. 10.23, the C/A curve is almost invariant by increasing temperature. This is related to the dominant effect of surface energy in comparison with the bulk Gibbs energy since the particle size of the amorphous region is extremely small. Moreover, as the surface energy was assumed to be invariant with temperature changes, the C/A curve is approximately fixed versus temperature.



**Fig. 10.24** The 3-D phase diagram for the *n*-YSZ system from different angles [71]

By combining the *n*-YSZ phase diagrams at different temperatures, a 3-D contour phase diagram was developed, in which the phase regions are predicted based on the mole fraction of yttria, particle size, and temperature. Different angles of the 3-D phase diagram for the *n*-YSZ system are shown in Fig. 10.24.

## 10.5 Summary

There have been extensive experimental investigations on the cathode-electrolyte of SOFC, especially the cathode and electrolyte conductivity optimization, thermomechanical property control, and the long-term degradation on the cathode side. However, most of the research was based on the traditional trial-and-error approach; the comprehensive thermodynamic understanding was missing due to the complicated nature of the system. Fortunately, computational thermodynamics has made significant progress in the past decade especially on the most popular systems in SOFC. This book chapter has mainly covered the recent critical progress on the application of computational thermodynamics in SOFCs. Here four critical considerations are described in this book chapter:

1. The detail defect chemistry analysis has been carried out for the most popular LSM cathode. The quantitative Brouwer diagram was developed with the CALPHAD approach.
2. Coupling the quantitative Brouwer diagram and the electron mobility, the electronic conductivity has been predicted for LSM for the first time. The modeling covers the effect of temperature, oxygen partial pressure, and *A* site deficiency. The ionic conductivity of YSZ electrolyte can be also predicted using the above methodological approach.
3. The cathode side plays a critical role in the long-term degradation of SOFC. It may due to the chemical reactions between cathode and electrolyte and the impurities from the *air*. The phase stabilities at TPBs have been simulated to provide guidance on the cathode composition optimization to prevent/reduce the

formation of harmful zirconates (LZO and SZO). The effect of gas impurities like CO<sub>2</sub> to the phase stability at the cathode side has been investigated. Formation of Sr-containing secondary phases was predicted to be the main reason for blocking ORR path and lowering the conductivity.

4. YSZ has been adopted as the most common electrolyte material. It was shown how to develop a (nano) *n*-YSZ phase diagram by applying the CALPHAD approach. It has provided the guidance on the phase transformation and coarsening for nanoparticles.

There are still a lot of areas to explore the application of computational thermodynamics in SOFC in the future, for example, how to optimize the mixed ionic-electronic conductivities (MIEC) for the cathode materials, reduce the cathode-electrolyte CTE mismatch, improve the chemical compatibility between the new cathode-electrolyte during sintering and operation conditions, and control the cathode stoichiometry and phase stability under various gas impurities including CO<sub>2</sub>, SO<sub>2</sub>, and H<sub>2</sub>O. With the help of computational thermodynamics, it is possible to systematically design the cathode-electrolyte of SOFC to meet all these requirements for the first time.

**Acknowledgments** This work is partially supported by the start-up funding from Florida International University for Dr. Yu Zhong and also the grant from the American Chemical Society Petroleum Research Fund (PRF#54190-DNI10). The Doctoral Evidence Acquisition (DEA) Fellowship from the graduate school of Florida International University is also appreciated for the financial support for Ms. Shadi Darvish and Mr. Mohammad Asadikiya. The authors also gratefully acknowledge the helpful comments and suggestions of the reviewers, which have improved the presentation.

---

## References

1. *FCT – Fuel Cell Technologies – SOFC*. 2017 [cited 2017]. Available from: <http://fuelcelltoday.com/technologies/sofc>
2. T. Ishihara, *Perovskite Oxide for Solid Oxide Fuel Cells*, Fuel Cells and Hydrogen Energy (Springer, Boston, 2009)
3. F.-P. Negal, *Electricity from Wood through the Combination of Gasification and Solid Oxide Fuel Cells* (ETH/PSI, Zurich, 2008)
4. N. Sammes, Y. Du, Intermediate-temperature SOFC electrolytes, in *Fuel Cell Technologies: State and Perspectives*, (Springer, Dordrecht, 2005), pp. 19–34
5. B.C. Steele, A. Heinzl, Materials for fuel-cell technologies. *Nature* **414**(6861), 345–352 (2001)
6. T. Wolfgram, S. Ellialtioglu, *Electronic and Optical Properties of d-Band Perovskites* (Cambridge University Press, Cambridge, UK, 2006)
7. D.M. Smyth, *The Defect Chemistry of Metal Oxides* (Oxford University Press, New York, 2000)
8. S. Darvish et al., Quantitative defect chemistry analysis and electronic conductivity prediction of La<sub>0.8</sub>Sr<sub>0.2</sub>MnO<sub>3±δ</sub> perovskite. *J. Electrochem. Soc.* **162**(9), E134–E140 (2015)
9. S. Darvish, S.K. Saxena, Y. Zhong, Quantitative analysis of (La<sub>0.8</sub>Sr<sub>0.2</sub>)<sub>1-x</sub>MnO<sub>3±δ</sub> electronic conductivity using CALPHAD approach, in *Developments in Strategic Ceramic Materials: A Collection of Papers Presented at the 39th International Conference on Advanced Ceramics and Composites*, (Wiley Online Library, Hoboken, 2015)

10. Y. Yu et al., Effect of atmospheric CO<sub>2</sub> on surface segregation and phase formation in La<sub>0.6</sub>Sr<sub>0.4</sub>Co<sub>0.2</sub>Fe<sub>0.8</sub>O<sub>3</sub> thin films. *Appl. Surf. Sci.* **323**, 71–77 (2014)
11. Y. Tanaka et al., Improvement of electrical efficiency of solid oxide fuel cells by anode gas recycle. *ECS Trans.* **30**(1), 145–150 (2011)
12. S. Darvish et al., Thermodynamic prediction of the effect of CO<sub>2</sub> to the stability of (La<sub>0.8</sub>Sr<sub>0.2</sub>)<sub>0.98</sub>MnO<sub>3±δ</sub> system. *Int. J. Hydrog. Energy* **41**(24), 10239–10248 (2016)
13. S. Darvish, S. Gopalan, Y. Zhong, Thermodynamic stability maps for the La<sub>0.6</sub>Sr<sub>0.4</sub>Co<sub>0.2</sub>Fe<sub>0.8</sub>O<sub>3±δ</sub>-CO<sub>2</sub>-O<sub>2</sub> system for application in solid oxide fuel cells. *J. Power Sources* **336**, 351 (2016)
14. C. Wang et al., Effect of SO<sub>2</sub> poisoning on the electrochemical activity of La<sub>0.6</sub>Sr<sub>0.4</sub>Co<sub>0.2</sub>Fe<sub>0.8</sub>O<sub>3-δ</sub> cathodes of solid oxide fuel cells. *J. Electrochem. Soc.* **164**(6), F514–F524 (2016)
15. A. Arabaci, M.F. Öksüzömer, Preparation and characterization of 10 mol% Gd doped CeO<sub>2</sub> (GDC) electrolyte for SOFC applications. *Ceram. Int.* **38**(8), 6509–6515 (2012)
16. F.W. Poulsen, Defect chemistry modelling of oxygen-stoichiometry, vacancy concentrations, and conductivity of (La<sub>1-x</sub>Sr<sub>x</sub>)<sub>y</sub>MnO<sub>3-δ</sub>. *Solid State Ionics* **129**(1–4), 145–162 (2000)
17. X.D. Zhou, H. Anderson, A Global defect chemistry model for p-type mixed ionic and electronic conductors. *ECS Trans.* **25**(2), 2807–2814 (2009)
18. J. Nowotny, M. Rekas, Defect chemistry of (La,Sr)MnO<sub>3</sub>. *J. Am. Ceram. Soc.* **80**(191914), 67 (1998)
19. H. Kamata et al., High temperature electrical properties of the perovskite-type oxide La<sub>1-x</sub>Sr<sub>x</sub>MnO<sub>3-d</sub>. *J. Phys. Chem. Solids* **87**, 943–950 (1995)
20. J. Mizusaki et al., Electronic conductivity, Seebeck coefficient, defect and electronic structure of nonstoichiometric La<sub>1-x</sub>Sr<sub>x</sub>MnO<sub>3</sub>. *Solid State Ionics* **132**, 167–180 (2000)
21. G. Brouwer, A general asymptotic solution of reaction equations common in solid-state chemistry. *Philips Res. Rep.* **9**(5), 366–376 (1954)
22. J.A.M. van Roosmalen, E.H.P. Cordfunke, A new defect model to describe the oxygen deficiency in perovskite-type oxides. *J. Solid State Chem.* **93**(1), 212–219 (1991)
23. I. Yasuda, M. Hishinuma, Electrical conductivity and chemical diffusion coefficient of strontium-doped lanthanum manganites. *J. Solid State Chem.* **123**(2), 382–390 (1996)
24. J. Mizusaki et al., Nonstoichiometry of the perovskite-type oxide La<sub>1-x</sub>Sr<sub>x</sub>CrO<sub>3-δ</sub>. *Solid State Ionics* **12**, 119–124 (1984)
25. I. Yasuda, T. Hikita, Precise determination of the chemical diffusion coefficient of calcium-doped lanthanum chromites by means of electrical conductivity relaxation. *J. Electrochem. Soc.* **141**(5), 1268–1273 (1994)
26. B.F. Flandermeier et al., High-temperature stability of magnesium-doped lanthanum chromite. *High Temp. Sci.* **20**(259), 259–269 (1985)
27. J.H. Kuo, H.U. Anderson, D.M. Sparlin, Oxidation-reduction behavior of undoped and Sr-doped LaMnO<sub>3</sub> nonstoichiometry and defect structure. *J. Solid State Chem.* **83**(1), 52–60 (1989)
28. J. Mizusaki et al., Nonstoichiometry and defect structure of the perovskite-type oxides La<sub>1-x</sub>Sr<sub>x</sub>FeO<sub>3-δ</sub>. *J. Solid State Chem.* **58**(2), 257–266 (1985)
29. J.H. Kuo, H.U. Anderson, D.M. Sparlin, Oxidation-reduction behavior of undoped and Sr-doped LaMnO<sub>3</sub>: defect structure, electrical conductivity, and thermoelectric power. *J. Solid State Chem.* **87**(1), 55–63 (1990)
30. Y.-L. Lee, D. Morgan, Ab initio and empirical defect modeling of LaMnO<sub>3±δ</sub> for solid oxide fuel cell cathodes. *Phys. Chem. Chem. Phys.* **14**(1), 290–302 (2012)
31. B. Hu et al., Effect of CO<sub>2</sub> on the stability of strontium doped lanthanum manganite cathode. *J. Power Sources* **268**, 404–413 (2014)
32. B. Hu, M.K. Mahapatra, P. Singh, Performance regeneration in lanthanum strontium manganite cathode during exposure to H<sub>2</sub>O and CO<sub>2</sub> containing ambient air atmospheres. *J. Ceram. Soc. Jpn.* **123**(1436), 199–204 (2015)
33. D. Oh, D. Gostovica, E.D. Wachsman, Mechanism of La<sub>0.6</sub>Sr<sub>0.4</sub>Co<sub>0.2</sub>Fe<sub>0.8</sub>O<sub>3</sub> cathode degradation. *J. Mater. Res.* **27**(15), 1992–1999 (2012)

34. L. Zhao et al., Insight into surface segregation and chromium deposition on  $\text{La}_{0.6}\text{Sr}_{0.4}\text{Co}_{0.2}\text{Fe}_{0.8}\text{O}_{3-\delta}$  cathodes of solid oxide fuel cells. *J. Mater. Chem. A* **2**(29), 11114–11123 (2014)
35. S.P. Simmer et al., Degradation mechanisms of la-Sr-co-Fe-O<sub>3</sub> SOFC cathodes. *Electrochem. Solid-State Lett.* **9**(10), A478–A481 (2006)
36. M. Liu et al., Enhanced performance of LSCF cathode through surface modification. *Int. J. Hydrog. Energy* **37**(10), 8613–8620 (2012)
37. F.S. Baumann et al., Strong performance improvement of  $\text{La}_{0.6}\text{Sr}_{0.4}\text{Co}_{0.8}\text{Fe}_{0.2}\text{O}_{3-\delta}$  SOFC cathodes by electrochemical activation. *J. Electrochem. Soc.* **152**(10), A2074–A2079 (2005)
38. Y. Yu, A.Y. Nikiforov, T.C. Kaspar, J.C. Woicik, K.F. Ludwig, S. Gopalan, U.B. Pal, S.N. Basu, Chemical characterization of surface precipitates in  $\text{La}_{0.7}\text{Sr}_{0.3}\text{Co}_{0.2}\text{Fe}_{0.8}\text{O}_{3-\delta}$  as cathode material for solid oxide fuel cells. *J. Power Sources.* **333**, 247–253 (2016)
39. S. Lau, S. Singhal, Potential electrode/electrolyte interactions in solid oxide fuel cells, in *Corrosion '85*, (Boston, United States: National Association of Corrosion Engineers 1985)
40. O. Yamamoto et al., Stability of perovskite oxide electrode with stabilized zirconia, in *Electrochemical Society 1989 Fall Meeting (Abstracts)*, (United States: The Electrochemical Society 1990)
41. G. Stochniol, E. Syskakis, A. Naoumidis, Chemical compatibility between strontium-doped lanthanum manganite and Ytria-stabilized zirconia. *J. Am. Ceram. Soc.* **78**(4), 929–932 (1995)
42. A. Mitterdorfer, L. Gauckler,  $\text{La}_2\text{Zr}_2\text{O}_7$  formation and oxygen reduction kinetics of the  $\text{La}_{0.85}\text{Sr}_{0.15}\text{Mn}_y\text{O}_3$ ,  $\text{O}_2(\text{g})/\text{YSZ}$  system. *Solid State Ionics* **111**(3), 185–218 (1998)
43. K. Wiik et al., Reactions between strontium-substituted lanthanum manganite and Ytria-stabilized zirconia: I, powder samples. *J. Am. Ceram. Soc.* **82**(3), 721–728 (1999)
44. A. Grosjean et al., Reactivity and diffusion between  $\text{La}_{0.8}\text{Sr}_{0.2}\text{MnO}_3$  and  $\text{ZrO}_2$  at interfaces in SOFC cores by TEM analyses on FIB samples. *Solid State Ionics* **177**(19), 1977–1980 (2006)
45. J. Labrincha, J. Frade, F. Marques,  $\text{La}_2\text{Zr}_2\text{O}_7$  formed at ceramic electrode/YSZ contacts. *J. Mater. Sci.* **28**(14), 3809–3815 (1993)
46. C. Brugnoli, U. Ducati, M. Scagliotti, SOFC cathode/electrolyte interface. Part I: reactivity between  $\text{La}_{0.85}\text{Sr}_{0.15}\text{MnO}_3$  and  $\text{ZrO}_2\text{-Y}_2\text{O}_3$ . *Solid State Ionics* **76**(3–4), 177–182 (1995)
47. H.Y. Lee, S.M. Oh, Origin of cathodic degradation and new phase formation at the  $\text{La}_{0.9}\text{Sr}_{0.1}\text{MnO}_3/\text{YSZ}$  interface. *Solid State Ionics* **90**(1–4), 133–140 (1996)
48. N.Q. Minh, Solid oxide fuel cell technology – features and applications. *Solid State Ionics* **174**, 271–277 (2004)
49. S. Jiang, Development of lanthanum strontium manganite perovskite cathode materials of solid oxide fuel cells: a review. *J. Mater. Sci.* **43**(21), 6799–6833 (2008)
50. M. Mori et al., Thermal-expansion behaviors and mechanisms for Ca- or Sr-doped lanthanum manganite perovskites under oxidizing atmospheres. *J. Electrochem. Soc.* **147**(4), 1295–1302 (2000)
51. A. Hammouche, E. Siebert, A. Hammou, Crystallographic, thermal and electrochemical properties of the system  $\text{La}_{1-x}\text{Sr}_x\text{MnO}_3$  for high temperature solid electrolyte fuel cells. *Mater. Res. Bull.* **24**(3), 367–380 (1989)
52. M. Mori, Effect of B-site doing on thermal cycle shrinkage for  $\text{La}_{0.8}\text{Sr}_{0.2}\text{Mn}_{1-x}\text{MxO}_{3+\delta}$  perovskites (M=Mg, Al, Ti, Mn, Fe, Co, Ni;  $0 \leq x \leq 0.1$ ). *Solid State Ionics* **174**(1–4), 1–8 (2004)
53. M. Mori, Mechanisms of thermal expansion and shrinkage of  $\text{La}_{0.8}\text{Sr}_{0.2}\text{MnO}_{3+\delta}$  perovskites with different densities during thermal cycling in air. *J. Electrochem. Soc.* **152**(4), A732–A739 (2005)
54. B.P. McCarthy et al., Enhanced shrinkage of lanthanum strontium manganite ( $\text{La}_{0.90}\text{Sr}_{0.10}\text{MnO}_{3+\delta}$ ) resulting from thermal and oxygen partial pressure cycling. *J. Am. Ceram. Soc.* **90**(10), 3255–3262 (2007)
55. B.P. McCarthy et al., Low-temperature densification of lanthanum strontium manganite ( $\text{La}_{1-x}\text{Sr}_x\text{MnO}_{3+\delta}$ ),  $x=0.0\text{--}0.20$ . *J. Am. Ceram. Soc.* **92**(8), 1672–1678 (2009)



56. T. Soma, et al., Porous lanthanum manganite sintered bodies and solid oxide fuel cells. U.S. Patent No. 5,432,024 (1995)
57. J. Chevalier et al., The tetragonal-monoclinic transformation in zirconia: Lessons learned and future trends. *J. Am. Ceram. Soc.* **92**, 1901–1920 (2009)
58. J.R. Kelly, I. Denry, Stabilized zirconia as a structural ceramic: an overview. *Dent. Mater.* **24**, 289–298 (2008)
59. C.H. Wang et al., Phase transformation and nanocrystallite growth behavior of 2 mol% yttria-partially stabilized zirconia (2Y-PSZ) powders. *Ceram. Int.* **39**, 5165–5174 (2013)
60. Y. Li et al., Electrical conductivity of zirconia stabilized with yttria and calcia. *J. Mater. Sci. Lett.* **18**, 443–444 (1999)
61. A. Nakamura, J.B. Wagner, Defect structure, ionic conductivity, and diffusion in yttria stabilized zirconia and related oxide electrolytes with fluorite structure. *J. Electrochem. Soc.* **133**, 1542–1548 (1986)
62. W. Strickler, W.G. Carlson, Ionic conductivity of cubic solid solutions in the system  $\text{CaO-Y}_2\text{O}_3\text{-ZrO}_2$ . *J. Am. Ceram. Soc.* **47**, 122–127 (1963)
63. J. Goff et al., Defect structure of yttria-stabilized zirconia and its influence on the ionic conductivity at elevated temperatures. *Phys. Rev. B* **59**(22), 14202 (1999)
64. R.C. Garvie, R.H. Hannink, R.T. Pascoe, Ceramic steel? *Nature* **258**, 703–704 (1975)
65. O. Ruff, F. Ebert, Refractory ceramics: 1, the forms of zirconia dioxide. *Z. Anorg. Allg. Chem.* **180**, 19–41 (1929)
66. C. Wagner, Über den Mechanismus der elektrischen Stromleitung im Nernststift. *Naturwissenschaften* **31**(23–24), 265–268 (1943)
67. J.A. Krogstad et al., Effect of yttria content on the zirconia unit cell parameters. *J. Am. Ceram. Soc.* **94**, 4548–4555 (2011)
68. A. Suresh, M.J. Mayo, W.D. Porter, Thermodynamics for Nanosystems: grain and particle-size dependent phase diagrams. *Rev. Adv. Mater. Sci.* **5**, 100–109 (2003)
69. J.W. Drazin, R.H.R. Castro, Water adsorption microcalorimetry model: deciphering surface energies and water chemical potentials of nanocrystalline oxides. *J. Phys. Chem. C* **118**, 10131–10142 (2014)
70. J.W. Drazin, R.H.R. Castro, Phase stability in nanocrystals: a predictive diagram for yttria-zirconia. *J. Am. Ceram. Soc.* **1384**, 1377–1384 (2015)
71. M. Asadikiya et al., Phase diagram for a nano-yttria-stabilized zirconia system. *RSC Adv.* **6**(21), 17438–17445 (2016)
72. L. Kaufman, H. Bernstein, *Computer Calculation of Phase Diagrams with Special Reference to Refractory Metals* (Academic, New York, 1970)
73. N. Saunders, A.P. Miodownik, *CALPHAD (Calculation of Phase Diagrams): A Comprehensive Guide*, vol xvi (Pergamon, Oxford, 1998), p. 479
74. M. Hillert, The compound energy formalism. *J. Alloys Compd.* **320**(2), 161–176 (2001)
75. K. Hack (ed.), *The SGTE Casebook : Thermodynamics at Work*, Materials Modelling Series (Institute of Materials, London, 1996)
76. A.T. Dinsdale, SGTE data for pure elements. *Calphad* **15**(4), 317–425 (1991)
77. B. Sundman, J. Agren, A regular solution model for phases with several components and sublattices, suitable for computer applications. *J. Phys. Chem. Solids* **42**, 297–301 (1981)
78. J.O. Andersson et al., A compound-energy model of ordering in a phase with sites of different coordination numbers. *Acta Metall.* **34**, 437–445 (1986)
79. A.N. Grundy et al., Calculation of defect chemistry using the CALPHAD approach. *Calphad* **30**(1), 33–41 (2006)
80. M. Yang, Y. Zhong, Z.K. Liu, Defect Analysis and Thermodynamic Modeling of  $\text{LaCoO}_{3-\delta}$ . *Solid State Ionics* **178**, 1072–1032 (2007)
81. S.H. Lee et al., Defect chemistry and phase equilibria of  $(\text{La}_{1-x}\text{Ca}_x)\text{FeO}_{3-\delta}$  thermodynamic modeling. *J. Electrochem. Soc.* **160**(10), F1103–F1108 (2013)
82. M. Yang, *Thermodynamic Modeling of  $\text{La}_{1-x}\text{Sr}_x\text{CoO}_{3-d}$* . *Diss. Master Thesis* (The Pennsylvania State University, 2006)

83. J.E. Saal, Thermodynamic modeling of phase transformations and defects: From cobalt to doped cobaltate perovskites. *Diss. The Pennsylvania State University*, (The Pennsylvania State University, 2010), p. 268
84. W. Zhang, B. Rasmus, Investigation of degradation mechanisms of LSCF based SOFC cathodes – by CALPHAD modeling and experiments. *Diss. Department of Energy Conversion and Storage*, (Technical University of Denmark, 2012)
85. E.P. Karadeniz, *Thermodynamic database of the La-Sr-Mn-Cr-O oxide system and applications to solid oxide fuel cells* (Diss. ETH Zurich, 2008)
86. F.A. Kroeger, H.J. Vink, *Solid State Ionics* **3**, 307 (1956)
87. M. Seppanen, M. Kyto, P. Taskinen, Defect structure and nonstoichiometry of  $\text{LaCoO}_3$ . *Scand. J. Metall.* **9**, 3–11 (1980)
88. M. Hillert, B. Jansson, B. Sundman, Application of the compound-energy model to oxide systems. *Z. Met.* **79**(2), 81–87 (1988)
89. Scientific Group Thermodata Europe (SGTE), Thermodynamic properties of inorganic materials, in *Landolt-Boernstein New Series, Group IV*, (Springer, Berlin/Heidelberg, 1999)
90. A.N. Grundy et al., Assessment of the La-Mn-O system. *J. Phase Equilib. Diffus.* **26**(2), 131–151 (2005)
91. O. Redlich, A.T. Kister, Algebraic representations of thermodynamic properties and the classification of solutions. *Ind. Eng. Chem.* **40**(2), 345–348 (1948)
92. M. Asadikiya et al., Thermodynamic modeling and investigation of the oxygen effect on the sintering of  $\text{B}_4\text{C}$ . *J. Alloys Compd.* **699**, 1022–1029 (2017)
93. M. Asadikiya et al., The role of CALPHAD approach in the sintering of  $\text{B}_4\text{C}$  with  $\text{SiC}$  as a sintering aid by spark plasma sintering technique. *Additive manufacturing and strategic technologies in advanced ceramics. Ceram. Trans.* **258**, 185–191 (2016)
94. S. Gupta et al., Phase evolution and electrochemical performance of iron doped lanthanum strontium chromite in oxidizing and reducing atmosphere. *Int. J. Hydrog. Energy* **42**, 6262 (2016)
95. H. Sabarou, Y. Zhong, Investigation on the phase stability of perovskite in La-Sr-Cr-Fe-O system. *Advances in solid oxide fuel cells and electronic ceramics II. Ceram. Eng. Sci. Proc.* **37**(3), 127–135 (2017)
96. M. Asadikiya et al., The effect of sintering parameters on spark plasma sintering of  $\text{B}_4\text{C}$ . *Ceram. Int.* **43**(14), 11182–11188 (2017)
97. M. Chen, B. Hallstedt, L.J. Gauckler, Thermodynamic modeling of the  $\text{ZrO}_2\text{-YO}_{1.5}$  system. *Solid State Ionics* **170**, 255–274 (2004)
98. L. Kaufman, M. Cohen, Thermodynamics and kinetics of martensitic transformations. *Prog. Met. Phys.* **7**, 165–246 (1958)
99. M. Chen et al., Thermodynamic modeling of the La-Mn-Y-Zr-O system. *Calphad* **30**(4), 489–500 (2006)
100. S. Darvish, Y. Zhong, Quantitative defect chemistry analysis of  $(\text{La}_{1-x}\text{Ca}_x)_y\text{FeO}_{3\pm\delta}$  perovskite. *ECS Trans.* **78**(1), 565–572 (2017)
101. M. Barsoum, *Fundamentals of Ceramics* (Institute of Physics Publ, Bristol, 2003)
102. R. Casselton, Low field DC conduction in yttria-stabilized zirconia. *Phys. Status Solidi A* **2**(3), 571–585 (1970)
103. C. Zhang et al., Ionic conductivity and its temperature dependence of atmospheric plasma-sprayed yttria stabilized zirconia electrolyte. *Mater. Sci. Eng. B* **137**(1), 24–30 (2007)
104. R. Pomprasertsuk et al., Predicting ionic conductivity of solid oxide fuel cell electrolyte from first principles. *J. Appl. Phys.* **98**(10), 103513 (2005)
105. A. Ioffe, D. Rutman, S. Karpachov, On the nature of the conductivity maximum in zirconia-based solid electrolytes. *Electrochim. Acta* **23**(2), 141–142 (1978)
106. Z. Lu et al.,  $\text{SrZrO}_3$  formation at the interlayer/electrolyte Interface during  $(\text{La}_{1-x}\text{Sr}_x)_{1-\delta}\text{Co}_{1-y}\text{Fe}_y\text{O}_3$  cathode sintering. *J. Electrochem. Soc.* **164**(10), F3097–F3103 (2017)

107. C. Levy et al., Thermodynamic stabilities of  $\text{La}_2\text{Zr}_2\text{O}_7$  and  $\text{SrZrO}_3$  in SOFC and their relationship with LSM synthesis processes. *J. Electrochem. Soc.* **157**(11), B1597–B1601 (2010)
108. S. Darvish et al., Weight loss mechanism of  $(\text{La}_{0.8}\text{Sr}_{0.2})_{0.98}\text{MnO}_{3\pm\delta}$  during thermal cycles. *Mechanical Properties and Performance of Engineering Ceramics and Composites X: A Collection of Papers Presented at the 39th International Conference on Advanced Ceramics and Composites*. (John Wiley & Sons, Inc., 2015)
109. A.N. Grundy et al., Calculation of defect chemistry using the CALPHAD approach. *Calphad Comput. Coupling Phase Diagrams Thermochem.* **30**(1), 33–41 (2006)
110. H. Yokokawa et al., Thermodynamic representation of nonstoichiometric lanthanum manganite. *Solid State Ionics* **86**, 1161–1165 (1996)
111. J.O. Andersson et al., THERMO-CALC & DICTRA, computational tools for materials science. *Calphad Comput. Coupling Phase Diagrams Thermochem.* **26**(2), 273–312 (2002)
112. S. Gupta, M.K. Mahapatra, P. Singh, Lanthanum chromite based perovskites for oxygen transport membrane. *Mater. Sci. Eng. R. Rep.* **90**, 1–36 (2015)
113. T. Frolov, Y. Mishin, Temperature dependence of the surface free energy and surface stress: an atomistic calculation for Cu(110). *Phys. Rev. B* **79**, 1–10 (2009)



# Application of DFT Methods to Investigate Activity and Stability of Oxygen Reduction Reaction Electrocatalysts

# 11

Xin Chen, Qingan Qiao, and Fan Li

## Contents

11.1	Introduction .....	338
11.2	Density Functional Theory Methods .....	339
11.3	Methods to Evaluate ORR Activity .....	340
11.3.1	Binding Energy of ORR Intermediates .....	340
11.3.2	Potential Energy Surface .....	342
11.3.3	Linear Gibbs Energy Relationship to Determine Reversible Potentials .....	344
11.3.4	Reaction Barrier of ORR .....	346
11.3.5	Catalyst Electronic Structure .....	348
11.4	Methods to Evaluate ORR Stability .....	350
11.4.1	Metal Dissolution Potential .....	350
11.4.2	Metal Cohesive Energies .....	353
11.4.3	Binding Energies of Metal in the Active Sites .....	353
11.5	Conclusions .....	355
	References .....	355

## Author Contributions

X. Chen formulated the idea, Q. Qiao and F. Li helped with the literature survey and X. Chen wrote the paper.

X. Chen (✉)

The Center of New Energy Materials and Technology, College of Chemistry and Chemical Engineering, Southwest Petroleum University, Chengdu, China

e-mail: [chenxin830107@pku.edu.cn](mailto:chenxin830107@pku.edu.cn)

Q. Qiao

School of Chemistry and Materials Science, Ludong University, Yantai, China

F. Li

Beijing Key Laboratory for Catalysis and Separation, Department of Chemistry and Chemical Engineering, College of Environmental and Energy Engineering, Beijing University of Technology, Beijing, China

e-mail: [vanadiumli@bjut.edu.cn](mailto:vanadiumli@bjut.edu.cn)

## Abstract

Proton exchange membrane fuel cells (PEMFCs) are considered one of the most promising energy conversion devices due to their high-energy yield and low environmental impact of hydrogen oxidation. The oxygen reduction reaction (ORR) at cathode plays a crucial role during operation of the PEMFCs. However, for various classes of ORR catalysts, the detailed mechanism and the origin of activities require an in-depth understanding. This chapter focuses on the application of density functional theory (DFT) methods in investigating the activity and stability of ORR electrocatalysts to advance the PEMFC performance. The authors systematically reviewed the descriptors to evaluate the catalyst activity, such as adsorption properties of ORR intermediates, potential energy surfaces, reversible potentials, reaction barriers, and catalyst electronic structures. They also discussed various methods implemented to evaluate the ORR stabilities, such as metal dissolution potentials, metal cohesive energies, and binding energies of metal in the active sites.

## 11.1 Introduction

The fuel cells are electrochemical devices that spontaneously convert the chemical energy of a fuel into electrical energy by electrochemical reactions. One family of the fuel cells, known as proton exchange membrane fuel cells (PEMFCs), is considered a potential future power source due to their ability to generate electrical energy using flexible fuel supplies with negligible harmful emissions. Currently, a key obstacle in the wide commercialization of the PEMFC platform is the high cost of component materials, specifically the platinum (Pt)-based electrocatalysts to mediate the oxygen reduction reaction (ORR) at the cathode. The ORR is a very complex process under the electrochemical conditions. This ORR involves multi-electrons, various intermediates, and many possible reaction pathways [1, 2]. Although many different experimental characterization technologies such as X-ray photoemission spectroscopy (XPS) [3], ultraviolet photoemission spectroscopy (UPS) [4], and electron energy loss spectroscopy (EELS) [5] have been employed to study the ORR process, the nature of mechanism still requires an in-depth investigation. The density functional theory (DFT) method is a valid tool complementing state-of-the-art experimental techniques. The DFT can provide important insights to understand the adsorption properties, reaction thermodynamics and kinetics, and electronic structure at catalyst/gas interfaces. Theoretical modeling is becoming an indispensable tool in the electrochemical area.

In the current field of catalyst study, the researchers implement the theoretical modeling not only to explain some experimental results but also to design new efficient ORR catalysts. This requires researchers to find out the nature of the ORR catalysis process. There are two key perspectives, including what determines the performance of a catalyst and what indicators could be used to evaluate an unknown ORR catalyst. Through extensive theoretical research on many catalyst materials, which have been well-defined structures, such as face-centered cubic (*fcc*) Pt, transition metal

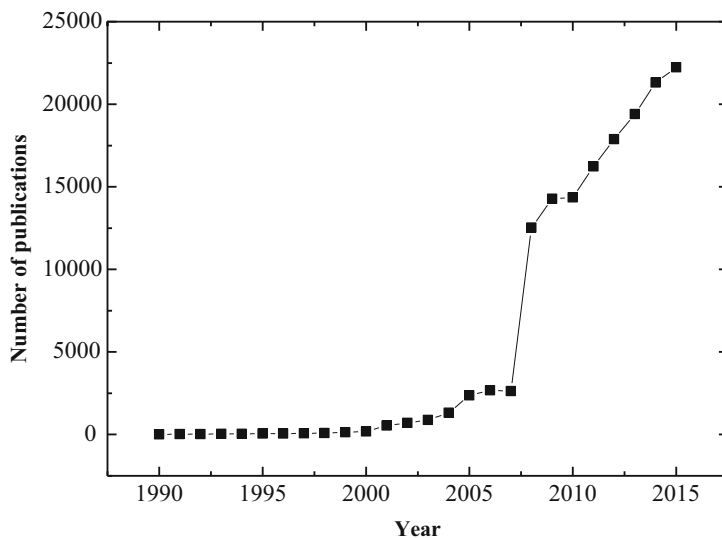
macrocyclic complexes, and graphene. One could obtain some useful parameters to evaluate whether a material has potential to serve as an ORR catalyst or not.

This chapter focuses on the application of DFT methods to investigate the activities and stabilities of the ORR electrocatalysts with an aim to improve PEMFC performance. As mentioned previously, some descriptors to evaluate the catalyst activity will be reviewed. To restate, these descriptions consist of adsorption properties of ORR intermediates, potential energy surfaces, reversible potentials, reaction barriers, and catalyst electronic structures. In addition, various methods to evaluate the ORR stabilities will be also illustrated. These methods are mainly metal dissolution potentials, metal cohesive energies, and binding energies of metal in the active sites.

## 11.2 Density Functional Theory Methods

The DFT approach has become increasingly the method of the choice for the solution of large systems, not only because of its sufficiently high accuracy but also its computational simplicity. Figure 11.1 shows the number of publications using DFT methods from 1990. The publications are based on the search from Web of Science database using “density functional theory” or “DFT” as the keywords. It can be clearly seen that the number of publications is increasing every year and a dramatic increase is observed starting from the year 2008. The DFT methods are no doubt becoming widely used by computational chemists.

In the DFT methods, the total energy of a many-electron system is considered as a function of its density only. By using the variation principle, a one-particle Schrödinger-like equation, i.e., the Kohn-Sham equation with an effective potential,



**Fig. 11.1** A number of publications that employ DFT each year

is obtained [6]. Since the exact form of the exchange-correlation function for an inhomogeneous electron gas is still unknown, several different types of approximate functions such as local-density approximation (LDA) and generalized gradient approximation (GGA) are used. The LDA is very successful for many systems, but LDA fails in systems where weak molecular bonds exist. To account for the inhomogeneity of the electron density, a nonlocal correlation is often added to the exchange energy; this is the so-called GGA [7]. There are many exchange-correlation functionals such as *Perdew 86* (P86, LDA); *Perdew and Wang 91* (PW91, GGA); *Becke-Perdew-Wang 91* (BPW91, exchange functionals); *Lee-Yang-Parr* (LYP, GGA); *Becke-Lee-Yang-Parr* (BLYP, hybrid functionals); *Perdew-Burke-Ernzerhof* (PBE, GGA); and *Becke, three-parameter, Lee-Yang-Parr* (B3LYP, hybrid functionals) correlation or exchange functionals. In general, as the exchange-correlation functionals contain both exchange and Coulomb correlation terms, the DFT methods could provide better results for most reaction systems.

---

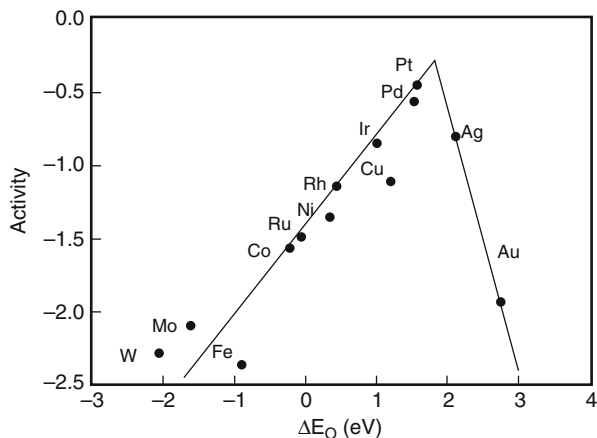
## 11.3 Methods to Evaluate ORR Activity

### 11.3.1 Binding Energy of ORR Intermediates

As is well known that Pt is the best catalyst material for the ORR, its catalytic process has been extensively studied both by experiment and by computational modeling. Yeager proposed two mechanistic pathways for the ORR in acidic medium [8]: (1) a “direct” four-electron pathway where  $O_2$  is reduced directly to water without involvement of hydrogen peroxide ( $H_2O_2$ ), which was summarized as  $O_2 + 4H^+ + 4e^- \rightarrow 2H_2O$ , and (2) a “series” pathway in which  $O_2$  is reduced to  $H_2O_2$ , which was also summarized as  $O_2 + 2H^+ + 2e^- \rightarrow H_2O_2$  followed by its further reduction to  $H_2O$ , proceeded by the following reaction,  $H_2O_2 + 2H^+ + 2e^- \rightarrow 2H_2O$ . The above two pathways can be processed via the intermediate OOH, O, and OH. Since there is no simple adequate spectroscopic method for identifying the adsorbed intermediates, computational studies can be used to investigate the structures and adsorption properties of reduction intermediates. Nørskov et al. found that the binding energy of O is a good parameter to describe ORR activity of Pt and other transition metal catalysts [9]. An activity volcano plot with an excellent coefficient of correlation appears, as shown in Fig. 11.2.

The volcano plot in Fig. 11.2 shows that Pt is indeed the best catalyst among all the pure metals; other metals have either stronger or weaker bonding to atomic O than Pt and as a result are poorer ORR catalysts. For example, Ni binds to atomic O so strongly on the surface that the bonding will lead to a slow proton-transfer step. In contrast, the weak bonding of atomic O on Au indicates that the barrier for molecular  $O_2$  dissociation is large, due to the fact that there is a linear dependence between the atomic O binding energy and the barrier for molecular  $O_2$  dissociation [10]. It can also be seen from Fig. 11.2 that pure Pt is not a perfect catalyst due to its higher than optimum binding energy. Metals with a somewhat lower atomic O binding energy than Pt should have a higher rate of oxygen reduction. This has already been

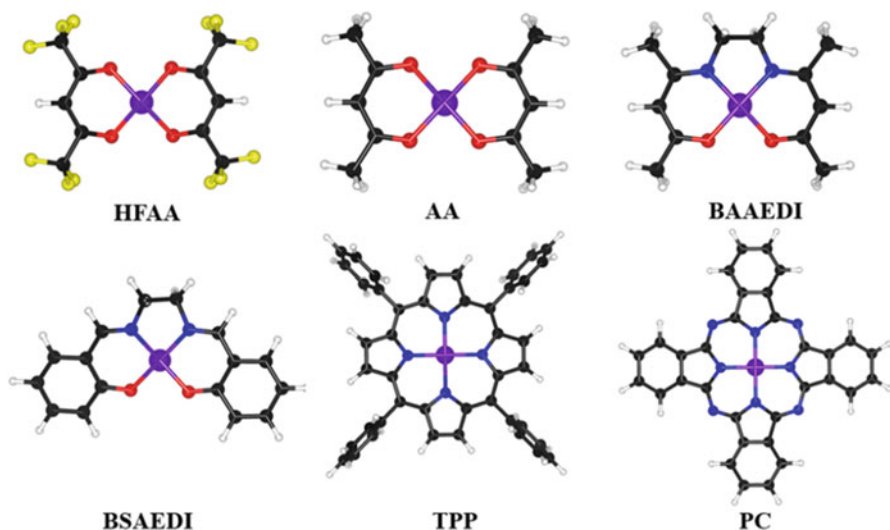
**Fig. 11.2** Trends in ORR activity plotted as a function of the O binding energy [9]



confirmed by experiment. For example, DFT calculations have shown that Pt alloys with Ni, Co, Fe, and Cr have smaller O binding energies than pure Pt [11, 12], and these alloys indeed have a higher ORR rate than pure Pt [13–15]. Nørskov also pointed out that the O binding energy is not the sole factor in determining the activity of a surface for ORR; the OH binding energy is another important consideration. Stephens et al. demonstrated that the OH binding energy can be used as an experimental descriptor for the surface activity of a catalytic reaction [16]. They confirmed that only a slight weakening of the OH binding energy, by  $\sim 0.1$  eV, relative to Pt{111}, will lead to approximately eightfold enhancement in ORR activity over Pt{111}. Lee et al. combined theoretical and experimental approaches to study the ORR activities of Pd alloys [17]. They implemented a simple trimer cluster model to calculate the binding energy of atomic O on these Pd-alloy catalysts. It was found that the Pd-Co alloy possesses the closest O binding energy to Pt in simple theoretical model calculations, suggesting the highest ORR activity. This prediction was further confirmed experimentally, suggesting that the single parameter of O binding energy can be a useful guide to developing non-Pt ORR catalysts. The obtained results have been confirmed on other families of catalysts, such as Fe-phthalocyanine and Co-phthalocyanine [18].

By using the atomic O binding energy as an activity descriptor, the candidacy of potential ORR catalysts can be evaluated. Recently, we investigated the catalytic ORR activity of various metal chelates by DFT methods [19]. Six chelating ligands, namely, hexafluoro-acetylacetonone (HFAA), acetylacetonone (AA), bis-acetylacetonone-ethylene-diimine (BAAEDI), bis-salicyl-aldehyde-ethylene-diimine (BSAEDI), tetraphenyl-porphine (TPP), and phthalocyanine (PC), were studied. The optimized structures of the cobalt chelates are shown in Fig. 11.3. The DFT results indicated that the ORR activity is determined by both the identity of the central metal ions and chelating ligands, whose unique combination influences the ORR. For the same ligand, the central metal ions Fe, Co, or Mn demonstrated high ORR activity, while the other combinations exhibited negligible catalytic activity. This trend may be explained by virtue of the molecular  $\text{O}_2$  and oxygen-containing species, which are





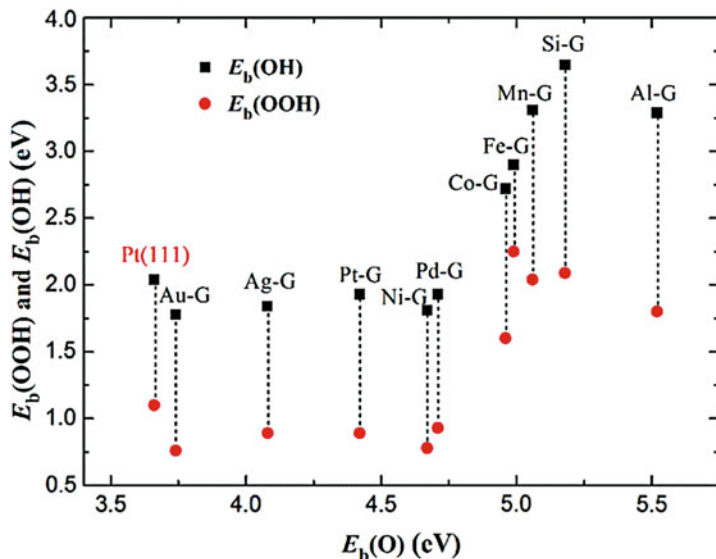
**Fig. 11.3** Optimized structures of cobalt chelates. The purple circles are cobalt atoms, the blue circles are nitrogen atoms, the black circles are carbon atoms, the red circles are oxygen atoms, the yellow circles are fluorine atoms, and the white circles are hydrogen atoms

either excessively adsorbed (on central Cr) or difficult to be adsorbed on the active sites (for central Zn, Cu, or Ni).

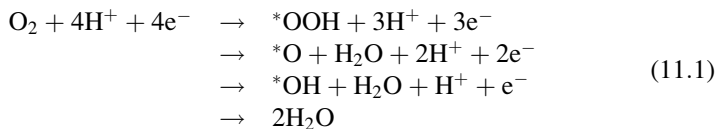
As discussed above, a single atomic O binding energy provides a facile method to evaluate ORR catalysts. The ability to port this DFT functional to an arbitrary catalyst was investigated by using metal-doped graphene as a model catalyst and using DFT to compute the ORR [20]. Ten different metal atoms, namely, Al (main block); Si (semiconductor); Mn, Fe, Co, and Ni (3d block); Pd and Ag (4d block); and Pt and Au (5d block) elements, respectively, were incorporated into surface vacancies on graphene to generate as yet unsynthesized metal-doped graphene constructs. The results indicated that the binding energies of atomic O and OH do not exhibit a linear dependence, relative to each other, which is different to the linear dependence found on metal surfaces. Furthermore, for Ni-doped graphene, the linear relationship is not possible, as shown in Fig. 11.4. These findings suggested that the value of O or OH binding energy alone is not sufficient to evaluate the catalytic activity of a catalyst, especially of nonmetal materials. This requires us to find other parameters and/or methods, such as the calculation of the potential energy surface.

### 11.3.2 Potential Energy Surface

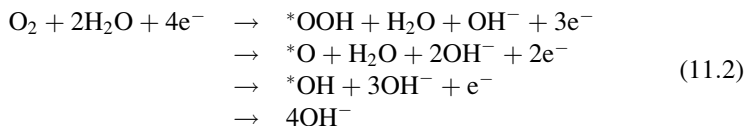
To analyze the potential energy surface, the relative energies of reaction intermediates in the ORR processes must be calculated. Generally, the electrochemical ORR from  $O_2$  to  $H_2O$  in an acid solution is proceeded as:



**Fig. 11.4** Binding energy variation of OOH and OH with O [20]

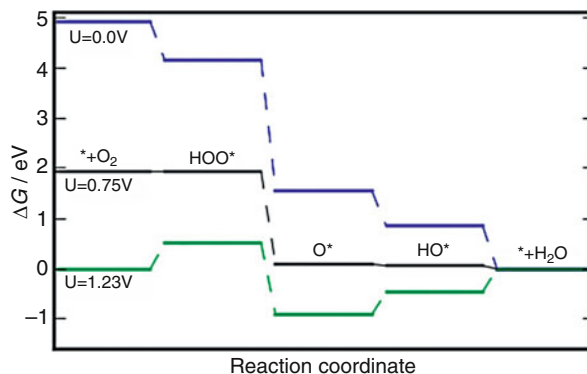


In an alkaline solution, the same processes can be expressed as:



From the above equations, it was hypothesized that the adsorbed intermediates along the reaction coordinate are independent of the concentration of protons. The only change is the chemical potential of the protons and that the proton donor changes from being  $H^+$  in an acid solution to being  $H_2O$  in an alkaline solution. Based on the theoretical electrochemistry method [9, 21, 22], the potential energy of the intermediates on the Pt{111} can be obtained at a given potential, as shown in Fig. 11.5. A perfect catalyst should be characterized by all steps having the same height at zero potential, i.e., by a flat potential energy landscape at the equilibrium potential. As can be seen, some steps have larger free energy changes than others, meaning that Pt is not a perfect catalyst for the ORR. Another application of potential energy surface profile is for estimating the highest ORR potential  $U_{rev}$ . We can define the  $U_{rev}$  at which all steps are just

**Fig. 11.5** The free energy of the intermediates along ORR on Pt{111} [21]

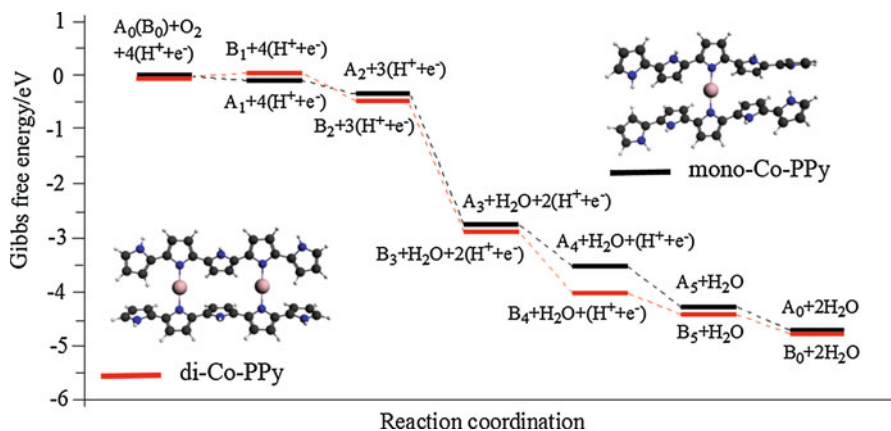


downhill in the potential energy landscape. The higher the  $U_{\text{rev}}$  is, the better the catalyst.

In addition to the application to Pt, this method has also been successfully applied to other materials, such as transition metal-doped conductive polymer [23, 24], M-N<sub>x</sub> (M = Fe, Co, Ni;  $x = 1-4$ ) embedded graphene [25, 26], and metal oxide catalysts [27, 28]. For example, we investigated the ORR catalyzed by cobalt-polypyrrole catalysts, demonstrating the active site structure and the origin of the catalytic activity [23]. We constructed two cobalt-polypyrrole models, one contains ten pyrrole rings with only one Co atom (mono-Co-PPy), and the other contains ten pyrrole rings with two Co atoms (di-Co-PPy). The potential energy surface of ORR on the two catalysts is shown in Fig. 11.6. It can be clearly seen that the relative total energy of each ORR step of mono-Co-PPy is higher than that for di-Co-PPy. The largest energy difference between these two systems is in the third reduction step ( $*\text{O} + \text{H}^+ + \text{e}^- \rightarrow *\text{OH}$ ). Therefore, the ORR steps catalyzed by di-Co-PPy are energy favored compared with those catalyzed by mono-Co-PPy. Further structural analysis showed that the dihedral angles between the pyrrole units have no regular pattern for mono-Co-PPy. But for di-Co-PPy, the angles show a perfect arrangement. This kind of structure of di-Co-PPy is helpful in electron transfer in its chain and makes the nitrogen atoms become active and the donation site of electrons to the ORR process. Therefore, a Co-PPy catalyst containing many cobalt atoms between two long PPy chains with periodic structure should show the good catalytic ability for ORR.

### 11.3.3 Linear Gibbs Energy Relationship to Determine Reversible Potentials

As discussed above, potential energy surface can provide much useful information regarding the reaction details, such as the free energy and the highest ORR potential. Anderson's group has developed a simple theoretical approach for calculating the reversible potentials [29–39]. From the calculated bond strengths of ORR



**Fig. 11.6** Potential energy surface for the ORR of the two reaction systems [23]

intermediates, reversible potentials can be determined using a linear Gibbs energy relationship. Consider an electrochemical reaction at equilibrium described in Eq. 11.3:



The linear Gibbs energy relationship for this reaction has the form described in Eqs. 11.4 and 11.5:

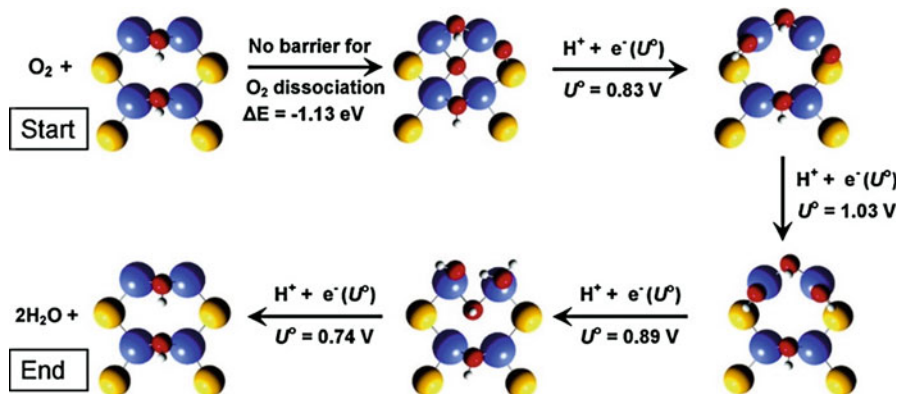
$$\Delta G_{\text{rev}} = \Delta G^\circ - \Delta E(\text{adsorption}) \quad (11.4)$$

and

$$U_{\text{rev}} = U^\circ + \Delta E(\text{adsorption})/nF \quad (11.5)$$

where  $\Delta G^\circ$  is the standard Gibbs energy change of reaction,  $\Delta E$  (adsorption) is the total adsorption bond strength of the products minus the total adsorption bond strength of the reactants,  $n$  is the number of the electrons transferred,  $F$  is the Faraday constant, and  $U^\circ$  is the standard solution-phase potential. Based on this approximate Eq. 11.5, the adsorption bond strengths can be used to make predictions of reversible potentials. On the basis of comparisons of predictions using this model with experimental measurements, the reversible potentials made using the model have errors of  $\sim 0.2$  V.

The above linear Gibbs energy relationship has been successfully applied to many ORR catalysts. For example, Sidik and Anderson investigated the ORR reversible potentials on  $\text{Co}_9\text{S}_8$  catalyst [33]. They predicted the steps of the ORR cycle on the partially OH-covered surface. The results are shown in Fig. 11.7. They found that after the first reduction at 0.83 V, the O on sulfur is reduced spontaneously to adsorbed OH



**Fig. 11.7** The reduction cycle for  $\text{O}_2$  on the partially OH-covered surface of  $\text{Co}_9\text{S}_8$  [33]

because its reversible potential is higher, 1.03 V. The sequential reduction of the adsorbed OH to  $\text{H}_2\text{O}$  occurs at relatively favorable potentials of 0.89 and 0.74 V, respectively. The 0.74 V step determines the overpotential for the overall four-electron ORR, suggesting that partially OH-covered surface is active toward ORR and should have overpotential behavior similar to that observed for Pt catalysts. Based on the above results, they concluded that an even better catalyst will be one to which  $\text{O}_2$  bonds and dissociates with less released heat.

Very recently we investigated the ORR catalyzed by B and N-doped  $\alpha$ - and  $\gamma$ -graphyne catalysts and predicted their ORR reversible potentials based on linear Gibbs energy relationship; some results are shown in Table 11.1 [40]. Our results indicated that the B and N single-doped  $\alpha$ -graphynes showed relatively low catalytic activities, owing to some unfavorable reversible potential in their ORR steps, while doped  $\gamma$ -graphyne could display ORR performance. We also found that co-doping with separated B and N could convert low active  $\alpha$ -graphyne to the active form. However, the activity of bonded B and N co-doped  $\alpha$ -graphyne ( $\alpha$ - $\text{B}_1\text{N}_2\text{G}$ ) was still low due to an unfavorable reduction potential in the last step, which was similar to that observed on doped carbon nanotubes (CNTs). We further determined that increasing the nitrogen contents in separated B and N co-doped constructs could effectively improve the onset potential as well as the electrocatalyst efficiency.

### 11.3.4 Reaction Barrier of ORR

Generally, to investigate the detailed reaction mechanism and to predict the catalytic performance of an ORR catalyst, the reaction barrier of each elementary step should be calculated and be analyzed. But unfortunately, only a few literature reports have been published in this direction. Anderson and Albu [41] carried out theoretical studies of activation energies for uncatalyzed ORR. The electrode was modeled by a non-interacting electron donor molecule with a chosen ionization potential. To locate

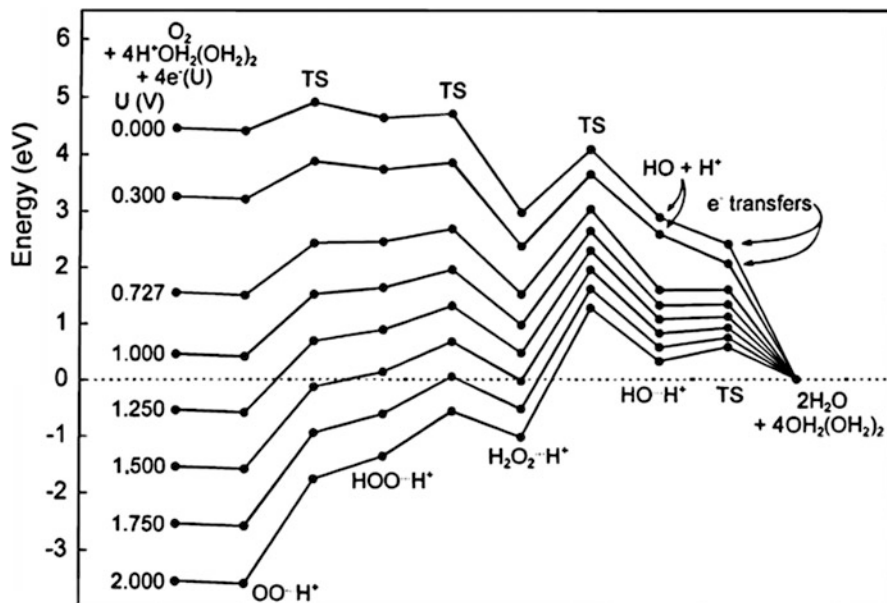
**Table 11.1** Standard reversible potential and reversible potential for each ORR step on the studied models [40]

$U_{\text{rev}}$ (V/SHE)									
Reaction step	$U^\circ$ (V/SHE)	$\alpha$ -B <sub>1</sub> G	$\alpha$ -N <sub>2</sub> G	$\alpha$ -B <sub>1</sub> N <sub>2</sub> G	$\alpha$ -B <sub>1</sub> N <sub>3</sub> G	$\alpha$ -B <sub>1</sub> N <sub>4</sub> G	$\alpha$ -B <sub>1</sub> (N <sub>4</sub> ) <sub>3</sub> G	$\gamma$ -BG	$\gamma$ -NG
1	-0.125	0.565	0.96	0.985	0.898	0.699	0.78	0.858	0.498
2	0.21	4.052	2.932	3.038	3.044	3.091	1.658	3.058	0.324
3	2.12	-0.234	0.966	1.039	0.957	0.829	2.074	0.793	3.534
4	2.72	0.542	0.067	-0.137	0.026	0.306	0.413	0.216	0.569
Overall	1.23	1.23	1.23	1.23	1.23	1.23	1.23	1.23	1.23

the transition state, the potential surface scan was deployed. Once the transition state was located, the energy difference between the transition state structure and reactant energy was taken as the activation energy. They calculated the activation energy of the four-electron transfer steps. The electron transfer was assumed to occur when the electron affinity of the reaction complex equaled the ionization potential of the electrode. They studied activation energies for the four-electron transfer steps at potentials ranging between 0 and 2 V (vs. standard hydrogen electrode, SHE). The results in Fig. 11.8 showed that as the electrode potential increases, the activation barriers also increased. The third electron and proton-transfer step has the highest activation energy. From their calculation results, it was evident that an efficient four-electron ORR electrocatalyst must not liberate hydrogen peroxide but activate the first and third reduction steps without deactivating the other two steps. The complete dissociation of HOOH on the electrode surface should lead to good activity, based on the low activation energy calculated for adsorbed OH reduction.

The Anderson group employed a similar method to study the catalytic effect of Pt on ORR. A single Pt atom was used to model the system. The results suggested that the Pt atom had a significant catalytic effect on the most difficult step of the ORR, i.e.,

$\text{H}_2\text{O}_2 \rightarrow \text{OH} + \text{H}_2\text{O}$ . Activation energies dropped about 1 eV over the 0–2 V potential range. The activation energies for the other reduction steps are also substantially reduced. In all cases, the activation energies are predicted to increase with increasing potential. In order to simplify the calculations, the neutral H atom instead of  $\text{H}^+$  proton was used to investigate the proton-transfer activation energy because the whole reaction system was charged neutral [42–46]. For example, Kattel and Wang studied the reaction pathway for ORR on  $\text{FeN}_4$  embedded graphene [46]. The adsorption sites of intermediates and the possible reaction pathways are shown in Fig. 11.9. Their DFT results indicated that the rate-determining step is the molecular  $\text{O}_2$  dissociation reaction with an activation energy of 1.19 eV in the molecular  $\text{O}_2$  dissociation pathway, the OOH dissociation reaction with an activation energy of 0.56 eV in the OOH dissociation pathway, and the OH diffusion step with an activation energy of 1.15 eV in the HOOH dissociation pathway. Therefore, the OOH dissociation pathway is the kinetically most favorable one to follow on the  $\text{FeN}_4$  embedded graphene. Compared with the activation energy of the rate-

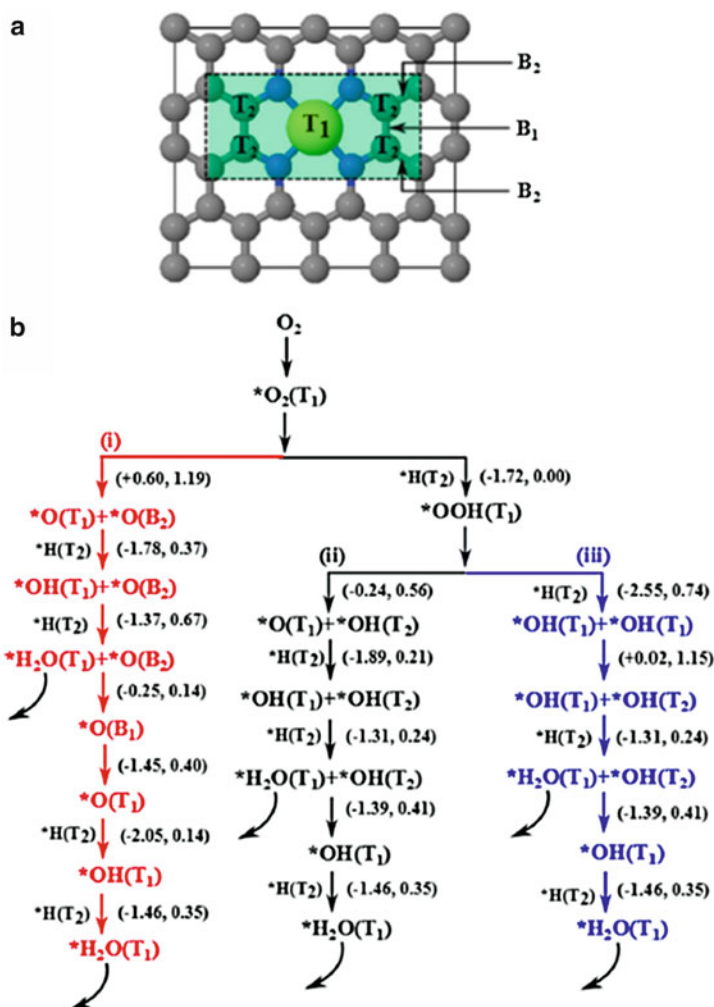


**Fig. 11.8** Energies as functions of electrode potential for the reaction system from beginning to end of the ORR [41]

determining step on the Pt{111} (0.79 eV) and Pt{100} surfaces (0.80 eV), they concluded that the FeN<sub>4</sub> embedded graphene possesses the catalytic activity for ORR comparable to (or greater than) that of precious Pt catalysts.

### 11.3.5 Catalyst Electronic Structure

As discussed above, some parameters, such as atomic O binding energy is a good descriptor of the ORR activity of a given surface in many cases, the question arises as to which property of the catalyst determines the ORR the most accurately. For metal-based catalysts, it was well-established that surface bond energies correlate with the average energy of the d states on the surface atoms to which the adsorbate binds (the d-band center) [47–51]. For example, Stamenkovic et al. investigated the ORR on polycrystalline alloy films of the type Pt<sub>3</sub>M (M = Ni, Co, Fe, and Ti) [51]. They measured the d-band center for all of the alloys by using synchrotron-based high-resolution photoemission spectroscopy (PES) and compared results with DFT-based calculations. They found that the ORR activity versus d-band center position at 0.9 V exhibited a classical volcano-shaped dependence, which agrees well with the activity predicted from DFT calculations. For the catalysts which bind to oxygen too strongly, the rate was limited by the removal of surface oxide, while for catalysts that bind oxygen too weakly, the rate was limited by the transfer of electrons and protons to adsorbed molecular O<sub>2</sub>.



**Fig. 11.9** Various adsorption sites and possible reaction pathways on the  $FeN_4$  embedded graphene [46]

For nonmetal catalysts, it was demonstrated that the energy gap between the highest occupied molecular orbital (HOMO) and the lowest unoccupied molecular orbital (LUMO) can be used to evaluate the chemical reactivity of a catalyst. A small HOMO-LUMO gap (HLG) implies low kinetic stability and high chemical reactivity [52]. In addition, for an ORR electrocatalyst, the energy level of the HOMO is also important because the electrons would be transferred to the  $O_2$  molecule to weaken the O-O bond. The above point of view has been illustrated in some of our works [53–55]. For example, we studied the ORR activity and the mechanism on doped



single-walled  $\gamma$ -graphyne nanotubes (GNTs) [55]. Four of the most commonly used doping elements, N, B, P, and S atoms, were used to investigate the doping effects. The electronic structure analysis showed that the N-GNT had the highest ORR catalytic activity among the studied catalysts, but its HLG (energy gap between LUMO and HOMO levels) is still relatively too small (or the HOMO level is too high), which leads to a relatively strong binding energy of ORR species. However, too large HLG would lead to too weak adsorption, just like the case of the S-GNT. Therefore, we concluded that if the GNT-based ORR catalysts will possess the catalytic activity comparable to that of Pt, their HLG and/or HOMO levels should be in the range between that of N- and S-GNTs. Similarly, Zhang and Xia studied the origin of the ORR activity catalyzed by N-doped graphene [56]; the results of charge distribution and spin density distribution on this catalyst are shown in Fig. 11.10. Their results suggested that both the atomic charge densities and spin densities can play roles in determining the catalytic activity. Substituting N atoms in N-graphene can lead to the asymmetry in spin densities and atomic charge densities, thus making it possible for N-graphene to show high electrocatalytic activities for the ORR.

## 11.4 Methods to Evaluate ORR Stability

### 11.4.1 Metal Dissolution Potential

An efficient ORR catalyst should not only have the high activity but also high catalytic stability under electrochemical conditions. The ORR stability of Pt-based materials has been extensively studied. It was demonstrated by Shao et al. that the Pt nanoparticle with a particle size of  $\sim 2.2$  nm would exhibit the maximum mass activity [57]. But unlike bulk Pt, the structural and electrochemical integrities of Pt nanoparticles are not fixed when they are exposed to acid solutions and high electrode potentials. It was reported that the Pt nanoparticles of less than 3 nm sizes can dissolve in acid media [58]. Since the electrochemical dissolution of catalyst atoms is directly related to the catalytic stability, an accurate understanding of the electrochemical degradation process at the atomic scale is an important step toward the development of high-stability catalysts. Han and co-workers investigated the electrochemical stability of Pt and Pt-based nanoparticle catalysts [59–61]. For pure Pt particles, they used Eq. 11.6 to calculate the dissolution potential:

$$U_{\text{diss}} = U_{\text{bulk}} + \frac{1}{2me} \{E(\text{Pt}_{n-m}) + mE(\text{Pt}_{\text{bulk}}) - E(\text{Pt}_n)\} \quad (11.6)$$

where  $U_{\text{diss}}$  is the dissolution potential of the nanoparticle;  $U_{\text{bulk}}$  is the dissolution potential of bulk Pt;  $E(\text{Pt}_n)$  and  $E(\text{Pt}_{n-m})$  are the total energies of nanoparticles consisting of  $n$  and  $n-m$  Pt atoms, respectively; and  $E(\text{Pt}_{\text{bulk}})$  is the energy per atom of bulk Pt. The calculated dissolution potentials of Pt nanoparticles were plotted as a function of the size of the initial model system, as shown in Fig. 11.11 [59]. The candidate with the lowest dissolution potential was selected for simultaneous

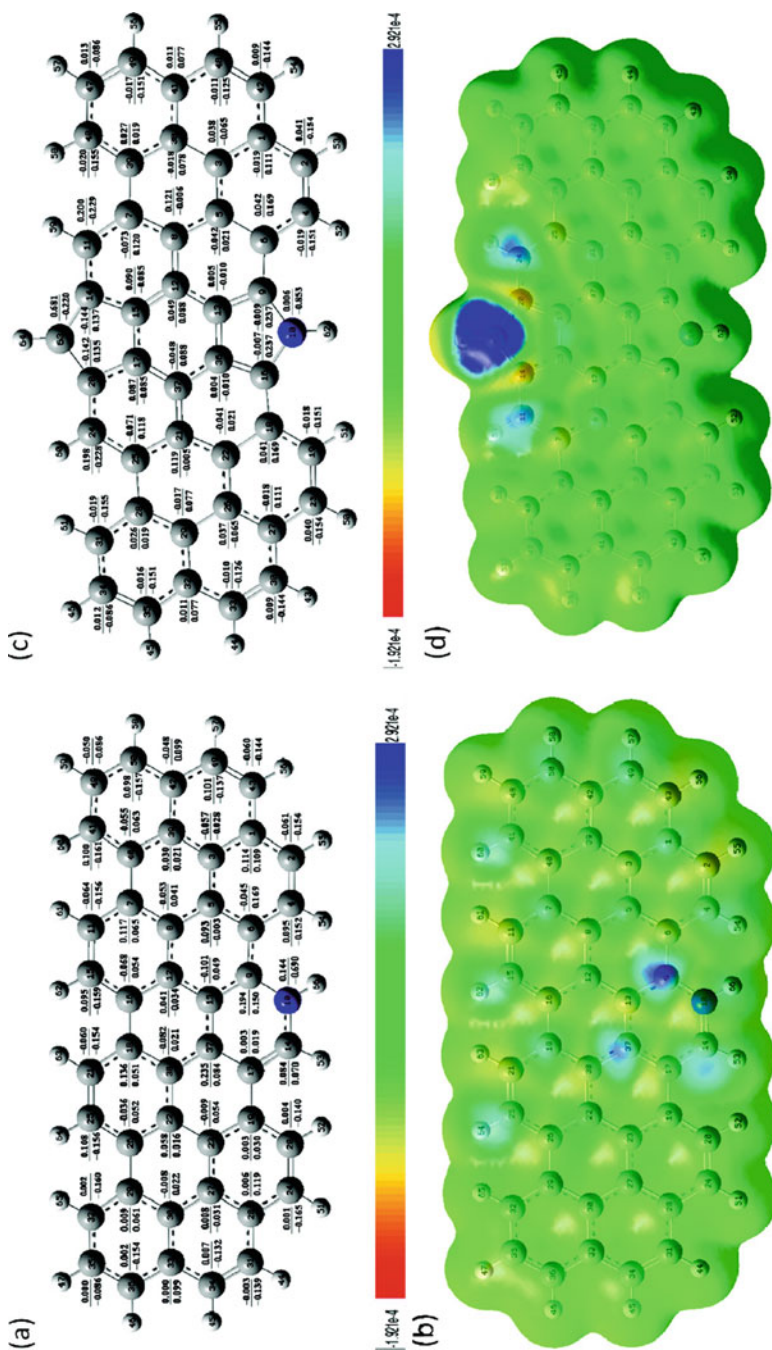
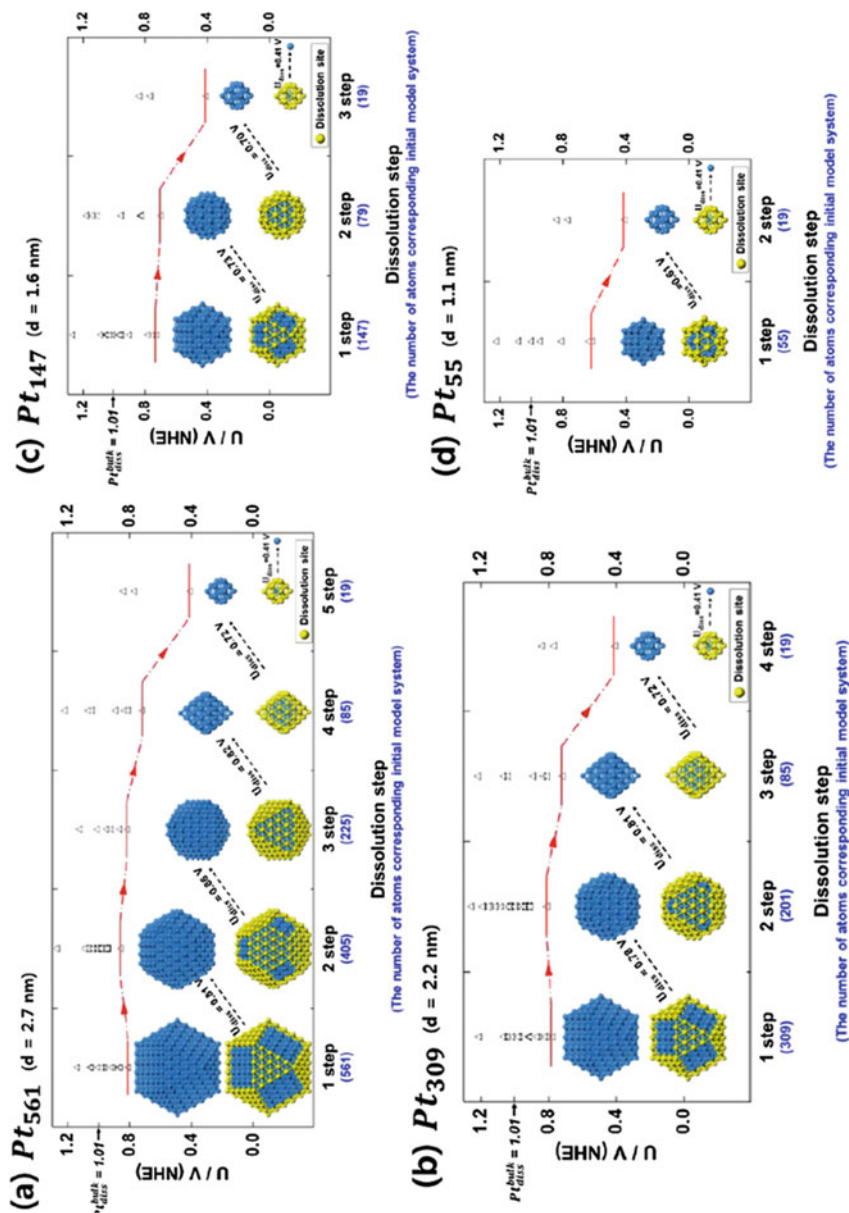


Fig. 11.10 Charge distribution and spin density distribution on the N-graphene [56]



**Fig. 11.11** The electrochemical dissolution of the nanoparticle (diameters of model systems were 2.7, 2.1, 1.6, and 1.1 nm) [59]

removal of the atomic sites marked in yellow in Fig. 11.11. The nanocluster thus obtained served as the initial model system for the next dissolution step. The procedure was continued until a single atom remained. Their results indicated that for model systems Pt<sub>561</sub> and Pt<sub>309</sub>, the nanoparticle obtained after the first step is more durable than the model system itself, but the dissolution potential subsequently decreases rapidly as the nanoparticle size also decreases. Therefore, it seems that in addition to the surface energy, the thermodynamics of the dissolution mechanism also influenced by the size of the nanoparticle. In general, the Pt nanoclusters with sizes smaller than approximately 3 nm have electrochemical stabilities weaker than that of bulk Pt (1.01 V relative to SHE).

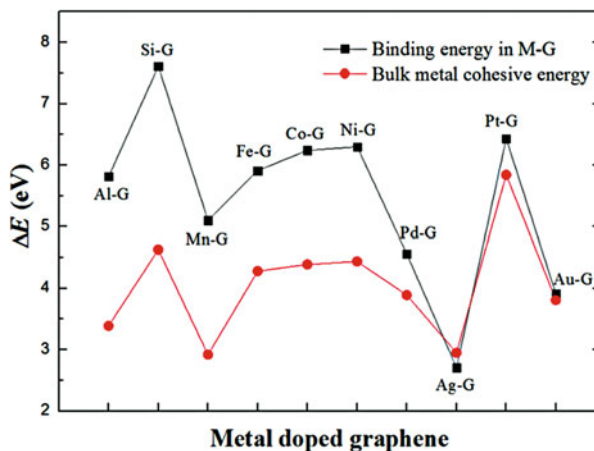
### 11.4.2 Metal Cohesive Energies

During the electrochemical dissolution process, the metal atoms could migrate from the surface of the material into the solution and thus create surface vacancies. This degradation process is thought to be addressed by studying the surface cohesive energy of Pt atoms [62]. The surface cohesive energy can be directly related to the dissolution energy, and the change in dissolution energy can be further related to the change in dissolution potential. Matanovic et al. used surface cohesive energy to investigate the stability of PtNi alloy, Pt nanotubes, and nanowires [63–65]. Their results indicated that the Pt nanotubes with a smaller diameter of ~0.5 nm have a much lower surface cohesive energies than the bulk Pt and thus will dissolve at much lower potentials. Most of the larger tubes with the diameter of ~1 nm have higher surface cohesive energies than the smaller tubes, but their stability is still lower than the bulk Pt. In contrast, both Pt<sub>3</sub>Ni and PtNi alloys were demonstrated to have higher surface cohesive energies than Pt, and it can thus be expected that the alloy will have a lower thermodynamic predisposition to electrochemical dissolution relative to Pt. For small metal clusters, the cluster cohesive energy is also a commonly used descriptor of stability. It is usually calculated as the difference between the energy of the cluster and the sum of the energies for each component atom within the cluster, calculated with the same functional and basis set [66, 67] based on correlation, exchange, or hybrid functionals. Zanti and Peeters investigated the stability of Pd<sub>n</sub> clusters [68]. They found that the cohesive energy increased with the cluster size. However, the increase was not constant and was attenuated with the cluster size, tending at the limit to an asymptotic behavior. It may be explained by noting the sphere of coordination of palladium atoms tends to a limit as the cluster nuclearity increases.

### 11.4.3 Binding Energies of Metal in the Active Sites

The methods to evaluate the catalyst stability are usually applied to metal-based materials. For nonmetal catalysts such as M-N<sub>x</sub>/C, the commonly used methods are

**Fig. 11.12** The binding energy of metal incorporated into graphene and the corresponding cohesive energy of bulk metals [20]



calculating the binding energies of metal in the active sites or the energies for removal of the metal from the active sites. Also, using metal-doped graphene as an example [20], we determined the binding energy. Our calculated binding energy of the metal atoms incorporated into the vacancy and then comparison of these values with the corresponding cohesive energy of bulk metals are summarized in Fig. 11.12. The results show that the binding energy of a metal incorporated into the vacancy is higher than the corresponding bulk metal cohesive energy. Interestingly, the variation of the calculated binding energy is very similar to that of bulk metal cohesive energy, namely, if a metal possesses a larger cohesive energy, then the corresponding M-G will generally possess a higher binding energy. These results indicated that a strong metal-carbon hybridization could be formed in M-G structures, making them very thermodynamically stable and thus avoiding metal dissolution from the active site. In other words, the stability of the screened M-G structures is even higher than that of the bulk metal surfaces. Note that electrochemical ORR is a complex process; the stability of a catalyst can be affected by many factors. For example, the stability of a catalyst depends not only on its electronic nature but also on the practical catalytic conditions and processes. The binding energy is only one of the parameters to simply evaluate the stability of M-G catalysts.

In addition to calculating the binding energy of the metal in the active sites, Lu et al. performed first-principle molecular dynamics calculations to investigate the stability of  $\text{MnN}_4$  embedded graphene [69]. In a time period of 1000 fs (1 ps) calculations at the temperature of 300 K, 500 K, 800 K, and 1000 K, the Mn, N, and C atoms are almost in the same plane with slight distortion. The  $\text{MnN}_4$  embedded graphene can be even stable to a period of 2 ps at 1000 K with only very slight distortion over time. These results indicated that the structure of the  $\text{MnN}_4$  embedded graphene was highly stable and can play roles in efficient ORR process.

## 11.5 Conclusions

In summary, we reviewed the application of DFT methods in investigating the activity and stability of ORR electrocatalysts for PEMFC. Some descriptors and methods to evaluate the catalyst performance (activity and stability) are discussed. These related research provide a better understanding of the catalytic mechanism to assist in the design of proposed novel ORR electrocatalysts. Furthermore, unlike the experimental methods that usually tend to become more expensive with time, the computational methods will become cheaper as computational power increases. Therefore, with the rapid progress of new electronic structure theory and computational methods, the computational approaches for the discovery and development of efficient catalysts hold great promise in the future.

**Acknowledgments** This work is supported by the National Natural Science Foundation of China (Agreement code No. 51602270). Two publications *Lecture Notes in Energy*, Volume 9 (2013), *Electrocatalysis in Fuel Cells: A Non- and Low-Platinum Approach*, and Screening of catalytic oxygen reduction reaction activity of metal-doped graphene by density functional theory, *Applied Surface Science* Volume 379, 30 August 2016, pages 291–295, have been cited and are duly acknowledged. The authors appreciated the scientists who described useful views that were cited in this chapter.

---

## References

1. A.J. Appleby, Electrocatalysis of aqueous dioxygen reduction. *J. Electroanal. Chem.* **357**(1–2), 117–179 (1993)
2. N.M. Markovic, P.N. Ross Jr., Surface science studies of model fuel cell electrocatalysts. *Surf. Sci. Rep.* **45**(4–6), 117–229 (2002)
3. A.C. Luntz, M.D. Williams, D.S. Bethune, The sticking of O<sub>2</sub> on a Pt(111) surface. *J. Chem. Phys.* **89**(7), 4381–4395 (1988)
4. J. Grimbolt, A.C. Luntz, D.E. Fowler, Low-temperature adsorption of O<sub>2</sub> on Pt(111). *J. Electron Spectrosc. Relat. Phenom.* **52**, 161–174 (1990)
5. B.A. Sexton, Identification of adsorbed species at metal-surfaces by electron-energy loss spectroscopy (EELS). *Appl. Phys. A Mater. Sci. Process.* **26**(1), 1–18 (1981)
6. E. Jensen, R.A. Bartynski, T. Gustafsson, E.W. Plummer, Angle-resolved photoemission study of the electronic structure of beryllium: bulk band dispersions and many-electron effects. *Phys. Rev. B* **30**(10–15), 5500–5507 (1984)
7. X. Chen, D. Xia, Z. Shi, J. Zhang, Theoretical study of oxygen reduction reaction catalysts: from Pt to non-precious metal catalysts, in *Electrocatalysis in Fuel Cells*, ed. by M. Shao (Ed), (Springer, London, 2013), pp. 339–373
8. E. Yeager, Electrocatalysts for O<sub>2</sub> reduction. *Electrochim. Acta* **29**(11), 1527–1537 (1984)
9. J.K. Nørskov, J. Rossmeisl, A. Logadottir, L. Lindqvist, J.R. Kitchin, T. Bligaard, H. Jonsson, Origin of the overpotential for oxygen reduction at a fuel-cell cathode. *J. Phys. Chem. B* **108**(46), 17886–17892 (2004)
10. J.K. Nørskov, T. Bligaard, A. Logadottir, S. Bahn, L.B. Hansen, M. Bollinger, H. Bengaard, B. Hammer, Z. Sljivancanin, M. Mavrikakis, Y. Xu, S. Dahl, C.J.H. Jacobsen, Universality in heterogeneous catalysis. *J. Catal.* **209**(2), 275–278 (2002)
11. Y. Xu, A.V. Ruban, M. Mavrikakis, Adsorption and dissociation of O<sub>2</sub> on Pt–Co and Pt–Fe alloys. *J. Am. Chem. Soc.* **126**(14), 4717–4725 (2004)

12. J.R. Kitchin, J.K. Nørskov, M.A. Barteau, J.G. Chen, Modification of the surface electronic and chemical properties of Pt(111) by subsurface 3d transition metals. *J. Chem. Phys.* **120**(21), 10240–10246 (2004)
13. U.A. Paulus, A. Wokaun, G.G. Scherer, T.J. Schmidt, V. Stamenkovic, V. Radmilovic, N.M. Markovic, P.N. Ross, Oxygen reduction on carbon-supported Pt-Ni and Pt-Co alloy catalysts. *J. Phys. Chem. B* **106**(16), 4181–4191 (2002)
14. M. Min, J. Cho, K. Cho, H. Kim, Particle size and alloying effects of Pt-based alloy catalysts for fuel cell applications. *Electrochim. Acta* **45**(25–26), 4211–4217 (2000)
15. M. Neergat, A.K. Shukla, K.S. Gandhi, Platinum-based alloys as oxygen-reduction catalysts for solid-polymer-electrolyte direct methanol fuel cells. *J. Appl. Electrochem.* **31**(4), 373–378 (2001)
16. I.E.L. Stephens, A.S. Bondarenko, F.J. Perez-Alonso, F. Calle-Vallejo, L. Bech, T.P. Johansson, A.K. Jepsen, R. Frydendal, B.P. Knudsen, J. Rossmeisl, I. Chorkendorff, Tuning the activity of Pt(111) for oxygen electro-reduction by sub surface alloying. *J. Am. Chem. Soc.* **133**(14), 5485–5491 (2011)
17. K.R. Lee, Y. Jung, S.I. Woo, Combinatorial screening of highly active Pd binary catalysts for electrochemical oxygen reduction. *ACS Comb. Sci.* **14**(1), 10–16 (2012)
18. R. Chen, H. Li, D. Chu, G. Wang, Unraveling oxygen reduction reaction mechanisms on carbon-supported Fe-phthalocyanine and Co-phthalocyanine catalysts in alkaline solutions. *J. Phys. Chem. C* **113**(48), 20689–20697 (2009)
19. X. Chen, The role of chelating ligands and central metals in the oxygen reduction reaction activity: a DFT study. *Russ. J. Electrochem.* **52**(6), 555–559 (2016)
20. X. Chen, S. Chen, J. Wang, Screening of catalytic oxygen reduction reaction activity of metal-doped graphene by density functional theory. *Appl. Surf. Sci.* **379**, 291–295 (2016)
21. H.A. Hansen, J. Rossmeisl, J.K. Nørskov, Surface pourbaix diagrams and oxygen reduction activity of Pt, Ag and Ni(111) surfaces studied by DFT. *Phys. Chem. Chem. Phys.* **10**(25), 3722–3730 (2008)
22. J. Rossmeisl, J. Greeley, G.S. Karlberg, Electrocatalysis and catalyst screening from density functional theory calculations, in *Fuel Cell Catalysis*, ed. by M. T. M. Koper (Ed), (Wiley, Hoboken, 2009), pp. 57–92
23. X. Chen, F. Li, X. Wang, S. Sun, D. Xia, Density functional theory study of the oxygen reduction reaction on a cobalt-polypyrrole composite catalyst. *J. Phys. Chem. C* **116**(23), 12553–12558 (2012)
24. X. Chen, S. Sun, X. Wang, F. Li, D. Xia, DFT study of polyaniline and metal composites as nonprecious metal catalysts for oxygen reduction in fuel cells. *J. Phys. Chem. C* **116**(43), 22737–22742 (2012)
25. S. Kattel, P. Atanassov, B. Kiefer, Density functional theory study of Ni–N<sub>x</sub>/C electrocatalyst for oxygen reduction in alkaline and acidic media. *J. Phys. Chem. C* **116**(33), 17378–17383 (2012)
26. S. Kattel, P. Atanassov, B. Kiefer, Catalytic activity of Co–N<sub>x</sub>/C electrocatalysts for oxygen reduction reaction: a density functional theory study. *Phys. Chem. Chem. Phys.* **15**(1), 148–153 (2013)
27. H.Y. Su, Y. Gorlin, I.C. Man, F. Calle-Vallejo, J.K. Nørskov, T.F. Jaramillo, J. Rossmeisl, Identifying active surface phases for metal oxide electrocatalysts: a study of manganese oxide bi-functional catalysts for oxygen reduction and water oxidation catalysis. *Phys. Chem. Chem. Phys.* **14**(40), 14010–14022 (2012)
28. G. Wang, F. Huang, X. Chen, C. Gong, H. Liu, S. Wen, F. Cheng, X. Zheng, G. Zheng, M. Pan, A first-principle study of oxygen reduction reaction on monoclinic zirconia (̄111), (̄101) and (110) surfaces. *Catal. Commun.* **69**, 16–19 (2015)
29. J. Roques, A.B. Anderson, Theory for the potential shift for OH<sub>ads</sub> formation on the Pt skin on Pt<sub>3</sub>Cr(111) in acid. *J. Electrochem. Soc.* **151**(3), E85–E91 (2004)
30. A.B. Anderson, R.A. Sidik, Oxygen electroreduction on Fe<sup>II</sup> and Fe<sup>III</sup> coordinated to N<sub>4</sub> chelates. Reversible potentials for the intermediate steps from quantum theory. *J. Phys. Chem. B* **108**(16), 5031–5035 (2004)

31. J. Roques, A.B. Anderson, Pt<sub>3</sub>Cr(111) alloy effect on the reversible potential of OOH(ads) formation from O<sub>2</sub>(ads) relative to Pt(111). *J. Fuel Cell Sci. Technol.* **2**(2), 86–93 (2005)
32. H. Schweiger, E. Vayner, A.B. Anderson, Why is there such a small overpotential for O<sub>2</sub> electroreduction by copper laccase? *Electrochem. Solid-State Lett.* **8**(11), A585–A587 (2005)
33. R.A. Sidik, A.B. Anderson, Co<sub>9</sub>S<sub>8</sub> as a catalyst for electroreduction of O<sub>2</sub>: quantum chemistry predictions. *J. Phys. Chem. B* **110**(2), 936–941 (2006)
34. R.A. Sidik, A.B. Anderson, O<sub>2</sub> reduction on graphite and nitrogen-doped graphite: experiment and theory. *J. Phys. Chem. B* **110**(4), 1787–1793 (2006)
35. E. Vayner, H. Schweiger, A.B. Anderson, Four-electron reduction of O<sub>2</sub> over multiple Cu<sup>I</sup> centers: quantum theory. *J. Electroanal. Chem.* **607**(1–2), 90–100 (2007)
36. E. Vayner, A.B. Anderson, Theoretical predictions concerning oxygen reduction on nitrated graphite edges and a cobalt center bonded to them. *J. Phys. Chem. C* **111**(26), 9330–9336 (2007)
37. E. Vayner, R.A. Sidik, A.B. Anderson, Experimental and theoretical study of cobalt selenide as a catalyst for O<sub>2</sub> electroreduction. *J. Phys. Chem. C* **111**(28), 10508–10513 (2007)
38. K.A. Kurak, A.B. Anderson, Nitrogen-treated graphite and oxygen electroreduction on pyridinic edge sites. *J. Phys. Chem. C* **113**(16), 6730–6734 (2009)
39. K.A. Kurak, A.B. Anderson, Selenium: a nonprecious metal cathode catalyst for oxygen reduction. *J. Electrochem. Soc.* **157**(1), B173–B179 (2010)
40. X. Chen, Q. Qiao, L. An, D. Xia, Why do boron and nitrogen doped  $\alpha$ - and  $\gamma$ -Graphyne exhibit different oxygen reduction mechanism? A first-principles study. *J. Phys. Chem. C* **119**(21), 11493–11498 (2015)
41. A.B. Anderson, T.V. Albu, Ab initio determination of reversible potentials and activation energies for outer-sphere oxygen reduction to water and the reverse oxidation reaction. *J. Am. Chem. Soc.* **121**(50), 11855–11863 (1999)
42. J. Zhang, Z. Wang, Z. Zhu, The inherent kinetic electrochemical reduction of oxygen into H<sub>2</sub>O on FeN<sub>4</sub>-carbon: a density functional theory study. *J. Power Sources* **255**, 65–69 (2014)
43. X. Zhang, Z. Lu, Z. Fu, Y. Tang, D. Ma, Z. Yang, The mechanisms of oxygen reduction reaction on phosphorus doped graphene: a first-principles study. *J. Power Sources* **276**, 222–229 (2015)
44. Z. Duan, G. Wang, A first principles study of oxygen reduction reaction on a Pt(111) surface modified by a subsurface transition metal M (M = Ni, Co, or Fe). *Phys. Chem. Chem. Phys.* **13**(45), 20178–20187 (2011)
45. Z. Duan, G. Wang, Comparison of reaction energetics for oxygen reduction reactions on Pt(100), Pt(111), Pt/Ni(100), and Pt/Ni(111) surfaces: a first-principles study. *J. Phys. Chem. C* **117**(12), 6284–6292 (2013)
46. S. Kattel, G. Wang, Reaction pathway for oxygen reduction on FeN<sub>4</sub> embedded graphene. *J. Phys. Chem. Lett.* **5**(3), 452–456 (2014)
47. B. Hammer, J.K. Nørskov, Why gold is the noblest of all the metals. *Nature* **376**(6537), 238–240 (1995)
48. B. Hammer, Y. Morikawa, J.K. Nørskov, CO chemisorption at metal surfaces and overlayers. *Phys. Rev. Lett.* **76**(12), 2141–2144 (1996)
49. L.A. Kibler, A.M. El-Aziz, R. Hoyer, D.M. Kolb, Tuning reaction rates by lateral strain in a palladium monolayer. *Angew. Chem. Int. Ed.* **44**(14), 2080–2084 (2005)
50. V.R. Stamenkovic, B. Fowler, B.S. Mun, G. Wang, P.N. Ross, C.A. Lucas, N.M. Marković, Improved oxygen reduction activity on Pt<sub>3</sub>Ni(111) via increased surface site availability. *Science* **315**(5811), 493–497 (2007)
51. V. Stamenkovic, B.S. Mun, K.J.J. Mayrhofer, P.N. Ross, N.M. Markovic, J. Rossmeisl, J. Greeley, J.K. Nørskov, Changing the activity of electrocatalysts for oxygen reduction by tuning the surface electronic structure. *Angew. Chem. Int. Ed.* **45**(18), 2897–2901 (2006)
52. J. Aihara, Reduced homo-lumo gap as an index of kinetic stability for polycyclic aromatic hydrocarbons. *J. Phys. Chem. A* **103**(37), 7487–7495 (1999)
53. X. Chen, F. Li, N. Zhang, L. An, D. Xia, Mechanism of oxygen reduction reaction catalyzed by Fe(Co)–N<sub>x</sub>/C. *Phys. Chem. Chem. Phys.* **15**(44), 19330–19336 (2013)



54. X. Chen, Oxygen reduction reaction on cobalt–(*n*)pyrrole clusters from DFT studies. *RSC Adv.* **6**(7), 5535–5540 (2016)
55. X. Chen, Graphyne nanotubes as electrocatalysts for oxygen reduction reaction: the effect of doping elements on the catalytic mechanisms. *Phys. Chem. Chem. Phys.* **17**(43), 29340–29343 (2015)
56. L. Zhang, Z. Xia, Mechanisms of oxygen reduction reaction on nitrogen-doped graphene for fuel cells. *J. Phys. Chem. C* **115**(22), 11170–11176 (2011)
57. M. Shao, A. Peles, K. Shoemaker, Electrocatalysis on platinum nanoparticles: particle size effect on oxygen reduction reaction activity. *Nano Lett.* **11**(9), 3714–3719 (2011)
58. K. Sasaki, H. Naohara, Y. Cai, Y.M. Choi, P. Liu, M.B. Vukmirovic, J.X. Wang, R.R. Adzic, Core-protected platinum monolayer shell high-stability electrocatalysts for fuel-cell cathodes. *Angew. Chem. Int. Ed.* **49**(46), 8602–8607 (2010)
59. J.K. Seo, A. Khetan, M.H. Seo, H. Kim, B. Han, First-principles thermodynamic study of the electrochemical stability of Pt nanoparticles in fuel cell applications. *J. Power Sources* **238**, 137–143 (2013)
60. S.H. Noh, M.H. Seo, J.K. Seo, P. Fischer, B. Han, First principles computational study on the electrochemical stability of Pt–Co nanocatalysts. *Nanoscale* **5**(18), 8625–8633 (2013)
61. S.H. Noh, B. Han, T. Ohsaka, First-principles computational study of highly stable and active ternary PtCuNi nanocatalyst for oxygen reduction reaction. *Nano Res.* **8**(10), 3394–3403 (2015)
62. C.D. Taylor, M. Neurock, J.R. Scully, First-principles investigation of the fundamental corrosion properties of a model Cu<sub>38</sub> nanoparticle and the (111), (113) surfaces. *J. Electrochem. Soc.* **155**(8), C407–C414 (2008)
63. I. Matanović, F.H. Garzon, N.J. Henson, Theoretical study of electrochemical processes on Pt–Ni alloys. *J. Phys. Chem. C* **115**(21), 10640–10650 (2011)
64. I. Matanović, P.R.C. Kent, F.H. Garzon, N.J. Henson, Density functional theory study of oxygen reduction activity on ultrathin platinum nanotubes. *J. Phys. Chem. C* **116**(31), 16499–16510 (2012)
65. I. Matanović, P.R.C. Kent, F.H. Garzon, N.J. Henson, Density functional study of the structure, stability and oxygen reduction activity of ultrathin platinum nanowires. *J. Electrochem. Soc.* **160**(6), F548–F553 (2013)
66. Y. Okamoto, Comparison of hydrogen atom adsorption on Pt clusters with that on Pt surfaces: a study from density-functional calculations. *Chem. Phys. Lett.* **429**(1), 209–213 (2006)
67. J.M. Seminario, L.A. Agapito, L. Yan, P.B. Balbuena, Density functional theory study of adsorption of OOH on Pt-based bimetallic clusters alloyed with Cr, Co, and Ni. *Chem. Phys. Lett.* **410**(4–6), 275–281 (2005)
68. G. Zanti, D. Peeters, DFT study of small palladium clusters Pd<sub>*n*</sub> and their interaction with a CO ligand (*n* = 1–9). *Eur. J. Inorg. Chem.* **2009**(26), 3904–3911 (2009)
69. Z. Lu, G. Xu, C. He, T. Wang, L. Yang, Z. Yang, D. Ma, Novel catalytic activity for oxygen reduction reaction on MnN<sub>4</sub> embedded graphene: a dispersion-corrected density functional theory study. *Carbon* **84**, 500–508 (2015)



# Hydrogen Fuel Cell as Range Extender in Electric Vehicle Powertrains: Fuel Optimization Strategies

# 12

Roberto Álvarez and Sergio Corbera

## Contents

12.1	Introduction .....	360
12.1.1	The Rebirth of Electric Powered Vehicles .....	361
12.1.2	Criticism and Recent Initiatives Fostering Fuel Cell Vehicles .....	362
12.2	Fuel Cell as Range Extender .....	364
12.3	Vehicle Drivetrain Approach .....	365
12.4	Vehicle Drivetrain Model .....	367
12.4.1	Vehicle Dynamics .....	368
12.4.2	Electric Engine .....	368
12.4.3	Battery Mode .....	369
12.4.4	Fuel Cell Stack Model .....	370
12.4.5	Power Distributor Unit .....	370
12.5	Switching Control Strategy .....	370
12.5.1	Problem Formulation .....	372
12.5.2	Genetic Algorithms .....	372
12.5.3	Switching Control Strategy .....	374
12.6	Results .....	374
12.6.1	Battery-Only Test .....	374
12.6.2	Range Extender Without GA Control Strategy .....	377
12.6.3	Range Extender with a Global Control Strategy Based on GAs .....	379
12.7	Conclusions .....	380
	References .....	381

## Author Contributions

Roberto Álvarez conceived the presented idea, developed the theoretical framework, and worked out almost all of the technical details. Sergio Corbera performed the analytic calculations and the numerical simulations. Both authors analyzed the results and contributed to the final version of the manuscript.

R. Álvarez (✉) · S. Corbera

Department of Engineering, Universidad Nebrija, Madrid, Spain

e-mail: [ralvarez@nebrija.es](mailto:ralvarez@nebrija.es); [scorbera@nebrija.es](mailto:scorbera@nebrija.es)

---

**Abstract**

The transformation of mobility is now beginning through the introduction of hydrogen ( $H_2$ ) as an energy carrier, coupled with fuel cell electric vehicles that can utilize  $H_2$  without greenhouse gas emissions. A current disadvantage of these vehicles lies in the limited infrastructure in terms of  $H_2$  refill or electric recharge stations, which has hindered their widespread applicability. There is a sense of déjà vu in the current development in automobile design between battery electric and fuel cell vehicle. This race is similar to a competition when the internal combustion engine-driven Ford Model T automobile became the dominant transportation platform in displacing battery and steam-driven automobiles in the United States a century ago and opened up a new industry. In this chapter, we propose a change in the architecture of the power plant of the fuel cell and battery electric vehicles. The objective is that these vehicles can be presently used until the development of an electric and/or hydrogen recharge network allows both being useful with the current status. We present a drivetrain set model, which is a combination of a plugged-in battery and a fuel cell that works as a range-extender system. Different strategies are applied in order to determine the working conditions that will lead to better vehicle performance and higher range. The vehicle performance is referred to the capacity of both energy sources, namely, electricity stored in a lithium-ion battery and hydrogen gas in high-pressure storage tanks. –The possibilities presented in the chapter may open the door to strategic advantages and innovation for car designers in the future.

---

## 12.1 Introduction

Nowadays, citizens of urban cities breathe an atmosphere whose concentration on harmful emissions has steadily grown throughout the twentieth century. The recent annual *Conference of Parties* (COP21) has revealed a global concern regarding the extreme climate changes in the near future if no action is taken today. The agreements reached in that conference highlighted the commitments undertaken by most of the nations. A new paradigm has to be developed in order to reduce and control greenhouse gas (GHG) emissions, focusing not only on the most pollutant activities but also on the common daily events, such as combustion of fossil fuels for electricity generation, transport, and household usages. The recent air pollution crises all over the world have revealed the need to accelerate such efforts to control and cap GHGs, which can be mitigated by our proposed powertrain strategies.

The use of internal combustion engines (ICE) for cars and trucks mostly burns fossil fuels, and it represents a strong contribution to the increase of GHGs and pollutant particles. There is no doubt that there exists a discussion about if the traditional transport model has become depleted. For example, pollutant exhaust tailpipe gases have been reduced in the European Union (EU) through a series of directives, each amendment to the 1970 Directive 70/220/EEC, which constitute the current legal EU framework for controlling transportation emissions. In this sense,

both manufacturers and governments had been working to develop newer and greener technologies as solutions.

The stronger control of environmental care in the big cities suggests that mobile fleet must probably change within the next 20–30 years [1, 2]. These transformations will require global actions, through a progressive decarbonization process based on utilization of low-carbon power sources. Therefore, the low-carbon sources in the transport sector can lead to a minimal output of the GHG emissions. Lower emission can be modeled on improvements of fuel efficiency and reduction of carbon intensity of fuels ( $\text{CO}_{2\text{eq}}/\text{MJ}$ ). The proposed targets can be met if not only technological solutions are applied but also policies that promote significant changes in human life and behavior [3]. The future solutions to mitigate carbon emissions related to transport and particularly passenger cars will need a new paradigm, involving automakers, consumers, urban planners, and policy makers.

The new and optimized powertrain technologies with the focus on energy optimization, which diminishes range anxiety<sup>1</sup> [3] and greenhouse gas emissions, should be supported and popularized. This approach will result in no fossil fuel combustion and zero tailpipe emissions, achieving an acceptable driving range and quick and easy refueling.

### 12.1.1 The Rebirth of Electric Powered Vehicles

Most of the automakers have opted for the rebirth of electric powertrain as the one and only suitable solution to reduce GHG emissions [45], but differing on the specific way [37] mainly due to the restrictions (technological as well as market development) of the different technologies of energy storage availability [4]. It is known that batteries offer a good dynamic response, while their discharge time is shorter than required and the charging time is longer than required. In spite of these drawbacks, full-electric (EV) or battery electric vehicle (BEV) availabilities in the market today are not a suitable option for many customer requests [5]. Automakers have found a temporary short-term market solution in the plug-in hybrid electric vehicle (PHEV), as it can be charged with electricity like BEVs, but also run on gasoline with an internal combustion engine (ICE) and using lower battery packs to improve fuel efficiency [6]. There are two leading PHEV technologies:

- The parallel hybrid, in which both the electric motor and the combustion engine are mechanically coupled to the wheels through a transmission (i.e. Toyota Prius).
- The series hybrid, also known as an extended-range electric vehicle (EREV), in which the electric motor is directly coupled to the wheels and the combustion engine is only used to recharge the batteries (i.e. BMW i3).

---

<sup>1</sup>Worry on the part of a person driving an electric car that the battery will run out of power before the destination or a suitable charging point is reached.

Although there are evident advantages in the range achieved by PHEVs, diminishing the range anxiety phenomenon, i.e.; they also have certain limitations as an increased price due to the need of two engines and additional power converters [7] and, in the end, they keep using fossil fuels.

On the other hand, hydrogen-powered fuel cell vehicles (FCVs) convert compressed hydrogen contained in storage tanks into electricity using a fuel cell stack that provides the energy needed to propel a car forward. A battery pack is still used in these vehicles. The battery pack is smaller than that used in BEVs, as it is necessary to assist the fuel cell stack to prevent disruptions at times of high power demand and to recover the excess of energy from the hydrogen fuel cell or through regenerative braking. The Hyundai Tucson ix35 fuel cell vehicle (Tucson FCEV), Honda FCX Clarity, and Toyota Mirai are examples of FCVs. They generate zero tailpipe emissions and enjoy good range characteristics. The range is determined by the capacity of the tank(s), which can be refilled within 5 min similar to the 10-gal capacity gasoline tank. The infrastructure needed and fuel widespread acceptance are the current main barriers for widespread use of FCVs.

### 12.1.2 Criticism and Recent Initiatives Fostering Fuel Cell Vehicles

On the one hand, there is the point of view of the fuel cell vehicle automakers that affirm “well-to-wheel emissions for hydrogen vehicles sourced from natural gas are lower than battery electric vehicles, and less than half of equivalent gasoline vehicle emissions” [19] or “The next generation of environmentally conscious motorist demands newer, cleaner forms of transportation. Recognizing hydrogen’s potential to answer that demand, we are producing fuel cell vehicles alongside our other alternative fuel vehicles to power a better future. A driving experience that’s on par with a gasoline engine, but without any CO<sub>2</sub> emissions” [42].

On the other hand, Tesla’s viewpoint (CEO Elon Musk) is that hydrogen-powered cars are a bad move. Specifically, Mr. Musk thinks that the technology is “incredibly dumb” [8]. Dr. Joseph J. Romm affirmed that the production of hydrogen by electrolysis of water, its transportation, pumping, and fuel cell conversion, is a low-efficiency process, which leaves about 20–25% of the original electricity. On the contrary, the process of electricity transmission, charging and discharging the battery, would achieve a 75–80% efficiency, making BEVs at least three times more energy efficient [39]. These affirmations cause considerable controversy, which only makes the situation more confusing. There exist several methods to obtain hydrogen, but it is not a mature infrastructure for hydrogen to allow a true comparison with electricity storage in equal conditions. It is clear that both extremes are fully charged with competitive posturing.

It seems that the competition between storing electricity in batteries or by hydrogen in tanks to power an electric vehicle is a *déjà vu* (patrol vs. electricity in 1900). What would have happened if Henry Ford had opted for the electric vehicle and the development of batteries instead of the internal combustion engines and fossil fuels? Did anyone give any chance to battery technology at that time? Is it not at least similar to what it is happening today with the use of fuel cells in automotive and hydrogen infrastructure?

The data reflects that the public infrastructure for BEV charging is significantly more advanced than the public hydrogen refueling network. According to the [44], there are currently 15,553 electric public charging stations (2017 February data) and 40,819 charging outlets across the United States while the number of hydrogen stations is 64 (half of them are located in California). If we look at European data, only 79 public access hydrogen stations are available [34], while the number of public electric charging stations is near 114,000. One of the reasons for this difference could be the cost associated. Compared with hydrogen stations, public electric charging devices are thousands of times cheaper and easier to construct. Nevertheless, 92 new hydrogen refueling stations have been opened throughout the world in 2016, the largest number of new stations ever. As of January 2017, the total number of hydrogen refueling stations in operation was 274 [43].

Several policy initiatives in several countries all over the world are promoting the development of a hydrogen refueling network. Hydrogen Mobility Europe – consisting of the projects H2ME1 and H2ME2 – is a flagship project giving fuel cell electric vehicle drivers access to the first truly pan-European network of hydrogen refueling stations (€68 million demonstration project co-funded with €32 million from the European Union’s Horizon 2020 program). California State has committed a funding for the development of hydrogen fueling stations through the Advanced Clean Cars Program [32, 33], including a provision to fund 100 hydrogen stations. Japan’s government proposed \$71 million to build hydrogen stations, and the United Kingdom announced over \$752 million of new capital investment between 2015 and 2020 in support of ultra-low emission vehicles, including FCVs [9]. Germany expects to have 400 hydrogen fueling stations by 2023 with the creation of a joint venture group known as H<sub>2</sub> MOBILITY Deutschland, consisting of Air Liquide, Linde, Daimler, OMV, Shell, and Total with investments of around EUR 400 million [10]. Norway, Sweden and Denmark are developing the Scandinavian Hydrogen Highway to make the Scandinavian region the first in Europe where hydrogen is commercially available in a network of refueling stations [35]. Italy is establishing a similar highway, designed to connect the country in a hydrogen way to Germany and Scandinavia [41]. General Motors and Honda will invest \$85 million to form a joint venture to produce advanced hydrogen fuel cell systems at a factory in Michigan [40].

Nevertheless, the development of refueling infrastructure is slow, and this, added to the current vehicle cost, is clearly the most important hurdles keeping FCVs from storming the market en masse. Therefore, given these figures, it is clear that it is necessary to analyze the sales volume, and the figures talk by themselves (Table 12.1):

Top selling FCEV passenger cars are Hyundai, Honda, and Toyota, but the figures are clearly poor. Worldwide sales of FCV in 2016 were 2268; plug-in vehicles, 777,497; and ICEs, 88.1 million units. The electric car sales also include all BEV and PHEV passenger car sales, light trucks in the United States/Canada, and the light commercial vehicle in Europe [8, 11, 12, 36]. The fuel cells themselves have made dramatic improvements in efficiency and cost, but the infrastructure needed to support them remains a weak point. Therefore, here is the chicken and egg problem: we have a hydrogen fuel cell vehicle technologically suitable for driving, but it is not

**Table 12.1** Fuel cell electric vehicle sales evolution (2012–2016)

Model	2016	2015	2014	2013	2012
Hyundai IX 35/Tucson FCEV	160	213	40	37	0
Toyota Mirai	2039	498			
HONDA Clarity FCV	113				

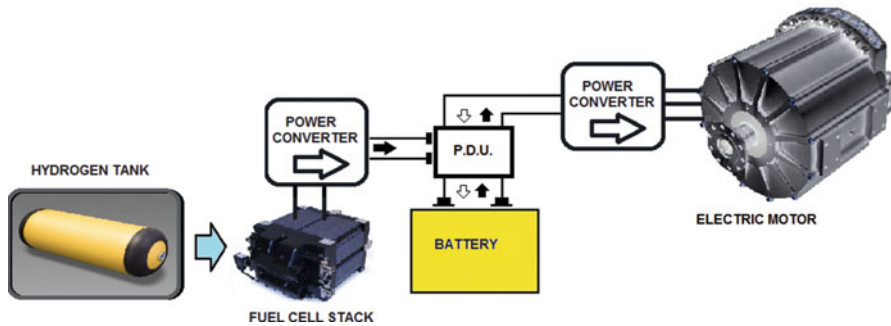
salable because there is a lack of infrastructure for its charge and vice versa. Nevertheless, several authors have emphasized that, in the future, zero emission powertrains driven by electricity stored in batteries and/or by hydrogen [13, 14] will lead the market.

## 12.2 Fuel Cell as Range Extender

In this work, we present modeling simulation and optimization of a fuel cell-based powertrain that trends to avoid all aforementioned BEV and FCEV's drawbacks. The powertrain includes a plug-in battery that would achieve a minimum range of 100 km fully charged of electric energy and a range extender based on a fuel cell that increases the range. Figure 12.1 shows the architecture of this power train and its major components as described in a previous work [15].

As Fig. 12.1 shows, the electric motor is directly coupled to the wheels and the fuel cell stack is used to charge the batteries through a power distributor unit (PDU) controller [31]. The fuel cell stacks do not need to be sized to match the peak rating of the traction electric motor due to their availability of the higher energy stored and the power of the battery pack. The ambition of this powertrain architecture is to be suitable today and in the near future, waiting for an optimistic scenario, explained as follows:

- **Future scenario:** There is a fully developed hydrogen charge network similar to the current fossil fuel one. In this case, the vehicle would achieve a range similar to current ICE vehicles with an easy and quick hydrogen refuel and allow for conventional electric charging too.
- **Current scenario:** Today's hydrogen fueling station network remains in an early development stage. The vehicle will be fueled with the electricity stored in the battery and could be charged using a grid electrical power at a recharging point placed (or not) at home. This battery pack would achieve a 100-km range in electric mode. Several studies have emphasized that the average daily distance traveled is about 41–44 km [4, 5, 16] and mainly the charging of the vehicles would be at home during nighttime [17]. So the vehicle mainly uses the battery for most of its driving, thereby reducing emissions, noises, and air pollutants. Its range-extender hydrogen powertrain would mitigate driver's range anxiety phenomena (one of the main barriers for electric vehicle commercialization).



**Fig. 12.1** Fuel cell range-extender power train architecture

The most relevant challenges are those related to the dimensions and management of the fuel(s), as energy consumption for a trip is influenced by some uncertain factors. The range represents a barrier to the commercialization of electric vehicles, and it is always a point confusing the information provided by the automakers. Clear information about the range of the electric vehicle is one of the weaknesses of this technology. As the proposed power architecture manages two different fuels, electricity in the battery and hydrogen stored in tanks, the use of optimization algorithms may assess the optimum selection/consumption/storage of each type of fuel searching for the usability of the vehicle in different scenarios.

### 12.3 Vehicle Drivetrain Approach

Based on the aforementioned aspects of the fuel cell range-extender architecture, we are going to focus on the following aspects:

- Energy storage. Battery dimensions:** Table 12.2 summarizes the published characteristics of the four FCVs available at the moment. All these vehicles have similar characteristics: electric motor power level, the capacity of battery and hydrogen gas storage, fuel tank and battery technologies. But the most important common characteristics are that all of them use a very low capacity battery storage (mainly to help the fuel cell when there is high power demand) and also that none of them is plug-in because it is recharged with regenerative energy. The first change in the range-extender topology is using the battery as the main power supplier, which will be plug-in, and its design variables will meet the capacity needed. This capacity must cover the driving range determined for the vehicle without using hydrogen, as it is required by the constraints of the current scenario. The volume of hydrogen stored in the tank(s) and the strategy of fuel consumption will have to be known necessarily to take into account upper limits for range estimation.



**Table 12.2** FCEV powertrain characteristics

	Honda Clarity	Toyota Mirai	Hyundai ix35
Electric motor	DC permanent magnet 100 kW	114 kW	AC induction 100 kW
Electric energy storage	Lithium-ion (Li-ion)	Nickel-metal-hydride (NiMH) 1.6 kWh	Lithium-ion polymer (Li-Po) 0.95 kWh
Driving range (cycle)	386 km (EPA test data)	483 km (EPA test data)	525 km (NEDC)
Fuel capacity (mass-pressure-volume)	3.92 kg – 350 bar	5 kg – 700 bar – 122.4 l	5.64 kg – 700 bar – 144 l
Fuel cell power	100 kW	100 kW	100 kW
Fuel consumption (kg hydrogen/100 km)	1.015	1.03	1.07

- Non-algorithm-based range extender.** As the battery will be the main power supplier in the range-extender powertrain, it will be drained when supplying the power requirements from the engine for a given route. The state of charge (SoC) of a battery indicates its remaining capacity, and it will be the parameter taken to control the battery performance. Figure 12.2 shows the control scheme for a given route. The battery begins its discharge (depleting mode) from 90% SoC (fully charged) and begins its depletion until it reaches  $SoC_d$  (this is a design value). Automatically the fuel cell begins its work and helps to charge the battery at a fixed current  $I_{FC}$  (another design value). The SoC will be increased until it reaches a maximum value  $SoC_h$  (design value), and then the fuel cell stops and the depleting cycle restarts. Fuel cell performance is sensitive to load variations (because of the low voltage and high current output characteristics), therefore the charge current supplied by the cell stack should be a constant value during the periods of range-extender mode in order to obtain a better result in terms of efficiency.

When simulating without the use of algorithms, the assumptions taken in order to simplify the problem are key to improve fuel cell response. In this sense, the fuel cell stack will be adjusted to transmit its maximum power working at a constant intensity ( $I_{FC}$ ) to provide a better operation. Therefore, the  $I_{FC}$  will be fixed at a constant value to maximize the fuel cell efficiency (empirical values are needed). Taking into account the safety of Li-ion batteries performance. It can be evaluated by the values for  $SoC_d$  and  $SoC_l$ , which are 30% and 20%, respectively. The lower limit of  $SoC_l$  (20%) is set to mitigate potential risk in discharging the Li-ion batteries. The optimum value of  $SoC_h$  is open for discussion with an aim to lower the consumption of hydrogen if possible with current hydrogen charging network. Hence if we want to minimize the risk of arriving at destiny with the highest charge in the battery and the lower hydrogen in the tank,  $SoC_h$  lowest values will be, a priori, more suitable.

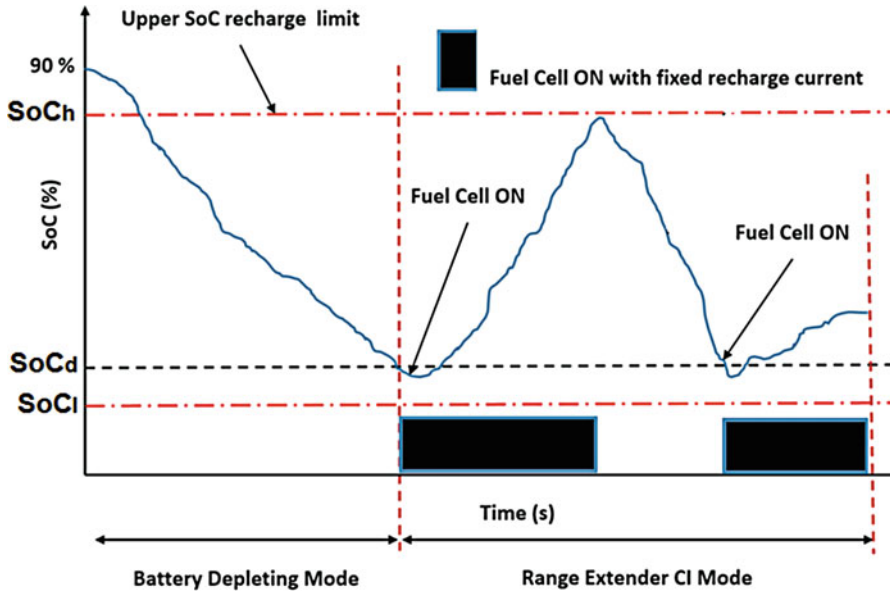
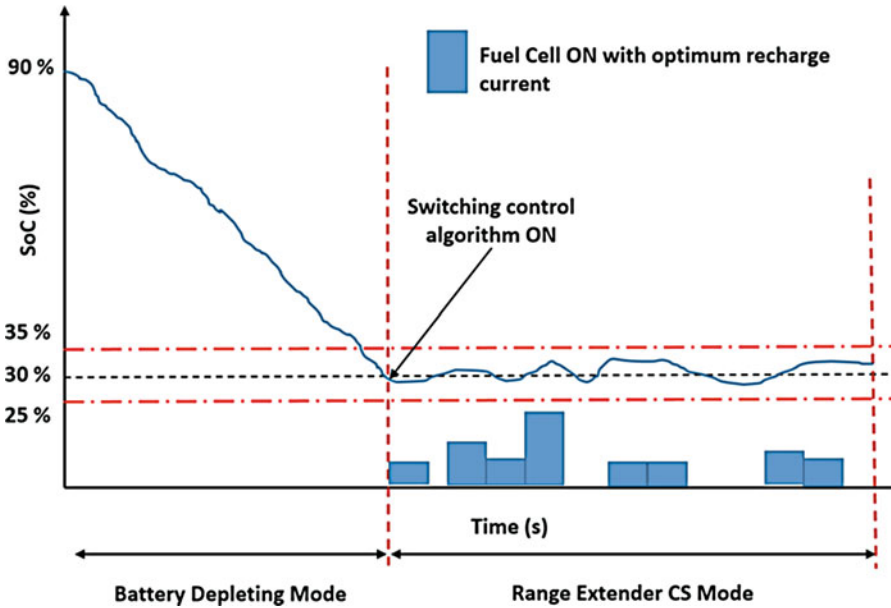


Fig. 12.2 Nonalgorithm-based fuel cell range-extender control strategy

- Algorithm-based range extender.** A simulation was applied using optimization algorithms to lower hydrogen usage by taking a few assumptions in order to simplify the fuel consumption problem. The constraints assumed were using  $SoC_d$  and  $SoC_l$  values, 35% and 25%, respectively, to achieve safe and optimal battery performance by limiting hydrogen consumption. When the constraint of  $SoC_h$  being equal to  $SoC_d$  was modeled, the simulation indicated the highest volume of hydrogen would remain in the storage tank. Algorithms will allow in obtaining the consecutive values for  $I_{FC}$  that minimizes the consumption of hydrogen, allowing for an arrival to a destination with the lowest consumption of hydrogen and battery charge, respectively (Fig. 12.3).

## 12.4 Vehicle Drivetrain Model

A MATLAB/Simulink vehicle model has been developed to estimate the energy consumption. The purpose of this study is to find out trends on the range of the vehicle with the new power plant architectures. This MATLAB-Simulink block set series allow modeling in a unique simulation environment, both the electrical and mechanical systems. The model proposed is based on Hyundai ix35 as a starting point. The electric power plant is described in the following points, including literature references.



**Fig. 12.3** Algorithm-based fuel cell range-extender control strategy

### 12.4.1 Vehicle Dynamics

Vehicle dynamics block calculates the required torque and the speed of the electric motor. The model considers the aerodynamic drag, gravitational effects, rolling resistance, and longitudinal tire effects. As it is an electric vehicle configuration, the regenerative braking is taken into account, but it is limited in order to prevent the front wheels from becoming locked [18]. The optimal braking energy in the front wheels depends on the acceleration requirement and the dynamic weight distribution. Using this resistance force, it is possible to calculate the power and torque. The torque and the speed of the drive shaft are the inputs for the electric motor operational point. Table 12.3 presents the Hyundai ix35 vehicle dimensions necessary to complete the simulation requirements of this block [19].

### 12.4.2 Electric Engine

The Hyundai ix35 drivetrain model includes a powerful 100 kW induction motor. This electric engine offers constant maximum torque, 200 Nm (0–3600 rpm), and constant power, 100 kW (3600–7200 rpm). A constant (V/f) control strategy is applied until it reaches the nominal speed. At speed greater than the nominal speed, the voltage cannot be increased and it is fixed to its nominal value, but the frequency could still be changed. A power converter unit controls the electric motor

**Table 12.3** Vehicle dynamics data set [19]

Vehicle dynamics (units)	Values
Overall length (mm)	4410
Overall width (mm)	1820
Overall height (mm)	1650
Wheelbase (mm)	2640
Front wheel tread (mm)	1585
Rear wheel tread (mm)	1586
Front over hang (mm)	880
Rear over hang (mm)	890
Cargo area (VDA) (liter)	551
Lightest curb weight (kg)	2250
Heaviest curb weight (kg)	2290
Gross vehicle weight (kg)	2290

**Table 12.4** Battery data set

Battery data set	Values (units)
Energy content	16 kWh
Capacity (per cell)	40 Ah
Technology	Li-ion
Number of cells	108
Nominal voltage	400 V
Max. voltage	448 V
Min. voltage	324 V
Discharge cont. (power)	200 A (80 kW)
Discharge peak (power)	400 A (160 kW)
Max. charging current	80 A (32 kW)

and converts voltage direct current from the PDU into alternating current (see Fig. 12.1), which is then used to operate the electric motor. This power unit also controls the rotating speed and torque of the motor.

### 12.4.3 Battery Mode

Considering the working conditions of the battery packs on BEVs, the methodology to estimate the state of charge (SoC) is the Coulomb counting (known as Ah method), which is widely used. This method calculates the SoC evolution by integrating the discharge current in time. Parameters of the battery model are summarized in Table 12.4. This battery has to achieve a minimum range value (100 km) in electric-only driving. The battery model presented by us in this chapter is a Li-ion one, and it has been tested in our previous studies [3, 20].

#### 12.4.4 Fuel Cell Stack Model

A proton exchange membrane (PEM) fuel cell stack system for an automobile is modeled following literature procedures [21–23]. The model output data explain the stack efficiency and consumption; therefore, it is able to be used in combination with a fuel tank subsystem, whose capacity is 142 l, pressured at 700 bar. The exact conditions of the Hyundai ix-35 fuel cell stack were summarized in Table 12.2.

#### 12.4.5 Power Distributor Unit

The battery and the fuel cell stack consumptions are controlled through a power distribution unit, consisting of a device fitted with multiple outputs designed to provide safe distribution of high electric power. The model essentially works as it is described in the workflow (Fig. 12.4): the power demand arrives from the complete dynamic plus the electric motor model; then a converter adjusts that demand according to the battery instant working voltage and transforms it into a current. The PDU decides whether the depletion of the battery requires a demand of energy coming from the fuel cell stack system or not. If it is required, this intensity is derived and the corresponding power delivered by the fuel cell is reflected in a hydrogen consumption.

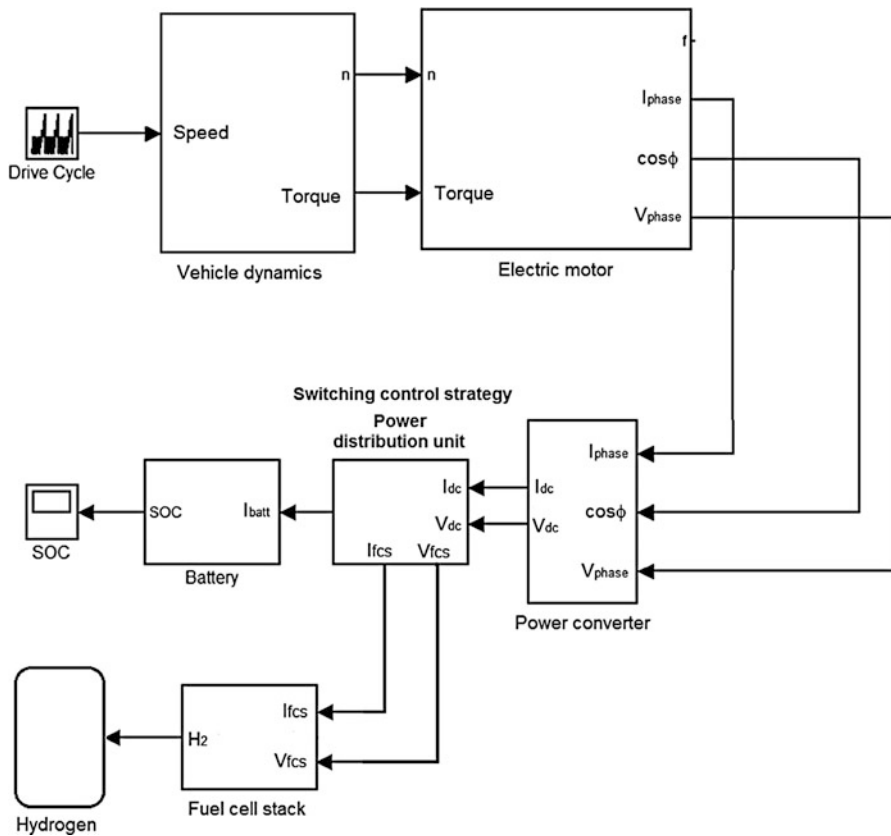
The input of the unified model is the drive cycle, and it offers the following outcomes: SoC evolution in the battery pack, current through the battery, voltage in the battery, power delivered by the battery, effective energy delivered by the battery, voltage and intensity generated by the fuel cell, consumption of hydrogen, power delivered by the fuel cell, and estimation about how many driving cycles would the configuration stand.

---

### 12.5 Switching Control Strategy

When a proposed hybrid powertrain is used in a vehicle, an additional complexity arises on how to manage the available fuel sources. There are many research publications related to management strategies for hybrid powertrains. These strategies include global optimization, dynamic and static real-time [24], which are well-known in this research area. These parameters are based on the use of advanced algorithms that manage when and what energy level of each power source is used in each moment, aiming to achieve high efficiency, energy savings, and emission's reduction.

Global optimization techniques include fuzzy logic methods [25] and genetic algorithms [26]. These methods are not applicable in real-time control systems because they require a priori known driving cycle. Dynamic real-time control strategies include



**Fig. 12.4** Simulink model schematic

adaptive fuzzy logic, which minimizes the fuzzy rules to obtain the desired behavior [6, 27], and adaptive fuel consumption minimization strategy (AFCMS).

For this study, a global optimization approach applying genetic algorithms (GAs) has been chosen as appropriated for switching control strategy. We are aware that the use of GAs can result in a dubious decision since it is well-known they require the knowledge of entire driving pattern, driving conditions, driver response and the route. However, technological advances and improvement in telecommunications networks will make it possible to access the data related to driving conditions and route characteristic information in an easy manner. This approach will increase the use of global optimization as a management strategy in a near future scenario. Therefore, despite their drawbacks, we have considered this control strategy as a good starting point to exemplify the benefits of the powertrain shown in Fig. 12.1 when the fuel consumption is efficiently managed.

### 12.5.1 Problem Formulation

The implemented PDU's switching control strategy can be treated as an optimization problem (OP). The main goal of any OP is to find optimal or near-optimal solutions with respect to some preestablished goals. When a battery electric powertrain includes a hydrogen range extender managed by a switching control strategy, the main objective is to manage the hydrogen consumption in an optimal manner. We are aware that this powertrain control involves many decisions and parameters that increase the OP complexity, but if we only refer to the optimization of the hydrogen consumption, we can formulate the problem as follows:

$$\min \text{ subject to: } \begin{cases} \text{Hydrogen}(\vec{x}) \\ \text{SoC}_{\max}(\vec{x}) \leq 35A & i = 1 \dots t_g \in S \\ \text{SoC}_{\min}(\vec{x}) > 25A & j = 1 \dots t_h \end{cases}$$

where

- $\text{Hydrogen}(\vec{x})$  represents the hydrogen consumption for a given driving cycle
- $\vec{x}$  represents the decision variable vector, which contains the response of the fuel cell in terms of amperes supplied by the range-extender device at each sampling time. The response of the fuel cell range extender should be different for each demand of power during the driven cycle. The number of decision variables is a function, depending on each vehicle speed cycle. According to the parameters of the battery model shown in Table 12.4, the maximum charge current is 80 A. The lower and upper bound values for the current supplied by the fuel cell range extender are 0 and 80 A, respectively. This could be a key factor to evaluate the possible fuel cell stack downsizing.
- $\text{SoC}_{\max}(\vec{x})$  and  $\text{SoC}_{\min}(\vec{x})$  are the upper and lower limits for charge and discharge battery limits, respectively.

### 12.5.2 Genetic Algorithms

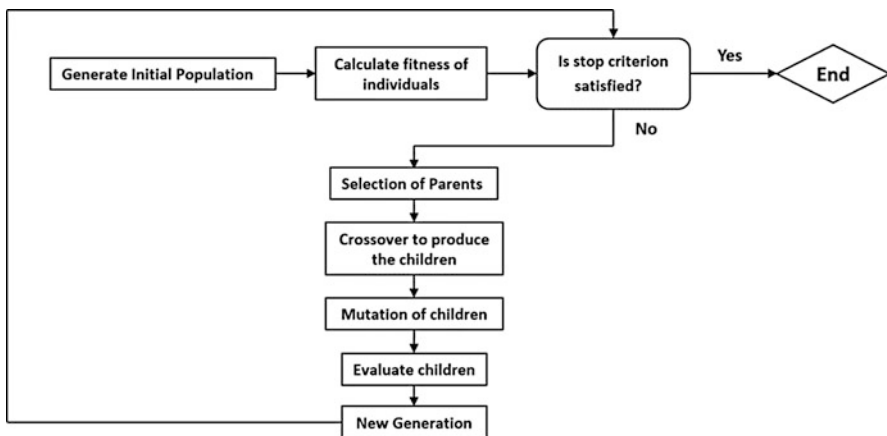
The genetic algorithms (GAs) are adaptive heuristic search algorithms based on the evolutionary idea of natural selection and genetics [28, 29]. These algorithms are applied in a vast number of ways; as such, they represent an intelligent exploitation of a random search in order to solve an optimization problem. The GAs are random algorithms, meaning the course taken by the algorithm is determined by random numbers, but the GA-based response is not random; instead of the GA output, it also explicitly utilizes historical information to point the search through the region of better performance within the search space. The basic techniques of GAs were designed to simulate natural processes necessary for evolution, especially those following the

principles laid down by Charles Darwin about evolution and natural selection. The GAs simulate the survival of the fittest among individuals over consecutive generations for solving a problem. Each generation consists of a population of character strings that are analogous to the chromosome that composes human deoxyribonucleic acid (DNA). Each individual represents a point in a search space and a possible solution. The individuals in the population are then made to go through a process of evolution. The GAs are based on an analogy with the genetic structure and behavior of chromosomes within a population of individuals using the following foundations:

- Individuals in a population compete for resources and mates.
- Those individuals most successful in each competition will produce more offspring than those individuals that perform poorly.
- Genes from good individuals propagate throughout the population so that two good parents will sometimes produce offspring that are better than either parent.
- Thus each successive generation will become more suited to their environment.

Given a clearly defined problem to be solved, a simple GA works as follows (Fig. 12.5):

1. Start with a random initial population (candidate solutions to the problem).
2. Calculate the fitness  $f(\vec{x})$  of each individual in the population.
3. Select the parents for crossover operation, the probability of selection being an increasing function fitness.
4. Crossover operation to form the children.
5. Mutate operation.
6. Replace the current population with the new population.
7. If the criterion stop is satisfied, the process ends, but go to step 2.



**Fig. 12.5** Genetic algorithm flowchart



### 12.5.3 Switching Control Strategy

Figure 12.6 shows a switching control flowchart based on GAs. The control strategy turns ON when the condition of  $\text{SoC} < 30\%$  is true. At this moment an iterative process to find the optimal  $I_{FC}$  supplied by the fuel cell starts. A vector, which contains the  $I_{\text{DEMAND}}$  at each time, is linked to the GA as input data. On the other hand, the objective of the switching control is to minimize the hydrogen consumption, so a link between the tank hydrogen and the GA is needed in evaluating each candidate solution. Once the switching control is activated, the GA works following the steps described before until the convergence is reached.

The GA and their link with the vehicle model have been developed specifically for this study. We have selected a well-known language programming as MATLAB in order to carry out the interaction with the Simulink vehicle model. Regarding the GA setup, the initial population size is equal to 100 candidates, which will be evolved during 4000 generations. Therefore, a total of 400,000 potential solutions could be evaluated once the switching control turns ON. A uniform crossover strategy with a constant probability equal to 0.6 and a mutation rate of 0.01 is implemented. The algorithm stops as soon as the number of generations reaches the maximum value (4000) or when the value of the fitness function for the best candidate does not change during 100 generations.

---

## 12.6 Results

In the present work, the New European Driving Cycle (NEDC) has been used as driving cycle in the tests. The NEDC cycle is composed of two parts, ECE-15 (urban driving cycle), repeated four times and plotted from 0 to 780 s, and extra-urban driving cycle (EUDC) plotted from 780 to 1180 s. The complete cycle is described in Fig. 12.7.

The objective of the present study is to determine which working conditions and strategies will lead to a better efficiency and performance in the combined energy storage system. For this purpose, this section shows the results of the simulation tests carried out with the aim of observing how the different operation modes affect energy consumption and therefore the vehicle range.

### 12.6.1 Battery-Only Test

Figure 12.8 presents the variation of battery SoC obtained when the vehicle is operating in electric mode. A continuous repetition of NEDC cycle is performed. It can be seen that there are some existing recharge notable points produced by the regenerative braking (i.e., points A and B in the graph). Figure 12.8 clearly points out how the simulation of SoC exceeds nine NEDC cycles. Each cycle of NEDC covers 11,023 m; therefore the goal of 100 km is fully achieved. As it can be seen, SoC varies from 90% to 10% for battery protection. Several studies cut the battery

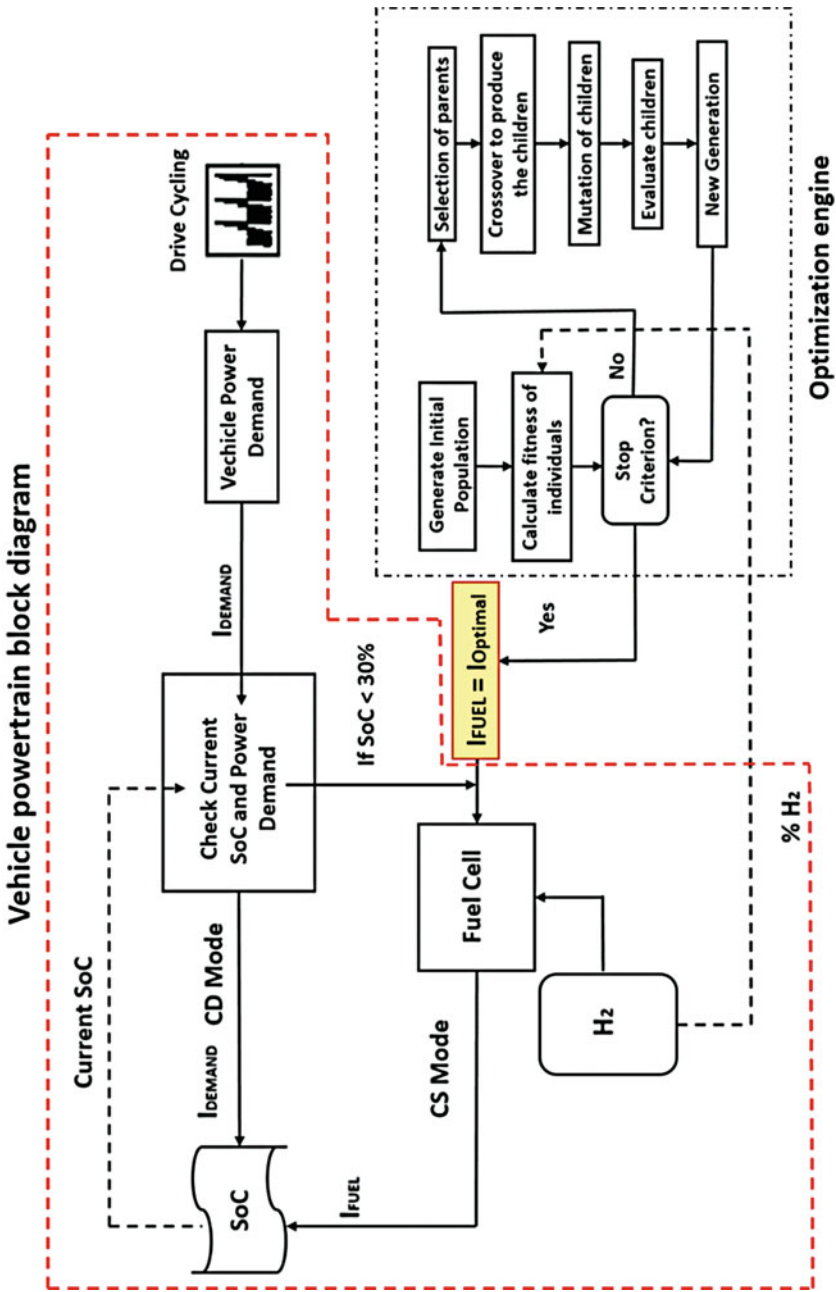


Fig. 12.6 PDU switching control flowchart

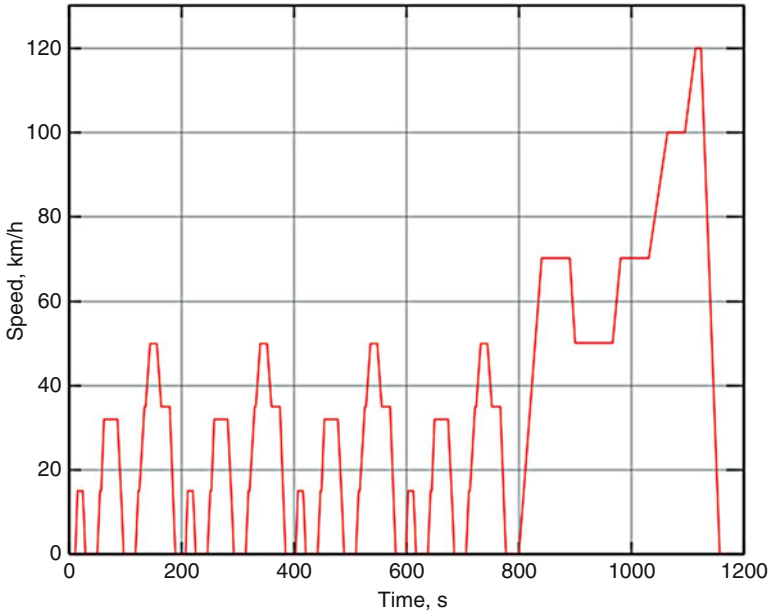


Fig. 12.7 NEDC cycle

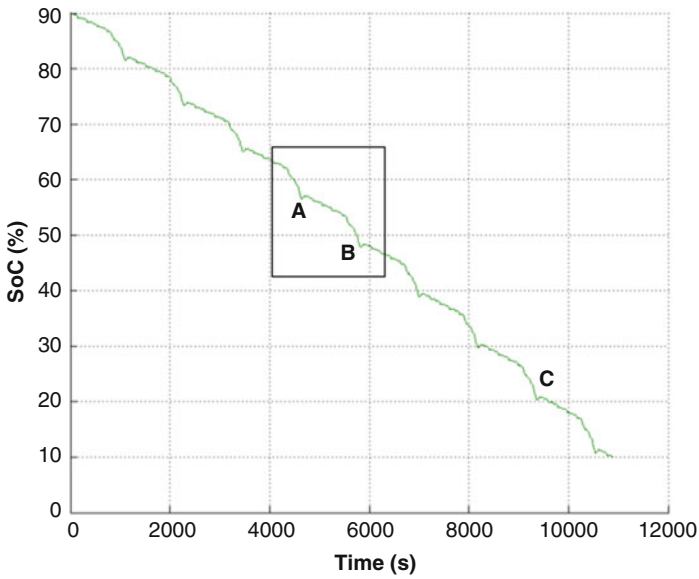
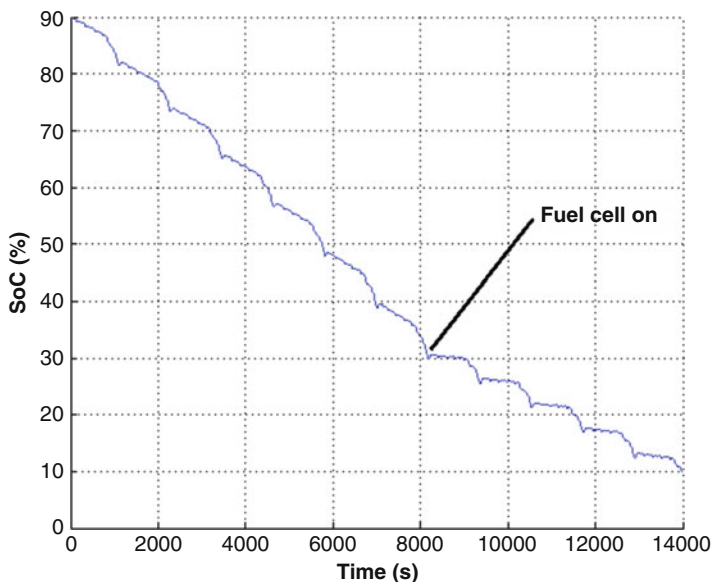


Fig. 12.8 SoC evolution in battery electric mode



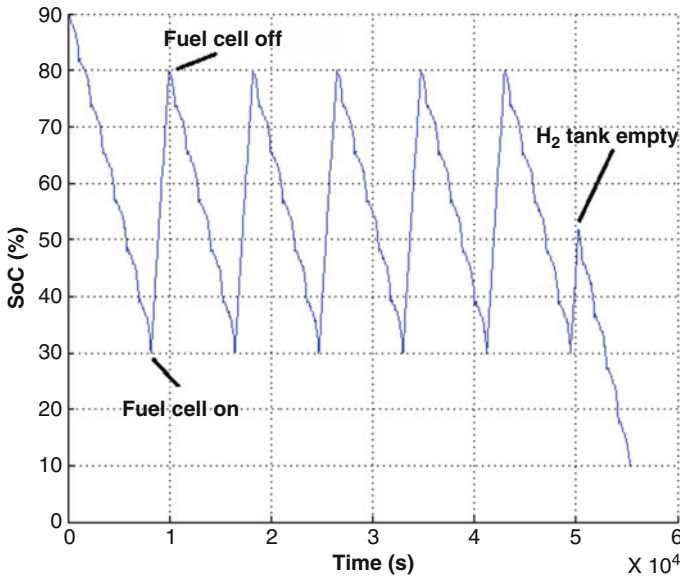
**Fig. 12.9** SoC evolution in battery ( $I_{FC}$  10 A)

power when SoC reaches 20% (point C in Fig. 12.8). In this case, the range achieved with the proposed battery pack would be 90 km.

### 12.6.2 Range Extender Without GA Control Strategy

In this case study, the range extender is connected with different recharging strategies based on the variation of the charging amperage (maximum value 80 A as seen in Table 12.4). This is a crucial design point because the results obtained will show the power of the fuel cell needed. Figures 12.9 and 12.10 represent the most extreme cases. Figure 12.9 shows that if we reduce to the minimum the power of the fuel cell, maximum  $I_{FC}$  current is 10 A. The power delivered by the fuel cell is not sufficient in any case to recharge the battery, therefore the battery discharges more slowly but ends reaching the lower SoC limit (10%).

If the power of the fuel cell used allows supplying the maximum current 80 A (see Fig. 12.10), the lithium-ion battery will be charged and discharged between the limits (30–80% SoC) five times. And finally the battery will be discharged and will drop below 10% SoC when there is no hydrogen in the storage tank. It was observed that the lower limit to activate the fuel cell range-extender device is 30% SoC. This is a requirement for battery safety reasons, but it may vary according to the algorithms applied (20% is the lower realistic limit).



**Fig. 12.10** SoC evolution in battery ( $I_{FC}$  80 A)

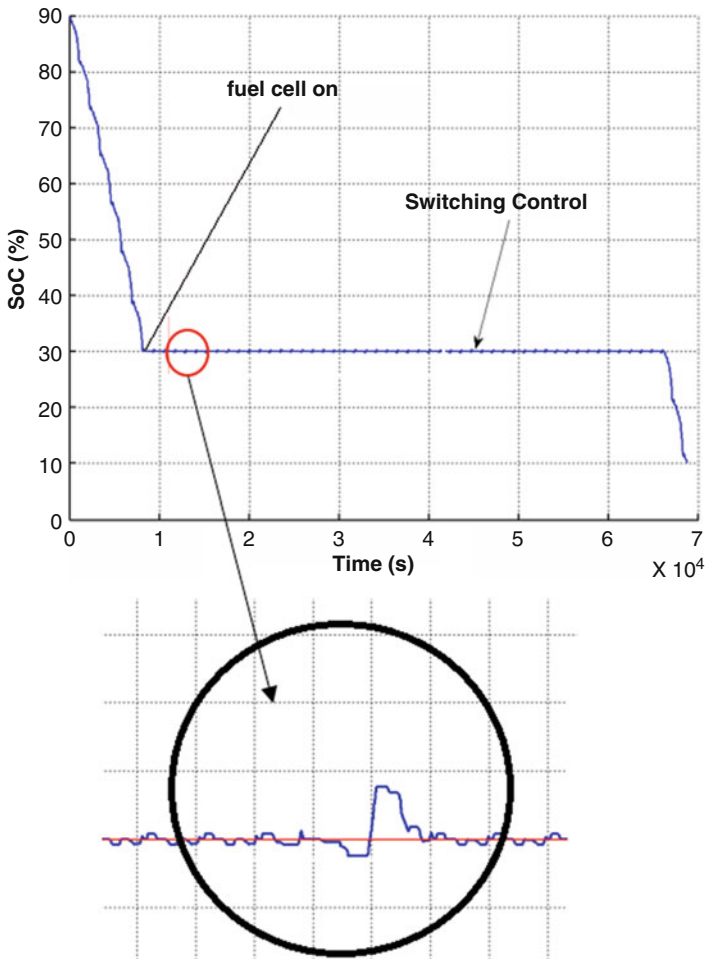
**Table 12.5** Vehicle performance (NEDC)

Recharge current (A)	Range (km)	Minimum fuel cell power (kW)
80 (2C)	588	32
70 (1.75C)	575	28
60 (1.5C)	578	24
50 (1.25C)	570	20
40 (1C)	530	16
30 (0.75C)	520	12
20 (0.5C)	497	8
10 (0.25C)	151	4
0 (electric-only)	108	0

Table 12.5 reflects the collection of data performance with the different recharging current. The range values obtained are near to 600 km with a fuel cell extended range charge of 80 A. The range extender at different charging current levels from 80 A (high level) to 10 A (low level) allows for a design of a different fuel cell power. It is clear that it is possible to substitute the 100 kW power fuel cell needed by the Tucson FCEV drivetrain by a new configurable fuel cell stack (4–32 kW). A reduction in the power of the fuel cell will allow for a reduction in the cost of the vehicle that would compensate the increment in cost for the new Li-ion battery included.

### 12.6.3 Range Extender with a Global Control Strategy Based on GAs

Figure 12.11 shows the SoC plot using this strategy based on GAs. It can be seen that the behavior is a charge depleting until the battery is drained and reaches 30% SoC. The observation was similar to that obtained in the case study b. But as soon as this depletion point is reached, the switching control strategy, applying the optimization algorithm, is initiated. The GA system determines the current requirements to achieve two objectives, to sustain the value of SoC at 30% and to consume the minimum amount of hydrogen fuel as possible. The NEDC cycles are repeated until the battery finishes its draining cycle when hydrogen tanks have been completely emptied. At the end of this cycle, the power from the battery is cut off.



**Fig. 12.11** SoC evolution in battery (algorithm-based)

Figure 12.11 reflects the ability of the algorithm to stabilize the variation of SoC, keeping the curve between 25% and 35% SoC level and achieving a theoretical range of around 640 km. The limitation in the use of these algorithms lies in the response to the real behavior because the fuel cell does not work very efficiently when abrupt changes of power are required. Therefore, it is necessary to establish transitory times in the evolution from one state to another, avoiding nonrealistic solutions. Those transitory times and the variation of power in the fuel cell will need empirical data to contrast the simulated results. However, the fact that the fuel cell is used to charge the battery rather than to propel the vehicle is an advantage in this sense, since it would not affect the driving sensation of the vehicle.

The fuel cell range-extender powertrains are not available in the market for passenger vehicles, but it is possible to find them in buses and vans. For example, the Kangoo ZE-H2 [30] is a short series of light commercial vehicles with a fuel cell range extender from Symbio FCell. This van consists of a Renault Kangoo ZE chassis but includes a hydrogen range-extender fuel cell, 5 kW power plant, that stores 2.1 kg of hydrogen in a tank pressured at 700 bar and a 22 kWh onboard battery. This power plant enables to drive for 160 km in battery range and 300 km hydrogen range. In electric mode, the Kangoo allows 7.3 km/kWh, compared to the 6.8 km/kWh obtained using our simulated model. Hyundai Tucson fuel cell vehicle, containing 5.6 kg of hydrogen, allows 497–588 km, extending the range with different (8–32 kW) power fuel cells [38]. Its fuel efficiency corresponds to 72–90 km/kg, while Kangoo achieves a hydrogen range of 70 km/kg. Although there is no information available on the driving cycle used to obtain Kangoo's consumption and range data, the simulation results are sufficiently coherent in order of magnitude with the Kangoo's.

---

## 12.7 Conclusions

Although today's battery electric powered vehicles show higher electric ranges annually, enough for most daily trips, the market demand reflects that this approach does not satisfy all customers' expectations. Additionally, there exists a mature vehicle technology developed for hydrogen-powered vehicles that score higher ranges, are available in the market, but are infeasible to be sold due to its impossibility to be charged.

A new powertrain based on the use of the fuel cell stack as a range-extender system powering the battery of a BEV has been explained. The range and fuel consumption with different energy management strategies has been studied by applying different tests aiming to mitigate the commercialization problem associated with these vehicles. The proposed powertrain allows the car designers to prioritize the fuel selection and/or consumption, by considering:

1. Higher ranges (with NEDC drive cycle test) compared to current FCEV and BEV powertrains
2. Reduced power in the fuel cell stack and its dimensions (about one-third of the required in an equivalent FCEV)
3. Reduced/increased hydrogen consumption and increased/reduced battery consumption (the fuel selection/consumption becomes a driver decision)
4. Customized (reduced/increased) hydrogen tanks and/or reduced battery capacity, understood as the stored hydrogen in liters in the case of the fuel cell and as the cell capacity in ampere hours in the case of the battery
5. Recharging of the battery at higher/lower C rates to preserve its health

The results show a powertrain concept that could avoid the commercialization problem associated with these vehicles and open the door for designers because the discussed powertrain could be the starting point for a driver-oriented management battery system and sizing of fuel storage dimensions.

**Acknowledgments** We gratefully acknowledge the helpful comments and suggestions of Javier Arboleda, Senior Service Manager at Hyundai Motor in Spain, and Gema María Rodado Nieto, engineer at National Hydrogen Centre (CNH2) in Spain. We wish to thank the editors for allowing us to extend our previously published review [Álvarez, R., Beltrán, F., Villar, in the *International Journal of Hydrogen Energy*, 2016] with new data from 2017, based on our research and other cited works in the field.

---

## References

1. J.D.K. Bishop, N. Molden, A.M. Boies, Real-world environmental impacts from modern passenger vehicles operating in urban settings. *Int. J. Transp. Dev. Integr.* **1**(2), 203–211 (2017)
2. K.E. Kakosimos, O. Hertel, M. Ketzel, R. Berkowicz, Operational street pollution model (OSPM)—a review of performed application and validation studies, and future prospects. *Environ. Chem.* **7**(6), 485–503 (2010)
3. R. Álvarez, A. López, N. De la Torre, Evaluating the effect of a driver's behaviour on the range of a battery electric vehicle. *Proc. Inst. Mech. Eng., Part D: J. Automob. Eng.* **229**(10), 1379–1391 (2015)
4. E. Graham-Rowe, B. Gardner, C. Abraham, S. Skippon, H. Dittmar, R. Hutchins, J. Stannard, Mainstream consumers driving plug-in battery-electric and plug-in hybrid electric cars: a qualitative analysis of responses and evaluations. *Transp. Res. A Policy Pract.* **46**(1), 140–153 (2012)
5. B. Junquera, B. Moreno, R. Álvarez, Analyzing consumer attitudes towards electric vehicle purchasing intentions in Spain: technological limitations and vehicle confidence. *Technol. Forecast. Soc. Chang.* **109**, 6–14 (2016)
6. P. Pisu, G. Rizzoni, A comparative study of supervisory control strategies for hybrid electric vehicles. *IEEE Trans. Control Syst. Technol.* **15**(3), 506–518 (2007)
7. C.C. Chan, The state of the art of electric, hybrid, and fuel cell vehicles. *Proc. IEEE* **95**(4), 704–718 (2007)
8. Business Insider, David Scutt, 2016 was a record-breaking year for global car sales, and it was almost entirely driven by China, (2016), <http://www.businessinsider.com/2016-was-a-record-breaking-year-for-global-car-sales-and-it-was-almost-entirely-driven-by-china-2017-1>



9. J.E. Kang, T. Brown, W.W. Recker, G.S. Samuelsen, Refuelling hydrogen fuel cell vehicles with 68 proposed refuelling stations in California: measuring deviations from daily travel patterns. *Int. J. Hydrog. Energy* **39**(7), 3444–3449 (2014)
10. H2 Mobility, (2017), <http://h2-mobility.de/en/>
11. Electriccarsreport.com, Global Plug-in Vehicle Sales for 2016 (2016), <http://electriccarsreport.com/2017/02/global-plug-vehicle-sales-2016/>
12. Forbes, Robert Rapier, U.S. electric vehicle sales soared in 2016 (2016), <https://www.forbes.com/sites/rpapier/2017/02/05/u-s-electric-vehicle-sales-soared-in-2016/#5c85cdcd217f>
13. S. Hardman, R. Steinberger-Wilckens, D. van der Horst, Disruptive innovations: the case for hydrogen fuel cells and battery electric vehicles. *Int. J. Hydrog. Energy* **38**(35), 15438–15451 (2013)
14. P. Maniatopoulos, J. Andrews, B. Shabani, Towards a sustainable strategy for road transportation in Australia: the potential contribution of hydrogen. *Renew. Sust. Energ. Rev.* **52**, 24–34 (2015)
15. R. Álvarez, F. Beltrán, I. Villar, A new approach to battery powered electric vehicles: a hydrogen fuel cell based range extender system. *Int. J. Hydrog. Energy* **41**, 4808–4819 (2016)
16. A. Glerum, L. Stankovikj, M. Thémans, M. Bierlaire, Forecasting the demand for electric vehicles: accounting for attitudes and perceptions. *Transp. Sci.* **48**(4), 483–499 (2013)
17. D. Kettles, *Electric Vehicle Charging Technology Analysis and Standards (No. FSEC-CR-1996-15)* (Florida Solar, Cocoa, 2015)
18. J. Larminie, J. Lowry, *Electric Vehicle Technology Explained* (Wiley, Chichester, 2004)
19. Hyundai, ix35 fuel cell. Realizing the dream (2015), <http://worldwide.hyundai.com/WW/Showroom/Eco/ix35-Fuel-Cell/PIP/index.html>. Accessed 11 Nov 2015
20. R. Álvarez, S. Zubezu, G. Díaz, A. López, Analysis of low carbon super credit policy efficiency in European Union greenhouse gas emissions. *Energy* **82**, 996–1010 (2015)
21. V. Di Dio, D. La Cascia, R. Liga, R. Miceli, Integrated mathematical model of proton exchange membrane fuel cell stack (PEMFC) with automotive synchronous electrical power drive. in *Electrical Machines, 2008. ICEM 2008. 18th International Conference on IEEE* (2008), pp. 1–6
22. S.S. Kocha, Polymer electrolyte membrane (PEM) fuel cells, automotive applications, in *Fuel Cells* (Springer, New York, 2013), pp. 473–518
23. J. T. Pukrushpan, A. G. Stefanopoulou, H. Peng, Modeling and control for PEM fuel cell stack system, in *American Control Conference, 2002. Proceedings of the 2002*, vol. 4 (IEEE, 2002) pp. 3117–3122
24. A. Meintz, M. Ferdowsi, Control strategy optimization for a parallel hybrid electric vehicle, in *Vehicle Power and Propulsion Conference, 2008. VPPC'08* (IEEE, 2008), pp. 1–5
25. J.S. Won, R. Langari, Intelligent energy management agent for a parallel hybrid vehicle-part II: torque distribution, charge sustenance strategies, and performance results. *IEEE Trans. Veh. Technol.* **54**(3), 935–953 (2005)
26. A. Piccolo, L. Ippolito, V. zo Galdi, A. Vaccaro, Optimisation of energy flow management in hybrid electric vehicles via genetic algorithms, in *Advanced Intelligent Mechatronics, 2001. Proceedings 2001 IEEE/ASME International Conference on*, vol. 1 (IEEE, 2001), pp. 434–439
27. F.U. Syed, H. Ying, M. Kuang, S. Okubo, M. Smith, Rule-based fuzzy gain-scheduling pi controller to improve engine speed and power behavior in a power-split hybrid electric vehicle, in *Fuzzy Information Processing Society, 2006. NAFIPS 2006. Annual Meeting of the North American* (IEEE, 2006), pp. 284–289
28. D.E. Goldberg, J.H. Holland, Genetic algorithms and machine learning. *Mach. Learn.* **3**(2), 95–99 (1988)
29. D. E. Goldberg, in *Genetic Algorithms in Search, Optimization, and Machine Learning* (Addison-Wesley, Massachusetts, 1989)
30. Symbio (2016), <http://www.symbiofccl.com/vehicles/kangoo-ze-h2-en/>
31. Brusa: on-line product catalogue, PDU254 datasheet, <http://www.brusa.biz/en/products/system/hv-distribution/pdu254.html>

32. California Environmental Protection Agency, Advanced clean cars portal. <https://www.arb.ca.gov/msprog/acc/acc.htm>
33. California Environmental Protection Agency, Hydrogen Fueling Infrastructure Assessments <https://www.arb.ca.gov/msprog/zevprog/hydrogen/h2fueling.htm>
34. EAFO, <http://www.eafo.eu/infrastructure-statistics/hydrogen-filling-stations>
35. Eur-Lex, <http://eur-lex.europa.eu/legal-content/EN/TXT/?uri=celex:52013SC0005>
36. EV Volumes, <http://www.ev-volumes.com/country/total-world-plug-in-vehicle-volumes/>
37. D. L. Greene, G. Duleep, Status and prospects of the global automotive fuel cell industry and plans for deployment of fuel cell vehicles and hydrogen refuelling infrastructure. Oak Ridge National Laboratory (2013)
38. HYUNDAI, (2017), [https://www.hyundaiusa.com/abouthyundai/news/corporate\\_hyundai\\_offers\\_tucson\\_fuel\\_cell\\_hydrogen-powered\\_electric\\_vehicle\\_to\\_retail\\_customers\\_in\\_s-20131120.aspx](https://www.hyundaiusa.com/abouthyundai/news/corporate_hyundai_offers_tucson_fuel_cell_hydrogen-powered_electric_vehicle_to_retail_customers_in_s-20131120.aspx)
39. J. Romm, Tesla Trumps Toyota part II: The Big Problem with Hydrogen Fuel Cell Vehicles. The Energy Collective (2014), <http://www.theenergycollective.com/josephromm/462826/tesla-trumps-toyota-part-ii-big-problem-hydrogen-fuel-cell-vehicles>
40. B. Snavely, GM, Honda to make hydrogen fuel cells at Michigan factory. USA today. <http://www.usatoday.com/story/money/cars/2017/01/30/general-motors-honda-fuel-cell-deal/97240096/>
41. The Scandinavian Hydrogen Highway, <http://www.scandinavianhydrogen.org/>. Accessed 13 Oct 2016
42. Toyota, <https://ssl.toyota.com/mirai/fuel.html>
43. TÜV SÜD, <http://www.tuv-sud.com/news-media/news/92-new-hydrogen-refuelling-stations-worldwide-in-2016>
44. US Department of Energy, Fuel cell technologies market report 2015 (2016), [https://energy.gov/sites/prod/files/2016/10/f33/fcto\\_2015\\_market\\_report.pdf](https://energy.gov/sites/prod/files/2016/10/f33/fcto_2015_market_report.pdf)
45. J. Weinert, J. Ogden, D. Sperling, A. Burke, The future of electric two-wheelers and electric vehicles in China. *Energy Policy* **36**(7), 2544–2255 (2008)



# Totalized Hydrogen Energy Utilization System

# 13

Hiroshi Ito and Akihiro Nakano

## Contents

13.1	Introduction .....	386
13.2	Description of Totalized Hydrogen Energy Utilization System (THEUS) .....	388
13.2.1	Unitized Reversible Fuel Cell (URFC) System .....	388
13.2.2	Metal Hydride Tank (MHT) for Hydrogen Storage .....	392
13.3	THEUS Operation .....	395
13.3.1	Definition of Efficiencies of THEUS .....	395
13.3.2	Continuous Operation of THEUS for 3 Days .....	398
13.3.3	THEUS Operation with Fluctuating Renewable Energy Sources (RESs) .....	401
13.4	Summary .....	404
	References .....	405

## Abstract

The totalized hydrogen energy utilization system (THEUS) proposed here is a hydrogen-based energy system originally designed to have both functions of load leveling and cogeneration in commercial buildings. In addition, THEUS has the potential to capture fluctuating energy input from renewable energy sources such as solar photovoltaics (PVs) and wind power. The main components of THEUS are a unitized reversible fuel cell (URFC) and metal hydride tank (MHT). In this chapter, first, the performances of URFC and MHT were verified individually.

## Author Contribution

The authors acknowledge publishers (Hydrogen Energy Publications, LLC, and Elsevier B.V.) in permitting us to reuse contents in published articles. The authors thank the editors in allowing us to extend our previously published articles [4, 5, 6, 11, 12, 17].

H. Ito (✉) · A. Nakano

Research Institute for Energy Conservation, National Institute of Advanced Industrial Science and Technology (AIST), Tsukuba, Japan

e-mail: [ito.h@aist.go.jp](mailto:ito.h@aist.go.jp); [a.nakano@aist.go.jp](mailto:a.nakano@aist.go.jp)

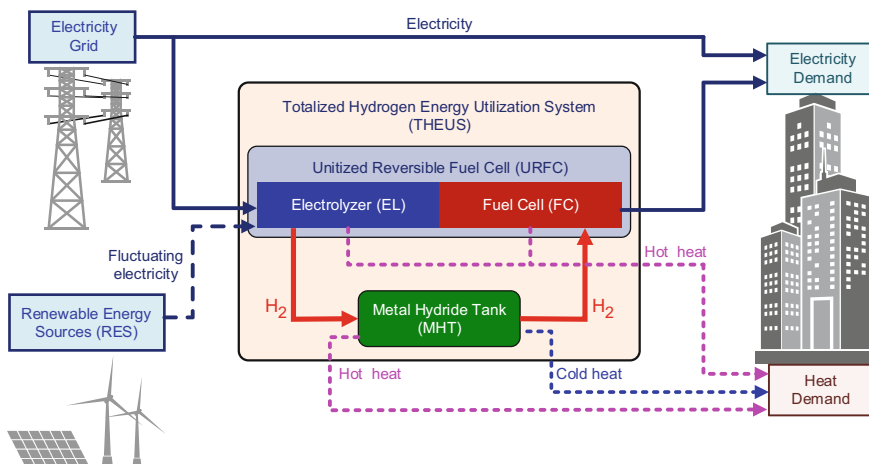
Then, a 3-day continuous operation of THEUS was evaluated. Finally, the potential of THEUS for capturing fluctuating energy input was verified experimentally. These experimental results clearly indicate the promising potential of THEUS as an innovative energy facility in stationary applications.

### 13.1 Introduction

The difficult issues of both global warming and depletion of fossil fuel resources require energy conservation, namely, reduction in fossil fuel consumption, and thus impose important technical challenges in various energy sectors. In Japan, because the share of fossil fuels (coal, oil, and natural gas) in primary energy consumption has been about 92% (in 2014) [1] and almost all of it imported (>90%), the reduction in fossil fuel consumption has been a national issue in terms of the environment, economy, and national security. Based on data for energy use in Japan in 2014 [1], the share of heat use used in domestic hot water (DHW) and space heating/cooling was about 44% in the commercial sector including schools and hospitals and about 53% in the residential sector. This means that about half of the primary energy is converted to heat (hot or cold) of the total energy use in these sectors via various equipment such as a heater, boiler, and air conditioners. In addition, in Japan, the large difference in electricity demand between daytime and nighttime leads to overcapacity and less capacity factor (operation time) of power generation facilities. Here, the development of an innovative energy utility system that has both functions of “energy storage” and “cogeneration of heat and power (CHP)” is needed.

On the other hand, the capacity of “new” renewable energy facilities installed worldwide, such as solar photovoltaics (PVs) and wind turbines, has increased rapidly during the past 10–15 years [9]. These new renewable energy sources (RES) such as solar and wind are distributed evenly compared to fossil fuels, and the cost of RES facilities has decreased significantly during the past 10 years. However, the electricity generated by these RESs is fluctuating in nature, due to variation in wind or light patterns. The capacity of such newly installed RES has already exceeded the limit of the grid stabilization capacity in some areas, though their contribution to the total worldwide energy supply is still minor (<10%). Therefore, “energy storage” is crucial for accelerating the installation of RES.

Attention is currently focusing on hydrogen (H<sub>2</sub>) as an energy medium for stationary energy applications because it offers many advantages for energy storage; (1) hydrogen can be produced via water electrolysis even from fluctuating electricity of intermittent RES (e.g., solar and wind), (2) produced hydrogen can be stored in numerous forms (e.g., compressed, liquefied, or metal hydride) without self-discharge over time, (3) carbon-free electricity production can be achieved using a fuel cell, and (4) system power (kW) and stored energy (kWh) can be independently optimized. Based on these advantages, hydrogen-based energy systems for energy storage and conversion have been receiving much attention [3, 8, 10].



**Fig. 13.1** Schematic overview of the concept of “totalized hydrogen energy utilization system (THEUS)”

Based on this background, we propose a concept called “totalized hydrogen energy utilization system (THEUS),” which is a stationary system of energy utilization using hydrogen as the energy medium. Figure 13.1 shows a schematic overview of the concept of THEUS, whose main components are a water electrolyzer (EL), fuel cell (FC), metal hydride tank (MHT), and connecting pipes.

Both ELs and FCs can be categorized into several types based on their electrolyte and operating temperature, e.g., proton exchange membrane (PEM), alkaline, or solid oxide. Among them, PEM-based devices (FCs and ELs) are attractive due to their simple system and their excellent performance of load following and/or start-and-stop characteristics. In addition, PEM-ELs and PEM-FCs have a similar cell/stack design using a common PEM as the electrolyte. From the technical viewpoint, it is possible to establish a unitized cell/stack of these two electrochemical devices. A unitized reversible fuel cell (URFC) based on PEM has been studied for several decades [2, 7, 18, 21], and its high potential as an energy conversion device for both functions (i.e., energy storage and heat/power cogeneration) has been proven. As an energy conversion device in stationary systems, URFCs have several advantages over the discrete installation of both an electrolyzer and a fuel cell: (1) lower cost for the total system, (2) higher operating ratio, (3) reduced maintenance, and (4) smaller footprint. That is why in THEUS, the URFC has been applied as the key energy conversion device using hydrogen medium.

Several options for the form of hydrogen storage are also available, such as compressed, liquefied, synthesized natural gas, or metal hydride. Among them, hydrogen storage using a metal hydride tank has two significant advantages for application in commercial buildings, that is, high volume density and low pressure [19, 22]. High volume density enables compact energy storage, which is beneficial to

practical applications. Low-pressure hydrogen storage is desirable due to the strict safety regulations in commercial buildings.

The cogeneration ability of THEUS enables not only hot but also cold thermal energy. Hot heat (thermal energy) can be extracted from both EL and FC operation modes. Furthermore, because hydrogen absorption and desorption via metal hydride is an exothermic and endothermic reaction, respectively, hot heat and cold heat can be, respectively, obtained from this hydrogen absorption and desorption processes. Because commercial buildings have a relatively high demand for both hot and cold thermal energy, cogeneration ability of the THEUS is advantageous in commercial and high-rise residential buildings. As for the energy storage function, the Japanese electricity price at night is much cheaper than that during the day due to the difference in demand. According to a feasibility study by an energy engineering company [14], installation of THEUS into certain commercial buildings in Japan might be economically beneficial because of its load leveling function due to its energy storage ability. THEUS would also be an energy storage (buffer) device for fluctuating electricity from RES. This energy storage function is expected to promote the installation of THEUS into a wide range of applications.

A pilot-scale of THEUS (Fig. 13.2) was installed in our laboratory (AIST, Japan) and comprehensively evaluated experimentally. Based on the obtained data for electricity, material (hydrogen), and recovered heat, our research group examined the performance of each component and of the total system by including the energy consumption of the balance of plants (BOPs) [4, 11]. Our group also experimentally evaluated the energy storage ability of THEUS of fluctuating electricity from RES [5, 6]. In the current chapter, we summarize these results to determine the potential of THEUS as a stationary energy utilization system.

---

## 13.2 Description of Totalized Hydrogen Energy Utilization System (THEUS)

This section introduces the specifications and performance of system components (URFC and MHT) of a pilot-scale of THEUS installed in our laboratory.

### 13.2.1 Unitized Reversible Fuel Cell (URFC) System

A pilot-scale URFC system (Fig. 13.2) was installed in our laboratory [11, 12]. The URFC stack and its balance of plants (BOPs) were designed and manufactured by Takasago Thermal Engineering Co. (Japan). In this pilot system, the nominal hydrogen production rate in the EL operation mode was 1.0 Nm<sup>3</sup>/h, and nominal power production capacity in the FC mode was 0.8 kW, when the energy consumption of BOPs during FC mode was about 0.3 kW and net power production capacity of FC mode was about 0.5 kW (see Sect. 13.3.1 and Fig. 13.9). The system included a URFC stack, pipeline system, valves, pumps, air blower, chiller, and two power devices (a DC power and a DC load), all of which were enclosed in a cabinet whose



**Fig. 13.2** Photo of the THEUS installed in AIST: left, metal hydride tank (MHT); center, unitized reversible fuel cell (URFC); and right, personal computer (PC) for controlling and monitoring the operating parameters

dimensions were 1280 (width)  $\times$  740 (length)  $\times$  1361 (height) mm (Fig. 13.2). Also enclosed within this cabinet was a system to control the stack current ( $I_{\text{stack}}$ ), stack temperature ( $T_{\text{stack}}$ ), hydrogen pressure ( $P_{\text{H}_2}$ ), and valve switching and to monitor all the operating parameters such as stack voltage ( $V_{\text{stack}}$ ) and flow rates of working fluids ( $\text{H}_2$ , air, and water).

The URFC stack in this pilot-scale system consisted of ten rectangular cells, with an active electrode area ( $A$ ) of  $250 \text{ cm}^2$ , and each cell consisted of a membrane electrode assembly (MEA) and bipolar plates [12]. The MEA was a composite of a catalyst-coated membrane (CCM) and gas diffusion layers (GDLs) on both sides of the CCM. Table 13.1 lists the specifications of the cell and stack. The stack had six pipeline connections for fluids (Fig. 13.3), that is, the inlet and outlet lines of each fluid, namely,  $\text{H}_2$ ,  $\text{O}_2$  (or air), and cooling water. Each fluid line in the stack passed through the bipolar plates and membranes. The manifolds were designed to distribute both gases ( $\text{H}_2$  and either  $\text{O}_2$  or air) to one side of each cell. Each bipolar plate had a terminal to measure the cell voltage ( $V_{\text{cell}}$ ).

The fabrication of an efficient URFC system must include the design of the BOP. To ensure an overall compact system, lines in the piping system must be shared by both operation modes as much as possible. Figure 13.3 is a piping and flow diagram of the present system, showing the six major line systems: inlet and outlet lines of  $\text{H}_2$  (left side of URFC stack in Fig. 13.3), inlet and outlet lines of either air or  $\text{O}_2$ , electrolysis water circulation line (right side of URFC stack), and cooling water circulation line (upper side of URFC stack). The outlet line of  $\text{H}_2$  and that of either air or  $\text{O}_2$  were shared by both the EL and FC operation modes.



**Table 13.1** Specifications of URFC stack

Material		
Membrane		Nafion 115
Catalyst	H <sub>2</sub> side	Pt
	O <sub>2</sub> side	Pt + IrO <sub>2</sub>
Gas diffusion layer (current collector)	H <sub>2</sub> side	Carbon paper
	O <sub>2</sub> side	Titanium felt
Bipolar plate		Titanium (Pt coated)
Cell/stack configuration		
Electrode active area	250 cm <sup>2</sup>	
Number of cells in series	10	

Figure 13.4 shows representative results of continuous operation of the URFC system for about 2.5 h with switching between EL and FC modes. In this case, the URFC was operated first at the EL mode for about 60 min, and then switched to FC mode for about 60 min, and then switched again to EL mode. In the first EL mode, the URFC was operated at the rated condition ( $T_{\text{stack}} = 50\text{ }^{\circ}\text{C}$ ,  $P_{\text{H}_2} = 1.0\text{ MPa}$ , and  $i_{\text{stack}}$  (current density of stack ( $= I_{\text{stack}}/A$ )  $= 1.0\text{ A cm}^{-2}$ ), and all the operating parameters ( $i_{\text{stack}}$ ,  $V_{\text{stack}}$ ,  $T_{\text{stack}}$ , and  $P_{\text{H}_2}$ ) were stable, when  $T_{\text{stack}}$  was regulated by the cooling water and  $P_{\text{H}_2}$  by the back pressure valve. In the switching procedure, dry nitrogen ( $\text{N}_2$ ) was introduced into both sides of the stack, and remaining water and gases were discharged. The switching procedure took about 5–10 min. At the beginning of FC mode,  $T_{\text{stack}}$  remained around  $50\text{ }^{\circ}\text{C}$ , which was rather low for FC operation, and thus there was a possibility of flooding occurring at high  $i_{\text{stack}}$ . To avoid such flooding,  $i_{\text{stack}}$  was increased gradually as shown in Fig. 13.4.  $T_{\text{stack}}$  increased with increasing  $i_{\text{stack}}$  and reached  $70\text{ }^{\circ}\text{C}$ . When  $T_{\text{stack}} > 70\text{ }^{\circ}\text{C}$ , stack cooling with circulating water was activated for regulating  $T_{\text{stack}}$ . Small spikes observed in  $P_{\text{H}_2}$  during FC mode were caused by the draining and recharging of  $\text{H}_2$  in the recirculation line. At the rated operation of FC ( $T_{\text{stack}} = 70\text{ }^{\circ}\text{C}$  and  $i_{\text{stack}} = 0.5\text{ A cm}^{-2}$ ) (110–130 min in Fig. 13.4), again the operating parameters were stable, the same as in the EL mode. The flow rate of produced  $\text{H}_2$  was monitored with a digital flow meter. Under the  $P_{\text{H}_2}$  range in the EL operation in this study (0.1–1.0 MPa), no relationship was observed between  $P_{\text{H}_2}$  and Faraday (current) efficiency, which was near 1 at  $i_{\text{stack}} = 1.0\text{ A cm}^{-2}$ . Here, the stoichiometric ratio of  $\text{H}_2$  during FC operation was always near 1.

Figure 13.5 shows the measured  $i_{\text{stack}} - \text{average cell voltage}$  ( $V_{\text{cell\_avg}}$ ) for EL and FC modes under different  $T_{\text{stack}}$ , where  $V_{\text{cell\_avg}}$  was obtained by dividing  $V_{\text{stack}}$  by the number of cells (i.e., 10). The heat source for the stack was the self-heating (Joule heat) resulting from the overpotential during both EL and FC modes. Because the overpotential during EL was smaller than that during FC,  $T_{\text{stack}}$  during EL was limited to  $50\text{ }^{\circ}\text{C}$ , whereas  $T_{\text{stack}}$  during FC reached  $70\text{ }^{\circ}\text{C}$ . During EL operation,  $P_{\text{H}_2}$  was set at 1.0 MPa. As expected, the EL performance was improved at higher  $T_{\text{stack}}$ ,



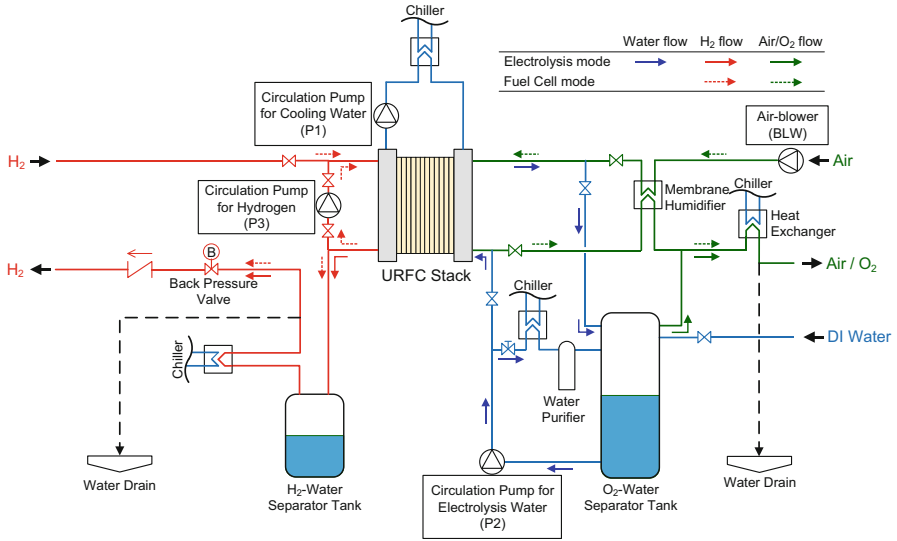


Fig. 13.3 Piping and flow diagram of URFC system

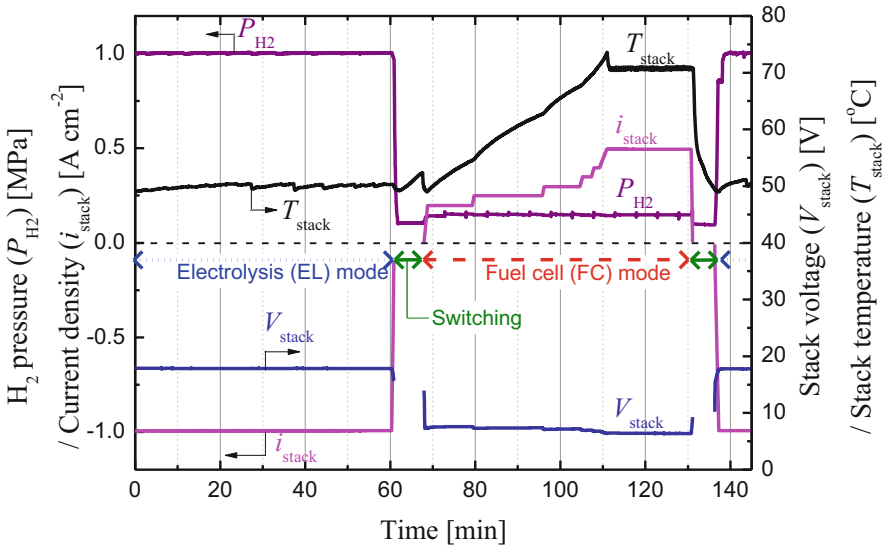
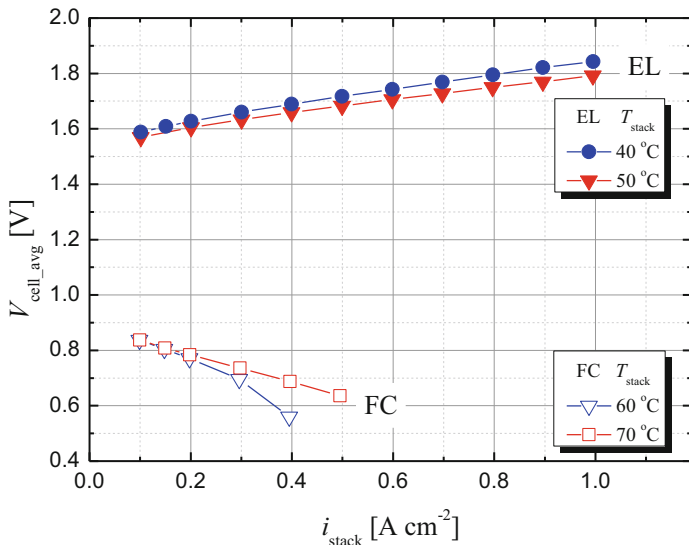


Fig. 13.4 Change in hydrogen pressure ( $P_{H_2}$ ), stack temperature ( $T_{stack}$ ), stack voltage ( $V_{stack}$ ), and stack current density ( $i_{stack}$ ) during continuous operation of URFC system from electrolysis (EL)→switching→fuel cell (FC) mode

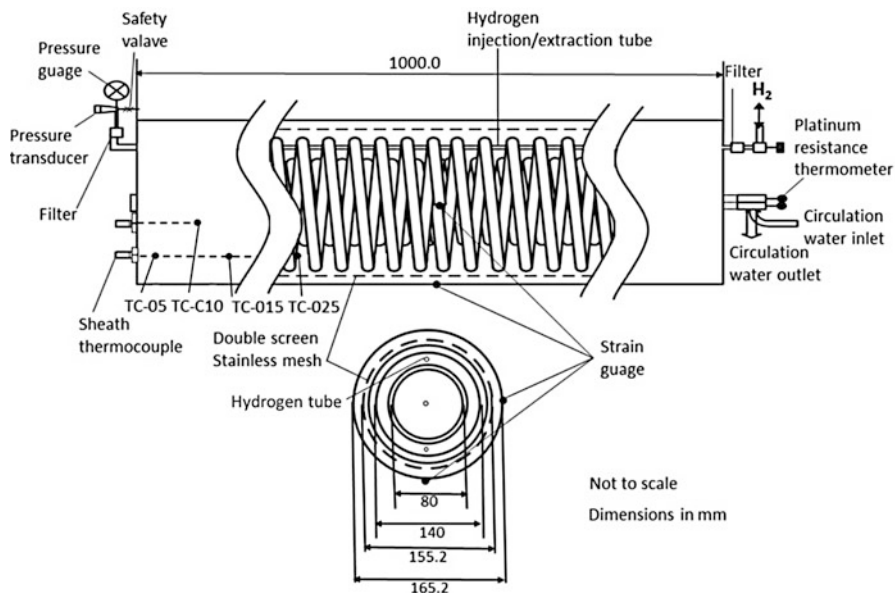


**Fig. 13.5** Current density ( $i_{stack}$ ) – average cell voltage ( $V_{cell,avg}$ ) characteristics of EL and FC modes at various stack temperature ( $T_{stack}$ ).  $P_{H_2}$  during EL was 1.0 MPa

because both activation and ohmic overpotentials decreased as  $T_{stack}$  was increased. As for FC operation, a significant difference in  $V_{cell,avg}$  between two different  $T_{stack}$  is evident at  $i_{stack} > 0.2$  A cm<sup>-2</sup>. The rapid decrease in  $V_{cell,avg}$  (i.e.,  $V_{stack}$ ) at  $T_{stack} = 60$  °C indicates “flooding,” that is, condensed liquid water in the cell/stack had accumulated at the electrode and thus hindered the mass transport of reactive gases to the electrode surface. The dew point of air passing through the membrane humidifier was estimated at around 60 °C under the constant flow rate of the air regardless of  $T_{stack}$ . Therefore, relative humidity ( $RH$ ) of the air in the cathode gas channel reached near 100% when  $T_{stack} = 60$  °C.

### 13.2.2 Metal Hydride Tank (MHT) for Hydrogen Storage

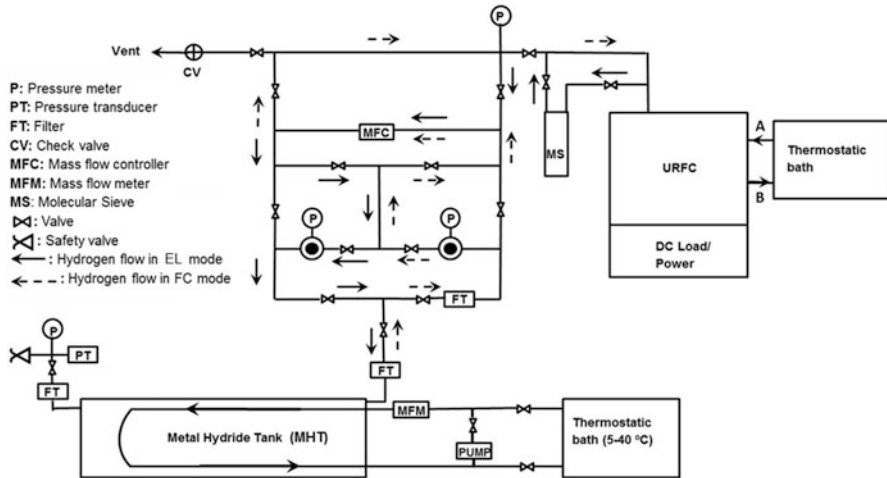
Several types of MHT have been designed and tested by our research group [13, 15, 16, 20]. As a component of the present pilot-scale THEUS, a new horizontal-type MHT has been designed by our group and installed in our laboratory (AIST) [17]. Specifications of this MHT unit and the unit test results are described in this section. Figure 13.6 shows schematics of this horizontal-type MHT, whose total length was 1 m with an outer diameter of 165.2 mm and the inner diameter of 155.2 mm. This MHT contained 50 kg of MmNi<sub>5</sub> (Mm is mischmetal), (AB<sub>5</sub>) metal hydride alloy whose grain size was 500 μm, and whose reaction heat for absorption was 28.934 kJ/mol H<sub>2</sub> and that for desorption was 27.867 kJ/mol H<sub>2</sub>. The total weight of the MHT with the MmNi<sub>5</sub> hydride was approximately 85 kg. A double coil-type heat exchanger made of copper was adopted for recovering the reaction



**Fig. 13.6** Schematic of the metal hydride tank (MHT). Four sheath thermocouples (TC-C10, TC-O25, TC-O15, and TC-O5) were inserted to measure temperature at various locations in the tank

heat of the metal hydride. Four sheath thermocouples were inserted into the tank to measure the temperature at the respective location as follows. The thermocouple (TC) with one measurement point was set at 26 mm from the center of the side wall and 10 cm from the outer surface of the side wall (TC-C10). The thermocouple with three measurement points was fixed at 55 mm from the center of the side wall, and the measurement points were at 25 cm, 15 cm, and 5 cm from the outer surface of the side wall (TC-O25, TC-O15, and TC-O5), respectively. The pressure in the MHT was measured by using a pressure transducer. The safety valve was set to 1.2 MPa. To reduce cost, a specially designed hydrogen injection/extraction tube [16] was adopted, and a commercial sintered stainless filter with a pore diameter of 0.5  $\mu\text{m}$  was used outside of the tank. The tank was covered with a 6-cm-thick thermal insulation foam (Aeroflex) to prevent heat loss from the outer surface.

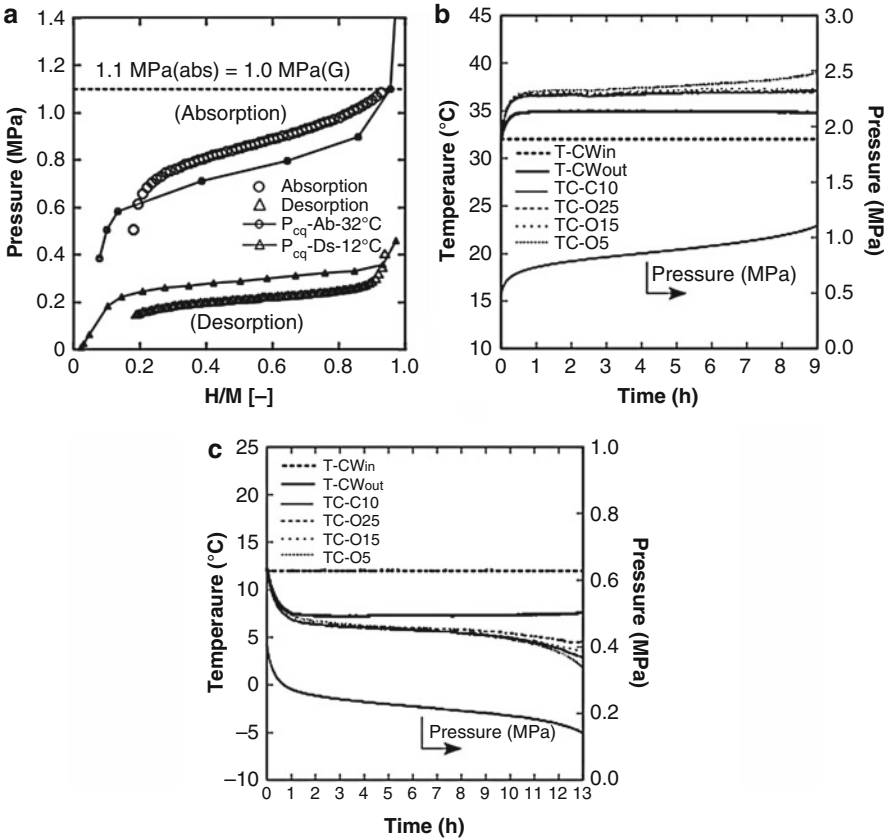
Figure 13.7 shows the piping and flow diagram for the experimental setup of the THEUS in our laboratory. For the unit test of this MHT, the hydrogen was supplied from hydrogen cylinders instead from the URFC. The hydrogen flow rate was regulated by a mass flow controller (MFC). The inlet and outlet of the heat exchanger in the MHT were connected to a thermostatic bath to regulate the temperature of the circulation fluid. The circulation fluid was composed of water (85 vol.%) and ethylene glycol (15 vol.%). A bypass line with a small pump was added to the circulation line so that the circulation fluid could be circulated without entering the



**Fig. 13.7** Piping and flow diagram of a THEUS in AIST (Fig. 13.2)

thermostatic bath. This pump and bypass line were used in the experiments for the absorption/desorption continuous test.

The pressure-composition ( $P$ - $C$ ) isotherms, the temperature change in selected locations in the tank (TC-C10, TC-O25, TC-O15, and TC-O5), and the inlet temperature and outlet temperature of the circulation fluid (TC-CWin and TC-CWout, respectively) were assessed to determine the fundamental characteristics of the MHT. Figure 13.8 shows the result of the individual unit absorption-desorption test for the MHT. Figure 13.8a shows the  $P$ - $C$  isotherm, Fig. 13.8b shows the time variation in  $P$ , TC-C10, TC-O25, TC-O15, TC-O5, TC-CWin, and TC-CWout for absorption, and Fig. 13.8c shows that for desorption. The composition hydrogen-to-metal ( $H/M$ ) of 0.18 was selected as the starting point, and hydrogen was absorbed for 9 h. During the 9-h absorption process (Fig. 13.8b), the hydrogen flow rate was 11.0 normal liters per minute (NL/min), and the circulation water flow rate was 1.12 L/min at 32 °C. During the 13-h desorption process (Fig. 13.8c), the hydrogen flow rate was 7.6 NL/min and the circulation water flow rate 0.46 L/min at 12 °C. In the  $P$ - $C$  results (Fig. 13.8a), the solid lines with the circles and the triangles show the equilibrium pressures at absorption and desorption ( $P_{eq-Ab}$  and  $P_{eq-Ds}$ , respectively) at 32 and 12 °C, respectively. Also shown in Fig. 13.8b, c is the time variation in pressure ( $P$ ) during absorption and desorption, respectively. The hydrogen supply was stopped when the composition,  $H/M$ , reached 0.94, which corresponded to  $P = 1.1$  MPa. In total, 5920 NL of hydrogen was absorbed during this unit test. The temperature data during the absorption process remained relatively steady, except at the measurement point TC-O5, which was a location very close to the side wall. Note that Fig. 13.8c indicates an inhomogeneous temperature distribution during the last stage of the desorption process (>10 h). The difference between TC-CWin and TC-CWout was kept at 3 °C during the absorption process and at 5 °C desorption process.

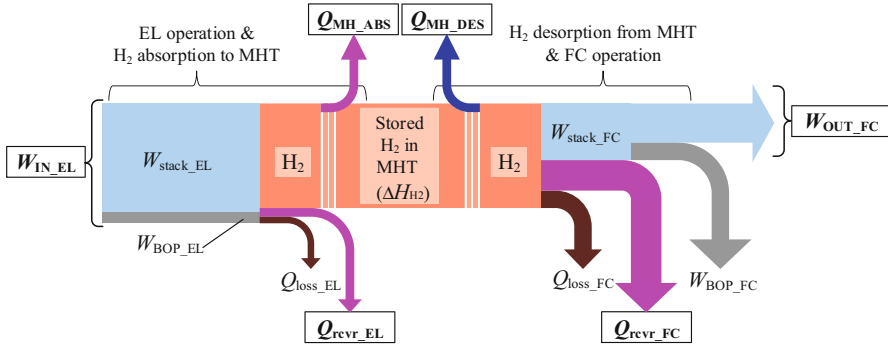


**Fig. 13.8** Individual absorption-desorption test of MHT; (a) P-C isotherm, (b) temperature changes in the tank and circulation water (fluid) during absorption, and (c) temperature changes during desorption

### 13.3 THEUS Operation

#### 13.3.1 Definition of Efficiencies of THEUS

This section describes the evaluation of the performance of THEUS. First, the performance of THEUS was evaluated at the system level in which the energy consumption of BOP was considered. Then, considering combined heat and power (CHP) application with URFC, the heat recovery (HR) with cooling water of URFC was included in the evaluation. Finally, the HR from the MHT during the absorption/desorption process was considered. Thus, three different efficiencies were defined and calculated for both the EL/absorption and FC/desorption modes: (1) energy conversion efficiency of EL/FC ( $\eta_{EL}/\eta_{FC}$ ), (2) efficiency including heat recovery



**Fig. 13.9** Schematic of energy flow from power input into electrolysis (EL) mode to power output from fuel cell (FC) mode (right edge)

(HR) during EL/FC operation ( $\eta_{EL+HR}/\eta_{FC+HR}$ ), and (3) efficiency including HR from MHT during the absorption/desorption process ( $\eta_{EL+HR+MH}/\eta_{FC+HR+MH}$ ). Also calculated were two different round-trip efficiencies: (1)  $\eta_{URFC}$ , defined by merging  $\eta_{EL+HR}$  and  $\eta_{FC+HR}$ , and (2)  $\eta_{THEUS}$ , defined by merging  $\eta_{EL+HR+MH}$  and  $\eta_{FC+HR+MH}$ . The energy flow of THEUS is schematically shown in Fig. 13.9. All five efficiencies, namely,  $\eta_{EL}$  (or  $\eta_{FC}$ ),  $\eta_{EL+HR}$  (or  $\eta_{FC+HR}$ ),  $\eta_{EL+HR+MH}$  (or  $\eta_{FC+HR+MH}$ ),  $\eta_{URFC}$  and  $\eta_{THEUS}$ , were evaluated based on the energy amount (J or kWh), and no loss related to hydrogen storage was considered here. The enthalpy change of H<sub>2</sub> was calculated based on the high heating value (HHV) of H<sub>2</sub> (i.e., 285.83 kJ mol<sup>-1</sup>).

In the case of EL operation,  $\eta_{EL}$  was defined using Eq. 13.1 as the ratio of the enthalpy of produced H<sub>2</sub> ( $\Delta H_{H_2\_prod}$ ) during a certain period ( $t_{EL}$ ) of EL operation to the total energy input into the URFC during EL operation ( $W_{IN\_EL}$ ):

$$\eta_{EL} = \frac{\Delta H_{H_2\_prod}}{W_{IN\_EL}} \tag{13.1}$$

where  $W_{IN\_EL}$  is the summation of energy input into the stack for EL ( $W_{stack\_EL} = I_{stack} \times V_{stack} \times t_{EL}$ ) and the BOP power consumption during EL operation ( $W_{BOP\_EL}$ ). Similarly,  $\eta_{FC}$  was defined using Eq. 13.2 as the ratio of the useful electrical energy output during a certain period ( $t_{FC}$ ) of FC operation to the enthalpy of consumed H<sub>2</sub> ( $\Delta H_{H_2\_cons}$ ):

$$\eta_{FC} = \frac{W_{OUT\_FC}}{\Delta H_{H_2\_cons}} \tag{13.2}$$

where  $W_{OUT\_FC}$  was calculated by subtracting the BOP power consumption during FC operation ( $W_{BOP\_FC}$ ) from the energy output from the stack for FC ( $W_{stack\_EL} = I_{stack} \times V_{stack} \times t_{FC}$ ).

Assuming a CHP application of the URFC system, thermal energy recovered from the stack was then considered. The recovered heat (thermal energy) from the URFC was calculated based both on the difference between TC-CWin and

TC-CWout and on the flow rate of the cooling water. In both EL and FC, the ratio of recovered heat was calculated by dividing the recovered thermal energy for each operation mode ( $Q_{\text{rcvr\_EL}}$ ,  $Q_{\text{rcvr\_FC}}$ ) by the total energy input for EL and FC ( $W_{\text{IN\_EL}}$ ,  $\Delta H_{\text{H}_2\text{\_cons}}$ ), respectively, and then added to  $\eta_{\text{EL}}$  and  $\eta_{\text{FC}}$  to obtain the efficiency including HR during EL and FC operation ( $\eta_{\text{EL+HR}}$  and  $\eta_{\text{FC+HR}}$ ), using Eqs. 13.3 and 13.4, respectively:

$$\eta_{\text{EL+HR}} = \frac{\Delta H_{\text{H}_2\text{\_prod}} + Q_{\text{rcvr\_EL}}}{W_{\text{IN\_EL}}} \quad (13.3)$$

$$\eta_{\text{FC+HR}} = \frac{W_{\text{OUT\_FC}} + Q_{\text{rcvr\_FC}}}{\Delta H_{\text{H}_2\text{\_cons}}} \quad (13.4)$$

Finally, the recovered thermal energy (hot/cold) from MHT during absorption/desorption of  $\text{H}_2$  was added to  $\eta_{\text{EL+HR}}$  and  $\eta_{\text{FC+HR}}$ , respectively. In the case of EL operation, the produced  $\text{H}_2$  by URFC was directly absorbed by the MHT. Because the absorption process is exothermic, hot heat could be extracted via the cooling fluid. This recovered heat ( $Q_{\text{MH\_ABS}}$ ) was added to  $\eta_{\text{EL+HR}}$  described in Eq. 13.5 as

$$\eta_{\text{EL+HR+MH}} = \frac{\Delta H_{\text{H}_2\text{\_prod}} + Q_{\text{rcvr\_EL}} + Q_{\text{MH\_ABS}}}{W_{\text{IN\_EL}}} \quad (13.5)$$

In the case of FC operation, desorbed  $\text{H}_2$  from MHT was directly supplied to URFC. During this desorption process, cold heat could be extracted from the MHT, because the desorption process is endothermic. In the same manner as EL/absorption, recovered cold heat ( $Q_{\text{MH\_DES}}$ ) during desorption was added to  $\eta_{\text{FC+HR}}$  to obtain the overall efficiency of FC/desorption described in Eq. 13.6 as

$$\eta_{\text{FC+HR+MH}} = \frac{W_{\text{OUT\_FC}} + Q_{\text{rcvr\_FC}} + Q_{\text{MH\_DES}}}{\Delta H_{\text{H}_2\text{\_cons}}} \quad (13.6)$$

Because no loss related to hydrogen storage was considered here,  $\Delta H_{\text{H}_2\text{\_prod}}$  was assumed to be equal to  $\Delta H_{\text{H}_2\text{\_cons}}$  for one cycle between EL/absorption and FC/desorption (Fig. 13.9). Based on this assumption, the total energy efficiency of URFC including HR during both operation modes ( $\eta_{\text{URFC}}$ ) can be defined in Eq. 13.7 as

$$\eta_{\text{URFC}} = \frac{W_{\text{OUT\_FC}} + Q_{\text{rcvr\_EL}} + Q_{\text{rcvr\_FC}}}{W_{\text{IN\_EL}}} \quad (13.7)$$

In addition, HR from the MHT was included to obtain the total energy efficiency of THEUS ( $\eta_{\text{THEUS}}$ ) defined in Eq. 13.8 as

$$\eta_{\text{THEUS}} = \eta_{\text{URFC}} + \frac{Q_{\text{MH\_ABS}} + Q_{\text{MH\_DES}}}{W_{\text{IN\_EL}}} \quad (13.8)$$

As in the case of URFC, the recovered thermal energy (hot/cold) from MHT was calculated based both on the difference between TC-CWin and TC-CWout and on the flow rate of the cooling water. The HR rate during absorption/desorption of H<sub>2</sub> from the MHT ( $\varepsilon_{\text{MH\_ABS/DES}}$ ) was defined in Eq. 13.9 as

$$\varepsilon_{\text{MH\_ABS/DES}} = \frac{Q_{\text{MH\_ABS/DES}}}{Q_{\text{MH\_REACT}}} \quad (13.9)$$

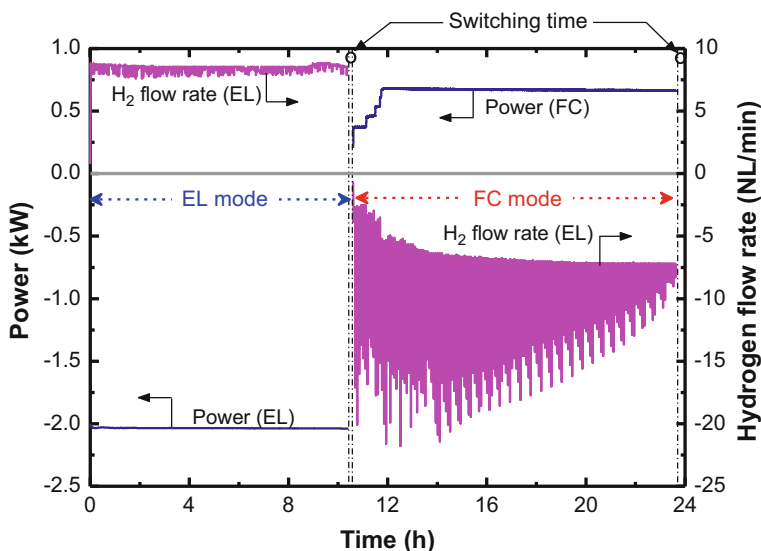
where  $Q_{\text{MH\_REACT}}$  is the reaction heat of MH. The value of  $Q_{\text{MH\_REACT}}$  is estimated as the product of the volume of H<sub>2</sub> absorbed/desorbed by MH and the reaction heat per volume.

### 13.3.2 Continuous Operation of THEUS for 3 Days

Both functions of THEUS, that is, load leveling and cogeneration of heat and power, were evaluated by testing the THEUS system continuously for 3 days [4]. Figure 13.10 shows the power and hydrogen flow rate during Day 1 operation. THEUS was operated in EL mode for 10 h 44 min and in FC mode for 13 h. The switching time between EL and FC in URFC was about 8 min. In Fig. 13.10, the positive power indicates the power output from the URFC, and the negative hydrogen flow rate indicates hydrogen supplied to the URFC from the MHT. During FC operation, spikes observed in the hydrogen flow rate were due to the hydrogen recirculation by the hydrogen circulation pump every 5 min. The hydrogen flow rate was also increased proportionally to the FC power output to prevent flooding as mentioned in Sect. 13.2.1. The URFC during FC mode took about 1 h 14 min to reach the predefined output, after which the power output remained steady until the end of this FC mode. Power input to the THEUS in EL mode was fixed at 2.05 kW, and power output from the THEUS in FC mode was fixed at 0.68 kW. During EL mode, the hydrogen flow rate was kept between 7.8 and 8.8 NL/min with an average of 8.4 NL/min, and during FC mode, the range was 3–23 NL/min with an average of 7 NL/min. During Day 2, the heat output from the URFC in EL mode ( $Q_{\text{rcvr\_EL}}$ ) and FC mode ( $Q_{\text{rcvr\_FC}}$ ) was 8.88 MJ and 17.81 MJ, respectively, with an average of 0.23 kW and 0.38 kW, respectively.

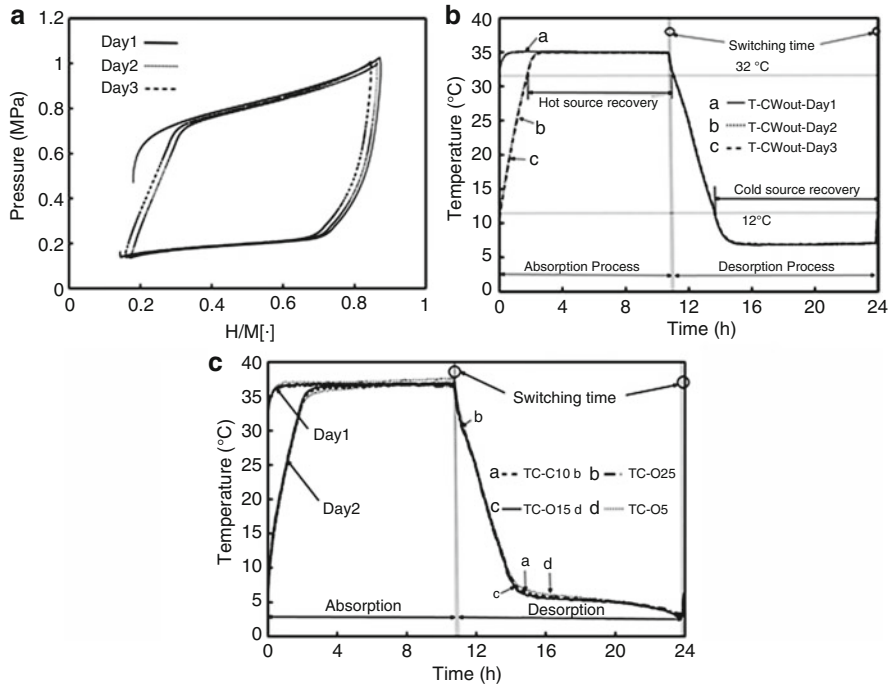
Figure 13.11a shows the dynamic pressure-composition (P-C) isotherm of MH during the 3-day continuous operation. During the first absorption process, the P-C isotherm showed the same pattern as during the individual MHT unit test (Fig. 13.8a), after which the pressure profile exhibited a closed loop that consisted of a switching time, the end point of the desorption process, again switching time, and vice versa. Except in the first absorption process, the starting point of the desorption process in the continuous operation occurred at a higher temperature and that at absorption process at a lower temperature as compared with the individual test. The maximum H/M of the MHT was 0.87. The maximum and minimum MHT pressures were 1.02 MPa and 0.136 MPa, respectively, for both EL and FC modes.





**Fig. 13.10** Change in power and hydrogen flow rate during Day 1 of THEUS operation

Figure 13.11b shows TC-CWout during the 3-day continuous operation. The Day 1 absorption temperature profile was similar to the individual MHT unit test result shown in Fig. 13.8b, because the initial temperature of MHT during absorption was 32 °C, which was regulated by the circulating water and the same as that of unit tests discussed in Sect. 13.2.2. To recover the heat from the MHT during the switching time, the circulation water flow rate was increased to 1.12 L/min because, at the end of the absorption process, the MHT temperature was still high at around 35 °C. After the switching, the URFC was started in FC mode, but the MHT temperature was still higher than the assumed desorption temperature of 12 °C. Hence, the MHT was self-cooled by using the endothermic reaction heat of MH during the desorption process. The circulation water was recirculated using a bypass valve and pump without passing through the thermostatic bath. Once the TC-CWout reached 12 °C, again the circulation water was fed into the thermostatic bath and the circulation water flow rate was decreased to 0.39 L/min. At the end of the desorption process, the MHT temperature was still below 12 °C. For recovering the cold energy from the MHT during the switching time, the circulation water flow rate was increased again to 1.12 L/min. After switching, the URFC was started in EL mode, but the temperature of the MHT was still lower than the assumed absorption temperature of 32 °C. Again the MHT was self-heated by using the exothermic reaction heat of MH during the absorption process. The circulation water was recirculated by using the bypass valve and pump without being fed into the thermostatic bath. Once TC-CWout reached 32 °C, again the circulation water was fed into the thermostatic bath and the circulation water flow rate was decreased to 0.77 L/min. The above procedure was



**Fig. 13.11** A 3-day continuous test of MHT; (a) P-C isotherm, (b) changes in outlet temperature of the circulation water (fluid), and (c) temperature changes in the tank during Day 1 and during EL operation on Day 2

repeated continuously for 3 days. The variation in TC-CWout after the first absorption process was similar for the entire 3 days.

Figure 13.11c shows the temperature profiles measured inside the tank during Day 1 and during the EL operation on Day 2. The starting point in the temperature profile differs between Day 1 and Day 2 because in Day 1 the MHT initial temperature was 32 °C, whereas in Day 2, the initial temperature depended on the preceding FC operation. The MHT tank takes some time to reach 32 °C by exothermic reaction heat. The Day 3 temperature profiles were the same as those for Day 2 and thus are not shown here.

The calculated efficiencies obtained from this 3-day continuous operation are summarized in Table 13.2. In these experiments, the reaction heat recovery (HR) rate in the absorption process ( $\epsilon_{\text{MH\_ABS}}$ ) was 81% (Day 1), 67% (Day 2), and 67% (Day 3) and that in desorption ( $\epsilon_{\text{MH\_DES}}$ ) was constant at 62% for all 3 days. These rates (except the absorption in Day 1) were smaller than those in the individual unit tests ( $\epsilon_{\text{MH\_ABS}} = 79\%$ , and  $\epsilon_{\text{MH\_DES}} = 74\%$ ) due to part of the reaction heat being used for self-cooling or self-heating of the MHT during the desorption or absorption process, respectively. In summary, THEUS was successfully tested continuously for

**Table 13.2** Calculated efficiencies for the THEUS in continuous 3-day operation

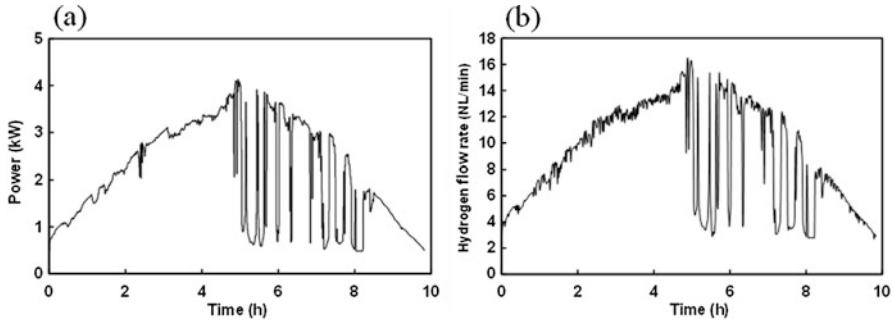
		Energy conversion efficiency		Efficiency including heat recovery from URFC		Efficiency including heat recovery from URFC and MHT		Heat recovery rate from MHT	
		$\eta_{EL}$		$\eta_{EL+RH}$		$\eta_{EL+RH+MH}$		$\varepsilon_{MH\_ABS}$	
Day 1	EL/absorption	$\eta_{EL}$	0.82	$\eta_{EL+RH}$	0.93	$\eta_{EL+RH+MH}$	0.99	$\varepsilon_{MH\_ABS}$	0.81
	FC/desorption	$\eta_{FC}$	0.24	$\eta_{FC+RH}$	0.49	$\eta_{FC+RH+MH}$	0.56	$\varepsilon_{MH\_DES}$	0.62
	Overall			$\eta_{URFC}$	0.52	$\eta_{THEUS}$	0.64		
Day 2	EL/absorption	$\eta_{EL}$	0.82	$\eta_{EL+RH}$	0.93	$\eta_{EL+RH+MH}$	0.98	$\varepsilon_{MH\_ABS}$	0.67
	FC/desorption	$\eta_{FC}$	0.24	$\eta_{FC+RH}$	0.49	$\eta_{FC+RH+MH}$	0.56	$\varepsilon_{MH\_DES}$	0.62
	Overall			$\eta_{URFC}$	0.52	$\eta_{THEUS}$	0.63		
Day 3	EL/absorption	$\eta_{EL}$	0.82	$\eta_{EL+RH}$	0.92	$\eta_{EL+RH+MH}$	0.98	$\varepsilon_{MH\_ABS}$	0.67
	FC/desorption	$\eta_{FC}$	0.24	$\eta_{FC+RH}$	0.49	$\eta_{FC+RH+MH}$	0.55	$\varepsilon_{MH\_DES}$	0.62
	Overall			$\eta_{URFC}$	0.51	$\eta_{THEUS}$	0.62		

3 days without any interruption, and the results confirm that THEUS achieves both functions of load leveling and cogeneration.

### 13.3.3 THEUS Operation with Fluctuating Renewable Energy Sources (RESs)

When fluctuating energy input from renewables is applied to EL operation for H<sub>2</sub> production, the flow rate of the produced H<sub>2</sub> fluctuates accordingly. If this fluctuating H<sub>2</sub> could be stored successfully in MHT, applications of THEUS would be significantly extended not only by load leveling and cogeneration in office buildings but also by capturing fluctuating renewable energy at various sites. To prove this applicability of THEUS, the system performance using various fluctuating energy inputs has been evaluated comprehensively [5, 6]. The experimental results verified that the desorption behavior of stored H<sub>2</sub> in the MHT was independent of hydrogen flow pattern during the absorption process, that is, regardless of constant or fluctuating flow patterns. Therefore, here, our scope focused on EL/absorption process using fluctuating energy inputs. As for the experiments shown in this section, a special designed vacuum thermal insulator with the thickness of 6 mm and a thermal insulation foam (Aeroflex) with the thickness of 1 cm were wrapped around the MHT to reduce the total tank size without reducing the thermal insulation performance.

The fluctuating energy input applied for EL was pseudo-power input that simulates actual energy output from photovoltaics (PV) or wind turbines [5, 6]. First, the results of EL/absorption process using solar PV power are presented here. The EL operation of URFC was carried out by using simulated solar PV power data based on

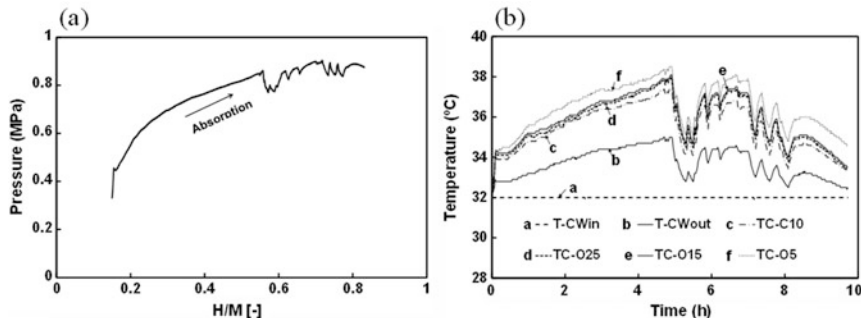


**Fig. 13.12** Electrolysis (EL) operation with pseudo-energy pattern simulating solar PV output. (a) Power input for EL and (b) hydrogen flow rate produced by EL

the irradiance data of a partly cloudy day. The URFC was operated in EL mode for 9 h 50 min, where the weather condition was very fair in the morning (for about the first 5 h) and then occasionally cloudy in the afternoon. Figure 13.12a, b shows the power input and hydrogen production rate during EL mode. The total amount of hydrogen produced by the EL was 5314 NL with the average flow rate of 9 NL/min. Figure 13.13a shows the dynamic P-C isotherm curve for the absorption process. Figure 13.13b shows TC-C10, TC-O25, TC-O15, TC-O5, TC-CWin, and TC-CWout during the absorption process. The maximum pressure of the MHT during absorption was 0.90 MPa. The wavy pattern in MHT pressure during the second half of the absorption process shown in Fig. 13.13a corresponds to large fluctuations in the hydrogen flow rate (seen in Fig. 13.12b). The effect of intermittent hydrogen flow on the temperature inside the MHT can be seen clearly in Fig. 13.13b. Table 13.3 summarizes the measured EL performance data that uses fluctuating energy input to simulate solar PV.

Next, the results of EL/absorption process using wind power data are presented. The URFC was operated based on simulated wind turbine power generation data. In this case, the URFC was successfully operated in EL mode for about 12 h. Figure 13.14 shows the results. Figure 13.14a, b shows the power input and the corresponding hydrogen production rate during EL operation. The hydrogen flow rate pattern entirely depended on the power input pattern of the URFC. The hydrogen flow rate was in the range of 0–12 NL/min with an average of 7.0 NL/min. The total amount of  $H_2$  produced by the EL was 5066 NL. Figure 13.15 shows the result of the absorption process in the MHT. Figure 13.15a shows the dynamic P-C isotherm curve during  $H_2$  absorption, and Fig. 13.15b shows the temperature profiles of the MHT and TC-CWin and TC-CWout. The final pressure of the MHT during the absorption was 0.97 MPa. In the absorption process, TC-CWin and flow rate of the circulation water were fixed at the same value as in the experiment with solar PV.

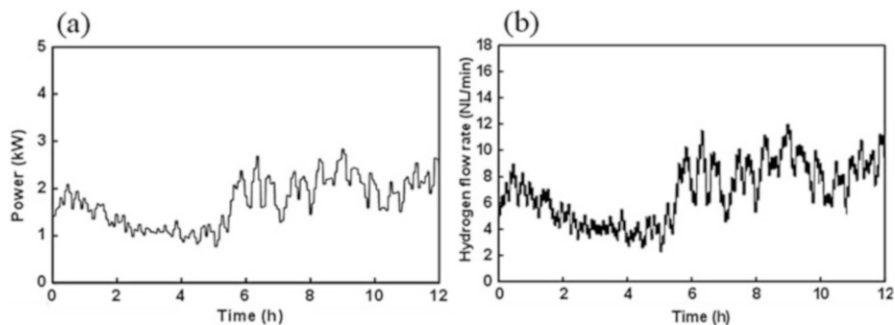
These experimental results with the fluctuating power input to EL operation reveal the following. The EL mode of the URFC could be successfully operated with fluctuating energy input as seen in Figs. 13.12 and 13.14. On the other hand,



**Fig. 13.13** Hydrogen absorption in the MHT with pseudo-energy pattern simulating solar PV output; (a) P-C isotherm and (b) temperature changes in the tank and circulation water (fluid) during absorption

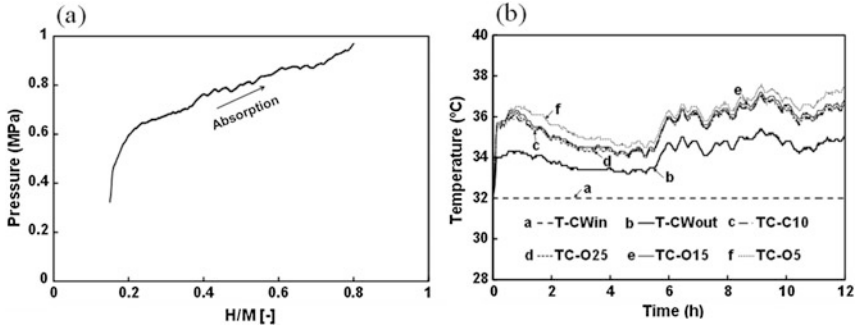
**Table 13.3** Comparison of electrolysis (EL) performance using pseudo-energy pattern simulating solar PV and wind power

Parameters		Solar PV	Wind turbine
Duration		9 h 50 m	12 h
Total energy input for EL ( $W_{IN\_EL}$ )	[MJ]	79.99	80.08
Total volume of produced $H_2$ ( $V_{H2\_prod}$ )	[NL]	5314	5066
Total enthalpy of produced $H_2$ ( $\Delta H_{H2\_prod}$ )	[MJ]	67.96	64.79
EL efficiency ( $\eta_{EL}$ )		0.85	0.81



**Fig. 13.14** Electrolysis (EL) operation with pseudo-energy pattern simulating wind power output; (a) power input for EL and (b) hydrogen flow rate produced by EL

electrolysis efficiency ( $\eta_{EL}$ ) with the fluctuating energy input (Table 13.3) was comparable (wind power) or slightly higher (solar PV) than that with constant energy input (Table 13.2). This is explained by the  $i$ - $V$  characteristics of EL operation (i.e.,  $i_{stack}$ - $V_{cell-avg}$  seen in Fig. 13.5) as follows, where the overpotential was observed smaller at lower  $i$ . At a given energy consumption for BOP ( $W_{BOP\_EL}$ ),  $\eta_{EL}$  would be higher at lower  $i$ . In the case of solar PV, as shown in Fig. 13.12a, the fluctuating



**Fig. 13.15** Hydrogen absorption in the MHT with pseudo-energy pattern simulating wind power output; (a) P-C isotherm and (b) temperature changes in the tank and circulation water (fluid) during absorption

energy inputs applied here were lower than that of constant energy input (2.05 kW) for most of the operation time. In EL operation, a lower energy input yields a lower  $i$  and higher  $\eta_{EL}$ . On the other hand, in the case of wind power, as shown in Fig. 13.14a, the fluctuations were relatively small, and the average energy (power) input (1.85 kW) was close to the constant energy input (2.05 kW) during continuous operation and thus explains why  $\eta_{EL}$  using wind power was very close to that using constant power. As for the absorption process in the MHT with fluctuating  $H_2$  supply, the temperature inside the MHT is more sensitive to the hydrogen flow rate than is the MHT pressure. Particularly in the case of solar PV, a large decrease in MHT temperature was observed at about 5.5-h operation time (Fig. 13.13b) due to the decrease in power (Fig. 13.12) and, correspondingly, an immediate decrease in  $H_2$  pressure in the MHT. Nevertheless, the fluctuations in  $H_2$  pressure in the MHT were smaller than those for either power or temperature, and all of the  $H_2$  produced by EL operation could be successfully stored in the MHT. In conclusion, the EL/absorption process was successful as an energy storage process with fluctuating energy input.

## 13.4 Summary

A THEUS concept proposed here is a hydrogen-based energy system designed to have both functions of load leveling based on energy storage and of cogeneration of heat and power. In addition, THEUS has the potential to capture fluctuating energy input from renewable energy sources such as solar PV and wind power. The main components of THEUS are URFC and MHT. First, the performances of URFC and MHT were verified individually. Then, the THEUS was operated continuously for 3 days, and the various efficiencies were calculated and evaluated. Finally, the potential of THEUS for capturing fluctuating energy input from renewable energy sources was verified experimentally. These experimental results clearly indicate the promising potential of THEUS as an innovative energy facility in stationary applications.

**Acknowledgments** This work has been financially supported by the Ministry of Economy, Trade and Industry (METI) and Japan Science and Technology Agency (JST) through the Japan-U.S. Cooperation Project for Research and Standardization of Clean Energy Technologies and the CONCERT-Japan joint research program. And a part of this study was supported by the New Energy and Industrial Technology Development Organization (NEDO). The authors would like to especially thank Dr. Satya Sekhar Bhogilla, Mr. Atsushi Kato, and Mr. Naoki Miyazaki for their remarkable contributions.

The authors also gratefully acknowledge the helpful comments and suggestions of the reviewers, which have improved the presentation.

---

## References

1. Agency for Natural Resources and Energy (ANRE) of Japan, FY2015 annual report on energy (Energy White Paper 2016) (2016), <http://www.enecho.meti.go.jp/about/whitepaper/2016html/> [in Japanese]
2. R. Baldwin, M. Pham, A. Leonida, J. McElroy, T. Nalette, Hydrogen-oxygen proton-exchange membrane fuel cells and electrolyzers. *J. Power Sources* **29**, 399–412 (1990)
3. F. Barbir, PEM electrolysis for the production of hydrogen from renewable energy sources. *Sol. Energy* **78**, 661–669 (2005)
4. S.S. Bhogilla, H. Ito, A. Kato, A. Nakano, Research and development of a laboratory scale totalized hydrogen energy utilization system. *Int. J. Hydrog. Energy* **41**, 1224–1236 (2016)
5. S.S. Bhogilla, H. Ito, A. Kato, A. Nakano, Experimental study on a laboratory scale totalized hydrogen energy utilization system for the solar photovoltaic application. *Appl. Energy* **177**, 309–322 (2016)
6. S.S. Bhogilla, H. Ito, A. Kato, A. Nakano, Experimental study on a laboratory scale totalized hydrogen energy utilization system using wind power data. *Int. J. Hydrog. Energy* (2017). <https://doi.org/10.1016/j.ijhydene.2016.12.125>
7. M. Gabbasa, K. Sopian, A. Fudholi, N. Asim, A review of unitized regenerative fuel cell stack: material, design, and research achievements. *Int. J. Hydrog. Energy* **39**, 17765–17778 (2014)
8. G. Gahleitner, Hydrogen from renewable electricity: an international review of power-to-gas pilot plants for stationary applications. *Int. J. Hydrog. Energy* **38**, 2039–2061 (2013)
9. International Energy Agency (IEA), Key renewables trend 2016 (2016), <https://www.iea.org/publications/freepublications/publication/renewables-information—2016-edition—excerpt—key-renewables-trends.html>
10. D. Ipsakis, S. Voutetakis, P. Seferlis, F. Stergiopoulos, C. Elmasides, Power management strategies for a stand-alone power system using renewable energy sources and hydrogen storage. *Int. J. Hydrog. Energy* **34**, 7081–7095 (2009)
11. H. Ito, N. Miyazaki, M. Ishida, A. Nakano, Efficiency of unitized reversible fuel cell systems. *Int. J. Hydrog. Energy* **41**, 5803–5815 (2016)
12. H. Ito, N. Miyazaki, M. Ishida, A. Nakano, Stack performance of proton exchange membrane based unitized reversible fuel cells. *Int. J. Microgravity. Sci. Appl.* **33**, 330305 (2016). <https://doi.org/10.15011/jasna.33.330305>
13. T. Maeda, K. Nishida, M. Tange, T. Takahashi, A. Nakano, H. Ito, Y. Hasegawa, M. Masuda, Y. Kawakami, Numerical simulation of the hydrogen storage with reaction heat recovery using metal hydride in the totalized hydrogen energy utilization system. *Int. J. Hydrog. Energy* **36**, 10845–10854 (2011)
14. M. Masuda, Y. Kozawa, A feasibility study on deployment of hydrogen energy carrier to realize a comprehensive energy system for building facilities. *Therm. Sci. Eng.* **8**, 47–56 (2000). [in Japanese]
15. A. Nakano, T. Maeda, H. Ito, M. Masuda, Y. Kawakami, M. Tange, T. Takahashi, K. Nishida, Study on absorption/desorption characteristics of a metal hydride tank for boil-off gas from liquid hydrogen. *Int. J. Hydrog. Energy* **37**, 5056–5062 (2012)

16. A. Nakano, H. Ito, T. Maeda, T. Munakata, T. Motyka, C. Corgnale, S. Greenway, J.M. Perez-Berrios, Study on a metal hydride tank to support energy storage for renewable energy. *J. Alloys Compd.* **580**, 5418–5422 (2013)
17. A. Nakano, H. Ito, S.S. Bhogilla, T. Motyka, C. Corgnale, S. Greenway, B.C. Hauback, Research and development for a metal hydride tank with double coil type heat exchanger below 1.0 MPa (G) operation. *Int. J. Hydrog. Energy* **40**, 2663–2672 (2015)
18. J. Pettersson, B. Ramsey, D. Harrison, A review of the latest developments in electrodes for unitized regenerative polymer electrolyte fuel cells. *J. Power Sources* **157**, 28–34 (2006)
19. L. Schlapbach, A. Züttel, Hydrogen-storage materials for mobile applications. *Nature* **414**, 353–358 (2001)
20. M. Tange, T. Maeda, A. Nakano, H. Ito, Y. Kawakami, M. Masuda, T. Takahashi, Experimental study of hydrogen storage with reaction heat recovery using metal hydride in a totalized hydrogen energy utilization system. *Int. J. Hydrog. Energy* **36**, 11767–11776 (2011)
21. Y. Wang, D.Y.C. Leung, J. Xuan, H. Wang, A review on unitized regenerative fuel cell technologies, part-a: unitized regenerative proton exchange membrane fuel cells. *Renew. Sust. Energ. Rev.* **65**, 961–977 (2016)
22. V.A. Yartys, M.V. Lototsky, An overview of hydrogen storage methods. *NATO Sci. Ser II Math Phys. Chem.* **172**, 75–104 (2005). [https://doi.org/10.1007/1-4020-2669-2\\_7](https://doi.org/10.1007/1-4020-2669-2_7)





# Influence of Air Impurities on the Performance of Nanostructured PEMFC Catalysts

# 14

Olga A. Baturina, Boris Dyatkin, and Tatyana V. Reshetenko

## Contents

14.1	Introduction .....	408
14.2	PEMFC Contamination by Airborne Contaminants .....	409
14.2.1	Pt-Based Cathodes .....	409
14.2.2	Pt-Based Alloys Cathodes .....	416
14.3	PEMFC Recovery Strategies .....	417
14.4	Modeling .....	421
14.5	Emerging Catalysts for Fuel Cell Cathodes .....	428
14.5.1	Fe/N/C Catalysts and Their Tolerance to SO <sub>2</sub> , NO <sub>2</sub> , and CO Poisoning .....	428
14.5.2	Nitrogen-Doped Graphitic Carbons .....	432
14.6	Conclusion .....	433
	References .....	435

## Abstract

This chapter provides an overview of proton exchange membrane fuel cell (PEMFC) performance issues that stem from exposure to airborne pollutants. The PEMFCs must adapt to various functional environments and operate within well-established air quality thresholds in order to become commercially viable.

## Author Contribution

O.A. B. wrote § 14.1, 14.2, and 14.6, B. D. § 14.4 and 14.6, and T.V. R. § 14.1, 14.3, 14.5, and 14.6. The authors further acknowledge that there is no financial relationship with the editors or publisher, and all the cited literature is acknowledged and appropriately cited with copyright permission.

O. A. Baturina · B. Dyatkin

Naval Research Laboratory, Washington, DC, USA

e-mail: [olga.baturina@nrl.navy.mil](mailto:olga.baturina@nrl.navy.mil); [boris.dyatkin.ctr@nrl.navy.mil](mailto:boris.dyatkin.ctr@nrl.navy.mil)

T. V. Reshetenko (✉)

Hawaii Natural Energy Institute, University of Hawaii, Honolulu, HI, USA

e-mail: [tatyanar@hawaii.edu](mailto:tatyanar@hawaii.edu)

Ambient air is the most convenient oxidant for PEMFCs; however, it may contain various contaminants that can cause significant performance loss in these energy conversion systems. The discussion focuses on the effects of organic and inorganic impurities on nanostructured electrocatalysts, such as Pt and novel material alternatives. This chapter compares different contamination mechanisms, electrochemically driven impurity evolution and transformation on catalyst nanoparticles, and the effects of these processes on the oxygen reduction reaction and PEMFCs' subsequent performance. Finally, the chapter highlights possible PEMFC performance recovery and contaminant mitigation strategies. The discussion presents an overview of the experimental and computational approaches and efforts to reconcile observed performance with phenomenological modeling.

---

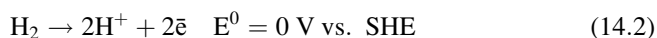
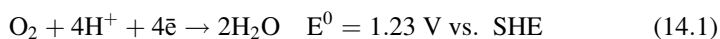
## 14.1 Introduction

Proton exchange membrane fuel cells (PEMFCs) offer a viable, efficient, and environmentally benign alternative to internal combustion engines and other energy conversion and storage systems. However, their successful commercial deployment requires high operational reliabilities, low costs, and long cycle lives that are independent of different, and often rugged, operating and environmental conditions. Air is the most practical and economic cathode-side oxidant for automotive and stationary fuel cell applications. However, ambient air may contain a broad range of airborne impurities that compromise PEMFC performance [10, 31, 100, 117]. Air impurities include organic and inorganic compounds as well as fine particles and aerosols. These contaminants originate from natural as well as anthropogenic emission sources. Volcanic activity and seawater mist in marine environments are natural and significant sources of sulfur dioxide [SO<sub>2</sub>], hydrogen sulfide [H<sub>2</sub>S], and chloride ions [Cl<sup>-</sup>], which affect PEMFC performance. Therefore, these air impurities influence fuel cell operation in areas with high volcanic activity and close proximity to the sea [10, 11, 31, 37, 68, 100, 117, 118]. Anthropogenic contamination of the atmosphere originates from combustion and burning of fossil fuels by energy-generating power plants and vehicles. The resulting exhaust gases contain SO<sub>2</sub>, nitrogen oxide/dioxides [NO and NO<sub>2</sub>, (NO<sub>x</sub>)], and incompletely combusted hydrocarbons. An additional significant and serious road side source of polycyclic aromatic hydrocarbon (PAC) contaminants is freshly paved asphalt on, for example, road surfaces [18]. Industrial and agricultural human activity results in the emission of chemical reagents, solvents, welding fuels, pesticides, and insecticides in to the atmosphere. This is particularly critical in urban environments and raises concerns for fuel cell applications, especially in systems that do not have air filtration units due to weight and/or volume restrictions.

The PEMFC contamination effects can be separated into three main categories that differ by the affected membrane electrode assembly (MEA) components: kinetic, ohmic, and mass transfer effects. The kinetic effects are related to the inhibition of the electrocatalytic activity of nanostructured catalysts that is caused by an absorption and/or reaction of the contaminant on the catalyst surface. Pollutants and/or their derivatives may also interact with an ionomer in the membrane and

catalyst layers, reducing the proton conductivity and increasing the ohmic losses. Finally, the adsorption of airborne contaminants can modify the hydrophobicity and availability of the MEA components, which alters the mass transfer properties. In actuality, true contamination impact is a combination of all of these processes and depends on the chemical nature of individual air impurities.

The main focus of this book chapter is on kinetic losses at the nanostructured fuel cell cathode catalysts that are caused by the airborne impurities. The PEMFC performance is defined by the two electrochemical reactions that are summarized in Eqs. 14.1 and 14.2. They are, respectively, the sluggish oxygen reduction reaction (ORR) at the cathode and the fast hydrogen oxidation reaction (HOR) at the anode [32]:



The  $E^0$  denotes the equilibrium potential at steady-state conditions, and SHE denotes the standard hydrogen electrode potential. Both reactions require a catalyst, and the most common material employed at the anode and cathode is platinum (Pt) nanoparticles (3–5 nm in diameter). The majority of airborne impurities adversely affect the kinetics of the ORR by adsorbing on Pt surface and inhibiting Pt electrocatalytic activity. While a great deal of research is focused on the influence of airborne contaminant on the electrocatalytic activities of polycrystalline surfaces, we will concentrate our effort on the behavior of nanostructured catalysts, which are currently used or can be employed at PEMFC cathodes. Understanding the mechanisms of the influence of impurities on the performance of the nanostructured catalysts will help design better catalysts, which are less susceptible to contamination, and develop mitigation and recovery strategies for existing catalysts. The discussion below is limited to literature that had been published within the last 5 years, as comprehensive earlier reviews on the subject are readily available.

---

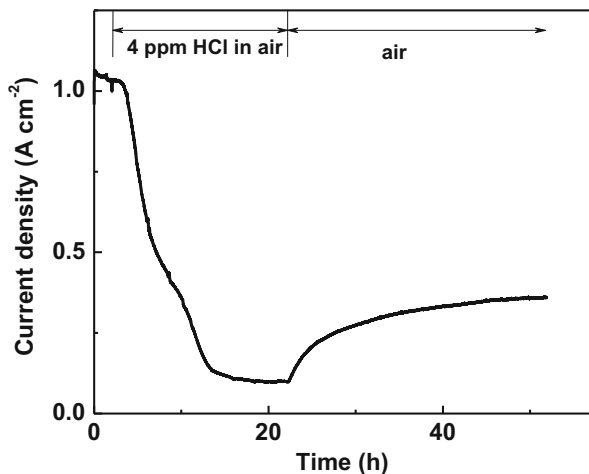
## 14.2 PEMFC Contamination by Airborne Contaminants

### 14.2.1 Pt-Based Cathodes

Platinum nanoparticles are susceptible to performance-inhibiting adsorption of both inorganic and organic species. This section analyzes the effect of chloride ions on the activity of supported Pt nanoparticles in the PEMFC environment because (1) some peculiarities of adsorption of chloride ions are typical for all inorganic anions and (2) presented information will help explain the effects of halogen-containing organic compounds such as bromomethane [ $\text{CH}_3\text{Br}$ ] and chlorobenzene [ $\text{C}_6\text{H}_5\text{Cl}$ ] on activity of Pt nanoparticles toward the ORR.

Effects of inorganic chloride ions on fuel cell performance and degradation have been extensively studied.  $\text{Cl}^-$  can be introduced to the cathode from multiple

**Fig. 14.1** The current density (per geometric surface area) vs. time curve measured during exposure of the fuel cell cathode to 4 ppm HCl in the air at 0.6 V. Exposure to HCl was preceded and followed by exposure to neat air for 1 and 30 h, respectively. Conditions: 80 °C, 100% RH, 0.4|1.0 standard liters per minute (SLPM) (Reproduced with permission from Baturina et al. [9]. Copyright (2011), The Electrochemical Society)

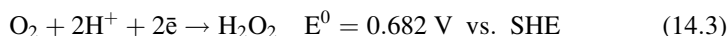


sources, both externally (air) and internally (humidified water or residual  $\text{Cl}^-$  from a catalyst precursor).

An example of the effect of chloride ions on the performance of a fuel cell cathode is demonstrated in Fig. 14.1 [9]. A 4 ppm level of hydrochloric acid [HCl] in ambient air that is supplied to the cathode held at 0.6 V causes almost an order of magnitude decrease in fuel cell (FC) performance. The FC performance can be partially recovered by the replacement of HCl in the air stream by the flow of neat air. However, no full recovery has been observed even after prolonged exposure to neat air (100 h).

The four major effects of  $\text{Cl}^-$  ions on the Pt nanostructured catalyst can account for performance loss during FC operation: (1) blocking of the Pt active sites, (2) shifting of the ORR pathway from  $4e^-$  to  $3.5e^-$  due to promotion of hydrogen peroxide [ $\text{H}_2\text{O}_2$ ] generation, (3) Pt dissolution to chloroplatinate ions [ $\text{PtCl}_4^{x-}$ ], and (4) growth of Pt nanoparticles due to Pt dissolution-redeposition.

At the electrode/solution interface, chloride ions reversibly adsorb on the surface of Pt nanoparticles up to approximately 1.0 V vs. reversible hydrogen electrode (RHE). Single crystal studies [101] demonstrate the blocking effect of  $\text{Cl}^-$  ions on the ORR on the  $\{111\}$  and  $\{110\}$  Pt planes, the most active toward the ORR. This effect does not affect the  $4e^-$  reaction pathway. Unlike  $\{111\}$  and  $\{110\}$  planes, adsorption of  $\text{Cl}^-$  ions on  $\{100\}$  plane is so strong that it suppresses adsorption of molecular oxygen [ $\text{O}_2$ ] and reduces the number of available Pt sites that are needed to break down the  $\text{O}=\text{O}$  bond. As a result, the reaction mechanism changes from a purely  $4e^-$  mechanism (Eq. 14.1) to a less efficient mixed pathway (Eq. 14.3), in which both  $\text{H}_2\text{O}_2$  and  $\text{H}_2\text{O}$  are generated.  $\text{H}_2\text{O}_2$  formation proceeds via the  $2e^-$  pathway, as shown in Eq. 14.3:

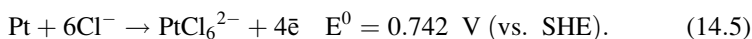
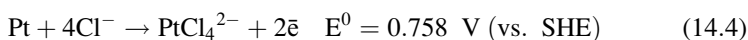


The Pt nanoparticles can be represented as a superposition of  $\{111\}$ ,  $\{110\}$ ,  $\{100\}$  planes, edges, and corners. Accordingly, the activity of Pt nanoparticles toward the ORR is expected to be a sum of contributions of different magnitudes

from these geometrical features. Since Pt {111} and Pt {100} crystal facets constitute the majority (75%) of the surface of 4 nm Pt nanoparticles, and most of those (63%) are occupied by {111} planes, the Pt {100} planes do not significantly contribute to the ORR pathway. However, H<sub>2</sub>O<sub>2</sub> generation in the presence of chloride ions was detected both for ORR on carbon-supported Pt (Pt/C) nanoparticles at electrode/solution interface [86] and at the PEMFC cathode [65].

The blocking of active sites of Pt nanoparticles by adsorbed Cl<sup>-</sup> ions was considered a dominant factor for the dependence of fuel cell current on the cell voltage [8]. The decrease in chloride coverage was clearly correlated to the observed fivefold current increase for the cells held at 0.4 V versus those held at 0.6 V. However, a Pt dissolution also contributed to performance loss.

At certain potentials, Cl<sup>-</sup> adsorption may lead to Pt dissolution, according to (Eqs. 14.4 and 14.5):



While the dissolution of Pt nanoparticles at the electrode/solution interface is observed at potentials more positive than 1.0 V [115], they dissolve more readily in the fuel cell environment. For example, Pt dissolution to chloroplatinate ions within the cathode catalyst layers was confirmed for single cells held at a cell voltage of 0.6 V for 20 h [9]. This leads to a loss of electrochemical surface area (ECSA) through two different mechanisms. The first mechanism involves diffusion of chloroplatinate ions toward the catalyst/membrane interface or inside the Nafion membrane, where hexachloroplatinate [PtCl<sub>6</sub><sup>2-</sup>] can be reduced to zerovalent state [Pt<sup>0</sup>] by crossover hydrogen [65]. If electrically isolated, these Pt<sup>0</sup> species no longer contribute to the ORR catalysis. The second mechanism is, most likely, related to the growth of Pt nanoparticles through Pt dissolution-redeposition (Ostwald ripening), driven by a decrease in the surface energy of platinum nanoparticles. The appreciable growth of Pt nanoparticles after exposure to chloride ions was experimentally confirmed by direct high-resolution transmission electron microscopy (HRTEM) observations.

Surprisingly, Pt nanoparticles yield chloroplatinate ions even after exposure to HCl in the air in ambient conditions [9]. A fresh Gore catalyst-coated membrane (CCM) soaked in 0.1 M HCl solution for 2 h demonstrated a pre-edge feature in Cl K-edge X-ray absorption near-edge structure (XANES) spectrum, which is typical for chloroplatinate ions.

Interestingly, the effect of CH<sub>3</sub>Br on FC performance [76] closely resembles that of chloride ions. Bromomethane has natural and anthropogenic atmospheric sources, which include emission from oceans, biomass burning, vehicle exhausts, and agricultural usage as pesticides. Owing to its ozone-destructive capabilities, the chemistry of atmospheric CH<sub>3</sub>Br has been previously extensively studied. Figure 14.2 demonstrates the effect of CH<sub>3</sub>Br on FC performance versus neat air measured in a segmented fuel cell, which represents a more advanced version of a single cell.

While single cell tests allow one to obtain average values of current, voltage, and impedance, spatial characterization reveals unique information about locally resolved data over the electrode area. Figure 14.2 presents profiles of the segment voltages and current densities normalized to initial values vs. experiment time at total cell current of  $1.0 \text{ A}\cdot\text{cm}^{-2}$ . The PEMFC performance under  $\text{CH}_3\text{Br}$  exposure revealed three well-defined operating regimes: (1) lack of any changes in the cell performance in the first 0–9 h, (2) fast degradation from 0.650 to 0.440 V for 45 h of exposure (62 h of total operation), and (3) slow degradation (0.440–0.335 V) (Fig. 14.2a, b). At the same time, the voltage loss was accompanied by noticeable current redistributions for the three regimes. During the first stage, the current

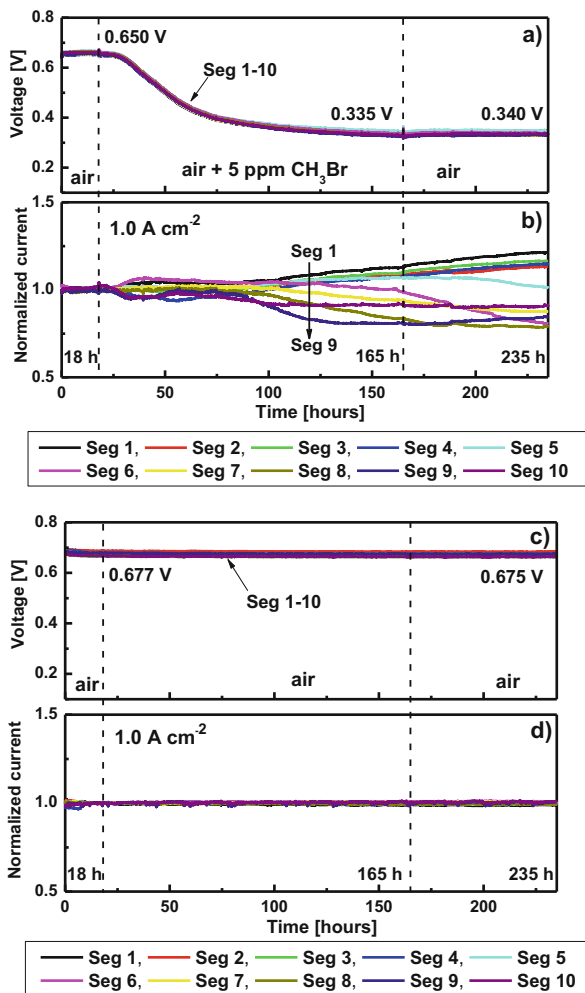
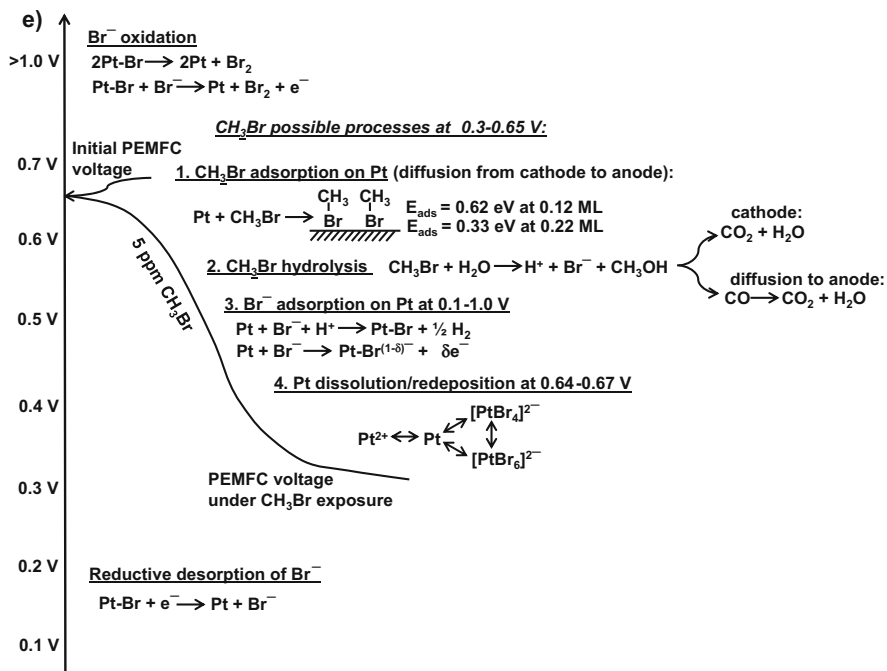


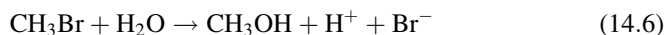
Fig. 14.2 (continued)



**Fig. 14.2** Voltage (a) and normalized current densities (b) of individual segments of PEMFC exposed to 5 ppm CH<sub>3</sub>Br; voltage (c) and normalized current densities (d) for PEMFC operated without CH<sub>3</sub>Br. Cell inlet is at segment 1, outlet is at segment 10. An overall current density is 1.0 A·cm<sup>-2</sup>. Anode/cathode: H<sub>2</sub>/air, 1.059/2.522 L·min<sup>-1</sup>, 100/50% RH, 48.3/48.3 kPa gauge, 80 °C. Schematic of the proposed processes occurring during exposure of the PEMFC cathode to CH<sub>3</sub>Br in the air (e) (Reprinted with permission from Reshchenko et al. [76] Copyright (2017), Elsevier)

density distribution was not affected. At the second stage, the current densities of segments 1 and 6 slightly increased, segments 2, 3, 5, 7, and 8 did not show significant changes, while current densities of segments 4, 9, and 10 decreased. The third stage started when the voltage reached an inflection point of 0.440 V. Inlet segments 1–5 increased performance during the third stage, while the performances of outlet segments 6–10 declined. At steady state, the inlet segments demonstrated better performances than the outlet segments. The current density redistribution ranged from +12% for segment 1 to –19% for segment 9 due to the operation of the cell in a galvanostatic mode, which required an overall constant current.

An analogy in PEMFC behavior under Cl<sup>-</sup> and CH<sub>3</sub>Br exposure suggests similar poisoning mechanisms [8, 9, 55, 65, 68]. CH<sub>3</sub>Br has been shown to slowly hydrolyze in aqueous media as demonstrated in Eq. 14.6 [26, 60]:

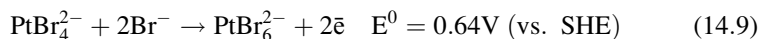
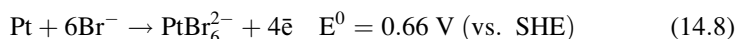
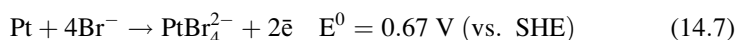


Methanol [CH<sub>3</sub>OH] generated during hydrolysis of CH<sub>3</sub>Br can be further oxidized to carbon dioxide [CO<sub>2</sub>] and water [H<sub>2</sub>O] at the fuel cell cathode by chemical or electrochemical pathways [34], which leaves Br<sup>-</sup> as the most probable cause of performance decline. Indeed, the presence of Br species both in the anode and cathode compartment after exposure to CH<sub>3</sub>Br was confirmed by X-ray photoelectron spectroscopy (XPS). Bromide, similar to chloride ions, is strongly adsorbed on Pt {111}, {100}, and {110} in the 0.2–1.0 V potential range with a maximum coverage of 0.42–0.7 monolayer [33, 64, 72, 85, 110]. The data obtained by rotating ring-disk electrode (RRDE) technique show that, through suppression of O<sub>2</sub> adsorption and diminished numbers of available Pt sites required for breaking O = O double bonds, this coverage is sufficient for the inhibition of the ORR. Moreover, the noticeable formation of H<sub>2</sub>O<sub>2</sub> indicates a change in the ORR mechanism from a 4e<sup>-</sup> to a 2e<sup>-</sup> pathway [33, 64].

Neither the cell nor its segments recovered their performance after stopping the CH<sub>3</sub>Br poisoning for 70 h, and the current distribution continued to evolve. The lack of self-recovery demonstrates a more pronounced effect of CH<sub>3</sub>Br on the PEMFC performance vs. that of Cl<sup>-</sup> ions (see a recovery in the air in Fig. 14.1).

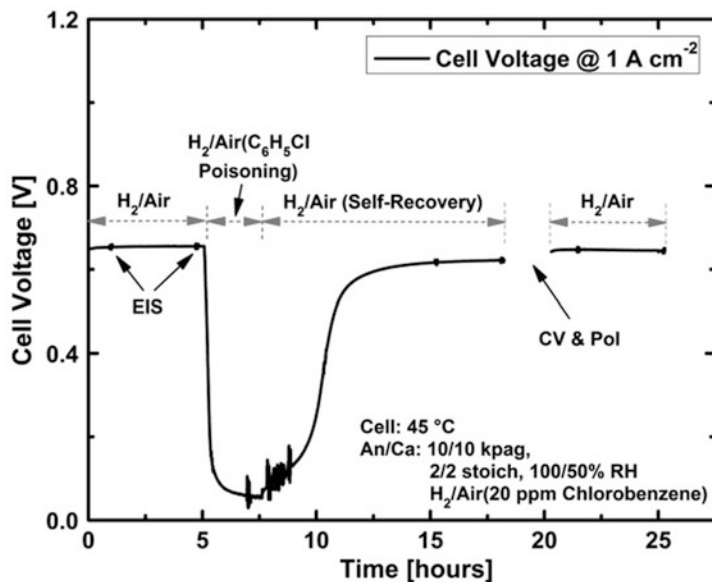
In the neat air, PEMFC performance was very stable during 235 h, and no spatial current density redistributions were observed (Fig. 14.2c, d). A comparison of PEMFC performance in the presence of CH<sub>3</sub>Br to that of contaminant-free air (Fig. 14.2b, d, respectively) clearly shows the effects of air pollutant on local currents, demonstrating propagation of the contamination along the flow field.

Similar to exposure to HCl, loss of Pt ECSA was observed due to the growth of Pt nanoparticles in the presence of CH<sub>3</sub>Br. Contrary to the Cl<sup>-</sup> case, both cathode (52% loss) and anode (57% loss) ECSAs were significantly impacted. The Pt nanoparticle size increased from an initial 2.4 nm to 3.8 nm (cathode) and 3.3 nm (anode). The growth of Pt nanoparticles was attributed to particle coalescence as well as Ostwald ripening, following Pt dissolution into bromoplatinate ions, according to the Eqs. 14.7, 14.8, and 14.9 [35]:



The confusion may arise when comparing E<sup>0</sup> of 0.64–0.67 V to cell voltages of 0.34–0.65 V in Fig. 14.2, because the first range is more positive vs. the experimental cell voltage range. This comparison is meaningless because (1) E<sup>0</sup> is reported for 1 M bromide solutions vs. SHE and (2) cell voltages need to be converted to electrode potentials vs. SHE in order to make a valid comparison. Also, E<sup>0</sup> assigned to Eqs. 14.7, 14.8, and 14.9 does not include contributions from different crystalline faces as well as corners and edges of Pt nanoparticles into their energetics at the electrode/solution interface. Contributions from these features with sharp curvatures may be significant, and the dissolution potentials on edges and pits of Pt {111} are





**Fig. 14.3** The cell voltage response to exposure by 20 ppm  $C_6H_5Cl$  in the cathode air stream under  $1.0 \text{ A}\cdot\text{cm}^{-2}$  and  $45 \text{ }^\circ\text{C}$  (Reprinted with permission from Zhai et al. [119] Copyright (2015), American Chemical Society)

approximately 500 mV lower than on planar surfaces [50]. Recovery procedure for  $CH_3Br$ -exposed cathode was also reminiscent of one for the  $HCl$ -exposed cathode. The near-complete recovery of the PEMFC performance was achieved by a hydrogen/nitrogen [ $H_2/N_2$ ] purge of the anode/cathode compartments and subsequent cyclic voltammetry (CV). The proposed mechanism of the influence of  $CH_3Br$  in the air on the performance of PEMFC cathode as a function of a cell voltage is summarized in Fig. 14.2e [76].

Another halogen-containing organic compound,  $C_6H_5Cl$ , originates in the atmosphere from industrial solvents, heat transfer agents, deodorants, degreasers, disinfectants, pesticides, and herbicides [58, 109]. Its effect on cathode structure and performance is a notable example of remarkably different degradation behavior in PEMFCs. This contaminant causes fast cathode catalyst performance degradation, followed by fast and also complete recovery solely by being exposed to neat air, as shown in Fig. 14.3 [119]. The reason for a rapid performance decline immediately following the introduction of chlorobenzene is, most likely, strong adsorption of this compound on the Pt surfaces at potentials of PEMFC operation [93]. Adsorption at low potentials of 0.1–0.3 V is destructive, as confirmed by detection of  $Cl^-$  ions in the cathode effluent water and benzene [ $C_6H_6$ ] in the gas phase by gas chromatography coupled to mass spectrometry (GC-MS) [119]. Although, the presence of chloride ions on the surface of Pt nanoparticles after recovery in the neat air was indirectly confirmed by analysis of CV curves, the impact of chloride ions was much less significant as compared to either the effect of  $Cl^-$  alone or  $Br^-$  ions (produced by hydrolysis of  $CH_3Br$ ).

Following analysis of the three compounds that contain halogen anions (produced at certain stages of chemical/electrochemical reactions), the subsequent logical step would be to compare the effect of anions to that of cations. Inorganic cations can leach into fuel cell cathodes externally from ocean spray or mist on the roads after deicing. Alternatively, de-alloying of Pt alloys that outperform Pt in the ORR is an internal source of these contaminants.

Cations are known to decrease the proton conductivity of the FC membrane and catalyst layers due to the replacement of protons in the Nafion ionomer and membrane [68]. However, thorough comparison of the effect of cations on the ORR at the electrode/solution interface and the triple phase boundary (TPB) reveal that cations cause not only decrease in proton conductivity but also impact mass transport and kinetics of the ORR [120]. The effect was found to be correlated to a cation charge. At the electrode/solution interface, the negative effect of potassium  $[K^+]$ , lithium  $[Li^+]$ , cobalt  $[Co^{2+}]$ , and aluminum  $[Al^{3+}]$  cations on the activity of Pt nanoparticles toward the ORR was more pronounced for multivalent cations and decreased in the following order:  $Al^{3+} > Co^{2+} > K^+ \sim Li^+$ . Although, these positive ions do not specifically adsorb on the surfaces of Pt nanoparticles in the ORR potential region, their presence on the interface may stabilize adsorbed  $OH_{ads}$  groups on the Pt surface, which partially block the Pt surface from adsorption of molecular oxygen. In addition, cations decrease the oxygen diffusion coefficient, solubility, and kinematic viscosity of electrolyte and, subsequently, modify the  $O_2$  transport conditions. At the TPB, the presence of  $Co^{2+}$  cations also negatively impacted both the kinetic and the diffusion regions of the ORR. While the effect of  $Co^{2+}$  ions at the TPB was thought to be similar to that at electrode/solution interface, subsequent research has not supported this prediction. The ORR transport limitations at a TPB have been assigned to inhibited molecular  $O_2$  diffusion through the shrunken channels between the hydrophilic domains of the Nafion film.

### 14.2.2 Pt-Based Alloys Cathodes

The Pt nanoparticle alloy with transition metals such as Co and nickel [Ni] exhibits superior electrocatalytic activity toward the ORR than pure Pt [32, 102]. This is attributed to a compressive strain in the outer shell and delayed adsorption of  $OH_{ads}$  groups on the Pt-enriched layer formed upon leaching of transition metals in acidic environments [1, 103]. The influence of impurities on the performance of nanostructured Pt alloys is novel and, as a result, has been explored in much less detail as compared to Pt. Interestingly, chloride ions not only inhibit the ORR on PtNi alloys in acidic solutions but also promote their de-alloying [48]. Even low concentrations of  $Cl^-$  ions ( $10^{-4}$  M) were sufficient to accelerate Ni dissolution from electrochemically deposited nanostructured PtNi alloys by CV. Furthermore, potential cycling has been found to promote  $\{100\}$  faceting of Pt or Pt-enriched shell in the chloride-free electrolyte or in the presence of  $Cl^-$  ions, respectively. This plane is the least active toward the ORR and most active toward  $Cl^-$  adsorption. Subsequently, faceting of  $\{100\}$  Pt makes kinetics of ORR on nanostructured catalysts even more sluggish. However, the detrimental effect of  $Cl^-$  adsorption (two orders of

magnitude decrease in the ORR activity in the presence of  $10^{-4}$  M  $\text{Cl}^-$ ) is less pronounced for PtNi alloys versus Pt likely due to the fact that subsurface Ni inhibits  $\text{Cl}^-$  adsorption on the surface of Pt nanoparticles.

Similar to chloride ions among inorganic ions, sulfur dioxide is a “classical” example of neutral molecule that has been extensively studied regarding its effect on the performance of the nanostructured Pt catalysts. However, only a few papers report the effect of  $\text{SO}_2$  on the catalytic activity of nanostructured Pt alloys in PEMFC environment. The results reported for electrode/solution interface [30] and PEMFC environment [11] both suggest that carbon-supported  $\text{Pt}_3\text{Co}$  nanoparticles are more susceptible to  $\text{SO}_2$  poisoning than Pt nanoparticles for a given Pt loading. However, the activity of  $\text{Pt}_3\text{Co}/\text{C}$  catalyst, having higher sulfur coverage, restores easier than carbon-supported platinum [Pt/C]. This was attributed to the enhanced reactivity of  $\text{Pt}_3\text{Co}/\text{C}$  catalyst with respect to sulfur/sulfur dioxide  $\text{S}^0/\text{SO}_2$  oxidation to sulfate [ $\text{SO}_4^{2-}$ ]. The specific effect may include either greater mobility of adsorbed oxygen species or higher reactivity of vacancies, which are typically present on cobalt-leached alloy surface, toward dissociation of  $\text{H}_2\text{O}$  or molecular oxygen. The latter  $\text{O}[\text{H}]_{\text{ads}}$  species are mandatory for  $\text{S}^0$  oxidation to sulfate (oxidation number increased from zero to positive six) [51, 83].

---

### 14.3 PEMFC Recovery Strategies

The performance degradation of the fuel cell after exposure to airborne contaminants can be separated into reversible and irreversible losses. Irreversible performance losses are usually associated with deterioration of catalysts and ionomer or degradation of electrode structures. For example, the growth of nanoparticle size, which is enhanced by present halides, causes an irreversible decrease in ECSA and performance due to increased activation overpotentials [76]. Reversible losses are connected to recoverable contaminant effects on the catalyst and/or ionomer. Most importantly, in the latter case, fuel cell performance can be restored by applying appropriate techniques.

The performance recovery requires removal of impurities from the electrode layer: catalyst surface, ionomer, and gas phases. Some self-recovery is often observed as soon as neat air is introduced to a cathode compartment due to fast desorption of a contaminant from the catalyst and lack of contaminants interaction with other components of the electrode structure [77, 79]. However, some impurities like  $\text{Cl}^-$ ,  $\text{Br}^-$ ,  $\text{SO}_2$ , and acetonitrile [ $\text{CN}_3\text{CN}$ ] strongly adsorb to the surface or form products that may additionally affect catalyst and ionomer [9, 11, 76, 78, 118]. These impurities are more difficult to remove. The fundamental chemical and electrochemical properties of contaminants, as well as their possible reactions during PEMFC operation, determine the necessary recovery strategies and approaches. It is well-known that adsorption and desorption of any compounds on Pt are potential-dependent processes and can be accompanied with their electrooxidation or electroreduction. Subsequently, dynamic potential cycling is the most basic, simple, and effective method to remove the adsorbed impurities and clean Pt surfaces.

In order to restore fuel cell performance exposed to  $\text{Cl}^-$  and  $\text{Br}^-$  (from  $\text{CH}_3\text{Br}$ ), the potential of the cathode should be lowered. The desorption of halides takes place at potentials below the potential of zero charges of Pt nanoparticles ( $\sim 0.27$  V vs. RHE for 5 nm nanoparticles [66]) at which Pt surface becomes negatively charged and where reductive desorption of halides occurs [22, 28, 85] and is summarized in Eq. 14.10.

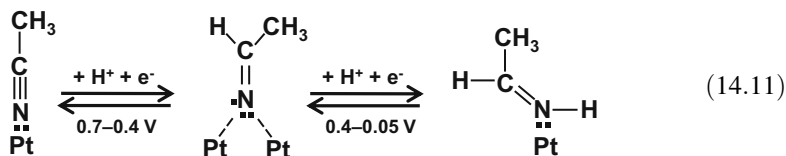


Exposure to low potentials (0 V vs. SHE) was previously used by V.S. Bagotsky et al. [7] to desorb chloride ions from a platinum surface in aqueous 0.5 M sulfuric acid [ $\text{H}_2\text{SO}_4$ ] solutions.

Moreover, halide ions should be simultaneously washed out from the electrode layer to prevent their re-adsorption. Thus, the simplest recovery procedure should include a purging of anode and cathode by fully humidified hydrogen and nitrogen, respectively, which ensures the cathode potential of  $\sim 0.1$  V. The best conditions for desorption in the FC environment is achieved by purging the fuel cell cathode with molecular hydrogen, which brings cathode potential to 0.0 V vs. potential at the anode. However, desorption of halides ions from Pt surface does not lead to the restoration of the FC performance. Because  $\text{Cl}^-$  and  $\text{Br}^-$  ions remain in the cathode compartment after being desorbed from Pt surface, they re-adsorb onto Pt during electrochemical cycling of the fuel cell, i.e., in the 0.5–0.9 V range. Only multiple exposures to low potentials lead to a complete recovery of the fuel cell performance in the potential region dominated by diffusion of molecular oxygen (0.5–0.7 V). Due to irreversible losses of Pt ECSA, performance in the kinetic region (0.8–0.9 V) is never fully restored.

The electrochemical and chemical transformation of pollutants on Pt during operation of the FC can lead to the production of derivatives, which may serve as additional sources of contaminants of catalysts and ionomers. The most studied airborne impurity illustrating this pathway is sulfur dioxide.  $\text{SO}_2$  was shown to reduce to elemental sulfur on Pt or  $\text{Pt}_3\text{Co}$ , block ECSA, and alter ORR mechanism [12, 29]). Recovering of the catalyst surface proceeds through electrooxidation of sulfur to sulfates/bisulfates [ $\text{S}^0 \rightarrow \text{SO}_4^{2-}/\text{HSO}_4^-$ ] at 1.2 V and their further desorption at potentials below the point of zero charges ( $\sim 0.1$ – $0.3$  V), which can be achieved by potential cycling. Also, running multiple successive polarization curves was demonstrated to recover the PEMFC performance after  $\text{SO}_2$  poisoning [10].

In addition to various inorganic compounds,  $\text{CH}_3\text{CN}$  also forms products that affect the catalyst as well as ionomer [78]. Acetonitrile is an airborne impurity that mainly originates from a broad range of common processes in chemical industry. Chemisorption of  $\text{CH}_3\text{CN}$  on Pt is coupled with its reduction via two consecutive electron and proton transfer reactions. A fast reversible process at 0.7–0.4 V is followed by a second slow reduction at 0.4–0.05 V. Steric limitations promote the formation of a bent  $\text{sp}^2$  imine-type structure [4, 43, 69, 104], illustrated in Eq. 14.11:

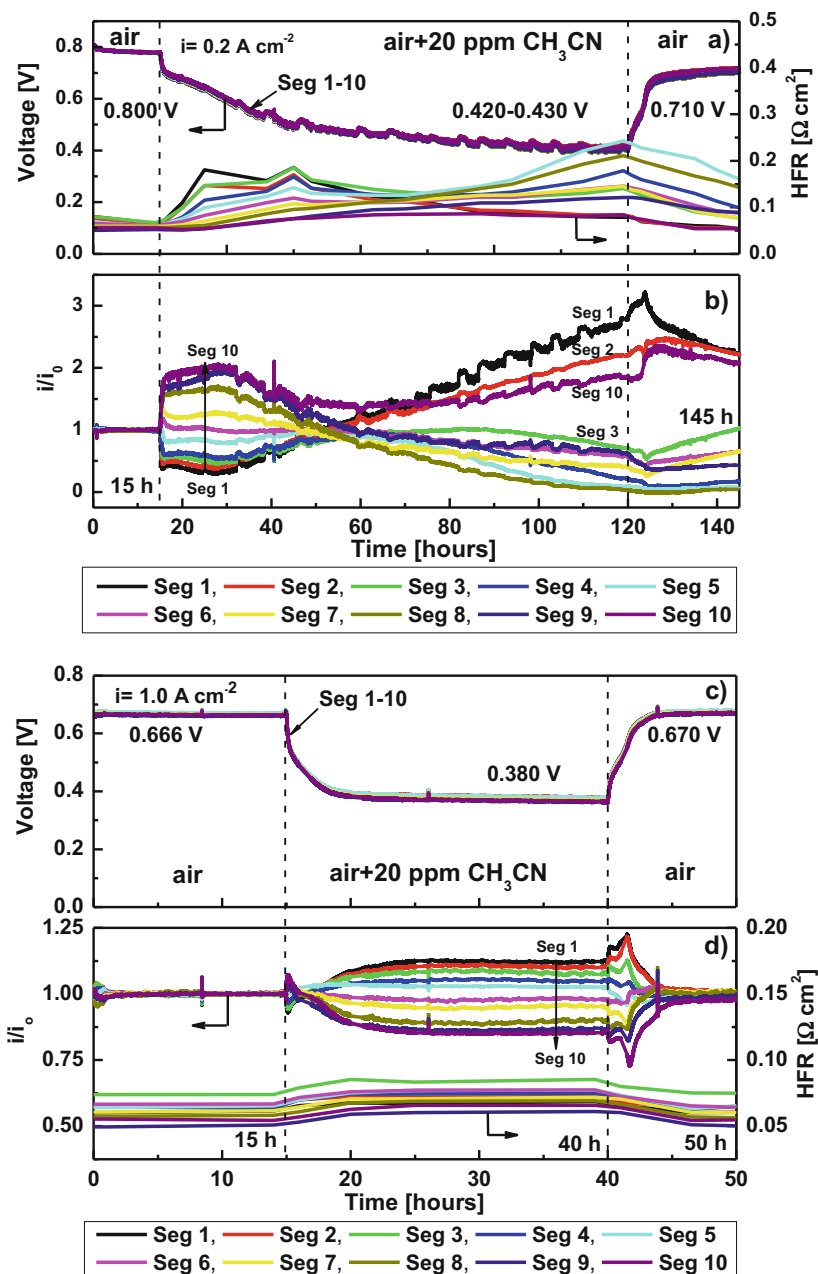


The acetonitrile and imine-type species tend to hydrolyze during fuel cell operations and, subsequently, produce ammonia  $[\text{NH}_3]$ , acetic acid  $[\text{CH}_3\text{COOH}]$ , and acetaldehyde  $[\text{CH}_3\text{COH}]$  [4, 43]. Therefore, acetonitrile not only alters the oxygen reduction mechanism [25, 94] but also generates ammonium ion  $[\text{NH}_4^+]$ , which both affects the ORR pathway and impacts ionomer proton conductivity, high-frequency resistance (HFR), and ohmic losses [39, 42, 59, 73].

The effects of  $\text{CH}_3\text{CN}$  on the localized high-frequency resistance (HFR) and current densities depended on PEMFC running conditions and were found to be severe in the case of low current operation ( $0.2 \text{ A}\cdot\text{cm}^{-2}$ ), when water production at the cathode was not very significant (Fig. 14.4). At low current density, acetonitrile and ammonia can accumulate in the catalyst layer and the ionomer. This causes a considerable increase in the HFR and only partial self-recovery to 0.71 V instead of the initial cell voltage of 0.80 V (Fig. 14.4a, b). Furthermore, a comparison of ECSA before and after the acetonitrile exposure at  $0.2 \text{ A}\cdot\text{cm}^{-2}$  shows a clear loss of  $\sim 20\%$ . The current voltage (IV) measurements demonstrated significant performance drop as well. At high current densities, the produced water could remove  $\text{NH}_3$  and  $\text{CH}_3\text{CN}$ , which is miscible in water, from the cathode and mitigate any negative effects. This also leads to full self-recovery (Fig. 14.4c, d).

Research into mechanisms of  $\text{CH}_3\text{CN}$  suggests several possible recovery approaches. Operations at high current densities may restore cell performances after  $\text{CH}_3\text{CN}$  poisoning at low currents. The operation of the contaminated cell for  $\sim 10 \text{ h}$  at a constant voltage of 0.6 V led to the improvement of the produced current from 0.95 to  $1.3 \text{ A}\cdot\text{cm}^{-2}$ . Additionally, the ECSAs of the anode and the cathode were determined after this operation, and the results confirmed the recovery of the Pt catalyst surface. The ECSA loss was 9.2% and 2.8% for the anode and the cathode, respectively [78].

The proposed recovery techniques can be easily implemented in the case of single cell operation in a laboratory environment, where potential cycling and purging electrodes by different gases is accessible. However, practical commercial application of these recovery approaches for an FC stack in a vehicle or stationary energy source system poses logistical challenges and may be impossible. In order to ensure reliable FC stack operation, air impurities must not affect the performance, and/or contamination should be avoided. The first approach is conditional on the successful future development of catalysts that are more tolerant to air pollutants than existing nanostructures. Currently, Pt/C is the most active catalyst for ORR in acid media, and emerging various Pt-free catalytic systems cannot surpass it. On the other hand, it is impossible to design a catalyst that is tolerant to all known airborne contaminants. The second approach – to prevent stack cathode poisoning by using and adding a reliable filtration system – requires the development of a filtration material, design of the system, and its employment to a balance of plant (BOP).



**Fig. 14.4** Voltage and high-frequency resistance (a), normalized current densities (b) of individual segments vs. time for an overall current density of  $0.2 \text{ A cm}^{-2}$ . Voltage (c), normalized current densities, and high-frequency resistance (d) of individual segments vs. time for an overall current density of  $1.0 \text{ A cm}^{-2}$ . Cell inlet is at segment 1, outlet is at segment 10. Anode/cathode:  $\text{H}_2/\text{air}$ , 20 ppm  $\text{CH}_3\text{CN}$  in the air stream, 2/2 stoichiometry, 100/50% RH, 48.3/48.3 kPa gauge,  $80 \text{ }^\circ\text{C}$  (Reprinted with permission from Reshetyenko and St-Pierre [78]. Copyright (2015), Elsevier)

## 14.4 Modeling

A computational approach that investigates effects of air impurities on PEMFC catalysts presents several important advantages. The resulting phenomenological models identify reaction mechanisms that may either more properly correlate with existing fuel cell degradation studies or assess the effects of additional, previously unexplored contaminants. The cyclability experiments often involve long-duration (over 5000) tests, and predictive calculations will streamline and accelerate the empirical validation of nanostructured catalysts [89]. The simulation results may quantify fuel and air purity standards and aid in the design of new fuel cell components. Finally, contaminants influence the long-term degradation of catalysts at extremely low levels (~1 ppb). Although, these concentrations are large enough to affect the surface kinetics and structural changes of Pt-based catalysts, they are difficult to precisely detect and control in an experimental setting. Therefore, a well-designed computational approach may more accurately evaluate minute changes in contaminant concentrations.

Computational modeling approaches to evaluate Pt degradation have existed since at least 2003. Researchers R. Darling and P. Meyers developed a kinetic rate equation system to evaluate Pt oxidation and dissolution during normal operations. The model did not incorporate any contaminant infusions into the air stream [23]. Researchers W. Bi and T. F. Fuller expanded on this work in 2008 and developed a one-dimensional physics-based model that included a Pt dissolution “band” in the membrane [14]. The computational approach included (1) Pt electrochemical dissolution, (2) Pt oxidation, and (3) Pt reduction by H<sub>2</sub>. The model evaluated different particle size distributions. The simulation poorly agreed with experimental results, which led to the authors’ conclusion of a possible additional (as of yet undetermined and unaccounted) mechanism that also influenced catalyst degradation.

A 2008 study accounted for the presence of NO<sub>2</sub> in the air stream [99]. The model incorporated mass balance equations that correlated nitrous oxide [N<sub>2</sub>O] concentration (in the air stream) with Pt’s ECSA. The NO<sub>2</sub>-Pt surface interactions were not taken into account, and the authors used Langmuir adsorption kinetics. The Tafel behavior of the ORR was applied to derive the surface blockage kinetic factor and output the FC’s voltage as a function of contaminant coverage. The model was simple and accounted for time, air flow pressure, and relative concentrations of reactants and contaminants. However, it was not sufficiently well-developed to properly correlate with experimental results.

An appropriate Pt catalyst model aims to (1) observe and validate experimental results, (2) understand the fundamental mechanisms and build a framework to predict performance, and (3) use these findings to develop mitigation and recovery strategies [14]. With those goals in mind, several computation-based studies have simulated PEMFC operation and durability at different physical scales. They successfully used a “bottom-up” (MEMEPhys<sup>®</sup>) approach, which analyzed the fundamental physics and kinetics at the nanoscale and gradually scaled them up to a full PEMFC-scale level, and integrated it with a macroscale mass-transport model to



determine the influence of FC operating regimes on resulting long-term catalyst stability. The key findings, which corroborated other work, highlighted the detrimental effect of dynamic operation (power cycling) and correlated Pt's ECSA with time-resolved operating potentials [82]. The authors' model also predicted that nanoparticle degradation was particularly localized in the immediate vicinity of the air inlet; subsequently, the composition of the air source was expected to significantly influence the health and operating capabilities of the entire PEMFC.

Different modeling approaches have used varying degrees of complexity in their models. The initial attempts relied on a zero-dimensional (0D) transient kinetic model for Pt dissolution and platinum (II) oxide [PtO] formation. It did not output resulting PEMFC cell voltage. Subsequent work upgraded it to a one-dimensional (1D) and, subsequently, a two-dimensional (2D) transient model that assessed Pt<sup>+</sup> dissolution through the MEA based on electrochemical/chemical reactions. It incorporated mass and charge balances but did not account for ohmic losses [16]. Ongoing efforts have implemented 3D models that account for ohmic losses and predict PEMFC cell voltages based on impurity concentrations and resulting overpotentials. Although, PtO commonly forms during regular (contaminant-free operation), its effects on PEMFC performance, such as reduced ECSA and cathode overpotentials, resemble effects of contaminants and serve as a good platform for the subsequent development of models for air impurities.

Most thermokinetic models of cell degradation report the time-resolved potential of a cell. The use of variables is described in Eq. 14.12 [117]:

$$V_{\text{Cell}} = E_0 - \eta_A - \eta_C - R_0 I_C \quad (14.12)$$

The equation denotes  $E_0$  as the equilibrium potential;  $\eta_A$  and  $\eta_C$  as, respectively, the anode and cathode overpotentials;  $R_0$  as the PEMFC's internal resistance; and  $I_C$  as the current density. The latter term depends on the number of ECSA sites and degrades as catalyst coverage sites become overwhelmed with contaminants (or particles dissolve). A thermokinetic equation for the cathode overpotential has been developed using the ORR (following Tafel kinetics), surface sorption of the contaminant, and the electrode reaction mechanism described in Eq. 14.13 [67]:

$$\eta_C = \frac{1}{\beta} \ln \left( \left( \frac{I}{\delta \alpha i_0} \right) (1 - y)^{-1.5} \right) \quad (14.13)$$

The equation sets  $y$  as the fraction of contamination in the ionomer at the catalyst layer,  $1/\beta$  as the Tafel slope (assumed to be 0.060 V/decade),  $\delta$  as the catalyst layer thickness,  $\alpha$  as the ECSA of the catalyst normalized by volume, and  $i_0$  as the initial current density.

The existing models identify the following species as components of the total ECSA of the material: Pt, Pt-O<sub>2</sub>, Pt-OH, Pt<sub>*n*</sub>-P (contaminant), and Pt<sub>*n*</sub>-P' (oxidized form of the contaminant). Taken together their contributions add up to the total surface area summarized in Eq. 14.14 (typically expressed as  $\theta$  or 1, with other parameters being fractions of that value) [54]:



$$1 = \theta_{\text{Pt}} + \theta_{\text{PtO}_2} + \theta_{\text{PtO}_{2\text{H}}} + \theta_{\text{Pt}_{n-P}} + \theta_{\text{Pt}_{n-P'}} \quad (14.14)$$

While the oxide phases of Pt arise from natural operation (and are a part of the typical degradation behavior associated with the ORR process), the latter two terms depend on the presence of impurity species in the air stream. The authors calculated the rate of change of concentrations of the five phases and determined the following relationship described in Eq. 14.15 for the cathode current density:

$$I_C = n_{\text{O}_2} F \gamma_C k_{2f} \frac{k_{1f}}{k_{1b}} C_{\text{O}_2} A C_{\text{H}^+} \exp\left(-\frac{\alpha_2 n_2 \eta_C F}{RT}\right) \times \left[1 - \exp\left(-\frac{\alpha_2 n_2 \eta_C F}{RT}\right)\right] (1 - \theta_{\text{Pt}_{n-P}} + \theta_{\text{Pt}_{n-P'}}) \quad (14.15)$$

The equation uses  $n_{\text{O}_2}$  as the electron transfer number,  $\gamma$  as the ratio of active surface to total surface of the cathode catalyst layer,  $k_f$  or  $k_b$  is the forward or backward reaction rate,  $\alpha$  as the electron transfer coefficient,  $A$  is the ECSA, and  $C$  as the concentration of specific species ( $\text{H}^+$  or  $\text{O}_2$ ) at the cathode.

Several further modeling efforts by J. St-Pierre successfully developed simulations for possible behaviors for different types of contaminants and correlated their predicted adsorption properties with resulting PEMFC performance. The initial approach simulated contaminant sorption (from air stream) on cathode layer, reconciled adsorption time scales ( $>10$  h) with ORR time scales (0.06–0.6 s), and derived change in cell potential as a function of fractional impurity coverage ( $\theta_p$ ) assuming Tafel kinetics of ORR described in Eq. 14.16 [96]:

$$\Delta V = \frac{RT}{F} \ln(1 - \theta_p) \quad (14.16)$$

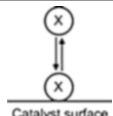

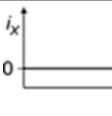
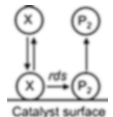
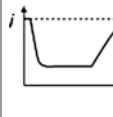
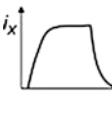
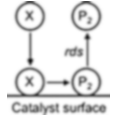
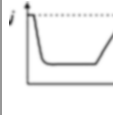
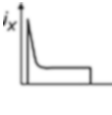
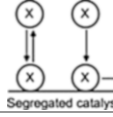
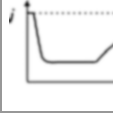
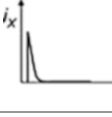
The modeling approach further defined a time-resolved ( $t$ ) relationship between contaminant coverage and kinetic rate of contaminant desorption ( $k_{\text{des}}$ ) and Pt molar density ( $\rho$ ) summarized in Eq. 14.17:

$$\ln\left(\frac{1 - e^{\frac{F\Delta V}{RT}}}{\theta_p}\right) = \frac{-k_{\text{des}}}{\rho} t \quad (14.17)$$

This approach is applicable to a broad range of airborne contaminants, and effects of common chemical pollutants in transportation and industrial environments including carbon monoxide [CO],  $\text{SO}_2$ ,  $\text{NO}/\text{NO}_2$ , and hydrogen sulfide [ $\text{H}_2\text{S}$ ] on PEMFC behavior were analyzed [95]. The relative concentration ratios of oxygen (reactant) to the contaminant species, as well as the adsorption kinetics and electrochemical activity behavior, significantly influenced resulting fuel cell performance. The possible modeled outcomes are summarized in Table 14.1.

The modeling efforts demonstrated that the unique chemistries of different contaminants yielded different effects on overpotentials [92]. The kinetic loss mathematical model showed different effects between uniform surfaces and

**Table 14.1** Effect of sorption mechanism, contaminant electrochemical activity, and contaminant/reactant ratio on resulting fuel cell performance (Reprinted with permission from St-Pierre [96]. Copyright (2010), Elsevier)

Activity of contaminant X	Rate-determining step	Scheme	Fuel cell performance (reactant present)	Fuel cell performance (reactant absent)
Electroinactive	X adsorption or desorption			
Electronegative contaminant X that produces product P <sub>2</sub>	X reaction			
	Desorption of P <sub>2</sub>			
	Irreversible adsorption of P <sub>2</sub>			

segregated reaction sites. The model calculated current densities with and without reactants. The simulation was able to predict future performance of PEMFCs based on several critical parameters. Based on estimates of catalyst recovery and impurity concentration thresholds, the model established a 0.65 ppb contaminant level minimum for performance loss of no greater than  $1 - \rho_1/\rho$  ( $\rho_1$  and  $\rho$  are, respectively, Pt site molar density associated with the reversibly adsorbed contaminant and Pt site molar density). Furthermore, the model predicts that a reduction of the Pt catalyst loading from its current common  $0.4 \text{ mg}\cdot\text{Pt}\cdot\text{cm}^{-2}$  value to  $0.1 \text{ Pt}\cdot\text{cm}^{-2}$  increases that concentration threshold up to 0.9 parts-per-billion (ppb).

For that initial simulation setup, the computational predictions for PEMFC performance closely matched experimentally determined effects of contaminants on cell voltage. The modeling approaches were subsequently extended and applied to permeation of contaminants through the ionomer layer (assuming Fick diffusion kinetics) [98]. This approach was further expanded recently and accounted for impurity ion exchange with protons in the membrane in order to derive tolerance limits as a function of ion valence. This model is a very good complement to the catalyst degradation simulation and, in unison, presents a comprehensive framework for fuel cell performance decay. Such a model will be important for the further evaluation of organic molecule impurities and other airborne contaminants.

While initial thermokinetic models limited their focus to small molecules (CO, NO<sub>2</sub>, H<sub>2</sub>S, etc.), others expanded their computational approach to more complex contaminants. Several kinetic models specifically focused on toluene [C<sub>7</sub>H<sub>8</sub>], which is a common industrial chemical and may often leach into air intake streams. Efforts

by investigator Z. Shi et al. assumed Langmuir adsorption kinetics for toluene. However, the process is complex and may involve vertical or flat orientation of the adsorbed molecule. The model simulated competitive adsorption of toluene vs. molecular  $O_2$  and was robust enough to calculate and predict both transient and steady-state cell performance [90]. The predicted results, which agreed with empirical data, showed that a  $0.2 \text{ A}\cdot\text{cm}^{-2}$  current density and a 750 ppb concentration resulted in a Pt ECSA drop from 59% to 48%. A current density of  $1.0 \text{ A}\cdot\text{cm}^{-2}$  decreased operating cell voltage by 48 mV for the same contaminant concentration. Despite the model's good agreement with experimental data, it has limitations: it assumes only a single site for molecular  $O_2$  adsorption and fails to account for either the temperature or the structure of the Pt catalyst.

The various modeling approaches all converge around the critical importance of accessible Pt ECSA. While most studies have focused on adsorption of contaminants, other approaches have also attempted to simulate Pt particle dissolution or coarsening. A one-dimensional model simulated an acidic media (which may be created with a broad range of airborne contaminants) and combined different thermokinetic rate models to estimate particle size evolution. In particular, fractions of  $N_2$  and air in the input stream influenced Pt dissolution and subsequent Ostwald ripening [57]. This work also analyzed anode catalyst layer evolution and transport of ions through the ionomer layer. A different thermokinetic model of Pt particle oxidation and dissolution demonstrated the dependence of the net reaction rate and long-term PEMFC performance on the Pt particle size distribution (including both the mean and the variance of the particle size distribution) [41]. The modeling approach evaluated the size of the  $Pt^+$  ion sink and found that, due to coarsening, larger initial particle sizes (4–5 nm diameter) are more stable than smaller, commonly used Pt particles (2–3 nm). Although, this approach did not incorporate effects of impurities, it can be effectively adapted to address contaminant-induced degradation.

Recent efforts by researcher S.G. Rinaldo et al. have applied Lifshitz-Slyozov-Wagner and Smoluchowski models to simulate electrochemically driven particle size evolution [80]. The authors determined the kinetics of particle dissolution, redeposition, coagulation, and detachment and the effects of PEMFC operation dynamics on the resulting Pt catalyst layer particle size distributions. The authors successfully correlated modeled particle size evolution with experimentally measured (via TEM) structural characterization. The main takeaway of the study was a dependence of high potential with lower particle surface tension and subsequent accelerated dissolution.

Various efforts have investigated the formation of platinum oxide species on the catalyst layer surface (driven primarily by overpotential). These studies show a complicated relationship between the formation of this electrochemically inactive material and the total available ECSA. In particular, this oxide formation may slow down Pt particle dissolution. Several modeling efforts assumed oxide formation on Pt particle edges and planar sites and simulated resulting surface area changes to accurately predict cyclic voltammograms [45]. Furthermore, particle coarsening may proceed by Ostwald ripening (driven by particle sizes and ions in solution) and

particle coalescence. The latter mechanism describes Pt particle movement on the surface and their subsequent aggregation. This process is also likely to be influenced by impurities in the air stream, especially by insoluble, large particulates (soot, etc.) that may dislodge Pt particles during mechanical impacts. Future modeling efforts should evaluate these processes.

Several recent studies have also evaluated the performance of novel Pt-based alloy catalysts and their performance as FC electrodes. A Monte Carlo simulation is coupled with non-equilibrium thermokinetics to assess the effects of CO sorption on  $\text{Pt}_x\text{Co}_y$  anodes [49]. Since CO is a common byproduct of hydrocarbon fuel combustion, it may infiltrate the  $\text{H}_2$  flow stream (during fuel reforming) and block adsorption sites on the catalyst. Subsequently, CO may impede the HOR and factor in as an important contaminant in the PEMFC. A separate computational study suggested CO adsorption onto pure Pt catalyst surfaces using Butler-Volmer kinetics, which added a temperature dependence component to the simulation (not a factor in the  $\text{Pt}_x\text{Co}_y$  approach). The Monte Carlo simulation used electric current density,  $\text{H}_2/\text{CO}$  reactant stream ratios, and catalyst particle compositions as input parameters and developed pseudoequilibrium atomic repartition of  $\text{Pt}_x\text{Co}_y$  nanoparticles. While PtCo (homogeneous Pt and Co distribution on the surface) tolerated CO adsorption better than  $\text{Pt}_3\text{Co}$  (Pt shell over a Co core), the  $\text{Pt}_3\text{Co}$  degraded slower than PtCo in the presence of CO. The simulations showed that CO concentration led to overpotential conditions, which, in turn, accelerated Co de-alloying and its subsequent dissolution into the MEA. Since a Pt-M (ruthenium [Ru], Co, Ni, etc.) nanostructured alloy will be likely incorporated in novel cathode catalyst layers, this model will be very useful to evaluate similar effects of contaminants in the air stream.

Although, BOP contamination sources differ from air intake impurities, some of the molecules (toluenes, benzyl alcohols [ $\text{C}_6\text{H}_6\text{R}_x\text{H}_2\text{yO}$ ], and ethers [ROR']/ether acetates [R'-COO-R], where R and R' represent the alkyl or aryl groups) may originate from a variety of sources [20]. Efforts by researchers B. Tavakoli and J.W. Weidner evaluated the effects of these organic molecules on the degradation of the Pt cathode catalyst layer [105]. The model assumed Tafel kinetics and described three distinct phenomena: adsorption on Pt sites, adsorption into the catalyst layer, and ion exchange with the monomer. The model described changes to the cell potential as a function of lost Pt ECSA. The authors evaluated recovery profiles and found that specific impurities, which differed according to their ion-exchange behavior in the ionomer, showed partial or full recovery. This model is applicable to a broad range of impurities and correlates well with reported experimental results.

The majority of the previously mentioned work has been based on systems of thermokinetic equations. However, a "computational simulation" approach encompasses a broad array of techniques that have been effectively used for phenomenological modeling. A coarse-grained molecular dynamics (CG-MD) process simulated the corrosion of the underlying nanostructured carbon support under zero-current conditions and during power cycling [62]. The simulation captured the evolution of the Pt-C bond (Pt  $d$  orbital and  $\pi$  bonding in carbon) and analyzed the microstructure of catalyst as a function of carbon loss. The approach was very

comprehensive and factored in additional effects, including ionomer and H<sub>2</sub>O morphology and coverage, and used the microstructure to gauge cell potential evolution. The simulation also captured ionomer phase evolution and detected conditions that propagated Nafion sorption on Pt surfaces (yet another possible BOP contaminant source). A separate CG-MD approach coupled this simulation method with dissipative particle dynamics (DPD) and smoothed particle hydrodynamics (SPH) to simulate self-organization of the microstructured catalyst layers and the reactive transport of fuel and oxidants through the porous media [114]. These approaches are highly customizable and can incorporate and evaluate effects of airborne contaminants.

Most modeling results output the cell overpotential, total voltage, and/or current density vs. time or cycle number. While these values properly gauge fuel cell performance, they do not describe structural transformations at the nanoscale level. If future computational models of degradation can correlate contaminant injection with electrochemically induced Pt particle growth or lattice restructuring, the simulation results will yield important fundamental insights. Furthermore, many current models apply nearly identical approaches to chemically different contaminants. However, experimental evidence shows divergent cell degradation behaviors for different contaminants (even those with similar electrochemical activities). Impurity species in the air intake stream are complex molecules with different dimensions, polar and nonpolar bonds, steric hindrances, and self-diffusion behaviors. The subsequent modeling work must further take these properties into account and incorporate these critical parameters. As similar Pt-metal alloys gain prominence as PEMFC cathode and anode catalysts, such approaches will more accurately assess the effects of nanoparticle composition on subsequent impurity-induced degradation behaviors.

Many contamination modeling exercises have focused on individual PEMFC materials (cathode catalyst layer, underlying carbon support, ionomer). However, some impurity molecules (such as NH<sub>3</sub> and toluene) are likely to permeate through and degrade multiple components [97]. These processes may run in series and in parallel and include competing for reactions with different kinetics. The experimentally measured results, in actuality, are a convoluted combination of these processes. More complex models that can combine these separate systems into more comprehensive simulations may more accurately capture the effects of contaminants on both catalyst degradation and fuel cell degradation as a whole.

While emerging thermokinetic models design extensive and descriptive systems of equations (such as those listed as Eqs. 14.15 and 14.17), these simulations rely on a very large number of parameters, which sometimes do not have well-defined physical meaning. These variables may have limited practical value, as certain inherent properties of intermolecular interactions and rate constants are difficult to measure or control in PEMFCs. While their use may help accurately validate the simulation and reconcile predicted performance with experimental results, the end result may overstate and mislead the precision and universality of such approaches. Models with fewer parameters, as well as models that define their parameters based on controllable experimental conditions, will provide more insights into effects of air contaminants.

Additional in situ material characterization techniques will provide in-depth structural information that will assess the ECSA changes, particle dissolution, and coarsening of Pt particles and selective surface reactions with different lattice plains. A recent effort conducted focused ion beam/scanning electron microscopy (FIB/SEM) imaging and relied on electron tomography to visualize the porous catalyst layer to assess its degradation. The technique provided time-dependent information about the size of catalyst and pores and compared particle changes against equation data for mass transport [87]. A different *in operando* X-ray absorption spectroscopy (XAS) method obtained extended X-ray absorption fine structure (EXAFS) spectra to correlate experimentally determined Pt-O growth with model predictions [74]. These techniques, along with other in-depth characterization methods (X-ray and neutron reflectometry, in situ Raman/infrared (IR) spectroscopy), may be adapted to studies of contaminants and refine existing models.

---

## 14.5 Emerging Catalysts for Fuel Cell Cathodes

The PEMFCs must become substantially less expensive in order to be commercially viable for their target applications. Existing MEAs of all pre-commercial fuel cell stacks utilize platinum or platinum group metals (PGM) on anodes and cathodes. The high price of PGM electrocatalysts accounts for 30–50% of the total stack cost. The substitution of platinum with inexpensive catalysts has been explored since the mid-1960s [47]. Despite decades of research into novel platinum group metal-free (PGM-free) electrocatalysts for oxygen reduction, only the last couple of years have yielded significant breakthroughs. In particular, recent studies reported progress in development of iron nitrogen-doped graphitic carbon [Fe/N/C] catalysts [46, 52, 53, 88, 112] and nitrogen-doped graphitic carbons (CN<sub>x</sub>) [19, 36, 40, 61, 91]. The PGM-free substitute catalysts should have similar activities as platinum, high durability, and high versatility for all types of fuel cell applications, such as in automobiles and electrical backup systems. Regardless of catalyst choice, the long-term operation of fuel cell devices is highly dependent on air quality. Therefore, emerging PGM-free catalysts should also resist degradation induced by major airborne contaminants, especially those emitted from cars (CO, NO<sub>x</sub>) and coal-fed power plants (SO<sub>2</sub>).

### 14.5.1 Fe/N/C Catalysts and Their Tolerance to SO<sub>2</sub>, NO<sub>2</sub>, and CO Poisoning

The impact of small-molecule poisons including CO, thiocyanate [SCN<sup>-</sup>], cyanide [CN<sup>-1</sup>], halides, [F<sup>-</sup>, Cl<sup>-</sup>, and Br<sup>-</sup>], azide [N<sub>3</sub>], ethanethiol [CH<sub>3</sub>CH<sub>2</sub>S], H<sub>2</sub>S, NO<sub>x</sub>, and SO<sub>2</sub> on ORR at PGM-free catalysts has been mainly studied in an attempt to develop methods to probe and separate iron-containing catalytically active sites: Fe-N<sub>4</sub>/C and Fe-N<sub>2</sub>/C moieties.

Common precursors for Fe/N/C, such as Fe-porphyrin and Fe-phthalocyanine, are well-known to have a higher affinity for CO than O<sub>2</sub>. Therefore, the Fe-N<sub>4</sub>/C and Fe-N<sub>2</sub>/C sites were expected to strongly chemisorb carbon monoxide, and effects of CO on the ORR activity of Fe/N/C catalysts were studied [6, 15, 21, 71, 84, 111]. It was observed that steric factors of ligands in Fe-porphyrin complexes can reduce affinity to CO or even suppress any CO binding at atmospheric pressure [21, 84]. Additional studies of Fe-porphyrin interactions with CO in aqueous solutions using in situ X-ray absorption spectroscopy showed the formation of CO-Fe-porphyrin adduct, which disappeared at a 0.6 V potential and released the CO molecules [6]. Moreover, recent publications have confirmed CO tolerance of Fe/N/C catalysts [15, 71, 111].

Further, attempts to identify active sites on Fe/N/C catalysts revealed that CN<sup>-</sup> had strong poisoning effects [38, 56, 106]. The authors proposed that CN<sup>-</sup> bound at an axial position on the sites inhibited oxygen reduction and shifted the reaction pathway from 4e<sup>-</sup> to 2e<sup>-</sup>. The catalytic activity was restored after rinsing a poisoned electrode in water [106]. At the same time, ORR on Fe/N/C electrocatalysts obtained from Fe-phthalocyanine precursor was shown to be unaffected by F<sup>-</sup> or SCN<sup>-</sup> [106]. In contrast, halide ions (F<sup>-</sup>, Cl<sup>-</sup> and Br<sup>-</sup>) and sulfur-containing species (SCN<sup>-</sup>, SO<sub>2</sub>, and H<sub>2</sub>S) appeared to suppress oxygen reduction on Fe/N/C catalysts that had been derived from poly-*m*-phenylenediamine [111]. Additionally, this electrocatalyst was found to be insensitive to NO<sub>x</sub> [111], whereas authors [63] suggested the use of NO<sub>x</sub> to quantify active sites for Fe/N/C. Analysis of prior reported publications demonstrated that no clear conclusion can be reached on poisoning effects of contaminants on Fe/N/C catalysts. Furthermore, all ORR studies described here primarily relied on rotating disk electrode (RDE) and CV techniques.

Evaluation of PGM-free cathode PEMFCs under realistic FC operating conditions and exposure to air contaminants, such as CO, SO<sub>2</sub>, and NO<sub>2</sub>, are very critical for efforts to understand durability and environmental adaptability of the new catalytic materials. However, published Papers that addresses these issues are quite limited.

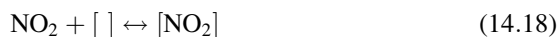
A detailed investigation recently reported on the performance of PGM-free PEMFCs and their tolerance to main air contaminants (SO<sub>2</sub>, NO<sub>2</sub>, and CO) using a segmented cell setup with 76 cm<sup>2</sup> MEAs [75]. The Fe/N/C catalyst was synthesized using iron (III) nitrate [Fe(NO<sub>3</sub>)<sub>3</sub>] and 4-amino antipyrine [C<sub>11</sub>H<sub>13</sub>N<sub>3</sub>O] as precursors by a sacrificial support method. The performance of PGM-free cathode PEMFC was found to be limited by high activation overpotentials. These were attributed to the lower activity of the Fe/N/C cathodes in oxygen electroreduction than those levels for Pt-based catalysts. Additionally, due to a high Fe/N/C catalyst loading (~3 mg·cm<sup>-2</sup>), mass transfer losses became pronounced and reduced both overall and local segment performance. The composition and structure of PGM-free gas diffusion electrodes (GDEs) significantly contributed to the fuel cell output. In particular, the ratio between the catalyst and Nafion coating layer loadings on the top of the catalyst materials at GDE appeared to be responsible for appropriate HFR, catalyst utilization, and performance.



The exposure of Pt-based PEMFC to a mixture of air and 1–10 ppm SO<sub>2</sub> resulted in a significant decrease in the performance [10, 11, 37, 118]. In contrast, the performance of Fe/N/C cathode PEMFC was not affected by the presence of SO<sub>2</sub>. Figure 14.5a, b presents profiles of the segment voltages and normalized current densities vs. experiment time at total cell current of 0.2 A·cm<sup>-2</sup> during SO<sub>2</sub> poisoning. For the first 2 h, the cell operated with pure air, resulting in a cell voltage of 0.390 V. The initial current density distribution ranged from 0.23 to 0.17 A·cm<sup>-2</sup> for segments 1 and 10, respectively, due to downstream oxygen consumption and water accumulation. The injection of 10 ppm of SO<sub>2</sub> for 7 h did not cause any noticeable changes in segments/cell voltage and current distribution similar to previously published work [24].

To understand the differences in the performances of Fe/N/C cathodes in the presence of airborne contaminants, density functional theory (DFT) was used to calculate the oxygen and contaminant binding energies at the proposed catalytic sites: Fe-N<sub>4</sub>/C, Fe-N<sub>2</sub>/C, and N-doped graphene [75]. According to Sabatier's principle, oxygen reduction activity is strongly dependent on the interaction of oxygen with the catalyst. Using DFT with functionals employing Perdew-Burke-Ernzerhof (PBE) correlation, the adsorption energies of molecular oxygen on the Fe-N<sub>4</sub>/C, Fe-N<sub>2</sub>/C, and N-doped graphene sites were calculated as -1.01, -2.34, and -0.15 eV, respectively (Table 14.2). Comparisons of the adsorption energies of SO<sub>2</sub> with those of molecular O<sub>2</sub> showed that SO<sub>2</sub> interactions with Fe-N<sub>4</sub>/C and Fe-N<sub>2</sub>/C are weaker than with O<sub>2</sub> (-0.81 and -1.63 eV). Hence, SO<sub>2</sub> cannot be strongly adsorbed by Fe-containing centers and should not affect oxygen reduction and performance.

Exposure of the Fe/N/C cathode to 2 and 10 ppm NO<sub>2</sub> resulted in a performance loss of 30 and 70–75 mV, respectively (Fig. 14.5c, d), which is lower than in a Pt cathode fuel cell with a performance drop of ~80–100 mV under exposure of 2 ppm NO<sub>2</sub> [3, 31]. The finding clearly demonstrated that the non-precious catalyst was more tolerant to NO<sub>2</sub> poisoning than the Pt catalyst. The impact of NO<sub>2</sub> on the Fe/N/C and Pt electrocatalysts could be attributed to NO<sub>2</sub> adsorption and its further transformation. The NO<sub>2</sub> molecules adsorb onto the Fe-N<sub>2</sub>/C, Fe-N<sub>4</sub>/C, and Pt sites, causing performance drops [17, 27, 44, 81] and are summarized in Eqs. 14.18 and 14.19:

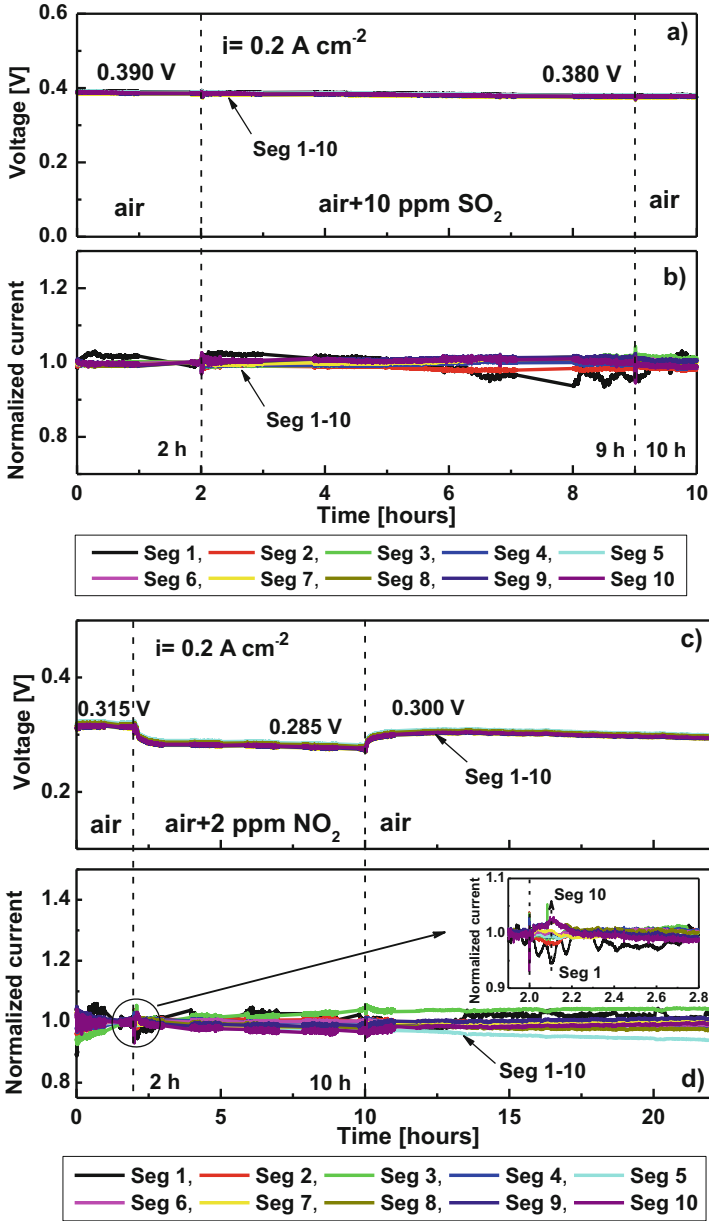


The adsorbed NO<sub>2</sub> can reversibly dissociate into NO and O:



The produced NO has an affinity toward Fe<sup>n+</sup> centers (Fe<sup>2+</sup> and Fe<sup>3+</sup>) [70, 81, 113] and can either slowly desorb from Pt and Fe-N<sub>x</sub>/C into the gas phase or be released as nitric acid [HNO<sub>3</sub>] [27]. Moreover, DFT results confirmed that the adsorption energies





**Fig. 14.5** Voltage and normalized current densities of individual segments vs. time for PGM-free PEMFC exposed to  $\text{SO}_2$  (a, b) and  $\text{NO}_2$  (c, d) at  $0.2 \text{ A cm}^{-2}$ . Cell inlet is at segment 1, outlet is at segment 10. Anode/cathode:  $\text{H}_2/\text{air}$ , 2/2 stoichiometry, 100/50% RH, 2/2 atm gauge,  $80 \text{ }^\circ\text{C}$  (Reprinted with permission from Reshетенko et al. [75] Copyright (2016), Elsevier)

**Table 14.2** Adsorption energies of O<sub>2</sub>, NO, NO<sub>2</sub>, and SO<sub>2</sub> on Fe-N<sub>4</sub>/C, Fe-N<sub>2</sub>/C, and N-doped graphene (Reprinted with permission from Reshetyenko et al. [75] Copyright (2016), Elsevier)

Adsorbate	Adsorption energy [eV]		
	Fe-N <sub>4</sub> /C	Fe-N <sub>2</sub> /C	N-doped graphene
O <sub>2</sub>	-1.01	-2.34	-0.15
SO <sub>2</sub>	-0.81	-1.63	-0.17
NO	-1.97	-3.37	-0.09
NO <sub>2</sub>	-1.45	-2.63	-0.43
CO	-1.61	-2.09	-0.01

of NO<sub>2</sub> and NO were greater than that of O<sub>2</sub> on Fe-N<sub>2</sub>/C and Fe-N<sub>4</sub>/C sites (Table 14.2). This implied that NO<sub>x</sub> can substitute molecular O<sub>2</sub> and poison catalytically active sites, inhibit oxygen reduction, and result in a performance loss.

The introduction of 5 or 20 ppm of CO into the air stream did not affect Fe/N/C [75], which is in agreement with RDE data [15, 71, 111]. The CO in air stream also did not cause any changes for Pt PEMFCs performance. The adsorption of CO on Fe-N<sub>2</sub>/C and N-doped graphene was not favorable in comparison with O<sub>2</sub>, but CO competes with O<sub>2</sub> for strong adsorption at Fe-N<sub>4</sub>/C sites (Table 14.2). The discrepancy between the computational and experimental data might be also explained by the very fast CO removal due to its oxidation on the Fe-N<sub>4</sub>/C similar to the Pt-based cathodes.

The long-term operation of Fe/N/C fuel cells resulted in a gradual performance degradation, which became pronounced when O<sub>2</sub> was used as the cathode feed gas. The degradation was mainly caused by increased activation overpotentials. Detailed XPS studies confirmed that PEMFC performance declines were due to catalyst degradation and ionomer oxidation, the latter being promoted by the presence of air contaminants.

### 14.5.2 Nitrogen-Doped Graphitic Carbons

In parallel with Fe/N/C catalysts, significant work has been done on studies of nitrogen-doped nanotubes (CN<sub>x</sub>) as ORR catalysts in alkaline and acid conditions [19, 36, 61, 91]. All of these materials are primarily produced via decomposition of nitrogen-containing hydrocarbons (acetonitrile, cyanamide [NH<sub>2</sub>CN], ethylenediamine [C<sub>2</sub>H<sub>8</sub>N<sub>2</sub>], and pyridine [C<sub>5</sub>H<sub>5</sub>N]) over iron- or cobalt-based catalysts at elevated temperatures. The resulting carbon structures were treated by acid/base to remove any accessible catalytic materials. Despite this purification treatment, the carbon nanotubes (CNTs) still retain metal particles with 5–30 nm diameters that are covered by layers of turbostratic carbon. Subsequently, they appear to be inaccessible for oxygen. The CN<sub>x</sub> electrocatalysts were studied by RDE and demonstrated good ORR performance in alkaline media [19, 61], while in acid conditions they are less active compared to Fe/N/C and Pt [92].

The described preparation method for  $CN_x$  catalysts likely resulted in the appearance of multiple active centers for ORR with metallic center (Fe-N<sub>4</sub>/C or Fe-N<sub>2</sub>/C) and without metallic center (pyridinic nitrogen). Metal-containing site formation may occur through hydrocarbon decomposition over 3d metal catalysts (Ni, Co, Fe). The growth of carbon nanotubes/fibers involves adsorption and dissociation of hydrocarbon precursor on 3d metal particles, carbon diffusion through the particles, and its deposition as graphitic layers [2, 116]. Multiple repetitions of catalytic cycles deactivate the catalyst due to encapsulation of the metal active center by formed graphite layers. Research of this phenomenon [5] suggested another mechanism of the catalyst deactivation: “atomic” intercalation or erosion of the active particle. During this process, the deposited graphite layers capture catalytic material and incorporate metal atoms in a carbon matrix.

Since the presence of multiple active sites cannot be eliminated, and the observed performance might be also due to metal centers with high activity, the nature of active sites in the  $CN_x$  catalysts is still not clear and debated. To clarify this question, Ozkan group [107, 108] deliberately poisoned the  $CN_x$  catalyst with H<sub>2</sub>S, CO, and cyanide and found that the catalyst retained its ORR activity based on RDE measurements. These results supported the hypothesis that pyridinic nitrogen is the active site, and  $CN_x$  catalysts do not have any metal-containing catalytic centers [92]. Additionally, these findings also demonstrated tolerance of  $CN_x$  to some possible air pollutants and revealed the potential of the catalyst for applications operated at harsh environmental conditions. As it was mentioned previously, the  $CN_x$  catalysts were studied only at RDE conditions and cannot provide any predictable information about PEMFC performance and behavior in the presence of air pollutants due to different operating conditions (temperature and back pressure) and environments (gaseous vs. aqueous). Therefore, additional work is required in order to identify the tolerance threshold of this novel catalyst.

---

## 14.6 Conclusion

Impurities in the air stream negatively impact nanostructured Pt-based catalysts of PEMFC cathodes, and resulting detrimental effects present a serious roadblock in the pathway toward viable commercialization of fuel cells. These contaminants originate from a broad range of sources and environments, and fuel cells that operate outside of pristine laboratory conditions are likely to encounter them. Most of the inorganic and organic salts, solvents, exhaust gases, and industrial combustion products interact with Pt nanoparticles and negatively impact the oxygen reduction reaction. Moreover, even extremely minute concentrations (~1 ppb) of some contaminants are sufficiently significant and may cause significant damage to the PEMFC. Unless commercialized fuel cells employ highly efficient air filters, impurity-induced cathode degradation will impede the performance of these energy conversion systems and require materials- and operations-focused solutions.

Primary fundamental processes that contribute to fuel cell performance degradation involve adsorption of contaminants on nanoparticle surfaces, which reduces the available electrochemical surface area, shift of the ORR pathway from  $4e^-$  to less electrochemically efficient mixed  $4e^-$  and  $2e^-$  mechanism, and catalyst nanoparticle dissolution or coarsening. Furthermore, some contaminants promote side reactions that are driven by an electrochemical potential and yield additional impurity products that impede the electrocatalytic activities of Pt. Although, each contaminant exhibits distinct performance degradation behavior, the processes are ubiquitous. The phenomenological modeling of contaminant-induced cathode catalyst degradation typically involves a system of thermokinetic equations that derive the cell's potential and current density as a function of the available surface area. Simulation efforts have underscored the significance of Pt particle dimensions and found optimal particle size distributions that facilitate efficient oxidation reduction yet minimize Pt coarsening. However, other predictive modeling approaches, such as coarse-grained molecular dynamics, may provide more insights and account for particle dissolution, Ostwald ripening, and coalescence effects.

Recovery steps, which are inherently simple, typically counter the effects of contaminant introduction into the air stream, adsorption onto catalytic surfaces, and subsequent electrochemical processes. The most common fuel cell rehabilitation approach involves electrochemical cycling that is coupled with repeated flushing with neat (contaminant-free) air. While, in many cases, this operation successfully desorbs impurities and restores PEMFC cathodes to their full operating capabilities, it cannot undo the damage of irreversible electrochemical reactions. Furthermore, such a recovery procedure deviates from the fuel cells' standard operating routine and serves as a significant drawback to their commercial viability.

Material modifications to the nanostructured platinum catalyst have yielded some improvement of tolerance to impurities. Although Pt-based alloys, such as  $Pt_3Co$  and  $PtNi$ , do not significantly inhibit adsorption of impurities versus platinum, the former promotes faster recovery from  $SO_2$ . However, fundamental studies of adsorption of inorganic and organic species on nanostructured alloys are still in their infancy. Platinum-free catalysts, which aim to address both durability and cost of novel fuel cells, may more effectively resist poisoning by certain contaminants and retain their active centers. Fe/N/C and nitrogen-doped graphitic carbons show promising oxygen reduction reaction activities and tolerance to  $SO_2$ ,  $NO_2$ , and CO. However, relatively few studies have addressed their performance in the presence of airborne contaminants in the PEMFC environment, and future efforts must address this knowledge gap. These novel materials, along with other nanostructured catalysts, have highly versatile geometrical configurations, particle sizes, electron band structures, and electrochemically driven adsorption and reaction capabilities. Future catalyst research efforts must incorporate effects of impurities in their efforts to abstain from the use of precious metals and design efficient and inexpensive PEMFCs.

**Acknowledgments** This work is supported by the Office of Naval Research (N00014-12-1-0496) and the Department of Energy (DE-EE0000467). B. Dyatkin (B.D.) is supported by the National Research Council (NRC) Research Associateship Program (RAP). The authors also gratefully acknowledge the helpful comments and suggestions of the reviewers. The authors thank the editors for allowing us to review our previously published papers [8, 9, 11–13, 30, 75, 76, 78].

## References

1. R.R. Adzic, J. Zhang, K. Sasaki, M.B. Vukmirovic, M. Shao, J.X. Wang, A.U. Nilekar, M. Mavrikakis, J.A. Valerio, F. Uribe, Platinum monolayer fuel cell electrocatalysts. *Top. Catal.* **46**, 249–262 (2007)
2. I. Alstrup, A new model explaining carbon filament growth on nickel, iron, and Ni-Cu alloy catalysts. *J. Catal.* **109**, 241–251 (1988)
3. M. Angelo, J. St-Pierre, The effect of common airborne impurities and mixtures on PEMFC performance and durability. *ECS Trans.* **64**, 773–788 (2014)
4. H. Angerstein-Kozłowska, B. Macdougall, B.E. Conway, Electrochemisorption and reactivity of nitriles at platinum electrodes and the anodic H desorption effect. *J. Electroanal. Chem.* **39**, 287–313 (1972)
5. L.B. Avdeeva, O.V. Goncharova, D.I. Kochubey, V.I. Zaikovskii, L.M. Plyasova, B.N. Novgorodov, S.K. Shaikhutdinov, Coprecipitated Ni-alumina and Ni-Cu-alumina catalysts of methane decomposition and carbon deposition. II. Evolution of the catalysts in reaction. *Appl. Catal. A.* **114**, 117–129 (1996)
6. I.T. Bae, D.A. Scherson, In situ X-ray absorption of a carbon monoxide-iron porphyrin adduct adsorbed on high-area carbon in an aqueous electrolyte. *J. Phys. Chem. B* **102**, 2519–2522 (1998)
7. V.S. Bagotzky, Y.B. Vassilyev, J. Weber, J.N. Pirtskha, Adsorption of anions on smooth platinum electrodes. *J. Electroanal. Chem.* **27**, 31–46 (1970)
8. O.A. Baturina, A. Epshteyn, P. Northrup, K.E. Swider-Lyons, The influence of cell voltage on the performance of a PEM fuel cell in the presence of HCl in the air. *J. Electrochem. Soc.* **161**, F365–F372 (2014)
9. O.A. Baturina, A. Epshteyn, P.A. Northrup, K.E. Swider-Lyons, Insights into PEMFC performance degradation from HCl in the air. *J. Electrochem. Soc.* **158**, B1198–B1205 (2011a)
10. O.A. Baturina, Y. Garsany, B.D. Gould, K.E. Swider-Lyons, Contaminant-induced degradation, in *PEM Fuel Cell Failure Mode Analysis*, ed. by H. Wang, H. Li, X. Z. Yuan (CRC Press, New York, 2012)
11. O.A. Baturina, B.D. Gould, Y. Garsany, K.E. Swider-Lyons, Insights on the SO<sub>2</sub> poisoning of Pt<sub>3</sub>Co/VC and Pt/VC fuel cell catalysts. *Electrochim. Acta* **55**, 6676–6686 (2010)
12. O.A. Baturina, B.D. Gould, A. Korovina, Y. Garsany, R. Stroman, P.A. Northrup, Products of SO<sub>2</sub> adsorption on fuel cell electrocatalysts by a combination of sulfur K-edge XANES and electrochemistry. *Langmuir* **27**, 14930–14939 (2011b)
13. O.A. Baturina, B.D. Gould, P.A. Northrup, K.E. Swider-Lyons, SO<sub>2</sub> adsorption products on Pt nanoparticles as a function of electrode potential and oxidative properties of carrier gas: in situ sulfur K-edge XANES approach. *Catal. Today* **205**, 106–110 (2013)
14. W. Bi, T.F. Fuller, Modeling of PEM fuel cell Pt/C catalyst degradation. *J. Power Sources* **178**, 188–196 (2008)
15. L. Birry, J.H. Zagal, J.P. Dodelet, Does CO poison Fe-based catalysts for ORR? *Electrochem. Commun.* **12**, 628–631 (2010)
16. F.N. Büchi, M. Inaba, T.J. Schmidt, *Polymer Electrolyte Fuel Cell Durability* (Springer, New York, 2009)

17. M. Busch, A. Kompch, S. Suleiman, C. Notthoff, U. Bergmann, R. Theissmann, B. Atakan, M. Winterer, NO<sub>x</sub> conversion properties of a novel material: iron nanoparticles stabilized in carbon. *Appl. Catal. B.* **166–167**, 211–216 (2015)
18. M.A. Butler, G. Burr, D. Dankovic, R.A. Lunsford, A. Miller, M. Nguyen, L. Olsen, D. Sharpnack, J. Snawder, L. Stayner, Hazard review: health effects of occupational exposure to asphalt (U.S. Department of Health and Human Services, Public Health Service Centers for Disease Control and Prevention, National Institute for Occupational Safety and Health, December 2000)
19. Z. Chen, D. Higgins, H.S. Tao, R.S. Hsu, Z.W. Chen, Highly active nitrogen-doped carbon nanotubes for oxygen reduction reaction in fuel cell applications. *J. Phys. Chem. C* **113**, 21008–21013 (2009)
20. H.-S. Cho, J.W. Van Zee, An isothermal model for predicting performance loss in PEMFCs from the balance of plant leachates. *J. Electrochem. Soc.* **161**, F1375–F1388 (2014)
21. J.P. Collman, X.M. Zhang, P.C. Herrmann, E.S. Uffelman, B. Boitrel, A. Straumanis, J.I. Brauman, Congruent multiple Michael addition for the synthesis of biomimetic heme analogs. *J. Am. Chem. Soc.* **116**, 2681–2682 (1994)
22. B.E. Conway, Y. Phillips, S.Y. Qian, Surface electrochemistry and kinetics of anodic bromine formation at platinum. *J. Chem. Soc. Faraday Trans.* **91**, 283–293 (1995)
23. R.M. Darling, J.P. Meyers, Kinetic model of platinum dissolution in PEMFCs. *J. Electrochem. Soc.* **150**, A1523–A1527 (2003)
24. D.H. Deng, L. Yu, X.Q. Chen, G.X. Wang, L. Jin, X.L. Pan, J. Deng, G.Q. Sun, X.H. Bao, Iron encapsulated within pod-like carbon nanotubes for oxygen reduction reaction. *Angew. Chem. Int. Ed.* **52**, 371–375 (2013)
25. M.S. El-Deab, F. Kitamura, T. Ohsaka, Impact of acrylonitrile poisoning on oxygen reduction reaction at Pt/C catalysts. *J. Power Sources* **229**, 65–71 (2013)
26. S. Elliott, F.S. Rowland, Methyl halide hydrolysis rates in natural waters. *J. Atmos. Chem.* **20**, 229–236 (1995)
27. A.A. Franco, B. Barthe, L. Rouillon, O. Lemaire, Mechanistic investigations of NO<sub>2</sub> impact on ORR in PEM fuel cells: a coupled experimental and multiscale modeling approach. *ECS Trans.* **25**, 1595–1604 (2009)
28. N. Garcia-Araez, V.C. Climent, E. Herrero, J.M. Feliu, On the electrochemical behavior of the Pt (100) vicinal surfaces in bromide solutions. *Surf. Sci.* **560**, 269–284 (2004)
29. Y. Garsany, O.A. Baturina, K.E. Swider-Lyons, Impact of sulfur dioxide on the oxygen reduction reaction at Pt/Vulcan carbon electrocatalysts. *J. Electrochem. Soc.* **154**, B670–B675 (2007)
30. Y. Garsany, O.A. Baturina, K.E. Swider-Lyons, Oxygen reduction reaction kinetics of SO-contaminated Pt<sub>2</sub>Co and Pt/Vulcan carbon electrocatalysts. *J. Electrochem. Soc.* **156**, B848–B855 (2009)
31. F.H. Garszon, F.A. Uribe, Effects of contaminants of catalyst activity, in *Handbook of Fuel Cells – Fundamentals, Technology, and Applications*, ed. by W. Vielstich, H. A. Gasteiger, A. Lamm (Wiley, Weinheim, 2010)
32. H.A. Gasteiger, S.S. Kocha, B. Sompalli, F.T. Wagner, Activity benchmarks and requirements for Pt, Pt-alloy, and non-Pt oxygen reduction catalysts for PEMFCs. *Appl. Catal. B.* **56**, 9–35 (2005)
33. H.A. Gasteiger, N.M. Markovic, P.N. Ross, Bromide adsorption on Pt(111): adsorption isotherm and electrosorption valency deduced from RRD(Pt(111))<sub>E</sub> measurements. *Langmuir* **12**, 1414–1418 (1996)
34. S. Gilman, D. Chu, Methanol effects on the O<sub>2</sub> reduction reaction, in *Handbook of Fuel Cells – Fundamentals, Technology, and Applications*, ed. by W. Vielstich, H. A. Gasteiger, A. Lamm, H. Yokokawa (Wiley, Weinheim, 2010)
35. R.N. Goldberg, L.G. Hepler, Thermochemistry and oxidation potentials of the platinum group metals and their compounds. *Chem. Rev.* **68**, 229–252 (1968)

36. K.P. Gong, F. Du, Z.H. Xia, M. Durstock, L.M. Dai, Nitrogen-doped carbon nanotube arrays with high electrocatalytic activity for oxygen reduction. *Science* **323**, 760–764 (2009)
37. B.D. Gould, O.A. Baturina, K.E. Swider-Lyons, Deactivation of Pt/VC proton exchange membrane fuel cell cathodes by SO<sub>2</sub>, H<sub>2</sub>S, and COS. *J. Power Sources* **188**, 89–95 (2009)
38. S. Gupta, C. Fierro, E. Yeager, The effects of cyanide on the electrochemical properties of transition metal macrocycles for oxygen reduction in alkaline solutions. *J. Electroanal. Chem.* **306**, 239–250 (1991)
39. R. Halseid, P.J.S. Vie, R. Tunold, Influence of ammonium on conductivity and water content of Nafion 117 membranes. *J. Electrochem. Soc.* **151**, A381–A388 (2004)
40. D.C. Higgins, J. Wu, W. Li, Z. Chen, Cyanamide derived thin film on carbon nanotubes as metal free oxygen reduction reaction electrocatalyst. *Electrochim. Acta* **59**, 8–13 (2012)
41. E.F. Holby, D. Morgan, Application of Pt nanoparticle dissolution and oxidation modeling to understanding degradation in PEM fuel cells. *J. Electrochem. Soc.* **159**, B578–B591 (2012)
42. K. Hongsirikam, J.G. Goodwin Jr., S. Greenway, S. Creager, Influence of ammonia on the conductivity of Nafion membranes. *J. Power Sources* **195**, 30–38 (2010)
43. G. Horányi, E.M. Rizmayer, Formation of ethane during the electroreduction of acetonitrile at a platinized platinum electrode. *J. Electroanal. Chem.* **113**, 305–309 (1980)
44. M. Iwasaki, H. Shinjoh, Analysis of the adsorption state and desorption kinetics of NO<sub>2</sub> over Fe–zeolite catalyst by FT-IR and temperature-programmed desorption. *Phys. Chem. Chem. Phys.* **12**, 2365–2372 (2010)
45. T. Jahnke, G. Futter, A. Latz, T. Malkow, G. Papakonstantinou, G. Tsotridis, P. Schott, M. Gérard, M. Quinaud, M. Quiroga, A.A. Franco, K. Malek, F. Calle-Vallejo, R. Ferreira de Morais, T. Kerber, P. Sautet, D. Loffreda, S. Strahl, M. Serra, P. Polverino, C. Pianese, M. Mayur, W.G. Bessler, C. Kompis, Performance and degradation of proton exchange membrane fuel cells: state of the art in modeling from atomistic to system scale. *J. Power Sources* **304**, 207–233 (2016)
46. F. Jaouen, E. Proietti, M. Lefevre, R. Chenitz, J.P. Dodelet, G. Wu, H.T. Chung, C.M. Johnston, P. Zelenay, Recent advances in nonprecious metal catalysts for oxygen-reduction reaction in polymer electrolyte fuel cells. *Energy Environ. Sci.* **4**, 114–130 (2011)
47. R. Jasinski, A new fuel cell cathode catalyst. *Nature* **201**, 1212–1213 (1964)
48. K. Jayasayee, J.A.R. Van Veen, E.J.M. Hensen, F.A. de Bruijn, Influence of chloride ions on the stability of PtNi alloys for PEMFC cathode. *Electrochim. Acta* **56**, 7235–7242 (2011)
49. S. Kian Cheah, O. Sicardy, M. Marinova, L. Guetaz, O. Lemaire, P. Gélin, A.A. Franco, CO impact on the stability properties of Pt<sub>x</sub>Co<sub>y</sub> nanoparticles in PEM fuel cell anodes: mechanistic insights. *J. Electrochem. Soc.* **158**, B1358–B1367 (2011)
50. V. Komanicky, K.C. Chang, A. Menzel, N.M. Markovic, H. You, X. Wang, D. Myers, Stability and dissolution of platinum surfaces in perchloric acid. *J. Electrochem. Soc.* **153**, B446–B451 (2006)
51. C. Korzeniewski, W. McKenna, S. Pons, An in situ infrared studies of the oxidation of sulfur-dioxide on platinum-electrodes. *J. Electroanal. Chem.* **235**, 361–368 (1987)
52. U.I. Kramm, J. Herranz, N. Larouche, T.M. Arruda, M. Lefevre, F. Jaouen, P. Bogdanoff, S. Fiechter, I. Abs-Wurmbach, S. Mukerjee, J.P. Dodelet, Structure of the catalytic sites in Fe/N/C-catalysts for an O<sub>2</sub> reduction in PEM fuel cells. *Phys. Chem. Chem. Phys.* **14**, 11673–11688 (2012)
53. M. Lefevre, E. Proietti, F. Jaouen, J.P. Dodelet, Iron-based catalysts with improved oxygen reduction activity in polymer electrolyte fuel cells. *Science* **324**, 71–74 (2009)
54. H. Li, S. Knights, Z. Shi, J.W. Van Zee, J. Zhang, *Proton Exchange Membrane Fuel Cells: Contamination and Mitigation Strategies* (CRC Press, New York, 2010a)
55. H. Li, H.J. Wang, W.M. Qian, S.S. Zhang, S. Wessel, T.T.H. Cheng, J. Shen, S.H. Wu, Chloride contamination effects on proton exchange membrane fuel cell performance and durability. *J. Power Sources* **196**, 6249–6255 (2011)

56. W. Li, A. Yu, D.C. Higgins, B.G. Llanos, Z. Chen, Biologically inspired highly durable iron phthalocyanine catalysts for oxygen reduction reaction in polymer electrolyte membrane fuel cells. *J. Am. Chem. Soc.* **132**, 17056–17058 (2010b)
57. Y. Li, K. Moriyama, W. Gu, S. Arisetty, C.Y. Wang, A one-dimensional Pt degradation model for polymer electrolyte fuel cells. *J. Electrochem. Soc.* **162**, F834–F842 (2015)
58. C. Long, Q.F. Li, Y. Li, Y.A. Liu, A.M. Li, Q.X. Zhang, Adsorption characteristics of benzene-chlorobenzene vapor on hyper cross-linked polystyrene adsorbent and a pilot-scale application study. *Chem. Eng. J.* **160**, 723–728 (2010)
59. T. Lopes, J. Chlistunoff, J.-M. Sansiñena, F.H. Garzon, Oxygen reduction reaction on a Pt/carbon fuel cell catalyst in the presence of trace quantities of ammonium ions: an RRDE study. *Int. J. Hydrog. Energy* **37**, 5202–5207 (2012)
60. W. Mabey, T. Mill, Critical-review of hydrolysis of organic compounds in water under environmental conditions. *J. Phys. Chem. Ref. Data* **7**, 383–415 (1978)
61. S. Maldonado, K.J. Stevenson, Influence of nitrogen doping on oxygen reduction electrocatalysis at carbon nanofiber electrodes. *J. Phys. Chem. B* **109**, 4707–4716 (2005)
62. K. Malek, A.A. Franco, Microstructure-based modeling of aging mechanisms in catalyst layers of polymer electrolyte fuel cells. *J. Phys. Chem. B* **115**, 8088–8101 (2011)
63. D. Malko, A. Kucernak, T. Lopes, In situ electrochemical quantification of active sites in Fe–N/C non-precious metal catalysts. *Nat. Commun.* **7**, 13285 (2016)
64. N.M. Markovic, C.A. Lucas, H.A. Gasteiger, P.N. Ross, Bromide adsorption on Pt (100): Rotating ring Pt (100) disk electrode and surface X-ray scattering measurements. *Surf. Sci.* **365**, 229–240 (1996)
65. K. Matsuoka, S. Sakamoto, K. Nakato, A. Hamada, Y. Itoh, Degradation of polymer electrolyte fuel cells under the existence of anion species. *J. Power Sources* **179**, 560–565 (2008)
66. K.J.J. Mayrhofer, B.B. Bliznac, M. Arenz, V.R. Stamenkovic, P.N. Ross, N.M. Markovic, The impact of geometric and surface electronic properties of Pt-catalysts on the particle size effect in electrocatalysis. *J. Phys. Chem. B* **109**, 14433–14440 (2005)
67. B.A.T. Mehrabadi, H.N. Dinh, G. Bender, J.W. Weidner, Effect of system contaminants on the performance of a proton exchange membrane fuel cell. *J. Electrochem. Soc.* **163**, F1527–F1534 (2016)
68. M.S. Mikkola, T. Rockward, F.A. Uribe, B.S. Pivovar, The effect of NaCl in the cathode air stream on PEMFC performance. *Fuel Cells* **7**, 153–158 (2007)
69. S. Morin, B.E. Conway, G.J. Edens, M.J. Weaver, The reactive chemisorption of acetonitrile on Pt (111) and Pt (100) electrodes as examined by in situ infrared spectroscopy. *J. Electroanal. Chem.* **421**, 213–220 (1997)
70. G. Mul, J. Pérez-Ramírez, F. Kapteijn, J.A. Moulijn, NO adsorption on ex-framework [Fe,X] MFI catalysts: novel IR bands and evaluation of assignments. *Catal. Lett.* **80**, 129–138 (2002)
71. T.S. Olson, B. Bliznac, B. Piela, J.R. Davey, P. Zelenay, P. Atanassov, Electrochemical evaluation of porous non-platinum oxygen reduction catalysts for polymer electrolyte fuel cells. *Fuel Cells* **9**, 547–553 (2009)
72. J.M. Orts, R. Gomez, J.M. Feliu, Bromine monolayer adsorption on Pt(110) surfaces. *J. Electroanal. Chem.* **467**, 11–19 (1999)
73. M.R. Rahman, M.I. Awad, F. Kitamura, T. Okajima, T. Ohsaka, A comparative study of ORR at the Pt electrode in ammonium ion-contaminated H<sub>2</sub>SO<sub>4</sub> and HClO<sub>4</sub> solutions. *J. Power Sources* **220**, 65–73 (2012)
74. E.L. Redmond, B.P. Setzler, F.M. Alamgir, T.F. Fuller, Elucidating the oxide growth mechanism on platinum at the cathode in PEM fuel cells. *Phys. Chem. Chem. Phys.* **16**, 5301–5311 (2014)
75. T. Reshетенko, A. Serov, K. Artyushkova, I. Matanovic, S. Stariha, P. Atanassov, Tolerance of non-platinum group metals cathodes proton exchange membrane fuel cells to air contaminants. *J. Power Sources* **324**, 556–571 (2016)
76. T.V. Reshетенko, K. Artyushkova, J. St-Pierre, Spatial proton exchange membrane fuel cell performance under bromomethane poisoning. *J. Power Sources* **342**, 135–147 (2017)



77. T.V. Reshетенko, J. St-Pierre, Study of acetylene poisoning of Pt cathode on proton exchange membrane fuel cell spatial performance using a segmented cell system. *J. Power Sources* **287**, 401–415 (2015a)
78. T.V. Reshетенko, J. St-Pierre, Study of the acetonitrile poisoning of platinum cathodes on proton exchange membrane fuel cell spatial performance using a segmented cell system. *J. Power Sources* **293**, 929–940 (2015b)
79. T.V. Reshетенko, J. St-Pierre, Study of the aromatic hydrocarbons poisoning of platinum cathodes on proton exchange membrane fuel cell spatial performance using a segmented cell system. *J. Power Sources* **333**, 237–246 (2016)
80. S.G. Rinaldo, P. Urchaga, J. Hu, W. Lee, J. Stumper, C. Rice, M. Eikerling, Theoretical analysis of electrochemical surface-area loss in supported nanoparticle catalysts. *Phys. Chem. Chem. Phys.* **16**, 26876–26886 (2014)
81. M. Rivallan, G. Ricchiardi, S. Bordiga, A. Zecchina, Adsorption and reactivity of nitrogen oxides (NO<sub>2</sub>, NO, N<sub>2</sub>O) on Fe–zeolites. *J. Catal.* **264**, 104–116 (2009)
82. C. Robin, M. Gerard, A.A. Franco, P. Schott, Multi-scale coupling between two dynamical models for PEMFC aging prediction. *Int. J. Hydrog. Energy* **38**, 4675–4688 (2013)
83. K.I. Rozental, V.I. Veselovskii, Izuchenie mekhanizma i kinetiki reaktsii elektrokhimicheskogo okisleniya metodom anodnoi polyarografii na platinovom elektrode. *Zh. Fiz. Khim.* **27**, 1163–1171 (1953)
84. C. Ruzie, P. Even, D. Ricard, T. Roisnel, B. Boitrel, O<sub>2</sub> and CO binding to tetraaza-tripodal-capped iron(II) porphyrins. *Inorg. Chem.* **45**, 1338–1348 (2006)
85. G.N. Salaita, D.A. Stern, F. Lu, H. Baltruschat, B.C. Schardt, J.L. Stickney, M.P. Soriaga, D.G. Frank, A.T. Hubbard, Structure and composition of a platinum (111) surface as a function of pH and electrode potential in aqueous bromide solutions. *Langmuir* **2**, 828–835 (1986)
86. T.J. Schmidt, U.A. Paulus, H.A. Gasteiger, R.J. Behm, The oxygen reduction reaction on a Pt/carbon fuel cell catalyst in the presence of chloride anions. *J. Electroanal. Chem.* **508**, 41–47 (2001)
87. H. Schulenburg, B. Schwanitz, N. Linse, G.G. Scherer, A. Wokaun, J. Krbanjevic, R. Grothausmann, I. Manke, 3D imaging of catalyst support corrosion in polymer electrolyte fuel cells. *J. Phys. Chem. C* **115**, 14236–14243 (2011)
88. A. Serov, K. Artyushkova, P. Atanassov, Fe-N-C oxygen reduction fuel cell catalyst derived from carbendazim: synthesis, structure, and reactivity. *Adv. Energy Mater.* **4**, 1301735 (2014)
89. A.A. Shah, K.H. Luo, T.R. Ralph, F.C. Walsh, Recent trends and developments in polymer electrolyte membrane fuel cell modeling. *Electrochem. Acta* **56**, 3731–3757 (2011)
90. Z. Shi, D. Song, H. Li, K. Fatih, Y. Tang, J. Zhang, Z. Wang, S. Wu, Z.-S. Liu, H. Wang, J. Zhang, A general model for air-side proton exchange membrane fuel cell contamination. *J. Power Sources* **186**, 435–445 (2009)
91. D. Singh, I.I. Soykal, J. Tian, D. von Deak, J. King, J.T. Miller, U.S. Ozkan, In situ characterization of the growth of CN<sub>x</sub> carbon nanostructures as oxygen reduction reaction catalysts. *J. Catal.* **304**, 100–111 (2013)
92. D. Singh, J. Tian, K. Mamtani, J. King, J.T. Miller, U.S. Ozkan, A comparison of N-containing carbon nanostructures (CN<sub>x</sub>) and N-coordinated iron-carbon catalysts (FeNC) for the oxygen reduction reaction in acidic media. *J. Catal.* **317**, 30–43 (2014a)
93. M.P. Soriaga, A.T. Hubbard, Determination of the orientation of adsorbed molecules at solid-liquid interfaces by thin-layer electrochemistry – aromatic-compounds at platinum-electrodes. *J. Am. Chem. Soc.* **104**, 2735–2742 (1982)
94. I. Srejić, M. Smiljanić, Z. Rakočević, S. Štrbac, Oxygen reduction on polycrystalline Pt and Au electrodes in perchloric acid solution in the presence of acetonitrile. *Int. J. Electrochem. Sci.* **6**, 3344–3354 (2011)
95. J. St-Pierre, PEMFC contamination model: competitive adsorption followed by an electrochemical reaction. *J. Electrochem. Soc.* **156**, B291–B300 (2009)

96. J. St-Pierre, Proton exchange membrane fuel cell contamination model: competitive adsorption followed by a surface segregated electrochemical reaction leading to an irreversibly adsorbed product. *J. Power Sources* **195**, 6379–6388 (2010)
97. J. St-Pierre, PEMFC contaminant tolerance limit – foreign cations in ionomers. *Int. J. Hydrog. Energy* **36**, 5527–5535 (2011a)
98. J. St-Pierre, PEMFC contamination model: neutral species sorption by ionomer. *ECS Trans.* **41**, 307–315 (2011b)
99. J. St-Pierre, N. Jia, R. Rahmani, PEMFC contamination model: competitive adsorption demonstrated with NO<sub>2</sub>. *J. Electrochem. Soc.* **155**, B315–B320 (2008)
100. J. St-Pierre, Y. Zhai, M.S. Angelo, Effect of selected airborne contaminants on PEMFC performance. *J. Electrochem. Soc.* **161**, F280–F290 (2014)
101. V. Stamenkovic, N.M. Markovic, P.N. Ross, Structure-relationships in electrocatalysis: oxygen reduction and hydrogen oxidation reactions on Pt (111) and Pt (100) in solutions containing chloride ions. *J. Electroanal. Chem.* **500**, 44–51 (2001)
102. V. Stamenkovic, B.S. Mun, K.J.J. Mayrhofer, P.N. Ross, N.M. Markovic, J. Rossmeisl, J. Greeley, J.K. Norskov, Changing the activity of electrocatalysts for oxygen reduction by tuning the surface electronic structure. *Angew. Chem. Int. Ed.* **45**, 2897–2901 (2006)
103. P. Strasser, S. Koh, T. Anniyev, J. Greeley, K. More, C.F. Yu, Z.C. Liu, S. Kaya, D. Nordlund, H. Ogasawara, M.F. Toney, A. Nilsson, Lattice-strain control of the activity in dealloyed core-shell fuel cell catalysts. *Nat. Chem.* **2**, 454–460 (2010)
104. M. Szklarczyk, J. Sobkowski, The behavior of high polar organic solvents at platinum electrode – II. Adsorption and electrode reactions of acetonitrile. *Electrochim. Acta* **25**, 1597–1601 (1980)
105. B. Tavakoli, J.W. Weidner, Effect of contaminants on the performance of a proton exchange membrane fuel cell. *ECS Trans.* **66**, 77–90 (2015)
106. M.S. Thorum, J.M. Hankett, A.A. Gewirth, Poisoning the oxygen reduction reaction on carbon-supported Fe and Cu electrocatalysts: evidence for metal-centered activity. *J. Phys. Chem. Lett.* **2**, 295–298 (2011)
107. D. von Deak, D. Singh, E.J. Biddinger, J.C. King, B. Bayram, J.T. Miller, U.S. Ozkan, Investigation of sulfur poisoning of CN<sub>x</sub> oxygen reduction catalysts for PEM fuel cells. *J. Catal.* **285**, 145–151 (2012a)
108. D. von Deak, D. Singh, J.C. King, U.S. Ozkan, Use of carbon monoxide and cyanide to probe the active sites on nitrogen-doped carbon catalysts for oxygen reduction. *Appl. Catal. B* **113–114**, 126–133 (2012b)
109. C. Wang, D. Ma, X. Bao, Transformation of biomass into porous graphitic carbon nanostructures by microwave irradiation. *J. Phys. Chem. C* **112**, 17596–17602 (2008)
110. J.X. Wang, N.S. Marinković, R.R. Adžić, Structure of Br adlayers in the course of electrocatalytic reactions O<sub>2</sub> reduction of Pt (111) and Au (100). *Colloids Surf. A Physicochem. Eng. Asp.* **134**, 165–171 (1998)
111. Q. Wang, Z.Y. Zhou, Y.J. Lai, Y. You, J.G. Liu, X.L. Wu, E. Terefe, C. Chen, L. Song, M. Rauf, N. Tian, S.G. Sun, Phenylenediamine-based FeN<sub>x</sub>/C catalyst with high activity for oxygen reduction in acid medium and its active-site probing. *J. Am. Chem. Soc.* **136**, 10882–10885 (2014)
112. G. Wu, K.L. More, C.M. Johnston, P. Zelenay, High-performance electrocatalysts for oxygen reduction derived from polyaniline, iron, and cobalt. *Science* **332**, 443–447 (2011a)
113. Q. Wu, G. Mul, R. van de Krol, Efficient NO adsorption and release at Fe<sup>3+</sup> sites in Fe/TiO<sub>2</sub> nanoparticles. *Energy Environ. Sci.* **4**, 2140–2144 (2011b)
114. Y. Xiao, J. Yuan, B. Sundén, Modeling of micro/mesoscale reactive transport phenomena in catalyst layers of proton exchange membrane fuel cells. *Int. J. Low-Carbon Tech.* **7**, 280–287 (2012)
115. A.P. Yadav, A. Nishikata, T. Tsuru, Effect of halogen ions on platinum dissolution under potential cycling in 0.5 M H<sub>2</sub>SO<sub>4</sub> solution. *Electrochim. Acta* **52**, 7444–7452 (2007)

116. R.T. Yang, J.P. Chen, Mechanism of carbon filament growth on metal catalysts. *J. Catal.* **115**, 52–64 (1989)
117. N. Zamel, X. Li, Effect of contaminants on polymer electrolyte membrane fuel cells. *Prog. Energy Combust. Sci.* **37**, 292–329 (2011)
118. Y. Zhai, G. Bender, S. Dorn, R. Rocheleau, The multi process degradation of PEMFC performance due to sulfur dioxide contamination and its recovery. *J. Electrochem. Soc.* **157**, B20–B26 (2010)
119. Y. Zhai, O. Baturina, D. Rarnaker, E. Farquhar, J. St-Pierre, K. Swider-Lyons, Chlorobenzene poisoning and recovery of platinum-based cathodes in proton exchange membrane fuel cells. *J. Phys. Chem. C* **119**, 20328–20338 (2015)
120. J. Durst, M. Chatenet, F. Maillard, Impact of metal cations on the electrocatalytic properties of Pt/C nanoparticles at multiple phase interfaces. *Phys. Chem. Chem. Phys.* **14**, 13000–13009 (2012)



# Solid-State Materials for Hydrogen Storage 15

Rolando Pedicini, Irene Gatto, and Enza Passalacqua

## Contents

15.1	Introduction .....	444
15.2	Physisorption .....	446
15.3	Chemical Hydrides .....	448
15.3.1	Complex Metal Hydrides .....	448
15.3.2	Nonmetal Hydrides .....	450
15.3.3	Metal Hydrides [MeH <sub>x</sub> ] .....	451
15.4	Innovative Materials .....	454
15.4.1	Hybrid Materials .....	454
15.4.2	Natural Material .....	462
15.5	Conclusions .....	464
	References .....	465

## Author Contribution

ROLANDO PEDICINI, National Research Council-Institute for Advanced Energy Technologies (CNR-ITAE)IRENE GATTO, National Research Council-Institute for Advanced Energy Technologies (CNR-ITAE)ENZA PASSALACQUA, National Research Council-Institute for Advanced Energy Technologies (CNR-ITAE). The authors further acknowledge that there is no financial relationship with the editors or publisher and have contributed original work in this chapter, other than what was acknowledged or appropriately cited with copyright permission.

R. Pedicini (✉)

Institute for Advanced Energy Technologies, Messina, Italy

Dipartimento di Fisica, Università della Calabria, Arcavacata di Rende, CS, Italy

e-mail: [rolando.pedicini@itaecnr.it](mailto:rolando.pedicini@itaecnr.it)

I. Gatto · E. Passalacqua

Institute for Advanced Energy Technologies, Messina, Italy

## Abstract

Hydrogen ( $H_2$ ) is a promising replacement energy carrier and storage molecular due to its high energy density by weight. For the constraint of size and weight in vehicles, the onboard hydrogen storage system has to be small and lightweight. Therefore, a lot of research is devoted to finding an efficient method of hydrogen storage based on both mechanical compression and sorption on solid-state materials. An overview of the current research trend and perspectives on materials-based hydrogen storage including both physical and chemical storage is provided in the present paper. Part of this chapter was dedicated to recent results on two innovative materials: hybrid materials based on manganese oxide anchored to a polymeric matrix and natural volcanic powders. A prototype  $H_2$  tank, filled with the developed hybrid material, was realized and integrated into a polymer electrolyte membrane (PEM) single fuel cell (FC) demonstrating the material capability to coupling with the FC.

## 15.1 Introduction

The need for an alternative to fossil fuels is escalating due to the increasing problem of global warming and climate change, not to mention worries over energy security and adverse health effects [1].

New alternative energy sources are required to replace fossil fuels, for example, by using energy generated from the wind and/or solar energy. One of the actively explored concepts is to convert solar energy directly to hydrogen and then to use hydrogen as an energy carrier and a fuel for, e.g., cars. Considering that water covers about 71% of the earth's surface, we have almost an unlimited source of hydrogen. Hydrogen has an extremely high gravimetric energy density ( $142 \text{ MJ kg}^{-1}$ ), which is at least three times larger than the equivalent value for liquid hydrocarbons ( $47 \text{ MJ kg}^{-1}$ ). Hydrogen as the fuel is also environmentally friendly as the only exhaust product in both combustion and fuel cell engines is water vapor. Therefore, hydrogen is an attractive candidate for replacement of petrol or diesel in cars or other vehicles.

Hydrogen can be used as a fuel in cars with slightly modified combustion engines. However, combustion engines are not a sustainable solution due to the relatively low efficiency (fuel for useful work ratio) of  $\sim 25\%$ . On another hand, cars can be powered by fuel cells (FCs), electrochemical devices, which combine hydrogen and oxygen to produce electricity. Fuel cells convert hydrogen into electricity with an efficiency of 50–60% and release only water and heat as side products. The main obstacle for widespread application of FCs is the absence of sufficiently good and compact, lightweight hydrogen storage systems which are capable of delivering hydrogen gas to an FC at nearly room temperature and at pressures not much higher than atmospheric pressure. An average modern car equipped with a combustion engine needs approximately 30–35 l of petrol or diesel to travel 500 km, and the

combined weight of the fuel and the tank is about 80 kg. A car equipped with an FC engine would need about 5 kg of hydrogen to travel the same distance. The problem is that 5 kg of hydrogen at normal conditions (room temperature and atmospheric pressure) occupy ~56,000 l of space which is equivalent to a balloon of the diameter of 5 m. In this contest, the storage of hydrogen is identified as one of the major problems to be solved in the short and medium terms.

In a hydrogen storage system, aspects such as safety, reversible hydrogen uptake and the release rate, cost, weight, and volume must also be taken into account. According to multi-annual work plan (2014–2020) of *Fuel Cells and Hydrogen Joint Undertaking* (FCH JU) group under The *Horizon 2020* program [2], the targets for hydrogen storage for transportation are 600 euros-per-kilogram-hydrogen (€/Kg H<sub>2</sub>) for system cost and 0.023 Kg × L<sup>-1</sup> and 5 wt.% of the volumetric and gravimetric capacity of H<sub>2</sub> tank system, respectively.

There are three possible ways in which hydrogen can be stored: gas compression, liquefaction, and storage within solid-state materials. Compressed gas is currently the most common form of hydrogen storage. Typically, tanks are made from steel and used at an operating pressure from 200 to 350 bar. However, lightweight composite cylinders have operating pressures up to 800 bar, where hydrogen has a volumetric density of 36 kg × m<sup>-3</sup>. The amount of energy used to compress hydrogen gas depends on what pressure it is being compressed from and to, as well as the method using the gas compression. The ideal (isothermal, ΔT = 0) compression of hydrogen from 1 to 800 bar requires 2.21 kWh × kg<sup>-1</sup> of energy, which is ca. 5% of the energy content in hydrogen. In a real process, the work consumption is significantly higher because compression is not isothermal. In fact, adiabatic compression (V<sup>γ</sup>P = constant, where γ is the adiabatic exponent) requires over 16% of the energy content in hydrogen.

Liquid hydrogen must be stored below its low critical temperature (33 K) and pressure (13 bar); typically it is stored at its boiling point (20.3 K). The volumetric density of liquid hydrogen is 70.8 kg m<sup>-3</sup> almost twice that of compressed hydrogen gas. The significant disadvantages of storing hydrogen as a liquid are boil-off and the relatively large amount of energy required for the liquefaction (30% of the lower heating value). However, boil-off losses are reduced when large-scale storage vessels are used due to the small surface-to-volume ratio, as the evaporation rate decreases as the size of the storage tank increases.

The hydrogen storage by solid-state materials has definite advantages from a safety perspective. Extensive efforts have been made on new hydrogen storage systems, including metal-organic frameworks (MOFs), zeolites, metal hydrides (MH), metal nitrides (M<sub>x</sub> N<sub>2</sub>), metal imides (MNR), doped polymers, hollow glass microspheres, and carbon-based materials. In solid-state storage, hydrogen is bonded by either physical, e.g., MOF and carbon-based materials, or chemical forces, e.g., hydrides, imides, and nitrides. Physisorption has the advantages of higher energy efficiency and faster adsorption/desorption cycles, whereas chemisorption results in the adsorption of larger amounts of gas but, in some cases, is not reversible and requires a higher temperature to release the adsorbed gas.

## 15.2 Physisorption

The large surface areas of porous materials, especially of nanostructures, allow the adsorption of large quantities of hydrogen; for this reason, the use of porous materials and their simplicity of physisorption attract scientific interests. Two fundamental parameters have to be taken into account for optimal hydrogen storage: the average surface available per unit volume of the adsorbent and the characteristic binding energy of the hydrogen molecule with the material. Physisorption involves weak van der Waals forces, and this weak physisorption interaction requires cryogenic temperatures (typically 77 K) and high pressure to reach reasonable hydrogen storage values. Porous carbonaceous materials have been identified to be attractive for hydrogen storage. Experimental and theoretical studies have shown that the interaction energies between H<sub>2</sub> and pure carbon materials are in the range from 4 kJ mol<sup>-1</sup> for activated carbon and graphite to 15 kJ·mol<sup>-1</sup> for internal and interstitial sites of single-walled nanotubes (SWNTs), very low for storing large amounts of hydrogen at room temperature and relatively low pressures. Optimal interaction energies should be over 100 kJ·mol<sup>-1</sup>.

Since the first studies [3], carbon nanotubes (CNTs), single-walled and multi-walled carbon nanotubes (SWNTs and MWNT), have been investigated extensively as potential hydrogen storage materials because of their low density, wide variety of structural forms, extensive pore structure, good chemical stability, and the ability to modify the structures using wide range of preparation, carbonization, and activation condition. Many of the reported results are controversial, with H<sub>2</sub> sorption that varies from less than 0.1 wt.% to more than 10 wt.% depending on measurement method and operating conditions. High values were obtained in cryogenic conditions unsuitable for mobile applications; when ambient conditions are used, this value is less than 1 wt.% [4].

To improve the hydrogen sorption properties of carbon materials, a chemical activation has been proposed. Activated carbons (AC) produced using potassium hydroxide [KOH] as an activating agent exhibit high surface areas, large pore volumes, and uniform micropore-size distributions suitable for hydrogen sorption. In particular, AC with a two-step procedure in which physical activation (with carbon dioxide [CO<sub>2</sub>]) was followed by a chemical (KOH) activation step exhibited a hydrogen adsorption capacity up to 7.08 wt.% at 469 K and 2 MPa H<sub>2</sub> pressure [5]. Changes in hydrogen uptakes of porous carbons were found with nitrogen incorporation into carbon. Starting from hydrothermally carbonized chitosan and successive activation with KOH, a hydrogen storage at 77 K of 1.75–2.71 wt.% and 4.23–6.77 wt.% at 1 bar and 20 bar was, respectively, obtained [6].

Among carbon materials for hydrogen storage, graphene recently was cited as a promising adsorbent material due to its high surface area up to 2630 m<sup>2</sup> g<sup>-1</sup>, but H<sub>2</sub> uptake for bulk graphene-related materials evaluated at ambient temperature and 77 K does not exhibit superior hydrogen storage (generally less than 1 wt.% at room temperature and 120 bar) compared to other nanostructured carbon materials like activated carbons, CNTs, or nano-fiber. The use of transition metals to obtain decorated graphene has been proposed, to increase the hydrogen storage capacity

through a spillover mechanism at ambient conditions. Recent results report a highly enhanced hydrogen storage capacity (3.19 wt.%) under a practical operating condition of 298 K at 100 bar for a bioinspired graphene foam based on polydopamine (PD,  $-\text{[C}_8\text{H}_5\text{NO}_2\text{]}_p - \text{[C}_8\text{H}_7\text{NO}_2\text{]}_o - \text{[C}_8\text{H}_9\text{NO}_2\text{]}_n - \text{[C}_8\text{H}_{11}\text{NO}_2\text{]}_m-$ , where  $p$ ,  $o$ ,  $n$ , and  $m$  represent the monomers) and decorated with Pt nanoparticles shown [7].

Another efficient approach for the fabrication of porous carbon materials is the template carbonization method, which allows obtaining materials with controlled physical and chemical properties. Among them, zeolites,  $\left[\text{M}^{\frac{x}{n}} \left( \text{AlO}_2 \right)_x \left( \text{SiO}_2 \right)_y \right]_m \cdot \text{H}_2\text{O}$ , where M is the ion balancing the charge of the aluminosilicate ion, are attractive due to their versatility and three-dimensional pore channels. A large number of zeolites with a variety of pore structures have been used, and it has been reported that zeolites can store up to 4.5 wt.% of hydrogen at 35 K and 0.96 MPa and 1.81 wt.% at 77 K and 1.5 MPa. Several modifications were carried out to improve the  $\text{H}_2$  capacity, such as a combined liquid impregnation/chemical vapor deposition (CVD) process on a commercially available zeolite as a hard template to produce a porous carbon with hydrogen uptake capacities in the range of 3.4–6.3 wt.% (at 77 K and 20 bar).

Metal-organic frameworks (MOFs) could be considered an interesting candidate for hydrogen storage due to their high crystallinity, purity, porosity, and tunable structural characteristics. The MOF's interconnections provide an ordered network of channels or pores wherein molecular  $\text{H}_2$  can be reversibly captured and released. An MOF is an interconnect structure which mainly consists of an organic linker and a metal cluster with high surface area and is typically only available in the form of loose powders, which can be problematic to incorporate into the relevant device structures. In 2003, the initial  $\text{H}_2$  storage data were reported for *isorecticular metal-organic framework-1* (IRMOF-1, also known as MOF-5) (4.5 wt.% at 77 K and 1 atm), which were prepared from benzene-1,4-dicarboxylate (BDC) and Zn(II) salt. The structure consists of  $\text{Zn}_4 \text{O}$  nodes with BDC linkages between the nodes [8].

To increase the surface area, a multi-ligand strategy was used for porous *University of Michigan Crystalline Material-2* (UMCM-2) MOF of the surface area of  $5200 \text{ m}^2 \text{ g}^{-1}$ , consisting of  $\text{Zn}_4 \text{O}$  metal clusters linked together by two linear dicarboxylates and four trigonal planar ligands arranged in an octahedral geometry with a hydrogen capacity of 6.9 wt. at 77 K and 4.6 MPa [9]. Other studies have reported a mesoporous *Technical University of Denmark-6* (DTU-6) MOF using a secondary linker to stabilize a highly open framework structure, leading to an  $\text{H}_2$  uptake of 5.64 wt.% at 77 K and 5 MPa.

Chromium-based metal-organic framework (Cr-MOF) has been explored as potential material, and to lower the production cost waste, polyethylene terephthalate (PET) bottles were used as a source of terephthalic acid (BDC) linker for the synthesis. The PET-derived Cr-MOF materials showed a 2.1 wt.% of  $\text{H}_2$  adsorption at 77 K and 1 bar higher than commercial-derived in the same conditions (1.8 wt.%).

Improvements in  $\text{H}_2$  adsorption of Cr-based MOF were obtained from a hybrid composite of zeolite template carbon (ZTC) and Cr-based *Matériau Institut Lavoisier-101* (MIL-101) MOF. The hydrogen uptake capacities of individual MIL-101 and zeolite template carbon (1.91 wt.% and 2.39 wt.%, respectively) were enhanced



to 2.55 wt.% at 77 K and 1 bar [10]. However, the high gravimetric storage capacities at cryogenic temperatures for MOF fall down at  $\sim 1$  wt % at 298 K and 100 bar.

Although microporous materials consist of inorganic materials, a class of organic microporous polymers has attracted the interest of researchers for their “intrinsic microporosity” (PIM). The PIM class of materials is amorphous organic microporous materials resulting from repeated experiments on phthalocyanine material in the 1990s. A network of PIMs shows higher surface areas and hydrogen uptake compared to nonnetwork PIMs with an  $H_2$  capacity ranging from 1.83 wt.% to 1.92 wt.% at 1 bar and 77 K and a greater uptake of 3.94 wt.% at higher pressure (10 bar) [11]. Therefore, PIMs have shown hydrogen uptake results comparable to that of inorganic and organic porous materials such as zeolites and MOFs and even carbon materials with similar surface areas.

The metal-organic coordination polymers (M-CP) with the large internal surface area are one of the promising materials; new M-CPs have been synthesized with different conformations, improved surface area, and pore size. Dual-metal manganese copper (MnCu) ferrocenyl [ $C_{10}H_9Fe$ ] coordination polymer microspheres with hollow structure have been synthesized, and an  $H_2$  uptake of 3.12 wt.% at 163 K was reported.

---

## 15.3 Chemical Hydrides

The use of alternative fuels, especially in a liquid form, is one of the most attractive storage approaches since liquid fuels are unmatched in terms of transportability and energy density, and they can rely on existing infrastructure [12]. Chemical hydrides are materials that contain hydrogen bonded chemically. They are able to store a large amount of hydrogen, even if they are not rechargeable on board. In any case, due to a higher binding energy ( $190\text{--}290\text{ kJ} \times \text{mol}^{-1}$ ) than physisorbed hydrogen ( $4\text{--}15\text{ kJ} \times \text{mol}^{-1}$ ), these materials are preferred to another form of hydrogen storage. The chemical hydrides can be classified into different categories such as complex metal hydrides, nonmetal hydrides, and the most known metal hydrides.

### 15.3.1 Complex Metal Hydrides

The complex metal hydrides are materials that contain hydrogen atoms covalently bound with a polyatomic anion. They are usually bound to lithium [Li], magnesium [Mg], sodium [Na], calcium [Ca], or less commonly transition metals.

#### 15.3.1.1 Amides and Imides

The amide/imide systems are considered very interesting for the onboard application due to the possibility to store about 6.5 wt.% of  $H_2$  [13]. The most common materials are based on Li. However, these systems have several drawbacks, such as slow reaction kinetics, high hydrogen release temperature, and bad cycling stability. To

enhance the hydrogen storage property of these systems, many authors have mixed different additives to improve their properties; some of these have introduced potassium fluoride [KF] to a mixture of lithium amide-lithium hydride [ $\text{LiNH}_2 - \text{LiH}$ ] improving the cyclic performance of about four times; others have reduced the onset temperature for the dehydrogenation from 403 to 353 K, by introducing magnesium borohydride [ $\text{Mg}(\text{BH}_4)_2$ ] in  $2\text{LiNH}_2$ /magnesium hydride [ $\text{MgH}_2$ ]. Zhang et al. [14] investigated the effect of doping iron(III) chloride [ $\text{FeCl}_3$ ] in  $\text{LiNH}_2 - 2\text{LiH}$ . They found a shift to low temperature and a reduction of dehydrogenation energy due to the formation of a new solid cubic phase of lithium imide chloride. One of the problems of these materials is the ammonia [ $\text{NH}_3$ ] generation during the decomposition, which is a poison for fuel cells; a different approach was investigated to solve this drawback. One of these was that the introduction of  $\text{Li}_3\text{AlH}_6$  in  $2\text{LiNH}_2 - \text{MgH}_2$  suppresses the  $\text{NH}_3$  release and in addition improves the dehydrogenation kinetics at low temperature. Baricco et al. [15] studied a mixed lithium amide/magnesium hydride compound to realize a storage hydrogen system to be integrated with a high-temperature proton exchange membrane (HT-PEM) fuel cell stack. The tank was designed to feed the stack for 2 h. The integration was possible due to the relatively low temperature for hydrogen release of this material.

### 15.3.1.2 Alanates [ $\text{MeAlH}_4$ ]

The alanates class of materials are based around aluminohydride in which the hydrogen evolution takes place upon contact with water. They are good candidates for hydrogen storage due to the high theoretical hydrogen storage capacity, about 10 wt.%, and mild pressure and temperature of work. The alanates desorb hydrogen through chemical decomposition, by the formation of a hexahydro-aluminate as intermediate. Unfortunately, they present a slow kinetics during hydrogen cycling, so many efforts have been made to synthesize mixed alanates with good kinetics and thermodynamic properties. The  $\text{NaAlH}_4$  has attracted much interest for high  $\text{H}_2$  storage capacity (up to 5 wt.%) and desirable operating pressure and temperature. Zhang et al. [16] used zirconium dioxide on carbon [ $\text{ZrO}_2/\text{C}$ ] as a catalyst for the dehydrogenation and hydrogenation of  $\text{NaAlH}_4$  and found a significant reduction in the operating temperature and improvement in the kinetics. Also, the introduction of niobium pentoxide [ $\text{Nb}_2\text{O}_5$ ] and titanium(III) chloride [ $\text{TiCl}_3$ ] in the sodium alanate produces a beneficial effect in terms of kinetics due to a modification of the crystallographic structure of the alanates. Similarly, Zou et al. [17] demonstrated that the titanium(IV) oxide [ $\text{TiO}_2$ ] strongly affects the catalytic activity for the dehydrogenation of  $\text{NaAlH}_4$  obtaining a dehydrogenation capacity of about 4 wt. % stable for more than ten cycles. The dehydrogenation capacity of  $\text{NaAlH}_4$  was improved by the addition of only 3 mol % of nickel ferrite [ $\text{NiFe}_2\text{O}_4$ ] permitting to reach a good cycle stability at 423 K. In addition to the  $\text{NaAlH}_4$ , other metal aluminohydrides (where Me represents metal cations around the tetrahedral [ $\text{AlH}_4$ ] anions), such as potassium,  $\text{KAlH}_4$ ; lithium,  $\text{LiAlH}_4$ ; yttrium,  $\text{Y}(\text{AlH}_4)_3$ ; and magnesium,  $\text{Mg}(\text{AlH}_4)_2$ , alanates, were studied [18].

### 15.3.1.3 Borohydrides [Me(BH<sub>4</sub>)<sub>n</sub>]

The borohydrides are promising materials for H<sub>2</sub> storage due to very high potential hydrogen contents up to 18 wt.%. Unfortunately, they are limited by the higher temperature of dehydrogenation. To overcome this problem, a possible way is to destabilize the materials by incorporating additives in the structure or by confining it into nanoporous structures. In the first case, different compounds such as lithium borate [Li<sub>3</sub>BO<sub>3</sub>] [19], niobium(V) fluoride [NbF<sub>5</sub>], or scandium [Sc] were used to improve the sluggish kinetics or favor the reversibility of the re-hydrogenation process. Regarding the effect of the nano-confinement, many papers report the results on the entrapping of the borohydrides into aerogel carbon, in carbon nanocages, or in graphitic nanosheets. Many papers demonstrate the real applicability of borohydrides as hydrogen storage system to feed a PEMFC. Li et al. [20] developed an on-demand hydrogen generation based on NaBH<sub>4</sub> able to continuously supply H<sub>2</sub> for a 3kW PEMFC.

## 15.3.2 Nonmetal Hydrides

The nonmetal hydrides are less common than metal hydrides and complex metal hydrides. However, since one of the metal hydrides' drawbacks is the high weight, the nonmetal hydrides have increased their popularity in the last period. They usually contain boron [B], carbon [C], nitrogen [N], and oxygen [O] that are very reactive and can interact with H<sub>2</sub>.

### 15.3.2.1 Nitrogen Hydrides [N<sub>x</sub>H<sub>y</sub>]

Among nitro-hydrides, the most promising materials are ammonia and hydrazine [N<sub>2</sub>H<sub>4</sub>]. In particular, the ammonia presents two advantages: the high H<sub>2</sub> contents 17 wt.%, and the well-known production technology. The disadvantage of NH<sub>3</sub> is related to the high temperature required to release H<sub>2</sub>. For this reason catalysts able to help the ammonia decomposition have been studied. The most common catalysts are ruthenium [Ru] supported on oxides such as alumina [Al<sub>2</sub>O<sub>3</sub>], nickel [Ni], or copper [Cu]. The hydrazine, containing 12 wt.% of H<sub>2</sub>, reacts explosively with oxidizing agents but diluted in water or in inert gas is stable, and its reaction of decomposition is controllable by catalysts. The most common catalysts are Ni, palladium [Pd], and platinum [Pt] supported on graphene nanosheets [21], graphene oxide [C<sub>x</sub> : O, where x = 2.1 – 2.9], and graphene doped with boron.

### 15.3.2.2 Boron and Nitrogen Hydrides

The most common amine-boranes (ammonia borane [NH<sub>3</sub>BH<sub>3</sub>], hydrazine borane [N<sub>2</sub>H<sub>4</sub>BH<sub>3</sub>]) present very high hydrogen content, but their use is limited by slow kinetics and thermodynamic to release H<sub>2</sub>. The H<sub>2</sub> release can occur by decomposition, with exothermic steps that require high temperature, or by a hydrolytic process that requires efficient catalysts to improve the sluggish kinetic. The ammonia

borane has a hydrogen capacity of about 19 wt.%; to improve the kinetics reaction, different supported catalysts are studied [22]. Similarly, the confinement of  $\text{NH}_3\text{BH}_3$  in aerogel or mesoporous silica produces a beneficial effect due to the reduction of decomposition temperature [23]. Hydrazine borane has a gravimetric hydrogen storage capacity of 15 wt.%. It can release  $\text{H}_2$  by hydrolysis using different catalysts [24] or by thermolysis. In the last case to facilitate the decomposition reaction,  $\text{N}_2\text{H}_4\text{BH}_3$  is mixed with alkali metal hydrides such as LiH, NaH, and KH [25] or destabilized by using graphene nano-fibers.

### 15.3.3 Metal Hydrides [ $\text{MeH}_x$ ]

The hydrogen absorption mechanism on metal hydrides occurs under certain temperature and pressure conditions due to strong interactions between the metal surface and the hydrogen molecule dissociation.

The kinetics of this process is much slower in comparison to the adsorption of molecular hydrogen in porous materials, but atomic hydrogen in metal hydrides binds via chemical bonds with an around ten times stronger enthalpy of formation. This fact implies that higher temperatures are required in order to break the bonds and remove absorbed hydrogen from the structure.

The chemical reaction of hydrogen and metal powder to form a metal hydride is given by the overall equation (15.1) where Me denotes any kind of metal or alloy able to absorb hydrogen ( $\text{H}_2$ ), MeH the corresponding metal hydride, and  $\Delta H$  the enthalpy of the reaction:



It is a reversible process, and, according to the principle of Le Chatelier-Braun, a pressure increase shifts the equilibrium to the right (hydrogen is absorbed), whereas a temperature increase shifts it to the left [26]. A release of hydrogen (desorption) from the metal hydride is therefore possible by either reducing the hydrogen pressure (P) or increasing the temperature (T). As the hydrogen absorption is generally exothermic, the endothermic desorption tends to cool the metal powder.

The stability in desorption phase (dissociation P) of the metal hydride is one important issue for its applicability. Technically, pressure and temperature conditions of the metal-hydrogen reaction depend on the desired application and can be typically assumed as  $P \approx 1 - 100$  bar and  $T \approx 240 - 750$  K. Pure, low electronegative metals (so-called A-metals, e.g., Li, Na, K, cesium [Cs], Mg, Ca, lanthanum [La], Ti, or Zr) form stable hydrides with high dissociation T and/or low equilibrium P. Therefore only a few, e.g., Mg (at a desorption pressure of 1 bar temperature of 573 K), seem interesting for technical applications. More electronegative metals (so-called B-metals, e.g., Cu, Ni, Co, Fe, Mn, Cr, or molybdenum [Mo]) form unstable hydrides at relevant T and P. Van Vucht et al. [27] evaluated the possibility of alloying A- and B-metals to produce intermetallic compounds with practicable metal hydride phase stability.

The absorption and desorption characteristics of the metal hydride can be varied by partial substitution of alloy elements. Therefore, an adaptation of the metal hydride to the respective application is possible. A smaller particle size is advantageous because the surface area is increased and the diffusion distance for dissolved hydrogen in the metal hydride bulk is decreased.

As the density of the metal hydride is smaller than the density of the respective metal, a hydrogenation stresses the lattice and therefore collapses the brittle metal hydride bulk. For this reason, activation process during the first several absorptions (ab-) and desorption (de-) cycles have been carried out to reduce the particle size in the order of 1–20  $\mu\text{m}$  [28, 29] depending on the metal hydride.

A commonly used method to characterize metal hydrides is the pressure-concentration isotherm (PCI) measurement. The hydrogen uptake is generally given as a storage capacity of the metal hydride, which is the ratio between the absorbed hydrogen mass and the metal mass (%).

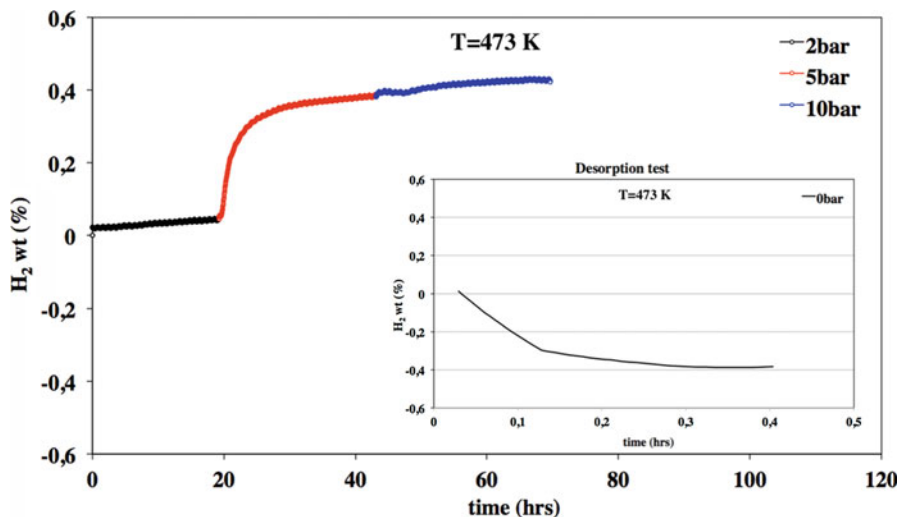
The absorption pressure is always higher than desorption pressure because, during the formation of the hydride phase, the lattice is expanded up to 30%. The induced stresses and deformations lead to a consumption of free enthalpy and contribute to the pressure hysteresis [27]. The hysteresis is an important characteristic that determines the applicability of the alloy. Especially in sorption systems, a small as possible hysteresis is necessary to increase the efficiency of the system.

High reaction enthalpy, combined with high density and low thermal conductivity of metal hydride powders, complicates experimental investigations of metal-hydrogen systems under isothermal conditions. The hydrogen uptake of a metal hydride can be determined either on gravimetric or on volumetric measurements. The gravimetric method requires a high precision balance to observe the absorption and desorption, whereas the volumetric method is based on the mass conservation in a closed system with known volume. If the system is fully sealed, the hydrogen uptake is proportional to the measured pressure loss in the system. Both principles and their respective advantages are described and compared in detail in [27].

Wang et al. [30] divided the hydriding process into three separated steps and developed a single equation for:

1. Dissolution of hydrogen on the surface
2. Diffusion of hydrogen through the lattice
3. Phase transformation or nucleation and growth

Different A/B-metal combinations were investigated, and the variety of the obtained intermetallic compounds can be summarized as follows [31]:  $A_2B(\text{Zr}_2\text{Cu}, \text{Ti}_2\text{Pd}, \text{Mg}_2\text{Ni})$ , AB (LaNi, MgNi, TiFe, ZrCo),  $A_2B(\text{TiMn}_2, \text{CaNi}_2, \text{gadolinium cobalt} [\text{GdCo}_2], \text{ZrMn}_2, \text{ZrCr}_2, \text{TiCr}_2)$ , and  $AB_5(\text{LaNi}_5, \text{YCo}_5, \text{europium nickel} [\text{EuNi}_5], \text{CaNi}_5, \text{LaCo}_5)$ . The most significant results were obtained for  $\text{Mg}_2\text{Ni}$  with a 10 wt.%  $\text{H}_2$  uptake at 423–573 K at 25 bar and for  $\text{LaNi}_5$  with 1.4 wt.%  $\text{H}_2$  uptake at 298 K at 2 bar [32].



**Fig. 15.1** Hydrogen sorption and desorption tests at 473 K

The formation of metal alloys before the hydride development is another approach. In this contest, Tuissi et al. [33] have proposed a new hydrogen storage Cr/Ti alloy. Pure metals Ti and Cr were melted by means of a vacuum arc furnace obtaining an atomic Cr/Ti ratio of 1.78:1.

The obtained Cr/Ti metal alloy, tested by using a Sievert apparatus type, has undergone a treatment before the test for activation, by repeatedly cycling P at different T. The kinetic of absorption reaction is influenced by the temperature with any H<sub>2</sub> sorption value at 298 K at 2 bar and 0.04 wt.% at 473 K in same P condition.

An interesting H<sub>2</sub> sorption trend (0.4 wt.%) is revealed at 5 bar, in which the kinetic reaction is faster than the other two pressures (Fig. 15.1). The reversibility of the process at the same temperature condition is verified, as reported in Fig. 15.1, and the total H<sub>2</sub> desorption is reached after about 20 min.

This hydrogen storage capacity is comparable to that of transition metals and/or rare earth alloy powders, commonly used for hydrogen storage applications at a temperature below 423 K, even if in this case the H<sub>2</sub> sorption measure was carried out at 473 K.

The interaction between alloy and hydrogen was confirmed by X-ray diffraction (XRD) spectroscopy. The XRD patterns of the material before and after H<sub>2</sub> absorption show diffraction signals shifted toward lower 2θ values, according to larger lattice parameters extracted from Rietveld refinements. On the basis of tabulated values for TiCr<sub>2</sub>-based hydrates, the crystallographic cell dimensions should correspond to a rough composition TiCr<sub>2</sub>H<sub>0.4</sub> [34].

## 15.4 Innovative Materials

### 15.4.1 Hybrid Materials

The reversibility of charge/discharge cycles in drastic conditions is a critical and fundamental aspect. The materials used for storage are subjected to strong mechanical stress that causes the collapse of structures.

For this reason, the attention is been addressed on polymeric composite materials even if only a few papers have been published about the use of synthetic polymers in this specific application. Moreover, the mechanical properties of the polymers damp down the mechanical stress that the embedded hydrogen storage material (e.g., a metal hydride) can undergo during sorption cycles, though there is still the open question whether the hosting polymer plays a role in modifying the hydrogen storage capacity of compounds like metal hydride. A possible explanation could be the interactions between hydrogen and the polymer chains and/or metal hydrides supported on these polymers. These interactions are generally a combination of covalent, ionic, metallic, H-bonds, and van der Waals [35]. Other important aspects that make polymer-based systems attractive for hydrogen storage are the low density and costs of the materials and the relative ease of synthesis, functionalization, and loading of the polymer matrix.

Some transition metal oxides, such as  $\text{TiO}_2$  and manganese(IV) oxide [ $\text{MnO}_2$ ], have been tested as dopants to improve the hydrogen sorption properties of light metals [36] and complex [37] hydrides and could possibly play a positive role for the interaction of the hydrogen also with the polymer matrix. Following these results, an alternative approach was taken by Pedicini et al. [38] to obtain a hybrid material based on a functionalized polymer containing a nanometric metal oxide.

A commercial polyether-ether-ketone (PEEK,  $[(\text{C}_{19}\text{H}_{12}\text{O}_3)_m^-]$ ) was selected as a matrix for its chemical-physical characteristics. A manganese oxide was linked onto a highly chlorosulfonated (100% $[\text{SO}_2(\text{OH})\text{Cl}]$ ) PEEK to generate the sulfonated

derivative  $\left( \text{SPEEKCl} - \left[ \left( \text{CH}_2 \right)_3 - \underset{\text{H}}{\overset{\text{Cl}}{\text{C}}} - \left( \text{CH}_2 \right)_3 \right]_n - \left[ \underset{\text{Cl-SO}_2}{\overset{\text{H}}{\text{C}}} - \right]_m \right)$  polymeric matrix as

a metal compound able to promote the hydrogen storage. The chlorosulfonation of PEEK increases its surface area from 9.72 to 19.16  $\text{m}^2 \text{g}^{-1}$  due to the introduction of chlorosulfonic groups, and the anchoring of the metal oxide does not change the surface area.

The manganese oxide was chosen as a hydrogen storage material for both its crystalline structure and its easy production method based on an in situ reaction.

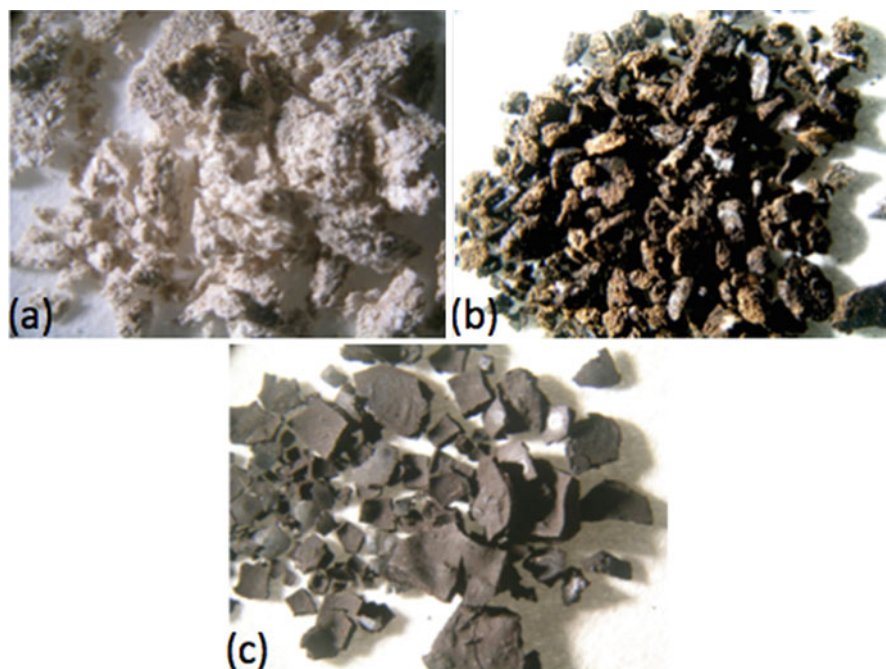
Acting on precursor concentration potassium permanganate [ $\text{KMnO}_4$ ], reaction time and temperature of several powders with the amount of Mn oxide ranging from 7 to 78 wt.% were obtained as shown in Table 15.1.

The variation of Mn oxide content, determined by different synthesis parameters conditions, is evidenced by the change in color and appearance of the powders



**Table 15.1** SPMnO powder characteristics

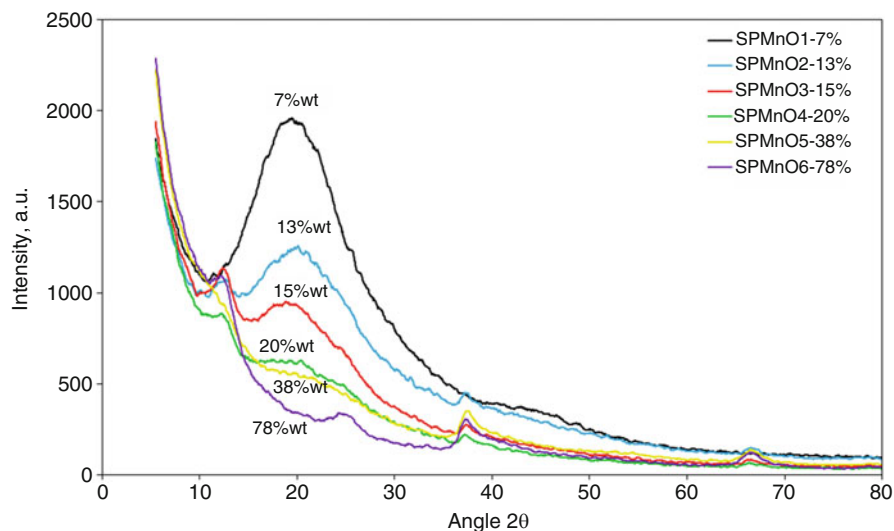
Sample	[KMnO <sub>4</sub> ], mmoles	T, K	Time, h	Mn oxide, wt.%
SPMnO1	2	323	1	7
SPMnO2	3.2	323	1	13
SPMnO3	4	323	1	15
SPMnO4	4	323	3	20
SPMnO5	20	323	1	38
SPMnO6	20	323	3	78

**Fig. 15.2** SPMnO1 (a), SPMnO2 (b), and SPMnO6 (c) (Photos; reproduced with permission of Elsevier)

observed with an optical microscope. In Fig. 15.2, the photos relative to SPMnO1, SPMnO2, and SPMnO6 samples are shown.

The SPMnO1 sample (Fig. 15.2a), with the lowest percentage of manganese oxide (7 wt.%), shows spongy appearance and dirty white color very similar to the polymeric precursor as reported in [38]. Increasing the metal oxide content, the material tends to become darker and less spongy. When the amount is very high (78 wt.%, Fig. 15.2c), the predominance of the oxide is evident and the material becomes hard with the typical black color of Mn oxides.





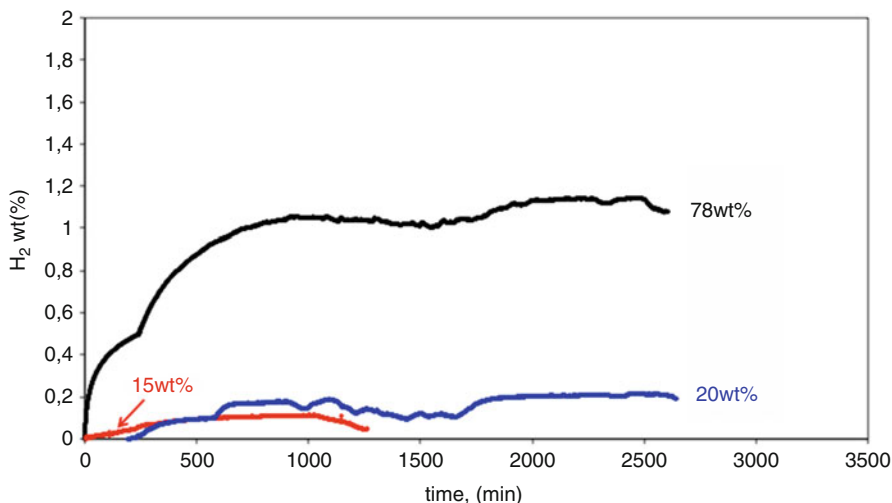
**Fig. 15.3** SPMnO XRD comparison (Reproduced with permission of Elsevier)

The influence of the oxide amount on the structural properties of the prepared samples is evidenced by XRD profiles of all samples, as shown in Fig. 15.3. The peak centered at about  $20^\circ$   $2\theta$  is due to the amorphous structure of the chlorosulfonated PEEK; this profile is maintained in all the developed samples and decreases by increasing the manganese oxide content and almost disappears in the SPMnO6 sample. All the samples present three characteristic peaks ( $12^\circ$ ,  $37^\circ$ , and  $66^\circ$   $2\theta$ ) of the layered manganese oxide of birnessite type. The crystal planes related to the birnessite structure, by following JCPDS data n° 05-673, have angles  $12^\circ$   $2\theta\{100\}$ ,  $37^\circ$   $2\theta\{003\}$ Z, and  $66^\circ$   $2\theta\{005\}$ Z.

Another peak at about  $25^\circ$   $2\theta$ , particularly for the SPMnO5 and SPMnO6, is clearly visible and further confirms the structure of the oxide [39]. Furthermore, the oxide crystalline profile is not well defined as in pure oxide due to the presence of polymeric matrix.

To verify the possible  $H_2$  sorption capability, three synthesized powders SPMnO3, SPMnO4, and SPMnO6 have been characterized by using a Sievert's type gas sorption analyzer. The tests have been performed at 323 K and 383 K. For each test a sequence of different steps of hydrogen pressure was used to charge the samples: in particular, in all tests, 10, 20, 40, and 60 bar of hydrogen pressure has been charged subsequently. Figure 15.4 shows the hydrogenation curves obtained for the three samples at 383 K. The maximum hydrogen uptake increases the manganese oxide content inside the sample.

Interestingly, for sample SPMnO3 (15 wt.%), the hydrogen saturation (0.10 wt.%) is reached with a hydrogen pressure (i.e., 40 bar) lower than that required for sample SPMnO4 (20 wt.%) for which  $H_2$  sorption starts not before 60 bar with higher value of around 0.18 wt.%.



**Fig. 15.4** SPMnO H<sub>2</sub> sorption comparison

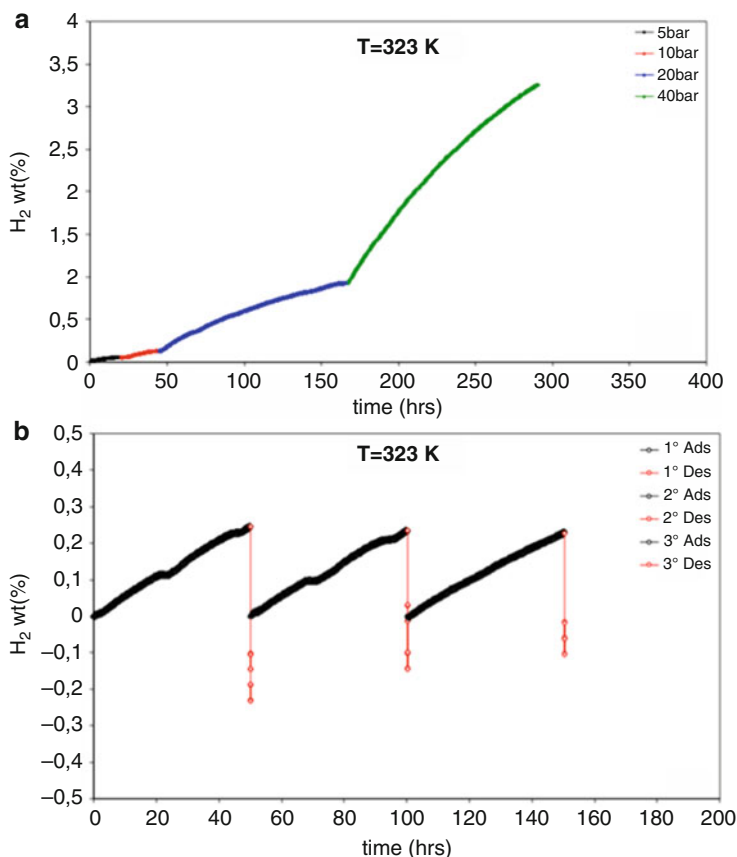
A remarkable result was obtained for sample SPMnO6; the sample showed a high hydrogen capacity, compared to the other samples, already at 10 bar (0.5 wt.%). Once the system was approaching the saturation at 10 bar, a successive step was directly performed at 60 bar. Surprisingly, the sample was able to reach H<sub>2</sub> saturation more than after 1 wt.% after 1000 min, which is, up to now, a value never reached for polymer-based systems at no cryogenic conditions.

Encouraged by these promising results, the measurement temperature of this last sample was lowered at 323 K. The behavior is shown in Fig. 15.5a. The H<sub>2</sub> sorption does not reach the saturation in any P step, and the kinetic reaction is very slow. In any case, at 20 bar, the H<sub>2</sub> sorption is more than 1 wt.%, which is the highest value obtained at 383 K, while at 40 bar, the maximum H<sub>2</sub> sorption value was more than 3 wt.%. The reversibility of the H<sub>2</sub> sorption/desorption cycles was performed, at 323 K, with the aim of evaluating the stability of the material after sorption tests.

The limited number of sorption/desorption cycles was caused by technical reasons; anyway, reversible cycles were reached, and the previous H<sub>2</sub> sorption value at 20 bar was confirmed (in same time range). In addition, the short time of desorption process (5 min) was sufficient to evacuate H<sub>2</sub> completely since subsequent H<sub>2</sub> sorption steps are reproduced.

A further confirmation of the stability of the developed material after the volumetric test was obtained by XRD analysis, in which the profiles before and after test did not show substantial differences maintaining unaltered the crystallographic structure.

A modeling study by ab initio density functional theory (DFT) was carried out on this kind of material. A supercell, containing  $2 \times 2 \times 3$  unit cells of MnO<sub>2</sub> and having 24 Mn and 48 O, was used. The hydrogen atoms were gradually placed in different locations inside the voids. For each number of H atoms, several



**Fig. 15.5** (a) H<sub>2</sub> sorption test and (b) H<sub>2</sub> ads/des cycles of SPMnO<sub>6</sub> (Reproduced with permission of Elsevier)

configurations were calculated (with H atoms in different locations) in order to find the one with the lowest energy. Figure 15.6 shows the lowest energy configurations with 6, 12, and 24 H atoms (b, c, and d, respectively).

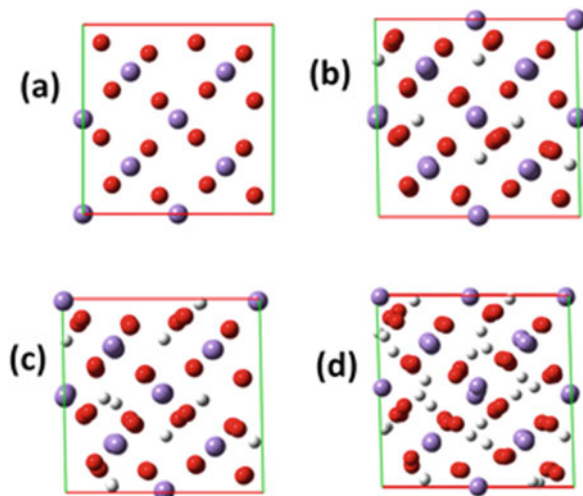
The desorption energy was calculated with Eq. 15.2:

$$\Delta E = 2(E(\text{Mn}_{24}\text{O}_{48}) + n/2E(\text{H}_2) - E(\text{Mn}_{24}\text{O}_{48}\text{H}_n))/n \quad (15.2)$$

The  $\Delta E$  starts from the high value of about 365 kJ/mol for  $n = 2$  and constantly drops to about 150 kJ mol<sup>-1</sup> for  $n = 36$ . This starting value is higher than some metal hydrides, for instance, MgH about 100 kJ mol<sup>-1</sup> or BeH about 240 kJ mol<sup>-1</sup> [40].

Starting from the experimental H<sub>2</sub> sorption value (it was considered 1.7 wt.% instead of 3 wt.% really obtained), it was calculated the number of the respective H atoms corresponds to 36, with desorption energy value of 150 kJ mol<sup>-1</sup>.

**Fig. 15.6** The xy cross section of the lowest energy configurations for  $Mn_{24}O_{48}H_n$  with  $n = 0, 6, 12,$  and  $24$  H atoms (**a**, **b**, **c**, and **d**, respectively). Mn, O, and H atoms are shown as blue, red, and white spheres, respectively (Reproduced with permission of Elsevier)



**Table 15.2** SPMnO powder characteristics and  $H_2$  storage values at 383 K/60 bar

Sample	[KMnO <sub>4</sub> ], mmoles	T, K	Time, h	Mn oxide, wt.%	H <sub>2</sub> sorption, wt.%
SPMnOC	30	353	1	83	0.62
SPMnOD	30	323	3	81	0.95
SPMnOE	12	368	1	78	0.97
SPMnOF	14.2	368	3	85	1.16

To verify the influence of Mn oxide amount on  $H_2$  storage capacity, other samples were developed using more drastic preparative conditions to obtain loading over 78 wt.%. The maximum reachable value was 85 wt.%, but the corresponding  $H_2$  sorption value was about 1 wt.% almost constant for any loading. These results are reported in Table 15.2.

Moreover, the samples obtained in such drastic operative conditions did not show any  $H_2$  reversibility capacity. This behavior was confirmed by XRD postmortem analyses where a structural change was detected. A crystalline structure of the test corresponding to  $Mn_2O_3$  was detected, meaning that the  $H_2$  reacted with the oxide reducing  $Mn^{+4}$  to  $Mn^{+3}$ .

The encouraging results in terms of hydrogen absorption reached on sample SPMnO6 have promoted this material for application in a prototype tank; in fact, its lightweight and easy to handle render this material promising for real application.

An integrated small-scale system consisting of a hydrogen tank, having a capacity of 5–8 normal liters (NL) of hydrogen and a 25 cm<sup>2</sup> single polymer electrolyte fuel cell (PEFC), has been realized and tested to assess the performance of the innovative hydrogen storage material [41]. A precautionary  $H_2$  sorption value of 1.1 wt.% ( $T = 383$  K and  $P = 60$  bar) was considered. Starting from these features, 20 g of material is necessary to feed a 25 cm<sup>2</sup> single cell, and the following parameters (Table 15.3) were considered to size the tank:

**Table 15.3** Theoretical electrochemical parameters with 20 g of sample; reproduced from [42] with permission of Elsevier

Parameter	Amount	Units
H <sub>2</sub> stoichiometry	1	–
Composite material amount	20	g
Absorption ratio	1	% mass
Absorbed H <sub>2</sub>	0.20	g
PM H <sub>2</sub>	2	g mol <sup>-1</sup>
Absorbed H <sub>2</sub> moles	0.10	mol
Constant molar volume	22.41	NL mol <sup>-1</sup>
Absorbed H <sub>2</sub> volume	2.24	NL
H <sub>2</sub> volume at 50 bar	0.04	L
Single-cell active area	25	cm <sup>2</sup>
Specific power	400	mW cm <sup>-2</sup>
Single-cell power	10	W
Cell potential	0.60	V
Cell current	16.67	A
H <sub>2</sub> consumed	8.636E-05	mol s <sup>-1</sup>
Lifetime	1158	s
Lifetime	19.30	min

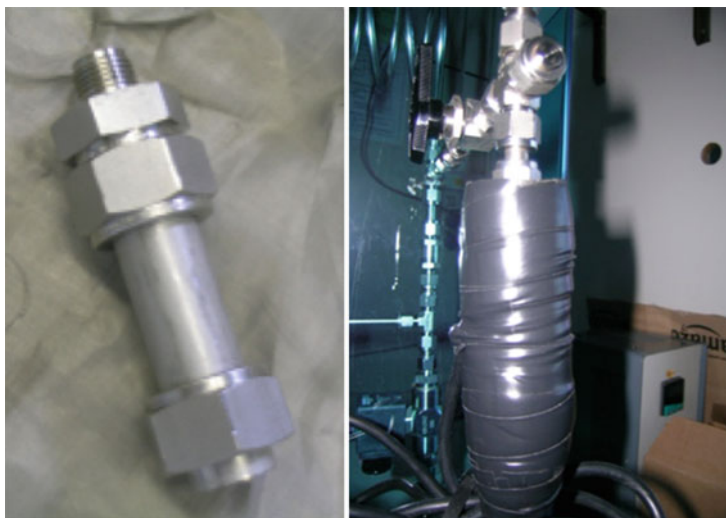
The lifetime of the test was calculated from the molar consumption of reagents (Faraday's law) of the cell at the fixed current, while the potential was chosen to compare the data with other tests performed in a fuel test station. From this data sheet, the cylinder has an H<sub>2</sub> molar volume of 2.24 NL, able to feed a 25 cm<sup>2</sup> single cell with a 400 mW cm<sup>-2</sup> power density at 0.6 V, corresponding a total power of 10 W.

The prototype tank before and after the loading of the material is shown in Fig. 15.7.

Two types of test were performed to measure the performance of the small tank. The first test includes the measurement of the quantity of gas released by the tank. The tests were performed at two constant flow rates, 100 mL min<sup>-1</sup> and 200 mL min<sup>-1</sup>. After each test, the hydrogen tank was recharged at 60 bar (g) and 383 K and different recharge time. The recharge time is recorded to understand the most convenient value relative to desorption performance. A total of six tests have been performed and their results summarized in Table 15.4. The net discharge time was considered taking into account the dead volume related to piping and connections.

Test results show a pretty constant performance in terms of gas output. The average duration of the gas flow is approximately 15 min at a flow rate of 200 mL min<sup>-1</sup> (tests n. 4–6) and 23 min at 100 mL min<sup>-1</sup> (tests n. 1–3).

The discharge time versus charge time is then plotted to highlight their correlation (i.e., the tendency to a plateau which shows the end of the absorption process) and any possible anomaly (i.e., significant gas leakage) (Fig. 15.8). As shown in Fig. 15.8, an increase of charge time did neither lead to a proportional increase nor a constant value of discharge time; the adsorption process requires a longer time than the desorption process.



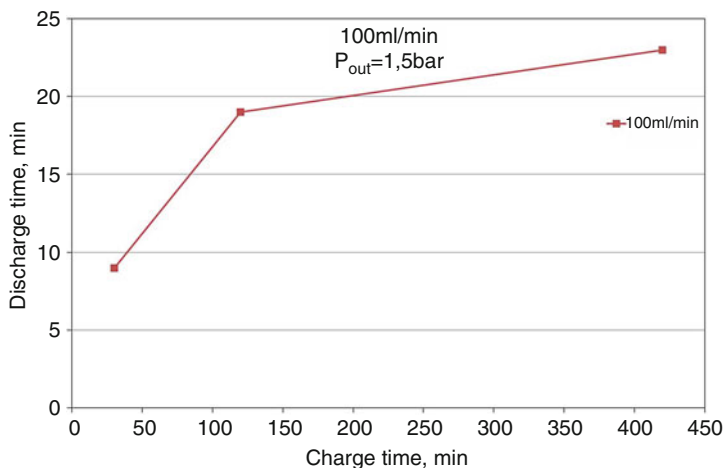
**Fig. 15.7** Prototype tank (Reproduced from [42] with permission of Elsevier)

**Table 15.4** Experimental data for charge/discharge of prototype tank

Test	Charge, min	Net discharge time, min	Flow, mL min <sup>-1</sup>
1	30	9	100
2	120	19	100
3	420	21	100
4	60	7	200
5	120	11	200
6	220	8	200

Successively, the prototype tank was connected to a 25 cm<sup>2</sup> (active area) single cell operating in dead-end mode, so that the hydrogen desorption and the consumption rate can be theoretically estimated by using Faraday's law and measuring the current of the fuel cell. The single cell was previously tested at 353 K and 100% RH by supplying air and H<sub>2</sub> from the laboratory pipeline, to obtain the performance baseline. Figure 15.9a shows a comparison between the baseline fuel cell performance (blue line) and the electrochemical test, performed with the actual system (green line). The two curves were obtained under the same operative conditions at 353 K 1.5 bar and 0.6 V fixed potential, but dry hydrogen was used to feed anode side in the prototype configuration. Unstable behavior was recorded under potentiostatic condition because, in this case, the mass flow controller must manage the flow according to any current fluctuation, leading to flow instability.

The same comparison was carried out at fixed current as shown in Fig. 15.9b. The different performance of the PEFC single cell (blue line vs. green line) is related to the different operative conditions when the cell is fed with the hydrogen from the pipeline (3 bar, 353 K, fully humidified hydrogen, 2.5 stoichiometric at 15 A) or



**Fig. 15.8** Discharge versus charge time at 100 mL min<sup>-1</sup>; (Reproduced from [42] with permission of Elsevier)

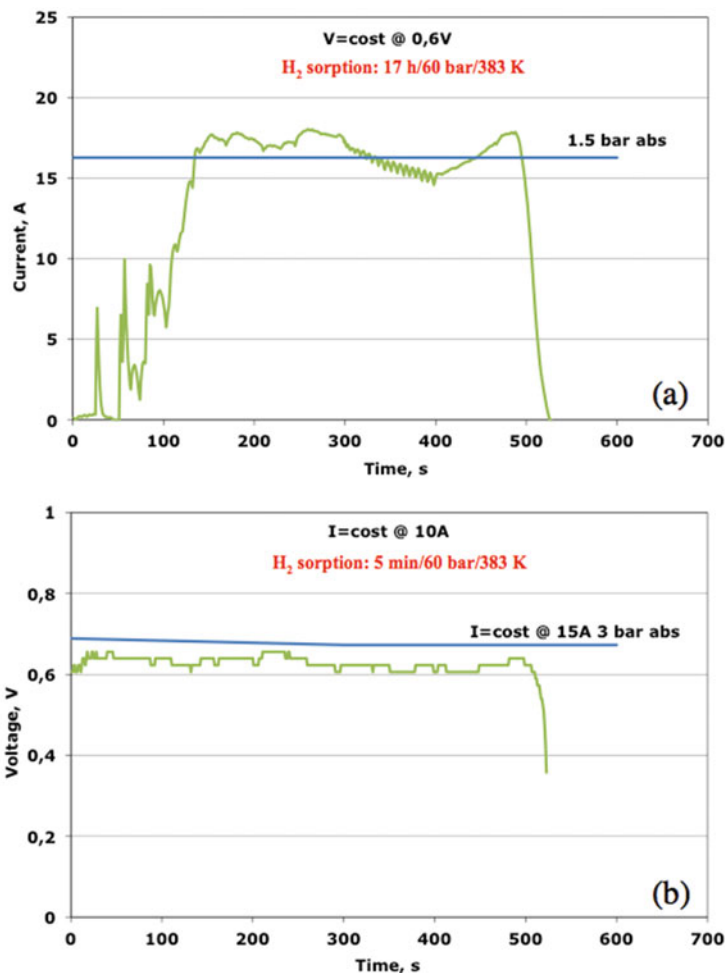
from the tank (353 K, 1.5 bar, dry H<sub>2</sub>, stoichiometric value at 10 A). In the galvanostatic test, a more stable behavior was recorded because the gas consumption rate is constant; hence the mass flow controller follows the set point.

The test lasted 10 min instead of the foreseen discharge time of 20 min due to the hydrogen leakage that reduced the tank autonomy.

As shown in Fig. 15.9b, the fuel cell performances of the prototype system are comparable to that laboratory system when appropriate test conditions were used. Therefore, the innovative material could be used for practical applications with further improvement in terms of material storage capacity and system design.

## 15.4.2 Natural Material

Due to the large variety of elements present in natural volcanic powders [42], this material was taken into consideration for a possible application in hydrogen storage. Two different volcanic samples were analyzed for this study. The first sample (sample red) is coming from an 1892 Etna Vulcan eruption showing oxidized metals, due to a long exposition to the atmospheric agents. The second sample (sample gray) is a lava rock, sampled during a 2006 summit eruption, and was not contaminated by the atmospheric agents. Both of these samples show phenocryst assemblage, which is common to most Etnean volcanics. From X-ray fluorescence spectrometer analyses, the following composition was revealed: <1% for silicon(IV) oxide [SiO<sub>2</sub>], TiO<sub>2</sub>, Al<sub>2</sub>O<sub>3</sub>, MnO, total Fe in Fe<sub>2</sub>O<sub>3</sub><sup>(tot)</sup>, MgO, CaO, and K<sub>2</sub>O; <5% sodium oxide [Na<sub>2</sub>O] and phosphorus(V) oxide [P<sub>2</sub>O<sub>5</sub>]; and between 5% and 10% for all trace elements. From volumetric analyses, sample red has shown a hydrogen storage

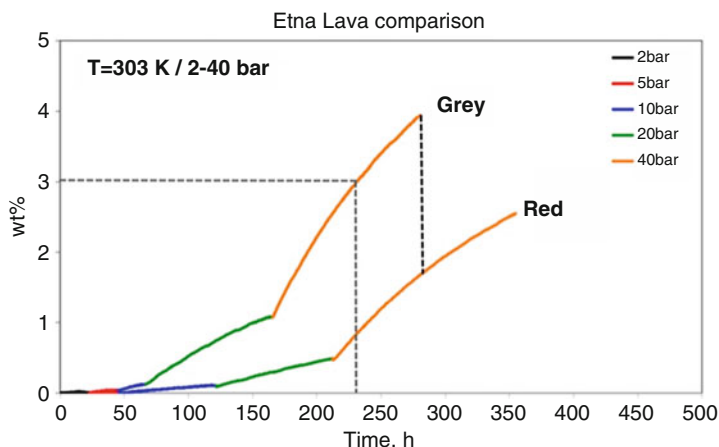


**Fig. 15.9** Comparison of fuel cell performance at fixed potential (a) and current (b) by using standard and prototype H<sub>2</sub> feeding (Reproduced from [42] with permission of Elsevier)

capability of about 2.5 wt.% at 303 K and 40 bar, while sample gray has supplied a higher capability reaching a value of about 4 wt.% in the same operative conditions (Fig. 15.10).

This value was obtained after 280 h; on the contrary, the first sample, at the same time, stores about one-half of H<sub>2</sub>, meaning that the hydrogen sorption kinetic of sample gray is faster than sample red. This wide difference could be attributable to different factors such as high purity of sample gray, not polluted by the atmospheric agents and smaller and homogeneously dispersed particles. From a structural





**Fig. 15.10** Comparison of hydrogen sorption

postmortem characterization by XRD was verified that the hydrogen sorption tests do not produce any modification in the structure of the materials. In conclusion, good and promising results were obtained using natural samples based on volcanic rocks in very mild conditions.

## 15.5 Conclusions

The need to use hydrogen as a carrier for energy has pushed the research toward the study of hydrogen storage with the aim to find available solid-state materials that have suitable requisites for the use in mobile applications. Several classes of materials have been investigated based on  $H_2$  physisorption (carbonaceous, high surface area (HSA) materials) and chemisorption (complex metal hydride, metal hydrides). Generally, all these materials present high  $H_2$  sorption capacity in cryogenic conditions not fully satisfactory for real application. For this reason, the interest toward innovative materials is increased. Recently, a hybrid material based on a functionalized polymer (PEEK) containing different percentages of nanometric Mn oxides was investigated. The XRD patterns highlighted that the developed manganese oxide presents the fundamental peaks of  $MnO_2$  corresponding to lamellar birnessite structure. A low amount of Mn oxide (15 wt.%) and  $H_2$  sorption of 1.2 wt.% was obtained in cryogenic conditions (77 K at 1 bar). Very promising results were reached in mild conditions when a load of 80 wt.% Mn oxides were used. From Sievert apparatus,  $H_2$  sorption values of 3 wt.% at 323 K at 40 bar and 1.1 wt.% at 383 K and 60 bar were obtained.

Furthermore, by short  $H_2$  sorption/desorption cycles, a total reversibility was demonstrated. These results made possible the application of this material in a prototype tank integrated to a polymer electrolyte single cell. The results were comparable to those obtained in a laboratory system. Through a modeling study,

ab initio density functional theory, a desorption energy value comparable to metal hydrides was found, supporting the results obtained in this study.

Among innovative materials, natural volcanic powders coming from Etna Vulcan eruptions were investigated. These materials, containing a large variety of elements, could promote the H<sub>2</sub> sorption. From preliminary H<sub>2</sub> sorption tests, an H<sub>2</sub> uptake of about 4 wt.% at 303 K and 40 bar was recorded on a summit lava rock coming from the 2006 eruption. Despite the significant advances in solid-state material for H<sub>2</sub> storage and many encouraging results, extensive research in this field is in constant evolution.

**Acknowledgments** The hybrid material activity was developed within the Research Project AdP CNR-MSE and financing from the Research Fund for the Electrical System, with theme: International Project “Nuclear, Hydrogen, Fuel Cells” e Activity 2.6: Polymeric materials for hydrogen storage.

The authors are grateful to Dr. Ausonio Tuissi (CNR-ICMATE) for his collaboration in TiCr development and Dr. Lucia Miraglia (INGV) for his support in lava material characterizations.

---

## References

1. S. Borowitz, *Farewell Fossil Fuels*, Springer Science book ISBN 978-0-306 45781-4, (1999)
2. <http://www.fch.europa.eu/page/multi-annual-work-plan>
3. S. Iijima, *Nature* **354**, 56 (1991); A.C. Dillon, K.M. Jones, T.A. Bekke-dahl, H. Kiang, D.S. Bethune, M.J. Heben, Storage of hydrogen in single-walled carbon nanotubes. *Nature* **386**, 377–379 (1997)
4. E. Poirier, R. Chahine, T.K. Bose, *Int. J. Hydrog. Energy* **26**, 831 (2001)
5. H. Wang, Q. Gao, J. Hu, High hydrogen storage capacity of porous carbons prepared by using activated carbon. *J. Am. Chem. Soc.* **131**, 7016–7022 (2009)
6. Z. Wang, L. Sun, F. Xu, H. Zhou, X. Peng, D. Sun, J. Wang, Y. Du, Nitrogen-doped porous carbons with high performance for hydrogen storage. *Int. J. Hydrogen Energy* **41**, 8489–8497 (2016)
7. H. Jung, K.T. Park, M.N. Gueye, S.H. So, C.R. Park, Bio-inspired graphene foam decorated with Pt nanoparticles for hydrogen storage at room temperature. *Int. J. Hydrogen Energy* **41**, 5019–5027 (2016)
8. N.L. Rosi, J. Eckert, M. Eddaoudi, D.T. Vodak, J. Kim, M. O’Keeffe, O.M. Yaghi, Hydrogen storage in microporous metal-organic frameworks. *Science* **300**, 1127–1129 (2003)
9. K. Koh, A.G. Wong-Foy, A.J. Matzger, A porous coordination copolymer with over 5000 m<sup>2</sup>/g BET surface area. *J. Am. Chem. Soc.* **131**, 4184–4185 (2009)
10. N.M. Musyoka, J. Ren, P. Annamalai, H.W. Langmi, B.C. North, M. Mathe, D. Bessarabov, Synthesis of a hybrid MIL-101(Cr)/ZTC composite for hydrogen storage applications. *Res. Chem. Intermed.* **42**, 5299–5307 (2016)
11. D. Ramimoghadam, E. MacA Gray, C.J. Webb, Review of polymers of intrinsic microporosity for hydrogen storage applications. *Int. J. Hydrogen Energy* **41**, 16944–16965 (2016)
12. O. Elishav, D.R. Lewin, G.E. Shter, G.S. Grader, The nitrogen economy: economic economic feasibility analysis of nitrogen-based fuels as energy carriers. *Appl. Energy* **185**, 183–188 (2017). <https://doi.org/10.1016/j.apenergy.2016.10.088>
13. P.L. Bramwell, S. Lentink, P. Ngene, P.E. De Jongh, Effect of pore confinement of LiNH<sub>2</sub> on ammonia decomposition catalysis and the storage of hydrogen and ammonia. *J. Phys. Chem. C* **120**(48), 27212–27220 (2016). <https://doi.org/10.1021/acs.jpcc.6b10688>

14. Y.Z. Ge, W.Y. Ye, Z.H. Shah, X.J. Lin, R.W. Lu, S.F. Zhang, PtNi/NiO clusters coated by hollow silica: novel design for highly efficient hydrogen production from ammonia-borane. *ACS Appl. Mater. Interfaces* **9**(4), 3749–3756 (2017). <https://doi.org/10.1021/acsami.6b15020>
15. M. Baricco, M. Bang, M. Fichtner, B. Hauback, M. Linder, C. Luetto, P. Moretto, M. Sgroi, SSH2S: Hydrogen storage in complex hydrides for an auxiliary power unit based on high-temperature proton exchange membrane fuel cells. *J. Power Sources* **342**, 853–860 (2017). <https://doi.org/10.1016/j.jpowsour.2016.12.107>
16. X. Zhang, R.Y. Wu, Z.Y. Wang, M.X. Gao, H.G. Pan, Y.F. Liu, Preparation and catalytic activity of a novel nanocrystalline  $ZrO_2@C$  composite for hydrogen storage in  $NaAlH_4$ . *Chem-Asian J* **11**(24), 3541–3549 (2016). <https://doi.org/10.1002/asia.201601204>
17. G. Zou, B. Liu, J. Guo, Q. Zhang, C. Fernandez, Q. Peng, Synthesis of nanoflower-shaped MXene derivative with unexpected catalytic activity for dehydrogenation of sodium Alanates. *ACS Appl. Mater. Interfaces* **9**(8), 7611–7618 (2017). <https://doi.org/10.1021/acsami.6b13973>
18. J.R. Ares, J. Zhang, T. Charpentier, F. Cuevas, M. Latroche, Asymmetric reaction paths and hydrogen sorption mechanism in mechanochemically synthesized potassium alanate ( $KAlH_4$ ). *J. Phys. Chem. C* **120**(38), 21299–21308 (2016). <https://doi.org/10.1021/acs.jpcc.6b07589>
19. Y.F. Ma, Y. Li, T. Liu, X. Zhao, L. Zhang, S.M. Han, Y.J. Wang, Enhanced hydrogen storage properties of  $LiBH_4$  generated using a porous  $Li_3BO_3$  catalyst. *J. Alloys Compd.* **689**, 187–191 (2016). <https://doi.org/10.1016/j.jallcom.2016.07.313>
20. S.C. Li, F.C. Wang, The development of a sodium borohydride hydrogen generation system for proton exchange membrane fuel cell. *Int. J. Hydrog. Energy* **41**(4), 3038–3051 (2016). <https://doi.org/10.1016/j.ijhydene.2015.12.019>
21. D. Lu, G.F. Yu, Y. Li, M.H. Chen, Y.X. Pan, L.Q. Zhou, K.Z. Yang, X. Xiong, P. Wu, Q.H. Xia, RuCo NPs supported on MIL-96(Al) as highly active catalysts for the hydrolysis of ammonia borane. *J. Alloys Compd.* **694**, 662–671 (2017). <https://doi.org/10.1016/j.jallcom.2016.10.055>
22. L.M. Zhou, J. Meng, P. Li, Z.L. Tao, L.Q. Mai, J. Chen, Ultrasmall cobalt nanoparticles supported on nitrogen-doped porous carbon nanowires for hydrogen evolution from ammonia borane. *Mater. Horiz.* **4**(2), 268–273 (2017). <https://doi.org/10.1039/c6mh00534a>
23. M. Rueda, L.M. Sanz-Moral, J.S.B. Jose, A. Martin, Improvement of the kinetics of hydrogen release from ammonia borane confined in silica aerogel. *Microporous Mesoporous Mater.* **237**, 189–200 (2017). <https://doi.org/10.1016/j.micromeso.2016.09.030>
24. Z.J. Zhang, Y.Q. Wang, X.S. Chen, Z.H. Lu, Facile synthesis of NiPt-CeO<sub>2</sub> nanocomposite as an efficient catalyst for hydrogen generation from hydrazine borane. *J. Power Sources* **291**, 14–19 (2015). <https://doi.org/10.1016/j.jpowsour.2015.05.012>
25. R. Moury, K. Robeyns, Y. Filinchuk, P. Miele, U.B. Demirci, In situ thermodiffraction to monitor synthesis and thermolysis of hydrazine borane-based materials. *J. Alloys Compd.* **659**, 210–216 (2016). <https://doi.org/10.1016/j.jallcom.2015.11.052>
26. P. Chen, E. Akiba, S. Orimo, A. Züttel, L. Schlapbach, Hydrogen storage by reversible metal hydride formation in the *Book: Hydrogen Science and Engineering: Materials, Processes, Systems and Technology* (2016)
27. G. Friedlmeier, M. Groll, Experimental analysis and modeling of the hydriding kinetics of Ni-doped and pure Mg. *J. Alloy Compd.* Elsevier-Amsterdam, **253–254**, 550–555 (1997)
28. H. Wang, H.J. Lin, W.T. Cai, L.Z. Ouyang, M. Zhu, Tuning kinetics and thermodynamics of hydrogen storage in light metal element based systems – a review of recent progress. *J. Alloys Compd.* **658**, 280–300 (2016)
29. M. Ron, The normalized pressure dependence method for the evaluation of kinetic rates of metal hydride formation/decomposition. *J. Alloy Compd.* **283**, 178–191 (1999)
30. C.S. Wang, X.H. Wang, Y.Q. Lei, C.P. Chen, Q.D. Wang, The hydriding kinetics of  $MiNi_5$  – I. Development of the model. *Int. J. Hydrogen Energy* **21**, 471–478 (1996)
31. J. Yang, A. Sudik, C. Wolverton, D.J. Siegel, High capacity hydrogen storage materials: attributes for automotive applications and techniques for materials discovery. *Chem. Soc. Rev.* **39**, 656–675 (2010)

32. K. Sanjay, H. Miyaoka, T. Ichikawa, G.K. Dey, Y. Kojima, Micro-alloyed Mg<sub>2</sub>Ni for better performance as negative electrode of Ni-MH battery and hydrogen storage. *Int. J. Hydrog. Energy* **42**, 5220–5226 (2017)
33. R. Pedicini, I. Gatto, M. Coduri, C.A. Biffi, A. Tuissi, Preliminary investigation on metal alloy based on Cr/Ti, HYPOTHESIS XII Conference, Syracuse, 28–30 June 2017
34. H. Imoto, M. Sasaki, T. Saito, Y. Sasaki, *Bull. Chem. Soc. Jpn.* **53**(6), 1584–1587 (1980)
35. W.R. Schmidt, Activity report of the United Technologies Research Center for the Polymer Dispersed Metal Hydride program, DOE contract DEFC36-00G010535
36. Z. Liu, Z. Lei, Cyclic hydrogen storage properties of Mg milled with nickel nano-powders and MnO<sub>2</sub>. *J. Alloys Compd.* **443**, 121–124 (2007)
37. Y. Suttisawat, P. Rangsunvigit, B. Kitiyanan, S. Kulprathipanja, Effect of co-dopants on hydrogen desorption/absorption of HfCl<sub>4</sub>- and TiO<sub>2</sub>- doped NaAlH<sub>4</sub>. *Int. J. Hydrog. Energy* **33**, 6195–6200 (2008)
38. R. Pedicini, A. Saccà, A. Carbone, E. Passalacqua, Hydrogen storage based on the polymeric material. *Int. J. Hydrog. Energy* **36**, 9062–9068 (2011)
39. G. Zhu, H. Li, L. Deng, Z.H. Liu, Low-temperature synthesis of δ-MnO<sub>2</sub> with large surface area and its capacitance. *Mater. Lett.* **64**, 1763–1765 (2010)
40. A.D. Zdetsis, M.M. Sigalas, E.N. Koukarasad, *Phys. Chem. Chem. Phys.* **16**, 14172–14182 (2014)
41. R. Pedicini, F. Matera, G. Giacoppo, I. Gatto, E. Passalacqua, *Int. J. Hydrogen Energy* **40**, 17388–17393 (2015)
42. R. Pedicini, L. Miraglia, A. Carbone, E. Passalacqua, I. Gatto, Interesting hydrogen storage behavior of volcanic powders, The III Energy & Materials Research Conference – EMR 2017 Lisbon, 5–7 Apr 2017
43. L. Miraglia, *Tech. Report INGV* **261**, 5–24 (2013)



# Stress Distribution in PEM Fuel Cells: Traditional Materials and New Trends

# 16

Javier de la Cruz, Tatiana Romero, and Ulises Cano

## Contents

16.1	Introduction .....	470
16.2	Mechanical Stress on a PEM Fuel Cell Stack .....	472
16.2.1	Dimensions: Effect of Temperature and Presence of Water .....	476
16.2.2	Stress Modes in a Fuel Cell Stack .....	476
16.2.3	Stress Distribution Measurements .....	478
16.2.4	Materials Trend in Fuel Cell Technology .....	478
16.3	Bipolar Plates .....	479
16.3.1	Conventional Materials .....	481
16.3.2	New Tendencies in BPs .....	482
16.3.3	Distribution Stress in Bipolar Plates .....	484
16.3.4	Mechanical Characterization of Bipolar Plates .....	484
16.4	Proton Exchange Membrane .....	485
16.4.1	PEM Structure .....	485
16.4.2	Mechanical Properties of Commercially Available PFSA's .....	486
16.4.3	Assembled Membranes .....	490
16.4.4	Alternative Proton Exchange Membranes .....	491

## Author Contribution

All authors contributed significantly to the Introduction. UC was the main contribution for Sect. 16.2 “Mechanical Stress on a PEM Fuel Cell Stack” and partially on Sect. 16.3 “Bipolar Plates,” where Javier de la Cruz contributed the remaining material. DIC was also was in charge of carrying out the 3D simulations presented in Sect. 16.2.3. TR wrote Sect. 16.4 “Proton Exchange Membrane” and contributed as editor of the whole document. The authors further acknowledge that there is no financial relationship with the editors or publisher and have contributed original work in this chapter, other than what acknowledged or appropriately cited with copyright permission.

J. de la Cruz (✉)

CONACYT-INEEL, Cuernavaca, Mexico

e-mail: [javier.delacruz@iie.org.mx](mailto:javier.delacruz@iie.org.mx)

T. Romero · U. Cano

INEEL, Cuernavaca, Mexico

e-mail: [tr Romero@iie.org.mx](mailto:tr Romero@iie.org.mx); [ucano@iie.org.mx](mailto:ucano@iie.org.mx)

16.5 Conclusion .....	492
References .....	493

### Abstract

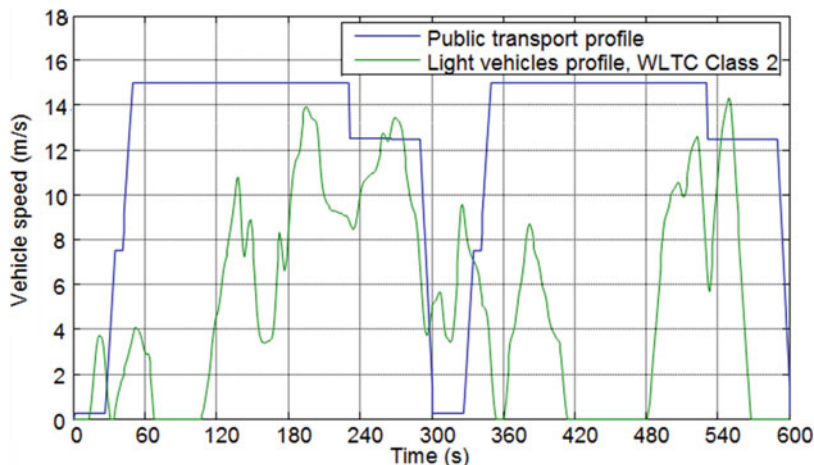
The even distribution of mechanical stress along the fuel cell is an important metric to observe in order to preserve the integrity of the system's components. The diversity of the fuel cell's comprising materials and dimensions, ranging from thin polymers, porous electrocatalyst and gas diffusion layers, graphite blocks, gaskets, and seals to metallic foils and plates, produces different load transmission patterns. These variations in load when combined with their particular mechanical properties may promote localized stresses deriving in accelerated degradation or, even worse, in early unsafe failure.

In transport applications, main fuel cell mechanical stressors, such as the fuel cell assembly torque, operational parameters, and vibration, can induce harsh conditions altering the lifetime of the system. The ionomeric membrane and bipolar plates are critical components in the fuel cell that may fail through mechanical means; therefore, understanding their limitations to withstand mechanical stress is important in redesigning these components to prevent unintended damage and failure.

In this chapter, we give a personal perspective account of the mechanical properties of the fuel cell's most sensitive components, i.e., the proton exchange membrane (PEM) and the bipolar plate (BP) are examined in the scope of their current material limitations; alternative material's substitution is discussed for improving the endurance of the integrated fuel cell device. This chapter is designed to give the fuel cell practitioner real hands-on experience on the actual engineering aspects of FC bench testing and associated testing specifications including US Department of Energy guidelines and targets.

## 16.1 Introduction

Fuel cell technology has rapidly developed in the last few years intended for many applications ranging from stationary to mobile, where the latter is the more developed application toward fuel cell electric vehicles as the main market target. In particular, the proton exchange membrane (PEM) low-temperature fuel cells (FCs) have developed, as they are very convenient for start-up and operation at low ambient temperatures. This particular type of fuel cell uses a very thin solid polymer electrolyte, able to exchange protons (proton exchange membrane) during the fuel cell operation, with the possibility of a highly increased power density required for the transport industry. It is precisely in the transportation application market where the fuel cell is likely to experience mechanical conditions, which may result in component failure, conditions that go from vibrations associated with the movement of the vehicle and the friction with the ground to collisions when accidents may

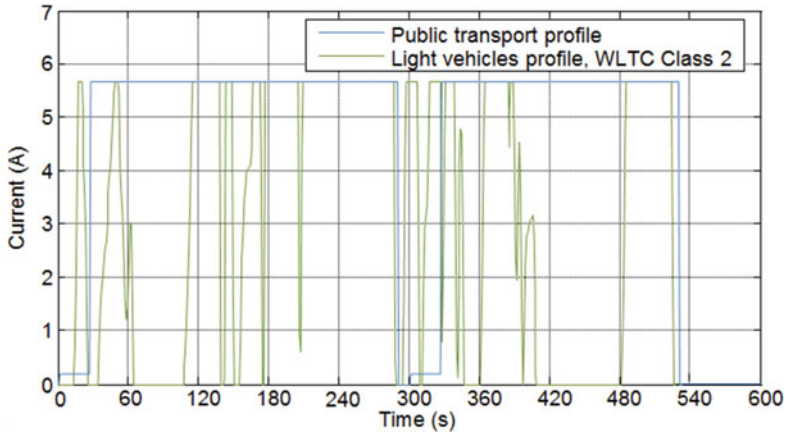


**Fig. 16.1** Driving cycles in transportation applications: public transport and light personal vehicle

occur while driving on the roads. Although some fuel cell vehicles like the Toyota Mirai possess a body with high rigidity (i.e., torsional rigidity of 40–60%; higher than another automobile model, manufactured by the Toyota car company [40]), the fuel cell power plant should withstand potential exposure to vibration and shock impact to a certain extent, without compromising FC performance. That means that the integrity of a fuel cell stack should fulfill operation requirements and robustness for the intended application.

Figure 16.1 shows two driving cycles for (a) public transport and (b) light personal vehicle [1]. As is shown in the figure, the public transport profile requires a steady speed, which translated to the fuel cell requirement involving mostly a steady-state operation: constant power for long periods. On the other hand, the light vehicle profile shows a constant speed variation with frequent starts and stops. This power demand represents a harsh operating condition in the fuel cell stack with variations in the power, resulting in frequent cycles of temperature and water production, known as hygrothermal cycles. Such cycles are one of the main causes of degradation including mechanical, induced degrading conditions on some of the most sensitive components in the fuel cell.

The design of the fuel cell should consider the power supply related to the energy demand profile. The driving profile helps to define the power configuration, whether the fuel cell will cover the whole demand or will do it partially, with support from an auxiliary power source such as a battery. In the latter case, the current demand peaks of 6 amperes (A), shown in Fig. 16.2, are delivered potentially by a combination of fuel cell supported by the battery or the battery supplemented by the FC. Figure 16.2 shows the delivered current of the fuel cell along each drive cycle. In any case, the profile of the light vehicle could cause accelerated fuel cell out-of-specification mechanical conditions including fatigue.



**Fig. 16.2** Current demand at each driving cycle

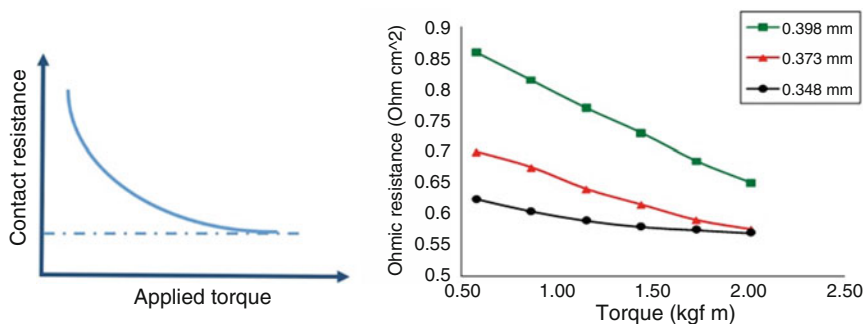
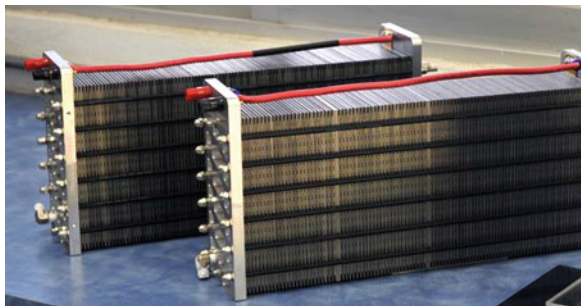
## 16.2 Mechanical Stress on a PEM Fuel Cell Stack

A fuel cell stack is a series of components integrated and held together through a mechanism in which some force, commonly an application of compression force, to keep its elements to stay in place. By compressing the components together, the applied force will distribute according to the component's properties and in a manner that corresponds to the particular geometrical and spatial design of the fuel cell. There are certain challenges to this compression, which may contribute to component failure. For example, the mechanical properties of these components may vary up to two orders of magnitude [2] which represents a big challenge for parts designers, as components should be compatible mechanically. Material compatibility is achieved at the design stage, where component designers consider materials selection and their associated properties in the environment and conditions expected during operation.

A fuel cell stack is the power plant of an application device based on that technology, where all assembled components are integrated into a subsystem or sub-device through mechanical compression. The compression procedure should combine the different parts together to operate as specified during its design and manufacture. As a single cell only gives a low voltage, which is insufficient for practical applications, several cells are connected in series in the form of a stack to generate the required power. The geometrical aspects of the fuel cell stack influence the mechanical stability. For example, a long stack, although convenient for heat dissipation of the exothermic reaction, is mechanically less stable. The Fig. 16.3 shows two identical fuel cell stacks, each with 98 single cells. Usually, the cell's area determines the total current in a series configuration to give the nominal power of the device. This seems simple, but it requires several considerations in order to



**Fig. 16.3** Two fuel cell stacks composed of 98 single cells connected in series fabricated at the INEEL



**Fig. 16.4** Fuel cell stack contact resistance as a function of torque [3]

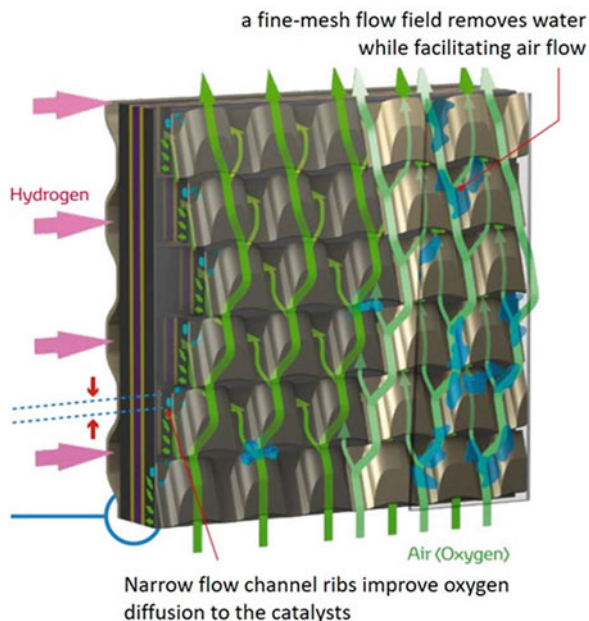
guarantee that all processes needed to generate electricity and operate the generator occur in a controlled manner, deliver the specified power, and maintain mechanical stability within the range of the properties of the components.

The compression force used to maintain components together is also important for two additional reasons. First, as conductive components are aligned together to transmit electrical current, that is, they are electrically connected in series, the effective electrical conduction will be a function of the force applied to bring them in close contact. That is, the appropriate conduction along each connected cell can only be achieved if they have a tight physical contact. Figure 16.4 shows the contact resistance as a function of the applied torque in a fuel cell stack through a series of bolts; on the left, there is a general behavior schematic and on the right an experimental case. The figure on the right shows that different thicknesses of the same gasket material, in this case, rubber used as a sealant, cause a decrease in the contact resistance value along with the increase in torque. A second reason for the application of a compression force is related to safety as many sealing systems are based on compression acting as seal materials that need to be deformed in order to exert an opposite direction force thanks to their elastic properties and isolate the fuel-containing regions from the outside. Clearly, this is of paramount importance as hydrogen is the usual fuel in a fuel cell stack and may be very reactive depending on certain conditions, which may, in turn, generate safety concerns.

To understand why stress distribution within a fuel cell stack is important and why it should be known a priori before the technology performs during operation, it is worth to remember how an FC is constituted. The two basic components in a fuel cell stack are the bipolar plates (BP) and the membrane-electrodes assemblies (MEA). From the manufacturing point of view, there is an advantageous tendency of integrating into a single constituent several components so that the final integrations of a device, such as a fuel cell plant, become a fast and simple process, therefore favoring higher production volumes and lowering production costs. An example of this approach is the fabrication of the MEA, which contains the electrolyte and the electrodes but which is often composed of additional components such as the gas diffusion layers (GDL), a porous conductive material, and a reinforcing frame or sub-gasket that provides better mechanical stability to the delicate electrolyte. In this way, an MEA may become a constituent formed by seven or more layers. This seven-layer MEA integrates one polymer (electrolyte), a conductive catalyst layer composed of a support in the micrometer scale made of conductive carbon materials for the catalyst (usually platinum (Pt) often alloyed with another metal), and an additional electrolyte and binding made of a different polymer. All of these components have different and distinctive characteristics, not only physically but also chemically different, but need to be constructed within the MEA to function. Within a fuel cell stack, several different processes take place, for example, the electrochemical reactions at the anode and cathode (fuel oxidation and oxygen from air reduction, respectively). These redox reactions are exothermic which generate heat that is exchanged by the refrigeration system (which is either air or liquid based). Inside the fuel cell stack, reactants are fed separately to anode and cathode, but reaction products also need to be considered. The redox reaction at the cathode produces water as a by-product that needs to be removed, to maintain the reactant flow access. Removal is effected by movement of air flow at large volumes. This air flow is often humidified to maintain optimum electrolyte conductivity unless the design allows for self-humidification which provides a more compact and cheaper fuel cell system.

The stack is provided with electrical connectors by which reactants are fed and products are removed. For proper functioning the fuel stacks require conduits, pores, or channels known as gas flow fields (GFF), to facilitate liquid or gas transport, meaning the bipolar plate (BP) is not a continuous solid but have a geometric configuration that may be very intricate or very simple depending on the technology. Such configuration will, in turn, behave mechanically depending on such their design and assembly. For example, the greater the number of “voids” (GFF), the greater the porosity of the BP which should be constructed of materials with the greater tensile strength to take account of the higher porosity of the assembled subsystem. The BP will distribute the transmitted stress depending on its geometry, i.e., volume and shape. From Ohm’s law it is evident that a larger transverse area will provide with more conduction sites, so if a BP design is defined with more channels or these channels are wide, their effective electrical conduction will be poorer due to less contact area. Also from the mechanical point of view, the device

**Fig. 16.5** Gas flow field in Toyota's fuel cell stack used in the commercially available FCV Mirai



will be subjected to higher stress derived from a smaller cross-sectional area increasing the load on the BP. Figure 16.5 shows a very complex but effective configuration used by the fuel cell in the Toyota Mirai [4]. Here, the cathode plates have a 3D fine mesh design to maintain the humidity inside the cells but are still capable of removing the excess water, while at the same time, the plates provide access to reactant air.

Generally, such plates are used to reinforce structurally other components with lower mechanical properties, for example, the polymeric membrane (PEM), the porous gas diffusers (GDL), porous electrodes also called catalyst layer (CL), and other sealing materials. As expected, such combination of materials imposes a great challenge from the mechanical point of view when designing a mechanism of integrating and holding all components in the right place. This integration process should be packaged, after a thorough analysis of mechanical aspects prior to full production. The analysis should take into account factors such as chemical and mechanical material properties. These include but are not limited to the elastic modulus, yield stress limit, elongation at break, flexural strength, yield strength, and tensile strength, which allows the designer in determining how components will behave under FC operating conditions. As the fuel cell suffer from thermal changes during its functioning, other properties like their thermal expansion coefficients need to be available. Such consideration if modeled will give designers feedback on likely redesign areas and if correctly implemented will reduce the likelihood of material or device failure under real operating conditions.

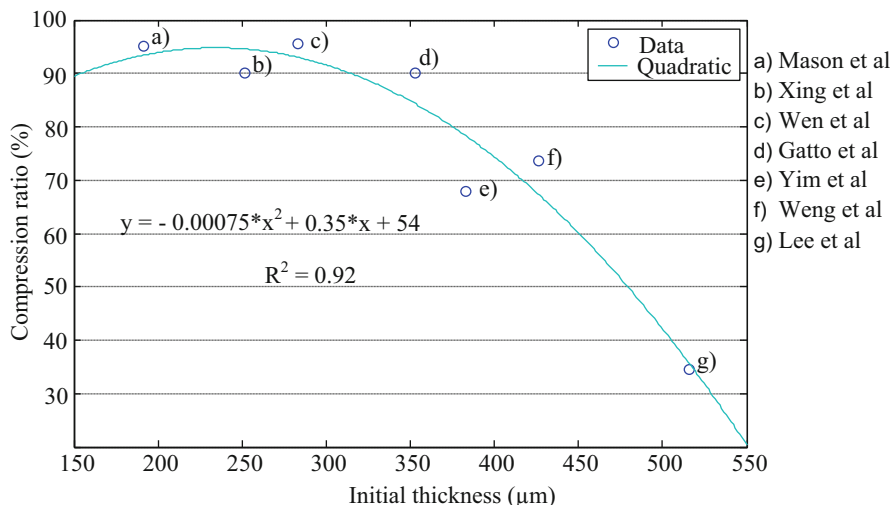
### 16.2.1 Dimensions: Effect of Temperature and Presence of Water

The components in a fuel cell are designed in dimensions that vary from a few millimeters down to micrometers in thickness, so this should also be taken into consideration as any dimension variation in one or more components may greatly affect the mechanical condition of another on a smaller scale. Most low-temperature PEM fuel cells operate in the range of 60–80 °C, which means that dimensional changes of components might occur to a different extent, as they will have different thermal expansion coefficients. This parameter describes the dimensional changes a material will suffer because of a change in temperature, and it is expressed as the ratio of the fractional change in size to the change in temperature; that is why its units are in  $^{\circ}\text{K}^{-1}$  or  $^{\circ}\text{C}^{-1}$ . Many of the components in a fuel cell may present anisotropic structures either due to the way there are manufactured or on purpose because of functional designs. These geometries should be considered as some materials may suffer more from longitudinal change during temperature changes and not necessarily an isotropic (volume) change. If a fuel cell stack is not properly designed, then heat conduction may occur heterogeneously meaning that a gradient of temperatures could exist along several or all of the stack components imposing heterogeneously dimensional changes creating potentially unwanted mechanical conditions.

The presence of water inside a fuel cell is the product of the fuel and oxidant global reaction [ $\text{O}_2 + 4\bar{e} + 4\text{H}^+ \rightarrow 2\text{H}_2\text{O}$  at the cathode]. A good stack design will provide a means of escape for the excess water in the form of liquid or vapor to avoid the blockage of gases or reactants entering the power plant or even product accumulation. In order to simplify system complexity, engineers design is aimed at avoiding humidification subsystems and using the in situ water produced by the operation of the stack. The presence of water causes an important component, the membrane, to swell not only changing dimensions but also creating much localized mechanical conditions causing other stress modes like shear stress or even tension loads in this component and potentially in adjacent elements. The estimation of such stresses and modes is very important, as they have to be considered as to avoid such conditions and protect the integrity of one of the most delicate components, i.e., the membrane that serves also as a separator of the two reactants.

### 16.2.2 Stress Modes in a Fuel Cell Stack

The usual method of keeping the fuel cell stack's components together is by applying a predesigned compression force. A compression force like any force has a direction, and in a fuel cell, this is perpendicular to the cross-sectional area of the individual cells and of the BP aligned in series. In a conventional fuel cell stack besides BPs and MEAs, the stack also integrates two final plates (one at each end of the series connection) which are pressed through a compression press and kept together by some locking means or through compression bolts which torque is estimated to apply a particular force on the fuel cell stack. The end plates are usually specified to withstand higher loads as they provide the mechanism to distribute the applied force



**Fig. 16.6** Effect of compression on the GDL thickness

to the entire stack. During manufacturing of fuel cell stacks, developers usually employ compression systems that ensure the correct alignment of components and the correct application of the compressive load on the stack, while at the same time allowing locking the stack in position once the pressure force has been applied. If alignment is not correct, there is a risk of having regions with unwanted mechanical stress, for example, overlapping components will make them interact, potentially creating hotspots of high loads. This is because some components are not continuous elements and may contain porous of different sizes. Also, their porosity, i.e., the ratio of empty space (pores) to solid volume, plays an important role and should be maintained under control. These components, catalyst layer (CL) gas diffusion layer (GDL), gas diffusion electrodes (GDE), etc., react in a particular manner when mechanical pressure is applied to them but most tend to maintain their volume unless spatially restricted. If the latter happens, the porosity will be compromised. When defining a compression value for a fuel cell stack, porous components should not be extremely deformed as they usually provide paths for reactants and products. This is the case of the GDL, which normally suffers a level of compression reaching compression ratios of about 0.92; see Fig. 16.6 [5].

Usually, these porous elements may present a load component orthogonal to the applied compressive load, because of their ability to deform in such planar mode. This resultant force may affect adjacent elements with mechanical strength lower than the resultant force. For this reason, many developers use reinforcing material components such as frames or sub-gaskets for the PEM or for the entire MEA, which may encounter additional shear stresses or even tension loads. The second mode for mechanical loading present in PEM fuel cells is due to the swelling of the electrolyte during FC operation. Here the Nafion membrane is saturated with water causing

membrane swelling. It is important to note that the degree of swelling is depending on the fabrication method; conventional Nafion membranes will swell either isotropically or anisotropically, depending on the membrane and MEA design. This, in turn, may generate loads in one, two, or three directions potentially with different magnitudes, which ideally should be anticipated at the design stage.

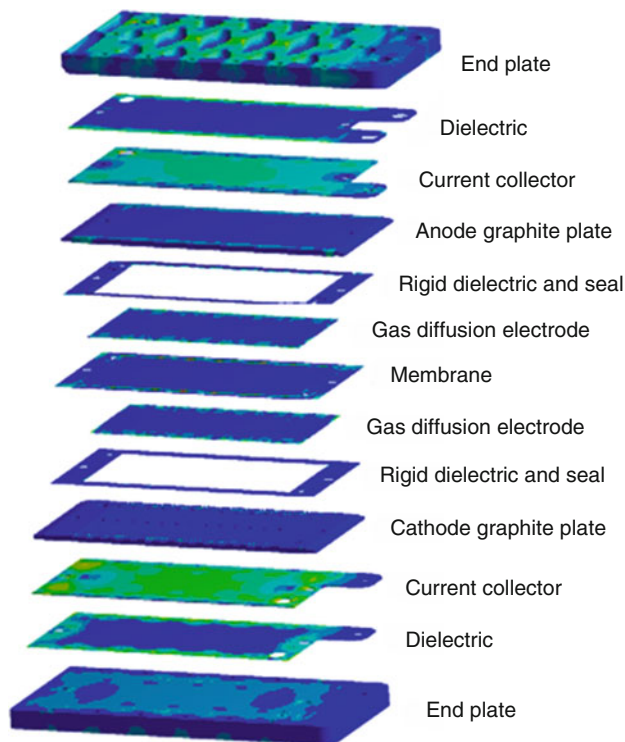
### 16.2.3 Stress Distribution Measurements

In order to estimate how stress is distributed in a fuel cell stack, finite element analysis (FEA) is normally used together with adequate models to account for the applied forces. During such studies, component's mechanical properties are required and considered within the model as to evaluate their mechanical response and potential deformation. In case that evaluated stress levels exceed strength values of components that represent mechanical limits, the design of the component must be modified in order to prevent failures. Several commercial software packages allow the evaluation of mechanical distribution in different systems. The geometrical design is considered as a starting point by the software and during the establishment of the boundary conditions during the evaluation. Once a geometrical model is defined, the FEA requires developing a grid system to solve relevant equations to estimate stress levels in each predefined element. The commercial software packages include different options of mechanical models to be used depending on the system to be studied, but often a von Mises model will be adequate for the simulation and evaluation of such mechanical conditions along the fuel cell stack. Also, principal stresses are estimated for some fragile material components like graphite BP.

Figure 16.7 illustrates these cell's components in a disassembled view and their corresponding stress distribution. There is not a unique scale of stress values. Each component shows how the force is transmitted between end plates. In this example, the dielectric components used here to protect excessive porous component deformation concentrate the load on the lateral edges, because end plate tends to flex in that region due to the applied force, and so it transmits it to other elements. Current collector plates, made with metallic materials, transmit the force in a uniform way because of its rigidity and strength properties. Graphite BP presents a stress concentration in areas where the force is transmitted by the effect of rigid dielectric sheets. The same situation happens on the membrane. Gas diffusion electrodes receive force according to the path of the bipolar plate's flow channels (GFF).

### 16.2.4 Materials Trend in Fuel Cell Technology

The mechanical effects on fuel cells are of interest to designers, for example, the material interaction between various subsystems and components has been extensively reviewed elsewhere (see monographs by [6–10] and [11] related to these topics and considerations in FC design). Such effects are very relevant aspects for the competitiveness of the technology, including performance, safety, durability, and



**Fig. 16.7** Stress's distribution on the fuel cell's components

cost. It is important to mention that each fuel cell stack design should include a mechanical analysis to determine stress distributions during operation of the fuel cell; moreover thermal aspects and dynamic operation influence on material behavior should be included in a thorough analysis in order to ensure integrity and performance as specified. As seen from Fig. 16.5, new approaches in PEM fuel cells include metallic components and new designs that require less conventional structures like in the case of the Toyota fuel cell, where the GFF is provided through a metal 3D mesh. Such changes are taken into consideration as the mechanical response of a mesh structure is totally different compared with a solid continuous material when a more conventional GFF is used.

### 16.3 Bipolar Plates

In the last 20 years, there have been changes in the basic design of fuel cell stacks regarding materials used for their construction. Perhaps the one with more impact from the mechanical point of view has been the substitution of graphite-based bipolar plates by metallic alternatives. These changes have taken a long time as

the role BP should play within the stacks is very demanding mechanically, electrically, and chemically, and therefore the solution required has been very challenging. The BP should electrically connect single cells and provide means for feeding reactants and get rid of the unwanted excess water. These two requirements mean that BP should have great electrical conductivity and be unreactive to the gases used, i.e., hydrogen and air, therefore oxygen, as well as to deionized water. They should be resistant to corrosion and be manufactured by conventional technologies to decrease costs. Metallic BPs have been seen for several years as the logical substitutes for graphite-based plates as they have good electrical properties, are mechanically strong, and have a general low permeability to reactants at the low pressures found in practice in an operating fuel cell, and their manufacturability is well known and established. Unfortunately, BP is also exposed to conditions in which they should perform well without affecting their other properties. An example of this is the fact that they should be corrosion resistant and good electric conductors, but if the first property fails, corrosion products such as oxides will no longer conduct as their metallic precursor. The fuel cell stacks have liquid deionized water that enters into contact with the BP and are often working under oxidant conditions due to the high electrical potentials on the cathode side. That is why these conditions require that the BP be corrosion resistant while at the same time maintaining good electrical conductivity, two properties that are usually not compatible in most cost-effective metals. Some low-cost solutions are possible and have recently been introduced in the form of metallic BP in FC stacks. Some fuel cell developers have used metallic plates that undergo a surface treatment to make them corrosion resistant and at the same time good conductors; this has been the case of stainless steels often coated by a protective yet conductive film. Although this has been introduced in some products, developers have discovered that some ions that result from minor oxidation become unwanted contaminants. Although gold has been used as a protective and conductive coating, titanium is often used as in the case of Toyota's fuel cell stack where a film layer of carbon coating,  $\pi$ -conjugated amorphous carbon (PAC) is applied on the metal. This substitution should be taken into consideration from the mechanical and from the general component properties' point of view. Metallic plates have better mechanical properties, but also their thermal properties are better compared to their counterparts made of graphite. Although considered a heavier material, metallic plates can be made thinner than their graphite counterparts, as they have higher mechanical strength. One important property associated with such mechanical advantage is the fact that metallic BP is a lot stiffer than graphite plates, which are more fragile, a property that has forced developers to make thicker graphite BP. The thinner metal BP allows the increase in energy and power density of fuel cell stacks and systems making them more competitive in many applications.

Some characteristics of the BPs have been published as technical targets. The goal is to keep the fuel cell operation in a safe way with an enhanced performance. Table 16.1 shows some technical targets published by the US Department of Energy [12].

It is important to highlight that bipolar plates add about 80% of the fuel cell weight and 30% or 40% of the total cost [13], and it may consume up to the 90% of total volume of the stack [14]. The use of alternative materials also alters these figures so



**Table 16.1** Technical targets: bipolar plates for transportation applications

Characteristics	2015 status	2020 target
Cost (\$/kW <sub>net</sub> )	7	3
Plate weight (kg/kW <sub>net</sub> )	<0.4	0.4
Plate H <sub>2</sub> permeation coefficient (Std cm <sup>3</sup> /(sec × cm <sup>2</sup> Pa) @ 80 °C, 3 atm 100% RH)	0	1.3 × 10 <sup>-14</sup>
Corrosion, anode (μA/cm <sup>2</sup> )	No active peak	<1 and no active peak
Corrosion, cathode (μA/cm <sup>2</sup> )	<0.1	<1
Electrical conductivity (S/cm)	>100	>100
Area-specific resistance (ohm cm <sup>2</sup> )	0.006	<0.01
Flexural strength (MPa)	>34	>25
Formal elongation (%)	20–40	40

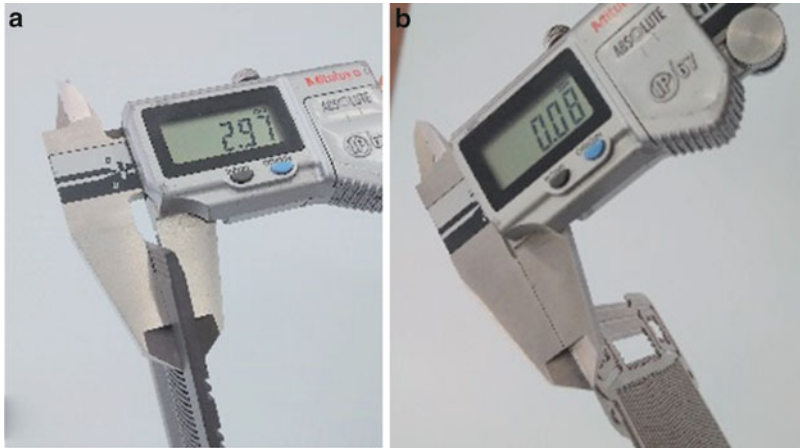
any developer's consideration as to improve mechanical properties and fulfill other BP requirements should also maintain performance and costs industry targets.

### 16.3.1 Conventional Materials

#### 16.3.1.1 Composite Graphite and Metallic

The graphite plates have been for many years the most widely used material in PEMFC. These materials have been considered because they provide good chemical resistance and good thermal and electrical conductivity [15] and their manufacture process is well known. However, graphite plates present some undesirable features such as their brittleness and poor mechanical strength and traditionally a high manufacturing cost. BP volume is usually an issue because the regular thickness of the graphite plates, used in PEMFC stacks, is between 2.5 and 4 mm, as shown in Fig. 16.8a. It means that a stack of 100 membrane electrode assemblies could be at least 25 cm or 40 cm high. The metallic plates, to some extent, can be considered as next-generation components and therefore conventional materials. More than a decade ago [16], these materials were considered as the best alternatives for increasing the power density and reducing the manufacturing cost in PEMFC. However, as mentioned before metals are more susceptible to corrosion that can adversely affect the fuel cell performance.

In its *Hydrogen and Fuel Cells Program Record on Fuel Cell System Cost 2016* (Record # 16020), the DOE reexamines state-of-the-art materials and manufacturing process of BP. The report found that metal BP design and required stamping force for its GFF result in a substantial increase in press tonnage increasing manufacturing capital cost from \$530 k to \$2.1 M. This also results in a decrease in the stamping rate, affecting production volume, and an increase in tooling costs from \$100 k to \$660 k/die. The typical thickness of a metallic material varies between 0.08 and 0.16 mm, as shown in Fig. 16.8b. Therefore, a fuel cell stack composed of metallic bipolar plates is between 15 and 50 times smaller than a stack composed of graphite plates.



**Fig. 16.8** Bipolar plates: (a) graphite, (b) metallic

## 16.3.2 New Tendencies in BPs

### 16.3.2.1 Coated Materials

The BP coating materials can be used to address concerns arising from potential low conductivity and fast corrosion of bare metallic bipolar plates. The aim of coating BPs is not only to decrease the negative effects of corrosion but also to increase the fuel cell power density (using metallic BPs) as well as the fuel cell mechanical performance. Table 16.2 presents the most common coating materials used in metallic bipolar plates [17].

Stainless steel is one of the most popular metals for the manufacture of coated metallic BPs, as it features good mechanical properties, low costs, and well-known machining process to make it a preferred candidate to many developers.

### 16.3.2.2 Carbon-Based Composites Materials

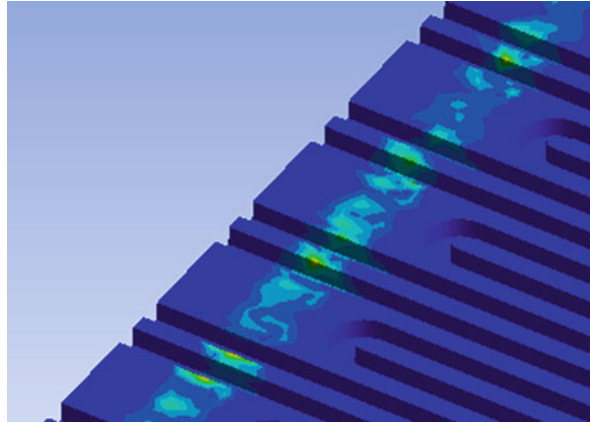
Composites materials can be considered as a polymer binder with a filler component for structural reinforcement. The polymers used in the building process of bipolar plates may be divided into two categories, thermoset and thermoplastic. Thermoset is more brittle than thermoplastics. At high temperatures, more than 120 °C, thermoset can maintain the dimension and thermal stability better than thermoplastics. The category of thermoset BP has been described in the literature as bipolar plates manufactured using materials such as epoxy, phenolic, and vinyl ester [18]. Due to their high viscosity, thermoplastics are usually less suitable than thermosets because they can incorporate fewer amounts of fillers than thermoset resins. However, the associated shorter synthesis time coupled with a solvent-free fabrication process can overcome this material disadvantage. The most popular thermoplastic used on bipolar plates is polypropylene. A low-cost material combines good processing

**Table 16.2** Coating materials used in bipolar plates

Base plate material				
Metallic BP↓	Aluminum	Stainless steel	Titanium	Nickel
Coating material(s)	x			
Conductive polymer		x		
Chromium		x		
Chromium nitride	x			
Diamond-like carbon	x		x	
Gold		x		
Gold-titanium		x		
Gold-nickel	x		x	x
Graphite foil	x	x	x	x
Graphite topcoat	x			
Indium tin oxide		x		
Lead oxide		x		
Nickel		x		
Niobium	x			
Organic mono polymer			x	
Platinum		x		
Silicon carbide		x		
Silver		x		
Silver-PTFE	x			
Titanium-aluminum		x		
Titanium nitride oxide		x		
Zirconia		x		

conditions and mechanical properties. There are thermoplastic polymers used on bipolar plates, i.e., polyvinylidene fluoride  $[-(C_2H_2F_2)_n-]$ , polyphenylene sulfide  $((C_6H_4S)_n-)$ , polyethylene  $[-(C_2H_4)_x-]$ , polyphenylene oxide  $[C_6H_4O)_n-]$ , nylon  $[-(CH_2)_6-]$   $[-(CH_2)_4-]_n$ , and liquid crystalline materials. Polymers are good electrical insulators; however, there are two kinds of fillers used to increase the conductivity. One is based on metallic conductors and the other is derivatives of carbon. Natural graphite could be converted to expanded graphite by using a muffle oven at a temperature higher than 800 °C. Expanded graphite could reach a conductivity of  $12,500 \text{ S} \cdot \text{cm}^{-1}$  [18]. Carbon fibers, like graphite, present a high aspect ratio, which helps in strengthening and increases stiffness to the material, while conductivity is sacrificed. The carbon black is another form of elementary carbon. Its form is like pellets, which are  $100 \mu\text{m} \times 2 \text{ mm}$  in size. The electrical conductivity is higher than with carbon fibers. The low mechanical properties are the material limitation. Carbon nanotubes (CNTs) consist of tubular structures having a diameter of  $1 \times 50 \text{ nm}$  and of length of 1 mm to few centimeters. The CNTs have a density similar to that of graphite with higher mechanical properties. However, CNTs are more expensive fillers than the DOE criteria for bipolar plates ( $<5 \text{ \$/kW}$ ). Graphene

**Fig. 16.9** Stress distribution on graphite bipolar plate ribs



has excellent mechanical and electrical conductivity properties and it is known as one of the strongest material ever tested [18], but as with CNTs, its high manufacture costs constraints its use in mass production of BPs.

### 16.3.3 Distribution Stress in Bipolar Plates

The main function of the bipolar plates is to supply the reactant gases to the gas diffusion electrode through the flow channels. In addition, electric current flows through BPs in order to close the electric circuit in the fuel cell stack. A normal force is applied to the bipolar plates not only to confine the gases in the flow channel's volume but also to assure the electric contact. The graphite bipolar plates are commonly used with a special consideration regarding their fracture point. This specific task could be complicated to deal with, due to the brittle and weak properties of graphite material when that is the used material. Figure 16.9 shows how stress distribution could present on graphite bipolar plates. This stress distribution was obtained by finite element analysis (FEA) software.

The stress distribution is highly concentrated on the ribs of the bipolar plate as it is complicated to get soft edges through the machining process. This stress concentration could provoke cracks on the bipolar plate or small fractures at the edges. These drawbacks could be overcome if metallic bipolar plates are manufactured. The machining process of metallic plates is easier than graphite plates. The machining process on metallic plates produces soft edges. The stronger nature of metallic bipolar plates allows reducing the plate thickness, while the stress distribution along the BP maintains safety levels.

### 16.3.4 Mechanical Characterization of Bipolar Plates

According to the DOE [19], there are two basic mechanical parameters to take into account in bipolar plates: first is the flexural strength that is an established parameter

considered on the DOE technological target list. The second is the tensile strength that is on the way to be considered by DOE [19]. These parameters are obtained through standardized methods. The method to be used depends upon the bipolar plate material and dimension. For example, the specification test conditions that need to be met for consideration of a viable application to the DOE are listed below. All of these targets will most likely need to be met by the DOE 2020 target list:

- ASTM D790-10 Standard Test Method for Flexural Properties of Unreinforced and Reinforced Plastics and Electrical Insulating Materials
  - Determination of flexural properties of unreinforced and reinforced plastics formed as rectangular bars molded directly or cut from sheets, plates, or molded shapes
- ASTM D638-14 Standard Test Method for Tensile Properties of Plastics
  - Materials as unreinforced and reinforced plastics in a test specimen are dumbbell-shaped. Pretreatment condition as temperature, humidity, and machine speed is defined. Testing materials of thickness up to 14 mm
- ASTM E8/E8M-16a Standard Test Methods for Tension Testing of Metallic Materials
  - This method covers the tension testing of metallic materials in any form at room temperature. It is a method of determination of yield strength, yield point elongation, tensile strength, elongation, and reduction of area.

---

## 16.4 Proton Exchange Membrane

### 16.4.1 PEM Structure

The proton exchange membrane (PEM) materials for fuel cells have been extensively researched to improve endurance, performance, and cost to be able to make fuel cells an affordable technology for clean electrical energy production. Recent works have focused on improving the material's thermal, mechanical, and chemical stability associated with operating conditions in the fuel cell. Up to recently, Nafion<sup>®</sup> from DuPont (based on  $[(C_7HF_{13}O_5S \cdot C_2F_4)_x]$ ) was considered the most stable and efficient PEM for the fuel cell market. Nafion<sup>®</sup> is a perfluorosulfonic acid (PFSA) membrane and is a copolymer formed of a chemical polytetrafluoroethylene ( $-(C_2F_4)_n-$ , PTFE)-based backbone providing rigidity and dimension stability; meanwhile, its sulfonic side ( $-HSO_3F-$ ) chains add flexibility and water sorption to the ionomer. The conductivity of Nafion for proton transport has improved in the last years with the reduction of membrane thickness, reaching values of 50  $\mu\text{m}$  and even as low as 25  $\mu\text{m}$  thick; yet, despite extensive research, the membrane mechanical strength is poor. The thin membranes are prone to fast degradation due to chemical and mechanical mechanisms creating pinholes, cracks, shorting, etc. Its water content and temperature resistance limit the conductivity of Nafion. It is known that the presence of water is essential to conduct protons through the Nafion membrane. The higher the membrane water content, the greater the conductivity.

**Table 16.3** DOE technical targets for polymer electrolyte membrane

Durability		2015 status	2016 status
Mechanical	Cycles until $>15 \text{ mA/cm}^2 \text{H}_2$ crossover <sup>a</sup>	23,000 <sup>b</sup>	20,000
Chemical	Hours until $>15 \text{ mA/cm}^2$ crossover or $>20\%$ loss in OCV	742 <sup>b</sup>	$>500$
Combined chemical/mechanical	Cycles until $>15 \text{ mA/cm}^2$ crossover or $>20\%$ loss in OCV	–	20,000

<sup>a</sup>For air or N<sub>2</sub> testing, an equivalent crossover metric of 0.1 sccm/cm<sup>2</sup> at a 50 kPa pressure differential, 80 °C, and 100% RH may be used as an alternative

<sup>b</sup>Reinforced and chemically stabilized PFIA membrane. M. Yandrasits et al. (3M), US Department of Energy Hydrogen and Fuel Cells Program 2015 Annual Progress Report

In addition, Nafion has a glass transition temperature at 120 °C; therefore, the temperature range for ensuring durability is always below 100 °C. The variations of water concentration during fuel cell operation produce Nafion to swell and shrink, with the consequential mechanical stress for the constant dimensional change. This water uptake in PFSA is determined by a number of hydrophilic sites in the polymeric chain, as defined by the ion exchange capacity (IEC) of the ionomer. The Nafion membrane can be mechanically reinforced and chemically stabilized in the form of Nafion XL. The composite offers a 20-fold longer lifetime, over unreinforced Nafion. The reinforcement is added by a microporous PTFE support layer, and the stabilizers are silica-based additives on the membrane surface. This arrangement promotes lower water uptake and shrinkage, lowering the mechanical tension by dimensional changes occurring by the temperature and humidity cycles. The plastic properties of the PTFE reduce the crack initiation that is frequent in the unreinforced Nafion [20]. The major technical barriers related to PEM development are related to its durability, cost, and performance. The technical targets for PEM proposed by the DOE are summarized in Table 16.3 [21].

According to the DOE's project proposed for "New fuel cell membranes with improved durability and performance," the main objectives were to produce chemical and mechanically improved membranes using polymer technology based on multi-acid side chain ionomers and electrospun nanofiber structures to obtain reinforced membranes. The chemical stability was planned to be enhanced with peroxide scavenging additives. The reports from this project indicated that the performance and durability of the perfluoroimide  $[-(\text{CF}_2)_2\text{n}-(\text{CF}_2 - \text{C})\text{n}]_n$  where  $\text{X} = -\text{O}(\text{CF}_2)_4 - \text{O}_3\text{S} - \text{NH} - \text{O}_3\text{S} - (\text{CF}_2)_3\text{OHO}_3\text{S}$ , PFIA)-based membrane were according to the expected, with 14-mm-thick membranes with exceptional proton conductivity [21].

### 16.4.2 Mechanical Properties of Commercially Available PFSA

Numerous research reports regarding the mechanical properties for PFSA demonstrate the effect the different stressors have on these types of materials within operational fuel cells. Below is a brief account of these reports that are presented

for a variety of the most common ionomers found in the market. The quantification of the measured mechanical properties, the analysis techniques used, and the correlation of materials properties with degradation phenomena are discussed to give an overview of the fuel cell operating conditions that conduce to a longer lifetime.

The mechanical and chemical degradation processes are the main cause of early failure in the membrane, and their prevention is key step to guarantee longer operational lifetime. Regarding the mechanical aspect, the membrane undergoes dimensional variations produced by hygrothermal cycling during fuel cell operation. These cycles occur as a response to the power demand the fuel cell receives, as shown in the graph of Fig. 16.1. In self-humidified fuel cells, when the current density increases, there is more heat and water produced increasing the swelling of the membrane. In the low power demand mode, dehydration and shrinking of the membrane will frequently occur. The hygrothermal cycles thus give rise to the main mechanical failures of the membrane producing cracks and pinholes and, eventually, gas crossover and short-circuiting. Within the fuel cell, the constrained membrane develops large in-plane stresses during swelling, causing permanent plastic deformation. Then, during shrinking, the stress from the deformation develops tensile residual stress, which, in some occasions, causes the membrane to reach tensile yielding [22, 23]. The mechanical and chemical attack can also occur in combination. The chemical degradation occurs as result of mechanical compression. It is believed that the membrane strain energy alters the molecular energy of the polymer chain weakening the attack-site bonds. Chemical attacks then occur especially at high potentials or when the fuel cell operates in idle (open circuit voltage) mode for long periods. Under this mode the chemical damage to the membrane is faster than the mechanical damage from thermocycling [24, 25]. Several studies have shown that PFSA-based membranes become flexible with an increase in temperature and water sorption up to 50 °C. The mechanical behavior of Nafion-117<sup>®</sup> has been reported by means of differential scanning calorimetry (DSC) and dynamic mechanical analysis (DMA). These tests determined the effect of temperature and water activity on Nafion mechanical properties [32]. In temperatures below 50 °C ca., water produces a plasticizing effect on the membrane. By measuring tensile creep on Nafion 1110, under constant load and controlled temperature and water activity, it was confirmed the plasticizing effect of water over the membrane, from room temperature up to 40 °C. Above 50 °C, when water activity was increased, the creep decreased, confirming that the membrane became stiff in a first stage; but further increase of water activity increased the creep. Table 16.4 illustrates the plasticizing effect of water in Nafion; Young's modulus [ $E = (F/A)/(\Delta L/L_0)$ ] (where  $F$  is the force exerted on an object under tension;  $A$  is the actual cross-sectional area through which the force is applied;  $\Delta L$  is the amount by which the length of the object changes; and  $L_0$  is the original length of the object) is also shown. Young's modulus ( $E$ ) changed from 249 to 114 MPa, when the water activity is increased at 23 °C. The elasticity goes further down to 64 MPa when the temperature was increased to 100 °C and the membrane is fully saturated. In addition, temperatures above 50 °C can result in membrane stiffening as opposed to plasticization. This reversal of plasticity above 50 °C may be due to formation of a network of

**Table 16.4** Comparison of mechanical properties as function of temperature and RH on commercial PFSA membranes and MEAs (Adapted from [26–28])

Membrane	Conditions	Yield strength		Maximum tensile strength (MPa)			Elastic modulus (MPa)			Elongation at break		Notes
		MD <sup>a</sup>	TD <sup>b</sup>	MD	TD	TD	MD	TD	MD	TD	TD	
Nafion	Dry <sup>c</sup>			29.8		24.7						d
Nafion 115, 117, 110	23 °C, 50% RH			43		32		249		22	5	e
Nafion 115, 117, 110	Water soaked, 23 °C			34		26		1	14	20	0	e
Nafion 115, 117, 110	Water soaked, 100 °C			25		24		64	18	0		
Nafion	23 °C, 50% RH	14.4	14.0	30.5		28.0		272	253	253	235	e
NR-111	80 °C, 100% RH	4.4	4.6	8.9		9.5		23.9	25.1	159	188	e
Aquivion	23 °C, 50% RH	9–13	9–13	20–40		20–35				90	200	e
E79-03S												
Gore-Select	Dry <sup>c</sup>			34.4		23.9						d
Gore-Select	25 °C, 50% RH <sup>f</sup>	19		43		49		560	490	120		e
MEA	25 °C, 50% RH	8.5 ± 0.6	8.7 ± 0.5	22.5 ± 1.7		24.1 ± 1.1		223 ± 11	244 ± 33			e

<sup>a</sup>MD machine direction<sup>b</sup>TD transverse direction<sup>c</sup>Oven dried<sup>d</sup>[27]<sup>e</sup>[26]<sup>f</sup>Values approximated from graphs provided<sup>g</sup>[28]



hydrophilic clusters within the polymer and then stabilized by hydrogen bonding. Bauer et al. found that at low humidity, the OH strength bonds in Nafion resemble those of bulk water; in the medium range, from 50% to 80%, the bonding strength decreased and then increased with higher humidity to reaching the maximum above 50 °C [29, 30]. For dry Nafion, the tensile creep strain measurements with a fixed load and controlled environment were carried out to find a transition occurring between 80 and 100 °C producing the elastic modulus to decrease and creep to increase [31]. The authors mentioned the possibility of the glass transition temperature ( $T_g$ ) of Nafion being the cause for the Nafion flexibility and creep, although previous investigations have mentioned that Nafion's  $T_g$  occurs at 130 °C, which is higher than the temperatures investigated. It is important to note that when the dry membrane was put in contact with a small amount of water, it showed plasticization with increasing temperature contrary to the theory supporting membrane stiffening.

The improved mechanical properties of the reinforced Nafion XL were probed and showed that the PTFE layers on both sides of the membrane provide higher dimensional stability, especially in the in-plane direction, reducing the swelling-induced stress. This was distinct to the normal (unreinforced) Nafion, membrane, which lacks the additional cross-linking components. The reinforcement in the membrane produces anisotropy in the mechanical properties, as determined using DMA-based testing. The measured storage modulus of Nafion XL resembles that of PTFE, which indicates that the PTFE-based reinforcement dominates the mechanical response of the membrane, where the ionomer has no contribution to the modulus. The Nafion XL showed similar temperature dependence than normal Nafion, and similar transition between 80 and 120 °C, where the value of the storage modulus decreased [20]. Aquivion<sup>®</sup> from Solvay is another perfluorosulfonic acid ionomer that showed higher mechanical strength than Nafion due to its shorter side chains. This membrane possesses similar morphology and higher IEC than Nafion (1.29 vs. 0.91 mequiv g<sup>-1</sup>) and was found to have higher crystallinity [32], which may explain its better mechanical properties (cf. Table 16.4). In dry conditions, Aquivion 850 was found to decrease its elastic modulus [ $\lambda^{\text{def}} = \text{stress/strain}$ ] with increasing temperature, in the same way than Nafion<sup>®</sup> 1000 and 1100. It was found that the thermal transition for Aquivion 850 membrane occurs at ca. 95 °C compared to Nafion<sup>®</sup> 1100 for which its transition temperature is reached at ca. 60 °C [32]. For Aquivion, it was also confirmed the same water doubles function on PFSA leading to membrane plasticizing and later to membrane stiffening. It was also found that below the thermal transition, the water plasticizer effect occurred resulting in increasing creep and decreasing elastic modulus with increased water activity. However, above the transition temperature, the elastic modulus increased and the creep reduced dramatically in the beginning of the water activity ramp. A second reinforced composite perfluorinated PEM, Gore-Select<sup>®</sup>, offers thinner and stronger membranes to either Nafion or Aquivion. When tensile strength tested dry Gore-Select for tensile strength, the polymer showed similar strength than dry Nafion: 23.9 and 24.7 MPa, respectively. However, wet Gore-Select membrane showed lower plasticization than Nafion: 17.7 and 9.5 MPa, respectively. Comparing the tensile strength loss from dry to wet PEMs can be summarized as [27]:

- Nafion: 62% and 53%, respectively, in transverse direction (TD) and machine direction (MD)
- Gore-Select: 26% and 6%, in TD and MD, respectively

From these numbers, it is evident that the reinforced membrane has minimum softening effect by the presence of water, plus maintaining dimensional stability. In other studies, reinforced hydrated perfluorosulfonic acid (PFSA) membranes, Gore-Select, were mechanically tested in controlled environments within the ranges of 25–85 °C and 30–90% *RH*. These tests found that the reinforced membranes have much larger Young's modulus (*E*), limit of proportionality, stress, and break stress than unreinforced PEMs at all temperatures and humidity conditions. Similar to unreinforced PFSA, these properties decrease proportionally with an increase in temperature and humidity, and above 90 °C wet membranes become stiffer [24]. The data in Table 16.4 shows numerical evidence of the improved mechanical properties of the reinforced PFSA from Gore-Select.

### 16.4.3 Assembled Membranes

Studies have shown that restrained PEMs in a fuel cell, receive large in-plane stress during swelling, causing permanent deformation. During unloading, the membrane shrinks and the deformation stress develops tensile residual stress, which can cause tensile yielding [23]. For Nafion<sup>®</sup> 212, subjected to hygrothermal aging, it resulted in an increased modulus and tensile strength with aging [33]. Applying accelerated stress test on Nafion, the membrane became stiffer and more brittle upon humidity cycling. In numerical simulations of stress distribution within a fuel cell stack, the membrane was found to receive up to 27 MPa from a typical clamping pressure of 20 pounds-per-square inch (psi), in the outer area. In experimental measurements, similar stress values were observed even inside the active area, near the border, especially when water is present [2]. From this, the use of a sub-gasket to protect the membrane peripheral is considered critical to reducing the mechanical stress occurring in hygrothermal cycles.

In MEAs, the membrane constrained within the catalyst layers receives mechanical stress especially in the areas of the land of the flow field channels. These stressors cause mechanical fatigue developing cracks on the surface of the catalyst layer, as well as on the membrane. Tensile test performed by [28] on MEAs (Nafion<sup>®</sup> NR211 and Pt/C catalyst layers) confirmed that MEA can be considered isotropic for in-plane direction. Young's modulus obtained for the MEA showed values above the PEMs (210 MPa) indicating that the catalyst layer's Young's modulus is higher than PEMs (cf. Table 16.4). The mechanical tests also probed that MEAs, fabricated under thermomechanical stress, have a dependency on the temperature in the same way that PEMs reduced Young's modulus at increasing temperature and humidity (below 60 °C); but above 80 °C, the presence of water increases Young's modulus. The maximum stress and yield stress decrease with temperature, and rupture strain increases. What differed from PEM, in terms of the magnitude and variation in the

Young's modulus, is the alteration of the value at specific relative humidities (*RH*). In the MEA, *RH* did not alter the last three properties, unlike for the membranes. The mechanical response was independent of the water content for the MEA. It is thought to be due to the constraint caused by the catalyst layers limiting the deformation of PEM at high temperatures [28]. It was also observed that MEA under tensile stress showed crack formation on the surface of the catalyst layer. Under these test conditions, the MEA yielding is reached, as the catalyst layer cannot deform as easily as in the PEM. It was also found that tensile direction had no effect on the strain of the surface crack initiation and low temperature reduced the initiation point. However, using 3D visualization techniques, such as X-ray computed tomography in MEAs, it was found that half of the through-plane cracks occurred only within the membrane structure without connection with cracks in the catalyst layers [34]. This observation, using degraded MEAs by accelerated stress tests (AST), suggests a different mechanism of crack occurrence independent of the molecular movement in the catalyst layer as observed by Kai et al. These MEAs went through a combined mechanical and chemical degradation (AST) in order to reproduce typical voltage and relative humidity cycles imposed by automotive driving patterns on fuel cells.

#### 16.4.4 Alternative Proton Exchange Membranes

In the search for increased mechanical strength and chemical resistance on PEMs, there are reports of different chemical and physical methods to retard mechanical or chemical failure. The goal is to design thinner membranes that are resistant to pinholes, tears, and cracks and to increase performance and durability of PEMs and fuel cells. With thinner membranes, ohmic resistance decreases and water management improves, reducing manufacturing costs. With high-temperature-resistant PEMs, water management-associated failures also decrease. However, the mechanical strength still needs to be improved to warrant durability along expected operational lifetimes. The physical reinforcement also includes incorporation of inorganic materials and stable polymers, such as PTFE, polyimide film, polyethylene, and polyethylene terephthalate ( $[-C_{10}H_8O_4]_n^-$ ), to provide a porous matrix or polyvinylidene fluoride ( $[-C_2H_2F_2]_n^-$ ) or fluorine-containing polyimide ( $[-C_{41}H_{22}N_4O_{11}]^-$ ) as a polymer network. These approaches have probed mostly successful to improve the tensile strength and dimensional stability of PEMs; however, the incorporation of inorganic materials usually reduces the membrane proton conductivity. The reinforcement with polymers has been successful to reduce the liquid fuel crossover in direct alcohol fuel cells [26]. Recently, electrospinning was used to make porous nanofiber mats with the advantage of improved homogeneity and interconnections with an adaptable fabrication technique. Nano-sized inorganic particles, such as carbon nanotubes, binary metal oxides of silica (Si), titanium (Ti), or zirconium (Zr) such as  $SiO_2$ ,  $TiO_2$ , and  $ZrO_2$ , were used as fillers of PEMs in providing higher thermal stability and better water management as the inorganic nanoparticles improve water uptake. The carbon nanotubes were also used as fillers which offer the advantage of increasing the mechanical strength up to 29%,

with as minimum as 1 wt. % of CNT in a composite membrane made with Nafion 212 [35]. The challenges rely on the difficulty to scale up the process as well as to prevent the risk of short-circuiting if the concentration is kept high. Liu et al. also found that keeping the CNT concentration below the percolation threshold, the latter is prevented.

The chemical reinforcement approach relies on implementing cross-linking within the polymeric matrix. This technique is known to improve the mechanical strength of the polymer and can be the ionic or covalent type. Though there are mechanical advantages of the cross-linking, the chemical conditions are not easy to obtain in PEMs. The cross-linking sites must have the linkable functional groups, which require in some cases extensive chemical and thermal treatment to either convert the hydrophilic side chains or the incorporation of the cross-linkable functional groups [36]. The electron beam irradiation and plasma-induced grafting methods are examples of cross-linking techniques applied to polymers such as Nafion or polybenzimidazole ((C<sub>20</sub>H<sub>12</sub>N<sub>4</sub>)<sub>n</sub>, PBI) fiber to improve the membrane mechanical properties reducing the swelling and increasing elastic modulus. In the PBI membranes, the cross-linking resulted in thinner membranes with improved chemical stability to perform in high-temperature fuel cells [37]. To prevent the main degradation mechanism in PFSA's by the radical attack, fluorination of terminal H-containing groups was proposed to increase the durability of PFSA's without change of the tensile strength values; Nafion has shown double lifetime with this technique [38].

Graphene oxide (GO) has been considered a good candidate for nanohybrid PEMs, providing membranes with better mechanical, thermal, and chemical properties. The carbon-based GO provides the membrane with higher proton conductivity via proton hopping mechanism and improves water uptake. The different routes of hybridization for PEM with GO have been proposed. Even further, the GO's mechanical stability can be tuned by chemical grafting of charged functional groups. Graphite oxide (GtO) has been used to improve the PEM mechanical stability via surface modification. The drawback of this modified PEM is the increase in fuel crossover. Another variety with GtO is the paper electrolyte from flake graphite and cellulose acetate membrane (C<sub>6</sub>H<sub>7</sub>O<sub>2</sub>(OH)<sub>3</sub><sup>-</sup>) filter for direct methanol fuel cells [39].

---

## 16.5 Conclusion

The high relevance of mechanical aspects during the design and operation stages of PEM fuel cell technology is necessary to ensure the successful application of an efficient and clean energy system. A fuel cell stack is a very complex system that integrates a series of different components with different properties, which are exposed to mechanical stress from the way they are designed and also under their operating conditions. These aspects together with the environment in which the FC operates impose mechanical dynamics that may bring the hardware to unintended

conditions that may cause failure, earlier degradation, and even unsafe consequences, such as leakage of hydrogen fuel.

The fuel cell technologies are still evolving, and new proposed designs and materials keep bringing new complexities and testing specifications. Further, regimes need to be continually evaluated, including synergies among its components. These proposed changes shall bring improvements in the performance and costs convergence and eventually wide acceptance. Nevertheless, the mechanics related to FC component fabrication, integration, simulation, bench, and laboratory testing needs improvement and refinement to meet real operational constraints related to hours of operation, operating humidity, temperature, feed gases, and environmental fluctuations, in order to give developers the necessary data to develop FC that meet consumer expectations related to FC integrity, reliability, form factor, safety, low cost, and durability.

**Acknowledgments** This work is supported by the Mexican National Council of Science and Technology, CONACyT, through financial assistance to the projects No. 174689 and No. 246018.

---

## References

1. M. Tutuianu, A. Marotta, H. Steven, E. Ericsson, T. Haniu, N. Ichikawa, *Development of a Worldwide Worldwide Harmonized Light Duty Driving Test Cycle (WLTC)*. Technical report, United Nations Economic Commission for Europe (2013), <https://www.unece.org/fileadmin/DAM/trans/doc/2014/wp29grpe/GRPE-68-03e.pdf>. Accessed 14 May 2017
2. J. De La Cruz, U. Cano, T. Romero, Simulation and in situ measurement of stress distribution in a polymer electrolyte membrane fuel cell stack. *J. Power Sources* **329**, 273–280 (2016). <https://doi.org/10.1016/j.jpowsour.2016.08.073>
3. INEEL, Final report project no. 152485 SENER-CONACYT (2016)
4. T. Yoshida, K. Kojima, Toyota MIRAI fuel cell vehicle and progress toward a future. *Hydrogen society. Electrochem. Soc. Interf.* **24**, 45–49 (2015), [https://www.electrochem.org/dl/interface/sum/sum15/sum15\\_p45\\_49.pdf](https://www.electrochem.org/dl/interface/sum/sum15/sum15_p45_49.pdf). Accessed 23 June 2017
5. M. Ahmad, Benchmarking a PEM fuel cell stack compression process. *IREC 2015* (2015), [http://www2.warwick.ac.uk/fac/sci/wmg/education/researchdegrees/eportfolio/wmmbj/research/posters/mussawar\\_ahmad\\_irec\\_2015.ppsx](http://www2.warwick.ac.uk/fac/sci/wmg/education/researchdegrees/eportfolio/wmmbj/research/posters/mussawar_ahmad_irec_2015.ppsx). Accessed 23 June 2017
6. L. Shen, L. Xia, T. Han, H. Wu, S. Guo, Improvement of hardness and compression set properties of EPDM seals with the alternating multi-layered structure for PEM fuel cells. *Int. J. Hydrog. Energy* **48**, 23164–23172 (2016). <https://doi.org/10.1016/j.ijhydene.2016.11.006>
7. Y. Sung-Dae, K. Byun-Ju, S. Young-Jun, Y. Young-Gi, P. Gu-Gon, L. Won-Yong, K. Chang-Soo, K. Yong-Chai, The influence of stack clamping pressure on the performance of PEM fuel cell stack. *Curr. Appl. Phys.* **2**, S59–S61 (2010). <https://doi.org/10.1016/j.cap.2009.11.042>
8. A. Batex, S. Mukherjee, S. Hwang, S.C. Lee, O. Kwon, G.H. Choi, S. Park, Simulation and experimental analysis of the clamping pressure distribution in a PEM fuel cell stack. *Int. J. Hydrog. Energy* **38**, 6481–6493 (2013). <https://doi.org/10.1016/j.ijhydene.2013.03.049>
9. Y. Tang, M.H. Santare, A.M. Karlsson, S. Clegghorn, W.B. Johnson, Stresses in proton exchange membranes due to hygro-thermal loading. *J. Fuel Cell Sci. Technol.* **3**(2), 119–124 (2016). <https://doi.org/10.1115/1.2173666>
10. A. Evren-Firat, *Mechanical Analysis of PEM Fuel Cell Stack Design* (Cuvillier Verlag, 2016), [https://cuvillier.de/uploads/preview/public\\_file/9927/9783736992573\\_Leseprobe.pdf](https://cuvillier.de/uploads/preview/public_file/9927/9783736992573_Leseprobe.pdf). Accessed 24 June 2017

11. A.R. Maher, A.-B. Sadiq, A parametric study of assembly pressure, thermal expansion, and membrane swelling in PEM fuel cells. *Int. J. Energy Environ.* **7**(2), 97–122 (2016), <https://doi.org/article/0dd6b13f2c244d62b7e82a748fd6e44e> Accessed: 24 June 2017
12. US Department of Energy DOE, 2016 fuel cells section: 3.4 fuel cells (2016), [https://www.energy.gov/sites/prod/files/2016/06/f32/cto\\_myrd\\_fuel\\_cells\\_0.pdf](https://www.energy.gov/sites/prod/files/2016/06/f32/cto_myrd_fuel_cells_0.pdf). Accessed 24 June 2017
13. E. Planes, L. Flandin, N. Alberola, Polymer composites bipolar plates for PEMFCs. *Energy Procedia* **20**, 311–323 (2012). <https://doi.org/10.1016/j.egypro.2012.03.031>
14. A. Iwan, M. Malinowski, G. Pasciak, *Renew. Sust. Energy. Rev.* **49**, 954–967 (2015). <https://doi.org/10.1016/j.rser.2015.04.093>
15. A. Heinzel, F. Mahlendorf, C. Jansen, *Bipolar Plates* (University of Duisburg–Essen, Duisburg, 2009), <http://booksite.elsevier.com/brochures/ecps/PDFs/BipolarPlates.pdf>. Accessed 24 June 2017
16. X. Zi-Yuan, H. Wang, J. Zhang, D. Wilkinson, Bipolar plates for PEM fuel cells – from materials to processing. *J. New Mater. Electrochem. Syst.* **8**, 257–267 (2005), <http://www.groupe.polymtl.ca/jnmes/modules/journal/index.php/content0390.html>. Accessed 24 June 2017
17. K. Shahram, F. Norman, R. Bronwyn, F. Foulkes, A review of metallic bipolar plates for proton exchange membrane fuel cells: materials and fabrication methods. *Adv. Mater. Sci. Eng.* **2012**, 1–22 (2012). <https://doi.org/10.1155/2012/828070>
18. R. Taherian, A review of composite and metallic bipolar plates in proton exchange membrane fuel cell: materials, fabrication, and material selection. *J. Power Sources* **265**, 370–390 (2014). <https://doi.org/10.1016/j.jpowsour.2014.04.081>
19. P. Beckhaus, *Characterization of Composite and Metallic Bipolar Plates*, ZBT GmbH (Fuel Cell Research Center) (Germany, 2011). [http://www.zbt-duisburg.de/fileadmin/user\\_upload/01-aktuell/05-publikationen/05-vortraege/2011/hfc2011-beckhaus-tuesday-17-bpp.pdf](http://www.zbt-duisburg.de/fileadmin/user_upload/01-aktuell/05-publikationen/05-vortraege/2011/hfc2011-beckhaus-tuesday-17-bpp.pdf). Accessed 1 May 2017
20. S. Shia, A.Z. Weber, A. Kusoglu, Structure/property relationship of Nafion XL composite membranes. *J. Membr. Sci.* **516**, 123–134 (2016). <https://doi.org/10.1016/j.memsci.2016.06.004>
21. US Department of Energy, DOE, DOE technical targets for polymer electrolyte membrane fuel cell components (2015), <https://energy.gov/eere/fuelcells/doe-technical-targets-polymer-electrolyte-membrane-fuel-cell-components>. Accessed 14 May 2017
22. A. Kusoglu, A.M. Karlsson, M.H. Santare, S. Cleghorn, W.B. Johnson, Mechanical response of fuel cell membranes subjected to a hygro-thermal cycle. *J. Power Sources* **161**, 987–996 (2006). <https://doi.org/10.1016/j.jpowsour.2006.05.020>
23. A. Kusoglu, A.M. Karlsson, M.H. Santare, S. Cleghorn, W.B. Johnson, Mechanical behavior of fuel cell membranes under humidity cycles and effect of swelling anisotropy on the fatigue stresses. *J. Power Sources* **170**(2), 345–358 (2007). <https://doi.org/10.1016/j.jpowsour.2007.03.063>
24. H. Tang, S. Peikang, S. Jiang, F. Wang, M. Pan, A degradation study of Nafion® proton exchange membrane of PEM fuel cells. *J. Power Sources* **170**, 85–92 (2007). <https://doi.org/10.1016/j.jpowsour.2007.03.061>
25. A. Kusoglu, M. Calabrese, A.Z. Weber, Effect of mechanical compression on chemical degradation of Nafion membranes. *ECS Electrochem. Lett.* **3**(5), F33–F36 (2014). <https://doi.org/10.1149/2.008405eel>
26. S. Subianto, M. Pica, M. Casciola, P. Cojocaru, L. Merlo, G. Hards, D. Jones, Physical and chemical modification routes leading to improved mechanical properties of perfluorosulfonic acid membranes for PEM fuel cells. *J. Power Sources* **233**, 216–230 (2013). <https://doi.org/10.1016/j.jpowsour.2012.12.121>
27. M. Wilson, S. Zawodzinski, A. Thomas, S. Gottesfeld, *Advanced Composite Polymer Electrolyte Fuel Cell Membranes*. Proceedings of the First International Symposium on Proton Conducting Membrane Fuel Cells I Electrochemical Society Proceedings (1995), <http://>

[citeseerx.ist.psu.edu/viewdoc/download?doi=10.1.1.465.3459&rep=rep1&type=pdf](https://citeseerx.ist.psu.edu/viewdoc/download?doi=10.1.1.465.3459&rep=rep1&type=pdf).

Accessed 1 May 2017

28. Y. Kai, Y. Kitayama, M. Omiya, T. Uchiyama, M. Kato, Crack formation on membrane electrode assembly (Mea) under static and cyclic loadings. in *ASME 2012 10th International Conference on Fuel Cell Science, Engineering and Technology Collocated with the ASME 2012 6th International Conference on Energy Sustainability* (2012), FUEL CELL 2012, pp. 143–151. <https://doi.org/https://doi.org/10.1115/FuelCell2012-91164>
29. F. Bauer, S. Denneler, M. Willert-Porada, Influence of temperature and humidity on the mechanical properties of Nafion<sup>®</sup> 117 polymer electrolyte membrane. *J. Polym. Sci. B Polym. Phys.* **43**, 786–795 (2005). <https://doi.org/10.1002/polb.20367>
30. M. Laporta, M. Pegoraro, L. Zanderighi, Perfluorosulfonated membrane (Nafion): FT-IR study of the state of water with increasing humidity. *Phys. Chem. Chem. Phys.* **1**, 4619–4628 (1999). <https://doi.org/10.1039/A904460D>
31. P.W. Majsztzik, A.B. Bocarsly, J.B. Benziger, Viscoelastic response of Nafion. Effects of temperature and hydration on tensile creep. *Macromolecules* **41**, 9849–9862 (2008). <https://doi.org/10.1021/ma801811m>
32. Q. Zhao, J. Benziger, Mechanical properties of perfluoro sulfonated acids: the role of temperature and solute activity. *J. Polym. Sci. Part B Polym. Phys.* **51**, 915–925 (2013). <https://doi.org/10.1002/polb.23284>
33. S. Shi, G. Chen, Z. Wang, X. Chen, Mechanical properties of Nafion 212 proton exchange membrane subjected to hydrothermal aging. *J. Power Sources* **238**, 318–323 (2013). <https://doi.org/10.1016/j.jpowsour.2013.03.042>
34. Y. Singh, F. Orfino, M. Dutta, E. Kjeang, 3D visualization of membrane failures in fuel cells. *J. Power Sources* **345**, 1–11 (2017). <https://doi.org/10.1016/j.jpowsour.2017.01.129>
35. Y.H. Liu, B.I. Yi, Z.G. Shao, D.M. Xing, H.M. Zhang, Carbon nanotubes reinforced Nafion composite membrane for fuel cell applications. *Electrochem. Solid-State Lett.* **9**, A356–A359 (2006). <https://doi.org/10.1149/1.2203230>
36. W. Ma, C. Zhao, J. Yang, J. Ni, N. Zhang, H. Lin, J. Wang, G. Zhang, Q. Li, H. Na, Crosslinked aromatic cationic polymer electrolytes with enhanced stability for high-temperature fuel cell applications. *Energy Environ.* **5**, 7617–7625 (2012). <https://doi.org/10.1039/C2EE21521G>
37. S. Lai, J. Park, S. Cho, M. Tsai, H. Lim, K. Chen, Mechanical property enhancement of ultra-thin PBI membrane by electron beam irradiation for PEM fuel cell. *Int. J. Hydrog. Energy* **41**, 9556–9562 (2016). <https://doi.org/10.1016/j.ijhydene.2016.04.111>
38. D.E. Curtin, R.E. Lousenberg, T.J. Henry, P. Tangeman, M.E. Tisack, Advanced materials for improved PEMFC performance and life. *J. Power Sources* **131**, 41–48 (2004). <https://doi.org/10.1016/j.jpowsour.2004.01.023>
39. R. Pandey, G. Shukla, M. Manohar, V. Shahi, Graphene oxide based nanohybrid proton exchange membranes for fuel cell applications: an overview. *Adv. Colloid Interf. Sci.* **240**, 15–30 (2017). <https://doi.org/10.1016/j.cis.2016.12.003>
40. Y. Tanaka, TOYOTA's next generation vehicle strategy and Fuel Cell Vehicle MIRAI's Development, Product Planning Toyota Motor Corporation (2015), <http://www.taia.or.th/home/media/file/49923981428457602.pdf>. Accessed 23 June 2017





# Recent Progress on the Utilization of Nanomaterials in Microtubular Solid Oxide Fuel Cell

# 17

Mohd Hilmi Mohamed, Siti Munira Jamil,  
Mohd Hafiz Dzarfan Othman, Mukhlis A Rahman, Juhana Jaafar,  
and Ahmad Fauzi Ismail

## Contents

17.1	Introduction .....	498
17.2	Fabrication Method of MT-SOFC .....	498
17.2.1	Preparation of Spinning Suspensions .....	500
17.2.2	Phase Inversion-Based Co-extrusion Technique .....	503
17.2.3	Co-sintering Process .....	504
17.3	Nanoparticle Inclusion in MT-SOFC .....	506
17.4	Intermediate-Temperature System Using Ceria Gadolinium Oxide (CGO) Electrolyte .....	507
17.5	High-Temperature System Using Ytria-Stabilized Zirconia Electrolyte .....	510
17.6	Summary .....	513
	References .....	514

## Author Contributions

Mohd Hilmi Mohamed wrote the manuscript with input from all authors and contributed to the final version of the manuscript. Siti Munira Jamil carried out the experiment, wrote the manuscript, and contributed to the final version of the manuscript. Siti Halimah Ahmad carried out the experiment and wrote the manuscript. Mohd Hafiz Dzarfan Othman devised the project, the main conceptual ideas, and proof outline. He also supervised the project, discussed the results, and contributed to the final manuscript. Mukhlis A Rahman, Juhana Jaafar, and Ahmad Fauzi Ismail helped supervise the project, discussed the results, and contributed to the final manuscript.

M. H. Mohamed · S. M. Jamil · M. H. D. Othman (✉) · M. A. Rahman · J. Jaafar · A. F. Ismail  
Advanced Membrane Technology Research Centre, Universiti Teknologi Malaysia, Johor,  
Malaysia

Renewable Energy Research Group, Department of Energy Engineering, Faculty of Chemical and  
Energy Engineering, Universiti Teknologi Malaysia, Johor, Malaysia

e-mail: [hafiz@petroleum.utm.my](mailto:hafiz@petroleum.utm.my)



---

**Abstract**

This chapter describes the method of producing hollow fiber for a microtubular solid oxide fuel cell (MT-SOFC) using nanomaterial-based structures. This chapter focuses on the utilization of yttrium-stabilized zirconia (YSZ) and cerium-gadolinium oxide (CGO) nanomaterials for high and intermediate working temperatures of MT-SOFC, respectively. The chapter then discusses the nanomaterial available and a number of attempts to produce the nanomaterial for the electrolyte. Then, the advantages of using nanomaterial are also discussed. Finally, this chapter concludes the future of nanomaterial for MT-SOFC and its future challenges.

---

**17.1 Introduction**

The microtubular solid oxide fuel cell (MT-SOFC) is a breakthrough in the SOFC research due to its robustness to thermal shock, ease of sealing, and longer stability. The tubular shape is a cylindrical tube consisting all electrodes attached as a unit cell. The MT-SOFC can also be found operating at various temperatures with high power output. These features enable further development of SOFC in stationary and portable power applications, particularly when nanomaterial is a part of the SOFC fabrication systems [1]. The rationale for using nanomaterials in FC applications is due to their large surface area which leads to an increase in FC performance, a decrease in the conductivity, and an increase in the triple phase boundaries (TPB) [2]. This chapter summarizes the fabrication procedure of MT-SOFC and the utilization of nanomaterial-based components in an MT-SOFC to extend device robustness, ruggedness, operation at lower temperatures, and improved catalysis through better gas channeling.

---

**17.2 Fabrication Method of MT-SOFC**

Among many types of SOFC configuration, the planar design is the design of the most active research by investigators. The geometry of the planar consists of the electrode being attached to each other. The planar electrode comes in many sizes as long as they fit into the reactor casing. All electrodes are attached together as a unit cell. The fuel is channeled to the anode and air to the cathode compartments. The electrolyte separates the two electrodes and provides for charge mobility. The planar configuration is generally fabricated via tape casting method. Each electrode adheres via multiple steps of sintering. The planar configuration has been developed by several companies such as Siemens, Westinghouse, and Sulzer Hexis. The high power output from the electrode-based FCs and simplicity of fabrication make the planar configuration ripe for commercialization. Besides the planar geometry, FCs can also be configured with tubular and microtubular configurations.

Recently, a review of the recent fabrication techniques for anode-supported MT-SOFCs has been published [3]. The review analyzed the most common methods associated with fabrication, namely, the plastic mass ram extrusion method and the dry-jet wet extrusion method which was adopted from the fabrication method of polymeric membranes. Preliminary research led by Sammes and separately led by Suzuki laid the foundations to employ the plastic mass extrusion method in fabricating MT-SOFCs, whereas recent work by Li further refined fabrication of MT-SOFCs using dry-jet wet extrusion technique. For the ram extrusion technique, the anode materials are mixed overnight with a polymer binder, and an organic solvent to form a mass or viscous paste is formed. Prior to extrusion, a vacuum is applied to the paste in order to remove air trapped inside the mass. Then, the paste is extruded through a custom-made die using ram extruder to obtain the support tubes. The support tubes are dried and cut to the desired length before transforming to a stronger fiber by sintering process [4].

The main difference between the fabrication methods is that the spinning suspension or dope for the dry-jet wet extrusion is in liquid form, whereas for the ram extrusion, it is in paste or plastic mass form. Another major difference between the fabrication methods is the solidification process of the tube (or hollow fiber). In dry-jet wet extrusion, the solidification of the hollow fiber occurs via phase inversion process initiated by the solvent/non-solvent exchange, while in ram extrusion process, the tube is dried straightaway after the extrusion prior to the sintering. For dry-jet wet extrusion, the suspension is firstly prepared from the anode material mixture, an organic solvent, and a polymer binder, prior to the suspension extrusion through an extruder called spinneret to obtain hollow fiber shape. Bore fluid or internal coagulant is passed through at the center of the spinneret to form the hollow precursor. Then, the precursor free-falls into a non-solvent external coagulant bath to allow solidification process via solvent/non-solvent exchange, where the process commonly known as phase inversion [1]. These exchanges encourage the precipitation of the polymer in suspension and hold the ceramic materials in the desired configuration [2]. Finally, the hollow fiber support is dried and cut to specific length before subjected to sintering and reduction processes. The different fabrication methods of anode substrate would result in different anode structures [5]. For example, the mass ram extrusion technique generally produces a symmetrical structure of anode tubes [6], while dry-jet wet extrusion technique creates anode hollow fibers with an asymmetric structure [7]. The symmetric and asymmetric structures demonstrate the homogeneous and heterogeneous morphology, respectively.

In symmetric structures, microscopic pores are formed during the reduction of NiO to Ni which is distributed uniformly in the anode as viewed by cross-sectional examination of the anode. An advantage of this type of uniform dispersion is that the generated pores yield high resistance for gas transportation through the layer [3, 8]. Thus, some researchers had added degradable pore-forming agent such as graphite [9, 10] and polymethyl methacrylate (PMMA) beads [11] into the anode suspension in order to induce the macro-size pore in anode substrate during the sintering process. The artificial pore-forming agents should be chemically stable toward solvent so that the pore former will remain in its original shape after the extrusion process. The generated particles will be burnt off during the thermolysis

stage of the sintering process and consequently leave pores intact in the sintered tubes. In contrast, the solidification process through phase inversion in dry-jet wet extrusion system has led to the formation of the asymmetric structures consisting of fingerlike and spongelike regions. The resultant fingerlike structures enhance the permeability and the flow of fuel and reaction products, while spongelike structures intensify the mechanical strength and give high Ni particle continuity [12]. If structural control is one of the limitations of ram extrusion, the flexibility of dry-jet wet extrusion on producing desired morphology in anode structures can be achieved by simple adjustment of fabrication parameters such as additive loading in the suspension, air gap, and flow rate of bore fluid.

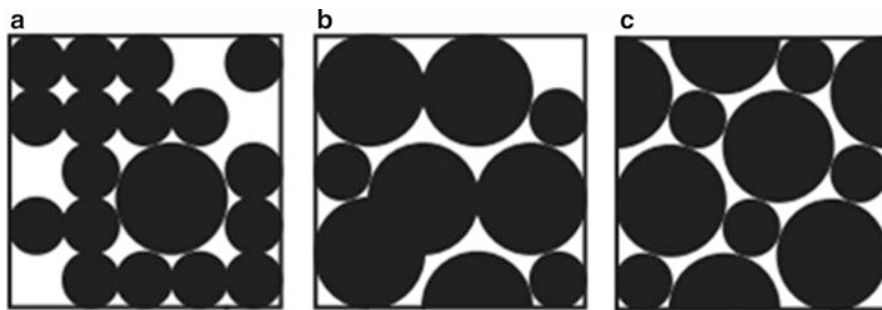
This approach can be extended in the fabrication of multilayer hollow fiber through multiple cycles creating a layer-by-layer deposition. A support layer is first developed to provide mechanical strength to the membrane and followed by fabrication of final separation layer after coating one or more intermediate layers on the support layer [4, 10]. After the fabrication of each layer, the anode electrode must undergo high-temperature heat treatment which requires time, money, and technician with expertise in the use of high-temperature furnaces [7]. By combining these steps into a single step, the fabrication process is simplified and greatly reduced associated costs, processing times, and expertise of the individual carrying out the procedures [13]. Li had employed the dry-jet wet extrusion technique for fabrication of anode-supported dual-layer hollow fiber by combining the phase inversion-based co-extrusion technique and co-sintering process. Two spinning suspensions are separately prepared and simultaneously co-extruded through a triple-orifice spinneret before undergoing the co-sintering process. The dual-layer anode-supported i.e., NiO-Ce<sub>0.9</sub>Gd<sub>0.1</sub>O<sub>1.95</sub>, in Ce<sub>0.9</sub>Gd<sub>0.1</sub>O<sub>1.95</sub> (NiO-CGO/GCO) has been successfully fabricated via this method, and cathode layers were then deposited onto the substrate to construct MT-SOFCs for intermediate-temperature applications. The resultant hollow fiber produced the maximum power densities of 450 Wm<sup>-2</sup> and 800 Wm<sup>-2</sup> at temperatures of 450 °C and 550 °C, respectively.

The phase inversion-based co-extrusion and co-sintering methods consist of three main steps, where each step plays a significant role in the production of desired hollow fiber:

- (i) Formation of particle suspensions by preparing anode and electrolyte spinning suspensions
- (ii) Packing of particle suspensions into a dual-layer hollow fiber precursor using phase inversion-based co-extrusion process
- (iii) Consolidation of dual-layer hollow fiber precursor by a heat treatment at a high temperature a process known as co-sintering

### 17.2.1 Preparation of Spinning Suspensions

A spinning suspension is a viscous mixture (or in liquid form) which consists of ceramic particles, solvent, a polymer binder, and additives, where each material



**Fig. 17.1** Schematic of random dense packing of (a) excessive small ceramic particles and (b) excessive large ceramic particles and (c) optimal packing where the small spheres fill all voids in large ceramic particle packing (Fig. 2.13 from Li et al., with permission. License # 4152300651973) [15]

composition has various influences on the resultant suspension. In order to prepare a spinning suspension, several steps are involved: (1) dissolution of dispersant with solvent, (2) addition of ceramic particles into the mixture, (3) disaggregation by ball milling of the suspension, (4) addition of polymer binder followed by re-milling, (5) addition of pore-forming agent followed by re-milling (for preparation of the anode suspension), and (6) degassing the suspension dope prior to the extrusion process. A ball milling machine with continuous rotary function is used to prevent agglomeration of particles in the spinning suspension. The major constituent of the typical anode and electrolyte spinning suspensions for the ceramic material contains around 50–70 wt. % out of the total suspension. In the high-temperature SOFC system, yttria-stabilized zirconia (YSZ) is widely used as an electrolyte ceramic material because of its availability, it is reasonable in price, and it can withstand at high operative temperature. The ceramic particle size is one of the important factors that greatly affect the dispersion and viscosity due to the particle packing principle and also influence the porosity and densification of fabricated fiber [14]. Figure 17.1 schematically illustrates the random dense packing when two different sizes of ceramic spheres are mixed. Thus, it is no longer possible to achieve high packing density because of the mismatch between quantities of small particles and the larger clusters since most of the voids become filled or partially filled leaving some voids which cannot be fully occupied. The optimal void filling may be achieved as long as the proportion of the smaller particles is sufficiently great such that the large particles are always in contact with three neighboring particles [16].

Tan reported a difficulty when using smaller particle diameter (i.e., 0.01  $\mu\text{m}$ ) of ceramic material during the preparation of spinning suspension [17]. Instead of becoming a dope solution, the suspension turned to ceramic paste when using the 0.01  $\mu\text{m}$  diameter particles either as particles alone or as a binary mixture of ceramic/binder at low binder mass %. The ultrafine powders promoted agglomeration during milling and mixing process. This is because the presence of a large surface area of small particles results in the formation of a suspension with less fluidity causing aggregation during the spinning procedure. Therefore, it is advisory to blend the

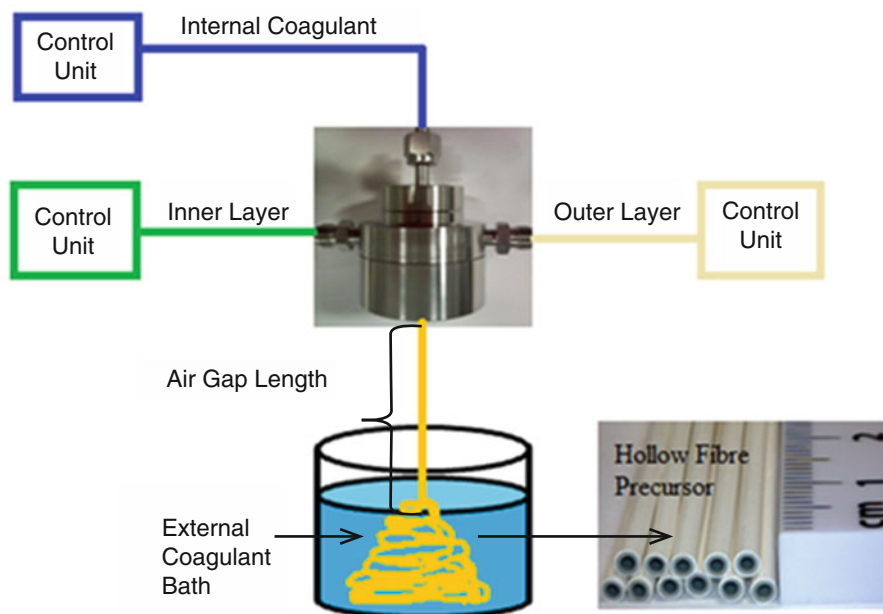
small particle diameter with particles of a large diameter in sufficient ratio to make a desirable spinning suspension. Besides preparing a suspension with spinnable properties, the suspensions should also be mixed sufficiently to ensure that YSZ particles are wholly surrounded by the binder. In phase inversion technique, the binder plays a vital role as it affects the viscosity of suspension and the solidification process of a hollow fiber. Although the binder is completely removed from the fiber body after undergoing high heat treatment, its inclusion does influence anode morphology and robustness. In addition to the use of a sacrificial binder, the pore-forming agent will also undergo pyrolysis and consequently be removed, although it will promote pore formation into the sintered fiber, prior to its removal. Tan also studied the effect of different ceramic/polymer ratios to pore size and porosity of hollow fibers [18]. They indicated that the pore size and surface porosity decreased as the ratio of ceramic/binder increased, promoting material density. Thus, in the fabrication of dense electrolyte layer, higher ceramic YSZ loading in electrolyte suspension must be maintained. At high loading, reduction in gas permeability is tailored through adjustment of the ceramic/binder ratio to promote the transformation of the material to a much denser structure. However, if the ratio of ceramic/binder is greater than 9 mol %/mol %, the experimental results revealed that it was hard to form a hollow fiber precursor due to inconsiderable viscosity during extrusion/co-extrusion processes. Most of the binders are long-chain polymers that dissolve in the polar solvent. The interaction between polymer binder and solvent determines the solidification of the polymer. Solvents used in the dry-jet wet extrusion technique must exhibit a high exchange rate with non-solvents or coagulants because the rates of solvent outflow and coagulant inflow also affect the morphology of the hollow fiber. The morphology of hollow fiber can be confirmed by characterizing using scanning electron microscopy (SEM).

A report done by Othman revealed the effect of the presence of solvent and non-solvent in a spinning dope [12]. The most common polar solvent is dimethyl sulfoxide (DMSO, 46.7 F/m) which has high freezing point and was empirically shown to inhibit the formation of fingerlike overgrowth of voids in the material when compared with more nonpolar solvents such as N-methyl-2-pyrrolidinone (NMP, 32.2 F/m) with water having a polarity index value of 80.1 F/m, indicating that NMP is more nonpolar than DMSO, while the addition of ethanol (24.5 F/m) as non-solvent in the mixture caused the formation of thick spongelike layers as ethanol increased the initial mixture volume and accelerated the precipitation of polymer binder during phase inversion [2]. In general, around 20–40 wt. % of solvent would be needed and very little amount of dispersant (0.1–1.5 wt. %) in the spinning suspension. The dispersant is used to improve the dispersion effect as it depends on the ability of dispersant to break the surface interaction between particles to allow them to remain separate. Finally, the preparations of spinning suspensions are considered complete after going through the degassing process. A degassing procedure is an essential step to remove any gas bubbles that may have been trapped during the milling process to prevent the incorporation of gas bubbles into hollow fiber structure [19]. The bubbles may cause defects in the fabricated fiber and lead to cracking during sintering. The simplest technique for degassing is under an applied

vacuum accompanied by gentle stirring. Several considerations in terms of rotation time, rotation speed, pump suction power, and tightness of the system are also important because it may alter the viscosity of the final suspension.

### 17.2.2 Phase Inversion-Based Co-extrusion Technique

The anode and electrolyte spinning suspensions will undergo a co-extrusion process in the presence of bore fluid (or known as non-solvent internal coagulant) to form a dual-layer hollow fiber precursor. The term “precursor” is used for extruding the hollow fiber before sintering that is comprised of ceramic material, a polymer binder, and dispersant. Figure 17.2 illustrates the flow of the co-extrusion process, where the components of the inner and outer suspensions and bore fluid are co-extruded simultaneously through specific small openings of the triple-orifice spinneret. The bore fluid is then passed through at the center of the spinneret to produce hollow side along the middle of the fiber. For anode-supported hollow fiber, an anode suspension is directed as the inner suspension, whereas the electrolyte suspension is directed as the outer suspension. As a result, a thin electrolyte outer layer supported by a thick anode inner layer is formed. The dual-layer hollow fiber travels vertically downward into non-solvent external coagulant bath where it forms a coil. A parameter such as extrusion rates (inner, outer, and bore fluid) and dimension of spinneret mostly



**Fig. 17.2** Schematic diagram of phase inversion-based co-extrusion process (Adapted from Fig. 17.1 from Othman et al., with permission. License # 4154670599480)

affects the resultant thickness of layers. While the bore fluid, external coagulant bath plays a great role in the final morphology, other factors also influence final form, such as the air gap which enables the production of controlled microstructures during formation of the hollow fiber.

Furthermore, operational conditions of spinneret are essential to the final form of the anode and need to be carefully controlled for uniform anode generation between batches. For instance, by keeping the spinneret temperatures at or lower than room temperature (i.e., 25 °C), interlayer diffusion phenomenon is inhibited resulting in the fabrication of a more robust electrode. The lower spinneret temperature also modulation of the viscosity of extruded dope to be maintained at a higher degree which in turn will reduce the diffusion rate of polymer molecules between two layers and increase electrode robustness [20]. For polymeric membrane, the interlayer diffusion in the dual-layer hollow fibers (HFs) is desired since it could enhance the adhesion between the layers. However, in ceramic membrane especially for SOFC application, the interlayer diffusion must be prevented because this can reduce the cell efficiency by the short-circuiting condition. During the co-extrusion process, the same concept of solvent/non-solvent exchange in dry-jet wet extrusion is applied to solidify the dual-layer hollow fibers. When the inner suspension attained high viscosity, the suspension is immediately administered with bore fluid (non-solvent). The generated binary mixture is hydrodynamically unstable due to the mismatch between their viscosities resulting in fingerlike morphologies being formed.

The resulting fingerlike formation on the inner surface alters the intrinsic porosity of the electrode but may assist with gas diffusion. When the phase inversion is complete, there is no solvent/non-solvent exchange, which in turn inhibits the viscous fingering phenomenon. Based on the results obtained by [21], 50–70% of fingerlike voids in anode layer can be considered as an ideal structure for producing high-performance MT-SOFCs with high gas diffusivity. The dense structure is required for the outer electrolyte layer instead of an asymmetric structure in anode layer. Based on this requirement, an air gap is set as high as 15 cm [20] to eliminate the fingerlike formations on the outer surface of hollow fiber. This is because the external surface of the nascent fiber experienced solvent evaporation and absorption of water moisture from the air, both of which will induce the solidification of the outer surface. It takes place before immersing the nascent fiber into the external coagulation bath, hence minimizing the viscous finger-type formation. But, spinning the suspension at too high, an air gap may interrupt (i.e., break off) the flow of nascent fiber due to the gravitational force. Table 17.1 summarizes factors that affect fiber properties.

### 17.2.3 Co-sintering Process

The co-sintering process is a high-temperature process where heat is treated to two different layers (i.e., anode and electrolyte layer) together in a furnace to develop the desired microstructure. During the process, a powder compact of the components is



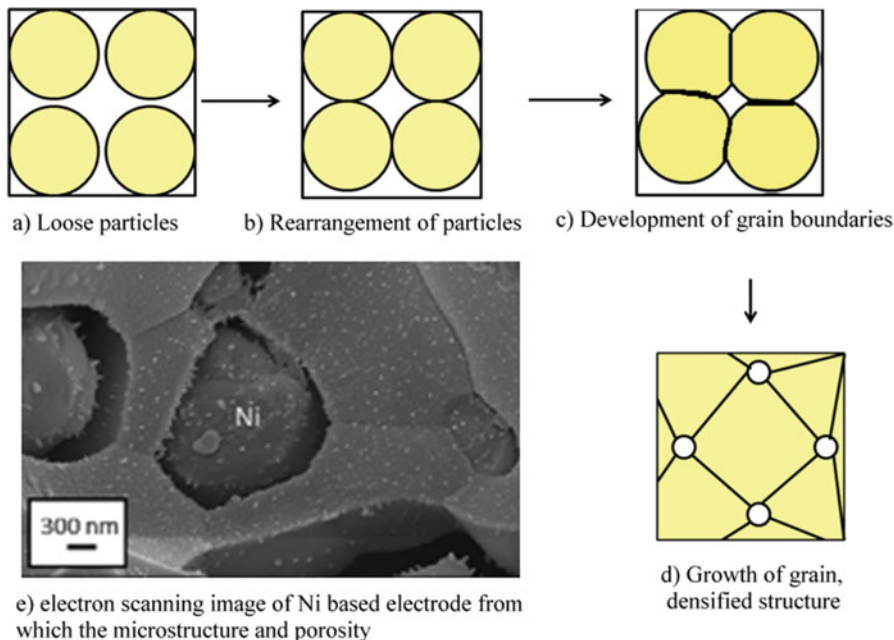
**Table 17.1** Features and influences of phase-inversion-based co-extrusion step to the fabricated hollow fiber properties

Features	Influences
Viscosity/homogeneous of suspension	Uniformity (bore shape)
Particle size/distribution	Particle packing density
Flow rate (inner suspension/outer suspension/bore fluid)	Morphology of precursor (dense/porous)
Air gap	Structure of precursor (symmetric/asymmetric)
Humidity and temperature of experiment	Thickness, dimensions, length of precursor
Dimension and condition of spinneret	Viscosity/homogeneous of suspension
Temperature (internal/external coagulant)	Pore diameter/morphology
Temperature of suspension	Pore density

fabricated that can transform into a strong and dense ceramic fiber without melting the fiber. There are three major stages of co-sintering the dual-layer hollow fiber precursor, (1) pre-sintering, (2) thermolysis, and (3) final sintering. The basic mechanism of sintering of ceramics is also applied to the co-sintering dual-layer hollow fiber. At pre-sintering stage (around 200 °C), the residual liquid that may remain after the co-extrusion process and any moisture adsorbed in the precursor is removed. The temperature is further increased at a low heating rate to prevent any cracks or fractures within the fiber. As the temperature rises to 800 °C, the thermolysis process can take place. During this period of time, organic compounds such as a binder, pore-forming agent, and dispersant will be sacrificed. The removal of the pore-forming agent will eventually leave pores without the cross-links. These two stages in fiber formation are important to be controlled because incomplete organic compounds removal and uncontrolled thermolysis may produce defects in the hollow fiber. The final stage of sintering is achieved at a temperature as high as 1400 °C. The structures of the ceramic particles undergo rearrangements, and later grain boundaries start to form. The ceramic particles will then bind together and form pore channels along the grain edges. The pores continue shrinking and some of them pinch off and become isolated at the grain corners as the temperature increases. Therefore, some of the spongelike structure that is formed during the phase inversion process become smaller and eliminated. As a consequence of their removal, the initial regions of spongelike morphology become densified and eventually become gas tight [22]. A potential nucleation and fiber formation mechanism can be proposed by observing the stages of the densification of ceramic particles as illustrated in Fig. 17.3.

As a result, the porosity of the fiber was greatly reduced after sintering due to the reduction of the pore quantity and pore size [24]. Such a structure is highly dependent on particle sizes and composition of spinning suspension besides the sintering effect. The smaller particle size diameter results in the fabrication of a much denser structure resulted from the higher shrinkage during the sintering process. However, in most of the cases, macrostructure of the precursor formed during the phase inversion process. The macrostructures which are formed as the result of the





**Fig. 17.3** Various stages (a–d) of sintering where ceramic microstructure is developed, including (e) electron scanning image of Ni based electrode from which the microstructure and porosity can be visualized (Part 3e (this work) from (b) insert from Liu et al., with permission license # 4152271238771) [23]

removal of pore-forming agent during the pre-sintering stage remain after lower-temperature sintering. The macrostructures generated form fingerlike voids which cannot be eliminated, although at high sintering temperature the probability is negligible relative to lower-temperature processes [22]. In addition to the influence of pore-forming agent on pore densities, the sintering temperature and sintering duration also play important roles in the process related to pore formation or elimination in hollow fibers. When the temperature or the duration of sintering process increases, the porosity of the fiber will significantly decrease, resulting in higher resistance to gas flow, but at the same time, the increase in porosity will also dramatically improve the mechanical strength of the fiber [24]. Therefore, it is vital to find suitable sintering temperature range that gives sufficient strength and permeation for fiber to be fabricated into a module without cracking.

### 17.3 Nanoparticle Inclusion in MT-SOFC

The fabrication of fibers of nanosize dimensions yields mechanical and electrical properties that are different from fibers at micrometer or greater dimension. These very small dimensions promote uniqueness and clean energy for SOFC. The

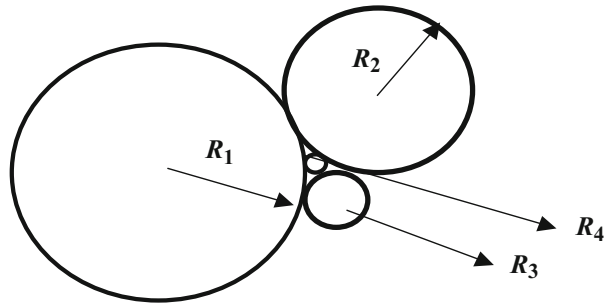
nanosize materials exhibit greater surface area leading to reaction area, oxygen vacancies, and reduction sites, due to a greater degree of reactive edges relative to bulk materials. The needs of developing nano-electrolyte were mostly due to the densification issue. The previous study had demonstrated that the electrolyte densification is dependent upon the diameters of the electrolyte composite material. The increase in material density is usually achieved by sintering at high temperatures [22]. Therefore, the nanomaterial-based electrolyte promotes the densification of the electrolyte at a lower temperature. The nanomaterial does not only facilitate to enhance the cell performance but also provides the reduction in the operating temperature. High operating temperature halted the development because of the fast degradation and poor reliability. Therefore, the option of lowering the sintering temperature can enable the generation of higher-density composite electrodes, without any unwanted chemical reactions between the cell components and degradation of the material. However, the reduction of temperature has its own drawbacks. The electrode polarization is also lost at sintering at lower temperatures. The performance of SOFC is affected by the morphology of the electrode. Nanomaterial-based materials have demonstrated improved performance from the current micro-sized electrodes by providing a channel for facile charge transfer. The charge transfer of the corresponding nanomaterial-based electrodes is thus greater due to the higher surface area. When the materials exhibit a grain size of  $<100$  nm, reaction area is increased as well as charge transfer. The anode (NiO) is in close proximity to the electrolyte material; if composed of nanomaterial, the reaction rate is increased, although the limiting factor in reaction rate is the availability of oxidants. Therefore, increasing the number of an oxygen ion, in turn, increases the reaction rate [2]. This chapter will focus on the application of the performance of SOFC using anodes sintered using the nanomaterial composites at two different temperature ranges, to facilitate the generation of different morphologies and pore densities. The nano-composite occurs after synthesis of the anode, from which the power density of the FC is determined and compared with anodes constructed using macro-sized materials.

---

## 17.4 Intermediate-Temperature System Using Ceria Gadolinium Oxide (CGO) Electrolyte

By lowering the sintering temperature a relatively high density of sintered for porous nickel (Ni)/ceria gadolinium oxide (CGO) anodes. The other advantage of lowering the CGO sintering temperature is a reduction of the processing cost and time and improved batch-to-batch fabrication consistency, due to avoidance of excessive grain coarsening, but also because it may serve as a solution to face the challenge in the SOFC fabrication during the fabrication process. The phase inversion method has been modified as the co-extrusion/co-sintering technique to prepare dual-layer microtubular SOFC. In this method, two layers of anode and electrolyte are generated in single step [20]. Thus, the sintering behaviors of the two layers must be synchronized to avoid the formation of cracks or defects during the high-temperature

**Fig. 17.4** The void at a three disk junction which is just filled by a touching disk of radius  $R_4$  (Fig. 2.12 from Li et al., with permission. License # 4152300651973) [15]

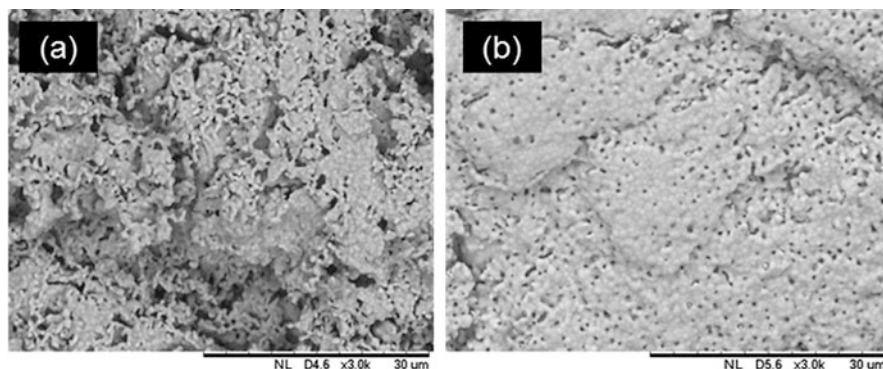


co-sintering. Hypothetically, there are several factors that can influence the sintering behavior and densification of ceramic particles. These include the size and shape of the powder particles, the porosity and initial density of the body, as well as chemical factors such as dopant content, impurities, and sintering additives [25–28]. The current problems are uneven densification and pore size, as well as varied morphologies, which contribute to material strain and lower power densities generated by the FC device. Since the last decade, many researchers have attempted to reduce the sintering temperature of the CGO composite to reduce these fabrication inconsistencies. Some improvements were achieved by using different powder preparation methods such as coprecipitation and hydrothermal method to synthesize active nanosize CGO powders [29–32]. However, the complex powder synthesis step with low yield and high cost makes it challenging for scalable practical applications with high batch-to-batch reproducibility. Hence, one approach is a systematic study to determine material computability to fabricate nanoparticle starting powder, which by virtue of their increased surface area contributes toward higher FC power densities [25, 33]. Theoretically, the smaller particle diameter introduced into the bulk packing will fill the voids without increasing the total number of beds to a higher degree when compared with micron-sized particles, resulting in the generation of materials with more homogeneous zones. Over the past 30 years, several studies have been conducted to look at two-dimensional structures using the disk and sphere synthesis approach [34]. The researchers demonstrated that the ratio of the particle diameter and composition of the mixture were the main factors that influenced material layering phenomenon in CGO fabrication. The ratio of the particle size determines the coordination number on the packaging of the highest packing density and is illustrated in Fig. 17.4, which is the optimal parameter to promote the most effective packing improvement and electrode material robustness.

Three existing disk apparatus have a radius consisting of three rotating disks of  $R_1$ ,  $R_2$ , and  $R_3$ . The fourth disk,  $R_4$ , has an intermediate radius and is in contact with the other disks. The effective packing consisting of particles with two distinct radii can be calculated as follows:

$$\frac{1}{R_4} = \frac{1}{R_1} + \frac{1}{R_2} + \frac{1}{R_3} + 2 \left[ \frac{1}{(R_1 R_2)} + \frac{1}{(R_1 R_3)} + \frac{1}{(R_2 R_3)} \right]^{1/2} \quad (17.1)$$

For the most effective packing improvement, the added particle should just touch the three adjacent particles. If the three large disks are equal in size,  $R_4$  was predicted to have a radius of 1/6.464 or 0.1547 (dimensionless unit) of the large disk radius, with the coordination number of three. As long as the proportion of the smaller spheres is sufficiently greater than the smaller sphere, the proportion of large spheres could reach a stage at which they touch each other resulting in an optimal packing. When there is a mismatch between the quantity and diameters of the two particles, such as an overabundance of the smaller diameter particles, the voids and filled and further addition will cause the larger particles to become too heavy and further addition will no longer increase the packing density. Li [15] sketched the basic behavior for a random dense packing in Fig. 17.3, which shows that the amount of packaging, called an “optimum” (volume-to-mass ratio), is a function of the composition of the mixture consisting of large and small spheres. It was observed that there was a maximum packing density composition to achieve “optimum.” The relative increase in the packing density depends on the ratio of large and small particle size. The fabrication of nanosize particles was previously demonstrated with the generation of CGO pellets with high densification produced at 1000 °C sintering temperature [35]. The weak agglomerates between the different materials and high crystallinity of the synthesized nanopowders were facilitated by the introduction of nanoparticles. Ruez reported that their synthesized nanopowder possessed excellent sinterability at low temperatures (1250 °C) and short reaction times (<1 h) [36]. Gil generated nano-CGO composite materials by co-sintering the nanosize electrolyte layer that was dip-coated on the NiO-CGO anode support at temperature 1300 °C with 98% relative density and ~10 μm thickness [33]. Glasscock also successfully sintered the CGO pellet at 1400 °C using nanosize CGO as the starting powder [25]. However, the final homogeneity and crystallinity of the as-generated powder are strongly depending on the fabrication technique and fabrication parameters. Nevertheless, most of the literature studies reported increased consistency, reproducibility, and robustness of the anode through the introduction of nanoparticles via pressing technique. To our knowledge, there are no published studies using phase inversion technique particularly in preparing the electrolyte for the microtubular SOFC application. The fabrication and parameterization offered by phase inversion technique, particularly in enabling sintering to be performed at a lower temperature by using nanopowders without compromising on pore density, have advantages of the other fabrication techniques cited in the literature [25, 36]. A study of technical parameters which influence the microstructure and densification temperature of the composite materials would fill a gap in their current literature regarding optimization of fabrication of nanosize CGO-type anode materials. Recently, the sintering temperature for the production of a dense CGO electrolyte layer was successfully lowered by incorporating nanosize CGO [21]. The sintering temperature was lowered to 1450 °C by introducing 30% loading of nanosize CGO. The loading of nanosize CGO (surface area 192 m<sup>2</sup> g<sup>-1</sup>, particle size 60 mesh d<sub>50</sub>) during powder suspension preparation played an important role in the densification temperature of the CGO electrolyte as prepared by phase inversion technique. The precursor of mixed particle size CGO was sintered and compared with the full micron precursors as shown in Fig. 17.5, whereby the zoomed area was focused at the center region of the flat sheet.



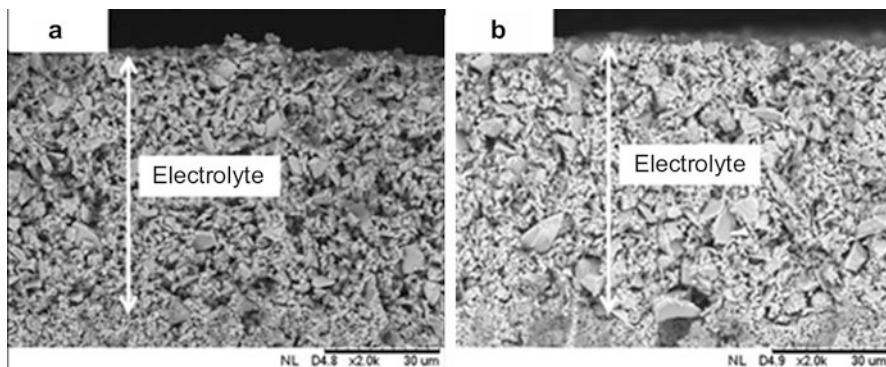
**Fig. 17.5** SEM cross-sectional images: (a) fully micron (b) mixed particle size CGO flat sheet electrolytes sintered at 1450 °C

The scanning electron microscope (SEM) micrographs shown in Fig. 17.5a, b show flat sheet morphology at the micron-sized and mixed particle size CGO sintered at 1450 °C for 12 h, respectively. In these images, newly grown CGO grains were observed. The porosity and pinhole decreased at the sintering temperature of 1450 °C. Besides, the grain boundaries have become gradually clear at this temperature especially in the mixed particle size which were visualized as flat sheet morphologies (Fig. 17.5b). This may be attributed to the existing nanosize particles which demonstrated a high driving force that can increase the rate of densification [25]. While the nanosize particles filled up the porosity, a dense structure was formed in this flat sheet structure. The pores and pinholes of the flat sheet almost disappeared due to homogeneous grain growth. The fully densified CGO with no porosity and cracks are desirable for the electrolytes of SOFCs [6, 22, 24–26].

The powders must achieve optimal packing in order to produce the desired rheology of electrolyte suspension to be compatible with such a technique. It may be concluded that the approach of mixed particle size electrolyte can be utilized as a strategy for reducing the sintering temperature that is both scientifically and technically relevant with an understanding on how to synergize between this approach and the fabrication technique and yield more robust electrodes and increased power densities in SOFCs.

## 17.5 High-Temperature System Using Ytria-Stabilized Zirconia Electrolyte

Even though the research now mainly focuses on reducing operational temperature of SOFC to low and intermediate temperatures, the high-temperature sintering process is the benchmark. This is due to YSZ material lower fabrication costs and greater compatibility to high-temperature sintering (in terms of ionic conductivity and stability at high temperature) as compared to CGO. The physical and chemical



**Fig. 17.6** SEM images of YSZ sintered at 1250 °C (a) without nano-YSZ (b) with the addition of nano-YSZ

properties of YSZ are similar to the CGO anode. The YSZ transport oxygen ion from the cathode to the anode at high temperature. The conductivity of YSZ was higher at the higher sintering temperatures as compared to CGO [37]. Despite the established method of phase inversion, fabrication using bulk materials and the optimal fabrication parameters using nanoparticle materials are still undefined. The behavior of nano-YSZ is not the same as the micron-sized YSZ. While preparing the suspension, the nano-YSZ tends to take longer time due to fine powder properties which is more difficult to get into a suspension. Furthermore, mixing with the micron-sized NiO while preparing suspension is a practical challenge in developing suspensions of uniform viscosity and consistency. This is due to the requirement to generate anode materials of a defined density, which for bulk materials are dependent upon sintering temperatures, heating rate, solvent type, and particle diameter ratio. The relative density of the YSZ composite material at certain sintering temperature exhibits a dense morphology. The pre- and post-sintering temperatures of the YSZ indicated a relative density change from 73% to 93% when sintered at 1250 °C as shown in Fig. 17.6 [38].

The densification at lower sintering temperature is a critical step in obtaining anode material with a high degree of porosity with the appropriate density, which is experimentally shown to generate the highest power densities in the operational FC. The introduction of YSZ mixture of nano- and submicron structures was able to reduce the sintering temperature improving electrode fabrication since the lower sintering temperature was able to reach the triple layer boundary consisting of the anode/electrolyte/cathode without the introduction of overpacking or introduction of different fingerlike morphologies into the electrode structure. The reduction of sintering temperature can reduce the thermal expansion mismatch and speed up batch construction due to the introduction of a single-step fabrication technique. The production of a nano-YSZ also had its own challenges, since the instrument and fabrication parameters to achieve “optimum” are not fully documented. Despite the lack of literature findings on nanosize particles for anode fabrication, a few methods



**Table 17.2** Comparison of anode-supported SOFCs performance

Ref	Year	Anode	Electrolyte	Cathode	Fuel stream	Temp (°C)	OCV (V)	Max. power density ( $\text{Wm}^{-2}$ )
[20]	2009	Ni-CGO	CGO	LSCF-CGO	H <sub>2</sub>	550	0.90	8000
[42]	2010	Ni-CGO	CGO	LSCF-CGO	H <sub>2</sub>	570	0.89	5800
[7]	2011	Ni-CGO	CGO	LSCF-CGO	H <sub>2</sub>	580	0.80	10,000
[43]	2017	NiO-YSZ	YSZ	LSM	H <sub>2</sub>	800	0.90	10,800
[44]	2008	NiO-YSZ	YSZ	LSCF-YSZ	H <sub>2</sub>	800	0.5	1800
[44]	2008	NiO-YSZ	YSZ	LSCF-YSZ	H <sub>2</sub>	800	0.5	1800
[41]	2011	NiO-YSZ	Nano-YSZ	LSM	H <sub>2</sub>	500	0.8	13,400

have been proposed such as hydrothermal, nitrate combustion, spray pyrolysis, and sol-gel method [2], to enable researchers to batch fabricate anodes with the desired consistency have not reached the same threshold as with anodes fabricated using bulk materials. To meet expected SOFC demand, the electrodes will need to be mass produced. At such large-scale production facilities, the reproduction of the electrodes must be at steady state in order to maintain the effectiveness and quality of the powders. In addition, the method must also be of low cost, simple, and efficient. The usage of nano-Ni-YSZ/YSZ/YSZ-LSM (lanthanum strontium manganite) as a unit cell shows the power density ranging from 0.2 to 1.2  $\text{Wcm}^{-2}$  at 600 and 800 °C with hydrogen as the fuel source [39]. The power density obtained was higher than previously reported using micron-sized Ni [40]. The use of nano-YSZ caused an extension of the TPBs, which in turn generated higher conductivity, while maintaining adequate porosity for facile gas diffusion. As mentioned earlier, the nanosize YSZ increased the densification rate as well as the material packing order. The denser electrolyte indicates that there is less fuel crossover and only allowed ions to transport across the electrolyte to generate charge. However, the weak connection of cathode and electrolyte contributed by the low sintering temperature during the fabrication process contributed to the slow oxygen reduction reaction (ORR) and low surface kinetics of YSZ-LSM that are major hurdles toward generating higher power densities for operational FCs. Chao showed that the YSZ electrolyte could achieve 13,400  $\text{Wm}^{-2}$  at 500 °C [41]. The power densities of a number of FC systems are compared and summarized in Table 17.2. This data summarized in Table 17.2 shows that the densified nano-YSZ had high activation energy barrier relative to micron-sized YSZ anodes, which are needed to achieve 11,000  $\text{Wm}^{-2}$  at 800 °C range of power densities. The high open circuit voltage (OCV), another benchmark for FC performance, also indicates that the electrolyte

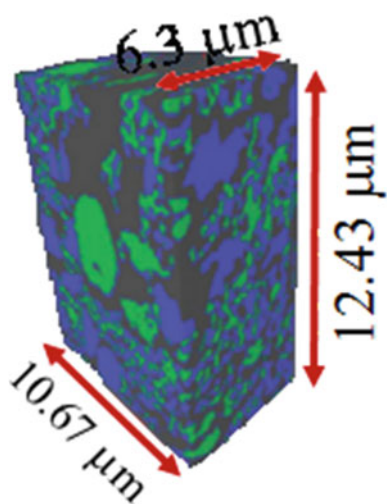
was fully in contact with the electrode within the gas tight membrane surface with minimal fuel crossover, contributing to the higher OCVs or measured power densities.

## 17.6 Summary

The application of nanomaterial in the SOFC is relatively a new area of research as measured by the number of peer-reviewed publications. The nanosize electrolyte enables the operational FC to output higher OCVs when compared with electrolyte and electrodes fabricated using micron-sized particles. The production of an MT-SOFC by phase inversion technique has a number of advantages such as lower production costs, fabrication time, and anode-to-anode fabrication consistency. The single-step fabrication procedure to generate hollow fiber (HF) by simultaneously employing anode and electrolyte suspensions to be able to reduce the sintering steps as advantages that non-expert technicians can be tasked to produce batches that are more reproducible, which in turn will lower overall production costs and facilitate mass commercialization of SOFC for stationary energy applications. The MT-SOFC was able to produce high power densities which increase the likelihood of its adaptation as a future renewable energy device. Although the introduction of nanoparticles in producing hollow fiber, as electrodes within the MT-SOFC, has advantages, the actual instrument and experimental optimum parameters to generate materials with the “correct” pore density, volume, and material fingerlike homogeneity are not fully documented in the literature and need to be empirically defined shown in Fig. 17.7.

The nanomaterial-based electrolyte is likely to enable the power densities of SOFC to exceed current values, which are based on bulk materials if the fabrication

**Fig. 17.7** Reconstructed 3D pore, CGO, and nickel (three different colors) within a  $10 \times 12 \times 6 \mu\text{m}$  cube of a Ni-CGO anode for SOFC after prolonged operation by FIB tomography and sectioning (Fig. 17.3a from Zekri et al., with permission. License # 4152530719706 [45])





parameters can be determined. With the nano-electrolyte, the sintering temperature could be reduced, enabling higher densification to be reached, that in turn enables higher power densities to be attained, although there is no linear correlation between material densification and power density, although both increase relative to each other. The incorporation of nanoparticles also increases the oxygen lattice within the anode, which in turn assists the transport of oxygen ions. This causes the reaction rate to increase with sufficient oxidant and is not the rate-limiting step in overall FC performance. The lowering of the operating temperature also reduces thermal stresses within the fabricated material and prolongs its operational life.

Overall, the addition of nanoparticles to the electrolyte or electrode enables higher power densities to be reached, if the fabrication process can be optimized and sintering temperatures lowered. The added nanoparticles must also be compatible with the materials used in the membrane and electrodes as well as facilitate charge transport to increased FC operational performance. The use of nanoparticle as components for electrolyte has been demonstrated to increase the FC performance by  $\times 3$  when compared with FC operating with micron-sized electrolytes. When the nanosize electrolytes are combined with the MT-SOFC, their improved cell design and increased robustness of the electrolyte can synergistically combine to further increase OCV and FC operability, although technical challenges remain in respect to material computability, optimal fabrication parameters, and charge carrier efficacy.

**Acknowledgments** The authors would like to express their gratitude to Universiti Teknologi Malaysia, Research University Grant Tier 1 (12H25), and UTMSHine Flagship Grant (03G29) for the support and funds.

---

## References

1. T.X. Cai, Y.W. Zeng, W. Zhang, C.J. Guo, X.W. Yang, Synthesis of nanocomposite nickel oxide/yttrium-stabilized zirconia (NiO/YSZ) powders for anodes of solid oxide fuel cells (SOFCs) via microwave-assisted complex-gel auto-combustion. *J. Power Sources* **195**(5), 1308–1315 (2010)
2. S. Zhuiykov (ed.), 7 – Nanostructured semiconductor composites for solid oxide fuel cells (SOFCs), in *Nanostructured Semiconductor Oxides for the Next Generation of Electronics and Functional Devices*, Woodhead Publishing, 321–373 (2014). <https://doi.org/10.1533/9781782422242.321>
3. S.M. Jamil, M.H.D. Othman, M.A. Rahman, J. Jaafar, A.F. Ismail, K. Li, Recent fabrication techniques for micro-tubular solid oxide fuel cell support: a review. *J. Eur. Ceram. Soc.* **35**(1), 1–22 (2015)
4. T. Suzuki, T. Yamaguchi, Y. Fujishiro, M. Awano, Fabrication, and characterization of micro tubular SOFCs for operation in the intermediate temperature. *J. Power Sources* **160**(1), 73–77 (2006)
5. J.H. Lee, J.W. Heo, D.S. Lee, J. Kim, G.H. Kim, H.W. Lee, H.S. Song, J.H. Moon, The impact of anode microstructure on the power generating characteristics of SOFC. *Solid State Ionics* **158** (3–4), 225–232 (2003)
6. H.T. Suzuki, T. Uchikoshi, K. Kayashi, T.S. Suzuki, T. Sugiyama, K. Furuya, M. Matsuda, Y. Sakka, F. Munakata, Fabrication of GDC/LSGM/GDC tri-layers on polypyrrole-coated NiO-YSZ by electrophoretic deposition for anode-supported SOFC. *J. Ceram. Soc. Jpn.* **117** (1371), 1246–1248 (2009)

7. M.H.D. Othman, N. Droushiotis, Z. Wu, G. Kelsall, K. Li, Novel fabrication technique of hollow fiber support for micro-tubular solid oxide fuel cells. *J. Power Sources* **196**(11), 5035–5044 (2011)
8. T. Suzuki, Y. Funahashi, T. Yamaguchi, Y. Fujishiro, M. Awano, Effect of anode microstructure on the performance of micro tubular SOFCs. *Solid State Ionics* **180**(6–8), 546–549 (2009)
9. X.X. Meng, X. Gong, N.T. Yang, X.Y. Tan, Z.F. Ma, Preparation and properties of direct-methane solid oxide fuel cell based on a graded Cu-CeO<sub>2</sub>-Ni-YSZ composite anode. *Acta Phys. Chim. Sin.* **29**(8), 1719–1726 (2013)
10. C.C. Wei, O.Y. Chen, Y. Liu, K. Li, Ceramic asymmetric hollow fiber membranes-one step fabrication process. *J. Membr. Sci.* **320**(1–2), 191–197 (2008)
11. A. Sarikaya, V. Petrovsky, F. Dogan, Effect of the anode microstructure on the enhanced performance of solid oxide fuel cells. *Int. J. Hydrog. Energy* **37**(15), 11370–11377 (2012)
12. M.H.D. Othman, Z. Wu, N. Droushiotis, U. Doraswami, G. Kelsall, K. Li, Single-step fabrication and characterizations of electrolyte/anode dual-layer hollow fibers for micro-tubular solid oxide fuel cells. *J. Membr. Sci.* **351**(1–2), 196–204 (2010)
13. O. Mohd Hafiz Dzarfan, A.R. Mukhlis, L. Kang, J. Juhana, H. Hasrinah, I. Ahmad Fauzi, Ceramic hollow-fiber support through a phase inversion-based extrusion/sintering technique for high-temperature energy conversion systems, in *Membrane Fabrication* (CRC Press, Florida, 2015), pp. 347–382
14. C.Y. Liu, J.Q. Wang, Z.H. Rong, Mesoporous MCM-48 silica membrane synthesized on a large-pore alpha-Al<sub>2</sub>O<sub>3</sub> ceramic tube. *J. Membr. Sci.* **287**(1), 6–8 (2007)
15. K. Li, Preparation of ceramic membranes, in *Ceramic Membranes for Separation and Reaction* (Wiley, 2007), pp. 21–57
16. S.L. Li, S.R. Wang, H.W. Nie, T.L. Wen, A direct-methane solid oxide fuel cell with a double-layer anode. *J. Solid State Electrochem.* **11**(1), 59–64 (2007)
17. X. Tan, K. Li, Inorganic hollow fiber membranes in catalytic processing. *Curr. Opin. Chem. Eng.* **1**(1), 69–76 (2011)
18. X. Tan, S. Liu, K. Li, Preparation and characterization of inorganic hollow fiber membranes. *J. Membr. Sci.* **188**(1), 87–95 (2001)
19. N. Droushiotis, U. Doraswami, D. Ivey, M.H.D. Othman, K. Li, G. Kelsall, Fabrication by co-extrusion and electrochemical characterization of micro-tubular hollow fiber solid oxide fuel cells. *Electrochem. Commun.* **12**(6), 792–795 (2010)
20. N. Droushiotis, M.H.D. Othman, U. Doraswami, Z. Wu, G. Kelsall, K. Li, Novel co-extruded electrolyte–anode hollow fibers for solid oxide fuel cells. *Electrochem. Commun.* **11**(9), 1799–1802 (2009)
21. N.H. Othman, Z. Wu, K. Li, Functional dual-layer ceramic hollow fibre membranes for methane conversion. *Procedia Eng.* **44**(0), 1484–1485 (2012)
22. B.F.K. Kingsbury, K. Li, A morphological study of ceramic hollow fiber membranes. *J. Membr. Sci.* **328**(1–2), 134–140 (2009)
23. B.H. Rainwater, M. Liu, M. Liu, A more efficient anode microstructure for SOFCs based on proton conductors. *Int. J. Hydrog. Energy* **37**(23), 18342–18348 (2012)
24. J. Liu, S.A. Barnett, Operation of anode-supported solid oxide fuel cells on methane and natural gas. *Solid State Ionics* **158**(1–2), 11–16 (2003)
25. J.A. Glasscock, V. Esposito, S.P.V. Foghmoes, T. Stegk, D. Matuschek, M.W.H. Ley, S. Ramousse, The effect of forming stresses on the sintering of ultra-fine Ce<sub>0.9</sub>Gd<sub>0.1</sub>O<sub>2-δ</sub> powders. *J. Eur. Ceram. Soc.* **33**(7), 1289–1296 (2013)
26. Y. Okawa, Y. Hirata, Sinterability, microstructures and electrical properties of Ni/Sm-doped ceria cermet processed with nanometer-sized particles. *J. Eur. Ceram. Soc.* **25**(4), 473–480 (2005)
27. V. Gil, C. Moure Jiménez, J. Tartaj, *Low-Temperature Synthesis and Sintering Behavior of Gd-Doped Ceria Nano Sized Powders: Comparison Between Two Synthesis Procedures*. Síntesis y sinterización de polvo nanométrico de ceria dopado con gadolinia: comparación entre dos procedimientos de síntesis, (2009)

28. M. Han, Z. Liu, S. Zhou, L. Yu, Influence of lithium oxide addition on the sintering behavior and electrical conductivity of Gadolinia doped ceria. *J. Mater. Sci. Technol.* **27**(5), 460–464 (2011)
29. A.I.Y. Tok, L.H. Luo, F.Y.C. Boey, Carbonate co-precipitation of Gd<sub>2</sub>O<sub>3</sub>-doped CeO<sub>2</sub> solid solution nano-particles. *Mater. Sci. Eng. A* **383**(2), 229–234 (2004)
30. D.H. Prasad, H.Y. Jung, H.G. Jung, B.K. Kim, H.W. Lee, J.H. Lee, Single step synthesis of nano-sized NiO–Ce<sub>0.75</sub>Zr<sub>0.25</sub>O<sub>2</sub> composite powders by glycine nitrate process. *Mater. Lett.* **62**(4–5), 587–590 (2008)
31. D.H. Prasad, J.W. Son, B.K. Kim, H.W. Lee, J.H. Lee, Synthesis of the nano-crystalline Ce<sub>0.9</sub>Gd<sub>0.1</sub>O<sub>1.95</sub> electrolyte by novel sol–gel thermolysis process for IT-SOFCs. *J. Eur. Ceram. Soc.* **28**(16), 3107–3112 (2008)
32. D. Hari Prasad, H.R. Kim, J.S. Park, J.W. Son, B.K. Kim, H.W. Lee, J.H. Lee, Superior sinterability of nano-crystalline gadolinium doped ceria powders synthesized by co-precipitation method. *J. Alloys Compd.* **495**(1), 238–241 (2010)
33. V. Gil, J. Gorauskis, R. Campana, R.I. Merino, A. Larrea, V.M. Orera, Anode-supported microtubular cells fabricated with gadolinia-doped ceria nanopowders. *J. Power Sources* **196**(3), 1184–1190 (2011)
34. H.H. Kausch, D.G. Fesko, N.W. Tschoegl, The random packing of circles in a plane. *J. Colloid Interface Sci.* **37**(3), 603–611 (1971)
35. P. Muralidharan, S.H. Jo, D.K. Kim, Electrical conductivity of submicrometer gadolinia-doped ceria sintered at 1000°C using precipitation-synthesized nanocrystalline powders. *J. Am. Ceram. Soc.* **91**(10), 3267–3274 (2008)
36. E. Ruiz-Trejo, J. Santoyo-Salazar, R. Vilchis-Morales, A. Benítez-Rico, F. Gómez-García, C. Flores-Morales, J. Chávez-Carvayar, G. Tavizón, Microstructure and electrical transport in nano-grain sized Ce<sub>0.9</sub>Gd<sub>0.1</sub>O<sub>2–δ</sub> ceramics. *J. Solid State Chem.* **180**(11), 3093–3100 (2007)
37. K. Kendall, N.Q. Minh, S.C. Singhal, Chapter 8 – Cell and stack designs, in *High Temperature and Solid Oxide Fuel Cells*, (John Wiley and Sons, Inc., Hoboken, NJ, Elsevier Science, Amsterdam, 2003), pp. 197–228
38. G. Ye, F. Ju, C. Lin, S. Gopalan, U. Pal, D. Seccombe, *Single-Step Co-Firing Technique for SOFC Fabrication*, in *Advances in Solid Oxide Fuel Cells: Ceramic Engineering and Science Proceedings*, ed. by N. P. Bansal (John Wiley and Sons, Inc., Hoboken, NJ, 2008), **26**(4), pp. 25–32. <https://doi.org/10.1002/9780470291245.ch3>
39. S.-D. Kim, H. Moon, S.-H. Hyun, J. Moon, J. Kim, H.-W. Lee, Nano-composite materials for high-performance and durability of solid oxide fuel cells. *J. Power Sources* **163**(1), 392–397 (2006)
40. C. Chen, M. Liu, L. Yang, M. Liu, Anode-supported micro-tubular SOFCs fabricated by a phase-inversion and dip-coating process. *Int. J. Hydrog. Energy* **36**(9), 5604–5610 (2011)
41. C.-C. Chao, C.-M. Hsu, Y. Cui, F.B. Prinz, Improved solid oxide fuel cell performance with nanostructured electrolytes. *ACS Nano* **5**(7), 5692–5696 (2011)
42. M.H.D. Othman, N. Droushiotis, Z. Wu, K. Kanawka, G. Kelsall, K. Li, Electrolyte thickness control and its effect on electrolyte/anode dual-layer hollow fibers for micro-tubular solid oxide fuel cells. *J. Membr. Sci.* **365**(1–2), 382–388 (2010)
43. D. Das, B. Bagchi, R.N. Basu, Nanostructured zirconia thin film fabricated by an electrophoretic deposition technique. *J. Alloys Compd.* **693**, 1220–1230 (2017)
44. C.C. Wei, K. Li, Yttria-stabilized zirconia (YSZ)-based hollow fiber solid oxide fuel cells. *Ind. Eng. Chem. Res.* **47**(5), 1506–1512 (2008)



# Nanostructured Materials for Advanced Energy Conversion and Storage Devices: Safety Implications at End-of-Life Disposal

# 18

Sajid Bashir, Pranitha Hanumandla, Hsuan-Yi Huang, and Jingbo Louise Liu

*Dedicated to Peter J. Derrick and Rakesh Prajpat.*

## Contents

18.1	Introduction .....	518
18.1.1	Historical Overview .....	519
18.1.2	Fuel Cell Electrocatalyst .....	520
18.1.3	General Comments About Toxicity .....	522
18.2	Experimental Procedure .....	523
18.2.1	Extraction of Natural Products .....	523
18.2.2	Synthesis of Magnetic Nanoparticles .....	523
18.2.3	Structural Characterization .....	524
18.2.4	Toxicological Evaluation of Magnetic Nanoparticles .....	525
18.2.5	Measurement of Reactive Oxygen Species (ROS) .....	525
18.3	Results and Discussions .....	525
18.3.1	Structural Evaluations of MNPs .....	525
18.3.2	Toxicological Evaluations of MNPs .....	528
18.4	End-of-Life Safety Implication .....	532
	References .....	538

## Author Contribution

The first draft of this manuscript was written by PH. The figures and images were supplied by PH and HH. This research was carried out under supervision by SB and LL. The manuscript was reviewed and edited by SB and LL.

S. Bashir (✉) · P. Hanumandla · H.-Y. Huang · J. L. Liu  
Department of Chemistry, Texas A&M University-Kingsville, Kingsville, TX, USA  
e-mail: [br9@tamuk.edu](mailto:br9@tamuk.edu); [kfjll00@tamuk.edu](mailto:kfjll00@tamuk.edu)

---

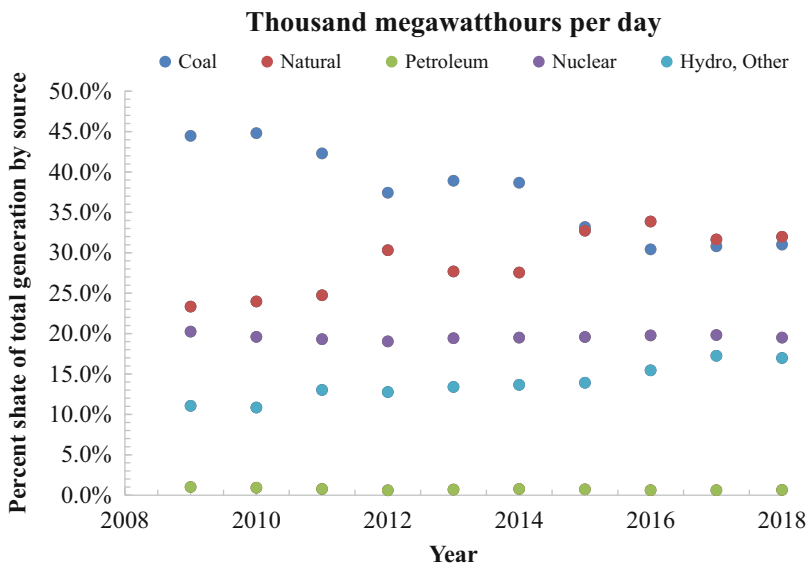
**Abstract**

The global demand for electricity has gradually increased to 20,000 TWh in 2016 at approximately 2% per decade. The top four resources to generate electricity are coal, natural gas, nuclear, and renewables. In the USA, natural gas has displaced coal as the primary source for the generation of electricity. In the transport sector, fossil fuels dominate. The two major drawbacks of using fossil fuels for energy and transport are the harmful emission of oxides of carbon, nitrogen, and sulfur and the limited availability of these resources if measured in centuries rather than years. To offset these short- and long-term problems, researchers have proposed the development of fuel cells (FCs) as a potential solution. The FCs convert fuels (such as hydrogen) into water and electricity with zero or near-zero emission of harmful gases. Hydrogen is generated using either water splitting or steam reformation of methane, coal gasification, or from methanol. The above alternative solutions require chemical and electrical energy and are not necessarily carbon dioxide neutral. To improve the efficiency and lower the cost of the fuel cell stack, researchers have focused on replacement of platinum anode/cathodes with other non-precious metals. Their potential toxicity and interactions with the environment, animals, and people have received little attention, unlike our understanding of the toxicity of gasoline volatiles, particulate matter, and organic residues. In this study, we evaluated the potential biological effects using core-shelled  $\text{Fe}_3\text{O}_4$  magnetic nanoparticles (MNPs) as an example. The toxicity results indicate that electrocatalyst with appropriate structural support may be biologically benign. The toxicity of these catalysts may be an issue in the near future since the number of electric and hydrogen-powered automobiles with fuel cells is expected to increase. This increased utilization will lower consumption of fossil fuels, as well as emission of greenhouses gases, but will increase a secondary risk of the effects of these electrocatalysts. Our results demonstrate the minimization of oxidative stress and cellular damage if encapsulated with natural product extracts.

---

**18.1 Introduction**

The world's energy demand over the last decade has increased approximately by 2%, although this slowed down in 2015, the lowest increase since 1998 (and the 2009 recession) [1]. In large part, increases in the demand for energy in the USA, Europe and particularly China were lower than expected, although China still recorded the largest increment in primary energy consumption, maintaining its dominant position for a 15th consecutive year [2]. The dip in primary energy usage also impacted fossil fuel prices [3]. The price of crude oil was the lowest since 1986 and natural gas since 1999, while coal prices also dropped for a fourth consecutive year since 2014 [4]. Global renewable consumption continued to rise to under 3% and accounted for more than 210 TWh of electricity with China and Germany using the most energy from renewables [2]. China also overtook Germany and the USA to become the



**Fig. 18.1** Domestic energy in 2017 by fuel sources [6]

dominant producer of electricity from solar sources [5]. The energy production by a source within the USA is summarized in Fig. 18.1 [6].

While there has been a slight drop in energy consumption, the overall trajectory is the energy demands are increasing, with natural gas (37%) overtaking coal (34%) as the primary source of energy for the generation of electricity in 2016. This is the reverse of the usual energy mix, for example, in 2007 natural gas accounted for 25% of the total electricity generated, while coal accounts for 46%, respectively [6]. The decline in coal usage is in part due to lower natural gas prices and more demand for “cleaner” energy sources [7]. The gasoline in the transport sector remains dominant, approximately 19.6 million barrels/day in 2016 of which 13 million barrels are used [8]. It is anticipated that improved efficiency in miles-per-gallon automobiles will reduce overall demand [9]. Although gasoline and diesel usage in light trucks and compact cars are anticipated to decrease, their aggregate use toward carbon dioxide (CO<sub>2</sub>) emissions and biologically harmful by-products is likely to increase until electric or hybrid including fuel cell-powered automobiles become dominant [10].

### 18.1.1 Historical Overview

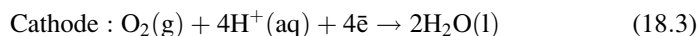
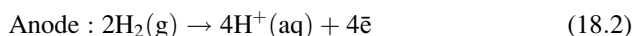
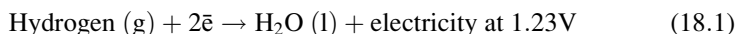
The internal combustion engine displaced the steam engine as the central “driving engine” in industry and leisure at the turn of the century when a significant percentage of the population could utilize these “horseless carriages” [11]. The ecological and toxicological impact of diesel was evaluated much later. Since diesel fuel is distilled at a higher temperature (<390 °C), the distillate contains longer

aliphatic carbons (<9–28 carbons), polycyclic aromatic hydrocarbons (PAHs), and sulfur (0.5 wt%) [12]. The final composition is highly dependent upon feedstock, extraction site, and additive inclusion. During ignition, PAHs are formed due to combustion of oil in the crankcase, or engine oil, or from the exhaust [13]. The incomplete combustion also yields particulate matter to be released with the tendency to be modified once in the atmosphere [14]. Factors which promote soot formation are engine load, the timing of the injection, cold start, and fuel-to-air ratio [15]. At very high temperatures (~2300 °C), reactive oxygen and nitrogen species are generated [16]. Exposure to diesel exhaust has a number of effects [17] in the environment, human health, and ecology. The physical effects, such as irritation to eyes, nose, and throat, resulted from diesel vapor, or oxides in the exhaust gas from nitrogen oxides (NO<sub>x</sub>) or sulfur dioxide (SO<sub>2</sub>). Both types of oxides can form mild acidic solutions in lungs and organs with moisture, for example, eyes, lips, tongues, and internal organs [18]. The biochemical effects are the interaction of carbon monoxide (due to incomplete combustion) with hemoglobin.

At higher temperatures in the engine block, PAHs and soot are produced, causing mutagenesis effects through interactions with deoxyribonucleic acid (DNA), cell damage through increased adduct formation [19], stimulated tumor formation through cell proliferation, and reduced particulate matter (PM) clearance through reactive oxygen species (ROS) formation [20]. In addition to the mechanical damage, soot elicits biochemical stress due to the release of adsorbed organics from its surface. PAHs undergo transformation into methyl-, nitro- and oxygenated derivatives that in turn are carcinogenic [21]. These previous studies have relevance to the current proliferation of fuel cell-based vehicles that utilize compressed hydrogen gas as a fuel [22]. These cars do not generate any CO<sub>2</sub> emissions; however, the biological impact remains to be evaluated on the electrocatalysts, such as platinum and/or non-platinum, to better qualify their end-of-life fate [23].

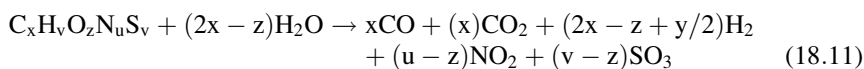
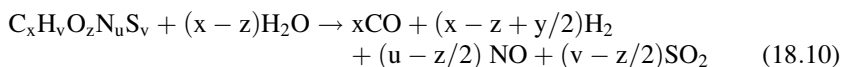
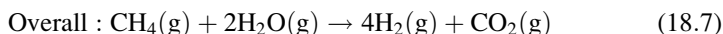
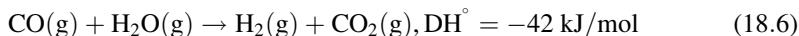
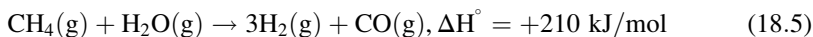
### 18.1.2 Fuel Cell Electrocatalyst

Platinum-based electrodes are used at the anode and cathode in proton exchange membrane fuel cells (PEMFCs) in which hydrogen is converted to water, while electricity generated, summarized in Eqs. 18.1, 18.2, 18.3, and 18.4 [24]:



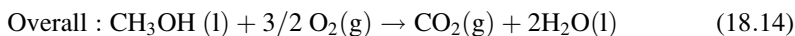
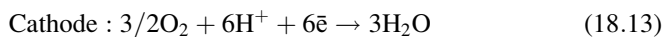
The hydrogen may be obtained from methane (Eqs. 18.5, 18.6, and 18.7) or methanol (Eqs. 18.8 and 18.9) or coal (Eqs. 18.10 and 18.11). Assuming that coal

contains negligible sulfur or nitrogen, the by-products are  $x\text{CO} + (x - z + y/2)\text{H}_2$  and  $(x)\text{CO}_2 + (2x - z + y/2)\text{H}_2$  (Dou et al. 2014):



The platinum (Pt) resource is limited to meet projected demands, therefore necessitates the development of non-precious alternates or decreased use of Pt [25]. The aim is to reduce Pt loading in membrane electrode assemblies to  $150 \text{ mg cm}^{-2}$  without degradation in measured power densities [26]. A literature survey indicates a broad range of Pt loading between 0.05 and  $0.15 \text{ mWmg Pt}^{-1}$  [27]. The hydrogen reduction reaction (HOR) at anode is facile [28]. More research has focused on Pt loading with other metals such as ruthenium (Ru) [29], tungsten (W) [30], tin (Sn) [31], cobalt (Co) [32], iridium (Ir) [33], manganese (Mn) [34], or composites [35]. Platinum is also the metal of choice for the oxygen reduction reaction (ORR) which is the rate-determining step in PEMFC performance [36]. This is a four-electron process mechanism with the intermediates share the electrode Pt oxide or hydroxide surface [37]. In direct methanol fuel cells, the Pt loading is higher than in PEMFCs with a focus on cobalt (Co) [38], nickel (Ni) [39], and iron (Fe) [40] as possible Pt replacements. In addition, other approaches use structured carbon supports such as Pd/titania nanotubes [41] or inner transition metal oxides such as ceria [42]. The hydrogen-to-carbon ratio, energy-per-gram, and amount of carbon dioxide released are summarized in Table 18.1 [43].

In the absence of compressed hydrogen, methanol (Eqs. 18.12, 18.13, and 18.14) and ethanol (Eqs. 18.15, 18.16, and 18.17) are the other common fuels. Their corresponding electrode redox reactions would be [44]





**Table 18.1** The energy content and physical properties of common fuels [43]

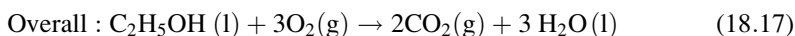
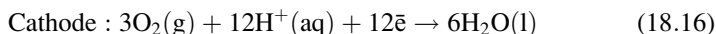
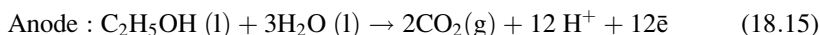
Fuel	H/C ratio	Energy (kJ/g)	CO <sub>2</sub> released (mol/MJ)	Density at 20 °C (g/mL)
Hydrogen	0	120	0	0.000089 at 0 °C
Methanol	4	20.0	1.2	0.79
Ethanol	3	27.3	1.6	0.79
Natural gas (CH <sub>4</sub> )	4	51.6	1.2	0.72 at 15 °C
Petroleum (octane)	2.25	43.6	1.6	0.737 at 15.5 °C
Coal	<1	39.3	2.0	833 kg/m <sup>3</sup> (bulk)

**Table 18.2** Energy and electrochemical properties of common fuels

Fuel	MW (g/mol)	n (ē)	n/MW (ē mol/g)	E° (V)	E <sub>SP</sub> (MJ/kg)	η (%)
Hydrogen	2.01	2	0.995	1.23	142	83
Methane	16.00	8	0.5	1.03	55.5	60
Methanol	32.04	6	0.187	1.21	19.7	97
Ethanol	46.07	12	0.260	1.15	26.4	97
Gasoline (octane)	114.22	6	0.05	18.07 <sup>a</sup>	46.4	20

1 MJ ≈ 0.28 kWh ≈ 0.37 HPh

<sup>a</sup>E° = -ΔG°/nF, where F = 96,485 A·s/mol, n is the number of electrons involved, and ΔG° is the Gibbs free energy of the redox reaction (kJ/mol) [45]



The number of electrons involved in a redox reaction is related to theoretical energy capacity of the fuel cell, and the energy conversion efficiency is close to 90%. The specific energy (E<sub>SE</sub>) is proportional to the number of electrons (n) and cell potential (E°) and is inversely proportional to the molar mass of the fuel (MW) as nE°/MW summarized in Table 18.2 [46].

### 18.1.3 General Comments About Toxicity

The above fuels are by definition highly flammable and asphyxiate (for compressed gases). Methanol is a poison while ethanol is an irritant [47]. With respect to the fuels, the most optimal fuel is hydrogen in terms of its high energy density and low toxicity [48]. The problem as described in Eqs. 18.5, 18.6, 18.7, 18.8, 18.9, 18.10, and 18.11 is that hydrogen is difficult to extract from precursor materials that require energy and generates carbon monoxide (a biological and fuel cell poison) and carbon dioxide, which is a greenhouse gas and also contributes to global warming [49].

The most practicable method of hydrogen storage is through compression that introduces other engineering and safety factors to be considered. In addition, since the volumetric compression ratio and density is different to compressed natural gas, a separate distribution and storage network must be created [50].

While the hazards of gasoline and hydrocarbons are better known, the potential biological effects of nanomaterials used in fuel cells are less known. Iron or lanthanide oxides, such as cerium oxide ( $\text{CeO}_2$ ) nanomaterials, have been used in solar cells [51] and fuel cells [52] and were evaluated to determine potential toxicity in both microorganism and human cells in vitro [53].

---

## 18.2 Experimental Procedure

Experimental procedures include extraction of medicinal plant and formation of magnetic nanoparticles using metal cations, such as  $\text{Fe}^{2+}$  and  $\text{Fe}^{3+}$ . In this study, an aqueous solution of starting materials was used to produce magnetic nanoparticles (MNPs). The medicinal product extracts will be used to functionalize the MNPs. The medicinal product extracts contain various fatty acids, carbohydrates, saponins, flavonols, and various proteins. The chemicals of  $\text{FeCl}_2 \cdot 6\text{H}_2\text{O}$  were used as a  $\text{Fe}^{2+}$  source and  $\text{Fe}(\text{NO}_3)_3$  as a  $\text{Fe}^{3+}$  source, respectively. Gum arabic was introduced as a dispersing agent to prevent particle agglomeration. *Chlorophytum borivilianum* and *Hygrophila auriculata* are the two traditional drugs which have various medicinal uses [54]. *Hygrophila auriculata* belongs to genus *Hygrophila*, while *Chlorophytum borivilianum* belongs to genus *Chlorophytum* [55] with known medical properties [56]. Seeds from these plants are obtained, cleaned, and extracted using distilled water. The extraction of this natural product was carried out over 8 h.

### 18.2.1 Extraction of Natural Products

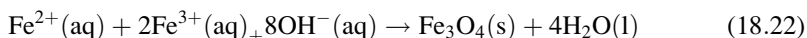
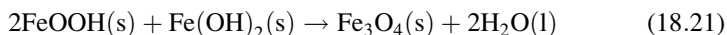
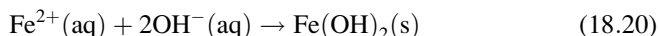
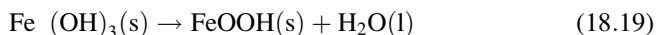
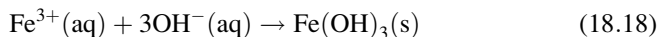
In the medicinal plant, there contain a significant amount of fatty acids and saponin, which contain both hydrophilic and hydrophobic groups permeable through the cell membrane. These amphiphilic groups will enhance the biocompatibility of MNPs with biological fluids. The active chemicals' different molecular percentages were used to functionalize the MNPs [57].

### 18.2.2 Synthesis of Magnetic Nanoparticles

Iron oxide MNPs were synthesized using a sol-gel method under ambient conditions. Initially, 0.5 g of gum arabic was dissolved in 100 mL distilled water and stirred using a mechanical agitation until it becomes a homogenous solution. Two starting materials,  $\text{FeCl}_2 \cdot 6\text{H}_2\text{O}$  (0.5 M) and  $\text{Fe}(\text{NO}_3)_3$  (0.5 M) as  $\text{Fe}^{2+}$  and  $\text{Fe}^{3+}$  precursors, were dissolved in 25 mL of distilled water, respectively. As  $\text{Fe}^{2+}$  cations are easily oxidized, the inert gas  $\text{N}_2$  was introduced to protect from oxidation. Five different formulations

of Fe<sub>3</sub>O<sub>4</sub> MNPs were generated for structural and biological evaluation. The crystalline and morphological structures were studied using X-ray powder diffraction and electron microscopy [59]. The toxicity against human cells (retinal pigment epithelium (RPE)) was evaluated using an *in vitro* bioassay for NO and ROS.

The chemical reactions to produce MNPs were shown in equation (Eqs. 18.18, 18.19, 18.20, 18.21, and 18.22) [58], and the overall reaction is represented by Eq. 18.22:



### 18.2.3 Structural Characterization

The Quanta 600 FEG is a field emission scanning electron microscope capable of generating and collecting high-resolution and low-vacuum images. It is equipped with an x-y-z tilt-rotate stage in which x and y with 150 mm and z with 65 mm. Field emission gun along with Schottky emitter source bearing voltage 10 kV and a beam current of >226  $\mu\text{A}$ . The pressures of the chamber and gun were controlled at  $4.58 \times 10^{-5}$  torr and  $2.81 \times 10^{-9}$  torr, respectively. SEM determines morphology and particle size distribution of prepared MNPs. The resolution is measured as gold particle separation on a carbon substrate [60]. Scanning transmission electron microscope (FEI Tecnai G2 F20) was used to evaluate the morphology and crystalline phase of Fe<sub>3</sub>O<sub>4</sub> MNPs. This utilizes ZrO<sub>2</sub>/W (100) Schottky Field emitter (FEG) with a resolution of 0.27 nm and information limit of 0.16 nm. The FEI Tecnai produces better coherence and higher brightness. In scanning transmission electron microscope (STEM) mode, high current is delivered to a fine probe with which microanalysis along with sub-nanometer spatial resolution is accessed [61]. The TEM was equipped with X-ray energy dispersive spectrometer (EDS) capabilities to obtain an elemental composition of MNPs. The instrument was operated in the TEM mode to obtain the high-resolution images and a high-angle angular dark-field (HAADF) detector. A probe size of 1 nm was used for EDS and STEM, at 150 mm camera length for the HAADF detector to collect for Rutherford scattered electrons. The gun and chamber vacuum were controlled at  $3.5 \times 10^{-5}$  Torr and  $3.0 \times 10^{-9}$  Torr for high resolution. Three-dimensional lattice structure and d-spacing of magnetic nanoparticles (MNPs) can be obtained using Bruker D8 Advance X-ray powder diffraction. X-rays generated in this process will not damage the powdered sample and can be used to map the major transition and main block elements which have the same wavelength. The scan range varied from 20 to 90° with a scanning rate at 2°/min. The voltage and current were

controlled at 40 kV and 44 mA [62]. Ultraviolet-visible (UV-Vis) spectroscopy is used to test the formed  $\text{Fe}_3\text{O}_4$  magnetic nanoparticle absorbance. MNPs are tested with Beckman Coulter DU 800 UV-VIS Spectrophotometer using quartz cuvette; the wavelength ranges from 200 to 800 nm. Initially, distilled water is used as blank and sample is scanned later on. Here  $\text{D}_1$  lamp used is deuterium and  $\text{D}_2$  lamp as tungsten. The intensity was controlled at 0.6 under ambient temperatures [63].

### 18.2.4 Toxicological Evaluation of Magnetic Nanoparticles

Immortalized human hTERT retinal pigmented epithelium (RPE) whole cells (WCs) [64] were grown in the dark (-RL) until confluent and then incubated with phosphate buffered saline (PBS) [65] or MNPs. The level of nitric oxide (NO) was measured as an indicator of cellular toxicity. This cellular signaling molecule is important for vascular tone, insulin secretion, airway tone, angiogenesis, neural development, and peristalsis. Chemical treatments using six cofactors (to be stated below) and MNPs were carried out to detect the cell viability. These WC-RL cells without treatment were used as a control. Cells were also treated using sodium nitrite ( $\text{NaNO}_2$ , NIT) as a generator for NO production and superoxide formation. Sodium nitroprusside ( $\text{Na}_2[\text{Fe}(\text{CN})_5\text{NO}]$ , NitroP) was used as another control due to its slow NO release. The 7-ethyl-10-hydroxy camptothecin (SN-38,  $\text{C}_{22}\text{H}_{20}\text{N}_2\text{O}_5$ ) was used to induce chemical stress and DNA fragmentation through inhibition of topoisomerase-1. The dithranol ( $\text{C}_{14}\text{H}_{10}\text{O}_3$ , DIT), known as a reducing agent, was used to lower the oxidative stress of cells. An oxidizing agent, hydrogen peroxide ( $\text{H}_2\text{O}_2$ , HP), was to enhance oxidative stress and promote cell death. An irreversible inhibitor of cytochrome c oxidase, sodium cyanide ( $\text{NaCN}$ , CN), was used to determine whether the oxidative stress occurred in the mitochondria. The toxicology of  $\text{Fe}_3\text{O}_4$  MNPs was evaluated by NO release and/or absorption measured in whole RPE WCs with a number of cofactors mentioned above.

### 18.2.5 Measurement of Reactive Oxygen Species (ROS)

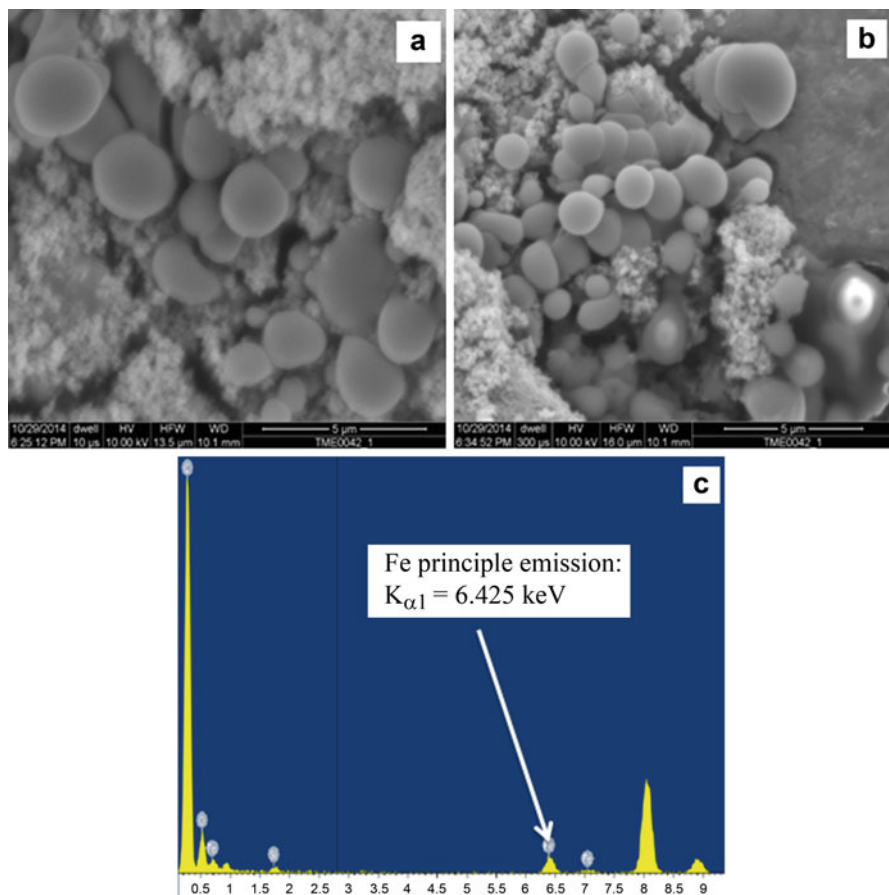
Dichlorofluorescein derivative dye is non-fluorescent until the acetate groups are removed by intracellular esterases and oxidation occurs within the cells [66]. This study provides a complementary indicator of oxidative stress to the measurement of NO.

---

## 18.3 Results and Discussions

### 18.3.1 Structural Evaluations of MNPs

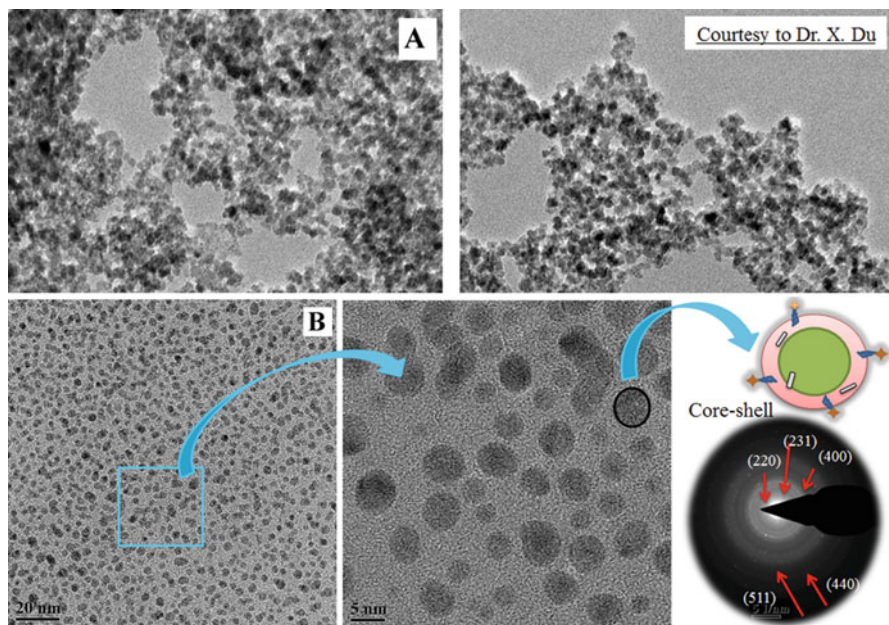
The scanning electron microscopic data (Fig. 18.2a, b) indicated that the pseudo-spherical particles were formed and the grain size was averaged at 25  $\mu\text{m}$ . It was found that  $\text{Fe}^{2+}$  oxidation was prevented by addition of medicinal plant extracts.



**Fig. 18.2** Scanning electron micrographs of core-shelled Fe<sub>3</sub>O<sub>4</sub> magnetic nanoparticles prepared by sol-gel method, (a) the spherical Fe<sub>3</sub>O<sub>4</sub> particles; (b) a different spot of the Fe<sub>3</sub>O<sub>4</sub> MNPs; and (c) the EDS analysis of the Fe<sub>3</sub>O<sub>4</sub> MNPs, showing the principle emission of Fe element

Meanwhile, the agglomeration of MNPs occurred due to the high surface tension. The energy dispersive spectroscopy (EDS) equipped with this SEM provided information on the elemental composition (Fig. 18.2c). It was found that the Fe principle emission occurred at  $k_{\alpha 1}$ : 6.425 keV [67].

The transmission electron microscopic analyses (Fig. 18.3a) indicated that the size of pure Fe<sub>3</sub>O<sub>4</sub> MNPs was averaged at 6.5 nm. The uniformity of the MNPs was found controlled well using natural product extracts as a dispersing agent. The ring pattern depicted highly crystalline MNPs were obtained using a feasible wet-chemistry method under moderate synthesis conditions. The crystalline phase was found to be in agreement with the X-ray powder diffraction data (discussed in the next section).



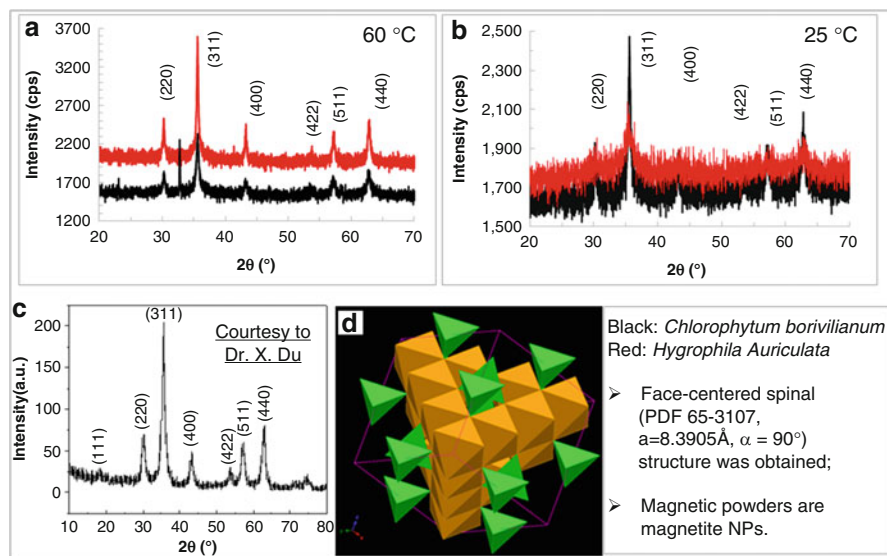
**Fig. 18.3** Transmission electron micrographs of core-shelled Fe<sub>3</sub>O<sub>4</sub> magnetic nanoparticles prepared by sol-gel method, (a) pure Fe<sub>3</sub>O<sub>4</sub> MNPs and (b) core-shelled Fe<sub>3</sub>O<sub>4</sub> MNPs and the insert showing formation of core-shelled structure

Upon functionalization using medicinal extract (*Hygrophila auriculata*), the core-shelled structure (Fig. 18.3b) was clearly detected [68]. The core is composed of Fe<sub>3</sub>O<sub>4</sub> MNPs based on the EDS elemental composition analysis. The shell composed of medicinal extract provides protection of MNPs from agglomeration and increases bioavailability for RPE cells. The tunability of the size, shape, and composition of MNPs enables the precise control of their cellular uptake.

The X-ray powder diffraction results (Fig. 18.4) indicated that the inverse spinel crystalline phase for the MNPs was formed. The results were well-indexed with the standard Fe<sub>3</sub>O<sub>4</sub> powders (PDF 65-3107,  $a = 8.3905\text{\AA}$ ,  $\alpha = 90^\circ$ ). The series of characteristic peaks at different diffraction angles are corresponding to the Miller indices as indicated in the XRD patterns [69]. It was found that the functionalization using the medicinal extract has no effect on the crystalline phase; however, the crystallinity was subject to decrease. The heat treatment to obtain the MNPs showed an increase in temperature essentially results in the increase in crystallinity [70].

Ultraviolet-visible (UV-Vis) spectroscopic analyses of core-shelled Fe<sub>3</sub>O<sub>4</sub> MNMs were carried out using Beckman Coulter DU 800. The results indicated that the plasmon of linoleic acid occurs at approximately 290 nm [71]. This linoleic acid is one of the major chemical constituents from the *Hygrophila auriculata* and *Chlorophytum borivilianum*, respectively. The absorbance at 290 nm resulted from the electrons, which were excited from nonbonding (n) to anti- $\pi$  bonding ( $\pi^*$ )





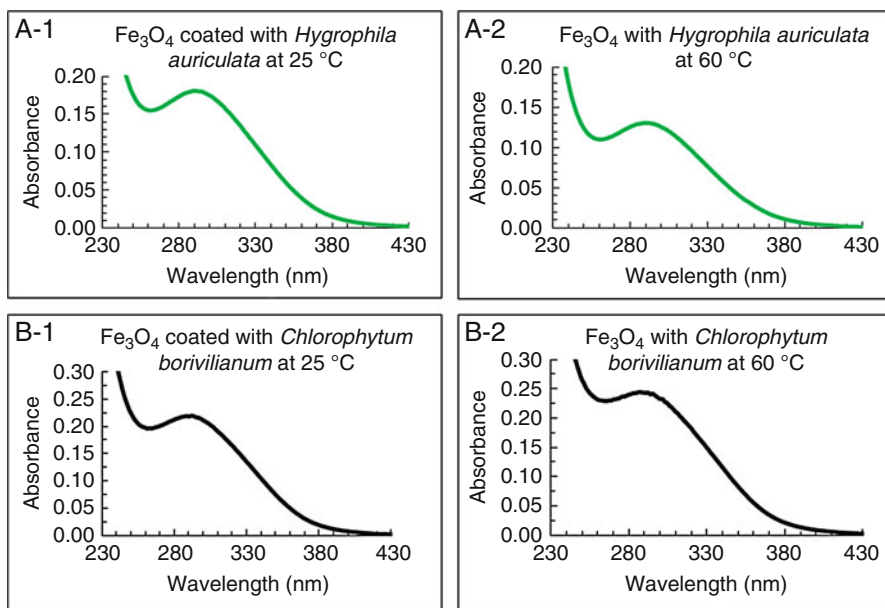
**Fig. 18.4** X-ray powder diffraction analyses of core-shelled  $\text{Fe}_3\text{O}_4$  magnetic nanoparticles prepared by sol-gel method, (a) core-shelled  $\text{Fe}_3\text{O}_4$  MNPs synthesized at 60 °C; (b) core-shelled  $\text{Fe}_3\text{O}_4$  MNPs synthesized at 25 °C; (c) pure  $\text{Fe}_3\text{O}_4$  MNPs as a reference; and (d) the crystal structure of the  $\text{Fe}_3\text{O}_4$  (magnetite)

orbitals. In this MNP core-shelled structure, the adsorption of  $\text{Fe}_3\text{O}_4$  MNMs was not detected, indicating the full coating of the  $\text{Fe}_3\text{O}_4$  core by the active chemicals extracted from natural products [72]. Both medicinal extracts as shells showed similar functions under UV-Vis characterization (Fig. 18.5a, b).

DeltaNu Advantage 200 A was used to collect Raman spectra under ambient conditions (Fig. 18.6). The results of core-shelled  $\text{Fe}_3\text{O}_4$  MNPs indicated that [73] vibration of Fe-O bond occurred at 582–640  $\text{cm}^{-1}$ . The Raman spectra of two medicinal plants (*Hygrophila auriculata* and *Chlorophytum borivilianum*) showed the different vibrational modes from the functional groups between the shell and core (Table 18.3). The OH in-plane stretching mode was found to occur at the wavenumber of 640  $\text{cm}^{-1}$ . At wavenumber of 1481  $\text{cm}^{-1}$ , the O-H bending [74] was observed, and at the wavenumber of 3195  $\text{cm}^{-1}$ , the asymmetrical mode of O-H was detected. These results demonstrated that the  $\text{Fe}_3\text{O}_4$  core was completely encapsulated by the medicinal extract without any shell defects.

### 18.3.2 Toxicological Evaluations of MNPs

The RPE cells incubated at 37 °C in the dark were measured using NO fluorescence at a wavelength of 562 nm. The % fluorescence change of NO or ROS of the no-cofactor control was used as a baseline to determine potential toxicity [75].

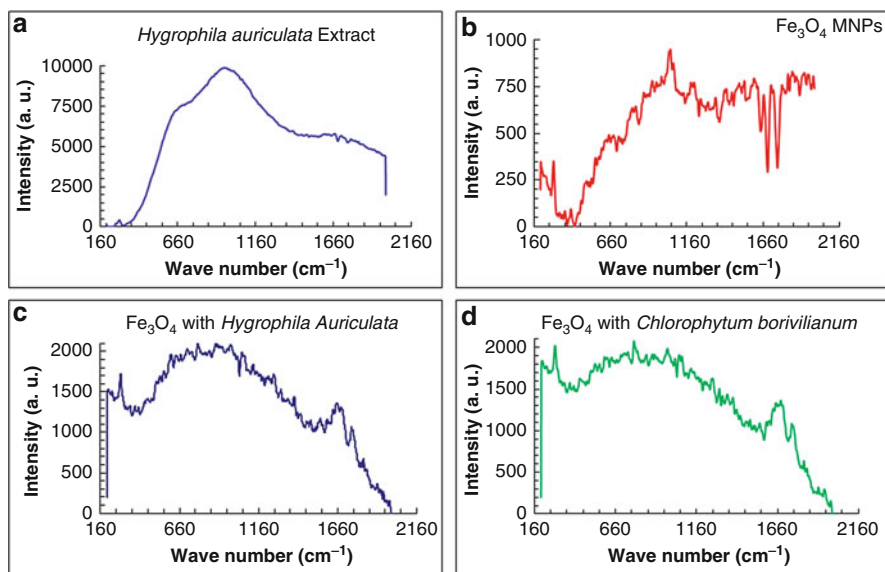


**Fig. 18.5** The spectra of ultraviolet-visible spectroscopy showing spectral graphs of core-shelled Fe<sub>3</sub>O<sub>4</sub> MNPs: (a) the UV-Vis spectra of Fe<sub>3</sub>O<sub>4</sub> coated with *Hygrophila auriculata* and (b) the UV-Vis spectra of Fe<sub>3</sub>O<sub>4</sub> coated with *Chlorophytum borivilianum* (MNPs were derived from two synthesis temperatures) (Note: The 290 nm results from electron transition from nonbonding to anti- $\pi$  bonding orbitals)

The high fluorescence of NO after addition of sodium nitrite (NIT) validates the bioassay design [76]. The data indicates that both SN-38 and hydrogen peroxide (HP) inhibit cell division, further cause cell death due to the ROS production, resulting in lower NO fluorescence [77]. Three cofactors, NIT, SN-38, and HP, were found to promote rapid cell death at threshold concentrations. In particular, it was observed that cells can be damaged within 30 min using NIT as an external fast NO-releasing cofactor. On the other hand, the damage was less severe using slow NO-releasing cofactors. Our study showed NitroP released NO slowly, suggesting low NO levels may trigger cell death [78]. The RPE cells showed the cellular stress within 10 h after addition of NitroP, implying a different biochemical pathway. It was hypothesized that the generation of ROS is one of the major reasons causing cell death. This generation of ROS can be minimized if the NO generation is controlled in a specific concentration window (100–1000  $\mu$ mol), depending on cell density, age, and type. If dithranol is added into RPE cells, the NO production increased slightly, suggesting the creation of a reducing environment to assist with cell recovery from oxidative damage. This observation confirms that one of the modes of cellular damage is the oxidizing environment.

To evaluate the toxicity of different formations of Fe<sub>3</sub>O<sub>4</sub> MNPs toward RPE cells, we employed the same procedure as mentioned above. Toxicity data indicated all MNPs exhibited similar NO profiles to those of control cells, indicating the core-



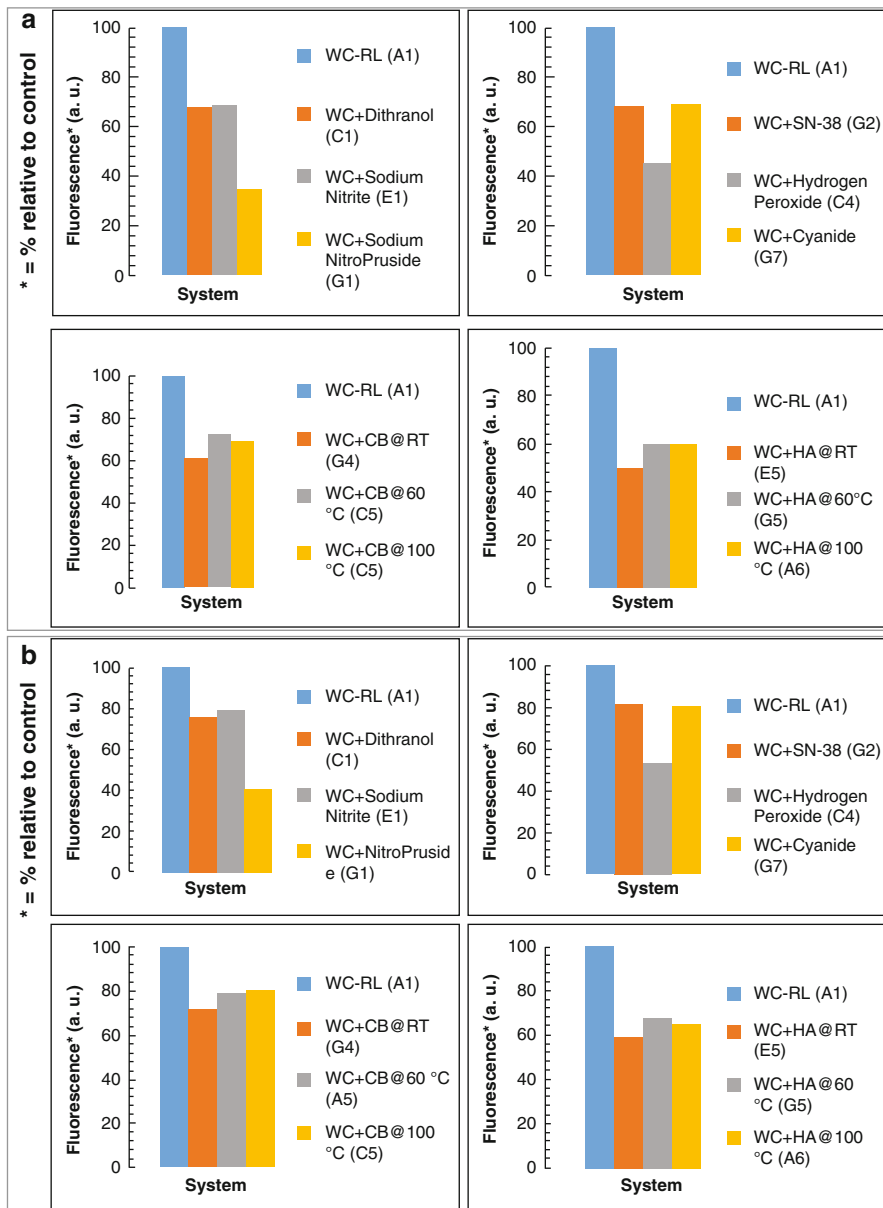


**Fig. 18.6** The Raman spectra of core-shelled  $\text{Fe}_3\text{O}_4$  MNPs: (a) the Raman spectra of *Hygrophila auriculata* extract; (b) the Raman spectra of  $\text{Fe}_3\text{O}_4$  without coating (MNPs were derived at  $60^\circ\text{C}$ ); (c) the Raman spectra of  $\text{Fe}_3\text{O}_4$  coated with *Hygrophila auriculata*; and (d) the Raman spectra of  $\text{Fe}_3\text{O}_4$  coated with *Chlorophytum borivilianum*

**Table 18.3** A summary of the functional groups of core-shelled  $\text{Fe}_3\text{O}_4$  MNPs using Raman analyses

Wavelength ( $\text{cm}^{-1}$ )	Vibrational mode
$640\text{ cm}^{-1}$	Fe-O stretching vibration
$1500\text{ cm}^{-1}$	C=O stretching vibration
$1660\text{ cm}^{-1}$	C=C stretching vibration
$1900\text{ cm}^{-1}$	Symmetric C=C
$1750\text{ cm}^{-1}$	O-H bending vibration

shelled  $\text{Fe}_3\text{O}_4$  MNPs (100 ppm) are not toxic. It was observed that MNPs encapsulated with *Chlorophytum borivilianum* aqueous extract at  $100^\circ\text{C}$  promoted cell proliferation. This proliferation was enhanced due to the elevation of the cell NO compared with the control [79]. When red seeds of *Hygrophila auriculata* (RS) were used as an aqueous extract, the extraction temperature appears to influence cell proliferation. It was found that MNPs synthesized at two extraction temperatures at 60 and  $100^\circ\text{C}$  were nontoxic, since cell NO level was similar to that of control. However, MNPs with extracts at room temperature (RT) or  $65^\circ\text{C}$  appear to be slightly cytotoxic since NO levels decreased at least by one-third compared with the control (Fig. 18.7). It was reasonable to conclude that  $\text{Fe}_3\text{O}_4$  MNPs acted as an oxidizing agent unless they were fully encapsulated. The degree of capsulation appears to be dependent on the extraction and reaction temperatures.



**Fig. 18.7** The bioassay of nitrogen monoxide (NO) release from RPE cells after introduction of standard cofactors and the core-shelled  $\text{Fe}_3\text{O}_4$  MNPs: (a) the bioassay of NO release within 10 min and (b) the bioassay of NO release within 30 min

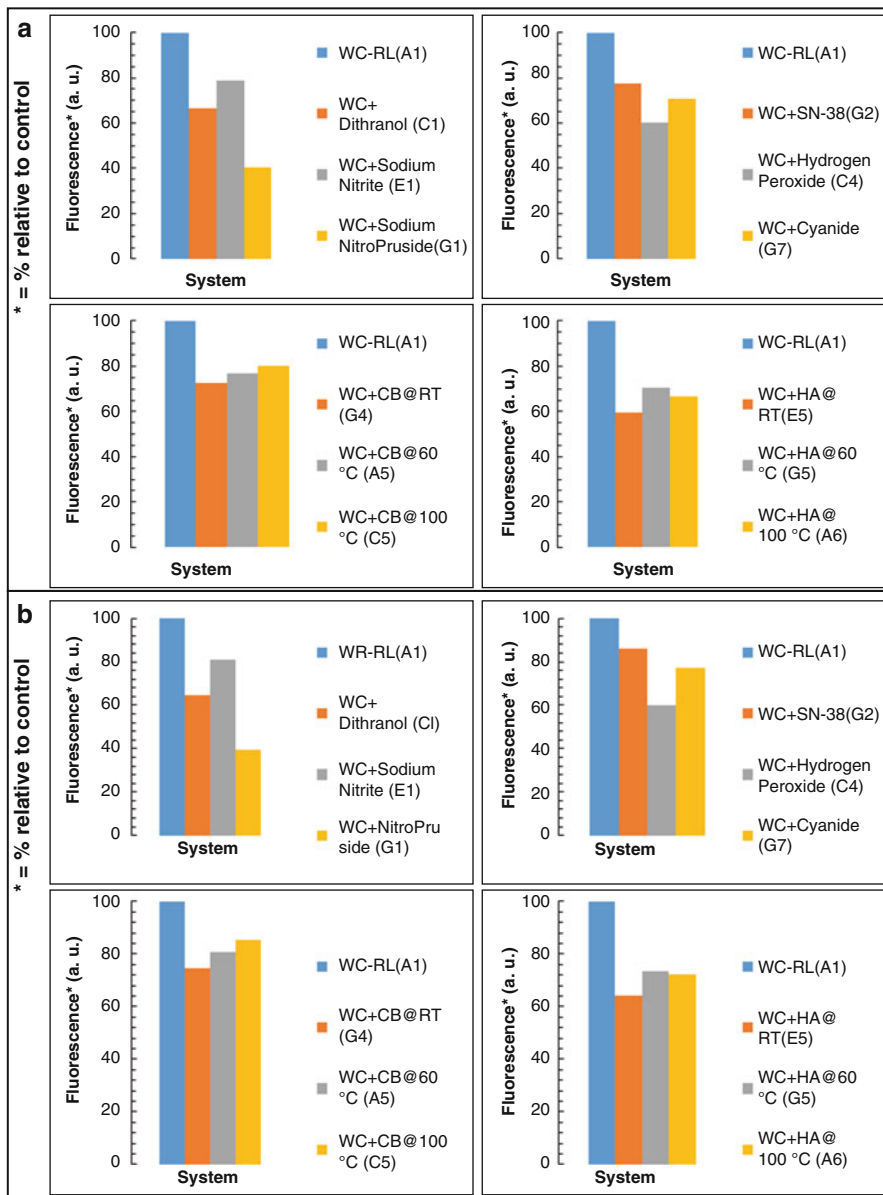
Reactive oxygen species (ROS) are mostly generated during the energy production from electron transport chain, due to the ionizing radiation interaction and by some enzymes like neutrophils. The generated ROS will react with hydrogen and forms peroxide radical ( $\text{HOO}\cdot$ ), which is much more reactive than hydroxyl radical ( $\text{HO}\cdot$ ) and can cause greater damage to the cell than  $\text{HO}\cdot$ -based ROS [80]. In our study, the fluorescent compound 5-(and-6)-carboxy-2',7'-dichlorofluorescein diacetate ( $\text{C}_{29}\text{H}_{17}\text{Cl}_2\text{NO}_{11}$ ), a succinimidyl ester, was used to measure the oxidative stress in RPE cells. This ester is colorless and non-fluorescent under ambient conditions but becomes brightly green fluorescent once it is hydrolyzed by intracellular esterases. The fluorescence change can be used as a gauge to estimate the cellular health. Fluorescence obtained from ROS data indicated an enhancement to 160% from 100% (control) by HP. When compared to control, the generated ROS will not damage the cells to the maximum extent (Fig. 18.8) but may cause damage to the oxidizing environment after a wide time window (30 min to 48 h, accordingly). This delay of cell death may be due to the passive diffusion of oxidizing species into cells through the membrane. This diffusion will lead to a covalent modification of intracellular proteins, resulting in a long-term cell labeling and loss of protein catalysis. Further, a loss of enzyme function can result in an eventual cell death at the later time than the initial oxidization.

Calcein acetoxymethyl ester ( $\text{C}_{46}\text{H}_{46}\text{N}_2\text{O}_{23}$ , calcein AM), a non-fluorescent, converts to the strongly green fluorescent calcein when it is hydrolyzed by intracellular esterases in live cells [81]. This cell permeable compound is widely used to determine cell viability since its fluorescence intensity is proportional to the number of live cells. Measurement of live cells using calcein AM dye showed less number of viable cells at 10 min when the *Hygrophila auriculata* encapsulated  $\text{Fe}_3\text{O}_4$  MNPs were tested. The fluorescence was found to be increased after incubation for 30 min, indicating an increase in viable cells. This proves that *Hygrophila auriculata* extracted at room temperature is not toxic to the cells (Fig. 18.9) although MNPs did generate high NO levels. It is hypothesized that the *Hygrophila auriculata* shell is not complete and exposed surface of  $\text{Fe}_3\text{O}_4$  MNPs was used to generate ROS, which led to an increase in intercellular NO levels.

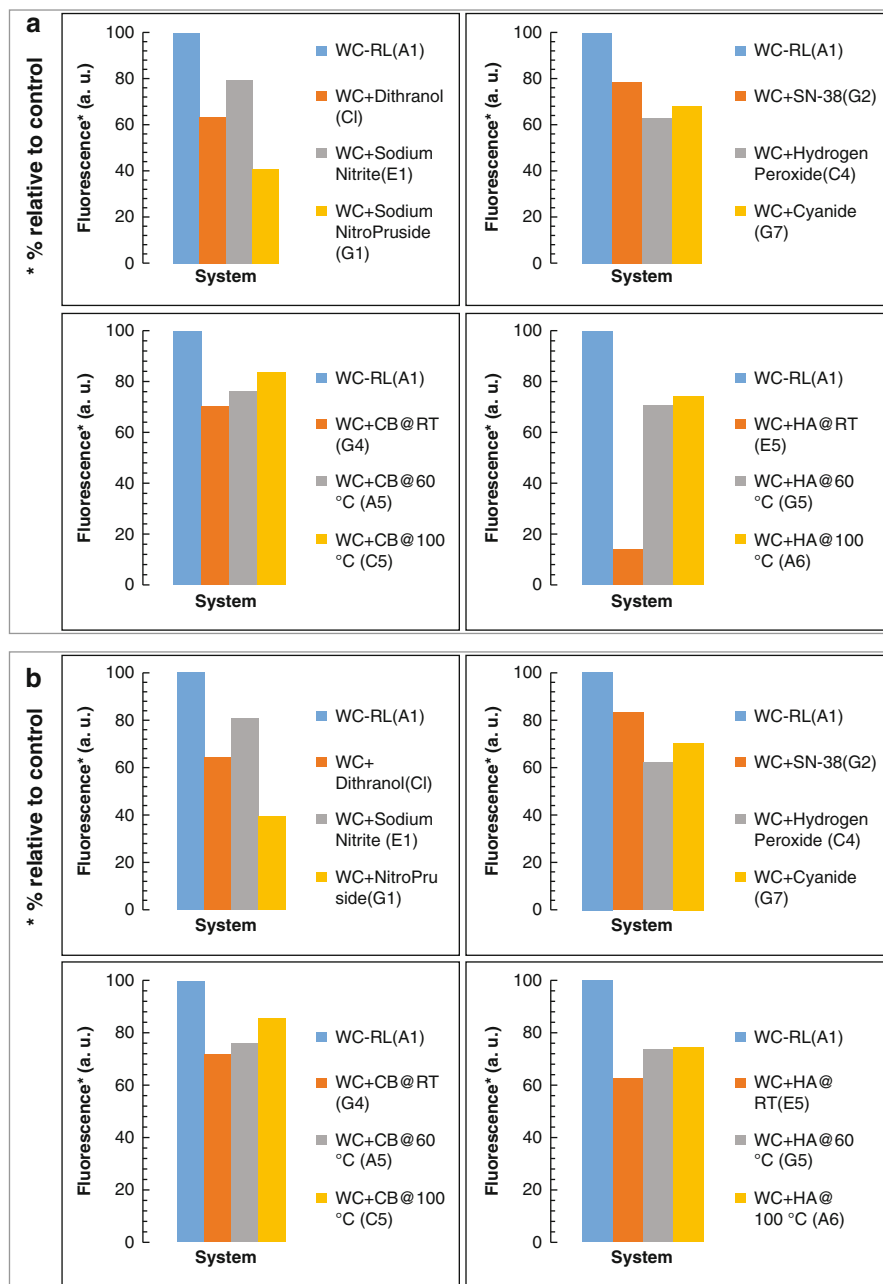
---

## 18.4 End-of-Life Safety Implication

Safety concerns with engineered catalysts for human health in vitro (TOX) were summarized in the toxicological section. The environmental life cycle assessment (LCA) and risk assessment (RA) were summarized in Table 18.4. The life cycle assessment is a comprehensive study of the potential impact on human health through degradation of the materials or transformation of natural matrices. The RA is a set of procedures established to estimate if a specific material or exposure to this material can cause adverse health or environmental effects. The comparison of these two studies provides guidelines for risk management of severity and probability of nanomaterial toxicity.



**Fig. 18.8** The bioassay of reactive oxygen species (ROS) from RPE cells after introduction of standard drug and the core-shelled  $\text{Fe}_3\text{O}_4$  MNPs under different temperatures: **(a)** the bioassay of ROS within 10 min and **(b)** the bioassay of reactive oxygen species within 30 min



**Fig. 18.9** The calcein live assay from RPE cells after introduction of standard drug and the core-shelled  $\text{Fe}_3\text{O}_4$  MNPs under different temperatures: (a) the calcein live assay within 10 min and (b) the calcein live assay within 30 min

**Table 18.4** The relationships between LCA and RA

Life cycle assessment (LCA)	Risk assessment (RA)
Standard operating procedure to assess the impact on environment and health [82]. This is broken down into ten steps	Standard operating procedure to reduce risk of exposure to humans or transformation of environmental matrices [83]
Life cycle identification	Identify each cycle and associated toxicity
Material identification	Initial hazards of materials, even ones that are encased
Qualitative exposure assessment	A dose response of the major nanomaterials on target cells such as nerve, skin, kidney, and liver cells
Identification of exposure potential at each life cycle stage	The use of derivatives that can be modified during the life cycle, such as Fe to Fe-OH for metal catalysts as an example of the type of analysis
Evaluation of nonhuman toxicities	The toxicity to fish, birds, and grasses should be examined, and materials that are disposed of in land fills should also be examined
Analysis of risk potential	The short-term (acute) and long-term (chronic) toxicity should be modeled
Identification of uncertainty and risk groups	The range at which these materials show acute toxicity should be modeled first including thresholds at which toxicity is measured and possible chronic effects such as low doses over prolonged time may be toxic, even though a single dose may not be toxic
Development of risk management strategies	What biomarkers are indicative of stress across cell lines, or different organisms need to be established
Gathering of information on materials and their end-fate	Severity versus probability rating, the severity is from low, medium, high, and very high reaction or response, and probability is extremely unlikely, less likely, and likely to probable
Review and modify LCA based on whether predicted RAs match measured RAs	The toxicity of a material should take into account material surface chemistries, shape, diameter, and solubility from which carcinogenicity, mutagenicity, dermal or reproductive toxicity is obtained. A dose-response relationship to acute and chronic conditions should also be determined and modeled

The combined LCA and RA approach should be structured to include information on impact but also on decision making on how the life cycle is defined [84]. Using particulate matter as a classical pollutant, the LCA component has a focus on product or processes, while RA component focus is on emissions and toxicity. The problem with

the classical approach is the RA has a focus on a single chemical, whereas fuel cell nanomaterials as shown in the toxicology section generate multiple of bioactive species [85] that can cause cellular stress and toxicity. Lastly, LCAs tend to cover a large array of environmental impact parameters, while RA covers toxicity. Therefore, the danger in disposal of nanomaterials used in fuel cells is greater scope than the limited danger using particulate matters (PM) [86]. By adjustment of the LCA approach, the model accuracy can be improved through incorporation of the functional units used to calculate exposure limits [87]. A similar method can be used to determine the toxicity if the functional unit is treated in an analogous manner to the assessment of the PM. The RA framework is broken down and simplified to that used to determine toxicity for bulk chemicals. A four-step procedure (Table 18.4) is adopted to model the risks associated with the functional units, (1) hazard identification, (2) dose-response relationships, (3) exposure assessment, and (4) risk characterization [88]. The hazard identification step is necessary to better understand the physicochemical properties of functional units and their biological interactions. The dose response is required to understand a quantitative estimation of chemical concentrations, which have health effects under both acute and chronic exposure scenarios. Exposure assessment is applied to the model for actually measured toxicity data to generate the predictive environmental concentration (PEC) threshold for specific scenarios. These three aspects are used to provide a risk characterization, ultimately generating a risk quotient that can be measured from predictive to actual conditions.

Our RA analyses indicated the Fe-based magnetic nanoparticles (MNPs) are toxic at 100 ppm thought in vitro measurement of reactive oxygen species (ROS) in retinal pigmented epithelium (RPE) cells, which was minimized through encapsulation of MNPs by *Hygrophila auriculata* and *Chlorophytum borivilianum* by measurement of nitric oxide (NO). The size of MNPs was controlled around 6.5 nm, and their toxicity was mediated through COO-Fe catalyzed ROS as determined by FT-IR ( $1430\text{ cm}^{-1}$ ). The effect of ROS on RPE was deoxyribonucleic acid degradation that was similar to one of the cofactors, SN-38. A literature survey indicates few studies that link RA and LCAs, which is required to generate meaningful scenarios for hazard, exposure assessments and toxicity impact in the environments. The current inventory lacks data on the effect of nanomaterials indoors and outdoors. There are few studies on the toxicity of the emissions into atmosphere or penetration into the soil and subsurface water table. The lack of empirical data limits our understanding of nanoparticle release into the soil and production of secondary species (such as Fe-OOH). The efficiency of local municipalities to remove these nanomaterials through incineration or filtration is unknown, although it is expected that these processes will be ineffective or generate more pollutants through aerosolization. Furthermore, the long-term (chronic) effects of nanoparticles to the water table are entirely unknown. Lastly, the indirect exposure to humans through drinking of this contaminated water source poses serious healthcare concerns that presently are under investigation.



*This chapter is dedicated to Professor Peter J. Derrick who passed away on February 06, 2017, during the writing of this chapter.*

***Tributes to Dr. P. Derrick by Dr. Sajid Bashir***

*Dr. Derrick was my Ph.D. advisor when I was at Warwick University. Dr. Derrick was someone who not only expected high academic rigor but also high ethical and professional standards. We mourn his loss deeply and celebrate his life and profession through the publication of peer-reviewed research. I also mourn the loss of my best friend Rakesh Prajapat whom we shared our childhood until I left for university. It seems incredible someone so young could not be here. I deeply miss his loving company and as always excellent counsel. I pass my deepest condolences to Miss Sophie Prajapat, who will carry out his legacy of being the utmost professional in his work, best friend, neighbor, and a decent human being. I am proud and privileged to call him "friend."*

***Tributes to Dr. P. Derrick by Dr. Jingbo Liu***

*Dr. Peter J. Derrick was a role model for me although we never and will always inspire me. Based on Dr. Bashir's learning trajectory and a strong sense of responsibility, I can envision Dr. Derrick as a shining star who led his crew to explore the new scientific frontier with the honesty, diligence, and talent. From Dr. Bashir's intonation and determination, I sensed clearly the important role model set by Dr. Derrick, who has been our academic Papa for 20 years. I have experienced three very sad experiences in my life: the death of my grandparents who raised me up and taught me to be a nice person, the death of my parents who gave me life and encouraged me to be a strong person, and the death of Dr. Derrick who guided Dr. Bashir and me through his example. I pray for the sweet, courageous, and dedicated scholar, mentor, and role model, Dr. Peter Derrick.*

**Acknowledgments** The authors wish to thank the College of Arts & Sciences (CoA&S, Dr. Bashir, 160336-00002), ACS-PRF (Liu, 53827-UR10), Summer Faculty Fellowship Program (Bashir), Welch Departmental Grant (AC-0006), NSF-MRI acquisition (Liu), University Research Awards (160315-00015, Liu), and RDF grants (160345-00005, Liu) at Texas A&M University-Kingsville (TAMUK) for funding and student support respectfully. The Microscopy and Imaging Center (MIC) at TAMU and the Department of Chemistry at TAMUK are also duly acknowledged for their technical support and nanostructure characterization. The Welch Foundation (AC-006) is further acknowledged in providing financial support to graduate students in their studies. Dr. Bashir would also like to acknowledge Dr. Wigle for access to the Triservice Laboratory (Fort Sam Houston, Air Force, EPA-07-029-HE-00-EPA) and assistance with *in vitro* cell assays.



The Materials Characterization Facility and Microscopy Imaging Center, TAMU, and technical support from TAMUK were acknowledged; Dr. Ying-Pin Chen from Zhou's group, Chemistry Department, TAMU, is duly acknowledged for her assistance with XRD and SEM data collection and analyses; and Drs. H. Kim and Wilson Serem, Texas A&M University, for assistance with other analyses are also acknowledged.

---

## References

1. R. G. Newell, Y. Qian, D. Raimi, Global energy outlook 2015 (No. w22075). National Bureau of Economic Research. (2016), <http://www.nber.org/papers/w22075>
2. S. Dale, The BP statistical review of the world (2016), <https://www.bp.com/content/dam/bp/pdf/energy-economics/statistical-review-2016/bp-statistical-review-of-world-energy-2016-full-report.pdf>
3. I. Chapman, The end of peak oil? Why this topic is still relevant despite recent denials. *Energy Policy* **64**, 93–101 (2014)
4. N. Bauer, I. Mouratiadou, G. Luderer, L. Baumstark, R.J. Brecha, O. Edenhofer, E. Kriegler, Global fossil energy markets and climate change mitigation—an analysis with REMIND. *Clim. Chang.* **136**(1), 69–82 (2016)
5. C. Li, H. Shi, Y. Cao, J. Wang, Y. Kuang, Y. Tan, J. Wei, A comprehensive review of renewable energy curtailment and avoidance: a specific example in China. *Renew. Sust. Energy. Rev.* **41**, 1067–1079 (2015)
6. EIA, (2017), <https://www.eia.gov/todayinenergy/detail.php?id=30832>
7. A. Cherp, J. Jewell, V. Vinichenko, N. Bauer, E. De Cian, Global energy security under different climate policies, GDP growth rates, and fossil resource availabilities. *Clim. Chang.* **136**(1), 83–94 (2016)
8. V. Court, F. Fizaine, Long-term estimates of the Energy-Return-on-Investment (EROI) of coal, oil, and gas global productions. *Ecol. Econ.* **138**, 145–159 (2017)
9. S.M. Chin, H.L. Hwang, D. Davidson, *Shared Freight Transportation and Energy Commodities Phase One: Coal, Crude Petroleum, and Natural Gas Flows* (No. ORNL/TM-2016/303) (Oak Ridge National Laboratory (ORNL), Oak Ridge, 2016), <https://info.ornl.gov/sites/publications/Files/Pub68388.pdf>
10. D.L. McCollum, J. Jewell, V. Krey, M. Bazilian, M. Fay, K. Riahi, Quantifying uncertainties influencing the long-term impacts of oil prices on energy markets and carbon emissions. *Nat. Energy* **1**, e16077 (18 pages) (2016), <https://www.nature.com/articles/nenergy201677>
11. Y. Niki, D. H. Yoo, K. Hirata, H. Sekiguchi, Effects of Ammonia Gas Mixed Into Intake Air on Combustion and Emissions Characteristics in Diesel Engine. In *ASME 2016 Internal Combustion Engine Fall Technical Conference* (pp. V001T03A004-V001T03A004). (American Society of Mechanical Engineers, 2016), <http://proceedings.asmedigitalcollection.asme.org/proceeding.aspx?articleid=2589990>
12. A. Karvountzis-Kontakiotis, A. Dimaratos, L. Ntziachristos, Z. Samaras, Exploring the stochastic and deterministic aspects of cyclic emission variability on a high-speed spark-ignition engine. *Energy* **118**, 68–76 (2017)
13. M.K. Balki, C. Sayin, M. Canakci, The effect of different alcohol fuels on the performance, emission and combustion characteristics of a gasoline engine. *Fuel* **115**, 901–906 (2014)
14. O. Popovicheva, G. Engling, K.T. Lin, N. Persiantseva, M. Timofeev, E. Kireeva, G. Wachtmeister, Diesel/biofuel exhaust particles from modern internal combustion engines: microstructure, composition, and hygroscopicity. *Fuel* **157**, 232–239 (2015)
15. E. Mattarelli, C.A. Rinaldini, V.I. Golovitchev, CFD-3D analysis of a light duty dual fuel (diesel/natural gas) combustion engine. *Energy Procedia* **45**, 929–937 (2014)
16. J.J. Schauer, Design criteria for future fuels and related power systems addressing the impacts of non-CO<sub>2</sub> pollutants on human health and climate change. *Ann. Rev. Chem. Biomol. Eng.* **6**, 101–120 (2015)

17. J.L. Vieira, G.V. Guimaraes, P.A. de Andre, F.D. Cruz, P.H.N. Saldiva, E.A. Bocchi, The respiratory filter reduces the cardiovascular effects associated with diesel exhaust exposure: a randomized, prospective, double-blind, controlled study of heart failure: the FILTER-HF trial. *JACC Heart Fail.* **4**(1), 55–64 (2016)
18. K. Berhane, Y. Zhang, M.T. Salam, S.P. Eckel, W.S. Linn, E.B. Rappaport, F.D. Gilliland, Longitudinal effects of air pollution on exhaled nitric oxide: the children's health study. *Occup. Environ. Med.* **71**(7), 507–513 (2014)
19. F. Christodoulou, A. Megaritis, Experimental investigation of the effects of simultaneous hydrogen and nitrogen addition on the emissions and combustion of a diesel engine. *Int. J. Hydrog. Energy* **39**(6), 2692–2702 (2014)
20. M. Tinajero-Trejo, K.J. Denby, S.E. Sedelnikova, S.A. Hassoubah, B.E. Mann, R.K. Poole, Carbon monoxide-releasing Molecule-3 (CORM-3; Ru (CO) 3Cl (Glycinate)) as a tool to study the concerted effects of carbon monoxide and nitric oxide on bacterial Flavohemoglobin Hmp applications and pitfalls. *J. Biol. Chem.* **289**(43), 29471–29482 (2014)
21. K.H. Kim, S.A. Jahan, E. Kabir, R.J. Brown, A review of airborne polycyclic aromatic hydrocarbons (PAHs) and their human health effects. *Environ. Int.* **60**, 71–80 (2013)
22. L.B. Braga, J.L. Silveira, M.E. da Silva, E.B. Machin, D.T. Pedrosa, C.E. Tuna, Comparative analysis of a PEM fuel cell and an internal combustion engine driving an electricity generator: technical, economical and ecological aspects. *Appl. Therm. Eng.* **63**(1), 354–361 (2014)
23. L.E. Arteaga-Pérez, Y. Casas-Ledón, W. Prins, L. Radovic, Thermodynamic predictions of performance of a bagasse integrated gasification combined cycle under quasi-equilibrium conditions. *Chem. Eng. J.* **258**, 402–411 (2014)
24. S. Verhelst, Recent progress in the use of hydrogen as a fuel for internal combustion engines. *Int. J. Hydrog. Energy* **39**(2), 1071–1085 (2014)
25. M.K. Debe, Electrocatalyst approaches and challenges for automotive fuel cells. *Nature* **486**(7401), 43–1–43–10 (2012), <http://search.proquest.com/openview/4fd6575f0c9c5af4ce49a704ba2995b0/1?pq-origsite=gscholar&cbl=40569>
26. H.A. Gasteiger, S.S. Kocha, B. Sompalli, F.T. Wagner, Activity benchmarks and requirements for Pt, Pt-alloy, and non-Pt oxygen reduction catalysts for PEMFCs. *Appl. Catal. B Environ.* **56**(1), 9–35 (2005)
27. Y. Yuan, J. Smith, G. Goenaga, D.J. Liu, B. Zhou, J. Liu, Performance improvement of fuel cells using platinum-functionalised aligned carbon nanotubes. *J. Exp. Nanosci.* **8**(6), 797–807 (2013)
28. J. Liu, Y. Yuan, S. Bashir, Functionalization of aligned carbon nanotubes to enhance the performance of fuel cell. *Energies* **6**(12), 6476–6486 (2013)
29. K. Suárez-Alcántara, O. Solorza-Feria, Kinetics and PEMFC performance of Ru x Mo y Se z nanoparticles as a cathode catalyst. *Electrochim. Acta* **53**(15), 4981–4989 (2008)
30. L.G.S. Pereira, F.R. dos Santos, M.E. Pereira, V.A. Paganin, E.A. Ticianelli, CO tolerance effects of tungsten-based PEMFC anodes. *Electrochim. Acta* **51**(19), 4061–4066 (2006)
31. J. Parrondo, F. Mijangos, B. Rambabu, Platinum/tin oxide/carbon cathode catalyst for high-temperature PEM fuel cell. *J. Power Sources* **195**(13), 3977–3983 (2010)
32. B.P. Vinayan, R. Nagar, N. Rajalakshmi, S. Ramaprabhu, Novel platinum–cobalt alloy nanoparticles dispersed on nitrogen-doped graphene as a cathode electrocatalyst for PEMFC applications. *Adv. Funct. Mater.* **22**(16), 3519–3526 (2012)
33. E. Slavcheva, I. Radev, S. Bliznakov, G. Topalov, P. Andreev, E. Budevski, Sputtered iridium oxide films as electrocatalysts for water splitting via PEM electrolysis. *Electrochim. Acta* **52**(12), 3889–3894 (2007)
34. I. Roche, E. Chaînet, M. Chatenet, J. Vondrák, Carbon-supported manganese oxide nanoparticles as electrocatalysts for the oxygen reduction reaction (ORR) in alkaline medium: physical characterizations and ORR mechanism. *J. Phys. Chem. C* **111**(3), 1434–1443 (2007)
35. A. Serov, C. Kwak, Review of non-platinum anode catalysts for DMFC and PEMFC application. *Appl. Catal. B Environ.* **90**(3), 313–320 (2009)
36. L. Dai, Y. Xue, L. Qu, H.J. Choi, J.B. Baek, Metal-free catalysts for oxygen reduction reaction. *Chem. Rev.* **115**(11), 4823–4892 (2015)

37. Y. Jiao, Y. Zheng, M. Jaroniec, S.Z. Qiao, Design of electrocatalysts for oxygen-and hydrogen-involving energy conversion reactions. *Chem. Soc. Rev.* **44**(8), 2060–2086 (2015)
38. H. Liu, C. Song, L. Zhang, J. Zhang, H. Wang, D.P. Wilkinson, A review of anode catalysis in the direct methanol fuel cell. *J. Power Sources* **155**(2), 95–110 (2006)
39. R. Bashyam, P. Zelenay, A class of non-precious metal composite catalysts for fuel cells. *Nature* **443**(7107), 63–66 (2006)
40. C.T. Hsieh, J.Y. Lin, Fabrication of bimetallic Pt–M (M= Fe, Co, and Ni) nanoparticle/carbon nanotube electrocatalysts for direct methanol fuel cells. *J. Power Sources* **188**(2), 347–352 (2009)
41. S.Y. Huang, P. Ganesan, S. Park, B.N. Popov, Development of a titanium dioxide supported platinum catalyst with ultrahigh stability for polymer electrolyte membrane fuel cell applications. *J. Am. Chem. Soc.* **131**(39), 13898–13899 (2009)
42. E.P. Murray, T. Tsai, S.A. Barnett, A direct- methane fuel cell with a ceria-based anode. *Nature* **400**(6745), 649–1–649–4 (1999), <https://www.nature.com/nature/journal/v400/n6745/pdf/400649a0.pdf?origin=ppub>
43. J. Graetz, New approaches to hydrogen storage. *Chem. Soc. Rev.* **38**(1), 73–82 (2009)
44. D.R. Palo, R.A. Dagle, J.D. Holladay, Methanol steam reforming for hydrogen production. *Chem. Rev.* **107**(10), 3992–4021 (2007)
45. K. Vasudeva, N. Mitra, P. Umasankar, S.C. Dhingra, Steam reforming of ethanol for hydrogen production: thermodynamic analysis. *Int. J. Hydrog. Energy* **21**(1), 13–18 (1996)
46. J.A. Turner, Sustainable hydrogen production. *Science* **305**(5686), 972–974 (2004)
47. T.R. Tephly, The toxicity of methanol. *Life Sci.* **48**(11), 1031–1041 (1991)
48. B.K. Nelson, W.S. Brightwell, D.R. MacKenzie, A. Khan, J.R. Burg, W.W. Weigel, P.T. Goad, Teratological assessment of methanol and ethanol at high inhalation levels in rats. *Fundam. Appl. Toxicol.* **5**(4), 727–736 (1985)
49. A. Demirbas, Progress and recent trends in biofuels. *Prog. Energy Combust. Sci.* **33**(1), 1–18 (2007)
50. A.L. Dicks, Hydrogen generation from natural gas for the fuel cell systems of tomorrow. *J. Power Sources* **61**(1–2), 113–124 (1996)
51. J. Zhang, W. Peng, Z. Chen, H. Chen, L. Han, Effect of cerium doping in the TiO<sub>2</sub> photoanode on the electron transport of dye-sensitized solar cells. *J. Phys. Chem. C* **116**(36), 19182–19190 (2012)
52. K. Eguchi, T. Setoguchi, T. Inoue, H. Arai, Electrical properties of ceria-based oxides and their application to solid oxide fuel cells. *Solid State Ionics* **52**(1–3), 165–172 (1992)
53. T.J. Brunner, P. Wick, P. Manser, P. Spohn, R.N. Grass, L.K. Limbach, W.J. Stark, In vitro cytotoxicity of oxide nanoparticles: comparison to asbestos, silica, and the effect of particle solubility. *Environ. Sci. Technol.* **40**(14), 4374–4381 (2006)
54. Choudhary, B. K. (1980). Bandyopadhyay. Important of mineral content and medicinal properties of *Moringa oleifera* and *Hygrophila auriculata*. *Sachitra Ayurved*, 50(7), 543–549
55. A.K. Dash, G.K. Dutta, K.K. Sardar, G. Sahoo, The ethnomedicinal importance of *Hygrophila spinosa* T. Anders: a review. *Plant Arch.* **12**(1), 5–9 (2012)
56. S. Ahmed, A. Rahman, M. Mathur, M. Athar, S. Sultana, Anti-tumor promoting activity of *Asteracantha long folio* against experimental hepatocarcinogenesis in rats. *Food Chem. Toxicol.* **39**(1), 19–28 (2001)
57. M.S. Hussain, S. Fareed, M. Ali, Hyphenated chromatographic analysis of bioactive gallic acid and quercetin in *Hygrophila auriculata* (K. Schum) Heine growing wildy in marshy places in India by validated HPTLC method. *Asian Pac. J. Trop. Biomed.* **2**(2), S477–S483 (2012)
58. N. Singh, G.J. Jenkins, R. Asadi, S.H. Doak, Potential toxicity of superparamagnetic iron oxide nanoparticles (SPION). *Nano Rev. Exp.* **1**(5358), 1–15 (2010), <http://www.tandfonline.com/doi/pdf/10.3402/nano.v1i0.5358>
59. S.J. Soenen, M. De Cuyper, Assessing iron oxide nanoparticle toxicity in vitro: current status and future prospects. *Nanomedicine* **5**(8), 1261–1275 (2010)
60. N. Kaushik, Saponins of *Chlorophytum* species. *Phytochem. Rev.* **4**(2), 191–196 (2005)

61. M.A. Lacaille-Dubois, Bioactive saponins with cancer related and immunomodulatory activity: recent developments. *Stud. Nat. Prod. Chem.* **32**, 209–246 (2005)
62. H. Meng, Z. Zhang, F. Zhao, T. Qiu, J. Yang, Orthogonal optimization design for the preparation of Fe<sub>3</sub>O<sub>4</sub> nanoparticles via chemical coprecipitation. *Appl. Surf. Sci.* **280**, 679–685 (2013)
63. Q.A. Pankhurst, J. Connolly, S.K. Jones, J.J. Dobson, Applications of magnetic nanoparticles in biomedicine. *J. Phys. D. Appl. Phys.* **36**(13), R167-1–R167-16 (2003), <https://isis.ku.dk/kurser/blob.aspx?feltid=20160>
64. W. Kai, X. Xiaojun, P. Ximing, H. Zhenqing, Z. Qiqing, Cytotoxic effects and the mechanism of three types of magnetic nanoparticles on human hepatoma BEL-7402 cells. *Nanoscale Res. Lett.* **6**(1), 480-1–48-10 (2011), <https://link.springer.com/article/10.1186/1556-276X-6-480>
65. A.G. Bodnar, M. Ouellette, M. Frolkis, S.E. Holt, C.P. Chiu, G.B. Morin, W.E. Wright, Extension of life-span by introduction of telomerase into normal human cells. *Science* **279** (5349), 349–352 (1998)
66. H. Wang, J.A. Joseph, Quantifying cellular oxidative stress by dichlorofluorescein assay using microplate reader. *Free Radic. Biol. Med.* **27**(5), 612–616 (1999)
67. M. Gotić, S. Musić, Mössbauer, FT-IR and FE-SEM investigation of iron oxides precipitated from FeSO<sub>4</sub> solutions. *J. Mol. Struct.* **834**, 445–453 (2007)
68. M. Sundrarajan, M. Ramalakshmi, Novel cubic magnetite nanoparticle synthesis using room temperature ionic liquid. *J. Chem.* **9**(3), 1070–1076 (2012)
69. O.M. Lemine, K. Omri, B. Zhang, L. El Mir, M. Sajieddine, A. Alyamani, M. Bououdina, Sol-gel synthesis of 8nm magnetite (Fe<sub>3</sub>O<sub>4</sub>) nanoparticles and their magnetic properties. *Superlattice. Microst.* **52**(4), 793–799 (2012)
70. H. Wang, T.B. Shrestha, M.T. Basel, R.K. Dani, G.M. Seo, S. Balivada, D. Moore, Magnetic-Fe/Fe<sub>3</sub>O<sub>4</sub> nanoparticle-bound SN<sub>38</sub> as a carboxylesterase-cleavable prodrug for the delivery to tumors within monocytes/macrophages. *Beilstein J. Nanotechnol.* **3**(1), 444–455 (2012)
71. S.A. Kulkarni, P.S. Sawadh, P.K. Palei, K.K. Kokate, Effect of synthesis route on the structural, optical and magnetic properties of Fe<sub>3</sub>O<sub>4</sub> nanoparticles. *Ceram. Int.* **40**(1), 1945–1949 (2014)
72. D. Yoo, J.H. Lee, T.H. Shin, J. Cheon, Theranostic magnetic nanoparticles. *Acc. Chem. Res.* **44** (10), 863–874 (2011)
73. J.T. Nurmi, P.G. Tratnyek, V. Sarathy, D.R. Baer, J.E. Amonette, K. Pecher, M.D. Driessen, Characterization and properties of metallic iron nanoparticles: spectroscopy, electrochemistry, and kinetics. *Environ. Sci. Technol.* **39**(5), 1221–1230 (2005)
74. M. Auffan, J. Rose, M.R. Wiesner, J.Y. Bottero, Chemical stability of metallic nanoparticles: a parameter controlling their potential cellular toxicity in vitro. *Environ. Pollut.* **157**(4), 1127–1133 (2009)
75. H. Markides, M. Rotherham, A.J. El Haj, Biocompatibility and toxicity of magnetic nanoparticles in regenerative medicine. *J. Nanomater.* **2012**, 13-1–13-11 (2012), <http://dl.acm.org/citation.cfm?id=2437971>
76. C. Xu, M.S. Inokuma, J. Denham, K. Golds, P. Kundu, J.D. Gold, M.K. Carpenter, The feeder-free growth of undifferentiated human embryonic stem cells. *Nat. Biotechnol.* **19**(10), 971-1–971-5 (2001), <http://search.proquest.com/openview/487240db7cd50ece7301a88928509889/1?pq-origsite=gscholar&cbl=47191>
77. C.J. Ku, W. Karunarathne, S. Kenyon, P. Root, D. Spence, Fluorescence determination of nitric oxide production in stimulated and activated platelets. *Anal. Chem.* **79**(6), 2421–2426 (2007)
78. K.M. Lee, K.H. Choi, M.M. Ouellette, Use of exogenous hTERT to immortalize primary human cells. *Cytotechnology* **45**(1), 33–38 (2004)
79. H. Matsunaga, J.T. Handa, A. Aotaki-Keen, S.W. Sherwood, M.D. West, L.M. Hjelmeland, Beta-galactosidase histochemistry and telomere loss in senescent retinal pigment epithelial cells. *Invest. Ophthalmol. Vis. Sci.* **40**(1), 197–202 (1999)
80. S. Naqvi, M. Samim, M.Z. Abidin, F.J. Ahmed, A.N. Maitra, C.K. Prashant, A.K. Dinda, Concentration- dependent toxicity of iron oxide nanoparticles mediated by increased oxidative stress. *Int. J. Nanomedicine* **5**, 983-1–983-7 (2010), <https://www.ncbi.nlm.nih.gov/pmc/articles/PMC3010160/pdf/ijn-5-983.pdf>

81. C. Cheng, K.H. Müller, K.K. Koziol, J.N. Skepper, P.A. Midgley, M.E. Welland, A.E. Porter, Toxicity and imaging of multi-walled carbon nanotubes in human macrophage cells. *Biomaterials* **30**(25), 4152–4160 (2009)
82. M. Finkbeiner, A. Inaba, R. Tan, K. Christiansen, H.J. Klüppel, The new international standards for life cycle assessment: ISO 14040 and ISO 14044. *Int J Life Cycle Assess* **11**(2), 80–85 (2006)
83. D.J. Briggs, A framework for integrated environmental health impact assessment of systemic risks. *Environ. Health* **7**(1), 61 (2008)
84. S. Ross, D. Evans, Use of life cycle assessment in environmental management. *Environ. Manage* **29**(1), 132–142 (2002)
85. S. Foss Hansen, B.H. Larsen, S.I. Olsen, A. Baun, Categorization framework to aid hazard identification of nanomaterials. *Nanotoxicology*, **1**(3), 243–250 (2007)
86. I. Linkov, T.P. Seager, Coupling multi-criteria decision analysis, life-cycle assessment, and risk assessment for emerging threats (2011)
87. S.J. Cowell, R. Fairman, R.E. Lofstedt, Use of risk assessment and life cycle assessment in decision making: a common policy research agenda. *Risk Anal* **22**(5), 879–894 (2002)
88. ECHA (European Chemicals Agency), 2010 Guidance on information requirements and chemical safety assessment. Chapter R.16: environmental exposure estimation. **2**, (2010)



# Correction to: Evaluation of Cell Performance and Durability for Cathode Catalysts (Platinum Supported on Carbon Blacks or Conducting Ceramic Nanoparticles) During Simulated Fuel Cell Vehicle Operation: Start-Up/Shutdown Cycles and Load Cycles

Makoto Uchida, Katsuyoshi Kakinuma, and Akihiro Iiyama

## Correction to:

**Chapter 3 in F. Li et al. (eds.), *Nanostructured Materials for Next-Generation Energy Storage and Conversion*, [https://doi.org/10.1007/978-3-662-56364-9\\_3](https://doi.org/10.1007/978-3-662-56364-9_3)**

The original version of this chapter unfortunately contained mistakes in the figure captions of Fig. 3.7, Fig. 3.9, and Fig. 3.27.

In the figure captions of Fig. 3.7, Fig. 3.9 and Fig. 3.27(d) “(1.0 MPa)” was incorrectly given instead of “(0.1 MPa)”.

In Fig. 3.7 the reference number [9] was incorrectly given instead of [13].

The corrected figure captions are given in the following:

**Fig. 3.7** Cell performance *I-E* curves for initial (open symbols) and after (filled symbols) durability testing for c-Pt/CB (○), c-Pt/GCB (Δ), Pt/GCB-HT (□), and n-Pt/GCB (∇) catalysts at 65 °C, 100% RH with H<sub>2</sub> and air (0.1 MPa). MEA: Pt loading (cathode/anode) 0.5 mg-Pt cm<sup>-2</sup>, Nafion (NRE212), active electrode-area 29.2 cm<sup>2</sup>, Japan Automotive Research Institute (JARI) standard cell [13]

The updated online version of the original chapter can be found at [https://doi.org/10.1007/978-3-662-56364-9\\_3](https://doi.org/10.1007/978-3-662-56364-9_3)

**Fig. 3.9** Effect of scan rate ( $0.50 \text{ V s}^{-1}$ ,  $0.10 \text{ V s}^{-1}$ , and  $0.05 \text{ V s}^{-1}$ ) for the triangular wave cycling and lower potential limit (0.8 V, 0.9 V, and 1.0 V) for the square wave cycling at  $80 \text{ }^\circ\text{C}$ , 100% RH with  $\text{H}_2$  and  $\text{N}_2$  (0.1 MPa). MEA: Pt loading (cathode/anode)  $0.5 \text{ mg-Pt cm}^{-2}$ , Nafion (NRE212), active electrode-area  $29.2 \text{ cm}^2$ , JARI standard cell [22]

**Fig. 3.27 (a)** Normalized ECA changes during the durability evaluations of load cycles with holding times of OCV/load ( $0.5 \text{ A cm}^{-2}$ ) between ca. 0.63 V and OCV at  $80 \text{ }^\circ\text{C}$  and 100% RH,  $\diamond$ : 3 s/3 s (A1),  $\circ$ : 3 s/60 s (A2),  $\square$ : 60 s/3 s (A3), **(b)** IR-free  $I$ - $E$  curves before and after the durability evaluations at  $80 \text{ }^\circ\text{C}$  and 100% RH under  $\text{H}_2$ /air, **(c)** Normalized ECA changes during the load cycles and the OCV holding at  $80 \text{ }^\circ\text{C}$  and 100% RH,  $\square$ : OCV/load holding time of 60 s/3 s (A3),  $\triangle$ : OCV holding time of 10,000 min (A4), **(d)** IR-free  $I$ - $E$  curves before and after the load cycles and OCV holding at  $80 \text{ }^\circ\text{C}$  and 100% RH under  $\text{H}_2$ /air (0.1 MPa), Pt loading (cathode/anode)  $0.1/0.5 \text{ mg-Pt cm}^{-2}$ , Nafion (NRE211), active electrode-area  $29.2 \text{ cm}^2$ , JARI standard cell [59]

The original chapter has been corrected.

# Index

## A

A-B binary system, 294  
A-site atoms, 242  
AA, *see* Acetylacetone  
Absorption/adsorbed, 119, 155, 277, 315, 388, 392, 394–404, 408, 411, 428, 451–453, 459, 460, 504  
AC, *see* Activated carbons  
Acetylacetone (AA), 341  
Activated carbons (AC), 18, 446  
Activation energy, 240, 284, 311, 347  
Activation polarization, 229, 230, 243, 262  
Adaptive fuel consumption minimization strategy (AFCMS), 371  
Adsorbed molecules, 93  
Adsorbed oxygen atoms, 176  
Advanced fuel cycle initiatives, 9  
AE, *see* Alkaline earth  
AES, *see* Auger electron spectroscopy  
AFC, *see* Alkaline fuel cell  
AFCMS, *see* Adaptive fuel consumption minimization strategy  
Ag, *see* Argentum/Silver  
Air start (AS), 71–74  
Alanates, 449  
ALD, *see* Atomic layer deposition  
Alkaline earth (AE), 291  
Alkaline fuel cell (AFC), 40–44, 50, 183  
Alloy/alloying, 17–19, 117, 118, 129, 131, 147, 161, 173–175, 178, 179, 181, 183–189, 192, 215, 216, 219, 241, 293, 295, 341, 348, 353, 392, 416–417, 426, 427, 434, 451–453, 474  
Amides, 448–449  
Ammonium persulfate (APS), 211  
Amorphous, 62, 92, 93, 161, 182, 292, 304, 305, 326–328, 448, 456, 480  
Amorphous phase modeling, 305

## Anode

flow field, 200  
polarization, 235  
Anode/electrolyte layer (A/E) interface, 504  
Anodic catalyst layer, 252  
Anodic oxidation catalyst, 202  
Antimony-doped tin oxide (ATO), 155  
APS, *see* Ammonium persulfate  
Argentum/Silver (Ag), 171, 173, 187, 188, 215, 234, 342  
ARSM, *see* Atmospheric resistive switching mechanism  
AS, *see* Air start  
Atmospheric resistive switching mechanism (ARSM), 54, 101–106  
ATO, *see* Antimony-doped tin oxide  
Atomic energy commission (AEC), 5, 7, 10  
Atomic layer deposition (ALD), 187, 233, 237  
Atomic oxygen, 340–342, 348  
Atoms for Peace, 3  
Au, *see* Auric/Gold  
Auger electron spectroscopy (AES), 289  
Auric/Gold (Au), 161, 171, 173, 181, 184, 186–188, 189, 191, 192, 203, 215, 340, 342

## B

B, *see* Boron  
B-site atoms, 242, 289, 308–310, 318, 324  
BAAEDI, *see* Bisacetylacetonethylenediimine  
Balance of plants (BoP), 388, 419  
Barium strontium cobalt (BSCF), 232–234  
Battery, 18, 20, 146, 172, 361, 362, 364–366, 367, 369, 370, 372, 374, 376–381, 471  
Battery electric vehicle(s) (BEV), 361–364, 369, 380, 381  
Benzene-1,4-dicarboxylate (BDC), 447



- BEV, *see* Battery electric vehicle(s)
- Binding energy, 178, 180, 183, 311, 340–343, 348, 350, 354, 446, 448
- Biomass, 8, 11, 14, 411
- Bioreclamation process, 192
- Bipolar plate (BP), 18, 254, 261, 277, 278, 389, 474, 478–485  
material, 485
- Birnessite type, 456
- Bis-acetylacetone-ethylene-diimine (BAAEDI), 341
- Bis-salicyl-aldehyde-ethylene-diimine (BSAEDI), 341
- BN, *see* Boron nitrides
- BoP, *see* Balance of plants
- Boranes, 451
- Borohydride(s), 149, 210, 211, 449, 450
- Boron (B), 450–451
- Boron nitrides (BN), 160
- Boundary conditions, 262–264, 478
- Braking energy, 19, 368
- Bridge carbonyls, 127
- Brouwer diagram(s), 287, 306, 307, 315, 316, 329
- Bruggemann's correction, 257
- BSAEDI, *see* Bis-salicyl-aldehyde-ethylene-diimine
- BSCF, *see* Barium strontium cobalt
- Butler-Volmer  
equation, 255, 256  
kinetics, 426
- C**
- C, *see* Carbon
- C/A, *see* Cubic/amorphous
- Calcination, 155, 237, 242
- CALCulation of PHase Diagram (CALPHAD), 293, 295, 305–330
- CALPHAD, *see* CALCulation of PHase Diagram
- Capture and storage technologies, 15
- Carbide(s), 88–90, 118, 147, 157–159, 163
- Carbon (C), 3, 40, 56, 116, 147, 172, 202, 228, 342, 361, 386, 411, 445, 474, 519
- Carbon black (CB), 58, 147, 149, 173, 185, 188, 216, 217, 483
- Carbon capture, 9
- Carbon dioxide (CO<sub>2</sub>), 13–15, 17, 200, 201, 414, 446, 519
- Carbon monoxide (CO), 12, 17, 117, 118, 120, 121, 123, 127–129, 130, 140, 141, 151, 175, 212, 216, 228, 423, 429, 522
- Carbon nanotube (CNT), 163, 183, 202–206, 218, 219, 346, 432, 433, 446, 483, 484, 491, 492  
film, 163, 183, 202–209, 218, 346, 432, 433, 446, 483, 491
- Carbon nanotube-membrane electrode assembly (CNT-MEA), 204–206
- Carbon oxidation reaction (COR), 58, 59, 75, 76, 78, 79, 106
- Carbon paper (CP), 202, 203, 205
- Carbon powders, 116, 123
- Carbon sequestration, 9
- Carbonyl ligands, 120, 127
- Catalyst  
stability, 353  
supported, 62, 66, 88, 92, 101, 147, 155, 159, 161, 210–217, 451
- Catalyst coated membrane (CCM), 75, 203, 389, 411
- Catalyst layer (CL), 18, 57, 58, 98, 153, 157, 190, 201–203, 209, 212, 234, 250–252, 254–256, 259–261, 272, 277, 409, 411, 416, 417, 419, 422, 423, 425–427, 428, 475, 477, 490, 491
- Catalytic activity, 66, 93, 103, 117–119, 121, 122, 126, 128–130, 131, 133, 141, 149, 151, 153, 155, 159, 161, 162, 185, 189, 190, 210, 211, 215, 216, 220, 230, 231, 235, 238–242, 285, 341, 344, 348, 350, 417, 429, 449
- Cathode  
catalyst layer, 58, 98, 153, 201  
current collector, 203, 204, 237  
thickness, 317
- CB, *see* Carbon black
- CCM, *see* Catalyst coated membrane
- CEM, *see* Compound energy model
- Ceria (CeO), 213, 233, 234, 237–239, 240, 242, 285, 286, 324, 507–510, 521
- CGO, *see* Gadolinium doped ceria
- Charge carrier, 94, 251, 288, 307, 514
- Charge disproportionation, 287, 288, 296, 297, 301, 306, 308, 309
- Charge-transfer, 32, 33
- Chemical energy conversion, 29, 33–35
- Chemical vapor deposition (CVD), 181, 234, 447
- CHP, *see* Cogeneration of heat and power
- Chromium (Cr), 118, 155, 238–240, 292, 341, 342, 447, 451, 453, 483
- Chronoamperometry, 123
- CL, *see* Catalyst layer
- Clean Air Act, 13

- Close-loop, 267, 398  
Clusters, 101, 115–141, 190, 210, 216, 218, 235, 287, 288, 341, 353, 447, 489, 501  
CNT, *see* Carbon nanotubes  
CO, *see* Carbon monoxide  
Co, *see* Cobalt  
CO Co-Oxidation, 151, 215  
Co hydrogenation, 127  
CO poisoning, 17, 18, 183, 213, 215, 428–432  
CO sorption, 426  
CO<sub>2</sub>, *see* Carbon dioxide  
Coal, 3, 5, 8–14, 20, 21, 386, 518–520  
Cobalt (Co), 118, 174, 217, 233, 239, 241, 284, 341, 342, 344, 416, 452, 521  
Coefficient of thermal expansion (CTE), 284, 324, 330, 475, 476  
Cogeneration of heat and power (CHP), 386, 387, 396, 398, 404  
Cohesive energy, 353, 354  
Coking, 228, 237, 239, 241  
Columbia charge, 215  
Competitive adsorption, 425  
Complex hydride, 448–450, 464  
Compound energy model (CEM), 294  
Compressed gas/compressed hydrogen gas/compression of hydrogen, 18, 19, 278, 445, 520  
Concentration polarization, 229, 230, 235  
Concus-Finn condition, 277  
Condensation/condenser, 121, 259, 260  
Cooling system, 264, 270, 271  
COR, *see* Carbon oxidation reaction  
Core-shell/core-shelled, 161, 174, 183, 184, 187–189, 192  
Corrosion, 19, 59, 60, 62–68, 70, 73, 86, 88, 99, 101, 103, 104, 106, 147, 149, 159, 160, 163, 173, 204, 210, 426, 480–482  
Corundum, 319  
Cost, 5, 8, 10, 11, 14, 17, 20, 21, 117–119, 136, 141, 163, 172–174, 181, 186, 187, 191–193, 209, 215, 216, 221, 228, 229, 240, 267, 268, 283, 285, 338, 363, 378, 386, 387, 393, 408, 428, 434, 445, 447, 454, 474, 479–481, 482, 484–486, 491, 493, 500, 507, 508, 510, 512, 513  
Cost of electricity, 388  
Coulomb/Coulomb's Law, 31, 32, 35, 256, 340, 369  
Covalent compounds, 120, 157, 448, 454, 492, 532  
CP, *see* Carbon paper  
Cr, *see* Chromium  
Critical radius, 190  
Crossover, 82–84, 202, 207, 209, 216, 373, 374, 411, 487, 491, 492, 512, 513  
CTE, *see* Coefficient of thermal expansion  
Cu, *see* Cuprum/Copper  
Cubic phase, 292, 449  
Cubic/amorphous (C/A), 328  
Cuboctahedral arrangement, 127  
Cuprum/Copper (Cu), 118, 124, 174, 183, 237–238, 342, 392, 448, 450, 451  
Current density, 41, 47, 48, 80–87, 94, 97, 99, 104, 118, 124, 131, 133, 134, 136–138, 154, 208–210, 212, 215, 221, 241, 255, 275, 276, 321, 323, 390–392, 410, 413, 414, 419, 420, 422, 423, 425, 430, 434  
Current-potential curves/IV performance (I-Es), 61, 64, 72–74, 80, 82, 83, 97, 99, 100, 105, 130, 132  
CV, *see* Cyclic voltammetry/cyclic voltammograms  
CVD, *see* Chemical vapor deposition  
Cyclic voltammetry/cyclic voltammograms (CV), 64, 66–69, 74, 80, 121, 123, 127–129, 132, 134, 151, 210–212, 213, 221, 415, 416, 425, 429  
Cytotoxicity, 21
- D**  
DARPA, *see* Defense Advanced Research Projects Agency  
Decarbonylation, 121, 125, 126, 129, 135  
Decomposition, 17, 29–34, 36, 37, 39, 40, 125, 129, 153, 182, 184, 239, 252, 432, 433, 449–451  
Defect reaction, 288, 295, 296, 301, 302, 306, 308, 309  
Defense Advanced Research Projects Agency (DARPA), 7  
Density functional theory (DFT), 176, 210, 290, 311, 339–340, 430, 457, 465  
Department Of Energy (DOE), 5–12, 67, 173, 174, 192, 480–486  
DFT, *see* Density functional theory  
DHW, *see* Domestic hot water  
Dibenzotetraazaanulenes (TAA), 118  
Dichlorofluorescein, 525, 532  
Diesel particulate matter, 12  
Diffusion barrier, 290  
Diffusion coefficient, 131, 255, 257, 258, 260, 265, 311, 416  
Diffusion layer (DL), 16, 17, 183, 190, 200–202, 207, 254, 259, 277, 278, 389, 474, 477

- Diffusion/diffusivity, 16–18, 44, 88–90, 97, 101, 131, 132, 157, 183, 189–191, 200–202, 207, 209, 230, 234, 235, 239, 242, 250, 254, 255, 257–259, 260, 265, 275, 276, 278, 290, 291, 311, 314, 347, 389, 411, 416, 418, 424, 429, 433, 452, 474, 479, 484, 504, 512, 532
- Direct electrostatic-to-chemical energy conversion, 33–35
- Direct methanol fuel cells (DMFC), 133, 157, 175, 183, 187, 191, 200–219, 221
- Dissolution, 57, 68, 74, 79–83, 85, 86, 100, 119, 156, 160, 183, 184, 189, 339, 350–353
- Dissolution potential, 339, 350–353, 414
- DMFC, *see* Direct methanol fuel cells
- DOE, *see* Department Of Energy
- Domestic hot water (DHW), 386
- Domestic oil production and usage, 4
- Dose-response, 536
- Drivetrain, 365–370, 378
- DTU, *see* Technical University of Denmark
- Dwight Eisenhower, 2, 3
- Dynamic viscosity, 259
- E**
- E-Tek, 154, 173
- ECA, *see* Electrochemical area
- ECSA, *see* Electrochemical surface area
- EDS, *see* Energy dispersive spectroscopy
- EELS, *see* Electron energy loss spectroscopy
- EL, *see* Water electrolyzer
- Electric power, 10, 27–50, 361–362, 367, 370, 372, 380
- Electrical conductivity, 18, 88, 89, 91, 93–95, 97, 98, 147–149, 151, 153, 156, 157, 159, 160, 183, 210, 218, 230, 233–235, 239, 242, 256, 285–289, 291, 292, 306–311, 480, 481, 483, 484
- Electrical energy, 16, 28, 29, 32, 200, 338, 396, 485
- Electro catalysts/electrocatalysis/  
electrocatalyst, 16, 60, 115–141, 146, 171–193, 220, 337–335, 408, 520
- Electro catalytic activity, 118, 127, 131, 149, 159, 162, 179, 181, 182, 184–186, 212, 218, 219, 239, 324, 350, 408, 409, 416, 434
- Electrocatalyst poisoning, 175, 178
- Electrocatalytic activity, 118, 127, 131, 149, 159, 162, 179, 181, 182, 184–186, 212, 218, 219, 239, 324, 350, 408, 409, 416, 434
- Electrochemical activity, 88, 128, 155, 159, 221, 242, 424, 427
- Electrochemical area (ECA), 60–62, 64–68, 71, 72, 82, 85, 86, 88, 89, 99–101, 104, 105, 338
- Electrochemical degradation, 350
- Electrochemical kinetics, 258
- Electrochemical quartz crystal microbalance (EQCM), 66
- Electrochemical reaction, 116, 117, 127, 191, 200–202, 230, 252, 256, 259–261, 275, 338, 345, 409, 416, 434, 474
- Electrochemical stability, 116, 147, 148, 155, 160, 350, 353
- Electrochemical surface area (ECSA), 159, 182, 211–215, 216, 221, 411, 414, 417–419, 421–423, 425, 426, 428
- Electrochemical surface area (ESA), 159, 221, 434
- Electrochemistry, 317, 343
- Electrode(s), 16, 29, 57, 116, 148, 174, 203, 227–243, 250, 284, 346, 389, 409, 474, 498, 520
- Electrolyte, 30, 97, 116, 149, 171–193, 210, 229, 250, 281–330, 387, 416, 459, 470, 498
- Electrolytic cells (ECs), 28–32, 39, 41, 44–48, 49
- Electrolytic polymer membrane, 16
- Electrolyzer, 28, 29, 38, 40–44, 50, 387
- Electromotive force (Emf), 31, 32, 36, 38–40
- Electron conduction, 94, 235
- Electron energy loss spectroscopy (EELS), 338
- Electron-holes, 287, 309, 310
- Electronic conducting phases, 162, 163
- Electronic conductivity, 116, 147, 148, 155, 156, 161–163, 179, 232, 237, 242, 284, 286, 287, 308–310, 324
- Electrons/electron mobility, 309, 329
- Electrooxidation/electro-oxidation, 80, 151, 155, 213, 215, 234, 417, 418
- Electrostatic energy, 29, 31, 33–35, 41
- Electrostatic-induction potential-superposed electrolysis (ESI-PSE), 28, 29, 36–42, 44–48, 50
- Electrostatic-induction potential-superposed water electrolysis, 29, 36–30
- Emf, *see* Electromotive force
- End plates, 17, 476, 478
- Energy consumption, 13, 365, 374, 386, 403, 518, 519
- Energy conversion, 28, 29, 33–35, 219, 228, 387, 433, 517–538

- Energy cycle, 28, 29, 40, 42–44, 50  
Energy demand, 2, 3, 518, 519  
Energy dispersive spectroscopy (EDS), 135, 240, 289, 524, 526, 527  
Energy policy, 3–6, 9, 20  
Energy-related research, 7, 9  
Entropy, 262, 272, 294, 298, 300–302  
Epitaxial growth or grows, 184  
EQCM, *see* Electrochemical quartz crystal microbalance  
EREVs, *see* Extended range electric vehicles  
ESA, *see* Electrochemical surface area  
ESI-PSE, *see* Electrostatic-induction potential-superposed electrolysis  
Ethanol, 8, 128, 129, 149, 155, 219, 239, 502, 521, 522  
Ethanol oxidation, 149, 219  
Ethylene glycol (EG), 149, 211–213, 393  
EUDC, *see* European union driving cycle  
European union driving cycle (EUDC), 374  
EXAFS, *see* Extended X-ray absorption fine structure  
Exchange-correlation functional, 340  
Exposure assessment, 536  
Extended range electric vehicles (EREVs), 361  
Extended X-ray absorption fine structure (EXAFS), 155, 428
- F**  
F, *see* Fluorine/fluoride  
Face centered cubic (FCC), 181, 338  
Faraday's law, 460, 461  
FCC, *see* Face centered cubic  
FCCJ, *see* Fuel Cell Commercialization Conference of Japan  
FCHJU, *see* Fuel Cells and Hydrogen Joint Undertaking  
FCs, *see* Fuel cells  
FCVs, *see* Fuel cell powered vehicles  
FCX, *see* Fuel Cell eXperimental (vehicle)  
Feedback controller, 265–268  
Ferrum (iron/ferrous/ferric) (Fe)  
FIB, *see* Focus(ed) ion beam  
Fickian, Stefan-Maxwell, 257  
First principle calculations, 324  
Flood/flooding, 17, 98, 201–206, 251, 275–277, 279, 390, 392, 398  
Flow field plate, 17  
Flow rate, 63, 66, 201, 204, 236, 264, 266, 268–270, 272, 275, 276, 278, 389, 390, 392–394, 397–399, 401–403, 404, 460, 500  
Fluorine/fluoride (F), 18, 31, 33, 35, 41, 342, 430, 491  
Focus(ed) ion beam (FIB), 428  
Forced convection, 272, 273  
Fossil fuels, 4, 8–10, 12, 14, 15, 172, 200, 221, 360–362, 364, 386, 408, 444  
Four-electron transfer step(s), 217, 347  
Fourth nearest-neighbor interactions, 311  
FSZ, *see* Fully stabilized zirconia  
Fuel cell(s) (FCs), 1–21, 28, 53–106, 115–141, 145–167, 171–193, 199–221, 227–243, 249–279, 281–330, 338, 359–381, 386, 408, 444, 469–493, 497–514, 519  
Fuel Cell Commercialization Conference of Japan (FCCJ), 57, 63, 64, 67  
Fuel Cell eXperimental (vehicle) (FCX), 18–20, 172, 362  
Fuel cell powered vehicles (FCVs), 8, 19, 48, 54–56, 57, 63, 66, 71, 74, 75, 78, 80, 105, 172, 362, 363, 365, 475  
Fuel cell tests, 124, 136, 153, 159  
Fuel Cells and Hydrogen Joint Undertaking (FCHJU), 445  
Full-Width-At-Half-Maximum (FWHM), 135  
Fully stabilized zirconia (FSZ), 292  
Fun, *see* Functional Unit  
Functional Unit (Fun), 536  
Future energy, 6–8, 361, 362, 364, 419, 424, 426, 427, 434, 513  
FWHM, *see* Full-Width-At-Half-Maximum
- G**  
GA, *see* Graphene Aerogel or Genetic Algorithm  
Gadolinium-doped ceria (GDC), 240, 285, 286  
Gas diffusion, 18, 88, 89, 101, 230, 235, 504, 512  
Gas diffusion electrodes (GDEs), 44, 45, 88, 183, 184, 207, 429, 477, 478, 484  
Gas diffusion layers (GDLs), 16–18, 183, 190, 202, 203, 205, 206, 254, 256, 257, 259–263, 275–277, 278, 389, 474, 475, 477  
Gas exchange process, 64  
Gas prices, 519  
Gasoline, 5, 8, 12–14, 15, 19, 21, 361, 362, 519, 523  
GCB, *see* Graphitized carbon black  
GDC, *see* Gadolinium-doped ceria  
GDEs, *see* Gas diffusion electrodes  
GDLs, *see* Gas diffusion layers

- Generalized differential quadrature (GQD), 218  
Generalized gradient approximation (GGA), 340  
Geothermal, 11  
GGA, *see* Generalized gradient approximation  
GHG, *see* Greenhouse gases  
Gibbs energy/Gibbs free energy, 34, 289, 290, 292–295, 297–306, 315, 320, 326, 328, 344–346, 522  
Glancing incidence X-ray diffraction (GIXD), 71, 73  
GNTs, *see* Graphene nanotubes  
GOA, *see* Graphene oxide aerogel  
GOs, *see* Graphene oxides  
GQD, *see* Generalized differential quadrature  
Grain boundaries, 94, 102, 289, 505, 510  
Graphene (G), 60, 149, 185, 202, 339, 430, 446, 483  
Graphene nanotubes (GNTs), 350  
Graphene oxide (GOs), 185, 207, 210, 211, 215, 220, 221, 450, 452  
Graphene oxide aerogel (GOA), 220, 221  
Graphene substrate, 210  
Graphitized carbon black (GCB), 59–63, 69, 70, 78, 80, 86–90, 95, 97–103  
Greenhouse gases (GHG), 3, 12, 13, 172, 360, 361, 522  
Gross domestic product, 10
- H**  
H, *see* Hydrogen/H<sub>2</sub>/H sorption  
HA, *see* Hygrophila Auriculata plant extract  
HAADF, *see* High-angle angular dark-field  
Hard X-ray photoelectron spectroscopy (HAXPES), 289, 290  
HAXPES, *see* Hard X-ray photoelectron spectroscopy  
Hazard identification, 536  
HCP, *see* Hexagonal close packing/packed  
Heat transfer, 251, 264, 273, 279, 415  
Heat treated/treatment (HT), 60, 94, 211, 289, 290, 313, 314  
Heptanuclear, 121  
Hexafluoro acetylacetone (HFAA), 341  
Hexagonal close packing/packed (HCP), 184  
Heyrovsky reaction, 134  
HFAA, *see* Hexafluoro acetylacetone  
HFR, *see* High-frequency resistance  
Hg, *see* Hydrargyrum (mercury)  
High-angle angular dark-field (HAADF), 524  
Highest occupied molecular orbital (HOMO), 349, 350  
High-frequency resistance (HFR), 419, 420, 429  
High-potential, 149  
High resolution transmission electron microscope (HRTEM), 411  
High superficial area, 277  
HLG, *see* HOMO-LUMO gap  
HOMO, *see* Highest occupied molecular orbital  
HOMO-LUMO gap (HLG), 349, 350  
Honda, 17–19, 20, 55, 56, 172, 362, 363  
HOR, *see* Hydrogen oxidation reaction  
HREG system, *see* Hydrogen generation system  
HRTEM, *see* High resolution transmission electron microscope  
HT, *see* Heat treated/treatment  
Humidified/humidifier/humidity, 17, 18, 70, 84, 86, 97, 99, 124, 136, 233, 237, 241, 250–252, 259, 264–267, 277, 279, 302, 352, 392, 410, 418, 461, 474, 475, 485, 486, 489–491  
Hydrargyrum (mercury) (Hg), 122, 173  
Hydration, 204, 206, 250, 251, 257, 275–277, 487  
Hydrocarbon fuels, 235, 237, 241, 426  
Hydrogel, 202, 207, 208, 220  
Hydrogen fuel, 8, 15, 216, 229, 235, 236, 266, 285, 493  
Hydrogen fuel cells, 21, 127, 172, 359–381  
Hydrogen generation (HREGs) system, 33, 40–50  
Hydrogen oxidation reaction (HOR), 58, 116–118, 119, 121, 123, 126, 127, 129–134, 140, 141, 175, 215–217, 219, 235, 240, 252, 409, 426, 521  
Hydrogen passivation, 75–79  
Hydrogen pressure, 272, 389, 391, 451, 456  
Hydrogen storage, 16, 19, 252, 387, 388, 392–397, 443–465, 523  
Hydrogen/H<sub>2</sub>/H sorption (H), 8, 27–50, 54, 116, 146, 172, 200, 229, 251, 285, 342, 359–381, 385–404, 408, 443–465, 473, 512, 520  
Hydrolysis, 414, 415, 451  
Hydrophilic/hydrophilicity, 97, 124, 151, 203, 277, 416, 485, 489, 492, 523  
Hydrophobic, 97, 203, 523  
Hydrothermal, 153, 159, 220, 445, 508, 512  
Hydroxide/hydroxyl ion, 211, 445, 521  
Hygrophila Auriculata plant extract (HA), 523, 527–529, 530, 532, 536

**I**

- I-Es, *see* Current-potential curves/IV performance  
ICEs, *see* Internal combustion engines  
Imides, 445, 448–449  
Import quotas, 5, 6  
Impregnation-thermal decomposition method, 153  
Incrustation processes, 119  
Indium oxides (ITOs), 155  
Indium tin oxide (ITO), 483  
INT, *see* Interface  
Inter-electrode voltage, 31  
Inter-particle distance, 189, 190  
Interaction parameter, 294, 300, 304  
Interface (INT), 31–33, 40, 73, 147, 149, 151, 160, 232, 237, 262, 275–277, 278, 286, 289–291, 338, 410, 411, 414, 416, 417  
Intermetallic compounds, 451, 452  
Internal combustion engines (ICEs), 15, 16, 172, 360–364, 408, 519  
Internal reforming (IR), 69, 85, 97, 99, 100, 105, 235  
Interstitial compounds, 157  
Intrinsic microporosity, 448  
Ionic, 31, 33, 35, 74, 85, 120, 229, 232, 233, 240, 252, 254–257, 283–285, 291, 292, 294–295, 304, 305, 309–311, 454, 492, 510  
Ionic conduction, 232, 240  
Ionization potential, 346, 347  
Iridium, 121, 122, 125–127, 129, 133–135, 138, 140, 149, 521  
Isothermal/isothermic state, 254, 445, 452  
ITO, *see* Indium tin oxide

**J**

- J, *see* Joule  
Jobs, 10, 13–15  
Joule, 390

**K**

- K, *see* Kalium (Potassium)  
Kalium (Potassium), 416  
Kinetic Monte Carlo simulation(s), 311  
KMC(s), *see* Kinetic Monte Carlo simulation(s)  
Kroger-Vink notation, 284, 296

**L**

- Lanthanum strontium chromium manganite, 238–240, 242  
Lanthanum strontium cobalt ferrite, 241, 284, 289, 290, 301, 302, 318–325  
Lanthanum strontium cobaltite, 232, 233  
Lanthanum strontium gallium magnesium oxide(s), 236, 237, 240, 242  
Lanthanum strontium gallium/Linear systems theory, 242  
Lanthanum strontium manganite, 232–234, 284, 286–292, 301, 302, 306–310, 312, 314–316, 324–325, 329, 512  
Lanthanum zirconium oxide(s), 290, 312, 313, 330  
Lattice Constant, 188  
LCA, *see* Life cycle assessment  
LDA, *see* Local density approximation  
Lewis base, 120  
Li, *see* Lithium  
Li-ion batteries, 366  
Life cycle assessment, 532, 535, 536  
Lifshitz-Slyozov-Wagner, 425  
Linear sweep voltammetry, 116, 121, 123, 127, 129  
Lithium, 416, 448, 449  
Load, 35, 43, 53–106, 117, 215, 216, 254, 266, 277, 291, 366, 387, 388, 398, 401, 404, 464, 475–478, 487, 489, 520  
Local density approximation, 340  
Low efficiency, 209, 362, 444  
Lowest unoccupied molecular orbital, 349, 350  
LSC, *see* Lanthanum strontium cobaltite  
LSCF, *see* Lanthanum strontium cobalt ferrite  
LSCM, *see* Lanthanum strontium chromium manganite  
LSGM(s)/LSGM(s) electrolyte, *see* Lanthanum strontium gallium magnesium oxide(s)  
LSM, *see* Lanthanum strontium manganite  
LST, *see* Lanthanum strontium gallium/Linear systems theory  
LUMO, *see* Lowest unoccupied molecular orbital  
LZO(s), *see* Lanthanum zirconium oxide(s)

**M**

- M/T, *see* Monoclinic/tetragonal  
Macroporous support, 157  
Magneli phase, 148–151, 163  
Magnetic nanoparticle(s), 523–534, 536

- Manganese, 238, 292, 308, 316, 341, 342, 354, 451, 457, 459, 521
- Manganese/manganese oxide, 238, 454–456, 464, 521
- Mass flow controller, 270, 393, 461, 462
- Mass fraction, 252, 257, 258, 262
- Mass transfer/mass transport, 32, 59, 88, 182, 201, 203, 205–207, 208, 229, 239, 262, 275, 277, 392, 408, 409, 421, 429
- Materials of Institut Lavoisier, 447
- MATLAB, 267, 367, 374
- Membrane electrode assembly, 16–18, 57, 58, 61, 64, 66, 68, 69, 72, 73, 88, 89, 95–101, 104–106, 124, 136, 138, 140, 200, 202–204, 207, 209, 251, 389, 408, 409, 422, 426, 474, 477, 478, 481, 488, 490, 491, 521
- MEMS, *see* Microelectromechanical system
- Metal hydride tank, 387–389, 392–404
- Metal hydride(s), 386–388, 393, 445, 448–454, 464
- Metal organic framework, 445, 447, 448
- Metal retrodonation, 120
- Metallic phthalocyanines, 118
- Methane, 8, 13, 230, 238, 239, 520, 522
- Methanol, 14, 17, 117, 119, 121, 123, 127–135, 140, 155, 175, 180, 200, 202–204, 206–218, 414, 492, 520–522
- Methanol oxidation, 129, 134, 212
- Methanol oxidation reaction, 119, 123, 129–135, 151–153, 158, 162, 164–166, 175, 179–181, 185, 186, 210–218, 220, 221
- MFC, *see* Mass flow controller
- MFFCS, *see* Multifunctional fuel cell system
- MHT, *see* Metal hydride tank
- Microcalorimetry, 292
- Microelectromechanical system, 200, 203
- Microwave irradiation/microwave-assisted method, 211, 213
- MIEC, *see* Mixed ionic and electronic conductor
- MIL, *see* Materials of Institut Lavoisier
- Mixed ionic and electronic conductor, 232, 233, 284, 330
- Mn, *see* Manganese
- MNP(s), *see* Magnetic nanoparticle(s)
- Mo, *see* Molybdenum
- Model/Modeling, 9, 14, 18, 30, 31, 82, 121, 228, 249–279, 287–289, 293–307, 309, 310, 315, 321, 329, 338, 340–342, 344, 345, 347, 350, 352, 353, 360, 364, 367–372, 374, 380, 421–428, 434, 457, 464, 471, 478, 536
- MOF, *see* Metal organic framework
- Molar fraction, 275
- Molybdenum, 117–119, 150, 151, 242, 451
- Monoclinic phase, 305
- Monoclinic/tetragonal, 292
- Monte Carlo simulation, 426
- MOR, *see* Methanol oxidation reaction
- Multi-walled carbon nanotube(s), 203, 446
- Multifunctional fuel cell system, 251
- MWNT(s), *see* Multi-Walled Carbon Nanotube(s)
- N**
- N<sub>2</sub>, *see* Nitrogen
- Nafion/Nafion ionomer, 61, 64, 68, 69, 72, 75, 82, 97, 123, 124, 157, 190, 203, 207, 251, 390, 411, 416, 427, 429, 477, 478, 485–490, 492
- Nano cage(s)/Nanocage(s), 181, 187, 188, 192
- Nano electrocatalyst(s), 179, 190
- Nano-catalyst(s), 147, 149, 179–186, 218, 236
- Nanomaterial(s)/Nanostructured, 119, 149, 152, 162, 171, 173, 179, 190, 192, 199–221, 227–243, 407–434, 449, 497–514, 517–539
- Nanoparticle(s), 53–106, 117, 119, 121, 132, 133, 147, 149, 151–153, 155, 157, 159–161, 166, 173, 178–180, 182–186, 189, 190, 192, 209, 211–213, 215, 216, 218, 220, 221, 232–235, 237–241, 292, 304–305, 325–330, 350, 352, 353, 409–411, 414, 416–418, 422, 427, 433, 434, 447, 491, 506–509, 511, 513, 514, 536
- Nanoporous, 450
- Nanosafety, 517–539
- Nanosheet/Nanosheet(s)/Nano-sheet(s), 152, 153, 184, 211, 215, 217, 220, 450
- Nanotube(s), 163, 166, 181, 183, 185, 233, 353, 521
- Nanowire(s), 87, 149, 182–187, 192, 219, 234, 353
- National Science Foundation, 6

- Natural gas, 3, 5, 8–11, 14, 16, 21, 362, 386, 387, 518, 519, 522, 523
- Natural oil, 5
- NCL-RGO(s), *see* Nitrogen-doped carbon layer-reduced graphene oxide(s)
- NEDC, *see* New European Driving Cycle
- Net exporter of energy, 3
- New European Driving Cycle, 366, 374, 376, 378, 379, 381
- Ni, *see* Nickel
- Nickel, 12, 118, 174, 229, 235–237, 239–241, 242, 285, 292, 340–342, 344, 348, 416, 417, 426, 433, 450, 451, 483, 499, 500, 506, 507, 512, 513, 521
- Niobium, 155, 450, 483
- Nitrogen, 13, 73, 80, 92, 116, 118, 123, 125, 126, 135, 203, 207, 217, 254, 258, 317, 342, 344, 346, 390, 415, 418, 433, 446, 450, 520, 521
- Nitrogen hydride(s), 450–451
- Nitrogen oxide(s), 12, 48, 520
- Nitrogen-doped carbon layer-reduced graphene oxide(s), 211–213
- NO, *see* Nitrogen oxide(s)
- Noble metal, 118, 147, 149–151, 157, 161, 165, 166, 171–193, 211, 215
- Noble metal lixiviation, 118
- Non-carbon catalysts support materials, 154
- Non-metal hydride(s), 448, 450–451
- Nonfaradaic process, 31
- Nonlinear dynamics, 268, 269
- NP(s), *see* Nanoparticle(s)
- Nuclear energy, 3, 8–10, 20
- Nuclearity, 121, 127, 353
- Numerical solution, 36, 49
- Nusselt number correlation, 264
- O**
- O, *see* Atomic Oxygen
- O<sub>2</sub>, *see* Oxygen
- OCV, *see* Open circuit voltage
- ODA, *see* Oxygen depleted air
- OER, *see* Oxygen evolution reaction
- OH binding, 189, 341, 342
- Ohmic losses/Ohmic resistance, 59, 64, 97–99, 229, 230, 236, 240, 277, 409, 419, 422, 491
- Onboard fuel reforming, 17
- Onboard high-pressure hydrogen tank(s), 19
- One-dimensional, 35, 162, 181–184, 219, 421, 422, 425
- OP, *see* Optimization problem
- Open circuit, 39, 124, 133, 136, 202, 234, 255 voltage, 41, 42, 47, 54, 56, 58, 80–87, 106, 486, 487, 512–514
- Optimization problem, 372
- ORR, *see* Oxygen reduction reaction
- Os, *see* Osmium
- Osmium, 119, 121, 122, 125–127, 135, 140, 173
- Ostwald ripening, 56, 80, 84, 100, 183, 186, 411, 414, 425, 434
- Outlook survey, 2
- Over potential or Overpotential(s), 117, 119, 134, 202, 229, 255, 262, 291, 346, 390, 392, 403, 417, 422, 423, 425–427, 429, 432
- Oxidation environments, 154
- Oxidation/Oxidizing/Oxide layer/Oxide(s), 13, 17, 41, 42, 56–58, 66, 79–83, 85, 102, 117, 119, 120, 127–129, 147, 153, 154, 157, 159, 160, 163, 165, 173, 175, 182, 202, 212, 213, 215, 230, 238, 239, 242, 283, 287, 291, 417, 421, 425, 432, 434, 450, 480, 523, 525, 529, 530, 532
- Oxidation reaction, 17, 28, 41, 43, 146, 200, 230, 237–239, 243
- Oxygen
- deficiency, 295–297, 301, 308
- depleted air, 251, 270, 271
- evolution reaction, 58, 59, 128
- reduction reaction, 58, 59, 70, 78, 88, 95, 104, 106, 116–119, 121, 123, 126, 127, 129–134, 140, 141, 146, 149–155, 158, 159, 161, 164–166, 173, 176–184, 186–189, 191, 192, 215–217, 220, 230–234, 243, 252, 283–286, 323, 330, 338–355, 409–411, 414, 416–419, 421–423, 428, 429, 432–434, 512, 521
- surface exchange process, 234
- transfer, 239
- vacancy concentration, 292, 310
- Ozone, 12, 13
- P**
- P, *see* Phosphorus
- p*-type oxide(s), 308, 309
- PAHs, *see* Polycyclic aromatic hydrocarbon(s)



- Palladium, 118, 149, 152, 161, 162, 173, 178, 180, 181, 183, 184, 186–189, 191, 192, 215, 216, 219, 239, 242, 341, 342, 353, 450
- PANI, *see* Polyaniline
- Partially stabilized zirconia, 292
- Particle growth, 79–82, 85, 86, 189, 427
- Particulate matter, 12, 13, 520, 536
- PBCO(s), *see* Praseodymium barium cobaltite oxide(s)
- PBFM(s), *see* Praseodymium barium ferrite magnesium oxide(s)
- PBMO(s), *see* Praseodymium barium magnesium oxide(s)
- Pc, *see* Phthalocyanine
- PCI, *see* Pressure-concentration isotherm
- PD, *see* Polydopamine
- Pd, *see* Palladium
- PDU, *see* Power Distributor Unit
- PEC, *see* Predictive environmental concentration
- PEEK, *see* Poly-ether-ether-ketone
- PEFC(s), *see* Polymer electrolyte fuel cell(s)
- PEM, *see* Proton exchange membrane
- PEMFC(s), *see* Polymer Electrolyte Membrane Fuel Cell(s)
- Pentanuclear, 121
- Perfluorosulfonic acid, 17, 250, 251, 485–490, 492
- Perovskite, 118, 230, 232, 233, 238–242, 284, 286, 289, 291–302, 306, 307, 309, 314–325
- Petroleum, 3, 9, 10, 14, 21, 522  
importation, 3
- PFSA, *see* Perfluorosulfonic acid
- PGM(s), *see* Platinum group metal(s)
- Phase structure, 233, 242
- PHEV(s), *see* Plug-in hybrid electric vehicle(s)
- Phosphoric acid electrolyte, 153
- Phosphorus, 462
- Photovoltaic(s), 15, 191, 386, 401–404
- Phthalocyanine, 341, 448
- Physisorbed hydrogen, 448
- Physisorption, 445–448, 464
- PIM, *see* Intrinsic microporosity
- Platinum catalyst/Platinum electrocatalyst(s), 16, 17, 118, 129, 131–133, 138, 139, 141, 434
- Platinum group metal(s), 173, 191, 428, 429
- Platinum nanoparticle(s), 132, 133, 409, 411
- Platinum/Platinum alloy, 15, 53–106, 117–119, 127, 128, 132, 134, 137, 138, 140, 141, 146, 147, 158, 162, 164, 172, 173, 184, 191, 210–213, 251, 409, 411, 417, 418, 428, 434, 450, 474, 483, 520, 521
- Plug-in hybrid electric vehicle(s), 361–363
- Polarization curve(s), 69, 129–132, 141, 150, 151, 154, 159, 217, 418
- Policy/Policies, 1–21, 361, 363
- Poly(vinylidene fluoride) cross-linked with divinylbenzene, 17
- Poly-ether-ether-ketone, 454, 456, 464
- Polyaniline, 119, 162, 166
- Polycyclic aromatic hydrocarbon(s), 13, 408, 520
- Polydopamine, 447
- Polymer electrolyte fuel cell(s), 63, 66, 67, 70, 71, 75, 78, 86–88, 95, 101, 106, 172–175, 177, 178, 181, 182, 184, 185, 187, 189, 190, 192, 193, 459, 461
- Polymer electrolyte membrane fuel cell(s), 250
- Polymer membrane conductivity, 118
- Polymorph(s), 292, 303, 304, 326, 327
- Polynuclear metal transition(s), 121
- Polypyrrole, 118, 162, 344
- Polytetrafluoroethylene, 17, 203, 485, 486, 489, 491
- Polyvinylidene fluoride, 203, 483, 491
- Porous electrode, 230, 254, 322, 475
- Porous/Porosity, 95, 116, 135, 136, 147, 149, 157, 160, 161, 163, 182–184, 186, 190, 201, 202, 204, 207–209, 219, 230, 232, 233, 235–237, 238, 242, 254, 256, 259–261, 278, 284, 285, 322, 427, 428, 446–448, 451, 474, 475, 477, 478, 491, 501, 502, 504–506, 508, 510–512
- Potential energy surface, 339, 342–345
- Potential/Potential cycling, 57, 62, 63, 70, 71, 74, 79, 80, 83, 180, 184, 416–419
- Power cycling, 422, 426
- Power density, 124, 136, 137, 141, 206, 233–237, 240–242, 460, 470, 480–482, 507, 512, 514
- Power distributor unit, 364, 370, 375
- PPy, *see* Polypyrrole
- Pr, *see* Platinum/Platinum alloy
- Praseodymium barium cobaltite oxide(s), 242
- Praseodymium barium ferrite magnesium oxide(s), 242
- Praseodymium barium magnesium oxide(s), 241
- Praseodymium strontium cobalt iron niobium oxide(s), 241
- Pre-exponential factor, 311
- Predictive environmental concentration, 536
- President Eisenhower, 3–6, 9, 10, 20
- Pressure-concentration isotherm, 452

- Proton exchange membrane, 175, 200, 250, 387, 470, 485–492
- Proton-transfer activation energy, 347
- PSCFN(s), *see* Praseodymium strontium cobalt iron niobium oxide(s)
- PSZ, *see* Partially stabilized zirconia
- Pt cluster(s), 216
- Pt dissolution, 57, 74, 80, 82, 83, 85, 86, 189, 410, 411, 414, 421, 422, 425
- Pt loading, 61, 62, 64, 68, 69, 72, 75, 82, 88, 92–94, 97, 99, 154, 155, 158, 160, 164, 165, 172, 173, 175, 190, 192, 216, 218, 221, 417, 521
- Pt nanoparticle(s), 59, 60, 63, 66, 69, 87, 88, 92–94, 100, 101, 106, 147, 149, 151, 153, 155, 159, 160, 166, 173, 179, 180, 189, 190, 211–213, 216, 218, 220, 221, 239, 350, 409–411, 414, 416–418, 433, 447
- Pt oxidation/Pt oxide/Pt oxide(s), 66, 68, 76–78, 81, 82, 106, 189, 421
- Pt reduction, 421
- PTFE, *see* Polytetrafluoroethylene
- PV(s), *see* Photovoltaic(s)
- PVDF, *see* Polyvinylidene fluoride
- Pyrolysis, 122, 124–126, 134, 135, 138, 502, 512
- Q**
- Q-HQ, *see* Quinone-hydroquinone
- Quaternary, 179, 306
- Quinone-hydroquinone, 68
- R**
- RA, *see* Risk Assessment
- Radical oxidative degeneration, 176
- Radio frequency, 88
- Raman, 59–63, 73, 101, 103, 106, 124, 428, 528, 530
- Random-defect model, 287, 288, 307
- Rd, *see* Reductant
- RDE, *see* Rotating disk electrode(s)
- Reactive oxygen species, 520, 524, 525, 528, 529, 532, 533, 536
- Red seed extract of *Hygrophilia auriculata* (RS), 530
- Redox couple, 151, 242
- Reduced graphene oxide(s), 207
- Reductant, 210
- Regulatory framework, 5
- Rehydrogenation, 252
- Relative humidity/humidities, 70, 81, 124, 136, 259, 265, 275–277, 279, 392, 491
- Renewable energy sources, 10, 14, 386, 388, 404
- Renewable(s)
- energies, 10, 14, 15, 386, 401, 513
- portfolio standards, 11
- RES, *see* Renewable energy sources
- Resistance/Resistivity, 19, 36, 37, 59, 60, 64, 88, 94, 97–99, 101–105, 118, 119, 133, 159, 160, 163, 173, 175, 190, 201, 203, 204, 207, 210, 215, 228–231, 233–237, 239–241, 243, 261, 272, 275–277, 278, 285, 291, 368, 419, 420, 422, 473, 481, 485, 491, 499, 506
- Retinal pigment epithelium, 524, 525, 527–529, 531–534, 536
- Reversible hydrogen electrode, 60, 63, 64, 66, 72, 88, 94, 147, 410, 418
- RF, *see* Radio frequency
- RGO(s), *see* Reduced graphene oxide(s)
- Rh, *see* Rhodium
- RH(s), *see* Relative Humidity/humidities
- RHE, *see* Reversible hydrogen electrode
- Rhodium, 122, 125–127, 129, 138, 140, 173, 242
- Riccati equation, 267, 268
- Rietveld refinements, 453
- Risk assessment, 532, 535, 536
- Risk characterization, 536
- Risk quotient, 536
- Room temperature, 40, 95, 122, 138, 148, 208, 210, 211, 278, 292, 304, 314, 316, 319, 326, 327, 444–446, 485, 530, 532
- ROS, *see* Reactive oxygen species
- Rotating disk electrode(s), 88, 92–95, 121–123, 127, 129, 131, 150, 161, 217, 429, 432, 433
- Rotating ring disk electrode, 151, 217, 414
- RPE, *see* Retinal pigment epithelium
- RRDE, *see* Rotating ring disk electrode; Rotating ring-disk electrode
- RS, *see* Red seed extract of *Hygrophilia auriculata* (RS)
- RT, *see* Room temperature
- Ru, *see* Ruthenium
- Ruthenium, 117, 119, 121, 122, 127, 140, 153, 158, 173, 210, 212, 239, 426, 450, 521 oxide, 153
- S**
- S, *see* Sulfur
- Samaria strontium cobaltite, 232, 234, 235
- Santa Barbara Amorphous Type Mesoporous Silica, 161

- SBA, *see* Santa Barbara Amorphous Type Mesoporous Silica
- Scanning electron microscope, 64, 65, 68, 95, 98, 105, 124, 135, 136, 204, 207, 208, 221, 238, 240, 428, 502, 510, 511, 524, 526
- Scanning transmission electron microscopy, 64, 240, 524
- Scientific Group Thermodata Europe, 293, 300
- Segregation kinetics, 290
- SEM, *see* Scanning electron microscope
- SGTE, *see* Scientific Group Thermodata Europe
- SHE, *see* Standard hydrogen reference electrode
- Single voltage source electrolysis, 31, 32, 37, 38
- Single-walled carbon nanotube(s), 446
- SMMO(s), *see* Strontium magnesium molybdenum oxide(s)
- Smoluchowski, 425
- SMSI(s), *see* Strong metal-support interaction(s)
- Sn, *see* Tin
- SnO, *see* Tin oxide
- SoC, *see* State of charge
- Sodium nitrite, 525, 529
- SOFC(s), *see* Solid oxide fuel cell(s)
- Solar, 8, 10–12, 14, 386, 401–404, 444, 519, 523
- Solid oxide fuel cell(s), 15, 227–243, 250, 281–330, 498, 501, 504, 506, 507, 509, 510, 512, 513
- Specific heats, 272–274
- Spinel, 118, 230, 319, 321, 527
- Square wave cycling, 64, 65
- SSC, *see* Samaria strontium cobaltite
- SSE, *see* Single voltage source electrolysis
- SSFF, *see* Stainless steel fiber felt
- Stack temperature, 270, 272, 391, 392
- Stack/fuel stack, 15, 17, 19, 117, 474
- Stainless steel fiber felt, 207, 208
- Standard hydrogen reference electrode, 347, 353, 409, 414, 418
- Start-up/Shutdown, 53–106
- State of charge, 366, 369, 370, 374, 376–380
- Steady state, 251, 266, 267, 279, 324, 409, 413, 425, 471, 512
- STEM, *see* Scanning transmission electron microscopy
- Stoichiometric coefficient/Stoichiometries/Stoichiometry, 242, 251, 270, 276, 277, 279, 290, 308, 330, 420, 431, 460
- Storage tank, 13, 362, 377, 445
- Strong metal-support interaction(s), 149, 151, 153–155, 158, 159
- Strontium magnesium molybdenum oxide(s), 239
- Strontium zirconate, 290, 312, 313, 330
- Strontium zirconia, 233
- SU/SD, *see* Start-up/Shutdown
- Sublattice, 293–298, 300, 301, 304, 305, 310
- Submonolayer, 161
- Sulfonated polybenzimidazoles, 17
- Sulfonated polyether ketones, 17
- Sulfur, 151, 228, 237, 239, 241, 345, 417, 418, 520, 521
- Sulfur oxide(s), 12
- Surface cohesive energy, 353
- Surface diffusion, 242
- Surface energy, 182, 292, 304, 326–328, 353, 411
- Surface segregation, 289
- Sweep mode, 64
- Sweep rate(s), 80, 128, 130
- SWNT(s), *see* Single-walled carbon nanotube(s)
- Symmetry, 60, 127
- SZO, *see* Strontium zirconate
- T**
- T/C, *see* Tetragonal/cubic
- TaC, *see* Tantalum carbide
- Tafel curve(s), 132
- Tafel kinetics, 422, 423, 426
- Tafel reaction, 133
- Tafel slope, 68, 70, 88, 132, 133, 151, 422
- Tantalum carbide, 220
- Tax credits/Tax credits and incentives/Taxation, 5, 6, 11, 12, 15, 20
- Technical University of Denmark (DTU), 447
- Teflon, 251
- TEM, *see* Transmission electron microscope
- Temperature-programmed reduction, 240
- Ternary, 117, 118, 174, 286, 306
- Tetragonal phase, 292, 305, 328
- Tetragonal/cubic, 292, 304, 326, 328
- Tetrametoxiphenyl porphyrins, 118
- Tetraphenyl porphine, 341
- TGA, *see* Thermogravimetric analysis
- Thermal conductivity, 18, 210, 261, 277, 278
- Thermal model, 270–273
- Thermodynamic equilibrium, 314, 316
- state, 34
- Thermodynamic model parameters, 306

- Thermogravimetric analysis, 125, 295  
Thermolysis/Thermolytic reaction, 121, 122,  
124, 125, 129, 134, 135, 138, 139, 218,  
451, 499, 505  
Threshold diagram, 319–321, 323  
Ti, *see* Titanium  
TiB, *see* Titanium boride(s)  
TiC, *see* Titanium carbide(s)  
TiN, *see* Titanium nitride(s)  
Tin, 521  
Tin oxide, 94, 155, 483  
Titanium, 238, 240, 390, 449, 480,  
483, 491  
Titanium boride(s), 87  
Titanium carbide(s), 87–90, 106, 157, 165  
Titanium nitride(s), 87–90, 98, 106, 153, 159,  
160, 165  
TMPP, *see* Tetrametoxiphenyl porphyrins  
Total energy, 10, 29, 33, 40, 41, 339, 386,  
396, 397, 403  
Total reflection X-ray fluorescence,  
289, 322  
Toxicology, 525, 536  
TPB, *see* Triple phase boundary  
TPP, *see* Tetraphenyl porphine  
TPR, *see* Temperature-programmed reduction  
Transition metals, 119–121, 127, 155,  
219, 232, 238, 241, 338, 416, 446,  
448, 453  
Transmission electron microscope (TEM), 60,  
65, 68, 71, 80, 83, 86, 88, 89, 91–93,  
95, 98, 100, 102, 155, 156, 188,  
211–213, 214, 425, 524  
Transport/Transport pathways/Transportation,  
8–10, 13, 44, 49, 50, 59, 81, 85,  
88, 102, 147, 172, 174, 182, 190,  
193, 200, 201, 205–208, 229, 230,  
251, 254, 257, 261–262, 264,  
275–279, 285, 360–362, 392, 416,  
421, 423, 425, 427, 428, 445, 470,  
471, 474, 481, 485, 499, 511, 512,  
514, 519, 532  
Triangular potential cycle, 57, 63  
Triangular wave cycling, 64, 65  
Trifluoro styrene, 17  
Triple phase boundary, 232, 234, 237, 242,  
290, 312–313, 322, 416, 498  
Tubular structure, 233, 483  
Tungsten, 151, 521, 525  
carbide, 157  
oxide, 151  
TXRF, *see* Total reflection X-ray  
fluorescence
- U**  
Ultrasonic spray pyrolysis, 157  
Ultraviolet, 13, 338  
Unitized reversible fuel cell(s), 387–393,  
395–399, 401, 402, 404  
Uranium, 3, 5  
URFC(s), *see* Unitized reversible fuel cell(s)  
USP, *see* Ultrasonic spray pyrolysis  
UV, *see* Ultraviolet
- V**  
V, *see* Vanadium  
Vacancy/Vacancies, 148, 210, 232, 238,  
242, 284, 287, 290–292, 296–298,  
301, 303, 309–311, 315, 316, 342, 354,  
417, 507  
Van Der Waals/Van Der Waals force, 446, 454  
Vanadium, 12  
Viability, 172, 191, 193, 434, 525, 532  
Volatile organics, 12, 13  
Volcano plots/Volcano-shaped, 178, 179,  
340, 348
- W**  
W, *see* Tungsten  
Water circulation, 389  
Water content, 81, 85, 201, 251, 257, 265,  
485, 491  
Water electrolysis, 29–31, 33, 45, 50, 386  
Water electrolyzer (EL), 29, 40, 41, 50, 387,  
389–391, 392, 395–404  
Water evaporation, 205, 206  
Water gas shift reaction(s), 151  
Water management, 201, 202, 251, 276,  
277, 491  
WC, *see* Tungsten carbide(s)  
WGSR, *see* Water gas shift reaction(s)  
Wind, 8, 10–12, 14, 15, 386, 401–404, 444
- X**  
X-ray absorption spectroscopy, 180, 220,  
428, 429  
X-ray diffraction, 71, 74, 90, 124, 135, 136,  
155, 193, 221, 453, 456, 457, 459,  
464, 527

- 
- X-ray photoelectron spectroscopy, 149, 151,  
155, 156, 159, 180, 193, 220, 290, 338,  
414, 432
- XAS, *see* X-ray absorption spectroscopy
- XPS, *see* X-ray photoelectron spectroscopy
- XRD, *see* X-ray diffraction
- Z**
- Zeolite template carbon, 447
- Zeolites, 445, 447, 448
- Zinc, 342, 447
- Zn, *see* Zinc
- ZTC, *see* Zeolite template carbon